

<b>REPORT DOCUMENTATION PAGE</b>				Form Approved OMB No. 0704-0188	
<small>Public reporting burden for this collection of information is estimated to average 1 hour per response, including the time for reviewing instructions, searching existing data sources, gathering and maintaining the data needed, and completing and reviewing the collection of information. Send comments regarding this burden estimate or any other aspect of this collection of information, including suggestions for reducing the burden, to Department of Defense, Washington Headquarters Services, Directorate for Information Operations and Reports (0704-0188), 1215 Jefferson Davis Highway, Suite 1204, Arlington, VA 22202-4302. Respondents should be aware that notwithstanding any other provision of law, no person shall be subject to any penalty for failing to comply with a collection of information if it does not display a currently valid OMB control number.</small> <b>PLEASE DO NOT RETURN YOUR FORM TO THE ABOVE ADDRESS.</b>					
<b>1. REPORT DATE (DD-MM-YYYY)</b> 16-03-2005		<b>2. REPORT TYPE</b> Conference Proceedings		<b>3. DATES COVERED (From – To)</b> 17 June 2002 - 21 June 2002	
<b>4. TITLE AND SUBTITLE</b>  Nanostructures: Physics and Technology 10th International Symposium				<b>5a. CONTRACT NUMBER</b> F61775-02-WF037	
				<b>5b. GRANT NUMBER</b>	
				<b>5c. PROGRAM ELEMENT NUMBER</b>	
<b>6. AUTHOR(S)</b>  Ioffe Institute				<b>5d. PROJECT NUMBER</b>	
				<b>5d. TASK NUMBER</b>	
				<b>5e. WORK UNIT NUMBER</b>	
<b>7. PERFORMING ORGANIZATION NAME(S) AND ADDRESS(ES)</b> Ioffe Institute 26 Polytechnicheskaya, Str. St. Petersburg 194021 Russia				<b>8. PERFORMING ORGANIZATION REPORT NUMBER</b>  N/A	
<b>9. SPONSORING/MONITORING AGENCY NAME(S) AND ADDRESS(ES)</b>  EOARD PSC 802 BOX 14 FPO 09499-0014				<b>10. SPONSOR/MONITOR'S ACRONYM(S)</b>	
				<b>11. SPONSOR/MONITOR'S REPORT NUMBER(S)</b> CSP 02-5037	
<b>12. DISTRIBUTION/AVAILABILITY STATEMENT</b>  Approved for public release; distribution is unlimited.					
<b>13. SUPPLEMENTARY NOTES</b> Copyright 2002 by Ioffe Institute and individual contributors. Available from: Ioffe Physico Technical Institute, 26 Politekhicheskaya, St Petersburg, 194021, Russia. The Department of Defense has permission to use for government purposes only. All other rights are reserved by the copyright holder.					
<b>14. ABSTRACT</b>  The Final Proceedings for 10th International Symposium 'Nanostructures: Physics and Technology', 17 June 2002 - 21 June 2002  Far-infrared and THz phenomena in nanostructures; Nanostructure characterization; Nanostructure technology; Optical and electrical phenomena in nanostructures; Opto- and electronic devices based on nanostructures; Physics of heterostructures with quantum wells and superlattices; Physics of heterostructures with quantum wires and quantum dots; Physics of silicon-based nanostructures; Quantum Computing; Self-organization phenomena in nanostructures; Single electron phenomena Wide gap materials					
<b>15. SUBJECT TERMS</b> EOARD, semiconductor devices, Nanotechnology					
<b>16. SECURITY CLASSIFICATION OF:</b>			<b>17. LIMITATION OF ABSTRACT</b> UL	<b>18. NUMBER OF PAGES</b> 649	<b>19a. NAME OF RESPONSIBLE PERSON</b> MATTHEW MORGAN, Lt Col, USAF
<b>a. REPORT</b> UNCLAS	<b>b. ABSTRACT</b> UNCLAS	<b>c. THIS PAGE</b> UNCLAS			<b>19b. TELEPHONE NUMBER</b> (Include area code) +44 (0)20 7514 4505

# **NANOSTRUCTURES: PHYSICS AND TECHNOLOGY**

10th International Symposium

St Petersburg, Russia, June 17–21, 2002

Co-Chairs

*Zh. Alferov*

*L. Esaki*

## **P R O C E E D I N G S**

Ioffe Institute  
St Petersburg, 2002

Published by  
Ioffe Physico-Technical Institute  
26 Politekhnikeskaya, St Petersburg 194021, Russia  
<http://www.ioffe.rssi.ru/>

Publishing license AP No 040971 of June 16, 1999.

Copyright © 2002 by Ioffe Institute and individual contributors. All rights reserved. No part of this publication may be multiple copied, stored in a retrieval system or transmitted in any form or by any means, electronic, mechanical, photocopying, recording or otherwise, without the written permission of the publisher. Single photocopies of single articles may be made for private study or research.

ISBN 5-93634-008-2

The International Symposium “Nanostructures: Physics and Technology” is held annually since 1993. The first Symposium was initiated by Prof. Zh. Alferov and Prof. L. Esaki who are its permanent co-chairs. More detailed information on the Symposium is presented on the World Wide Web <http://www.ioffe.rssi.ru/NANO2002/>

The Proceedings include extended abstracts of invited talks and contributed papers to be presented at the Symposium. By tradition this book is published before the beginning of the meeting.

The volume was composed at the Information Services and Publishing Department of the Ioffe Institute from electronic files submitted by the authors. When necessary these files were converted into the Symposium L<sup>A</sup>T<sub>E</sub>X 2<sub>ε</sub> style without any text revisions. Only minor technical corrections were made by the composers.

*Design and layout:* N. Vsesvetskii

*Desk editor:* L. Solovyova

Information Services and Publishing Department  
Ioffe Physico-Technical Institute  
26 Politekhnikeskaya, St Petersburg 194021, Russia  
Phones: (812) 247 2617, 247 9932  
Fax: (812) 247 1017  
E-mail: [vgrig@eo.ioffe.rssi.ru](mailto:vgrig@eo.ioffe.rssi.ru)

Printed in Russian Federation

The Symposium is held under the auspices of  
*the Russian Academy of Sciences*

### **Organizers**

*Scientific Engineering Center for  
Microelectronics at the Ioffe Institute  
Ioffe Physico-Technical Institute*

in association with

*Research Council for the Project  
“Physics of Solid State Nanostructures”  
at the Ministry of Industry, Science and Technologies of Russian Federation  
and*

the institutions of the Russian Academy of Sciences

*Division of General Physics and Astronomy  
St Petersburg Scientific Center*

### **Acknowledgments**

The Organizers gratefully acknowledge the following  
for their contribution to the success of the Symposium:

*Russian Academy of Sciences  
Ministry of Industry, Science and Technologies of Russian Federation  
Russian Foundation for Basic Research  
AIXTRON AG, Germany  
European Office of Aerospace Research and Development  
Air Force Office of Scientific Research  
United States Air Force Research Laboratory  
United States Office of Naval Research, Europe  
U.S. Army Research Laboratory European Research Office  
SPIE—The International Society for Optical Engineering*

### **Location and Date**

Symposium is held in St Petersburg, June 17–21, 2002  
and arranged as a river tour  
along a circular route (St Petersburg–Kizhi–Valaam–St Petersburg).



## Advisory Committee

Zh. Alferov ( <i>Russia</i> )	N. Holonyak Jr. ( <i>USA</i> )
Y. Arakawa ( <i>Japan</i> )	L. Keldysh ( <i>Russia</i> )
A. Aseev ( <i>Russia</i> )	G. Landwehr ( <i>Germany</i> )
D. Bimberg ( <i>Germany</i> )	J. Merz ( <i>USA</i> )
L. Esaki ( <i>Japan</i> )	M. Shur ( <i>USA</i> )
S. Gaponov ( <i>Russia</i> )	M. Skolnick ( <i>United Kingdom</i> )
E. Gornik ( <i>Austria</i> )	R. Suris ( <i>Russia</i> )
Yu. Gulyaev ( <i>Russia</i> )	B. Zakharchenya ( <i>Russia</i> )

## Programme Committee

R. Suris, Chair (*St Petersburg*)

V. Evtikhiev, Secretary (*St Petersburg*)

A. Andronov ( <i>Nizhny Novgorod</i> )	V. Kulakovskii ( <i>Chernogolovka</i> )
N. Bert ( <i>St Petersburg</i> )	M. Kupriyanov ( <i>Moscow</i> )
A. Chaplik ( <i>Novosibirsk</i> )	I. Merkulov ( <i>St Petersburg</i> )
V. Dneprovskii ( <i>Moscow</i> )	V. Panov ( <i>Moscow</i> )
B. Egorov ( <i>St Petersburg</i> )	E. Poltoratskii ( <i>Moscow</i> )
A. Gippius ( <i>Moscow</i> )	N. Sibel'din ( <i>Moscow</i> )
S. Gurevich ( <i>St Petersburg</i> )	V. Timofeev ( <i>Chernogolovka</i> )
Yu. Kopaev ( <i>Moscow</i> )	V. Volkov ( <i>Moscow</i> )
P. Kop'ev ( <i>St Petersburg</i> )	L. Vorobjev ( <i>St Petersburg</i> )
Z. Krasil'nik ( <i>Nizhny Novgorod</i> )	

## Organizing Committee

M. Mizerov, Chair (*Center for Microelectronics*)

B. Egorov, Secretary (*Ioffe Institute*)

D. Donskoy (*St Petersburg Scientific Center*)

V. Grigor'yants, (*Ioffe Institute*)

P. Kop'ev (*Ioffe Institute*)

G. Mikhailov (*Ioffe Institute*)

N. Sibel'din (*Lebedev Physical Institute*)

E. Solov'eva (*Ioffe Institute*)

V. Zayats (*Division of General Physics and Astronomy*)

## Award Committee

Zh. Alferov, Chair ( <i>Russia</i> )	M. Heuken ( <i>Germany</i> )
G. Abstreiter ( <i>Germany</i> )	K. von Klitzing ( <i>Germany</i> )
C. Chang-Hasnain ( <i>USA</i> )	M. Shur ( <i>USA</i> )
L. Eaves ( <i>United Kingdom</i> )	R. Suris ( <i>Russia</i> )
L. Esaki ( <i>Japan</i> )	V. Timofeev ( <i>Russia</i> )

# Contents

## Opening Plenary Session

OPS.01i	<i>K. von Klitzing</i> Physics and applications of Quantum Hall effect (QHE) . . . . .	1
OPS.02i	<i>G. Abstreiter</i> Control of charge and spin in novel semiconductor nanostructure devices . . . . .	2

## Nanostructure Technology

NT.01i	<i>P. Hoffmann</i> , I. Utke and F. Cicoira Limits of 3-D nanostructures fabricated by focused electron beam (FEB) induced deposition . . . . .	5
NT.03	M. Meixner, R. Kunert, <i>E. Schöll</i> , V. A. Shchukin and D. Bimberg Monte Carlo simulation of self-organized quantum dot structures: crossover from kinetics to thermodynamics . . . . .	12
NT.04	<i>R. Oga</i> , W. S. Lee, Y. Fujiwara and Y. Takeda Room-temperature electroluminescence at 1.55 $\mu\text{m}$ from InAs quantum dots grown on (001) InP by droplet hetero-epitaxy . . . . .	16
NT.05	<i>D. L. Huffaker</i> , S. Birudavolu and A. A. El-Emawy Structural and optical characteristics of MOCVD-grown quantum dots . . . . .	20
NT.06p	A. G. Banskchikov, N. F. Kartenko, A. K. Kaveev, M. M. Moisseeva and N. S. Sokolov Growth and structural characterization of $\text{ZnF}_2$ epitaxial layers on Si . . . . .	22
NT.07p	A. V. Bobyl, S. G. Konnikov, D. V. Shantsev, A. A. Sitnikova, R. A. Suris and V. P. Ulin Nanostructures in porous substrate for mismatched film technology and lateral growth model . . . . .	26
NT.08p	D. V. Brunev, A. N. Karpov, I. G. Neizvestny, <i>N. L. Shwartz</i> and Z. Sh. Yanovitskaya 2D $\rightarrow$ 3D growth mode transition through Stranski–Krastanov mode during epitaxial growth . . . . .	30
NT.09p	A. V. Chemakin, I. G. Neizvestny, <i>N. L. Shwartz</i> , Z. Sh. Yanovitskaja and A. V. Zverev Pore sealing during epitaxy and annealing on Si(001) surface . . . . .	34
NT.10p	<i>M. J. Fernée</i> , J. Warner, A. Watt and H. Rubunsztein-Dunlop Size/shape selective epitaxial overgrowth of nanocrystalline lead sulfide . . . . .	38
NT.11p	<i>V. M. Kozhev</i> , D. A. Yavsin, M. A. Zabelin, S. A. Gurevich, I. N. Yassievich, T. N. Rostovshchikova and V. V. Smirnov The impact of charge state on catalytic activity of metallic nanostructures . . . . .	41
NT.12p	<i>N. V. Kryzhanovskaya</i> , A. G. Gladyshev, D. S. Sizov, A. R. Kovsh, A. F. Tsatsul'nikov, J. Y. Chi, J. S. Wang, L. Wei and V. M. Ustinov The carriers localization influence on the optical properties of GaAsN/GaAs heterostructures grown by molecular-beam epitaxy . . . . .	45

NT.13p	<i>D. Litvinov, A. Rosenauer, D. Gerthsen, P. Kratzert, M. Rabe and F. Henneberger</i> Influence of ZnSe cap layer growth on the morphology and Cd distribution in CdSe/ZnSe quantum dot structures . . . . .	49
NT.14p	<i>A. I. Nikiforov, V. A. Cherepanov, and O. P. Pchelyakov</i> Variation of in-plane lattices constant of Ge islands during MBE growth on Si and SiO <sub>2</sub> surfaces . . . . .	53
NT.15p	<i>Yu. G. Sadofyev, Y. Cao, S. Chaparo, A. Ramamoorthy, B. Naser, J. P. Bird, S. R. Johnson and Y.-H. Zhang</i> High-mobility InAs/AlSb heterostructures for spintronics applications . . . . .	57
NT.16p	<i>D. S. Sizov, N. V. Kryzhanovskaya, A. G. Gladyshev, Yu. B. Samsonenko, G. E. Cirlin, N. K. Polyakov, V. A. Egorov, A. A. Tonkih, Yu. G. Musikhin, A. F. Tsatsul'nikov, N. N. Ledentsov and V. M. Ustinov</i> Investigation of the formation of InAs QD's in a AlGaAs matrix . . . . .	60
NT.17p	<i>N. S. Sokolov, S. M. Suturin and V. P. Ulin</i> Surface morphology evolution at early stages of CaF <sub>2</sub> (110) epitaxial growth on Si(001) . . . . .	64
NT.18p	<i>I. P. Soshnikov, B. V. Volovik, A. R. Kovsh, A. E. Zhukov, A. F. Tsatsul'nikov, O. M. Gorbenko, N. N. Ledentsov, V. M. Ustinov, P. Werner, N. D. Zakharov and D. Gerthsen</i> Formation specificity of InAs/GaAs submonolayer superlattice . . . . .	68

## Wide Band Gap Nanostructures

WBGN.01i	<i>B. Monemar, P. P. Paskov, H. Haratizadeh, G. Pozina, J. P. Bergman, S. Kamiyama, M. Iwaya, H. Amano and I. Akasaki</i> Optical properties of InGaN/GaN and AlGaN/GaN multiple quantum well structures . . . . .	72
WBGN.02	<i>N. Shapiro, H. Feick and E. R. Weber</i> Carrier recombination in InGaN nanostructures: carrier localization in quantum-dots, carrier separation by quantum-confined Stark effect . . . . .	77
WBGN.03	<i>V. Yu. Davydov, A. A. Klochikhin, V. V. Emtsev, A. V. Sakharov, S. V. Ivanov, V. A. Vekshin, F. Bechstedt, J. Furthmüller, J. Aderhold, J. Graul, A. V. Mudryi, H. Harima, A. Hashimoto, A. Yamamoto, J. Wu, H. Feick and E. E. Haller</i> Band gap of hexagonal InN and InGaN alloys . . . . .	78
WBGN.04	<i>H. Protzmann, G. Gerstenbrandt, A. Alam, O. Schoen, M. Luenenbuerger, Y. Dikme, H. Kalisch, R. H. Jansen and M. Heuken</i> Production scale MOVPE reactors for electronic and optoelectronic applications . . . . .	82
WBGN.05	<i>V. V. Strelchuk, M. Ya. Valakh, M. V. Vuychik, S. V. Ivanov, P. S. Kop'ev and T. V. Shubina</i> High-efficient up-conversion of photoluminescence in CdSe/ZnSe nanostructures . . . . .	85
WBGN.06p	<i>M. García-Rocha and I. Hernández-Calderón</i> Photoluminescence study of CdTe/ZnTe ultra-thin quantum wells grown by pulsed beam epitaxy . . . . .	89
WBGN.07p	<i>A. S. Gurevich, G. V. Astakhov, R. A. Suris, V. P. Kochereshko, D. R. Yakovlev, W. Ossau, S. A. Crooker and G. Karczewski</i> Filling-factor dependence of magneto-luminescence in II–VI QWs with 2DEG . . . . .	93
WBGN.08p	<i>D. K. Nelson, M. A. Jacobson, N. Grandjean, J. Massies, P. Bigenwald and A. Kavokin</i> Influence of high excitation on excitonic states in GaN/AlGaN quantum wells . . . . .	97

<b>WBG.N.09p</b>	<i>S. Shapoval, V. Gurtovoi, A. Kovalchuk, L. Eastman, A. Vertjachih, C. Gaquiere and D. Theron</i> Improvement of conductivity and breakdown characteristics of AlGaIn/GaN HEMT structures in passivation experiments . . . . .	101
------------------	---	-----

## Microcavity and Photonic Crystals

<b>MPC.01</b>	<i>A. L. Efros and A. L. Pokrovsky</i> Electrodynamics of left-handed materials . . . . .	105
<b>MPC.02</b>	<i>V. G. Golubev, A. V. Il'inskii, D. A. Kurdyukov, A. V. Medvedev, A. B. Pevtsov, A. V. Scherbakov, A. V. Sel'kin and E. B. Shadrin</i> The control of light by the phase transition in opal-VO <sub>2</sub> photonic crystals . . . .	108
<b>MPC.03</b>	<i>S. R. Kennedy, M. J. Brett, O. Toader and S. John</i> Fabrication of square spiral photonic crystals by glancing angle deposition . . .	112
<b>MPC.04</b>	<i>M. N. Makhonin, D. N. Krizhanovskii, A. N. Dremin, A. I. Tartakovskii, V. D. Kulakovskii, N. A. Gippius, M. S. Skolnick and J. S. Roberts</i> Influence of temperature and free carries on four-wave mixing in semiconductor microcavities . . . . .	116
<b>MPC.05p</b>	<i>A. V. Baryshev, A. A. Kaplyanskii, V. A. Kosobukin, M. F. Limonov, K. B. Samusev and D. E. Usvyat</i> Three-dimensional Bragg diffraction in growth-disordered opals . . . . .	120
<b>MPC.06p</b>	<i>D. Birkedal, V. G. Lyssenko and J. M. Hvam</i> Coherent inter-polariton scattering on moving gratings in microcavity with 25 nm GaAs/AlGaAs single quantum well . . . . .	124
<b>MPC.07p</b>	<i>L. I. Deych and A. A. Lisyansky</i> Local polariton modes in planar optical micro-cavities . . . . .	127
<b>MPC.08p</b>	<i>D. V. Gaikov, E. V. Kolobkova, A. A. Lipovskii, V. G. Melehin and V. G. Petrikov</i> Whispering gallery modes in glass microspheres made by simple technology . .	131
<b>MPC.09p</b>	<i>G. Gajiev, V. G. Golubev, D. A. Kurdyukov, A. B. Pevtsov and V. V. Travnikov</i> Three-dimensional GaN photonic crystals for visible spectral range . . . . .	134
<b>MPC.10p</b>	<i>S. G. Tikhodeev, A. L. Yablonskii, E. A. Muljarov and N. A. Gippius</i> Quasi-guided modes and optical response in 2D photonic crystal slabs . . . . .	138

## Nanostructure Characterization and Novel Atomic-scale Probing Techniques

<b>NC.01i</b>	<i>J. Schmidt</i> Optical and magnetic-resonance spectroscopy of single molecules . . . . .	140
<b>NC.02i</b>	<i>N. Miura, T. Ikaida, K. Uchida, T. Yasuhira, K. Ono, Y. H. Matsuda, G. Springholz, M. Pinczolits, G. Bauer, E. Kurtz, C. Klingshirn, Y. Shiraki and Y. Hirayama</i> Magneto-optical and cyclotron resonance study of semiconductor nanostructures in very high magnetic fields . . . . .	147
<b>NC.03</b>	<i>P. I. Arseev, N. S. Maslova, V. I. Panov and S. V. Savinov</i> Many-particle interaction in the tunnelling nanostructures and STM/STS measurements . . . . .	154
<b>NC.04</b>	<i>A. Ankudinov, A. Titkov, V. Evtikhiev, E. Kotelnikov, N. Bazhenov, G. Zegrya, H. Huhtinen and R. Laiho</i> Study of high power GaAs-based laser diodes operation and failure by cross-sectional electrostatic force microscopy . . . . .	157
<b>NC.05p</b>	<i>M. Chernyshova, V. V. Voloubeu, L. Kowalczyk, A. Yu. Sipatov and T. Story</i> Magnetic interactions in ferromagnetic EuS-PbS semiconductor multilayers . .	160

NC.06p	V. Yu. Davydov, A. N. Smirnov, I. N. Goncharuk, R. N. Kyutt, M. P. Scheglov, M. V. Baidakova, W. V. Lundin, E. E. Zavarin, M. B. Smirnov, S. V. Karpov and H. Harima Raman studies as a tool for characterization of the strained hexagonal GaN/Al <sub>x</sub> Ga <sub>1-x</sub> N superlattices . . . . .	164
NC.07p	Yu. S. Gordeev, V. M. Mikoushkin, V. V. Brysgalov, A. G. Zabrodskii, M. V. Alekseenko and H. Grimmeiss Plasma diagnostics of Ge-clusters in Si <sub>1-x</sub> Ge <sub>x</sub> mixed crystals . . . . .	168
NC.08p	Yu. E. Lozovik, S. P. Merkulova, M. M. Nazarov, A. P. Shkurinov and P. Masselin Time resolved nonlinear surface plasmon optics . . . . .	172
NC.09p	A. M. Mintairov, P. A. Blagnov, J. L. Merz, V. M. Ustinov, A. S. Vlasov, A. R. Kovsh, J. S. Wang, L. Wei and J. Y. Chi Quantum-dot-like composition fluctuations in near-field magneto-photo-luminescence spectra of InGaAsN alloys . . . . .	175
NC.10p	V. A. Volodin, D. A. Orehov, M. D. Efremov, V. A. Sachkov, B. A. Kolesov, N. D. Zakharov, V. A. Egorov, G. E. Cirlin and P. Werner Raman study of Ge quantum dots formed by submonolayer Ge coverages in Ge/Si superlattices . . . . .	179

## Silicon Based Nanostructures

SBNS.01	Yu. N. Drozdov, Z. F. Krasilnik, D. N. Lobanov, A. V. Novikov, M. Ya. Valakh, N. V. Vostokov, A. N. Yablonsky and V. A. Yukhymchuk Room-temperature photoluminescence of GeSi/Si(001) self-assembled islands in a 1.3–1.7 $\mu$ m wavelength range . . . . .	183
SBNS.02	S. D. Ganichev, U. Rössler, W. Prettl, E. L. Ivchenko, V. V. Bel'kov, R. Neumann, K. Brunner and G. Abstreiter Removal of spin degeneracy in SiGe based nanostructures . . . . .	187
SBNS.03	A. I. Yakimov, A. V. Dvurechenskii, V. V. Kirienko and A. I. Nikiforov Hole transport in Ge/Si quantum-dot field-effect transistors . . . . .	191
SBNS.04p	T. M. Burbaev, I. P. Kazakov, V. A. Kurbatov, M. M. Rzaev and V. I. Vdovin Growth and characterization of Si–Si <sub>1-x</sub> Ge <sub>x</sub> –GaAs heterostructure with InGaAs quantum dots . . . . .	195
SBNS.05p	I. P. Ipatova, O. V. Proshina and G. Benedek Surface polaritons at nanoporous carbon-silicon interface . . . . .	199
SBNS.06p	D. V. Kozlov, V. Ya. Aleshkin and V. I. Gavrilenko Shallow acceptors in Si/SiGe QW heterostructures . . . . .	203
SBNS.07p	D. I. Tetelbaum, V. A. Burdov, A. N. Mikhaylov and S. A. Trushin About the “phosphorus” sensitization of silicon quantum dots in SiO <sub>2</sub> photoluminescence . . . . .	206
SBNS.08p	M. V. Yakunin, G. A. Alshanskii, Yu. G. Arapov, V. N. Neverov and O. A. Kuznetsov Parallel magnetic field induced strong negative magnetoresistance in a wide p-Ge <sub>1-x</sub> Si <sub>x</sub> /Ge/p-Ge <sub>1-x</sub> Si <sub>x</sub> quantum well . . . . .	210

## Quantum Wells and Superlattices

QW/SL.01	Yu. E. Lozovik and I. V. Ovchinnikov New optical phenomena in Bose-condensed exciton system in quantum wells . .	214
QW/SL.02	G. Kocherscheidt, W. Langbein and R. Zimmermann Spectral speckle analysis: A new method to measure coherence and dephasing in semiconductor nanostructures . . . . .	217

QW/SL.03	<i>D. M. Gaponova, V. Ya. Aleshkin, V. I. Gavrilenko, D. V. Kozlov, V. N. Shastin, R. Kh. Zhukavin, B. N. Zvonkov, E. A. Uskova, J. N. Hovenier and A. F. G. van der Meer</i> Resonant states of carbon acceptor in p-InGaAs/GaAs $\delta$ -doped quantum well heterostructure . . . . .	221
QW/SL.04	<i>H. C. Lee, K. W. Sun and C. P. Lee</i> Structure effects on inter- and intra-band scattering of electrons in GaAs/Al <sub>x</sub> Ga <sub>1-x</sub> As and strained In <sub>x</sub> Ga <sub>1-x</sub> As/GaAs quantum wells . . . . .	225
QWSL.05p	<i>V. Ya. Aleshkin, D. M. Gaponova, D. G. Revin, L. E. Vorobjev, S. N. Danilov, V. Yu. Panevin, N. K. Fedosov, D. A. Firsov, V. A. Shalygin, A. D. Andreev, A. E. Zhukov, N. N. Ledentsov, V. M. Ustinov, G. E. Cirlin, V. A. Egorov, F. Fossard, F. Julien, E. Towe, D. Pal, S. R. Schmidt and A. Seilmeier</i> Light absorption and emission in InAs/GaAs quantum dots and stepped quantum wells . . . . .	229
QW/SL.06p	<i>V. Ya. Demikhovskii and D. V. Khomitsky</i> Optical and transport properties of p-type heterojunctions with lateral surface superlattice in perpendicular magnetic field . . . . .	233
QW/SL.07p	<i>M. V. Entin, L. I. Magarill and M. M. Mahmoodian</i> Friedel oscillations of the magnetic field penetration in systems with spatial quantization . . . . .	237
QW/SL.08p	<i>J. Erland, V. N. Grigoriev, K. L. Litvinenko, V. G. Lyssenko and J. M. Hvam</i> Phase relations and fringe contrast of coherent emission from single and multiple quantum wells at homogeneous and inhomogeneous broadening . . . . .	241
QW/SL.09p	<i>A.-K. Jappsen, A. Amann, A. Wacker, E. Schomburg and E. Schöll</i> Synchronization of dipole domains in GHz driven superlattices . . . . .	245
QW/SL.10p	<i>A. Yu. Silov, B. Aneeshkumar, M. R. Leys, N. S. Averkiev, P. C. M. Christianen and J. H. Wolter</i> Separate electron-hole confinement in composite InAs <sub>y</sub> P <sub>1-y</sub> /Ga <sub>x</sub> In <sub>1-x</sub> As quantum wells . . . . .	249
QW/SL.11p	<i>Z. N. Sokolova, D. I. Gurylev, N. A. Pikhtin and I. S. Tarasov</i> Auger recombination in strained InGaAsP quantum wells with $E_g = 0.7-1.6$ eV . . . . .	252
QW/SL.12p	<i>E. E. Vdovin, Yu. N. Khanin, Yu. V. Dubrovskii, L. Eaves, P. C. Main, M. Henini and G. Hill</i> Effective mass anisotropy of $\Gamma$ -electrons in GaAs/AlGaAs quantum well with InAs layer . . . . .	256

## Quantum Wires and Quantum Dots

QWR/QD.01i	<i>P. M. Petroff</i> Nanoscale self assembly and physics with semiconductors . . . . .	260
QWR/QD.02i	<i>E. L. Ivchenko</i> Electron-hole exchange interaction in nanostructures . . . . .	261
QWR/QD.03	<i>M.-E. Pistol, U. Håkanson, M. K.-J. Johansson, W. Seifert and L. Samuelson</i> Tunneling induced luminescence of individual InP quantum dots . . . . .	263
QWR/QD.04	<i>S. V. Goupalov, R. A. Suris, P. Lavallard and D. S. Citrin</i> On the zero phonon line homogeneous broadening in semiconductor QDs . . .	266
QWR/QD.05	<i>A. V. Chaplik</i> Aharonov-Bohm effect for few-particle and collective excitations (excitons, trions, plasmons) . . . . .	270

<b>QWR/QD.06</b>	<i>C. Kapteyn</i> , J. Ehehalt, R. Heitz, D. Bimberg, G. E. Cirlin, V. M. Ustinov and N. N. Ledentsov Optical memory concepts with self-organized quantum dots — material systems and energy-selective charging . . . . .	271
<b>QWR/QD.07</b>	<i>P. N. Brunkov</i> , A. Patanè, A. Levin, L. Eaves, P. C. Main, Yu. G. Musikhin, B. V. Volovik, A. E. Zhukov, V. M. Ustinov and S. G. Konnikov Escape of carriers photoexcited in self-organized InAs/GaAs quantum dots . . .	275
<b>QWR/QD.08</b>	<i>A. V. Baranov</i> , V. Davydov, A. Fedorov, H.-W. Ren, S. Sugou and Yasuaki Masumoto Heterostructure optical phonons in dynamics of quantum dot electronic excitations: new experimental evidences . . . . .	279
<b>QWR/QD.09p</b>	<i>B. H. Bairamov</i> , B. P. Zakharchenya, V. V. Toporov, V. A. Voitenko, F. B. Bairamov and M. Henini Inelastic inter-valence-band scattering of photoexcited holes in quantum dot structures . . . . .	283
<b>QWR/QD.10p</b>	<i>V. S. Dneprovskii</i> , O. A. Shaligina, E. A. Zhukov, V. P. Evtikhiev and V. P. Kochereshko Time-resolved luminescence of self-assembled CdSe/ZnSe quantum dots . . . .	287
<b>QWR/QD.11p</b>	<i>M. V. Entin</i> and M. M. Mahmoodian Distribution of persistent currents and magnetic field in quantum wire and disc . . . . .	290
<b>QWR/QD.12p</b>	<i>V. A. Gaisin</i> , A. Kh. Akopyan, B. S. Kulinkin, B. V. Novikov, V. N. Petrov, V. M. Ustinov and G. E. Cirlin The influence of temperature and hydrostatic pressure on luminescence spectra of InAs/GaAs quantum dots . . . . .	292
<b>QWR/QD.13p</b>	<i>I. Larkin</i> and A. Vagov Auger type relaxation of excitons in self assembled quantum dots via resonance scattering . . . . .	296
<b>QWR/QD.14p</b>	<i>V. A. Sablikov</i> and Ya. Gindikina Soft collective charge mode in a 1D electron system . . . . .	300
<b>QWR/QD.15p</b>	<i>A. A. Starikov</i> , I. I. Yakimenko, K.-F. Berggren, A. C. Graham, K. J. Thomas, M. Pepper and M. Y. Simmons Effects of accidental microconstriction on the quantized conductance in long wires . . . . .	303

## 2D Electron Gas

<b>2DEG.02</b>	E. E. Takhtamirov and V. A. Volkov Zero spin splitting of Landau levels in 2D electron systems: role of sign of Landé factor . . . . .	307
<b>2DEG.03</b>	<i>S. V. Dubonos</i> , K. S. Novoselov, A. K. Geim and J. C. Maan Quenching of the Hall effect in localised high magnetic field region . . . . .	311
<b>2DEG.04</b>	<i>N. S. Averkiev</i> and S. A. Tarasenko Quantum interference in magnetooscillation phenomena in two-dimensional electron gas . . . . .	315
<b>2DEG.05p</b>	<i>V. Yu. Kachorovskii</i> , I. S. Lyubinskiy and L. D. Tsendin Kinetic mechanism of current stratification in two-dimensional structures . . . .	319
<b>2DEG.06p</b>	<i>I. N. Kotel'nikov</i> , S. E. Dizhur and F. V. Shtrom Many-body lines in tunneling spectra of Al/ $\delta$ -GaAs junctions near resonant polaron threshold . . . . .	323

2DEG.07p	A. M. Martin, <i>L. Eaves</i> and K. A. Benedict The breakdown of the integer quantum Hall effect: a microscopic model with a hydronamical analogy . . . . .	327
2DEG.08p	<i>V. G. Popov</i> , Yu. V. Dubrovskii, E. E. Vdovin, Yu. N. Khanin, J.-C. Portal, D. K. Maude, T. G. Andersson and S. Wang Pinning of Landau levels in open two dimensional electron systems . . . . .	331

---

## Nanostructure Devices

---

ND.02	<i>Kazuhiko Matsumoto</i> Ultra-high coulomb energy in position controlled grown carbon nanotube . . . .	335
ND.03	<i>L. V. Litvin</i> , V. A. Kolosanov, D. G. Baksheev, V. A. Tkachenko, K. P. Mogilnikov, A. G. Cherkov and A. L. Aseev Ti/TiO <sub>x</sub> /Ti lateral tunnel junctions for single electron transistor . . . . .	339
ND.04p	A. Yu. Kasumov, R. Deblock, M. Kociak, B. Reulet, H. Bouchiat, S. Gueron, I. I. Khodos, Yu. B. Gorbatov, V. T. Volkov, V. I. Nikolaichik, <i>Yu. A. Kasumov</i> , C. Journet, P. Bernier, M. Burghard and D. V. Klinov Towards superconducting molecular nanoelectronics . . . . .	343
ND.05p	<i>E. B. Dogonkin</i> and G. G. Zegrya Current-induced cooling of nanostructures . . . . .	346
ND.06p	S. V. Dubonos, V. I. Kuznetsov and A. V. <i>Nikulov</i> Segment of an inhomogeneous mesoscopic loop as a dc power source . . . . .	350
ND.07p	I. Grekhov, <i>L. Delimova</i> , I. Liniichuk, D. Mashovets and I. Veselovsky Strongly modulated conduction in Ag/PLZT/LSCO ferroelectric field-effect transistor . . . . .	354
ND.08p	V. D. Kalganov, N. V. Mileshekina and <i>E. V. Ostroumova</i> The operating modes of the Auger-transistor and the photo-field detectors under strong electric field . . . . .	357
ND.09p	<i>M. E. Levinshstein</i> The origin of the $1/f$ noise in GaN-based HFETs: Is it tunneling? . . . . .	361
ND.10p	<i>M. P. Pires</i> , C. V.-B. Tribuzy, B. Yavich and P. L. Souza Optimization of InGaAs/InAlAs strained multiple quantum wells for amplitude modulators . . . . .	364
ND.11p	<i>D. B. Suyatin</i> , E. S. Soldatov, I. A. Maximov, L. Montelius, L. Samuelson, G. B. Khomutov, S. P. Gubin and A. N. Sergeev-Cherenkov Metal nanoelectrodes for molecular transistor and investigation of electron transport in molecular systems . . . . .	368
ND.12p	J. Unkelbach, A. Amann, <i>P. Rodin</i> and E. Schöll From bistability to spatio-temporal chaos in a resonant-tunneling diode . . . . .	371

---

## Lasers and Optoelectronic Devices

---

LOED.02i	<i>P. Borri</i> , W. Langbein, S. Schneider, U. Woggon, R. L. Sellin, D. Ouyang and D. Bimberg Temperature dependent homogeneous broadening and gain recovery dynamics in InGaAs quantum dots . . . . .	375
LOED.03	K. D. Moiseev, M. P. Mikhailova, <i>Yu. P. Yakovlev</i> and A. Krier Interface luminescence and lasing at a type II single broken-gap heterojunction . . . . .	381
LOED.04	<i>A. V. Platonov</i> , C. Lingk, J. Feldmann, M. Arzberger, M.-C. Amann and G. Abstreiter Ultrafast switch-off of an electrically pumped InAs/GaAs quantum dot laser . .	385



LOED.05	O. Drachenko, C. Becker, V. Rylkov, H. Page, D. Smirnov, <i>J. Leotin</i> and C. Sirtori Observation of phonon bottleneck in quantum box cascade lasers . . . . .	389
LOED.06	<i>P. G. Eliseev</i> , A. A. Ukhanov, A. Stintz and K. J. Malloy Gain and linewidth enhancement factor in InAs-quantum-dot and InAs-quantum-dash laser heterostructures . . . . .	392
LOED.07	<i>A. R. Kovsh</i> , A. E. Zhukov, N. A. Maleev, S. S. Mikhlin, A. V. Vasil'ev, Yu. M. Shernyakov, D. A. Livshits, M. V. Maximov, D. S. Sizov, N. V. Kryzhanovskaya, N. A. Pikhtin, V. A. Kapitonov, I. S. Tarasov, N. N. Ledentsov, V. M. Ustinov, J. S. Wang, L. Wei, G. Lin and J. Y. Chi High power lasers based on submonolayer InAs-GaAs quantum dots and InGaAs quantum wells . . . . .	395
LOED.08	<i>N. A. Maleev</i> , A. R. Kovsh, A. E. Zhukov, S. S. Mikhlin, A. P. Vasilev, E. S. Semenova, Yu. M. Shernyakov, E. V. Nikitina, N. V. Kryzhanovskaya, D. S. Sizov, I. P. Soshnikov, M. V. Maximov, N. N. Ledentsov, V. M. Ustinov, D. Bimberg and Zh. I. Alferov MBE growth of low-threshold long-wavelength QD lasers on GaAs substrates . . . . .	399
LOED.09p	Y. Boucher, A. G. Deryagin, V. I. Kuchinskii and <i>G. S. Sokolovskii</i> Near-threshold spectral and modal characteristics of a curved-grating quantum-well distributed-feedback laser (c-DFB) . . . . .	403
LOED.10p	V. P. Evtikhiev, E. Yu. Kotelnikov, D. V. Dorofeyev and <i>G. G. Zegrya</i> Non-linear power-current characteristics of quantum well lasers at high injection . . . . .	407
LOED.11p	<i>A. Khitun</i> and K. L. Wang Semiconductor quantum dot superlattice for coherent acoustic phonon emission . . . . .	410
LOED.12p	N. V. Fetisova, <i>N. A. Pikhtin</i> , E. G. Golikova, A. Yu. Leshko, A. V. Lyutetskiy, S. O. Slipchenko, Z. N. Sokolova and I. S. Tarasov 14XX nm pump lasers for Raman and $\text{Er}^{3+}$ doped fiber amplifiers . . . . .	414
LOED.13p	J. Puls, <i>G. V. Mikhailov</i> , F. Henneberger, D. R. Yakovlev and A. Waag Optical gain and lasing of trions in delta-doped ZnSe quantum wells . . . . .	418
LOED.14p	<i>I. S. Tarasov</i> , G. G. Zegrya, G. V. Skrynnikov, N. A. Pikhtin and S. O. Slipchenko SC DHS InGaAsP/InP lasers ( $\lambda = 1.5\text{--}1.6\ \mu\text{m}$ ) with above-threshold internal quantum efficiency $\eta_i^{\text{st}}$ about 100% . . . . .	421
LOED.15p	G. B. Venus, A. Gubenko, <i>E. L. Portnoi</i> , E. A. Avrutin, J. Frahm, J. Kubler and S. Schelhase The use of nanostructure-cluster-based ion-implantation-induced saturable absorbers in multisection high-power $1.5\text{-}\mu\text{m}$ picosecond laser diodes . . . . .	425
LOED.16p	D. A. Yanson, E. U. Rafailov, <i>G. S. Sokolovskii</i> , V. I. Kuchinskii, A. C. Bryce, J. H. Marsh and W. Sibbett Self-focused distributed Bragg reflector QW laser diodes . . . . .	429
LOED.17p	<i>I. N. Yassievich</i> , M. S. Bresler, O. B. Gusev and A. S. Moskalenko Er-doped $\text{SiO}_2$ with silicon nanocrystals as a new active optical medium . . . . .	433
LOED.18p	G. G. Zegrya, <i>I. A. Kostko</i> , N. A. Gunko and E. B. Dogonkin Influence of intraband relaxation processes on threshold and power-current characteristics of quantum well lasers . . . . .	437

## Infrared Phenomena in Nanostructures

IRP.01	T. N. Adam, R. T. Troeger, S. K. Ray, U. Lehmann and <i>J. Kolodzey</i> Terahertz emitting devices based on intersubband transitions in SiGe quantum wells . . . . .	441
IRP.02	<i>M. S. Kagan</i> , I. V. Altukhov, E. G. Chirkova, K. A. Korolev, V. P. Sinis, R. T. Troeger, S. K. Ray and J. Kolodzey Stimulated THz emission of acceptor-doped SiGe/Si quantum-well structures . .	445
IRP.03	<i>A. Andronov</i> , I. Nefedov and A. Sosnin Proposed Terahertz Bloch superlattice oscillator . . . . .	449
IRP.04p	<i>M. A. Odnoblyudov</i> , A. Blom, I. N. Yassievich and K.-A. Chao Impurity induced resonant states in modulation doped heterostructures . . . . .	453
IRP.05p	<i>A. A. Prokofiev</i> , M. A. Odnoblyudov, I. N. Yassievich and K.-A. Chao Resonant acceptor states in delta-doped SiGe nanostructures . . . . .	457

## Spin Related Phenomena in Nanostructures

SRPN.01i	<i>S. D. Ganichev</i> Circular photogalvanic effects induced by spin orientation in quantum wells . .	461
SRPN.02	O. Krebs, S. Cortez, A. Jbeli, X. Marie, J.-M. Gérard, T. Amand and <i>P. Voisin</i> Spin polarization dynamics in n-doped InAs/GaAs quantum dots . . . . .	463
SRPN.03	<i>I. A. Yugova</i> , I. V. Ignatiev, S. Yu. Verbin, I. Ya. Gerlovin, V. K. Kalevich, A. Yu. Shiryayev, K. V. Kavokin and Y. Masumoto Gateable spin memory in InP quantum dots . . . . .	465
SRPN.04	<i>S. A. Tarasenko</i> and E. L. Ivchenko Spin orientation of two-dimensional electron gas under intraband optical pumping . . . . .	469
SRPN.05p	K. Aulenbacher, J. Schuler, D. v. Harrach, E. Reichert, J. Röthgen, <i>A. Subashiev</i> , V. Tioukine and Y. Yashin The picosecond time scale spin-polarized electron kinetics in thin semiconductor layers . . . . .	473
SRPN.06p	<i>L. E. Golub</i> Spin splitting and interband photogalvanic effect in quantum wells . . . . .	477
SRPN.07p	<i>S. Yu. Verbin</i> , Yu. P. Efimov, V. V. Petrov, I. V. Ignatiev, Yu. K. Dolgikh, S. A. Eliseev, I. Ya. Gerlovin, V. V. Ovsyankin and Y. Masumoto Spin memory in the n-doped GaAs/AlGaAs quantum wells . . . . .	481

## Quantum Computing

QC.01i	<i>Guido Burkard</i> and Daniel Loss Spintronics and quantum information processing in nanostructures . . . . .	485
QC.02i	<i>G. L. Snider</i> , A. O. Orlov, R. K. Kumamuru, R. Ramasubramaniam, G. H. Bernstein, C. S. Lent, M. Lieberman and T. P. Felhner Experimental progress in quantum-dot cellular automata . . . . .	486
QC.03	<i>A. O. Orlov</i> , R. Kumamuru, R. Ramasubramaniam, C. S. Lent, G. H. Bernstein and G. L. Snider Clocked quantum-dot cellular automata devices . . . . .	491
QC.04	<i>A. M. Bychkov</i> and D. Bouwmeester Single-photon storage in a single quantum dot for the implementation of a solid-state quantum repeater . . . . .	495

QC.05p	<i>A. Khitun</i> , S. Hong and K. L. Wang Semiconductor tunneling structure with self-assembled quantum dots for multi-logic cellular automata module . . . . .	497
QC.06p	<i>A. Khitun</i> , R. Ostroumov and K. L. Wang Feasibility study of the spin wave quantum network . . . . .	501
QC.07p	<i>A. A. Kokin</i> and K. A. Valiev The proposed large-scale ensemble silicon-based NMR quantum computers . .	505

## Transport in Nanostructures

TN.01	<i>B. M. Ashkinadze</i> , E. Cohen and Arza Ron Dimensional magnetoplasma resonance in GaAs/AlGaAs heterostructures . . .	508
TN.02	<i>S. V. Zaitsev-Zotov</i> , Yu. A. Kumzerov, Yu. A. Firsov, and P. Monceau Magnetoresistance in long InSb nanowires . . . . .	512
TN.03	<i>V. A. Kulbachinskii</i> , R. A. Lunin, V. A. Rogozin, A. V. Golikov, V. G. Kytin, B. N. Zvonkov, S. M. Nekorkin, D. O. Filatov and A. de Visser Hopping conductivity and magnetic-field-induced quantum Hall-insulator transition in InAs/GaAs quantum dot layers . . . . .	516
TN.04p	<i>I. L. Drichko</i> , A. M. Diakonov, I. Yu. Smirnov, V. V. Preobrazhenskii, A. I. Toropov and Y. M. Galperin Persistent high-frequency hopping photoconductivity in GaAs/AlGaAs heterostructures in the quantum Hall regime . . . . .	520
TN.05p	A. Koeder, <i>W. Schoch</i> , S. Frank, R. Kling, M. Oettinger, V. Avrutin, W. Limmer, R. Sauer and A. Waag Ferromagnetic GaMnAs for spintronic devices . . . . .	524
TN.06p	<i>A. A. Farajian</i> , H. Mizuseki and Y. Kawazoe Spin-polarized transport through doped nanotube junctions in presence of applied magnetic field . . . . .	528
TN.07p	<i>A. N. Ionov</i> , V. A. Zakrevskii, V. M. Svetlichny and R. Rentzsch Super high conductivity effect in metal-polymer-metal structures . . . . .	531
TN.08p	<i>G. M. Mikhailov</i> , L. I. Aparshina, A. V. Chernykh, I. V. Malikov, V. Y. Vinnichenko, J. C. Maan, S. Olsthoorn, C. Possanzini and H. Jonge Ballistic effects in magnetoresistance of the planar point contact composed of single crystalline tungsten . . . . .	534
TN.09p	<i>G. M. Minkov</i> , A. V. Germanenko, O. E. Rut, A. A. Sherstobitov, B. N. Zvonkov, E. A. Uskova and A. A. Birukov The conductivity of disordered 2D systems: from weak to strong localization . .	538
TN.10p	<i>K. D. Moiseev</i> , V. A. Berezovets, M. P. Mikhailova, V. I. Nizhankovskii, R. V. Parfeniev and Yu. P. Yakovlev Magnetotransport of 2D-electrons and holes at a type II broken-gap single heterojunction doped with acceptor impurity . . . . .	542
TN.11p	M. P. Trushin, <i>V. A. Margulis</i> and A. V. Shorokhov Quantized acoustoelectric current in the ballistic channels . . . . .	546
TN.12p	<i>I. P. Zvyagin</i> Conduction in nanocomposites: hopping on a fractal . . . . .	550

## Tunnelling Phenomena

TP.01i	<i>L. Eaves</i> Tunnel spectroscopy of self-assembled quantum dots: wavefunction mapping and addressing the dots with electrostatic gates . . . . .	554
--------	---	-----

TP.02	D. Meinhold, V. G. Lyssenko, K. Leo and B. Rosam Polarization revival of a Bloch-oscillating wave packet at resonant Zener tunneling in GaAs shallow superlattice . . . . .	556
TP.03	Yu. V. Dubrovskii, P. C. Main, L. Eaves, V. A. Volkov, D. Yu. Ivanov, E. E. Vdovin, Yu. N. Khanin, V. G. Popov, D. K. Maude, J.-C. Portal, M. Henini and G. Hill Tunnel gaps in the two-dimensional electron system in a magnetic field . . . . .	559
TP.04	Yu. V. Dubrovskii, V. A. Volkov, D. K. Maude, J.-C. Portal, M. V. Chukalina, D. Yu. Ivanov, E. E. Vdovin, L. Eaves, P. C. Main, M. Henini and G. Hill Magnetotunnelling spectroscopy of the electron states in the quantum well with embedded self-assembled quantum dots: studies in magnetic fields up to 28 T . . . . .	563
TP.05p	A. V. Germanenko, G. M. Minkov, V. A. Larionova and O. E. Rut Resonant broadening of two-dimensional states in semiconductors with inverted band structure . . . . .	566
TP.06p	G. G. Kareva, M. I. Vexler, I. V. Grekhov and A. F. Shulekin Resonant tunneling metal-oxide-silicon nanostructure . . . . .	570
TP.07p	C. Möller, J. Böttcher and H. Künzel GaAs-based tunnel junctions . . . . .	574
TP.08p	E. V. Sukhorukov, G. Burkard and D. Loss Noise of a quantum-dot system in the cotunneling regime . . . . .	577
TP.09p	A. Vercik, M. J. S. P. Brasil, Y. G. Gobato and G. E. Marques Tunneling of photogenerated holes through Landau levels in GaAs/AlGaAs double barrier diodes . . . . .	581

## Excitons in Nanostructures

EN.01i	M. Bayer, G. Ortner, A. Larionov, A. Kress, A. Forchel, P. Hawrylak, K. Hinzer, M. Korkusinski, S. Fafard, Z. Wasilewski, T. L. Reinecke and Yu. Lyanda-Geller Entangled exciton states in quantum dot molecules . . . . .	584
EN.02	J. Puls, P. Kratzert, A. Hundt, M. Rabe and F. Henneberger Magneto-optical properties of self-assembled (Cd,Mn)Se quantum dots . . . . .	588
EN.03	D. R. Yakovlev, G. V. Astakhov, W. Ossau, Q. McCulloch, S. A. Crooker and A. B. Dzyubenko Singlet and triplet states of charged excitons in ZnSe-based QWs probed by high magnetic fields . . . . .	591
EN.04	V. P. Kochereshko, G. V. Astakhov, D. R. Yakovlev, W. Ossau, G. Landwehr, T. Wojtowicz, G. Karczewski and J. Kossut Combined exciton and trion excitations in modulation doped quantum well structures . . . . .	594
EN.05p	P. Díaz-Arencibia and I. Hernández-Calderón Modeling of the photoluminescence spectra of localize excitons in $\text{Zn}_{1-x}\text{Cd}_x\text{Se}$ quantum wells . . . . .	598
EN.06p	A. V. Koudinov, Yu. G. Kusrayev, B. P. Zakharchenya, D. Wolverson, J. J. Davies and J. Kossut Pauli blockade in spin-flip Raman scattering via donor bound excitons . . . . .	602
EN.07p	V. V. Ovsyankin, Yu. K. Dolgikh, B. V. Stroganov and V. S. Zapasskii, S. A. Eliseev, Yu. P. Efimov and V. V. Petrov Molecular states of 2D excitons in the GaAs-SQW-structures and the coherent transient spectroscopy of the phase-conjugate response . . . . .	606

EN.08p	A. Reznitsky, A. Klochikhin, S. Permogorov, I. Sedova, S. Sorokin, S. Ivanov, M. Schmidt, H. Kalt and C. Klingshirn Exciton states of nano-islands in ZnCdSe quantum wells . . . . .	610
EN.09p	T. V. Teperik and V. V. Popov Inhomogeneous luminescence of slow polaritons from near-surface two-dimensional excitonic system . . . . .	614

**Closing Plenary Session**

CPS.03i	M. S. Shur, S. L. Rumyantsev and R. Gaska Nanostructures on flexible substrates . . . . .	618
---------	--	-----

<b>Author Index</b> . . . . .	623
-------------------------------	-----

**Unprinted Papers**

The papers listed below are included in the Symposium Programme, but not printed in the Proceedings, as the authors had not submitted electronic files in due time.

NT.02i	P. Ajayan Building architectures with carbon nanotubes and exploring their applications	
2DEG.01i	I. V. Kukushkin Microwave spectroscopy of composite fermions	
ND.01i	J. H. Wolter Challenges in integration of opto-electronic quantum devices on InP	
LOED.01i	C. J. Chang-Hasnain A new look at quantum dot devices and their enabling applications	
CPS.01i	G. Pomrenke Title will be defined later	
CPS.02i	J. Feldmann Optical switching and sensing with individual nanoparticles	
TP.10p	L. P. Rokhinson, L. J. Guo, S. Y. Chou, D. C. Tsui, E. Eisenberg, R. Berkovits and B. L. Altshuler Coherent electron transport in a Si quantum dot dimer	

## AIXTRON Young Scientist Award

In 1999, the Symposium Programme Committee and the Board of AIXTRON AG (Germany) established a special award to honour a young scientist who will present at the Symposium the best paper in the field of solid state nanostructures. The award comprises a diploma and a \$500 reward sponsored by AIXTRON.

The AIXTRON Young Scientist Award recipients are:

- 1999 **Alexey R. Kovsh**, Ioffe Institute, St Petersburg, Russia  
 2000 **Thomas Gruber**, Physikalisches Institut, Universität Würzburg, Würzburg, Germany  
 2001 **Ivan Shorubalko**, Department of Solid State Physics, Lund University, Lund, Sweden.

### Mr. Ivan Shorubalko

became the recipient of AIXTRON Award for the presentation of the paper:

### Room-temperature operation of GaInAs/InP based ballistic rectifiers at frequencies up to 50 GHz

Co-authors: *P. Omling, L. Samuelson, W. Seifert, A. M. Song and H. Zirath.*

**Education:** 1992 finished Gulbene secondary school, Latvia. 1992–1995 University of Latvia, Faculty of Physics and Mathematics. 1995–1996 The Netherlands, University of Groningen, Faculty of Mathematics and Physics. 1996–1997 University of Latvia, Faculty of Physics and Mathematics. Bachelor's degree in physics. 1997 Master study in solid state physics at University of Latvia, Faculty of Physics and Mathematics. 1998 Sweden, Lund University, dept. of Solid State Physics. Masters degree in physics. 1999 Sweden, Lund University, dept. of Solid State Physics, PhD student.



**Experience:** Since 1998 Post-graduate study in the group of electron transport physics, dept. of Solid State Physics, Lund University, Sweden. 1998 Master thesis work, dept. of Solid State Physics, Lund University, Sweden. Title: “Fabrication and electron transport properties of GaInAs/InP based quantum wires”. Prof. Per Omling was a supervisor for this work. 1996–1997 Laboratory assistant, Institute of Solid State Physics, Physics and Mathematics department, University of Latvia. 1996 Project work in the group of Physics of Thin Layers, Faculty of Mathematics and Physics, University of Groningen, The Netherlands. Prof. T. M. Klapwijk was a supervisor of this work. The work was used for bachelor theses. 1994–1995 Laboratory assistant, Institute of Solid State Physics, Physics and Mathematics department, University of Latvia.

**Current Research:** Fabrication and electron transport properties of GaInAs/InP based, novel, ballistic nanodevices. Currently nonlinear electron transport behavior of the so called ballistic rectifiers and three terminal ballistic junctions (T-branches) has been investigated. The working principles of these devices are completely different from the conventional devices used in today's electronics, which gives functionality of these novel devices at very high frequencies. Small size (nanoscale) of these devices makes it possible to observe ballistic phenomena up to room temperature. Therefore, these novel ballistic nanodevices are very promising candidates for the building blocks of the future electronic circuits.

**Experimental work:** Optical and electron beam lithography, wet chemical etching, inspections in scanning electron microscope and atomic force microscope, electrical measurements.



## Physics and applications of Quantum Hall effect (QHE)

*K. von Klitzing*

Max-Planck-Institut für Festkörperforschung, D-70569 Stuttgart, Germany

The QHE is today a synonym for different kind of phenomena related to electrons in strong magnetic fields with connections not only to different topics in solid state physics (superconductivity, magnetism, metal-insulator transition, quantum computation etc) but also to other research areas like astrophysics (edge states in gravity and black hole physics), high energy physics (quantum Hall quarks), and metrology (fundamental constants), which explains the popularity of QHE research with about one publication per day.

For practical applications, the accuracy of the quantized Hall resistance and his connection to the fundamental constant  $h/e^2$  is used for the high precision determination of the fine-structure constant, the realization of a resistance and capacitance standard and more recently (together with the Josephson effect) for an accurate determination of Planck's constant and alternatively for a new realization of the kilogram, the unit of mass.

Most of the recent activities in the field of QHE research focus on interaction phenomena in two-dimensional electron gases with very high mobility. The electron-electron interaction, which leads to the fractional quantum Hall effect (FQHE), is nicely covered by the composite fermion (CF) picture where strongly interacting electrons in a magnetic field  $B_{CF}$  (corresponding to an even number of flux quanta per electron) are replaced by composite fermions which do not feel the external magnetic field. Many experiments including recent focusing experiments of composite fermions (unpublished measurements of Jörn Göres) show the similarity between electrons at zero magnetic field and transport phenomena at the magnetic field  $B_{CF}$  so that the FQHE can easily be discussed as an integer QHE in an effective magnetic field  $|B - B_{CF}|$ . Since the effective mass and therefore the cyclotron energy of composite fermions changes approximately with the square root of the magnetic field  $B$  (see contribution of Igor Kukuchkin at this conference) contrary to the Zeeman energy with a linear increase, level crossings are expected as a function of  $B$  and interesting interaction phenomena are predicted if the two different spin orientations are degenerate and each of the two levels is half filled. Recent experiments by Jurgen Smet [1, 2] demonstrate, that the magnetoresistance at this transition point for the spin orientation shows properties of an Ising ferromagnet and is strongly modified by the nuclear spin polarization. The influence of the hyperfine interaction on the electronic properties is discussed in detail.

## References

- [1] J. H. Smet, R. A. Deutschmann, W. Wegscheider, G. Abstreiter and K. von Klitzing, *Phys. Rev. Lett.* **86**, 2412 (2001)
- [2] J. H. Smet, R. A. Deutschmann, F. Ertl, W. Wegscheider, G. Abstreiter and K. von Klitzing, *Nature* **415**, 281 (2002)



## Control of charge and spin in novel semiconductor nanostructure devices

*Gerhard Abstreiter*

Walter Schottky Institut, Techn. Univ. Munich, D-85748 Garching

Semiconductor nanostructures have attracted a lot of interest recently due to their possible applications in optoelectronics, nanoelectronics, quantum information processing and chemical/biological sensing. There are many different experimental approaches to realize well controllable nanostructure devices. In the past few years we have concentrated our efforts on the fabrication of such devices based on two methods, cleaved edge overgrowth and self-assembly of quantum dots.

Cleaved edge overgrowth allows the realization of atomically precise potential landscapes for electrons or excitons in GaAs based heterostructures. This allowed for example the study of electron transport in nearly perfect quantum wires [1–3] and the luminescence of coupled quantum dots with well defined coupling strength [4, 5]. Very recently we were able to fabricate a new type of superlattice transistor which allows the controlled variation of the Fermi level in minibands in atomically precise superlattices resulting for example in strong evidence for electrically driven Bloch oscillations and quantum interference in artificial bandstructures [6, 7]. In such transistors, whose design is shown schematically in Fig. 1, the density driven quantum phase transition between unpolarized and fully spin polarized fractional quantum Hall states could be studied in detail [8, 9]. It was also demonstrated that the hyperfine interaction with nuclear spins of the host semiconductor is important for the observed hysteresis in the two-dimensional ferromagnetic domain formation. Subsequently this interaction was used to demonstrate the gate-voltage control of spin interactions between electrons and nuclei, a first direct electrical control and measurement of the spin degree of freedom in a field effect transistor which may be a step towards an all-solid-state-electronics approach for quantum information processing [10].

Another very interesting development in the area of semiconductor nanostructures is the control of charge and spin population of self-assembled quantum dots. Here often spectroscopy is used to control and measure the quantum dot electronic states. Conventional optical spectra, probing many dots at the same time, are broadened inhomogeneous due to variations in size, shape, and composition. Sharp spectral lines in absorption and emission, which are important for most of the novel applications mentioned above, are only observed

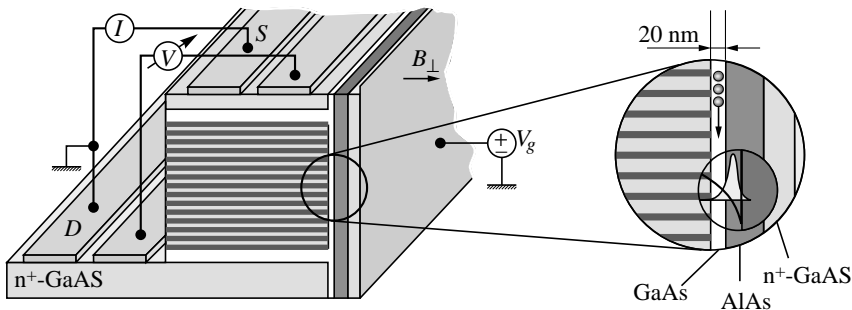


**Fig. 1.** Schematics of the superlattice field effect transistor fabricated by the cleaved edge overgrowth method.

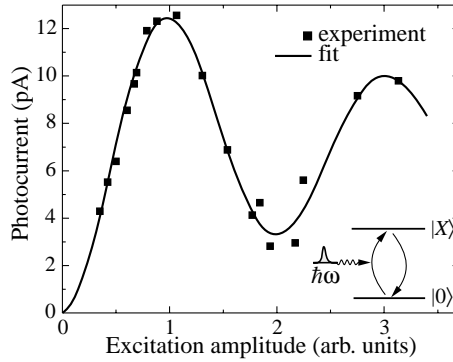


**Fig. 2.** Rabi oscillations in the photocurrent of a single dot photodiode.

when individual quantum dots are studied. The work on single dot spectroscopy started nearly a decade ago [11–17]. In the past 5 years several hundred papers appeared in the literature, reporting on various aspects of single dot spectroscopy demonstrating the vastly growing interest in this field of research [18]. Spectroscopy with high spatial resolution concomitant with separation of dots in space or in transition energy has been used to study the population of single or coupled dots populated with one or a few electron-hole pairs. Photoluminescence (PL) and photoluminescence excitation spectroscopy (PLE) with and without applied magnetic field allows the identification of ground-state and excited electronic levels as well as phonon-assisted processes. The formation of biexcitons (2 electrons and 2 holes in the dot) and filling of higher states is observed in PL with increasing excitation power [12, 19] and via a resonant 2-photon absorption process [12]. In special electrically tunable semiconductor structures it is also possible to study charged excitons and to obtain a well defined controllable population of the dots [20, 21, 22]. In magnetic fields characteristic features with respect to the spin population and spin dynamics are observed, which may be also of interest to future quantum information processing. The sequential decay of excitons in a single quantum dot can be used for example as triggered single photon source [23–26]. Very recently also coherent effects of excitons and biexcitons in individual quantum dots have been observed in time-resolved spectroscopy manifesting itself for example in Rabi oscillations [27, 28]. Under resonance excitation also spectrally sharp and tunable photocurrent is obtained in reverse biased single dot photodiodes [29, 30]. Such photodiodes are first single dot optoelectronic devices which resemble a quantum mechanical two-level system with electric contacts. Very recently Rabi oscillations in the photocurrent has been demonstrated using such single dot photodiodes [31, 32]. The deterministic oscillating photocurrent with increasing amplitude of the exciting laser pulse is shown in Fig. 2.

This overview of recent achievements with semiconductor nanostructures based on cleaved edge overgrowth and self-assembled quantum dots is based on the work of various PhD-students at the Walter Schottky Institut under the supervision of Artur Zrenner and Werner Wegscheider whose important and valuable contributions can be seen from the references. We also profited from the many collaborations with other groups which are partially included in the list of references as well.

#### *Acknowledgments*

The work was supported financially by DFG via SFB 348 and by BMBF via Verbundprojekt III–V-Quantenstrukturen.

## References

- [1] A. Yacoby *et al*, *Phys. Rev. Lett.* **77**, 4612 (1996).
- [2] O. M. Auslaender *et al*, *Phys. Rev. Lett.* **84**, 1764 (2000).
- [3] M. Rother *et al*, *Physica E* bf6, 551 (2000), see also M. Rother, thesis TU Munich (2000), ISBN 3-932749-33-2.
- [4] W. Wegscheider *et al*, *Phys. Rev. Lett.* **79**, 1917 (1997).
- [5] G. Schedelbeck *et al*, *Science* **278**, 1677 (1997).
- [6] R. A. Deutschmann *et al*, *Appl. Phys. Lett.* **79**, 1564 (2001), see also R. A. Deutschmann, thesis TU Munich (2001), ISBN 3-932749-42-1
- [7] R. A. Deutschmann, W. Wegscheider, M. Rother, M. Bichler, G. Abstreiter, C. Albrecht and J. H. Smet, *Phys. Rev. Lett.* **86**, 1857 (2001).
- [8] J. H. Smet, R. A. Deutschmann, W. Wegscheider, G. Abstreiter and K. von Klitzing, *Phys. Rev. Lett.* **86**, 2412 (2001).
- [9] see also: J. Eom *et al*, *Science* **289**, 2320 (2000).
- [10] J. H. Smet, R. A. Deutschmann, F. Ertl, W. Wegscheider, G. Abstreiter and K. von Klitzing, *Nature* **415**, 281 (2002).
- [11] K. Brunner, U. Bockelmann, G. Abstreiter, M. Walther, G. Böhm, G. Tränkle and G. Weimann, *Phys. Rev. Lett.* **69**, 3216 (1992).
- [12] K. Brunner, G. Abstreiter *et al*, *Appl. Phys. Lett.* **64**, 3320 (1994) and *Phys. Rev. Lett.* **73**, 1183 (1994).
- [13] A. Zrenner, L. V. Butov, M. Hagn, G. Abstreiter, G. Böhm and G. Weimann, *Phys. Rev. Lett.* **72**, 3382 (1994).
- [14] H. F. Hess, E. Betzig, T. D. Harris, L. N. Pfeiffer and K. West, *Science* **264**, 1740 (1994).
- [15] J.-Y. Marzin, J.-M. Gerard, A. Izrael, D. Barrier and G. Bastard, *Phys. Rev. Lett.* **73**, 716 (1994).
- [16] M. Grundmann *et al*, *Phys. Rev. Lett.* **74**, 4043 (1995).
- [17] D. Gammon *et al*, *Phys. Rev. Lett.* **76**, 3005 (1996) and *Science* **273**, 87 (1996).
- [18] for a recent overview see: Proc. of the International Conference on Semiconductor Quantum Dots (physica status solidi, vol. 224, nrs. 1-3, 2001), eds.: U. Woggon and A. Zrenner.
- [19] F. Findeis *et al*, *Solid State Comm.* **114**, 227 (2000), see also F. Findeis, thesis TU Munich (2001), ISBN 3-932749-34-0.
- [20] R. J. Warburton *et al*, *Nature* **405**, 926 (2000).
- [21] F. Findeis, M. Baier, A. Zrenner, M. Bichler, G. Abstreiter, U. Hohenester and E. Molinari, *Phys. Rev.* **B63**, 121309R (2001).
- [22] M. Baier, F. Findeis, A. Zrenner, M. Bichler and G. Abstreiter, *Phys. Rev.* **B64**, 195326 (2001).
- [23] C. Santori *et al*, *Phys. Rev. Lett.* **86**, 1502 (2001).
- [24] P. Michler *et al*, *Science* **290**, 2282 (2000).
- [25] Z. Yuan *et al*, *Science* **295**, 102 (2002).
- [26] E. Moreau *et al*, *Phys. Rev. Lett.* **87**, 183601 (2001).
- [27] T. H. Stievater *et al*, *Phys. Rev. Lett.* **87**, 133603 (2001).
- [28] Gang Chen *et al*, *Phys. Rev. Lett.* **88**, 117901 (2002).
- [29] F. Findeis, M. Baier, E. Beham, A. Zrenner and G. Abstreiter, *Appl. Phys. Lett.* **78**, 2958 (2001).
- [30] E. Beham, A. Zrenner, F. Findeis, M. Bichler and G. Abstreiter, *Appl. Phys. Lett.* **79**, 2808 (2001).
- [31] E. Beham, A. Zrenner, S. Stufler, F. Findeis, M. Bichler and G. Abstreiter, *Proc. of the 12th Int. Winterschool*, Mauterndorf Austria (2002) (preprint).
- [32] A. Zrenner, E. Beham, S. Stufler, F. Findeis, M. Bichler and G. Abstreiter, submitted to *Science*.

## Limits of 3-D nanostructures fabricated by focused electron beam (FEB) induced deposition

*P. Hoffmann, I. Utke and F. Cicoira*

Institute of Imaging and Applied Optics, School of Engineering (STI),  
Ecole Polytechnique Fédérale de Lausanne, CH-1015 Lausanne-EPFL, Switzerland

**Abstract.** The focused electron beam of an electron microscope (SEM or TEM) decomposes tailored precursor molecules on substrates into functional deposits. Extremely high aspect ratios of more than 10 can easily be obtained. During the last years several materials could be deposited, most of them composed of metal nanoparticles embedded in amorphous matrices. The deposition process depends on the precursor supply, its surface adsorption behavior, and the beam induced chemical decomposition path of the molecule on one hand, and on the other hand on the electron beam properties like beam current, electron energy, and beam distribution. The limits in minimal size, growth rate, and chemical composition arise from all mentioned parameters, which are interdependent.

### Introduction

Since the first “contamination” carbon deposits with a broad [1] and a focused [2] electron beam, several attempts were made to improve the focused electron beam (FEB) induced deposition process with respect to high resolution and deposit purity. Pioneers in the field of metal containing deposits are Matsui and Mori [3] and Koops and coworkers [4, 5]. The physical understanding of FEB deposition was strongly improved by models of Christy [6], Scheuer and Koops [5] and Reimer [7], describing the process as decomposition of surface adsorbed molecules by secondary electrons (SE). One can divide the limiting factors of the process into physical, physico-chemical, and chemical contributions. As physical factors we consider the primary electron beam distribution as well as the resulting secondary electron distribution. They are predominantly responsible for the minimal structure size of the deposits. Physico-chemical parameters are transport phenomena like effusion of molecules, surface diffusion rate, residence time, desorption rate, and adsorption enthalpy. They determine mainly the processing speed, i. e. the maximum deposition rate. The chemical contributions taking place like electron beam induced ionization and fragmentation, thermal decomposition reactions and surface catalyzed decomposition are less known compared to the above mentioned physical and physico-chemical parameters, but are responsible for the chemical composition, i. e. purity, and thus for deposit functionality. During the last years we tried to extend the understanding of FEB induced deposition using novel carbon free precursors like  $\text{AuClPF}_3$  and  $\text{Rh}_2\text{Cl}_2(\text{PF}_3)_4$ . Our system comprises a SEM (Cambridge S 100) with a thermionic tungsten filament as electron emitter and an oil free pumping system, allowing to study deposition in an electron energy range of 2–25 keV and with beam currents of several nA down to 5 pA.

### 1. Physical properties — Size limits — Electron probe size — Secondary Effects

Generally, FEB deposition electron microscopes have electron energies ranging from several hundreds of eV up to several hundreds of keV. The focused electron beam diameter and

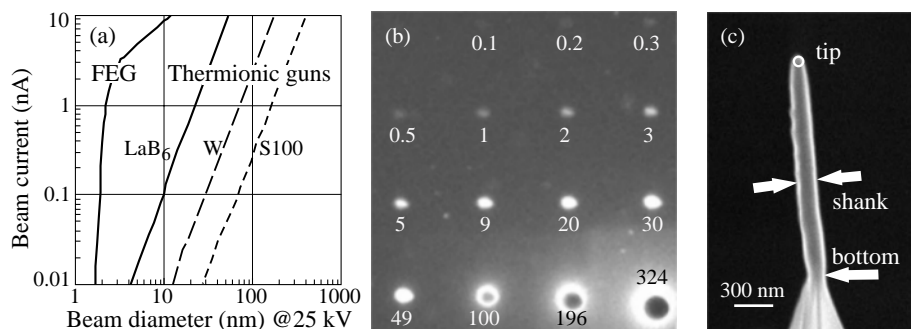


**Fig. 1.** (a) Electron beam diameter ( $1/e^2$ ) versus electron beam current for different electron gun emitters at 20–25 kV (FEG: field emission gun,  $\text{LaB}_6$ : lanthanum hexaboride, W: tungsten) taken from [Reimer, 1998 #2848]. In comparison our W-emitter SEM Cambridge S100, one of the first commercially available SEMs, shows the largest beam diameter. (b) Short time deposits (0.1–324 s) at 25 pA and 25 kV of  $\text{Rh}_2\text{Cl}_2(\text{PF}_3)_4$  on thin carbon film. Horizontal dot distance is 1  $\mu\text{m}$ . (c) Magnetic supertip from Co-carbonyl on top of pyramidal Si tip at 100 pA and 25 kV. Note the different diameters.

its electron distribution are described by a gaussian shaped beam increasing its diameter with increasing current according to Fig. 1(a). Depending on emitter and electron optics one obtains a distribution of electrons down to several nanometers spot size. It is straightforward that the electron beam distribution will be one important limiting factor for the smallest lateral dimensions that can be obtained. However, electron microscope resolution does not correspond 1:1 to the electron beam diameter because contrast filters allow for additional confinement of the obtained secondary or transmitted electron images. Alternatively, the knife-edge method for beam distribution measurements is complicated due to effects of partial primary electron transmission and increased edge emission of secondary electrons.

We applied short time exposures for deposition of Rhodium containing nano-composite on thin carbon films, see Fig. 1(b). With decreasing time the deposit diameter saturates at a value corresponding to the knife-edge measured beam diameter. The deposit thickness profile was measured ex-situ by TEM and shows a gaussian shape at the outer deposit region. The central part of the deposits is flat since deposition is precursor flux limited, as will be discussed in the next chapter. The advantage of deposition on thin carbon films is that it avoids generation of backscattered electrons and electromagnetic radiation (X-rays) due to the low excitation volume. If plane bulk substrates are used backscattered electrons result in thin “halo” deposits around the principal deposit [8]. On non-planar substrates as shown in Fig. 1(c) the bottom, shank, and apex diameter of tip deposits can be distinguished. The tip apex diameter corresponds to the measured beam diameter (at  $1/e^2$ ) whereas the cylindrical shank diameter is about 2 times larger due to increased beam broadening with increasing penetration depth of electrons. Monte Carlo simulations show that  $> 80\%$  of impinging electrons exit the cylindrical deposit wall and induce additional radial growth. This effect can be avoided by depositing free-standing horizontal rods by scanning the electron beam laterally. Optimized lateral scan speeds result in deposit diameters corresponding to the beam size. However, the ultimate physical limit should be given by the escape thickness of secondary electrons in the deposit the value of which varies between 5–10 nm (for Al: 5 nm [9]). The smallest ever published freestanding rods have a diameter of 15 nm and were produced in a TEM at 200 keV [10] using a tungsten precursor. Dots of Pt containing

carbonaceous material with 20 nm diameter were recently obtained [11]. We can conclude that for a given beam diameter the minimum deposit dimensions depend on its geometry. For dot deposits resolution depends on aspect ratio (time), for vertical deposits on electron scattering (beam broadening) and for horizontal free standing rods on scan speed.

## 2. Physico-chemical limits — Growth rates — Mass transport versus electron current

For all serial processes speed is of paramount importance. FEB deposition rates up to 150 nm/s are reported in literature [12]. As a localized Chemical Vapor Deposition (CVD) process FEB deposition underlies the same rules as all CVD processes; the growth rate can either be limited by the mass transport or by the chemical reaction rate. The adsorption rate  $dn/dt$  of precursor molecules can be expressed as

$$\frac{dn}{dt} = sJ \left(1 - \frac{n}{n_0}\right) - \frac{n_0}{\tau} - \sigma n f + D \nabla^2 n \quad (1)$$

with  $s$  the sticking coefficient,  $J$  the precursor flux,  $n_0$  the monolayer density,  $\tau$  the mean dwell time,  $\sigma$  the interaction cross section,  $D$  the diffusion coefficient and  $f$  the electron flux. The first term describes molecule adsorption as dependence of monolayer coverage, the second term desorption, the third term decomposition by electrons and the forth term diffusion (see also Fig. 2(a)). Solving Eq. (1) for equilibrium conditions results in constant growth rates. If diffusion is neglected the steady state growth rate  $R$  is given by [5]:

$$R = v s J \left(1 + \frac{n_0 + s \tau J}{n_0 \tau \sigma f}\right)^{-1} \quad (2)$$

with  $v$  the volume of the (decomposed) molecule. It should be noted that experimentally observed deposition rates for tip deposits decrease with time.

### 2.1. Precursor effusion

An oriented tube from which the precursor effuses onto the substrate has the advantage that byproducts are more efficiently pumped away from the reaction zone. The precursor

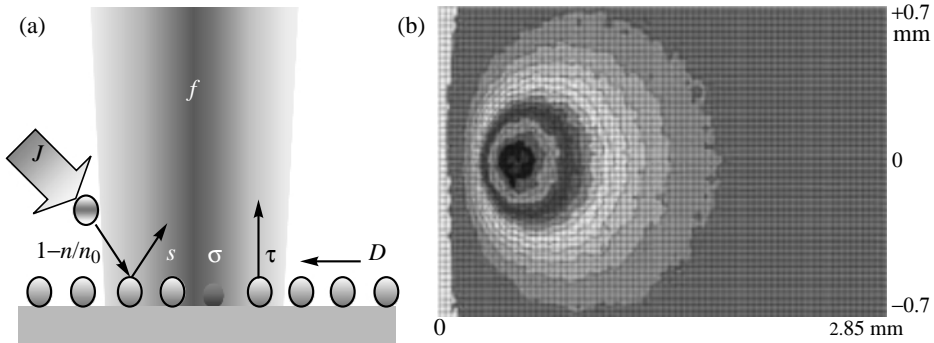


**Fig. 2.** (a) Mechanisms determining the adsorption rate in the focused electron beam irradiated area. Sticking, dwelltime, decomposition, and coverage are symbolized, see also Eq. (1). Molecule size is not at scale. (b) Mapping of precursor molecules arriving from a  $45^\circ$  inclined micro-tube with a radius  $R = 285 \mu\text{m}$  and a length  $L/R = 21$  on a horizontal substrate. The tube axis is aligned to  $y = 0$ . Mean free path  $\lambda$  is  $46.8 \mu\text{m}$  and  $\lambda/R = 0.16$ . An almost cosine distribution is obtained due to intermolecular collisions. The color code is as follows: precursor flux  $J$  = maximum for black center,  $J = 0$  for white on the left side, color increment is 6.25%.

flow arriving on the substrate depends on the tube dimensions, the molecular mass of the precursor, its vapor pressure, and the vacuum chamber pressure into which the precursor effuses. The orientation (e.g.  $45^\circ$  angle) and position of the tube relative to the substrate surface where the electron beam impinges is also important. A schematic demonstration is given in Fig. 4. Distributions of molecules impinging on the substrate are obtained from simulations for the molecular flux regime taking into account collisions between molecules [13], see Fig. 2(b).

## 2.2. Precursor diffusion

Precursor surface diffusion can be studied at contamination deposits. No precursor is supplied and deposition occurs due to decomposition of residual fragments from pump oils adsorbed onto the otherwise clean surface. In Fig. 3, a series of tip deposits with varying time was performed. The deposition rate reduces drastically by about one order of magnitude at a tip height of about 400 nm owing to the increasing diffusion path. The apex diameter is constant, however, the bottom diameter increases steadily due to surface diffusion into the decomposition zone.

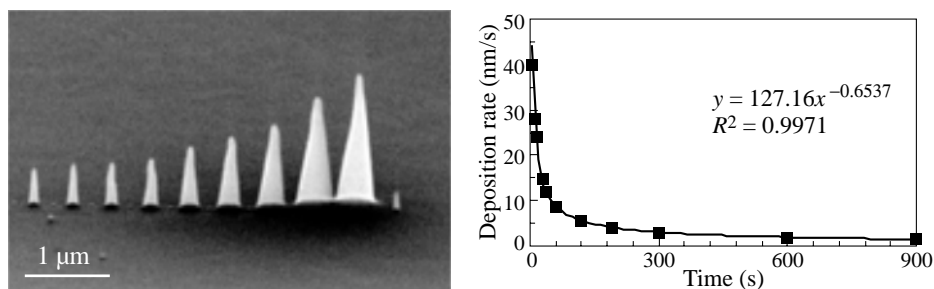


**Fig. 3.** Example of surface diffusion limited deposition. Contamination deposits in a JEOL 6400 (LaB<sub>6</sub>) at 40 kV, 70 pA, working distance 15 mm. Chamber pressure  $6 \times 10^{-7}$  mbar. Note the growth of the deposit diameter at the bottom.

The ratio between surface diffusion and gas phase transport during FEB deposition could be studied by varying the distance from the tube exit, if the surface residence time of the precursor molecules were known. A decrease in deposition rate (due to a decrease in precursor flux) and a shape evolution can be monitored with increasing distance obtained with Rh<sub>2</sub>Cl<sub>2</sub>(PF<sub>3</sub>)<sub>4</sub>, see Fig. 4. However, deposits at large distances from the tube exit (1 mm) still show features oriented to the precursor tube exit, i.e. molecules impinging directly from the gas phase contribute to the deposition rate under these conditions.

For surface diffusion limited growth the vertical deposition rate is higher at low currents than at high currents. Due to the increased beam size with increasing electron current, precursor molecules are decomposed on their way to the center of the electron beam. The vertical deposition rate seems to be limited by the lateral deposition reducing the amount of precursor reaching the central part of the electron beam. In this region with highest electron densities we are always precursor transport limited.

## 3. Chemical decomposition reaction — Ionization — Fragmentation — Composition of deposit

The most complex and less understood part of FEB deposition is the decomposition of the adsorbed precursor molecules. The electron dissociation cross sections as function of electron energy was published by Cosby [14] for a simple compound, carbon-monoxide CO

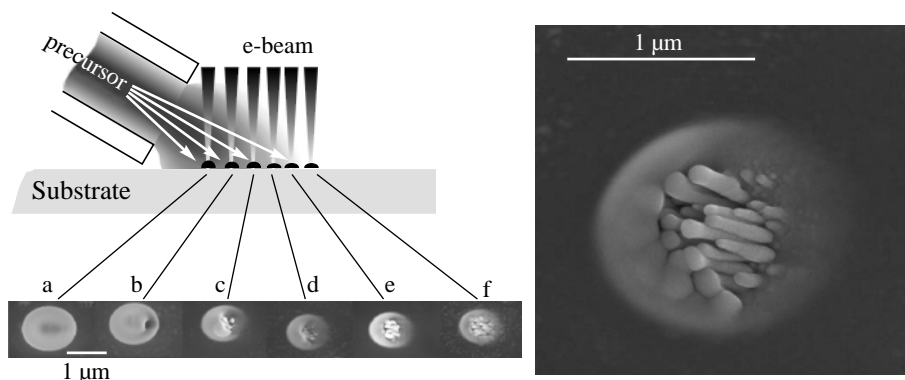


**Fig. 4.** Schematic drawing of the orientation of the precursor flux onto the substrate (see also Fig. 2(b)) with the corresponding SEM top view pictures of FEB deposits. The deposition conditions are 25 keV acceleration voltage, as precursor:  $\text{Rh}_2\text{Cl}_2(\text{PF}_3)_4$  on oxidized Si as substrate, beam current 1 nA, deposition time for every spot was 180 s. The distances from *a* to *f* were 10, 150, 430, 570, 800, 1000 micrometers respectively, from the upper edge of the tube. The latter deposit is shown at higher magnification on the right.

( $\sigma = 0.75 \times 10^{-16} \text{ cm}^2$  at 50 eV) and for osmium carbonyl the electron dissociation cross section was estimated to be  $\sigma = 0.15 \times 10^{-16} \text{ cm}^2$  from FEB deposition at 40 keV [5]. However, no studies are found describing the molecular fragmentation path resulting in deposits. One of the reasons is that the amount of decomposed precursor and of deposited material is very small (picograms).

We performed quadrupole mass spectrometry measurements to determine the fragmentation path of the inorganic  $\text{Rh}_2\text{Cl}_2(\text{PF}_3)_4$  precursor. The detected positively charged fragments of the electron induced ionization process show, that the dissociation of  $\text{PF}_3$  groups is the predominant decomposition path. No fragments indicating the separation of fluorine from phosphorous were detected. These findings were confirmed by density functional theory (DFT) calculations of the decomposition of the precursor molecule [15]. However, the deposit composition determined by Auger electron spectroscopy shows up to 60 at% Rh (as 4–8 nm nano-crystals, see Fig. 5(a–c)) with P and Cl as main contaminants, which is in contradiction to the above measurements of electron induced fragmentation of precursor molecules in the gas phase. This fact shows, that it is very difficult to extrapolate the FEB deposit composition from mass spectrometry data. Probably surface catalyzed reactions, rearrangements, and polymerization reactions play an important role during FEB-deposition.

FEB deposition of another chemical compound of the same family,  $\text{AuClPF}_3$  results in deposits of almost pure gold, proven by 4-point probe measurements of highly electrically conducting gold nanowires having an electrical resistivity of  $22 \mu\Omega \text{ cm}$ , (Au:  $2.4 \mu\Omega \text{ cm}$  at room temperature). A very high nanowire resolution of 50 nm was obtained with our microscope, as can be seen in Fig. 5(d).

#### 4. Conclusions

Focused Electron Beam (FEB) induced chemistry like deposition and etching are important processes for future rapid prototyping tools in nanotechnologies. There are many challenging applications of this extremely flexible technology, like mask and device repair in microelectronics and micro-optoelectronics, prototype production of nano-electrodes



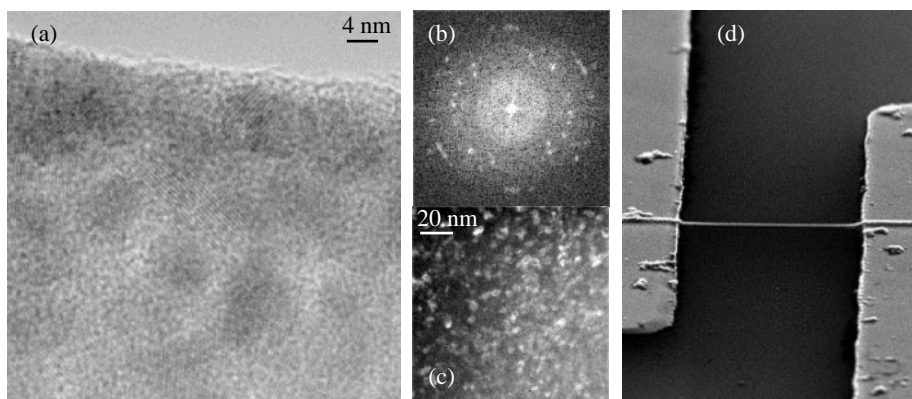


**Fig. 5.** TEM images of a deposit grown with 15 kV at 8 nA beam current from  $\text{Rh}_2\text{Cl}_2(\text{PF}_3)_4$ : (a) HRTEM image showing Rh lattice planes of nanocrystals of 4...8 nm in diameter. (b) Electron diffraction pattern, proving the polycrystalline nature. (c) dark field image of Rh-clusters. (d) Tilted SEM image of a gold line with resistivity of  $22 \mu\Omega \text{ cm}$  ( $10\times$  Au bulk value) deposited from  $\text{AuCIPF}_3$ . The distance of the photo-lithographically deposited gold electrodes is  $5 \mu\text{m}$ .

for studies in a large variety of research fields, and prototypes of nano-optical devices like 3 dimensional photonic crystal structures, see for example Fig. 6. FEB deposition of other materials like magnetic Co nanoparticles (2–4 nm in diameter) embedded in an amorphous oxidation protecting carbon film, deposited on silicon cantilevers and used for high resolution magnetic force microscopy studies (see Fig. 1(c)) present first impacts in applications. The demand for local three dimensional structuring of surfaces is increasing, and spans over a very large number of materials and functionalities.

Historically the first deposits were obtained from “contamination” in SEM or TEM machines, being condensed vapors of pump oil. The obtained deposits contain carbon, often called diamond-like carbon. Recently, we measured the mechanical properties of such deposits showing a very high elasticity modulus of 0.4 TPa, responsible for the name of the carbon deposits. In this case, not even the precursor compound is precisely known, that results in the high performing deposits. This is an example of the basic research still

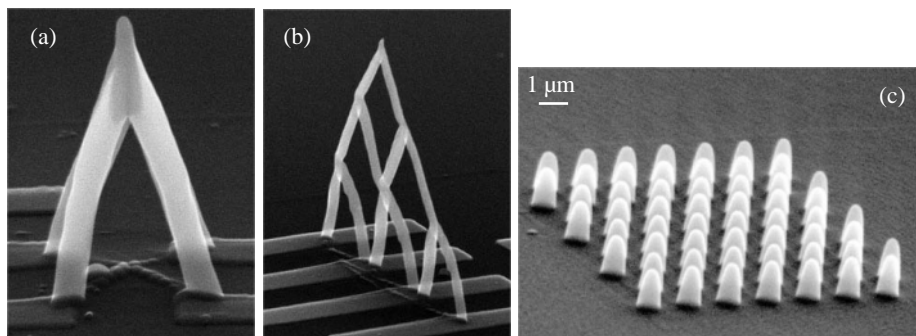


**Fig. 6.** (a) and (b) 3D FEB deposits on Au electrodes from Dimethyl-hexafluoroacetylacetonate  $(\text{CH}_3)_2\text{Au}(\text{hfa})$ , fabricated by e-beam lithography and lift-off process. Distance between electrodes is 500 nm. (c) SEM image of hexagonal tip arrays deposited with FEB. The deposition time gives control over the tip height. Additionally, the tip inclination angle can be varied moving the electron beam with the lithography program during exposure. Tips contain about 80 wt% Au and 20 wt% carbon.

needed to improve the performance of FEB deposition. With the present work we tried to inform about the complexity of the FEB deposition process and the state of the art of the understanding of the ongoing processes. The influences of the physical and physico-chemical parameters of the FEB deposition process on the limiting size of deposits and growth rates of the deposits will become clear in the near future. On the other hand, the electron induced chemical fragmentation reactions are still not understood. Exceptions happen, using thermally fragile precursor molecules (decomposition temperatures below 100 °C) containing noble metals, which result in high quality deposits probably due to electron induced local heating. We have shown that high deposit purity and therefore high functionality can be obtained by a proper precursor choice. But for specific tailoring of precursors for FEB deposition, the understanding of the electron beam induced chemical processes of molecules close to surfaces is still insufficient.

### Acknowledgements

The authors are grateful to Benjamin Dwir (IPEQ/EPFL) as participant in all FEB deposition projects, Simone Amorosi and Giacomo Benvenuti (both IOA/EPFL) for the Monte Carlo simulations, Klaus Leifer (IPEQ/EPFL) and Philippe-André Buffat (CIME/EPFL) for the TEM work, Hans-Jorg Mathieu and Nicolas Xanthopoulos (both LMCH/DMX/EPFL) for the Auger measurements, Pascal Doppelt (ESPCI, Paris) for the synthesis of the precursors, Patrick Seuret, Jacques Weber, and Thomas Wesolowski (University Geneva) for the density functional theory calculations, and EPFL, CTI and ETH-Rat financing the TOP NANO 21 program, and the Swiss National Science Foundation for financial support.

### References

- [1] S. R. Lariviere, *Phys. Rev.* **45**, 488–490 (1934).
- [2] A. E. Ennos, *Brit. J. Appl. Phys.* **5**, 27–31 (1954).
- [3] S. Matsui and K. Mori, *J. Vac. Sci. Technol. B* **4**, 299–304 (1986).
- [4] H. W. P. Koops, R. Weiel, D. P. Kern and T. H. Baum, *J. Vac. Sci. Technol. B* **6**, 477–481 (1988).
- [5] V. Scheuer, H. Koops and T. Tschudi, *Microelectron. Engin.* **5**, 423–430 (1986).
- [6] R. W. Christy, *J. Appl. Phys.* **31**, 1680 (1960).
- [7] L. Reimer, *Scanning Electron Microscopy*; 2nd ed.; Springer: Berlin, Vol. 45, 1998.
- [8] P. Hoffmann, I. Utke, F. Cicaira, B. Dwir, K. Leifer, E. Kapon and P. Doppelt, *Proc. Mater. Res. Soc. Spring Meeting* vol. 624 p. 171–177, 2000.
- [9] D. C. Joy, *Monte Carlo Modeling for Electron Microscopy and Microanalysis* Oxford University Press: New York, 1995.
- [10] S. Matsui and T. Ichihashi, *Appl. Phys. Lett.* **53**, 842–4 (1988).
- [11] H. W. P. Koops, 2001, personal communication
- [12] H. W. P. Koops, A. Kaya and M. Weber, *J. Vac. Sci. Technol. B* **13**, 2400–2403 (1995).
- [13] G. Benvenuti, S. Amorosi, I. Utke, A. Luisier and P. Hoffmann, (to be published).
- [14] P. C. Cosby, *J. Chem. Phys.* **98**, 7804–7818 (1993).
- [15] P. Seuret, J. Weber, T. Wesolowski, F. Cicaira and P. Hoffmann, (to be published).

## Monte Carlo simulation of self-organized quantum dot structures: crossover from kinetics to thermodynamics

M. Meixner<sup>†</sup>, R. Kunert<sup>†</sup>, E. Schöll<sup>†</sup>, V. A. Shchukin<sup>‡§</sup> and D. Bimberg<sup>‡</sup>

<sup>†</sup> Institut für Theoretische Physik, Technische Universität Berlin,  
D-10623 Berlin, Germany

<sup>‡</sup> Institut für Festkörperphysik, Technische Universität Berlin,  
D-10623 Berlin, Germany

<sup>§</sup> Ioffe Physico-Technical Institute, St Petersburg, Russia

**Abstract.** We study the heteroepitaxial growth of self-assembled quantum dots in strained semiconductors in the Stranski–Krastanov growth mode using kinetic Monte Carlo simulations. Optimization of growth parameters such as temperature, deposition rate, coverage, and growth interruption time is discussed. In particular, we investigate the crossover between kinetically controlled and thermodynamically limited growth, and thereby resolve the seemingly contradictory temperature dependence of the average dot size.

The growth of high density, dislocation free quantum dot layers for applications in modern semiconductor devices is a major challenge for process engineering. A promising way to obtain highly efficient dot layers is the use of self-organization effects present in the Stranski–Krastanov or Volmer–Weber growth mode [1].

In this work we model the growth of strained sub-monolayer islands forming precursors of quantum dots on top of the wetting layer in the Stranski–Krastanov growth mode by means of a kinetic Monte Carlo simulation. In contrast to previous phenomenological work [2] we calculate the strain field, which is responsible for spatially correlated island growth [3], self-consistently from elasticity theory.

If the quantum dot array is allowed to equilibrate, the average size of the dots follows from thermodynamics [4]. Due to the effect of entropy, the average dot size  $N_{\text{opt}}$  decreases with increasing temperature  $T$  down to single adatoms at very high temperatures according to  $N_{\text{opt}}(T) = N_0 - \frac{2\sqrt{N_0}}{c_2} kT \ln(8\pi kT N_0^{7/2} / (c_2 q^2))$  where  $N_0$  corresponds to  $T = 0$ ,  $q$  is the total coverage,  $c_2 = 0.1$  eV is determined by the strain field, and island-island interactions have been neglected. On the other hand, often a contradictory effect can be found experimentally, particularly if the system is cooled down or capped immediately after the formation of the dot layer. Here the average dot size increases with increasing temperature. Due to the higher mobility of adatoms at higher temperatures the attachment to existing islands is more favorable than the nucleation of new islands. Thus for low temperatures many small islands are formed, whereas for high temperatures few large islands are observed. The size distribution is dominated by kinetic effects. For a given experiment it is generally not clear if the growth dynamics is dominated by thermodynamic equilibration or by kinetics. In this paper we address this question and, in particular, focus on the crossover from kinetic island formation to thermodynamically controlled size distributions [5].

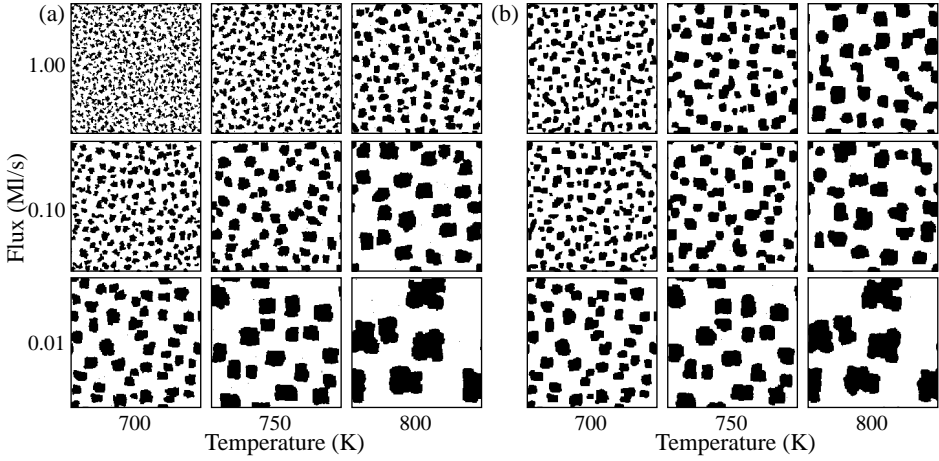


**Fig. 1.** (a) Monte Carlo simulations of quantum dots for different growth temperatures and flux rates for a coverage of  $c = 30\%$  after the end of deposition. (b) Same after 50s simulation time (grid of  $200 \times 200$  square lattice sites with periodic boundary conditions,  $E_s = 1.3$  eV,  $E_b = 0.3$  eV,  $\lambda = 2.9 \times 10^{11}$  erg/cm<sup>3</sup>,  $\mu = 3.5 \times 10^{11}$  erg/cm<sup>3</sup> corresponding to InAs).

We simulate the heteroepitaxial growth of quantum dots by means of a continuous time kinetic Monte Carlo (MC) scheme [2]. This technique allows us to simulate the nucleation and growth of sub-monolayer islands far from equilibrium as well as to analyse the processes relevant during equilibration. The basis of our simulations is a model of activated diffusion incorporating self-consistently the local elastic strain field. The hopping probability of an adatom onto a nearest neighbour site is given by the Arrhenius law  $p = \nu_0 \exp[-(E_s + nE_b - E_{str}(x, y)/k_bT)]$  where  $\nu_0 = 10^{13} \text{ s}^{-1}$  is the attempt frequency,  $E_s$  and  $E_b$  are the binding energies to the surface and to the  $n \leq 4$  nearest neighbour atoms, respectively.  $E_{str}(x, y)$  is the energy correction due to the local strain field generated by the growing islands. The strain field is treated in the framework of the continuum theory of elastic media using a Green's function formalism. The elastic displacements  $u_i(\mathbf{r}) = -\oint_S d^2r' G_{ij}(\mathbf{r}, \mathbf{r}') P_j(\mathbf{r}')$  are calculated by means of the static Green's tensor  $G_{ij}(\mathbf{r}, \mathbf{r}')$  of elasticity theory. The line forces  $P_i(\mathbf{r})$  appear at the island edges and act as the sources of the strain. Therefore the integration is carried out along all island boundaries  $S$ . The strain energy is then calculated from the displacements by

$$E_{str} = \frac{\lambda}{2} \left( \sum_i \frac{\partial u_i}{\partial x_i} \right)^2 + \mu \sum_{ij} \frac{1}{4} \left( \frac{\partial u_i}{\partial x_j} + \frac{\partial u_j}{\partial x_i} \right)^2$$

with elastic constants  $\lambda$  and  $\mu$ .

By varying experimentally accessible growth parameters like temperature, deposition rate, and coverage  $c$  of the adatoms above the wetting layer, we are able to identify optimum growth conditions where narrow size distributions and good spatial ordering can be achieved (Fig. 1(a,b)).

Generally, in the kinetically controlled regime, an increase of the temperature  $T$  leads to an increase of the average island size and to a broadening of the size distribution. The same effect is observed with decreasing deposition rate  $F$  (see Fig. 1(a)). The density  $n$  of nucleated islands decreases with increasing ratio of diffusion to deposition rate. If the diffusion constant  $D(T) = D_0 \exp(-E/kT)$  with diffusion barrier  $E$  and  $D_0 = \frac{1}{4} a_0^2 \nu_0$

(where  $a_0$  is the lattice constant) increases, deposited atoms can — on average — travel farther between deposition events and aggregation to existing islands becomes more likely than nucleation processes. During deposition a characteristic diffusion length of adatoms  $l \sim (D(T)/F)^\gamma$  with  $\gamma = 1/4$  can be defined as the average distance between nucleation sites [6]. It determines the radius of the area from which an existing island can draw adatoms. The kinetically controlled average island size  $N_{\text{kin}}(T)$  is proportional to  $l$ , and thus increases with  $T$  approximately as  $N_{\text{kin}}(T) \sim (D_0 e^{-E/kT}/F)^\gamma$ . For high temperature and small flux clustering of islands occurs, while in the opposite case many small islands nucleate. As a general trend we predict that growth interruptions enhance the spatial ordering, which is mediated by weak, long-range island–island interactions through the strain field. The size distribution, too, can be improved by growth interruption times of a few 10 seconds (Fig. 1(b)). Good spatial ordering of the islands and a sharp size distribution is found with coverages of about  $c = 30\%$  if the other parameters are chosen appropriately.

In order to clarify the crossover from the kinetic regime to the thermodynamic regime we have performed simulations at low coverage of 4% such that equilibration occurs within a much shorter time than in Fig. 1(b). In Fig. 2(a) the temporal evolution of the average island size  $\langle \sqrt{N} \rangle$ , where  $N$  is the number of atoms in an island, is displayed for temperatures of  $T = 675 \text{ K} \dots 750 \text{ K}$ . Fig. 2(b) shows the histograms of the size distributions taken at a time  $t = 35 \text{ s}$ . For low temperatures, the size distribution has a well pronounced maximum. Mostly large islands are present and only very few individual adatoms or small groups can be found. With increasing temperature the size distribution broadens and the number of single adatoms increases due to the entropy contribution to the free energy. The maximum of the distribution shifts towards smaller islands. For the highest temperature  $T = 750 \text{ K}$  a distinct maximum of the size distribution is hardly visible and the tail of small islands becomes dominant. For even higher temperatures the maximum of large islands disappears and only single atoms or small clusters can be found.

From Fig. 2(a) it is evident that in the initial stages of island growth the size distribution is clearly kinetically controlled. At lower temperatures the nucleation of many small islands

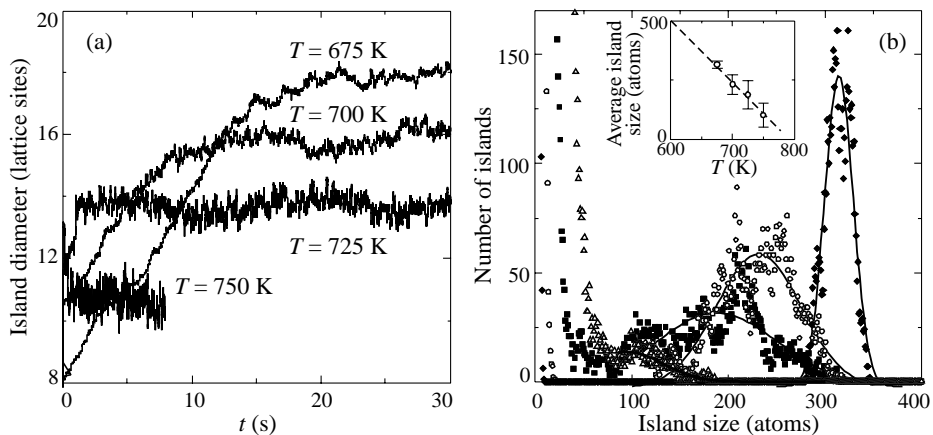


**Fig. 2.** (a) Temporal evolution of the average island size for different temperatures  $T$  ( $F = 1 \text{ ML/s}$ ,  $c = 4\%$ ,  $E_s = 0.7 \text{ eV}$ ,  $E_b = 0.3 \text{ eV}$ ,  $250 \times 250$  grid). (b) Equilibrium size distributions for  $T = 675 \text{ K}$  (diamonds),  $T = 700 \text{ K}$  (open circles),  $T = 725 \text{ K}$  (squares) and  $T = 750 \text{ K}$  (open triangles) taken at  $t = 35 \text{ s}$ . The inset shows the dependence of average island size on  $T$  (dotted line: thermodynamics, open circles: MC).

is the dominant process. Since the adatom mobility is low, the density of single adatoms increases fast during the deposition and pairs of atoms are formed randomly. Those act as nuclei for islands. With increasing temperature the adatoms become more and more mobile. A single adatom can travel a long distance until it finds an existing island to which it will attach, and the nucleation of new islands is suppressed. The spatial configuration in the kinetically controlled regime therefore exhibits few and large islands. Right after the deposition, however, the islands begin to equilibrate. The system is now in an intermediate state between kinetically and thermodynamically controlled growth conditions. The slow increase of island sizes and a crossover of the average island size for systems of different temperatures is characteristic for this regime.

For low temperatures the growth process is the slowest, and the higher the temperature becomes, the faster the islands approach their average equilibrium size. Once the equilibrium size distribution is reached, the average island diameter remains constant. In the course of equilibration the islands at lower temperatures continue to grow until they reach their equilibrium size at an average diameter above that of the islands at higher temperature. For the highest temperature  $T = 750$  K, equilibration is very fast and the equilibrium size distribution is reached almost directly after the end of deposition. The average island size is larger in the kinetically controlled regime and islands have to shrink to reach their equilibrium size distribution. This effect might be caused by oversaturation where the attachment of adatoms to existing islands is strongly favored as opposed to nucleation of new islands. Only if enough island nuclei have been generated, the excess atoms of large islands can be removed.

The average island sizes extracted from our kinetic MC results after longer simulation times (Fig. 2(b)) are indeed in good quantitative agreement with the thermodynamic behavior following from a free energy consideration [5].

#### Acknowledgments

We acknowledge support by Deutsche Forschungsgemeinschaft in the framework of Sfb 296. V.A.Sh. is grateful to the Alexander von Humboldt Foundation and to the Russian Foundation for Basic Research.

#### References

- [1] D. Bimberg, M. Grundmann and N. Ledentsov, *Quantum Dot Heterostructures* (Wiley, New York, 1999),  
I. Daruka and A.-L. Barabási, *Appl. Phys. Lett.* **72**, 2102 (1998),  
V. Shchukin and D. Bimberg, *Rev. Mod. Phys.* **71**, 1125 (1999), G. Springholz, M. Pinczolits, P. Mayer, V. Holy, G. Bauer, H. Kang and L. Salamanca-Riba, *Phys. Rev. Lett.* **84**, 4669 (2000).
- [2] E. Schöll and S. Bose, *Sol. State El.* **42**, 1587 (1998),  
B.-G. Liu and E. Schöll, *Vacuum* **61**, 145 (2001).
- [3] M. Meixner, E. Schöll, M. Schmidbauer, H. Raidt and R. Köhler, *Phys. Rev. B* **64**, 245307 (2001).
- [4] V. A. Shchukin, N. N. Ledentsov, P. S. Kop'ev and D. Bimberg, *Phys. Rev. Lett.* **75**, 2968 (1995).
- [5] M. Meixner, E. Schöll, V. A. Shchukin and D. Bimberg, *Phys. Rev. Lett.* **87**, 236101 (2001),  
*ibid* **88**, 059901 (2002).
- [6] M. Schroeder and D. E. Wolf, *Phys. Rev. Lett.* **74**, 2062 (1995).

## Room-temperature electroluminescence at 1.55 $\mu\text{m}$ from InAs quantum dots grown on (001) InP by droplet hetero-epitaxy

*R. Oga, W. S. Lee, Y. Fujiwara and Y. Takeda*

Department of Materials Science and Engineering, Graduate School of Engineering,  
Nagoya University, Furo-cho, Chikusa-ku, Nagoya 464-8603, Japan

**Abstract.** We have successfully observed room-temperature electroluminescence (EL) from InAs quantum dots (QDs) on (001) InP substrates. The InAs QDs were grown by droplet hetero-epitaxy using low-pressure organometallic vapor epitaxy (OMVPE). There were two kinds of InAs QDs; large and small QDs. The small InAs QDs with the average diameter and height of 40 nm and 7 nm were present at the density of  $3 \times 10^{10} \text{ cm}^{-2}$ . In photoluminescence (PL) measurements at 77 K, a peak with full width of 84 meV at half maximum was observed around at 1506 nm. Room-temperature electroluminescence was successfully observed from InAs QDs embedded in InP matrix around at 1560 nm, together with InP emission at 980 nm. With increasing injection current density from  $3 \text{ A/cm}^{-2}$  to  $33 \text{ A/cm}^{-2}$ , the shape of the spectra was unchanged, suggesting that the broadness of the luminescence is due to the size distribution of InAs QDs.

### Introduction

Quantum dot (QD) lasers are expected to attain remarkable reduction in threshold current, temperature-insensitive operation and large modulation due to atom-like density of state which increases optical gain and limits thermal carrier distribution [1–4]. In recent years, a variety of fabrication techniques have been developed to realize device-quality semiconductor QD structures. Among them, injection lasers containing InAs and InGaAs QDs embedded in GaAs matrix have been successfully demonstrated and show improved characteristics as predicted [5, 6]. Most researches have focused on InAs or InGaAs QDs on GaAs substrates, and operating wavelengths emitted from the QDs were shorter than 1.3  $\mu\text{m}$ . On the other hand, InAs QDs on InP substrates are very attractive since they are expected to emit radiation around 1.5  $\mu\text{m}$  region. We have studied droplet hetero-epitaxy for the fabrication of InAs QDs on InP substrates [7]. We succeeded in formation of InAs QDs with the density of  $9.8 \times 10^9 \text{ cm}^{-2}$  on (001) InP substrates. The photoluminescence (PL) was observed around 1.6  $\mu\text{m}$  at room temperature. In this article, we report on the first observation of room-temperature electroluminescence (EL) from InAs QDs grown on (001) InP substrates by droplet hetero-epitaxy. The QDs are also investigated with atomic force microscope (AFM) and PL measurements.

### 1. Fabrication of InAs QDs

The samples were grown by a low-pressure organometallic vapor phase epitaxial system with a vertical cold-wall quartz reactor. Reactor pressure was fixed at 76 Torr.  $\text{H}_2$  carrier gas was Pd-purified, and the total  $\text{H}_2$  flow rate in the reactor was maintained at 4 slm. Trimethylindium (TMIn), tertialybutylphosphine (TBP) and tertialybutylarsine (TBAs) were used as source materials for group-III and -V, respectively. Diethylzinc (DEZn) was used for p-type InP contact layer. The growth was carried out after thermal treatment

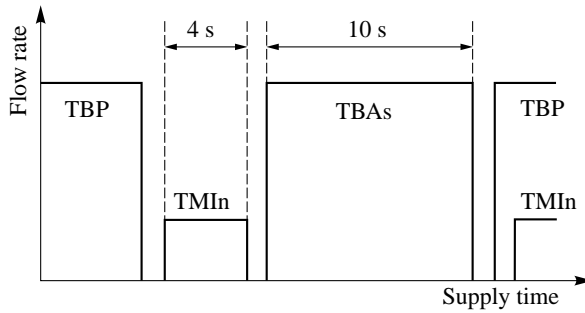
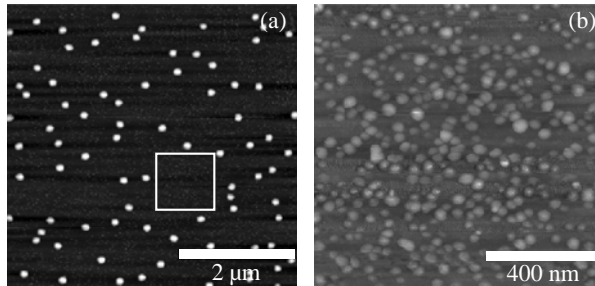


**Fig. 1.** Gas flow sequence for the formation of InAs QDs by droplet hetero-epitaxy. Flow rates of TMIIn and TBAs were  $1.68 \times 10^{-7}$  mol/s and  $3.35 \times 10^{-6}$  mol/s, respectively.

in TBP ambient for 30 min at the same temperature as the growth. Figure 1 shows a gas sequence for droplet hetero-epitaxy. The substrate temperature was fixed at 530 °C. TMIIn was supplied at  $1.68 \times 10^{-7}$  mol/s for 4 s to form In droplets. Then, the In droplets were exposed to TBAs ambient for 10 s in order to crystallize the droplets to InAs dots. The TBAs was supplied at  $3.35 \times 10^{-6}$  mol/s. We grew three types of samples for PL, AFM and EL. For PL and AFM, InAs QDs were grown on Fe-doped (001) InP substrates. The sample for PL was cooled down in TBP ambient after the growth of a 10 nm InP cap layer. On the other hand, the sample which was cooled down in TBAs ambient without any InP cap layer was prepared for AFM observation. In order to measure EL spectra, InAs QDs were grown on n-type Sn-doped (001) InP substrates with carrier concentration of  $10^{18} \text{ cm}^{-3}$ . After the growth of InAs QDs and a 10 nm undoped InP layer, Zn-doped InP ( $p = 4 \times 10^{18} \text{ cm}^{-3}$ ) was grown at 620 °C.

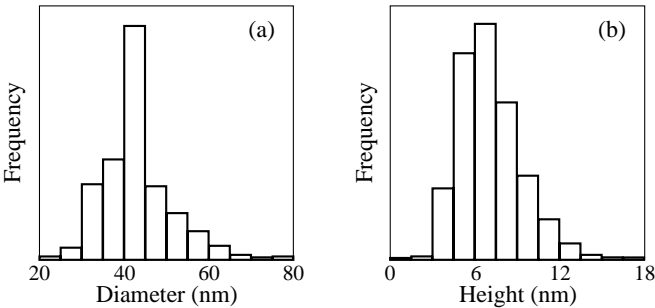
## 2. Results and discussion

Figure 2 shows AFM images of the sample with InAs QDs grown by droplet hetero-epitaxy, which were taken with different magnifications. There are two kinds of InAs QDs. Large InAs QDs are present at the density of  $3 \times 10^8 \text{ cm}^{-2}$ . Their average diameter and height are 160 nm and 48 nm, respectively. Small QDs are also observed together with large QDs. The areal density is at  $3 \times 10^{10} \text{ cm}^{-2}$ . Distributions of the diameter and height of small QDs are shown in Fig. 3. The average diameter and height are 40 nm and 7 nm, respectively. Some large QDs have grooves on the face. It indicates that large QDs are formed by coalescence between small dots.



**Fig. 2.** AFM images; (a)  $5 \times 5 \mu\text{m}^2$  and (b)  $1 \times 1 \mu\text{m}^2$ . There are two kinds of InAs QDs. Areal densities of large and small QDs are  $3 \times 10^8 \text{ cm}^{-2}$  and  $3 \times 10^{10} \text{ cm}^{-2}$ , respectively.





**Fig. 3.** Distributions of the diameter and height of small InAs QDs; (a) diameter and (b) height. The average diameter and height are 40 nm and 7 nm, respectively.

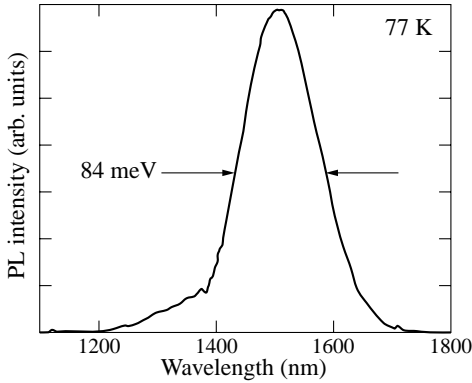


**Fig. 4.** 77 K PL spectrum of InAs QDs embedded in InP matrix. The peak with FWHM of 84 meV is observed around at 1506 nm.

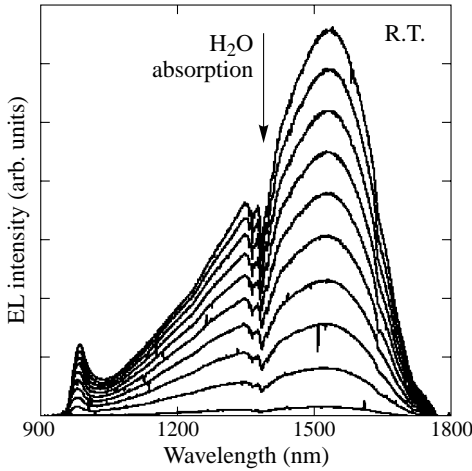


**Fig. 5.** Room-temperature EL spectra. Injection current density was varied from 3 A/cm<sup>-2</sup> to 33 A/cm<sup>-2</sup>. The shape of the spectra are unchanged against the injection current density.

Figure 4 shows low-temperature PL spectrum. PL measurement was carried out on the sample directly immersed into liquid nitrogen at 77 K. The photoexcitation source was an Ar<sup>+</sup> laser with incident power of 50 mW. Broad luminescence originating from InAs QDs is observed with the peak around at 1506 nm. The full width at half maximum (FWHM) is 84 meV, which is well coincident with that of InAs QDs grown on exact (001) InP substrates by using Stranski–Krastanov mode [8]. This is an evidence that the droplet hetero-epitaxy is one of the useful techniques to form InAs QDs on InP. Figure 5 shows room-temperature EL spectra. Injection current density was varied from 3 A/cm<sup>-2</sup> to 33 A/cm<sup>-2</sup>. The absorption of H<sub>2</sub>O around 1390 nm should be ignored, since the spectra are not corrected for the spectral response of the system. Two peaks are clearly observed at 980 nm and 1560 nm. The 980 nm peak is due to the emission of InP as a matrix. The emission due to InAs QDs is peaked around at 1560 nm. The spectra are broad especially in the shorter wavelength region. New luminescence is never observed even with the higher current density. It indicates that the broad luminescence is due to the size distribution of InAs QDs, not due to the contribution of excited quantum states of the QDs.

### 3. Conclusion

We have successfully observed room-temperature electroluminescence from InAs QDs on (001) InP substrates. InAs QDs were grown by droplet hetero-epitaxy. There were two kinds of InAs QDs; large and small. Small QDs with the average diameter and height of 40 nm and 7 nm were observed at the density of  $3 \times 10^{10}$  cm<sup>-2</sup>. Some large QDs had grooves on the face, suggesting that the large QDs are formed by the coalescence between small QDs. Optical properties of InAs QDs were investigated with PL and EL. In PL measurement at 77 K, a peak with FWHM of 84 meV was observed at 1506 nm. This FWHM is well coincident with that of InAs QDs grown on exact (001) InP substrates by using Stranski–Krastanov mode. Room-temperature electroluminescence was successfully observed from InAs QDs at 1560 nm, together with InP emission at 980 nm. The spectra were broad especially in the shorter wavelength region. Any new luminescence was not observed even with increasing injection current density. It indicates that the broad luminescence is due to the size distribution of InAs QDs, not due to the contribution of excited quantum states of InAs QDs.

### References

- [1] Y. Arakawa and H. Sasaki, *Appl. Phys. Lett.* **40**, 939 (1982).
- [2] M. Asada, Y. Miyamoto and Y. Suematsu, *IEEE J. Quantum Electron.* **QE-22**, 1915 (1986).
- [3] K. J. Vahala, *IEEE J. Quantum Electron.* **24**, 523 (1988).
- [4] H. Sasaki, *Jpn. J. Appl. Phys.* **28**, L314 (1989).
- [5] N. Kirstaedter, N. N. Ledentsov, M. Grundmann, D. Bimberg, V. M. Ustinov, S. S. Ruvimov, M. V. Maximov, P. S. Kop'ev, Zh. I. Alfenov, U. Richter, P. Werner, U. Gösele and J. Heydenreich, *Electron. Lett.* **30**, 1416 (1994).
- [6] K. Kamath, P. Bhattacharya, T. Sosnowski, T. Norris and J. Phillips, *Electron. Lett.* **32**, 1374 (1996).
- [7] Y. Nonogaki, T. Iguchi, S. Fuchi, Y. Fujiwara and Y. Takeda, *Mat. Sci. & Eng. B* **51**, 118 (1998).
- [8] H. Marchand, P. Desjardins, S. Guillon, J.-E. Paulter, Z. Bougrioua, R. Y.-F. Yip and R. A. Masut, *Appl. Phys. Lett.* **71**, 527 (1997).

## Structural and optical characteristics of MOCVD-grown quantum dots

*D. L. Huffaker, S. Birudavolu and A. A. El-Emawy*

Center for High Technology Materials, University of New Mexico  
1313 Goddard SE, Albuquerque, New Mexico 87106, USA

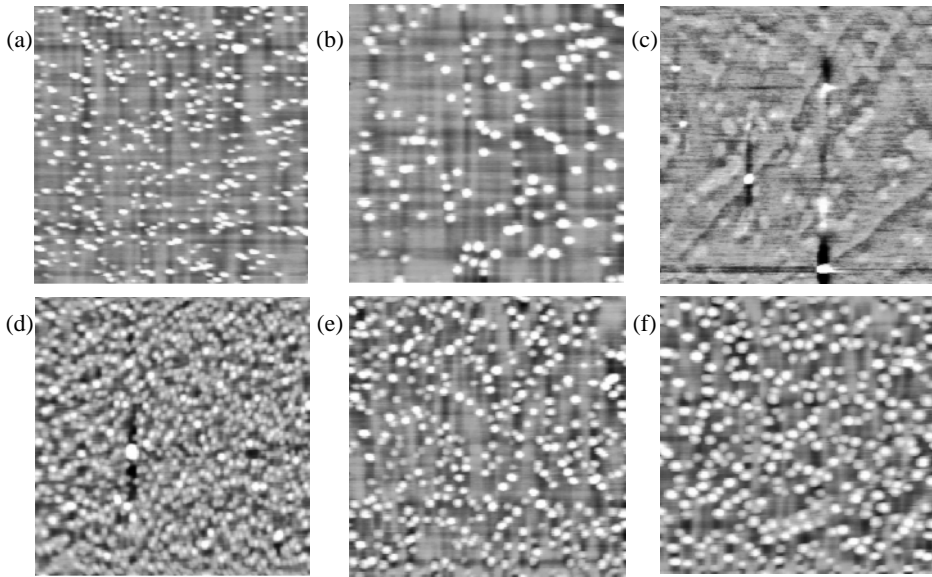
**Abstract.** There are few reports [1–3] of 1.3  $\mu\text{m}$  emission from MOCVD-grown QDs and to date, the 1.3  $\mu\text{m}$  QD laser grown by MOCVD has not been demonstrated. As we optimize the MOCVD-QD ensemble for laser application, we have studied formation trends and characterization of InAs surface and capped QDs. By varying growth temperature and buffer layer composition, we achieve surface densities of  $8 \times 10^{10}/\text{cm}^2$ . Photoluminescence spectra from uncovered QDs show an emission wavelength of 1550 nm with a FWHM of 140 meV. After overgrowth, the emission wavelength is 1.32  $\mu\text{m}$  with a 40 meV linewidth.

All samples are grown on (100) SI-GaAs in a 60 Torr MOCVD reactor. The epilayers consist of 2200 Å GaAs layer, a 5 ML buffer layer (GaAs or  $\text{In}_{0.15}\text{Ga}_{0.85}\text{As}$ ) followed by 2.5 MLs of InAs. The growth rate and V/III ratio are kept constant at 0.5 ML/s and 52.5, respectively, during QD growth. For capped QDs, growth is interrupted for 60s after InAs deposition. The QDs are capped with 45 Å  $\text{In}_{0.15}\text{Ga}_{0.85}\text{As}$  then 330 Å GaAs layers.

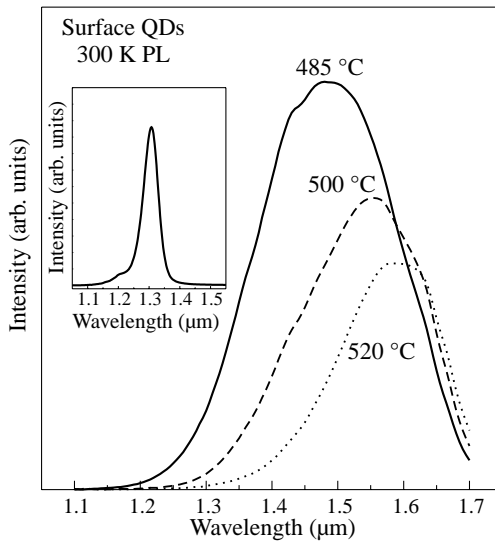
Figures 1(a)–1(f) show AFM images of surface QDs grown on a GaAs (1(a)–1(c)) and an  $\text{In}_{0.15}\text{Ga}_{0.85}\text{As}$  buffer (1(d)–1(f)) at temperatures ranging from 460 °C to 520 °C. Under these conditions, the QDs on GaAs form in a narrow temperature range of 460 °C to 485 °C. Within this temperature range, the QD formation trends are explained by the increased surface atom mobility with temperature, i.e. QD size increases as QD density decreases. From AFM scans, we measure an average QD height of 40 Å (45 Å), a density of  $3.5 \times 10^{10}/\text{cm}^2$  ( $1.5 \times 10^{10}/\text{cm}^2$ ) at 460 °C (485 °C). Outside of this range, QD formation does not occur due to lack of surface mobility at  $T \leq 460$  °C and In evaporation at  $T \geq 500$  °C. The QDs on  $\text{In}_{0.15}\text{Ga}_{0.85}\text{As}$  show a significantly higher dot density due to increased In content and perhaps faster QD nucleation. At  $T = 485$  °C, the density is  $8 \times 10^{10} \text{ cm}^{-2}$  with a height of 30 Å. For  $T > 485$  °C, the density decreases ( $3.5 \times 10^{10}/\text{cm}^2$ ) as the QD height increases (45 Å) at 520 °C.

Figure 2 shows RT-PL spectra from the surface QDs grown on  $\text{In}_{0.15}\text{Ga}_{0.85}\text{As}$ . The peak wavelengths range from 1.46  $\mu\text{m}$  (485 °C) to  $\sim 1.6 \mu\text{m}$  (520 °C). The FWHM ranges from 160 meV to 120 meV. The peak PL intensity and FWHM decrease with temperature due to the decrease in dot density. The inset of Fig. 2 shows an RT-PL spectrum from capped QDs grown on  $\text{In}_{0.15}\text{Ga}_{0.85}\text{As}$  at 500 °C. The PL wavelength is observed at 1.32  $\mu\text{m}$  with a narrow linewidth of 40 meV.

The longer wavelength and broader FWHM of surface QDs is partially due to larger and less uniform QDs. The free surface allows the strained In atoms to slightly relax which also increases the wavelength. However, the surface electronic barrier provides a deep confinement potential that is essentially the InAs electron affinity ( $\sim 5$  eV). The deep confinement likely contributes a blue-shift to the resulting emission wavelength and increases the separation between energy levels. At 77 K, we are not able to excite higher energy levels, even after the ground state has saturated suggesting a single confined state exists for the surface QD. Higher energy levels with separations of 39 meV can be excited in the capped QDs. We will discuss this data and more in our presentation.



**Fig. 1.** Atomic force microscope images of InAs QDs grown on GaAs at (a) 460 °C, (b) 485 °C and (c) 500 °C and on 5 MLs  $\text{In}_{0.15}\text{Ga}_{0.85}\text{As}$ , at (d) 485 °C, (e) 500 °C and (f) 520 °C. The scan size is  $1\text{ }\mu\text{m} \times 1\text{ }\mu\text{m}$ .



**Fig. 2.** Room-temperature PL spectra from surface InAs QDs grown on 5 MLs of  $\text{In}_{0.15}\text{Ga}_{0.85}\text{As}$  at 485 °C to 520 °C. The inset shows PL spectrum of capped InAs QDs grown on  $\text{In}_{0.15}\text{Ga}_{0.85}\text{As}$  at 500 °C. The cap layers, grown at 500 °C, are 45 Å of  $\text{In}_{0.15}\text{Ga}_{0.85}\text{As}$  and 330 Å of GaAs.

## References

- [1] K. Mukai, N. Ohtsuka, M. Sugawara and S. Yamazaki, *J. J. Appl. Phys. Part 2 (Letters)* **33**, L1710 (1994).
- [2] A. Passaseo, G. Maruccio, M. De Vittorio, R. Rinaldi, R. Cingolani and M. Lomascolo, *Appl. Phys. Lett.* **78**, 1382 (2001).
- [3] J. Tatebayashi, M. Nishioka and Y. Arakawa, *Appl. Phys. Lett.* **78**, 3469 (2001).

## Growth and structural characterization of $\text{ZnF}_2$ epitaxial layers on Si

A. G. Banshchikov, N. F. Kartenko, A. K. Kaveev, M. M. Moiseeva  
and N. S. Sokolov

Ioffe Physico-Technical Institute, St Petersburg, Russia

### 1. Introduction

In recent years studies of II-group and rare-earth fluoride layers on semiconductors have been quite active. The fluorides have a number of features that make them attractive for epitaxial growth on the most important semiconductors for both practical applications and basic studies. Among other fluorides,  $\text{ZnF}_2$  is known for its unusual features which are of special interest. The rutile structure of  $\text{ZnF}_2$  is similar to the  $\text{MnF}_2$  structure. Moderate ( $\Delta a/a = -3.34\%$ ,  $\Delta c/c = -5.38\%$ ) lattice mismatch allows [1]  $\text{MnF}_2$  epitaxial growth on  $\text{ZnF}_2$ . Zinc fluoride is diamagnetic, and magnetically ordered epitaxial films separated by thin diamagnetic layers are of interest in terms of low-dimensional effects [2, 3]. Polymorphous structural transitions at high pressures and temperatures (100–400 °C, 30–160 KBar) have been found [4] in  $\text{ZnF}_2$ . Electronic properties of  $\text{ZnF}_2$  differ from those of II a-group metal fluorides. So, after doping by some trivalent impurities, zinc fluorite, being a wide band gap insulator, converses into an n-type semiconductor with the binding energy of shallow donors of about 0.07–0.25 eV [5, 6]. Other attractive feature is an effective electroluminescence in rare-earth doped bulk crystals and polycrystalline films [7]. Depending on the impurity, the radiation wavelength changes from IR to UV. Efficient luminescence, in addition to high free electron concentrations, makes zinc fluorite a promising compound for electroluminescent device applications. In this work, we studied the epitaxial growth and structural properties of zinc fluoride films grown on silicon using fluorite buffer layer.

### 2. Experimental

Zinc fluoride films were grown on Si(111) and Si(001) substrates by molecular beam epitaxy (MBE). Calcium fluoride buffer layer was deposited before the  $\text{ZnF}_2$  growth. The Shiraki method [8] was used for chemical cleaning of the Si substrates. The remaining thin oxide layer was evaporated under UHV conditions by heating the substrates up to 1250 °C for 1–2 minutes. This procedure produced atomically clean  $7 \times 7$  Si(111) or  $2 \times 1$  Si(001) faces. The crystal quality of the layer was characterized in situ by reflection high-energy electron diffraction (RHEED) with the electron energy of 15 KeV. The films were covered with a few  $\text{CaF}_2$  monolayers in order to protect them from the ambient humidity. X-ray diffraction measurements (XRD) were carried out on a DRON system with  $\text{CuK}_\alpha$  (Ni-filter) radiation. The  $\Theta - 2\Theta$  curves were measured in symmetrical Bragg geometry in the (20–132°)  $2\Theta$  range. Side reflections were measured in a manual regime. The surface morphology measurements were carried out using a P4-SPM-MDT atomic-force microscope manufactured by NT-MDT (Zelenograd, Russia).

### 3. Results and discussion

It is known that both  $\text{ZnF}_2$  and  $\text{MnF}_2$  bulk crystals crystallize in the rutile structure. It is also found that the  $\text{ZnF}_2$  rutile structure is more stable than that of  $\text{MnF}_2$ . In accordance with the Goldshmidt criteria, this can be due to a smaller  $\text{Zn}^{2+}$  ionic radius than in  $\text{Mn}^{2+}$ .

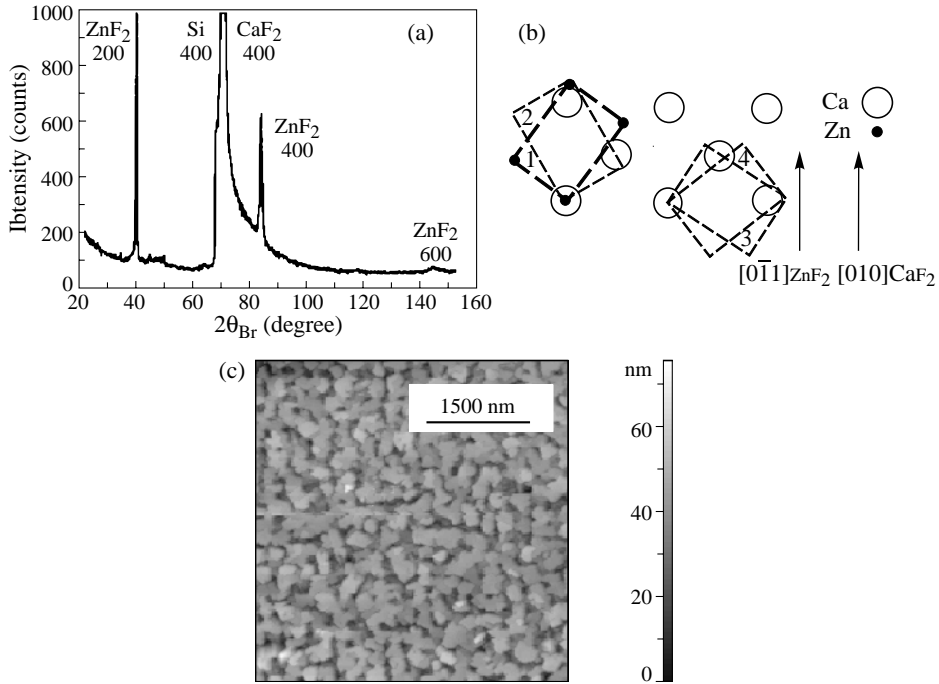


**Fig. 1.** The X-ray diffraction  $\Theta - 2\Theta$  scan (a), epitaxial relations in the (001)-plane (b), and an AFM image (c) of the ZnF<sub>2</sub> 180 nm layer grown on the CaF<sub>2</sub> (001) surface.

It has recently been found that MnF<sub>2</sub> epitaxial films grown on Si [9] have the  $\alpha$ -PbO<sub>2</sub>-type structure, which is metastable to bulk crystals. It was tempting to explore the possibility of ZnF<sub>2</sub> epitaxial growth on Si and, if successful, to examine the crystal structure of the films and epitaxial relations.

It was found by light microscopy that at elevated temperatures ZnF<sub>2</sub> molecules etch the Si surface. To prevent this chemical reaction, a CaF<sub>2</sub> buffer layer of 20–100 nm thick was usually grown on the silicon substrate. It was earlier shown that a 2D growth mode results in a flat CaF<sub>2</sub> (111) surface on the Si(111) [10]. In the same work it was shown that in case of the growth on Si(001) at a temperature lower than 550 °C, CaF<sub>2</sub> tends to form an array of uniformly distributed pyramidal islands with {111} facets. In these islands, the (001)-plane is parallel to the plane of the substrate. It has been found [11] that in case of CaF<sub>2</sub> growth on Si(001) at a temperature higher than 650 °C, a grooved and ridged fluorite surface morphology is observed. In this layer, the (110)-plane is parallel to the (001)-plane of the substrate. To obtain a relatively smooth (001)-surface of the buffer layer, we grew about 30 nm fluorite at 300–400 °C and applied rapid thermal annealing at 850 °C for 45 s, which is known to flatten the CaF<sub>2</sub> (001) surface [12].

On the top of the CaF<sub>2</sub> buffer layer, a 180 nm ZnF<sub>2</sub> film was grown at 350 °C. The RHEED patterns observed during the zinc fluoride deposition indicated the epitaxial growth of the film. The X-ray diffraction measurements confirmed a good crystallinity of the ZnF<sub>2</sub> film. The  $\Theta - 2\Theta$  XRD curve (Fig. 1(a)) shows 3 orders of the film diffraction peaks with the interlayer distance corresponding to  $a = 4.711 \text{ \AA}$  for the rutile phase of <sub>2</sub>. Side reflection measurements allowed determination of the epitaxial relations (Fig. 1(b)):  $[100]_{\text{ZnF}_2} \parallel [001]_{\text{CaF}_2}$ ,  $[0\bar{1}1]_{\text{ZnF}_2} \parallel [010]_{\text{CaF}_2}$ . Note that the distance between the opposite

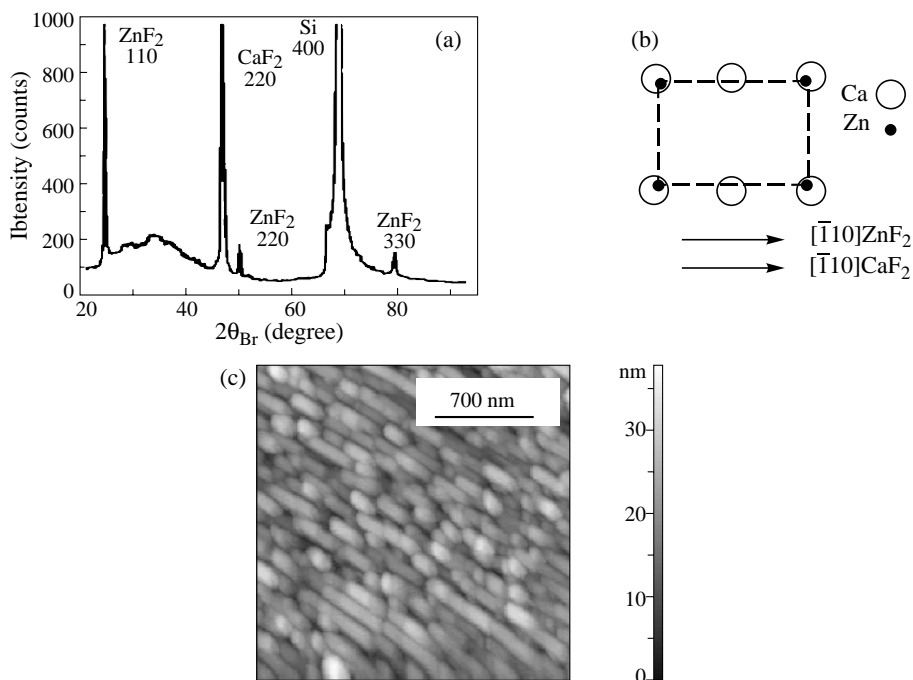


**Fig. 2.** The X-ray diffraction  $\Theta - 2\Theta$  scan (a), epitaxial relations in the (110)-plane (b), and an AFM image (c) of the  $\text{ZnF}_2$  50 nm layer grown on the  $\text{CaF}_2$  (110) surface.

Zn ions lying on the diagonal in the (100) face of the tetragonal unit cell equal to  $5.656 \text{ \AA}$  appeared to be quite close to the lattice parameter on the  $\text{CaF}_2$  (001) surface ( $5.46 \text{ \AA}$ ). These epitaxial relations are suggestive of four types of structural domains (in addition to the above —  $[011]\text{ZnF}_2 \parallel [010]\text{CaF}_2$ ,  $[011]\text{ZnF}_2 \parallel [100]\text{CaF}_2$  and  $[0\bar{1}1]\text{ZnF}_2 \parallel [100]\text{CaF}_2$ ). This assumption is in agreement with the surface morphology of the layer presented in Fig. 1(c), where several orientations of the crystallites can be observed. These observations show the predominant rutile phase of  $\text{ZnF}_2$  under the growth conditions given, in contrast to  $\text{MnF}_2$ , which in similar conditions tends to form the  $\alpha\text{-PbO}_2$ -type structure [9].

To avoid the multi-domain structure of the  $\text{ZnF}_2$  layer, we used a  $\text{CaF}_2$  (110) buffer layer with a highly anisotropic surface [11]. Such layers, with a typical thickness of about 50–60 nm, were grown at high temperatures (700–770 °C), with grooves and ridges along the  $[110]$ -direction observed at this surface. A zinc fluoride layer of 50 nm thick was grown at 350 °C on the top of the buffer. In the  $\Theta - 2\Theta$  XRD curve obtained from this structure (Fig. 2(a)), one can see 3 orders of the film diffraction peaks due to the (110)-planes in the  $\alpha\text{-PbO}_2$  type of  $\text{ZnF}_2$  structural phase. Side reflection measurements allowed determination of the epitaxial relations (Fig. 2(b)):  $(110)\text{ZnF}_2 \parallel (110)\text{CaF}_2$ ,  $[\bar{1}10]\text{ZnF}_2 \parallel [\bar{1}10]\text{CaF}_2$  and  $[001]\text{ZnF}_2 \parallel [001]\text{CaF}_2$ . The distance ( $7.34 \text{ \AA}$ ) between two adjacent Zn atoms in the  $[\bar{1}10]$ -direction of the (110)-plane is quite close to the distance ( $7.72 \text{ \AA}$ ) between two Ca atoms lying opposite on the face diagonal. Thus the single-domain character of this structure has been found, which is in agreement with the AFM observations (Fig. 2(c)). On the AFM-image islands stretched along the  $[110]$ -direction can be seen. All the observations for this case show predominant crystallization of  $\text{ZnF}_2$  in the  $\alpha\text{-PbO}_2$  phase, similar to  $\text{MnF}_2$  in the same conditions.

It was also found that zinc fluoride grows on  $\text{CaF}_2(111)$  in the rutile structure with the (110)-plane parallel to the (111)-plane of the buffer layer. The  $\Theta - 2\Theta$  XRD curve have shown 3 orders of film diffraction peaks. The lattice parameter calculated from this curve ( $a = 4.706 \text{ \AA}$ ) was found to be close to the value  $a = 4.711 \text{ \AA}$  characteristic of bulk crystals.

#### 4. Summary

Epitaxial  $\text{ZnF}_2$  films as thick as 200 nm have been grown on  $\text{Si}(001)$  and  $\text{Si}(111)$  substrates. XRD measurements have shown that  $\text{ZnF}_2$  is capable to form the  $\alpha\text{-PbO}_2$  and rutile structural phases during the MBE growth. Stabilization of the orthorhombic  $\alpha\text{-PbO}_2$  structure was found to be possible for  $\text{ZnF}_2/\text{CaF}_2$  (110) similar to the previous results [9] for  $\text{MnF}_2$ . The appearance of certain structural phase depends on the buffer surface orientation. XRD measurements in asymmetrical Bragg geometry allowed determination of the epitaxial relations for both structural phases. Optical measurements of the  $\text{ZnF}_2$  layers doped with rare-earth ions are underway.

#### Acknowledgements

The authors appreciate stimulating discussions with V. P. Ulin. This study was partially supported by Russian Ministry of Sciences, INTAS (Grant No 97-10528) and Swiss National Science Foundation (Grant No 7SUPJ062359).

#### References

- [1] M. Lui, J. Drucker, A. King, J. Kotthaus, P. Hansma and V. Jaccarino, *Sov. Phys. Semicond.* **53**, 7720 (1986).
- [2] C. Ramos, M. Caceres and D. Lederman, *Phys. Rev. B* **53**, 7890 (1996).
- [3] D. Lederman, C. Ramos, V. Jaccarino and J. Cardy, *Phys. Rev. B* **48**, 8365 (1993).
- [4] L. Lityagina, M. Kachan, S. Kabalkina and L. Vereshchagin, *Dokl. Acad. Sci. USSR* **216**, 1066 (1974).
- [5] N. Miura, T. Ishikawa, T. Sasaki, T. Oka, H. Ohata, H. Matsumoto and R. Nakano, *Jpn. J. Appl. Phys.* **31**, Pt. 2, No 1A/B, 46 (1992).
- [6] D. Morton and F. Williams, *Appl. Phys. Lett.* **35**, 671 (1979).
- [7] N. Miura, T. Sasaki, H. Matsumoto and R. Nakano, *Jpn. J. Appl. Phys.* **31** Part 1, 51 (1992).
- [8] A. Ishizaka and Y. Shiraki, *J. Electrochem. Soc.* **133**, 666 (1986).
- [9] A. G. Banskchikov, O. V. Anisimov, N. F. Kartenko, M. M. Moiseeva, N. S. Sokolov and V. P. Ulin, *Proc. 9<sup>th</sup> Int. Symp. "Nanostructures: Physics and Technology", St Petersburg, Russia, June 18-22, p 25, 2001.*
- [10] L. J. Schowalter and R. W. Fathauer, *J. Vac. Sci. Technol.* **A4**, 1026 (1986).
- [11] N. S. Sokolov and S. M. Sutorin, *Appl. Surf. Sci.* **175-176**, 619-628 (2001).
- [12] T. Asano, H. Ishiwara and S. Furukawa, *Jpn. J. Appl. Phys.* **27**, 1193 (1988).



## Nanostructures in porous substrate for mismatched film technology and lateral growth model

A. V. Bobyl, S. G. Konnikov, D. V. Shantsev, A. A. Sitnikova, R. A. Suris  
and V. P. Ulin

Ioffe Physico-Technical Institute, St Petersburg, Russia

A porous GaAs (100) substrate was prepared with nanoscale (5–20 nm) surface roughness,  $10^8 \text{ cm}^{-2}$  density of nanoscale inlet holes at the surface, and a network of pores (20–100 nm) along [111] on the 50–100 nm depth. The lattice misfit of the heterostructure GaSb/GaAs with the porous substrate was 22% less than that for the same rigid substrate. The structure of pores is discussed in connection with possible electrochemical processes of pore formation in  $\text{A}_3\text{B}_5$  materials.

The initial stage of growth has been analysed assuming a strain dependence of the lateral growth rate at the side film/pore interface. This dependence accounts for the formation of bridges over the pores followed by a smooth growth of continuous film. Using a strain distribution calculated for a model heterostructure of two mismatched layers with pores we estimated the dynamics of bridging and evolution of the crystallisation front.

Use of porous substrates in homo- and hetero-epitaxy allows for significant reduction of elastic stresses near the interface [1]. In particular, it can improve a device performance [2, 3] when the misfit is not very large ( $f_m < 2\%$ ). It is still unclear, however, how promising the porous substrates are for a much more difficult problem of epitaxial growth for large misfits. The solution should be obviously sought in nanoscale range since the critical number of lattice spacing is approximately given by  $f_m^{-1}$ .

In order to estimate the strain distribution in an epitaxial film grown on a mismatched porous substrate one can consider a simple model structure: a thin strip of a finite width  $2l$  on an infinite substrate. Analytical calculations show that the stress relaxation due to the presence of the strip edges is significant when the ratio of the strip width to its thickness  $h$  is small,  $2l/h < 3$  [1, 4]. Moreover, it follows from the theory that a film with small enough lateral dimensions can be grown infinitely thick without appearance of misfit dislocations.

Experiment is in a good agreement with these theoretical predictions, as seen, e.g., from the InGaAs growth on mesa-GaAs [5], GaN growth on porous GaAs [2], 4H-SiC on porous SiC [6], Si on porous Si [7], InP on porous InP [3]. There, however, remains one question: how can a continuous film be formed on the top of the porous layer? One could expect that the pores should be completely filled by the growing material. There is a simple reason why bridges over the pores can be formed faster than the pores are filled. The elastic strain due to the lattice mismatch becomes smaller farther from the interface. This decrease can be estimated as  $\exp(-\pi z/2l)$ , where  $z$  is the height above the interface [1]. One has all grounds to expect that the growth proceeds faster (or slower) where the strain is less, i.e., at the top layers of the film. It naturally leads to bridging over the pores and subsequent formation of a continuous film layer with confined pores underneath.

In this work to clarify situation taking place in or near the significantly mismatched ( $f_m \approx 8\%$ ) hetero interface the results of microscopy investigation of porous GaAs substrates, as well as epitaxial GaSb films grown on them and rigid one are described. The

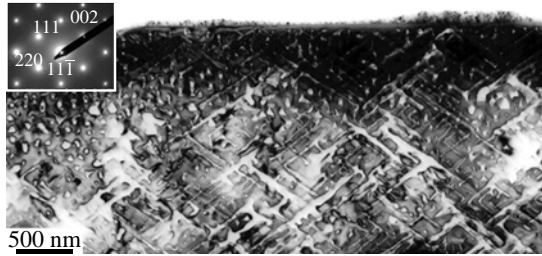


**Fig. 1.** TEM section (110) image of GaAs porous substrate with pore direction along [111]. Inset shows the picture of electron microdiffraction and the reflex indexes.

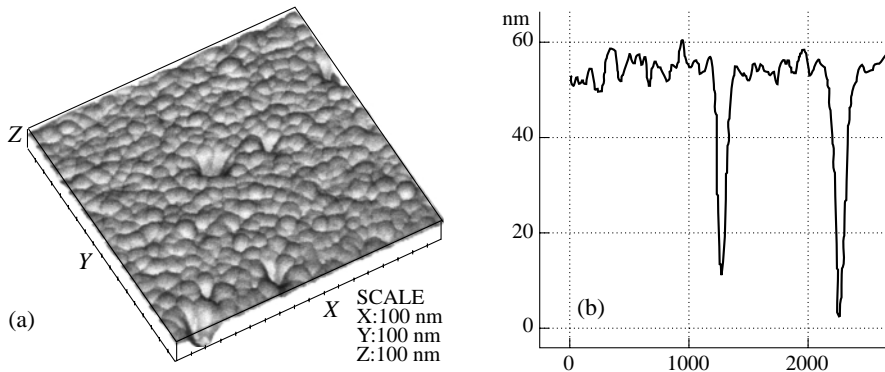


**Fig. 2.** AFM image of GaAs porous substrate surface (100) (a) and surface depth relief (b).

mechanism of bridging over the pores due to a strain dependence of the growth under a constant inflow of atoms from gas or melt is developed.

Porous layers (9–12  $\mu\text{m}$ ) were fabricated by the electrochemical etching of GaAs substrates according technology described in [2, 3]. During pore processing there is anisotropic pore spreading along [111] direction (Fig. 1.) It points at adulteration of antibonding ( $\text{sp}^3$ )\*-lattice atom orbital in forming of transfer complexes while pores arise and spread. They have triangular section and surface cut close to (211). In a polar crystal with sphalerit structure exists two sets from four equivalent directions — [111]A and [111]B. The pores shown in Fig. 1 spread and branch out only along one of them — [111]B. It is seen from Fig. 1 inset that the porouse sample part has only point reflexes. It indicates its monocrystallinity, no-polycrystals and mosaic inclusions there. It is important that surface layer (top black part of Fig. 1) was electrically shunted and participate in electrochemical etching only by forming narrow nanosize inlet holes with density  $\sim 10^7 \text{ cm}^{-2}$ , shown in Fig. 2. Here we can see nanoerosion of the surface, existence nanosize channels and hillocks, that create favorable conditions for mismatched film growth.

Epitaxial GaSb films were grown on described above porous and rigid GaAs substrates by vapor phase epitaxion. Figure 3(a,b,c) demonstrates the images of three samples. By using electron microdiffraction the following misfit values  $f_m$  were determined: (a) 7.4%, (b) 7.0%, (c) 5.8%. The last number is a main technology result of this paper. It means the 22% decreasing of the misfit between epitaxial GaSb films and porous part of GaAs substrate (Fig. 3(c)) in comparison with their rigid part (Fig. 3(a)). It is seen that strain relaxation on the rigid substrate interface accounted for by a big amount of dislocations  $\sim 10^9 \text{ cm}^{-2}$ . Their amount is less in non-optimal situation with big porous (one of them

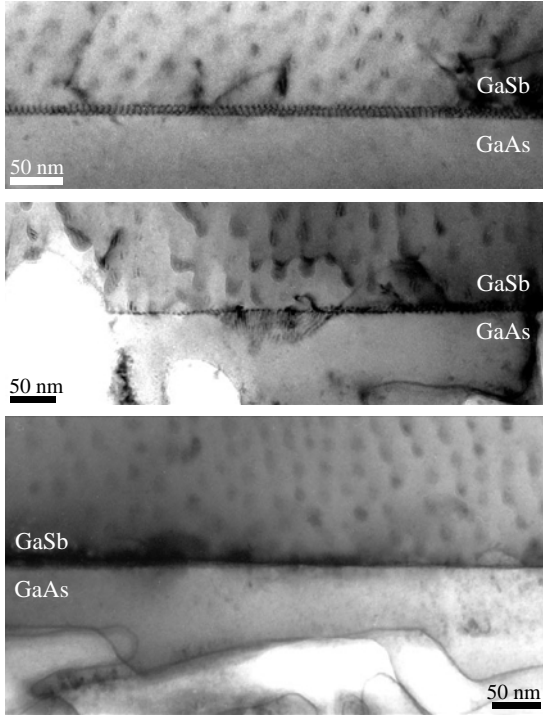


**Fig. 3.** TEM section (110) image of epitaxial structures GaSb/GaAs grown on: (a) rigid substrate, (b) porous substrate with big inlet holes  $\sim 150$  nm and their density  $\sim 10^9$  cm $^{-2}$  and (c) porous substrate with nanoerosion of the surface, little inlet holes  $\sim 20$  nm and their density  $\sim 10^8$  cm $^{-2}$ .

shown in Fig. 3(b)). The dislocations are practically absent on the optimal substrate with nonstructured porous interface (Fig. 3(c).) which shows the maximal decreasing of  $f_m$ .

Let us consider a mechanism of bridging over the pores due to a flow of atoms from the frontal plane to the side surfaces. In this case the crystallization front will obviously be non-uniform. We will use a model of two-component diffusion over the plane with a source, which is accompanied by formation of immobile complexes [8]. We will also take into account a strain dependence of the lateral growth rate at the side film/pore interface. The rate of such growth was found in [9] for a surface with bends separated by distance  $\lambda$ :

$$V \approx \frac{\Delta T}{T} \left( \frac{a}{\lambda} \right)^2 a v \frac{\Delta H}{k T_{ml}} \exp \left( -\frac{\Delta H}{k T_{ml}} \right) \exp \left( -\frac{E}{k T} \right). \quad (1)$$

Here  $\Delta T$  is overcooling at the crystallization front,  $E$  is an energy barrier at the phase boundary,  $\Delta H$  is sublimation heat,  $a$  is the lattice spacing,  $v$  is a phonon frequency ( $v \approx 10^{13}$  s $^{-1}$ ). Using that  $\Delta H \gg E$ , one can assume that the sublimation heat depends linearly on the strain  $\Delta H = \Delta H_0 + A\epsilon$ , where  $A$  is in the range of  $10^0$ – $10^1$  eV [10]. The value of  $\Delta H/kT$  can be in the range 3–20 depending on the materials and on the type and parameters of epitaxial growth. Since the crystallisation front is distorted during the growth,  $\lambda$  will depend on the angle  $\varphi$  between the surface and the crystal axis. For small  $\varphi$ ,

$$\lambda = \left[ 1 - 1/2 (\lambda_0/a)^2 \varphi^2 \right] \lambda_0, \quad (2)$$

where  $\lambda_0$  is a distance between the bends for  $\varphi = 0$  formed due to thermal fluctuations,  $\lambda_0 = a[\exp(\omega/kT) + 2]/2$ ,  $\omega$  is the energy of bend formation. For large  $\varphi$  one has  $\lambda = a \sin \varphi$ . For  $\omega/kT < 0.7$  the surface appears as a set of randomly distributed aggregates.

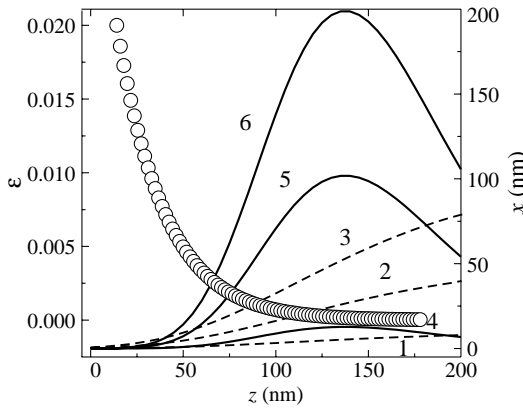


**Fig. 4.** The strain distribution  $\varepsilon$  ( $\circ$ ) and the position of lateral growth fronts at the side film/pore interface: dotted curve 1–3 — in 2, 10 and 30 s after growth start, respectively, for  $a/\lambda = 30$ ; full curve 4–6 — in 2, 4 and 5 s, respectively, taking into account  $\lambda(\varphi)$ -dependency.

For very large  $\omega/kT$ , when the mean free path of atoms becomes smaller than  $\lambda$ , we enter the island-mode of the growth at facets, where Eq. (1) is not applicable.

A strain distribution in a strip of width  $2l$  is calculated within a 2D model by equation

$$\varepsilon = f_m \exp\left(-\frac{\pi \gamma^{1/2} z}{2l}\right) \cos(\pi x/2l). \quad (3)$$

Here  $\gamma = C_{11}/C_{44} \approx 2$ . The last factor in (3) is determined by boundary conditions: zero in-plane strain at the side facets. For the given growth temperature this condition is violated by thermal fluctuations and the sublimation heat dependence on the bulk parameters. One may consider this factor as being close to unity. The strain distribution and the position of lateral growth front were calculated and shown in Fig. 4. The following parameter values were used  $\Delta T/T = 1/30$ ,  $a = 0.6$  nm,  $\Delta H/kT_{ml} = 20$ ,  $A = 25$  eV,  $f_m = 0.1$ ,  $2l = 300$  nm. For  $\varepsilon = 0$  from (1) we can get growth rate  $V = 5$  nm/s. It is seen that the curve 6 (Fig. 4.) quantitatively fits well big porous dome shown the left side of Fig. 3(b). So the strain dependence of the lateral growth rate at the side film/pore interface can really account for the formation of bridges over the pores.

#### Acknowledgements

This work is supported by grants INTAS No 0175wp, Integracija No 0200, RFBR No 010217585, Scientific School No 001599082, No 001596812.

#### References

- [1] S. Luryi and E. Suhir, *Appl. Phys. Lett.* **49**, 140 (1986).
- [2] V. V. Mamutin *et al*, *Pis'ma ZTF* **25**, 3 (1999).
- [3] I. N. Arsentev *et al*, *Pis'ma ZTF* **27**, (2002).
- [4] A. Atkinson *et al*, *J. Appl. Phys.* **77**, 1907 (1995).
- [5] S. Guha *et al*, *Appl. Phys. Lett.* **56**, 2304 (1990).
- [6] M. Mynbaeva *et al*, *Appl. Phys. Lett.* **78**, 117 (2001).
- [7] S. Jin *et al*, *J. Cryst. Growth* **212**, 119 (2000).
- [8] S. V. Byl'jarskij and V. I. Fistyl, *Thermodynamics and Kinetics of Coupling Defects in Semiconductors*, Nauka, M: 1997, 351 p.
- [9] *Sovremennaja Kristallografija* Pt. 3, Ed. by A. A. Chernov *et al*, Nauka, M: 1980, 407 p.
- [10] A. V. Bobyl *et al*, *J. Appl. Phys.* **82** (1274) 1997.

## 2D → 3D growth mode transition through Stranski–Krastanov mode during epitaxial growth

D. V. Brunev, A. N. Karpov, I. G. Neizvestny, *N. L. Shwartz*  
and Z. Sh. Yanovitskaya  
Institute of Semiconductor Physics RAS SB,  
13 pr. Lavrenteva, Novosibirsk, 630090, Russia

**Abstract.** Using a kinetic Monte Carlo model atomic interlayer exchange influence on the Stranski–Krastanov (SK) growth mode was investigated. With the increase of the deposited dose, transition from 2D to 3D growth mode within SK region without changing interlayer exchange and the growth parameters, was observed. Limit parameter values corresponding to 2D → SK and SK → 3D transitions were determined.

During heteroepitaxy in systems with misfit lattices 3D island formation takes place on the wetting layer according to the Stranski-Krastanov (SK) mechanism. In the case of the Ge/Si system 3D islands are formed on the wetting layer with the thickness of 3–5 monolayers (ML) [1–3]. Atomic transitions to the upper layers lead to strain field relaxation. Using a kinetic Monte Carlo model the transition from layer-by-layer to the 3D growth mode during the epitaxial process at various parameters of atomic interlayer exchange was obtained [4]. Simulations were carried out under the assumption that probability  $P_{\text{up}}$  of atom hops from the step edge to the upper layers may be larger than probability  $P_{\text{down}}$  to the lower ones. The phase diagram in coordinates  $P_{\text{up}}-P_{\text{down}}$ , where the SK growth mode separates the 2D growth mode from 3D island formation, was obtained by simulation [4]. The boundaries of SK → 3D and 2D → SK transitions in the phase diagram were determined in present work. 3D growth starts after critical dose deposition. The critical dose depends on interlayer exchange parameters.

The probabilities  $P_{\text{up}}$ ,  $P_{\text{down}}$  control the atomic flows  $N_{\text{up}}$  to the upper atomic layers and  $N_{\text{down}}$  to the lower ones. The ratio  $\eta = N_{\text{up}}/N_{\text{down}}$  depends not only on  $P_{\text{up}}$  and  $P_{\text{down}}$ , but on the island sizes and step perimeter too. The thermodynamic equilibrium for 3D islands was demonstrated to be formed only for  $\eta > 1$ .

The coverage in each atomic layer depending on the monolayer number for different parameters  $\chi = P_{\text{up}}/P_{\text{down}}$  was examined. The coverage in  $(m+1)$  monolayer  $\theta_{m+1}$  at the deposited dose  $\theta = m$  ML was calculated. As can be seen from Fig. 1  $\theta_{m+1}$  is rather low during the 2D growth mode. With increasing  $\chi$  the coverage in  $(m+1)$  layer enhances, as the larger amount of the material transfers to the higher layers from the wetting layer. For some  $\chi = \chi_c$  there is maximum in this dependence, with position independent of  $m$ . The further decrease of  $\theta_{m+1}$  with increasing  $\chi$  is due to upper layers formation, that is typical for 3D growth. In the inserts (Fig. 1) one can see the model surfaces corresponding to the points indicated by arrows. At  $\chi > \chi_c$  compact 3D islands without wetting layer are grown. At  $\chi < \chi_c$  in the initial stage of growth wetting layer formation takes place. At  $\chi = \chi_c$  wetting layer practically disappears. Therefore  $\chi = \chi_c$  was chosen as borderline value, that separates the SK and 3D growth regions.

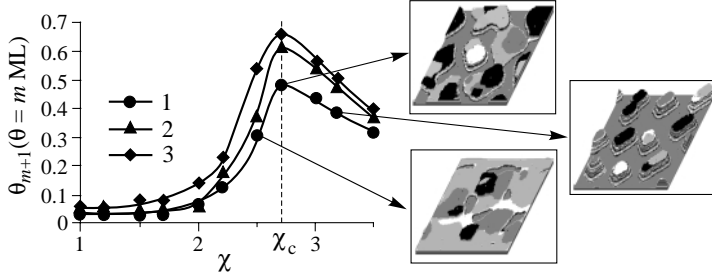


**Fig. 1.** Dependence of coverage in the  $(m + 1)$  layer  $\theta_{m+1}$  after deposition  $\theta = m$  ML on  $\chi$  ( $b = 0.02$ ,  $\lambda = 20$ ): 1 —  $m = 3$ , 2 —  $m = 5$ , 3 —  $m = 9$ . In the inserts: the model surfaces after 3 ML deposition corresponding to points are indicated by arrows.

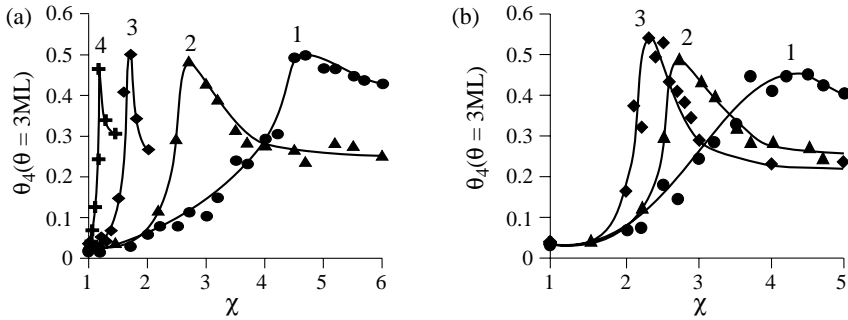


**Fig. 2.** Dependence of coverage in the forth layer  $\theta_4$  after 3 ML deposition on  $\chi$  (a) for different  $b$ : 1 —  $b = 0.01$ , 2 —  $b = 0.02$ , 3 —  $b = 0.04$ , 4 —  $b = 0.08$  ( $\lambda = 20$ ); (b) for different  $\lambda$ : 1 —  $\lambda = 10$ , 2 —  $\lambda = 20$ , 3 —  $\lambda = 25$  ( $b = 0.02$ ).

$\chi_c$  depends on nearest-neighbors binding energy  $E_b$  and adatom diffusion length  $\lambda$  ( $\lambda^4 = D/F$ , where  $D$  is adatom diffusion coefficient,  $F$  is the flux intensity;  $\lambda$  is measured in atomic lattice units). As one can see in Fig. 2(a)  $\chi_c$  increases with decreasing  $b$  ( $b = \exp(-E_b/kT)$ ).

The dependence  $\theta_{m+1}(\chi)$  for given  $b$  and different  $\lambda$  is presented in Fig. 2(b). As  $\lambda$  decreases, maximum is shifted to higher  $\chi$  values. Dependence  $\chi_c(b)$  is due to different atomic hops defining the upward and downward atomic flows. The increase of  $\chi_c$  with decreasing  $\lambda$  is due to higher adatom flux on the surface for lower  $\lambda$  leading to enhance of  $N_{\text{down}}$ . So to sustain a given  $\eta$  value the higher  $\chi$  value is necessary.

The importance of correlation between  $\chi$  and  $\eta$  is evident. The parameter  $\chi$  in the model crystal determines peculiarities of atomic diffusion across the steps, but for relief formation the governing factor is  $\eta = N_{\text{up}}/N_{\text{down}}$  rather than  $\chi$ . Figure 3 demonstrates  $\eta(\chi)$  dependencies for different  $b$  and  $\lambda$  at  $\theta = 3$  ML.

One can see three practically linear portions in  $\eta(\chi)$  dependence with different slopes. The first portion of the curve corresponds to the 2D growth mode with  $\chi > 1$  and  $\eta < 1$ . The second portion, where the slope of the curve increases abruptly, includes the SK region and the region of 3D growth with islands having shape of truncated cone. The third portion corresponds to the 3D growth mode with pointed cone islands. For these  $\chi$  values the slope of the curve again is reduced. Figure 3(b) demonstrates  $\eta(\chi)$  dependence at different  $\lambda$ . Curves are shifted toward higher  $\chi$  with decreasing  $\lambda$ . Such dependence on  $\lambda$  is due to the decrease of average island size at the same coverage. Dotted lines in Fig. 3 indicate area

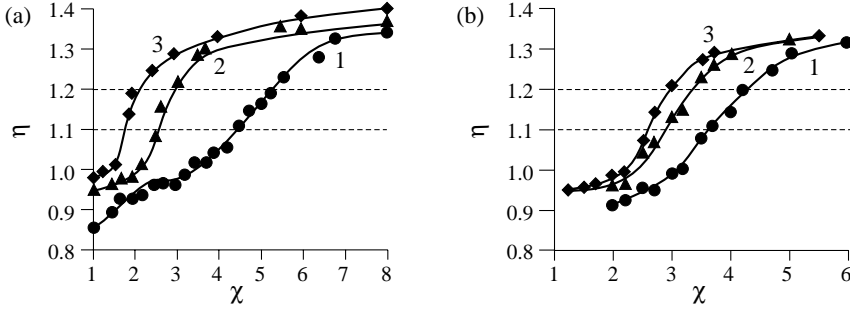


**Fig. 3.**  $\eta$  versus  $\chi$ ,  $\theta = 3$  ML: (a) for different  $b$ : 1 —  $b = 0.01$ , 2 —  $b = 0.02$ , 3 —  $b = 0.04$  ( $\lambda = 20$ ); (b) for different  $\lambda$ : 1 —  $\lambda = 10$ , 2 —  $\lambda = 15$ , 3 —  $\lambda = 20$  ( $b = 0.02$ ). Doted lines restrict area of SK  $\rightarrow$  3D transition.

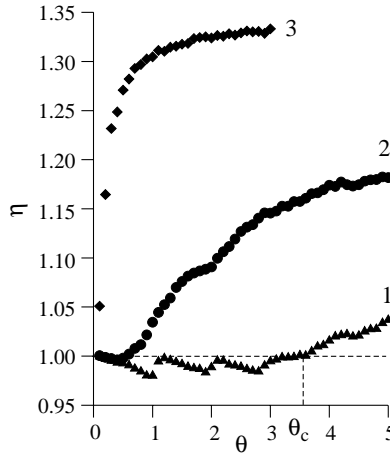


**Fig. 4.** Dependence  $\eta$  on  $\theta$  for different  $\chi$ : 1 —  $\chi < \chi_c$ , 2 —  $\chi = \chi_c$ , 3 —  $\chi > \chi_c$  ( $\lambda = 20$ ,  $b = 0.02$ );  $\theta_c$  — critical dose (at  $\theta > \theta_c$  3D island formation on wetting layer starts).

of parameters where SK  $\rightarrow$  3D transition takes place. As one can see this transition occurs at  $1.1 < \eta < 1.2$  over a wide range of  $b$  and  $\lambda$ .

In SK region the change of growth mode during epitaxy process without changing parameters of growth takes place. Behavior of  $\eta(\theta)$  in SK region ( $1 < \chi < \chi_c$ ) for determination the critical coverage for 3D growth transition was analyzed. In curve 1 (Fig. 4) one can see oscillations with period equals to deposition time of 1 ML. By this is meant that  $\eta$  is defined by distribution of material in the atomic layer rather than by coverage. If the average  $\eta$  value enlarges with increasing coverage and from some  $\theta = \theta_c$ ,  $\eta$  becomes greater unity one can see the transition from the 2D to 3D growth mode. At this moment disappear step density oscillations. The higher  $\chi$ , the earlier this transition takes place (the lower  $\theta_c$ ). As is seen from Fig. 4 for  $\chi = \chi_c$   $\theta_c < 1$  ML, and for  $\chi > \chi_c$   $\theta_c \ll 1$  ML.

The experimental criteria for 2D  $\rightarrow$  3D transition during the deposition process is RHEED oscillations breakdown [1, 2]. Experimental observation reveals that this transition takes place during 1 ML deposition [1, 3]. In the model experiments step density oscillation breakdown was observed, however 2D  $\rightarrow$  3D growth transition is smoother. The model

situation was distinct from the experimental one, as in simulation we didn't assume variation of  $\chi$  during the growth process that could take into account strain field increase with enlarging of wetting layer depth. The transition from 2D to SK growth mode occurs at  $\chi = 1$ . For  $\chi < 1$  at any  $b$ ,  $\lambda$  and  $\theta$  the 2D growth mode is realized.

The nature of predominant upward flow during heteroepitaxial growth could be due not only to strain fields, but for instance to different chemistry of the substrate and adsorbate, the presence of surfactants on the surface.

Using simulation influence of interlayer atomic exchange on the SK region width was investigated. The parameter values corresponding to  $2D \rightarrow SK$  and  $SK \rightarrow 3D$  transitions were determined. In the SK region transition from 2D to 3D growth mode at some coverage  $\theta = \theta_c$  was observed without variation of interlayer exchange and growth parameters.

#### *Acknowledgements*

This work was supported by the Russian Foundation for Basic Research and the Federal Target-Orientated Program "Investigation and development of prospective science and technology lines for civil purposes".

#### **References**

- [1] V. A. Markov, H. H. Cheng, Chih-ta Chia, A. I. Nikiforov, V. A. Cherepanov, O. P. Pchelyakov, K. S. Zhuravlev, A. V. Talochkin, E. McDlynn and M. O. Henry, *Thin Solid Films* **369**, 79 (2000).
- [2] R. Koch, G. Wedler, J. J. Schulz and B. Wassermann, *Phys. Rev. Lett.* **87**, 136104 (2001).
- [3] B. Voigtlander, *Surf. Science Rep.* **43**, 127 (2001).
- [4] D. V. Brunev, I. G. Neizvestny, N. L. Shwartz and Z. Sh. Yanovitskaya, *Nanotechnology* **12**, 413 (2001).



## Pore sealing during epitaxy and annealing on Si(001) surface

A. V. Chemakin, I. G. Neizvestny, *N. L. Shwartz*,  
Z. Sh. Yanovitskaja and A. V. Zverev

Institute of Semiconductor Physics RAS SB,  
13 pr.Lavrenteva, Novosibirsk, 630090, Russia

**Abstract.** Using 3D Monte Carlo model evolution of Si(001) surface during epitaxy and high temperature annealing was investigated. The surface relief in the form of pyramidal pits is developed in the wide range of deposition rate. This relief prevents simultaneous creation of flat surface and thin solid layer formation over pores on Si(001) surface. Critical dose on (001) surface at the same deposition rates and temperatures was found to be an order of magnitude larger than on (111) surface.

3D Monte Carlo model of epitaxy and annealing on (001) and (111) surfaces of diamond-like crystal was used for simulation of homoepitaxy process on porous Si surfaces. Our 3D-model includes possibility to watch hops of tracer atoms and groups of atoms. Simulation was performed giving estimation of surface morphology and necessary dose for complete pores sealing (critical dose). Simulations were carried out in the ranges of substrate parameters and regime of growth according to experimental work [1]. Pores were perpendicular to the surface with the density approximately equal  $10^{10} - 10^{12} \text{ cm}^{-2}$ . Pores diameter was varied from 2.7 to 20 nm and pores depth achieved 50 nm, deposition rate  $V = 0 - 1.3 \text{ nm/s}$ .

Simulation of pores sealing on Si(111) was carried out in [2–3]. The present work is devoted to Si(001) porous surface. Porous Si(001) surface was found to be rough after epitaxy as against of Si(111) being practically flat. The critical dose dependencies on deposition rate, pore diameter and porosity were obtained. Surface relief and reasons of it development were investigated.

Figure 1 demonstrates evolution of surface relief on porous Si(001) during epitaxy. Long before sealing at pore edges (111) facets start to form. At further deposition these facets are enlarged. Formation of these facets is due to higher diffusivity along (111) surface than along (001) one, as for diamond-like crystal (111) surface is the face with minimal free energy [4]. Owing to high mobility atoms impinged from the flux on these facets reach their edges and attach them creating additional bond. As surface reconstructions couldn't be considered by lattice models, adatom diffusion along (111) surface is higher than along (001) surface. Such situation is close to reality as on rough porous Si(001) surfaces there are no dimer rows. Facet formation results in slow pore sealing as sealing is realized through monolayer growing on these facets. Most of deposited material therewith goes to creation "ridges" round external edge of the pit forming on the surface, rather than to pore sealing. At the moment of complete pore sealing the pit represents regular quadrangular pyramid, that is well seen in Fig. 1(b,c). During further deposition thickness of the solid layer over the pore increases, but pits and "ridges" around pore are smoothing slowly (Fig. 1(d)). Without overlapping pit linear sizes with high accuracy are proportional to pore diameter.

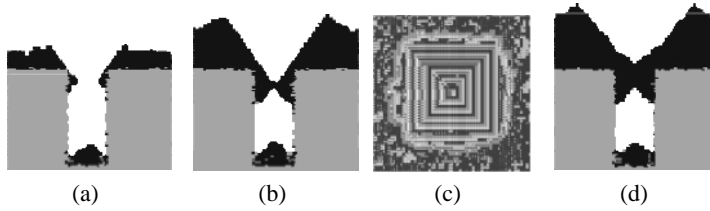


**Fig. 1.** Kinetics of pore sealing on Si(001) surface during homoepitaxy at  $T = 800$  K, deposition rate 2 monolayer per second (ML/s), pore diameter 5 nm, pore initial depth 25 nm. Pore cross-sections after deposition: (a) 15 ML; (b) 37 ML, (d) 48 ML (substrate material is marked in gray and deposited material in black) and (c) top view after deposition 37 ML.

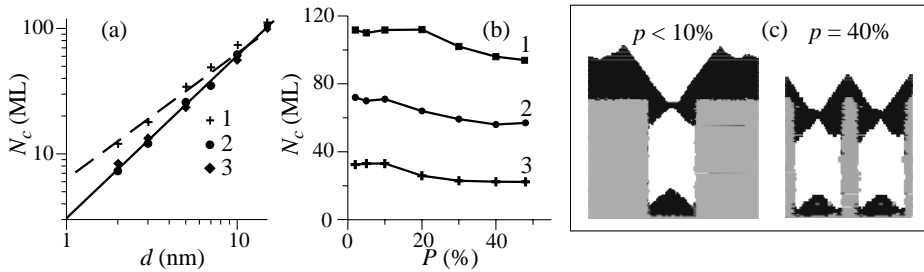


**Fig. 2.** Critical dose dependence  $N_c$  (a) on diameter  $d$  (1 —  $P = 10\%$ , 2 —  $P = 25\%$ , 3 —  $P = 48\%$ ) dashed line —  $N_c \sim d$ , solid line —  $N_c \sim d^{4/3}$ ; (b) on porosity  $P$  (1 —  $d = 20$  nm, 2 —  $d = 10$  nm, 3 —  $d = 5$  nm); (c) surface cross-sections at the moment of pore sealing.

In log-log scale critical dose  $N_c$  dependence on pore diameter  $d$  for three porosity is presented in Fig. 2(a). At low porosity ( $< 10\%$ ) this dependence is linear, and at higher porosity  $N_c \sim d^{4/3}$ . In Fig. 2(b) critical dose dependence on porosity for three pore diameters is shown. One can see two regions: without dependence on porosity for  $P < 10\%$  and with dependence for  $P > 40\%$ . Exponent change in  $N_c(d)$  dependence in Fig. 2(a) corresponds to transition between these two regions. Figure 2(c) demonstrates two different solid layer morphologies over pore. For low porosity pits over pores are not overlapped but for high porosity overlapping becomes essential. For low porosity critical dose is higher. Over a wide range of porous surface parameters and growth conditions geometric figure forming from deposited material in the pore mouth has the same shape, thus its volume  $V_p \sim d^3$ . Linear dependence  $N_c(d)$  can be explained as follows: due to linear dependence of pyramidal pit sizes on pore diameter dependence of facets area, where from material for three-dimensional figure overlapping pore is gathered, is square. Thus figure volume over pore at the moment of sealing:  $V_p \sim t_c d^2$ , where  $t_c$  — time necessary for pore sealing  $t_c = N_c/V$ ,  $V$  — deposition rate. On this basis one results  $N_c \sim d$ . With porosity increasing distance between pores decreases and pits over neighbor pore meet (Fig. 2(c)). Facet size is dependent on porosity in this case and more complex dependence on pore diameter arises ( $N_c \sim d^{4/3}$ ). Figure 2(b) represents critical dose dependence on porosity for different pore diameters. At low porosity critical dose is independent of porosity. Only after reaching some critical porosity when “ridges” around neighbor pores start to couple dependence  $N_c$  on porosity is noticeable. The decrease of critical dose with increasing porosity is associated with decreasing of material amount between pores.

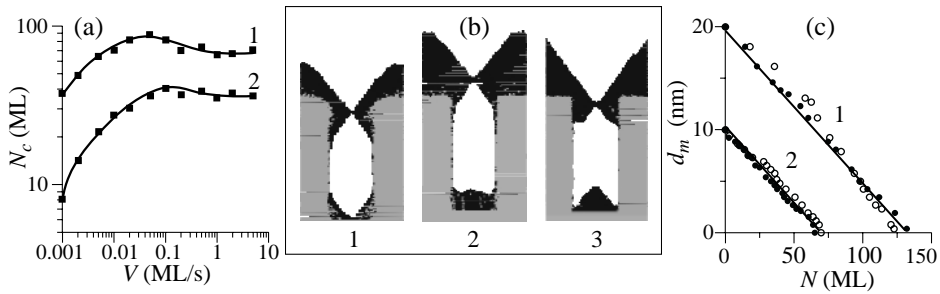


**Fig. 3.** (a)  $N_c$  versus  $V$  (1 —  $d = 10$  nm, 2 —  $d = 5$  nm); (b) pore cross-section ( $d = 10$  nm, depth  $h = 25$  nm) for different deposition rates (1 —  $V = 0.001$  ML/s, 2 —  $V = 0.05$  ML/s, 3 —  $V = 1$  ML/s); (c) dependence of pore mouth diameter  $d_m$  on deposited dose  $N$  for different values of initial pore diameters (1 —  $d = 20$  nm, 2 —  $d = 10$  nm) (hole circles —  $V = 0.2$  ML/s, solid circles —  $V = 2$  ML/s).

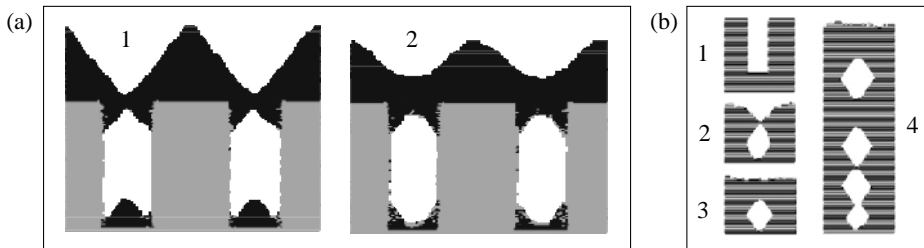


**Fig. 4.** Pores cross-sections during high temperature annealing process at  $T = 1400$  K: (a) 1 — after critical dose deposition, 2 — the same surface after annealing during 3 seconds; (b) annealing of shallow pore (1, 2, 3 —  $d = 3$  nm,  $h/d = 3$ ): 1 — before annealing, 2 — after  $t = 4$  ms annealing (the moment of pore sealing), 3 — after  $t = 14.4$  ms annealing; 4 — deep pore ( $h/d = 12$ ) after 500 ms annealing.

Figure 2(c) demonstrates pore cross-section at the moment of pore sealing. As is evident from Fig. 2(c) amount of deposited material in the pore for low porosity is greater than for high porosity, as in the first case disproportional enhancement of material between pores takes place.

In Fig. 3(a) critical dose dependence on deposition rate  $V$  for different pore diameters is shown. At low deposition rate atoms of initial substrate are of considerable importance in pore sealing. As deposition rate increases, movement of substrate atoms is of no importance and critical dose enhances with  $V$  increasing. Some following decrease of critical dose with deposition rate increasing is due to reduction of atomic flow through pore mouth. Figure 3(b) demonstrates pore cross-section for three deposition rates: to the left of maximum in the curve in Fig. 3(a), in the maximum and to the right of it. Figure 3(c) shows variation of size of pore mouth during pore sealing. If one plots  $d_m$  versus deposited dose  $N$ , then  $d_m = d - kN$  and rate of pore mouth overlapping  $k$  is independent neither of initial diameter, nor of deposition rate.

Figure 4 demonstrates porous surface evolution during high temperature annealing process at  $T = 1400$  K. Such temperature is certainly higher than annealing temperature in experiments. We have chosen such temperature to watch surface relief evolution within

short modeling time. The tendency of model relief evolution adequately reflects slower morphology evolution at lower temperatures. Figure 4(a) demonstrates smoothing of the surface relief created after deposition process during high temperature annealing. Relief smoothing is only outlined (3 seconds annealing at  $T = 1400$  K corresponds approximately to  $10^6$  seconds at  $T = 800$  K). Figure 4(b) presents kinetics of shallow pore sealing (1,2,3) and demonstrates deep pore fragmentation during annealing (4). Similar simulation results were obtained during annealing of porous Si(111) surfaces [3].

#### *Acknowledgements*

This work was supported by the Russian Foundation for Basic Research and the Federal Target-Orientated Program "Investigation and development of prospective science and technology lines for civil purposes".

#### **References**

- [1] S. I. Romanov, V. I. Mashanov, L. V. Sokolov, A. Gutakovski and O. P. Pchelyakov, *Appl. Phys. Lett.* **75**, 4118 (1999).
- [2] A. V. Zverev, I. G. Neizvestny, N. L. Schwartz and Z. Sh. Yanovitskaya, *Izvestija AN, Physical series* **65**, 192 (2001) (in Russian).
- [3] A. V. Zverev, I. G. Neizvestny, N. L. Shvarts and Z. Sh. Yanovitskaya, *Semiconductors* **35**, 1022 (2001).
- [4] A. A. Chernov *et al*, *Modern Crystallography, Crystal Growth*, vol. 3, M.: Nauka, 1980.

## Size/shape selective epitaxial overgrowth of nanocrystalline lead sulfide

*M. J. Fernée, J. Warner, A. Watt and H. Rubunsztein-Dunlop*

Centre for laser science, Dept. of Physics, University of Queensland,  
Qld., Australia, 4072

**Abstract.** We have developed a technique for photoluminescence activation of colloidal solutions of lead sulfide (PbS) nanocrystallites using epitaxial overgrowth of cadmium sulfide (CdS). The photoluminescence excitation spectrum reveals a substantial increase in spectral detail compared to the absorption spectrum, including a well defined band-edge and a previously unobserved excited state. From measurements of the band-edge we find an extremely narrow size distribution of less than 4%, which is significantly narrower than the original PbS nanocrystallite distribution. This luminescent sub-ensemble exhibits significant above-band-edge emission, which is one characteristic of a strongly quantised system where efficient energy transfer to the band-edge is restricted due to "phonon bottleneck".

### Introduction

Strong quantum confinement, which gives rise to discreet atomic-like electronic energy levels in semiconductor quantum dots (QD's), should suppress intra-band energy relaxation due to phonon interactions if the level spacings are significantly greater than individual phonon energies [1, 2]. However, this "phonon bottleneck" is not readily observed in QD's [3]. PbS is an excellent candidate for observing "phonon bottleneck" due to strong quantum confinement of both electrons and holes [4]. Band-edge shifts of up to 1.6 eV are easily achieved in nanocrystals of around 2 nm diameter. Such QD colloidal solutions have strong transitions in the visible and UV spectrum [4].

### 1. Results

Epitaxial overgrowth of cadmium sulfide (CdS) (a wide band-gap semiconductor) is used for passivating the surface trap states in PbS QD's. The overgrowth is carried out in aqueous solution under conditions unsuitable for individual CdS nanocrystallite growth [5]. After the CdS growth phase, we find strong visible photoluminescence from the solution when irradiated with a UV lamp. The solutions are then mixed with a polymer and dried into thin films.

In Figure 1 we present both photoluminescence (PL) and photoluminescent excitation (PLE) spectra of a PbS/CdS nanocrystallite film. From the PLE spectrum we identify the band-edge at approximately 1.95 eV as well as a previously unobserved state near 2.2 eV. The upper figure shows a higher resolution scan of the band-edge with an associated Gaussian fit. We use the FWHM of the Gaussian to estimate the size distribution of the luminescent nanocrystallites as less than 4%, which is as narrow as the most monodisperse samples of nanocrystallites yet produced [6]. Furthermore, we find that this distribution broadens at room temperature to approximately 80 meV, indicating some residual homogeneous acoustic phonon broadening.

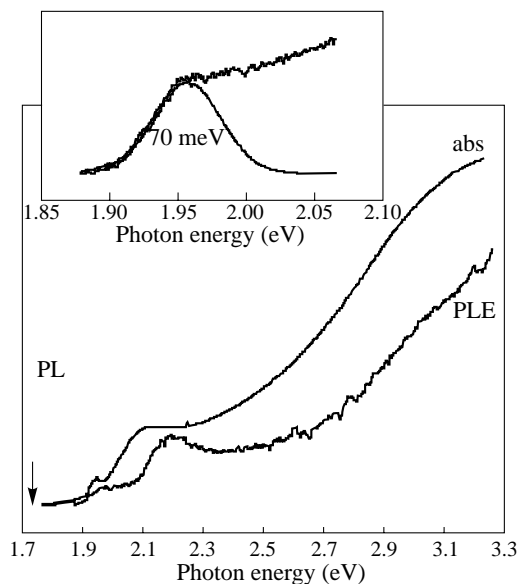


**Fig. 1.** PLE and PL and absorption scans of a polymer film containing PbS/CdS core/shell nanocrystallites. The arrows indicate the excitation and monitoring energies for the PL and PLE scans respectively. The upper plot represents a high resolution PLE scan of the band-edge region with an associated gaussian fit. The PL and PLE data were taken at 77 K.

The bulk absorption spectrum is also included in Fig. 1 for comparison with the PLE spectrum. From TEM images, a PbS size dispersion of approximately 10% has been deduced. This then illustrates the size selectivity of the overcoating process. However, the over coated nanocrystallites are clearly visible in the TEM images as a much smaller ensemble, suggesting that shape selectivity is also occurring. We suggest that this process results from the mismatch in crystal types between PbS and CdS, whereby CdS can only form a good epitaxial coating on PbS nanocrystallites with appropriately terminated [111] surfaces. During the synthesis, we encourage the growth of sulfur terminated [111] surfaces by injection of slight excess of  $\text{H}_2\text{S}$ , thereby increasing the luminescence of the colloid.

Such a size/shape selectivity has never before been reported and is potentially useful for the preparation of nearly identical nanocrystallites for further nanotechnological applications. As the overcoated nanocrystallites have both a different size and chemical surface compared to the remaining uncoated nanocrystallites, it should be possible to separate and purify the overcoated nanocrystallites.

Significant above-band-edge emission is illustrated in Fig. 2 for a range of excitation energies ranging from the near UV at 380 nm to blue (460 nm) in 10 nm steps. We also include a PLE curve monitoring the above-band-edge emission at 2.2 eV, indicating the extremely sharp cut-off in energy transfer. The nature of this energy transfer has also been probed using 2-photon spectroscopy, where we find a significantly reduced above-band-edge contribution to the PL while retaining a strong band-edge contribution. In both cases the energy transfer is either strongly dependent on the photon energy or excited state symmetry. This type of behaviour is characteristic of state-symmetry dependent radiative energy transfer or “phonon bottleneck”. Other results using polarization spectroscopy also support this, indicating that the excited states near 2.2 eV have opposite symmetry to those near the band-edge at 1.95 eV. This also provides direct evidence that energy relaxation

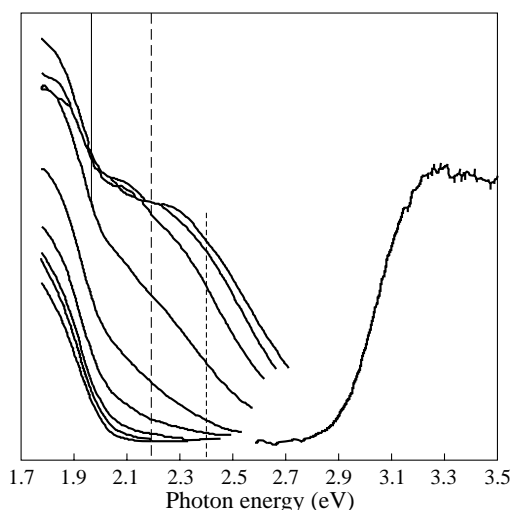


**Fig. 2.** Series of PL scans of a polymer film containing PbS/CdS core/shell nanocrystallites, taken at 77 K. The data are taken with the excitation source varied from 380 nm to 460 nm in 10 nm steps. On the right of the graph is a PLE scan monitoring the above-band-edge emission near 2.2 eV. A solid line indicates the band-edge near 1.95 eV, a dashed line indicates the excited state near 2.2 eV and a dotted line indicates the CdS bulk band-edge.

preserving the state-symmetry in this system, even at room temperature. Such processes are characteristic of atomic systems, suggesting possible use for PbS/CdS nanocrystallites as an artificial atom for use in emerging quantum technologies.

## References

- [1] U. Bockelmann and G. Bastard, *Phys. Rev. B* **42** 8947 (1990).
- [2] R. Heitz *et al*, *Phys. Rev. B* **64** 241305 (2001).
- [3] V. Klimov and D. W. McBranch, *Phys. Rev. Lett.* **80** 4028 (1998).
- [4] I. Kang and F. W. Wise, *J. Opt. Soc. Am. B* **14** 1632 (1997).
- [5] A. Mews, V. Kadavanich, U Banin and A. P. Alivisatos, *Phys. Rev. B* **53** R13242 (1996).
- [6] C. R. Kagan, C. B. Murray and M. G. Bawendi, *Phys. Rev. B* **54** 8633 (1996).

## The impact of charge state on catalytic activity of metallic nanostructures

V. M. Kozhevnikov<sup>†</sup>, D. A. Yavsin<sup>†</sup>, M. A. Zabelin<sup>†</sup>, S. A. Gurevich<sup>†</sup>,  
I. N. Yassievich<sup>†</sup>, T. N. Rostovshchikova<sup>‡</sup> and V. V. Smirnov<sup>‡</sup>

<sup>†</sup> Ioffe Physico-Technical Institute, St Petersburg, Russia

<sup>‡</sup> Chemistry Department, Moscow State University

**Abstract.** We report on ultra-high catalytic activity of metallic structures consisting of densely packed assemblies of nano-size metallic (Cu) granules. These nanostructures are fabricated by a new method of laser electrodispersion. The major results on experimental studies of catalytic activity of Cu nanostructures are presented by the example of dichlorobutene isomerization. The observed high catalytic activity of granulated Cu nanostructure is explained by the presence of charges appeared at the granules due to thermally activated inter-granule electron tunneling. The charge state of the structure is analyzed by using newly developed Monte-Carlo model.

### 1. Introduction

Metal-based catalysts are widely used in oil refining, toxic exhaust decomposition, new material synthesis, etc. In modern catalysis the major tendency consists in diminishing the sizes of a metallic particles, which provides the enhancement of the reaction rate [1]. This enhancement is usually associated with increased density of the reaction activation centers at the surface of small metallic particles. In this area the main problem is associated with creating the catalyst structures comprising nanometer particles of well-defined size, having identical chemical properties. In common structures, wide size dispersion and related variations of the particle surface properties lead to drastic decrease of catalyst selectivity because the rate and even the direction of catalytic reaction may be strongly affected by the size of catalyst particle. Recently it was proposed to use a method of laser electrodispersion for controllable fabrication of monodisperse metallic nanostructures [2]. The method is based on laser ablation of Cu target with subsequent cascade fission of liquid metallic droplets ejected from the target. The experiments performed with these structures have shown that they possess extremely high catalytic activity, which can not be attributed to only small granule sizes and narrow size dispersion. In this paper we suggest that the observed extraordinary catalytic activity can be explained by specific charge state of densely packed assembly of granules appearing due to inter-granule electron tunneling.

### 2. Metallic nanostructures fabricated by laser electrodispersion

The method of nanostructure fabrication is based on laser ablation of metallic (Cu) target. In this process liquid metallic drops of sub-micron size are first splashed from the target. Being charged in the laser torch plasma the drops became to be unstable due to capillary instability [3] and then brake up in cascade way [4] so that the flux of charged nanometer size droplets (5 nm in diameter) is produced. Nanometer size droplets having narrow size dispersion are forced to the substrate by the electric field. The deposited structure is self-assembled in a densely packed layer(s) due to Coulomb interaction of charged particles at the substrate surface (quartz or thermally oxidized Si). Finally the structure is oxidized



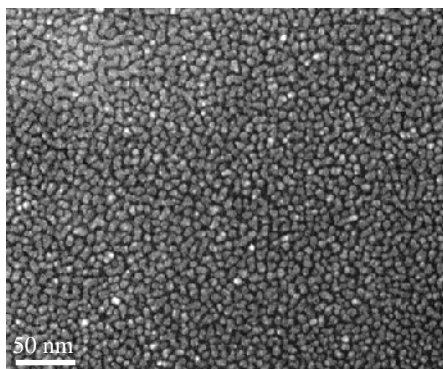
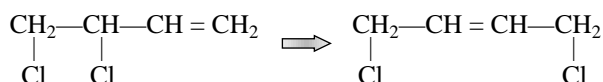


**Fig. 1.** TEM image of the granulated film deposited during 10 min.

in ambient atmosphere and as a result each granule is covered by about 1 nm thick  $\text{Cu}_2\text{O}$  shell. Figure 1 shows TEM view of the fabricated nanostructure.

### 3. Experiments on dichlorobutene isomerization by Cu nanostructures

In the experiments the reaction of dichlorobutene isomerization was studied which is catalyzed by Cu. This reaction is described by the following formula:



The rate of reaction product formation was measured and this rate was compared with those known from the literature for other advanced Cu-based catalysts [5]. The results are presented in Fig. 2 where the bottom symbols denote the technology of catalyst formation. One can see the superior catalytic activity of nanostructure produced by laser electrodispersion.

The hypothesis of the role of charge state in provision of high catalytic activity of nanometer size metallic granules has been suggested in [5]. This idea is further developed in our experiments in which the surface density of granules (deposition time) as well as

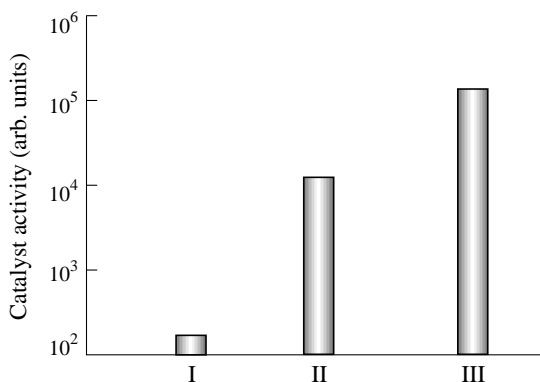


**Fig. 2.** Comparison of catalytic activities of different catalysts. I — catalyst fabricated by impregnation of Cu with the salt solution with further disoxidation, II — Cu nanostructures formed by condensation of Cu vapor and monomer under the low temperature condition, III — Cu nanostructure formed by laser electrodispersion.

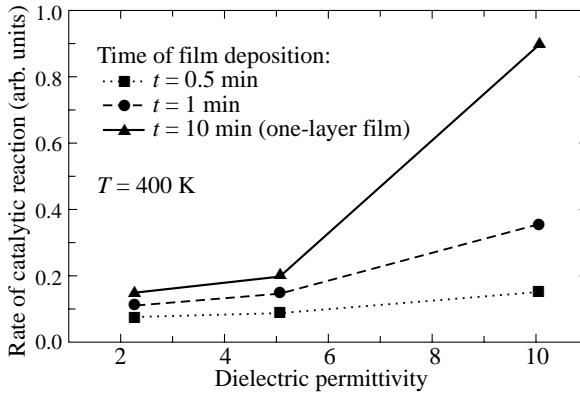


**Fig. 3.** Reaction rate vs. dielectric permittivity of the reaction solution.

dielectric permittivity of the solution was intentionally varied in order to control the charge state of the metallic nanostructure. The results of these experiments are presented in Fig. 3. The curve labeled by  $t = 0.5$  min corresponds to the structure with rear-standing Cu granules in which the gaps between particles is at least 4 nm such that the electron exchange between the granules is highly improbable. Contrary to this the curve  $t = 10$  min corresponds to the film consisting of one densely-packed layer of granules (see Fig. 2). As it is discussed below in this case a lot of granules are charged owing to thermally activated electron tunneling. It is also important that in densely-packed granulated structures the value of average charge and charge density increase with the permittivity of the solution in which the reaction takes place. This follows from the fact that charging energy and activation energy for the electron hops between the granules are inversely proportional to the dielectric permittivity of the medium. Thus, the results shown in Fig. 3 manifest that charge generation results in strongly increased catalytic activity of nanostructure.

#### 4. Discussion

The charge state of the granulated structure was examined by means of Monte-Carlo model in which thermally activated inter-granule electron hops are accomplished according to the transition probability calculated from the potential distribution in the system of granules. This potential distribution is calculated before and after each electron hope accounting for the charge state of all granules. The simulations were performed for the structures consisting of one layer of granules assuming that they are densely packed so that the time for establishing the equilibrium of charge distribution is much less than the characteristic time of catalytic reaction. In calculations the variable parameters were granule size and density as well as the temperature and permittivity of the solution. Shown in Fig. 4 are the calculated densities of differently charged granules vs. the dielectric permittivity of the medium. As indicated in this figure the number of charged grains is growing up with increasing of dielectric permittivity. One can relate this increasing charge density with the enhancement of catalytic activity presented in Fig. 3 by the curve  $t = 10$  min. The experimental results can be best fitted by using the following relation:

$$R \propto n_0 + n_1 + 4n_2 + 200n_3 \quad (1)$$

where  $R$  is the reaction rate,  $n_q$  are the relative densities of granules with the charges  $|q| = 0, 1, 2, 3$  (measured in elementary electron charge). The densities  $n_q$  are taken from

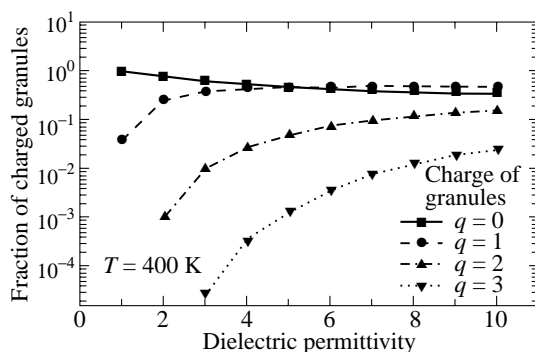


**Fig. 4.** Fraction of charged granules vs. dielectric permittivity of the reaction solution.

the data of Fig. 4. As one can see from the above expression the values of coefficients standing in front of  $n_q$  are strongly increasing with the granule charge. This means that the more is the granule charge the higher is catalytic activity of the granule. Obviously the sign of the charge is also of importance because the reaction involves both the excitation of the reagent molecule by electron attachment and further quenching the excitation by electron detachment. The appearance of negative charge at the granule offers considerable transformation of the tunnel barrier, which electron should surpass in order to be trapped by the molecule, and owing to this the probability of the molecule excitation is strongly increased. Contrary to this at the positively charged granule the probability of electron detachment from the molecule to the granule is increased.

The simulations show that the considered structure is characterized by essential correlation of neighboring charges so that these charges form dipoles. The reason is the dipole arrangement is energetically preferable. It is believed that the formation of the dipoles may also be important in providing high catalytic activity. This idea is supported by simple estimation, which shows that mean displacement of the exited molecule moving with thermal velocity is comparable with the average inter-granular gap in dense structures. Thus, the molecule can be easily exited at the negatively charged side of dipole and then the excitation can be quenched at the positively charged granule.

Summing up, we propose that the appearance of spontaneously generated charges in dense granulated metal structures leads to their extremely high catalytic activity.

#### Acknowledgements

This work was supported by RFBR, grants 01-02-17827 and 02-03-32609.

#### References

- [1] B. C. Gates, *Chem. Rev.* **95**, 511 (1995).
- [2] V. M. Kozhevnikov, D. A. Yavsin, V. M. Kouznetsov, V. M. Busov, V. M. Mikushkin, S. Yu. Nikonov, S. A. Gurevich and A. Kolobov, *JVST B* **18**, 1402 (2000).
- [3] J. W. S. Rayleigh, *Philos. Mag.* **14**, 184 (1882).
- [4] A. I. Grigor'ev, S. O. Shiryaeva and S. S. Verbitskii, *J. Coll. Interface Sci.* **146**, 137 (1990).
- [5] P. S. Vorontsov, E. I. Grigir'ev, S. A. Zav'yalov, L. M. Zav'yalova, T. N. Rostovschikova and O. V. Zagorskaya, *Chem. Phys.* **21**, 1 (2002).

## The carriers localization influence on the optical properties of GaAsN/GaAs heterostructures grown by molecular-beam epitaxy

*N. V. Kryzhanovskaya*<sup>†</sup>, *A. G. Gladyshev*<sup>†</sup>, *D. S. Sizov*<sup>†</sup>, *A. R. Kovsh*<sup>†</sup>,  
*A. F. Tsatsul'nikov*<sup>†</sup>, *J. Y. Chi*<sup>‡</sup>, *J. S. Wang*<sup>‡</sup>, *L. Wei*<sup>‡</sup> and *V. M. Ustinov*<sup>†</sup>

<sup>†</sup> Ioffe Physico-Technical Institute, St Petersburg, Russia

<sup>‡</sup> Industrial Technology Research Institute, Hsinchu 310, Taiwan, R.O.C.

**Abstract.** Optical properties of GaAsN/GaAs heterostructures with different N contents grown by molecular-beam epitaxy were investigated. We show that under the certain grows regimes the optical properties of the GaAsN layers are determined by recombination via localized states which is due to composition fluctuation. An increase in the N concentration leads to increase in composition fluctuation and, correspondingly, to increase in energy of localized states. Thermal annealing reduces nonuniformity distribution of nitrogen atoms. In short-period GaAsN/GaAs superlattice the effects of phase separation can be enhanced.

### Introduction

In the past few years Ga(In)AsN/GaAs has been one of the most interesting system due to its large optical bowing coefficient. A possibility to vary the band gap of this alloy over a wide range makes it very attractive in application for lasers, operating in the near infrared range. Ga(In)AsN combined with GaAs is promising to overcome the poor temperature stability of characteristics of conventional GaInAsP/InP based lasers due to the high electron confinement as a result of the large conduction band offset [1]. Moreover GaAs/AlAs distributed Bragg reflectors can be easily grown on a GaAs substrate and GaAsInN based for vertical cavity surface-emitting lasers were fabricated [2]. In this work we investigated optical properties of different types of samples 0.2  $\mu\text{m}$  thick GaAsN layers in GaAs matrix with varied content of N, short-period superlattice GaAs<sub>0.95</sub>N<sub>0.05</sub>/GaAs (0.4 nm/1.2 nm) and 0.1  $\mu\text{m}$  thick GaAs<sub>0.998</sub>N<sub>0.012</sub> layer formed by periodical nitridization of thin 1.2 nm GaAs insertions. Peculiarity of the growth of GaAsN caused by the large difference between the radii of As and N atoms leads to phase separation even in the case of a few percent of nitrogen. It was shown that optical properties of GaAsN quantum wells (QW) are determined by recombination via localized states resulting from thickness modulation of QW [3, 4] and composition fluctuation (phase separation) [5].

### Experiment

The samples under investigation were grown in a Riber Epineat machine with solid sells for group III elements and arsenic and UNI Bulb RF Plasma Source (Applied EPI) for nitrogen. The nitrogen concentration of the samples and crystal quality were evaluated by x-ray diffraction. Photoluminescence was excited by Ar<sup>+</sup> laser ( $\lambda \sim 514.5$  nm,  $P \sim 100$  W/cm<sup>2</sup>) or pulsed N<sub>2</sub> laser ( $\lambda \sim 312$  nm,  $P \sim 100$  kW/cm<sup>2</sup>). Transmission spectra were recorded under quartz-halogen bulb excitation. Resulting photoluminescence (PL) was detected with a cooled Ge photodiode.

## Result and discussion

Figure 1 show PL spectra of 2.0  $\mu\text{m}$  thick GaAsN layers with different N content for different temperatures. At the low temperatures only one peak ( $E_2$ ) was revealed in the PL spectra. Increase in temperature leads to appearance PL line denoted as  $E_1$ , which become dominating at room temperature. Maximum of the line is blue-shifted relatively  $E_2$ . Such behavior of PL spectra is typical for localized states caused by fluctuation in localization energy. At low temperatures all low-energy states are occupied. Increase in temperature results in activation of carriers and exited states are occupied. This leads to arising of  $E_1$  line in the PL spectrum.

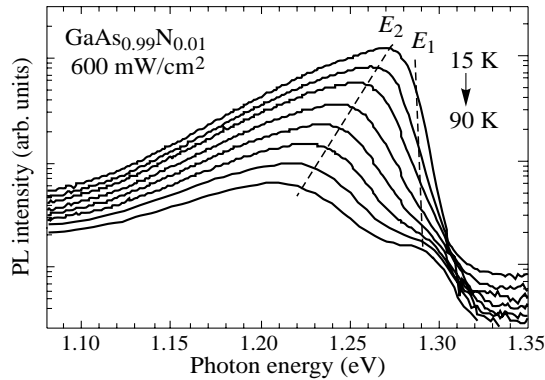


**Fig. 1.** PL spectra of sample  $\text{GaAs}_{0.99}\text{N}_{0.01}$  for different temperatures.

With further increasing of temperature the intensity  $E_2$  line is decreased and at room temperature there is only one peak  $E_1$ . This fact displays that at high temperatures recombination originates from localized centers having smaller energy of localization ( $E_1$ ), whose density is higher, obviously. The temperature dependences confirms, that temperature changing of shape of PL spectra is due to carriers redistribution between localized states. To investigate effect of N content on the localization of carriers comparison of PL and transmission spectra was carried out. Figure 2 shows temperature dependence of PL maxima and edge of transmission. It can be seen that point of intersection dependencies of PL maxima and edge of transmission shifts towards higher temperature with increasing of N content. So, one can conclude, that emission comes via the localized states up to room temperature for the sample with 1.3% of N content. Increasing in N content from 0.6% till 1.3% results in increasing of Stokes shift from 14 till 43 meV (inset in Fig. 2) at low temperature. Stokes shift is determined as energy space between absorption edge and maximum of PL spectra.

We applied a post-grown annealing for this samples to investigate the changes in nitrogen distribution. Post-grown annealing was performed for 15 min at 850° C, in  $\text{H}_2$  gas. PL spectra recorded before and after annealing is shown in Fig. 3. This shows that annealing results in blue shift and narrowing of PL emission for samples with N concentration 1% and 1.3%. Comparison of the PL spectra of the samples before and after annealing shows that maxima of emission of annealed samples nearly coincide with absorption edges of initial samples. So one can conclude that annealing of the GaAsN layers leads to suppress of nonuniform distribution of nitrogen atoms. For the  $\text{GaAs}_{0.994}\text{N}_{0.006}$  layers a broaden line, which is due to emission from localized states remains in the PL spectra even after

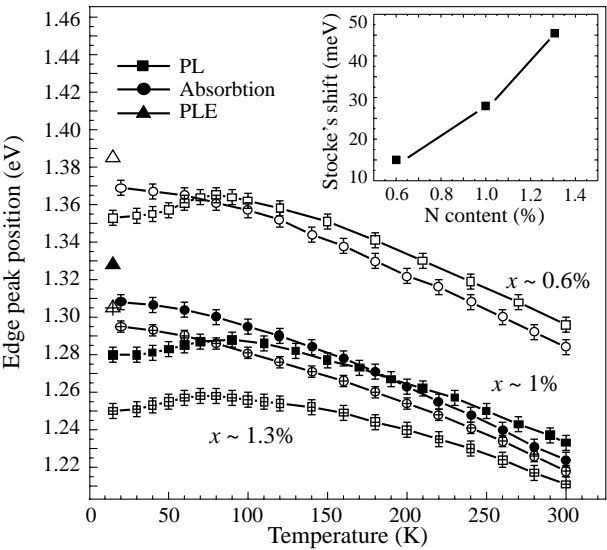


**Fig. 2.** Temperature dependence of PL maximum and edge of transmission of GaAsN layers 0.2  $\mu\text{m}$  thick.

annealing. This fact indicates that thermal stability of nonuniform N distribution in the sample with low N content is more stable. Figure 4 shows PL spectra of the samples with GaAsN layers grown by different methods: conventional, with applying of nitridization of GaAs surface and using of deposition of short-period GaAs/GaAsN<sub>0.05</sub> SL. For all PL spectra of samples one can see two peaks: a short wavelength peak, which usually is

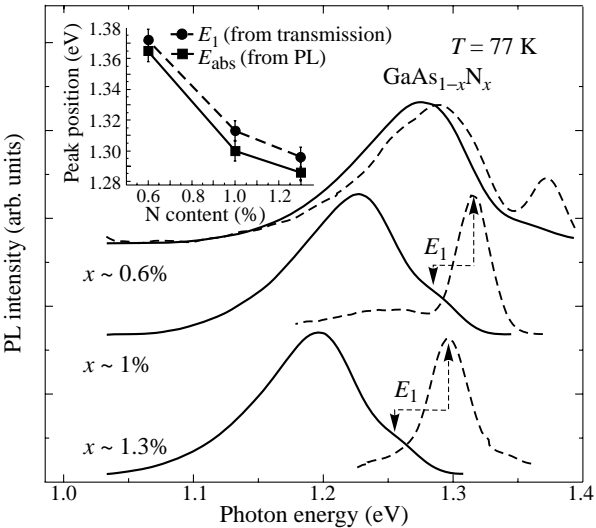


**Fig. 3.** PL spectra recorded before and after annealing GaAsN layers 0.2  $\mu\text{m}$ .

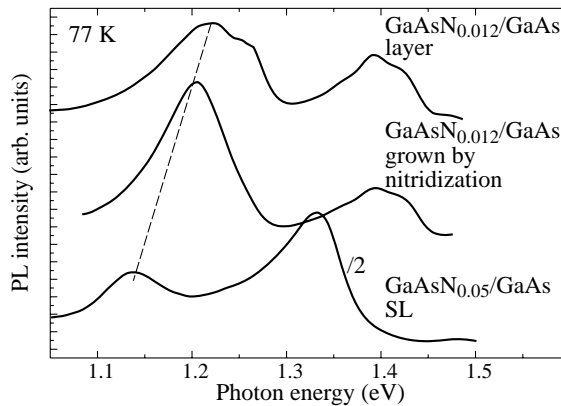


**Fig. 4.** PL spectra at 77 K of the samples with GaAsN layers grown by different methods: conventional, with applying of nitridization of GaAs surface and short-period GaAs/GaAsN<sub>0.05</sub> SL.

associated with emission from transition layers, which appears at the moment of turning on RF plasma source, and long wavelength peak which is due to emission from GaAsN layers. The dashed line in Fig. 4 indicates the red shift of maximum emission for investigated samples. This fact demonstrate that using of GaAs surface nitridization and deposition GaAs/GaAsN SL increases non-uniform distribution of N atoms. For sample grown at conventional regime long wavelength peak is strongly broaden and it is seen, that peak is superposition of several peaks, i.e. recombination originate via localized states resulting from random alloy composition. In case of applying GaAs surface nitridization or short-period GaAs/GaAsN<sub>0.05</sub> SL long wavelength peaks are also broaden. But width of the emission of these samples is smaller than one for layer GaAsN, grown in conventional regime, and intensity of these peaks increased. Thus, we can conclude that incorporation of N can be controlled by using different growth methods.

#### Acknowledgements

This program was supported by RFBR, NATO science for Peace Program (SfP-972484), CRDF grant (RE1-2217), Joint scientific program between Ioffe Institute (Russia) and ITRI (Taiwan).

#### References

- [1] M. Kondow, K. Uomi, A. Niwa, T. Kitatani, S. Watahiki and Y. Yazawa, *Jpn. J. Appl. Phys.* **35**, 1273 (1996).
- [2] G. Steinly, F. Mederer, M. Kicherer, R. Michalzik, G. Kristen, A. Y. Egorov, H. Riechert, H. D. Wolf and K. J. Ebeling, *Electron. Lett.* **37**, 632 (2001).
- [3] H. P. Xin, K. L. Kavanagh, Z. Q. Zhu and C. W. Tu, *J. Vac. Sci. Technol. B* **17**, 1649 (1999).
- [4] B. V. Volovik, A. R. Kovsh, W. Passenberg, H. Kuenzel, N. Grote, N. A. Cherkashin, Yu. G. Musikhin, N. N. Ledentsov, D. Bimberg and V. M. Ustinov, *Semicond. Sci. Technol.* **16**, 186 (2001).
- [5] I. P. Soshnikov, N. N. Ledentsov, B. V. Volovik, A. Kovsh, N. A. Maleev, S. S. Mikhrin, O. M. Gorbenko, W. Passenberg, H. Kuenzel, N. Grote, V. M. Ustinov, H. Kirmse, W. Neuman, P. Werner, N. D. Zakharov, D. Bimberg and Zh. I. Alferov, *Proc. 9th Int. Symp. "Nanostructures. Physics and Technology"*, St Petersburg, Russia, June 18-22, 2001.

## Influence of ZnSe cap layer growth on the morphology and Cd distribution in CdSe/ZnSe quantum dot structures

*D. Litvinov*<sup>†</sup>, *A. Rosenauer*<sup>†</sup>, *D. Gerthsen*<sup>†</sup>, *P. Kratzert*<sup>‡</sup>, *M. Rabe*<sup>‡</sup>  
and *F. Henneberger*<sup>‡</sup>

<sup>†</sup> Laboratorium für Elektronenmikroskopie, Universität Karlsruhe,  
D-76128 Karlsruhe, Germany

<sup>‡</sup> Institut für Physik, Humboldt Universität, D-10115 Berlin, Germany

**Abstract.** The morphology and Cd distribution in CdSe/ZnSe quantum dot structures grown by molecular beam epitaxy is compared before and after the ZnSe cap layer deposition. Atomic force microscopy is applied to study the surface topography of uncapped samples without removing the samples from the ultra-high vacuum. The capped structures are analyzed by transmission electron microscopy. It is observed that only a highly specific growth procedure involving a thermal activation step leads to a Stranski–Krastanow morphology with three-dimensional CdSe islands on a thin wetting layer which are preserved after the overgrowth with ZnSe.

### Introduction

Heterostructures containing CdSe with a nominal thickness of a few monolayers (ML) embedded in a ZnSe matrix have been the subject of intense interest in the past few years which is motivated by the prospect of obtaining CdSe/ZnSe quantum dot structures for fundamental studies and novel device applications. On the first sight, the CdSe/ZnSe system with a lattice-parameter mismatch of 7% is comparable to the InAs/GaAs system where three-dimensional (3D) InAs islands nucleate on a two-dimensional (2D) wetting layer (Stranski–Krastanow (SK) growth) [1]. In fact, there are reports about reflection high electron energy diffraction (RHEED) studies where a growth mode transition from 2D to 3D is observed for CdSe on ZnSe [2–4].

However, up to now, transmission electron microscopy (TEM) performed on structures capped with ZnSe show a ternary CdZnSe layer with Cd-rich inclusions which does not correspond to the expected SK morphology [5–7].

The main goal of the present work is the study of the possible modification of the CdSe layer morphology by the ZnSe overgrowth. For that purpose, the CdSe surface topography was analyzed by atomic force microscopy (AFM) immediately after the molecular beam epitaxy (MBE) deposition without removing the sample from the ultra-high vacuum.

The Cd distribution and morphology of capped samples was studied by conventional and high-resolution (HR)TEM in combination with quantitative chemical analysis techniques.

### 1. Experimental techniques

The structures were grown by MBE on GaAs (001) substrates. 3 ML CdSe were deposited at 230 °C on a strain-relaxed 1  $\mu\text{m}$  thick ZnSe buffer layer. Sample 1 was immediately covered by ZnSe, while sample 2 was hold for 2 h at 230 °C before the overgrowth. The RHEED pattern of the CdSe surface remained streaky during this period. For sample 3, the substrate temperature was increased shortly after the CdSe deposition to 310 °C. During



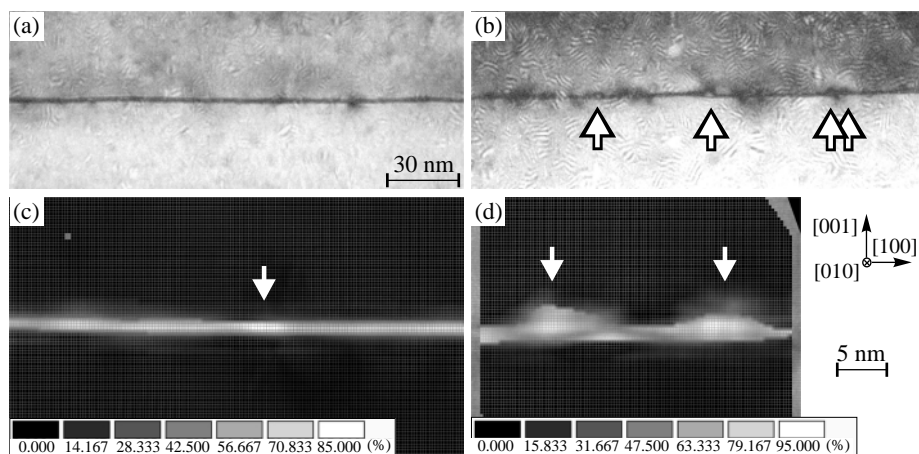


**Fig. 1.** (002) dark-field cross-section images for (a) sample 1 and (b) sample 3 and grey-scale coded CELFA maps of the Cd distribution for (c) sample 1 and (d) sample 3.

this thermal activation, the RHEED pattern undergoes a distinct transition from a streaky to spotty [2]. Sample 3 was capped after annealing it for 40 min at 310 °C. In all cases, ZnSe cap layers of several 10 nm were grown at 310 °C.

Since artifacts appear when exposed to air [8], the study of the surface topography of the uncapped CdSe layers was carried out in ultra high vacuum by an atomic force microscope directly attached to MBE chamber. The AFM images show that 3D islands with a lateral extension below 10 nm and an average height of  $(1.6 \pm 0.1)$  nm are exclusively formed on the surface of the thermally activated sample [9]. Their density is  $(1.1 \pm 0.2) \times 10^{11} \text{ cm}^{-2}$ . The surfaces of the other samples only show an atomic scale roughness.

The capped structures were studied by TEM in plan-view and cross-section geometry using a Philips CM 200 FEG/ST electron microscope with an electron energy of 200 keV. To prevent defect generation during the plan-view specimen preparation, which is known to occur during the final  $\text{Ar}^+$ -ion milling, only careful dimpling and mechanical polishing was applied. The [010] cross-section specimens were prepared by the standard technique with final  $\text{Ar}^+$  or  $\text{Xe}^+$  ion milling. The Cd distribution in the cross-section samples was quantitatively analyzed by the composition evaluation by lattice fringe (CELFA) technique [10] and the evaluation of (002) two-beam dark-field images [6]. Both techniques are based on the chemical sensitivity of the {002} reflections of the sphalerite structure.

## 2. Results and discussion

Figure 1 presents TEM results for samples 1 and 3. The overview (002) dark-field image of sample 1 (Fig. 1(a)) reveals a CdZnSe layer with homogeneous thickness. The Cd distribution of sample 1 (Fig. 1(c)) displayed in a grey-scale coded CELFA map shows that small Cd-rich inclusions (arrow) with lateral extensions below 5 nm are embedded in the layer. The full width at half maximum (FWHM) of the Cd concentration profiles extracted from the CELFA maps along the [001] growth direction were used to measure the thickness of the Cd-rich regions (5.5–6 ML) and the layer between inclusions (5 ML) which do not differ significantly. For that reason, the Cd-rich regions can be considered as 2D islands. For sample 3, the layer morphology (Fig. 1(b)) and the character of the Cd

distribution (Fig. 1(d)) is completely different. Bright regions (arrows) in the dark CdZnSe layer are visible in the overview image which occur if the Cd concentration  $x_{\text{Cd}}$  exceeds 40% [6]. Islands with  $x_{\text{Cd}}$  close to 100% and a height of 8 to 10 ML can be recognized which significantly exceed the region between the islands (FWHM  $\approx$  5 ML). The height of the islands is consistent with the values obtained by the AFM investigations before the cap layer growth. These islands can clearly be denoted as 3D islands. It can be assumed that the core of the islands consists of pure CdSe because the TEM sample thicknesses are in the range between 10 and 20 nm which can lead to a reduction of the measured Cd concentration if an island with high  $x_{\text{Cd}}$  is embedded in the ZnSe at the investigated sample area. CELFA analyses of further areas containing 3D islands show that the lateral island extensions vary between 5 and 15 nm.

The TEM investigation of the plan-view specimens (not shown here) displays contrast features related to 3D islands only in sample 3. Regions with a coffee-bean contrast with a density of  $4 \times 10^{10} \text{ cm}^{-2}$  occur. The coffee-bean contrast is primarily induced by stacking fault pairs [12] which are most likely generated in the vicinity of islands with high  $x_{\text{Cd}}$  and strain. In addition, small dark spots with a density of approximately  $1 \times 10^{10} \text{ cm}^{-2}$  are observed which could be caused by small 3D islands without defects or small defects which cannot be resolved. If the two contrast types are interpreted in terms of islands, the overall island density is  $5 \times 10^{10} \text{ cm}^{-2}$  in the capped structure.

The Cd distribution in samples 1 and 2 is typical for most CdSe/ZnSe samples with CdSe coverages between 0.7 and 3.6 ML [5–7]. It is a characteristic feature of the 2D islands that they are already present at very low CdSe coverages below the critical thickness for the 2D/3D transition indicating that they might not directly related to the SK growth mode.

The broadening of the CdZnSe layer with respect to the nominal CdSe coverage in all samples could be induced by Cd/Zn interdiffusion or Cd segregation during the ZnSe cap layer growth. Almost identical CdZnSe layer thicknesses in sample 1 and 2 being kept for distinctly different time intervals at 230 °C indicate that interdiffusion does not play a dominant role. The shape of the Cd-concentration profiles which can be extracted from the CELFA maps of Fig. 1(c) and (d) show a pronounced asymmetry with a steep increase at the lower interface and a gradual decline of the Cd concentration towards the ZnSe cap. The profile asymmetry is typical for segregation [11] which can be considered to be the dominant mechanism for the layer broadening and an important consequence of the ZnSe cap layer growth.

### 3. Conclusions

It could be clearly demonstrated by the present work, that three-dimensional Stranski–Krastanow islands are only formed by the application of a well-defined thermal activation procedure applied within an growth interruption. Although the SK CdSe layer is modified by the ZnSe overgrowth by Cd segregation and lateral CdSe redistribution, it has to be emphasized, that the 3D character of islands is preserved. Other growth conditions lead to 2D islands embedded in a CdZnSe layer with a homogeneous thickness.

### References

- [1] A. Madhukar, *Thin Solid Films* **8**, 231 (1993).
- [2] M. Rabe, M. Löwisch and F. Henneberger, *J. Crystal Growth* **184/185**, 248 (1998).
- [3] D. Schikora, S. Schwedhelm, D. J. As, K. Lischka, D. Litvinov, A. Rosenauer, D. Gerthsen, M. Strassburg, A. Hoffmann and D. Bimberg, *Appl. Phys. Lett.* **76**, 418 (2000).

- [4] F. Flack, N. Samarth, V. Nikitin, P. A. Crowell, J. Shi, J. Levy and D. D. Awschalom, *Phys. Rev. B* **54**, R17312 (1996).
- [5] T. Kümmell, R. Weigand, G. Bacher, A. Forchel, K. Leonardi, D. Hommel and H. Selke, *Appl. Phys. Lett.* **73**, 3105(1998).
- [6] N. Peranio, A. Rosenauer, D. Gerthsen, S. V. Sorokin, I. V. Sedova and S. V. Ivanov, *Phys. Rev. B* **61**, 16015 (2000).
- [7] D. Litvinov, A. Rosenauer, D. Gerthsen and N. N. Ledentsov, *Phys. Rev. B* **61**, 16819 (2000).
- [8] M. Grün, F. Funfrock, P. Schunk, Th. Schimmel, M. Hetterich and C. Klingshirn, *Appl Phys. Lett.* **73**, 1343 (1998).
- [9] P. R. Kratzert, M. Rabe and F. Henneberger, *Phys. Stat. Sol. B* **224**, 179 (2001).
- [10] A. Rosenauer and D. Gerthsen, *Ultramicroscopy* **76**, 49 (1999).
- [11] K. Muraki, S. Fukatsu, Y. Shirakia and R. Ito, *Appl. Phys. Lett.* **61**, 557 (1992).
- [12] D. Litvinov, A. Rosenauer, D. Gerthsen, H. Preis, S. Bauer and E. Kurtz, *J. Appl. Phys.* **89**, 4150 (2001).

## Variation of in-plane lattices constant of Ge islands during MBE growth on Si and SiO<sub>2</sub> surfaces

A. I. Nikiforov, V. A. Cherepanov, and O. P. Pchelyakov

Institute of Semiconductor Physics, 630090 Novosibirsk, Russia

**Abstract.** Variations in the lattice constant of Ge film were determined by RHEED in the course of the MBE film growth on the silicon surface. Oscillations of the in-plane atomic cell constant were observed for the Ge film growing according to the 2D mechanism. Variations in the two-dimensional lattice constant at the stage of 2D growth are caused by elastic deformation of edges of two-dimensional islands. It was shown that the germanium film growth on silica, unlike the growth on the pure silicon surface, proceeds without formation of the wetting layer.

### Introduction

The Ge/Si heterosystem is an ideal object for studying the heteroepitaxial growth and the 2D to 3D growth mode transition (the Stranski-Krastanov mechanism). Dependence of the island lattice constants on the deposition conditions makes it necessary to provide continuous monitoring the situation at the growth surface of the substrate. The traditionally used technique is reflection high-energy electron diffraction (RHEED). The RHEED technique was used [1] for plotting phase diagrams of the structures formed at the surface during Ge epitaxy on Si. A variation in the diffraction pattern is a qualitative illustration of morphological rearrangements of the growing film. The quantitative information can be obtained by recording the intensity of the diffraction pattern.

Of particular interest are the data on strains in the growing layer which are exactly the main driving force for the observed morphological rearrangements. The strains can be estimated from variations in the lattice constant in the growing Ge film. The variations can be established during heteroepitaxy from the reflection positions in the RHEED patterns. This approach was used to determine the relaxation points in systems Ge/Si [2] and InAs/GaAs [3]. The assumption of the island deformation in the course of 2D growth was supported by observations of periodical changes in the size of the surface 2D cell for A<sub>3</sub>B<sub>5</sub> and metals [4, 5]. The present work was aimed at studying the behaviour of the constant of the growing Ge lattice at the Si(100) and SiO<sub>2</sub> surfaces under the conditions of 2D growth.

### 1. Results and Discussion

A MBE installation Katun-C equipped with two electron beam evaporators for Si and Ge was used for synthesis. Analytical equipment of the chamber included a quadrupole mass spectrometer, a quartz thickness monitor and a high energy electron (20 kV) diffractometer. Diffraction patterns were monitored during the growth using a CCD camera on line with a PC. The software allowed both the whole images and chosen fragments of the diffraction patterns to be monitored at the rate of 10 frames/s. Ge grew at the rate of 10 ML/min, temperature was varied up to 600 °C. Silicon wafers misoriented by less than 0.5° were used as substrates. Before a Ge film started growing, the substrate was annealed and a

buffer Si layer was grown to reconstruct the original surface. An MBE installation was used for oxidation at oxygen supply up to  $10^{-4}$  Pa and the substrate temperature  $500^\circ\text{C}$ .

The 2D mechanism occurs at the growth of several initial Ge monolayers (the so-called wetting layer) in the Ge/Si system. Elastic relaxation of 2D islands formed during the 2D growth results in distortion of the unit cell of the heteroepitaxial film. RHEED technique allows the deformation to be *in situ* registered as a variation in the size ( $a_{\parallel}$ ) of the in-plane surface 2D atomic cell. To do that, variations in the intensity of the diffraction pattern was recorded along the line going across the streaks and bulk spots. The distance between the spots assigned to  $0\bar{1}$  and  $01$  reflections oscillates during the growth that indicates changes in the  $a_{\parallel}$  value at the plane of the Ge film.

Figure 1 shows variations in the 2D surface cell constant (as percentage with respect to the  $a_{\parallel}$  value of the pure silicon surface) during growth of a Ge film at the Si(100) surface at  $250^\circ\text{C}$ . The corresponding intensity variations of the RHEED specular beam reflected by the substrate surface is shown in the same figure. The  $a_{\parallel}$  value is seen to change, in periodical manner, during the growth, while the oscillation range reaches 2%. The periodic variations in the lattice constant of the 2D Ge cell in (100) plane is of the same nature as the specular beam intensity oscillations. Hence, there is the same reason for variations both in  $a_{\parallel}$  and in the specular beam intensity, *viz.* the periodical changes in the surface roughness of the growing film. It is common knowledge that these changes observed for 2D growth mode are caused by nucleation and coalescence of 2D islands. However, 2D lattice constant oscillations are half-period shifted with respect to the corresponding specular electron beam oscillations. The maximum of the lattice constant oscillations coincides with the minimum of the intensity oscillations at half monolayer coverage. Such behaviour means that the elastic deformation of 2D islands is maximal at the maximal surface roughness, and the atomic cell has the maximal lattice constant. When each monolayer is completed, the islands coalesce to form a smooth surface and the 2D surface cell of the film reaches its minimum. A decrease in  $a_{\parallel}$  of the smooth surface indicates the maximal increase in the surface sell to occur at the edge of the islands; the island coalescence results in a decrease in the in plane elastic deformation. The mean constant of the 2D cell during growth of the

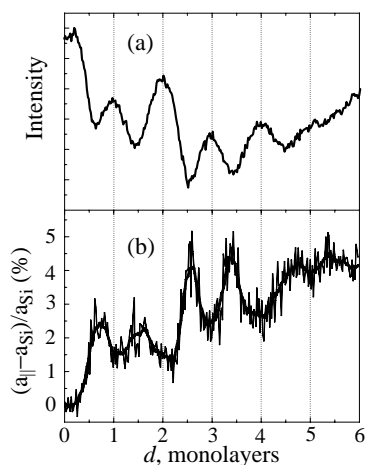


**Fig. 1.** Variations in specular beam intensity (a) and surface 2D cell constant (b) during growth of Ge film of Si(100) at  $250^\circ\text{C}$ .

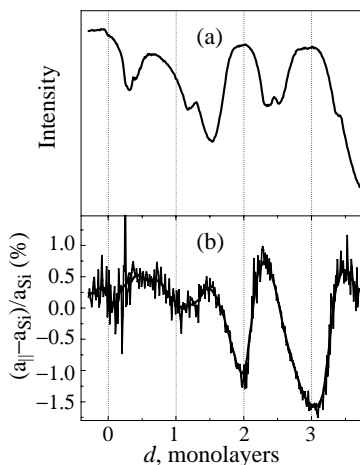


**Fig. 2.** Variations in specular beam intensity (a) and surface 2D cell constant (b) during growth of Ge film of Si(111) at  $370^\circ\text{C}$ .

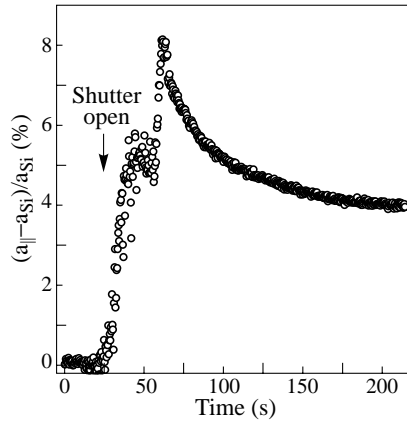


**Fig. 3.** In-plane lattice constant changes during growth of the germanium film on the oxidized Si(100) surface at 600 °C.

wetting Ge layer increases progressively. The whole pattern of  $a_{||}$  variations for various stages of Ge growth on the Si(100) surface is given elsewhere [6].

The cyclic nature of the roughness variations causes oscillations of the observed constants. The smooth surface of the continuous layer corresponds to the maximum in oscillations of the specular beam and to the minimum in oscillations of the 2D cell lattice constant. The presence of 2D islands at the growth surface results in a decrease in the specular beam intensity, and the lattice distortion at the island edges gives rise to the observed enlargement of the surface cell of the Ge film. Oscillations of the  $a_{||}$  parameter are detected over all ranges of temperature and growth rate when oscillations of the RHEED specular beam are observed. The fashion of the surface cell constant variations at the growth temperature range between 250 and 500 °C remains the same as that shown in Fig. 1.

Oscillations of the intensity and parameter  $a_{||}$  during Ge growth on Si(111) at the substrate temperature 370 °C are shown in Fig. 2. A characteristic feature of the growth on this surface is variations in the in-plane constant of the surface atomic cell of the Ge film around zero value, i.e. the  $a_{||}$  value of silicon. Parameter  $a_{||}$  is ca. 1% increased at the maximal roughness and ca. 1% decreased at the minimal roughness. Another distinctive feature is a slight variation in  $a_{||}$  at the thickness range corresponding to one monolayer. This behaviour is characteristic of a wide temperature range and independent of the presence or absence of intensity oscillations at this thickness. It is known that the intensity variations corresponding to the first monolayer is observed at not all growth temperatures that is accounted for by the double-level growth mode at the given stage.

The oxidation process is accompanied by an increase in in-plane constant that indicates the presence of an elastically strained layer at the silicon-oxide interface. The wetting layer is not formed during growth of Ge islands on the oxidized silicon surface proceeds, but the process is accompanied by remarkable changes in the surface cell. The process begins with growth of elastically strained islands similar to the growth on the pure surface of Si(100) but then in-plane constant decreases to the value of bulk germanium that indicates complete relaxation of the islands (Fig. 3). It is seen that the changes in the surface lattice of Ge relative to the surface lattice of Si also reaches 8% like in the case of the growth on the pure silicon surface.

## 2. Conclusions

Variations in the lattice constant of Ge film were determined in the course of the MBE film growth on silicon (100), (111) and SiO<sub>2</sub> surfaces. Oscillations of the in-plane atomic cell constant were observed for the Ge film growing according to the 2D mechanism. The in-plane constant oscillates in the same manner as the specular beam intensity but is half period shifted. Variations in the two-dimensional lattice constant at the stage of 2D growth are caused by elastic deformation of edges of two-dimensional islands. It was shown that the germanium film growth on silica, unlike the growth on the pure silicon surface, proceeds without formation of the wetting layer and the changes in the surface lattice of Ge relative to the surface lattice of Si like in the case of the growth on the pure silicon surface.

### Acknowledgements

The authors thank A. I. Yakimov for technical assistance. The study was supported by the Russian Foundation for Basic Research (Projects 00-02-18012 and 00-02-17638).

## References

- [1] O. P. Pchelyakov, V. A. Markov, A. I. Nikiforov and L. V. Sokolov, *Thin Solid Films* **306**, 299 (1997).
- [2] L. Kubler, D. Dentel, J. L. Bischoff, C. Ghica, C. Ulhag-Bouillet and J. Werckmann, *Appl. Phys. Lett.* **73**, 1053 (1998).
- [3] A. Ohtake, M. Ozeki and J. Nakamura, *Phys. Rev. Lett.* **84**, 4665 (2000).
- [4] N. Grandjian and J. Massies, *J. Crystal Growth* **134**, 51 (1993).
- [5] P. Turban, L. Hennet and S. Andrieu, *Surface Science* **446**, 242 (2000).
- [6] A. I. Nikiforov, V. A. Cherepanov and O. P. Pchelyakov, *Thin Solid Films* **380**, 158 (2000).

## High-mobility InAs/AlSb heterostructures for spintronics applications

*Yu. G. Sadofyev*<sup>†</sup>, *Y. Cao*<sup>‡</sup>, *S. Chaparo*<sup>‡</sup>, *A. Ramamoorthy*<sup>‡</sup>, *B. Naser*<sup>‡</sup>,  
*J. P. Bird*<sup>‡</sup>, *S. R. Johnson*<sup>‡</sup> and *Y.-H. Zhang*<sup>‡</sup>

<sup>†</sup> P. N. Lebedev Physical Institute of RAS, Moscow, 117924 Russia

<sup>‡</sup> Department of Electrical Engineering & Center for Solid State Electronics Research,  
Arizona State University, Tempe, AZ 85287-5706, USA

**Abstract.** High-mobility InAs single quantum well with symmetrical AlSb and asymmetrical AlSb and  $\text{Al}_{0.8}\text{Ga}_{0.2}\text{Sb}$  barriers were grown on GaAs (100) by MBE. Magneto-transport studies revealed enhancement of sufficient effective  $g$ -factor in a quantizing magnetic field. This enhancement is quite sensitive to the layer composition of the epitaxially-grown structures. The implications of these results for the implementation of InAs-based spintronics structures are discussed.

### Introduction

High-mobility heterojunctions and quantum wells using InAs as the conducting channel layer are promising for spintronics applications. Bulk InAs is known to exhibit a large effective  $g$ -factor ( $g^* = -15$ ), which is expected to allow for a strong enhancement of any intrinsic spin-splitting in the presence of even a moderate magnetic field. Another useful feature of this material system is its small effective mass ( $m^* = 0.024m_0$ ), which yields large energy splittings in nanostructures such as quantum wires and dots [4, 6]. For these reasons, InAs has been proposed as one of the ideal systems for realizing a novel spin-filter structure, which exploits spin-dependent tunneling through a magnetic, quantum-point-contact, barrier [7]. Heterostructures such as InAs/AlSb can be exploited in systems with asymmetric bandedge profiles to realize large spin splittings at zero magnetic field [1, 3]. For all these potential physics study and applications, a high electron mobility is desirable. In our presentation, we will therefore describe the epitaxial growth of high-mobility InAs/AlSb quantum wells on GaAs substrates and their transport properties. Magneto-transport studies reveal a low-temperature (4 K) electron density of  $5 \times 10^{11} \text{ cm}^{-2}$  with a mobility of  $4 \times 10^5 \text{ cm}^2 \text{ s}^{-1}$ . We also discuss the results of studies of the  $g$ -factor enhancement in a quantizing magnetic field [8], the details of which we find to be quite sensitive to the layer composition of the epitaxially-grown structures.

### 1. Sample preparation

The samples were grown on semi-insulating GaAs(100) substrates, in a VG VH80 MBE machine equipped with solid-phase sources for Group III and V materials. Valved cracker cells were used to produce  $\text{As}_2$  and  $\text{Sb}_2$  fluxes and the quantum wells were formed on a complicated buffer layer, as described previously by Nguyen et al. [9]. To promote the formation of a smooth substrate, and to help the subsequent nucleation of AlSb, this process proceeds with the growth of 200 nm of GaAs and 10 nm of AlAs, which are deposited at a temperature of 610 °C, 100 nm of AlSb was then grown at 570 °C, followed by the deposition of a 2.4 nm buffer of either AlSb (samples A839, A856), or GaSb (sample B824), at a substrate temperature of either 570 or 510 °C, respectively. A ten-period



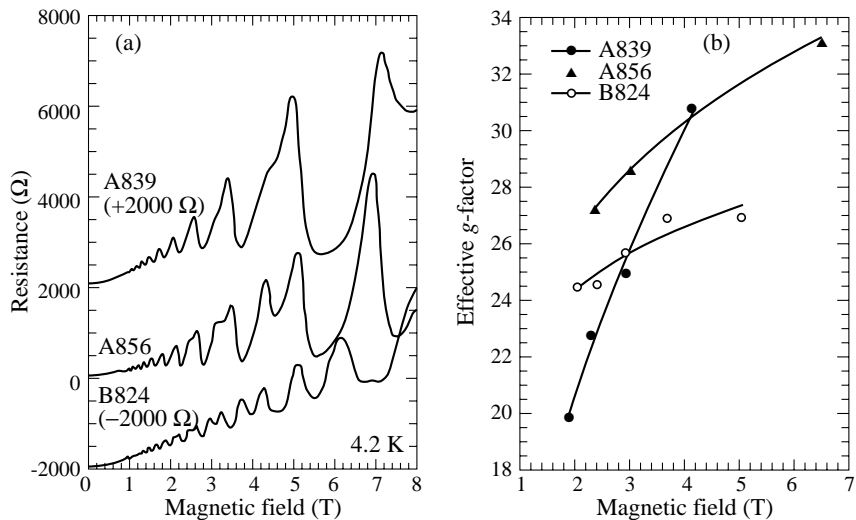


**Fig. 1.** (a) Shubnikov–de Haas oscillations in the three samples at 4.2 K. (b)  $g$ -factor variation inferred for the three different samples.

superlattice (2.5 nm GaSb 2.5 nm AlSb) followed this buffer section and was grown at a substrate temperature of 490 °C. The active quantum well in these structures consisted of a 15 nm InAs layer, sandwiched between two barriers. In all samples studied, the lower barrier consisted of 12 nm of AlSb. The upper barrier was formed from 40 nm of AlSb in sample A839 and B824, and from 30 nm of  $\text{Al}_{0.8}\text{Ga}_{0.2}\text{Sb}$  in sample A856. In all three samples, the layer structure was completed by the deposition of a 6 nm GaSb layer. The shutter sequence employed during MBE growth provided for the formation of InSb-like chemical bonds at the top and bottom interfaces (InAs/AlSb or InAs/GaAsSb) [10]. The  $\text{Sb}_{2:\text{III}}$  flux ratio was equal to 1.2 for all Sb containing layers while the  $\text{As}_{2:\text{In}}$ -flux ratio was 1.5. All layers exhibited mirror-like surfaces, and quite good ( $1\times 3$ ) or ( $2\times 4$ ) surface reconstructions were seen in the RHEED patterns for the (Al,Ga)Sb, and InAs layers, respectively. An infrared pyrometer was used as a substrate temperature controller and the growth rates were 6 nm/min for the InAs and 12 nm/min for the Sb-containing layers. The key layer parameters for the different samples are summarized in Table 1 below.

**Table 1.** Electronic properties of the different samples.

	$\mu_{300\text{ K}}$ $\text{cm}^2/\text{Vs}$	$n_{300\text{ K}}$ $\times 10^{11} \text{ cm}^{-2}$	$\mu_{4\text{ K}}$ $\text{cm}^2/\text{Vs}$	$n_{4\text{ K}}$ Hall $\times 10^{11} \text{ cm}^{-2}$	$n_{4\text{ K}}$ SdH $\times 10^{11} \text{ cm}^{-2}$
A839	30540	11.5	184550	5.53	5.12
A856	27420	11.7	444350	5.01	5.27
B824	28510	15.7	413600	7.45	6.56

## 2. Results

In order to characterize the electrical quality of the samples, the Shubnikov–de Haas and Quantum-Hall effects were investigated at temperatures between 0.01 and 10 K, using a Hall bar geometry with soldered In contacts. In Table 1, we list the 4 K carrier densities of the

three different quantum-well samples, as determined from measurements of the Shubnikov–de Haas oscillations and the low-field Hall effect. We also list their 4 K mobilities, which vary by a factor of two for the three different samples. In Fig. 1(a), we show the Shubnikov–de Haas oscillations in the 4 K magneto-resistance, while in Fig. 1(b) we show the variation of the effective  $g$ -factor, as determined from the magnetic-field splittings of the Shubnikov–de Haas oscillations.

The origins of the different  $g$ -factor variations noted in Fig. 1(b), and the implications of these results for the implementation of InAs-based spintronic structures, will be discussed in further detail in our presentation.

## References

- [1] J. Luo, H. Munekata, F. F. Fang and P. J. Stiles, *Phys. Rev. B* **41**, 7685 (1990).
- [2] G. Engels, J. Lange, Th. Schäpers and H. Luth, *Phys. Rev. B* **55**, R1958 (1997).
- [3] J. Nitta, T. Akazaki, H. Takayanagi and T. Enoki, *Phys. Rev. Lett.* **78**, 1335 (1997).
- [4] T. Sugaya, J. P. Bird, M. Ogura, Y. Sugiyama, D. K. Ferry and K.-Y. Jang, *Appl. Phys. Lett.* **80**, 434 (2002).
- [5] T. Sugaya, M. Ogura, Y. Sugiyama, T. Shimizu, K. Yonei, K.-Y. Jang, J. P. Bird and D. K. Ferry, *Appl. Phys. Lett.* **79**, 371 (2001).
- [6] T. Maemoto, T. Kobayashi, T. Karasaki, K. Kita, S. Sasa, M. Inoue, K. Ishibashi and Y. Aoyagi, *Proceedings of the 12th International Conference on Nonequilibrium Carrier Dynamics in Semiconductors*, Physica B, in press.
- [7] M. J. Gilbert and J. P. Bird, *Appl. Phys. Lett.* **77**, 1050 (2000).
- [8] Th. Englert, D. C. Tsui, A. C. Gossard and Ch. Uihlein, *Surf. Sci.* **113**, 295 (1982).
- [9] C. Nguyen, B. Brar, C.R. Bolognesi, J. J. Pekarik, H. Kroemer, J. H. English, *J. Elec-tron. Mater.* **22**, 255 (1993).
- [10] G. Tuttle, H. Kroemer and J. H. English, *J. Appl. Phys.* **67**, 3032 (1990).

## Investigation of the formation of InAs QD's in a AlGaAs matrix

*D. S. Sizov, N. V. Kryzhanovskaya, A. G. Gladyshev, Yu. B. Samsonenko, G. E. Cirlin, N. K. Polyakov, V. A. Egorov, A. A. Tonkih, Yu. G. Musikhin A. F. Tsatsul'nikov, N. N. Ledentsov and V. M. Ustinov*

*Ioffe Physico-Technical Institute, St Petersburg, Russia*

**Abstract.** Optical and structural properties of self organised InGaAs quantum dots (QD), deposited in  $\text{Al}_{0.3}\text{Ga}_{0.7}\text{As}$  matrix, were investigated. Samples were grown by molecular-beam epitaxy (MBE). It is shown, that deposition of 1.7–4 monolayer of InAs on  $\text{Al}_{0.3}\text{Ga}_{0.7}\text{As}$  surface results in formation of nanoscale QDs on 1–2 monolayer thick wetting layer (Stranski–Krastanov growth mode) [1]. Large exciton localization energy of the InAs QDs in  $\text{Al}_{0.3}\text{Ga}_{0.7}\text{As}$  in compare with QDs in GaAs is demonstrated. This is due to increase in size of these QDs and significant bandgap offset in the case of InAs/AlGaAs system in compare with InAs/GaAs one.

### Introduction

At recent time, progress in the development of light emitting devices and injection lasers based on self-organised In(Ga)As QDs become evident [2]. Lasers grown on GaAs substrates with QD-based active region allow to realize  $1.3\ \mu\text{m}$  emission. This lasers are promising for using in fiber optic communication systems. Vertical cavity surface emitting lasers with AlGaAs distributed Bragg reflector and QD based active region, were fabricated. Deep carrier localization in QDs leads to another advantage of QD-based devices — temperature stability of the parameters of lasers with QD's in active region [3]. Localization energy more than 800 meV can be achieve in In(Ga)As/ $\text{Al}_{0.3}\text{Ga}_{0.7}\text{As}$  QD's system. In principle, up to now main investigations were concentrated on In(Ga)As QD's in GaAs matrix [4]. In this work we have investigated InAs QD's grown in  $\text{Al}_{0.3}\text{Ga}_{0.7}\text{As}$  matrix which exhibit photoluminescence (PL) in wide optical range ( $0.98\text{--}1.3\ \mu\text{m}$ ).

Wide bandgap  $\text{Al}_{0.3}\text{Ga}_{0.7}\text{As}$  allows dramatically increase carrier localization in QD. Localization energy of about 0.7 eV for InAs QDs in a  $\text{Al}_{0.3}\text{Ga}_{0.7}\text{As}$  matrix was achieved that exceed the value for the same QD's in GaAs matrix (about 0.46 eV). Obtained result indicates that InGaAs QDs in AlGaAs can be used for fabrication of high temperature stability injection laser [5].

### Experiment

Investigated structures were grown by molecular beam epitaxy on GaAs [100] substrates. The samples contain active region with InAs QD embedded in  $\text{Al}_{0.3}\text{Ga}_{0.7}\text{As}$  matrix. This active region was confined from both sides by AlAs/GaAs superlattices, to prevent leakage of the carriers to defect areas which located near buffer layer and surface. The substrate temperature during the deposition of QDs and following  $50\ \text{\AA}$   $\text{Al}_{0.3}\text{Ga}_{0.7}\text{As}$  layer was  $485\ ^\circ\text{C}$ . The other layers of the structures were grown at  $600\ ^\circ\text{C}$ . PL was excited by  $\text{Ar}^+$  laser ( $\sim 500\ \text{W}/\text{cm}^2$ ) and registered by cooled Ge photodiode. Transmission electron microscopy (TEM) measurements were performed using a Phillips EM 420 microscope in plan-view and cross-section geometry at an acceleration voltage of 100 kV.

## Result and discussion

Cross section and plain view TEM pictures of the structures with QDs obtained by the deposition of 2.5 ML of InAs in the  $\text{Al}_{0.3}\text{Ga}_{0.7}\text{As}$  and GaAs matrixes are presented in Fig. 1. WL was revealed in the images that indicate Stransky–Krastanov growth mode for both cases. Lateral size of the QDs grown in  $\text{Al}_{0.3}\text{Ga}_{0.7}\text{As}$  matrix is about 18 nm, whereas, lateral size of QDs in GaAs matrix is about 12 nm. This effect can be connected with roughness of  $\text{Al}_{0.3}\text{Ga}_{0.7}\text{As}$  surface or different growth mechanism for InAs on  $\text{Al}_{0.3}\text{Ga}_{0.7}\text{As}$ .

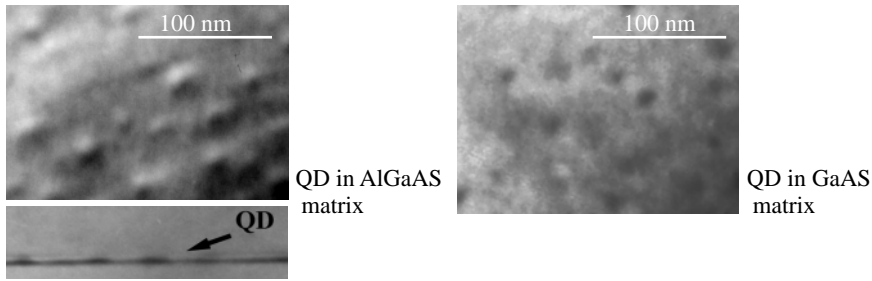


**Fig. 1.** TEM pictures of structure with QDs in AlGaAs matrix in compare with structure with QDs in GaAs matrix.

PL lines associated with recombination via ground state of the QDs for the samples with different InAs average coverage in  $\text{Al}_{0.3}\text{Ga}_{0.7}\text{As}$  matrix are presented in Fig. 2. Observed lines are inhomogeneously broadened, and they have Gauss function shape. QD peak shifts in red side with increase in InAs layer thickness up to 4.5 ML.

Dependencies of the QD peak position on InAs average thickness for the QDs in GaAs and  $\text{Al}_{0.3}\text{Ga}_{0.7}\text{As}$  are shown in Fig. 3. In case of GaAs matrix, red shift of QD peak can be observed with increasing of InAs coverage up to 2.5 ML and then the shift of emission saturates [6]. In case of AlGaAs matrix, this red shift continue up to 3 ML, and saturate over these value. Energy separation between InAs ground states and matrix states can be achieved of 0.7 eV for the AlGaAs matrix in compare with 0.46 eV for GaAs matrix. This large shift is due to significant localization of the carriers in QDs, that results in

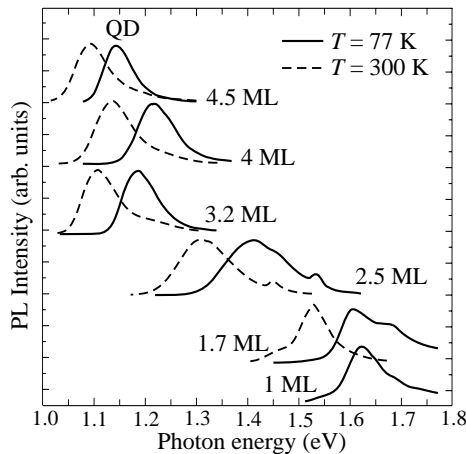


**Fig. 2.** PL spectra of structures with QDs in AlGaAs matrix. QD peak shift with in red side increasing InAs average coverage up to 4.5 ML.

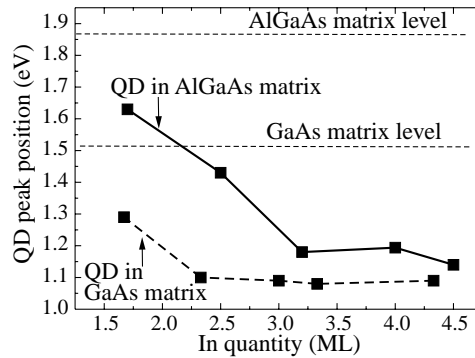


**Fig. 3.** Dependences of the QD peak position on InAs coverage for the QDs in GaAs and AlGaAs.

smaller effect of matrix bandgap on energy levels in QDs. Beside, conservation of the shape of QDs at overgrowth of the QDs by AlGaAs, resulting in red shift of emission was demonstrated [7].

It's known, that overgrowth of InAs QDs by  $\text{In}_{0.15}\text{Ga}_{0.85}\text{As}$  alloy leads to considerable redshift of the QD emission. This method allows to achieve  $1.3 \mu\text{m}$  lasing in structures with InGaAs/GaAs QD [6]. We propose apply this method for QD embedded in  $\text{Al}_{0.3}\text{Ga}_{0.7}\text{As}$  matrix.

Active region of this sample contains 2.5 ML thick InAs layer overgrown by 5 nm  $\text{In}_{0.15}\text{Ga}_{0.85}\text{As}$  layer. PL spectrum of this sample is presented in Fig. 4. Maximum QD peak position wavelength corresponds to  $1.25 \mu\text{m}$ . Further optimization of growth parameters can increase QD emitting wavelength, and so emission at  $1.3 \mu\text{m}$  can be achieved.

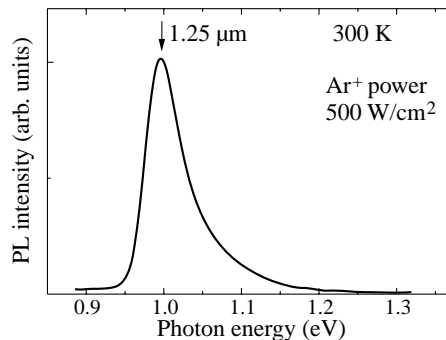


**Fig. 4.** PL spectrum of structure with InAs QD overgrown by  $\text{In}_{0.15}\text{Ga}_{0.85}\text{As}$  in AlGaAs matrix.

## Conclusions

It was demonstrated, that InAs QDs are grown in Stransky-Krastanov growth mode in  $\text{Al}_{0.3}\text{Ga}_{0.7}\text{As}$  matrix. These QDs have larger lateral size in compare with QDs in GaAs matrix. This fact, as well significant bandgap offset in the InAs/AlGaAs system, allows fabricate QDs with localization energy about 0.7 eV. Possibility to achieve PL at  $1.3 \mu\text{m}$  wavelength by using of InAs QDs overgrown by InGaAs layer was demonstrated.

## Acknowledgments

This work was supported by: RFBR NanoOp Program, Intas and CRDF grant (RE1-2217).

## References

- [1] V. M. Ustinov, A. E. Zhukov, A. Yu Egorov, A. R. Kovsh, A. F. Tsatsul'nikov, M. V. Maximov, S. V. Zaitsev, N. Yu Gordeev, P. S. Kop'ev and Zh. I. Alferov, *Proc. Int. Symp. on Compound Semiconductors*, St Petersburg, Russia, 1996.
- [2] V. M. Ustinov and A. E. Zhukov, *Semicond. Sci. Technol.* **15**, R41 (2000).
- [3] L. V. Asryan and R. A. Suris, *Semicond. Sci. Technol.* **11**, 554 (1996).
- [4] N. N. Ledentsov, V. M. Ustinov, V. A. Shchukin., P. S. Kop'ev, Zh. I. Alferov and D. Bimberg, *Semiconductors* **32**, 4 (1998).
- [5] P. S. Kop'ev, N. N. Ledentsov, V. M. Ustinov, I. V. Kochnev, N. A. Bert, A. Yu. Egorov, A. E. Zhukov, V. V. Komin, A. O. Kosogov, I. L. Krestnikov, M. V. Maximov, S. S. Ruvimov, V. A. Shchukin, Yu. M. Shernyakov, A. F. Tsatsul'nikov, S. V. Zaitsev, Zh. I. Alferov and D. Bimberg, *Tech. Dig. Series, Conference Edition*, **10**, pp. 383-384 (1996), [Proc. Conf. on Quantum Electronics and Laser Science (Anaheim, CA, USA, 2-7 June, 1996), Washington, DC, USA: Opt. Soc. America, 1996, pp. 181-182].
- [6] M. V. Maximov, A. F. Tsatsul'nikov, B. V. Volovik, D. S. Sizov, Yu. M. Shernyakov, I. N. Kaniander, A. E. Zhukov, A. R. Kovsh, S. S. Mikhlin, V. M. Ustinov, Zh. I. Alferov, R. Heitz, V. A. Shchukin, N. N. Ledentsov, D. Bimberg, Yu. G. Musikhin and W. Neumann, *Phys. Rev. B* **62**, 16671 (2000).
- [7] A. F. Tsatsul'nikov *et al*, *Proc. 26th Int. Symp. on Compound Semiconductors (ISCS 1999)*, Berlin, Germany, 1999.

## Surface morphology evolution at early stages of $\text{CaF}_2(110)$ epitaxial growth on $\text{Si}(001)$

*N. S. Sokolov, S. M. Suturen and V. P. Ulin*

Ioffe Physico-Technical Institute, St Petersburg, Russia

### 1. Introduction

The initial stage studies of  $\text{CaF}_2$  molecular beam epitaxy (MBE) on  $\text{Si}(111)$  provide a lot of new information important for understanding basic mechanisms of the heteroepitaxy and interface formation between dissimilar materials (see, for example recent review [1]). Unlike  $\text{CaF}_2$  on  $\text{Si}(111)$  system, which has been thoroughly studied by many groups, the interaction of  $\text{CaF}_2$  molecules with a technologically important  $\text{Si}(001)$  surface until recently remained almost unexplored except for the TEM and STM studies [2, 3], where strong anisotropy at the initial stages of  $\text{CaF}_2$  growth on  $\text{Si}(001)$  was observed. In our previous work [4], it was found that a so-called "wetting layer" forms during the initial stage of fluorite growth at above 650 °C. This layer influences much the following stages of fluorite growth and determines unusual (110)-orientation of  $\text{CaF}_2$  nanostructures, grown on  $\text{Si}(001)$  surface. The wetting layer formation was accompanied by transformation of the initially two-domain ( $2 \times 1$  and  $1 \times 2$ ) silicon surface to single-domain. However, microscopic mechanism of this transformation remained unclear.

In this work, we used atomic force microscopy to thoroughly investigate the evolution of the silicon substrate surface during the wetting layer formation. We have found the basic microscopic mechanism governing the transition between single- and two-domain surface morphology and revealed more details on nucleation and evolution of  $\text{CaF}_2$  linear ridge-like nanostructures described in [4] as appearing at higher surface coverage.

### 2. Experimental

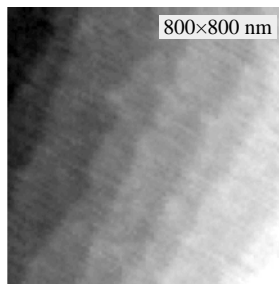
Growth experiments were carried out in a custom MBE system. After standard chemical cleaning, Si substrate was transferred into growth chamber and thermally cleaned at 1250 °C for  $\sim 1.5$  min. Prior to the growth it was kept at 1000 °C for 15 min to flatten the surface. The RHEED pattern of the prepared substrate showed a well pronounced  $2 \times 1$  superstructure which is characteristic of the clean  $\text{Si}(001)$  surface. Calcium fluoride was deposited at the rate of 1–2 nm/min from the molecular beam formed by sublimation of single-crystal  $\text{CaF}_2$  pieces in an amorphous carbon crucible. The growth was carried out at 770 °C, the temperature calibrated with optical pyrometer. Just after the end of the deposition the substrate heater was switched off and the sample cooled down to below 100 °C within a few minutes.

The surface morphology of the samples was studied in the ambient conditions using the tapping mode of a P4-SPM atomic force microscope produced by NT-MDT (Zelenograd, Russia). Typical lateral resolution of the AFM measurements was about 10 nm, depending on the sharpness of the cantilever tip, the height resolution was better than 0.1 nm. Ambient conditions were found not to influence much the surface morphology during at least an hour after exposing the surface to the atmosphere in the laboratory. In the testing experiments no features except surface steps were found on the bare silicon surface within 60 min after it was taken out to the air and this was a sufficient time for accurate AFM measurements.

The surface oxidation became noticeable only after 1.5–2 hours exposition of the sample to the atmosphere.

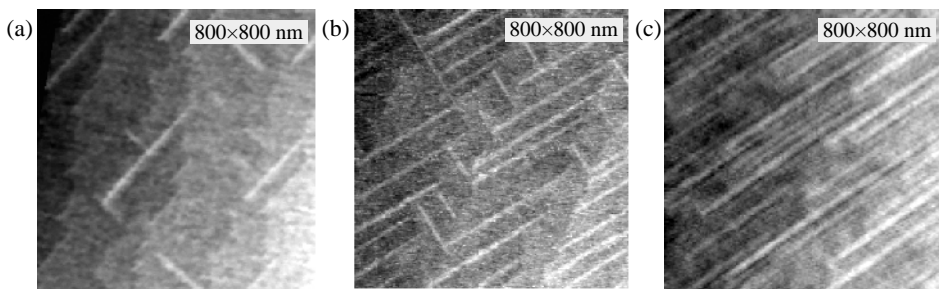
### 3. Results and discussion

Figure 1 shows an AFM image of a Si(001) substrate surface morphology before the deposition of calcium fluoride. Terraces 50–100 nm in width and steps a single atom high are clearly seen on the surface. The integral areas of “even” and “odd” terraces are comparable, which indicates that this is a two-domain surface with orthogonal direction of silicon dimers on the neighboring terraces. The conclusion is supported by RHEED observations showing half-order streaks in both orthogonal  $[110]$  and  $[1\bar{1}0]$  directions. This is obviously due to the superposition of  $2\times 1$  and  $1\times 2$  reconstructions on the “even and odd” terraces.



**Fig. 1.** Si(001) surface prior to fluorite growth. Step height:  $\sim 1.3 \text{ \AA}$ . Average terrace width:  $\sim 150 \text{ nm}$ .

After the deposition of  $\sim 0.1 \text{ ML}$  of  $\text{CaF}_2$ , one can notice narrow nano-strips running along  $[110]$  and  $[1\bar{1}0]$  directions, Fig. 2(a). The nano-strips are longer in  $[1\bar{1}0]$ -direction, which is closer to the average direction of the step edges. One can also see that the nano-strips do not cross each other forming T-joints. At slightly higher  $\text{CaF}_2$  coverage presented in Fig. 2(b), a drastic change on the surface is observed. The terraces with the nano-strips along  $[1\bar{1}0]$ -direction become much broader than the neighboring terraces. The density of



**Fig. 2.** (a) Nucleation of the nano-strips on Si(001) surface at  $\sim 0.1 \text{ ML}$   $\text{CaF}_2$  coverage. Nano-stripe height:  $3 \text{ \AA}$ . Nano-stripe width:  $< 100 \text{ \AA}$ . (b) Redistribution of Si(001) surface terraces induced by the nano-strips growth. Coverage  $\sim 0.15 \text{ ML}$ . (c) Domination of  $[110]$ -nano-strips on the Si substrate with the step direction close to  $[110]$ . Misorientation azimuth  $10 \text{ deg.}$  from  $[110]$  direction.



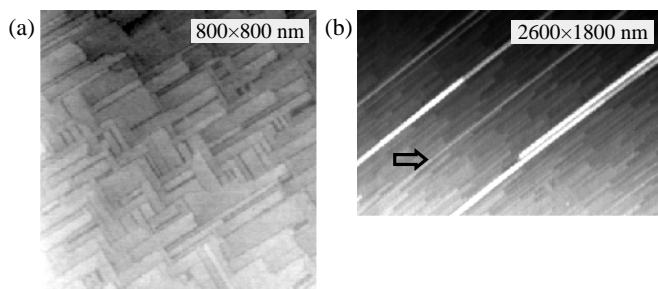


**Fig. 3.** (a) Wetting layer formation at  $\sim 1$  ML  $\text{CaF}_2$  coverage. (b) Long  $\text{CaF}_2$  ridges form on top of the wetting layer at above 1 ML coverage. Ridge height:  $< 5$  nm. Ridge length: several microns. An arrow indicates an apex of one of the ridges.

the long  $[1\bar{1}0]$ -type nano-strips is much higher than the orthogonal  $[110]$ -type ones. It is clearly seen that each nano-stripe is confined within a single terrace and do not cross the silicon substrate steps. A nano-stripe does not propagate below the terrace edge, however it spreads in the upward direction, consuming the silicon atoms from the upper terrace. Thus, the redistribution of the areas between the terraces covered by  $[1\bar{1}0]$  and  $[110]$  nano-strips takes place, resulting in the domination of the latter. This domination appears to be higher for the substrates with the step direction closer to  $[1\bar{1}0]$ . (See for example Fig. 2(c) where almost no  $[110]$  nano-strips are present).

As the fluorite coverage reaches 1 ML, the nano-strips coalesce to form flat terraces with rectangular edges (Fig. 3(a)). As most of the terraces consist of the same type of nano-strips, we come to the surface with a dominating single-axis anisotropy. This anisotropy is confirmed by completely different RHEED patterns in two orthogonal  $[1\bar{1}0]$  and  $[110]$  directions. This stage corresponds to the formation of the wetting layer observed earlier in [4].

Quite similar surface morphology was found in UHV STM measurements of a “row-like layer”, obtained in [3] after room temperature deposition of two  $\text{CaF}_2$  monolayers on  $\text{Si}(001)$  followed by annealing at  $670^\circ\text{C}$ . Analyzing STM images measured at biases of both polarities, the authors of the work concluded that Ca atoms in the row-like layer are in  $1+$  charge state which is different from  $2+$  charge state in the bulk. Metastable He atom deexcitation spectroscopy measurements described in [5] also indicated the presence of  $\text{Ca}^+$  ions in the wetting layer, leading to the conclusion that Ca atoms at the interface are bound to Si.

As  $\text{CaF}_2$  coverage reaches  $\sim 1$  ML, the growth switches to 3-dimensional mode. Long ridges  $\sim 1\text{--}3$  nm in height appear at the surface parallel to the direction in which most of the nano-strips run (Fig. 3(b)). However, unlike the nano-strips, the ridges are not confined to a single terrace. Having length of several microns they cross many steps on the way. The RHEED measurements carried out during the growth showed that the  $(110)$   $\text{CaF}_2$  planes in the ridges are parallel to  $(001)$  surface of Si, the  $[1\bar{1}0]$  direction of  $\text{CaF}_2$  coinciding with that of Si. These epitaxial relations being quite unusual for  $\text{CaF}_2$  on Si are assumed to come from the underlying wetting layer. Inclined streaks observed at the RHEED pattern indicate that the side slopes of the ridges are formed by  $\text{CaF}_2$   $\{111\}$  planes. This is consistent with the fact that  $\{111\}$  planes have minimal surface free energy in the fluorite lattice [6]. Most of the ridges observed by AFM are uniform in width. However, height and width of the ridges whose up-the-steps ends fall within the image bounds (see for

example arrow indication in Fig. 3(b)), noticeably increase along the ridge in the down-the-steps direction, most likely compensating for the decrease in the absolute height induced by the steps. Thus it can be assumed that the ridge is roof-like with the side slopes formed by step-free  $\{111\}$  surfaces. Far from the thin end saturation of the ridge width is observed, which is probably related with strain effect due to large lattice misfit across the ridge. It is likely that the ridge nucleates at its apex (the thinner end) and grows preferentially in the down-the-steps direction. The further increase of the coverage leads to higher density of the ridges.

#### 4. Conclusion

Using conventional atomic force microscopy operating in the ambient conditions, we could resolve essential details in the initial stages of the wetting layer formation. We could reveal the basic microscopic mechanism of the transformation between the initial two-domain ( $2 \times 1$  and  $1 \times 2$ ) silicon surface to the single domain surface of the wetting layer observed here and in our earlier work [4]. It was also found that  $\text{CaF}_2$  ridges observed at the coverage exceeding 1 ML grow mainly in the down-the-steps direction and maintain  $\{111\}$  step-free facets at least in the vicinity of the nucleation end. After reaching the critical height of  $\sim 3$  nm they stop growing in width and height most likely because of the strain effects. To determine the chemical composition as well as the atomic arrangement of the wetting layer, synchrotron experiments on surface sensitive photoelectron spectroscopy and photoelectron diffraction are needed.

#### Acknowledgements

This study was partially supported by Russian Ministry of Sciences, INTAS (Grant No 97-10528) and Swiss National Science Foundation (Grant No 7SUPJ062359).

#### References

- [1] M. A. Olmstead, *Thin Films: Heteroepitaxial Systems* W. K. Liu and M. B. Santos (eds.) World Scientific, Singapore, pp. 211–265, 1999.
- [2] D. Loretto, F. M. Ross and C. A. Lucas, *Appl. Phys. Lett.* **68**, 2363 (1996).
- [3] T. Sumiya, T. Miura, H. Fujinuma and S. Tanaka, *Surf. Sci.* **376**, 192 (1996).
- [4] N. S. Sokolov and S. M. Sutorin, *Appl. Surf. Sci.* **175–176** 619–628 (2001).
- [5] L. Pasquali, S. D'Addato, G. Selvaggi, S. Nannarone, N. S. Sokolov, S. M. Sutorin and H. Zogg, *Nanotechnology* **12**, 403–408 (2001).
- [6] L. J. Schowalter and R. W. Fathauer, *J. Vac. Sci. Technol.* **A4**, 1026 (1986).

## Formation specificity of InAs/GaAs submonolayer superlattice

*I. P. Soshnikov*<sup>†</sup>, *B. V. Volovik*<sup>†</sup>, *A. R. Kovsh*<sup>†</sup>, *A. E. Zhukov*<sup>†</sup>,  
*A. F. Tsatsul'nikov*<sup>†</sup>, *O. M. Gorbenko*<sup>†</sup>, *N. N. Ledentsov*<sup>†</sup>, *V. M. Ustinov*<sup>†</sup>,  
*P. Werner*<sup>‡</sup>, *N. D. Zakharov*<sup>§</sup> and *D. Gerthsen*<sup>§</sup>

<sup>†</sup> Ioffe Physico-Technical Institute, St Petersburg, Russia

<sup>‡</sup> MPI für Mikrostrukturphysik, Weinberg 2, D-06120 Halle, Germany,

<sup>§</sup> Universität Karlsruhe, D76128 Karlsruhe, Germany

### Introduction

Heterostructures with submonolayer insertions attract interest due to optical properties and to possibility of the studying of the self-organization effect. Besides, investigation of SML heterostructures is retarded as consequence of problems of the structural and composition characterization [1–5]. The situation is changed on account of development of quantitative methods for HREM image analysis [6–8]. There formation of superlattice heterostructures with InAs submonolayer insertions in GaAs matrix and them optical properties are investigated in the work.

### 1. Experimental

Investigated structures were grown by solid-source molecular beam epitaxy in a Riber 32P apparatus on GaAs(100) substrates. The SML superlattices were formed by deposition of 20 pairs of InAs (0.5 ML thick) — GaAs (thickness of dsp) layers on a GaAs buffer layer. In sample with  $d_{sp} = 15 \text{ \AA}$  number of pairs was reduced to 10 to keep total In content below critical and eliminate degradation of structural and optical properties. Growth temperature for GaAs buffer and cladding layers was 600 °C. The InAs/GaAs superlattices was grown at 485 °C to prevent reevaporation and surface segregation of indium atoms.

Structural characterization was performed using a JEM 4000EX electron microscope at accelerate voltage of 400 kV and using a PHILIPS CM 200 FEG/ST electron microscope at accelerating voltage of 200 kV. TEM specimens were prepared using a typical method with 4 keV Ar ion etching at liquid nitrogen cooling as finished operation. HREM images were processed by special software [7] for the investigation of the In distribution. Optical investigations were carried out in a helium flow cryostat. PL was excited by either Ar<sup>+</sup>-ion laser with  $\lambda = 514.5 \text{ nm}$  or tunable Ti-sapphire laser and detected by CCD camera.

### 2. Results and discussion

HREM images of (110) cross section of studied samples are demonstrated in Fig. 1(a,b,c). These images illustrate that examined structures are coherent and non-defect. Besides, existing (or absence) of the cluster structure in the InAs SML insertions connected to self organization effect can not be ascertained in these images without special analysis. Processing results of HREM images are displayed in Fig. 1(d,e,f). It is seen that In is non-uniformity distributed in these insertions. In these layers have been noted modulation of the composition. The modulation is likely clarified by SML In cluster formation. An averaged lateral size of these clusters is varied from 4 up to 11 nm in according with the spacer thickness. Obtained maps of In content were analyzed for revealing of correlation

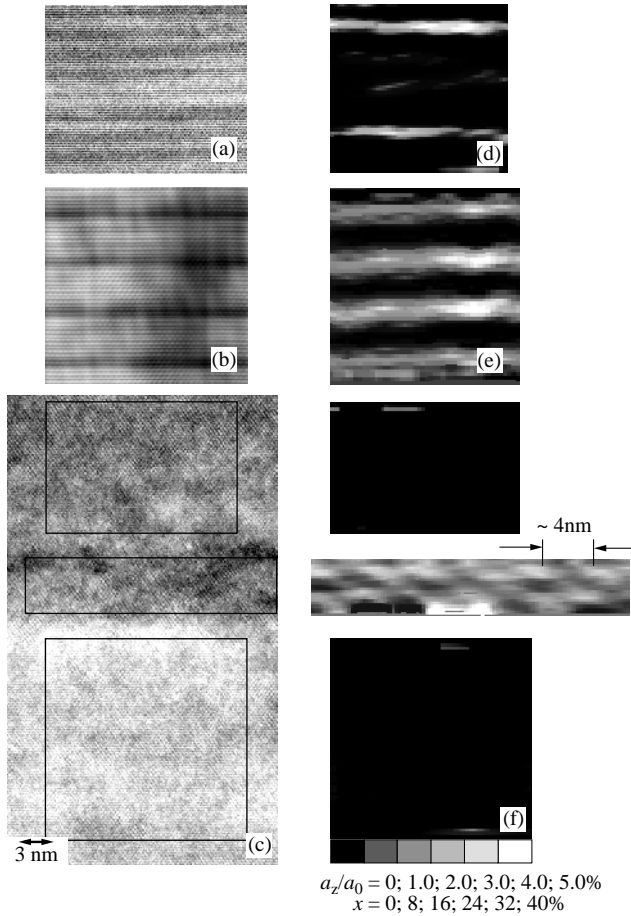


**Fig. 1.** HRTEM images of the (110) cross section of the SML superlattice structures with spacer thickness: 1.4 (a), 3 (b), 10 (c) nm and maps (d, e, f correspondently) of local [002] interplane distance.

self-organization effect by method based Fourier transformation. Figure 2 illustrates dependence of Fourier transformed image for correlated and anticorrelated structures. Fourier image can be expressed as combination of correlated, anticorrelated and random components with

$$I = F(x) \left( C \sum_k [c_k \exp\{iky(f_v)_c\}] + A \sum_k [a_k \exp\{iky(f_v)_a\}] \right) + R(x, y),$$

$$A + C = 1$$

$$\int [a_k \exp\{iky(f_v)_a\}] dk = \int [c_k \exp\{iky(f_v)_c\}] dk = 1$$

where  $F(x)$  is dependence on horizontal direction;  $A$  and  $C$  are coefficients of anticorrelated and correlated fractions of structures;  $\sum_k [c_k \exp\{iky(f_v)_c\}]$  and  $\sum_k [a_k \exp\{iky(f_v)_a\}]$  are normalized Fourier sequences of anticorrelated and correlated components, respectively;

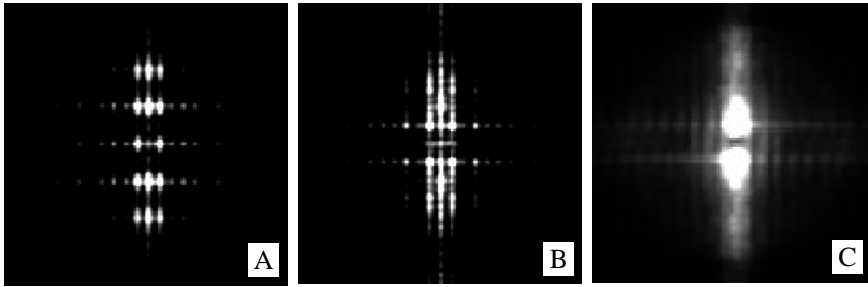


**Fig. 2.** Fourier images of simulated correlated (A) and anticorrelated (B) structures and Fourier transform image of map of LID demonstrated in Fig. 1(f).

$R(x, y)$  is random signal. It is found that correlation and anticorrelation coefficients for heterostructures with 10 and 6 nm spacers are equal about  $C = 0.4$  and  $0.45$  and  $A = 0.6$  and  $0.55$ , respectively. Obtained values are accorded for random and likely partially anticorrelated positions of In rich nanoclusters. Besides, notice that volume of analyzed ranges in these case is a small there we have a problem of accuracy. At the time coefficients of correlated (C) and anticorrelated (A) components are equal  $C = 0.63 \pm 0.1$  and  $A = 0.47 \pm 0.1$ . These values shown that in the structure is likely partially correlated. Obtained values for structure with 1.4 nm spacers are  $C = 0.2 \pm 0.1$  and  $A = 0.8 \pm 0.1$  that are indicative for predominantly anticorrelated structure. Obtained results can be explained using a theory of SML heterostructures formation [2] by parameter value of  $p < 0.5$ .

Figure 3 demonstrates PL spectra of the investigated samples. Line denoted as SML is associated with the recombination via ground state of the SML insertions. It has been seen that decreasing of spacer thickness results in red shift of the PL line. Obtained structural and optical results are agreement.

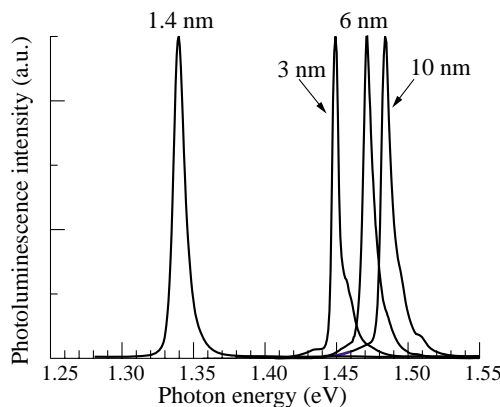


**Fig. 3.** PL spectra of the investigated samples different spacer thickness.

Thus, formation of the nanoscale InGaAs islands in a GaAs matrix was studied. It is demonstrated formation of In rich nanoclusters islands in SML insertions with lateral size from 3.5 up to 10 nm. We found that the nanoclusters are predominantly anticorrelated arrangement for SML insertions separated by 1.4 nm GaAs spacers. Increasing of spacers

thickness leads to predominantly random arrangement of these nanoclusters.

#### *Acknowledgements*

The work was supported by the BMBF and RFBR programs.

#### **References**

- [1] L. Goldstein, F. Glass, J. Y. Marzin, M. N. Charasse and G. Le Roux, *Appl. Phys. Lett.* **47**, 1099 (1985).
- [2] V. A. Shchukin, D. Bimberg, V. G. Malyshev and N. N. Ledentsov, *Phys. Rev. B* **57**, 12262 (1998),
- [3] G. E. Cirlin, V. A. Egorov, B. V. Volovik, A. F. Tsatsul'nikov, V. M. Ustinov, N. N. Ledentsov, N. D. Zakharov, P. Werner and U. Gosele, *Nanotechnology* **12**, 417 (2001).
- [4] O. Brandt, H. Lage and K. Ploog, *Phys. Rev. B* **43**, 14285 (1991).
- [5] M. Gherasimova, B. Gaffey, P. Mitev, L. J. Guido, K. L. Chang, K. C. Hsieh, S. Mitha and S. Spear, *MRS Internet J. Nitride Semicond. Res.* **4S1**, G3.44, (1999).
- [6] A. Rosenauer, U. Fischer, D. Gerthsen and A. Forster, *Ultramicroscopy* **72**, 121 (1998).
- [7] I. P. Soshnikov, O. M. Gorbenko, A. O. Golubok and N. N. Ledentsov, *Semiconductors* **35**, 347 (2001).
- [8] V. L. Indenbom and S. B. Tochilin, *Soviet Physics - Doklady* **35**, 955 (1990).

## Optical properties of InGaN/GaN and AlGaN/GaN multiple quantum well structures

*B. Monemar*<sup>†</sup>, P. P. Paskov<sup>†</sup>, H. Haratizadeh<sup>†</sup>, G. Pozina<sup>†</sup>, J. P. Bergman<sup>†</sup>,  
S. Kamiyama<sup>‡</sup>, M. Iwaya<sup>‡</sup>, H. Amano<sup>‡</sup> and I. Akasaki<sup>‡</sup>

<sup>†</sup> Department of Physics and Measurement Technology, Linköping University,  
S-581 83 Linköping, Sweden

<sup>‡</sup> Department of Electrical Engineering and Electronics and High-Tech Research  
Center, Meijo University, 1-501 Shiogamaguchi, Tempaku-ku, Nagoya 468, Japan

**Abstract.** We report on low temperature photoluminescence (PL) in  $\text{In}_x\text{Ga}_{1-x}\text{N}$  multiple quantum wells (MQWs) with  $x$  in the range 0.1 and highly Si doped barriers of  $\text{In}_{0.01}\text{Ga}_{0.99}\text{N}$ . One sample with 3 QWs of width 3.5 nm and barriers of width 10.5 nm had the MQW in the depletion region of the outer surface. Two PL peaks were observed, one QW exciton from the QW closest to the GaN buffer, one lower energy peak related to a 2DEG at the interface to the GaN buffer layer. In a second similar sample 5 QWs of width 3 nm and with 6 nm highly Si doped  $\text{In}_{0.01}\text{Ga}_{0.99}\text{N}$  barriers the MQW was placed in the n-side depletion region of a pn-junction. At low temperatures the PL and electroluminescence (EL) spectra are quite different at no, low, or reverse bias, the PL appearing at higher energy. At high forward bias a spectral component at the EL position appears. This proves a strong influence of the depletion field on the optical spectra. Preliminary results are also reported for n-doped  $\text{Al}_{0.07}\text{Ga}_{0.93}\text{N}/\text{GaN}$  structures, with near surface MQWs.

## Introduction

A special property of the III-nitride materials is the presence of strong polarization charges at surfaces and interfaces in all device structures [1]. Both spontaneous (sp) and piezoelectric (pz) polarizations are in general important [2, 3]. At an outer surface the sp polarization charges are expected to have a strong influence on the pinning of the Fermi level. In the common case of Ga(In) face surfaces a pinning at the valence band edge, or possibly in the lower part of the bandgap in the case of a large number of surface states, is expected [4], and a depletion region is present close to the surface [3–5]. For the common case of an n-doped MQW structure ending at the surface the QWs will experience a strong depletion field, which is also expected to vary strongly between the different QWs in the MQW region, leading to different optical spectra for each QW [6]. A similar situation is expected for an n-type MQW present on the n-side of a pn-junction. Since the QWs are present in a strong field gradient in these cases, optical excitation producing free carriers will cause a change in the potential profile of the structure, due to drift of the photo-excited carriers in the strong electric field [7].

## 1. Samples and experimental

Results for two specific InGaN/GaN samples are discussed in this paper. Both are grown by MOVPE on a (0001) sapphire substrate with AlN buffer layer, followed by a nominally undoped GaN layer [8]. Finally, for sample A three InGaN quantum wells of width 3.5 nm were grown on the top of such a GaN layer. The In composition in the QWs was about 0.1. The barriers of thickness 10.5 nm were  $\text{In}_y\text{Ga}_{1-y}\text{N}$  with a small In composition ( $y = 0.01$ ),

doped with Si to about  $5 \times 10^{18} \text{ cm}^{-3}$ . A second sample B had five 3 nm  $\text{In}_{0.1}\text{Ga}_{0.9}\text{N}$  QWs separated by 6 nm Si doped  $\text{In}_{0.01}\text{Ga}_{0.99}\text{N}$  barriers with a similarly low In content, but had a p-type contact on top, and a semitransparent top metallisation as well. The MQW part was grown at a constant growth temperature of about  $800^\circ\text{C}$  in both samples. The  $\text{AlGaIn}/\text{GaIn}$  samples discussed here were also MOCVD grown MQWs with 5 QWs about 3 nm wide and with  $\text{Al}_{0.07}\text{Ga}_{0.93}\text{N}/\text{GaIn}$  barriers about 7 nm. Most samples were highly Si-doped near surface structures.

For optical excitation in the PL measurements we have used a 266 nm cw laser. For the transient PL data we used the third harmonics ( $\lambda = 266 \text{ nm}$ ) from a Ti:sapphire femtosecond pulse laser. Some PL spectra were obtained as time-integrated signals with short pulse excitation. The PL transients were detected either by a time-correlated photon counting system with time resolution better than 200 ps, or with a UV sensitive streak camera system. PL excitation (PLE) spectra were obtained with a simple arrangement using a Xe lamp and a monochromator as excitation source. The samples were placed in a variable temperature cryostat for measurements at 2–300 K.

## 2. Results for $\text{InGaIn}/\text{GaIn}$ MQWs and discussion

The PL spectra from the two MQW samples discussed here are shown in Fig. 1. At the lowest excitation the PL linewidth of the main peak Q1 is about 40 meV. We interpret the Q1 peak as a QW exciton transition, in a QW having a substantial electron filling. A weaker low energy peak Q2 is observed about 0.1 eV below the main PL peak in sample A (Fig. 1(a)). This peak is due to a separate PL transition, i. e. not an LO replica of Q1. The Q2 transition is increased in strength with increasing excitation intensity, and shifts to higher energy [9]. With increasing temperature the low energy PL spectrum disappears, leaving only the Q1 transition at room temperature [9].

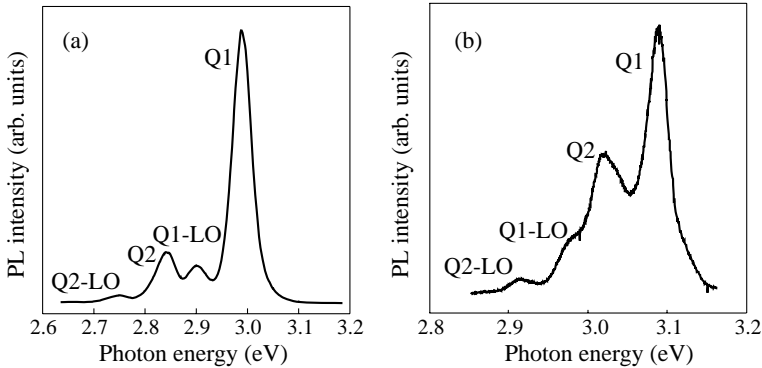


**Fig. 1.** Photoluminescence spectra of sample A (a) and sample B (b) at 2 K and low cw excitation intensity.

The PL spectrum of sample B, measured under open circuit conditions with similar excitation as in Fig. 1(a) at 2 K, is shown in Fig. 1(b). The Q1 transition in this case is also quite narrow, about 35 meV. Sample B also shows the presence of two different peaks, but here the peak Q2 is situated much closer to Q1, at a distance about 60 meV at low excitation. LO-replicas of both Q1 and Q2 are also seen. In fact at somewhat elevated temperature the Q2 peak develops into a doublet structure in this sample. We point out that none of these



samples shows any TEM evidence of phase separation involving nm-size regions of higher In composition [10].

PLE spectra for sample A at 2 K were recently reported [9]. The results (Fig. 2(a)) provide strong evidence for the interpretation of the origin of the Q2 transition as related to an electron potential minimum at the interface to the GaN buffer layer, as shown schematically in Fig. 2(b). We suggest that this potential is mainly induced by the optical excitation, and is very shallow in this sample, explaining the fact that Q2 disappears already above about 20 K at low (cw) excitation.

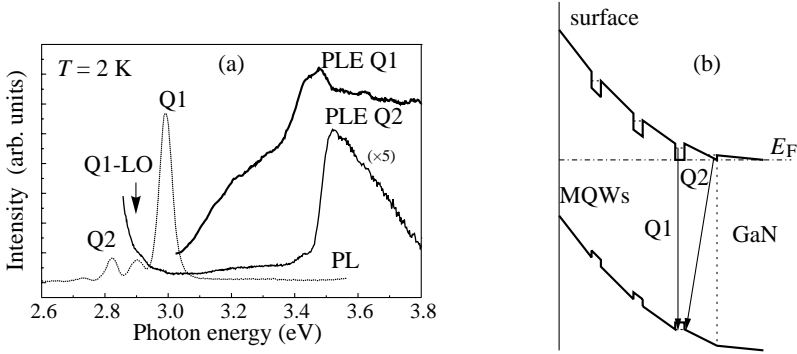


**Fig. 2.** (a) Photoluminescence excitation spectra of sample A. (b) Sketch of the potential variation across the MQW region for sample A.

The transient PL data for sample A reveal a PL decay time of about 5 ns at 2 K [5, 9], which is close to the expected radiative lifetime of excitons at 2 K in a 3 nm InGa<sub>N</sub>/Ga<sub>N</sub> QW [11]. The PL decay is very slow for the Q2 peak, about 200 ns at 2 K [9]. For sample B the Q1 peak has a decay time about 3.5 ns at 2 K [9]. The Q2 peak has a slower decay, the value is about 12 ns. This is much faster than the corresponding transition for sample A, consistent with a tunneling type recombination process (Fig. 2(b)) with a much thinner barrier width in sample B. This transition seems to overlap with a second QW PL with a low electron filling, and thus a higher internal field than for Q1.

For sample B a series of PL spectra has been obtained with varying bias, at temperatures from 2 K to 300 K. The spectra were obtained time-integrated with pulsed excitation, and therefore show some spectral broadening compared to Fig. 1(b). Figure 3(a) shows a collection of such spectra obtained at 2 K, in Fig. 3(b) the corresponding data at 200 K are shown. In both cases the electroluminescence (EL) spectra obtained for different cw forward bias but without laser excitation are also shown. It is clear that the optical excitation induces a higher energy part of the PL spectrum (at low temperatures) that is not present in the EL spectra.

The above data clearly show the presence of a strong potential gradient already for the region close to the GaN buffer layer. Such a strong gradient is necessary to leave the transition Q2 at lower energy than Q1 (see Fig. 2(b)). The observed Q1 transition is here interpreted as the excitonic PL from the lowest QW closest to the GaN buffer layer (Fig. 2(b)). The high Si doping in the barriers is expected to cause a high electron filling in the QWs, so that the internal polarization-induced electric field in the QWs is rather well screened. The optical excitation will produce carriers that will affect this filling, and presumably also the electron pocket close to the GaN buffer, responsible for the Q2

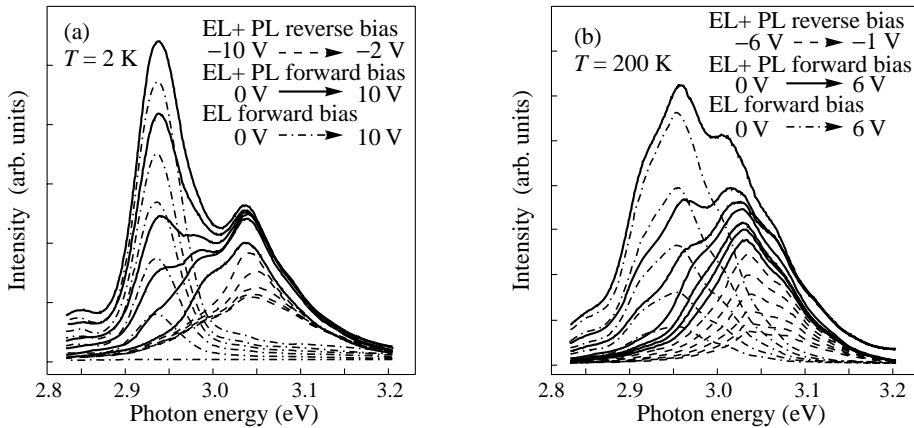


**Fig. 3.** Photoluminescence (PL) and electroluminescence (EL) of sample B at different applied biases: (a)  $T = 2$  K; (b)  $T = 200$  K.

transition. The high depletion field close to the surface may cause the carriers to leak out of the QWs, however. The depletion field is much higher for the near surface QWs,  $> 1$  MV/cm for the doping used in this sample. In the case when the QWs will not hold the carriers, the internal piezoelectric field will also be important. The PL spectra of the two outer QWs would be expected to be noticeably redshifted [6], and cannot be accounted for within the narrow linewidth of Q1. No trace is observed of additional QW spectra at lower energies, apart from the Q2 spectrum. We conclude that the two outer QWs are empty, and optically inactive.

The conclusions from the data without forward bias for sample B with 5 QWs in a pn-junction depletion field are similar. It seems like also for the pn-junction LED case one QW dominates the PL at 2 K, indicating that the QWs close to the pn-junction are not active. The situation is then expected to be different for EL under forward bias. Clearly the EL spectrum appears at lower energy than the PL spectrum from the lowest QW, and there is a gradual development of spectral contributions towards lower energy as the forward bias is increased (Fig. 3). This indicates involvement of additional QWs in the radiative PL process as the depletion field is decreased. The difference between PL and EL spectra at low  $T$  suggests that the QWs close to the pn-junction have no electron filling, and are dominated by the pz-induced internal field under forward bias. In addition the hole diffusion length is small at low  $T$  so that the QWs close to the buffer layer may not be reached with electrical injection. This will be different at room temperature, in which case the PL and EL spectra are similar.

### 3. Results for AlGaIn/GaN MQWs

A large number of samples doped with Si were studied (Fig. 4). For the modulation-doped samples clear signs of band gap renormalization were observed. An interesting result is the strong hole localisation in these samples, making the PL decay time doping independent at 2 K [12]. In Fig. 4(b) is shown an interesting difference in the PL spectra for the case of Si doping in the barrier and the well respectively. In the latter case a lower energy PL emission dominates, possibly related to a donor band. In all spectra there is evidence for spectral overlap between inequivalent QWs, due to the variation in the surface depletion

field between different QWs. This also explains the apparent rather large linewidth in most spectra, the linewidth for a single QW in these samples is of the order 20 meV.

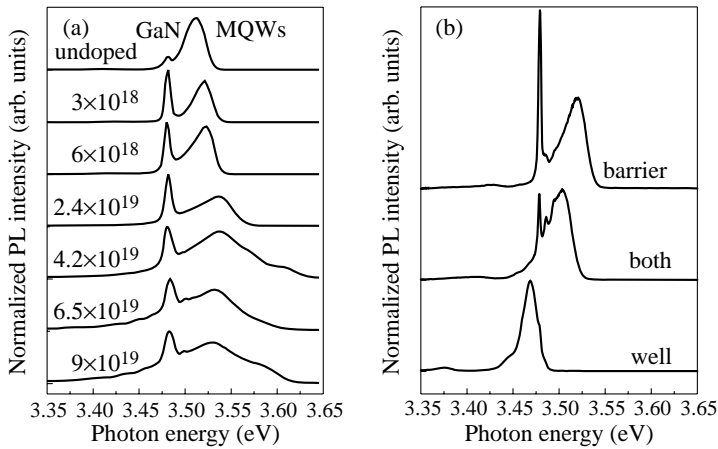


**Fig. 4.** Photoluminescence spectra of Si-doped  $\text{Al}_{0.07}\text{Ga}_{0.93}\text{N}/\text{GaN}$  MQW samples measured at  $T = 2$  K. (a) Doping in the barrier with different doping level. (b) Different doping position with the same doping level,  $6 \times 10^{18} \text{ cm}^{-3}$ .

## References

- [1] F. Bernadini, V. Fiorentini and D. Vanderbilt, *Phys. Rev. B* **56**, R10024 (1997).
- [2] T. Takeuchi, H. Takeuchi, S. Sota, H. Sakai, H. Amano and I. Akasaki, *Jpn. J. Appl. Phys.* **36**, L177 (1997).
- [3] B. Monemar and G. Pozina, *Progress in Quantum Electronics* **24**, 239 (2000).
- [4] O. Mayrock, H. J. Wunsche and F. Henneberger, *Phys. Rev. B* **62**, 16870 (2000).
- [5] G. Pozina, J. P. Bergman, B. Monemar, M. Iwaya, S. Nitta, H. Amano and I. Akasaki, *Appl. Phys. Lett.* **77**, 1638 (2000).
- [6] V. Fiorentini, F. Bernadini, F. Della Sala, A. Di Carlo and P. Lugli, *Phys. Rev. B* **60**, 8849 (1999).
- [7] J. P. R. David, T. E. Sale, A. S. Pabla, P. J. Rodrigues-Girones, J. Woodhead, R. Grey, G. J. Rees, P. N. Robson, M. S. Skolnick and R. A. Hogg, *Appl. Phys. Lett.* **68**, 820 (1996).
- [8] H. Amano, N. Sawaki, I. Akasaki and Y. Toyoda, *Appl. Phys. Lett.* **48**, 35 (1986).
- [9] B. Monemar, P. P. Paskov, J. P. Bergman, G. Pozina, T. Paskova, M. Iwaya, S. Kamiyama, H. Amano and I. Akasaki, *Proc. PLMCN-1 (Rome 2001)*, *Phys. Stat. Sol. (a)* **190**, No1 (2002).
- [10] Yu. G. Musikhin, D. Gerthsen, D. A. Bedarev, N. A. Bert, W. V. Lundin, A. F. Tsatsulnikov, A. V. Sakharov, A. S. Usikov, Zh. I. Alferov, I. L. Krestnikov, N. N. Ledentsov, A. Hoffmann and D. Bimberg, *Appl. Phys. Lett.* **80**, 2099 (2002).
- [11] M. Nardelli, K. Rapcewicz and J. Bernholc, *Appl. Phys. Lett.* **71**, 3135 (1997).
- [12] H. Haratizadeh, P. P. Paskov, G. Pozina, P. O. Holtz, B. Monemar, S. Kamiyama, M. Iwaya, H. Amano, and I. Akasaki, *Appl. Phys. Lett.* **80**, 1373 (2002).

## Carrier recombination in InGaN nanostructures: carrier localization in quantum-dots, carrier separation by quantum-confined Stark effect

Noad Shapiro, Henning Feick and *Eicke R. Weber*

Department of Materials Science and Engineering,  
University of California, Berkeley, CA 94720, USA

InGaN quantum well structures are the active layer of most nitride-based short-wavelength LED and laser structures for blue and blue-green light emission. However, fundamental properties of these quantum wells are still not yet well understood. They are the topic of ongoing controversies.

Structural analysis techniques such as TEM reveal evidence that the distribution of In in InGaN quantum well layers is inhomogeneous on the nanoscale. These kind of inhomogeneities, together with fluctuations of the quantum well width, can lead to regions with smaller bandgap and thus carrier localization.

On the other side, the strong electric fields from spontaneous polarization in these hexagonal crystals, plus piezoelectric fields caused by residual biaxial strain, can result in separation of electrons and holes caused by the quantum-confined Stark effect (QCSE).

We have developed spectroscopic tools that include the study of the optical emission characteristics as a function of injection intensity, temperature, and externally applied biaxial strain to distinguish between these two competing effects that control the carrier recombination process. The analysis of the emission energy as a function of the applied biaxial strain can be analyzed in terms of a single parameter, which we call the effective localization parameter.

We will discuss the results of this type of analysis of structures grown by different methods, and compare them with structural analysis by TEM techniques. The key issue to be discussed finally is how to better control the carrier recombination process in these nanostructures.

Results of these studies have been published in the following articles:

### References

- [1] P. Perlin, C. Kisielowski, V. Iota, B. A. Weinstein, L. Mattos, N. A. Shapiro, J. Krüger, E. R. Weber and J. Yang, *Appl. Phys. Lett.* **73**, 2778 (1998).
- [2] N. A. Shapiro, P. Perlin, C. Kisielowski, L. S. Mattos, J. W. Yang and E. R. Weber, *MRS Internet J. Nitride Semicond. Res.* **5**, 1 (2000).
- [3] N. A. Shapiro, Y. Kim, H. Feick, E. R. Weber, P. Perlin, J. W. Yang, I. Akasaki and H. Amano, *Phys. Rev.* **B 62**, (*Rapid Commun.*), R 16318 (2000).
- [4] N. A. Shapiro, H. Feick, N. F. Gardner, W. K. Gotz, P. Waltereit, J. S. Speck and E. R. Weber, *Phys. Stat. Sol.* **B 228**, 147 (2001).
- [5] Noad A. Shapiro, Henning Feick, William Hong, Nathan F. Gardner, Werner K. Götz, J. W. Yang and Eicke R. Weber, *MRS Symp. Proc.* (2002), to be published.

## Band gap of hexagonal InN and InGaN alloys

V. Yu. Davydov<sup>1</sup>, A. A. Klochikhin<sup>1</sup>, V. V. Emtsev<sup>1</sup>, A. V. Sakharov<sup>1</sup>,  
S. V. Ivanov<sup>1</sup>, V. A. Vekshin<sup>1</sup>, F. Bechstedt<sup>2</sup>, J. Furthmüller<sup>2</sup>, J. Aderhold<sup>3</sup>,  
J. Graul<sup>3</sup>, A. V. Mudryi<sup>4</sup>, H. Harima<sup>5</sup>, A. Hashimoto<sup>6</sup>, A. Yamamoto<sup>6</sup>, J. Wu<sup>7</sup>,  
H. Feick<sup>8\*)</sup> and E. E. Haller<sup>8</sup>

<sup>1</sup> Ioffe Physico-Technical Institute, St Petersburg, Russia

<sup>2</sup> Institut für Festkörpertheorie und Theoretische Optik, Friedrich-Schiller-Universität  
Jena, Max-Wien-Platz 1, D-07743 Jena, Germany

<sup>3</sup> LfI University of Hannover, Schneiderberg 32, 30167 Hannover, Germany

<sup>4</sup> Institute of Solid State and Semiconductor Physics, Belarus Academy of Sciences,  
Brovki 17, 220072 Minsk, Belarus

<sup>5</sup> Department of Electronics and Information Science, Kyoto Institute of Technology,  
Matsugasaki, Sakyo-ku, Kyoto 606-8585, Japan

<sup>6</sup> Department of Electronics Engineering,  
Fukui University, Bunkyo, Fukui 910-8507, Japan

<sup>7</sup> Applied Science and Technology, University of California,  
Berkeley, CA 94720, USA

<sup>8</sup> Department of Materials Science and Engineering, University of California,  
Berkeley, CA 94720, USA

\*) on leave from 'Center of Advanced European Studies and Research'

**Abstract.** We present results of photoluminescence studies of the band gap of non-intentionally doped single-crystalline hexagonal InN layers and In-rich  $\text{In}_x\text{Ga}_{1-x}\text{N}$  alloy layers ( $0.36 < x < 1$ ). The band gap of InN is found to be close to 0.7 eV. This is much smaller than the values of 1.8 eV to 2.1 eV cited in the current literature. A bowing parameter of  $b \approx 2.5$  eV allows one to reconcile our and the literature data for the band gap values of  $\text{In}_x\text{Ga}_{1-x}\text{N}$  alloys in the entire composition region.

InN and In-rich  $\text{In}_x\text{Ga}_{1-x}\text{N}$  alloys have not been investigated thoroughly because of difficulties associated with the growth of these compounds. At the same time, knowledge of their fundamental parameters is vitally important for the development of In-based nanostructures. Recently improved growth techniques have made it possible to obtain single-crystalline InN layers. Optical measurements on these layers revealed a strong photoluminescence (PL) band near the absorption edge in a range of 0.75 eV to 0.9 eV [1]. In the present work we argue that the PL bands of non-intentionally doped InN samples studied are similar to the high energy bands in PL spectra of heavily doped III–V or II–VI crystals. The analysis of the PL data leads to the conclusion that the InN band gap is much smaller than the value of 1.8 eV reported previously [2]. These findings are supported by PL studies of In-rich  $\text{In}_x\text{Ga}_{1-x}\text{N}$  alloys.

Single-crystalline n-type InN epilayers were grown on (0001) sapphire substrates by the metal-organic chemical vapor deposition [3] (sample 1), and metalorganic molecular-beam epitaxy [4] (samples 2, 3 and 4) techniques. Hall measurements revealed free carrier

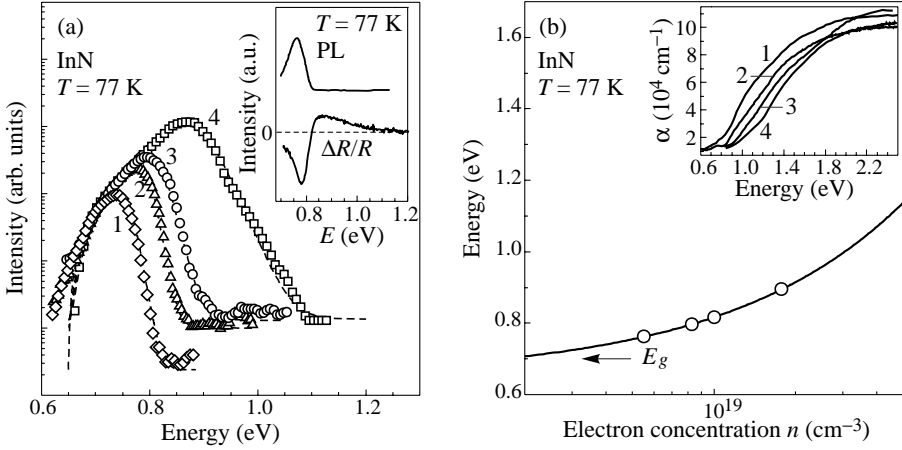


**Fig. 1.** (a) Open symbols, semilog PL spectra of InN layers with different carrier concentrations:  $6 \times 10^{18} \text{ cm}^{-3}$  (1),  $9 \times 10^{18} \text{ cm}^{-3}$  (2),  $1.1 \times 10^{19} \text{ cm}^{-3}$  (3), and  $4.2 \times 10^{19} \text{ cm}^{-3}$  (4). Dashed lines, fitted curves. (b) Calculated shift of optical absorption edge due to Burstein-Moss effect in n-type InN (solid line). Open circles mark  $E_g + E_F$  positions estimated from PL spectra in our samples. The inset shows absorption edge of InN samples.

concentrations of  $6 \times 10^{18}$ ,  $9 \times 10^{18}$ ,  $1.1 \times 10^{19}$  and  $4.2 \times 10^{19} \text{ cm}^{-3}$  in samples 1 to 4, respectively. A set of  $\text{In}_x\text{Ga}_{1-x}\text{N}$  alloys in the composition range of  $0.36 < x < 1$  was grown by plasma-assisted molecular-beam epitaxy under conditions similar to those for InN [1]. Only InN and  $\text{In}_x\text{Ga}_{1-x}\text{N}$  films with hexagonal structure, showing no traces of other polymorphs, as determined by x-ray and Raman measurements were investigated. An argon laser (2.54 eV) was used as an excitation source in the PL measurements.

The high energy PL band in heavily doped semiconductors results from recombination of degenerate electrons with photoholes near the top of the valence band. The valence-conduction band diagram given in [6] combined with the results of [7] lead in the energy region  $\hbar\omega > E_G$  to the following shape of the PL band

$$I(\hbar\omega) \sim [\hbar\omega - E_G]^{\gamma/2} f(\hbar\omega - E_G - E_F), \quad (1)$$

where  $E_G$  is charge carrier concentration-dependent parameter related to the band gap  $E_g$ ,  $E_F$  is the Fermi energy for the degenerate electrons, and  $f(\hbar\omega - E_G - E_F) = 1/[\exp\{(\hbar\omega - E_G - E_F)/kT\} + 1]$  is the Fermi distribution function. The value of  $\gamma = 1$  if only vertical interband transitions are allowed,  $\gamma = 4$  if the momentum conservation law is completely broken as a result of influence of defects and/or impurities on the hole states.

The shape of the PL band of the degenerate electron gas has two characteristic features. The first one is a high energy wing of the band which shows an exponential decrease in the region of  $(\hbar\omega - E_G) \approx E_F$  due to a decrease of the electron population in accordance with Fermi function  $f(\hbar\omega - E_G - E_F)$ . The second is the low energy wing of the PL band at  $\hbar\omega < E_G$  which typically demonstrates the Urbach tail which can overlap with PL bands related to the recombination of electrons with deeper localized states of holes.

Figure 1(a) shows PL spectra obtained at 77 K for the investigated InN samples and the fitted curves obtained using Eq. (1). The temperature estimated from the exponential slope of the high-energy wing of the PL bands is close to the measurement temperature

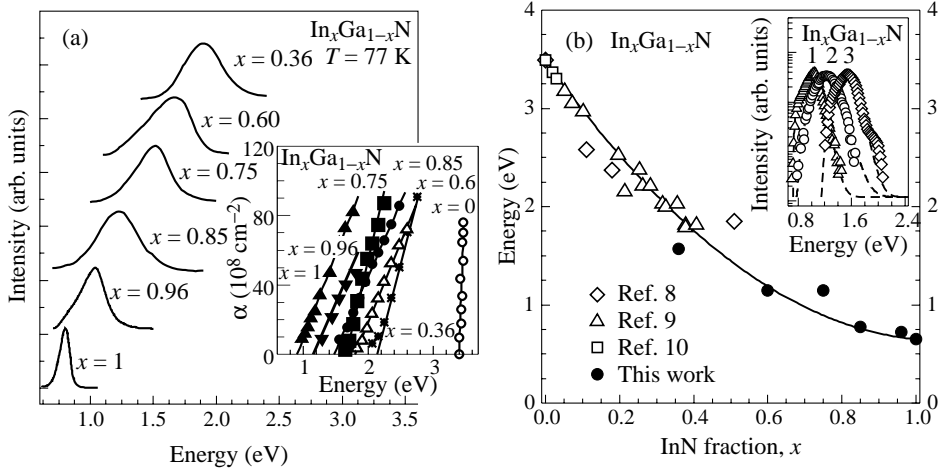


**Fig. 2.** (a) PL spectra and absorption edge of In-rich  $\text{In}_x\text{Ga}_{1-x}\text{N}$  layers. (b)  $E_g$  estimated for In-rich alloys studied in this work, and positions of PL band maxima in Ga-rich alloys taken from [8–10] as a function of  $\text{In}_x\text{Ga}_{1-x}\text{N}$  composition. The inset shows semilog PL spectra and fitted curves obtained using Eq. (1) for most perfect alloys:  $x = 0.96$  (1),  $x = 0.85$  (2), and  $x = 0.75$  (3).

for all crystals except the InN sample 4. This discrepancy is probably due to sample inhomogeneity and a very high doping level. The fitting further shows that  $\gamma$  close to 4 should be used in Eq. (1) for the InN samples studied. It follows from Eq. (1), that the low-energy parts of the fitted curves go to zero at  $\hbar\omega \rightarrow E_g$  defining the parameter  $E_g$ . The  $E_g$  value obtained from the fitting procedure was found to be close to 0.65 eV. It coincides for all InN samples studied within the accuracy of the model used. Taking into account uncertainties in the estimation procedure using Eq. (1) for reference heavily doped n-GaAs, it is safe to state that the  $E_g$  of hexagonal InN lies between 0.65 eV and the PL band maximum at 0.73 eV for sample 1. The mean value of  $E_g \sim 0.7\text{ eV}$  is slightly smaller than that suggested by calculations [1].

The inset in Fig. 1(a) shows the PL and photomodulated reflectance (PR) spectra obtained for one of the InN samples. The zero point of the PR spectrum is close to the energy  $(\hbar\omega - E_g) = E_F$ , and the shape of the PR spectrum indicates that the Fermi distribution of the electrons is affected by the photomodulation.

The Fermi energies  $E_F$  estimated from PL spectra are 112.5, 147.5, 167.5 and 245 meV in samples 1 to 4, respectively. The  $E_F$  as a function of electron concentration  $n$  ( $\text{cm}^{-3}$ ) under the assumption of isotropic electron band with the effective mass  $m^* = 0.1m_0$  is given by  $E_F = 16.6(m_0/m^*)(n \times 10^{-19})^{2/3}\text{ meV}$ . The electron concentrations calculated from the Fermi energies are in good agreement with Hall measurements. The shift of the optical absorption edge of n-type InN due to the Burstein-Moss effect calculated in this model is presented in Fig. 1(b). It can be seen that the absorption edge shifts considerably as the electron concentration increases.

Figure 2(a) shows the PL spectra of the  $\text{In}_x\text{Ga}_{1-x}\text{N}$  layers studied. It is evident that the PL bands shift toward higher energies as the Ga content in the alloy increases. The FWHMs of PL bands for alloys are larger than that for InN, and they are about 300 meV at 77 K. Figure 2(b) depicts  $E_g$  for In-rich alloys studied in this work as a function of alloy

composition. The alloy composition was estimated, according to Vegard's law, from the lattice constant  $c$  obtained from x-ray measurements. This figure also presents the position of the PL band maxima taken from the papers of other authors for Ga-rich  $\text{In}_x\text{Ga}_{1-x}\text{N}$  alloys. The experimental points in Fig. 2(b) are scattered to some extent, but they can be fitted by a smooth curve  $E_g = 3.493 - 2.843x - bx(1-x)$  where the bowing parameter is taken to be  $b = 2.5$  eV. It is clear that the data obtained from the PL spectra of  $\text{In}_x\text{Ga}_{1-x}\text{N}$  layers ( $0.36 < x < 1$ ) confirm the small band gap of InN.

To summarize, the analysis of PL data obtained on non-intentionally doped single-crystalline hexagonal InN leads to the conclusion that the true band gap of InN is  $E_g \approx 0.7$  eV. This finding is supported by studies of the PL bands in In-rich  $\text{In}_x\text{Ga}_{1-x}\text{N}$  alloys and photorefectivity measurements of InN layers. Our conclusions are also confirmed by first-principles calculations of the InN band gap. The discrepancy with the earlier data on  $E_g$  can be explained by the improved quality of InN layers. This explanation is supported by our study of InN samples with  $E_g$  of 1.8 eV, which, according to x-ray and Raman data, are polycrystalline and exhibit Hall concentrations of electrons exceeding  $4 \times 10^{20} \text{ cm}^{-3}$ .

#### Acknowledgments

The authors are grateful to Prof. S. A. Permogorov and Prof. B. V. Novikov for fruitful discussions. We thank V. A. Kapitonov, A. N. Smirnov, D. S. Sizov, N. V. Kryzhanovskaya and V. V. Mamutin for their assistance in measurements and MBE growth. This work is supported by the Programs "Lowdimensional Quantum Structures" and "Nanostructures", and CRDF (grant No. RP1-2258).

#### References

- [1] V. Yu. Davydov, A. A. Klochikhin *et al*, *phys. stat. sol.(b)* **229**, 1 (2002).
- [2] T. L. Tansley and C. P. Foley, *J. Appl. Phys.* **59**, 3241 (1986).
- [3] E. Kurimoto, H. Harima *et al*, *phys. stat. sol. (b)* **228**, 1,(2001).
- [4] J. Aderhold, V. Yu. Davydov *et al*, *J. Cryst. Growth* **222**, 701 (2001).
- [5] V. V. Mamutin, V. A. Vekshin *et al*, *phys. stat. sol. (a)* **176**, 247 (1999).
- [6] E. Burstein, *Phys. Rev.* **93**, 632 (1954).
- [7] A. P. Levanyuk and V. V. Osipov, *Sov. Phys. Usp.* **24**, 187 (1981) [*Usp. Fiz. Nauk* **133**, 427 (1981)].
- [8] M. H. Kim and J. K. Cho *et al*, *phys. stat. sol. (a)* **176**, 269 (1999).
- [9] K. P. O'Donnell *et al*, *J. Phys. Condens. Matt.* **13**, 6977 (2001).
- [10] A. Klochikhin, A. Reznitsky *et al*, *Proc. 9th Int. Symp. "Nanostructures: Physics and Technology"*, Ioffe Institute, St Petersburg, p. 554, (2001).



## Production scale MOVPE reactors for electronic and optoelectronic applications

H. Protzmann<sup>†</sup>, G. Gerstenbrandt<sup>†</sup>, A. Alam<sup>†</sup>, O. Schoen<sup>†</sup>,  
 M. Luenenbuerger<sup>†</sup>, Y. Dikme<sup>‡</sup>, H. Kalisch<sup>‡</sup>, R. H. Jansen<sup>‡</sup> and *M. Heuken*<sup>†</sup>  
<sup>†</sup> AIXTRON AG, D-52072 Aachen, Germany  
<sup>‡</sup> Institut für Theoretische Elektrotechnik, RWTH Aachen,  
 D-52074 Aachen, Germany

**Abstract.** In this letter a number of latest results from the process development on AIXTRON production scale MOVPE reactors will be reported. Growth of GaN on alternative substrates has been examined. Up to 900 nm crack free GaN layer were deposited on Si using a double nucleation interfacing technique. Low yellow band vs. band-edge related photoluminescence emission ratios have been observed and sheet resistances of up to 3500  $\Omega/\square$  have been achieved on 2" Si substrates. Also, first results are reported of the up-scaling of the Planetary Reactor<sup>®</sup> to 24×2". First results from fully loaded runs show an average 2" on wafer peak wavelength standard deviation of 3.8 nm, average wafer to wafer standard deviation across all wafers of 2.0 nm and average 3×2" disk to disk standard deviation of 1.6 nm at an average wavelength of 477.9 nm across all wafers (evaluated with peak integration and 2 mm edge exclusion for the 2" wafers). Photoluminescence peak intensity (area) varied with 13.6% standard deviation wafer to wafer and 12.8% disk to disk. On wafer intensity deviation was 11.3%.

## Introduction

Heterostructures in the material system AlGaInN/GaN have been accepted generally as the leading contender for display and lighting applications in the green to blue/UV spectral range. Furthermore, the AlGaInN/GaN structures are recognized to have a very high potential for electronic devices. The metal organic vapor phase epitaxy (MOVPE) has established itself as the layer growth method of choice for these (and other) semiconductor materials. AIXTRON's AIX 2000 G3 HT system family was developed to meet the needs of modern production facilities by low overall running costs and low cost of ownership while maintaining high standards for layer quality and uniformity on wafer and wafer to wafer.

### 1. Development of GaN/Si

Examining the growth of GaN on alternative substrates, growth on Si has been investigated in depth. Growth of GaN on Si(111) substrate was optimized using interlayers of low temperature (LT) AlN (cf. fig. 1 for the structure). The first LT buffer layer was grown at

GaN ( <i>d</i> , <b>1120°C–1170°C</b> )
AlN ( <b>12.45 nm</b> , <b>550°C–720°C</b> )
GaN (350 nm, <b>1120°C–1170°C</b> )
AlN (32 nm, 720°C)
Si-substrate

**Fig. 1.** Structure of the grown samples. Bold printed parameters were investigated.

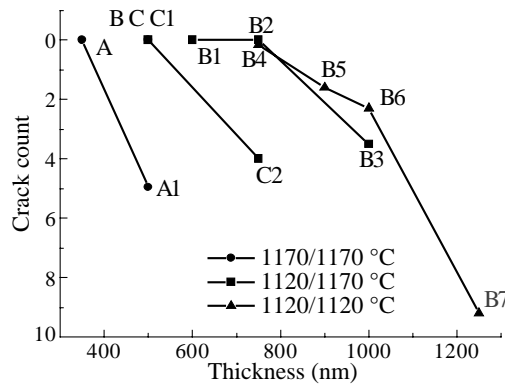


**Fig. 2.** Crack count as a function of the thickness of the second HT GaN layer.

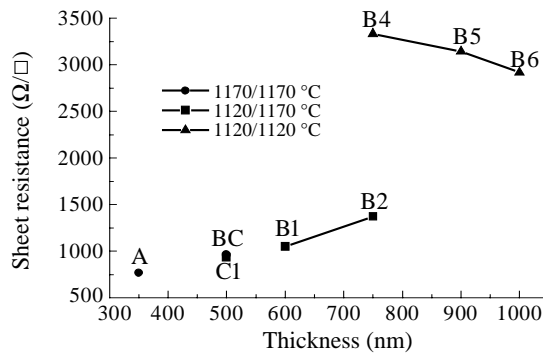


**Fig. 3.** Sheet resistance as a function of thickness of second HT GaN layer.

720 °C. In these experiments, we investigated the effects of the growth temperatures of the second LT buffer layer and the two HT buffer layers. The films were characterized by in-situ reflectance measurements, room temperature (RT) photoluminescence (PL) and sheet resistance measurements. We achieved best results using a growth temperature of 635 °C for the second LT buffer layer and 1120 °C for the HT buffer layers. We used crack counting in a defined area by optical microscope to classify the grown structures. In figure 2 the crack count of structures is shown as a function of the thickness of the second HT GaN layer. In this graph the groups A (550 °C), B (635 °C) and C (720 °C) represent the growth temperature of the second LT AlN-layer. The index designates different target thicknesses for any nucleation temperature series. Figure 3 shows the sheet resistance of the structures as a function of the thickness of second HT GaN layer. Up to 900 nm of crack-free GaN film with a smooth surface, low yellow PL band emission and high sheet resistance (3500 Ω/□) were achieved on 2'' Si substrates. This GaN film is well suited as the buffer for the subsequent deposition of high electron mobility transistors (HEMT).

## 2. Up-scaling to 24×2''

To increase the system throughput for mass production applications the reactor geometry has been scaled up to 24×2'' (8×3×2'') in the AIX 2600 HT G3 configuration recently. Numerical simulation of thermal field and decomposition chemistry has been performed for the new reactor set-up. From the simulation results initial values for the respective

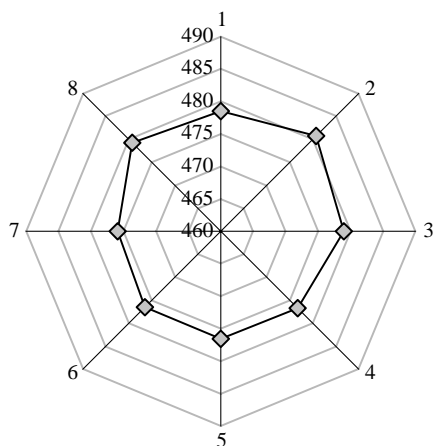


**Fig. 4.** Average photoluminescence wavelength per disk of a fully loaded  $24 \times 2''$  configuration: radius indicates the wavelength and position on the circumference is the disk load position.

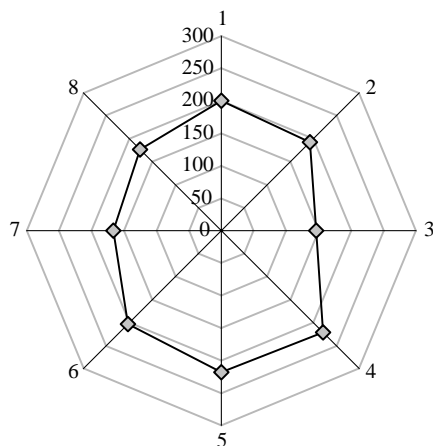


**Fig. 5.** Average photoluminescence peak intensity per disk of a fully loaded  $24 \times 2''$  configuration: radius indicates the intensity and position on the circumference is the disk load position.

process parameters have been chosen.

After preliminary tuning a first fully loaded growth run has been performed. The average on ( $2''$ ) wafer peak wavelength was 477.9 nm across all wafers. To eliminate the effect of thin layer interference on the observed peak wavelength the spectra have been evaluated by peak area integration. The wavelength of the area center is interpreted as peak wavelength. Additionally a 2 mm edge exclusion for the  $2''$  wafers has been applied. The standard deviation average for all wafers was 3.8 nm on wafer. The average wafer to wafer standard deviation across all wafers was 2.0 nm and the average  $3 \times 2''$  disk to disk standard deviation was 1.6 nm. The photoluminescence peak intensity (integrated area) varied with 13.6% standard deviation wafer to wafer and 12.8% disk to disk. On wafer intensity standard deviation was 11.3%.

## High-efficient up-conversion of photoluminescence in CdSe/ZnSe nanostructures

V. V. Strelchuk<sup>†</sup>, M. Ya. Valakh<sup>†</sup>, M. V. Vuychik<sup>†</sup>, S. V. Ivanov<sup>‡</sup>, P. S. Kop'ev<sup>‡</sup>  
and T. V. Shubina<sup>‡</sup>

<sup>†</sup> Institute of Semiconductor Physics of NAS, 03028 Kyiv, Ukraine

<sup>‡</sup> Ioffe Physico-Technical Institute, St Petersburg, Russia

**Abstract.** The intensive up-conversion photoluminescence (UPL) was observed at low temperatures in CdSe/ZnSe structures with single CdSe inserts of a nominal thickness of 1.5 and 0.6 ML. The quadratic-like dependence of UPL intensity on the excitation power was obtained. UPL mechanism was interpreted on the basis of non-linear process of two-step two-photon absorption (TS-TPA) through deep defect states including cation vacancies localised at the barrier-nanoisland heterointerface.

### Introduction

CdSe/ZnSe quantum nanostructures or self-assembled quantum dots (QD's) is of considerable interest as it offers the possibility for low-threshold-current optoelectronic devices for the green spectral range. As reported earlier [1], for the CdSe the QD's formation is more complicated and is not only restricted to an abrupt 2D-3D threshold transition which is peculiar to the Stranski–Krastanov growth mode. The transformation becomes more complex due to the interdiffusion processes at CdSe/ZnSe interfaces and Cd segregation. These processes are probably accelerated by a nonuniform strain distribution and nonequilibrium growth conditions which produce anomalously high density of cation vacancies. These defects are most likely expected to serve as a channel of non-radiative recombination of carriers, and they therefore decrease the effective emission of QD's. In PL experiments these defects act as traps for photoexcited electron and holes. A lifetime of the carrier trapped to the defect may be very long and, in principle, it becomes possible to release trapped carriers by means of below bandgap ( $h\nu_{\text{ex}} < E_g$ , where  $E_g$  is the bandgap of CdSe QD) optical excitation.

Low-temperature UPL, or anti-Stokes PL at the extremely low excitation intensity were observed in semiconductor heterojunctions, quantum wells (QW's) and QD's [2–5]. In most of these experiments UPL was caused by a radiative recombination in the wide-bandgap material.

In this paper we report on an experimental observation of an intensive UPL at low-temperature and low excitation intensity in CdSe/ZnSe self assembled QD's when the optical excitation energy being below QD's ground state.

### 1. Experimental set-up

Epitaxial layers were grown pseudomorphically on GaAs(001) substrates at a temperature of 280 °C. The thickness of ZnSe buffer and cap layers was 80 nm and 20 nm, respectively. CdSe epilayers of nominal thickness of 0.6 and 1.5 ML were grown by migration-enhanced epitaxy method. The growth process is described in [6]. PL spectra were measured using

DFS-24 spectrometer with a photon-counting system for detection and  $\text{Ar}^+$ -laser with different lines for excitation.

## 2. Results and discussion

In Fig. 1 are shown PL spectra (90 K) of CdSe/ZnSe heterostructure with a single CdSe inserts of nominal thickness of 1.5 ML. In the spectrum of an ordinary PL (Fig. 1(a)) there are an intensive band at  $\sim 2.564$  eV with linewidth  $\sim 35$  meV. The position of the maximum of this band and its low-energy asymmetry agree with the recent results [7] and are interpreted as simultaneous contribution to the spectrum of confined excitons from  $\text{Cd}_x\text{Zn}_{1-x}\text{Se}$  2D-layer (high-energy side) and of localised 0D excitons in the small intra-layers Cd-rich islands (low-energy side).

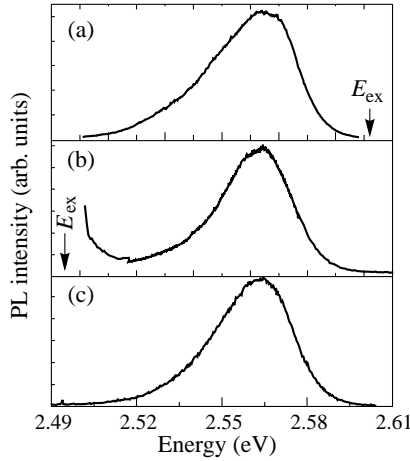


**Fig. 1.** UPL spectra of CdSe/ZnSe structure with single CdSe inserts of 1.5 ML thickness. (a)  $E_{\text{ex}} = 2.602$  eV, (b)  $E_{\text{ex}} = 2.497$  eV, (c)  $E_{\text{ex}} = 2.41$  eV.  $T = 90$  K.

When excitation quantum energy is lower than exciton energy maximum (Fig. 1(b,c)) an up-conversion emission is observed. The mechanism of UPL excitation can be interpreted on the basis of the model proposed for UPL in InAs and InP QD's [2,5], namely TS-TPA process of the excitation of electron-hole pair through the intermediate deep defect states, most probably localised at the barrier-nanoisland heterointerface. In our case, cation vacancies may serve as actual defect states. Firstly, the cation vacancies formation features  $\text{A}^2\text{B}^6$  semiconductors and they cause a series of absorption and radiation bands in these materials [8]. Secondly, the presence of deep traps for electrons was found in CdSe/ZnSe structures with QD's by DLTS method [9]. And thirdly, it should be noted that in the case of high density of nanoislands, when the distances between the islands are comparable with their size (for 1.5 ML the density of islands is  $\sim 10^{11} \text{ cm}^{-2}$  and the average distance between them is 15–20 nm [1]), an elastic interaction between the islands becomes essential as a result of penetration in the substrate of nonuniform strain field caused by the islands. This may lead to the gettering effect from nanoislands and barrier layers with the localization of defects at the interface.

To confirm our assumption concerning UPL excitation we have investigated the dependence of UPL intensity on the excitation power. The results shown in Fig. 2 for the sample with CdSe inserts of the thickness 1.5 ML gives an coefficient of the line slope near  $\sim 2$ .

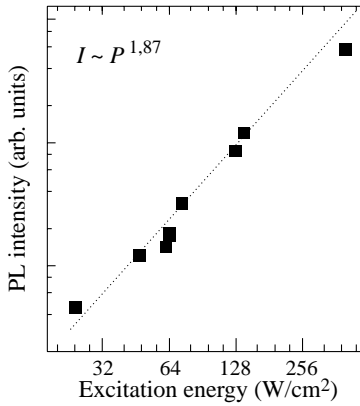


**Fig. 2.** Power dependence of UPL intensity of the CdSe/ZnSe (1.5 ML) structure ( $E_{\text{ex}} = 2.41$  eV). Double-logarithmic scale is used.

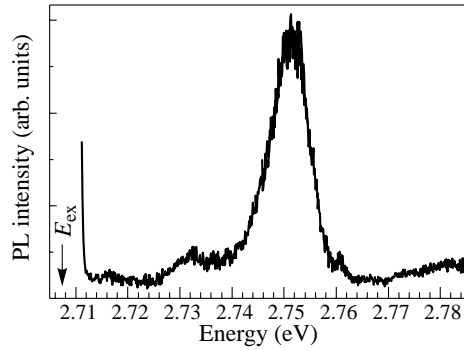


**Fig. 3.** UPL spectrum of CdSe/ZnSe structure with CdSe insert thickness of 0.6 ML ( $E_{\text{ex}} = 2.707$  eV).  $T = 5$  K.

It should be emphasised that the UPL efficiency at the excitation energy 2.41 eV make up several percents in comparison to the power-commensurable ( $P_{\text{ex}} \sim 10$  W/cm<sup>2</sup>) direct excitation with energy of 2.707 eV, e.g. we have an intensive enough process.

Other possible mechanism of UPL enhancement may be Auger recombination process. But in this case a cubic-like dependence of intensity on excitation power is expected, what contraries to our results. Besides the power of excitation was low enough ( $P_{\text{ex}} < 400$  W/cm<sup>2</sup>) for the contribution of a direct two-photo absorption to be insignificant.

Inasmuch as at low temperature (5 K) the band gap of ZnSe barrier is  $\sim 2.8$  eV, by excitation with quanta energy 2.41 eV, UPL was also observed, the energy level participating in TS-TPA is situated, at least,  $\sim 0.4$  eV lower (higher) than conduction (valence) band edge of ZnSe barrier.

UPL was also observed in the sample with the single CdSe inserts with thickness of 0.6 ML. The corresponding PL spectrum (5 K), obtained by the excitation energy  $\sim 2.707$ , is shown in Fig. 3. An intensive band is seen here at  $\sim 2.75$  eV with the linewidth  $\sim 9$  meV. The position of the UPL maximum corresponds to the Cd concentration  $x \approx 3\text{--}4\%$  of Cd<sub>x</sub>Zn<sub>1-x</sub>Se 2D-layer. It should be noted, that as well as in previous case UPL from ZnSe barrier was not registered. Two weak peaks at  $\sim 2.76$  eV and  $\sim 2.732$  eV that appeared in the PL spectra are not accounted for yet.

Thus the low-temperature UPL was revealed in CdSe/ZnSe heterostructures with the single CdSe inserts of the nominal thickness of 1.5 and 0.6 ML, forming Cd<sub>x</sub>Zn<sub>1-x</sub>Se nanoislands. This UPL is characterised by the anomalously high efficiency in comparison with the previously observed one in bulk semiconductors and QW structures. We suppose UPL to be connected with the TP-TPA of the nanoislands trough the defect states localised at the ZnSe barrier — Cd<sub>x</sub>Zn<sub>1-x</sub>Se nanoisland heterointerface. As such defects cation vacancies may serve, and the high concentration of the cation vacancies in the case of large density of nanoislands cause the anomalously high intensity of radiation.

## References

- [1] N. Peranio, A. Rosenauer, D. Gerthsen, S. V. Sorokin, I. V. Sedova and S. V. Ivanov, *Phys. Rev. B*, **61**, 16015 (2000);  
D. Litvinov, A. Rosenauer, D. Gerthsen and N. N. Ledentsov, *Phys. Rev. B*, **61**, 16819 (2000).
- [2] D. A. Mazurenko, A. V. Scherbakov, A. V. Akimov, A. J. Kent, M. Henini, *Semicond. Sci. Technol.*, **14**, 1132 (1999).
- [3] T. Kita, T. Nishino, C. Geng, F. Scholz and H. Schweizer, *Phys. Rev. B* **59**, 15358 (1999).
- [4] P. P. Paskov, P. O. Holtz, B. Monemar, J. M. Garcia, W. V. Schoenfeld and P. M. Petroff, *Jpn. J. Appl. Phys.* **40**, 2080 (2001).
- [5] I. V. Ignatiev, I. E. Kozin, H. W. Ren, S. Sugou and Y. Masumoto, *Phys. Rev. B* **60**, R14001 (1999).
- [6] S. V. Ivanov, A. A. Toropov, T. V. Shubina, S. V. Sorokin, A. V. Lebedev, I. V. Sedova, P. S. Kop'ev, G. R. Pozina, J. P. Bergman and B. Monemar, *J. Appl. Phys.* **83**, 3168 (1998).
- [7] C. S. Kim, M. Kim, S. Lee, J. K. Furdyna, M. Dombrowska, H. Rho, L. M. Smith and H. E. Jackson, *J. Cryst. Growth*, **214/215**, 761 (2000).
- [8] K. M. Lee, Le Si Dang and G. D. Watkins, *Solid State Commun.* **35**, 527 (1980).
- [9] V. G. Litvinov, V. I. Kozlovsky and Yu. G. Sadofyev, *Phys. Stat. Sol. (b)*, **229**, 513 (2002).

## Photoluminescence study of CdTe/ZnTe ultra-thin quantum wells grown by pulsed beam epitaxy

*M. García-Rocha* and I. Hernández-Calderón

Departamento de Física, Centro de Investigación y de Estudios Avanzados del IPN.  
Apdo. Postal 14-740, 07000 México, D.F., México

**Abstract.** CdTe ultra-thin quantum wells (UTQWs) within ZnTe barriers were grown by pulsed beam epitaxy (PBE) on GaAs(001) substrates. *In-situ* reflection high energy electron diffraction (RHEED) patterns and real-time spot intensity measurements indicated a high structural quality of the QWs. Low temperature photoluminescence (PL) experiments indicated a clear influence of the growth temperature on the structural properties of the samples. The 2 monolayer (ML) thick UTQW grown at  $T_s = 270^\circ\text{C}$  exhibited an intense and sharp peak at 2.26 eV whereas the 4 ML thick UTQW ( $T_s = 290^\circ\text{C}$ ) presented an intense peak at 2.13 eV and a weak one around 2.04 eV. This behavior is discussed in terms of Cd re-evaporation at the higher  $T_s$ .

### Introduction

Because of its energy band gap, 1.5 eV at room temperature (RT), CdTe has been considered as an ideal semiconductor for the fabrication of high efficiency solar cells [1]. Additionally, HgCdTe alloys have been used in infrared detectors and optoelectronic devices [2]. On the other hand, ZnCdSe based quantum wells (QWs), have been applied in the fabrication of light emitting devices in the blue-green spectral region [3, 4]. These devices are of great interest due to its technological application in the developing of flat panel color displays, and optical storage devices [5]. The fundamental optical transitions of CdTe/ZnTe QWs can be designed to be in the 1.5–2.3 eV range at RT, a very attractive region for infrared-green optoelectronic applications. In this work, we present our results on the structural and optical properties of CdTe ultra-thin quantum wells (UTQWs), grown by pulsed beam epitaxy (PBE), a growth method that allows the fabrication of monolayer and submonolayer structures [6].

### 1. Experimental details

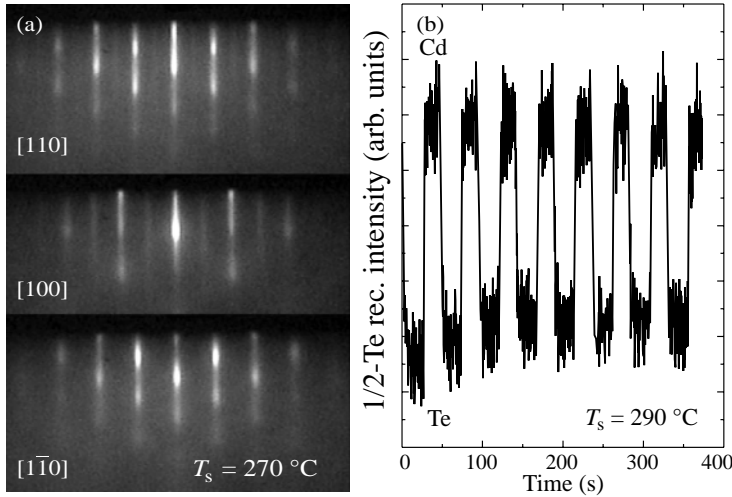
The epitaxial growth was carried out in a Riber 32P system with Cd, Zn and Te elemental sources. Previous to the deposition of the QWs, a  $0.5\ \mu\text{m}$  thick ZnTe buffer layer was grown on the GaAs(001) substrate. PBE of CdTe UTQWs was performed by alternate exposure of the substrate surface to individual fluxes of Cd (25 s) and Te (16 s). The Cd to Te flux ratio was 2:3. After each flux exposure, a 4 s dead time (flux interrupt) was applied to allow re-evaporation of excess material and migration of the atomic species. The ZnTe barriers were deposited by molecular beam epitaxy (MBE), from elemental sources with a 1:3 Zn to Te flux ratio. Two different samples were prepared: Sample 1 (S1) was grown at a substrate temperature ( $T_s$ ) of  $270^\circ\text{C}$ , and consisted of five CdTe UTQWs, each with four PBE-cycles. Sample 2 (S2), was grown at  $T_s = 290^\circ\text{C}$ , and also consisted of five UTQWs, but with eight PBE-cycles per QW. Under our growth conditions, a  $\sim 0.5$  ML coverage per cycle was expected [7, 8]. Then the UTQWs are nominally 2-ML thick in



S1, and 4-ML thick in S2. The growth was *in-situ* monitored by reflection of high energy electron diffraction (RHEED). The evolution of the  $(2 \times 1)$ -Te reconstruction in the  $[110]$  azimuth was monitored during the PBE growth. Low temperature photoluminescence (PL) experiments were performed in a closed cycle He refrigerator (APD Cryogenics) at 15 K with a 4880 Å line of an Ar<sup>+</sup> laser (Spectra Physics). The PL signal was analyzed with a 0.5 m monochromator (SPEX) equipped with a photomultiplier tube.

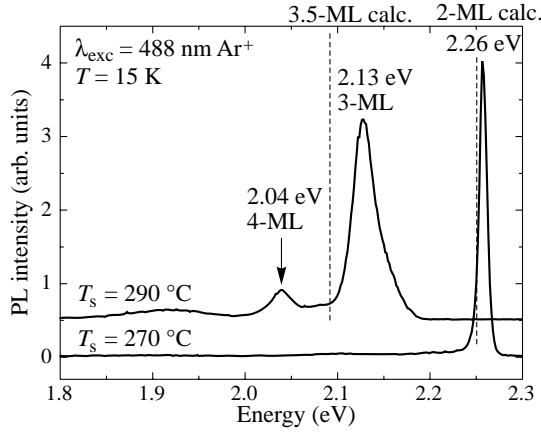
## 2. Results and discussion

Figure 1 shows typical RHEED patterns during PBE of S1, and real time spot intensity measurements in S2. The RHEED patterns along three different azimuths of S1 under Cd flux are shown in Fig. 1(a). A predominant streaky pattern indicates the good epitaxial growth of S1, despite the lattice mismatch of  $\sim 6.1\%$  between CdTe and ZnTe. Weak spots on the streaks of the RHEED pattern suggest that the CdTe QWs are formed by large islands. Slightly spottier RHEED patterns were observed during the growth of S2. Fig. 1(b) corresponds to real-time spot intensity measurements and shows the evolution of the intensity of the  $1/2$  spot reconstruction of the Cd-terminated surface along the  $[1\bar{1}0]$  azimuth during the PBE cycles. No evidence of roughness modulation during the 8 cycles was observed, a confirmation of the 2D epitaxial growth of CdTe UTQWs.



**Fig. 1.** (a) RHEED patterns along three different azimuths during the PBE growth of a CdTe UTQW in sample S1 (Cd cell open and Te cell closed). (b) Real time spot intensity during the PBE cycles of sample S2 along the  $[1\bar{1}0]$  azimuth. The evolution of the  $1/2$ -Cd reconstruction intensity shows clearly 8-cycles. A good epitaxial growth was also observed in this sample.

Figure 2 shows the PL spectra of S1 and S2 taken at 15 K with the 4880 Å line of an Ar<sup>+</sup> laser as excitation energy. The PL signal of S1 (2-ML), shows only a sharp (10 meV FWHM), and intense peak at 2.26 eV. This peak is due to the UTQWs and its position agrees quite well with the calculated excitonic transition energy for a 2-ML thick CdTe quantum well [9]. To our knowledge, the FWHM obtained for this sample is the narrowest up to date reported in the literature for a 2-ML CdTe QW. A very weak signal (not shown here), from the ZnTe barriers and buffer layer was observed for both S1 and S2. The



**Fig. 2.** PL signal of CdTe QWs at 15 K. A sharp and intense peak in S1 is indicative of the high quality of the 2 ML UTQWs. In the case of S2, instead of only a peak associated to the 4 ML UTQW, another one, more intense, associated to a 3 ML QW, is observed. This is attributed to the higher substrate temperature during growth of S2.

absence of a more intense signal from the barriers is attributed to a high diffusion length of the photogenerated carriers in the ZnTe barriers due to the good crystalline quality of our samples. In contrast to S1, the PL signal of S2 showed three peaks: an intense and broad peak at 2.13 eV (29 meV FWHM), a weaker signal at 2.04 eV and a weak band centered around 1.91 eV. We will see that this different behavior of the PL signal may be attributed to the higher substrate temperature (290 °C) during the PBE growth of the CdTe QWs. The emission around 2.13 eV is a bit larger than that of the calculated optical transition in a 3.5-ML CdTe QW [9] and the peak at 2.04 eV is closer to the expected transition of a 4 ML QW. Then, the larger signal may be attributed to a QW thinner than the expected 4 ML well. This result can be explained in terms of Cd re-evaporation at the higher growth temperature of S2, only around 3 ML of CdTe were effectively deposited during the 8 cycles ( $\sim 0.38$  ML/cycle) and only a minor region of the sample contains 4 ML thick QWs. Indeed, additional RHEED studies indicated that Cd terminated surfaces were not thermally stable at 290 °C.

### 3. Conclusions

We have successfully grown UTQWs of CdTe with ZnTe barriers by PBE on GaAs(001) substrates. RHEED and PL experiments support a 2D growth mode of the UTQWs. From the analysis of the PL spectra a clear effect of the substrate temperatures observed. While the sample grown at 260 °C presents only one, intense and sharp peak corresponding to the expected 2 ML thick UTQW, in the case of the structure grown at 290 °C, two peaks were observed, a weak one associated to the 4 ML nominal thickness of the UTQW, and an intense, but slightly broad peak, attributed to a 3 ML thick QW. The thinning of the QWs at the higher substrate temperature is attributed to Cd re-evaporation. Due to the high crystalline quality of the barriers, only a very weak emission from the ZnTe was observed. The CdTe UTQWs appear as attractive structures for application in the fabrication of novel optoelectronic devices in the infrared to green spectral region.

### Acknowledgments

This work was partially supported by CONACYT (Mexico). Authors appreciate the technical assistance from H. Silva, A. Guillén and Z. Rivera.

### References

- [1] N. Amin, T. Isaka, T. Okamoto, A. Yamada and M. Konagai, *Jap. J. Appl. Phys. Part 1* **38**, 4666 (1999).
- [2] Y. G. Sidorov, S. A. Dvoretzki, N. N. Mikhalov, M. V. Yakushev, V. S. Varavin and A. P. Antsiferov, *J. Optical Technol.* **67**, 31 (2000).
- [3] M. A. Haase, J. Qiu, J. M. Depuydt and H. Cheng, *Appl. Phys. Lett.* **59**, 1272 (1991).
- [4] A. Gerhard, J. Nürnberger, K. Schüll V. Hock, C. Schumacher, M. Ehinger and W. Faschinger, *J. Cryst. Growth* **184**, 1319 (1998).
- [5] R. A. Metzger, *Compound Semiconductor* **1**, 26 (1995).
- [6] V. Calvo, N. Magnea, T. Taliercio, P. Lefebvre, J. Allegre and H. Mathieu, *Phys. Rev. B* **58**, 15736 (1998).
- [7] W. Faschinger and H. Sitter, *J. Cryst. Growth* **99**, 566 (1990).
- [8] J. Hartmann, G. Feuillet, M. Charleux and H. Mariette, *J. Appl. Phys.* **79**, 3035 (1996).
- [9] Y. Teari, S. Kuroda, K. Takita, T. Okuno and Y. Masumoto, *Appl. Phys. Lett.* **73**, 3757 (1999).
- [10] Y. M. Yu, S. Nam, K. S. Lee, Y. D. Choi and B. O, *J. Appl. Phys.* **90**, 807 (2001).

## Filling-factor dependence of magneto-luminescence in II–VI QWs with 2DEG

A. S. Gurevich<sup>†</sup>, G. V. Astakhov<sup>‡†</sup>, R. A. Suris<sup>†</sup>, V. P. Kochereshko<sup>†</sup>,  
 D. R. Yakovlev<sup>‡†</sup>, W. Ossau<sup>‡</sup>, S. A. Crooker<sup>¶</sup> and G. Karczewski<sup>§</sup>

<sup>†</sup> Ioffe Physico-Technical Institute, St Petersburg, Russia

<sup>‡</sup> Physikalisches Institut der Universität Würzburg, 97074 Würzburg, Germany

<sup>¶</sup> National High Magnetic Field Laboratory, Los Alamos, 87545 NM, USA

<sup>§</sup> Institute of Physics, Polish Academy of Sciences, Warsaw, Poland

**Abstract.** Photoluminescence spectra of modulation-doped quantum well structures based on II–VI semiconductors (CdTe/CdMgTe and ZnSe/ZnBeMgSe) were studied in high magnetic fields in the range of 2D electron concentrations of  $(1–5) \times 10^{11} \text{ cm}^{-2}$ . The following peculiarities were found at low magnetic fields: (i) linear increase of the photoluminescence energy with increasing magnetic fields, (ii) jumps in this dependence at integer filling-factors, (iii) periodical changing of Zeeman splitting. The observed behavior is interpreted in a frame of a model which takes into account combined exciton electron recombination processes in the presence of magnetic fields.

## Introduction

Several recent publications reported about investigations of photoluminescence (PL) spectra of quantum well (QW) structures based on III–V and II–VI semiconductors with two-dimensional electron gas (2DEG) in concentration range from  $10^{10}$  up to  $10^{12} \text{ cm}^{-2}$  (i. e. with Fermi energy from 1 to 5 meV). These studies were carried out at high magnetic fields. A linear shift of observed PL lines to the high energies with increasing magnetic fields [1], jumps in the PL/absorption line position at integer filling-factors [2] and jumps of the PL intensity at integer filling factors [3, 5] were found. The observed picture is typical for 2D electron gas of high density — “metallic regime”. The observed behavior was interpreted in the terms of integer and fractional quantum Hall effects. On the other side when the filling-factor is less than 2, PL/absorption shows a behavior typical for the dielectric phase with the presence of exciton and trion lines [4]. Till now there is no satisfactory explanation for the observed effect of the “metal–insulator” transition.

In the present paper we analyze the PL spectra in magnetic fields up to 50 T taken from modulation-doped QWs based on CdTe/CdMgTe and ZnSe/ZnBeMgSe semiconductors with 2DEG concentration  $(1–5) \times 10^{11} \text{ cm}^{-2}$ . A qualitative explanation of the observed results by combined exciton electron recombination processes is presented.

## Experiment

We have studied modulation-doped CdTe and ZnSe -based single quantum well structures (SQW) grown by molecular-beam epitaxy on (100)-oriented GaAs substrates. The electron density in the QWs was varied from  $n_e \approx 5 \times 10^{10}$  to  $5 \times 10^{11} \text{ cm}^{-2}$ .

A CdTe/Cd<sub>0.7</sub>Mg<sub>0.3</sub>Te structures contain a 120 Å-thick SQW separated from the surface by a 750 Å-wide Cd<sub>0.7</sub>Mg<sub>0.3</sub>Te barrier. These structures contain  $\delta$ -layer doped by Iodine to a concentration of  $2 \times 10^{17} \text{ cm}^{-3}$  at a distance of 100 Å from the QW. Samples with

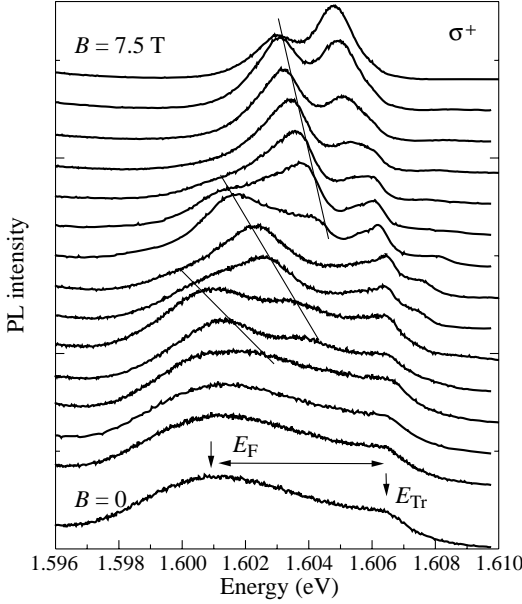


**Fig. 1.** Photoluminescence spectra taken from a 120 Å CdTe/Cd<sub>0.7</sub>Mg<sub>0.3</sub>Te SQW with electron concentration of  $2.5 \times 10^{11} \text{ cm}^{-2}$  in magnetic fields from zero to 7.5 T.

different electron densities were fabricated at the same substrate using the wedge growth mode. It allows to vary the doped level keeping all other QW parameters (QW width, barrier height, background impurity concentration, *etc.*) constant.

ZnSe/Zn<sub>0.71</sub>Be<sub>0.11</sub>Mg<sub>0.18</sub>Se structures consists a 67 Å-thick ZnSe SQW embedded between 1000 Å-thick Zn<sub>0.82</sub>Be<sub>0.08</sub>Mg<sub>0.10</sub>Se barriers. The structures contain a  $\delta$ -layer at a distance of 100 Å from the QW doped by Chlorine. A set of structures with different doping level varied from  $6 \times 10^{17} \text{ cm}^{-3}$  to  $8 \times 10^{18} \text{ cm}^{-3}$  was fabricated [5].

In the PL spectrum (Fig. 1) of the studied structures a wide band with two maxima was observed at zero magnetic field. The lowest in energy maximum of the line is located close to the trion resonance energy in weakly doped structure ( $\hbar\Omega_{\text{Tr}}$ ). The main, high energy,

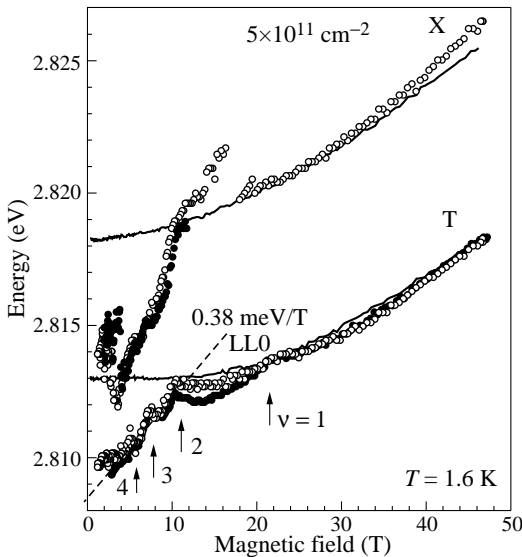


**Fig. 2.** Energies of PL maxima vs magnetic field for an 67 Å-thick ZnSe/Zn<sub>0.71</sub>Be<sub>0.11</sub>Mg<sub>0.18</sub>Se SQW  $5 \times 10^{11} \text{ cm}^{-2}$  detected in  $\sigma^+$  (open circles) and  $\sigma^-$  (solid circles) polarizations. (X) and (T) show exciton and trion lines in high magnetic fields [5]. Their diamagnetic shifts shown by solid lines are moved to lower energies by 7.7 meV.

maximum is located at the energy ( $\hbar\Omega_{\text{Tr}} - E_F$ ), (where  $E_F$  is the Fermi energy of the 2D electron gas).

In the presence of external magnetic fields the PL spectra modified strongly. First, the wide PL band starts narrowing and its low energy maximum moves to high energy one (i. e. to  $\hbar\Omega_{\text{Tr}}$ ). A weakly pronounced structure of maxima and minima appears on the line contour. This structure depends strongly on magnetic fields: the maxima shift to the low energies, the intensity of the maxima increases initially and then goes down at higher fields. At high enough magnetic fields instead of the wide PL band an arbitrary narrow PL line was observed. Such behavior was observed in CdTe-based structures as well as in ZnSe-based structures. Figure 1 illustrates the described above on an example of CdTe/CdMgTe SQW with electron density  $2.5 \times 10^{11} \text{ cm}^{-2}$ .

In Fig. 2 we show an example of the magnetic field dependence of the main (i. e. most intensive) PL maximum for ZnSe/ZnBeMgSe SQW structure. Here we can see that the main PL maximum moves to the high energies and has leaps at integer filling-factors. The similar behavior of the main maximum was observed also in QW structures based on GaAs [1] and CdTe [2].

## Discussion

We explain these modifications of the PL spectra by the following way: In the absence of magnetic fields we have a trion in an initial state. The binding energy of this trion, of cause, depends on the electron density because of screening, but in 2D case a weakly bound state is still remains. After the trion annihilation we have a photon plus one electron in the final state:  $Tr \rightarrow \hbar\omega_{\text{Tr}} + e^*$ . This residual electron  $e^*$  can be placed the empty states above the Fermi level only. Consequently, the energy of the emitted photon is:  $\hbar\omega_{\text{Tr}} = E_{\text{Tr}} - E^*$ , here:  $E^* \in (E_F, \infty)$  is the energy of the residual electron,  $E_{\text{Tr}}$  is the energy of the trion in the initial state. Obviously, in weakly doped samples the energy of the photon emitted in the trion annihilation ( $\hbar\omega_{\text{Tr}}$ ) is equal to the trion energy ( $E_{\text{Tr}}$ ). Although the residual electron after the trion annihilation can has any energy from the Fermi energy to infinity, the probability of such process decreases fast with increasing the electron energy. So, the maximum of the PL intensity is expected to be located at the energies close to  $(E_{\text{Tr}} - E_F)$ .

Therefor, the PL maximum at the trion annihilation in heavily doped samples is shifted to lower energies from the trion PL line position in weakly doped samples. The value of this shift is of the order of the Fermi energy.

In the presence of magnetic fields the energy of the emitted photon is  $\hbar\omega_c = E_{\text{Tr}}(H) - E^*$ , here:  $E^* = (N + 1/2)\hbar\omega_c$ ,  $N$  is integer. In the range of magnetic fields when the magnetic length is smaller the trion radius but higher the exciton radius the trion energy goes up as:  $E_{\text{Tr}}(H) \approx E_{\text{Tr}}(0) + 1/2\hbar\omega_c$ .

So that, at low temperature a fan of Landau PL lines should be observed shifting linearly to low energies from the trion resonance with increasing magnetic fields (these lines are so-called “shake-up” lines).

As the upper Landau levels become empty the maximum of the PL jumps closer to the trion energy. It shifts jumping from the higher Landau levels to the lower Landau levels as higher Landau levels become empty until it reaches the trion energy. It happens just when the filling-factor is equal to 2. These leaps are washed out when the temperature of the 2DEG increases. The similar behavior will be observed due to a broadening of the Landau levels caused by a scattering processes or inhomogeneity.

At sufficiently high temperature the leaps will disappear completely and the PL line will shifts to the high energies as  $1/2\hbar\omega_c$ . This situation is illustrated in Fig. 3 for three

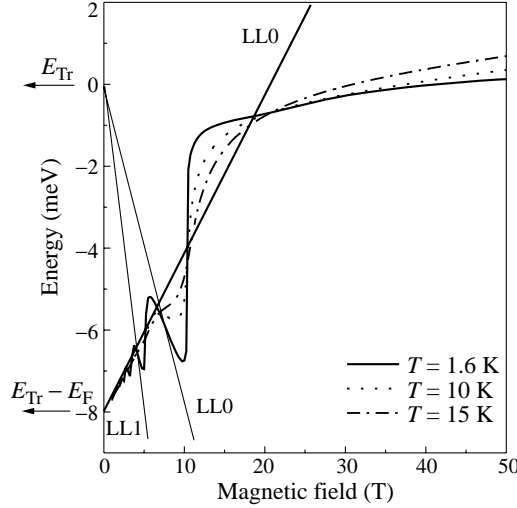


**Fig. 3.** Scheme of magnetic field dependence of the main PL peak position, which corresponds to the case of the trion annihilation when the residual electron is left on the Fermi level. LL0, LL1, ... shows the Landau level fan.

different temperatures and for the ZnSe/ZnBeMgSe sample with the same parameters as for the presented in Fig. 2 (see [5]). Qualitative coincidence of Fig. 3 and Fig. 2 is clearly seen.

In conclusion: PL spectra of modulation-doped QW structures based on II–VI semiconductors (CdTe/CdMgTe and ZnSe/ZnBeMgSe) were studied at high magnetic fields. The following peculiarities of the observed spectra were found: (i) shift of the PL line maxima to the high energies with increasing magnetic fields, (ii) leaps in this dependence at integer filling-factors. The observed experimental behavior is interpreted in a model, which takes into account a dependence of Fermi level on magnetic fields. Although we are speaking about trion processes we should have in mind that at high 2D electron densities the trions are screened and we have to consider them as an exponentially weak bound state of three particles. Nevertheless the processes considered above will conserve in a dense 2DEG until the excitons are unscreened and can be considered as whole particles.

#### Acknowledgments

The work was supported in part by grants: DFG Os98/6, RFBR 01-02-16990, “Nanostructures” of Russian Ministry of Sciences and Russian Academy of Sciences.

#### References

- [1] D. Gekhtman, E. Cohen, Arza Ron and L. N. Pfeiffer, *Phys. Rev. B* **54**, 10320 (1996).
- [2] F. J. Teran, M. L. Sadowski, M. Potemski, G. Karczewski, S. Mackowski and J. Jaroszinski, *Physica B* **256-258**, 577 (1998).
- [3] S. A. Crooker, D. G. Rickel, S. K. Lyo, N. Samarth and D. D. Awschalom, *Phys. Rev. B* **60**, R2173 (1999).
- [4] E. I. Rashba and M. Sturge, *Phys. Rev. B* **63**, 045305 (2001).
- [5] W. Ossau, D. R. Yakovlev, G. V. Astakhov *et al*, To be published in *Physica E* (2002).

## Influence of high excitation on excitonic states in GaN/AlGaIn quantum wells

D. K. Nelson<sup>†</sup>, M. A. Jacobson<sup>†</sup>, N. Grandjean<sup>‡</sup>, J. Massies<sup>‡</sup>, P. Bigenwald<sup>§</sup>  
and A. Kavokin<sup>§</sup>

<sup>†</sup> Ioffe Physico-Technical Institute, St Petersburg, Russia

<sup>‡</sup> Centre de Recherche sur l'Hetero-Epitaxie et ses Applications-CNRS,  
Rue B. Gregory, Sophia Antipolis, 06560 Valbonne, France

<sup>§</sup> LASMEA, Université Blaise Pascal Clermont II,  
CNRS 24 avenue des Landais, 63177 Aubiere Cedex, France

**Abstract.** Photoluminescence of GaN/AlGaIn quantum well structures was studied under high intensity of excitation. The blue shift of photoluminescence peak energy was observed when excitation intensity increased. The blue shift was most prominent for the wide wells, becoming smaller with decreasing the well width. We attribute the observed effect to the screening of the built-in electric field by photoexcited carriers, which leads to reducing of the initial red shift caused by the quantum confined Stark effect. The variation of exciton binding energy with carrier concentration also makes the contribution to the blue shift. The theoretical calculations of the blue shift were performed and compared with experimental data.

The present report is devoted to the study of the influence of high density of excitation on the excitonic states in GaN/AlGaIn quantum well (QW) structures. It is known [1, 2] that the huge (about 1 MV/cm) built-in electric field due to spontaneous polarization and piezoelectric effect exists in GaN/AlGaIn quantum wells. The existence of an electric field lead to the red shift of the excitonic states. Under high density of excitation photoexcited carriers can screen the electric field reducing the red shift, which will manifest itself in the blue shift of the excitonic state.

The samples under investigation were undoped GaN/AlGaIn quantum well structures grown on (0001) sapphire substrates by molecular-beam epitaxy (MBE) using  $\text{NH}_3$  as a nitrogen precursor. Before growing the quantum structures, a 2–3- $\mu\text{m}$ -thick GaN template was deposited by MBE on the substrate. Details of the growth procedure are given in [3]. The thickness of the QW was from 4 to 17 monolayers (ML, 1 ML = 2.59 Å) for different samples and the percentage of Al in  $\text{Al}_x\text{Ga}_{1-x}\text{N}$  barrier was  $x = 0.09$ –0.13. A pulsed nitrogen laser ( $\lambda = 337$  nm, high excitation) and He-Cd laser ( $\lambda = 325$  nm, low excitation) was used as excitation source for photoluminescence study. The excitation density (in high excitation regime) was varied from 10 to 1000  $\text{kW}/\text{cm}^2$ . The samples were mounted in an evaporation helium cryostat providing temperature variation from 6 to 60 K.

The luminescence spectra of GaN/AlGaIn quantum well samples under low-level excitation consist of the emission band of exciton localized on the fluctuations of the well width. The sample with a set of wells with different well thickness exhibits a set of bands with different peak energies. All the luminescence peaks are well resolved in our samples. When the excitation density increases the excitonic peak undergoes the blue shift. Figure 1 presents the luminescence spectra of one of the studied samples. The maximum value of the blue shift (about 10 meV at excitation power of 1  $\text{MW}/\text{cm}^2$  and at  $T = 6$  K) was observed



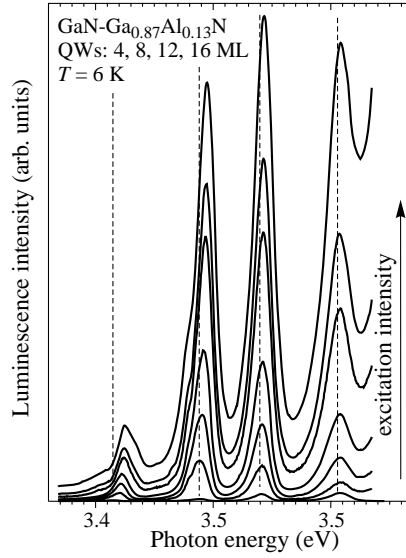


**Fig. 1.** Photoluminescence spectra of the quantum well sample in dependence on the excitation intensity. The dashed lines indicate the positions of the bands at low excitation level.

for the widest wells (with the thickness of 16 ML). For the narrower wells the blue shift is smaller ( $\sim 7$  meV for 12 ML QW,  $\sim 4$  meV for 8 ML QW and  $\sim 3$  meV for 4 ML QW at the same conditions). The dependencies of the blue-shift value on the excitation intensity for the sample with four quantum wells with different thickness are represented in Fig. 2. It can be mentioned that for the widest QW the blue shift starts at smaller excitation intensities than for narrower ones.

As it was mentioned above, in GaN/AlGaN QW structures strong electrostatic fields are built in. The origin of these fields is, at first, the significant lattice parameter mismatch among III-nitrides, which being accompanied with considerable piezoelectric constant leads to high piezoelectric field. Besides this, in semiconductors with wurtzite structure, spontaneous polarization exists along the (0001) polar axis even in the absence of strain [4]. Both these reasons lead to built-in electric fields as high as 0.5–1 MV/cm depending on the Al composition in a barrier and on the barrier thickness [2, 5]. As a result, the photoluminescence peaks appear to be significantly redshifted due to quantum-confined Stark effect. The red shift increases with increasing of the well width, so for the wide wells ( $\geq 40$  Å) the PL peak energy is lower than that of bulk GaN.

The photocreation of high densities of electron-hole pairs in such quantum wells leads to the blue shift of the transition energy. One can consider two components in the blue shift. The first part comes from the screening of the electric field in the well due to electron-hole plasma. Up to rather large values of the injected plasma density  $\sigma$  this blue-shift is linear with  $\sigma$ . The proportionality coefficient increases with the well width. The second part comes from exciton renormalization: due to screening of the dielectric constant, filling of bands, the kinetic energy increases and is not compensated by increase of potential term. The exciton binding energy diminishes and one has the second reason for the blue shift. This blue shift is not linear with the plasma density.

The sample in Fig. 2 is based on  $\text{Al}_{0.13}\text{Ga}_{0.87}\text{N}/\text{GaN}$  single quantum structures with nominal widths of 4/8/12/16 ML separated with 10 nm barriers. The fit of the observed

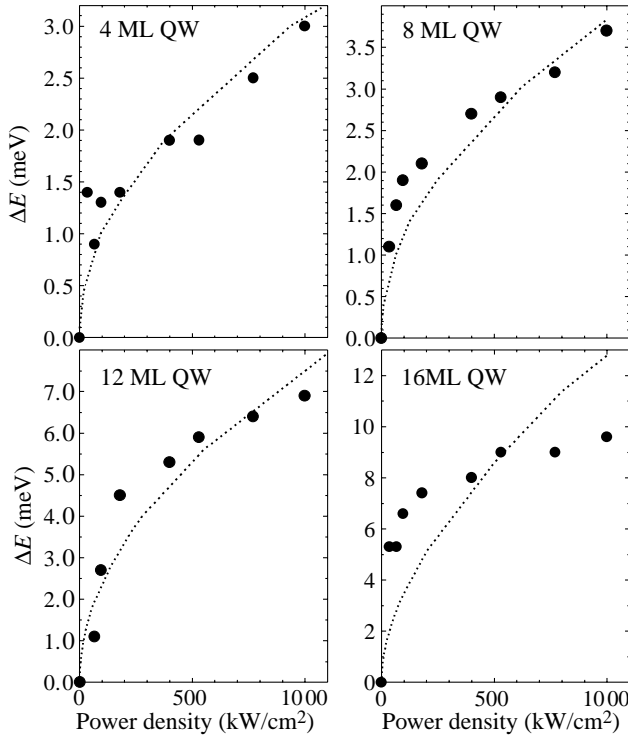


**Fig. 2.** The dependencies of the blue-shift value  $\Delta E$  on the excitation intensity for  $\text{Al}_{0.13}\text{Ga}_{0.87}\text{N}/\text{GaN}$  sample with the well thickness of 4 ML, 8 ML, 12 ML and 16 ML. Points — experimental data, dashed lines — theoretical calculations.

transition peaks at low power density give us the actual values of 5/8/12/17 ML that can be considered as a good agreement. We treated the calculation of each quantum well separately from the others since the particles, both electron and hole, are very heavy, the quantum wells are deep and the polarization fields assumed to be present in the wells are strong, being equal to 580 kV/cm. The other parameters used for the calculations are taken from the literature [6].

The calculations were made within the conventional effective mass approximation making the assumption that our base material, GaN, has the wurtzite hexagonal symmetry. Since we treat the problem of small to large densities of free carriers, the particles' wavefunctions are found after solving self-consistently the Schrödinger and Poisson equations. When dealing with a large number of carriers, the reciprocal space gets filled and the radiative transition will no longer occur at the zone center due to Pauli exclusion principle: no transitions are allowed for  $k < k_F$  ( $k_F$  is Fermi wavevector) at the absolute zero. It is then necessary to describe the system with a potential Hamiltonian that accounts both for this phenomenon and for the screening of the electron-hole interaction. For this purpose we used the approach developed by Averkiev [7] and Pikus [8]. In detail the calculation procedure is described in [9].

The results of theoretical calculations are presented in Fig. 2. by dashed lines. From the best fit of calculations to the experimental data the following results were obtained. The power density producing in a well the carrier concentration of  $\sigma = 10^7 \text{ cm}^{-2}$  is  $P = 1.875 \text{ kW/cm}^2$ ,  $P = 1.25 \text{ kW/cm}^2$ ,  $P = 0.275 \text{ kW/cm}^2$ , and  $P = 0.125 \text{ kW/cm}^2$

for the well width of 5 ML, 8 ML, 12 ML, and 17 ML respectively. The proportionality coefficient between  $\sigma$  and band to band blue shift increases with the well width, for  $\sigma = 8 \times 10^{10} \text{ cm}^{-2}$ , the shift equals respectively 0.66, 0.89, 1.77 and 3.38 meV for the same well widths. Finally, for the same values of the well widths (5, 8, 12 and 17 ML) and of  $\sigma = 8 \times 10^{10} \text{ cm}^{-2}$ , the exciton binding energy is respectively reduced by 10.8, 10.8, 9.7 and 7.5 meV. The agreement between calculations and experiment appears to be rather well, at least for the narrower wells. The discrepancy observed for the widest well can be overcome if the reduction of the lifetime with excitation power will be taken into account.

#### *Acknowledgement*

The work was partially supported by RFBR grant No 00-02-16952.

#### **References**

- [1] N. Grandjean, J. Massies and M. Leroux, *Appl. Phys. Lett.* **74**, 2361 (1999).
- [2] M. Leroux, N. Grandjean, J. Massies, B. Gil, P. Lefebvre and P. Bigenwald, *Phys. Rev. B* **60**, 1496 (1999).
- [3] N. Grandjean, J. Massies, P. Vennegues, M. Leroux, F. Demangeot, M. Renucci and J. Frandon, *J. Appl. Phys.* **83**, 1379 (1998).
- [4] F. Bernardini, V. Fiorentini and D. V. Vanderbilt, *Phys. Rev. B* **56**, R10024 (1997).
- [5] N. Grandjean, B. Damilano, S. Dalmaso, M. Leroux, M. Laugt and J. Massies, *J. Appl. Phys.* **86**, 3714 (1999).
- [6] *Group III Nitride Semiconductor Compounds: Physics and Applications*, ed. by B. Gil, Oxford University Press, 1998.
- [7] N. S. Averkiev *et al*, *Sov. Phys. Solid State* **30**, 1884 (1989).
- [8] F. G. Pikus, *Sov. Phys. Semicond.* **26**, 26 (1992).
- [9] P. Bigenwald, A. Kavokin, B. Gil and P. Lefebvre, *Phys. Rev. B* **61**, 15621 (2000).

## Improvement of conductivity and breakdown characteristics of AlGaIn/GaN HEMT structures in passivation experiments

S. Shapoval<sup>†</sup>, V. Gurtovoi<sup>†</sup>, A. Kovalchuk<sup>†</sup>, L. Eastman<sup>‡</sup>, A. Vertjachih<sup>‡</sup>,  
C. Gaquiere<sup>§</sup> and D. Theron<sup>§</sup>

<sup>†</sup> Institute of Microelectronics Technology RAS, 142432 Chernogolovka,  
Moscow district, Russia

<sup>‡</sup> Cornell University, School of Electrical and Computer Engineering,  
Ithaca, NY 14853-5401

<sup>§</sup> Institut d'Electronique et de Microelectronique du Nord,  
UMR-CNRS 9929, France

**Abstract.** We have studied interface properties of  $\text{Si}_3\text{N}_4/\text{GaN}$  structures by capacitance-voltage methods, paying attention to semiconductor surface treatments before insulator deposition. ECR plasma deposition of  $\text{Si}_3\text{N}_4$  and ECR plasma treatments of semiconductor surfaces have been used. The interface state density depends on the hydrogen incorporation in ECR silicon nitride and its composition, which are the function of ECR deposition parameters. Optical properties and H-content of the films were characterized by ellipsometry and Fourier transform infrared (FTIR) spectroscopy, respectively. Minimum interface state density ( $1 \times 10^{11} \text{ cm}^{-2} \text{ eV}^{-1}$ ) has been observed for optimized composition  $\text{Si}_3\text{N}_4$  films and ECR  $\text{O}_2$  and  $\text{CF}_4$  plasma treatment of GaN. After passivation by optimized  $\text{Si}_3\text{N}_4$  films, there were observed improvement in breakdown voltage, increase in saturation current, output power, and power added efficiency for AlGaIn/GaN HEMTs.

Due to the outstanding thermal and electric breakdown properties of GaN, this semiconductor becomes the material of choice for high power level and high temperature operation. In comparison with technologically developed GaAs and Si devices that have parameters near their physically possible limit, a lot of efforts should be done to approach theoretically predicted parameters for GaN based devices.

Very promising realization of AlGaIn/GaN HEMTs has been suggested in [1]. Nevertheless, carrier trapping effects (bulk unfilled dislocation states and/or surface states) result in current slump during high voltage or pulsed operation. Among different plasma methods, plasma-enhanced chemical vapor deposition (PECVD) of  $\text{Si}_3\text{N}_4$  with typical ion densities  $10^9 \text{ cm}^{-3}$  is widely used for device passivation and encapsulation in III/V technology. There were published results on  $\text{Si}_3\text{N}_4$  passivation of AlGaIn/GaN HEMTs by RF PECVD [2]. This passivation resulted in decreasing of breakdown voltage and output power. Moreover, there were problems to pinch off the devices when the silicon nitride deposition temperature was increased. In case of RF-plasma deposition of  $\text{Si}_3\text{N}_4$ , arising problems are due to high level of hydrogen bond concentration (more than 25%) and high deposition temperature. It has been reported that the trap densities increases with hydrogen concentration in silicon nitrides [4]. FET performance is also subjected to influence of hydrogen content in  $\text{Si}_3\text{N}_4$  films [5]. Depending on bonding configuration (Si-H or N-H), hydrogen can increase the wet etching rate, change electrical properties, N-H bonds are

responsible for the compressive stress of  $\text{Si}_3\text{N}_4$  films [6]. As for interface state density of  $\text{Si}_3\text{N}_4$  on n-GaN, this system has been studied recently for PECVD  $\text{Si}_3\text{N}_4$  [7].

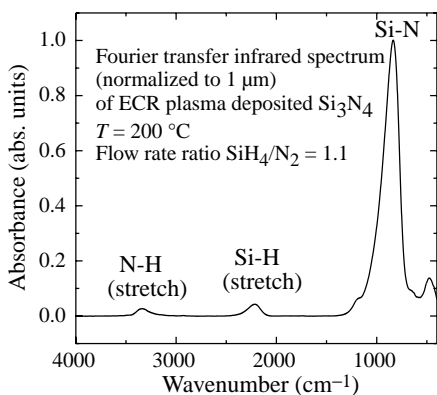


**Fig. 1.** FTIR spectrum of a  $\text{Si}_3\text{N}_4$  film.

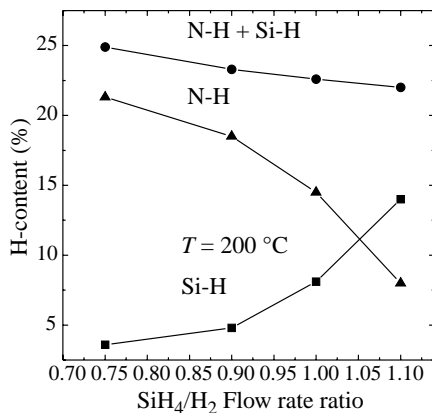


**Fig. 2.** Hydrogen content in  $\text{Si}_3\text{N}_4$  films as a function of  $\text{SiH}_4/\text{N}_2$  flow rate ratio.

Due to advantages of electron cyclotron resonance (ECR) plasma methods with high plasma density  $10^{12} \text{ cm}^{-3}$  and low ion energy (20 eV), they became very efficient tools for deposition and etching. Moreover, ECR  $\text{Si}_3\text{N}_4$  gives high quality films with improved step coverage [3]. But contrary to traditionally used PECVD, ECR CVD of  $\text{Si}_3\text{N}_4$  is not so extensively studied. In this work, we investigate the influence of different  $\text{Si}_3\text{N}_4$  ECR plasma deposition parameters and ECR plasma treatments of GaN on the interface state density. Optimized  $\text{Si}_3\text{N}_4$  films were used for improvement of conductivity and breakdown characteristics of AlGaIn/GaN HEMT structures in passivation experiments.

Silicon nitride films (100–200 nm) were deposited from monosilane ( $\text{SiH}_4$ ) and nitrogen diluted in argon (1:3) using an ECR plasma reactor and by varying substrate temperature (20–300 °C),  $\text{SiH}_4/\text{N}_2$  flow rate ratio (0.75–1.2), pressure (1–6 mTorr), and source power (200–500 W). To investigate  $\text{Si}_3\text{N}_4$  film properties, the films were deposited on Si (100) wafers (p-type, 10  $\Omega \text{ cm}$ ) and GaN on sapphire substrates. Silicon nitride refractive index in the range 1.96–2.03 was measured by varying the  $\text{SiH}_4/\text{N}_2$  flow rate ratio (0.9–1.1). Figure 1 shows the normalized FTIR spectrum of a typical silicon nitride film. The amount of hydrogen incorporation and bonding configuration was determined from the absorbance of the Si-H and N-H stretch modes at 2180 and 3340  $\text{cm}^{-1}$ , respectively. Hydrogen content in  $\text{Si}_3\text{N}_4$  films as a function of  $\text{SiH}_4/\text{N}_2$  flow rate ratio is shown in Fig. 2. For both Si-H and N-H bond content, sharp changes were observed for small deviations of  $\text{SiH}_4/\text{N}_2$  around 1, nevertheless, the total hydrogen incorporation remained nearly constant.

Prior to deposition of insulating films, samples were processed by the following surface treatments: (1) cleaning in organic solvents, (2)  $\text{O}_2$  ECR plasma treatment, (3) cleaning in both  $\text{O}_2$  and  $\text{CF}_4$  ECR plasma. Oxygen plasma treatment was used with the aim to remove organic contamination from the surface and  $\text{CF}_4$  ECR plasma treatment to etched remaining oxides. Auger depth profiling of the films showed that, they are homogeneous and stoichiometric with sharp and oxygen free interface. The oxygen content was lower than 0.5%, which was determined by detection limit of Auger spectrometer.

MIS structures for C–V measurements were fabricated with guard ring configuration and were characterized by high frequency (1 MHz) LCR bridge. The best results were achieved

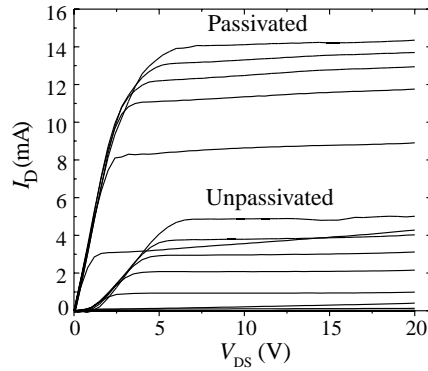


**Fig. 3.** DC I–V characteristics of GaN/AlGaIn HEMT (before and after passivation) with a gate of  $2 \times 50 \times 0.3 \mu\text{m}^2$ . Maximum  $V_G = +4 \text{ V}$ , step  $1 \text{ V}$ .

for the  $\text{SiH}_4/\text{N}_2$  flow rate ratio of 1.05 and cleaning in both  $\text{O}_2$  and  $\text{CF}_4$  ECR plasma (interface-trap density level was  $1 \times 10^{11} \text{ cm}^{-2} \text{ eV}^{-1}$ . From high frequency C–V measurements, interface-trap density level was determined to be rather low  $(1-5) \times 10^{11} \text{ cm}^{-2} \text{ eV}^{-1}$ , showing high quality of  $\text{Si}_3\text{N}_4/\text{GaN}$  interface.

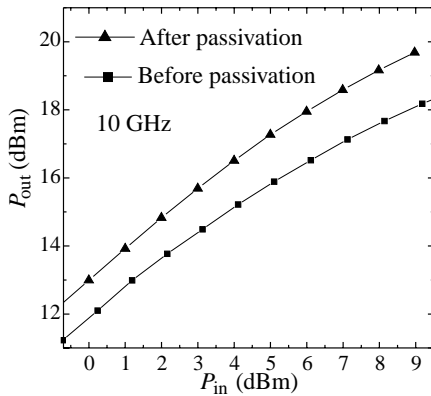


**Fig. 4.** Output power as a function of drive for a  $2 \times 37.5 \times 0.3 \mu\text{m}^2$  AlGaIn/GaN HEMT.

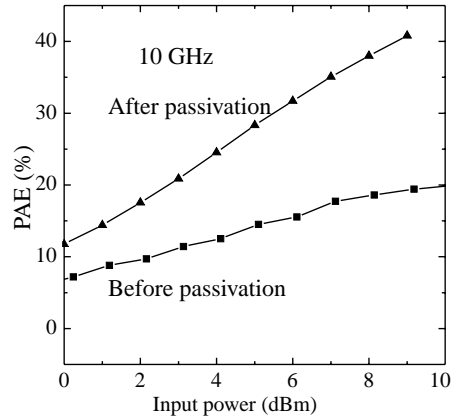


**Fig. 5.** Power-added efficiency as a function of drive for a  $2 \times 37.5 \times 0.3 \mu\text{m}^2$  AlGaIn/GaN HEMT.

A significant current reduction or frequency-dependent slump deteriorates the RF power performance of AlGaIn/GaN HEMTs [8]. This effect is caused by trapping states at the surface of semiconductor in exposed to environment gate-drain and gate-source regions. Therefore, the usage of  $\text{Si}_3\text{N}_4$  passivation layer could eliminate the surface effects limiting the RF current. We should note that different treatments of the semiconductor surface (such as cleaning, oxide removing, etc.) could be determining factors of passivation efficiency. Figure 3 shows an increase in the extrinsic transconductance and decrease in the parasitic source resistance for a GaN/AlGaIn transistor with a gate of  $2 \times 50 \times 0.3 \mu\text{m}^2$  (IEMEN, France) after passivation. All these moved  $f_T$  from 8 GHz to 12.5 GHz despite the increase

in  $C_{GD}$  caused by  $\text{Si}_3\text{N}_4$  passivation dielectric constant increase.

Large signal measurements before and after passivation were done for undoped GaN/AlGaIn devices on sapphire substrates with  $2 \times 37.5 \times 0.3 \mu\text{m}^2$  gate (Cornell University). Loadpull measurements using Maury harmonic loadpull powerbench were performed at 10 GHz ( $V_{ds} = 15 \text{ V}$ ,  $V_{gs} = -3.8 \text{ V}$ ). An increase in the output power of 40% was obtained (from 870 to 1220 mW/mm, Fig. 4).

Figure 5 shows the power-added efficiency (PAE) before and after passivation. A tremendous increase in PAE from 20 to 41% is observed. It is clear from these measurements that passivation strongly decreases depletion of the channel region under the gate-drain semiconductor surface resulting in pronounced capability to modulate the active channel conductivity.

#### Acknowledgement

This work is supported by a grant of the Program "Physics of Solid State Nanostructures".

#### References

- [1] L. F. Eastman, *Proc. of "24th Workshop on Compound Semiconductor Devices and Integrated Circuits (WOCSDICE 2000)"*, Greece, May 29–June 02, p. VIII-7 (2000).
- [2] C. Gaquiere, B. Boudart, R. Amokrane, Y. Crosnier, J. C. De Jaeger and F. Omnes, *Proc. of "24th Workshop on Compound Semiconductor Devices and Integrated Circuits (WOCSDICE 2000)"*, Greece, May 29–June 02, p. VIII-11 (2000).
- [3] F. Ren, D. N. Buckley, D. N. Lee *et al*, *Solid State Electron.* **38**, 2011 (1995).
- [4] S. Fujita, T. Ohishi, T. Toyoshima and A. Sasaki, *J. Appl. Phys.* **57**, 426 (1985).
- [5] C. S. Wu, G. L. Lan, C. K. Puo, S. Bar and M. Hu, *Mater. Res. Soc. Symp. Proc.* **300**, 41 (1993).
- [6] C. W. Pearce, R. F. Fetcho, M. D. Gross, R. F. Koefer and R. A. Pudliner, *J. Appl. Phys.* **71**, 1838 (1992).
- [7] S. Arulkumaran, T. Egava, H. Ishikawa, T. Jimbo and M. Umeno, *Appl. Phys. Lett.* **73**, 809 (1998).
- [8] S. C. Binari *et al*, *Solid-State Electron.* **41**, 1549 (1997).

## Electrodynamics of left-handed materials

A. L. Efros and A. L. Pokrovsky

Department of Physics, University of Utah,  
 Salt Lake City, Utah, 84112 USA

**Abstract.** The theory of diffraction in the system consisting from the left-handed and the right-handed materials is constructed. The theory is based upon the Huygens principle and the Kirchhoff integral and it is valid if the wavelength is smaller than any relevant length of the system. The theory is applied to the calculation of the smearing of the foci of the Veselago lens due to the finite wavelength. We show that the Veselago lens is a unique optical instrument for the 3D imaging, but it is not a “superlens” as it has been claimed recently. We analyze the possibility of obtaining a left-handed materials on the basis of the metallic photonic crystals. The recent experimental results on the LHM are discussed.

### Introduction

In his seminal work Veselago [1] has introduced the concept of the left-handed materials (LHM's). In a simplest case the LHM's are materials where in some frequency range both electric permittivity  $\epsilon$  and magnetic permeability  $\mu$  are negative. It is easy to show that in the LHM the vectors  $\mathbf{k}$ ,  $\mathbf{E}$ ,  $\mathbf{H}$  form a left-handed set, while in usual materials ( $\epsilon > 0$ ,  $\mu > 0$ ) they form a right-handed set. If imaginary parts of  $\epsilon$  and  $\mu$  are small, the electromagnetic waves (EMW's) propagate in the LHM but they have some unusual properties. All these properties originate from the fact that in the isotropic LHM the Poynting vector  $\mathbf{S} = \mathbf{E} \times \mathbf{H}$  is anti-parallel to the wave vector  $\mathbf{k}$ .

### 1. Diffraction in left-handed materials and theory of Veselago lens

Consider a propagation of the EMW from the point source located at a point  $z = -a$  through the infinite slab of a LHM of the thickness  $d$  with the usual right-handed material (RHM) at  $z < 0$  and  $z > d$  (Fig.1). It is obvious that  $S_z > 0$  everywhere at  $z > -a$  because the energy propagates from its source. The directions of vector  $\mathbf{k}$  for different rays are shown by arrows. They are chosen in such a way that at the boundary of RHM and LHM tangential component of vector  $\mathbf{k}$  is the same for all waves as it should be. Then in the LHM  $k_z$  is negative. It follows that the Snell's law for the RHM-LHM interfaces has an anomalous form:  $\sin i / \sin r = -n' / n$ , where  $i$  and  $r$  are the angles of incidence and refraction respectively,  $n' = \sqrt{|\epsilon'| |\mu'|} / \epsilon_0 \mu_0$  and  $n = \sqrt{\epsilon \mu} / \epsilon_0 \mu_0$  are positive refractive indexes for LHM and RHM respectively. The term “negative refractive index” is often used in connection with LHM's [2], but we do not think this is a proper term because in an infinite medium an EMW may propagate in any direction in both LHM and RHM and the only physical difference is that vector  $\mathbf{k}$  is directed from the source of the wave in the RHM, while in the LHM it is directed toward the source.

The device shown at Fig. 1 is a unique optical lens proposed by Veselago. In this lens  $\epsilon = -\epsilon'$  and  $\mu = -\mu'$ , then  $n' = n$  and  $i = -r$ . It is easy to show that the reflected wave is completely absent. Since all the rays going right from the source have  $i = -r$ , all of them have foci at points  $z = a$  and  $z = 2d - a$  as shown in Fig. 1. All the ideas above have



been put forward by Veselago about 35 years ago [1]. Recently the method of fabricating of the LHM's on the basis of metallic photonic crystals has been found and the San Diego group [2] has reported the first observation of the anomalous Snell's law. Since the LHM's become the reality it is time to develop a deeper understanding of their electrodynamic properties in order to understand the advantages of these materials.

One can see that the Veselago lens is an *absolute instrument* because it images stigmatically a three-dimensional domain  $-d \leq z \leq 0$  and optical length of any curve in the object space is equal to the optical length of its image [3]. The only other absolute instrument we are aware of is the famous fish-eye of Maxwell [3]. Note, that the definition of the absolute instrument assumes geometrical optics only. Since the LHM's have been already obtained [2] we think that the Veselago lens can be extremely important device for the 3D imaging.

Pendry [4] claims that the Veselago lens has a different unique property. Due to Pendry the resolution of this lens does not have a traditional wave length limitation which follows from the uncertainty principle. Pendry has introduced a new term "superlenses" with the Veselago lens as a first representative of this class. Two comments appeared recently [5, 6] where the work of Pendry has been criticized. In spite of Pendry's replies we mostly agree with the criticism. We are not going to analyze here this controversy. However, our results show that the Veselago lens is not a "superlens" at least at small wavelengths.

In this paper we propose a general scalar theory of diffraction in the LHM which is based upon the Huygens principle and the Kirchhoff integral. As any diffraction approach our theory works under condition that the wave length is much smaller than any relevant geometrical length in the problem. We apply this theory to the Veselago lens and calculate the smearing of the foci due to the finite wave length. Thus, our results do not support the idea of "superlens". Ziolkowski and Heyman [7] performed a computer simulations of the Veselago lens in the lossless regime. They have not found any focusing. We think that the main reason is that their  $a$  and  $d$  were of the order of the wave length. Due to the smearing calculated above we would not expect any focusing for such wave length.

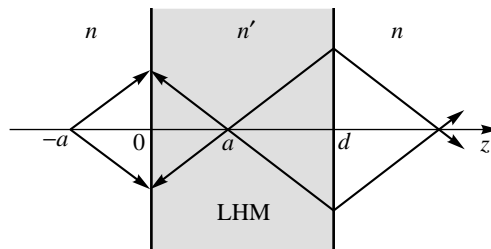


**Fig. 1.** The Veselago lens ( $n = n'$ ). Refraction of light rays outgoing from a point source at  $z = -a$  on the infinite slab of the LHM. The arrows represent the direction of the wave vector. The slab is surrounded by the usual RHM.

## 2. Electrodynamics of metallic photonic crystals and problem of left-handed materials

The idea that a metallic photonic crystal (MPC) may be a technological base for the LHM appears as a result of the computational and experimental study of a few groups [8–12] which have found the EMW's in the MPC propagating above a very low cutoff frequency. The

MPC's they have considered are three- or two-dimensional lattices of thin straight metallic wires. Their discovery is very interesting and important because the waves propagate under the condition  $f\sigma/\epsilon_0\omega \gg 1$ , where  $f\sigma$  is an average conductivity,  $f$  being the volume fraction of a metal in the system. This propagation must be due to the MPC structure, because it would be impossible in a homogeneous medium with the conductivity  $f\sigma$ .

Various groups obtained different cutoff frequencies and they understood them differently. The group of Soukoulis [10] qualitatively interpreted the effect of propagation in terms of waveguide modes, while the group of Pendry [11] presented a completely original physical picture based upon a new longitudinal mode, called "plasma mode". According to Pendry *et al.* [11] the resulting permittivity has a plasma-like behavior, however, the "plasma" frequency contains the light velocity and has a form

$$\omega_p^2 = \frac{2\pi c^2}{d^2 \ln(d/R)}, \quad (1)$$

where  $d$  is the lattice constant,  $R$  is the radius of the metallic wires.

The San Diego group has accepted the "plasma model" and considered the negative  $\epsilon$  at  $\omega < \omega_p$  as one of the two crucial conditions for creation of the LHM. They have reported the first observation of the waves with the NRI by adding the split ring resonators (SRR's) to the MPC [2, 13]. Due to Pendry *et al.* [14] such resonators create a negative bulk magnetic permeability.

We claim in this paper that the "plasma mode" in the MPC is in fact an EMW and that is why the experiments of the San Diego group cannot be simply understood using  $\epsilon$  of the MPC and  $\mu$  of the SRR's. In this paper we first discuss the arguments of Pendry *et al.* [11] in favor of the plasma model and the theoretical approach by Smith *et al.* [12]. Then we derive and solve an exact dispersion equation for the cutoff frequency  $\omega_0$  and find  $\epsilon(\omega)$ . The results are different from Eq. (1) but  $\omega_0$  is in a very good agreement with all computational and experimental data we are aware of. It follows that all groups discuss the same mode. The permittivity becomes negative at  $\omega < \omega_0$ . Then we show that the MPC does not support any waves if it is embedded in the medium with negative  $\mu$  and discuss this result together with the experimental results of the San Diego group.

#### Acknowledgment

The work has been funded by the NSF grant DMR-0102964.

#### References

- [1] V. G. Veselago, *Sov. Phys.-Solid State* **8**, 2854 (1967); *Sov. Phys. Uspekhi* **10**, 509 (1968).
- [2] R. A. Shelby, D. R. Smith and S. Schultz, *Science* **292**, 77 (2001).
- [3] M. Born and E. Wolf, *Principle of Optics*, Pergamon Press, 1980, p. 143.
- [4] J. B. Pendry, *Phys. Rev. Lett.* **85**, 3966 (2000).
- [5] G. W. 't Hooft, *Phys. Rev. Lett.* **87**, 249701 (2001).
- [6] J. M. Williams, *Phys. Rev. Lett.* **87**, 249703 (2001).
- [7] R. W. Ziolkowski and E. Heyman, *Phys. Rev. E* **64**, 056625 (2001).
- [8] D. F. Sievenpiper, M. E. Sickmiller and E. Yablonovitch, *Phys. Rev. Lett.* **76**, 2480 (1996).
- [9] D. R. Smith *et al*, *Appl. Phys. Lett.* **65**, 645 (1994).
- [10] M. M. Sigalas *et al*, *Phys. Rev. B* **52**, 11744 (1995).
- [11] J. B. Pendry *et al*, *Phys. Rev. Lett.* **76**, 4773 (1996);  
J. B. Pendry *et al*, *J Phys: Condens. Matter* **10**, 4785 (1998).
- [12] D. R. Smith *et al*, *Appl. Phys. Lett.* **75**, 1425 (1999).
- [13] D. R. Smith *et al*, *Phys. Rev. Lett.* **84**, 4184 (2000).
- [14] J. B. Pendry *et al*, *IEEE Trans. Microwave Theory Tech.* **47**, 2075 (1999).

## The control of light by the phase transition in opal-VO<sub>2</sub> photonic crystals

V. G. Golubev<sup>†</sup>, A. V. Il'inskii<sup>†‡</sup>, D. A. Kurdyukov<sup>†</sup>, A. V. Medvedev<sup>†</sup>,  
A. B. Pevtsov<sup>†</sup>, A. V. Scherbakov<sup>†</sup>, A. V. Sel'kin<sup>†</sup> and E. B. Shadrin<sup>†</sup>

<sup>†</sup> Ioffe Physico-Technical Institute, St Petersburg, Russia

<sup>‡</sup> BUAP, Puebla, Pue, 72000, Mexico

**Abstract.** Three-dimensional opal-VO<sub>2</sub> photonic crystals were synthesized by the chemical bath deposition technique. The Bragg reflection spectra from the (111) planes of the crystals were measured as a function of the temperature in the range between 15 and 100 °C. The thermal hysteresis loop of the reflection peak position due to the phase transition in VO<sub>2</sub> filling the opal voids was observed. A theoretical model of the periodic layered medium was proposed to describe quantitatively the reflection spectra of opal-like structures. The values of the dielectric constants of the VO<sub>2</sub> below and above the phase transition temperature have been estimated which give the best fit within the model considered.

### Introduction

One of the powerful way to control the propagation of electromagnetic waves is making use of photonic crystals [1], the materials with a periodically varying dielectric constant whose periodicity is of the same order of magnitude as the light wavelength. The Bragg diffraction of light in such a periodic structure gives rise to a photonic band gap (PBG) in the energy spectrum of electromagnetic modes of the crystal. This means that the light propagation in the PBG spectral range can be suppressed in a certain or all directions [2, 3]. Current interest in photonic crystals is primarily due to the search for new possibilities of their perspective applications in optoelectronic and photonic devices.

A representative of a three-dimensional photonic crystal is synthetic opal [4], possessing a fcc lattice composed of close-packed monodisperse amorphous SiO<sub>2</sub> spheres with a diameter varying within 100–1000 nm. The PBG position may be tuned in a wide spectral range (ultraviolet-near infrared) by varying the size of SiO<sub>2</sub> spheres. Filling the interconnected opal voids with various fillers of a dielectric constant different from that for SiO<sub>2</sub> allows variation of the average refractive index and optical contrast (the filler-to-SiO<sub>2</sub> refractive index ratio) of the resultant composite, thereby tuning the PBG position and width.

Many potential applications require special methods to control the PBG structure of a material in real time under external factors (electric field, strain, heating, etc.). To create the three-dimensional PBG material tunable in real time it was suggested [5] infiltrating the opal voids with vanadium dioxide (VO<sub>2</sub>), a material characterized by a metal–semiconductor phase transition. In this work, we studied electrical and optical properties of synthesized opal-VO<sub>2</sub> composites and demonstrated the possibility to govern their PBG structure via the metal–semiconductor phase transition in VO<sub>2</sub>.

### 1. Results and discussion

The initial templates used for preparing samples were commercial synthetic opals with a polydomain structure. The size of a domain with a high ordering degree of SiO<sub>2</sub> spheres

was 30 to 100  $\mu\text{m}$ , the diameter of the spheres being  $230 \pm 5$  nm. The opal-VO<sub>2</sub> composites were fabricated in filling opal voids with VO<sub>2</sub> by the chemical bath deposition technique so that VO<sub>2</sub> occupied about 80% of the available void volume [5].

The results on the temperature dependence of conductivity of the composite in the vicinity of the metal-semiconductor phase transition testify to the crystalline perfection of VO<sub>2</sub>. We measured the thermal hysteresis loop of the composite conductivity at direct current in the 20–90 °C temperature range. The heating branch of the loop starts at the temperature of 67 °C coinciding with that for a single crystal VO<sub>2</sub>. The hysteresis loop has the heating and cooling branches practically parallel to each other, which evidences for a low concentration of oxygen defects. A stepwise profile of the branches indicates size effects due to the martensitic nature of the metal-semiconductor phase transition in this compound. As a whole, the experimental results on conductivity fit well with available data [6,7] whose interpretation is based on the electronic nature of the phase transition in VO<sub>2</sub>. In this connection, the phase transition in the material synthesized in opal voids is expected to occur for a few hundred femtoseconds, and the idea to use the opal-VO<sub>2</sub> composite as a material for ultrafast tuning of PBG properties is validated.

To study the PBG properties of synthesized composites, we measured specular reflection spectra from the (111) lattice planes of the opal-VO<sub>2</sub>. To avoid any contribution of the opal polydomain structure and structural defects to the signal detected [8] we used the so-called light microscopic technique [9,10]. It allowed an investigation of a fragment of the sample surface within a single domain. In studying the phase transition effect on the PBG properties, the samples were heated by a resistance microheater.

In Fig. 1(a) we present the measured (symbols) reflection spectra from the (111) composite surface at the normal incidence of light. The spectra are given for two temperatures: below the phase transition point (the semiconductor phase,  $T = 15$  °C) and above it (the metallic phase,  $T = 75$  °C). The observable peaks are due to the Bragg diffraction of electromagnetic waves by the periodic structure of the samples and characterize the stop band in the [111] direction. Figure 1(b) demonstrates the thermal hysteresis loop of the Bragg peak position. The loop configuration and the temperature range correspond well to the electric measurements discussed above. Note that a good reproducibility of all spectral characteristics was observed in numerous heating-cooling cycles.

The spectral position  $\lambda_m$  of the Bragg peak at normal incidence can be only roughly estimated from the simple Bragg law  $\lambda_m = 2d_{111}\langle\epsilon\rangle^{1/2}$ , where  $d_{111}$  is the interplane distance in the fcc lattice of the composite for the [111] direction,  $\langle\epsilon\rangle$  is the average dielectric constant of the composite;  $\langle\epsilon\rangle = (1 - f)\epsilon_a + f\epsilon_b$ , where  $\epsilon_a$  and  $\epsilon_b$  are the dielectric constants of the voids (in filled with VO<sub>2</sub>) and amorphous SiO<sub>2</sub>, respectively, and  $f$  is the volume fraction of the spheres. For adequate description of the problem in question one needs, of course, more detailed analyses based on quantitative treatment of reflectance contours.

To simulate numerically the reflection spectra we modeled an opal-like 3D structure by a periodically-layered system with the dielectric function  $\epsilon(z)$  continuously varying along only the [111]  $z$  direction. The profile of  $\epsilon(z)$  was calculated according to the scheme suggested in Ref. [11] where, instead of  $\epsilon(z)$ , a refractive index as a function of  $z$  was modeled. Our scheme includes also effects of a sintering process on the shrinkage  $\Delta a$  of the lattice constant  $a$ . Numerical calculations of the reflectance spectra were performed by the one-dimensional transfer matrix method and used the sphere diameter  $D$ , dielectric constants ( $\epsilon_a$ ,  $\epsilon_b$ ) and shrinkage coefficient  $\eta = \Delta a/a$  as fitting parameters of the model. Besides, an imaginary part  $i\epsilon''$  was added to the dielectric function  $\epsilon(z)$  in order to describe

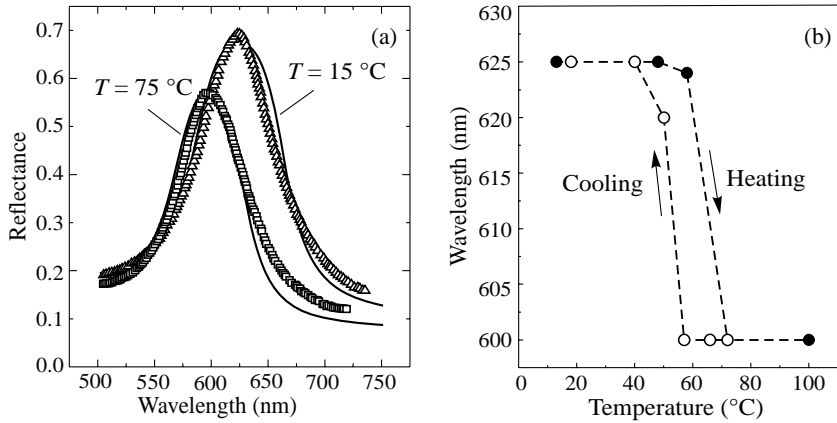


**Fig. 1.** (a) Experimental (symbols) and theoretical (solid lines) reflectance spectra from the (111) surface of the opal-VO<sub>2</sub> at the temperatures of 15  $^{\circ}\text{C}$ , and 75  $^{\circ}\text{C}$ , (b) The thermal hysteresis loop of the reflection peak position of the opal-VO<sub>2</sub> during the sample heating and cooling.

effectively scattering and absorption of light inside the crystal. It is noteworthy that the numerical values of  $D = 228\text{ nm}$ ,  $\varepsilon_a = 1.98$ , and  $\eta = 0.01$  were determined from the analysis of reflectance spectra of the initial bare opal used as a template for preparing the opal-VO<sub>2</sub> composite.

Solid lines in Fig. 1(a) show calculated reflection spectra which are in a good agreement with the experimental ones for the opal-VO<sub>2</sub> sample. The theoretical spectra are obtained at the values of  $D$ ,  $\varepsilon_b$  and  $\eta$  pointed above and  $\varepsilon_a$  being equal to 5.9 and 4.9 for the temperatures of 15  $^{\circ}\text{C}$  and 75  $^{\circ}\text{C}$ , respectively. The  $\varepsilon''$  value is found to be 0.14 for both temperatures when fitting the maximum values of reflectance. With an allowance for the fact that VO<sub>2</sub> occupies only a part ( $\sim 80\%$ ) of the available void volume, we can estimate the values of dielectric constants of VO<sub>2</sub> as  $\varepsilon_{\text{VO}_2} \approx 7.1$  at 15  $^{\circ}\text{C}$  and  $\varepsilon_{\text{VO}_2} \approx 5.9$  at 75  $^{\circ}\text{C}$ .

So, the phase transition in VO<sub>2</sub> induced by heating the sample brings about decreasing the value of  $\varepsilon_{\text{VO}_2}$  and thus an optical contrast between voids and spheres. As a result, the Bragg diffraction peak shifts toward the short-wavelength side by about 25 nm. The reflection band becomes narrower and its intensity is lowering in agreement with our model calculations.

## 2. Summary

We have studied optical and electrical properties of a three-dimensional opal-VO<sub>2</sub> photonic crystal synthesized by the chemical bath deposition technique. A controllable and reproducible variation in conductivity and the photonic band gap (PBG) properties of the crystal was achieved under its heating and cooling. Numerical calculations of reflectance spectra performed in the framework of the model of a periodic layered planar medium demonstrate well principle features in the temperature behavior of the spectra measured. It is shown that due to the metal-semiconductor phase transition in VO<sub>2</sub> a remarkable change in its dielectric constant occurs, which governs the PBG spectral shift of about 25 nm in the visible spectral range and allows an effective control of light propagation.

### Acknowledgements

This work was supported by the Russian R&D Program “Nanostructures” and the RAS Program “Low-dimensional quantum structures”. One of us (A.V.I.) is grateful for support of the work by CONACyT.

### References

- [1] J. D. Joannopoulos, R. D. Meade and J. N. Winn, *Photonic crystals: molding the flow of light*, Princeton University Press, Princeton, NJ 1995.
- [2] E. Yablonovitch, *Phys. Rev. Lett.* **58**, 2059 (1987).
- [3] S. John, *Phys. Rev. Lett.* **58**, 2486 (1987).
- [4] Y. Xia, B. Gates, Y. Yin and Y. Lu, *Adv. Mater.* **12**, 693 (2000).
- [5] V. G. Golubev, V. Yu. Davydov, N. F. Kartenko, D. A. Kurdyukov, A. V. Medvedev, A. B. Pevtsov, A. V. Scherbakov and E. B. Shadrin, *Appl. Phys. Lett.* **79**, 2127 (2001).
- [6] E. B. Shadrin and A. V. Il'inskii, *Phys. Solid State* **42**, 1126 (2000).
- [7] G. Stefanovich, A. Pergament and D. Stefanovich, *J. Phys. Condens. Matter* **12**, 8837 (2000).
- [8] Yu. A. Vlasov, V. N. Astratov, A. V. Baryshev, A. A. Kaplyanskii, O. Z. Karimov and A. A. Limonov, *Phys. Rev.* **E61**, 5784 (2000).
- [9] D. Kang, J. E. MacLennan, N. A. Clark, A. A. Zakhidov and R. H. Baughman, *Phys. Rev. Lett.* **86**, 4052 (2001).
- [10] Yu. A. Vlasov, M. Deutsch and D. J. Norris, *Appl. Phys. Lett.* **76**, 1627 (2000).
- [11] Yu. A. Vlasov, M. A. Kaliteevskii and V. V. Nikolaev, *Phys. Rev.* **B60**, 1555 (1999).

## Fabrication of square spiral photonic crystals by glancing angle deposition

*S. R. Kennedy*<sup>†</sup>, *M. J. Brett*<sup>†</sup>, *O. Toader*<sup>‡</sup> and *S. John*<sup>‡</sup>

<sup>†</sup> Department of Electrical and Computer Engineering, University of Alberta,  
Edmonton, AB, Canada, T6G 2V4

<sup>‡</sup> Department of Physics, University of Toronto,  
Toronto, ON, Canada, M5S 1A7

**Abstract.** Using Glancing Angle Deposition, a novel thin film deposition technique, it is possible to fabricate complex, periodic structures suited for applications in photonic band gap crystals. In comparison to complex lithography processes used to produce conventional structures on the scale of several nanometers, GLAD is ideally suited to a virtual single step deposition, producing a novel tetragonal square spiral crystal structure and having a large predicted band gap of up to 15%.

### Introduction

Photonic band gap (PBG) crystals are periodic dielectric structures that restrict the propagation of certain frequencies of electromagnetic waves falling within the characteristic band of the structure. This property of PBGs is analogous to the restricted bands of electron energies in the arrangement of atoms of a semiconductor crystal, and has been studied extensively in many applications such as light localization [1] and inhibited spontaneous emission [2]. The difficulty with fabricating these devices lies in the production of an appropriate complex structure with high uniformity and ideally three-dimensional periodicity on the size scale of a wavelength of light. In a recent paper by Toader and John [3], a new structure, the tetragonal square spiral, was proposed and is loosely based on the promising diamond lattice. This structure can be easily fabricated through a specialized thin film deposition process known as Glancing Angle Deposition (GLAD) [4], and is predicted to result in highly stable, large relative band gaps of up to 15%. In the following work, the fabrication of tetragonal square spiral structures using GLAD will be outlined, addressing some key issues that arise in the fabrication process.

### 1. Glancing angle deposition

The Glancing Angle Deposition process is a method used to create highly porous thin films with specifically tailored microstructure from a wide variety of materials [5–7]. Deposition by electron beam or thermal evaporation at highly oblique angles of incidence,  $\alpha = 80\text{--}90^\circ$ , is implemented in conjunction with advanced substrate motion to grow a wide variety of unique structures as diverse as helices, chevrons and posts. In the production of aperiodic GLAD thin films, a flat substrate is placed on a specialized mount able to accurately control the orientation of the substrate with respect to the source of material flux (Fig. 1(a)). Initial nucleation on the substrate shadows the region opposite the incoming flux due to the highly oblique orientation of the substrate, preventing further growth from occurring in these locations (Fig. 1(b)). Self-shadowing results in individual growths and with the further implementation of computer controlled substrate rotation,  $\varphi$ , it is possible to change the

apparent direction of the source so that various microstructures can be tailored as they ‘reach’ toward the incoming flux.

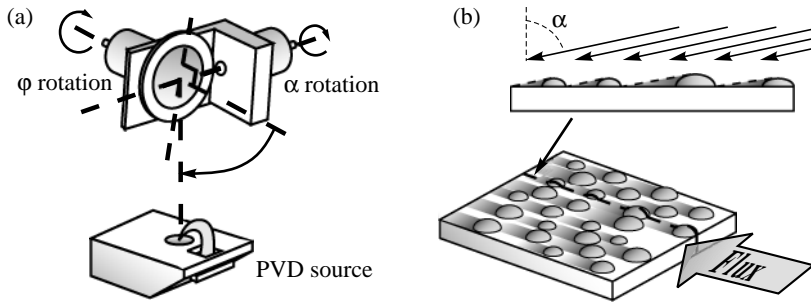


**Fig. 1.** (a) Schematic of the GLAD apparatus used in the production of square spiral crystals. (b) Self-shadowing that occurs at extreme angles of incidence,  $\alpha$ .

In creating PBG devices, dielectric materials must be arranged in a fully three-dimensional array, however the implementation of standard GLAD on a flat substrate yields an aperiodic distribution of structures that is dictated by the randomness of the nucleation process. To restrict growths to the desired, regularly spaced locations, the substrate must be first patterned to take advantage of the shadowing aspect of GLAD where growth occurs only at the higher points of the topography (Fig. 2(a)).

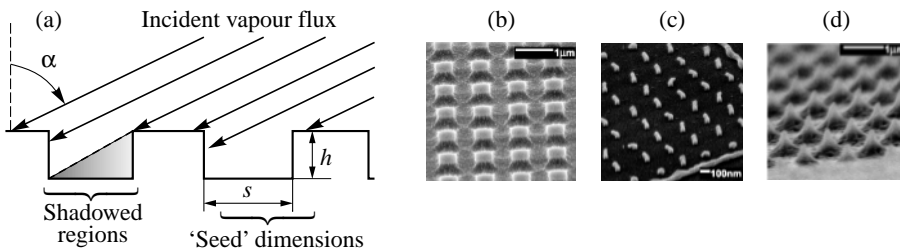


**Fig. 2.** (a) Schematic of shadowing occurring on a pre-patterned substrate and examples of actual seeded substrates created using (b) photolithography and reactive ion etching, (c) scanning electron microscope, and (d) plastic embossing [8].

Many techniques may be used to pattern the substrate where the key feature of a successful substrate lies in the aspect ratio of the topography rather than the sharpness of the features. Shown on the right hand side of Fig. 2 are three examples of patterned substrates used for producing periodic GLAD structures. These processing techniques, along with countless others may be used to pre-pattern the substrate where typically the requirement of feature size or pattern area dictate the use of one process over another.

## 2. Tetragonal square spiral crystal structures

The tetragonal square spiral crystal structure was first proposed by John and Toader [3] after observations of spiral symmetry in various PBG lattice structures by Chutinan and Noda [9]. The lattice is composed of a square array of staircase structures that emulate a non-conventional diamond lattice. The critical dimensions are the lattice spacing,  $a$ , and



the three structure parameters normalized to the lattice:  $L$ , the horizontal width of the spiral,  $c$ , the vertical period or pitch of the spiral, and  $r$ , the radius of the arms of the spiral.

To fabricate square spiral crystals, a substrate with seeds arranged in a square array is used to provide a layer from which the fundamental unit of the diamond lattice can be formed. From this starting layer, we are able to connect the basis points of the desired lattice by depositing a material such as silicon with a high index of refraction, while holding the substrate at a highly oblique angle. The orientation of the substrate is fixed during deposition until the arm of the spiral is of the desired length at which point the substrate is rotated through  $\pm 90^\circ$  depending on the desired handedness (right- and left-handed spirals are degenerate cases) [4]. These steps are shown in Fig. 3, where the initial arm is first grown on the seeded substrate, and subsequent arms are grown at right angles.

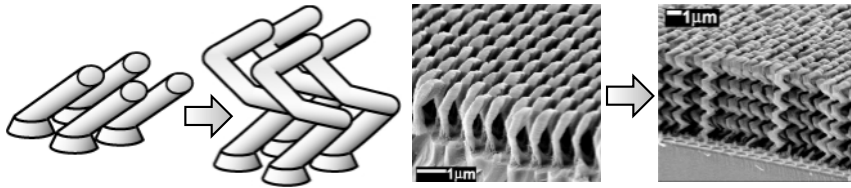


**Fig. 3.** Deposition of tetragonal square spiral crystals is done by the successive growth of arms at right angles to the previous structure. The film is deposited on a substrate that is composed of topographical relief arranged in a square array.

The GLAD process is very versatile in that the resulting structure can be easily modified through the simple variation of deposition parameters and substrate dimensions. In this way, the effect of the various changes on the resulting crystal structure and ultimately on its optical properties may be investigated. In particular, it is possible to vary the deposition angle, seed size and spacing, and rotation intervals so that all of the dimensions,  $a$ ,  $L$ ,  $c$  and  $r$  may be varied to provide a more complete view of the band properties of the crystal structure.

### 3. Results and discussion

The production of ideal structures with smooth, cylindrical arms is not realistic in practice, and some approximations must be made to overcome issues that arise in the fabrication

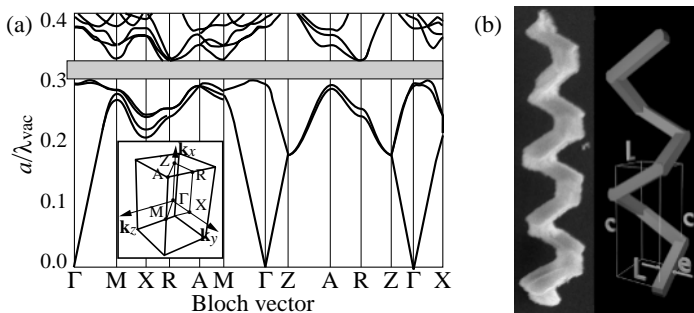


**Fig. 4.** (a) Band diagram for the square cross-section square spiral with  $[L, c, e] = [0.7, 1.3, 0.44]$ , (b) Images of the actual and CG spirals.

of square spiral photonic crystals. One of the issues of chief concern is the cross-section. Attempts to more realistically model the resulting structure can be seen in Fig. 4, where instead of simulating ideal circular arms of radius  $r$ , a square cross-section of side length  $e$  has been used. As can be seen from Fig. 4(b)), this is much closer to the actual deposited spiral. What is encouraging from this result, as seen in the band diagram of part (a) of the same figure, is that the gap still remains quite large at 9.3% without any further optimization of the structure.

The importance of photonic crystals is synonymous to that of semiconductors in that the true usefulness comes not from the band gap, but by defect states introduced to the gap. In addition to fabrication, the 'doping' process in GLAD deposited square spiral photonic crystals is extremely simple and can be done in several way such as by modifying growth sites to create microcavities, and planar defects can be introduced by a temporary change in the deposition parameters.

## References

- [1] S. John, *Phys. Rev. Lett.* **58**, 2486 (1987).
- [2] E. Yablonovitch, *Phys. Rev. Lett.* **58**, 2059 (1987).
- [3] O. Toader and S. John, *Science* **292**, 1133 (2001).
- [4] S. R. Kennedy, M. J. Brett, O. Toader and S. John, *Nano Lett.* **2**, 59 (2002).
- [5] K. Robbie and M. J. Brett, *J. Vac. Sci. Technol. A* **15**, 1460 (1997).
- [6] K. Robbie, J. C. Sit and M. J. Brett, *J. Vac. Sci. Technol. B* **16**, 1115 (1998).
- [7] K. Robbie and M. J. Brett, *US Patent* **5,866,204**, (1999).
- [8] B. Dick, J. C. Sit, M. J. Brett, I. M. N. Votte and C. W. M. Bastiaansen *Nano Lett.* **1**, 71 (2000).
- [9] A. Chutinan and S. Noda, *Phys. Rev. B* **59**, 2006 (1998).

## Influence of temperature and free carries on four-wave mixing in semiconductor microcavities

*M. N. Makhonin*<sup>†</sup>, *D. N. Krizhanovskii*<sup>†</sup>, *A. N. Dremin*<sup>†</sup>, *A. I. Tartakovskii*<sup>†‡</sup>,  
*V. D. Kulakovskii*<sup>†</sup>, *N. A. Gippius*<sup>¶</sup>, *M. S. Skolnick*<sup>‡</sup> and *J. S. Roberts*<sup>§</sup>

<sup>†</sup> Institute of Solid State Physics, RAS, Chernogolovka, 142432, Russia

<sup>‡</sup> Dept. of Physics and Astronomy, University of Sheffield, Sheffield S3 7RH, UK

<sup>§</sup> Dept. of Electronic and Electrical Engineering, University of Sheffield,  
Sheffield S1 3JD, UK

<sup>¶</sup> General Physics Institute RAS, Moscow, Russia

In semiconductor microcavities (MCs) with embedded quantum wells (QW) a strong two-dimensional (2D) confinement of the light in the growth direction leads to an enhanced exciton-photon interaction, which results in the formation of mixed exciton-photon states described in terms of quasi 2D-polaritons. The density of these states is strongly reduced compared to exciton one, due to a very small in-plane mass. As a result, one can hope that the high filling of the polariton states near the polariton band bottom can be achieved at relatively small total density without destroying the strong coupling regime. However such a filling never was reached at low excitation density range where the polariton relaxation to the polariton branch bottom is determined by the emission of acoustic phonons. The reason is in the fact that the polariton lifetime is comparable with phonon scattering time [1]. As a result, the energy distribution of polaritons clearly demonstrates ‘bottleneck effect’ both under the above band gap excitation and the resonant excitation below free exciton level [2, 3]. However the high occupation of polariton states near the band bottom is relatively easy reached under conditions of a strong resonant excitation into the lower polariton (LP) branch at particular wavenumbers close to the inflection point of the LP dispersion [4, 5]. It is explained as the result of stimulated hyper-Raman scattering (or four-wave mixing) of pumped polaritons with  $(E_p, k_p)$  to states with the energy and momentum  $[E_1, k_1 \sim 0]$  and  $[E_2 = 2E_p - E_1, k_2 = 2k_p]$ , which referred to as the ‘signal’ and ‘idler’, respectively.

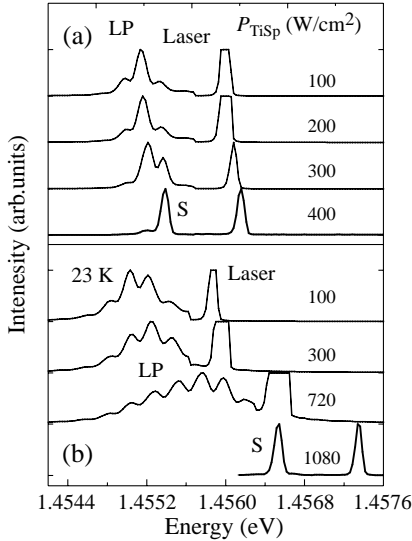
This scattering being an analogous to a so called hyper Raman scattering of polaritons in the bulk semiconductors has been found to demonstrate an unusual dependence on the excitation photon energy and wavenumber when the excitation occurs in the vicinity of the LP dispersion inflection point. In particular, it has been found that the signal and idler peaks are located out off the LP branch: they always appear at  $k \approx 0$  and  $\approx 2k_p$  whereas the energy conservation law is fulfilled due to their shift to the higher energies lying well above the LP ones at  $k \approx 0$  and  $\approx 2k_p$ , respectively. This phenomenon is still not explained. One can suppose that the four wave mixing in polariton range of MCs is highly influenced by the scattering with either phonons or excitons and carriers. In particular, it has been recently shown that the additional above band gap illumination or the rising temperature result in a highly enhanced relaxation of polaritons photoexcited resonantly into the LP branch below the free exciton energy.

Here we investigate the influence of a temperature and an additional above band gap excitation on the stimulated scattering in MCs. A GaAs/AlAs MC containing 6 InGaAs quantum wells in the active layer (Rabi splitting  $\Omega$  of 6–7 meV) has been investigated in a wide range of detunings between free exciton level and bottom of the photonic mode

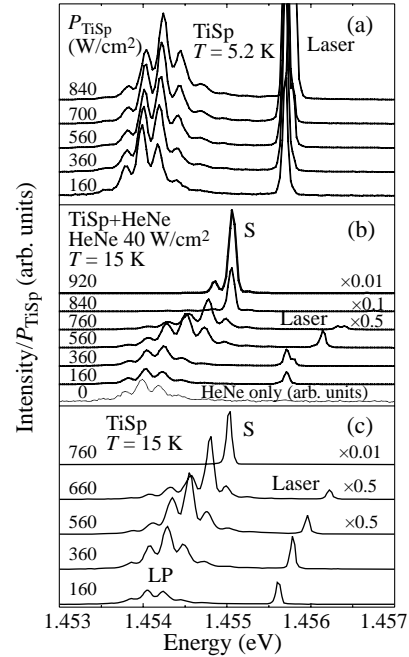
from  $\delta = 0$  to  $-3$  meV. The resonance excitation into an LP branch was carried out with a tunable Ti-sapphire laser. The HeNe laser was used for the additional above GaAs band gap excitation. The sample was mounted in a helium thermostat with the temperature control at  $T = 5-30$  K.

Figure 1 shows the behavior of the LP emission for the MC with approximately zero detuning at two temperatures  $T = 6$  and  $23$  K. The fine structure originates from the interference effect between the front and the rear surfaces of the sample. The peak intensity at  $23$  K is markedly smaller and the threshold excitation density for the stimulated scattering  $P_{\text{thr}}$  resulting in the appearance of the narrow signal line S is markedly higher. A similar increasing of  $P_{\text{thr}}$  was observed as well in experiments carried at  $5$  K when the MC was additionally excited with a rather weak ( $40 \text{ W/cm}^2$ ) HeNe laser beam generating hot excitons and free carriers. Such a behavior is well expected: the scattering with phonons and/or photoexcited hot excitons and carriers results in an enhanced decay of polariton states and, as a consequence, in an increased threshold density for the stimulated scattering process.

However the situation changes qualitatively in MCs with the negative detuning. That is illustrated in Fig. 2 that shows the experimental data for the MC with  $\delta \sim -1.5$  meV. Figure 1(a) displays the spectra recorded at  $T = 5.2$  K and  $k \sim 0$  with a Ti-sapphire laser excitation resonant with the LP branch at a magic angle near the inflection point ( $k_p \sim 2.4 \times 10^{-4} \text{ cm}^{-1}$ ) for different excitation powers  $P_{\text{TiSp}}$ . In the whole range of  $P_{\text{TiSp}}$  the maximum intensity of the LP line is reached at the same frequency of the exciting



**Fig. 1.** Emission spectra of LP-branch at  $\delta \approx 0$  recorded at  $k \sim 0$  for  $T = 5.2$  K (a) and  $T = 23$  K (b) under resonant excitation.



**Fig. 2.** Emission spectra of LP-branch at  $\delta < 0$  recorded at  $k \sim 0$  for  $T = 5.2$  K (a,b) and  $T = 15$  K (c) under resonant excitation with Ti-sapphire (a,c) and simultaneous excitation with both Ti-sapphire and HeNe lasers.

laser. With increasing  $P_{\text{Ti}}$ , the LP-line becomes wider, shifts slightly to higher energies and increases in the intensity nearly linearly with  $P_{\text{Ti}}$ , no stimulated scattering similar to that in the MC with zero detuning is observed. The situation changes with increasing temperature to 15 K. Figure 1(c) show that in contrast to the case of 5 K, already at as small  $P_{\text{Ti}}$  as  $360 \text{ W/cm}^2$  the LP line shifts markedly to the higher energies, increases highly superlinearly with  $P_{\text{Ti}}$ , becomes narrower and a strong narrow peak S corresponding to a stimulated scattering appears at  $P_{\text{Ti}} > 700 \text{ W/cm}^2$ . Figure 2(b) shows that a similar effect can be reached at 5 K if a relatively weak additional above band gap excitation is added. The spectra are recorded with as small as  $40 \text{ W/cm}^2$  HeNe laser excitation. The lowest spectrum in Fig. 2(b) shows the spectrum recorded with the excitation by the only HeNe laser. The intensity of the LP line is 10 times smaller than that obtained with the  $160 \text{ W/cm}^2$  excitation with the Ti-sapphire laser. However the effect of this small above band gap excitation on the efficiency of the four wave mixing process is drastic. Figure 2(b) shows that the line LP shifts to higher energies already at  $P_{\text{Ti}} > 360 \text{ W/cm}^2$  by  $\sim 0.5 \text{ meV}$  and the stimulated scattering appears at the highest excitation densities. Note that the highest emission at  $k = 0$  and the stimulated scattering is reached at  $E_S$  well above ( $\sim 0.7 \text{ meV}$ )  $E_{\text{LP}}(k_p)$  but still well below ( $\sim 1 \text{ meV}$ ) the cavity mode energy indicating that the system is still in the strong coupling regime.

Figure 3 displays dependencies of a cavity absorption  $A$ , an emission intensity  $I_0$  at  $k \approx 0$  and an emission maximum energy  $E_0$  on the excitation energy  $\hbar\omega_p(k_p)$  at 5 K. The power of Ti-sapphire laser was taken  $P_{\text{Ti}} = 800 \text{ W/cm}^2$ . No stimulated emission is observed in this case until an additional above band gap excitation is used. A comparison of Figs. 3(b) and (c) shows that under the only Ti-sapphire laser excitation the maximum of the emission intensity and the cavity absorption are observed at the same frequency of exciting laser. In contrast, in the experiments with a simultaneous excitation with two lasers the maximum emission is shifted to the higher energy by  $\sim 1 \text{ meV}$  compared to that for

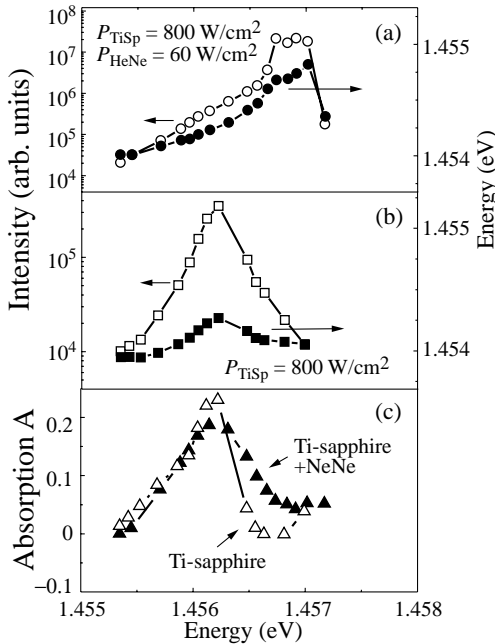


**Fig. 3.** Dependencies of the intensities and energies of the  $k = 0$  LP-line recorded under the excitation by both Ti-sapphire and HeNe lasers (a) and Ti-sapphire laser only (b) at  $T = 5.2 \text{ K}$ . (c) MC absorption as a function of the photon energy .

the maximum absorption. Comparison of Figs. 3(a) and c shows that the increase in the emission intensity reaches 2 orders of magnitude when the excitation energy  $\hbar\omega_p$  increases from 1.4562 eV to 1.4568 eV despite the absorption drops down more than 4 times. That indicates that the density of photoexcited excitons is not the decisive parameter determining the efficiency of stimulated parametric scattering.

In general, the four wave mixing efficiency depends both on the excitation density and the decay of the signal and idler states. The scattering of the polariton states with phonons and free excitons or carriers is to increase with temperature and/or above band gap excitation density. That is correlated with the increase of  $P_{\text{thr}}$  for stimulated parametric scattering in MCs with a zero detuning. The opposite effect observed in MCs with negative detuning points out that the effect of enhanced phonon and exciton (carrier) scattering is overcompensated by some another mechanism. Note that the idler states located at large wavenumbers are very similar in the MCs with zero and negative detuning. Thereby one has to suggest that the difference in the four wave mixing behavior in the MCs with zero and negative detuning is connected with the states near the LP band bottom. The most pronounced change for these states that can occur with the lowering of the LP energy seems to be connected with changes in the absorption coefficient at the LP energy due to the filling of localized states. At zero detuning the LP mode is located about 3 meV below the free exciton energy. The localized states at this energy are effectively emptying at temperatures above 10 K and with photoexcited hot excitons and carriers. In contrast, the delocalization of states located at 5–6 meV below the free exciton energy is still weak even at  $T < 20$  K. The filling of these states with photoexcited excitons results in a strong decrease of the absorption coefficient at LP energy [7]. That can explain the observed decrease rather than the increase of  $P_{\text{thr}}$  in MCs with negative detuning.

Within the framework of this explanation it is not clear why the most effective stimulated scattering occurs at  $\hbar\omega_p$  well above the maximum in the MC absorption. Calculations predict the shift of the maximum in the stimulated scattering to higher energies compared to the LP energy in the unexcited cavity due to the exciton-exciton interaction. However the maximum in the cavity absorption spectrum has to shift to the higher energies, too. The contradiction to the experiment can be taken away if the stimulated scattering has pulse rather than cw character with duty circle less than 10%. The pulse character of stimulated scattering can be connected with a gradual filling of localized states and their quick emptying when the stimulated process. Time resolved measurements in a ps time region have to be carried out in order to check this suggestion.

#### Acknowledgements

The authors are grateful to V. B. Timofeev for fruitful discussions. The work was supported by RFBR and INTAS.

#### References

- [1] F. Tassone *et al*, *Phys. Rev. B* **56**, 7554 (1997).
- [2] A. I. Tartakovskii *et al*, *Phys. Rev. B* **62**, R2283–R2286 (2000).
- [3] D. N. Krizhanovskii *et al*, *Solid. State. Comm.* **118/11** 583–587 JUN 2001.
- [4] P. G. Savvidis *et al*, *Phys. Rev. Lett.* **84** 1547 (2000).
- [5] A. I. Tartakovskii *et al*, *Phys. Rev. B* **62**, R13298 (2000).
- [6] Ciuti *et al*, *Phys. Rev. B* **62**, R4825 (2000).
- [7] D. N. Krizhanovskii *et al*, *Solid. State Comm.* **119**, 435–439 (2001).

## Three-dimensional Bragg diffraction in growth-disordered opals

A. V. Baryshev, A. A. Kaplyanskii, V. A. Kosobukin, M. F. Limonov,  
 K. B. Samusev and D. E. Usvyat  
 Ioffe Physico-Technical Institute, St Petersburg, Russia

### 1. Introduction

After [1] artificial opals as well as opal-based infilled and inverted composites are considered to be promising representatives of photonic crystal materials. Earlier, photonic stop gaps in opals were studied mainly in transmission or specular reflection geometries corresponding to "one-dimensional" Bragg diffraction, see [2] and references therein. On the contrary, this work was aimed at observing the typical patterns of optical Bragg diffraction in which phenomenon opal crystal structure acts as a three-dimensional diffraction grating. Although our experiments were performed for artificial opals possessing unavoidable imperfections a well-pronounced diffraction peaks were observed characteristic of a crystal structure. Each of the diffraction maxima reveals a photonic stop gap in the specified direction, while the spectral width of the peak is a measure of the photonic stop gap width.

### 2. Theoretical background

The intensity of optical scattering (Bragg diffraction) from a crystal is expressed as follows

$$I(\mathbf{Q} \rightarrow \mathbf{Q}') = A \cdot S(\mathbf{K}' - \mathbf{K}) \cdot \left| \varepsilon(\mathbf{K}' - \mathbf{K}) \right|^2. \quad (1)$$

This formula corresponds to the lowest (Born) approximation in the Fourier component  $\varepsilon(\mathbf{K})$  of a small periodic variation of dielectric permittivity  $\varepsilon$  that is typical of opals immersed in a liquid. The structure factor

$$\begin{aligned} S(\mathbf{K}' - \mathbf{K}) &= \frac{1}{N} \sum_{n,m} \exp \left[ -i \cdot (\mathbf{K}' - \mathbf{K}) \cdot (\mathbf{R}_n - \mathbf{R}_m) \right] \\ &= \left| \frac{1}{\sqrt{N}} \sum_n \exp \left[ -i \cdot (\mathbf{K}' - \mathbf{K}) \cdot \mathbf{R}_n \right] \right|^2 \end{aligned} \quad (2)$$

depends on the site positions  $\mathbf{R}_n$  that are occupied by silica spheres in an opal. Inside a crystal the wavevectors  $\mathbf{K}$  and  $\mathbf{K}'$  of direct and diffracted waves, respectively, are of the form

$$\mathbf{K} = (\omega/c) \sqrt{\varepsilon(0)} \left\{ (\mathbf{e}_x \cos \varphi + \mathbf{e}_y \sin \varphi) \sin \theta + \mathbf{e}_z \cos \theta \right\}. \quad (3)$$

Here,  $\varepsilon(0)$  is the space-averaged dielectric constant coinciding with the Fourier component  $\varepsilon(\mathbf{K})$  for  $\mathbf{K} = \mathbf{0}$ . The factor  $A$  in Eq. (1) describes transformation of polar angles according to the relation  $\sin \vartheta = \sqrt{\varepsilon(0)} \sin \theta$  when light wave passes the sample surface. The corresponding vector  $\mathbf{Q}$  (or  $\mathbf{Q}'$ ) measured in vacuum is obtained from  $\mathbf{K}$  (or  $\mathbf{K}'$ ) by changing  $\theta \rightarrow \vartheta$  and  $\sqrt{\varepsilon(0)} \rightarrow 1$  in Eq. (3).

According to a general diffraction theory [3] it is the structure factor (2) that defines predominantly the diffraction intensity (1). For an ideal crystal the most intensive (principal) maxima of (2) in the limit  $N \rightarrow \infty$  satisfy the Laue equation  $\mathbf{K}' - \mathbf{K} = \mathbf{b}$ , with  $\mathbf{b}$  being

a vector of the reciprocal lattice. Below, a solution  $\mathbf{b}$  of Eq. (4) with  $|\mathbf{K}'|=|\mathbf{K}|$  is denoted as  $\mathbf{b}_{(hkl)}$  where explicitly indicated is the plane  $(hkl)$  of the real-space face-centered cubic (f.c.c.) lattice. The  $(hkl)$  plane is responsible for Bragg diffraction and perpendicular to  $\mathbf{b}_{(hkl)}$ . In dealing with a disordered opal structure one should average [3] either the intensity (1) or structure factor (2), the operation providing the mean value  $\overline{S(\mathbf{K}'-\mathbf{K})}$ . A model of interlayer disorder is discussed below on this background.

### 3. Experimental

The artificial opal samples under study were made of highly monodisperse silica ( $\text{SiO}_2$ ) spheres whose average diameters could vary from 200 to 400 nm in different samples. The  $\text{SiO}_2$  spheres are closely packed in two-dimensional hexagonal layers. In turn, the layers stack in a sequence, possibly random, defined by the in-layer site positions A, B and C that are conventionally introduced in textbooks for the f.c.c. structure. Opal samples were characterized in [2], a f.c.c. lattice being established as a reference structure for the opals. For measurements, the most optically homogeneous samples were selected up, and their crystallographic parameters were determined with atomic force microscope.

Angle and frequency dependencies of the light intensity were measured in an optical scheme typical of scattering experiments, and the diffraction spots were seen directly at a screen by either vision or photographing. These diffraction patterns were investigated experimentally in the following two geometries. (i) Diffraction near the direction of specular reflection at oblique incidence of light beam on the growth surface (111) of an opal sample. (ii) Diffraction of the waves whose incidence directions lie in hexagonal layers, i.e. in the (111) growth plane of an opal. In both cases diffraction occurred from different representatives, either (111) or  $(\bar{1}\bar{1}\bar{1})$ , of the same  $\{111\}$  system of crystal planes.

(i) Figure 1(a) presents the spectral intensity of diffraction measured in the scheme shown by the inset in Fig. 1(b). Incident beam of white light makes an angle of  $\vartheta = 20^\circ$  with the internal normal to sample surface (111), while its spectral components diffract backwards at different angles  $\vartheta'$ . Figure 1(b) shows how the maxima of the spectral peaks from Fig. 1(a) depend on  $\vartheta'$ . The specular reflection condition  $\vartheta' = \vartheta = \vartheta_B$  met by the maximum intensity in Fig. 1(b) confirming that Bragg diffraction is caused by the (111) plane perpendicular to  $\mathbf{b}_{(111)}$ . When measured in vacuum, the Bragg wavelength  $\lambda_B$  and angle  $\vartheta_B$  corresponding to the maxima in Figs. 1(a) and 1(b), respectively, satisfy the generalized Bragg relation  $\lambda_B = 2d\bar{n} \cos \vartheta_B$ . Here,  $d$  is the period determined for  $\{111\}$ -

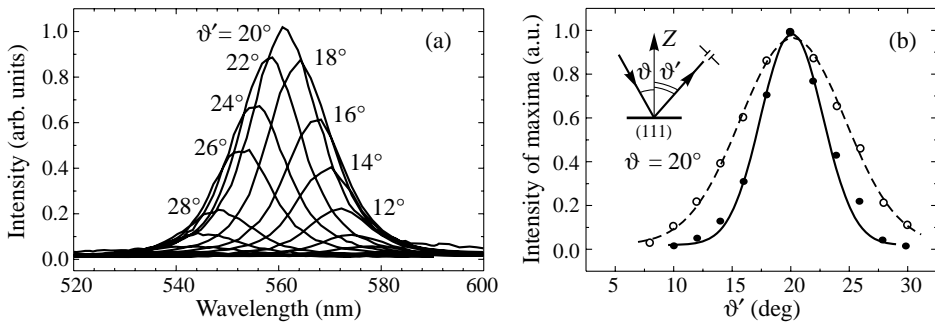
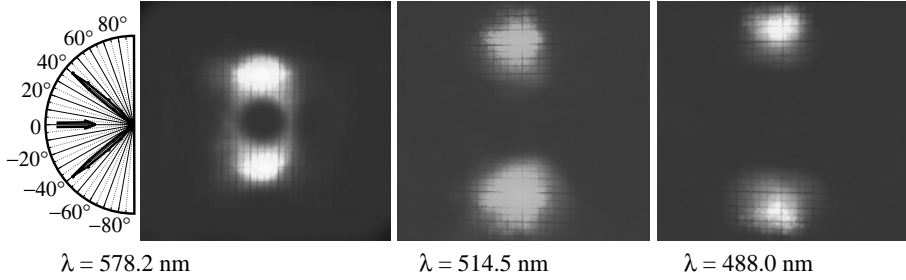


**Fig. 1.** (a) Experimental spectra of the Bragg  $\mathbf{b}_{(111)}$ -diffraction depending on the wavelength for different angles  $\vartheta'$ . (b) Intensity in the maxima as a function of the angle  $\vartheta'$  for white light (circles and dashed line for the eye) and monochromatic light with  $\lambda = 578.2$  nm (points and solid line). The incidence angle is  $\vartheta = 20^\circ$ , the angles  $\vartheta$  and  $\vartheta'$  are shown in the insert.



direction as  $d_{[111]} = R\sqrt{8/3}$  through the radius  $R$  of spheres in f.c.c. stacking, and  $\bar{n}$  is an effective refractive index ( $d_{[111]} \cdot \bar{n} = 300$  nm for the data of Fig. 1).

(ii) In the second geometry light beam was incident perpendicularly to the  $[111]$  growth axis and Bragg diffraction was studied in rotating the sample around this axis. In this case the diffraction spot patterns change essentially and periodically following anisotropy of single  $(111)$  layer. The simplest of the spot patterns is demonstrated in Fig. 2 at three different wavelengths of laser illumination. It is related with diffraction in the  $[\bar{2}11]$  direction providing the wavevectors of both incident and diffracted waves to belong to the  $(111)$  incidence plane. All patterns observed in this arrangement show a pair of spots located on the growth axis  $[111]$  symmetrically relative to light incidence direction.



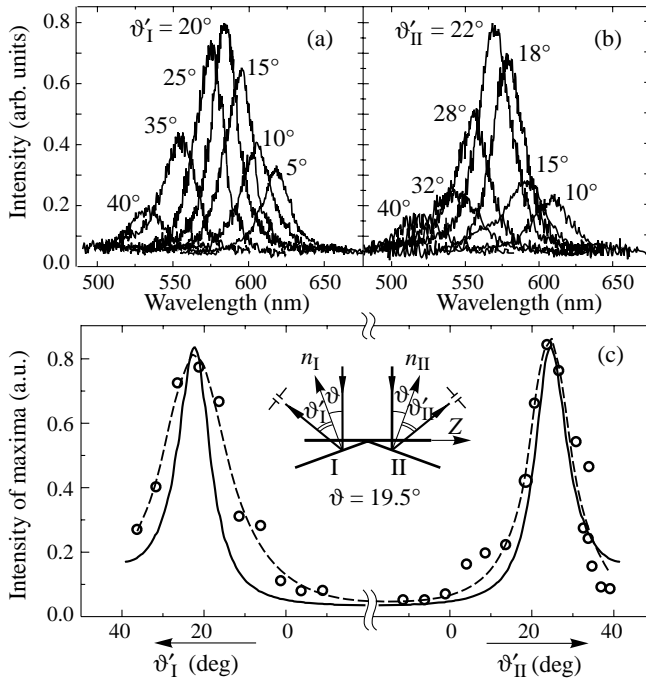
**Fig. 2.** Photographs of spot patterns caused by Bragg diffraction in the  $[\bar{2}11]$  direction incidence at three different wavelengths of illuminating light. Shown on the left is the scattering indicatrix for  $\lambda = 578.2$  nm.

Figure 3 presents the intensity of Bragg diffraction peaks for the  $[\bar{2}11]$  direction related to Fig. 2, an opal sample being illuminated with white light. Figures 3(a) and 3(b) show the intensity spectra at different angles  $\vartheta'$ , and Fig. 3(c) presents an envelope  $\vartheta'$ -dependence of the previous maxima. Note that when a light beam propagates along the  $[\bar{2}11]$  direction it makes an angle of  $\vartheta = 19.5^\circ$  with the normal to the  $(111)$  plane (see the insert in Fig. 3(c)).

#### 4. Discussion

We emphasize some features of the above Bragg diffraction whose interpretation fails if one presumes an ideal f.c.c. structure. First, we turn to the two-maxima patterns that appear in the  $[\bar{2}11]$  direction diffraction (Figs. 2 and 3). These can not be ascribed to a single f.c.c. lattice because the  $[\bar{2}11]$  direction does satisfy no symmetry conditions necessary for appearance of the two spots. Therefore we assume the opal sample to have a twinned structure, i.e. it consists of f.c.c. domains with the stacking sequences ABCABC... and ACBACB... that alternate along the growth axis. This assumption allowed us to attribute main features of the patterns to the diffraction from the  $(111)$  planes in each of the two above-mentioned twinning sequences.

Second, to interpret the angle dependence of intensity (Fig. 3(c)) we assumed Bragg diffraction from single hexagonal layers  $(111)$  to be essentially influenced by interlayer disorder. The latter was taken into account in numerical averaging the structure factor (2) within a random stacking model [5]. It is based on a probability  $\alpha$  that any three successive layers in a stack make up a fragment of f.c.c. structure. Within this model, the best fit values  $\vartheta = 22^\circ$ ,  $\lambda = 580$  nm and  $\alpha = 0.85$  were obtained, the former two being close to the figures characteristic of f.c.c. lattice. Comparing these results with the Bragg conditions ( $\vartheta_B = 19.5^\circ$ ,  $\lambda_B = 560$  nm) for  $(111)$  layers we conclude that the observed patterns are associated with Bragg diffraction from slightly disordered twinned f.c.c. structure.



**Fig. 3.** (a), (b) Experimental spectra of the Bragg diffraction in the  $[\bar{2}11]$  direction of incidence at different angles  $\vartheta'_I$  and  $\vartheta'_{II}$  (see the insert, where the indices I and II correspond two neighbour domains making a twin). (c) Experimental intensity in the maxima as a function of the angles  $\vartheta'_I$  and  $\vartheta'_{II}$  for white light (circles and dashed line for the eye)  $\mathbf{n}_I$ . The incidence angle relative to the normals  $\mathbf{n}_I$  and  $\mathbf{n}_{II}$  of the  $(1\bar{1}1)$  planes I and II is  $\vartheta = 19.5^\circ$ . Averaged structure factor calculated from Eq. (2) as a function of the angles  $\vartheta'_I$  and  $\vartheta'_{II}$  within a random stacking model (solid line).

## 5. Summary

To conclude, we have investigated three-dimensional Bragg diffraction of visible light from a photonic crystal structure of artificial opals. The light spot patterns can be considered as a direct visualization of diffraction events having analogues in X-ray diffraction from the same crystal lattice. We established that structure of the opal samples under study possess a twinned f.c.c. crystal lattice coexisting with random sequences of close-packed layers. The diffraction patterns observed in different scattering geometries were proved to be associated with Bragg diffraction from  $\{111\}$  planes.

## Acknowledgements

This work was supported, in parts, by the RFBR Grants 02-02-17689 and 02-02-17601.

## References

- [1] V. N. Astratov, V. N. Bogomolov, A. A. Kaplyanskii *et al*, *Nuovo Cimento* **D 17**, 1349 (1995).
- [2] A. V. Baryshev, A. V. Ankudinov, A. A. Kaplyanskii *et al*, *Phys. Solid State* **44**, (2002).
- [3] J. M. Ziman, *Models of Disorder* Cambridge, 1979.
- [4] R. M. Amos and J. G. Parity, *Phys. Rev.* **B 61**, 2929 (2000).
- [5] W. Loose and B. J. Ackerson, *J. Chem. Phys.* **101**, 7211 (1994).

## Coherent inter-polariton scattering on moving gratings in microcavity with 25 nm GaAs/AlGaAs single quantum well

D. Birkedal<sup>†</sup>, V. G. Lyssenko<sup>‡</sup> and J. M. Hvam<sup>†</sup>

<sup>†</sup> Research Center COM, Technical University of Denmark,  
DK-2800 Lyngby, Denmark

<sup>‡</sup> Institute of Microelectronics Technology, RAS,  
142432 Chernogolovka, Moscow District, Russia

**Abstract.** We report on a new coherent phenomenon in semiconductor microcavities at polariton selective resonance excitation by two femtosecond pulses, propagating along  $k_2$  and  $k_1$ , associated with exciton gratings, travelling in lateral direction  $\pm(k_2 - k_1)$ . Diffracted polaritons experience a frequency shift as observed in nondegenerate spectrally resolved transient four-wave mixing experiments.

### Introduction

Semiconductor microcavities offers opportunities to reach physical conditions not easily attained otherwise. This has led to a range of interesting effects, where in particular coherent scattering of polaritons have attracted considerably interest [1]. Coherent phenomena in semiconductor have most significantly been studied using transient four-wave mixing, where in the case of e.g. quantum wells a detailed understanding of the involved physics have resulted [2]. In contrast, relatively few reports have been published on transient four-wave mixing studies of semiconductor microcavities [3–6]. These studies have shown that the coherent nonlinear dynamics of semiconductor microcavities polaritons is modified from that of e.g. heavy-hole–light-hole excitons quantum beats in semiconductor quantum wells.

### 1. Travelling gratings

Here we report on a coherent nonlinear phenomenon in a semiconductor microcavities, which has no parallel for quantum well excitons. When two different polariton modes of the semiconductor microcavities are impulsively excited they will undergo normal mode oscillations with coherent energy exchange between the exciton and the cavity mode. In our experiment the two polaritons are excited with slightly different angles resulting in a travelling wave exciton grating. When a test polariton mode is excited it will scatter in the travelling grating producing amplitude modulation sidebands. This phenomenon produces a transient four-wave mixing signal, which is shifted in frequency from that of the test beam by the normal mode oscillation frequency. In our case, in the THz range corresponding to a grating velocity of  $\approx 1 \times 10^7$  m/s, which is four order of magnitude larger than the sound velocity. The presence of such travelling exciton grating have been predicted [5] but so far not observed directly experimentally.

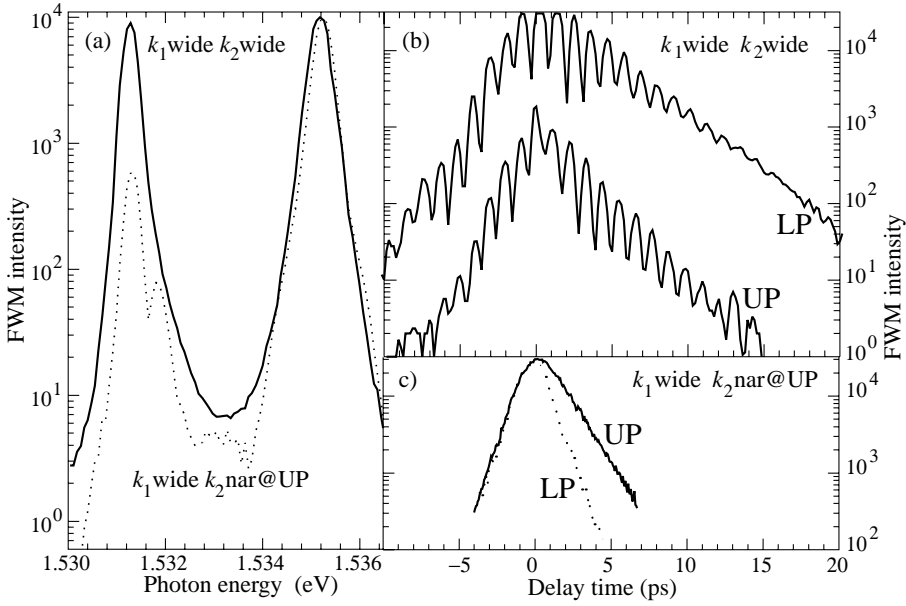


**Fig. 1.** (a) Spectrally resolved transient four-wave mixing at zero delay. Solid line for probing only the upper polariton (UP) and dashed line for probing simultaneously the upper and lower polariton (LP). (b) Transient four-wave mixing as a function of delay. Upper figure shows the signals at the upper and lower polaritons when both polaritons are probed simultaneously. Lower figure for probing selectively the upper polariton.

## 2. Results and discussion

The sample under investigation is a GaAs/AlGaAs  $\lambda$  cavity with a single 25 nm GaAs quantum well at the center [7]. The sample is held at 5 K in He cryostat and is excited by two pulses from a self-modelocked Ti:Sapphire laser, propagating in the directions  $k_1$  and  $k_2$ . The pulses are spectrally shaped to allow selective excitation of either of the polariton modes. The transient four-wave mixing signal is detected in the  $2k_2 - k_1'$  reflection geometry spectrally resolved and recorded as a function of the time delay between the two pulses. The present experiments are performed for near resonant conditions.

First we excite and probe both polaritons with spectrally broad pulses  $k_1$  and  $k_2$ . This results in transient four-wave mixing signal on the upper and lower polariton as shown in the spectrum in Fig. 1(a). In addition, strong beats in the transient four-wave mixing intensity is seen as a function of delay between the two pulses as shown in Fig. 1(b). This corresponds to our expectation from quantum well excitons and is in agreement with previous reports. In contrast, if we now probe selectively only one polariton, we observe a transient four-wave mixing signal resonant with the other polariton. This is shown here for selective probing of the upper polariton (Fig. 1(a): transient four-wave mixing spectrum; Fig. 1(b): delay dependence), where a strong signal resonant with the lower polariton is observed (Fig. 1(b)). We will demonstrate that these observations are in agreement with a theory based on the combined Maxwell and optical Bloch equations [5, 6, 8].

Thus, we discovered four-wave mixing signal at shifted frequency due to scattering on the polariton moving grating and developed theory, describing observed phenomena.

### Acknowledgements

This work was financially supported by the Danish Ministry of Science and Technology, Russian Foundation for Basic Research and Program “Physics and Technology of the Nanostructures”.

### References

- [1] P. G. Savvidas *et al*, *Phys. Rev. Lett.* **84**, 1547 (2000).
- [2] See e.g. J. Shah, *Ultrafast Spectroscopy of Semiconductors and Semiconductor Nanostructures*, (Springer, Berlin, 1997).
- [3] H. Wang *et al*, *Phys. Rev. B* **51**, 14713 (1995).
- [4] M. Kuwata-Gonokami *et al*, *Phys. Rev. Lett.* **79**, 1341 (1997).
- [5] H. Wang *et al*, *Phys. Rev. Lett.* **81**, 3255 (1998).
- [6] M. Koch, J. Shah and T. Meier, *Phys. Rev. B* **57**, 2049 (1998).
- [7] For details on the sample see e.g. J. R. Jensen, P. Borri, W. Langbein and J. M. Hvam, *Appl. Phys. Lett.* **76**, 3262 (2000).
- [8] H. J. Kimble, H. J. Carmichael *et al*, in *Cavity Quantum Electrodynamics*, **51**, ed. by P. R. Berman (Academic, Boston, 1994).

## Local polariton modes in planar optical micro-cavities

L. I. Deych and A. A. Lisyansky

Department of Physics, Queens College of CUNY, Flushing, NY 11367, USA

**Abstract.** An array of quantum dots in a microcavity is considered. It is shown that a vacancy in the array may give rise to one or two quasi-local states with a long life-time depending upon the structure of the array. One state always splits off the top of the polariton gap, and the other one may appear closer to the bottom of the gap. The life-time of the state is mostly determined by the exciton non-radiative relaxation and depends only weakly upon the properties of the cavity mirrors.

### Introduction

Optical microcavities containing a semiconductor quantum well or an organic film as an active material attract a great deal of attention [1, 2]. Confinement of the electromagnetic field inside the cavity leads to a strong enhancement of exciton-photon interaction. The result of this interaction is a new type of excitations — cavity polaritons, which are coherently mixed states of an exciton in an active material and a cavity photon. A significant feature of the spectrum of the cavity polaritons is a large splitting between lower and upper polariton branches (so called Rabi splitting) in the vicinity of the resonance frequency. This situation has been observed in a number of different microcavities, both with semiconductor [1] and organic [2] active elements. Novel types of microcavities with arrays of quantum dots are also being studied [3].

The spectral region between lower and upper polariton branches presents a photonic stop band, in which propagation of electromagnetic waves with wave vectors within a certain cone of directions is inhibited. This stop band also manifests itself in the significant decrease of the light emission in the respective directions. This fact invites an attempt to tailor emission properties of the cavity in this region using ideas developed in the physics of photonic crystals [4]. A point-like defect introduced in an active element of the cavity could give rise to a new state with a frequency inside the stop band and affect emission properties of the cavity. If the propagation of photons were forbidden for all directions of the wave vectors, the state would be a stationary local polariton state, in which both exciton and photon components are localized in the vicinity of the defect. The idea of local polaritons was first introduced in Refs. [5, 6] in the context of the substitution impurities in regular polar crystals. In this paper we extend this idea to microcavities with an array of quantum dots as an active element. When one of the dots in the array is absent or intentionally omitted, a point-like defect, or “vacancy”, arises. It was speculated [7] that this vacancy can be used as a source of emission in the spectral range of the polariton gap. In this paper we show that such a vacancy can give rise to a long-living quasi-stationary local polariton state.

### 1. Model and approach

In this paper, we use a continuous medium approach to describe of an active layer of a cavity. We also assume that the active layer of the cavity is thin, such that the excitons can

be considered two-dimensional. We can then present the polarization density  $\mathbf{P}(\rho)$  of the two-dimensional layer in the following form

$$P_i(\rho) = d\delta(z)\chi_{ij}(\omega)E_j(\omega, \rho, z), \quad (1)$$

where  $\rho$  is a position-vector in the plane of the active layer,  $z$  is the coordinate in the normal direction, the  $\delta$ -function takes care of the two-dimensional nature of the polarization,  $d$  is an effective thickness of the layer introduced in order to retain a correct dimension for the polarization density, and  $E_j(\omega, \rho, z)$  is the electric field of a monochromatic electromagnetic wave with frequency  $\omega$ . Neglecting direct interactions between quantum dots, we can assume that the effective two-dimensional exciton susceptibility  $\chi_{ij}(\omega)$  is local, and define it as

$$\chi_{ij}(\omega, \rho) = \frac{\Gamma^2}{\omega_0^2 - \omega^2}, \quad (2)$$

where  $\Gamma$  is the coupling exciton-photon constant, and  $\omega_0$  is the exciton resonance frequency.

The presence of the vacancy means that at a certain point within the layer the polarization vanishes. In order to account for the presence of such a defect, we introduce an additional term,  $\mathbf{P}^{\text{def}}$ , in our expression for the polarization, Eq. (1),

$$P_i^{\text{def}} = -da^2\chi_{ij}(\omega, \rho)\delta(z)\delta(\rho)E_j(\omega, \rho, z) \quad (3)$$

where the additional  $\delta$ -function reflects a point-like nature of the defect, and the factor  $a^2$  introduces its effective size,  $a$ . A solution for the Maxwell equations with the polarization term given by Eqs. (1) and (3) can be obtained with the use of the electromagnetic Green function,  $G_{i,j}(z, z'; \rho - \rho')$ , which must satisfy Maxwell equations and all the boundary conditions at the mirrors of the cavity, and at the active layer. Since the Green function retains its translational invariance in the plane of the cavity, we can use an in-plane wave vector  $\mathbf{k}$  in order to characterize the modes of our system. We choose the coordinate system such that the  $Y$ -axis lies along  $\mathbf{k}$ , the  $X$ -axis lies in the plane of the cavity perpendicular to  $\mathbf{k}$ , and the  $Z$ -axis is along the growth direction of the system. Accordingly, the values  $x$ ,  $y$  and  $z$  of polarization indexes  $i$ ,  $j$  correspond to  $T$ ,  $L$  and  $Z$  polarizations of the electromagnetic waves, respectively. Boundary conditions at the mirrors are taken care of by introducing complex reflection coefficients  $r_i$  of the mirrors, which can in principle depend upon the polarization, the in-plane wave number, and the frequency.

## 2. Results

The electric field at the defect site,  $\rho = 0$ , can have non-zero values only if the frequency  $\omega$  satisfies the dispersion equation for the local mode:

$$\det \left| \delta_{ik} - \frac{4\pi\omega^2}{c^2} da^2 G_{i,j}(0, 0) \chi_{jk}(\omega, \rho) \right| = 0. \quad (4)$$

If Eq. (4) has real valued solutions, they describe truly localized stationary modes. Solutions with a non-zero but small imaginary part correspond to quasi-stationary modes or resonances. The value of the Green's function at the location of the defect,  $G_{i,j}(0, 0)$ , turns out to be diagonal, which means that Eq. (4) decouples into three independent equations for each of the polarizations. Two of the Green's function's components are equal to each other,  $G_{xx} = G_{yy}$ , therefore, the dispersion equations for  $T$  and  $L$  polarizations are degenerate. The dispersion equation for the  $Z$  polarization does not have any solutions. Hence, the

electric field associated with the defect states may have an arbitrary direction in the plane of the active layer, while its  $z$ -component is equal to zero.

In the case of ideal mirrors, for which reflectivity for all polarizations is assumed to be equal to 1, the in-plane component of Eq. (4) can be presented as

$$1 + \frac{\omega^2 \Gamma^2 d a^2}{2c^2} [\Phi_T(\omega) + \Phi_L(\omega)] = 0, \quad (5)$$

where

$$\Phi_T(\omega) = \int_0^\infty dk \frac{k}{k_z} \frac{\sin \frac{k_z L}{2}}{(\omega_0^2 - \omega^2) \cos \frac{k_z L}{2} - \frac{\Gamma_T^2}{2} \sin \frac{k_z L}{2}} \quad (6)$$

and

$$\Phi_L(\omega) = \int_0^\infty dk \frac{k k_z}{k_0^2} \frac{\sin \frac{k_z L}{2}}{(\omega_0^2 - \omega^2) \cos \frac{k_z L}{2} - \frac{\Gamma_L^2}{2} \sin \frac{k_z L}{2}}. \quad (7)$$

The effective coupling constants  $\Gamma_T$  and  $\Gamma_L$  for  $T$ - and  $L$ -polarizations, respectively, can be defined in terms of the experimentally observable Rabi splitting,  $\Omega_R$ :  $\Gamma_T = \Omega_R \sqrt{\pi k_0 / 2 k_z}$  and  $\Gamma_L = \Omega_R \sqrt{\pi k_z / 2 k_0}$ . We also introduced parameters  $k_0 = \omega \sqrt{\epsilon_\infty} / c$ , and  $k_z = \sqrt{k_0^2 - k^2}$ .

The poles of the expressions in Eqs. (6) and (7) determine the dispersion equations of cavity polaritons of  $T$  and  $L$  polarizations respectively. For small  $k$ , these equations reduce to the familiar form of two coupled oscillators, which for the cavity tuned to resonance with the excitons describes Rabi splitting between two polariton branches at  $k = 0$ . For  $k > k_0$ ,  $k_z$  becomes imaginary and the pole of  $\Phi_T(\omega)$  describes a non-radiative mode with a dispersion curve asymptotically approaching  $\omega_0$  from below. Thus, for  $T$ -polarized modes, there is a gap between the exciton frequency,  $\omega_0$ , and the bottom of the upper polariton branch,  $\omega_0 + \Omega_R/2$ , which means that if  $\omega \in (\omega_0, \omega_0 + \Omega_R/2)$ , function  $\Phi_T$  remains real. Longitudinal modes described by poles of  $\Phi_L$ , for  $k > k_0$  fill out the gap region and the impurity mode, therefore, would decay into  $L$ -polarized non-radiative excitations. Estimates show, however, that the rate of this decay is very small compared to other decay mechanisms and can be neglected.

The existence of the solution for Eq. (5) depends upon the properties of the respective integrals in Eqs. (6) and (7). These integrals demonstrate an ultra-violet divergence caused by the  $\delta$ -functional descriptions of the active layer and the defect, as well as by the continuous medium approximation. The simplest way to regularize this divergence is to introduce a cut-off wave number  $k^*$ , which can be estimated as the inverse of the inter-dot distance. The integral also diverges at the  $\omega = \omega_0 + \Omega_R/2$ . As a result of this divergency, in the absence of exciton damping, Eq. (5) always has at least one solution, which splits off the top of the polariton gap if  $(ak^*)^2 / (4\pi) < 1$ . When  $(ak^*)^2 / (4\pi) > 1$  none or two solutions become possible. The exciton relaxation and non-ideal nature of the mirrors modifies these estimates. In order to evaluate these effects, we added the term  $2i\gamma_{ex}\omega$  to the denominator of the exciton susceptibility Eq. (2), and introduced non-zero transmission of the mirrors  $|t|^2 = 1 - |r|^2$ . Solving Eq. (5) numerically, we found that in the presence of the exciton relaxation the defect parameter  $ak_*$  must exceed certain critical value for the state to arise. More important, however, is that the life-time of the state remains long even in the presence of both exciton and cavity mode decay, Fig. 1. Studying the dependence of the decay rate upon the mirrors' reflectivity, we found that the characteristics of the mirrors do not significantly affect the properties of the impure state.



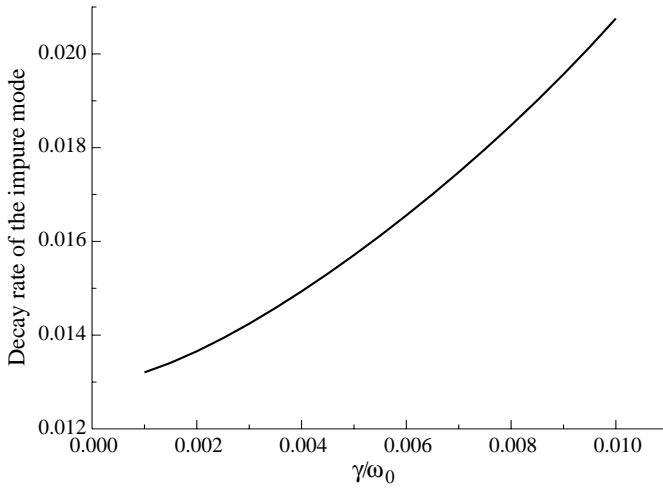


**Fig. 1.** Decay rate of the impure mode versus exciton relaxation. The decay rate is given in the units of the exciton frequency  $\omega_0$

## References

- [1] T. B. Norris, in: *Confined Electrons and Photons*, ed. E. Burstein and W. Weisbuch, New York: Plenum Press, 1995.
- [2] D. G. Lidzey, D. D. C. Bradley, T. Virgili, A. Armitage, M. S. Skolnick and S. Walker, *Phys. Rev. Lett.* **82**, 3316 (1999).
- [3] A. D. Yoffe, *Adv. Phys.* **50**, 1 (2001).
- [4] J. D. Joannopoulos, R. D. Meade and J. N. Winn, *Photonic Crystals: Molding the Flow of Light*, Princeton University Press, 1995.
- [5] L. I. Deych and A. A. Lisyansky, *Phys. Lett. A* **240**, 329 (1998).
- [6] V. Podolsky, L. I. Deych and A. A. Lisyansky, *Phys. Rev. B* **57**, 5168 (1998).
- [7] S. R. Forrest, private communication.

## Whispering gallery modes in glass microspheres made by simple technology

D. V. Gaikov<sup>†</sup>, E. V. Kolobkova<sup>†</sup>, A. A. Lipovskii<sup>†</sup>, V. G. Melehin<sup>‡</sup>  
and V. G. Petrikov<sup>†</sup>

<sup>†</sup> St Petersburg State Technical University,  
Politechnicheskaja 29, 195251 St Petersburg, Russia

<sup>‡</sup> Ioffe Physico-Technical Institute, St Petersburg, Russia

**Abstract.** A simple technique to form glass microresonators is proposed and used to make microresonators of samarium-doped phosphate glass. Measured in the vicinity of  ${}^4G_{5/2} - {}^6H_{7/2}$  transition of  $\text{Sm}^{3+}$  ion photoluminescence spectra of the microresonators gave the value of  $Q$ -factor  $\sim 6000$ . This exceeds the  $Q$ -factor of glass microsphere made with conventional flyway technique.

### Introduction

Most basic and applied interest to optical microresonators of different shapes, in particular, spherical ones, is due to whispering gallery modes existing in these structures [1, 2]. Whispering gallery modes were firstly studied by Rayleigh [3] in 1914 for acoustical range [3] and, for optical range by Garrett, Kaiser and Bond in 1961 [4]. These modes demonstrate low attenuation, and they are localized in subsurface region of a microresonator. That is why the density of electromagnetic field of whispering gallery modes is high even if the field contains only several quanta. This is essential for the usage of microresonators in the studies of the interaction of quantified electromagnetic fields with atoms, molecules or nanocrystals placed inside a resonating microsphere or on its surface. The applications of spherical glass resonators are related to low-threshold lasers [5], up-conversion lasers [6], bistable optical elements [7], filters and delay lines [8]. Most prospective for practice are resonators made of glass doped with rare-earth ions, but recently the interest to other dopants of high radiation efficiency, like CdSSe, has also arisen [9]. The techniques of making glass microspheres are flyway technique [10], blowing the microspheres with gas-burner [9], and laser heating of glass fibers with the formation of glass drop at the fiber end [11]. In flyway technique, which is being commonly used, prepared glass has to be milled, bolt using calibrated grids, and dropped in vertical furnace. While in free drop, the glass particles become spherical due to surface tension, and short duration of the processing prevents crystallization of the glass. Thus microspheres of optical quality can be formed.

### 1. Experimental

This study was aimed to the formation of microresonators, namely, microspheres of glass doped with samarium, using a simple alternative technique able to provide high optical quality of the glass both at the surface and in volume of the microresonators. The glass was synthesized using the next components:  $\text{Ba}(\text{PO}_3)_2$  (70%) –  $\text{SrF}_2$  (10%) –  $\text{MgF}_2$  (10%) –  $\text{BaF}_2$  (10%) (in mol. %), and 4–9 wt. % of  $\text{Sm}(\text{NO}_3)_3 \cdot 6\text{H}_2\text{O}$  were added in the glass batch. Glass of good optical quality has been synthesized in conventional glass-furnace. After

annealing close to glass transition temperature for removing thermal stresses the glass was milled and bolt. Then the glass particles were put on the plate of glassy carbon and, for a short term, inserted into glass-furnace, where the particles were melted. Due to the surface tension the particles before 150 microns took the shape, which was close to ideal sphere. Microscopic photograph of manufactured microspheres is presented in Fig. 1.

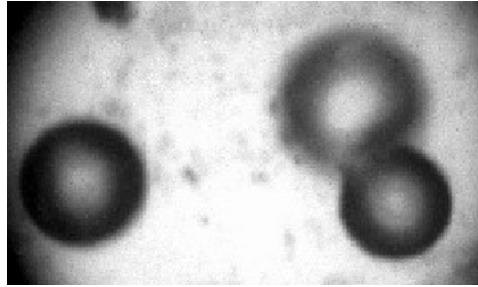


**Fig. 1.** Microscopic photo of the glass microspheres of several diameters.

The quality of the microspheres was evaluated through their photo luminescent (PL) properties. The luminescence was excited with Ar laser (488 nm, 200 mW), and PL spectra were measured with Ramanor U-1000 spectrometer (spectral resolution  $1.8 \text{ cm}^{-1}$ ). The measurements were performed at room temperature.

## 2. Results and discussion

Measured PL spectra of bulk glass and of one of formed microspheres are presented in Fig. 2. The spectra were measured in the vicinity of  $^4G_{5/2} - ^6H_{7/2}$  transition of  $\text{Sm}^{3+}$ . It is seen that broad PL bands typical for glasses doped with trivalent samarium ions transforms to periodical fine structure for the microresonator. Spectra of such kind are typical for microspheres of high bulk and surface quality, and the periodical structure is due to whispering gallery modes of the microsphere, that are the electromagnetic modes of high angular momentum. The period of the fine structure is  $\Delta\nu = 18 \text{ cm}^{-1}$ , and this value coincides with the distance between resonance mode of the sphere calculated using classical Mie theory [1]:

$$\Delta\nu = \frac{\arctan(z-1)^{0.5}}{\pi d n_2 (z-1)^{0.5}}; \quad z = \left(\frac{n_1}{n_2}\right)^2, \quad (1)$$

where  $d = 130 \text{ nm}$  is the diameter of the microsphere,  $n_1 = 1.552$  and  $n_2 = 1$  — indices of the glass (measured) and surrounding medium (air in our case), respectively.

The criterion of the microsphere quality is the  $Q$ -factor of the microresonator  $Q = \nu_l / \Delta\nu_l$ , where  $\nu_l$  and  $\Delta\nu_l$  — the frequency of resonance mode having angular momentum equal to 1, and the spectral width of this mode, respectively [1]. For most intensive modes in the range of  $16700 \text{ cm}^{-1}$  the evaluated  $Q$ -factor is  $\sim 6000$  (actually this value is higher since spectral width of the spectrometer slit has to be accounted in the evaluation of the spectral width of the mode). Measured  $Q$ -factor is of the same order of magnitude as that one of microspheres made with flyway technique ( $Q \approx 4000$  [7]). Finally, the developed simple technique allows the formation of glass microspheres doped with rare-earth ions. The quality of formed microresonators is comparable with the quality of microresonators formed with conventional, more complicated, techniques.

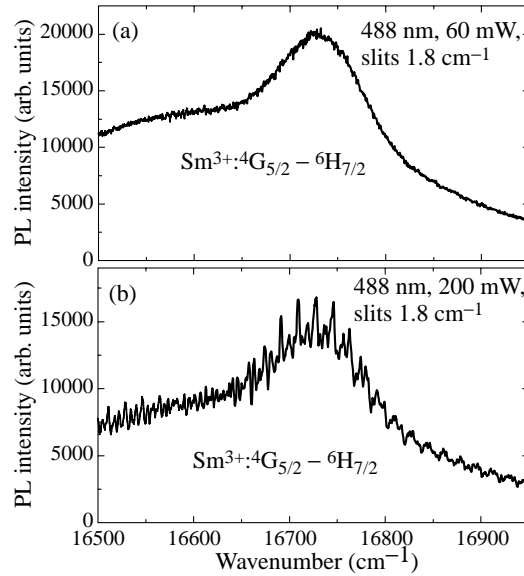


**Fig. 2.** Photoluminescence spectra of bulk Sm-doped glass (a) and microresonators formed of this glass (b). The spectra were measured in the vicinity of  $^4G_{5/2} - ^6H_{7/2}$  transition of Sm<sup>3+</sup>.

### Acknowledgement

This work was financially supported by Physics of Solid Nanostructures Program.

### References

- [1] P. V. Barber and R. K. Chang, eds., *Optical effects Associated with Small Particles*, Word Scientific, Singapore, 1998.
- [2] R. K. Chang and A. J. Chamillo, eds., *Optical processes in microcavities*, Word Scientific, Singapore, 1996.
- [3] J. W. Rayleigh, *Phil. Mag.* **27**, 100 (1914).
- [4] C. G. B. Garrett, W. Kaiser and W. L. Bond, *Phys.Rev.* **124**, 1807 (1961).
- [5] V. Sandoghdar, F. Treussart, J. Hare, V. Lefevre-Seguin, J.-M. Raimond and S. Haroche, *Phys. Rev. A* **54**, R1777 (1996).
- [6] W. Von Klitzing, E. Jahier, R. Long, F. Lissillour, V. Lefevre-Seguin, J. Hare, J.-M. Raimond and S. Haroche, *Electron.Lett.* **35**, 1745 (1999).
- [7] T. Hayakawa, H. Ooishi and M. Nogami, *Opt. Lett.* **26**, 84 (2001).
- [8] X. Fan, P. Palinginis, S. Lacey, H. Wang and M. C. Lonergan, *Opt. Lett.* **25**, 1600 (2000).
- [9] R. Jia, D.-S. Jiang, R.-H. Tan and B.-Q. Sun, *Appl. Phys. Lett.* **79**, 153(2001).
- [10] M. Nogami, J. Hayakawa and Y. Moriya, *J. Mater.Sci.* **17**, 2845 (1982).
- [11] D. S. Weiss, V. Sandoghdar, J. Hare, V. Lefevre-Seguin, J.-M. Raimond and S. Haroche, *Opt. Lett.* **20**, 1835 (1995).

## Three-dimensional GaN photonic crystals for visible spectral range

G. Gajiev<sup>†</sup>, V. G. Golubev, D. A. Kurdyukov, A. B. Pevtsov  
and V. V. Travnikov

Ioffe Physico-Technical Institute, St Petersburg, Russia

<sup>†</sup> On leave from Daghestan Institute of Physics, Makhachkala 367003, Russia

**Abstract.** Three-dimensional (3D) photonic crystals entirely consisting of GaN have been fabricated for the first time. Detailed investigations of optical Bragg diffraction spectra have shown a high quality of the prepared photonic crystals.

### Introduction

The wide bandgap GaN based semiconductor structures are highly attractive because of their great potential for development of stable optoelectronic devices in the visible-ultraviolet region [1]. Up to now main efforts of researchers have been directed on the use of properties of electron subsystem of the GaN based materials. The main goal of the presented work is to create a material where optical and electronic properties of the nitride semiconductors are combined with unique features of photonic crystals (PC) based on artificial opals. The novel properties of such materials open new possibilities to mould and control emission and propagation of light in optoelectronic devices [2]. The present work is aimed at synthesizing GaN PC, investigating their optical properties and effect of a photonic band gap (PBG) on the Bragg diffraction of light.

### 1. Results and discussion

To create GaN based 3D PC we used a template-directed method. As a temporary periodically structured 3D templates, highly ordered synthetic opals were used. The opals have the fcc structure formed by closed-packed  $\alpha$ -SiO<sub>2</sub> spheres with an ordered sublattice of interconnected voids. The fabricated samples were composed of  $\alpha$ -SiO<sub>2</sub> spheres of 245 nm in diameter. The opal voids were impregnated with Ga<sub>2</sub>O<sub>3</sub> precursor and the samples were annealed in an atmosphere of nitrogen hydrides. XRD, TEM, SEM, and Raman measurements confirmed the structural perfection of GaN in the opal-GaN composites [3]. Then, the silica template was selectively removed by etching off the  $\alpha$ -SiO<sub>2</sub> skeleton with HF. As a result we have prepared so-called inverse opal-GaN which is in fact 3D PC entirely consisting of GaN (Fig. 1).

Main attention at characterization of the fabricated samples were given to measuring of reflection spectra. Below we will present results obtained for s-polarization of diffracted light. The angle of observation was defined as the angle with respect to the [111] surface normal. The image of the sample was focused on the entrance slit of single spectrometer with 8-fold magnification.

Investigation of reflection spectra is one of the most simple and direct method to probe the band gap structure of PC [4]. Due to the periodic modulation of the dielectric constant photonic crystals have photonic band structures analogous to electronic band structures in solids and in particular forbidden energy gaps (stop bands) appear in the energy spectrum. Light waves with energies within these stop bands are Bragg reflected and cannot propagate

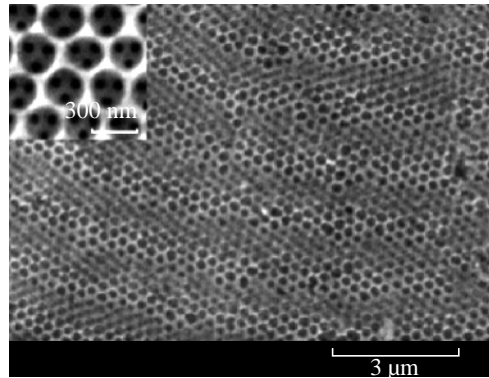


**Fig. 1.** SEM image of 3D GaN photonic crystal.

inside the crystal. As a result in reflection spectra maxima are appeared in the energy regions of such stop bands. Figure 2 shows reflection spectra of the initial opal-GaN nanocomposite for several angles of incidence. At small angles strong peaks are presented in the spectra due to constructive interference of waves reflected by (111) crystal planes [3]. With increasing of the incidence angle the peaks shift to higher energies following the well known Bragg law [3]. For angles starting near  $30^\circ$  an additional high energy peak appears in the reflection spectra (Fig. 2(a)). Figure 3 shows the center energies of all peaks as a function of incidence angle. It can be clearly seen from Fig. 3 that the center energies of low and high-energy peaks in the energy region near  $50^\circ$  are characterized by the pronounced avoided crossing behaviour. Such substantial deviation from the simple Bragg law is connected with the simultaneous Bragg diffraction by (111) and (200) PC planes [4]. Similar fine structure of optical diffraction was an important criterion for the quality of a 3D PC crystal [5]. In our case the avoided crossing behaviour is much more pronounced as compared with published data [4, 5]. It indicates to a good quality of our fabricated opal-GaN composite [5].

The important characteristic of a PC is the energy width of stop bands. The width of the stop bands ( $\Delta E$ ) in rather high accuracy can be identified with the full width of the reflection peaks at half height [4]. From the Bragg diffraction peak at normal incidence ( $0^\circ$ ) we have determined the relative stop band width in our opal-GaN composite as  $\Delta E/E_0 \approx 5.3\%$  ( $E_0$  is the energy of the peak maximum). It is not high value and the composites can be considered as a typical representative of weakly photonic crystals with stop bands in certain directions. Such crystals are characterized by the non-overlapping stop bands for different directions of light propagation. It is clearly seen from Fig. 2(a). For a example, there is no overlapping of diffraction peaks at  $0^\circ$  and  $50^\circ$  incident angles: points *h* and *l* which correspond to half height intensities of high- and low-energy side of corresponding peaks are separated by  $\sim 160$  meV energy range.

The strength of the interaction between light and a crystal is determined by the dielectric contrast - the ratio of the dielectric constants of PC constituents (GaN/SiO<sub>2</sub>, GaN/air here). Complete PBG are expected in strongly PC — crystals with the high dielectric contrast. In this case Bragg reflection bands from many differently oriented crystal planes can overlap. In our work we have chosen one of the promising way to obtain a strongly PC — fabrication of inverse opals [6].

The reflection spectra of the fabricated GaN PC (GaN inverse opal) for different incidence angles are presented in Fig. 2(b). The relative stop band width ( $\Delta E/E_0 \approx 10.5\%$ )

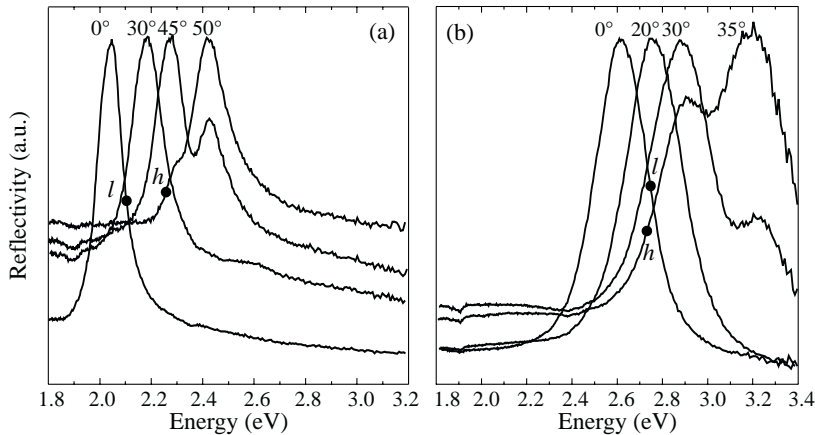


**Fig. 2.** The reflection spectra of the initial opal-GaN composite (a) and GaN photonic crystal (b) for various angles of incidence.

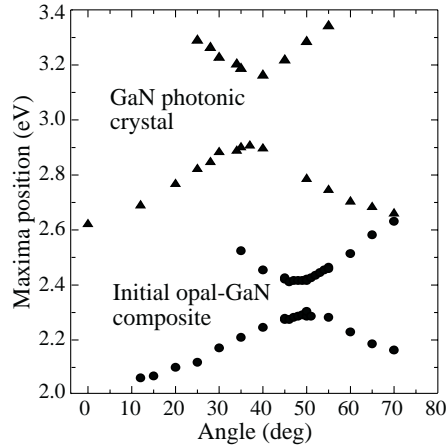


**Fig. 3.** Bragg reflection peak energies as a function of the angle of incidence.

is more than twice larger than one for initial opal-GaN composite. Figure 2 shows that the avoided crossing behaviour in this case is much more pronounced. The energy separation between the peaks in the avoided crossing region is about  $\sim 260$  meV (in the initial composite  $\sim 120$  meV) (see Fig. 3). This energy separation is a characteristic of coupled wave phenomena and its large value indicates to strong coupling of Bragg reflection events from the (111) and (200) crystal planes. The coupled diffraction considerably flattens the PBG on the surface of the Brillouin zone and keeps the stop bands on the same energy [4]. Figure 2(b) shows that low energy peaks are essentially overlapped at all incidence angles. Points *h* and *l* for extreme energy positions of low energy peaks are practically on the same energy. It indicates that photons with energies at the top of the stop band at  $0^\circ$  remain inside other stop bands corresponding to angles of more than  $\sim 40^\circ$ . It means, in turn, that for wide range of wave vectors light with such energies cannot enter the PC or no light can be emitted from inside. In according with [4] we have estimated that in our case about the

half of full ( $4\pi$ ) solid angle is forbidden for propagation of light in the energy region of the (111) Bragg reflection peak. It can lead to grossly altered both the density of states and the spontaneous emission rate.

## 2. Conclusions

3D opal-GaN and inverse opaline GaN PC have been fabricated. The doublet structure due to simultaneous Bragg reflection by the (111) and the (200) PC planes have been found. Pronounced avoided crossing behaviour of the doublet components which appear due to the multiple Bragg wave coupling effect [5] indicates on a high quality of the fabricated PC. The strong overlapping of observed reflection peaks for the wide incident angle range in the GaN PC shows that about the half of full solid angle is forbidden for propagation of light in the (111) Bragg reflection energy region. It should lead to changes in the optical density of states and as a result it opens the way to novel quantum optical effects.

### Acknowledgements

We thank A. V. Sel'kin for fruitful discussions. This work was supported by the NATO Program through Grant No PST.CLG.978079; the RAS Program "Low-dimensional quantum structures"; the Russian R&D Program "Nanostructures".

## References

- [1] S. Nakamura and G. Fasol, *The blue Laser Diode: GaN based Light Emitters and Lasers* Berlin, Springer 1997.
- [2] *Band Gap Materials*, ed. by C. M. Soukoulis. Advanced Studies Institute of NATO, Ser. E, vol. 315 (Kluwer, Dordrecht), 1996.
- [3] V. G. Golubev *et al*, *Semiconductors* **35**, 1320 (2001).
- [4] W. L. Vos *et al*, *Proc. NATO ASI Photonic Crystals and Light Localization*, ed. C. M. Soukoulis (Kluwer, Dordrecht), pp. 181–198, 2001.
- [5] S. G. Romanov *et al*, *Phys. Rev.* **E63**, 056603 (2001).
- [6] K. Bush and S. John, *Phys. Rev.* **E58**, 3896 (1998).



## Quasi-guided modes and optical response in 2D photonic crystal slabs

S. G. Tikhodeev, A. L. Yablonskii, E. A. Muljarov and N. A. Gippius

General Physics Institute, Russian Academy of Sciences, 119991 Moscow, Russia

**Abstract.** We calculate, via the scattering-matrix-based numerical method, the optical transmission properties and quasi-guided eigenmodes in a two-dimensionally (2D) square-lattice periodic photonic crystal slab (PCS) of finite thickness. We show that the appearance of dips in the transmission spectra of PCS is due to the interaction with resonant waveguide eigenmodes in the slab. The energy position and width of the dips in transmission provide the information on frequency and inverse radiative lifetime of the quasi-guided eigenmodes. We calculate the energies, linewidths and electromagnetic fields of such quasi-guided eigenmodes and analyze their symmetry and optical activity.

Recently, a considerable interest has been shown in the investigation of finite thickness slabs of two-dimensional (2D) photonic crystals. Such slabs demonstrate various interesting properties promising for future application in new active photonic devices. For example, if such photonic crystal slabs (PCS) support waveguide modes, their transmission spectra have well-pronounced narrow dips which exhibit a complicated behavior with the change of angle of light incidence and of the geometrical parameters of the system.

Recently we have developed a scattering matrix numerical method [1, 2, 3], based on a generalization of the method proposed by Whittaker and Culshaw [4], to model the properties of multilayered 1D and 2D patterned PCS, including case of frequency dispersive constituent materials. Our goal was to explain the experimentally measured [5],[2] transmission spectra in PCS containing an inorganic-organic semiconductor imbedded into a 1D or 2D periodically patterned quartz substrate. The narrow dips in transmission appear to be due to the excitation of quasi-guided (or leaky) modes, which play a crucial role in the optical properties of waveguiding PCS.

Here we illustrate the results of application of this method to a simplified dielectric PCS made of non-dispersive dielectric materials.

The structure of a simplified PCS and the geometry of light incidence is explained in the insert in Fig. 1, left panel. The substrate is quartz, the higher dielectric constant *active* material is assumed to be a semiconductor, but with non-dispersive dielectric constant. The symmetry of 2D periodicity of the model structure is taken square, with in-plane periods  $d_x = d_y = d \sim 680$  nm. The vertical thickness of the patterned layer is taken  $L_z \sim 120$  nm. The ratio of the in-plane size of the semiconductor squares to the thickness of quartz walls is taken  $\eta \sim 4$ . These parameters are close to the ones characteristic for the experiments [5, 2] with inorganic-organic semiconductor superlattices imbedded into a patterned quartz substrate, but neglecting the polariton dispersion of the active material.

An example of the calculated transmission spectra of the simplified PCS for different angles of incidence  $\vartheta$  is shown in Fig. 1, left panel. The theoretical analysis shows that the dips in the transmission spectra in this frequency region are due to the interaction of the incoming light with four TE-like and four TM-like quasi-guided modes in the corrugated waveguide. These quasi-guided modes originate from the 2-nd order Bragg resonance of the lowest TE and TM waveguide modes. The calculated wavevector dispersion (along  $\Gamma - X$  direction in the 1st Brillouin zone of the PCS) of the eigenenergy and linewidth (inverse lifetime) are shown in Fig. 1, right panel. The four lower modes are TE-like bands;

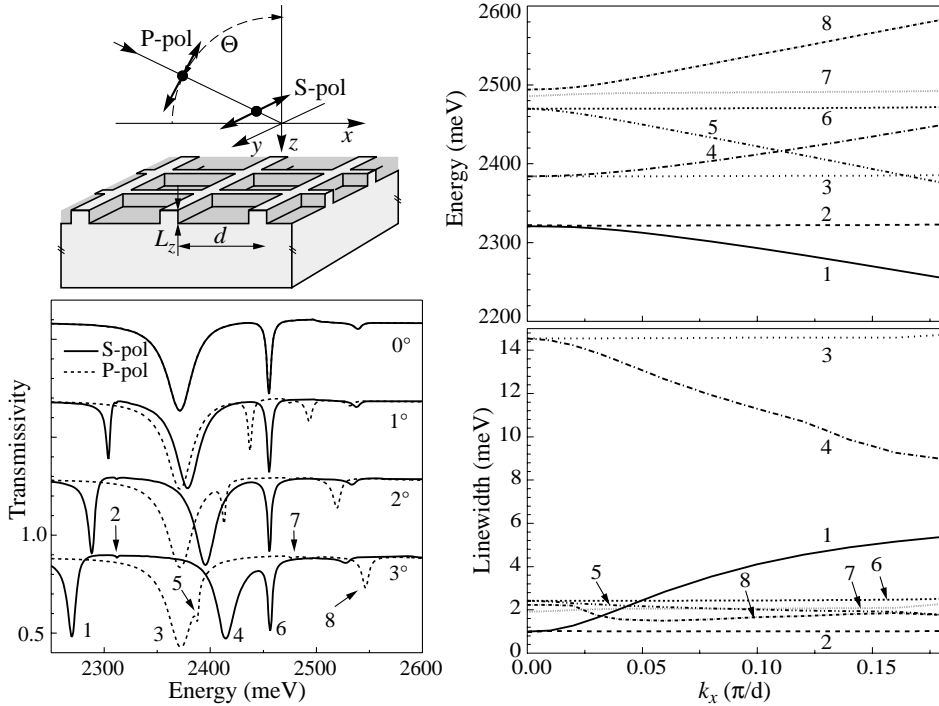


**Fig. 1.** The calculated transmission spectra of the simplified PCS (shown in insert) for S and P polarization and different angles of incidence (left panel). The calculated dispersion of the energies (right panel, top) and linewidths (left panel, bottom) of the four TE-type (1–4) and TM-type (5–8) quasi-guided eigenmodes in the same energy region.

in  $\Gamma$ -point there are two singlet modes (marked by numbers 1, 2 in Fig. 1) and one doublet mode (3, 4). The four higher modes are TM-like bands; in  $\Gamma$ -point there is one doublet mode (5, 6) and two singlet modes (7, 8). The different optical activity of different components of the TE-TM octet is caused by their different symmetry, and different electromagnetic field distributions.

The discussed here behavior of the TE-TM octet of quasi-guided eigenmodes explains, e.g., the evolution of measured spectra in a PCS filled with inorganic-organic layered perovskite semiconductor  $(\text{C}_6\text{H}_5\text{C}_2\text{H}_4\text{NH}_3)_2\text{PbI}_4$  [2].

#### Acknowledgements

This work was supported in part by Russian Foundation for Basic Research and Russian Ministry of Science program “Nanostructures”.

#### References

- [1] A. L. Yablonskii, E. A. Muljarov, N. A. Gippius, S. G. Tikhodeev, T. Fujita and T. Ishihara, *J. Phys. Soc. Japan* **70**, 1137 (2001).
- [2] R. Shimada, A. L. Yablonskii, S. G. Tikhodeev and T. Ishihara, *IEEE J. Quantum Electronics* (2002), to be published.
- [3] S. G. Tikhodeev, A. L. Yablonskii, E. A. Muljarov, N. A. Gippius and T. Ishihara, submitted to *Phys. Rev. B*.
- [4] D. M. Whittaker and I. S. Culshaw, *Phys. Rev. B* **60**, 2610 (1999).
- [5] T. Fujita, Y. Sato, T. Kuitani and T. Ishihara, *Phys. Rev. B* **57**, 12428 (1998).

## Optical and magnetic-resonance spectroscopy of single molecules

*J. Schmidt*

Huygens Laboratory, Department of Physics University of Leiden  
P.O.Box 9504, 2300 RA Leiden, The Netherlands

**Abstract.** In this contribution a short review is given of spectroscopic experiments on single molecules embedded in solid host materials at low temperatures. First it is shown how an individual pentacene molecule can be selected optically and how the magnetic-resonance transitions of its metastable triplet state can be observed. In addition it is shown that the magnetic-resonance transitions of a single nuclear spin, connected via hyperfine interactions to the single triplet spin can be observed. Single-molecule techniques can be applied with success to biologically relevant systems as is demonstrated by the first observation of the fluorescence-excitation spectra of individual light-harvesting complexes of photosynthetic bacteria. These results demonstrate unambiguously that the excited states of this complex must be described as Frenkel excitons, i.e., as excitations that are delocalised over the pigment molecules present in the complex.

### 1. Introduction

In the last decade techniques for the detection of single particles such as atoms, molecules, proteins, nanocrystals or single quantum dots have been developed and continuously refined. Scanning tunneling microscopy [1] and atomic force microscopy [2, 3] allowed for the first time the direct imaging of single atoms and molecules on surfaces. Optical detection of atoms was first realized by imaging the fluorescence of single atomic ions stored in radio-frequency traps [4–6]. This was rapidly followed by the first spectroscopic experiments on single organic dye molecules in the condensed phase [7, 8]. Since then a wide variety of systems have been investigated at the single-particle level providing valuable information that would otherwise be masked by ensemble averaging [9–15]. This contribution will focus on optical and magnetic-resonance experiments at cryogenic temperatures on individual pentacene molecules in a single crystal of *p*-terphenyl performed in our laboratory in Leiden.

The central problem in the field of single-molecule spectroscopy and microscopy is how to detect optically a single absorbing molecule surrounded by trillions of solvent or matrix molecules. Basically there are two important requirements to be fulfilled: (i) only one molecule in the irradiated volume must be in resonance with the excitation source, and (ii) the signal arising from the single molecule should be larger than that of any background signal. Practically all single-molecule experiments reported in the literature make use of the fluorescence that is emitted by the molecule after optical excitation by laser light. The physical mechanism leading to the fluorescence is schematically depicted in Fig. 1.

If the exciting laser wavelength  $\lambda_{\text{exc}}$  is in resonance with the purely electronic  $S_1 \leftarrow S_0$  transition, the molecule will absorb the photon and will be excited to  $S_1$ . After residing in  $S_1$  for typically a few nanoseconds it will decay to the ground state under emission of a fluorescence photon. A part of the emitted photons will be emitted at a wavelength longer than  $\lambda_{\text{exc}}$  caused by the decay of the molecule to a vibrationally excited state of  $S_0$ . These redshifted photons can be very efficiently separated from the overwhelming number

of excitation photons and allow the detection of a single molecule with a high signal-to-background ratio. The quantum yield for photon emission  $\Phi_F$  should of course be as high as possible preferably close to unity. Also care should be taken to minimize scattering background signals which may arise through Rayleigh scattering or from Raman scattering from the sample and the substrate.

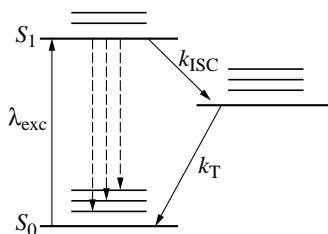


**Fig. 1.** A schematic representation of the electronic energy-level scheme of pentacene, a typical molecule used in single-molecule optical studies.  $S_0$  denotes the singlet ground state,  $S_1$  the first excited singlet state and  $T_1$  the lowest, metastable triplet state. For each electronic state, several vibronic levels are shown. The intersystem crossing and triplet decay rate are given by  $k_{ISC}$  and  $k_T$  respectively. The fluorescence emission corresponding to decay from  $S_1$  to a vibrational level of  $S_1$  is red-shifted (dashed lines) with respect to  $\lambda_{exc}$  and can therefore be spectrally separated from the excitation light.

The high signal-to-noise ratio necessary to achieve single-molecule sensitivity also depends crucially on the peak absorption cross section  $\sigma$  of the molecule. To optimise this value the total frequency width of the molecular absorption should be as narrow as possible, i.e., as close as possible to the lifetime-limited value. This situation is usually achieved at low (liquid-helium) temperatures where the electron-phonon coupling is weak. This can result in a peak absorption cross-section up to  $\sigma = 10^6 \text{ \AA}^2$ , i.e., 5 orders of magnitude larger than at room temperature and corresponding to about  $10^5$  times the molecular size.

One would expect that, upon increasing the incident laser power, optical saturation occurs at a maximum emission rate of  $\tau_1^{-1}/2$  photons per second, where  $\tau_1$  is the radiative lifetime of  $S_1$ . For a strongly allowed transition, with  $\tau_1 \approx 5 \text{ ns}$ , this would lead to a maximum emission rate of about  $10^8$  photons per second. This would be easily discernable from background contributions. However as is visible from Fig. 1, the maximum emission rate is often limited by excursions of the molecule from  $S_1$  to the meta-stable triplet state  $T_1$ . This state, due to the forbidden character of the triplet-singlet transition, can have lifetimes varying from microseconds to seconds. The maximum emission rate is then given by  $\tau_1^{-1}/(2 + k_{ISC}\tau_1)$ , where  $k_{ISC}$  is the population rate of the triplet state  $T_1$  from the excited singlet state  $S_1$  and  $\tau_1$  the lifetime of  $T_1$ . So intersystem crossing from the excited singlet into the metastable triplet state results in premature saturation of the emission rate of the molecule. This is of great importance for the signal-to-noise ratio that can be obtained for the fluorescence signal of a single molecule because the fluorescence intensity then saturates already at a relatively low level.

## 2. Experimental

An optimum signal-to-background ratio in the optical detection of single molecules requires a minimum excitation volume. The most commonly used method is that of confocal detection. In Figure 2 a schematic depiction of the cryogenic confocal microscope used for the single-molecule experiments described in this contribution is presented. A commercial

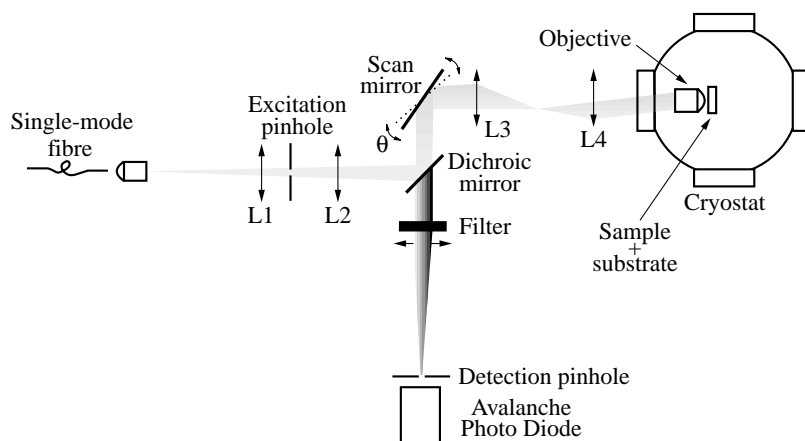


**Fig. 2.** The optical arrangement used to select and detect single molecules. In this confocal detection scheme the excitation by the laser light (light grey) and the collection of the fluorescence (dark grey) is performed by the same objective. Pinholes serve to suppress unwanted out-of-focus light.

microscope objective or an aspheric singlet lens is immersed in liquid helium and used to illuminate a volume of roughly  $1 \mu\text{m}^3$ . The mixture of back-reflected light and emitted fluorescence is captured by the same piece of optics that is responsible for the excitation focus. The laser beam, entering the microscope from a single-mode fiber to decouple the alignment of the optics on either end, is focussed by the L1 lens on the excitation pinhole. This pinhole serves as a spatial filter to achieve a Gaussian-shaped  $\text{TEM}_{00}$  mode of the excitation beam to ensure diffraction-limited focussing. The L2 lens forms an approximately parallel beam which is reflected by the scanning mirror. A pair of steering lenses L3 and L4 directs the laser onto the input plane of the objective in the cryostat. The luminescence from the sample which falls inside a critical angle defined by the numerical aperture of the objective follows the same way back through the objective and is transmitted by the dichroic mirror that is reflective for the excitation light but transparent for the red-shifted fluorescence light. After passing appropriate filters to suppress residual backscattered laser light, the fluorescence is focussed onto a photodetector. A confocal aperture is placed in front of the avalanche photo-diode, such that fluorescence from points on the sample that are not within the focal plane will be largely obstructed by the pinhole.

### 3. Magnetic resonance spectroscopy of a single electron spin

Because of its favourable photo-physical properties pentacene doped in a single crystal of *p*-terphenyl has emerged as the premier system for single-molecule type experiments [7, 8]. Pentacene has roughly the same shape and size as *p*-terphenyl so that pentacene guest molecules occupy one of four inequivalent lattice sites. Consequently the resulting four sharp  $S_1 \leftarrow S_0$  zero-phonon transitions are mutually displaced. By tuning the laser frequency to the 0–0 transition of the  $O_1$  site of a crystal with a concentration of approximately  $10^{-8}$  mol/mol pentacene in *p*-terphenyl, and by scanning the frequency of the single-mode laser, the fluorescence-excitation spectrum of individual pentacene molecules can be observed (see Fig. 3).

The single pentacene molecule, under the influence of the single-mode laser, undergoes repeated excitation-emission cycles between  $S_0$  and  $S_1$ . In addition to the fluorescence

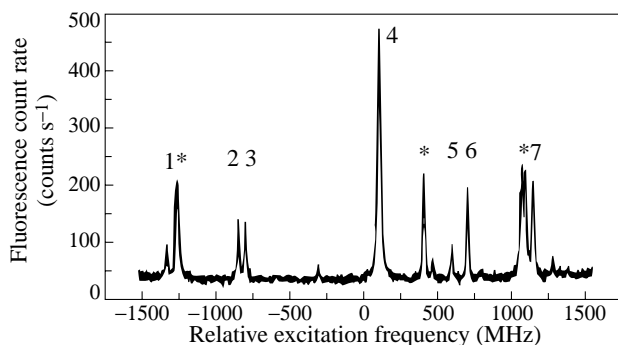


**Fig. 3.** Part of the fluorescence-excitation spectrum of pentacene in p-terphenyl taken at a wavelength of 592.20 nm. The peaks correspond to the excitations of individual pentacene molecules and exhibit a Lorentzian lineshape with a width that is determined by the lifetime of the  $S_1$  excited state. The features marked with an asterisk result from two or more molecules, the resonance frequencies of which coincide or almost coincide.

decay there is a small probability to cross over to the lower-lying triplet state  $T_1$ . The quantum yield for intersystem crossing (ISC) to  $T_1$  for the spectral site  $O_1$  is approximately 0.5%. The decay from  $T_1$  to the singlet ground state  $S_0$  proceeds via non-radiative processes with a mean lifetime of about 50  $\mu\text{s}$ .

The three sublevels of  $T_1$  labeled  $T_x$ ,  $T_y$  and  $T_z$ , are selectively populated upon inter-

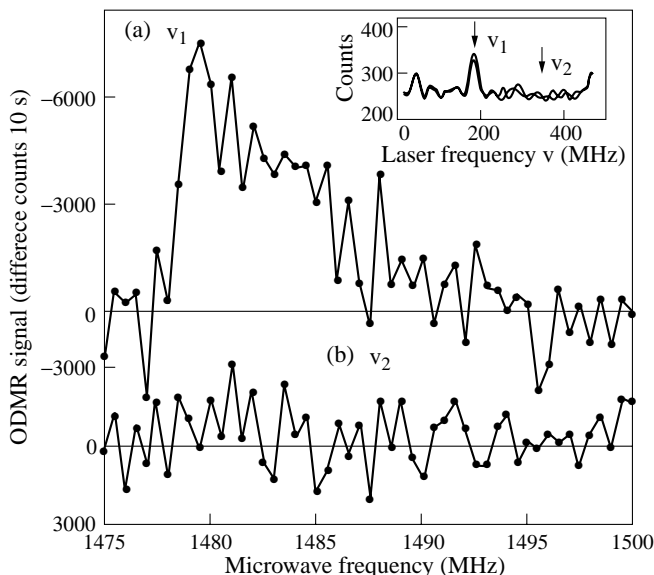


**Fig. 4.** (a) The optically detected magnetic-resonance spectrum of a single pentacene molecule in zero-magnetic field. The signal represents the  $T_x - T_z$  transition and corresponds to a decrease of the steady-state fluorescence intensity. (b) Change of the fluorescence intensity when the laser frequency is detuned from the fluorescence-excitation line of the single pentacene molecule. In the inset two consecutively recorded fluorescence-excitation spectra of the molecule are shown. These spectra are recorded with a lower laser intensity than that used for the fluorescence-detected magnetic-resonance signals.

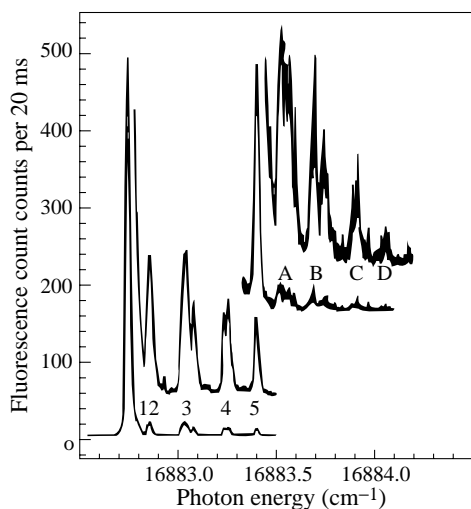


**Fig. 5.** The fluorescence-excitation spectrum of the  $O_1$  spectral site of pentacene in *p*-terphenyl. The satellites 1–5 result from pentacene molecules containing a single  $^{13}\text{C}$  nucleus in natural abundance. The satellites A–D are caused by molecules which contain two  $^{13}\text{C}$  nuclei.

system crossing. In this process the pentacene molecule most probably ends up in one of the two short-lived levels  $T_x$  or  $T_y$ . The flux of fluorescence photons is then temporarily interrupted because the molecule is shelved in the non-radiative triplet state. After decay to the ground state the molecule will again carry out excitation-emission cycles. Thus the fluorescence is emitted in bunches. This “photon bunching” is one of the signatures that the emission originates from a single molecule and not from an ensemble [16]. The average dark period corresponds to the mean residence time of the molecule in the triplet state. This residence time is changed under the influence of a resonant microwave field. Tuning the microwaves into resonance with a transition between one of the short-lived levels ( $T_x$  or  $T_y$ ) and the long-lived level  $T_z$  lengthens the dark period. When averaging over “light” and “dark” intervals one observes a reduction of the fluorescence intensity, i.e., one detects the microwave-induced transition between the two triplet sublevels of the single molecule. The influence of the resonant microwaves on the emission rate of a single pentacene molecule is illustrated in Fig. 4(a) for the  $T_x - T_z$  transition [17, 18]. Here the fluorescence-excitation spectrum of the single pentacene molecule is shown in the inset. To obtain the magnetic-resonance transition the laser is tuned to the peak of the fluorescence-excitation peak and the fluorescence is monitored while scanning the microwave frequency. The signal corresponds to a decrease of the average fluorescence intensity caused by the increased probability to populate the long-lived level  $T_z$  which lengthens the dark interval between the burst of photons. In Figure 4(b) it is shown that the microwave-induced signal vanishes if the laser is out of resonance with the optical transition of the molecule.

An interesting question is whether it is possible to perform nuclear magnetic-resonance experiments on single molecules. A first step towards this goal was the observation of the hyperfine interaction of a single triplet spin with a single nuclear spin. To observe the hyperfine interaction one has to create a situation in which the hyperfine interaction with one nuclear spin dominates. This can be achieved by optically selecting individual pentacene molecules which contain the rare isotope  $^{13}\text{C}$  ( $I = 1/2$ ) in natural abundance. This is illustrated in Fig. 5 in which the optical excitation spectrum is shown of a sample of pentacene in *p*-terphenyl. The laser beam has been moved over the crystal to find an area with a minimum amount of strain. The high quality of this part of the crystal is illustrated by the extremely narrow, inhomogeneously broadened  $O_1$  ensemble line. The

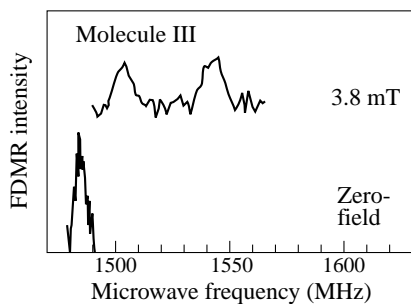


**Fig. 6.** The fluorescence-detected magnetic-resonance signals of the  $T_x - T_z$  transition of a single pentacene- $d_{14}$  molecule containing one  $^{13}\text{C}$  nucleus at the central carbon position in zero field and in the presence of a weak magnetic field of 7.5 mT.

line width of 750 MHz is only a factor of 100 larger than the homogeneous line width of about 8 MHz and allows for the observation of a set of weak satellites, numbered 1–5, in the high-energy wing. These satellites are caused by pentacene molecules which contain a single  $^{13}\text{C}$  nucleus [19, 20]. Given the small line width it is not surprising that such satellites are observed because the probability to find a pentacene molecule containing a  $^{13}\text{C}$  atom (natural abundance 1.108%) is no less than 19.3%. For a pentacene molecule of  $D_{2h}$  symmetry a  $^{13}\text{C}$  can occupy six inequivalent positions within the molecule and one expects to observe six satellites with an intensity ratio 4:4:4:4:4:2. As can be seen the observed spectrum confirms this prediction. In particular one predicts that the satellite at the highest energy corresponds to a pentacene molecule with a  $^{13}\text{C}$  spin at the central carbon position.

In Figure 6 the fluorescence-detected magnetic-resonance spectrum is shown for a single pentacene- $d_{14}$  molecule containing one  $^{13}\text{C}$  nucleus at the central carbon position in zero field and in the presence of a weak external magnetic field. The molecule is selected by tuning the laser to the satellite with the highest energy and by selecting a single molecule. In the presence of the magnetic field of 7.5 mT a shift and a splitting of the magnetic-resonance transition is observed. This splitting is caused by the hyperfine interaction of the single triplet electron spin with the single  $^{13}\text{C}$  nuclear spin [21]. The observation of this splitting indicates that the flip-flop time of the single  $^{13}\text{C}$  spin is short compared to the observation time of about 20 minutes. From an estimate [22] one obtains that this flip-flop time should be of the order of 0.1–1 s indeed much shorter than our observation time.

#### 4. Conclusion

The results presented here demonstrate that single-molecule optical and magnetic-resonance spectroscopy is feasible. Magnetic-resonance spectroscopy on single molecules is unfortunately limited to a few special cases that fulfil a number of stringent conditions as discussed in this contribution. At present most experiments concentrate on pure optical spectroscopy on single molecules that are of biological relevance. This is illustrated by our recent work on single light-harvesting complexes of photosynthetic bacteria that have allowed for the first time to visualise the effect of the coupling between strongly interacting bacteriochlorophyll-*a* molecules [23]. These kinds of experiments hold considerable promise for a detailed investigations of the mechanisms responsible for the efficient transfer of excitation energy in these complexes.

#### Acknowledgement

The author would like to thank all members of the group in Leiden that have contributed to the results presented in this contribution, i.e., Jürgen Köhler, Albert-Jan Brouwer, Antoine van Oijen, Michio Matsushita, Thijs Aartsma, Andreas Bloëß, Martijn Ketelaars and



Edgar Groenen. The work forms part of the research program of the “Stichting F.O.M” with financial support of the “Nederlandse Organisatie voor Wetenschappelijk Onderzoek (N.W.O.)”.

## References

- [1] G. Binnig and H. Rohrer, *Rev. Mod. Phys.* **59**, 615–625 (1987).
- [2] G. Binnig, C. F. Quate and Ch. Berber, *Phys. Rev. Lett.* **56**, 930–933 (1986).
- [3] D. Rugar and P. K. Hansma, *Physics Today* 23–30 (1990).
- [4] W. M. Itano, J. C. Bergquist and D. J. Wineland, *Science* **237**, 612–617 (1987).
- [5] H. Dehmelt, *Rev. Mod. Phys.* **62**, 525–530 (1990).
- [6] F. Diedrich, J. Krause, G. Rempe, M. O. Scully and M. Walther, *IEEE J. Quant. Elect.* **24**, 1314–1319 (1988).
- [7] W. E. Moerner and L. Kador, *Phys. Rev. Lett.* **62**, 2535–2538 (1989).
- [8] M. Orrit and J. Bernard, *Phys. Rev. Lett.* **65**, 2716–2719 (1990).
- [9] Th. Basché, W. E. Moerner, M. Orrit and U. Wild, *Single-Molecule Optical Detection, Imaging and Spectroscopy*. Verlag-Chemie München, 1997.
- [10] A. C. J. Brouwer, E. J. J. Groenen and J. Schmidt, *Phys. Rev. Lett.* **80**, 3944–3947 (1998).
- [11] W. E. Moerner and Th. Basché, *Angew. Chem. Int. Ed. Engl.* **32**, 457–476 (1993).
- [12] W. E. Moerner and M. Orrit, *Science* **283**, 1670–1676 (1999).
- [13] S. Nie and R. N. Zare, *Annu. Rev. Biophys. Biomol. Struct.* **26**, 567–596 (1997).
- [14] T. Plakhotnik, E. A. Donley and U. Wild, *Annu. Rev. Phys. Chem.* **48**, 181–212 (1997).
- [15] X. S. Xie and J. K. Trautman, *Annu. Rev. Phys. Chem.* **49**, 441–480 (1998).
- [16] J. Bernard, L. Fleury, H. Talon and M. Orrit, *J. Chem. Phys.* **98**, 850–859 (1993).
- [17] J. Köhler, J. A. J. M. Disselhorst, M. C. J. M. Donckers, E. J. J. Groenen, J. Schmidt and W. E. Moerner, *Nature* **363**, 242–244 (1993).
- [18] J. Wrachtrup, C. von Borczyskowski, J. Bernard, M. Orrit and R. Brown, *Nature* **363**, 244–245 (1993).
- [19] T. Basché, S. Kummer and C. Braüchle, *Chem. Phys. Lett.* **225**, 116–123 (1994).
- [20] A. C. J. Brouwer, J. Köhler, E. J. J. Groenen and J. Schmidt, *J. Chem. Phys.* **105**, 2212–2222 (1996).
- [21] J. Köhler, A. C. J. Brouwer, E. J. J. Groenen and J. Schmidt, *Science* **268**, 1457 (1995).
- [22] J. Köhler and J. Schmidt, *C.R. Acad. Sci. Paris.* **324**, 373–388 (1997).
- [23] A. M. van Oijen, M. Ketelaars, J. Köhler, T. J. Aartsma and J. Schmidt, *Science* **285**, 400–402 (1999).

## Magneto-optical and cyclotron resonance study of semiconductor nanostructures in very high magnetic fields

*N. Miura*<sup>†</sup>, *T. Ikaida*<sup>†</sup>, *K. Uchida*<sup>†</sup>, *T. Yasuhira*<sup>†</sup>, *K. Ono*<sup>†</sup>, *Y. H. Matsuda*<sup>†</sup>,  
*G. Springholz*<sup>‡</sup>, *M. Pinczolis*<sup>‡</sup>, *G. Bauer*<sup>‡</sup>, *E. Kurtz*<sup>§</sup>, *C. Klingshirn*<sup>§</sup>,  
*Y. Shiraki*<sup>¶</sup> and *Y. Hirayama*<sup>||</sup>

<sup>†</sup> Institute for Solid State Physics, University of Tokyo,  
Kashiwanoha, Kashiwa, Chiba 277-8581, Japan

<sup>‡</sup> Institut für Halbleiterphysik, Johannes Kepler Universität Linz,  
A-4040 Linz, Austria

<sup>§</sup> Institut für Angewandte Physik, Universität Karlsruhe,  
D-76128 Karlsruhe, Germany

<sup>¶</sup> Department of Applied Physics, University of Tokyo,  
Hongo, Bunkyo-ku, Tokyo 113-8656, Japan

<sup>||</sup> NTT Basic Research Laboratory, Morinosato-Wakamiya Atsugi,  
Kanagawa 243-0198, Japan

**Abstract.** We have studied new features of semiconductor nano-structures in cyclotron resonance and magneto-optical spectroscopy under very high magnetic fields up to a few megagauss. The new features are attributed to the shrinkage of wave-functions of electrons, holes and excitons. In PbSe/PbEuTe quantum dots that are regularly arranged to form an fcc-like lattice, sharp cyclotron resonance peaks from PbSe quantum dots were observed. It was found that the peaks show a number of anomalous features such as splitting, a remarkable dependence of the intensity on the wavelength, or a peculiar angular dependence of the resonance field. In the photoluminescence spectra of excitons for CdSe/ZnSe quantum dots, GaP/AlP and GaAs/AlAs short period superlattices, a remarkable decrease of the peak intensity and a red shift of the exciton peak were observed with increasing magnetic field; these effects are attributed to the general nature of excitons consisting of spatially separated electrons and holes.

### 1. Introduction

The high magnetic field is a powerful tool to study electronic states in semiconductor nano-structures. High magnetic fields reduce the extension of the wave-function of electrons and holes, and also of excitons. This effect competes with the confinement of the wave-functions by quantum potentials in nano-structure devices, causing a variety of new phenomena. These magnetic field effects can provide new insights regarding electronic states in the nano-structures. Recent advances in high magnetic field techniques have enabled us to generate very high magnetic fields which can be applied to experiments for solid state physics. We can now obtain pulsed high fields over 600 T by electromagnetic flux compression and over 300 T by the single-turn coil technique [1]. Long-pulse non-destructive fields up to 60 T can be obtained by using conventional pulsed magnets. These fields can be conveniently applied for many different kinds of experiments [2]. At 100 T, the extension of the wave-function is decreased to 2.6 nm; this is usually smaller than the size of quantum structures such as quantum well width, quantum wire width or the size of quantum dots. The wave-function extension of excitons is reduced considerably in high magnetic fields as well, but this is more complicated as it also depends on the reduced mass and on the dielectric constant. At first sight, therefore, we can expect that these systems should look

similar to the 3D systems in high magnetic fields. However, in real nano-devices such as quantum wells, superlattices, quantum wires or quantum dots, we often observe peculiar properties in high magnetic fields and these provide useful information on the electronic states and the characteristics of the devices.

In this paper, we present two topics of our recent studies on quantum dots and superlattices in high magnetic fields. Cyclotron resonance was measured in PbSe/PbEuTe quantum dots that are regularly arranged to form an fcc-like 3D crystal [3, 4]. The sharp cyclotron resonance from the PbSe quantum dots exhibits peak splitting, photon-energy-dependent change of the absorption intensity and a peculiar angular dependence with respect to the field direction. In CdSe/ZnSe quantum dots, photo-luminescence spectra of the excitons were measured. In relatively small dots, a remarkable decrease of the peak intensity and a red shift were observed with increasing magnetic field [5]. Similar phenomena were observed in GaP/AlP [6] and GaAs/AlAs short period superlattices [7]. These phenomena are due to the general properties of excitons consisting of electrons and holes that are spatially separated.

## 2. Experimental techniques

Pulsed high magnetic fields above 100 T were generated by the single-turn coil [1]. Although the pulse duration is as short as several microseconds, cyclotron resonance can be measured with high accuracy by using a CO<sub>2</sub> laser and a fast infrared detector. Long pulse fields up to 50 T, generated by non-destructive wire-wound magnets, were employed for photo-luminescence measurements. Photoluminescence spectra were measured by using an OMA system [8]. Samples of PbSe/PbEuTe quantum dots were grown at the Johannes Kepler Universität Linz by MBE on BaF<sub>2</sub> substrates [4]. By stacking many PbSe layers (20–100 layers) on which quantum dots are regularly arranged between PbEuTe matrix layers, quantum dots form an fcc-like crystal structure. Samples of CdSe/ZnSe quantum dots were grown at the Universität Karlsruhe by MBE [9]. We measured two samples: one is a relatively large quantum dot sample (EK34) with a lateral size of about 10 nm, and the other is a small dot sample (EK9) with a lateral size of about 5 nm. Short period superlattices of GaP/AlP and GaAs/AlAs were grown at the University of Tokyo [10] and the NTT Basic Research Laboratory, respectively.

## 3. Cyclotron resonance in PbSe/PbEuTe quantum dots

The arrays of PbSe quantum dots embedded in Pb<sub>1-x</sub>Eu<sub>x</sub>Te ( $x = 5-10\%$ ) were fabricated on BaF<sub>2</sub> (111) substrates. The dots have a nearly tetragonal shape with a side length of about 70 nm and a height of about 18 nm. In addition to samples with an fcc-like stacking (ABCABC) and with an AAAAAA-like stacking, samples with only a wetting layer of PbSe were measured. As the density of quantum dots was high in 3D space, a fairly large absorption of the cyclotron resonance was obtained. In the low photon energy range (15–114 cm<sup>-1</sup>) that was studied in the field range below 10 T, the dispersion cyclotron resonance of the Darwin-Fock type was observed which is characteristic for quantum dots. Figure 1 shows cyclotron resonance spectra for an fcc-like sample (sample MBEG921) in high magnetic fields for electron-active (right panel) and hole-active (left panel) circular polarization. The wavelength of the radiation of a CO<sub>2</sub> laser was varied between 9.25 μm and 10.6 μm. Broad peaks observed for the hole-active radiation are the cyclotron resonance of holes in the PbEuTe matrix mixed with the PbSe wetting layers.

Sharp peaks observed for the electron-active polarization are from electrons in PbSe quantum dots. It is known that when the magnetic field is applied in the (111) direction of

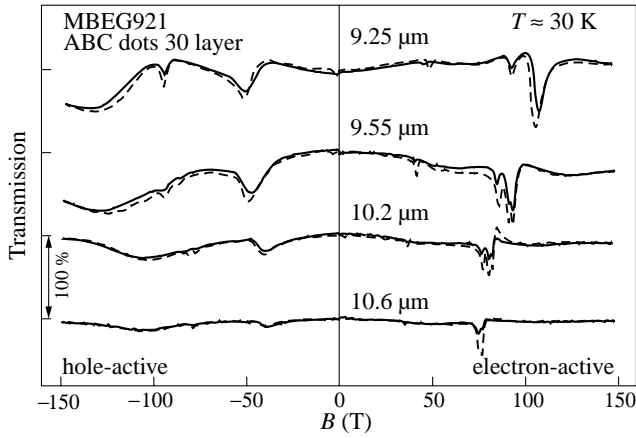


**Fig. 1.** Cyclotron resonance spectra in a PbSe/PbEuTe quantum dot sample (MBEG921) with ABCABC stacking. The radiation source was a CO<sub>2</sub> laser. Left handed and right handed circularly polarized radiation were used to observe the electron-active (right panel) and the hole-active (left panel) resonances.

a bulk PbSe crystal, two peaks are observed for heavy electron valleys (3-fold degenerate) and a light electron valley [11]. The peaks at 75–108 T and a peak at 35–46 T correspond to the heavy electron valleys and the light electron valley, respectively.

There are many peculiar features in the cyclotron resonance spectra as shown in Fig. 1. Firstly, we can see a remarkable wavelength dependence of the absorption intensity. As the wavelength is decreased from 10.6  $\mu\text{m}$  to 9.25  $\mu\text{m}$ , the absorption intensity increases dramatically. A completely opposite wavelength dependence of the absorption intensity was found in a different sample (sample MBEG1368) with an AAAAAA-type stacking. We found that the different behavior in function of the wavelength can be explained by multiple reflection of the radiation in the sample [12]. The thickness of the samples is 1.4  $\mu\text{m}$  for MBEG921 and 1.5  $\mu\text{m}$  for MBEG1368, respectively. If we take into account the large refractive index (6.6 for MBEG921 and 6.9 for MBEG1368), the wavelength of the radiation in the sample is comparable with the sample thickness. The absorption intensity will increase as the wavelength approaches the interference condition because the radiation undergoes multiple reflection in the sample. Thus the wavelength dependence of the absorption intensity can be well explained in terms of the multiple reflection effect.

Next, we notice a prominent splitting of the heavy electron peak. The splitting looks peculiar because the heavy electron peaks arising from the 3 heavy electron valleys are degenerate in bulk samples of PbSe. No straightforward argument can be given for the observed splitting of this peak. We found that the splitting gradually disappeared when the experiment was repeated on the same sample as shown in Fig. 2. This points to a strain-related effect due to the large lattice mismatch in this system; this may have been gradually relieved under the influence of the strong and steep field pulses or by thermal cycling.

In high magnetic fields as used in the present experiment, the cyclotron radius of electrons is much smaller than the dot size. Therefore, the cyclotron resonance spectra should be similar to those for bulk PbSe. In order to check on this point, we tilted the magnetic field direction from the  $\langle 111 \rangle$  axis that is parallel to the growth direction in the  $\langle 110 \rangle$  plane. In bulk samples, one of the degenerate peaks of the heavy electron valleys should shift to the heavier mass direction and the two others should shift to the lighter mass side. This was actually observed in a bulk PbSe sample. Figure 3 shows the angular dependence of the

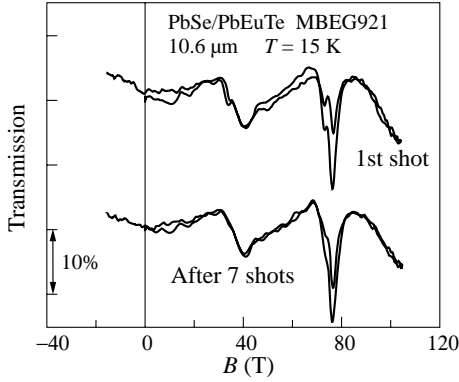


**Fig. 2.** Cyclotron resonance spectra in a PbSe/PbEuTe quantum dot sample (MBEG921) observed in the first run and after repeating 7 shots.

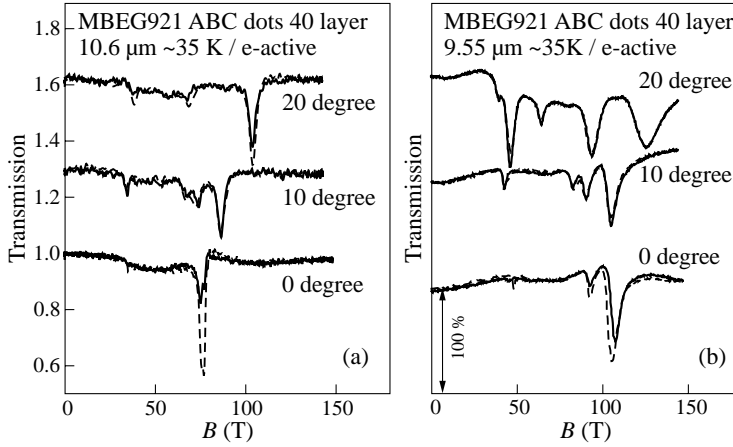


**Fig. 3.** Dependence of the cyclotron resonance spectra on the magnetic field direction. The field direction was tilted from the growth direction ( $\langle 111 \rangle$  axis) in the  $(110)$  plane. The wavelength of the radiation was (a)  $10.6 \mu\text{m}$  and (b)  $9.55 \mu\text{m}$ .

cyclotron resonance in sample MBEG921. For a wavelength of  $10.6 \mu\text{m}$ , the heaviest mass peak shifts to the higher field side as the tilt angle is increased. However, for a wavelength of  $9.55 \mu\text{m}$ , the heaviest mass peak shifts to the heavier mass side. This kind of behavior is seen when the Landau level-subband level crossover occurs in a 2-dimensional system. The present experimental results indicate that the electronic states in the quantum dots still keep some 2-dimensional character although the cyclotron radius is much smaller than the dot size. This may originate from the tetragonal shape of the quantum dots.

#### 4. Magnetic field effects on spatially separated excitons

Next we discuss the magnetic field dependence of the exciton lines in quantum dots and short period superlattices in high magnetic fields. As compared with the quantum dots of III-V compounds such as the InAs/GaAs system [13], much less has been known on quantum dots of II-VI compounds. We measured the magneto-photoluminescence spectra of excitons in CdSe/ZnSe quantum dots. In relatively large quantum dots the photon energy of the peak and the integrated intensity are increased as the field is increased. The energy shift (diamagnetic shift) is proportional to the square of the field below 30 T. From the diamagnetic shift  $\Delta E$ , we obtained the wave-function extent as  $\Delta x = 5.7 \text{ nm}$ . It should be

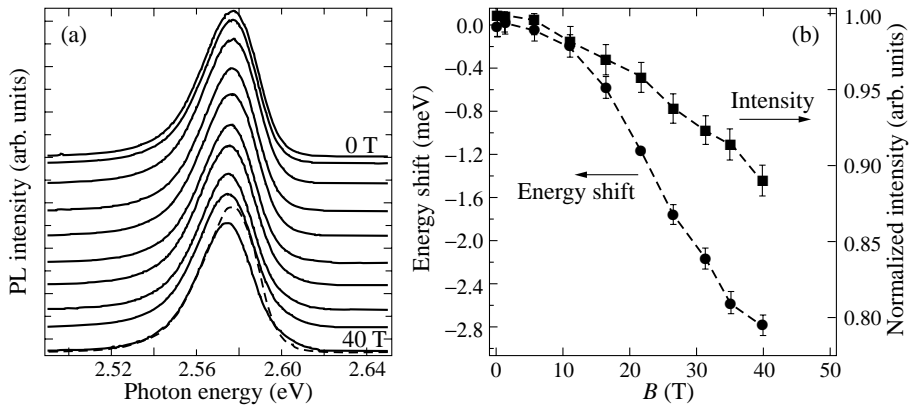


**Fig. 4.** (a) Magneto-photoluminescence spectra of excitons in CdSe/ZnSe quantum dots of small size (EK9) in magnetic fields applied parallel to the growth direction (Faraday configuration). The dotted line shows the zero-field spectra for comparison with the high field spectra. (b) Energy shift and intensity of the exciton peak.

noted that the  $\Delta x$  estimated from the diamagnetic shift is smaller than the geometrical dot diameter of 10 nm, but it is nearly equal to that in bulk CdSe ( $\sim 5.8$  nm). The PL intensity increases with increasing field as in the bulk crystal.

For the relatively small quantum dots in sample EK9, astonishing behavior of the excitons was observed in magnetic fields. Figure 4(a) shows the magneto-photoluminescence spectra and Fig. 4(b) the photon energy and the peak intensity as a function of magnetic field. Both the photon energy and the intensity of the peak are decreased as the field is increased; this is contrary to the normal behavior of excitons. These field dependences are also opposite to those for larger dots. Normally, the exciton wave-function extent is decreased, in other words, the distance between electrons and holes is decreased as the field is increased. That is the reason of the increase of the peak intensity with increasing field. For small CdSe dots, however, it seems that a completely opposite phenomenon occurs. This can be understood if we assume that electrons and holes are localized in the low potential region and spatially separated from each other. It has been reported that there is a Cd-rich region in CdSe/ZnSe quantum dots, such that electrons are easily trapped in this region and well confined in the dots. On the other hand, the valence band offset for the CdSe/ZnSe interface is considered to be very small and the hole confinement should be rather small. As the strain potential around the dots is fairly large due to the piezoelectric effect in II–VI compounds, holes would be trapped in the potential minimum around the quantum dots. Then an excitonic state would be created with spatially separated electrons and holes: an electron in the dot and a hole around the dot. With increasing magnetic field, wave-functions of both electrons and holes would shrink and the wave-function overlap would be decreased; this would lead to the decrease of the recombination rate, resulting in the decrease of the peak intensity.

The decrease of the recombination rate due to the wave-function shrinkage would also lead to a red shift of the exciton recombination energy due to the following mechanism. There is a considerable scatter of quantum dot size, and thus a potential fluctuation for excitons. Therefore, if the exciton recombination lifetime is prolonged by a magnetic field, the excitons would relax more to the lower energy region in the magnetic field. When the recombination lifetime  $\tau_r$  becomes comparable or longer than the characteristic time constant  $\tau_m$  for excitons to relax to the lower energy region, there will be a reduction of

the high energy part of the luminescence peak. Shubert and Tsang observed a red shift and the narrowing of the exciton line when reducing the excitation power in (GaIn)As alloy semiconductors, and explained the effect by a model as mentioned above [14]. When this process occurs, the line shape becomes asymmetric with a significant reduction of the intensity in the high energy region. Shubert and Tsang derived an expression for the asymmetric line shape that reproduced the observed line shape well. In the present experiment, the observed line shape actually has a similar asymmetry.

A similar red shift and intensity decrease of exciton lines were observed in the magneto-photoluminescence spectra in  $(\text{GaP})_m/(\text{AlP})_n$  short period superlattices ( $m$  and  $n$  are the number of monolayers). This system has the unique feature of showing a bright photoluminescence, in spite of the fact that both constituting materials have indirect band gaps. The conduction band minimum is located at the  $X$ -point in the AlP layers, while the valence band maximum is at the  $\Gamma$ -point in the GaP layers [15]. Thus the system is indirect both in real space and  $k$ -space. It was concluded that the intense photoluminescence arises from the localization of electrons and holes near the interface due to the imperfection of the interface.

The observed experimental results can be explained by the shrinkage of the wave-function of electrons and holes and their relaxation with an argument that is similar to the case of CdSe/ZnSe quantum dots. In short period superlattices there are fluctuations in the layer thickness. Electrons and holes would be trapped in the low potential region, separately forming a spatially indirect exciton. When a magnetic field is applied perpendicular to the layers, the wave-function of electrons and holes would be squeezed in the lateral direction in the potential valleys. Then the overlap between the electron and hole wave-function would decrease and the luminescence intensity would decrease. The photon energy of the peak would be decreased by the same relaxation mechanism as in the case of CdSe/ZnSe quantum dots. Thus the anomalous behavior in GaP/AlP short period superlattices is considered to have the same origin as in CdSe/ZnSe quantum dots. The only difference is the origin of the electron and hole localization.

In  $(\text{GaAs})_m/(\text{AlAs})_n$  short period superlattices, a similar band lineup is realized when the number of mono-layers is small. The conduction band minima are located at the  $X$ -point in the AlAs layers while the valence band top is located at the  $\Gamma$ -point in the GaAs layers. We measured the magneto-photoluminescence spectra of excitons in a short period

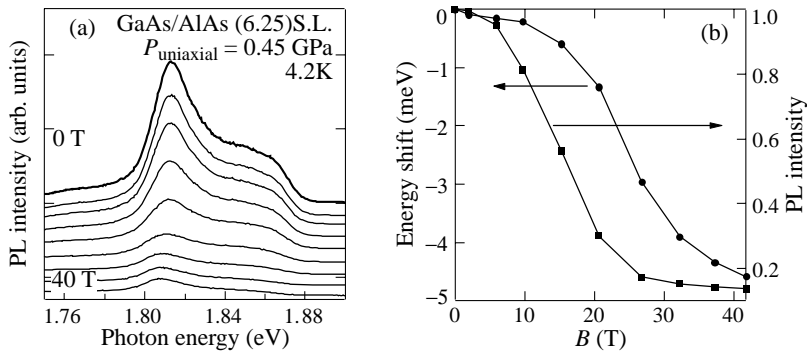


**Fig. 5.** (a) Magneto-photoluminescence spectra in a  $(\text{GaAs})_6/(\text{AlAs})_{25}$  short period superlattice under a uniaxial pressure of 0.45 GPa. (b) Magnetic field dependence of the intensity and of the photon energy of the photoluminescence peak for excitons in a  $(\text{GaAs})_6/(\text{AlAs})_{25}$  short period superlattice.

superlattice of  $(\text{GaAs})_6/(\text{AlAs})_{25}$ . At ambient pressure, the conduction band minima are located at the  $X_{xy}$  point, therefore the photoluminescence is not so large. When we apply a uniaxial pressure of 0.15 GPa to the normal direction of the superlattice ( $\langle 100 \rangle$  direction), the  $X_z - X_{xy}$  crossover takes place and above this pressure, the photoluminescence increases dramatically. Figure 5(a) shows the photoluminescence spectra of a  $(\text{GaAs})_6/(\text{AlAs})_{25}$  superlattice under uniaxial pressure of 0.45 GPa along the  $\langle 111 \rangle$  direction. The change of the intensity and the photon energy of the luminescence peak is shown in Fig. 5(b). We can see a dramatic decrease of the photoluminescence peak of excitons and the red shift with increasing magnetic field. These effects can be interpreted in terms of the same mechanism as observed in CdSe/ZnSe quantum dots and GaP/AlP short period superlattices. Thus the intensity decrease of the photoluminescence and the red shift are considered to be general characteristics of excitons consisting of electrons and holes that are spatially separated.

### Acknowledgments

The authors are obliged to Prof. F. Herlach for critically reading the manuscript and for valuable discussion. A part of the work is supported by the International Joint Research Grant Program by the New Energy and Industrial Technology Development Organization (NEDO).

### References

- [1] N. Miura, Y. H. Matsuda, K. Uchida, S. Todo, T. Goto, H. Mitamura, E. Ohmichi and T. Osada, *Physica B* **294-295**, 562 (2001).
- [2] N. Miura, Y. H. Matsuda, K. Uchida and H. Arimoto, *J. Phys.: Condens. Matter* **11**, 5917 (1999).
- [3] T. Ikaida, N. Miura, S. Tsujino, P. Xomalin, S. J. Allen, G. Springholtz, M. Pinczolits and G. Bauer, *Proceedings of the 10th International Conference on Narrow Gap Semiconductors and Related Small Energy Phenomena, Physics and Application*, (IPAP Conference Series 2), eds. N. Miura, S. Yamada and S. Takeyama (IPAP, 2001) p. 48
- [4] G. Springholz, V. Holy, M. Pinczolits and G. Bauer, *Science* **282**, 734 (1998).
- [5] N. Miura, K. Uchida, T. Yasuhira, E. Kurtz, C. Klingshirn, H. Nakashima, F. Issiki and Y. Shiraki, *Physica B* (to be published).
- [6] K. Uchida, N. Miura, J. Kitamura and H. Kukimoto, *Phys. Rev. B* **53**, 4809 (1996).
- [7] K. Ono, K. Uchida, N. Miura and Y. Hirayama, to be published.
- [8] T. Yasuhira, K. Uchida, Y. H. Matsuda, N. Miura and A. Towardowski, *J. Phys. Soc. Jpn.* **68**, 3436 (1999).
- [9] E. Kurtz, J. Shen, M. Baldauf, S. Wachter, M. Gruen, D. Litvinov, S. K. Hong, J. X. Shen, T. Yao, D. Gerhsen, H. Kalt and C. Klingshirn, *J. Crystal Growth* **214-215**, 712 (2000).
- [10] F. Issiki, S. Fukatsu and Y. Shiraki, *Appl. Phys. Lett.* **67**, 1048 (1995).
- [11] H. Yokoi, S. Takeyama, O. Portugall and N. Miura, *Physica B* **184**, 173 (1993).
- [12] M. von Ortenberg, *Solid State Commun.* **17**, 1335 (1975).
- [13] R. K. Hayden, K. Uchida, N. Miura, A. Polimeni, S. T. Stoddart, M. Henini, L. Eaves and P. C. Main, *Physica B* **246-247**, 93 (1998).
- [14] E. F. Schubert and W. T. Tsang, *Phys. Rev. B* **34**, 2991 (1986).
- [15] K. Uchida, N. Miura, T. Sugita, F. Issiki, N. Usami and Y. Shiraki, *Physica B* **249-251**, 909 (1998).



## Many-particle interaction in the tunnelling nanostructures and STM/STS measurements

P. I. Arseev<sup>†</sup>, N. S. Maslova<sup>‡</sup>, V. I. Panov<sup>‡</sup> and S. V. Savinov<sup>‡</sup>

<sup>†</sup> Lebedev Physical Institute of RAS, Moscow, Russia

<sup>‡</sup> Dpt of Physics, Moscow State University, Moscow, Russia

**Abstract.** The influence of many-particle interaction on tunnelling characteristics in low dimensional structures is analyzed theoretically and investigated experimentally by means of STM/STS methods. It is shown that indirect interaction (through band states of semiconductors) can often lead to increased tunnelling conductivity for bias range where the direct interaction between impurity states is not significant. New method for preparation of electronic states with definite spin configuration on neighboring atoms is suggested. The energy splitting of opposite spin electrons can be about 0.5–1 eV. The different types of tunnelling conductivity behavior in ultra small junction with superconductors is analyzed.

The qualitative changes in understanding of tunnelling phenomena in low-dimensional systems and in STM/STS contacts have occurred during last ten years. Low temperature STM/STS experiments revealed the significant importance of relaxation processes and non-equilibrium effects in behavior of tunnelling characteristics for ultra-small structures [1]. The developed general self-consistent theory of non-equilibrium tunnelling processes made it possible to analyze the obtained experimental data and to predict some new effects which can be observed in STM/STS experiments. Investigation of tunnelling spectra of nanometer scale interacting systems is very important and complicated problem. The presence of localized states in the contact area leads to appearance of non-equilibrium effects because the relaxation rates of electron distribution can be comparable with the tunnelling rate [2].

We present some new results of STM/STS investigations of non-equilibrium interaction effects depending on the distance between impurity atoms (Fig. 1) [3].

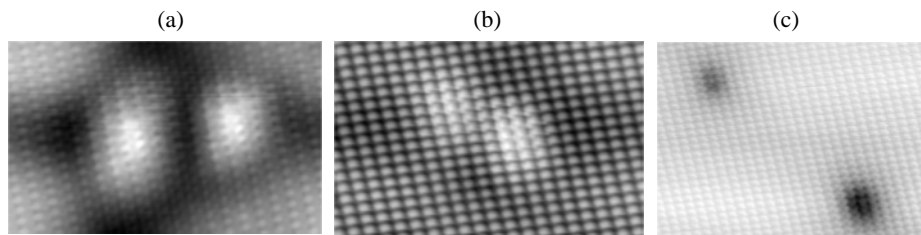


**Fig. 1.** STM topography images of doping atoms situated at different distances on GaAs(110) surface. (a) interacting atoms; (b) single cluster; (c) non-interacting atoms. (a), (b)  $10 \times 6$  nm; (c)  $14 \times 10$  nm.

If the distance between impurities is less than localization radius one has to deal with tunnelling characteristics determined by energy spectrum of total impurity cluster. Such cluster allows spatial separation of localized charges. The energy spectrum of this system depends on electron filling numbers not only through the total Coulomb interaction of localized charges, but also through hopping amplitude between the impurities, which is sensitive

to the presence of opposite spin electrons at neighboring site. That is why the energy spectrum of such cluster strongly depends on particular electron and spin configuration. The distance between tunnelling conductivity peaks measured above described impurity cluster strongly differs from the value of Coulomb repulsion even for weak coupling to the leads of STM junction (Coulomb blockade regime) (Fig. 2).

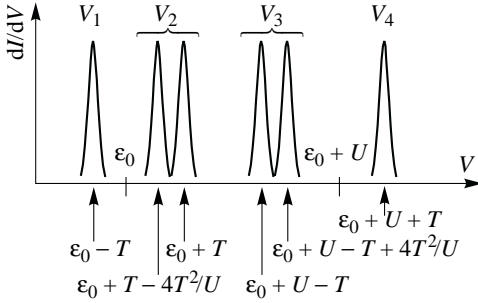


**Fig. 2.** The position of TC peaks in Coulomb blockade regime.

If the distance between impurities increases the behavior of tunnelling conductivity is determined by non-equilibrium charge redistribution changing the kinetics of tunnelling processes. In this case one of the interacting impurity atoms can transfer from “paramagnetic” state to “magnetic” one with changing of applied bias voltage as it was shown in previous report [4]. So, we have investigated theoretically and developed experimentally the new method for preparation of electronic states with definite spin configuration of neighboring impurity atoms on semiconductor surface. This method allows to obtain the energy splitting of opposite spin electron levels up to 0.5–1 eV. This value strongly exceeds the energy splitting in high magnetic field. Electron spin in each energy state can be fixed by applying very small perturbation — external magnetic field.

We have also analyzed indirect interaction between impurities (through band states of semiconductor). Indirect interaction can result in appearance of enhanced tunnelling conductivity in bias range where the direct interaction does not influence the tunnelling processes.

The important role of localized states in tunnelling spectroscopy of superconductors is proved [5]. Figure 3 shows high resolution STM image and experimental tunnelling spectra of BSSCO monocrystal surface. Superstructure along the *b*-axis is clearly visible (Fig. 3(a)). The tunnelling conductivity spectrum reveals asymmetric shape, non-zero

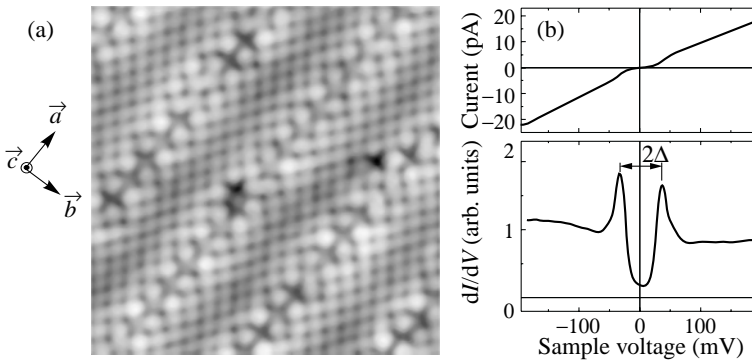


**Fig. 3.** (a) STM topography image and (b)  $I(V)$  and tunnelling conductivity curves for the same surface area.

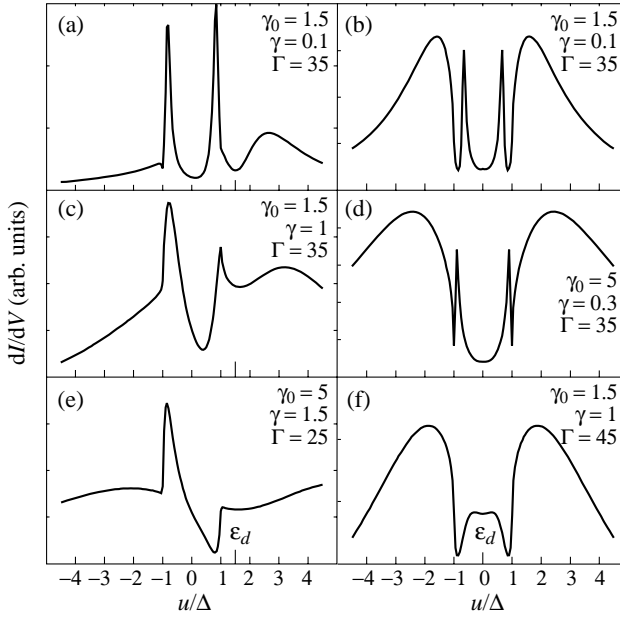


**Fig. 4.** Different types of the tunnelling conductivity  $dI/dV$  for various damping constants and two positions of the impurity level: left column for  $\varepsilon_d = 1.5$  and right column for  $\varepsilon_d = 0$ .

residual conductivity and a dip outside measured superconductive gap. Different types of tunnelling conductivity curves can be obtained by varying parameters of tunnelling junction due to non-equilibrium effects. Let us discuss some of the possible kinds of the  $dI/dU$  dependencies shown in Fig. 3(b).

For small enough values of impurity relaxation rate  $\gamma_0$  two sharp peaks appear inside the superconducting (SC) gap. These peaks correspond to new bound states. Note that both for impurity energy level  $\varepsilon_d$  lying inside and not too far outside the SC gap there is no maximum in the tunnelling conductivity at impurity level. The most remarkable fact is that the SC gap edges can be observed as dips in the conductivity curves. This is a consequence of strong changes in the SC local density of states in the vicinity of the impurity [5]. This situation is depicted in Fig. 4(a,b).

If the initial impurity energy lies inside the SC gap and tunnelling rate  $\Gamma$  increases, the peaks move toward the edges of the gap Fig. 4(d). Another behavior we see in Fig. 4(f), when relaxation rate increases and the peaks broaden. For large enough ratio  $\gamma_0/\Delta$  (impurity relaxation rate)/(band gap) values the peaks become unresolved and the SC gap disappeared. However the dips at the gap edges still remain.

## References

- [1] E. L. Wolf, *Principles of Tunneling Spectroscopy*, Oxford University Press. Oxford 1985.
- [2] P. I. Arseev, A. Depuydt, C. Van Haesendonck, N. S. Maslova, V. I. Panov and S. V. Savinov, *Phys. Rev. B* **60**, 2619 (1999).
- [3] P. I. Arseev, N. S. Maslova, V. I. Panov and S. V. Savinov, *JETP* **121**, 2213 (2002).
- [4] P. I. Arseev, N. S. Maslova, V. I. Panov, S. I. Oreshkin and S. V. Savinov, *JETP Lett.* **72**, 565 (2000).
- [5] P. I. Arseev and N. S. Maslova, *Sol. State Commun.* **108**, 717 (1998).

## Study of high power GaAs-based laser diodes operation and failure by cross-sectional electrostatic force microscopy

A. Ankudinov<sup>†</sup>, A. Titkov<sup>†</sup>, V. Evtikhiev<sup>†</sup>, E. Kotelnikov<sup>†</sup>,  
 N. Bazhenov<sup>†</sup>, G. Zegrya<sup>†</sup>, H. Huhtinen<sup>‡</sup> and R. Laiho<sup>‡</sup>

<sup>†</sup>Ioffe Physico-Technical Institute, St Petersburg, Russia

<sup>‡</sup>Wihuri Physical Laboratory, Turku University, Turku, FIN20014, Finland

One of the important factors that restricts the power limit of semiconductor lasers is a catastrophic optical mirror damage [1]. This process is significantly suppressed through decreasing the optical power density due to its redistribution over the broad transverse waveguide (BW). Recently it was shown that record-breaking values of the quasicontinuous and continuous-wave (QCW and CW) output power for 100- $\mu\text{m}$ -wide-aperture devices can be achieved by incorporating a broad transverse waveguide into 0.97  $\mu\text{m}$  emitting Al-free InGaAs(P)/InGaP/GaAs [2] and Al-containing InGaAs/AlGaAs/GaAs [3] separate confinement heterostructure quantum-well lasers (SCH-QWL). Another important factor limiting the CW output power is the Joule overheating of a laser diode due to an extra serial resistance. Traditionally, a decrease in the resistance is achieved by development of the contacts, whereas a voltage distribution across the device structure is not analyzed properly. At high operating currents the applied voltage can drop not only across the n-p-junction, but also at certain additional regions of the laser structure depending on a particular design of the device.

Electrostatic force microscopy (EFM) [4] provides a very promising method to study the voltage distribution across an operating device with a nanometer space resolution. An application of EFM for diagnostics of III-V laser diodes without and under applied biases

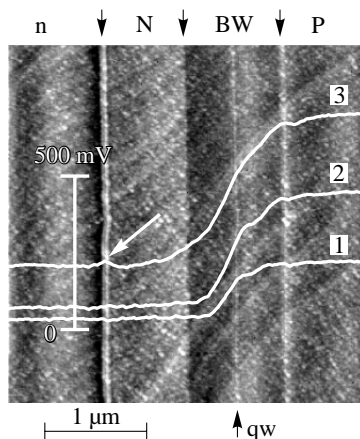


**Fig. 1.** EFM study of the cleavage of the mesa structure of a laser diode under various forward biases. The EFM data of the voltage drop are displayed over the gray scale topography image. Curves 1–3 were measured under the following biases on the p-contact of the laser: 1 — 513 mV; 2 — 1075 mV ( $I = 25 \text{ A/cm}^2$ ); 3 — 1735 mV ( $I = 720 \text{ A/cm}^2$ , lasing regime); the white arrow marks a peculiarity in the voltage drop profile related to the parasitic barrier.

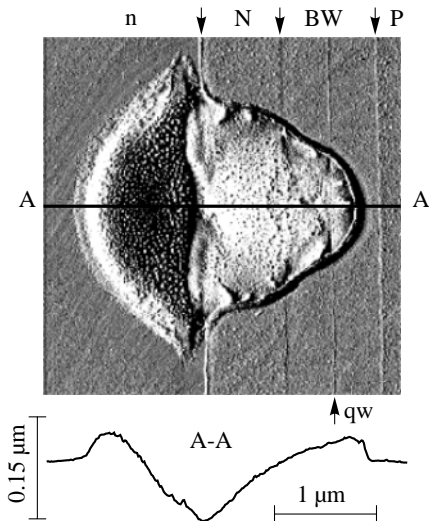


**Fig. 2.** Topography error image of the studied mesa cleavage after a failure at the injection current 9350 A/cm<sup>2</sup> (CW; the generation threshold is  $I_{th} = 500$  A/cm<sup>2</sup>). *A-A* — A height profile of the cleavage surface along the black line on the topography error image obtained from a simultaneously recorded topography image.

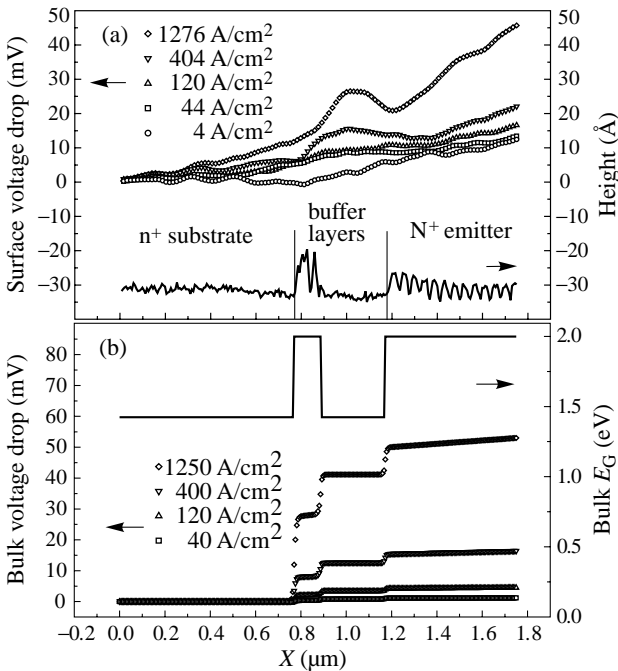


**Fig. 3.** Detailed EFM study of the parasitic barrier profile as a function of the injection current: *a*— experimental results of the surface voltage drop and corresponding topography cross-section of the parasitic barrier region, *b*— data of the bulk voltage drop obtained by simulating the part of the laser structure schematically presented as a bulk energy gap diagram.

have been recently demonstrated [5, 6, 7]. However, the most interesting range of the biases, the lasing regime, has not been studied yet.

In this work we use EFM to study BW InGaAs/AlGaAs/GaAs SCH-QW high power laser diodes at injection currents below and above the generation threshold. It is found that a surprisingly high power dissipation can occur at the initial calibration layer of the laser structure, where a parasitic drop of the applied bias is observed. EFM data shown in Fig. 1 reveal existence of a parasitic barrier at the calibration layer location. Studying the surface morphology of the laser diode mirror after the device failure, caused by an extremal injection current (Fig. 2), demonstrates that a catastrophic melting process at the mirror surface starts from the calibration layer. Profiles of the parasitic barrier versus the injection current are shown in Fig. 3. Behavior of the parasitic barrier was simulated theoretically. The results of such simulation shown in Fig. 3 are in good agreement with the experimental data. Thus, transport properties of auxiliary peripheral layers are an important factor for optimizing the structure of high power lasers, since such layers can cause device failures.

#### Acknowledgements

The work is supported by RFBR (grant No 00-02-16948) and by Programm of Russian Academy of Sciences "Low Dimensional Structures".

#### References

- [1] H. Casey and M. Panish, *Heterstructure Lasers*, Part B: *Materials and operating characteristics*, Chapter 8, New York, San Francisco, London: Academic Press, 1978.
- [2] A. Al-Muhanna, L. J. Mawst, D. Botez, D. Z. Garbuzov, R. U. Martinelli and J. C. Connolly, *Appl. Phys. Lett.* **73**, 1182 (1998).
- [3] E. Yu. Kotelnikov, A. A. Katsnelson, D. A. Livshits, W. Richter, V. P. Evtikhiev, I. S. Tarasov and Zh. I. Alferov, *8th Int. Symp. "Nanostructures: Physics and Technology"*, St Petersburg, p 31, (2000).
- [4] M. Nonemacher, M. P. O'Boyle and H. K. Wickmarmasing, *Appl. Phys. Lett.* **58**, 2091 (1991)
- [5] F. Robin, H. Jacobs, O. Homan, A. Stemmer and W. Bachtold, *Appl. Phys. Lett.* **76**, 2907 (2000).
- [6] A. Ankudinov, V. Marushchak, A. Titkov, V. Evtikhiev, E. Kotelnikov, A. Egorov, H. Riechert, H. Huhtinen and R. Laiho, *PLDS* **3/4**, 9 (2001).
- [7] A. V. Ankudinov, E. Yu. Kotelnikov, A. A. Katsnelson, V. P. Evtikhiev and A. N. Titkov, *Semiconductors* **35**, 840 (2001).

## Magnetic interactions in ferromagnetic EuS-PbS semiconductor multilayers

*M. Chernyshova*<sup>†</sup>, *V. V. Voloubey*<sup>‡</sup>, *L. Kowalczyk*<sup>†</sup>, *A. Yu. Sipatov*<sup>‡</sup>  
and *T. Story*<sup>†</sup>

<sup>†</sup> Institute of Physics, Polish Academy of Sciences, Al. Lotników 32/46,  
02-668 Warsaw, Poland

<sup>‡</sup> Kharkov National Technical University "KPI", 21 Frunze Str.,  
61002 Kharkov, Ukraine

**Abstract.** Magneto-optical Kerr effect and SQUID magnetometry were employed to study the temperature dependence of magnetization and magnetic hysteresis loops in ferromagnetic EuS-PbS semiconductor multilayers grown epitaxially on various substrates: KCl (100), BaF<sub>2</sub> (111), and PbS (100). We observe experimentally that ferromagnetic EuS layers are exchange-coupled via ultrathin (1nm) nonmagnetic PbS spacer layer. This interlayer coupling is antiferromagnetic for structures grown along (100) crystallographic direction but ferromagnetic for structures with (111) growth axis.

### Introduction

EuS-PbS multilayers (superlattices or trilayers) are ferromagnetic epitaxial structures composed entirely of semiconductor materials. Europium sulfide (EuS) is a non-metallic Heisenberg ferromagnet — a member of the well known family of magnetic semiconductors (europium chalcogenides) [1]. Lead sulfide (PbS) is a IV–VI compound semiconductor with a narrow energy gap. PbS is a diamagnetic material and serves as a nonmagnetic spacer layer in the EuS-PbS multilayer structures. Both materials crystallize in cubic (rock salt) crystal structure. Their lattice parameters  $a$  match very well ( $\Delta a/a = 0.5\%$ ). Therefore, pseudomorphic EuS-PbS structures can be grown with an overall thickness exceeding 100nm. Electronic structure of EuS-PbS multilayers can be described as multiple quantum well of PbS confined by the ferromagnetic barriers of EuS with a type I ordering of band edges at the EuS-PbS hetero-interfaces [2, 3].

Magnetic properties of EuS-PbS multilayers grown epitaxially either on KCl (100) or BaF<sub>2</sub> (111) substrates were examined in Ref. [4]. The measurements of magnetization,  $ac$  magnetic susceptibility, and ferromagnetic resonance showed that the ferromagnetic transition in EuS-PbS multilayers is observed even for ultrathin EuS layers of only 2 monolayers (2 ML). The Curie temperature  $T_C$  was found to decrease with decreasing EuS thickness for layers thinner than about 10 ML = 3 nm [4]. The ferromagnetic transition temperature in EuS-PbS multilayers depends also on thermal stress caused by the differences between thermal expansion coefficients of the substrate and the multilayer [4]. Figure 1 summarizes the Curie temperatures of the EuS-PbS structures studied by us. It also includes the recent data for trilayers grown on PbS (100) substrate.

EuS-PbS multilayers form a ferromagnetic-nonmagnetic multilayer system with negligibly small (as compared to metals) carrier concentration both in ferromagnetic and in nonmagnetic layer. Therefore, they constitute a model system to study the mechanisms of interlayer exchange interactions via nonmetallic spacers. These interactions proved to be

of importance for both basic and applicational research on metallic magnetic multilayers. They also play an important role in new semiconductor spintronic magneto-transport and magneto-optical structures. The aim of our work is to provide new experimental evidence for the interlayer exchange interactions in EuS-PbS structures using magneto-optical Kerr (MOKE) technique and SQUID magnetometry for the analysis of the temperature and the magnetic field dependence of magnetization  $M(H, T)$ .

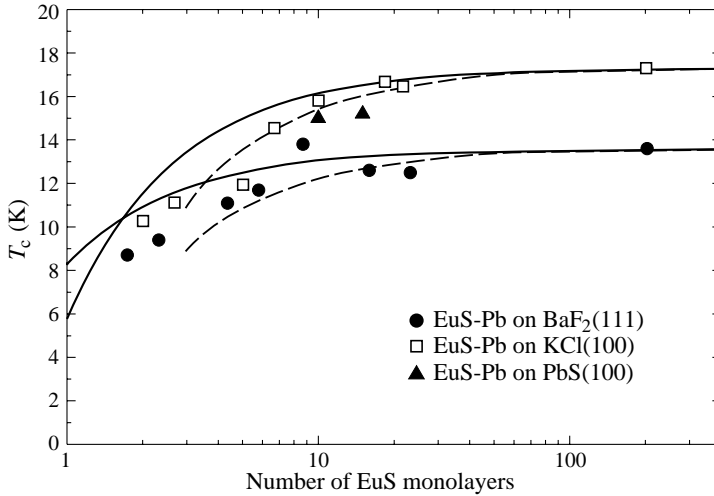


**Fig. 1.** The dependence of the ferromagnetic Curie temperature of EuS-PbS multilayers grown on various substrates on the thickness of ferromagnetic layer. Solid and broken lines correspond to mean-field theoretical description for sharp and intermixed (2 monolayers) interfaces, respectively [4].

## 1. Experimental

We studied magnetic properties of EuS-PbS multilayers and trilayers grown on two insulating transparent substrates KCl (100) and BaF<sub>2</sub> (111) as well as on n-type PbS (100) conducting substrate. The typical multilayer consisted of 10 or 20 repetitions of a basic EuS-PbS bilayer with EuS thickness in the range  $d_{\text{EuS}} = 3\text{--}8$  nm and PbS spacer thickness varying between  $d_{\text{PbS}} = 0.8\text{--}10$  nm. The multilayers were grown on 50 nm thick PbS buffer layer using the method of vacuum evaporation of EuS and PbS on monocrystalline substrates. The measurements of the longitudinal MOKE were carried out in the temperature range 3–35 K in liquid helium continuous-flow cryostat. The external magnetic field ( $H \leq 150$  Oe) was applied in the plane of the multilayer. The angle of incidence of light on the layer was about 30 degrees. In order to establish the optimal experimental conditions we studied the spectral dependence of the Kerr effect in EuS-PbS in the wavelength range  $\lambda = 500\text{--}825$  nm covering the fundamental electronic transitions in EuS. In agreement with the experimental data for bulk EuS crystals, we found two maxima of Kerr rotation: for  $\hbar\omega = 1.65$  eV (corresponding to the absorption edge of EuS), and for  $\hbar\omega = 2.1$  eV (corresponding to the maximum of absorption in EuS) [1, 2]. In our measurements we used the wavelength  $\lambda = 625$  nm which corresponds to the second maximum.



## 2. Discussion and conclusions

Two representative magnetic hysteresis loops of EuS-PbS multilayers obtained from Kerr rotation measurements are shown in Fig. 2. The EuS-PbS structures grown on BaF<sub>2</sub> (111) show a much softer loop than those grown on KCl (001) substrates. The former show a magnetic remanence of about 95%, whereas the remanence of the latter is only about 20%. The strong reduction of the magnetic remanence in EuS-PbS/KCl multilayers results from the presence of the antiferromagnetic coupling between EuS layers. This conclusion is supported by the characteristic temperature dependence of magnetization observed in antiferromagnetically coupled layers. While the structures with the thick PbS spacer ( $d_{\text{PbS}} > 2$  nm) show the standard mean-field-like increase of the magnetization with the decreasing temperature, the structures with thinner spacer ( $d_{\text{PbS}} \simeq 1$  nm) show an anomalous non-monotonic dependence of  $M(T)$  in low external magnetic fields ( $H \leq 30$  Oe). The “normal”  $M(T)$  behavior is observed only in the presence of sufficiently high external magnetic fields ( $H \geq 40$  Oe). These experimental findings can be explained in a simple model that considers the temperature dependent competition of the Zeeman energy of magnetic layers in external magnetic field (which favors ferromagnetic alignment of magnetization vectors of all EuS layers), and the exchange energy of antiferromagnetic interlayer coupling (which favors antiferromagnetic alignment of magnetization in coupled layers). The decrease in the net magnetic moment with the decrease in temperature is due to the increasing strength of antiferromagnetic interlayer coupling. Our theoretical simulations of the  $M(T)$  curve with the inclusion of the antiferromagnetic interlayer coupling and using a mean-field Weiss theory for the description of magnetization of EuS layers qualitatively reproduce the observed anomaly. No anomaly in the temperature dependence of the magnetization is observed in all the structures grown on BaF<sub>2</sub> (111) substrates, even for samples with very thin PbS spacer layers ( $d_{\text{PbS}} \simeq 1$  nm). This result is consistent with our suggestion concluded from the qualitative analysis of the Kerr hysteresis loops and favors the explanation that the high remanence in the structures grown on BaF<sub>2</sub> indicates that the magnetic layers are ferromagnetically coupled.

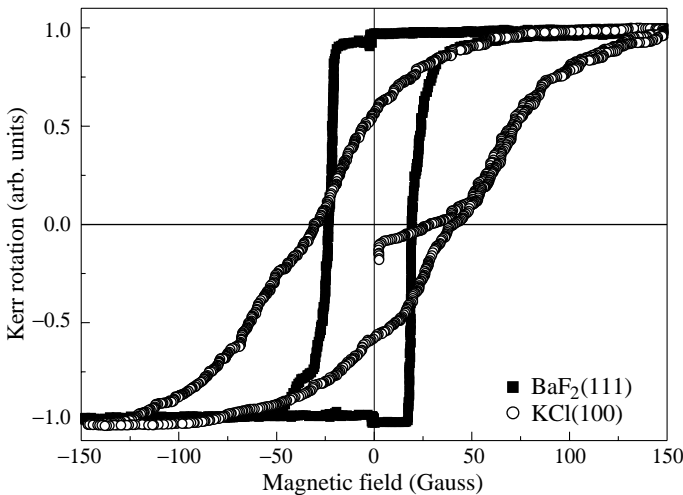


**Fig. 2.** The characteristic Kerr rotation (magnetization) hysteresis loops for EuS-PbS multilayers grown on KCl(100) and BaF<sub>2</sub> (111) substrates.

In conclusion, our study of magnetic properties of EuS-PbS multilayers shows the presence of antiferromagnetic interlayer coupling (of the order of  $0.01 \text{ mJ/m}^2$  for 1 nm PbS spacer) in films grown along (100) crystallographic direction (both on KCl (100) and PbS (100) substrates). For EuS-PbS multilayers grown along (111) direction (on  $\text{BaF}_2$  substrates), ferromagnetic interlayer coupling is observed. This is in agreement with the recent study of the interlayer coupling in EuS-PbS/KCl and EuS-PbS/ $\text{BaF}_2$  applying neutron techniques [5].

### Acknowledgements

This work was partially supported by the Committee for Scientific Research (KBN) project No. 2 P03B 154 18 and within European Community program ICA1-CT-2000-70018 (Center of Excellence CELDIS). We acknowledge the cooperation with the group of prof. W.J.M. de Jonge (Eindhoven University of Technology).

### References

- [1] A. Mauger and C. Godart, *Phys. Reports* **141**, 51 (1986).
- [2] I. V. Kolesnikov, V. A. Litvinov, A. Yu. Sipatov, A. I. Fedorenko and A. E. Yunovich, *Zh. Eksp. Teor. Fiz.* **94**, 239 (1988).
- [3] I. Stolpe, N. Puhlmann, O. Portugal, M. von Ortenberg, W. Dobrowolski, A. Yu. Sipatov and V. K. Dugaev, *Phys. Rev B* **62**, 16798 (2000).
- [4] A. Stachow-Wójcik, T. Story, W. Dobrowolski, M. Arciszewska, R. R. Gałązka, M. W. Kreijveld, C. H. W. Swüste, H. J. M. Swagten, W. J. M. de Jonge, A. Twardowski and A. Yu. Sipatov, *Phys. Rev. B* **60**, 15220 (1999).
- [5] H. Kępa, J. Kutner-Pielaszek, J. Blinowski, A. Twardowski, C. F. Majkrzak, T. Story, P. Kacman, R. R. Gałązka, K. Ha, H. J. M. Swagten, W. J. M. de Jonge, A. Yu. Sipatov and T. M. Giebultowicz, *Europhys. Lett.* **56**, 54 (2001).

## Raman studies as a tool for characterization of the strained hexagonal GaN/Al<sub>x</sub>Ga<sub>1-x</sub>N superlattices

V. Yu. Davydov<sup>†</sup>, A. N. Smirnov<sup>†</sup>, I. N. Goncharuk<sup>†</sup>, R. N. Kyutt<sup>†</sup>,  
M. P. Scheglov<sup>†</sup>, M. V. Baidakova<sup>†</sup>, W. V. Lundin<sup>†</sup>, E. E. Zavarin<sup>†</sup>,  
M. B. Smirnov<sup>‡</sup>, S. V. Karpov<sup>‡</sup> and H. Harima<sup>§</sup>

<sup>†</sup> Ioffe Physico-Technical Institute, St Petersburg, Russia

<sup>‡</sup> Fock Institute of Physics, St Petersburg State University, 198904  
St Petersburg, Russia

<sup>§</sup> Department of Electronics and Information Science, Kyoto Institute of Technology,  
Matsugasaki, Sakyo-ku, Kyoto 606-8585, Japan

**Abstract.** It is shown that such parameters of GaN/Al<sub>x</sub>Ga<sub>1-x</sub>N superlattice as the period, build-in strain, composition of the alloy, and individual layer thicknesses can be extracted from the energy positions, intensities, and line shapes of various optical and acoustical modes detected in Raman scattering.

### 1. Introduction

Recent progress in the growth technology of III–V nitrides such as GaN, AlN and Al<sub>x</sub>Ga<sub>1-x</sub>N alloys has made possible the demonstration of different optoelectronic devices based on this important class of semiconductors. Semiconductor superlattices (SLs) are of great interest because of their unique physical properties and potential for device applications. At present there is a growing need for precise non-destructive characterization of these nanostructures. One of the most efficient, sensitive, and direct techniques for the quantitative characterization of SLs is Raman spectroscopy [1, 2]. However, only fundamental problems of lattice dynamics in GaN/AlN or GaN/Al<sub>x</sub>Ga<sub>1-x</sub>N SLs were studied by Raman spectroscopy in a few works [3, 4]. The goal of our work was to show that many important parameters of GaN/Al<sub>x</sub>Ga<sub>1-x</sub>N SLs can be extracted from Raman measurements.

### 2. Sample characterization

The structures were grown by MOCVD and consisted of 500–1000-nm GaN or Al<sub>x</sub>Ga<sub>1-x</sub>N buffer layers grown directly on sapphire substrates followed by SLs [5]. The SL period was varied from 2.5 nm to 40 nm. The GaN well and Al<sub>x</sub>Ga<sub>1-x</sub>N barrier thicknesses were equal, and the total thickness of every SL was about 3 microns. The SLs were characterized by x-ray diffraction, electron probe microanalysis (EPMA), and atomic force microscopy (AFM). By fitting the simulating rocking curves to the experimental ones, the SL period, Al content in the alloy, and the strain in the alternating layers were estimated. The SL parameters obtained from AFM measurements correlated well with the x-ray measurements. Raman spectra of GaN/Al<sub>x</sub>Ga<sub>1-x</sub>N SLs were measured in a backscattering configuration at room temperature, with an Ar<sup>+</sup> laser ( $\lambda = 488$  nm) excitation.

### 3. Experimental results and discussion

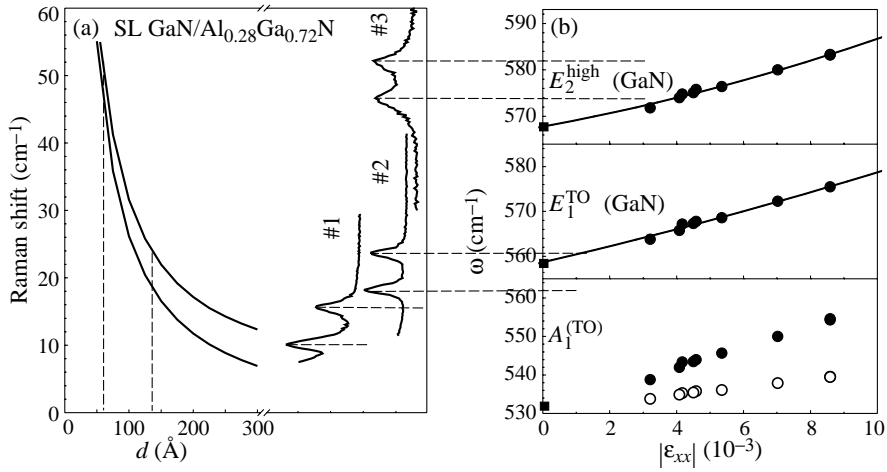


**Fig. 1.** (a) Calculated frequencies of the first folded-acoustic doublets as a function of SL period  $d$  ( $q = 6 \times 10^5 \text{ cm}^{-1}$ ). Raman spectra of SLs with different  $d$  are shown in the right part of the panel. (b) Top and middle panels: the positions of  $E_2(\text{high})$  and  $E_1(\text{TO})$  optical modes as functions of in-plane strain in SLs. Bottom panel: the measured positions of the  $A_1(\text{TO})$  line (full circles) and the positions of this line derived from the strains in SLs measured (open circles).

### 3.1. SL period

It was shown in Ref. [4] that the observed low-energy modes in the Raman spectra of  $\text{GaN}/\text{Al}_x\text{Ga}_{1-x}\text{N}$  SLs result from Brillouin-zone folding of the acoustic-phonon spectrum. We used the energy position of the folded phonons for an accurate determination of the SL period  $d$  in  $\text{GaN}/\text{Al}_x\text{Ga}_{1-x}\text{N}$  ( $x = 0.28$ ) SLs. The positions of the lines comprising the first folded doublet as functions of the SL period were calculated in the elastic continuum limit [6]. The sound velocity of  $\text{Al}_x\text{Ga}_{1-x}\text{N}$  alloy at  $x = 0.28$ , used in calculations, was obtained from our measurements. At first the value of average sound velocity  $v = 8600 \text{ m/s}$  was estimated from splitting of the doublets detected in Raman spectra. Then a sound velocity in the alloy of  $v_2 = 9200 \text{ m/s}$  was extracted from  $v$  [6]. Figure 1a shows calculated curves and the spectra of SLs with different periods. It is seen that the folded-acoustic-phonon doublet shifts to higher energies with decreasing SL period. By comparing the positions of the doublets with the calculated energies, we found the SL periods to be  $d = 225 \text{ Å}$  (No. 1),  $d = 135 \text{ Å}$  (No. 2), and  $d = 60 \text{ Å}$  (No. 3). The results obtained from Raman measurements are in excellent agreement with x-ray and AFM measurements.

### 3.2. Build-in strain

As our studies of SLs have shown,  $E_2(\text{high})$  and  $E_1(\text{TO})$  optical phonons can be regarded as the modes confined to their respective layers. It was also found that, due to a high scattering efficiency, the  $E_2(\text{high})$  and  $E_1(\text{TO})$  phonons observed in the Raman spectra can be ascribed to the GaN layer. The frequency positions of these modes in the SLs with different periods and alloy compositions were measured. The analysis of the data leads to the conclusion that the positions of the  $E_2(\text{high})$  and  $E_1(\text{TO})$  phonons can be explained by the build-in strain. The strain in GaN layers inferred from Raman data using phonon deformation potentials from [7] was found to be consistent with the strains estimated from

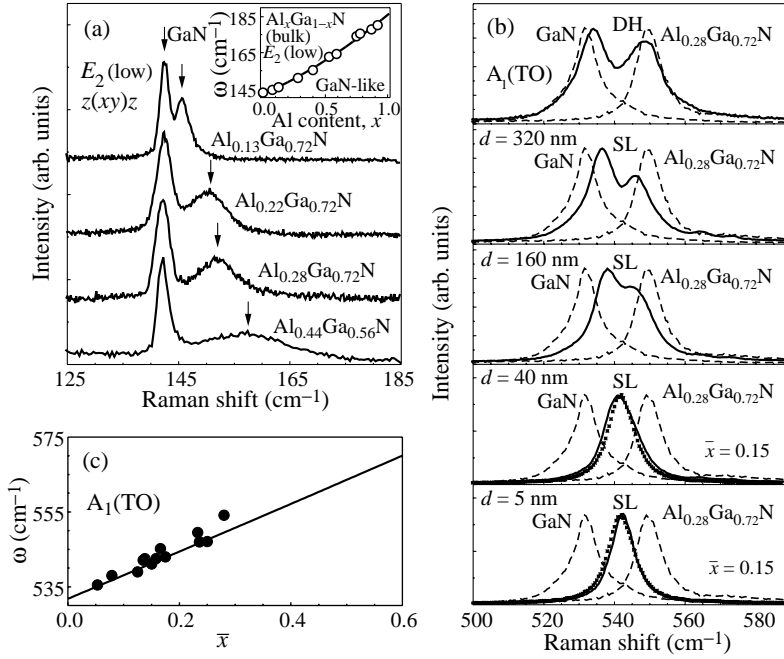


**Fig. 2.** (a) Raman spectra of SLs with different Al contents in the region of the  $E_2(\text{low})$  phonon. (b) Raman spectra of SLs for the scattering geometry corresponding to the  $A_1(\text{TO})$  phonon. (c) Behavior of  $A_1(\text{TO})$  phonon mode as a function of Al content averaged over SL period.

x-ray diffraction data. Figure 1b shows the positions of the  $E_2(\text{high})$  and  $E_1(\text{TO})$  GaN-like Raman lines as functions of the in-plane strain in SLs. A high sensitivity of the  $E_2(\text{high})$  and  $E_1(\text{TO})$  phonons to the build-in strain is convenient for estimating this parameter in GaN/ $\text{Al}_x\text{Ga}_{1-x}\text{N}$  SLs. Positions of the  $E_2(\text{high})$  and  $E_1(\text{TO})$  phonons as a functions of in-plane strain can be approximated by:

$$E_2(\text{high}) = 567.8 + 1.38 |\varepsilon_{xx}| \times 10^3 - 0.06 |\varepsilon_{xx}| \times 10^3 (1 - |\varepsilon_{xx}| \times 10^3) \text{ and} \\ E_1(\text{TO}) = 558.8 + 1.76 |\varepsilon_{xx}| \times 10^3 - 0.03 |\varepsilon_{xx}| \times 10^3 (1 - |\varepsilon_{xx}| \times 10^3).$$

The positions of the  $A_1(\text{TO})$  line measured in the same set of SLs are shown by full circles of the bottom panel of Fig. 1(b). The open circles show the positions of this line derived from the strain measured in SLs. It is seen that the shift of the  $A_1(\text{TO})$  line cannot be explained by the build-in strain. A more detailed description of the  $A_1(\text{TO})$  line behavior will be presented below.

### 3.3. Alloy composition

Figure 2(a) shows Raman spectra in the region of the  $E_2(\text{low})$  phonon for the SLs with the same period, but different alloy compositions. It is clearly seen that the  $E_2(\text{low})$  phonons can be regarded as the modes confined to their respective layers. It was established that the frequency positions of these modes exhibit a low sensitivity to the in-build strain. This fact and a high sensitivity of the  $E_2(\text{low})$  phonon to the Al content (see inset in Fig. 2a) are suitable for estimating the composition of alloys in GaN/ $\text{Al}_x\text{Ga}_{1-x}\text{N}$  SLs. The dependence of  $E_2(\text{low})$  mode on Al content can be approximated by equation  $E_2(\text{low}) = 142.8 + 43.5x - 14.5x(1-x)$ . Estimates of the alloy composition in SLs using this

equation are in good agreement with the data obtained by EPM measurements.

### 3.4. Average composition of SL

The  $A_1(\text{TO})$  phonon was observed as two lines corresponding to GaN and  $\text{Al}_x\text{Ga}_{1-x}\text{N}$  layers for the SLs with the periods larger than 160 nm. For the SLs with smaller periods, this phonon was detected as one line (Fig. 2(b)). Our studies revealed that the positions of this line correspond to the positions for the alloy with the Al concentration averaged over the SL period (Fig. 2(c)). These findings suggest that the  $A_1(\text{TO})$  phonon is a propagating mode rather than a confined one. This is consistent with the theoretical predictions [8] that some optical phonons in  $\text{GaN}/\text{Al}_x\text{Ga}_{1-x}\text{N}$  low-dimensional structures can be regarded as propagating due to the energy overlap between optical phonon regions of GaN and the alloy. From the position of the  $A_1(\text{TO})$  phonon, which is propagating through the whole SL and therefore reflects the average characteristics of the system, the average Al content in the structure can be obtained. Note that the propagating phonons are supposed to be insensitive to the strain due to different signs of strains in GaN and  $\text{Al}_x\text{Ga}_{1-x}\text{N}$  layers. The knowledge of three parameters  $x$ ,  $\bar{x}$ , and  $d$  gives the possibility to estimate individual layer thicknesses of the layers comprising the SL:  $\bar{x} = (d_2/d)x$ , where  $d = d_1 + d_2$ . It has been found that the difference in the layer thicknesses grows with increasing Al content in SL (Fig. 2(c)).

## 4. Summary

We have demonstrated that Raman scattering from folded acoustical modes can be used for accurate determination of the  $\text{GaN}/\text{Al}_x\text{Ga}_{1-x}\text{N}$  SL period. The knowledge of the specific features in the behavior of optical phonons in  $\text{GaN}/\text{Al}_x\text{Ga}_{1-x}\text{N}$  SLs provides the possibility to quantitatively estimate the build-in strain and alloy composition. Combined information about acoustical and optical phonons obtained from Raman scattering allows estimation individual layer thicknesses.

### Acknowledgments

This work is supported by the Programs “Low-dimensional Quantum Structures”, “Physics of Solid State Nanostructures”, RFBR (No 01-02-18011) and CRDF (grant No RP1-2258).

## References

- [1] B. Jusserand, D. Paquet *et al*, *Phys. Rev. B* **35**, 2808 (1987).
- [2] H. Brugger, G. Abstreiter *et al*, *Phys. Rev. B* **33**, 5928 (1986).
- [3] J. Gleize, J. Frandon *et al*, *Mat. Sci. Eng. B* **83**, 27 (2001).
- [4] V. Yu. Davydov, A. A. Klochikhin *et al*, *phys. stat. sol. (a)* **188**, 863 (2001).
- [5] W. V. Lundin, A. V. Sakharov *et al*, *phys. stat. sol. (a)* **188**, 885 (2001).
- [6] S. M. Rytov, *Akust. Zh* **2**, 71 (1956) [*Sov. Phys. Acoust.* **2**, 68 (1956)].
- [7] V. Yu. Davydov, N. S. Averkiev *et al*, *J. Appl. Phys.* **82**, 5097 (1997).
- [8] H. Grille and F. Bechstedt, *J. Raman Spectrosc.* **27**, 207 (1996).

## Plasma diagnostics of Ge-clusters in $\text{Si}_{1-x}\text{Ge}_x$ mixed crystals

*Yu. S. Gordeev*<sup>†</sup>, *V. M. Mikoushkin*<sup>†</sup>, *V. V. Brysgalov*<sup>†</sup>, *A. G. Zabrodskii*<sup>†</sup>,  
*M. V. Alekseenko*<sup>†</sup> and *H. Grimmeiss*<sup>‡</sup>

<sup>†</sup> Ioffe Physico-Technical Institute, St Petersburg, Russia

<sup>‡</sup> Lund University, SE-221 00 Lund, Sweden

**Abstract.** Mixed Crystals of  $\text{Si}_{1-x}\text{Ge}_x$  ( $x < 0.05$ ) grown by the method of zone melting have been studied by Electron Energy Loss Spectroscopy (EELS) in recoil. The contribution of Ge-bulk plasmon spectrum was revealed in the plasmon spectra of Mixed Crystals, and the conclusion has been made that an essential part of Ge atoms are included into Ge clusters. Plasma diagnostics of clusters in SiGe alloys is suggested on the basis of EEL spectroscopy.

### Introduction

Mixed Crystal  $\text{Si}_{1-x}\text{Ge}_x$  films have found a place in Si-based electronics because of their higher mobility that increases the operating frequency of bipolar transistor (e.g. [1]). However, the progress in the field of designing high frequency devices in Si-based electronics has not met expectations in full scale. Imperfection of Mixed Crystals, namely structural and content inhomogeneities, was suggested to be a barrier on the way of the frequency increase of bipolar transistor [2–5]. Among these inhomogeneities, there may be dislocations, strain fluctuations that can be expected in dislocation-rich materials, content fluctuations and clusters. The last can be created by the decoration of the mentioned defects by impurities or by one of the alloy elements. Therefore the development of effective quantitative diagnostics of such objects is a key task of the problem of high frequency Si-based electronics. It is also important for general problem of cluster formation. The most prevalent way of study of the alloy inhomogeneity is at present a Transmission Microscopy (TM). Unfortunately the common version of this method is not a quantitative one. It does not give information about element and chemical composition of clusters, its resolution is limited in the region of small cluster sizes, and it implies destruction of initial sample in the course of thin film preparation. The task of identification of atom in cluster and determination of the amount of atoms in clusters may be correctly solved by x-ray Photoelectron Spectroscopy (XPS) taking into account chemical shift and intensity of photoelectron line. Though the XPS method is effective only for the essentially heterogeneous systems, such as metallic clusters in dielectric matrices (e.g. [6]). In the case of Ge clusters in Si-Ge alloy, this method is completely inapplicable because of coincidence of Ge-core level binding energies in bulk germanium [7] (or in Ge-cluster) and in Si-Ge alloy [8] due to similar electron structure of Ge and Si. Thus the conclusion can be made that there are no direct methods of determination of Ge amount in Ge clusters of Si-Ge alloys today. A new approach is suggested in this work for the solution of the pointed problem. This approach is based on the excitation and observation of local plasma oscillations (plasmon) of cluster electron system whose energy differs from those of matrix.

### 1. Experiment

Mixed Crystals of  $\text{Si}_{1-x}\text{Ge}_x$  (111) with germanium content  $x < 0.05$  were studied. The aim of the work was to determine the portion of the Ge atoms merged into clusters. Low

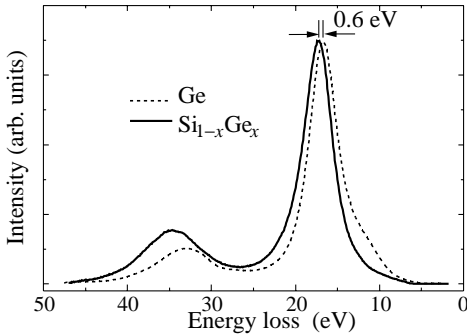


**Fig. 1.** EELS spectra of Ge (dashed line) and  $\text{Si}_{1-x}\text{Ge}_x$  ( $x = 3\%$ ) (solid line). The primary electron energy is  $E_0 = 1500$  eV. Zero loss-energy corresponds to the peak center of elastically scattered electrons.

germanium content was chosen in spite of the experimental difficulties because Si-rich ( $x < 0.05$ ) and Ge-rich ( $x > 0.95$ ) alloys are known as homogeneous ones contrary to the case of intermediate values of  $x$  when only polycrystals have been grown up to now [4]. SiGe Crystals were grown by electron beam crucibles zone melting. Two additional samples were used as the reference ones: samples with Ge content  $x = 0\%$  and  $x = 100\%$ , that is pure silicon and pure germanium crystals (111) also grown by zone melting. The bulk concentration of Ge had been preliminarily determined by x-ray microanalysis. Surfaces of different samples were polished and chemically etched by the same way. It led to the same roughness of different samples and made possible to compare Auger line intensities of these samples. Two  $\text{Si}_{1-x}\text{Ge}_x$  ( $x = 2.5\%$  and  $x = 5\%$ ) crystals and both reference samples were transferred first into the preparation chamber and then into the analytical chamber of the electron spectrometer “Leybold-11 AG”. The samples were heavily etched and cleaned from initial native oxide layer by  $\text{Ar}^+$  ions with an energy  $E_i = 2500$  eV in the first chamber. The major part of the amorphous layer was removed away by  $\text{Ar}^+$  ions with an energy  $E_i = 500$  eV in the second chamber. The pressure of residual gases was not higher than  $P = 2 \times 10^{-10}$  Torr. Nevertheless an essential rate of oxidation of upper monolayer by the oxygen of residual atmosphere was observed for the studied Mixed Crystals during long measurements needed for good statistics in the case of low Ge content. This rate was found to be much higher than that in the case of silicon wafer grown by the Chochralsky method. The oxidation extend was controlled by measuring the oxygen Auger line intensity and Si LVV Auger line shape. Relatively high oxidation rate of studied Si-Ge alloys is obviously related to the large concentration of defects and dislocations. The observed peculiarity might be used for the integral characterization of the defect concentration. The Ge content in the near surface layer ( $\approx 2$  nm) has been measured after ion etching by comparison of the Auger line intensity of Ge  $2p_{3/2}/23d^2$  line in  $\text{Si}_{1-x}\text{Ge}_x$  Mixed Crystal and in pure Ge. The Ge content turned out to be more than one third lower than in prior bulk measurements.

## 2. The idea and results of the plasma diagnostics

The suggested way of the Ge cluster diagnostics is based on the idea to observe a collective plasma excitation of electron system of rather large groups of Ge atoms. Separate Ge atoms incorporated into the alloy lattice can not take part in such an excitation on the contrary to any other electron excitations resulting for example in photo- or Auger emission. Another starting point of the diagnostics is an essential difference of plasma oscillation spectra (plasmon) in germanium and in silicon. This difference is illustrated by Fig. 1 which shows the Electron Energy Loss Spectra (EELS) in experiment with 1.5 keV electrons being reflected by surfaces of Si (oxidated up to  $\text{SiO}_2$  state) and Ge samples. The most prominent peak, whose center coincides with the onset of energy loss scale, corresponds



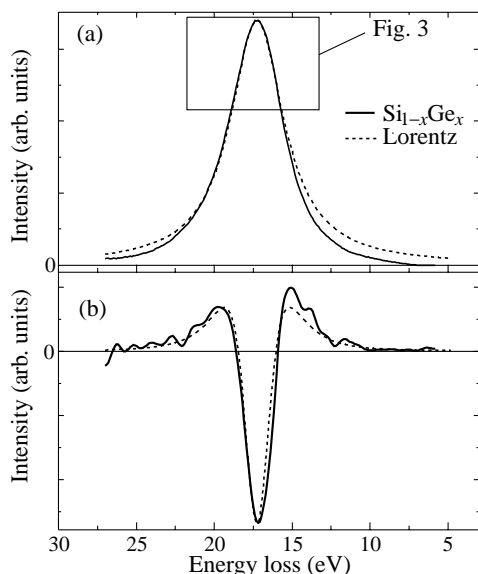


**Fig. 2.** (a) Initial EELS spectrum of  $\text{Si}_{1-x}\text{Ge}_x$  ( $x = 3\%$ ) alloy. (b) Its second derivative (solid line). Lorentz approximation is pointed by dashed line.

to the elastically scattered electrons. The next peaks correspond to the inelastic scattering with excitation of one or two bulk plasmons. It is seen that the energies of the Ge and Si plasmons are different. Figure 1 demonstrates the plasmon energy difference of about 0.6 eV. (Note that this difference strongly depends on the extent of the alloy oxidation: the smaller oxidation the larger difference.) Thus, the problem of the content determination of the Ge atoms incorporated into Ge clusters is reduced to the routine problem of the decomposition of plasmon peak of SiGe alloy into composing plasmon peaks of Ge and Si likewise the decomposition of any complicated spectral lines (e.g. XPS lines). It is assumed here that the plasmon energy of the  $\text{Si}_{1-x}\text{Ge}_x$  alloy with low Ge content ( $x < 5\%$ ) is close to that of pure Si, and that the plasmon energy of Ge cluster is close to that of the bulk Ge.

Figure 2(a,b) shows the initial plasmon spectrum of  $\text{Si}_{1-x}\text{Ge}_x$  ( $x = 3\%$  according to the Auger measurements) alloy measured with a very good statistics after background subtracting and its second derivative (solid line). The important feature of this starting stage of the research is that the spectrum was measured at the moment when the surface of the sample was practically completely oxidized in high vacuum chamber in the course of long measurements. It made minimal (0.6 eV) the difference between plasmon energies of alloy and Ge. But there were no plasmon energy shifts due to the redistribution of the intensities of the plasmon energies of Si and  $\text{SiO}_2$  during the measurement. The spectrum shown in Fig. 2 was measured by the multiply scanning procedure with a very good statistics. Dashed line corresponds to the approximation of the experimental spectrum by Lorentz function and its derivative. Lorentz function was taken because the natural widths of the plasmon peaks are much larger than the apparatus width estimated from the peak of elastically scattered electrons (Fig. 1). This function can not describe adequately the tails of the initial experimental line, probably because of rather rough line procedure of background subtraction. (The validity of this procedure is in a low background intensity). Nevertheless the tails are completely described in the differentiated spectrum. Much attention was given to the good description of the main part of the line where the bulk plasmons of Si-Ge alloy (or Si) and Ge are centered. This part is represented in Fig. 3 in more details. It can be seen that studied spectra of SiGe alloy, both initial and especially differentiated, can not be completely

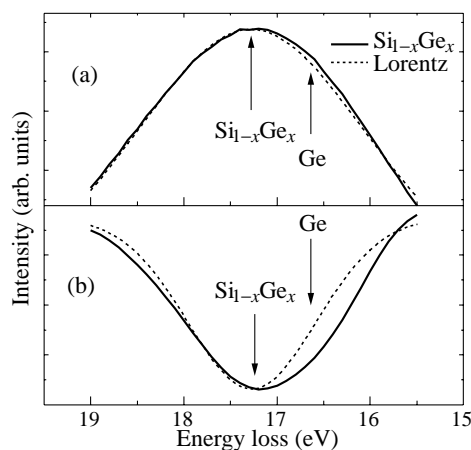


**Fig. 3.** EELS spectra of Fig. 2 represented in narrower loss-energy region in more details.

described by the single Lorentz line of Si (Fig. 2(a)). Some small contribution of the Ge plasmon is necessary to describe the complete spectrum.

Thus, the conclusion can be made that an essential part of Ge atoms of studied  $\text{Si}_{1-x}\text{Ge}_x$  ( $x < 0.05$ ) Mixed Crystals are included into Ge clusters. The size region of the displayed Ge rich particles can be ranged from the large segregates to clusters consisting of only several atoms, taking into account that plasmons can be excited in very small supported clusters [9]. More accurate determination of the Ge amount in clusters seems possible by increasing accuracy of EEL spectra measurements and background subtracting. The sensitivity and accuracy of the suggested diagnostics may be increased also by studying pure samples without oxide phases because the plasmon energy difference is much larger in this case. As a conclusion, plasma diagnostics of clusters in SiGe alloys is possible on the basis of EEL spectroscopy.

#### Acknowledgements

This work was supported by the Russian Academy of Sciences (Program “Low Dimensional Quantum Structures”), the Russian MNTF (Program “Nanostructures”), and by Swedish Academy of Sciences.

#### References

- [1] D. L. Harnage, J. H. Comfort, J. D. Cressler, E. F. Crabbe, J. Y. -C. Sun, B. S. Meyerson and T. Tice, *IEEE Trans. Electron. Devices* **42**, 455 (1995).
- [2] E. -L. Hellqvist, V. Nagesh, H. G. Grimmeiss *et al*, *Appl. Phys. A* **53**, 43 (1991).
- [3] G. Kissinger and H. G. Grimmeiss, *Phys. Stat. Sol. (a)* **145**, K5 (1994).
- [4] A. G. Zabrodskii, V. A. Evseev, R. F. Konopleva *et al*, *Sov. Phys. Semicond.* **20**, 1278 (1986).
- [5] W. Jantsch, Z. Wilamowski, N. Sandersfeld and F. Schaffler, *Physica B* **273-274**, 944, (1999).
- [6] S. A. Gurevich, *et al.*, T. A. Zarskaya, S. G. Konnikov, V. M. Mikoushkin, S. Yu. Nikonov, A. A. Sitnikova, S. E. Sysoev, V. V. Khorenko, V. V. Shnitov and Yu. S. Gordeev, *Appl. Phys. Lett.* **764**, 2031 (1994).
- [7] D. Briggs and M. P. Sikh, *Practical Surface Analysis by Auger and x-ray Photoelectron Spectroscopy*, John Wiley & Sons (1983).
- [8] E. A. Ogryzlo, L. Zheng, B. Heinrich, K. Myrtle and H. Lafontaine, *Thin Solid Films* **321**, 196 (1998).
- [9] V. M. Mikoushkin, *Technical Physics* **44**, 1077 (1999).

## Time resolved nonlinear surface plasmon optics

*Yu. E. Lozovik*<sup>†</sup>, *S. P. Merkulova*<sup>†</sup>, *M. M. Nazarov*<sup>‡</sup>, *A. P. Shkurinov*<sup>‡</sup>  
and *P. Masselin*<sup>§</sup>

<sup>†</sup> Institute of Spectroscopy, 142190 Moscow region, Troitsk, Russia

<sup>‡</sup> Department of Physics and International Laser Center, Moscow State University, Moscow, 119899, Russia

<sup>§</sup> Laboratoire de PhysicoChimie de l'Atmosphere, CNRS UMR 8101, Universite du Littoral, 145 avenue Maurice Schumann, 59140, Dunkerque, France

**Abstract.** A new surface-sensitive method of time-resolved optical studies is proposed. The method consists in the independent excitation of several surface electromagnetic waves (SEW) by two laser femtosecond pulse beams with varied time delay  $\Delta\tau$  and distance  $\Delta r$  between corresponding excitation regions on surface. To fulfill phase matching condition for plasmon-photon coupling metal grating is used. Due to nonlinear plasmon interaction, the optical radiation with  $\omega_1 + \omega_2$  and  $2\omega_1 - \omega_2$ , (where  $\omega_1, \omega_2$  are correspondent laser beam frequency) is generated. The intensity of this nonlinear response *versus*  $\Delta\tau$  and  $\Delta r$  are studied. The direct measurements of the SEW temporal properties are presented. Experiments of this type are important for the development of the femtosecond surface plasmon optics for study of ultrafast phenomena in nanostructures.

The use of surface electromagnetic wave (SEW) is an effective tool for interface studies. SEW have various applications in matter diagnostics, nonlinear optics and spectroscopy. Many optical effects are difficult to observe, because of a weak nonlinear response or small amount of substance. To avoid this difficulty, one can concentrate laser radiation energy in space and time. The advantage of using SEW is the concentration of light energy near the interface. Special experimental geometry can be used to fulfill phase matching condition for effective SEW excitation. We use metal grating for this purpose. It is essential for nonlinear processes to have high peak intensity, but the average field must be moderated, otherwise the sample will be damaged. Femtosecond laser pulses fit to these requirements.

In the present work we suggest new surface-sensitive method of time-resolved studies based on the use of interacting SEW, excited by two femtosecond laser beams with varying time delay and distance between corresponding excitation regions on the surface. This interaction leads to the generation of optical waves at frequency equal to the second harmonic or the sum frequency of incoming beams. Four waves mixing (FWM) process  $2\omega_1 - \omega_2$  is also investigated. We are mainly interested in temporal behavior to demonstrate that time-resolved studies on a grating surface can potentially have temporal resolution up to few femtosecond. The sensitivity and selectivity to the properties of the surface are achieved with the second-harmonic (SHG) and sum frequency generation (SFG) processes because these processes are forbidden in the bulk of the isotropic medium. The results show that our method based on the interaction of noncollinear SEW has femtosecond time-resolution and much more possibilities for experimental realizations in comparison with other surface-sensitive optical techniques.

We carry out experiments in different geometry of the incoming beams. Collinear

scheme is used in the case of degenerated SFG. We demonstrate the possibility of non-collinear experiments on the example of degenerated and nondegenerated SFG and FWM.

The SEW is generated according to the relation  $\mathbf{k}_{t,i}^\omega + n_i \mathbf{q} = \mathbf{K}_{\text{SEW},i}^\omega$ , where  $i = 1, 2$  denote beam number,  $\mathbf{q} = 2\pi/d$  is reciprocal lattice vector,  $d$  is grating period,  $\mathbf{k}_{t,i} = \mathbf{k}_i \sin \theta_i$  is laser radiation wave vector projection on a grating plane,  $\theta_i$  is the angle of incidence of laser beam relative to the normal of the grating,  $n_i$  is diffraction order.  $\mathbf{K}_{\text{SEW},i}^\omega$  is SEW wave vector.

The generated SEW waves radiate waves at combinational optical frequency if phase matching conditions for optical waves at frequencies  $\omega_1$  and  $\omega_2$  are satisfied simultaneously with the relation between interacting SEW wave vectors:  $\mathbf{K}_{\text{SEW},1}^{\omega_1} + \mathbf{K}_{\text{SEW},2}^{\omega_2} + n_3 \mathbf{q} = \mathbf{k}_{t,3}^{\omega_1 + \omega_2}$  for nondegenerated SFG and  $2\mathbf{K}_{\text{SEW},1}^{\omega_1} - \mathbf{K}_{\text{SEW},2}^{\omega_2} \pm \mathbf{q} = \mathbf{k}_{t,3}^{2\omega_1 - \omega_2}$  for FWM process. The angle  $\varphi$  is the angle between the optical wave vector and the reciprocal lattice vector of the grating. The proper choice of angles  $\varphi$  and  $\theta$  leads to simultaneous satisfaction of phase matching condition of surface plasmon excitation and of the nonlinear process. We highlight that when  $\varphi$  is equal to 90 degree (symmetrical case) excitation of two SEWs with wave vectors  $\mathbf{k}_t^\omega + \mathbf{q}$  and  $\mathbf{k}_t^\omega - \mathbf{q}$  respectively takes place simultaneously.

First we describe the case of two collinear plasmon interaction in symmetrical scheme ( $\varphi = 90^\circ$ ) with  $\omega_1 = \omega_2 = \omega$ . We measure the emission of signal at frequency  $2\omega$  and compare it with the autocorrelation function (ACF) of the fundamental beams. When spatial and temporal overlapping of the pulses occurs degenerated collinear SFG wave is radiated in specular direction. SFG is recorded as function of the delay (plasmon correlation function PCF). This experimental scheme is the same as in an autocorrelator.

We perform the same experiment in a noncollinear geometry. In this geometry SHG from each beam and degenerated SFG occurs. SFG wave vector projection on the surface is  $\mathbf{k}_{t,3}^{2\omega} = \mathbf{K}_{\text{SEW},1}^\omega + \mathbf{K}_{\text{SEW},2}^\omega$  and then the SFG signal emission occurs in the direction  $\theta_3 \approx (\theta_1 + \theta_2)/2$ , different from  $\theta_1$  and  $\theta_2$ . The recorded signal is then background free.

We realise also noncollinear nondegenerate SFG and FWM with two synchronised femtosecond laser beams with different frequencies. Symmetrical scheme is used for both beams with frequencies  $\omega_1$  and  $\omega_2$  like in the degenerate collinear scheme. Beams have different incidence angles as in degenerate noncollinear scheme. To characterize laser pulses we use cross-correlation function (CCF) of beam 1 and beam 2 pulses.

At SEW excitation we observe four nonlinear signals  $2\omega_1$ ,  $2\omega_2$ ,  $\omega_1 + \omega_2$ ,  $2\omega_1 - \omega_2$  separated in frequencies and in radiation emission angle. Note that  $2\omega_1 - \omega_2$  process has different nature, it is third order nonlinear process and its efficiency is determined by  $\chi_3$  not by  $\chi_2$ . Where  $\chi_2$  and  $\chi_3$  are correspondent nonlinear susceptibility tensors. Such properties as spectral width, pulse duration, polarization direction for FWM proved to be different from second order processes — SHG, SFG — for our experimental conditions. FWM absolute intensity is higher than SFG or SHG.

The PCF signal is the cross-correlation of SEW<sub>1</sub> and SEW<sub>2</sub> fields. In turn SEW field is the convolution of the plasmon lifetime  $\tau_{pl}$  and laser pulse duration. From the comparison of ACF and PCF duration it is then possible to obtain the plasmon lifetime. In the symmetrical (collinear and degenerated) SFG case we measure the SEW lifetime to be 70 fs. For nonsymmetrical case (noncollinear degenerate) this lifetime decreases to 20 fs. For nondegenerate symmetrical noncollinear case SEW lifetime (60 fs) is smaller than in degenerate symmetrical case due to higher SEW absorption on frequency of  $\omega_2$ . But it is greater than in nonsymmetrical case.

As plasmon propagates on the metal surface it exponentially decays (in time and in space) through several channels: Ohmic losses, radiation damping and Landau damping.

Besides metal is also in nonequilibrium state after SEW excitation and absorption, and electron relaxation can manifest itself in measured values.

In principle in time resolved SEW experiments it is possible to observe not only SEW lifetime, but also interface relaxation time through processes described above, if a parameter of nonlinear process depends essentially on temperature or metal electrons distribution.

In conclusion, the method of femtosecond surface plasmon spectroscopy is suggested and experimentally demonstrated. It is based on resonance excitation of several surface SEWs by femtosecond synchronised laser beams. These SEWs interact on the surface, allowing us to enhance various nonlinear optical effects, sensitive to the surface properties. That was demonstrated in the present work on the sum-frequency generation and four-wave mixing process. Nonlinear optical response originated from the interacting SEWs reflects the spatial and temporal behaviour of these SEWs. As an example, we measured the SEW lifetime on the surface of the gold grating, which proved to be 60 fs for symmetrical case and less than 20 fs for nonsymmetrical case. For the first time we observed simultaneously SHG, SFG and FWM enhanced by SEW on the grating. The described experiments open practical possibility for the development of time-resolved femtosecond surface plasmon optics and spectroscopy for study of ultrafast phenomena in nanostructures on the surface.

#### *Acknowledgements*

The authors thank Yu. P. Strelnikov for gratings fabrication, A. V. Balakin and I. A. Ozheredov for assistance in the experiments. The work was supported by INTAS, RFBR and Program "Physics of Solid Nanostructures".

## Quantum-dot-like composition fluctuations in near-field magneto-photoluminescence spectra of InGaAsN alloys

A. M. Mintairov<sup>†‡</sup>, P. A. Blagnov<sup>†</sup>, J. L. Merz<sup>‡</sup>, V. M. Ustinov<sup>†</sup>, A. S. Vlasov<sup>†</sup>,  
A. R. Kovsh<sup>†§</sup>, J. S. Wang<sup>§</sup>, L. Wei<sup>§</sup> and J. Y. Chi<sup>§</sup>

<sup>†</sup> Ioffe Physico-Technical Institute, St Petersburg, Russia

<sup>‡</sup> Dept. of Electrical Engineering, University of Notre Dame, IN 46556, USA

<sup>§</sup> Industrial Technology Research Institute, Hsinchu, Taiwan

**Abstract.** A series of narrow emission lines (halfwidth 0.5–2 meV) corresponding to quantum-dot-like compositional fluctuations have been observed in low temperature near-field photoluminescence spectra of GaAsN and InGaAsN alloys. The estimation of the size, density, and nitrogen excess of individual compositional fluctuations (clusters) using scanning near-field magneto-spectroscopy reveals phase-separation effects in the distribution of nitrogen. We found a strong effect of In on the exciton  $g$ -factor in InGaAsN alloys.

### Introduction

In<sub>x</sub>Ga<sub>1-x</sub>As<sub>1-y</sub>N<sub>y</sub> ( $x \sim 0-0.08$ ,  $y \sim 0-0.05$ ) alloys have recently attracted considerable attention as promising materials for laser diodes in the 1.3–1.5  $\mu\text{m}$  range as well as more efficient solar cells. In the present paper we use near-field magneto-photoluminescence measurements to study optical and structural properties of quantum-dot-like compositional fluctuations in InGaAsN alloys with the different nitrogen ( $y = 0.01$  and  $0.03$ ) and indium ( $x = 0, 0.03$  and  $0.08$ ) content. We found an increase of the cluster size and decrease of their density with increasing N content. We also observed an increase of the exciton  $g$ -factor with increasing In content.

### 1. Experiment

Coherently strained GaAs<sub>1-y</sub>N<sub>y</sub> and lattice matched In<sub>x</sub>Ga<sub>1-x</sub>As<sub>1-y</sub>N<sub>y</sub> ( $x \sim 0.03-0.08$ ,  $y \sim 0.01-0.03$ ) layers with thickness 0.1–1  $\mu\text{m}$  were grown by solid source MBE on (001) semi-insulating GaAs substrates at temperature 450–520 °C.

Near-field photoluminescence (NPL) spectra with spatial and spectral resolution of 300 nm and 0.4 nm (0.5 meV), respectively, were taken in collection-illumination mode. The spectra were excited by 20 mW of Ar ion laser excitation at 514.5 nm, measured in the temperature range 5–300 K and magnetic field strengths 0–10 T.

### 2. Results and discussion

#### 2.1. Near-field spectra

In Fig. 1(a) we present 5 K NPL spectra of two GaAsN ( $x = 0$ ) layers having  $y = 0.01$  and  $0.03$  and one InGaAsN ( $x = 0.37$ ) multiple quantum well having  $y = 0.02$ . Figure 1(b) shows Gaussian contour decomposition of the InGaAsN layer having  $x = 0.08$  and  $y = 0.03$ . We can see that the spectra of all samples reveal structure, consisting of the series of multiple narrow lines (halfwidth  $\gamma = 0.05-2$  meV) superimposed on broader

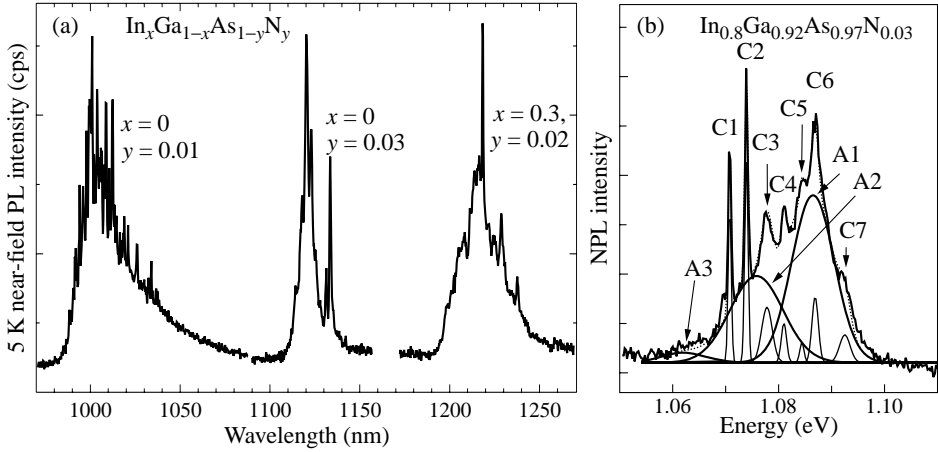


**Fig. 1.** (a) 5 K-near-field spectra of GaAsN layers (left  $y = 0.1$  and central  $y = 0.03$ ) and InGaAsN MQW (right  $x = 0.37$ ,  $y = 0.02$ ); (b) experimental (thick solid) and multiple Gaussian peak modeling (dotted — whole spectra and thin solid — constituents) of 5 K near-field PL spectra of  $\text{In}_{0.08}\text{Ga}_{0.92}\text{As}_{0.97}\text{N}_{0.03}$ .

( $\gamma = 20\text{--}60$  meV) band. We denote narrow lines as C1, C2 ... Cn (see Fig. 1(b)). We can resolve up to 30 C-lines for  $y = 0.01$  and up to 10 lines for  $y = 0.03$ . Thus the number of lines decrease with increasing N content. We observed that C-lines disappear in the spectra at temperatures above 70 K [1].

We attribute the C-lines to emission of excitons localized on QD-like composition fluctuations (N-rich clusters). Using temperature dependent near-field spectroscopy we estimated the exciton localization energy in the cluster to be 10–60 meV for  $T = 5$  K [1, 2].

## 2.2. Magneto-NPL spectra

We used magneto-photoluminescence measurements to estimate the size of the composition fluctuations. Figure 2(a-d) presents the magnetic field dependence of the C-lines in the GaAsN (a, c) and InGaAsN (b, d) samples having nitrogen content 0.01 (a, b) and 0.03 (c, d). We did not observe Zeeman splitting (zero exciton  $g$ -factor) of the C-lines in GaAsN. But InGaAsN has clear Zeeman splitting (subscript H and L denote high and low energy components in Fig. 2(b, d)). The splitting energy increased with increasing In content and has values of 0.7 ( $g$ -factor  $\sim 1$ ) and 1.7 ( $g$ -factor  $\sim 2$ ) meV at 10 T for  $y = 0.01$  and 0.03, correspondingly. Strong dependence of the Zeeman splitting in InGaAsN on In content can be related to a large value of the electron  $g$ -factor of InAs ( $-15$ [3]) compared with the same in GaAs ( $-0.44$ [3]) and in GaN[4].

We observed a clear diamagnetic shift for the C-lines in both GaAsN and InGaAsN alloys. We found that the value of the diamagnetic coefficient ( $\beta$ ) increases with increasing N content but shows little dependence on the presence of In (see Fig. 3(a)).  $\beta$  has values  $0.3\text{--}3 \mu\text{eV/T}^2$  for  $y = 0.01$  and  $3\text{--}12 \mu\text{eV/T}^2$  for  $y = 0.03$ . The cluster radius for different emission energies deduced from  $\beta$  [3] is presented in Fig. 3(b). It has average value 6 and 10 nm for  $y = 0.01$  and 0.03 correspondingly.

## 2.3. NPL imaging

Figure 4 presents selected spectra and monochromatic NPL intensity images (scans a-e) of the  $2 \times 2 \mu\text{m}$  area of the  $\text{GaAs}_{0.99}\text{N}_{0.01}$ , revealing spatial resolution of 300 nm (seen upper left section in scan c and in scan e).

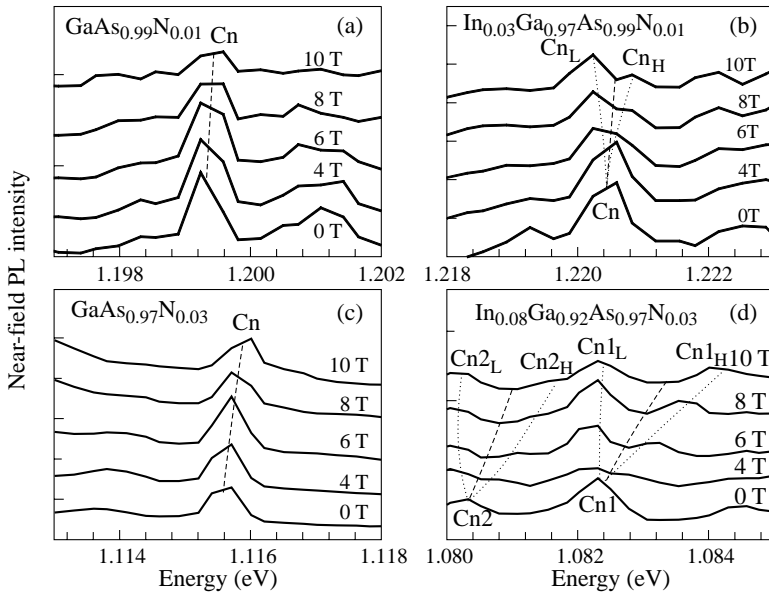


**Fig. 2.** 5 K near-field PL spectra of  $\text{In}_x\text{Ga}_{1-x}\text{As}_{1-y}\text{N}_y$ : (a)  $x = 0$ ,  $y = 0.01$ ; (b)  $x = 0.03$ ,  $y = 0.01$ ; (c)  $x = 0$ ,  $y = 0.03$  and (d)  $x = 0.08$ ,  $y = 0.03$  at magnetic field strengths  $B = 0, 4, 6, 8$  and  $10$  T.

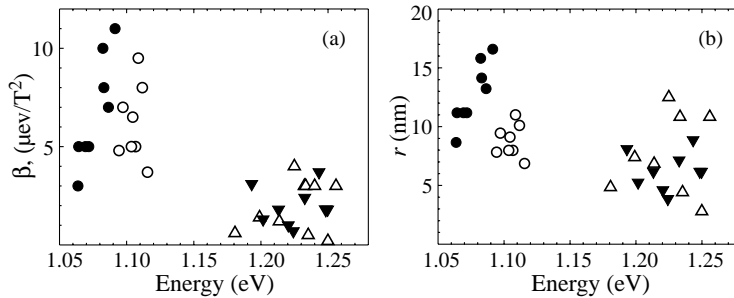


**Fig. 3.** Diamagnetic coefficient  $\beta$  (a), and corresponding cluster radius  $r$  (b): open triangles —  $x = 0$ ,  $y = 0.01$ , solid triangles  $x = 0.03$ ,  $y = 0.01$ , open circles  $x = 0$ ,  $y = 0.03$  and solid circles  $x = 0.08$ ,  $y = 0.03$  versus emission energy of C-lines.

All scans presented (except scan e) show locations for which at least five clusters are emitting at wavelengths within  $1$  nm of the detection wavelength. The separation of the clusters varies from  $0.4 \mu\text{m}$  (upper left  $1 \times 1 \mu\text{m}$  section) to  $< 0.2$  nm (lower left section) this revealing a strong inhomogeneity of the layer on a length scale of  $1 \mu\text{m}$ .

We estimate the density of the QD-like clusters in our samples to be  $(1-3) \times 100 \mu\text{m}^{-3}$ , which is ten orders of magnitude higher than that predicted for random alloy, and suggests their spontaneous formation.

#### Acknowledgments

The authors wish to acknowledge the NATO Science for Peace Program (grant SFP-972484), the W. M. Keck Foundation and the ITRI-Ioffe Joint Scientific Program.



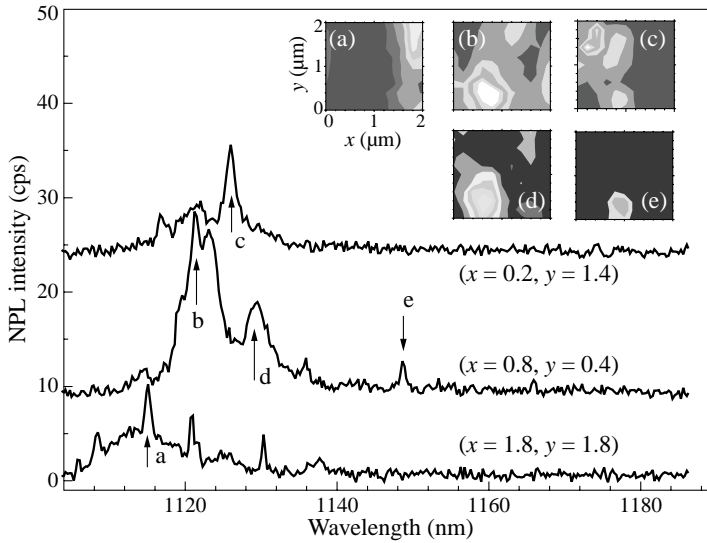


**Fig. 4.** NPL spectra and monochromatic intensity scans of a  $2 \times 2 \mu\text{m}$  area (inserts a-e) of  $\text{GaAs}_{0.97}\text{N}_{0.03}$ . Arrows show detection wavelength in corresponding scans taken at positions  $(x, y)$ ,  $\mu\text{m}$ : (0.2, 1.4), (0.8, 0.4) and (1.8, 1.4).

## References

- [1] A. M. Mintairov *et al*, *Phys. Rev. Lett.* **87**, 244701 (2001).
- [2] A. M. Mintairov *et al*, (in press).
- [3] *Semiconductors: group IV elements and III-V compounds* ed. O. Madelung, Berlin-New York: Springer-Verlag, 1991.
- [4] R. Stepniewski *et al*, *Phys. Rev. B* **60**, 4438 (1999).

## Raman study of Ge quantum dots formed by submonolayer Ge coverages in Ge/Si superlattices

V.A. Volodin<sup>1</sup>, D.A. Orehov<sup>1</sup>, M.D. Efremov<sup>1</sup>, V.A. Sachkov<sup>2</sup>, B.A. Kolesov<sup>3</sup>,  
 N. D. Zakharov<sup>4</sup>, V. A. Egorov<sup>4,5</sup>, G. E. Cirilin<sup>4,5</sup> and P. Werner<sup>4</sup>

<sup>1</sup> Institute of Semiconductor Physics SB RAS,  
 pr. Lavrentjeva 13, Novosibirsk 630090, Russia,

<sup>2</sup> Institute of Sensor Microelectronics SB RAS, pr. Mira 55a, Omsk 644077, Russia

<sup>3</sup> Institute of Inorganic Chemistry, pr. Lavrentjeva 3, Novosibirsk 630090, Russia

<sup>4</sup> Max-Planck Institute of Microstructure Physics, Halle/Saale, Germany

<sup>5</sup> Ioffe Physico-Technical Institute, St Petersburg, Russia

### 1. Introduction

Many attempts to create Si/Ge heterostructures with enhanced opto-electronic properties have been made since beginning of 90-th. Previously these hopes were connected with theoretical assumption that stressed ultra-thin Ge/Si superlattices (SLs) should have direct band gap structure [1]. Recently, the great excitement of researchers was generated by promising optical properties of self-organizing Ge quantum dots (QDs) embedded in a Si matrix. Traditionally, Ge QDs are formed using relatively thick Ge deposition as a result of structural reconstruction of stressed system in order to minimize elastic energy (Stranski–Krastanow mechanism) [2]. It should be noted, that in this case there is always the wetting layer and the lateral sizes of Stranski–Krastanow QDs usually relatively high (tens of nanometers), which defines weak vanishing of the wave-vector selection rules in the lateral direction. More recently, the mechanism of QDs formation using submonolayer (SML) insertions of a narrow-band semiconductor in a wide-band semiconductor matrix was proposed [3]. In this case the average sizes of QDs are usually very small and its densities are very high. According to electron diffraction, electron microscopy and photoluminescence (PL) data the Ge QDs were formed in Ge/Si SLs with SML Ge insertions [4]. Such Ge/Si heterostructures containing dense arrays of small Ge islands looks more promising for opto-electronic applications.

### 2. Experimental

The experimental samples were grown using molecular-beam epitaxy (MBE) technique. The used MBE setup was described elsewhere [4]. Parameters of the studied Ge/Si SLs are shown in the Table. The Raman spectra were registered at room temperature in back-

**Table 1.** Specifications of the studied Ge/Si superlattices.

No	Growth temperature (°C)	Thickness of Ge	Thickness of Si, (Å)	Number of periods
828b	650	0.7 Å, 0.5 ML	44	20
829b	750	0.7 Å, 0.5 ML	44	20
830a	700	0.7 Å, 0.5 ML	44	20
901a	700	1.4 Å, 1.0 ML	44	20

scattering geometry in  $Z(XY)\bar{Z}$  polarization geometry. The directions of the axes  $X$  (polarization of incident light) and  $Y$  (polarization of scattered light) are corresponded to the crystallographic directions  $\langle 100 \rangle$  and  $\langle 010 \rangle$ , the axis  $Z$  (wave vector of incident light) is corresponded to growth direction  $\langle 001 \rangle$ . This geometry was chosen because in this case the scattering on optical phonons is allowed and the second order scattering on transversal acoustical (TA) and longitudinal acoustical (LA) phonons in Si is forbidden. The line 488 nm of Ar laser was used for excitation of the Raman scattering. The power of laser beam reaching the sample (20 mW) was focused in a spot with diameter  $2 \mu\text{m}$ .

### 3. Results and discussion

The Raman spectra in region of Ge optical vibrations of samples with 0.5 ML Ge insertions grown at temperatures 650 and 700 °C are shown in Fig. 1.

As one can see, in the both samples there are peaks related to scattering by optical vibration of Ge–Ge bonds. The positions of peaks in both cases are  $318 \text{ cm}^{-1}$ , the frequencies of longitudinal optical (LO) and transversal optical (TO) phonons in bulk Ge is  $302 \text{ cm}^{-1}$ , such shift may be caused by mechanical stresses in Ge clusters. If one analyzes this data according to calculations in work [5], the in-plane stress in Ge clusters should be nearly as high as in totally not relaxed structure. It should be noted, that the high-energy shift in stressed Ge QDs can reach  $320 \text{ cm}^{-1}$  [6]. According to high resolution electron microscopy (HREM) data, the lateral size of Ge QDs in the structures grown in similar conditions was less than 8 nm, and its size in growth direction was less than 3.5 nm [4]. The observed low-energy shoulder in region about  $300 \text{ cm}^{-1}$  may be caused by scattering on Ge optical vibration of higher orders (including laterally confined phonons). To investigate the influence of growth temperature on structure of the studied heterostructures, the Raman spectra of samples 828b and 829b (see Table) were registered in region of frequencies of Ge–Si bond optical vibrations (Fig. 2).

As one can see, the integral intensity of peak related to scattering on Ge–Si bond vibrations for sample grown at 750 °C more than 2 times higher than for sample grown at 650 °C. It seems that in the case of higher growth temperature the Ge had formed solid mixture rather than QDs. It should be noted that in samples grown at 650 °C there was

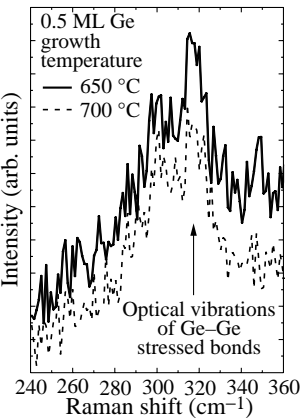


**Fig. 1.** Raman spectra of samples containing Ge QDs.

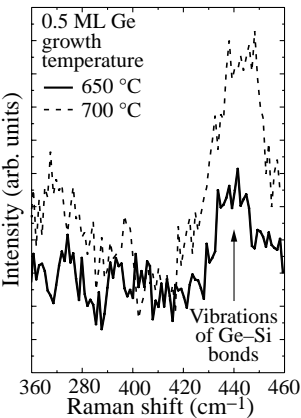


**Fig. 2.** Raman spectra of samples 828b and 829b.

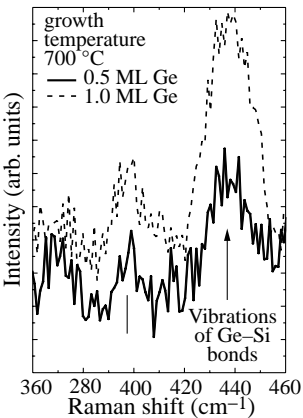


**Fig. 3.** Raman spectra of samples 830a and 901a.

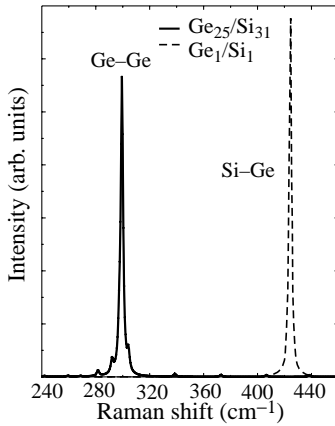


**Fig. 4.** Calculated Raman spectra of flat Ge/Si SLs.

strong PL signal from Ge QDs and for high-temperature grown sample PL efficiency was very low [4]. The PL data were correlated with HREM data [4]. The effects of influence of Ge thickness on Raman spectra are presented in Fig. 3.

The results of peak approximations using Lorentz curves give the ratio 2.5 between intensities of Ge–Si vibrations related peaks for sample with 1 ML Ge and 0.5 ML Ge. So, one can conclude, that in the case of thicker Ge insertions almost all Ge atoms are in Ge–Si solid mixture. It should be noted that no PL signal from Ge QDs was observed for sample grown in similar conditions with 1 ML Ge insertions [4]. One can see two peaks related to scattering on Ge–Si bond vibrations (about 400 and 440  $\text{cm}^{-1}$ ). The similar two peaks structure was observed by other authors [5] for stressed Ge–Si solid mixtures. For interpretation of the experiment the calculation of phonon dispersion and Raman spectra were made. The calculations of the phonon frequencies and the vectors of atomic displacements had been made within the frame of extended Born–von-Karman model. The force constants in the model were obtained using approximation of calculated phonon dispersion and the data of neutron scattering for bulk Ge [7]. The unit cells of SLs were built in mass substitution model. The Raman spectra were calculated using the bond polarisability model of Wolkenstein. Because the unit cells of real systems with QDs are very big, the model calculations were made for flat (001) oriented SLs. The results are presented in Fig. 4.

One can see intensive peak at approximately 300  $\text{cm}^{-1}$  caused by scattering on Ge–Ge bond vibrations for  $\text{Ge}_{25}/\text{Si}_{31}$  SLs (thickness of Ge and Si is given in MLs). The thickness of Ge in this case corresponds to thickness of Ge QDs in experimental samples (3.5 nm). As it was mentioned, the mechanical stresses can shift the position of peak to experimental value (318  $\text{cm}^{-1}$ ). The pure Ge–Si bond vibrations were modeled using  $\text{Ge}_1\text{Si}_1$  SL. In this SL there are only Ge–Si bonds, and the frequency of its vibrations is about 425  $\text{cm}^{-1}$ . This frequency can also be shifted by mechanical stress and stoichiometry of Ge–Si solid mixture [5]. Returning to Ge–Ge bond vibrations it should be noted that LO like Ge–Ge bond vibrations overlaps in frequency region with Si LA vibrations and for some Ge and Si thicknesses can not be confined.

#### 4. Conclusions

It was demonstrated, that Raman scattering spectroscopy powered by calculations can be effective, fast and not-destructive technique for study of Ge/Si heterostructures with Ge QDs. The conclusions about Ge QDs formation and PL efficiency of such structures can

be derived from intensity ratios of Raman peaks related to scattering on Ge–Ge and Ge–Si vibrations. Good correlations of Raman scattering and PL and HREM data were achieved.

#### *Acknowledgements*

G.E.C. is acknowledged Alexander von Humboldt foundation. V.A.V. is grateful to the Scientific Council of the Institute of Semiconductor Physics SB RAS for the Stipend for Young Scientists. This work was partially supported by the Russian Scientific Program “Physics of Low-Dimensional Structures”.

#### **References**

- [1] J. D. White, G. Fasol, R. A. Ghanbari, M. A. Gell, C. J. Gibbings and C. G. Tuppen, *Appl. Phys. Lett.* **57**, 1523 (1990).
- [2] O. P. Pchelyakov *et al*, *Semiconductors (Rus. Fizika i Technika Poluprovodnikov)* **34**, 1281 (2000).
- [3] N. N. Ledentsov, I. L. Krestnikov, M. Strasburg *et al*, *Thin Solid Films* **367**, 40 (2000).
- [4] N. D. Zakharov, G. E. Cirlin, P. Werner *et al*, *Proc. 9th Int. Symp. Nanostructures: Physics and Technology*, St Peterburg, Russia, June 18-22, 2001, p. 21.
- [5] J. Groenen, R. Carles, S. Christiansen, M. Albrecht, W. Dorsch, H. P. Strunk, H. Wawra and G. Wagner, *Appl. Phys. Lett.* **71**, 3856 (1997).
- [6] A. Milekhin, N. P. Stepina, A. I. Yakimov, A. I. Nikiforov, S. Schultze and D. R. T. Zahn, *Eur. Phys. J. B* **16**, 355 (2000).
- [7] G. Nelin and G. Nilsson, *Phys. Rev. B* **5**, 3151 (1972).

## Room-temperature photoluminescence of GeSi/Si(001) self-assembled islands in a 1.3–1.7 $\mu\text{m}$ wavelength range

Yu. N. Drozdov<sup>†</sup>, Z. F. Krasilnik<sup>†</sup>, D. N. Lobanov<sup>†</sup>, A. V. Novikov<sup>†</sup>,  
M. Ya. Valakh<sup>‡</sup>, N. V. Vostokov<sup>†</sup>, A. N. Yablonsky<sup>†</sup> and V. A. Yukhymchuk<sup>‡</sup>

<sup>†</sup> Institute for Physics of Microstructures, RAS, 603950,  
Nizhny Novgorod, GSP-105, Russia

<sup>‡</sup> Institute of Semiconductor Physics, NASU, 03028, Kiev, Ukraine

**Abstract.** The dependence of photoluminescence spectra of SiGe/Si(001) structures with self-assembled islands on Ge deposition temperature was investigated. Due to inhibition of SiGe alloying and an increase of the Ge content in islands the photoluminescence peak from the islands significantly shifted to low energy with a lowering temperature. The maximum of the peak from the island grown at 600 °C was observed at energies less than the energy of the bandgap for bulk Ge. As a result of holes localization in islands the photoluminescence peak from the islands was observed up to room temperature. Sufficient enhancement of the room-temperature intensity of the photoluminescence signal at 1.55  $\mu\text{m}$  was obtained for structures with islands grown on pre-deposited  $\text{Si}_{1-x}\text{Ge}_x$  layer. It is associated with a more effective capturing of holes by densely packed islands in structures with a pre-deposited  $\text{Si}_{1-x}\text{Ge}_x$  layer.

## Introduction

In recent years an active search has been conducted for ways of integrating opto-electronic devices such as light-emitting diodes, photodetectors and light modulators into modern highly developed Si-based electronics. The SiGe/Si(100) structures with self-assembled islands are a promising candidate for realization of these aims. The main advantages of island structures as against SiGe/Si(100) planar structures are (i) a photo- and electroluminescence signal at wavelengths up to 1.55  $\mu\text{m}$  which cannot be reached in the planar structures [1] and (ii) a increase of the temperature quenching threshold of the photoluminescence (PL) signal from islands due to 3D localization of the holes in the islands [2].

The aim of this work is to search for ways of increasing a PL signal at 1.55  $\mu\text{m}$  from GeSi/Si(001) structures with self-assembled islands by varying Ge deposition temperature and using pre-deposition of  $\text{Si}_{1-x}\text{Ge}_x$  layer in island growth. .

## 1. Experimental results and discussion

The samples under investigation were grown by solid-source MBE on Si (001) substrates. The structures consist of a Si buffer layer and a Ge layer deposited at  $T_g = 600\text{--}700$  °C. The structures for the investigations of islands growth on GeSi layers were grown at  $T_g = 700$  °C. and consist of a Si buffer layer, a  $\text{Si}_{0.9}\text{Ge}_{0.1}$  layer with the thickness  $d = 8\text{--}10$  nm and a Ge layer with the equivalent thickness of 5.5–13 monolayers (ML) ( $1\text{ L} \approx 0.14$  nm). The samples for PL measurements were capped by a Si layer. Sample morphology was determined by atomic force microscopy (AFM). X-ray diffraction measurements were performed with a double-crystal diffractometer. The Raman spectra were recorded by the Jobin Ivon Raman microprobe system. They were excited in the backscattering geometry

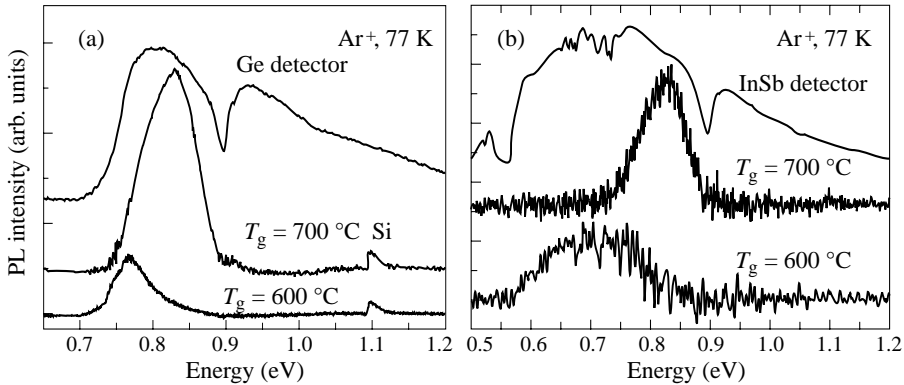


**Fig. 1.** PL spectra obtained at 77 K from structures with islands grown at various  $T_g$ . PL spectra detected by Ge (a) and InSb (b) cooled detectors. Upper curves on figures are spectral features of the detectors (decline in region 0.9 eV corresponds to absorption in quartz glass of spectrometer).

by an  $\text{Ar}^+$  laser (514.5 nm). PL was analyzed by a BOMEM DA3.36 Fourier spectrometer and detected by the Ge and InSb cooled detectors. PL spectra were excited by an  $\text{Ar}^+$  (514.5 nm) and  $\text{Kr}^+$  (647 nm) lasers.

One way to enhancement of the intensity and the temperature quenching threshold of the PL signal from the islands is an increase of the valence band offset between the island and the Si matrix, which results in a better localization of holes in the islands. However, it was shown [3] that strain-driven alloying occurs in islands at  $T_g \geq 600^\circ\text{C}$ . Formation of a GeSi alloy in islands causes a decrease in the valence band offset between the island and the Si matrix. Lowering of  $T_g$  suppresses alloy formation and result in increase of Ge content in islands [3]. The average Ge content ( $x$ ) in free-standing dome-islands, obtained by Raman spectroscopy and X-ray analysis, increases from about 50–55% at  $T_g = 700^\circ\text{C}$  to 70–75% at  $T_g = 600^\circ\text{C}$ . The Ge content in islands significantly decreases after overgrowth of islands. According to X-ray diffraction and Raman spectroscopy data the fraction of Ge in islands grown at  $T_g = 600^\circ\text{C}$  decreases from 70–75% to 60–65% after growth of Si cap layer.

PL investigations showed that a wide peak from the islands shifts to lower energies with a lowering  $T_g$  (Fig. 1). The PL peak from islands grown at  $T_g = 600^\circ\text{C}$  arises at the low energy edge of a Ge cooled detector (Fig. 1(a)). The spectra recorded by the InSb cooled detector showed that a PL signal from the islands grown at  $T_g = 600^\circ\text{C}$  spreads down to 0.6 eV ( $\lambda \sim 2 \mu\text{m}$ ) (Fig. 1(b)). This value of energy is less than the energy bandgap for bulk Ge and a strain  $\text{Ge}_x\text{Si}_{1-x}$  layer with  $x = 60\text{--}65\%$ . Such a dependence of the island PL peak on  $T_g$  is well described by the model of spatial indirect recombination of holes confined within Ge rich islands and electrons localized in Si on heterojunction with islands [4]. The redshift of the island PL signal with a lowering  $T_g$  is related to the increase of the valence band offset between the SiGe island and the Si matrix due to an increase of Ge content in the island. The energy of the optical transitions for islands grown at  $600^\circ\text{C}$  was calculated using model [4] and the islands composition values obtained by X-ray analysis and Raman spectroscopy. The calculated energy is in good agreement with the experimental energy position of island related PL peak.

The island PL peak was observed up to room temperature (Fig. 2). Contrary to our

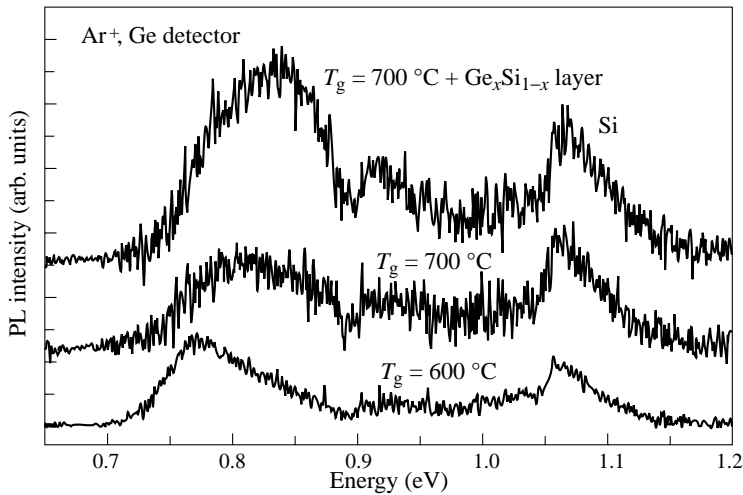


**Fig. 2.** Room-temperature PL spectra for island structures grown at various  $T_g$ . Upper curve on figures is PL spectrum from islands grown on  $\text{Si}_{0.9}\text{Ge}_{0.1}$  layer. The peak at 1.06 eV originates from free exciton recombination in Si layers and substrate.

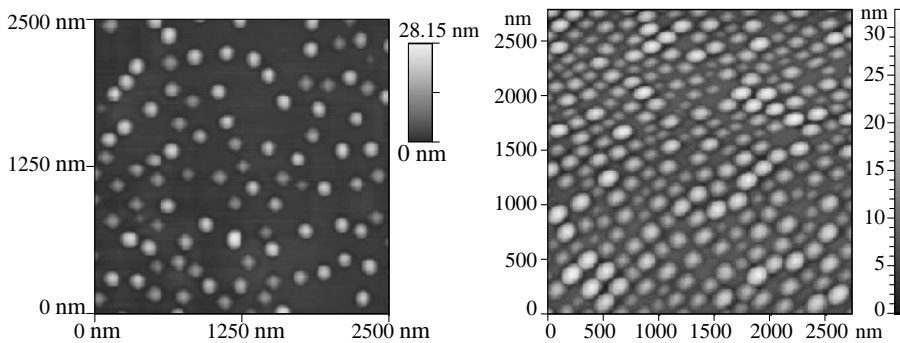


**Fig. 3.** AFM images of the samples without (left) and with (right) pre-deposition of  $\text{Si}_{1-x}\text{Ge}_x$  layer. The equivalent thickness of the deposited Ge layer is the same for both samples and equals 7 ML.

expectations of a better holes localization within the islands grown at  $T_g = 600^\circ\text{C}$  the PL signal at  $1.55\ \mu\text{m}$  (0.8 eV) from such islands is weaker than the PL signal from the islands grown at  $T_g = 700^\circ\text{C}$ . One reason for this is the redshift of PL signal from islands with a lowering  $T_g$ . The maximum of PL signal for islands grown at  $T_g = 600^\circ\text{C}$  is situated at wavelengths larger than  $1.55\ \mu\text{m}$  (Fig. 2). Another reason for the low intensity of the PL signal for islands grown at low temperatures is degradation of crystal quality of structures.

Another way to increase the PL signal from the islands is to increase a possibility of hole capturing by the islands. One can do it by increasing of the sizes and surface density of islands. In this paper the growth of Ge islands on pre-deposited  $\text{Si}_{1-x}\text{Ge}_x$  ( $x \sim 10\%$ ) layer was used for this purpose. AFM images revealed that the pre-deposition of  $\text{Si}_{1-x}\text{Ge}_x$  layer increases the roughness of surface. Besides that, the elastic energy accumulated in



the  $\text{Si}_{1-x}\text{Ge}_x$  layer decreases the Ge wetting layer thickness. Both of these reasons cause an increase of Si content in islands. The Si content in islands obtained by X-ray analysis increases from 45–50% for islands grown on Si to 55–60% in the case of islands growth on  $\text{Si}_{1-x}\text{Ge}_x$  layer. The increase of Si content in islands result in a considerable increase of islands volume (Fig. 3). As clearly seen from AFM images (Fig. 3), the islands on structures with pre-deposited  $\text{Si}_{1-x}\text{Ge}_x$  layer are densely packed and occupy much larger part of the surface. Besides, ordering of the island arrangement associated with the elastic interaction between the neighboring islands was observed on the surface of structures with a  $\text{Si}_{1-x}\text{Ge}_x$  layer. Due to a larger volume of the islands and part of surface occupied by islands the structures with islands grown on pre-deposited  $\text{Si}_{1-x}\text{Ge}_x$  layer more effectively capture the carriers (holes) generated by light and, as a consequence, have a larger intensity of room-temperature PL peak in the region of  $1.55\text{ }\mu\text{m}$  in comparison with structures without a  $\text{Si}_{1-x}\text{Ge}_x$  layer (Fig. 2).

#### Acknowledgements

This work was supported by the RFBR (grants No 00-02-16141 and No 02-02-16792 and CRDF Grant No RESC-02).

#### References

- [1] K. Eberl, M. O. Lipinski, Y. M. Manz, W. Winter, N. Y. Jin-Philipp and O. G. Schmidt, *Physica E* **9**, 164 (2001).
- [2] H. Sunamura, Y. Shiraki and S. Fukatsu, *Appl. Phys. Lett.* **66**, 953 (1994).
- [3] A. V. Novikov, B. A. Andreev, N. V. Vostokov, Yu. N. Drozdov, Z. F. Krasilnik, D. N. Lobanov, L. D. Moldavskaya, A. N. Yablonskiy, M. Miura, N. Usami, Y. Shiraki, M. Ya. Valakh, N. Mesters and J. Pascual, *Material Science and Engineering B* **89**, 62 (2002).
- [4] V. Ya. Aleshkin, N. A. Bekin, N. G. Kalugin, Z. F. Krasilnik, A. V. Novikov and V. V. Postnikov, *JETP Lett.* **67**, 48 (1998).

## Removal of spin degeneracy in SiGe based nanostructures

S. D. Ganichev<sup>†‡</sup>, U. Rössler<sup>†</sup>, W. Prettl<sup>†</sup>, E. L. Ivchenko<sup>‡</sup>, V. V. Bel'kov<sup>‡</sup>,  
R. Neumann<sup>§</sup>, K. Brunner<sup>§</sup> and G. Abstreiter<sup>§</sup>

<sup>†</sup> Fakultät Physik, University of Regensburg, 93040, Regensburg, Germany

<sup>‡</sup> Ioffe Physico-Technical Institute, St Petersburg, Russia

<sup>§</sup> Walter Schottky Institute, TU Munich, D-85748 Garching, Germany

**Abstract.** The photogalvanic effects, which require a system lacking inversion symmetry, become possible in SiGe based quantum well (QW) structures due to their built-in asymmetry. We report on the removal of spin degeneracy in the  $\mathbf{k}$ -space of SiGe nanostructures. This is concluded from the observations of the circular photogalvanic effect induced by infrared radiation in asymmetric  $p$ -type QWs. We discuss possible mechanisms that give rise to spin-splitting of the electronic subband states.

### Introduction

The spin-degree of freedom of charge carriers and its manipulation has become a topical issue in material science under the perspective of spin-based electronic devices [1]. Recently it has been demonstrated that in QW structures based on III–V compounds, a directed current can be induced by circularly polarized light [2]. This effect belongs to the class of photogalvanic effects [3] known for bulk semiconductors and represents the circular photogalvanic effect (CPGE). In QWs this effect is caused by the optical spin orientation. The occurrence of the current needs the removal of spin degeneracy in the  $\mathbf{k}$ -space i.e.  $\mathbf{k}$ -linear spin splitting [2]. In zinc-blende semiconductors, like III–V and II–VI, the reduction of dimensionality leads to a such removal of spin degeneracy. On the other hand, the diamond lattice has a center of inversion and for SiGe based QWs with symmetrical interfaces CPGE is forbidden. However, this effect becomes possible due to the structure inversion asymmetry. This is demonstrated by the experiments presented below where the inversion symmetry was broken by preparation of compositionally stepped QWs and asymmetric doping of compositionally symmetric QWs. The observation of CPGE proves the removal of spin degeneracy in the  $\mathbf{k}$ -space and is of importance in view of possible applications in spintronics based on SiGe.

### 1. Experiment

The measurements were carried out on  $p$ -type SiGe QW structures MBE-grown on (001)- and (113)-oriented substrates. The compositionally stepped samples consisted of ten QWs ( $\text{Si}_{0.75}\text{Ge}_{0.25}$ (4 nm)/ $\text{Si}_{0.55}\text{Ge}_{0.45}$ (2.4 nm)), separated by 6 nm Si barriers. The asymmetrically doped structures had a single QW of  $\text{Si}_{0.75}\text{Ge}_{0.25}$  composition with boron acceptors on one side only. All these samples had free carrier densities of about  $8 \cdot 10^{11} \text{ cm}^{-2}$  and were studied at room temperature. Ohmic contact pairs were centered at opposite sample edges.

A high power pulsed mid-infrared (MIR) TEA- $\text{CO}_2$  laser and a far-infrared (FIR)  $\text{NH}_3$ -laser have been used as radiation sources delivering 100 ns pulses with radiation power  $P$  up

to 100 kW. Several lines of the CO<sub>2</sub> laser between 9.2 and 10.6  $\mu\text{m}$  and of the NH<sub>3</sub>-laser [4] between  $\lambda = 76 \mu\text{m}$  and  $280 \mu\text{m}$  have been used for excitation in the MIR and FIR range, respectively. The laser light polarization could be modified from linear to circular using for the MIR light a Fresnel rhombus and quartz  $\lambda/4$  plates for the FIR radiation. The helicity of the incident light was varied according to  $P_{\text{circ}} = \sin 2\varphi$  where  $\varphi$  is the angle between the initial plane of linear polarization and the optical axis of the polarizer.

With illumination by the MIR radiation of a TEA CO<sub>2</sub> laser in (001)-oriented samples with asymmetric QWs a current signal proportional to the helicity  $P_{\text{circ}}$  is observed under oblique incidence indicating an observation of CPGE. The current changes sign if the circular polarization is switched from left to right handed. The spectral dependence of the photocurrent in the MIR corresponds to direct transitions between hole subbands. In the FIR range, where radiation causes indirect optical transitions within the lowest heavy-hole subband, a more complicated dependence of the current as function of helicity has been observed. In (001)-grown asymmetric QWs as well as in (113)-grown samples the dependence of the current on the phase angle  $\varphi$  may be described by a sum of two terms, one being  $\propto \sin 2\varphi$  and the other  $\propto \sin 2\varphi \cos 2\varphi$ . The first term  $\propto \sin 2\varphi$  is again caused by CPGE. The second term  $\propto \sin 2\varphi \cos 2\varphi$  vanishes for the circularly polarized radiation and is caused by the linear photogalvanic effect [5], it is out of the scope of this presentation. In symmetrically grown and symmetrically doped SiGe QWs no photogalvanic current has been observed.

## 2. Microscopical theory

The principal microscopical aspect of a photon helicity driven current is the removal of spin-degeneracy in the subband states due to the reduced symmetry of the quantum well structure [2, 6]. Thus the experimental observation of CPGE in asymmetric SiGe nanostructures unambiguously proves the lifting of spin degeneracy. This is described by  $\mathbf{k}$ -linear terms in the Hamiltonian,

$$H^{(1)} = \beta_{lm} \sigma_l k_m \quad (1)$$

where the real coefficients  $\beta_{lm}$  form a pseudo-tensor and  $\sigma_l$  are the Pauli spin matrices. Below several scenarios will be presented which could contribute to  $\beta_{lm}$  in SiGe QWs with symmetries  $C_{2v}$  or  $C_s$  corresponding to investigated structures. As discussed in [2] the coupling between the carrier spin ( $\sigma_l$ ) and momentum ( $k_m$ ) together with the spin-controlled dipole selection rules yields a net current under circularly polarized excitation.

Spin degeneracy results from the simultaneous presence of time-reversal and spatial inversion symmetry. If one of these symmetries is broken the spin degeneracy is lifted. In our SiGe QW systems the spatial inversion symmetry is broken (the point groups  $C_{2v}$  and  $C_s$  do not contain the inversion operation) and, as a consequence,  $\mathbf{k}$ -linear terms appearing in the electron Hamiltonian lead to a splitting of the electronic subbands at a finite in-plane wave vector. Microscopically different mechanisms can lead to  $\mathbf{k}$ -linear terms, which will be discussed here briefly.

In the context of spin related phenomena in QW structures most frequently the so-called Rashba term [7] is taken into account. It is a prototype spin-orbit coupling term of the form  $\alpha(\nabla V \times \mathbf{p}) \cdot \boldsymbol{\sigma}$ , where  $\mathbf{p}$  is the momentum of the particle moving in the potential  $V$  and  $\boldsymbol{\sigma}$  is the vector of the Pauli spin matrices. The weighting factor  $\alpha$  depends on the material in which the QW structure, giving rise to the potential  $V$ , is realized. The Rashba term has an axial symmetry and can exist as well in systems invariant under  $C_{2v}$  and  $C_s$ .  $\nabla V$  can be identified with the electric field leading to the asymmetric confinement and is parallel to the growth direction of the QW structure. In the context of  $\mathbf{k} \cdot \mathbf{p}$  theory the Rashba term

can be understood as resulting from the couplings between conduction and valence band states mediated by the momentum operator ( $\mathbf{k} \cdot \mathbf{p}$ -coupling) and the space coordinate  $z$  in the electric field term  $V = eFz$ . The Rashba term has the form  $\sigma_x k_y - \sigma_y k_x$  and leads to a  $\mathbf{k}$ -linear contribution to the subband dispersion. For hole states it has been discussed in [8].

Invoking the theory of invariants [9], the Hamiltonian acting in the twofold space of particles with spin 1/2 can be represented in terms of 4 independent  $2 \times 2$  matrices (the unit matrix and the Pauli spin matrices). In addition to the Rashba term (which has this form) there could be similar expressions but with higher powers of the wave vector (or the electric field). The  $4 \times 4$  Hamiltonian for holes, usually described in the basis of angular momentum eigenstates with  $J = 3/2$ ,  $M = \pm 3/2, \pm 1/2$ , requires for its most general form 16 independent matrices formed from angular momentum matrices  $J_x, J_y, J_z$ , their powers and products. Thus in combination with tensor operators, composed of components of the momentum (or wave vector) and the electric field, new terms are possible under  $C_{2v}$  and  $C_s$ . Some of these, which can be regarded as generalized Rashba terms, give rise to  $\mathbf{k}$ -linear contributions in the hole subbands. The  $4 \times 4$ -Luttinger Hamiltonian, describing the valence band dispersion of bulk Si or Ge close to the center of the Brillouin zone, can be split into a spherical symmetric part (giving rise to an isotropic dispersion of spin degenerate bands) and an anisotropic term causing warping of these bands. In (*hhl*)-grown QWs with symmetry  $C_s$  the spherical part leads to a subband Hamiltonian, which includes heavy-light hole coupling even at zero in-plane wave vector (angular momentum  $M$  ceases to be a good quantum number under  $C_s$ ). In addition the warping term mediates also a coupling between light and heavy hole states. Combining these two couplings, that derive from the Luttinger Hamiltonian, yields terms of the form  $J_z k_x$ . These terms are invariants under  $C_s$  and result in a spin-splitting of the hole subbands.

Finally we mention a mechanism to create  $\mathbf{k}$ -linear terms and spin-splitting which comes from the  $C_{2v}$  symmetry of a (001)-grown SiGe interface and gives rise to coupling between heavy and light hole states [10]. The mixing may be described by the coupling Hamiltonian

$$H_{l-h} = \frac{\hbar^2}{m_0 a_0 \sqrt{3}} t_{l-h} \{J_x, J_y\} \delta(z - z_{if}) . \quad (2)$$

Here  $\{J_x, J_y\}$  is the symmetrized product of angular momentum matrices with  $J = 3/2$ ,  $z_{if}$  is the interface coordinate along the growth axis,  $m_0$  the free electron mass,  $a_0$  the lattice constant, and  $t_{l-h}$  a dimensionless coupling coefficient. Note that a shift of the interface by one atomic layer interchanges the role of the axes  $[1\bar{1}0]$  and  $[110]$ , which as a consequence, leads to a sign change of  $t_{l-h}$  reversing the current. This heavy-light hole coupling in combination with that one inherent in the Luttinger Hamiltonian for QWs leads again to spin-dependent  $\mathbf{k}$ -linear terms.

### 3. Conclusions

In our experiments carried out for different  $p$ -doped SiGe based nanostructures, we have demonstrated a possibility to create a photon helicity driven stationary current due to the circular photogalvanic effect. We analyze the symmetry of the QWs under investigation and present different scenarios that can lead to spin-dependent  $\mathbf{k}$ -linear terms in the hole subband Hamiltonian, which are prerequisite for the appearance of the observed photocurrent. Our results provide the important information that spin-related phenomena, which so far have been considered to be specific for QW structures based on zinc-blende materials, exist also in the SiGe QW systems. In particular spin sensitive bleaching of optical absorption may

be recorded by the saturation of CPGE at high power levels allowing to conclude on spin relaxation times [11].

### Acknowledgements

Financial support from the DFG, the RFBR, INTAS and NATO Linkage Grant is gratefully acknowledge.

### References

- [1] S. A. Wolf, D. D. Awschalom, R. A. Buhrman, J. M. Daughton, S. von Molnar, M. L. Roukes, A. Y. Chtchelkanova and D. M. Treger, *Science* **294**, 1488 (2001).
- [2] S. D. Ganichev, E. L. Ivchenko, S. N. Danilov, J. Eroms, W. Wegscheider, D. Weiss and W. Prettl, *Phys. Rev. Lett.* **86**, 4358 (2001).
- [3] E. L. Ivchenko and G. E. Pikus, *Superlattices and Other Heterostructures. Symmetry and Optical Phenomena*, Springer Series in Solid State Sciences, vol. 110, Springer-Verlag, 1995; second edition 1997; Ch. 10.
- [4] S. D. Ganichev, *Physica B* **273-274**, 737 (1999).
- [5] S. D. Ganichev, H. Ketterl, W. Prettl, E. L. Ivchenko and L. E. Vorobjev, *Appl. Phys. Lett.* **77**, 3146 (2000).
- [6] S. D. Ganichev, E. L. Ivchenko and W. Prettl, *Physica E*, in press.
- [7] Yu. A. Bychkov and E. I. Rashba, *J. Phys. C* **17**, 6039 (1984).
- [8] R. Winkler, *Phys. Rev. B* **62**, 4245 (2000).
- [9] G. L. Bir and G.E. Pikus, *Symmetry and Strain-induced Effects in Semiconductors*, Wiley, New York, 1974.
- [10] E. L. Ivchenko, A. Yu. Kaminski and U. Rössler, *Phys. Rev. B* **54**, 5852 (1996).
- [11] S. D. Ganichev, S. N. Danilov, V. V. Bel'kov, E. L. Ivchenko, M. Bichler, W. Wegscheider, D. Weiss and W. Prettl, *Phys. Rev. Lett.* **88**, 057401 (2002).

## Hole transport in Ge/Si quantum-dot field-effect transistors

A. I. Yakimov, A. V. Dvurechenskii, V. V. Kirienko and A. I. Nikiforov  
Institute of Semiconductor Physics, 630090 Novosibirsk, Russia

**Abstract.** We report on the transport properties of Si field-effect transistors with an array of  $\sim 10^3$  10-nm-diameter Ge self-assembled quantum dots embedded into the active channel. The drain current versus gate voltage characteristics show oscillations caused by Coulomb interaction of holes in the fourfold-degenerate excited state of the dots even at room temperature. A dot charging energy of  $\sim 43$  meV (i.e.,  $> kT = 26$  meV at  $T = 300$  K) and disorder energy of  $\sim 20$  meV are determined from the oscillation period and the temperature dependence study of current maxima, respectively.

### Introduction

Epitaxial growth of highly strained semiconductors in the Stranski–Krastanov growth mode enables *in situ* fabrication of arrays of 10-nm-scale quantum dots (so called self-assembled quantum dots (SAQDs)). Electronic and opto-electronic nanodevices implemented on Ge self-assembled quantum dots in Si matrix have attracted much attention due to their compatibility with modern Si-based complementary metal-oxide-semiconductor (CMOS) circuitry. This would offer a substantial reduction in complexity and cost of future high performance electronics. Despite the large effort to study the fundamental properties of Ge/Si SAQDs, there are only several attempts of incorporating Ge/Si islands as active element of semiconductor devices, such as infrared photodetectors, light-emitting and resonant-tunneling diodes. Little work has been done on the Ge/Si quantum dot field effect transistors (QDFETs), which utilize the quantum transport through discrete energy states in zero-dimensional systems. To date, most work in the field of QDFETs has concentrated on InAs/GaAs SAQDs [1, 2] and on Si-based quantum dots (QDs) defined by very sophisticated patterning techniques, such as *e*-beam lithography in combination with anisotropic etching [3, 4] and selective oxidation [5, 6], or by tunable gates [7].

In order to rise the operation temperature of QDFETs up to 300 K, the size of QDs has to be smaller than 10 nm. This requirement considerably restrict the possibility of using the lithographic processes for fabrication ultra-small QDs. In this way the Ge/Si SAQDs, which are formed without additional lithography procedure and whose diameter can be achieved as small as  $\sim 10$  nm [8], are more advantageous and hence more relevant for application in QDFETs operating at room temperature. In this paper, we report on the transport phenomena in Ge/Si QDFETs.

### 1. Samples

The starting material was a silicon-on-insulator (SOI) substrate prepared by the separation by implanted oxygen (SIMOX) technique with a 150-nm-thick *p*-type superficial Si film. First, the SOI layer was thinned to 47 nm by repeated thermal oxidation and subsequent wet etching process. After removing  $\text{SiO}_2$ , a 20-nm-thick undoped Si buffer layer was grown at 800 °C by molecular beam epitaxy. Next, the Ge self-assembled dots were

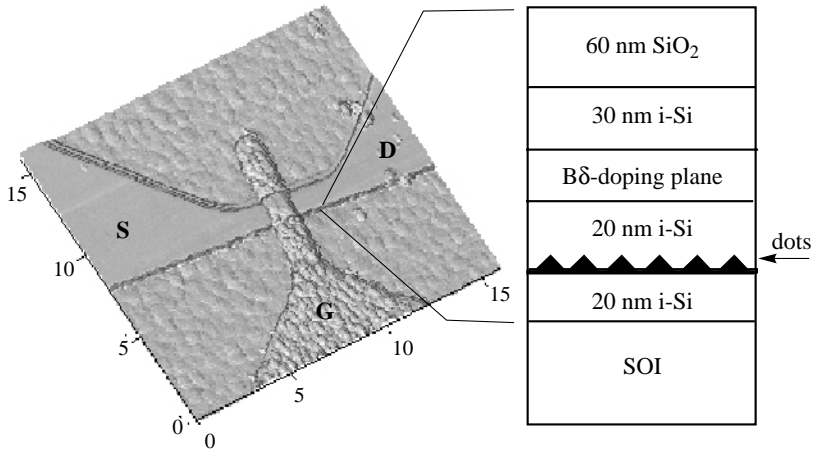


**Fig. 1.** Atomic force microscopy (AFM) image and schematic cross section of the transistor channel. The source, drain and the gate are indicated by S, D and G, respectively. The figures in the AFM picture are microns.

grown at 300 °C with nominal thickness of 8 monolayers and subsequently embedded in 20-nm of Si. The average in-plane diameter and height of the Ge dots are 10 and 1 nm, respectively. The density of the dots is  $4 \times 10^{11} \text{ cm}^{-2}$ . To supply holes on the dots, a boron delta-doping ( $6 \times 10^{12} \text{ cm}^{-2}$ ) Si layer inserted 20 nm above the Ge layer was grown. A 30-nm-thick undoped Si cap layer was then deposited at 500 °C. The channel was patterned by photolithography to form a Si island of 4- $\mu\text{m}$  length and 1- $\mu\text{m}$  width, etched down to the underlying SiO<sub>2</sub>. Source and drain electrodes were made using Al evaporation and annealing at 450 °C in a N<sub>2</sub> atmosphere. A plasma-enhanced chemical-vapor deposition silicon dioxide of 60-nm thickness was deposited as the gate insulator and, finally, a Al gate of 4- $\mu\text{m}$  width and 1- $\mu\text{m}$  length was formed. The amount of oxide charge, estimated from the admittance measurements, was about  $3 \times 10^{10} \text{ cm}^{-2}$ . Figure 1 shows an atomic force microscopy picture of the transistor. Several samples with designed channel widths  $W$  ranging from 2 to 1  $\mu\text{m}$  are fabricated. The sidewall depletion width is determined to be 0.9  $\mu\text{m}$  from measurements of drain current versus  $W$  at zero gate voltage. Assuming a uniform density of 4000 dots per  $\mu\text{m}^2$  the different gate areas of the samples contain number of active dots from 400 to 4000.

The hole concentration in the boron  $\delta$ -doping Si layer is sufficient to fill, after spatial transfer, all hole bound states in the Ge islands and to populate two-dimensional states in the Ge wetting layer. As a result, the channel conductance at zero gate voltage is found to show the non-activated behavior and depend only slightly on temperature.

## 2. Experimental results

The drain current ( $I_d$ ) as a function of the gate voltage ( $V_g$ ) was measured at different temperatures with the drain voltage fixed at 5 mV. Figure 2 shows the typical  $I_d - V_g$  characteristics of the 1- $\mu\text{m}$ -gate QD transistor. When a positive bias is applied to the gate the channel is depleted and current flow between the source and drain contacts is suppressed. Above the threshold voltage  $V_{th} \simeq 4 \text{ V}$  the deep hole states in the dots come into resonance with the Fermi energy and the current starts to oscillate.

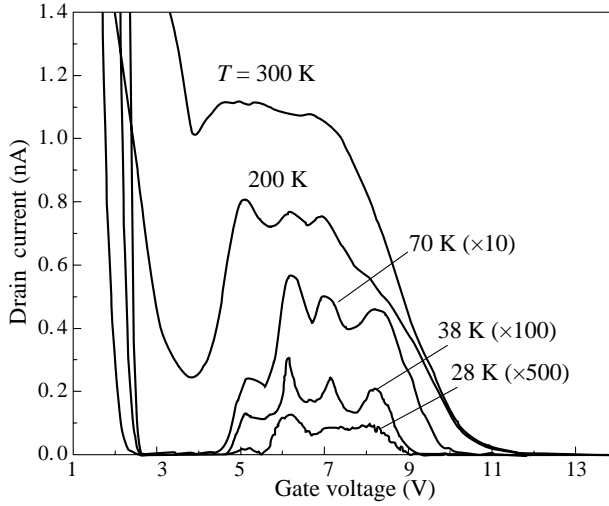


**Fig. 2.** Gate voltage dependence of drain current at various temperatures.

At room temperature, the current bump is clearly observable around 6 V. As the temperature decreases, four well-pronounced equidistant peaks with a gate voltage separation  $\Delta V_g \simeq 1.1$  V appear after onset of the conductance. The number and relative position of the peaks are well reproducible at different cold cycles and in different samples of similar sizes. A very similar fine-structure consistent with four maxima, separated by the Coulomb blockade energy  $E_C$ , has been observed by us in the admittance spectra of Si-based Schottky diodes with Ge SAQDs [9] and in the  $I_d - V_g$  characteristics of 100- $\mu\text{m}$ -scale Ge/Si QD-FETs [10], and ascribed to the hole transport through the fourfold-degenerate first excited state in the Ge QDs.

The charging energy ( $E_C$ ) of the dots can be determined by using  $E_C = \eta e \Delta V_g$ , where the gate modulation coefficient  $\eta$  relates the gate voltage to the hole energy inside the dots. This coefficient can be calculated from the temperature dependence of the full width at half maximum (FWHM) of the current peaks, which, for a single dot showing Coulomb blockade oscillations, should be broadening with  $T$  as  $3.5k_B T / (\eta e)$  [11], where  $k_B$  is Boltzmann's constant. By measuring the FWHM averaged over four peaks as a function of temperature, we obtain  $\eta = (3.9 \pm 0.3) \times 10^{-2}$ , with a residual FWHM  $V_0 = 0.49 \pm 0.05$  V which is a result of statistical fluctuations of the dot sizes and Coulomb potentials from randomly-distributed charged QDs in the dot ensemble. Based on this calculation, the estimated charging energy is  $43 \pm 3$  meV.

The disorder energy,  $E_d$ , in ensemble of the dots can be found from residual FWHM using  $E_d = \eta e V_0$ . For  $V_0 = 0.49 \pm 0.05$  V and  $\eta = (3.9 \pm 0.3) \times 10^{-2}$ , we obtain  $E_d = 19 \pm 3$  meV.

### 3. Summary

We have demonstrated Ge/Si quantum-dot metal-oxide-semiconductor field-effect transistor with the active channel containing  $\sim 10^3$  Ge self-assembled islands. The drain current shows Coulomb blockade oscillations even at room temperature. The charge-transfer mechanism in the transistor channel is identified as being due to nearest-neighbor hopping of



holes between the Ge dots with the typical hopping energy determined by disorder in the quantum dot ensemble. Further work is in progress to reduce the number of dots in the channel.

### Acknowledgements

We acknowledge the support of the Russian Foundation of Basic Research (Grants Nos 00-02-17885, 99-02-39051/NSNFC), Russian Ministry of Industry and Science (Zh. Alferov Program), and the Program of the Russian Academy of Sciences aiming to support research projects of young scientists.

### References

- [1] J. Phillips, K. Kamath, T. Brock and P. Bhattacharya, *Appl. Phys. Lett.* **72**, 3509 (1998).
- [2] K. H. Schmidt, M. Versen, U. Kunze, D. Reuter and A. D. Wieck, *Phys. Rev. B* **62**, 15 879 (2000).
- [3] T. Sakamoto, H. Kawaura and T. Baba, *Appl. Phys. Lett.* **72**, 795 (1998).
- [4] N. Takahashi, H. Ishikuro and T. Hiramoto, *Appl. Phys. Lett.* **76**, 209 (2000).
- [5] L. Zhuang, L. Guo and S. Y. Chou, *Appl. Phys. Lett.* **72**, 1205 (1998).
- [6] T. H. Wang, H. W. Li and J. M. Zhou, *Appl. Phys. Lett.* **78**, 2160 (2001).
- [7] J. W. Park, K. S. Park, B. T. Lee, C. H. Lee, Jung B. Choi, K.-H. Yoo, J. Kim, S. C. Oh, S. I. Park, K. T. Kim and J. J. Kim, *Appl. Phys. Lett.* **75**, 566 (1999).
- [8] A. I. Yakimov, A. V. Dvurechenskii, Yu. Yu. Proskuryakov, A. I. Nikiforov, O. P. Pchelyakov, S. A. Teys and A. K. Gutakovskii, *Appl. Phys. Lett.* **75**, 1413 (1999).
- [9] A. I. Yakimov, A. V. Dvurechenskii, A. I. Nikiforov and O. P. Pchelyakov, *Phys. Low-Dim. Struct.* **3/4**, 99 (1999).
- [10] A. I. Yakimov, A. V. Dvurechenskii, V. V. Kirienko, Yu. I. Yakovlev, A. I. Nikiforov and C. J. Adkins, *Phys. Rev. B* **61**, 10 868 (2000).
- [11] C. W. J. Beenakker, *Phys. Rev. B* **44**, 1646 (1991).

## Growth and characterization of Si–Si<sub>1–x</sub>Ge<sub>x</sub>–GaAs heterostructure with InGaAs quantum dots

T. M. Burbaev†, I. P. Kazakov†, V. A. Kurbatov†, M. M. Rzaev†  
and V. I. Vdovin‡

† P. N. Lebedev Physical Institute, RAS, 119991 Moscow, Russia

‡ Institute for Chemical Problems of Microelectronics, 109017 Moscow, Russia

**Abstract.** Heterostructure with In<sub>x</sub>Ga<sub>1–x</sub>As quantum dots on Si (001) substrate was grown by molecular beam epitaxy (MBE). Step graded Si–Si<sub>1–x</sub>Ge<sub>x</sub>–Ge buffer layers and In<sub>x</sub>Ga<sub>1–x</sub>As quantum dots (QDs) in GaAs matrix were deposited consecutively in two different MBE systems. Optical and structural characterizations of heterostructure were performed by photoluminescence (PL) at 77 K and 300 K and transmission electron microscopy (TEM), respectively. Si–Si<sub>1–x</sub>Ge<sub>x</sub>–GaAs heterostructure with InGaAs QDs exhibited intense photoluminescence in range 1.3 μm at room temperature.

### Introduction

One of the moving questions of semiconductor technology is a direct growth of A<sup>3</sup>B<sup>5</sup> compounds on Si substrates. This is required to provide the optical performance needed for interchip and intrachip communication links. Current integration between optoelectronic devices and Si circuitry must rely on a complex flip-chip, hybridization, epitaxial liftoff methods, specific growth regimes and postgrowth treatments [1, 2], using of a Si–Si<sub>1–x</sub>Ge<sub>x</sub>–Ge buffer layers where  $x$  slowly graded from 0 to 1 [3]. The most promising tendency in such integration is the getting of A<sup>3</sup>B<sup>5</sup> based light-emitters on Si substrate for the 1.3–1.55 μm range for telecommunication, for example: QDs lasers [4]. Numerous studies on the growth of InAs QDs embedded in silicon have been performed at last years [5–7]. Recently we have reported successful growth of InGaAs islands in GaAs matrix on Si substrate with Si<sub>1–x</sub>Ge<sub>x</sub> step graded buffer layers exhibited intense photoluminescence (PL) in range 1.3 μm at room temperature [8]. In the present work we study structural and optical properties of Si–Si<sub>1–x</sub>Ge<sub>x</sub>–GaAs heterostructure with InGaAs QDs by PL at 77 K and 300 K and TEM, respectively.

### 1. Experimental details

The growth of heterostructure was carried out consecutively in two different MBE systems. Si<sub>1–x</sub>Ge<sub>x</sub> step graded buffer layers were grown in KATUN MBE system equipped with two e-beam evaporators for Si and Ge. Then GaAs layers containing InGaAs QDs was grown in TSNA-25 solid source MBE system. 3"Si (001) wafers were used as substrates. The removal of silicon oxide from substrates was accomplished in growth chamber by anneal under weak silicon flow at substrate temperature ( $T_s$ ) 1000 °C. A 100 nm Si buffer was first grown at 750 °C, followed by a low-temperature (LT) Si layer deposited at 400 °C with thickness of 50 nm. Recent reports indicated that the use of LT Si buffer layer provides high-quality strain-relaxed SiGe buffer layers and could significantly reduce threading dislocation density in the Si/SiGe heterostructures [9]. By using the LT technique we

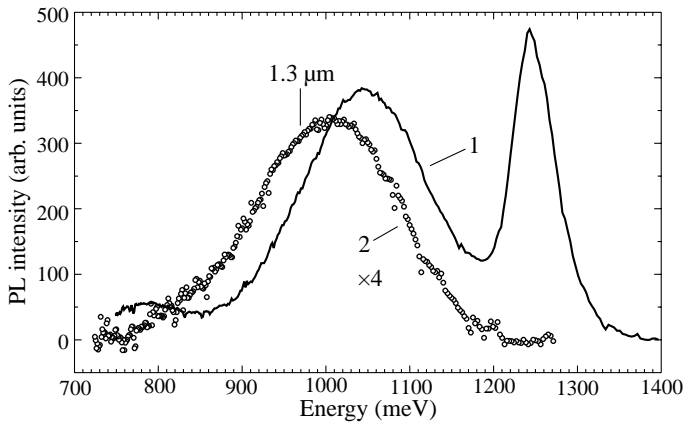


**Fig. 1.** PL spectra of Si-Si<sub>1-x</sub>Ge<sub>x</sub>-GaAs heterostructure with QDs of InGaAs. 1 —  $T = 77$  K, 2 —  $T = 300$  K.

have grown Si<sub>1-x</sub>Ge<sub>x</sub> layers ( $x = 0.3; 0.62; 1.0$ ). Each of this layers consist of 50 nm LT-Si<sub>1-x</sub>Ge<sub>x</sub> ( $T_s = 250$  °C) followed by a 150 nm Si<sub>1-x</sub>Ge<sub>x</sub> grown at  $T_s = 500$  °C. The heterostructure was capped by 5 nm Si. Then structure was carried through atmosphere into TSNA-25 MBE system. Cleaning procedure in A<sup>3</sup>B<sup>5</sup> growth chamber consisted of the heating of heterostructure at  $T_s = 800$  °C in Ga flow. After this step GaAs layer with 200 nm thickness was grown at  $T_s = 700$  °C, followed by the growth of In<sub>x</sub>Ga<sub>1-x</sub>As ( $x \approx 0.5$ ) QDs layer at  $T_s = 650$  °C, and 20 nm-GaAs cap layer ( $T_s = 650$  °C). QDs were grown by cyclical deposition of the InAs (2 sec.)/GaAs (2 sec.) with nominal thickness 3 nm.

The cleaning and growth processes were controlled by in situ reflection high energy electron diffraction (RHEED). After the deposition of In<sub>0.5</sub>Ga<sub>0.5</sub>As QDs layer, transition from 2D to 3D growth mode was monitored through coexisting of streaky and spotty RHEED patterns. RHEED measurements allowed us to value lattice constant ratio  $a_{\text{InGaAs}}/a_{\text{GaAs}} = 1.034$ . This value corresponds to the In composition of  $x \approx 0.5$  except strain appeared due to QDs and GaAs matrix lattice mismatch.

PL spectra were measured at 77 K and 300 K with the use of a MDR-2 monochromator. A semiconductor laser with wavelength of  $\lambda = 0.66$   $\mu\text{m}$  (quantum energy  $h\nu = 1.87$  eV) served as an excitation source. The maximum radiation power was of 70 mW, with the power density incident on a sample equal to 4 W/cm<sup>2</sup>. The emission from the samples was recorded using a liquid-nitrogen cooled germanium p-i-n photodiode. The structural studies were performed by TEM (JEM-200CX) on cross-sectional and plan-view samples.

## 2. Results and discussion

The PL spectrum at 77 K shows (Fig. 1 (line 1)) recombination lines from 2D wetting layer (1235 meV) as well as 3D InGaAs QDs (1045 meV). At room temperature, the PL intensity from QDs (Fig. 1 (line 2)) is about four times lower. The large full width at half-maximum (FWHM) of the QDs emission line in this sample can be explained by fluctuations in InGaAs QDs size as well as their composition. It is well known that segregation of InGaAs on the rough surface leads to the lateral change in alloy composition of islands due to different migration lengths of In and Ga [10]. In our in situ RHEED measurements we observed such mixed 2D-3D structure. After removing GaAs/InGaAs layers by wet etching

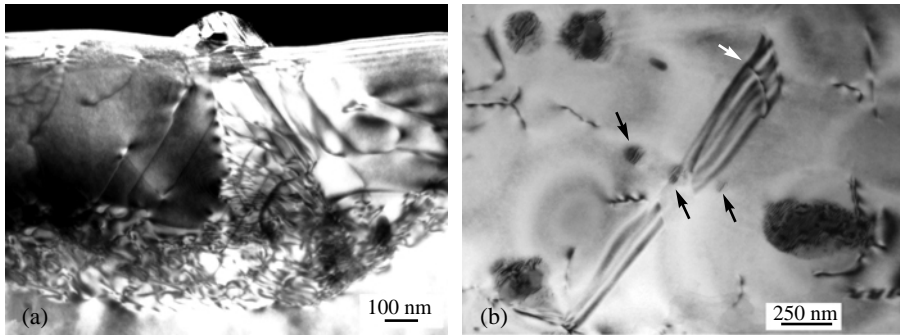


**Fig. 2.** TEM micrographs of structural defects in the heterostructure: (a) — cross-sectional image (dark field); (b) — plan-view image of the top layers. White arrow indicates the antiphase boundary in the GaAs layer. Black arrows indicate separate small islands with moiré contrast.

in  $\text{H}_2\text{SO}_4\text{:H}_2\text{O}_2\text{:H}_2\text{O}$  we observed recombination lines from  $\text{Si}_{1-x}\text{Ge}_x$  buffer layers and weak line of bound exciton with emission of TO phonon in PL spectrum at 77 K. It is clear that GaAs/InGaAs layers are the new more powerful channel an radiative recombination.

The structural studies show that a highly developed relief has been formed at the heterostructure surface because of a corrugation of interfaces in the SiGe buffer layer (Fig. 2a). Nevertheless, a deep strain relaxation has been achieved in this layer, which allowed getting almost unstained GaAs layer. The GaAs layer consists of the antiphase domains (Fig. 2b) and contains a high density,  $\sim 10^9 \text{ cm}^{-2}$ , of the threading dislocations (TDs). Numerous islands are observed by TEM on both plan-view and cross-sectional foils. There is a great spread in the height and lateral sizes of the islands. Small islands with height less than 10 nm are no uniformly arranged on the surface with the density  $\sim 10^8 \text{ cm}^{-2}$ . Such islands are free of the extended defects because they do not contact with TDs. Large islands with height of about 10–60 nm are the agglomerates of the small islands. They possess pyramidal shape and contain dislocations and microtwins (Fig. 2a). The same parallel moiré contrast is observed under all islands. We can suggest that more than 70% of the small islands are included into the large agglomerates, which can be attributed to the influence of the corrugated surface on the island nucleation.

### 3. Conclusion

The possibility of growing  $\text{In}_{0.5}\text{Ga}_{0.5}\text{As}$  QDs growth on Si substrate with relatively thin Si- $\text{Si}_{1-x}\text{Ge}_x$ -Ge-GaAs buffer layer has been demonstrated. Despite the fact that heterostructure contains a high structural defects density we have achieved intense PL in range  $1.3 \mu\text{m}$  at room temperature. This effect can be explained by a localization of the radiative recombination processes in QDs with perfect crystalline structure, which are nucleated apart from any structural defects.

### Acknowledgements

This research work was supported by Program's: RFBR (No 01-02-17732); Government support of scientific schools (No 00-15-96568); "Physics on solid-state nanostructures" and "Advanced devices for micro- and nanoelectronics" (No 204-1(00)-P).

### References

- [1] E. Gil-Lafon, A. Videcoq, J. Napierrala, D. Castelluci, A. Pimpinelli, B. Gerard, J. Jimenez and M. Avella, *Optical Materials* **17**, 267 (2001).
- [2] Z. I. Kazi, T. Egawa, M. Umeno and T. Jimbo, *J. Appl. Phys.* **90**, 5463 (2001).
- [3] S. M. Ting and E. A. Fitzgerald, *J. Appl. Phys.* **87**, 2618 (2000).
- [4] D. Bimberg, M. Grundmann, F. Heinrichsdorff, N. N. Ledentsov, V. M. Ustinov, A. E. Zhukov, A. R. Kovsh, M. V. Maximov, Y. M. Shernyakov, B. V. Volovik, A. F. Tsatsul'nikov, P. S. Kop'ev and Zh. I. Alferov, *Thin Solid Films* **367**, 235 (2000).
- [5] G. E. Cirlin, N. K. Polyakov, V. N. Petrov, V. A. Egorov, D. V. Denisov, B. V. Volovik, V. M. Ustinov, Zh. I. Alferov, N. N. Ledentsov, R. Heitz, D. Bimberg, N. D. Zakharov, P. Werner and U. Gosele, *Materials Science and Engineering* **B80**, 108 (2001).
- [6] L. Hansen, F. Bensing and A. Waag, *Thin Solid Films* **367**, 85 (2000).
- [7] T. Uragami, H. Fujioka, I. Waki, T. Mano, K. Ono, M. Oshima, Y. Takagi, M. Kimura and T. Suzuki, *Jap. J. Appl. Phys. Part 1* **39**, 4483 (2000).
- [8] T. M. Burbaev, I. P. Kazakov, V. A. Kurbatov, M. M. Rzaev, V. A. Tsvetkov, V. I. Tsekhosh and A. G. Touryanski, *Proc. of the 5th Russian Conference on Semiconductor Physics*, Nizhii-Novgorod, Russia, 10–14 September 2001.
- [9] C. S. Peng, H. Chen, Z. Y. Zhao, J. H. Li, D. Y. Dai, Q. Huang, J. M. Zhou, Y. H. Zhang, C. H. Tung, T. T. Sheng and J. Wang, *J. Cryst. Growth* **201/202**, 530 (1999).
- [10] K. Kamath, J. Phillips, J. Singh and P. Bhattacharya, *J. Vac. Sci. Technol.* **B14**, 2312 (1996).

## Surface polaritons at nanoporous carbon-silicon interface

I. P. Ipatova<sup>†</sup>, O. V. Proshina<sup>‡</sup> and G. Benedek<sup>‡</sup>

<sup>†</sup> Ioffe Physico-Technical Institute, St Petersburg, Russia

<sup>‡</sup> Università degli Studi di Milano - Bicocca, 20125 Milano, Italy

**Abstract.** This paper deals with the effect of the electromagnetic field enhancement in three-layered system due to the propagation of a polariton wave at the interface of nanoporous carbon film — silicon substrate.

Nanostructured carbon films grown by supersonic cluster beam deposition [1] are known to be highly porous and self-affine. The surface corrugation and the intrinsic porosity of the film is assumed to be the vehicle for a direct conversion of the incident photon into a polariton and viceversa.

It is known from literature [2] that polaritons propagate at the interface with negative dielectric function medium. Carbon and silicon are semiconductors the dielectric function of which becomes negative in the region of anomalous dispersion caused by exciton absorption. While  $\varepsilon_{Si}(\omega)$  is known from current literature, Raman spectra of the carbon nanoporous films performed by Milani et al. in [1] show that the carbon films are essentially graphitic-like with the presence of high number of distorted  $sp^2$  bonds and they have some  $sp^3$  bonding, at a level of approximately 10–12%. Similar  $sp^2$  bonding is well known for graphite crystals. The resemblance allows us to use the dispersion dependence of dielectric function of graphite from Johnson and Dresselhaus [3] for the dielectric function of the porous carbon  $\varepsilon_C(\omega)$ . The imaginary parts of  $\varepsilon_C(\omega)$  and  $\varepsilon_{Si}(\omega)$  can be neglected in our calculations.

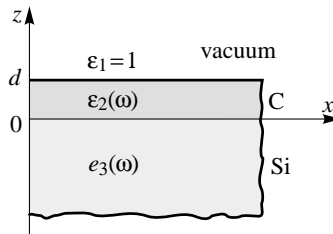


**Fig. 1.** Three-layered system.

The three-layered system consisting of a silicon substrate suspended in vacuum and covered on the upper side by a nanoporous carbon film of average thickness  $d$  is considered, see Fig. 1. We are interested in the possibility of polariton wave propagation on the boundary between carbon film (medium 2) and silicon substrate (medium 3). The polariton electric field propagating in the system is assumed to have the form

$$\mathbf{E}(z) = \mathbf{E}_1 \exp[-|\kappa_1|z] \exp i[\mathbf{K}\mathbf{R} + \omega t] \quad z > d \quad (1)$$

$$\mathbf{E}(z) = (\mathbf{E}_2 \exp[|\kappa_2|z] + \mathbf{F}_2 \exp[-|\kappa_2|z]) \exp i[\mathbf{K}\mathbf{R} + \omega t] \quad 0 < z < d \quad (2)$$

$$\mathbf{E}(z) = \mathbf{E}_3 \exp[|\kappa_3|z] \exp i[\mathbf{K}\mathbf{R} + \omega t] \quad z < 0, \quad (3)$$

respectively. Quantities  $\kappa_1$ ,  $\kappa_2$  and  $\kappa_3$  must be imaginary, i.e.  $\kappa_{1,2,3} = i |\kappa_{1,2,3}|$ , if the solution is to represent a wave which decays away from the interface.

From the Maxwell equations

$$\nabla \times \mathbf{E} = -\frac{1}{c} \frac{\partial \mathbf{H}}{\partial t}, \quad \nabla \cdot \mathbf{E} = 0, \quad (4)$$

$$\nabla \times \mathbf{H} = \frac{\varepsilon}{c} \frac{\partial \mathbf{E}}{\partial t}, \quad \nabla \cdot \mathbf{H} = 0. \quad (5)$$

one can get the following wave equation

$$\nabla^2 \mathbf{E}(z) = -k^2 \varepsilon(\omega) \mathbf{E}(z) \quad (6)$$

where  $k \equiv \omega^2/c^2$ . The substitution of Eqs. (1)–(3) into Eq. (6) leads to dispersion relations

$$\kappa_1^2 = K^2 - k^2, \quad z > d \quad (7)$$

$$\kappa_2^2 = K^2 - k^2 \varepsilon_2(\omega), \quad 0 < z < d \quad (8)$$

$$\kappa_3^2 = K^2 - k^2, \varepsilon_3(\omega) \quad z < 0. \quad (9)$$

Here we take for the carbon film  $\varepsilon_2(\omega) = \varepsilon_C(\omega)$  and for the silicon substrate  $\varepsilon_3(\omega) = \varepsilon_{Si}(\omega)$ , whereas for the vacuum region  $\varepsilon_1 = 1$ . The polariton wave vector  $\mathbf{K}$  on this boundary is defined by Eqs. (7)–(9). The substitution of Eqs. (1)–(3) into Eq. (4) results in four relationships among normal  $z$  and parallel  $x$  components of the field amplitudes in the three dielectric regions:

$$E_{1z} = \frac{iK}{\kappa_1} E_{1x}, \quad z > d \quad (10)$$

$$E_{2z} = -\frac{iK}{\kappa_2} E_{2x}, \quad F_{2z} = \frac{iK}{\kappa_2} F_{2x}, \quad 0 < z < d \quad (11)$$

$$E_{3z} = -\frac{iK}{\kappa_3} E_{3x}, \quad z < 0. \quad (12)$$

The continuity conditions of the parallel component of the electric field and of the normal component of the displacement field at the two interfaces which can be combined with Eqs. (10)–(12) leads to the system of two linear homogeneous equations in the components  $E_{2x}$  and  $F_{2x}$ :

$$\left( \frac{1}{\kappa_1} \exp[\kappa_2 d] + \frac{\varepsilon_2}{\kappa_2} \exp[\kappa_2 d] \right) E_{2x} + \left( \frac{1}{\kappa_1} \exp[-\kappa_2 d] - \frac{\varepsilon_2}{\kappa_2} \exp[-\kappa_2 d] \right) F_{2x} = 0, \quad (13)$$

$$\left( \frac{\varepsilon_3}{\kappa_3} - \frac{\varepsilon_2}{\kappa_2} \right) E_{2x} + \left( \frac{\varepsilon_3}{\kappa_3} + \frac{\varepsilon_2}{\kappa_2} \right) F_{2x} = 0. \quad (14)$$

The solvability condition of Eqs. (13), (14) leads to

$$\left( \frac{\varepsilon_3 \kappa_2}{\varepsilon_2 \kappa_3} - 1 \right) \left( \frac{1}{\varepsilon_2 \kappa_1} - 1 \right) \exp[-2\kappa_2 d] = \left( \frac{\varepsilon_3 \kappa_2}{\varepsilon_2 \kappa_3} + 1 \right) \left( \frac{1}{\varepsilon_2 \kappa_1} + 1 \right) \quad (15)$$

which gives in an implicit form of the dispersion relation  $[\omega \text{ vs } \mathbf{K}]$  of the polariton in the system. We see from this equation that as  $d \rightarrow \infty$  it yields the two equations

$$\frac{1}{\varepsilon_2 \kappa_1} + 1 = 0, \quad (16)$$

$$\frac{\varepsilon_2}{\varepsilon_3} \frac{\kappa_3}{\kappa_2} + 1 = 0 \quad (17)$$

that are the dispersion relations for surface polaritons at the vacuum-carbon film interface and at the carbon film–silicon substrate interface, respectively. Equations (7)–(9) and Eqs. (16), (17) may be solved for the four unknown quantities  $K$ ,  $\kappa_1$ ,  $\kappa_2$ ,  $\kappa_3$ . Solutions have the form

$$K = \frac{\omega}{c} \sqrt{\frac{\varepsilon_2(\omega)\varepsilon_3(\omega)}{\varepsilon_2(\omega) + \varepsilon_3(\omega)}}, \quad (18)$$

$$\kappa_1 = i \frac{\omega}{c} \frac{1}{\sqrt{\varepsilon_2(\omega) + 1}}, \quad \kappa_2 = i \frac{\omega}{c} \frac{\varepsilon_2(\omega)}{\sqrt{\varepsilon_2(\omega) + \varepsilon_3(\omega)}}, \quad \kappa_3 = -i \frac{\omega}{c} \frac{\varepsilon_3(\omega)}{\sqrt{\varepsilon_2(\omega) + \varepsilon_3(\omega)}}. \quad (19)$$

It follows from Eq. (18) that the polariton wave vector  $\mathbf{K}$  is the real quantity when the sum  $\varepsilon_2(\omega) + \varepsilon_3(\omega)$  is negative

$$\varepsilon_2(\omega) + \varepsilon_3(\omega) < 0 \quad (20)$$

while either  $\varepsilon_2$  or  $\varepsilon_3$  must be positive quantity, i.e.

$$\varepsilon_2 > 0; \quad \varepsilon_3 < -\varepsilon_2. \quad (21)$$

Dielectric functions of graphite and Si are plotted on the similar scale in Fig. 2.

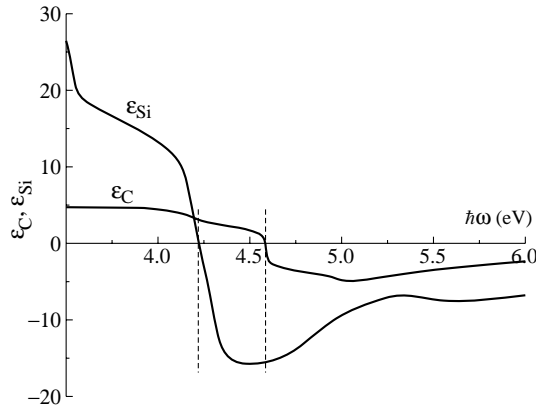


**Fig. 2.** Interval of the surface polariton propagation

It is seen that combination of C-film with Si-substrate opens the unique possibility to get the propagation of the surface polariton wave in the frequency interval

$$\Delta \hbar\omega \approx 4.2\text{--}4.5 \text{ eV} \quad (22)$$

where the anomalous dispersion of the silicon dielectric function occurs. In the frequency interval Eq. (22),  $\varepsilon_{Si}(\omega)$  is the steep function and  $\varepsilon_C(\omega)$  has slow dependence on frequency. The condition Eq. (21) holds:  $\varepsilon_C > 0$  and  $\varepsilon_{Si} < -\varepsilon_C$ . Therefore the interface polariton propagation is allowed in this interval.

The distribution of the electric field within the carbon layer can be obtained from ratio of amplitudes in Eq. (14) at the bottom (medium 3) and at the top of the carbon film



(medium 2), respectively:

$$\frac{E_{3x}(0)}{E_{2x}(d)} = \frac{2 \frac{\varepsilon_2}{\kappa_2}}{\left(\frac{\varepsilon_2}{\kappa_2} + \frac{\varepsilon_3}{\kappa_3}\right) \exp[\kappa_2 d] + \left(\frac{\varepsilon_2}{\kappa_2} - \frac{\varepsilon_3}{\kappa_3}\right) \exp[-\kappa_2 d]} \quad (23)$$

By substitution of C-Si interface polariton dispersion relation Eq. (17) into Eq. (23), one can get

$$\frac{E_{3x}(0)}{E_{2x}(d)} = \exp[\kappa_2 d]. \quad (24)$$

The relation Eq. (24) shows that electric field of the surface polariton increases exponentially with the thickness of the carbon film  $d$ . The exponential increase is limited by the absorption which is not taken in account. It means that there is an optimum value of the carbon film thickness  $d_{\text{opt}}$  which corresponds to the maximum field ratio.

The effect of polariton field enhancement could be observed in Raman scattering. The Raman scattering cross section should be the nonmonotonous function of the carbon film thickness  $d$ . The comparison with experimental data of the width of “exciton window”, the optimum value of  $d_{\text{opt}}$ , the dispersion law of the surface polariton would allow to see the difference between parameters of nanoporous film and parameters of graphite.

#### Acknowledgements

This work was supported in different parts by the RFBR, grants 00-15-96812, 01-02-04012; by Federal Program 1.107 “Surface Atomic Structures”; by Federal Program 97-2014 “Physics of Solid State Nanostructures”; by RAS Program “Low-dimensional quantum structures”, grant 6.4.

#### References

- [1] P. Milani, M. Ferretti, P. Piseri, C. E. Bottani, A. Ferrari, A. Li Bassi, G. Guizzetti and M. Patrini, *J. Appl. Phys.* **82**, 5793 (1997).
- [2] E. Burstein, A. Hartstein, J. Schoenwald, A. A. Maradudin, D. L. Mills and R. F. Wallis, *Polaritons*, Pergamon, New York, 1974, p. 89.
- [3] L. G. Johnson and G. Dresselhaus, *Phys. Rev. B* **7**, 2275 (1973).

## Shallow acceptors in Si/SiGe QW heterostructures

*D. V. Kozlov, V. Ya. Aleshkin and V. I. Gavrilenko*

Institute for Physics of Microstructures of Russian Academy of Sciences,  
 GSP-105, Nizhny Novgorod, 603950, Russia

**Abstract.** The new theoretical method for calculation of acceptor spectra in Si/SiGe heterostructures using  $6 \times 6$  Luttinger Hamiltonian, taking into account the anisotropy effects has been developed.

### Introduction

The energy spectrum of a shallow impurity in a quantum well (QW) heterostructure is known to be sensitive to both the well width and the impurity position in the well. The problem is the most complicated for the acceptors in strained heterostructures [1–2]. The ‘built-in’ deformation splits the light and heavy hole subbands thus reducing the effective masses and the binding energy of acceptors. The QW confinement on the one hand leads to stronger localization of the hole wave function near the impurity ion and increases the binding energy and, on the other hand, it also results in light and heavy hole subbands splitting thus increasing the effect of built-in strain. At last the binding energy depends significantly on the impurity position in the well. The paper deals for the first time with shallow acceptors in Si/SiGe heterostructures with strained SiGe quantum wells grown on Si(001) substrates. Recently in such heterostructures excited by high electric fields the stimulated far IR emission has been observed, the effect being attributed to the radiative transitions between shallow acceptor levels [3].

### 1. Theoretical formalism

Shallow acceptors spectra in Si/SiGe QW heterostructures have been calculated in the framework of the envelope function approximation. The acceptor Hamiltonian used is  $6 \times 6$  matrix operator included Luttinger Hamiltonian which takes into account the spin-split subband [4], the deformation term [5], the confinement potential due to valence-band discontinuity and the potential of an impurity center. Similar to the work [6] the acceptor envelope function has been expanded in the basis of free hole envelope functions in the QW ( $g_n^s(\mathbf{k}, z)e^{i\mathbf{k}\rho}$ ), which are the eigenstates of the Hamiltonian not containing the Coulomb potential:

$$F^s(\mathbf{r}) = \sum_n \int d\mathbf{k} R_n(\mathbf{k}) g_n^s(\mathbf{k}, z) e^{i\mathbf{k}\rho}. \quad (1)$$

Here  $n$  is the number of a subband,  $\mathbf{r}$  is the radius-vector,  $\rho$  is the in-plane radius-vector,  $\mathbf{k}$  is the hole wave vector, and  $s = (-3/2, -1/2, 1/2, 3/2)$  is the spin projection on the  $z$  axis. The expansion coefficients depend on both the value ( $k$ ) and the direction (determined by the angle  $\alpha$ ) of the wave vector  $\mathbf{k}$ . The acceptor wave function is transformed according the irreducible representation of the group  $C_4$ . Therefore expansion coefficients and free hole envelope functions is transformed at the rotation around  $z$  axis as:

$$C_4[g_n^s(k, \alpha, z) R_n(k, \alpha)] = g_n^s(k, \alpha, z) R_n(k, \alpha) \exp\left(im\frac{\pi}{4}\right) \quad (2)$$

where  $m = \pm 3$  or  $\pm 1$ , which corresponds to the different irriducible representation of group  $C_4$ .

By substituting expansion (1) into the Schrödinger equation for the envelope function the integral equations for the above expansion coefficients are obtained. The integrals have been approximated by discrete sums over the hole momentum  $k$  and the angle  $\alpha$ . The step difference by  $k$  has been chosen much less than the inverse Bohr radius and the step by  $\alpha$  has been set of  $\pi/4$ . The sums have been interrupted at  $k$  much greater than the inverse Bohr radius. Therefore, the problem has been reduced to diagonalization of the finite symmetric matrix.

## 2. Results and discussion

The calculation results on the shallow acceptor spectrum in a typical Si/SiGe heterostructure are given in the Table 1 in comparison with those for the bulk Si. In both cases the chemical shifts is not taken into account. It is clearly seen, that the binding energies of acceptors states in the strained QW heterostructure are much less than those in bulk Si.

**Table 1.**

	Si/Si <sub>0.8</sub> Ge <sub>0.2</sub> heterostructure ( $\epsilon = 5 \times 10^{-3}$ , $d_{QW} = 180 \text{ \AA}$ )	Bulk Si (envelope function approximation)
Ground state (s-like)	17.0 meV	31.5 meV [8]
1st excited state (p-like)	6.5 meV	15.6 meV [7]
2nd excited state	3.0 meV	11.4 meV [7]

Figure 1 represents the shallow acceptor ground and lowest excited state energies versus QW width. One can see that the ionization energy reaches the minimum value of 16.5 meV at  $d_{QW} = 150 \text{ \AA}$ . Such nonmonotonous dependence of the binding energy on QW width reflects the above mentioned dual effect of the quantum confinement on the acceptor spectrum.

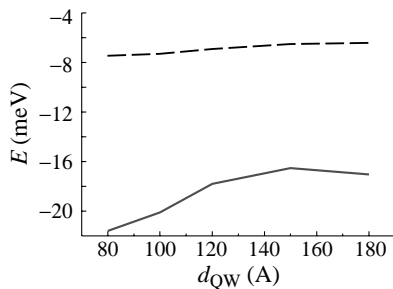


**Fig. 1.** Calculated binding energies of the ground and the lowest excited states of on- center acceptors (i.e acceptors placed at QW center) in Si/Si<sub>0.8</sub>Ge<sub>0.2</sub> ( $\epsilon = 5 \times 10^{-3}$ ) QW heterostructure versus the well width. Solid line: ground states, dashed line: the lowest excited p-like state.

Figure 2 presents the binding energy dependences on the impurity position in QWs. It is clearly seen that the binding energy of on-center acceptor is much greater than that of on-edge (i.e. placed at the heterointerface) acceptor.

In order to compare the calculation results with the available experimental data we have to take into account the chemical shift of the binding energy which is known to be significant for shallow acceptors in Si. The smallest chemical shift of the ground is observed for the borom impurity:  $\Delta E_{chem} = 15.2 \text{ meV}$  [7]. For the shallow impurity in a QW structure one can estimate the chemical shift from the following simple considerations. The shift is determined by the squared amplitude of the acceptor wave function in position of impurity

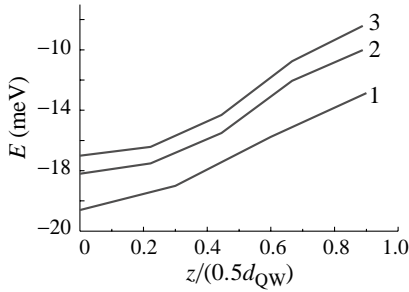


**Fig. 2.** Calculated binding energies of the ground states for some heterostructures versus the displacement from the center to the edge of QW. Line 1 correspond to the heterostructures Si/Si<sub>0.85</sub>Ge<sub>0.15</sub> ( $\epsilon = 3.75 \times 10^{-3} d_{\text{QW}} = 100 \text{ \AA}$ ), line 2: Si/Si<sub>0.85</sub>Ge<sub>0.15</sub>  $\epsilon = 3.75 \times 10^{-3} d_{\text{QW}} = 180 \text{ \AA}$ , line 3: Si/Si<sub>0.8</sub>Ge<sub>0.2</sub>  $\epsilon = 5 \times 10^{-3} d_{\text{QW}} = 180 \text{ \AA}$ .

ion [9]:  $\Delta E_{\text{chem}} \sim f^2(\mathbf{r} = 0)$ . By this reason the chemical shift for the p-like states should be negligible. For s-like states, as it follows from normalization conditions,  $f^2(\mathbf{r} = 0) \sim 1/a^3$  where  $a$  is the Bohr radius. On the other hand,  $E_i \sim 1/a^2$  where  $E_i$  is the binding energy. In that way:  $\Delta E_{\text{chem}} \sim E_n^{3/2}$ . Therefore, for the ground state of boron acceptor in Si/Si<sub>0.8</sub>Ge<sub>0.2</sub> heterostructure (1st line in the Table 1) one can estimate the chemical shifts as  $(17 \text{ meV}/31.5 \text{ meV}) \cdot 15.2 \text{ meV} \approx 6 \text{ meV}$ . Thus for this boron doped structure the ground state binding energy could be estimated as  $(17 + 6) \text{ meV} = 23 \text{ meV}$  and the separation between the ground and the 1st excited p-like state as  $(17 + 6 - 6.5) \text{ meV} = 16.5 \text{ meV}$ .

Charge transport in  $\delta$ -doped with boron Si/Si<sub>0.85</sub>Ge<sub>0.15</sub> heterostructure ( $d_{\text{QW}} = 200 \text{ \AA}$ ) was investigated in [10]. From the temperature dependence of the conductivity the activation energy of 18 eV was determined for on-center acceptors. This number corresponds fairly well to the estimated above energy separation between the ground and the first excited state of on-center boron acceptor. By the authors of Ref. [10] opinion the holes from the upper state of on-center acceptor can pass into the valence band in the QW by tunneling due to transverse electric field that incline the valence band thus making an excited state resonant.

### Acknowledgements

The research described in this publication was made possible in part by RFBR (Grants 00-02-16568, 01-02-16106) and the Russian Scientific Program "Leading Scientific School" (00-15-96618).

### References

- [1] A. Pasquarello, L. C. Andreani and R. Buczko, *Phys. Rev. B* **40**, 5602 (1989).
- [2] Loehr and J. Singh, *Phys. Rev. B* **41**, 3695 (1990).
- [3] I. V. Altukhov, M. S. Kagan *et al*, *Thin solid films* **380**, 237 (2000).
- [4] J. M. Luttinger, *Phys. Rev. B* **102**, 1030 (1956).
- [5] G. L. Bir and G. E. Pikus, *Symmetry and Strain-Induced Effects in Semiconductors*, John Wiley and Sons, New York, 1974.
- [6] V. Ya. Aleshkin, B. A. Andreev, V. I. Gavrilenko, I. V. Erofeeva, D. V. Kozlov and O. A. Kuznetsov, *Semiconductors* **34**, 563 (2000).
- [7] A. Baldereschi, N. O. Lipari and M. Altarelli, *Bull. of the Academy of Science, Physical Series* (in Russian) **42**, 1179 (1978).
- [8] A. Baldereschi and N. O. Lipari, *Phys. Rev. B* **9**, 1525 (1974).
- [9] E. I. Voevodin, E. M. Hershinson, G. N. Gol'zman and N. G. Pitsina, *Semiconductors* **23**, 1356 (1989).
- [10] I. V. Altukhov, M. S. Kagan *et al*, *Thin Solid Films* **380**, 218 (2000).

## About the “phosphorus” sensitization of silicon quantum dots in SiO<sub>2</sub> photoluminescence

D. I. Tetelbaum<sup>†</sup>, V. A. Burdov<sup>‡</sup>, A. N. Mikhaylov<sup>†</sup> and S. A. Trushin<sup>†</sup>

<sup>†</sup> Physico-Technical Research Institute of University of Nizhnii Novgorod,  
603950 Nizhnii Novgorod, Russia

<sup>‡</sup> University of Nizhnii Novgorod, 603950 Nizhnii Novgorod, Russia

**Abstract.** The question about the mechanisms of the photoluminescence enhancement of the system of silicon nanocrystals embedded into silica matrix at phosphorus doping is described. Both the experimental and theoretical arguments are presented.

### Introduction

The system of silicon quantum dots in SiO<sub>2</sub> (SiO<sub>2</sub>:Si) attracts a great attention due to the prospects of its application in optoelectronics (saving silicon as a basis material). The capability for the luminescence in the red — near IR region is one of the most important characteristics of given system. In this connection, the question about the ways of the enhancement of the photoluminescence (PL) effectiveness (quantum yield) is very actual. In [1], at the first time, there was shown that one of the methods of PL sensitization is phosphorus doping (the system was synthesized by Si<sup>+</sup> ion implantation in SiO<sub>2</sub> and subsequent annealing at 1000°, phosphorus was introduced also by ion implantation). Later, this fact was confirmed in some another works [2–5]. However, the nature of “phosphorus” sensitization is not yet clear. In [1], we have suggested two mechanisms which are responsible for this effect: the passivation of dangling bonds on silicon nanocrystal (NC) interfaces and the presence of the phosphorus atoms inside NC. We have presented the experimental data and some theoretical arguments speaking in favor of these mechanisms.

### 1. Experiments and discussion

The thermal oxidised samples of Si (specific resistance  $\sim 10 \Omega \text{ cm}$ ) with the SiO<sub>2</sub> thickness of 300 nm are used. The room temperature Si<sup>+</sup> implantation was provided at the energy  $E = 150 \text{ keV}$  and at the Si<sup>+</sup> dose  $\Phi = 10^{17} \text{ cm}^{-2}$ . One part of the samples was additionally implanted by different P<sup>+</sup> doses with the same energy  $E = 150 \text{ keV}$ . After implantation, the samples were annealed at 1000°C, 2h in N<sub>2</sub> stream. The PL spectra were measured at room temperature for excitation wavelength  $\lambda = 488 \text{ nm}$ .

In Fig. 1, the dependence of the PL intensity on the radiation wavelength is presented for the cases of phosphorus doping (curves 2–5) and without doping (curve 1). It is seen that intensity magnitude steadily grows with P dose. According an estimation, each NC contains more than one phosphorus atom at the dose of  $\sim 10^{16} \text{ cm}^{-2}$  and at the random distribution of P atoms. This speaks against the suggestion [4, 5] that the quenching role of P (which they have observed at high impurity concentration) is connected with Auger recombination when P atoms appear inside NC's. Certainly it is not a decisive argument.

So, what might be the “phosphorus” sensitization mechanisms? One of them is saturation of dangling bonds at NC/SiO<sub>2</sub> interface. Saturation is possible due to the presence of

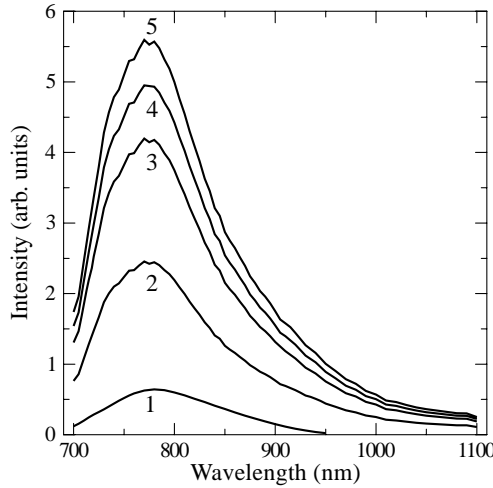


**Fig. 1.** Dependence of the PL intensity on the photon wavelength for undoped sample (1) and for the samples, doped with various P implantation doses ( $\Phi_P$ ,  $10^{16} \text{ cm}^{-2}$ ): 2 — 0.1; 3 — 0.3; 4 — 1; 5 — 3.

the five valence electrons of the phosphorus atom, four of which can participate in regular bonds and fifth one can close dangling bond (similar to the hydrogen). The second mechanism is the presence of free electrons in doped NC's even in the absence of excitation that provides additional channel for radiative recombination after throwing valence electron up to one of the energy level of  $\text{SiO}_2$  matrix. In condition of steady state excitation at room temperature, electrons can be thrown up to the conduction band (not necessary out of the valence band) both by the light and by thermal excitation.

There is one more factor that promotes “phosphorus” sensitization. It is connected with the difference of probabilities of radiative interband recombination at the presence via the absence of donor atoms in quantum dot. This factor is considered below.

## 2. Theoretical consideration

Let us consider the spherical silicon quantum dot of radius  $R$ , placed into a wide-band material, such as dielectric matrix. We must determine the possibility of an electron-hole recombination, accompanied by the photon radiation. This possibility is described by the Fermi golden rule

$$P_{if} = \frac{2\pi}{\hbar} \sum_{\mathbf{q}, \sigma} |V_{if}|^2 \delta[E_i - E_f - \hbar\omega(\mathbf{q})]. \quad (1)$$

Here  $V_{if}$  is the matrix element, calculated between initial and final states,  $E_i$  and  $E_f$  are the energies of these states and  $\omega(\mathbf{q})$  is the frequency of photon with the wave vector  $\mathbf{q}$  and polarization  $\sigma$ . We'll have assumed that initial state corresponds to the lowest electron energy level in the conduction band, and final state corresponds to the highest energy level in the valence band of the quantum dot.

For determination of the wave functions both the initial and final states we must solve

the Shrodinger-like equation for the envelope functions  $F_j(\mathbf{r})$

$$\sum_j \hat{H}_{ij} F_j(\mathbf{r}) = E F_i(\mathbf{r}), \quad (2)$$

where  $\hat{H}_{ij}$  is the matrix differential operator, which is represented by  $3 \times 3$ -matrix for the valence band [6] and  $2 \times 2$ -matrix for the conduction band [7]. We neglect the spin-orbit interaction, because it is rather weak in silicon, therefore the spin variables can be omitted.

At first, we shall calculate the possibility (1) in the absence of impurity ions. Using the expressions for the envelope functions, which have been obtained in [8], and the expansion of Bloch functions on the Fourier series we shall have

$$P_{if} = \frac{e^2(E_i - E_f)}{8\pi^2 m_0^2 c^3 a^2} \left(\frac{a}{R}\right)^8 \sum_{\sigma=1}^2 |D_{\sigma}|^2, \quad (3)$$

where  $m_0$  and  $e$  are the mass and the charge of a free electron,  $c$  is a light velocity,  $a$  is the lattice constant and  $D_{\sigma}$  is a complex dimensionless parameter of the order of unity. As it is followed from Eq. (3), the recombination rate is determined by the eight order of  $(a/R)$ -ratio. It is a consequence of that the silicon is an indirect-gap material, and the electron-hole transitions in a bulk silicon are forbidden. This result may be easily obtained from Eq. (3) by supposing the dot radius to be equal to infinity.

The nonzero value of the possibility (3) for the quantum dots unlike the bulk silicon is explained by the Heizenberg uncertainties relation. The electron state in the quantum dot is a superposition of the  $\hat{\mathbf{k}}$ -operator eigenfunctions with the various wave vectors  $\mathbf{k}$ . In particular, there are some eigenfunctions in this superposition, which have a wave vector equal, or approximately equal to the distance between  $\Gamma$  and  $X$  points in  $\mathbf{k}$ -space. The quota of these eigenfunctions in the electron state in the quantum dot is rather small and determined by the relation  $(a/R)^4$ . Therefore the possibility of the electron-hole recombination is proportional to  $(a/R)^8$ .

When the quantum dot contains the hydrogen-like donors inside itself, the Coulomb interaction operator adds to the electron and hole ground states the wave functions of various high-energy states. In particular, the states with the typical wavelength of order the lattice constant  $a$  will be presented. These states do not arise in the electron and hole ground states when the impurity is absent, due to the specific kind of the Hamiltonian operator  $\hat{H}_{ij}$  both in the valence and conduction bands. All elements of the  $\hat{H}_{ij}$ -operator have the form  $\sim \hat{k}_i \hat{k}_j$ , and can bind the ground 1s-state (for example in the valence band) with the 1d-state only. Unlike this, the Coulomb interaction allows to bind the 1s-state with any other state in a quantum dot.

The quota of states with the typical wavelength  $\lambda \sim a$  in the ground states is  $\sim (a/R)^2 V/E_0$ , where  $V$  and  $E_0$  are the typical values of Coulomb matrix element and size quantization energy respectively. For the recombination possibility in the presence of donors the following estimation can be obtained

$$P_{if}(N) \sim \left(\frac{e^2 m R N}{\epsilon \hbar^2}\right)^2 P_{if}(0), \quad (4)$$

where  $N$  is the number of donors inside the quantum dot,  $m$  is an effective mass,  $\epsilon$  is the silicon permittivity and  $P_{if}(0)$  is determined by Eq. (3). For the typical values of  $R \sim 2$

nm, the coefficient before  $P_{if}(0)$  in Eq. (4) is proportional to  $N^2$ . If the number of donors inside the quantum dot is more than one, the intensity of the recombination processes can increase significantly.

### 3. Conclusions

- The enhancement of the photoluminescence under phosphorus doping can take place in the case of phosphorus atom located inside the silicon nanocrystals.
- The increase of the radiative interband transition probability for the case of phosphorus atom location in Si nanocrystals can serve as one of the cause “phosphorus” sensitization, especially for small nanocrystals sizes.

### Acknowledgements

The authors are grateful to V. K. Vasil’ev for the technical support in the ion implantation of the samples. The work was partially supported by INTAS grant No 00-0064 and by the program “Scientific researches of higher school in the foreground directions of science and technique” (subprogram 205).

### References

- [1] D. I. Tetelbaum, I. A. Karpovich, M. V. Stepikhova, V. G. Shengurov, K. A. Markov and O. N. Gorshkov, *Surface Investigation* **14**, 601 (1998).
- [2] D. I. Tetelbaum, O. N. Gorshkov, S. A. Trushin, D. G. Revin, D. M. Gaponova and W. Eckstein, *Nanotechnology* **11**, 295 (2000).
- [3] D. I. Tetelbaum, S. A. Trushin, V. A. Burdov, A. I. Golovanov, D. G. Revin and D. M. Gaponova, *Nucl. Instr. Meth. B* **174**, 123 (2001).
- [4] A. Mimuro, M. Fujii, S. Hayashi, D. Kovalev and F. Koch, *Phys. Rev. B* **62**, 12625 (2000).
- [5] M. Fujii, A. Mimuro, S. Hayashi, K. Yamamoto, C. Urakawa and H. Ohta, *J. Appl. Phys.* **87**, 1855 (2000).
- [6] A. I. Anselm, *Introduction to Semiconductor Theory*, Prentice-Hall, Englewood Cliffs (1981).
- [7] A. A. Kopylov, *Sov. Phys. Semicond.* **16**, 1380 (1982).
- [8] V. A. Burdov, *J. Exp. Theor. Phys.* **94**, 411 (2002).



## Parallel magnetic field induced strong negative magnetoresistance in a wide $p\text{-Ge}_{1-x}\text{Si}_x/\text{Ge}/p\text{-Ge}_{1-x}\text{Si}_x$ quantum well

*M. V. Yakunin*<sup>†</sup>, *G. A. Alshanskii*<sup>†</sup>, *Yu. G. Arapov*<sup>†</sup>, *V. N. Neverov*<sup>†</sup>  
and *O. A. Kuznetsov*<sup>‡</sup>

<sup>†</sup> Institute of Metal Physics RAS Ural branch, Ekaterinburg GSP-170, 620219 Russia

<sup>‡</sup> Scientific Research Institute at Nizhnii Novgorod State University, Russia

**Abstract.** A negative magnetoresistance (NMR) reaching maximum 30-40% of its zero-field value is observed under in-plane magnetic field for the hole gases confined in wide  $p\text{-Ge}_{1-x}\text{Si}_x/\text{Ge}/p\text{-Ge}_{1-x}\text{Si}_x$  quantum wells (QW), while in an analogous narrow QW the magnetoresistance doesn't exceed 1%. In the QWs of intermediate widths and hole densities, the NMR is explained as being caused by suppression of the intersubband scattering due to the upper subband depopulation. In the widest QWs with the highest hole densities the hole gas is self-divided into two 2D sublayers. A similar NMR observed in these samples is interpreted as also been due to suppression of the intersubband scattering, but subbands are the lowest symmetric and antisymmetric states of the formed double quantum well. The main effect of the in-plane magnetic field in this case is a relative shift of subbands along the wave vector, rather than the shift in energy.

A magnetic field oriented parallel to the layer cause changes in dissipation conditions of the current carriers, which constitute a spatially quantized gas confined in it. These effects manifest brightly when two or more confinement subbands are initially occupied. The parallel field gives rise to shifts in energy of different magnitude for levels with different energies due to different extent of their wave functions in the layer cross-section [1], and hence — to the changes in the intersubband dissipation [2]. Still more pronounced are the effects of parallel field in selectively doped structures with a sufficiently wide layer containing high density of carriers, in which the self-separation of the carrier gas occurs into two 2D sublayers located next to the opposite layer interfaces [3]. In this case the parallel field additionally induces relative shifts in  $k$ -space of the energy dispersion paraboloids pertaining to the emerged sublayers [4]. Existence of a small tunneling gap between levels of the formed sublayers manifests under parallel field in a complex configuration of the mutual energy dispersion surface consisting of two paraboloids shifted in  $k$  with a gap along the line of their intersection [5]. Dissipation of carriers in such a system depends on the Fermi level position relative singular points of this dispersion surface. Since the shift of paraboloids is proportional to the parallel field, the singular points move relative the Fermi level with field that manifests in a magnetoresistance of certain structure [6].

So far the effects of parallel field on the restricted orbital motion has been studied in layers with electron type of conductivity. Complex structure of the confinement subbands in the valence band due to existence of heavy and light holes [7] should lead to still more intricate effects of parallel magnetic field. These are due to considerable differences in curvature of the valence subbands, strong interaction between subbands in regions of their anticrossing that induces their high nonparabolicity etc. These anticipations are the stimuli for present researches.

Experiments are performed in  $\text{Ge}_{1-x}\text{Si}_x/\text{Ge}$  heterosystem, which is actual for the Si-based technology. The samples are  $\text{p-Ge}_{1-x}\text{Si}_x/\text{Ge}$  multy-quantum-wells with low temperature mobilities  $1\text{--}1.4\text{ m}^2/\text{V s}$ , different in the Ge layer width  $d_w$ , which is the quantum well (QW) for holes, and the hole density  $p_s$  in a Ge layer. The  $\text{Ge}_{1-x}\text{Si}_x$  barriers, sufficiently wide to prevent the inter-Ge-layer tunneling, are selectively doped with boron in their central parts. The sample parameters are given in Fig. 1 together with the experimental results.

As it has been found in our investigations of the quantum Hall effect (QHE), the hole gas is integrated through the whole Ge layer width (i.e. may be treated as a single quasi-2D hole gas) in structures 1123 and 1125, but is self-divided into two 2D sublayers in structures 475 and 476 with the widest wells and highest hole densities (see the inserts in Fig. 1). The brilliant indication of the differences between the integrated and divided hole gases is either existence or absence of the QH plateau for the filling factor  $\nu = 1$ . In samples 1123 and 1125 this plateau pronouncedly exists [8] concomitant with a deep minimum in the longitudinal magnetoresistance, while the  $\nu = 1$  peculiarities are missed in samples 475/476.

For sample 578 with the narrowest Ge layers,  $d_w \approx 8\text{ nm}$ , the magnetoresistance in parallel fields doesn't exceed 1% (Fig. 1(a)), indicating that the spin effects are negligible in the  $\text{p-Ge}_{1-x}\text{Si}_x/\text{Ge}$  system for our experimental conditions. Contrary, for the other samples with wider Ge layers a negative magnetoresistance (NMR) reaching 30–40% of its zero field value in fields  $B_{\parallel} \geq 12\text{ T}$  is observed (Fig. 1(b-d)).

In samples 1123 and 1125 this NMR may be explained in terms of the effect, well-known in the electron systems, of the diamagnetic shift of the upper electric subband that results in its depopulation and subsequent suppression of the intersubband scattering, initially present. The NMR may reach a value up to 50% for this mechanism [2]. Our numerical estimations made for the calculated QW potential relief of sample 1123 indicate that the parallel field  $B_{\parallel} \approx 10\text{ T}$  induces an increase of the intersubband distance  $\Delta E_{21} = E_2 - E_1$  of the order comparable to the Fermi level position  $E_F - E_2$  inside the  $E_2$  subband.

For sample 1123 the parallel field induced drop of MR is shifted to higher fields as compared to sample 1125 (Fig. 1(b,c)). This is in agreement with the deeper position of the Fermi level inside the second subband in sample 1123, found earlier from the structure of the QHE in these samples [9].

The  $\rho(B_{\parallel})$  curves for samples 475/476 are similar to those for sample 1125: the NMR that starts from the weakest fields and reaches the amplitude of  $\sim 30\%$  the zero field value (fig.1d). It is in spite of quite different layout of the energy levels in these samples (see the insert in Fig. 1(d)): the lowest levels  $E_1$  and  $E_2$  almost coincide, in accordance with nearly a complete separation of the hole gases into sublayers, and the Fermi level is much higher of them both. Thus, the simple picture of some level depopulation due to a diamagnetic shift doesn't fit this case.

Then, what is the cause of strong NMR in samples 475/476? The NMR may arise due to suppression of quantum corrections to the conductivity. They are valid for the case  $k_F l \gg 1$  ( $k_F$  — the Fermi wave vector,  $l$  — a mean free path) and have the value  $\sim 1/k_F l$ . For samples 457/476:  $k_F l = 10\text{--}15$ , so the maximum effect due to the quantum corrections should be less than 10%. These corrections may be responsible for NMR in relatively low fields, but cannot yield the observed strong NMR in high fields. All the other mechanisms known should lead to a positive magnetoresistance: MR in the vicinity of a metal-insulator transition [10]; MR due to increase of the in-plane mass in parallel field [11]; MR due to a strong coupling of the parallel field to the orbital motion in the quasi-2D systems [12] etc.

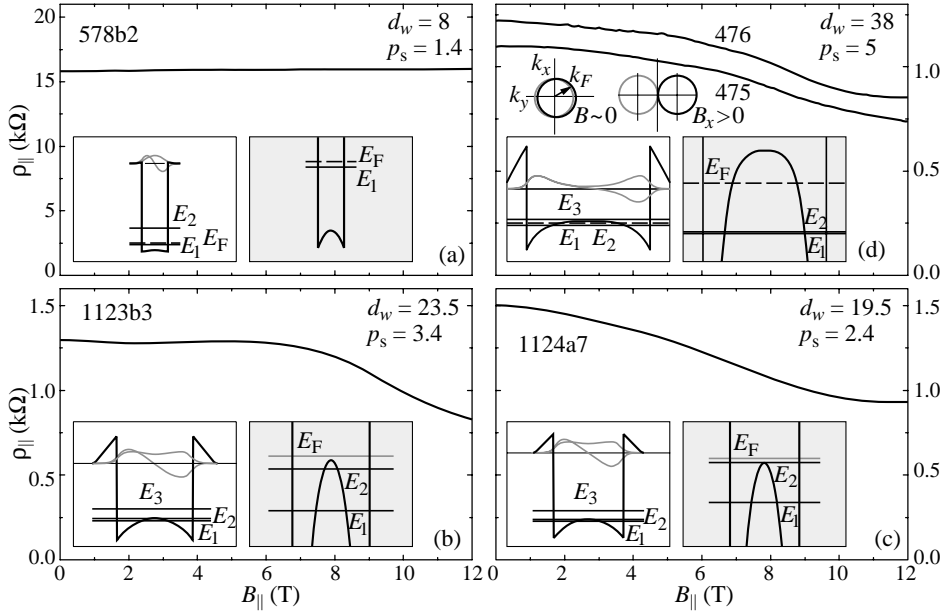


**Fig. 1.** Magnetoresistance in parallel magnetic fields of samples 578 (a), 1123 (b), 1125 (c) and 475/476 (d). Indicated are the well widths  $d_w$  [nm] and hole densities  $p_s$  [ $10^{15} \text{ m}^{-2}$ ]. In the insets: calculated energy profiles, energy levels, Fermi level and the wave functions. Left insets are the general views, and the right ones — the views enhanced in energy. Additional insets in (d) illustrate the shift of Fermi contours in  $B_{\parallel}$ .

We believe that nature of the NMR in samples 475/476 is also due to suppression of the intersubband scattering, but the mechanism of this scattering is unlike that in samples 1123 and 1125. The essential difference stems from that, while in samples 1123 and 1125 the potential in the Ge layer may be treated as a single QW, that of the samples 475/476 is effectively a double quantum well (DQW).

In a DQW, a parallel magnetic field  $B = B_x$  shifts the Fermi surfaces of the QWs in the plane direction along  $k_y$  on the value  $\Delta k_y = eBd/\hbar$ , with  $d$  - an effective distance between gases in the sublayers [13] (see the insets in Fig. 1(d)). While in a symmetrical DQW some finite probability exists for transitions between the two coinciding Fermi circles of the sublayers, it drops down as the circles shift relative each other in a parallel field. This drop has been directly observed in the tunneling current within a traditional DQW [14]. The remote impurity dominated inter-subband scattering is proportional to  $\exp(-2\Delta k_F L)$  [15] ( $\Delta k_F$  is the change of  $k$  in a scattering act;  $L$  — the spacer width) indicating that a shift of the Fermi contours causes the strong decrease of the in-plane resistivity as well. Additionally, the parallel field acts to increase the separation between sublayers [16] that also weakens transitions between them.

A considerable, up to  $\sim 30\%$ , NMR has been observed in some published experimental results in DQW structures [4, 6], albeit without comments. Notably, in a paper [4] experiments have been performed in the self formed DQW inside the wide QW, analogous to our case, but containing the electron gas.

A weak structure in the MR of samples 475/476 is superimposed on the monotonic background, in contrast to the smooth MR of samples 1123, 1125. A reasonable explanation

of this structure is in terms of weakly resolved complex structure of the energy dispersion surface of the DQW, self-formed in samples 475/476. This is the topic for further investigation.

#### *Acknowledgement*

The work is supported by RFBR, projects 02-02-16401 and 01-02-17685.

#### **References**

- [1] T. Ando, *J. Phys. Soc. Jpn.* **39**, 411 (1975).
- [2] Th. Englert, J. C. Maan, D. C. Tsui *et al*, *Sol. St. Commun.* **45**, 989 (1983).
- [3] Y. W. Suen, J. Jo, M. B. Santos *et al*, *Phys. Rev. B* **44**, 5947 (1991).
- [4] T. Jungwirth, T. S. Lay, L. Smrcka *et al*, *Phys. Rev. B* **56**, 1029 (1997).
- [5] S. K. Lyo, N. E. Harff and J. A. Simmons, *Phys. Rev. B* **58**, 1572 (1998).
- [6] J. A. Simmons, S. K. Lyo, N. E. Harff *et al*, *Phys. Rev. Lett.* **73**, 2256 (1994).
- [7] M. I. D'yakonov and A. V. Haetskii, *ZhETF* **82**, 1584 (1982).
- [8] Yu. G. Arapov, G. I. Harus *et al*, *Nanotechnology* **11**, 351 (2000).
- [9] Yu. G. Arapov, V. N. Neverov *et al*, *Semiconductors* **32**, 649 (1998).
- [10] T. Okamoto *et al*, *Phys. Rev. Lett.* **82**, 3875 (1999).
- [11] L. Smrcka and T. Jungwirth, *J. Phys.: Condens. Matter* **6**, 55 (1994).
- [12] S. Das Sarma, *cond-mat/9909452*.
- [13] G. S. Boebinger, A. Passner *et al*, *Phys. Rev. B* **43**, 12673 (1991).
- [14] J. P. Eisenstein, T. J. Gramila *et al*, *Phys. Rev. B* **44**, 6511 (1991).
- [15] W. Walukiewicz, H. E. Ruda *et al*, *Phys. Rev. B* **30**, 4571 (1984).
- [16] G. M. G. Oliveira, V. M. S. Gomes *et al*, *Phys. Rev. B* **35**, 2896 (1987).

## New optical phenomena in Bose-condensed exciton system in quantum wells

*Yu. E. Lozovik and I. V. Ovchinnikov*

Institute of Spectroscopy RAN, Moscow region, Troitsk, Russia, 142190

**Abstract.** The new effect — stimulated light backscattering and anomalous light transmission in Bose-condensed exciton system are considered. The effects are connected with photoinduced coherent recombination of two excitons from the condensate with production of two photons with opposite momenta. The effect of two-exciton coherent recombination leads also to the appearance of the second order coherence in exciton luminescence connected with squeezing between photon states with opposite momenta. Coherent 3- and 4-photon emission processes stimulated by respectively two and three laser beams are also considered.

The great progress has been made in the study of exciton Bose-condensation of exciton systems in quantum wells (QW) and  $\text{Cu}_2\text{O}$  (see, e. g. [1–7] and references therein). However, the study of various ways which exciton condensate should unambiguously reveal itself by its optical properties is still vital [3, 4].

We analyze the coherent coupling of photons with opposite momenta, originating from coherent recombination of two excitons from the condensate. We reveal that this process leads to new effect — stimulated light *backscattering* on exciton condensate. This effect can be viewed as a photoinduced coherent recombination of two *condensate* excitons with production of two photons with opposite momenta. We also consider analagous coherent many-photon processes.

Before we analyse the system of quasi-2D excitons in QW let us first consider the simpler case of 3D excitons in  $\text{Cu}_2\text{O}$ . Direct recombination of electron and hole in  $\text{Cu}_2\text{O}$  is a forbidden process and an exciton decays mainly with production of a photon as well as of an optical phonon (Fig. 1(a)). The process of two exciton recombination (Fig. 1(b)) has extra vertex of exciton–photon interaction and, therefore, is substantially weaker.

In the *Bose-condensed* phase of exciton system, exciton lines in Fig. 1(c) can belong to excitons from the condensate (see Fig. 1(c)). One-exciton recombination from the condensate has the only great factor  $\sqrt{N_0}$ , where  $N_0$  is the number of quanta in macroscopically

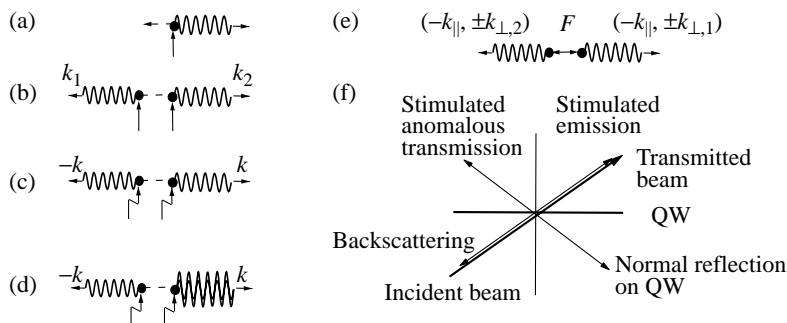


**Fig. 1.** (a) and (b) The diagrams of one- and two-exciton recombinations in  $\text{Cu}_2\text{O}$ . (c) Two-exciton recombination from exciton condensate. (d) Diagram of light backscattering from exciton Bose-condensate. (e) Two-exciton recombination in QW on GaAs. (f) Light backscattering and anomalous light transmission in exciton system in QW.

populated lowest quantum exciton state, while *two-exciton recombination has two such factors*. Additional factor can partly compensate the weakness of the process in comparison with the process of one-exciton recombination and thus make the rate of two-exciton recombination be of order of one-exciton recombination rate. In pure samples due to momentum and energy conservation laws two created photons have the same energy and opposite momenta.

It can be shown that the rate of two-exciton recombination is given as

$$W^{\text{spon}} = \frac{1}{\tau} \frac{4\pi c \rho_{\text{cond}}^2}{k_0^2 \omega_{phn}^2 \tau}, \quad (1)$$

where  $\rho_{\text{cond}}$  is condensate density,  $\tau$  is exciton lifetime, and  $\omega_{phn}$  is the frequency of optical phonon. Taking for estimation  $\rho_{\text{cond}} = 10^{19} \text{ cm}^{-3}$  we have that the rate of photon creation in coherent *two-exciton* recombination process is:

$$W_{\text{Cu}_2\text{O}}^{\text{spon}} \approx \frac{1.5 \cdot 10^{-2}}{\tau_{\text{Cu}_2\text{O}}} \times \rho_{\text{cond}}, \quad (2)$$

while the rate of photon creation in *one-exciton* recombination from the condensate process is  $\tau_{\text{Cu}_2\text{O}}^{-1} \times \rho_{\text{cond}}$ . Thus approximately every hundredth exciton in the condensate decays due to the process under consideration. Therefore, the spontaneous two-exciton recombination process is still weak in spite of extra bosonic (excitonic) factor  $\sqrt{N_0}$  in the matrix element of the process (Fig. 1(c)). But the process can be induced by resonant external laser radiation (Fig. 1(d)). At any act of such excitons stimulated recombination there is created *not only the photon propagating along inducing radiation direction but also the photon propagating in the opposite direction*. Consequently, it emerges that the process effectively acts as a light *backscattering* from the condensate. The rate at which photons are emitted in the opposite direction is multiplied by a factor  $(N_{\mathbf{k}} + 1)$ , where  $N_{\mathbf{k}}$  is the average number of quanta in the quantum state of inducing photon beam with the wave vector  $\mathbf{k}$ .

Consequently, inducing beam at the frequency  $\omega = \mu$  which has approximately hundred quanta per mode makes two-exciton recombination luminescence in opposite direction be of the same intensity with one-exciton recombination luminescence. Thus the effect of stimulated backscattering of laser beam on exciton condensate can be detected experimentally.

In the absence of inducing beam two-exciton recombination luminescence is squeezed between the photon states with opposite momenta (two-mode squeezing). Luminescence at a given direction does not possess statistical coherence. The only statistical correlation, which luminescence has, is the correlation between opposite direction luminescence intensities. This correlation can be detected by Hurbury–Brown–Twiss measurements with two detectors arranged diagonally with respect to the exciton system.

Consider now direct gap semiconductor with allowed interband transition such as GaAs. In GaAs, 3D excitons do not form Bose-condensate but, rather, gather in metallic electron-hole drops. Recently, excitons and their coherent properties are mainly studied in two dimensions — in coupled quantum wells GaAs/AlGaAs. In CQW spatially indirect excitons have electric dipoles and their interaction has strongly repulsive character, so that they can form stable Bose-condensate at  $T = 0$  (or quasi-long nondiagonal order superfluid phase with local quasi-condensate at temperatures smaller than the temperature of Kosterlitz-Thouless transition [4]). CQW is a quasi-2D system where only *2D in-plane momentum is conserved*.

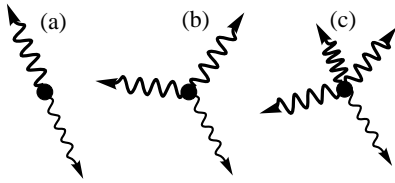


**Fig. 2.** The effects of N-exciton coherent emission stimulated by N-1 external laser beams in Cu<sub>2</sub>O. (a),(b) and (c) correspond to N = 2 (backscattering), N = 3 and N = 4 respectively.

We calculated the rate of two-exciton recombination process, whose diagram is given in Fig. 1(e). For exciton condensate  $\rho_{\text{cond}} = 10^{10} \text{ cm}^{-2}$  we have the estimate

$$W^{\text{spon}} \approx \frac{10^{-(1 \div 2)}}{\tau} \times \rho_{\text{cond}}.$$

This result shows that the effect of interest can be detected in the system of indirect excitons in GaAs/AlGaAs CQW.

Since in two dimensions the third component of photon wave vector is not fixed and is set only by energy conservation law, the differential process characterized by in-plane wave vector  $\mathbf{k}_{\parallel}$  in fact corresponds to *four processes* in which the photons with wave vectors  $(\mathbf{k}_{\parallel}, \pm \mathbf{k}_{\perp})$  and  $(-\mathbf{k}_{\parallel}, \pm \mathbf{k}_{\perp})$  are created. Therefore, stimulating laser light with in-plane wave vector component  $\mathbf{k}_{\parallel}$  induces *two processes* in which the photons with in-plane components  $\mathbf{k}_{\parallel}$  are emitted in two directions  $(-\mathbf{k}_{\parallel}, \pm \mathbf{k}_{\perp})$ , i.e. besides stimulated backscattering there arises *stimulated anomalous light transmission* in which only in-plane wave vector component changes its sign (see Fig. 1(f)).

The effects of coherent two-exciton coherent recombination can be generalized to the case of many-exciton coherent recombination processes with production of only photons. We have calculated the rates of 3- and 4-exciton recombination processes in Cu<sub>2</sub>O with simultaneous production of 3 and 4 photons respectively. Due to momentum conservation sum photon wave vector equals zero. At the same time, the lengths of photon wave vectors are the same since the energy of each photon equals approximately the energy of condensate excitons. This assures that wave vectors of photons have a certain relative orientation. For example, in case of 3-exciton coherent recombination photon propagation directions are complanar and make the angles of  $120^\circ$  to each other. These processes being induced by external N-1 laser beams appropriately relatively directed should result in appearance of emission coming out of exciton system. Estimations show that for the system of excitons with  $\rho_{\text{cond}} = 10^{18} \text{ cm}^{-3}$  these effects can be detected experimentally.

## References

- [1] S. A. Moskalenko and D. W. Snoke, *Bose-Einstein Condensation of Excitons and Biexcitons and Coherent Nonlinear Optics with Excitons*, Cambridge University Press, New-York (2000).
- [2] A. L. Ivanov, H. Haug and L. V. Keldysh, *Phys. Rep.* **296**, 237 (1998).  
See also L. V. Keldysh and Yu. V. Kopayev, *Fiz. Tverd. Tela* **6**, 2791 (1964) [*Sov. Phys. Solid State*, **6**, 2219 (1965)];  
A. N. Kozlov and L. A. Maximov, *JETP* **48**, 1184 (1965).
- [3] V. A. Gergel, R. F. Kazarinov and R. A. Suris, *JETP* **53**, 544 (1967).
- [4] Yu. E. Lozovik and O. L. Berman, *JETP Lett.* **64**, 526 (1996);  
Yu. E. Lozovik, O. L. Berman and V. G. Tsvetus, *Phys. Rev. B* **56**, 5628 (1999);  
Yu. E. Lozovik and A. V. Poushnov, *Phys. Rev. B* **58**, 6608 (1998).
- [5] L. V. Butov and I. V. Filin, *Phys. Rev. B* **58**, 1980 (1998).
- [6] E. Benson, E. Fortin and A. Mysyrowicz, *Solid State Comm.* **101**, 313 (1997).
- [7] A. V. Larionov, V. B. Timofeev *et.al.*, *JETP* **117**, 1255 (2000); *JETP Lett.* **71**, 174 (2000);  
*JETP Lett.* **73**, 342 (2001).

## Spectral speckle analysis: A new method to measure coherence and dephasing in semiconductor nanostructures

G. Kocherscheidt<sup>†</sup>, W. Langbein<sup>†</sup> and R. Zimmermann<sup>‡</sup>

<sup>†</sup> Experimentelle Physik IIb, Universität Dortmund,  
Otto-Hahn-Str. 4, 44221 Dortmund, Germany

<sup>‡</sup> Institut für Physik der Humboldt-Universität zu Berlin, 10117 Berlin, Germany

**Abstract.** A new method to measure the coherence of inhomogeneously broadened optical excitations in semiconductor nanostructures is presented. The secondary emission of excitons in semiconductor quantum wells is investigated. The spectrally-resolved coherence degree of resonantly-excited light emission is deduced from the intensity fluctuations over the emission directions (speckles). The spectral correlations of the speckles give direct access to the homogeneous line width as function of spectral position within the inhomogeneously broadened ensemble. The combination of static disorder and phonon scattering leads to a partially coherent emission. The temperature dependence of the homogeneous line width is well explained by phonon scattering.

The scattering of light into non-specular secondary emission (SE) directions by resonantly excited excitons in semiconductor nanostructures gives direct access to the scattering mechanisms of the excitons. Using the degree of temporal coherence between the SE and the exciting light, one can distinguish internal scattering mechanisms like interface roughness and phonon emission. If static disorder dominates, the scattering is elastic and is called resonant Rayleigh scattering (RRS), preserving the temporal coherence. Scattering by dynamic disorder, such as thermal phonons, results in incoherent luminescence. The coherent part of SE can be extracted by spectral interferometry [1], which retrieves the coherent electric field in amplitude and phase, as well as the spectrally resolved SE intensity. However, due to inconsistent speckle averaging in the detected RRS and SE, the results underestimate the absolute coherence degree of the emission. Time-resolved speckle analysis [2] can quantify the time-resolved intensity and coherence degree of the SE, allowing for a separate determination of pure dephasing and lifetime. However, the spectrally resolved coherence degree and dephasing was not accessible.

We present an extension of the speckle analysis technique into the spectral domain, which determines the spectrally resolved coherence degree and dephasing rate. Speckle analysis is a linear optical technique, while other methods to determine the microscopic damping of inhomogeneously broadened resonances such as spectral hole burning and photon-echo [3], are non-linear, limiting their applicability to high excitation densities.

The investigated samples are GaAs/Al<sub>0.3</sub>Ga<sub>0.7</sub>As single quantum wells (SQWs) with thicknesses of 5 nm and 8 nm, grown by molecular beam epitaxy. They are placed in a helium cryostat at a temperature varied between 1.5 and 30 K. The fundamental hh1-e1 1s exciton resonance is excited by optical pulses from a mode-locked Ti:sapphire laser of 0.3 to 1 ps pulse length. The secondary emission in various directions is passed through an imaging spectrometer and is detected by a nitrogen cooled CCD array with a spectral resolution of 20  $\mu$ eV. The angular resolution was adjusted to resolve a single speckle, *i.e.*



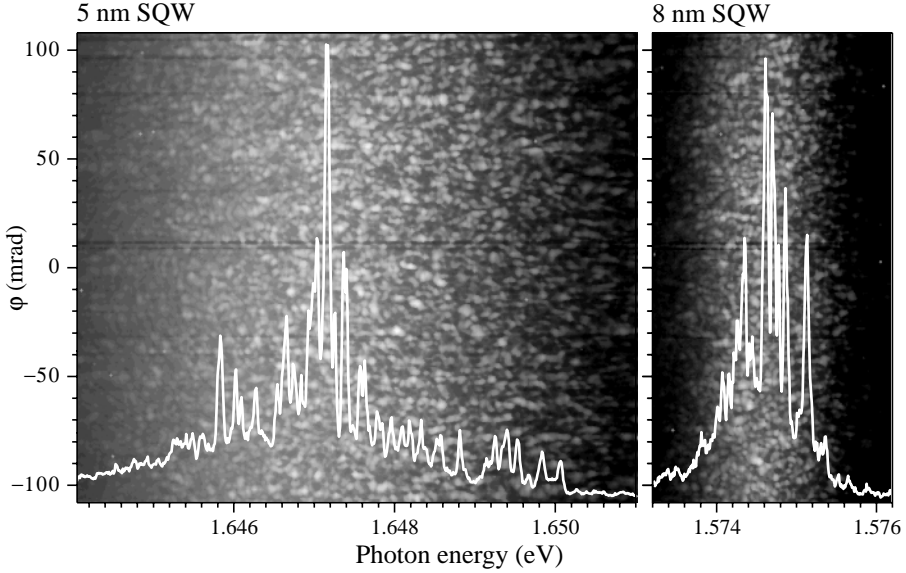


**Fig. 1.** Directionally and spectrally resolved emission intensity (2 decades logarithmic grey scale) of a 5 nm and a 8 nm GaAs SQW at 1.5 K. The white lines are spectra of single speckles.

better than the diffraction limit of the emission from the excited area on the sample. All presented data were taken with excitation in Brewster angle and detection centered normal to the sample, through an analyzer parallel to the linear excitation polarization.

The directional and spectral emission intensities are shown in Fig. 1 for the dominantly inhomogeneously broadened excitonic transitions in the 5 nm and 8 nm SQWs. Both data sets show strong intensity variations along the scattering direction and along the spectral energy, which represents a speckle pattern due to random interference of the temporally coherent part of the SE. The spectrally resolved emission intensity  $I(\hbar\omega)$  consists of a coherent and an incoherent part,  $I = I_{\text{coh}} + I_{\text{inc}}$ . We define the coherence  $c$  of the emission as the fraction  $c = \overline{I_{\text{coh}}}/\overline{I}$  where the average is taken over the scattering directions (at fixed energy  $\hbar\omega$ ). While  $I_{\text{inc}}$  has no significant variation over the direction,  $I_{\text{coh}}$  fluctuates over the speckles. The SE intensity shows a displaced exponential distribution, which is slightly modified taking into account the finite experimental resolution [2, 4]. Experimental intensity histograms from the 5 nm SQW are analyzed in Fig. 2. The coherence  $c$  can be determined from the intensity variance,  $c^2 = N_{\text{eff}}(\overline{I - \overline{I}})^2/\overline{I}^2$ . The full curves in Fig. 2 are predicted distributions for one-dimensional Gaussian correlated data [4], in which  $\overline{I_{\text{inc}}}$  and  $\overline{I_{\text{coh}}}$  were determined from average and variance of the data with  $N_{\text{eff}} = 1.2$  from the known experimental resolution.

As a model for the 1s excitons in a SQW with interface disorder, we consider an ensemble of localized states within the excitation focus, with Gaussian distributed transition frequencies  $\omega_j$  of variance  $\sigma$ . Each state has the same polarization decay rate due to radiative loss and phonon dephasing,  $\gamma = \gamma_{\text{rad}} + \gamma_{\text{phon}}$ . With these ingredients, a kinetic equation for the (non-diagonal) exciton density matrix is derived and solved for the emitted intensity  $I(t)$  as discussed in [2]. In the following we assume dominant inhomogeneous broadening,  $\sigma \gg \gamma$ . Within the present model the spectral coherence is then given by  $\gamma_{\text{rad}}/\gamma$ . However the model does not include transfer of density between the states, which

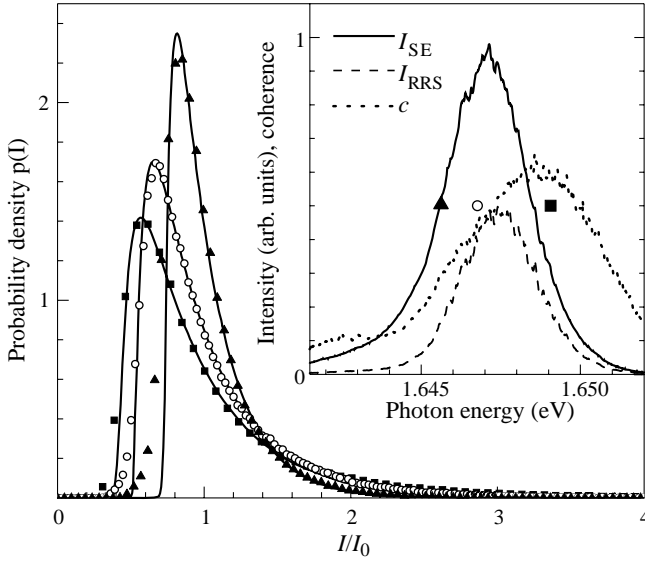


**Fig. 2.** SE intensity distribution at three different energies, indicated with equal symbols in the inset. Lines are calculated distributions for  $N_{\text{eff}} = 1.2$  (see text). Inset: Spectral dependence of the SE intensity (solid), the RRS intensity (dashed) and the coherence (dotted).

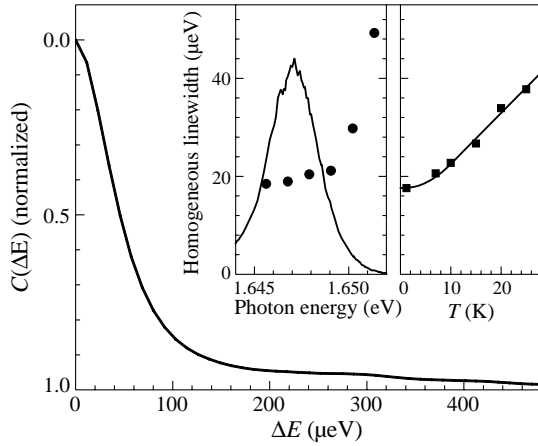


**Fig. 3.** Spectral speckle correlation  $C(E_0, \Delta E)$  of the 5 nm SQW for  $E_0 = 1.647 \text{ eV}$  at 1.5 K. Left inset: spectral dependence of the homogeneous line width  $\hbar\gamma$ . Right inset: temperature dependence of  $\hbar\gamma$  for the 8 nm SQW at  $E_0 = 1.5748 \text{ eV}$ .

is actually dominating the real phonon dephasing mechanism. This energy redistribution leads at low temperatures to a relaxation of the incoherent density to the low-energy part of the emission, reducing the coherence at lower energies and increasing it at higher energies (see inset of Fig. 2). A more detailed theory taking into account the transfer processes is thus necessary to explain the observed spectral dependence of the coherence. In general, the coherence of the emission is found to be around 50%, in deviation to previous lower findings [1].

The spectral intensity correlation of the speckle pattern  $C(\omega, \Delta\omega)$ , defined as

$$C(\omega, \Delta\omega) = \frac{\overline{I(\omega + \Delta\omega/2)I(\omega - \Delta\omega/2)}}{\overline{I(\omega + \Delta\omega/2)} \cdot \overline{I(\omega - \Delta\omega/2)}} - 1 \approx \frac{1}{\Delta\omega^2 + 4\gamma^2} \quad (1)$$

has for  $\sigma \gg \gamma$  a Lorentzian line shape of  $2\hbar\gamma$  width, and thus gives a direct access to the spectrally resolved homogeneous line width  $\hbar\gamma$ . Experimental results are given in Fig. 3. For the 5 nm SQW,  $\hbar\gamma$  is found to be around  $20 \mu\text{eV}$ , in good agreement with the expected radiative broadening. The increase of  $\hbar\gamma$  on the high energy side is probably due to increasing phonon-assisted relaxation. The temperature dependence of  $\hbar\gamma$  for the 8 nm SQW, shown in the inset, is described by an activated acoustic phonon scattering and a zero-temperature width  $\hbar\gamma_0$ .

$$\hbar\gamma(T) = \hbar\gamma_0 + \frac{aE_a}{k(\exp(-E_a/kT) - 1)}. \quad (2)$$

The radiative width  $\hbar\gamma_0$  is found to  $18 \mu\text{eV}$ , and the acoustic phonon coefficient to  $a = 2 \mu\text{eV/K}$  with an activation energy of  $E_a = 1.1 \text{ meV}$ . The activation energy should be interpreted as average energy of the interacting phonons.

In conclusion, we have presented a new method to measure the coherence of excitons in semiconductor nanostructures using speckle analysis in the spectral domain. As linear optical method, it allows to determine the coherence in a quantitative manner at low intensities, and without the need of an interferometric setup. For the investigated secondary emission of inhomogeneously broadened excitons in quantum wells, the spectrally resolved homogeneous line width and the spectrally resolved degree of emission coherence are determined.

#### Acknowledgements

The samples we grown by J. Riis Jensen and C. B. Sørensen at the III–V Nanolab, a joint laboratory between Research Center COM and the Niels Bohr Institute, Copenhagen University. This work was supported by the German Science Foundation (DFG) within the ‘Schwerpunktprogramm Quantenkohärenz in Halbleitern’.

#### References

- [1] D. Birkedal and J. Shah, *Phys. Rev. Lett.* **81**, 2372 (1998);  
G. R. Hayes, B. Deveaud, V. Savona and S. Haacke, *Phys. Rev. B* **62**, 6952 (2000).
- [2] W. Langbein, J. M. Hvam and R. Zimmermann, *Phys. Rev. Lett.* **82**, 1040 (1999).
- [3] W. Demtröder, *Laser Spectroscopy* (Springer, Berlin, 1991).
- [4] E. Runge and R. Zimmermann, *Phys. Rev. B* **61**, 4786 (2000).

## Resonant states of carbon acceptor in p-InGaAs/GaAs $\delta$ -doped quantum well heterostructure

*D. M. Gaponova*<sup>†</sup>, V. Ya. Aleshkin<sup>†</sup>, V. I. Gavrilenko<sup>†</sup>, D. V. Kozlov<sup>†</sup>,  
V. N. Shastin<sup>†</sup>, R. Kh. Zhukavin<sup>†</sup>, B. N. Zvonkov<sup>‡</sup>, E. A. Uskova<sup>‡</sup>,  
J. N. Hovenier<sup>§</sup> and A. F. G. van der Meer<sup>¶</sup>

<sup>†</sup> Institute for Physics of Microstructures RAS, 603950 N.Novgorod, Russia

<sup>‡</sup> Physical-Technical Institute of N.Novgorod State University,  
603600 N.Novgorod, Russia

<sup>§</sup> Delft University of Technology, P.O. Box 5046, 2600 GA Delft, The Netherlands

<sup>¶</sup> FOM Institute for plasma physics, Rijnhuizen, 3439 MN Nieuwegein,  
The Netherlands

**Abstract.** The photocurrent spectra in 27–37  $\mu\text{m}$  wavelength range of the InGaAs/GaAs heterostructure with carbon  $\delta$ -doping on the edge of the quantum wells has been investigated using free electron laser (FELIX). The resonant response has been revealed at the wavelength 34.3  $\mu\text{m}$ . The energy of observed photocurrent peak ( $\sim 36.2$  meV) is in a good agreement with the calculated energy of the hole transition from the ground state to the first excited resonant state of the impurity. The hole relaxation time to the acceptor ground state is estimated.

### Introduction

In recent years there has been considerable interest to the resonant states of shallow impurities in bulk semiconductors and quantum well (QW). The interest is stimulated by the laser action observed in the far IR range that is attributed to the optical transitions between the resonant and localized impurity states (see for example [1, 2]). The most interesting are the resonant states in quantum well since their parameters could be changed relatively easy. Yet so far the resonant states of the shallow acceptors were investigated in  $\text{Si}_{1-x}\text{Ge}_x/\text{Si}$  [2] and  $\text{Ge}_{1-x}\text{Si}_x/\text{Ge}$  [3, 4] heterostructures only. The present paper is devoted to the investigation of the carbon resonant state in InGaAs/GaAs heterostructure. The results of the experimental photocurrent measurements, carried out on the Free Electron Laser (FELIX), are compared with the theoretical calculations.

### 1. Experiment

The sample under investigation z2106 has been grown by MOCVD technique on semiinsulating GaAs(001) substrate. It consists of 20  $\text{In}_x\text{Ga}_{1-x}\text{As}$  quantum wells ( $x = 0.12$ ) of 63 Å width separated by broad (600 Å) GaAs barrier layers. Doping carbon  $\delta$ -layers have been introduced into one of the heterointerfaces in each QW ( $N_A = 2 \times 10^{11} \text{ cm}^{-2}$ ). For the photoconductivity spectra investigation the FELIX radiation tunable in 27 to 37  $\mu\text{m}$  wavelength range has been used. Pulsed FELIX radiation consists of 6 to 8 ps long repeated micropulses 1 ns apart forming the trains of 6 to 8  $\mu\text{s}$  in duration with repetition rate about 5 Hz. The maximum energy of each micropulse does not exceed 5  $\mu\text{J}$ , the beam diameter being about 1 cm. The photocurrent spectrum has been experimentally investigated under different excitation power densities. For the photocurrent measurements two strip electric

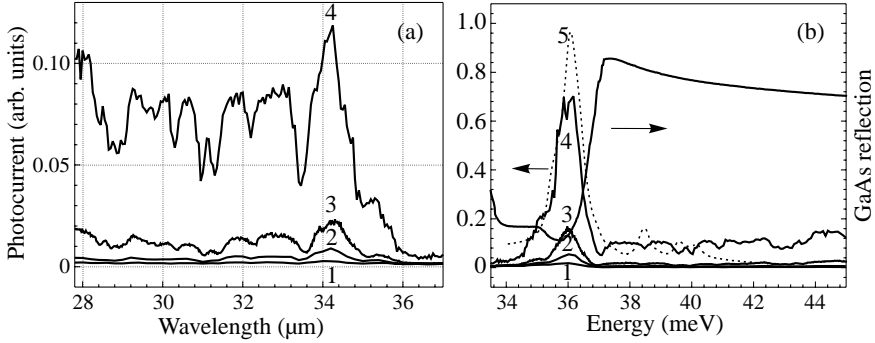


**Fig. 1.** (a) Photocurrent spectra of the heterostructure z2106 for different excitation power densities: 1—5 W/cm<sup>2</sup>; 2—50 W/cm<sup>2</sup>; 3— $5 \times 10^2$  W/cm<sup>2</sup>; 4— $5 \times 10^3$  W/cm<sup>2</sup>. (b) GaAs reflection spectrum and normalized measured photoconductivity spectra. Calculated photoconductivity spectrum is given by the dashed line 5.

contacts 3 mm apart have been deposited on the sample surface, the sample being biased by electrical voltage 2 V. The transmitted signal have been monitored with a Ge:Ga photodetector placed just behind the sample. All measurements have been carried out at 4.2 K. Boxcar integrator has been used for data acquisition.

In Fig. 1(a) the photocurrent spectra for the z2106 heterostructure in the range of 27–37  $\mu\text{m}$  (33.5–45 meV) corresponding to the different excitation power densities are shown. The peak at 36.2 meV about 1 meV in width is well distinguished. The peak intensity grows sublinearly with the laser power. The irregularity of both the transmitted signal and the photocurrent spectra observed originates from the water vapor absorption [5].

## 2. Theory

Spectra of shallow acceptors in GaAs/InGaAs QW heterostructures have been calculated using the developed nonvariational approach [6]. The acceptor Hamiltonian used is  $4 \times 4$  matrix operator included Luttinger Hamiltonian, the deformation term, the confinement potential due to valence-band discontinuity and the potential of an impurity center. Similar to the work [6] axial approximation is used; i.e. the Hamiltonian is considered to be invariant under rotation around the  $z \parallel [001]$  axis perpendicular to the plane of the structure. In this case the  $z$ -component of the total angular momentum  $J_z$  is a good quantum number and the acceptor states are two-fold degenerate by the sign of the component of the angular momentum [7]. The acceptor envelope function is expanded in the basis of free hole envelope functions in the quantum well, which are eigenstates of the Hamiltonian not containing the impurity potential. By substituting this function into the Schrödinger equation for the envelope function the integral equations for the above expansion coefficients are obtained. The integrals are approximated by the finite sums over the hole momentum  $k$ . Thus the problem is reduced to the diagonalization of the finite symmetric matrix.

Using the developed method the energies and the wavefunctions of the on-edge (i.e. placed at the heterointerface in the QW) acceptor states (corresponding to  $J_z = \pm 3/2$ ,  $J_z = \pm 1/2$  and  $J_z = \pm 5/2$ ) the heterostructure z2106 have been calculated. Dipole optical transitions from the acceptor ground state ( $J_z = \pm 3/2$ ) are allowed into the localized excited states and the states of the continuum corresponding to  $J_z = \pm 1/2$  and  $J_z = \pm 5/2$ . The calculated binding energy of the ground state is 11.5 meV (with respect to the edge of

the 1st hole subband in the QW). The binding energies of the two lowest resonant states with  $J_z = \pm 1/2$  and  $J_z = \pm 5/2$  bound with the 2nd hole subband are 4.2 and 2.6 meV correspondingly. The gap between the 1st and the 2nd hole subbands at  $k = 0$  is about 29 meV. In that way the optical transitions between the ground and the above resonant states should occur at photon energies 36.3 meV and 38 meV.

We have also calculated the photoconductivity spectrum for the heterostructure z2106. The energy levels halfwidth (FWHM) have been assumed of 0.25 meV. In the long wavelength range (photon energies 10 to 15 meV) the photoconductivity results from the optical transitions from the acceptor ground state to the continuum (to the first subband) and to the excited localized states (and subsequent thermoionization). In the short wavelength range (photon energies 30 to 45 meV) the photoconductivity is due to the transitions between the ground state and resonant states bound with 2nd subband of size quantization.

### 3. Discussion

In order to compare the experimental data with the calculated photoconductivity spectrum we have taken into account the lattice reflection. In the range of 34–44 meV the strong dependence of the reflection coefficient upon the wavelength takes place due to the reststrahlen (see Fig. 1(b)) [7]. The normalized (taking into account GaAs lattice reflectance) experimental spectra are shown in Fig. 1(b). From the comparison of the calculated and the measured spectra one can conclude that the main peak at 36 meV can be naturally attributed to the hole transitions from the ground to the lowest excited resonant state bound with the 2<sup>nd</sup> hole subband. It is worth mentioned that the calculations results reproduce not only the energy position, but also the form of the peak. Transitions into the higher resonant states are not resolved in the measured spectra. Possibly, these shallower resonant states are more broadened because of the overlapping of the wavefunctions of the neighbouring impurities.

In Fig. 2 the dependence of the peak photocurrent on the excitation power is shown. One can see that the photocurrent value is saturated with the enhancement of the excitation power density. It can be explained by the depletion of the impurity ground state. At the same time the photocurrent saturation is not observed out of the photocurrent peak, e.g. at  $\hbar\omega > 37$  meV where the absorption coefficient is significantly lower. The saturation takes place when  $\sigma N_s \tau \sim 1$ , where  $\sigma$  is photon absorption cross-section,  $\tau$  the time of the hole recombination into the ground state,  $N_s$  the photon flux density. From Fig. 2 one can obtain the value of the saturation parameter  $I_s \sim 2800$  W/cm<sup>2</sup> that corresponds to photon flux

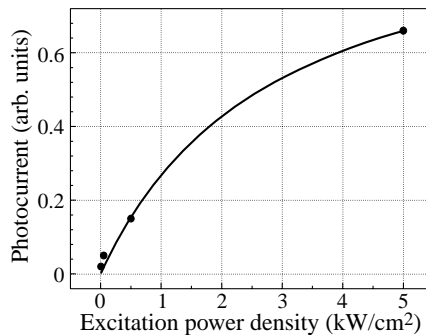


**Fig. 2.** The peak value photocurrent dependence on the excitation power density.

density of  $N_s \sim 6 \times 10^{23}$  photons/cm<sup>2</sup> × s. For the absorption cross-section  $\sigma \sim 10^{-15}$  cm<sup>2</sup> one readily gets  $\tau \sim 2 \times 10^{-9}$  s.

#### 4. Summary

Thus in the paper results of the experimental observation of the transitions from the acceptor ground to excited resonant conditions are presented. The hole relaxation time for the transitions from excited resonant to ground acceptor state is estimated.

#### Acknowledgements

This work was supported in part by the grants 00-02-16159, 01-02-16106 from RFBR, 00-15-96618 from the Russian Program "Leading Scientific Schools", 99-01242 from INTAS and the Deutsche Forschungsgemeinschaft (joint grant with RFBR 436 RUS 113/206/0 (R)).

#### References

- [1] I. V. Altukhov, M. S. Kagan *et al*, *JETP* **88**, 514 (1999).
- [2] M. S. Kagan, I. V. Altukhov *et al*, *Thin Solid Films* **380**, 237 (2000).
- [3] V. Ya. Aleshkin, B. A. Andreev, V. I. Gavrilenko, I. V. Erofeeva, D. V. Kozlov and O. A. Kuznetsov, *Semiconductors* **34**, 563 (2000)
- [4] V. Ya. Aleshkin, B. A. Andreev, V. I. Gavrilenko, I. V. Erofeeva, D. V. Kozlov and O. A. Kuznetsov, *Nanotechnology* **11**, 348 (2000).
- [5] J. Kauppinen, T. Karkkainen and E. Kyro, *J. Molec. Spectr.* **71**, 15 (1978).
- [6] W. Cochran, S. J. Johnson *et al*, *J. Molec. Spectr.* **71**, 15 (1978)
- [7] J. Kauppinen, T. Karkkainen and E. Kyro, *J. Appl. Phys.* **32**, 2102 (1961)
- [8] A. Pasquarello, L. C. Andrerani and R. Buczko, *Phys. Rev. B* **40**, 5602 (1989)

## Structure effects on inter- and intra-band scattering of electrons in GaAs/Al<sub>x</sub>Ga<sub>1-x</sub>As and strained In<sub>x</sub>Ga<sub>1-x</sub>As/GaAs quantum wells

H. C. Lee<sup>†</sup>, K. W. Sun<sup>‡</sup> and C. P. Lee<sup>†</sup>

<sup>†</sup> Department of Electronic Engineering and Institute of Electronics, National Chiao Tung University, Hsinchu, Taiwan, R.O.C.

<sup>‡</sup> Department of Physics, National Dong Hwa University, Hualien, Taiwan, R.O.C.

**Abstract.** Based on the dielectric continuum model, we have studied the dependence of electron-optical phonon scattering rates in GaAs/Al<sub>x</sub>Ga<sub>1-x</sub>As quantum wells with different structure parameters. It was found that the dependence of scattering rates of symmetric interface mode on Al composition in the barrier was stronger than that of the confined mode. The average phonon energy emitted by hot electrons in GaAs/Al<sub>x</sub>Ga<sub>1-x</sub>As quantum wells with various Al composition was estimated and the calculated value agrees with the experimental results qualitatively. For the dependence on the well width, scattering rates of the S+ mode dropped considerably as the well width is increased. The hot electron-neutral acceptor luminescence spectrum of the strained In<sub>x</sub>Ga<sub>1-x</sub>As/GaAs quantum well sample shows an oscillation period of about 22 meV which indicates that the hot electrons relaxed mostly through emissions of the InAs confined phonons.

### 1. Introduction

In the past, electron-phonon scattering rates in a quantum well structure were typically calculated using the bulk phonon model or the bulk-like phonon model. The bulk-like phonon model is that the optical phonon modes in the heterostructures were assumed the same as those of the bulk material while electron's wave function was treated with the quantum confined effect. More recently, the dielectric continuum model [1–4] (DCM) and Huang-Zhu model [5] were developed and found to be much better than the bulk and the bulk-like phonon models. The corresponding fundamental types of phonon modes [1, 4, 5] and electron-phonon Hamiltonian [2, 3, 5] in the heterostructures have become an interesting subject.

More recently, hot-electron neutral-acceptor luminescence [6] was also developed to study electron-optical phonon interaction due to its better spectral resolution and lower carrier excitation than that excited by an ultrafast laser. The experimental method was used to determine optical-phonon energy in GaAs/AlAs multiple quantum wells with different well widths and barrier thicknesses by Sapega [7–8]. Sun *et al.* have also studied [9] optical-phonon energy in GaAs/Al<sub>x</sub>Ga<sub>1-x</sub>As quantum wells with various Al compositions. Up to now, to our knowledge, there has not been any report on the calculations of the dependence of electron-optical phonon interaction on the Al composition. The purpose of this work is to calculate electron-optical phonon scattering rates in GaAs/Al<sub>x</sub>Ga<sub>1-x</sub>As quantum wells with various Al composition in the barrier based on the DCM in a quantum well structure. The calculations were compared with earlier experimental results.

### 2. Theory

#### 2.1. Phonon energy in GaAs/Al<sub>x</sub>Ga<sub>1-x</sub>As quantum wells

Base on DCM, there are six types of optical-phonon modes [3] in a dielectric slab. However, due to selection rules for intrasubband scattering only the confined LO mode, the half-space LO mode, symmetric interface modes were taken into consideration in our calculations.



The energy of the S+ and the S− interface phonon modes is given by the solution of

$$\varepsilon_1(\omega_{S\pm}) \tanh(q_{\parallel} L/2) + \varepsilon_2(\omega_{S\pm}) = 0,$$

where the subscripts 1 and 2 denote GaAs and  $\text{Al}_x\text{Ga}_{1-x}\text{As}$ , respectively,  $L$  is the well width, and  $q_{\parallel}$  is the in-plane phonon wave vector. The lattice dielectric function is given by  $\varepsilon_n(\omega_{S\pm}) = \kappa_{\infty n}(\omega_{S\pm}^2 - \langle\omega_{Ln}\rangle^2)/(\omega_{S\pm}^2 - \langle\omega_{Tn}\rangle^2)$ , where  $\kappa_{\infty n}$  is the high-frequency relative permittivity of the  $n$ th layer. In our calculations, all parameters of the  $\text{Al}_x\text{Ga}_{1-x}\text{As}$  alloy are taken from the work of Adachi [10]. In Fig. 1 we show the dependence of the phonon energy of the S+ mode and the S− mode on the Al composition in the barrier for minimum  $q_{\parallel\min}$  and maximum  $q_{\parallel\max}$  in-plane phonon wave vectors with a well width of 5 nm.

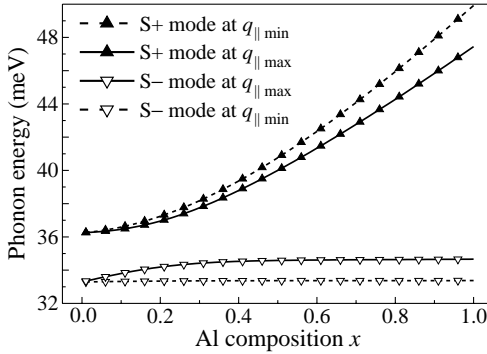


**Fig. 1.** The dependence of the phonon energy of the S+ mode and S− mode on the Al composition at  $q_{\parallel\min}$  and  $q_{\parallel\max}$ .

## 2.2. Electron-optical phonon scattering rates with and without dynamical screening

Electron-optical phonon interaction Hamiltonians for all modes in a dielectric slab are taken from the work of Ando *et al.* [3]. With the assumed average phonon energy in  $\text{Al}_x\text{Ga}_{1-x}\text{As}$  alloy shown earlier, intrasubband electron-optical phonon scattering rates in the lowest subband can be calculated using Fermi's golden rule. The scattering rates are obtained by integrating over all possible states using the two-dimensional density of state function with states restricted by energy and momentum conservation.

Dynamical screening in electron-phonon interaction is treated by random phase approximation, and the two-dimensional longitudinal dielectric function of plasma is given by

$$\varepsilon(q, \omega) = 1 - V_q \Pi_0(q, \omega)$$

where  $V_q = (e^2)/(2\varepsilon_0\kappa_{\infty n}q)$  is the two-dimensional Fourier transform of the Coulomb interaction, and

$$\Pi_0(q, \omega) = -\frac{n_{2D}}{E_F} \frac{k_F}{q} \left[ \frac{q}{k_F} - \left(a_+^2 - 1\right)^{1/2} + \left(a_-^2 - 1\right)^{1/2} \right]$$

is the zero-temperature polarizability function, where  $n_{2D}$  is the sheet charge density,  $k_F$  is Fermi wave vector,  $E_F$  is Fermi energy, and  $a_{\pm} = (\omega + i\gamma)/(qv_F) \pm (q)/(2k_F)$ , where  $\omega$  is the phonon energy, damping coefficient  $\gamma = (0.2-0.3)\omega$ , and  $v_F$  is the Fermi velocity.

## 3. Results and discussion

In Fig. 2 we show the calculated dependence of electron-optical phonon scattering rates on Al composition for various types of phonon modes in a GaAs/ $\text{Al}_x\text{Ga}_{1-x}\text{As}$  quantum well with a well width of 5 nm and a lattice temperature of 15 K. In Fig. 2 we also find that the screening effect for the S+ mode and the S− mode is not significant.

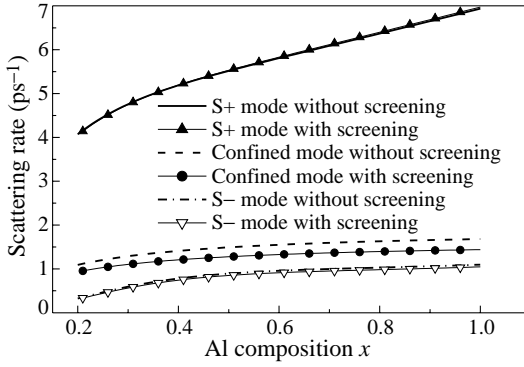


**Fig. 2.** The dependence of the electron-phonon scattering rate of the S+ mode, the confined mode, and the S- mode on the Al composition. The well width is 5 nm, the lattice temperature is 15 K, and the amount of the excess kinetic energy of the electron is 50 meV.

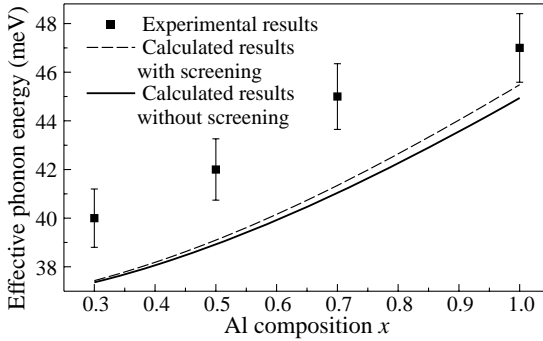


**Fig. 3.** The comparison of experimental results and calculated results for the dependence of the effective phonon energy on the Al composition. The well width is 5 nm, the lattice temperature is 15 K, and the amount of the excess kinetic energy of the electron is 180 meV.

Comparing to the S+ and the S- modes, the scattering rate of the confined phonon mode does not change very much with the Al composition in the range that we have investigated. The influence of screening for the confined mode is stronger than that of the S+ and the S- interface modes.

For the 5 nm well the electron wave function does not penetrate deeply into the barriers, therefore, the half-space mode's contribution to the scattering rate is insignificant comparing to the other three types of phonon modes and will not be considered here.

The calculated results were compared with experimental results [9] performed by hot electron neutral-acceptor luminescence for GaAs/Al<sub>x</sub>Ga<sub>1-x</sub>As quantum wells with various Al compositions. The calculated effective phonon energy ( $\omega_{\text{eff}}$ ) is given by the following equation.

$$\omega_{\text{eff}} = \frac{W_{S+}\omega_{S+} + W_{S-}\omega_{S-} + W_C\omega_C}{W_{S+} + W_{S-} + W_C}$$

where the  $W_{S+}$ ,  $W_{S-}$  and  $W_C$  are the scattering rates of the interface and confined modes.

In Fig. 3 we show the dependence of the effective phonon energy on the Al composition based on both the experimental result [9] and our calculations. The minor difference between the measured result and the calculated result on the effective phonon energy is attributed to the assumptions that we made in the calculations of the average phonon energy in Al<sub>x</sub>Ga<sub>1-x</sub>As alloy, which probably simplified the complexity in the ternary compound.

In Fig. 4 we show the dependence of scattering rates on the well width for various types of phonon modes in GaAs/Al<sub>x</sub>Ga<sub>1-x</sub>As quantum wells with an Al composition  $x = 0.3$ . Other parameters are the same as in previous calculations. There is a crossover point of the scattering rate for the confined mode and the S+ mode at a well width of 10 nm and an Al composition of 0.3. So the confined mode is the major relaxation channel for hot electrons in wide quantum wells. Although the total scattering rate only varies slightly with the well

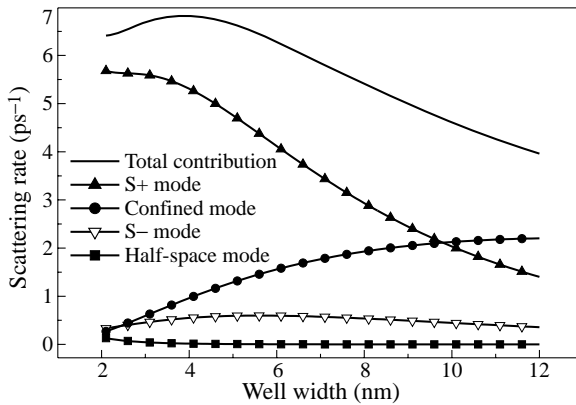


**Fig. 4.** The dependence of the electron-optical phonon scattering rate of the S+ mode, the confined mode, the S- mode, the half-space mode, and the total rate contributed by all types of phonon modes on the well width. The Al composition is 0.3, the lattice temperature is 15 K, and the amount of the excess kinetic energy of the electron is 50 meV.

width, there still can be a strong dependence of the average electron's energy-loss rate on the well width when the phonon energy of the corresponding modes is considered.

However, experimental wise, it is rather difficult to obtain decent hot electron luminescence spectra due to the deterioration of the AlAs morphology when wider wells and thick barriers were grown in the structures. Therefore, we turned to study the electron-optical phonon interactions in moderate wide  $\text{In}_x\text{Ga}_{1-x}\text{As}/\text{GaAs}$  strained quantum wells in order to determine the dominant LO phonon mode emitted by the hot electrons. The quantum well sample consisted of five layers of strained 10 nm  $\text{In}_{0.3}\text{Ga}_{0.7}\text{As}$  wells with GaAs barrier of 30 nm prepared on GaAs substrate. The central regions of 2 nm of the  $\text{In}_{0.15}\text{Ga}_{0.85}\text{As}$  wells were doped with Be to  $10^{18} \text{ cm}^{-3}$  in order to study its hot electron-neutral acceptor luminescence.

The energy difference between the peaks in the spectrum is about 22 meV and is close to the InAs confined phonon mode in the wells. Keep in mind that the GaAs-like phonon energy is close to 37 meV and the GaAs-like phonon mode was very unlikely the type of phonon emitted by the hot electrons excited in the wells. In comparing to the experimental results in the narrower GaAs/AlGaAs QWs, the phonon mode emitted by the hot electrons in the moderate wide QWs is now dominated by the confined phonon mode in the wells. The experimental results were also in good agreement with calculations qualitatively.

#### Acknowledgments

This work is supported by National Science Council of Republic of China under Grant No NSC89-2218-E009-055 and 89-2112-M-259-021.

#### References

- [1] Ronald Fuchs and K.L. Kliewer, *Phys. Rev.* **140**, A2076 (1965).
- [2] James J. Licari and Roger Evrard, *Phys. Rev. B* **15**, 2254 (1977).
- [3] N. Mori and T. Ando, *Phys. Rev. B* **40**, 6175 (1989).
- [4] R. Chen, D. L. Lin and Thomas F. George, *Phys. Rev. B* **41**, 1435 (1990).
- [5] Kun Huang and Bangfen Zhu, *Phys. Rev. B* **38**, 13377 (1988).
- [6] G. Fasol, W Hackenberg, H. P. Hughes, K. Ploog, E. Bauser and H. Kano, *Phys. Rev. B* **41**, 1461 (1990).
- [7] D. N. Mirlin, B. P. Zakharchenya, I. I. Reshina, A. V. Rodina, V. F. Sapega, A. A. Sirenko, V. M. Ustinov, A. E. Zhukov and A. Yu. Egorov, *Semicond.* **30**, 377 (1996).
- [8] V. F. Sapega, M. P. Chamberlain, T. Ruf, M. Cardona, D. N. Mirlin, K. Totemeyer, A. Fischer and K. Eberl, *Phys. Rev. B* **52**, 14144 (1995).
- [9] K. W. Sun, C. P. Lee *et al.*, *Solid State Commun.* **115**, 563 (2000)
- [10] Sadao Adachi, *J. Appl. Phys.* **58**, R1 (1985).

## Light absorption and emission in InAs/GaAs quantum dots and stepped quantum wells

V. Ya. Aleshkin<sup>1</sup>, D. M. Gaponova<sup>1</sup>, D. G. Revin<sup>1</sup>, L. E. Vorobjev<sup>2</sup>,  
S. N. Danilov<sup>2</sup>, V. Yu. Panevin<sup>2</sup>, N. K. Fedosov<sup>2</sup>, D. A. Firsov<sup>2</sup>,  
V. A. Shalygin<sup>2</sup>, A. D. Andreev<sup>3,8</sup>, A. E. Zhukov<sup>3</sup>, N. N. Ledentsov<sup>3</sup>,  
V. M. Ustinov<sup>3</sup>, G. E. Cirlin<sup>4</sup>, V. A. Egorov<sup>4</sup>, F. Fossard<sup>5</sup>, F. Julien<sup>5</sup>, E. Towe<sup>6</sup>,  
D. Pal<sup>6</sup>, S. R. Schmidt<sup>7</sup> and A. Seilmeier<sup>7</sup>

<sup>1</sup> Institute for Physics of Microstructures RAS, 603600 N. Novgorod, Russia

<sup>2</sup> St. Petersburg State Technical University, 195251 St. Petersburg, Russia

<sup>3</sup> Ioffe Physico-Technical Institute, St Petersburg, Russia

<sup>4</sup> Institute for Analytical Instrumentation RAS, 198103 St. Petersburg, Russia

<sup>5</sup> Universite Paris-Sud, 91405 Orsay, France

<sup>6</sup> University of Virginia, Charlottesville, VA 22903-2442, USA

<sup>7</sup> Institute of Physics, University of Bayreuth, Bayreuth D-95440, Germany

<sup>8</sup> Department of Physics, University of Surrey, Guildford, GU2 7XH, U.K.

**Abstract.** The results of optical phenomena investigations in quantum dot and quantum well structures under interband optical pumping are presented. Interband and intraband light absorption in nanostructures with quantum dots has been studied experimentally and theoretically. Photoluminescence and interband light absorption in stepped quantum wells have been investigated including PL studies under picosecond optical pumping. Experimental results have been compared with results of calculation of energy spectrum and transition probabilities. It is shown that inversion of population exists between the third and second excited levels of stepped quantum well.

### Introduction

The feasibility of bipolar mid-infrared laser based on intraband carrier transitions in QWs and QDs was considered elsewhere [1–4]. The first experimental studies of spontaneous mid-infrared emission under simultaneous generation of stimulated near-infrared radiation were carried out in classic heterolasers on QD and QW [5] and QD [3, 6] in condition of electrical injection.

The present paper is devoted to the investigation of optical phenomena in structures with QDs and QWs directed to the development of bipolar mid-infrared lasers.

### 1. Interband and intraband light absorption in quantum dots

Compared to PL studies, spectra of interband absorption enable to obtain more complete information about multilayered structures. The results of the first investigations of interband absorption in QD structures are presented in Fig. 1. Structure consisted of 15 InAs QD (2.5 ML) layers in  $\text{In}_{0.12}\text{Ga}_{0.88}\text{As}$  QW (50 Å) divided with 40 nm GaAs barriers. Multipass geometry of the sample was used (see inset in Fig. 1(b)). Light beam passed through QD layers 10 times. The observed absorption peaks can be attributed to carrier transitions between ground states, excited states and between states of wetting layer. Results of the optical matrix element calculations are also presented in Fig. 1. Calculations were carried out in frames of **kp** method taking into account strain, band mixing and wetting layer related

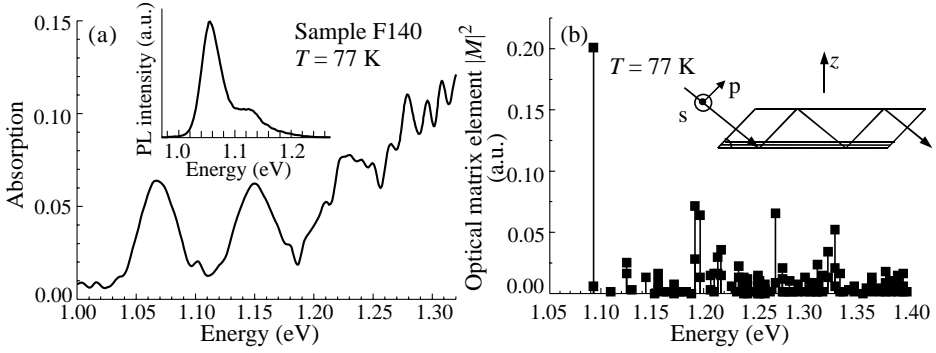


**Fig. 1.** Spectra of interband light absorption in QD structures: experiment (a) and calculation (b). Insets: PL spectrum and geometry of experiment.

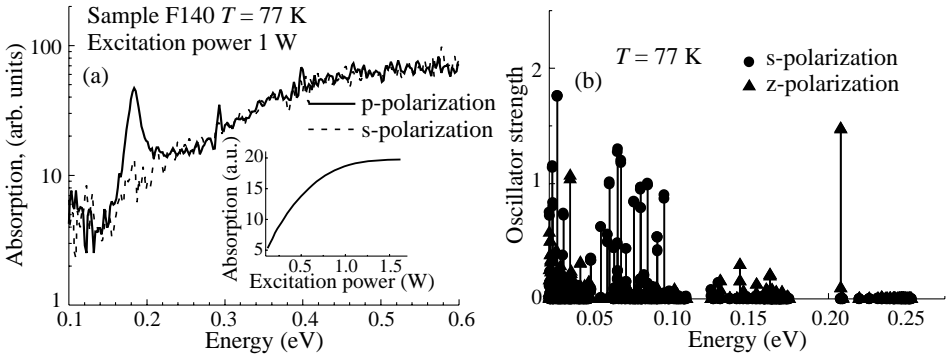


**Fig. 2.** Spectra of absorption (a) and calculated oscillator strength of intraband electron transitions (b). The saturation of absorption is presented in the inset.

states using wetting layer thickness of 0.28 nm and QD as truncated pyramid with the base area of  $16 \times 16 \text{ nm}^2$ , top area of  $4 \times 4 \text{ nm}^2$  and a height of 5.5 nm. A reasonable agreement between theory and experiment was found.

Experimental results of photoinduced absorption for *s*- and *p*-polarizations of light are presented in Fig. 2(a). Absorption peak for light of *p*-polarization only was observed in our experiments. Probably, this peak is connected with electron transitions from ground state to excited states (001) near the wetting layer. Oscillator strength  $f = 1.6$  estimated from absorption peak magnitude is in a good agreement with results of calculations (see Fig. 2(b)). Spectral peak position also correlates well with calculations. Filling the excited states and saturation of absorption occur under high intensity of optical pumping (see inset in Fig. 2(a)). According to calculations, absorption peaks for the light of *s*-polarization are located at the photon energies  $h\nu < 0.1 \text{ eV}$ .

As for interlevel light absorption by holes, it is essential for light of *s*-polarization only. In accordance with calculations this absorption belongs to spectral range  $h\nu < 0.08 \text{ eV}$  and is one order less in comparison with absorption by electrons.

## 2. Photoluminescence and light absorption in funnel shaped QWs

**2.1.** To find the intraband population inversion under optical pumping the surface photoluminescence was studied in the structure with a single funnel-shaped QW. The design of the structure and the interband electron transitions with the maximal optical matrix element are presented in Fig. 3(a). Experimental PL spectra are presented in Fig. 3(b), the calculated values of the transition energies are shown by the arrows. There are two peaks corresponding to  $e1 - hh1$  and  $e3 - hh5$  transitions. The calculated probabilities for both of them and for  $e2 - hh2$  transitions are equal approximately to  $1.4 \times 10^9 \text{ s}^{-1}$ . The calculated electron lifetimes on  $e3$  and  $e2$  levels related to intersubband transitions are equal to 4.3 and 0.5 ps, respectively. The lifetimes on  $e1$  and  $e2$  levels related to recombination processes are about 1 ns. Due to small electron lifetime on  $e2$  level there is no peak connected with  $e2 - hh2$  transitions in PL spectra under low pumping. Analyzing transition probabilities, electron lifetimes and PL peaks intensities one can conclude that there is a significant population inversion between  $e3$  and  $e2$  levels.

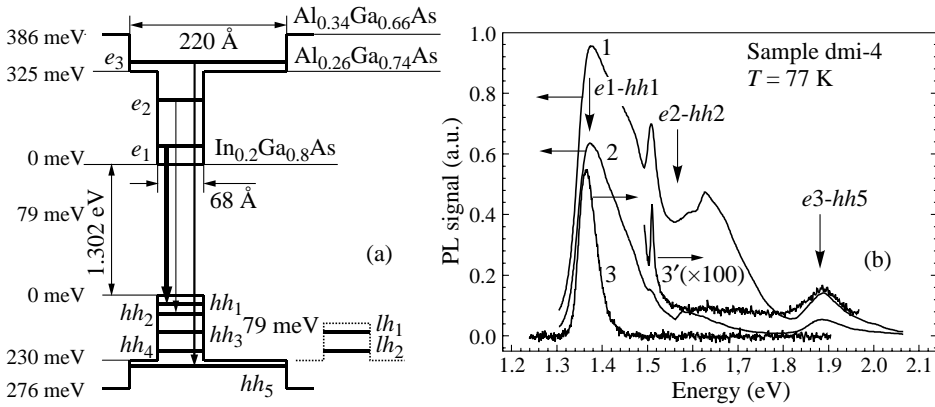


**Fig. 3.** (a) Potential profile, subband-edge energies and the main interband electron transitions in QW. (b) PL spectra for different levels of pulse (1 —  $3 \times 10^3 \text{ W/cm}^2$ , 2 —  $1.8 \times 10^3 \text{ W/cm}^2$ ) and continuous (3, 3' —  $20 \text{ W/cm}^2$ ) laser pumping.

**2.2.** Investigation of PL under intense optical pumping with the pulse duration comparable to the time of intersubband transitions with LO phonon emission is a powerful tool for the studies of energy spectrum in QW. The edge PL spectra measured in the structure consisted of  $20\text{In}_{0.24}\text{Ga}_{0.78}\text{As}/\text{Al}_{0.12}\text{Ga}_{0.88}\text{As}$  funnel-shaped QWs divided with 15 nm  $\text{Al}_{0.2}\text{Ga}_{0.8}\text{As}$  barriers are presented in the Fig. 4(a). Excitation was provided by 4 ps light pulse ( $\lambda = 0.523 \mu\text{m}$ ) with energy of 28  $\mu\text{J}$ . The peaks of PL and absorption spectra (Fig. 4) are in a good correlation. The calculated values of the  $e1 - hh1$  and  $e2 - hh2$  transition energies are shown by the arrows. PL connected with these transitions should be polarized in QW plane, and this was observed experimentally. Under used intensity of laser pumping the nonequilibrium carrier concentration exceeds  $10^{14} \text{ cm}^{-3}$ . Nevertheless we see sufficiently narrow PL peaks due to use of a very short laser pulse and pulse sampling registration because only a small part of electrons and holes get into  $e1$ ,  $e2$  and  $hh1$ ,  $hh2$  subbands and occupy the lower states there. In particular, one can see a sharp PL peak corresponding to the electron transitions from  $e2$  subband with small lifetime  $\tau_2 \approx 0.5 \text{ ps}$ . Analyzing the peak intensity one can estimate the times of the electron capture into QW levels.

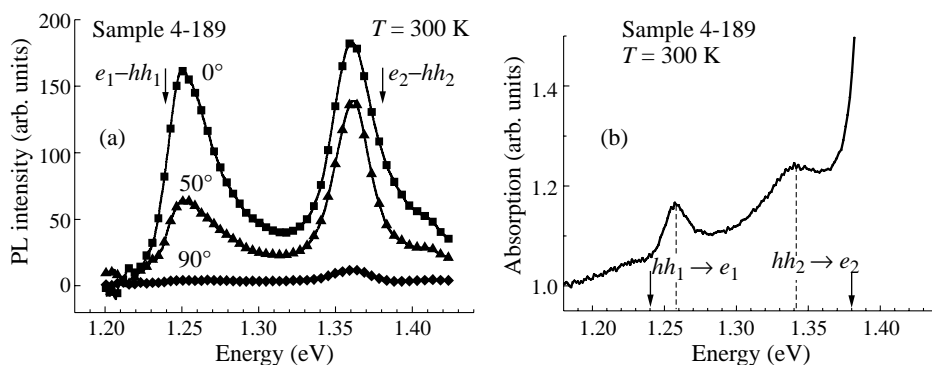


**Fig. 4.** PL spectra for different light polarizations (a) and spectrum of interband absorption in QW (b). The numbers near the curves indicate an angle between PL polarization and plane of QWs.

### Acknowledgements

This work was supported by grants of the INTAS (99-01242, 2001-0615); RFBR (02-17622); Russian Ministry of Education (E00-3.4-544) and Ministry of Science.

### References

- [1] J. Singh, *IEEE Photonics Technol. Lett.* **8** 488 (1996).
- [2] L. E. Vorobjev, *JETP Lett.* **68** 417 (1998).
- [3] M. Grundmann, A. Weber, K. Goede, V. M. Ustinov, A. E. Zhukov, N. N. Ledentsov, P. S. Kop'ev and Zh. I. Alferov, *Appl. Phys. Lett.* **77** 4 (2000).
- [4] A. Kastalsky, L. E. Vorobjev, D. A. Firsov, V. L. Zerova and E. Towe, *IEEE J. Quant. Electron.* **37** 1356 (2001).
- [5] L. E. Vorobjev, D. A. Firsov, V. A. Shalygin, V. N. Tulupenko, Yu. M. Shernyakov, N. N. Ledentsov, V. M. Ustinov and Zh. I. Alferov, *JETP Lett.* **67** 275 (1998).
- [6] S. Krishna, Q. Qasaimeh, P. Bhattacharya, P. J. McCann and K. Namjou, *Appl. Phys. Lett.* **76** 3335 (2000).

## Optical and transport properties of p-type heterojunctions with lateral surface superlattice in perpendicular magnetic field

*V. Ya. Demikhovskii* and D. V. Khomitsky

Nizhny Novgorod State University, 603950 Nizhny Novgorod, Russia

**Abstract.** We study the optics and transport in p-type heterojunctions with lateral surface quantum dot (antidot) superlattice and in the presence of perpendicular magnetic field. The Azbel'–Hofstadter problem is solved for holes in valence band described by  $4 \times 4$  Luttinger Hamiltonian. The probabilities of transitions between quantum states in magnetic subbands and monolayer of donors located inside heterojunction are calculated. The investigation of Hall conductance in the Integer Quantum Hall Effect (IQHE) mode in p-type heterojunctions with lateral surface superlattice has been performed. The mutual influence of heavy and light holes, and of the spin-orbit coupling on the quantization of Hall conductance was elucidated.

### Introduction

The problem of quantum states of 2D Bloch electrons subjected into magnetic field remains actual over several last decades. The fascinating physical phenomena occurring here are caused by interaction of lattice periodic potential which leads to band structure of spectrum with vector potential of uniform magnetic field tending to form discrete energy levels. During last years several significant theoretical aspects of discussed problem have been investigated. In particular, quantization of Hall conductance in the presence of additional periodic potential has been studied in [1, 2]. It was demonstrated that each magnetic subband gives a Hall conductance equal to an integer multiple for the entire Landau level. Recently the number of experimental studies have been performed in order to investigate optical and transport properties in n-type 2D heterojunctions with lateral periodic potential of quantum dots (antidots). The experiments in p-type heterojunctions have also become possible due to the progress in technology which substantially improved the quality of the p channels in GaAs/AlGaAs heterojunctions. The attempts of magneto-optical studies of interband transitions between conduction band and acceptor impurities [3] have been performed in n-type heterostructures. The first experimental evidences of Landau levels splitted into the set of magnetic subbands have been obtained in [4] by longitude magnetoresistance studies. Then, the measurements of Hall resistance in subband energy spectrum have also been performed [5].

In the present paper we study the problem of hole quantum states in p-type heterojunction with lateral quantum dot superlattice. The hole wavefunctions and energy spectrum in different subbands of size quantization are calculated in a four-band approximation for rational values of flux quanta penetrating the superlattice cell. We calculate the matrix elements between Bloch quantum states and impurities located in heterojunction subjected to magnetic field. Then we briefly discuss the quantization of Hall conductance in p-type heterojunctions with lateral surface superlattice.



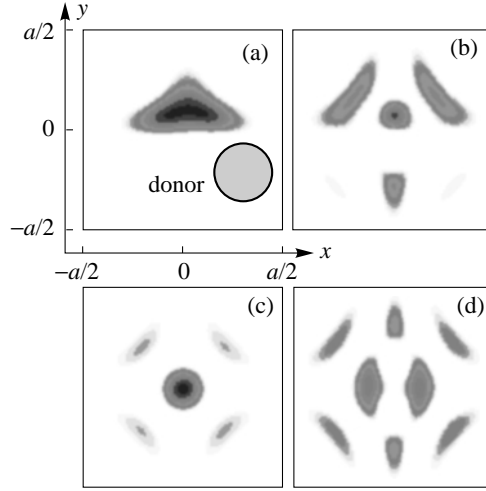


**Fig. 1.** Four components of  $Re\psi_j > 0$ -values for hole envelope wavefunction (1) at  $k_x = k_y = 0$  under the condition of strong subband overlap. The superlattice period  $a = 80 \text{ nm}$  and the amplitude of periodic potential  $V_0 = -10 \text{ meV}$ . The magnetic field  $H \approx 12.1 \text{ T}$  which corresponds to 20 flux quanta penetrating the elementary cell.

### 1. Matrix elements and transition probabilities between Bloch quantum states and impurities

The problem of calculation of transition probabilities between Bloch quantum states and impurities is preceded by the studies of energy spectrum and 2D Bloch magnetic wavefunctions. Such studies have been presented, for example, in [6] for the electrons in n-type and in [7] for the holes in p-type heterojunctions, respectively. In the latter case the four-component hole wavefunction written in  $|J; m_J\rangle$  basis is

$$\Psi_{k_x, k_y}(\mathbf{r}) = \psi_{k_x k_y}^{(1)}(\mathbf{r}) \left| \frac{3}{2}; \frac{3}{2} \right\rangle + \psi_{k_x k_y}^{(2)}(\mathbf{r}) \left| \frac{3}{2}; -\frac{1}{2} \right\rangle + \psi_{k_x k_y}^{(3)}(\mathbf{r}) \left| \frac{3}{2}; \frac{1}{2} \right\rangle + \psi_{k_x k_y}^{(4)}(\mathbf{r}) \left| \frac{3}{2}; -\frac{3}{2} \right\rangle. \quad (1)$$

It should be mentioned that the in-plane translational properties of each component  $\psi_{k_x k_y}^{(j)}(\mathbf{r})$  of envelope function are the same as for single-component electron wavefunction [6]. When the amplitude of external periodic potential exceeds the spacing between neighbouring hole Landau levels, the mixing of different components in (1) greatly increases. This is illustrated in Fig. 1 where the four-component hole envelope wavefunction is shown in one superlattice cell together with donor wavefunction (dark circle).

The calculation of matrix elements and transition probabilities between hole Bloch quantum states and monolayer of donors [7] is performed similar to the case of transitions between Bloch electrons and acceptors [3]. Namely, to obtain the transition probabilities one has to average the matrix elements over many possible donor configurations in a superlattice cell which corresponds to the movement of a circle in Fig. 1:

$$\overline{|M|_{k_x k_y}^2} = \frac{1}{N_A} \sum_{x_0, y_0} |M_{k_x k_y}(x_0, y_0)|^2, \quad (2)$$

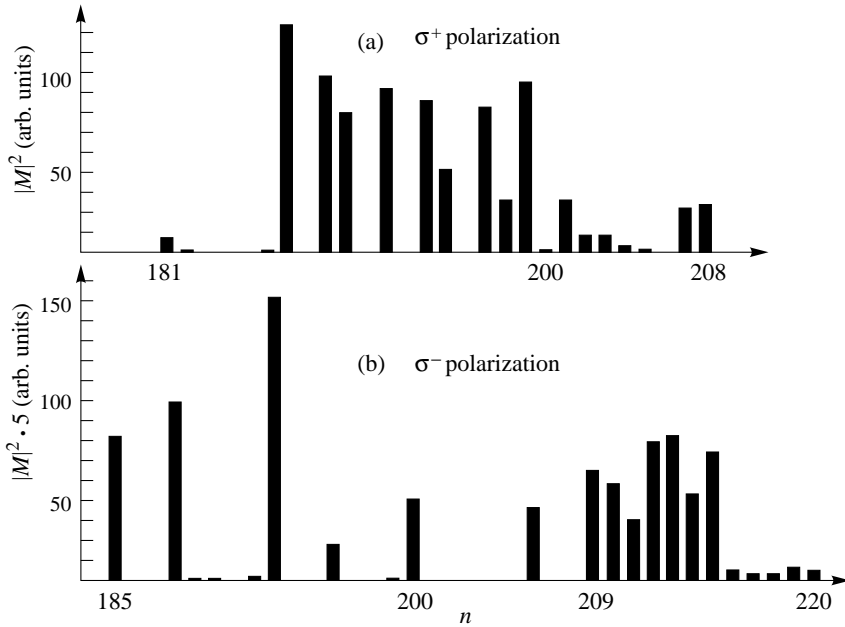


**Fig. 2.** Averaged square of matrix element module for transitions between hole magnetic subbands and donors under strong subband overlap at  $\sigma^+$  (a) and  $\sigma^-$  (b) polarization. The parameters  $a$ ,  $V_0$  and  $H$  are the same as in Fig. 1.

where  $N_A$  is total number of donor positions and the matrix element  $M_{k_x k_y}(x_0, y_0)$  is obtained as a sum of non-vanishing scalar products of hole and donor envelope functions determined by usual selection rules.

It should be noted that due to the random position of donor atom the matrix elements do not depend on the quasimomentum which classify the Bloch quantum state [7]. The results for (2) which determine the transition probabilities are shown in Fig. 2 for  $\sigma^+$  and  $\sigma^-$  polarizations. It is clearly seen that the switching from  $\sigma^+$  to  $\sigma^-$  leads to total decrease of matrix elements but their internal shape changes significantly mainly for subbands 209–220 which, as more detailed analysis shows [7], belong to the hole Landau level with dominating component  $\psi_{k_x k_y}^{(4)}(\mathbf{r})$  of wavefunction (1). The selection rules prescript these subbands to be illuminated by  $\sigma^+$  polarization only, which makes them experimentally observable even under the condition of strong subband overlap.

## 2. Quantization of hole Hall conductance in the presence of additional periodic potential

Here we generalize also the theoretical approaches developed in [1, 2] for the case of multi-band 2D hole spectrum in p-type heterojunctions. Such a generalization seems to be a non-trivial problem because it requires the consideration of both several subbands of size quantization and the multi-component character of hole wavefunction. The calculation of Hall conductance is performed using the Kubo formalism. These calculations are preceded by the analysis of analytical properties of hole envelope functions as a functions of quasimomentum. It is shown that the quantized value of Hall conductance is determined by the

type and the number of peculiarities for hole wavefunction as a function of quasimomentum in the magnetic Brillouin zone. However, the value of Hall conductance  $\sigma_{xy}$  always remains proportional to the integer multiple of  $e^2/h$ . The general results are illustrated on simple examples when  $p/q = 2, 3$ . The progress in this task allows to take into account the effects of spin and spin-orbit coupling on the behaviour of IQHE in the presence of additional periodic potential.

#### *Acknowledgements*

This work was financially supported by the Russian Foundation for Basic Research under Grant No. 01-02-17102, by the Ministry of Education RF under Grant No E00-3.1-413 and jointly by CRDF Foundation and Ministry of Education RF (Project REC-001).

#### **References**

- [1] D. J. Thouless *et al*, *Phys. Rev. Lett.* **49**, 405 (1982).
- [2] N. Usov, *Sov. Phys. JETP* **67**, 2565 (1988).
- [3] I. V. Kukushkin *et al*, *Phys. Rev. Lett.* **79**, 1722 (1997).
- [4] T. Schlösser *et al*, *Semicond. Sci. Technol.* **11**, 1582 (1996); *Europhys. Lett.* **33**, 683 (1996).
- [5] C. Albrecht *et al*, *Phys. Rev. Lett.* **86**, 147 (2001).
- [6] V. Ya. Demikhovskii and A. A. Perov, *Phys. Low-Dim. Struct.* **7/8**, 135 (1998).
- [7] V. Ya. Demikhovskii and D. V. Khomitsky, *arXiv.org:condmat/0112465*.

## Friedel oscillations of the magnetic field penetration in systems with spatial quantization

M. V. Entin, *L. I. Magarill* and M. M. Mahmoodian

Institute of Semiconductor Physics, Siberian Branch of the RAS,  
 630090 Novosibirsk, Russia

**Abstract.** The magnetic field, applied to a size-quantized system produces equilibrium persistent current non-uniformly distributed across the system. The distributions of dia- and paramagnetic currents and magnetic field in a quantum well is found. We discuss the possibility of observation of field distribution by means of NMR.

Traditionally, the magnetic field, penetrating into the system with spatial quantization is considered as uniform and coinciding with the external field. The magnetization of such system and diamagnetic currents are weak and the corrections to the external field are rather small. Nevertheless diamagnetic currents in quantum systems are essential in such phenomena as NMR. It is well known that the magnetic field acting on the atomic nucleus is partially screened by electron shells that results in the chemical shift of NMR line. This shift is measurable due to very narrow width of NMR line as compared with the typical electron relaxation rates. In a spatially quantized system non-uniform electronic currents of magnetization also produce the screening of the external field resulting in the change of effective magnetic field acting on nuclei.

The orbital magnetism in systems with spatial quantization was studied in a number of papers (see, e.g., [1]–[3]). These works consider the total magnetization of small systems. The purpose of the present paper is to find the current and magnetic field distribution in a quantum well.

### Diamagnetic contribution

Let the magnetic field  $\mathbf{B}$  to be directed along  $x$  axis in the film plane  $(x, y)$ . The magnetic field in the film is determined by the Maxwell equation  $\partial\mathbf{B}/\partial z = 4\pi\mathbf{j}(z)/c$ . The diamagnetic current density  $\mathbf{j}$  has the only  $y$  component. Since diamagnetism is weak we shall neglect corrections to the uniform external field in the expression for diamagnetic current. We shall consider diamagnetic current in linear in external magnetic field approximation. The equilibrium density of current can be found from the expression

$$j_y(z) = \text{Sp} \left[ \hat{j}_y(z) f(\hat{\mathcal{H}}) \right], \quad (1)$$

where  $\hat{\mathcal{H}} = (\hat{\mathbf{p}} + e\mathbf{A}/c)^2/2m + U(z)$  is the electron Hamiltonian,  $\mathbf{A} = (0, -B_0z, 0)$  is the vector potential of the external magnetic field  $\mathbf{B}_0$ ,  $U(z)$  is the confining potential,  $\hat{j}_y(z) = -e\{\hat{v}_y, \delta(z - \hat{z})\}/S$  is the orbital current density operator,  $\hat{\mathbf{v}} = (\hat{\mathbf{p}} + e\mathbf{A}/c)/m$  is the electron velocity operator,  $\{ \dots \}$  stand for the operation of symmetrization,  $f(E) = (\exp((E - \mu)/T) + 1)^{-1}$  is the Fermi function ( $\mu$ ,  $T$  are the chemical potential and the temperature),  $S$  is the surface area of the system. Here and below  $\hbar = 1$ .

The linear approximation in  $B_0$  yields:

$$j_y(z) = \frac{2e^2 B_0}{mcS} \sum_{n,\mathbf{p}} \left[ (z - z_{nn}) \varphi_n(z)^2 f(E_{n,\mathbf{p}}) + \sum_{n' \neq n} \frac{p^2}{2m} \varphi_n(z) \varphi_{n'}(z) z_{nn'} \frac{f_{n,\mathbf{p}} - f_{n',\mathbf{p}}}{E_{n,\mathbf{p}} - E_{n',\mathbf{p}}} \right]. \quad (2)$$

Here  $\varphi_n(z)$  are the transversal wave functions,  $\mathbf{p}$  is the longitudinal momentum,  $E_{n,\mathbf{p}} = E_n + p^2/2m$  is the energy of an electron in the  $n$ -th subband of transversal quantization,  $f_{n,\mathbf{p}} \equiv f(E_{n,\mathbf{p}})$ . In the model of a rectangular quantum well ("hard-wall" potential:  $U(z) = 0$  at  $0 < z < d$ ,  $U(z) = \infty$  for  $z < 0$  and  $z > d$ ) Eq. (2) can be simplified for  $T = 0$  as

$$j_y(E_F, 0; z) = \frac{e^2 B_0}{4\pi c d^2} \sum_{n=1} \frac{E_F - E_n}{E_n} \theta(E_F - E_n) \times \left[ (E_F + 3E_n) d(2z - d) \sin^2(\pi n z/d) - (E_F - E_n) n\pi z(z - d) \sin(2\pi n z/d) \right]. \quad (3)$$

Here  $E_F = \mu(T = 0)$  is the Fermi energy,  $E_n = \pi^2 n^2/2md^2$ .

The finite-temperature formula for current can be obtained from (3) using the relation

$$j_y(\mu, T; z) = \int dE j_y(E, 0; z) \left( -\frac{\partial f(E)}{\partial E} \right). \quad (4)$$

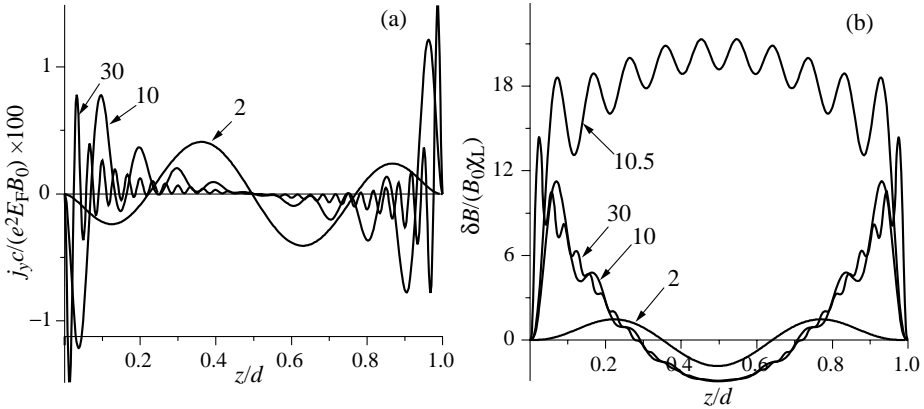


**Fig. 1.** Evolution of the current density (a) and magnetic field (b) for  $T = 0$  with the well width. The numbers of the occupied transversal subbands  $k_F d/\pi$  are marked on curves. For  $k_F d/\pi = 2, 10, 30$  the Fermi energy coincides with subbands bottoms, for  $k_F d/\pi = 10.5$  it lies between 10th and 11th bottoms.

Figure 1(a) depicts the current distribution in the quantum well with rectangular walls. The current density is antisymmetric in reference to the well center and oscillatory decays apart from the boundaries. The oscillations reflect the Friedel phenomenon, namely, the susceptibility singularity at the wave vector  $2k_F$ . The direction of current density alternates, so the term “diamagnetic”, strictly speaking, refers to the integrated surface current only.

In the low-temperature limit the current decay is slow. If the well width is larger than the Fermi wavelength,  $2\pi/k_F$ , the current density and magnetic field asymptotics on the small distance  $z \ll d$  to the boundary read

$$j_y = 3\chi_L c k_F B_0 \left( -\frac{\cos x}{x} + 3x^2 \int_x^\infty \frac{\sin t}{t^5} dt \right), \quad \frac{\delta B}{B_0} = 4\pi\chi_L \left( 1 - \frac{3\sin x}{2x} + \frac{3x^3}{2} \int_x^\infty \frac{\sin t}{t^5} dt \right) \quad (5)$$

Here  $\chi_L = -e^2 k_F / 12\pi^2 m c^2$  is the Landau diamagnetic susceptibility at  $T = 0$ ,  $x = 2k_F z$ . The first terms in Eq. (5) represent the asymptotics in the domain  $z \gg \pi/k_F$ . In particular, the constant contribution in  $\delta B/B_0$  gives exactly the Landau magnetic permeability of a bulk sample.

At finite temperature one can find for  $k_F z \gg 1$

$$\frac{\delta B}{B_0} = 4\pi\chi_L \left[ 1 - \frac{3\pi T}{4E_F} \frac{\sin(2k_F z)}{\sinh(z/l_T)} \right], \quad (6)$$

where the characteristic damping length  $l_T = k_F / (2\pi m T)$ . Note, that the impurity scattering also leads to the drop of  $\delta B(z)$  on a distance of mean free path from the surface.

Besides the oscillating surface diamagnetic current, Fig. 1(a) unexpectedly shows a small regular component of the current density, which is linear with the transversal coordinate. Asymptotically at  $k_F d / \pi \gg 1$  this contribution reads as

$$-\frac{e^2 B_0 k_F}{12mcd^2} (z - d/2) [1 + 6\zeta(\zeta - 1)], \quad \zeta = k_F d / \pi - [k_F d / \pi]. \quad (7)$$

The linear component is smaller than the surface current by the factor  $1/(k_F d)$ . The sign of the slope of the linear term alternates with the chemical potential. The linear term, averaged with respect to the chemical potential (ensemble averaging) vanishes. At the finite temperature the linear term is

$$-\frac{e^2 T B_0}{\pi c d} (z - d/2) \sum_{n=1}^{\infty} \frac{\cos(2nk_F d)}{n \sinh(nT/\theta)}, \quad (8)$$

where  $\theta = E_F (\pi k_F d)^{-1}$  is the characteristic temperature above which the linear term washes out.

The magnetic field corrections are shown in Fig. 1(b). The linear term in  $j_y$  produces the parabolic contribution to magnetic field, which is sensitive to the parameter  $\zeta$ . The linear term in the current density and the parabolic contribution to the magnetic field are connected with the orbital magnetism. In a quantum film the orbital contribution to the magnetic susceptibility fluctuatively grows with the width like  $k_F d$ , that corresponds to the growth of the parabolic contribution to the magnetic field.

### Paramagnetic current

In addition to the diamagnetic current, there is also a paramagnetic current, caused by electron spins. This contribution can be found from Eq. (1) with taking into account Pauli part of the Hamiltonian  $-\mu_B B_0 \sigma_x / 2$  and spin-related component of the current density

operator  $\hat{\mathbf{j}}^{(sp)} = cg\mu_B \nabla \times (\boldsymbol{\sigma}\delta(z - \hat{z}))/S$ . Here  $g$  is  $g$ -factor,  $\mu_B$  is the Bohr magneton,  $\sigma_i$  are Pauli matrices. As a result we find for the density of paramagnetic current

$$j_y^{(sp)} = \frac{g^2\mu_B^2cB_0}{2S} \sum_{n,\mathbf{p}} \left( -\frac{\partial f(E_{n\mathbf{p}})}{\partial E} \right) \frac{\partial \varphi_n^2(z)}{\partial z} \equiv \frac{g^2\mu_B^2cB_0}{4} \frac{\partial}{\partial \mu} \frac{\partial}{\partial z} n(z), \quad (9)$$

where  $n(z)$  is the local electron concentration. This current and corresponding magnetic field should be added to the diamagnetic contributions. The ratio of diamagnetic and paramagnetic contributions depends on  $g$ -factor and, in principle, may strongly vary in different materials.

In the specific case of square quantum well and  $T = 0$  we find

$$j_y^{(sp)} = -\frac{g^2\mu_B^2mk_F^2cB_0}{2\pi^2} \left( \frac{\cos x}{x} - \frac{\sin x}{x^2} \right), \quad \delta B = \frac{g^2\mu_B^2mk_F B_0}{\pi} \left( 1 - \frac{\sin x}{x} \right). \quad (10)$$

Let us consider the imaginary experiment of excitation of nuclear spin transition by the alternating gate voltage. Let 2D gated system is subjected to a magnetic field with  $z$  and  $x$  components. The normal component of field stays unscreened in an infinite 2D system. The  $x$ -component of magnetic field depends on the number of electrons and their state and hence can be controlled by acting on electron subsystem. In particular, the alternating voltage, applied to the gate will modulate the magnetic field and excite the NMR transitions. The excitation of NMR transitions is possible if the alternating component of magnetic field is orthogonal to the constant magnetic field. The resonance should be detected by the frequency (or magnetic field) dependence of the gate impedance. The magnetic field is non-uniform and hence different nuclei experience different in value magnetic fields. On the one hand, this leads to inhomogeneous signal broadening, on the other hand, provides the way of separate excitation of nuclei at different depths.

#### Acknowledgements

The work was supported by the Russian Fund for Basic Researches (grants 00-02-17658 and 02-02-16377).

#### References

- [1] M. Ya. Azbel, *Phys. Rev. B* **48**, 4592 (1993).
- [2] K. Richter, D. Ullmo and R. A. Jalabert, *Phys. Reports* **276**, 1 (1996).
- [3] E. Gurevich and B. Shapiro, *J. Phys. I France* **7**, 807 (1997).

## Phase relations and fringe contrast of coherent emission from single and multiple quantum wells at homogeneous and inhomogeneous broadening

J. Erland<sup>†</sup>, V. N. Grigoriev<sup>‡</sup>, K. L. Litvinenko<sup>‡</sup>, V. G. Lyssenko<sup>‡</sup>  
and J. M. Hvam<sup>†</sup>

<sup>†</sup> Research Center COM, Technical University of Denmark,  
DK-2800 Lyngby, Denmark

<sup>‡</sup> Institute of Microelectronics Technology, RAS,  
142432 Chernogolovka, Moscow district, Russia

**Abstract.** Phase-sensitive experiments in semiconductor nanostructures reveal how inhomogeneous broadening must be taken into account in contrast to previous coherent control experiments in atomic and molecular systems. With spectral resolution of the coherent control signal, the optical phases involved in the interplay between the homogeneous and inhomogeneous broadenings are measured. Based on these experiments, a model describing the optical fringe contrast using different detection schemes is established. This provides a spectroscopic tool to analyze contributions of inhomogeneous broadening to electronic resonances in semiconductor nanostructures.

### Introduction

The developments of coherent control techniques in optical spectroscopy have recently demonstrated population control and coherence manipulations when the induced optical phase is explored with phase-locked laser pulses. In experiments recording the secondary emission, after resonant excitation by phase-locked pulses, with a spectral filtering technique [1] or time-resolved [2, 3] using up-conversion, the coherent emission due to resonant Rayleigh scattering with optical fringes could be distinguished from incoherent photoluminescence without fringes. In the interpretation of these experiments and other experiments, based on differential reflection measurements [3], the exponential decay of the fringe contrast has been assigned to the homogeneous polarization decay with decay time  $T_2$  in an analogy with the concepts developed in atomic and molecular spectroscopy. This, however, neglects the inhomogeneous broadening in semiconductor samples due to stochastic alloy and size fluctuations. On the other hand, Wörner [4] and Garro [5, 6] state that, in general, it is not possible to interpret the decay of the coherent control in terms of  $T_2$ . They have experimentally observed an almost exponential decay of the fringe contrast versus delay between two pulses and ascribed this to the Fourier transform of the “real” exciton absorption line. In virtue of this, they come to the conclusion, that the measured dependence does not contain information about whether the investigated transition is homogeneously or inhomogeneously broadened. Moreover, in a number of recent papers [5, 6] the experimentally measured coherent control (CC) signals have been compared with three-level optical Bloch calculations, taking into consideration the inhomogeneous broadening of excited levels while no dephasing was included. On the basis of such a comparison, these authors come to the conclusion that the CC decay is inversely proportional to the inhomogeneous broadening. These obvious contradictions in the interpretation of similar CC results can be resolved by detecting phase-dependent spectrally resolved four-wave mixing (FWM) that demonstrates how inhomogeneous broadening contributes to the phase phase dynamics.



## 1. Experimental results and discussion

Our main experimental results are shown in Figs. 1(c,d) with the spectrally resolved FWM signal for probe pulse delay phase-locked pulse pair with time-delay  $\tau = 0.5$  ps, recorded at delays between two phase-locked pump pulses  $\tau_{cc} = 0$  ps, and  $\tau_{cc} = -3$  ps for 8 optical periods in the Michelson interferometer. In the direction of observation for the FWM signal, we simultaneously record PL from the sample on the low-energy side of the resonance (below 1.686 eV outside of the laser excitation bandwidth). The strong fringes, corresponding to the optical period, of these optical signals are caused by the interference between the two polarizations excited by phase-locked CC laser pulses. For

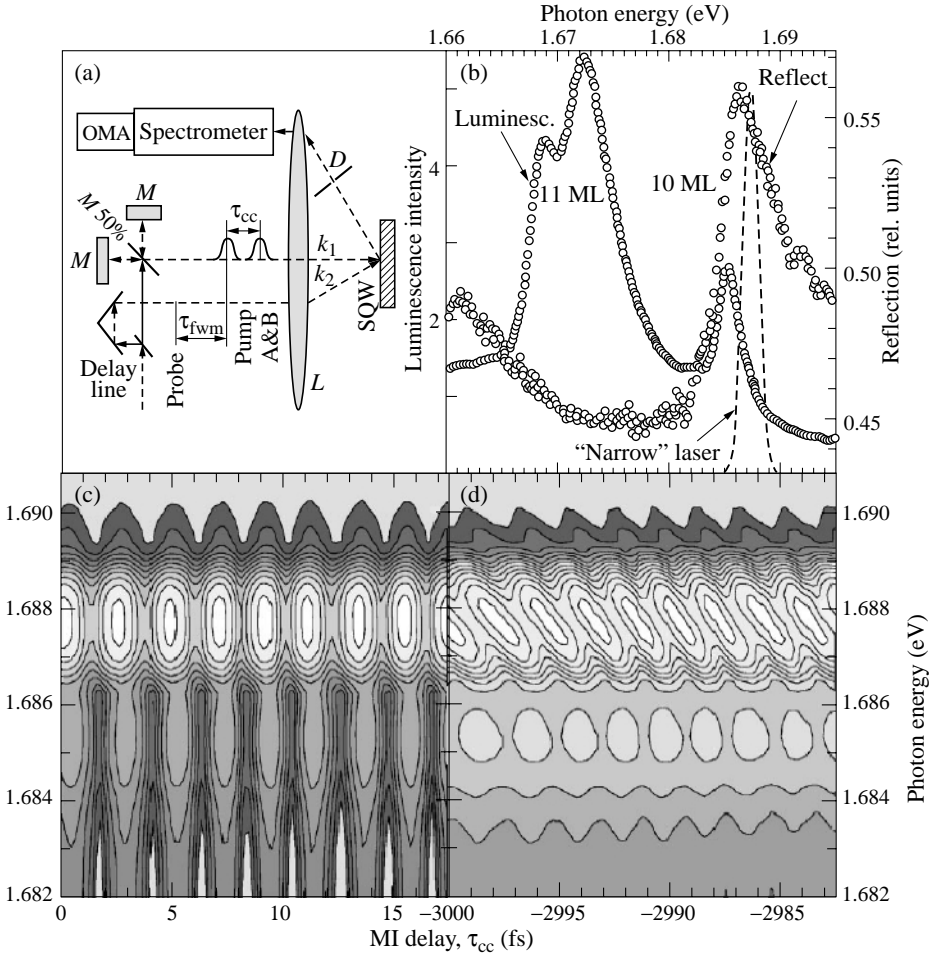


**Fig. 1.** (a) Experimental setup with Michelson interferometer for delay  $\tau_{cc}$ . The four-wave mixing generated by a time-delayed third pulse is spectrally resolved and detected with an OMA; (b) Luminescence (squares) and reflection (circles) spectra of the GaAs SQW revealing two regions with a thickness of 11 and 10 monolayers (ML). The pump laser spectrum is shown dashed; (c,d) FWM spectra at 12 K with photoluminescence ( $\hbar\omega = 1.686$  eV) for different phase delay  $\tau_{cc} = 0$  ps and  $\tau_{cc} = -3$  ps with  $\tau = 0.5$  ps.

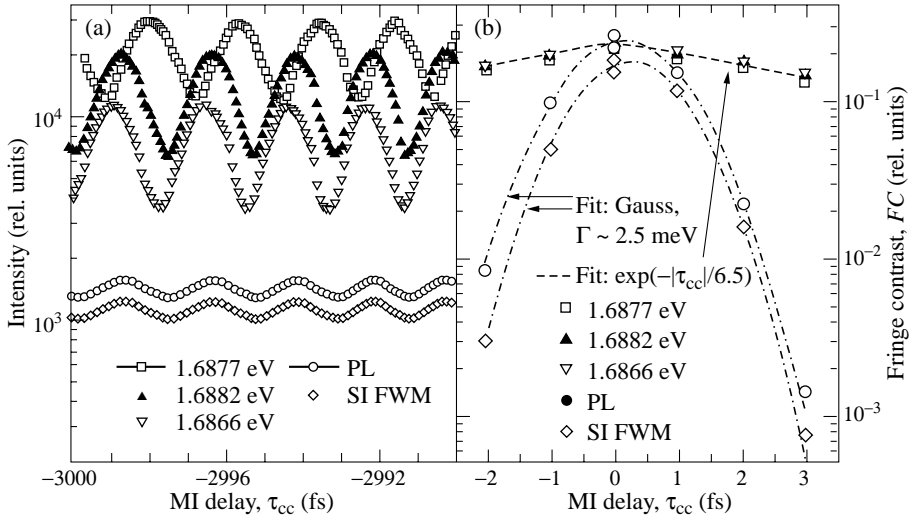


**Fig. 2.** (a) The FWM signal at photon energies 1.6877 (squares), 1.6882 eV (filled triangles), and 1.6866 eV (open triangles), the spectrally integrated (1.686–1.690 eV) FWM signal (diamond), and the PL signal (circles) versus  $\tau_{cc}$  (b) Corresponding decay of the fringe contrast with  $\tau_{cc}$ . The fits are exponential (dashed with decay time 6.5 ps) and Gaussian (dashed-dotted corresponding to  $\Gamma = 2.5$  meV).

the FWM signal, the resulting polarization  $P^{(1)}$ , after the two CC pulses, is probed by the delayed laser pulse resulting in the observed time-integrated signal proportional to  $P^{(3)}$ . In this way, the FWM configuration is used to record a collimated signal proportional to  $|P^{(3)}|^2$  but is otherwise not important for the conclusions of this paper. The striking time-delay dependence of the coherent control signals is evident from Figs. 1(c,d). For  $\tau_{cc} = 0$  ps in Fig. 1(c) we find no spectral variation of the PL and FWM signals, whereas for  $\tau_{cc} = -3$  ps in Fig. 1(d) the fringes in the FWM acquires a phase, dependent on the detected photon energy  $\hbar\omega$ , and the PL signal appears to be proportional to the spectrally integrated  $P = P(\hbar\omega, \tau_{cc})$  i.e., without any spectral variation. Indeed, in Fig. 2(a) we show how this phase change appears for the FWM signal and directly compares the spectrally integrated FWM signal with the PL signal demonstrating the proportionality between the two. On a longer time-delay scale in the CC experiment, we find much faster decay times for fringe contrast (FC) of the PL and spectrally integrated FWM signals compared to the FC of the spectrally resolved FWM signals, see Fig. 2(b). Only the decay times for the fringe contrast in spectrally resolved FWM signals corresponds to the pure FWM-determined polarization decay times  $T_2$  of the 10 ML resonance, which is shorter than the previously determined polarization decay times of the 11 ML resonance in the same sample. We can therefore conclude for inhomogeneous ensembles that the FC for spectrally resolved CC FWM signals decays with  $T_2$  whereas the FC for spectrally-integrated CC signals such as PL or FWM decay as a result of the interplay between inhomogeneous and homogeneous broadening. We develop simple expressions for the FC describing how the inhomogeneous and homogeneous broadening, the time-delay  $\tau_{cc}$ , and the detection configuration (PL and FWM) determine the FC in CC experiments.

Thus, we have developed an improved basis for optical coherent control in semiconductors, taking both homogeneous and inhomogeneous broadening into account. We demonstrate the important influence from even small inhomogeneous broadenings, comparable

to the homogeneous broadening, in spectrally resolved or spectrally integrated recordings of the coherent emission in coherent control experiments. Our model for the optical fringe contrast, developed on the basis of these experiments, successfully describes, in a simple way, the spectrally resolved detection of the coherent emission, as well as the detection of time-integrated photoluminescence used in most experiments. We make appropriate calculations to deduce information about the dependence of spectral FWM oscillations on the amplitude ratio of the two phase-locked pulses, including homogeneous and inhomogeneous broadening of the excited states. We show that the significant interference effects in the FWM spectra have a simple dependence on the homogeneous broadening, as well as on the inhomogeneous broadening. Experimental examples from a narrow GaAs quantum well sample is given, that demonstrating how the extracted phase information relates to the nature of the electronic resonances. This spectroscopy technique in semiconductor optics, using the phase information in coherently excited ensembles, is very important for extracting information on electronic dynamics in nanostructures and for coherent manipulations of populations.

#### *Acknowledgements*

This work was supported by the Danish Natural Science Research Council. V.L. acknowledges support from Otto Monsteds Foundation, RFBR and FTN.

#### **References**

- [1] M. Gurioli, F. Bogani, S. Ceccheroini and M. Colocci, *Phys. Rev. Lett.* **78**, 3205 (1997).
- [2] X. Marie, P. Le Jeune, T. Amand, M. Brousseau, J. Barrau, M. Paillard and R. Planel, *Phys. Rev. Lett.* **79**, 3222 (1997).
- [3] M. Wörner and J. Shah, *Phys. Rev. Lett.*, **81**, 4208 (1998).
- [4] A. P. Heberle, J. J. Baumberg and K. Köhler, *Phys. Rev. Lett.* **75**, 2598 (1995).
- [5] N. Garro, M. J. Snelling, S. P. Kennedy, R. T. Phillips and K. H. Ploog, *Phys. Rev. B* **60**, 4497 (1999).
- [6] N. Garro, M. J. Snelling, S. P. Kennedy, R. T. Phillips and K. H. Ploog, *J. Phys. C* **11**, 6061 (1999).

## Synchronization of dipole domains in GHz driven superlattices

A.-K. Jappsen<sup>†</sup>, A. Amann<sup>†</sup>, A. Wacker<sup>†</sup>, E. Schomburg<sup>‡</sup> and E. Schöll<sup>†</sup>

<sup>†</sup> Institut für Theoretische Physik, Technische Universität Berlin,  
 D-10623 Berlin, Germany

<sup>‡</sup> Institut für Angewandte Physik, Universität Regensburg,  
 D-93040 Regensburg, Germany

**Abstract.** We consider a semiconductor superlattice biased into the regime of negative differential conductivity and driven by an additional GHz ac voltage, and find frequency-locked or quasiperiodic propagating field domains. With increasing driving frequency, the complex impedance exhibits strong variations of its amplitude and phase. An anomalous phase shift appears as a result of phase synchronization of the traveling domains.

As predicted by Esaki and Tsu [1], semiconductor superlattices show pronounced negative differential conductivity (NDC). If the total bias is chosen such that the average electric field is in the NDC region, stable inhomogeneous field distributions (field domains) [2] or self-sustained oscillations [3] with frequencies up to 150 GHz at room temperature [4] appear. Which of these scenarios occurs depends on bias, doping, temperature, and the properties of the injecting contact [5]. For a more detailed discussion see Refs. [6, 7].

In order to apply the self-sustained oscillations as a high-frequency generator in an electronic device, it is crucial to know the response of the superlattice in an external circuit. A key ingredient for the analysis is the complex impedance of the superlattice in the respective frequency range. In this paper the complex impedance is evaluated numerically by imposing an additional ac bias to the superlattice. The interplay of the self-sustained oscillations and the external frequency causes a variety of interesting phenomena such as frequency locking following a devil's staircase, quasi-periodic and chaotic behavior which has been extensively studied both theoretically [8, 9] and experimentally [10, 11]. Here we focus on the response to the circuit and concurrent phase synchronization phenomena.

We describe the state of the superlattice by the electron densities per quantum well  $n_j(t)$  (in units of  $\text{cm}^{-2}$ ), where  $j = 1, 2, \dots, N$  is the well index. Deviations of the electron densities from the doping density  $N_D$  cause inhomogeneous field distributions via the discrete Poisson equation

$$\epsilon_r \epsilon_0 (F_j - F_{j-1}) = e(n_j - N_D) \quad (1)$$

where  $F_j$  is the average electric field between the wells  $j$  and  $j+1$ ,  $e < 0$  is the electron charge, and  $\epsilon_r, \epsilon_0$  are the relative and absolute dielectric constant, respectively. The fields have to satisfy the global voltage constraint  $U(t) = \sum_{j=0}^N F_j d$  where  $d$  denotes the superlattice period. The dynamical behavior of the electron densities is determined by the continuity equation

$$e \frac{d}{dt} n_j(t) = J_{j-1 \rightarrow j} - J_{j \rightarrow j+1}. \quad (2)$$

The current density  $J_{j \rightarrow j+1}$  between the wells  $j$  and  $j+1$  is evaluated within the model of sequential tunneling [7], and Ohmic boundary conditions  $J_{0 \rightarrow 1} = \sigma F_0$ ,  $J_{N \rightarrow N+1} =$

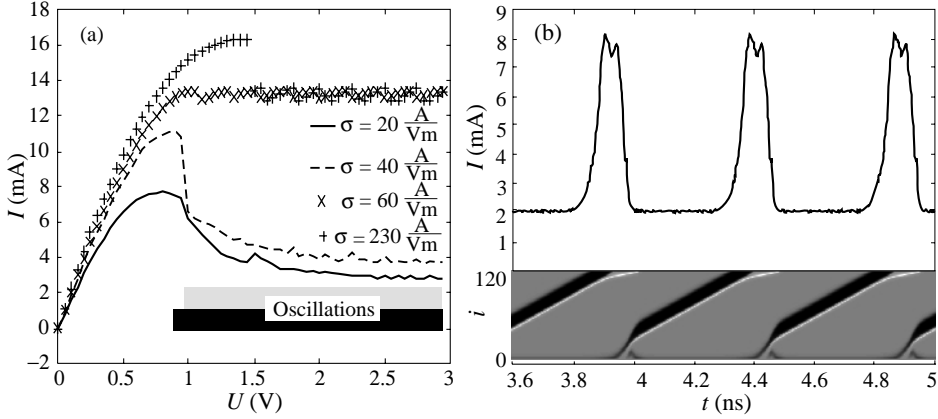


**Fig. 1.** (a) Calculated current–voltage characteristics for different contact conductivities  $\sigma$ , and  $U_{ac} = 0$ . For  $\sigma = 20 \text{ A/Vm}$  and  $40 \text{ A/Vm}$  self-sustained current oscillations are found in the indicated bias ranges. (b) Self-sustained oscillations for  $U_{dc} = 2 \text{ V}$ ,  $\sigma = 20 \text{ A/Vm}$ . The time series of the current  $I(t)$  and the space-time plot of the electron densities  $n_i(t)$  in the quantum wells is shown. Black indicates low electron density (depletion front), white indicates high electron density (accumulation front). The emitter is at the bottom, the collector at the top. ( $N = 120$  GaAs wells of width  $4.9 \text{ nm}$  separated by  $1.3 \text{ nm}$  AlAs barriers,  $n$ -doping  $8.7 \times 10^{10} \text{ cm}^{-2}$ ,  $T = 300 \text{ K}$  [11].)

$\frac{nN}{ND} \sigma F_N$  with a phenomenological contact conductivity  $\sigma$  are applied. In the following we consider a periodic bias signal  $U(t) = U_{dc} + U_{ac} \sin(2\pi \nu_1 t)$  and analyze the total current  $I(t) = A \sum_{j=0}^N J_{j \rightarrow j+1} / (N + 1)$ , where  $A = 64 (\mu\text{m})^2$  denotes the superlattice cross section. In particular we consider the Fourier component  $I_{ac}(\nu_1) \sin(2\pi \nu_1 t - \phi)$  which gives the complex impedance

$$Z(\nu_1) = \frac{U_{ac}}{I_{ac}(\nu_1)} e^{i\phi}. \quad (3)$$

In Fig. 1a we display the calculated current voltage characteristic for  $U_{ac} = 0$ . While for large values of the contact conductivity  $\sigma$  stationary field domains occur, self-sustained current oscillations (where pairs of accumulation and depletion fronts travel through the sample) are found for lower  $\sigma$  (Fig. 1b). This scenario is quite general for moderately doped samples [5, 7]. In the following we use  $\sigma = 20 \text{ A/Vm}$  giving best agreement with the measured current-voltage characteristic.

At  $U_{dc} = 2 \text{ V}$ , the self-sustained oscillations exhibit a frequency of  $\nu_0 = 2.1 \text{ GHz}$ . Now we study the change in the current signal by imposing an additional ac-bias amplitude  $U_{ac}$  with frequency  $\nu_1$ . Figure 2 displays the absolute value and the phase of the complex impedance given by Eq. (3). For both strengths of the ac amplitude one observes strong variations in the amplitude and phase of  $Z$ . In particular one observes pronounced minima in  $|Z|$  and a corresponding monotonic increase in  $\phi$  around frequencies  $\nu_1$  which are approximately integer multiples of  $\nu_0$ . This is due to frequency locking, where the external frequency  $\nu_1$  modifies the main oscillation frequency to  $\nu_0^*$  such that  $\nu_1/\nu_0^*$  is a rational number. While locking occurs in a rather wide frequency range for integer  $\nu_1/\nu_0^*$ , locking into rational numbers with larger denominators are less easy to observe. A more detailed examination indicates that the local minima in  $|Z|$  correspond to the locking regions marked by  $\nu_1/\nu_0^*$ , and  $\phi$  increases with  $\nu_1$  in those intervals, while a decrease is frequently observed outside these ranges where quasi-periodic or possibly chaotic behavior occurs. Thus the

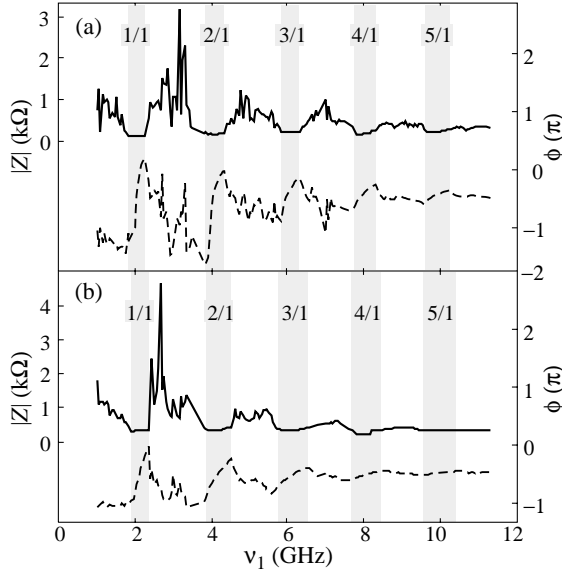


**Fig. 2.** Amplitude  $|Z|$  (full line) and phase  $\phi$  (dashed line) of the complex impedance  $Z$  as a function of the driving frequency for two different values of the ac bias: (a)  $U_{ac} = 0.2$  V, (b)  $U_{ac} = 0.6$  V. The shaded areas indicate locking intervals marked by  $\nu_1/\nu_0^*$  ( $U_{dc} = 2$  V,  $\sigma = 20$  A/Vm). (right) Current  $I$  (full line) and driving bias  $U$  (dashed line) versus time for different driving frequencies  $\nu_1$  ( $U_{ac} = 0.4$  V,  $U_{dc} = 2$  V).

presence of several locking intervals[11] explains the variety of peaks.

For high frequencies  $\nu_1 \gg \nu_0$  the variations of  $Z$  become less pronounced and  $|Z| \sim 300 \Omega$  and  $\phi \approx -\pi/2$  is observed. This corresponds to a capacitive current with an effective frequency-dependent capacitance  $C_{\text{eff}}(\nu_1) \approx 1/(2\pi\nu_1|Z|)$ . At  $\nu_1 = 10$  GHz this gives  $C_{\text{eff}} \approx 50$  fF. Note that this capacitance results from the interaction with the internal front dynamics in the superlattice structure; the intrinsic sample capacitance  $\epsilon_r\epsilon_0 A/(Nd) = 10$  fF is significantly smaller. While we have only shown results for  $U_{dc} = 2$  V and  $\sigma = 20$  A/Vm here, we checked that the features discussed above neither change for different biases nor different contact conductivities, albeit the main oscillation frequency  $\nu_0$  and the locking ranges change slightly.

Now we focus on the 1/1 locking region which is of interest if the device is used as an oscillator. In Fig. 3 we show the current and bias signal for different frequencies  $\nu_1$ . In parts (a) ( $\nu_1 = 1.95$  GHz) and (h) ( $\nu_1 = 2.3$  GHz) no complete locking occurs and the current does not exhibit a periodic signal. Between these frequencies the current signal is periodic with a frequency  $\nu_0^* = \nu_1$  imposed by the external bias. While the current peaks occur around the minima of the external bias for  $\nu_1 = 2$  GHz (corresponding to  $\phi \approx -\pi$ ), the delay between the minima of the current peaks and the bias maxima decreases with frequency until they are approximately in phase at the upper boundary of the locking range at  $\nu_1 = 2.25$  GHz (corresponding to  $\phi \approx 0$ ). It is intriguing to note that this behavior is just opposite to the response of a damped linear oscillator, where the phase between the driving signal and the response shifts from 0 to  $\pi$  with increasing driving frequency. The current peaks correspond to the formation of a domain at the emitter, while during the current minima the domain traverses the sample. The domain transit velocity is larger for smaller voltage. The phase shift between current and voltage adjusts such that the domain velocity

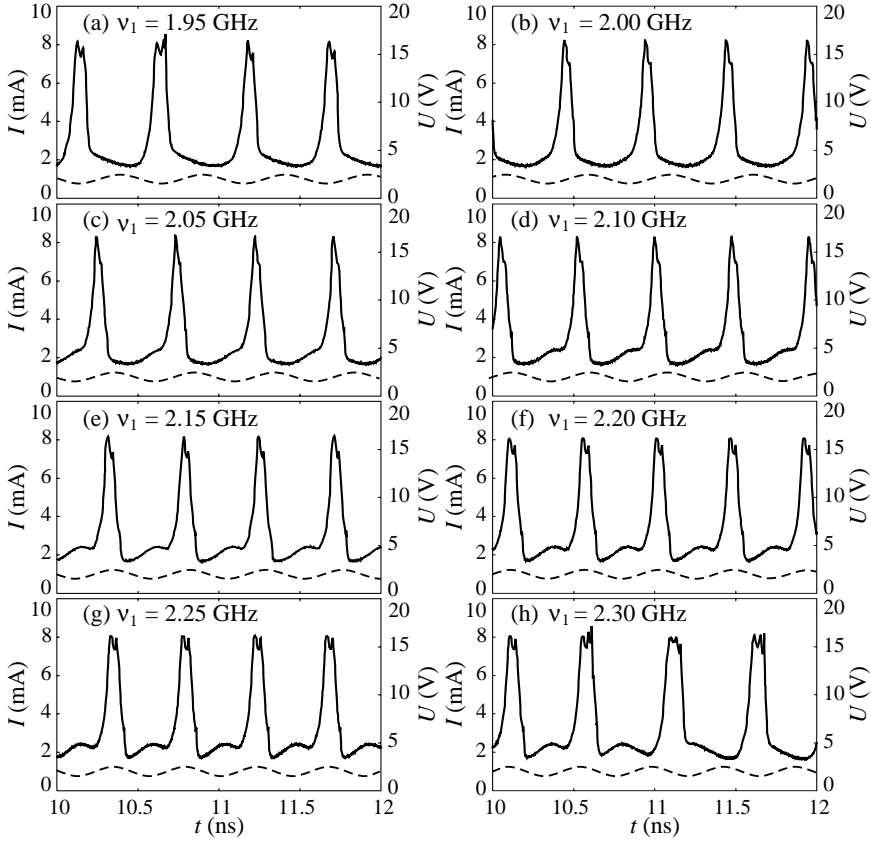


**Fig. 3.** Current  $I$  (full line) and driving bias  $U$  (dashed line) versus time for different driving frequencies  $\nu_1$  ( $U_{ac} = 0.4$  V,  $U_{dc} = 2$  V).

increases with increasing driving frequency during the whole locking interval. This is a phase synchronization effect induced by the domain dynamics.

## References

- [1] L. Esaki and R. Tsu, *IBM J. Res. Develop.* **14**, 61 (1970).
- [2] L. Esaki and L. L. Chang, *Phys. Rev. Lett.* **33**, 495 (1974).
- [3] J. Kastrup *et al*, *Phys. Rev. B* **52**, 13761 (1995).
- [4] E. Schomburg *et al*, *Electron. Lett.* **35**, 1491 (1999).
- [5] A. Amann, J. Schlesner, A. Wacker and E. Schöll, *Phys. Rev. B*, in print (2002).
- [6] E. Schöll, *Nonlinear spatio-temporal dynamics and chaos in semiconductors* (Cambridge University Press, Cambridge, 2001).
- [7] A. Wacker, *Phys. Rep.* **357**, 1 (2002).
- [8] O. M. Bulashenko and L. L. Bonilla, *Phys. Rev. B* **52**, 7849 (1995).
- [9] J. C. Cao and X. L. Lei, *Phys. Rev. B* **60**, 1871 (1999).
- [10] Y. Zhang, J. Kastrup, R. Klann, K. Ploog and H. T. Grahn, *Phys. Rev. Lett.* **77**, 3001 (1996).
- [11] E. Schomburg *et al*, *Phys. Rev. B* **65**, in press (15 April 2002).

## Separate electron-hole confinement in composite $\text{InAs}_y\text{P}_{1-y}/\text{Ga}_x\text{In}_{1-x}\text{As}$ quantum wells

A. Yu. Silov<sup>†</sup>, B. Aneeshkumar<sup>†</sup>, M. R. Leys<sup>‡</sup>, N. S. Averkiev<sup>¶</sup>,

P. C. M. Christianen<sup>§</sup> and J. H. Wolter<sup>†</sup>

<sup>†</sup> COBRA Inter-University, Eindhoven University of Technology,  
P.O. Box 513, 5600 MB Eindhoven, The Netherlands

<sup>‡</sup> Ghent University, Department of Information Technology,  
Sint Pietersnieuwstraat 41, B-9000 Ghent, Belgium

<sup>¶</sup> Ioffe Physico-Technical Institute, St Petersburg, Russia

<sup>§</sup> Research Institute for Materials, High Field Magnet Laboratory,  
University of Nijmegen, 6525 ED Nijmegen, The Netherlands

**Abstract.** Composite double quantum wells made from materials with a type-II band line-up have been grown to realize separate confinement in real space for electrons and holes. We have observed a substantial blue shift of the lowest energy transition in such composite double quantum wells. The photocurrent measurements demonstrate a linear Stark shift due to the separate confinement in real space for electrons and holes. The charge separation is up to 45 Å in the strain balanced  $\text{InAs}_{0.42}\text{P}_{0.58}/\text{Ga}_{0.67}\text{In}_{0.33}\text{As}$  samples. The experimental results agree very well with calculations in the framework of Bir-Pikus strain Hamiltonian.

### Introduction

Structures with separate confinement of electrons and holes in real space are good candidates for realizing a two dimensional exciton condensate [1] and for exploring the blue shifting nature of the absorption edge [2]. We demonstrate a blue shift in excess of 60 meV by using composite quantum well structures with separate confinement of electrons and holes. This has been accomplished by growing the composite well region out of materials with reverse band offset ratio with respect to the barrier material [3].

### 1. Samples

The composite quantum wells consist of  $\text{InAs}_y\text{P}_{1-y}$  and  $\text{Ga}_x\text{In}_{1-x}\text{As}$  layers in between InP barriers. At the  $\text{Ga}_x\text{In}_{1-x}\text{As}/\text{InP}$  interface the familiar value of 40:60 was assumed as conduction to valence band offset ratio. The photocreated electrons are confined within the  $\text{InAs}_y\text{P}_{1-y}$  layer (the band offset ratio of 70:30), while the holes are collected at the  $\text{Ga}_x\text{In}_{1-x}\text{As}$  part of the well *with no electric field applied*. The structures were grown by Chemical Beam Epitaxy [4]. The individual layer thickness in the double quantum well samples were measured from cross sectional transmission electron microscope images.

### 2. Photoluminescence results

During optical measurements, the samples were mounted in a He-flow cryostat. PL was excited by an estimated 400 mW/cm<sup>2</sup> of 532-nm second harmonic from a Nd:YAG laser. To perform PL excitation measurements and photocurrent experiments, tunable infrared light was generated by mixing a 1.064 μm Nd:YAG laser beam with a visible output from a synchronously pumped dye laser.



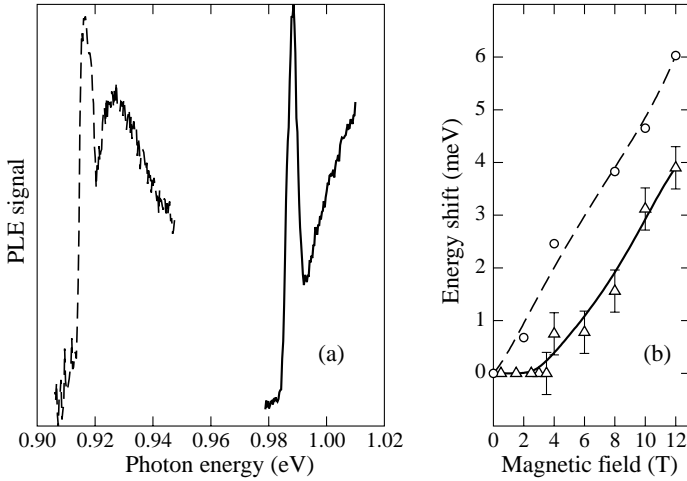


**Fig. 1.** (a) Photoluminescence excitation measurements: 35 Å Ga<sub>0.47</sub>In<sub>0.53</sub>As/10 Å InP/50 Å InAs<sub>0.40</sub>P<sub>0.60</sub> quantum well (dashed curve); 35 Å Ga<sub>0.67</sub>In<sub>0.33</sub>As/10 Å InP/50 Å InAs<sub>0.40</sub>P<sub>0.60</sub> (solid curve). (b) Photoluminescence shift in magnetic field: compression (circles) and the strain balanced sample (triangles).

Low-temperature photoluminescence (PL) on the sample containing 35 Å Ga<sub>0.47</sub>In<sub>0.53</sub>As/10 Å InP/50 Å InAs<sub>0.40</sub>P<sub>0.60</sub> as composite well proved that this asymmetrical quantum well, even though via an indirect in real space radiative transition, shows a strong PL band with a full width at half maximum of less than 10 meV. The PL band is shifted 175 meV towards the low energy side in respect to a reference InAs<sub>0.40</sub>P<sub>0.60</sub> structure containing wells of 35 Å.

We also studied strain balanced quantum wells: the Ga<sub>x</sub>In<sub>1-x</sub>As of the composite well was grown in tension by increasing the gallium content. The strain increases the spatial separation between electrons and holes, as coupling between InAs<sub>y</sub>P<sub>1-y</sub> and Ga<sub>x</sub>In<sub>1-x</sub>As conduction bands decreases. The corresponding PL peak shifts towards high energy with respect to the band of the sample with the Ga<sub>0.47</sub>In<sub>0.53</sub>As well.

### 3. Localized excitons

In all strain balanced samples we observe a phonon sideband of the main exciton photoluminescence. The phonon replica is centered at 33 meV below the principal PL peak, which is the GaAs-like longitudinal-optic phonon in the lattice mismatched Ga<sub>x</sub>In<sub>1-x</sub>As. These phonon sidebands are good indication of the excitons localized by the alloy fluctuations [5]. Figure 1(a) shows the results of PL-excitation measurements. PL-excitation spectra of the strain balanced samples show no Coulomb enhancement at the absorption edge, whereas samples with the lattice matched Ga<sub>x</sub>In<sub>1-x</sub>As display an almost ideal 2-D Sommerfeld factor. To probe the localization scale directly, we performed PL measurements in a magnetic field (see Fig. 1(b)). The peak position of the exciton transition displays no energy shift up to the in-plane magnetic length of 120 Å, that is, the localization length is much less than the Borh radius.

#### 4. Photocurrent experiments

For the photocurrent measurements, the quantum well region was grown in the intrinsic region of n-i-p structure. The experiments were performed at 100 K under reverse biasing. To determine the electron-hole separation, measurements were made in low electric fields.

The photocurrent measurements on samples with a 1.3% compression on the  $\text{InAs}_{0.42}\text{P}_{0.58}$  side of the composite quantum well and containing the lattice matched  $\text{Ga}_{0.47}\text{In}_{0.53}\text{As}$  show linear Stark shift in electric field up to 15 kV/cm. The initial linear Stark shift is a clear indication of the separated confinement for electrons and holes in real space. The photocurrent measurements on sample with 1.1% compression on the  $\text{InAs}_{0.35}\text{P}_{0.65}$  show that the slope of the linear red shift of the absorption edge is smaller. From this slope we can calculate the electron-hole separation. For the  $\text{InAs}_{0.42}\text{P}_{0.58}$  sample, the electron-hole separation is 40 Å, whereas for the sample with 1.1% compression it is decreased by 15%.

The maximum blue shift in excess of 60 meV was observed in the strain balanced samples. The energy shift is saturated in electric fields of 180 kV/cm, which is in a good agreement with calculations in the framework of Bir–Pikus strain Hamiltonian. The material constants used in the calculations are listed in Table 1.

**Table 1.** Values of the elastic stiffness constants  $C_{ij}$  ( $10^{11}$  dyn/cm<sup>2</sup>), the hydrostatic deformation potentials  $a$  (eV), the shear deformation potential  $b$  (eV), the Luttinger’s parameters  $\gamma_i$ , and the electron effective masses  $m_e^*$  ( $m_0$ ) used in calculations. Except for the hydrostatic deformation potentials, all values are taken from Landolt–Börnstein, *Semiconductors*, Vol. III-22a, edited by O. Madelung (Springer–Verlag, Berlin, 1987).

	$C_{11}$	$C_{12}$	$a^\dagger$	$b$	$\gamma_1$	$\gamma_2$	$\gamma_3$	$m_e^*$
InAs	8.329	4.526	−5.9	−1.7	19.7	8.4	9.3	0.023
InP	10.11	5.61	−7.4	−1.7	5.0	1.6	2.3	0.079
GaAs	11.26	5.71	−7.3	−2.0	6.8	2.1	2.9	0.065

$^\dagger$  C. G. Van de Walle, *Phys. Rev. B* **39**, 1871 (1989).

In conclusion, we have demonstrated the separate confinement in real space for electrons and holes in the composite  $\text{InAs}_y\text{P}_{1-y}/\text{Ga}_x\text{In}_{1-x}\text{As}$  quantum wells. We have observed both bright excitonic luminescence and strong excitonic resonances at the absorption edge from these structures. Due to the high asymmetry in the confinement, these structures can be used to achieve both red and blue shift of the absorption edge.

#### Acknowledgements

This work is a part of the research program of the “Stichting voor Fundamenteel Onderzoek der Materie (FOM)”, which is financially supported by the “Nederlandse Organisatie voor Wetenschappelijk Onderzoek (NWO)”.

#### References

- [1] L. V. Butov, A. V. Mintsev and Yu. E. Lozovik, *Phys. Rev. B* **62**, 1548 (2000).
- [2] P. N. Stavrinou, S. K. Haywood and G. Parry, *Appl. Phys. Lett.* **64**, 1251 (1994).
- [3] C. Monier *et al.*, *J. Cryst. Growth* **188**, 332 (1998).
- [4] C. A. Verschuren, M. R. Leys, R. T. H. Rongen, H. Vonk, J. H. Wolter, *J. Cryst. Growth*, **200**, 19 (1999).
- [5] A. Yu. Silov, T. Marschner, M. R. Leys, J. E. M. Haverkort and J. H. Wolter, *Phys. Stat. Solidi A* **164**, 145 (1997).

## Auger recombination in strained InGaAsP quantum wells with $E_g = 0.7\text{--}1.6\text{ eV}$

Z. N. Sokolova, D. I. Gurylev, N. A. Pikhtin and I. S. Tarasov  
Ioffe Physico-Technical Institute, St Petersburg, Russia

**Abstract.** Auger coefficients have been measured in five light emitting diodes (LEDs) with strained quantum wells in active region covered a wide range of wavelength. LED were fabricated from identical high efficient laser heterostructures. The obtained Auger coefficients increase from  $3 \times 10^{-30}$  to  $1.8 \times 10^{-28}\text{ cm}^6/\text{c}$  as wavelength changes from 0.78 to 1.8  $\mu\text{m}$ .

### Introduction

The nonradiative processes of Auger recombination are relevant at high carrier density in III–V semiconductors with bandgap  $E_g < 1.2\text{ eV}$ . In heterolasers the electron and hole densities in the active region are high and Auger processes are potentially important. The influence of Auger recombination on the threshold current in heterolasers with bulk active region based on InGaAsP was shown experimentally [1–3] and theoretically [4–7]. The difficulty with theories of Auger recombination is that information of the band parameters and the band structure at more than a bandgap away from the band edge must be known accurately. Therefore theories can predict the Auger rate to within an order of magnitude even in bulk case. The most reliable method of estimating Auger recombination is to use experimentally obtained Auger coefficients with the calculated or experimentally measured carrier density.

In quantum wells (QW), the band structure is converted into subbands and it is expected that the Auger rate is modified. There were two opposite predictions. It was predicted in [8, 9] that Auger coefficient should be reduced in long-wavelength quantum-well materials. Experiments [10] indicate a reduction of about 3 times in the Auger coefficient when comparing measurements of QW and bulk material. Otherwise theories [11, 12] predicted the increase of Auger coefficient in QW because of additional Auger process dominating in narrow QW.

In strained QW the dominant Auger processes can be suppressed because of the sufficient reduction of the in-plane heavy hole masses [13]. But this phenomenon could occur only in thin strained QW ( $\sim 75\text{ \AA}$ ). So in QW the Auger coefficients have to depend not only on the solution and stress but on the QW thickness and depth too. This accounts for the inconsistent experimental results [14–16].

Consequently Auger recombination in identical high efficient laser heterostructures with strained QW in active region covered a wide range of wavelength (0.78–1.8  $\mu\text{m}$ ) has been studied in this work. We could compare the role of Auger processes in different QW and found the values of Auger coefficients.

### 1. Experimental details

A series of identical InGaAsP/InP and InGaAsP/GaAs separate confinement double quantum well laser heterostructures have been MOCVD grown. The composition of the active

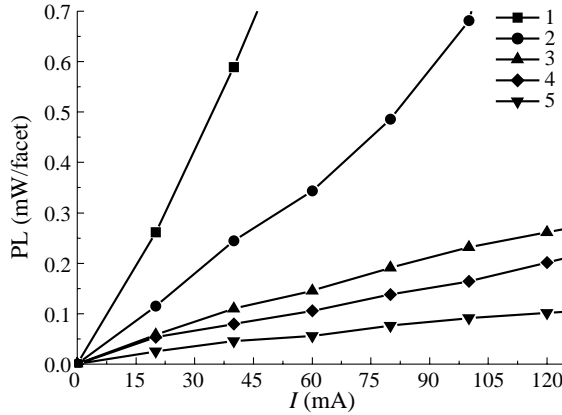


**Fig. 1.** CW light-current characteristics of broad area laser diodes based on conventional SCH QW InGaAsP/InP and InGaAsP/GaAs with symmetrical waveguide and different emitting wavelength: 1 — 0.78  $\mu\text{m}$ ; 2 — 0.95  $\mu\text{m}$ ; 3 — 1.26  $\mu\text{m}$ ; 4 — 1.6  $\mu\text{m}$ ; 5 — 1.8  $\mu\text{m}$ .

region, consisting of two 1% compressive strained QW of widths 60 Å, was verified for the achievement of electroluminescence peak around required wavelength. In order to improve some characteristics of heterostructure influencing on output parameters of laser diodes, namely the quantum efficiency, we have applied the symmetrical step-wise waveguide of full width 0.65  $\mu\text{m}$  in grown heterostructures. Then broad area laser diodes of mesa stripe construction with 100  $\mu\text{m}$  stripe width and 300  $\mu\text{m}$  cavity length have been fabricated from these heterostructures using the standard post-growth technique.

Spontaneous emission in five laser diodes with similar cavity length (300  $\mu\text{m}$ ) at below-threshold current density was measured. LEDs emitted at 0.78, 0.95, 1.26, 1.6 and 1.8  $\mu\text{m}$  wavelengths. CW light-current characteristics of these LED structures get from one mirror are shown in Fig. 1.

## 2. Results and discussion

The spontaneously generated optical output power  $P$  as function of injected current  $I$  is given by expression

$$P = \eta_i \eta_r \eta_c \frac{h\nu}{e} I. \quad (1)$$

$h\nu$  is a peak energy of LED.

Internal quantum efficiency  $\eta_i$  is a fraction of terminal current that generates carriers in the active region of laser. We estimated the values of  $\eta_i$  from CW light-current characteristics measured above threshold and selected structures with  $\eta_i \approx 95\%$  only.  $\eta_c$  is a net collection efficiency. The values of  $\eta_c$  were calculated for investigated structures and amounted to 2%.

A radiative efficiency  $\eta_r$  is a fraction of injected into active region carriers recombining radiatively. It can be defined as

$$\eta_r = \frac{C_{\text{sp}}}{C_{\text{rec}}}. \quad (2)$$

Recombination rate

$$C_{\text{rec}} = C_{\text{sp}} + C_{\text{nr}} + C_{\text{t}}. \quad (3)$$

$C_{sp}$  is a spontaneous recombination rate,  $C_{nr}$  is a nonradiative (Auger) recombination rate,  $C_l$  is a carrier leakage rate.

$$C_{sp} = Bnp.$$

$$C_{nr} + C_l \approx R_1 np^2 + R_2 n^2 p + An. \quad (4)$$

$n$ ,  $p$  are the electron and hole densities in QW. It was taken into account that in active region  $n < p$  by reason of electron escape from shallow QW. The density of escape electrons was evaluated as in [17]. The coefficient  $B$  is the bimolecular recombination coefficient. It was calculated for all compressive strained QW taking into account the reduction of in-plane heavy hole masses [13].  $R = R_1 + R_2$  is Auger coefficients. Coefficient  $A$  is connected with carrier leakage from QW.

The QW carrier density has been found using the experimental data (see Fig. 1) and expression

$$P_L = \eta_c C_{sp} h\nu V. \quad (5)$$

$V$  is the volume of QW.

Under steady-state conditions the generation rate of carriers in active region equals the recombination rate, i.e.

$$\eta_i I = e C_{rec} V. \quad (6)$$

The Auger coefficients for nongenerated carriers  $R_{ex}$  have been determined from Eq. (6) and Fig. 1 at different values of injected current  $I$  and are summarized in a the Table. The Auger coefficients  $R_{calc}$  calculated for bulk InGaAsP and InGaAs solid solutions [5, 18] are presented in the Table for comparison.

**Table 1.**

$\lambda$ ( $\mu\text{m}$ )	$R_{ex}$ ( $\text{cm}^6/\text{s}$ )	$R_{calc}$ ( $\text{cm}^6/\text{s}$ )
0.78	$3.0 \times 10^{-30}$	—
0.95	$1.8 \times 10^{-29}$	$1.4 \times 10^{-30}$
1.26	$3.2 \times 10^{-29}$	$5.2 \times 10^{-29}$
1.60	$3.8 \times 10^{-29}$	$3.5 \times 10^{-28}$
1.80	$1.8 \times 10^{-28}$	$7.0 \times 10^{-28}$

It can be seen from Table that measured values of Auger coefficients in investigated laser structures with compressive strained QW slightly depend on wavelength increase as compared to the calculated ones for the same bulk semiconductors.

#### Acknowledgements

This work was supported by the Russian Foundation for Basic Research (grants 01-02-17842, 01-02-17851) and Russian Programme “Physics of Solid State Nanostructures”.

#### References

- [1] Y. Horikoshi and Y. Furukawa, *Japan. J. Appl. Phys.* **18**, 809 (1979).
- [2] G. H. B. Thompson, *IEEE Proc.* **128**, 37 (1981).
- [3] D. Z. Garbuzov, V. V. Agaev *et al*, *Sov. Phys. Semiconductors* **18**, 665 (1984).
- [4] A. Sugimura, *Appl. Phys. Lett.* **39**, 21 (1981).
- [5] D. Z. Garbuzov, Z. N. Sokolova *et al*, *Sov. Phys. Semicond.* **16**, 707 (1982).
- [6] N. K. Dutta and R. J. Nelson, *J. Appl. Phys.* **53**, 74 (1982).
- [7] B. L. Gel'mont, Z. N. Sokolova *et al*, *Sov. Phys. Semiconductors* **17**, 280 (1983).

- [8] C. Smith, R. A. Abram and M. C. Burt, *Electron. Lett.* **20**, 893 (1984).
- [9] R. I. Taylor, R. W. Taylor and R. A. Abram, *Surface Sci.* **174**, 169 (1986).
- [10] S. Hausser, G. Fuchs *et al*, *Appl. Phys. Lett.* **56**, 913 (1990).
- [11] G. G. Zegrya, V. A. Kharchenko, *Sov. Phys. JETP* **101**, 327 (1992).
- [12] M. I. Dyakonov and V. V. Kocharovskii, *Phys. Rev. B* **49**, 17130 (1994).
- [13] E. P. O'Reilly, *Semicond. Sci. Technol.* **4**, 121 (1989).
- [14] V. P. Evtikhiev, I. V. Kudryashov *et al*, *Proc.ISCS-23* **155**, 795 (1996).
- [15] Y. Zou, J. S. Osinski, P. Grodzinski *et al*, *Appl. Phys. Lett.* **62**, 175 (1993).
- [16] G. Fuchs, C. Schiedel, A. Hangleiter *et al*, *Appl. Phys. Lett.* **62**, 396 (1993).
- [17] L. V. Asryan, N. A. Gunko *et al*, *Semicond. Sci. Technol.* **15**, 1131 (2000).
- [18] B. L. Gel'mont, Z. N. Sokolova *et al*, *Sov. Phys. Semiconductors* **16**, 382 (1982).

## Effective mass anisotropy of $\Gamma$ -electrons in GaAs/AlGaAs quantum well with InAs layer

*E. E. Vdovin*<sup>†</sup>, *Yu. N. Khanin*<sup>†</sup>, *Yu. V. Dubrovskii*<sup>†</sup>, *L. Eaves*<sup>‡</sup>, *P. C. Main*<sup>‡</sup>,  
*M. Henini*<sup>‡</sup> and *G. Hill*<sup>§</sup>

<sup>†</sup> Institute of Microelectronics Technology RAS, Chernogolovka, Russia

<sup>‡</sup> School of Physics and Astronomy, University of Nottingham,  
Nottingham NG7 2RD, UK

<sup>§</sup> Dept. of Electronic and Electrical Engineering, University of Sheffield,  
Sheffield S3 3JD, UK

**Abstract.** We use resonant magnetotunnelling spectroscopy, with the magnetic field applied parallel to the interfaces, to investigate the local band structure in the quantum well (QW) of a resonant tunnelling diode. By rotating the magnetic field in the plane of the interfaces, we investigate the energy surface at constant  $k_{\parallel}$ . Using this technique, we have studied two different types of double barrier structures. We obtain different results depending on whether or not the QW contains a narrow InAs layer.

### 1. Introduction

The exact band structure in GaAs close to the  $\Gamma$  conduction band minimum has been the focus of much attention. Experimental efforts in this context involved a determination of the in-plane effective mass of the electrons in GaAs/AlGaAs quantum wells and its dependence on the quantum well width with the help of magnetic fields applied perpendicular to the plane of the quantum well [1]. The theoretical predictions for the band structure were confirmed both qualitatively and quantitatively by these experiments. However, the experiments were not sensitive to any anisotropy in the effective mass parallel to the current direction. Recently, some of the authors have reported a small effective mass anisotropy for  $\Gamma$  electrons in GaAs/AlGaAs quantum wells [2, 3].

In this work, the resonances of a resonant tunnelling structure are probed by a magnetic field applied parallel to the interfaces, which enables us to investigate the local band structure in  $k$  space. By rotating the magnetic field in the plane of the interfaces, the energy surface at constant  $k_{\parallel}$  is investigated. Using this technique, we have studied two different types of double barrier structure (DBS) grown by molecular-beam epitaxy in the [001] direction. In a conventional double barrier structure (control sample), we see a small, two-fold anisotropy relative to the [110] direction, similar to that seen in [3]. This anisotropy can be understood in terms of the orthogonal [110] orientation of bond-planes at opposite interfaces of the quantum well. For a sample in which a wetting layer of InAs is embedded in the central plane of the GaAs quantum well, we observed a four-fold, “clover”-shaped anisotropy, defined by the [100] and [010] directions. These data reflect the  $\Gamma$  — minimum anisotropy of the bulk GaAs and are not associated with the interface.

### 2. Experimental

## 2.1. Samples

The DBSs were grown by molecular beam epitaxy on [001]  $n^+$ -doped GaAs substrates. A thin wetting layer of InAs (WL) was placed in the centre of a 11 nm wide GaAs quantum well (QW) with 8.3 nm  $\text{Al}_{0.4}\text{Ga}_{0.6}\text{As}$  confining barriers, sandwiched between two nominally-undoped 50 nm GaAs spacer layers. The intrinsic region is surrounded by graded  $n$ -type contact layers, with the doping concentration increasing from  $2 \times 10^{17} \text{ cm}^{-3}$  to  $3 \times 10^{18} \text{ cm}^{-3}$ . For comparison, we also studied control samples grown with the same sequence of layers, except that there is no InAs layer.

The presence of the narrow InAs WL modifies the electronic structure of the QW, lowering the ground state energy below the conduction band edge. In fact, the incorporation of the WL leads to a QW of more complicated form, with an additional narrow and very deep (0.6 eV) subwell in the centre of the main GaAs QW. Self-consistent calculations, using the Schrodinger and Poisson equation, show that the ground state in the QW of the samples incorporating the InAs WL is located about 35 meV below the GaAs conduction band edge with the result that, at zero bias, it is populated with electrons from the contact regions. Therefore, at zero bias, the ground state is in resonance with the 3D electrons in the contacts. In contrast, for the sample without the InAs WL, features due to resonant tunnelling through ground state are seen around a bias voltage of 100 mV.

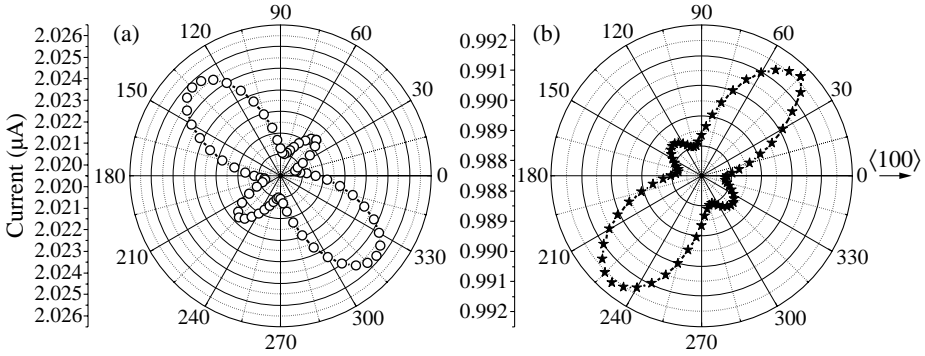
The samples with the InAs layer were characterized by photoluminescence (PL) spectroscopy, which confirmed the existence of the WL emission. Ohmic contacts were obtained by successive deposition of AuGe/Ni/Au layers and subsequent annealing. Mesa structures, with diameter between 50  $\mu\text{m}$  and 200  $\mu\text{m}$ , were fabricated by conventional chemical etching.

## 2.2. Results

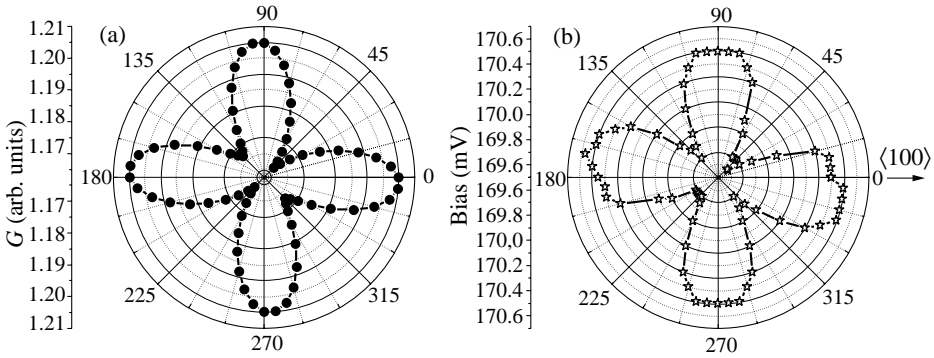
The in-plane dispersion  $E(k_{\parallel})$  of the QW subbands in DBS can be mapped in DBS, using magnetotunnelling spectroscopy with magnetic field  $B$  in the plane of the QW [4, 5]. Electrons tunnelling into the QW over a distance  $\Delta z$  acquire an extra in-plane momentum  $\hbar\Delta k_{\parallel} = eB\Delta z$  in the direction perpendicular to the magnetic field. In the ideal case (*without scattering*), the resulting peak shift  $\Delta V_{\text{peak}}$  is approximately proportional to  $E(k_{\parallel})$ . By rotating the field in the plane of the interfaces, it is possible to investigate any anisotropy between different crystal direction in this plane. The peak current also changes during the rotation, with a larger current in the same directions as the larger shifts in the voltage at which resonance occurs. The peak current is more sensitive to the anisotropy than peak bias [3, 5]. Typical experimental data, showing how the  $I(V)$  characteristic of the control sample is affected by the direction of the magnetic field, is shown in Fig. 1. A “butterfly”-like shape of the is observed, revealing a two-fold anisotropy in both forward, Fig. 1(a), and reverse bias, Fig. 1(b). The main axes of the current and bias anisotropy are oriented along the two orthogonal [110] directions, with a clear  $90^\circ$  rotation between forward and reverse bias. These maps reflect the dispersion relations at constant  $k_{\parallel}$ . They show that the constant energy surface of the QW subband is anisotropic with its principal axes oriented along the  $\langle 110 \rangle$  directions and that the constant energy surface is rotated by  $90^\circ$  on changing the bias polarity. On a qualitative level, the anisotropy can be understood by the orthogonal [110] orientation of bond-planes at opposite interfaces of the quantum well. The electric field breaks the symmetry by forcing the expectation value of the position of the electron wave function closer to one or other of the barriers, depending on the direction of electric field [3].

Figure 2(a) shows a plot of the peak current (or peak bias, Fig. 2(b)) vs magnetic field





**Fig. 1.** Polar plot of the peak current of the control sample for the first QW resonance, as the field is rotated in the plane of the interface. Magnetic fields of 8 T were applied in (a) the forward and (b) reverse bias direction, respectively.



**Fig. 2.** The peak current (a) and peak position (b) vs in-plane magnetic field direction, at 8 T, for the samples with embedded InAs monolayer in the GaAs QW.

direction for the samples in which a wetting layer of InAs is embedded in the central plane of the GaAs QW at  $B = 8$  T. The four-fold “clover”-shaped anisotropy, defined by the  $[100]$  and  $[010]$  directions, was observed in both forward and reverse bias. This anisotropy was independent of the direction of the electric field in contradiction to the anisotropy related to the influence of the interfaces [3]. Furthermore, the main axes of the anisotropy coincided with those predicted for the anisotropy of bulk GaAs [6]. Therefore, we consider that our data reflect the  $\Gamma$  — minimum anisotropy of the GaAs and are not related to any interface effect. To illustrate this, Fig. 3 shows the conduction band profile of the experimental samples with an InAs layer in the QW, together with the wave function of the electronic ground state, calculated using the Schrodinger and Poisson equations for bias  $V = 800$  mV. As shown in Fig. 3, the wave function for the samples with an InAs layer (solid line) is localised nearer the centre of the QW, reducing the influence of the interface. The wave function maximum of the samples without the InAs layer (dashed line) is much closer to the interface.

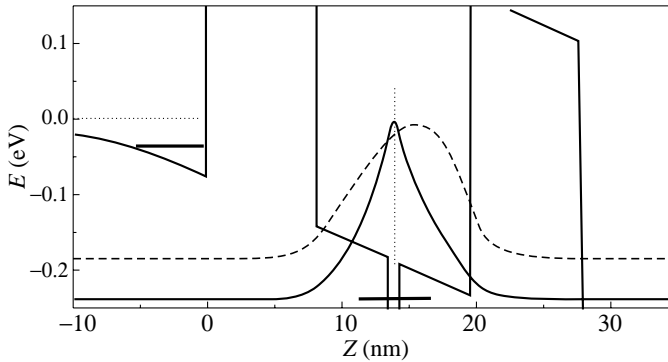


**Fig. 3.** The conduction band profile of the experimental samples with an InAs layer in the QW and wave functions of the electronic ground states in samples with InAs layer (solid line) and control samples (dotted line), calculated using the Schrödinger and Poisson equations for bias  $V = 800$  mV.

### 3. Conclusion

We see a small two-fold anisotropy along [110] for the control sample, similar to that seen in [3]. This anisotropy can be understood in terms of the orthogonal  $\langle 110 \rangle$  orientation of bond-planes at opposite interfaces of the quantum well. A four-fold, “clover”-shaped anisotropy, relative to the [100] and [010] directions, was observed for the samples in which a wetting layer of InAs is embedded in the central plane of the GaAs QW. These data reflect the  $\Gamma$ -minimum anisotropy of the bulk GaAs and are not related to the interface.

#### Acknowledgements

The work is partly supported by the INTAS, the RFBR, the Russian Ministry of Industry and Science, and the EPSRC (UK). EEV and YVD gratefully acknowledge supports from the Royal Society. We are gratefully to V. V. Belov and S. V. Morozov for technical assistance.

### References

- [1] E. E. Vdovin, Y. N. Khanin *et al*, *JETP Lett.* **74**, 41 (2001).
- [2] T. Reker, H. Im, L. E. Bremme *et al*, *Phys. Rev. Lett.* **88**, 056403 (2002).
- [3] R. K. Hayden, D. K. Maude, L. Eaves *et al*, *Phys. Rev. Lett.* **66**, 1749 (1991).
- [4] U. Gennser, V. P. Kesan, D. A. Syphers *et al*, *Phys. Rev. Lett.* **67**, 3828 (1991).
- [5] U. Rosser, *Solid State Comm.* **49**, 943 (1984).

## Nanoscale self assembly and physics with semiconductors

*P. M. Petroff*

Materials department, University of California, Santa Barbara, CA 93103, USA

In this paper we briefly the self assembly and self ordering of semiconductor quantum dots (QDs) using lattice strain engineering. We then will review some novel semiconductor devices which are made possible by the unique electronic properties associated with QDs. Among the important QDs characteristics which should provide new advances in semiconductor optoelectronic devices we list:

- (a) the three dimensional quantum confinement of carrier and excitons which bring into play important many body effects,
- (b) an ultra sharp density of states which confer to the QD "atom like properties" and
- (c) carrier and excitons localization which reduce their interactions with the surrounding material.

A wide variety of optoelectronic QDs devices have already been investigated. We cannot in this presentation give an exhaustive review of all of them. For example, we omit to cover the QDs laser and infrared detector devices which have made rapid progress. Instead we provide and discuss three examples of devices which make use of some of the unique QDs physical characteristics [1]. These are:

- An exciton storage which uses carrier localization in quantum dots to write information using photons to store the dissociated excitons (electron hole pairs) for long time periods (minutes) and to read the information as emitted photons at low temperature.
- A novel quantum dot spin injection light emitting diode which shows magnetically controlled circular polarization of its electroluminescence.
- A single photon quantum dot generator which produces a single photon on command.

## References

- [1] P. M. Petroff, A. Lorke and A. Imamoglu, *Physics Today* **46**, (2001).

## Electron–hole exchange interaction in nanostructures

*E. L. Ivchenko*

Ioffe Physico-Technical Institute, St Petersburg, Russia

The exchange interaction between an electron and a hole bound into an exciton in a semiconductor crystal was extensively investigated in the early 1970s in relation to the study of the fine structure of exciton levels [1–4] (see also [5–7]). The electron-hole exchange interaction is usually divided into the short-range (analytic) and long-range (non-analytic) contributions. The first contribution is governed by the short-range of the Coulomb potential and does not depend on the wave vectors of an electron and a hole involved. The second contribution only slightly varies at distances of the order of the lattice constant and depends non-analytically on the translational wave vector of the electron-hole pair.

In recent years the electron-hole exchange interaction in semiconductors has attracted a renewed attention in connection with extensive studies of the excitonic fine structure in quantum wells (see [7, 8] and references therein), type-II superlattices ([9, 10] and references therein) and quantum dots [11–16].

In addition to a general bird-eye review of the state-of-art in the physics of electron-hole exchange interaction, the talk is devoted to a controversial problem of the role of the long-range contribution to the level splitting for electron-hole pairs or excitons confined in spherical dots. According to [17, 18], the long-range interaction do not contribute to the singlet-triplet splitting of the exciton in a spherical quantum dot in case of nondegenerate conduction and valence bands. On the contrary, the consideration within the envelope function approach showed that the long-range exchange (i) leads as well to a  $R^{-3}$  law in the singlet-triplet splitting as a function of the dot radius  $R$  and (ii) can be comparable or even exceed the short-range contribution to the splitting of the  $\Gamma_6 \times \Gamma_7$  exciton in a spherical dot [19, 20].

In order to remove the existing controversy, in Ref. [21] the electron–hole exchange interaction has been analyzed in the framework of the empirical tight-binding method. It is demonstrated that intra-atomic and inter-atomic (or intrasite) contributions to the long-range interaction enter in an inequivalent way. In particular case of the  $\Gamma_6 \times \Gamma_7$  exciton in a spherical dot, the singlet-triplet splitting is given by

$$\Delta_{s-t}^{(\text{long})} = \frac{\pi C}{3} \hbar(\omega_{\text{LT}} - \omega_{\text{LT}}^{(\text{intra})}) \frac{a_{\text{B}}^3}{R^3}, \quad (1)$$

where  $C \approx 0.67$ ,  $a_{\text{B}}$  is the exciton Borh radius in the bulk material,  $\omega_{\text{LT}}$  is the longitudinal-transverse splitting for the bulk exciton and  $\omega_{\text{LT}}^{(\text{intra})}$  is the contribution to  $\omega_{\text{LT}}$  caused by the intraatomic transitions. Thus as compared to the envelope function approach valid for  $\omega_{\text{LT}}^{(\text{intra})} = 0$ , the splitting (1) differs by a factor

$$\frac{\omega_{\text{LT}} - \omega_{\text{LT}}^{(\text{intra})}}{\omega_{\text{LT}}} = 1 - \left( \frac{M_{\text{cv}}^{(\text{intra})}}{M_{\text{cv}}^{(\text{inter})} + M_{\text{cv}}^{(\text{intra})}} \right)^2, \quad (2)$$

where  $M_{cv}^{(inter)}$ ,  $M_{cv}^{(intra)}$  are the contributions to the interband optical matrix element due to the inter- and intra-atomic transitions in the tight-binding approach. For Frenkel excitons where  $M_{cv}^{(inter)}$  can be ignored,  $\Delta_{s-t}^{(long)} = 0$ .

Franceschetti *et al.* [22] numerically calculated exchange interaction in spherical nanocrystals by using the pseudopotential method. Their pseudopotential calculations show that, in the typical semiconductors, the monopole-monopole contribution to the long-range splitting is predominant which means that the intraatomic transitions give only a small correction to the interband matrix element  $M_{cv}$  as well as to the singlet-triplet splitting. The same was confirmed in the recent tight-binding numerical calculations of Lee *et al.* [23].

## References

- [1] G. E. Pikus and G. L. Bir, *Sov. Phys. JETP* **33**, 108 (1971); **35**, 174 (1972).
- [2] G. L. Bir and G. E. Pikus, *Symmetry and Strain-Induced Effects in Semiconductors* (Nauka, Moscow, 1972; Wiley, New York, 1974) ch. 4.
- [3] V. A. Kiselev and A. G. Zhilich, *Sov. Phys. Solid State* **14**, 1233 (1972); *Sov. Phys. Semicond.* **8**, 411 (1974).
- [4] M. M. Denisov and V. P. Makarov, *Phys. Stat. Sol. (b)* **56**, 9 (1973).
- [5] K. Cho, *Phys. Rev. B* **14**, 4463 (1976).
- [6] F. Bassani and G. Pastori Parravicini, *Electronic States and Optical Transitions in Solids* (Pergamon, Oxford, 1975; Nauka, Moscow, 1982).
- [7] E. L. Ivchenko and G. E. Pikus, *Superlattices and Other Heterostructures. Symmetry and Optical Phenomena* (Springer-Verlag, Berlin, Heidelberg, 1997).
- [8] S. V. Goupalov, E. L. Ivchenko and A. V. Kavokin, *JETP* **86**, 388 (1998).
- [9] E. L. Ivchenko, A. Yu. Kaminski and I. L. Aleiner, *JETP* **77**, 609 (1993).
- [10] E. L. Ivchenko, A. Yu. Kaminski and U. Rössler, *Phys. Rev. B* **54**, 5852 (1997).
- [11] M. Nirmal, D.J. Norris, M. Kuno, M.G. Bawendi, Al. L. Efros and M. Rosen, *Phys. Rev. Lett.* **75**, 3728 (1995).
- [12] D. J. Norris, Al. L. Efros, M. Rosen and M. G. Bawendi, *Phys. Rev. B* **53**, 16347 (1996).
- [13] Al. L. Efros, M. Rosen, M. Kuno, M. Nirmal, D. J. Norris and M.G. Bawendi, *Phys. Rev. B* **54**, 4843 (1996).
- [14] M. Chamarro, C. Gourdon, P. Lavallard, O. Lublinskaya and A. I. Ekimov, *Phys. Rev. B* **53**, 1336 (1996).
- [15] M. Chamarro, M. Dib, C. Gourdon, P. Lavallard, O. Lublinskaya and A. I. Ekimov, *Proceedings of Mat. Res. Soc. Symp.* (Boston, 1996), p 396.
- [16] U. Woggon, F. Gindele, O. Wind and C. Klingshirn, *Phys. Rev. B* **54**, 1506 (1996).
- [17] T. Takagahara, *Phys. Rev. B* **47**, 4569 (1993).
- [18] T. Takagahara, *J. Lumin.* **87-89**, 308 (2000).
- [19] S. V. Goupalov and E. L. Ivchenko, *J. Crystal Growth* **184/185**, 393 (1998); *Acta Physica Polonica A* **94**, 341 (1998).
- [20] S. V. Goupalov and E. L. Ivchenko, *Phys. Solid State* **42**, 1976 (2000).
- [21] S. V. Goupalov and E. L. Ivchenko, *Phys. Solid State* **43**, 1867 (2001).
- [22] A. Franceschetti, L. W. Wang, H. Fu and A. Zunger, *Phys. Rev. B* **58**, 13367 (1998).
- [23] S. Lee, L. Jönsson, J. W. Wilkins, G.W. Bryant and G. Klimeck, *Phys. Rev. B* **63**, 195318 (2001).

## Tunneling induced luminescence of individual InP quantum dots

*M.-E. Pistol*, U. Håkanson, M. K.-J. Johansson, W. Seifert and L. Samuelson  
Solid State Physics, Box 118 Lund University, SE-221 00 Lund, SWEDEN

**Abstract.** Quantum dots of InP have been investigated using a scanning tunneling microscope. The dots were situated close to the surface and thus easy to localise using tunneling microscopy. The photon emission from the dots was collected using a lens close to the sample and dispersed using a monochromator. Correlations between the luminescence and the topography have been made.

### Introduction

There is a strong interest in correlating structural and spectroscopic information of nanostructures such as quantum dots. Cathodoluminescence, where, for example, a semiconductor is excited using a scanning electron microscope is a useful technique which combines the imaging capabilities of scanning electron microscopy with photon maps of the same region of the sample [1].

Since many years there has been experiments reported on photon emission from surfaces where the excitation has been the tunneling current from a tip in close proximity to the surface. However only a few experiments have dealt with semiconductors and none have imaged surfaces using tunneling conditions. We here report on the investigation of semiconductor quantum dots using an STM for the excitation in tunneling mode. We show that it is possible to obtain photon maps of interesting structures. The sample consists of InP quantum dots grown by the Stranski–Krastanow mode on GaInP. As the growth technique we used metal-organic vapour phase epitaxy and the details of the growth can be found in Ref. [2]. The quantum dots were capped by 30 nm of GaInP and are thus situated quite close to the surface. The dots are shaped like truncated pyramids and have a height of 15 nm and a lateral extension of 40–50 nm according to transmission electron micrographs and atomic force micrographs [3, 4]. Previously, individual quantum dots in this system have been studied using photoluminescence (PL) [5], including time-resolved PL [6] and PL under electric field [7]. Realistic theoretical investigations have also been performed, using six-band  $k \cdot p$  theory [8], which give very good agreement with experiment. The GaInP is  $n$ -type with an electron concentration of about  $10^{18} \text{ cm}^{-3}$ .

The Fermi-level is thus situated close to the conduction band, which results in the quantum dots being highly charged with electrons [7]. The sample is also sulphur passivated. We use an ultra-high vacuum STM and the sample can be cooled to about 20 K. Tungsten tips were used and the tunneling current was typically 10 nA. The tip was positively biased relative to the sample. We typically used biases of 8–10 V. Under these conditions the Fermi-level of the tip is below the valence band edge of the GaInP and we extract electrons from the sample, which is equivalent to injecting holes. The injected holes recombine with electrons in the sample and photons are emitted. The photons are collected using a lens situated about 10 cm from the tip-sample area and focussed on the entrance slit of a monochromator. For detection we either used a cooled CCD-camera or a cooled GaAs photomultiplier. The CCD-camera was used for spectral measurements while the photomultiplier was used for imaging. Photon maps were obtained in about 10 minutes.

## Experimental results

In Figure 1 we show a photoluminescence spectrum of one sample. The emission consists of peaks corresponding to the GaInP barrier, the quantum dots and to the GaAs substrate [5]. The emission from the barrier is the most intense due to the comparably low density of quantum dots. The emission from the quantum dots is quite broad due to the fact that they are highly charged in this n-type material [7]. Thus several states in the conduction band are occupied by electrons which may recombine with holes in the ground state. In Figure 2(a) we show a constant current topograph of a sample.

A pattern of islands is seen. The islands correspond to overgrown quantum dots [9, 10], since the dots act as nucleation centers for the overlayer. The dots are typically situated in the center of the islands. If we take a photon map, using a detection energy of 1.6 eV, corresponding to the dot emission, we obtain the micrograph shown in Fig. 2(b). It can be seen that most of the islands contain a quantum dot giving emission in the relevant energy range. There are some exceptions and there are also a few islands that appear to contain more than one quantum dot. The presence of several closely spaced dots under one island has also been observed by transmission electron microscopy [10], but is not the subject of this report. In order to further investigate the technique we have taken spectra at different positions on the sample and the result is shown in Fig. 3. In positions 1 and 2 we obtain spectra which are typical of individual photoluminescence spectra of InP quantum dots. For instance, individual dots have several emission lines corresponding to different

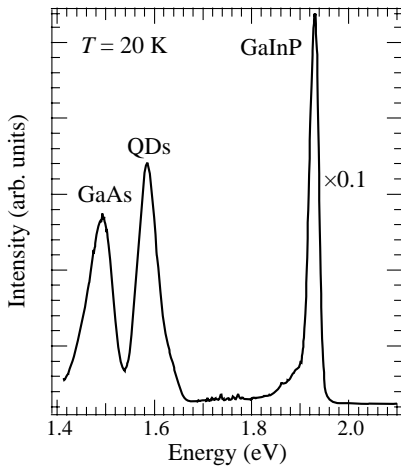


**Fig. 1.** A photoluminescence spectrum of a typical sample. The spectrum has three main peaks, one at 1.48 eV corresponding to the GaAs substrate, one at 1.6 eV corresponding to the InP quantum dots, and one at 1.94 eV corresponding to the GaInP layer.

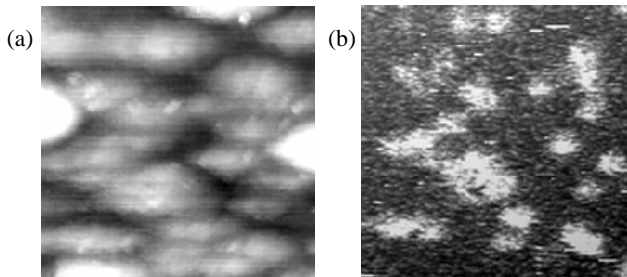


**Fig. 2.** (a) A constant current topograph of a sample with a size of 1 by 1  $\mu\text{m}$ . (b) the corresponding photon map where the emission from the quantum dots has been monitored.

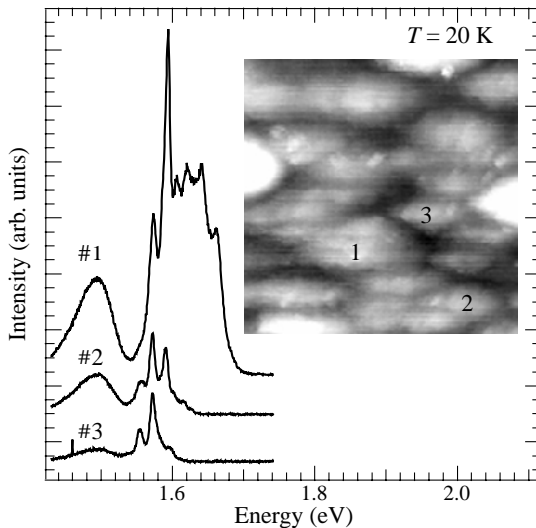


**Fig. 3.** Spectra obtained at three different position on the sample shown in the inset. The inset is a constant current topograph showing islands corresponding to overgrown InP quantum dots. In position 1 there are several quantum dots closely spaced whereas in positions 2 and 3 only one quantum dot is situated in the islands.

electrons which recombine with the holes. In position 3 we obtain a spectrum which in addition to the “normal” quantum dot also contain emission with a slightly higher energy (but still lower than the energy of the barrier).

## Conclusion

We have demonstrated that by collecting the photon emission from the tip-sample area it is possible to obtain photon maps using a scanning tunneling microscope, in the tunneling mode. It is additionally possible to obtain spectra at different locations on the sample.

## Acknowledgements

This work was performed within the nanometer consortium in Lund and was supported by SSF, NFR, TFR, Nutek and Ericsson.

## References

- [1] A. Gustafsson, M.-E. Pistol, L. Montelius and L. Samuelson, *J. Appl. Phys.* **84**, 1715 (1998).
- [2] N. Carlsson, W. Seifert, A. Peterson, P. Castrillo, M. E. Pistol and L. Samuelson, *Appl. Phys. Lett.* **65**, 3093 (1994).
- [3] M.-E. Pistol *et al.*, in *Proc. ICPS-23 (Berlin 1996)*, World Scientific, 1996, p. 1317.
- [4] K. Georgsson, N. Carlsson, L. Samuelson, W. Seifert and L. R. Wallenberg, *Appl. Phys. Lett.* **67**, 2981 (1995).
- [5] D. Hessman, P. Castrillo, M.-E. Pistol, C. Pryor and L. Samuelson, *Appl. Phys. Lett.* **69**, 749 (1996).
- [6] V. Zwiller, M.-E. Pistol, D. Hessman, R. Cederstrom, W. Seifert and L. Samuelson, *Phys. Rev. B* **59**, 5021 (1999).
- [7] D. Hessman, J. Persson, M.-E. Pistol, C. Pryor and L. Samuelson, *Phys. Rev. B* **64**, 233308 (2001).
- [8] C. Pryor, M.-E. Pistol and L. Samuelson, *Phys. Rev. B* **56**, 10 404 (1997).
- [9] U. Håkanson, M. K.-J. Johansson, J. Persson, J. Johansson, M.-E. Pistol, L. Montelius and L. Samuelson, *Appl. Phys. Lett.* **80**, 494 (2002).
- [10] M. K.-J. Johansson and U. Håkanson, unpublished.
- [11] J. Persson, M. Holm, C. Pryor, D. Hessman, W. Seifert, L. Samuelson and M.-E. Pistol, unpublished.



## On the zero phonon line homogeneous broadening in semiconductor QDs

*S. V. Goupalov*<sup>†‡</sup>, *R. A. Suris*<sup>‡</sup>, *P. Lavallard*<sup>§</sup> and *D. S. Citrin*<sup>†</sup>

<sup>†</sup> Georgia Institute of Technology, Atlanta, GA 30332-0250 USA

<sup>‡</sup> Ioffe Physico-Technical Institute, St Petersburg, Russia

<sup>§</sup> Groupe de Physique des Solides, Universités Paris 6 et 7, 75251 Paris, France

### Introduction

Dephasing of optical excitations in semiconductor quantum dots (QDs) has recently received much attention. A common model used for understanding such processes is a two-level electronic system interacting with phonons.

This model is applied to an optical transition between the QD ground state and a state where a localized exciton is optically excited. The nuclear system of the crystal is treated as the slowest one (adiabatic approximation). The relatively fast motion of the exciton localized in the QD is perturbed by the exciton-phonon interaction, which is assumed to be linear in the nuclear displacements. The perturbed energy of the localized exciton serves as an adiabatic potential for the nuclear system. The perturbation is usually considered up to the second order. As a result, parabolic adiabatic potentials for the nuclear motion (and, therefore, phonon Hamiltonians) corresponding to the QD ground state and to a state, where the localized exciton is optically excited, differ. The first-order perturbation term corresponds to terms linear in nuclear displacements in the difference of the phonon Hamiltonians and leads to a difference in the parabolic potential's minima positions. The second-order term corresponds to terms quadratic in nuclear displacements and leads to a difference in the parabolic potential's (phonon) frequencies. As a result, the phonon wave functions of the ground and the excited states are no longer orthogonal and multi-phonon-assisted transitions become possible.

Optical phonons can usually be treated within the Einstein model where all phonon modes are assumed to have the same frequency. The terms linear in nuclear displacements in the difference of the phonon Hamiltonians in the initial and optically excited states lead to the absorption spectrum consisting of a series of infinitely sharp lines representing multi-phonon-assisted transitions. If the exciton interaction with optical phonons is weak enough, then the zero optical phonon line (ZOPL) dominates the spectrum and only few replicas due to multi-phonon-assisted transitions make substantial contributions [1]. At low temperatures the ZOPL is broadened due to a strong exciton interaction with acoustic phonons [2]. However, the asymptotic behavior of the function describing this broadening at long times implies that the ZOPL consists of a broader line and a sharp peak [2]. The latter is analogous to the Mössbauer line in the  $\gamma$ -quanta absorption spectra of crystals [3] and will be referred to as the real zero phonon line (ZPL).

The spectral profiles in the form of a 'Prussian helmet' consisting of a broader line and a sharp peak have been recently observed experimentally using time-domain (photon echo [4, 5]) and frequency-domain (spectral hole burning [6]) nonlinear techniques in different QD systems. The use of nonlinear techniques is necessary to eliminate the effect of inhomogeneous broadening due to the size (shape) distribution of QDs usually present in a sample.

Available theoretical papers [7–10] discussing the ZPL homogeneous broadening are

contradictory. In the paper by Krivoglaz [7] a perturbative theory of the ZPL broadening was constructed where a phenomenological constant of the phonon damping constitutes one of the main parameters. In Refs. [8, 9] the electron-phonon interaction was treated non-perturbatively. However, the phonon damping was set equal to zero in the results and the difference of the phonon Hamiltonians in the initial and optically excited states was chosen in a form different from that of Ref. [7]. Thus, the result of Krivoglaz could not be obtained as a limiting case in Refs.[8, 9]. Very recently this result was misleadingly claimed to be exact [10].

In our work we construct a consistent non-perturbative theory of the ZPL homogeneous broadening and resolve the contradictions by pointing out the limits of validity of the theoretical papers mentioned above.

## 1. General formalism

From *e.g.* the Kubo formula it may be shown [1] that the optical absorption spectrum is determined by the function

$$U(t) \equiv e^{K(t)} = \left\langle e^{iH_i t} e^{-iH_f t} \right\rangle e^{i\Omega_0 t} = \left\langle T \exp \left[ -i \int_0^t \hat{V}(t_1) dt_1 \right] \right\rangle. \quad (1)$$

Here  $H_i = \sum_{\kappa} \omega_{\kappa} a_{\kappa}^+ a_{\kappa}$  and  $H_f$  are the phonon Hamiltonians in the initial and final states, respectively;  $\kappa$  enumerates different phonon modes,  $\omega_{\kappa}$  is the frequency of the mode  $\kappa$ ,  $a_{\kappa}^+$  ( $a_{\kappa}$ ) is the phonon creation (destruction) operator,  $\Omega_0$  is the difference in frequencies between the final and initial states of the electronic system,  $\hat{V}(t) = e^{iH_i t} V e^{-iH_i t}$ ,  $V = H_f - H_i - \Omega_0$ ,  $T$  is the time-ordering operator, and the brackets  $\langle \dots \rangle$  denote an average over phonon degrees of freedom. If  $V$  is such that  $K(t \rightarrow \infty) = \text{const}$ , then the ZPL is a  $\delta$ -function [3]. As far as we are interested in its broadening, interaction mechanisms leading to a non-constant long-time behavior of  $K(t)$  should be analyzed.

In what follows we will use the cumulant expansion of Eq. (1) defined by [11]

$$K(t) \equiv \sum_{n=1}^{\infty} K_n(t) = \sum_{n=1}^{\infty} \frac{(-i)^n}{n!} \int_0^t dt_1 \dots \int_0^t dt_n \left\langle T \hat{V}(t_1) \dots \hat{V}(t_n) \right\rangle_c. \quad (2)$$

Here the brackets  $\langle \dots \rangle_c$  denote the cumulant average [11]. This average is constructed in such a way that it is zero as soon as any two of the operators  $\hat{V}(t_i)$ ,  $\hat{V}(t_j)$  are not correlated. In other words, only connected diagrams contribute to  $K(t)$ .

## 2. Perturbative approach

In Ref. [7] the operator  $V$  was chosen in a simple form  $V = \sum_{\kappa} B_{\kappa} a_{\kappa}^+ a_{\kappa}$  implying that only the quadratic terms are present in the difference of the phonon Hamiltonians. Then  $V$  was considered as a perturbation and Eq. (1) was expanded up to the terms quadratic in  $B_{\kappa}$ . Using the phonon Green's function in the form  $d_{\kappa}(t, t') = -i \langle T \hat{a}_{\kappa}(t) \hat{a}_{\kappa}^+(t') \rangle$  or

$$i d_{\kappa}(t, t') = e^{-\gamma_{\kappa}|t-t'|} \left[ \theta(t-t') e^{-i\omega_{\kappa}(t-t')} (\bar{n}_{\kappa} + 1) + \theta(t'-t) e^{-i\omega_{\kappa}(t-t')} \bar{n}_{\kappa} \right] \quad (3)$$

[where  $\gamma_{\kappa}$  is the phenomenological constant of phonon damping,  $\theta(t)$  is the Heaviside function,  $\bar{n}_{\kappa} = (\exp \beta \omega_{\kappa} - 1)^{-1}$ , and  $\beta$  is the inverse temperature] to perform averaging

we obtain the result of Krivoglaz:

$$U(t) \approx \exp \left[ -i \sum_{\kappa} B_{\kappa} \bar{n}_{\kappa} t - \sum_{\kappa} \frac{B_{\kappa}^2 \bar{n}_{\kappa} (\bar{n}_{\kappa} + 1)}{4\gamma_{\kappa}^2} \left( 2\gamma_{\kappa} t - 1 + e^{-2\gamma_{\kappa} t} \right) \right]. \quad (4)$$

Since the perturbative expansion was used to derive Eq. (4), it is valid for small times only. In his original paper [7] Krivoglaz noticed that this result can be generalized for long times as well. However, the way of generalization suggested in Ref. [7] corresponds in fact to truncating the cumulant expansion of Eq. (2) at the second order. Indeed, one can see that  $U(t) \approx \exp[K_1(t) + K_2(t)]$  gives again Eq. (4). Below we show that the cumulant expansion up to the second order is not enough to describe the ZPL broadening and Eq. (4) does not hold for long  $t$ .

### 3. Nonperturbative approach

First of all, let us notice that Eq. (4) incorrectly leads to a finite ZPL line-width even in the case  $\gamma_{\kappa} \rightarrow 0$ . However, this case allows a simple exact solution. Namely,

$$U(t) = \left\langle \exp \left( -i \sum_{\kappa} B_{\kappa} n_{\kappa} t \right) \right\rangle = \prod_{\kappa} \frac{1 - e^{-\beta\omega_{\kappa}}}{1 - e^{-(\beta\omega_{\kappa} + iB_{\kappa}t)}} , \quad (5)$$

where  $n_{\kappa} = a_{\kappa}^{\dagger} a_{\kappa}$ . It is evident that  $U(t) \rightarrow \text{const} \neq 0$  when  $t \rightarrow \infty$ . This means that the long-living phonons cannot lead to the ZPL broadening even if the operator  $V$  contains terms quadratic in nuclear displacements, and that Eq. (4) does not hold in the limit  $t \rightarrow \infty$ . One may verify, however, that expansions of Eq. (4) with  $\gamma_{\kappa} = 0$  and Eq. (5) up to the second order in  $B_{\kappa}$  coincide.

Now let us analyze the long-time behavior of the function  $U(t)$  in the case when the phonon damping is finite. To that end let us notice that the  $n$ -th cumulant in the expansion (2) may be written in the form [8]

$$K_n(t) = (-i)^n \int_0^t d\tau_n \int_0^{\tau_n} d\tau_{n-1} \dots \int_0^{\tau_{n-1}} d\tau_1 \left\langle T \hat{V}(\tau_1 + \dots + \tau_{n-1}) \dots \hat{V}(\tau_{n-1}) \hat{V}(0) \right\rangle_c. \quad (6)$$

If  $t \gg \gamma_{\kappa}^{-1}$  then we can extend the upper limits of the integrals for  $\tau_{n-1} \dots \tau_1$  to infinity. We then obtain [8]

$$K_n(t) \approx t (-i)^n \int_0^{\infty} d\tau_1 \dots \int_0^{\infty} d\tau_{n-1} \left\langle T \hat{V}(\tau_1 + \dots + \tau_{n-1}) \dots \hat{V}(\tau_1) \hat{V}(0) \right\rangle_c. \quad (7)$$

Thus, the  $n$ -th cumulant is proportional to  $t$  for  $t \gg \gamma_{\kappa}^{-1}$  and, therefore, the ZPL line-shape is Lorentzian. The width of the Lorentzian is obtained by the summation of the cumulants of all orders. Choosing  $V = \sum_{\kappa} A_{\kappa} (a_{\kappa} + a_{\kappa}^{\dagger}) + \sum_{\kappa} B_{\kappa} a_{\kappa}^{\dagger} a_{\kappa}$  and adopting derivation of Ref. [8] or [9] for this form of  $V$  we find

$$K(t) \approx -t \sum_{\kappa} \left\{ \frac{i A_{\kappa}^2 \hat{d}_{\kappa}(0)}{1 - B_{\kappa} \hat{d}_{\kappa}(0)} + i B_{\kappa} \bar{n}_{\kappa} + \int_{-\infty}^{\infty} \frac{d\omega}{2\pi} \left[ \ln(1 - B_{\kappa} \hat{d}_{\kappa}(\omega)) + B_{\kappa} \hat{d}_{\kappa}(\omega) \right] \right\} \quad (8)$$

where we introduced the Fourier transform of Eq. (3)

$$\hat{d}_{\kappa}(\omega) = \frac{\bar{n}_{\kappa} + 1}{\omega - \omega_{\kappa} + i\gamma_{\kappa}} - \frac{\bar{n}_{\kappa}}{\omega - \omega_{\kappa} - i\gamma_{\kappa}} = \frac{\omega - \omega_{\kappa} - i\gamma_{\kappa}(2\bar{n}_{\kappa} + 1)}{(\omega - \omega_{\kappa})^2 + \gamma_{\kappa}^2}. \quad (9)$$

In Refs. [8, 9] an expression for a phonon Green's function with  $\gamma_{\kappa} = 0$  was used to evaluate  $K(t)$ . However,  $\gamma_{\kappa}$  has a physical meaning of the inverse phonon life-time and should be kept finite.

#### 4. Discussion of the results

Keeping  $\gamma_{\kappa}$  finite enables one to compare the result of Eq. (8) with that of Krivoglaz (Eq. (4)). The latter allows the limit  $t \gg \gamma_{\kappa}^{-1}$  in which Eq. (8) was obtained. Letting in Eq. (8)  $A_{\kappa} = 0$ , expanding it up to the second order in  $B_{\kappa}$  and performing integration by closing the contour in *e.g.* the upper complex semi-plane we obtain the result of Eq. (4) in which  $t \gg \gamma_{\kappa}^{-1}$ .

One can see from Eq. (8) that, as far as  $\gamma_{\kappa}$  is finite, a finite ZPL line-width can be due to the linear terms in the difference of the phonon Hamiltonians alone. The ZPL line-width is also finite at zero temperature if  $\gamma_{\kappa}$  remains finite in this limit.

To summarize, we have shown that (i) long-living phonons cannot lead to the ZPL homogeneous broadening, (ii) a non-zero ZPL line-width can be due to both linear and quadratic in nuclear displacements terms in the difference of the phonon Hamiltonians in the ground and optically excited states, and (iii) as far as phonon life-time is finite at zero temperature, the ZPL line-width is non-zero in this limit.

#### Acknowledgements

Support from INTAS (code 99-O-0858), the U.S. Office of Naval Research, the U.S. National Science Foundation (through ECS-0072986 and DMR-0073364), RFBR and the State of Georgia (through the Yamacraw program) is gratefully acknowledged.

#### References

- [1] G. D. Mahan, *Many-Particle Physics*, 2nd ed. (Plenum, New York, 1990).
- [2] S. V. Goupalov, R. A. Suris, P. Lavallard and D. S. Citrin, *Nanotechnology* **12**, 518 (2001).
- [3] E. D. Trifonov, *Sov. Phys. - Doklady* **7**, 1105 (1963).
- [4] K. Takemoto, B.-R. Hyun and R. Masumoto, *Solid State Commun.* **114**, 521 (2000); *J. Luminescence* **87-89**, 485 (2000).
- [5] P. Borri, W. Langbein, S. Schneider, U. Woggon, R. L. Sellin, D. Ouyang and D. Bimberg, *Phys. Rev. Lett.* **87**, 157401 (2001).
- [6] P. Palinginis and H. Wang, *Appl. Phys. Lett.* **78**, 1541 (2001).
- [7] M. A. Krivoglaz, *Sov. Phys.- Solid State* **6**, 1340 (1964).
- [8] D. Hsu and J. L. Skinner, *J. Chem. Phys.* **81**, 1604 (1984).
- [9] J. L. Skinner and D. Hsu, *J. Phys. Chem.* **90**, 4931 (1986).
- [10] A. V. Uskov, A.-P. Jauho, B. Tromborg, J. Mørk and R. Lang, *Phys. Rev. Lett.* **85**, 1516 (2000).
- [11] R. Kubo, *J. Phys. Soc. Japan* **17**, 1100 (1962).

## Aharonov–Bohm effect for few-particle and collective excitations (excitons, trions, plasmons)

*A. V. Chaplik*

Institute of Semiconductor Physics, Siberian Branch of the RAS,  
630090 Novosibirsk, Russia

The conventional Aharonov–Bohm effect is associated with the behavior of electrons in non-simply connected objects (quantum rings, nanotubes) placed in a magnetic field. The physical manifestation of the effect is the oscillatory dependence of macroscopic characteristics (like conductance, magnetic susceptibility etc.) on the magnetic flux piercing the ring or nanotube. In the present paper some more complicate formations are considered including neutral and charge excitons in quantum rings and collective oscillations of 2D electrons on the surface of nanotubes (plasma waves). It is shown that the Aharonov–Bohm effect occurs in these situations either and it is established which parameters of the considered systems reveal the oscillatory behavior when changing the magnetic flux.

The neutral exciton in a one-dimensional ring demonstrates the aharonov–bohm oscillations of the binding energy with the universal period equaled to the flux quantum  $h/e$ . With accounting for the radial degrees of freedom due to finite width of the ring these oscillations decay in accord with gaussian law as a function of the magnetic field; the decrement of the damping is linearly proportional to the ring radius.

In the case of trions (e–e–h complex) one meets to-date the only example of the non-universal period of the aharonov-bohm oscillations: the binding energy of the trion oscillates as a function of magnetic flux with the period depending on the ratio of effective masses of electrons and holes. However the persistent current produced by the trion in the ring depends on the flux with the universal period  $h/e$ .

Plasma oscillations of electrons in nanotubes placed in the magnetic field parallel to the tube axis are affected by the field only due to topological reasons: normally the 2D electrons do not “see” the in-plane magnetic field. Both types of the single-particle energy spectrum of nanotubes are considered. In the case of the semiconductor spectrum the plasmon frequency oscillates with the magnetic flux only if the spatial dispersion is taken into account (i.e. beyond the cold plasma approximation). On the contrary, for the gapless metallic type of spectrum the magnetic flux dependence appears “from the very beginning” because the magnetic field “opens” the gap in the single-particle spectrum of electrons. In both cases the period of oscillations is  $h/e$ . Some possibilities of experimental manifestations of the Aharonov–Bohm effects for plasmons via FIR absorption and Raman scattering are discussed.

## Optical memory concepts with self-organized quantum dots — material systems and energy-selective charging

C. Kapteyn<sup>†</sup>, J. Ekehalt<sup>†</sup>, R. Heitz<sup>†</sup>, D. Bimberg<sup>†</sup>,  
G. E. Cirlin<sup>‡</sup>, V. M. Ustinov<sup>‡</sup> and N. N. Ledentsov<sup>†‡</sup>

<sup>†</sup> Institut für Festkörperphysik, Technische Universität Berlin,  
Hardenbergstraße 36, 10623 Berlin, Germany

<sup>‡</sup> Ioffe Physico-Technical Institute, St Petersburg, Russia

**Abstract.** For memory structures based on optically induced charge in self-organized quantum dots, the concept of wavelength-domain multiplexing in the quantum dot ensemble is an essential prerequisite. The electric properties of quantum dots in various material systems as studied by time-resolved capacitance spectroscopy are summarized, and candidates suitable for future memory applications are discussed. By combining optical excitation and capacitance spectroscopy, direct evidence is obtained for energy-selective hole charge generation and storage in InAs/GaAs quantum dots. A clear dependence of the activation energy of the emitted holes on the energy of the excitation is observed.

### Introduction

The ultimate reduction of device size and charge in semiconductor memory devices naturally leads to the quantum regime. An ideal prototype to study few- and single-electron effects are semiconductor quantum dot heterostructures [1]. Early it was realized that self-organized quantum dots can be fabricated in a variety of material systems with a resulting broad range of electric and optical properties. As direct electrical addressing of huge ensembles of such quantum dots would involve enormous technological efforts, it was proposed to employ optical addressing to circumvent these difficulties [2,3]. Optical addressing is feasible only provided wavelength-domain multiplexing can be realized. Self-organized quantum dots exhibit a natural spectral distribution in their energy levels due to ensemble fluctuations in size and shape. They can also be fabricated with very high optical quality and very low defect density. Such quantum dot heterostructures are therefore a very promising system for studying wavelength-domain multiplexing techniques. Optical charging in suitable sample structures with quantum dots embedded has recently been reported [3–8]. A demonstration, however, that the generated charge retains the initial spectral information of the excitation process is, although crucial, still lacking.

Here, we discuss the prerequisites for memory applications based on self-organized quantum dots and study the optical charge generation process by combining optical charging with conventional capacitance spectroscopy. Our experimental results demonstrate the feasibility of energy-selective optical charging of sub-ensembles of quantum dots.

### 1. Material systems

Central issues for memory concepts are the energy level structure, the carrier retention time, and the escape mechanisms. A simple diode structure allows to directly detect the amount of charge in an embedded quantum dot layer, which is situated at a suitable distance from a Schottky- or pn-interface. Such a structure is an ideal device to study charging and escape processes in quantum dots with help of time-resolved capacitance spectroscopy. Based on the data evaluation methods of deep level transient spectroscopy (DLTS) [9], capacitance transients are recorded, emission time constants determined, escape mechanisms identified, and activation energies derived.

A variety of material combinations exhibiting quantum dot formation have so far been investigated [10–17]. The obtained activation energies are summarized in Table 1. For memory applications a high activation energy is desirable, since thermal escape of carriers is usually the limiting process for the charge storage time.

**Table 1.** Activation energies obtained from time-resolved capacitance measurements for various quantum dot material systems.

Material system	Carrier type	Activation energy	Reference
InAs/GaAs	electron	80–90 meV (*)	[11,12]
InAs/GaAs	hole	160–250 meV	[12,17]
GaSb/GaAs	hole	350–400 meV	[14,16]
InAs/InP	hole	440 meV	[15]
InP/GaInP	electron	220 meV	[10]
Ge/Si	hole	350 meV	[13]

(\*) Note that except for electrons in InAs/GaAs quantum dots, the activation energies for electrons and holes reflect the ground state energies relative to the conduction or valence band-edge of the matrix material, respectively.

From the experimental results one can estimate room temperature carrier retention times by extrapolation (e.g. a few ps for holes in InAs/GaAs quantum dots [12] and about one  $\mu$ s for holes in Ge/Si). These retention times are significantly shorter than retention times, which can be attained in suitable memory devices, where carrier storage of up to several seconds was observed [3–7]. The reduced retention times in time-resolved capacitance measurements are due to the presence of an electric field, which increases the effective emission rate. Typical memory structures make use of an optimized band structure and additional barriers in order to prevent unintentional carrier loss. Table 1 nevertheless clearly indicates in which material systems long intrinsic storage times may be expected. From this point of view, hole storage in Ge/Si, InAs/InP, or GaSb/GaAs quantum dots appears promising.

For the employment of wavelength-domain multiplexing techniques the optical properties of the material system are of great importance, too. As GaSb/GaAs has a type-II band line-up, only the hole states are fully quantized in all three dimensions and a true energy-selectivity might hence not be given for the absorption process. For a general test of the feasibility of the concept of optical multiplexing, InAs/GaAs quantum dots hence appear to be a very promising system. In previous experiments it was furthermore observed, that electron and hole escape processes, and hence the according emission rates in the InAs/GaAs material system, are significantly different [12]. This is reflected by the smaller thermal activation energy for electrons. A net hole charge can thus elegantly be created, simply by optical excitation of electron-hole pairs and fast release of electrons. Due to these reasons, we decided to focus on InAs/GaAs quantum dots for optical charging experiments.

## 2. Optical multiplexing

For optical addressing of sub-ensembles of self-organized quantum dots one can employ their natural fluctuations in the optical transition energies. Due to the quantum-size effect, larger quantum dots exhibit a smaller transition energy, whereas smaller quantum dots show a larger transition energy. Conclusively one can expect to charge large quantum dots by illumination at a lower energy than small quantum dots, which require a larger excitation energy. In order to avoid additional absorption in impurities or defects, and carrier loss due to charge-transfer into defects close to the quantum dots, a high material quality is required.

### 2.1. Experimental details

Based on time-resolved capacitance measurements, we have performed experiments with optical excitation. The sample structures are GaAs  $p^+n$ -diodes similar to devices previously used for purely electrical capacitance spectroscopy of quantum dots, see e.g. [11]. Details of the sample structure and the optical charging process will be presented elsewhere [17].

In our experiments, we record capacitance transients due to carrier emission from the quantum dots after illumination of the sample with monochromatic light with a resolution of about 6 meV for 10 ms. A conventional lamp with a monochromator was employed for these measurements. The temperature shift of the absorption was accounted for by adjusting the actual excitation wavelength according to the temperature. Here and in the following, only the respective excitation energies for 300 K are mentioned.

### 2.2. Results

Recording capacitance transients after illumination, a minority carrier DLTS signal is clearly observed (not shown). From the amplitude a hole charge of about 0.2 per quantum dot is deduced. The activation energy of the thermally activated emission process exhibits a pronounced dependence on the energy of the exciting light. The reference sample did not exhibit any optically induced DLTS signal. Bias dependent DLTS measurements of the quantum dot sample (not shown) prove that the quantum dot layer is the source of the observed carrier emission.

By increasing the excitation energy in the range between 1.02 eV and 1.09 eV, a shifting DLTS signal with an accordingly decreasing activation energy down to about 180 meV is observed, see Fig. 1. For further increasing excitation energy, the activation energy quickly raises again to about 230 meV at around 1.11 eV, until it decreases again down to about 170 meV for the highest excitation energies (up to 1.19 eV).

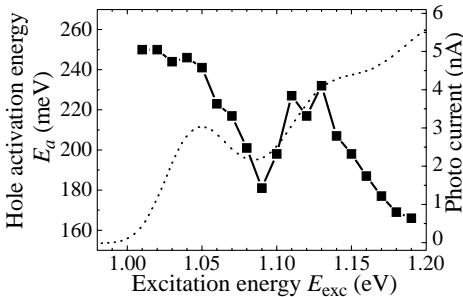


**Fig. 1.** The dependence of the hole activation energy as function of excitation energy (for 300 K) is shown as squares. The reverse bias was set to 8.3 V and optical pulses of 10 ms were applied. For comparison, the photo-absorption current at 300 K for a reverse bias of 8.3 V is displayed as dotted line.

These experimental findings are interpreted in terms of energy-selective charging of sub-ensembles of quantum dots by resonant absorption of light. In large quantum dots with a low ground state transition energy a net hole charge is generated, which exhibits a large activation energy. By increasing the excitation energy, smaller and smaller quantum dots are resonantly charged with holes, which are energetically closer to the GaAs valence band edge and hence lead to smaller activation energies. This process is even repeated for absorption in the first excited state, as the observed activation energies for excitation above around 1.11 eV reflect. These experimental results demonstrate, to our knowledge, the first direct proof for energy-selective charging of quantum dot sub-ensembles.

### 3. Concluding remarks

In order to charge quantum dots and hence “write” data in future memory structures, optical addressing is a very promising approach. Various quantum dot material systems have previously been studied by time-resolved capacitance spectroscopy. By comparing these results and also taking optical properties into account InAs/GaAs was identified as



a promising candidate for optical charging experiments. By combining resonant optical excitation and capacitance spectroscopy, it is demonstrated that optical multiplexing in quantum dot ensembles is feasible. Hole ground state activation energies in the range of 250 meV to 180 meV were observed for excitation energies between 1.02 eV and 1.09 eV, giving evidence for energy-selective charging. Similar energy-selective charging could also be conducted for optical charging of excited quantum dot states.

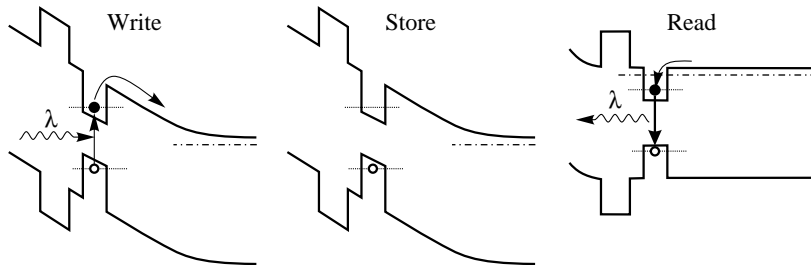


**Fig. 2.** Schematic band structure and basic operation principle of a memory structure based on energy-selective optical charging, similar to the sample investigated here. Note the additional barriers for increased hole storage times.

The development of memory structures based on optical multiplexing in self-organized quantum dot ensembles is still at a rather explorative stage. Recent results from the investigation of the electrical properties and carrier emission processes in quantum dots in various material systems, however, allow to conduct more dedicated research towards key functional ingredients of future devices, especially optical addressing.

In the future it is intended to increase the spectral resolution, to extend the investigations to other promising material systems (e.g. GaSb/GaAs), and to develop and study optimized sample structures for memory applications, which allow for increased carrier retention times and hence more realistic device operation.

#### Acknowledgements

This work was funded by the NANOMAT project of the European Commission's Growth Programme, contract number G5RD-CT-2001-00545, and SFB 296 of DFG.

#### References

- [1] D. Bimberg, M. Grundmann and N. N. Ledentsov, *Quantum Dot Heterostructures*, John Wiley & Sons, Chichester (1998)
- [2] S. Muto, *Jpn. J. Appl. Phys.* **34**, L210 (1995).
- [3] K. Imamura, Y. Sugiyama, Y. Nakata *et al*, *Jpn. J. Appl. Phys.* **34**, L1445 (1995).
- [4] G. Yusa and H. Sakaki, *Appl. Phys. Lett.* **70**, 345 (1997).
- [5] J. J. Finley, M. Skaltz, M. Arzberger *et al*, *Appl. Phys. Lett.* **73**, 2618 (1998).
- [6] Y. Sugiyama, Y. Nakata, S. Muto *et al*, *IEEE J. Sel. Topics in Quantum Electron.* **4**, 880 (1998).
- [7] T. Lundstrom, W. Schoenfeld, H. Lee *et al*, *Science* **286**, 2312 (1999).
- [8] H. Pettersson, L. Baath, N. Carlson *et al*, *Appl. Phys. Lett.* **79**, 78 (2001).
- [9] D. V. Lang, *J. Appl. Phys.* **45** (7), 3023 (1974).
- [10] S. Anand, N. Carlsson, M.-E. Pistol *et al*, *J. Appl. Phys.* **84** (7), 3747 (1998).
- [11] C. M. A. Kapteyn, F. Heinrichsdorff, O. Stier *et al*, *Phys. Rev. B* **60** (20), 14265 (1999).
- [12] C. M. A. Kapteyn, M. Lion, R. Heitz *et al*, *Appl. Phys. Lett.* **76** (12), 1573 (2000).
- [13] C. M. A. Kapteyn, M. Lion, R. Heitz *et al*, *Appl. Phys. Lett.* **77** (25), 4169 (2000).
- [14] R. Magno, B. R. Bennett and E. R. Glaser, *J. Appl. Phys.* **88** (10), 5843 (2000).
- [15] H. Pettersson, C. Pryor, L. Landin *et al*, *Phys. Rev. B* **61** (7), 4795 (2000).
- [16] M. Geller *et al*, *to be published*
- [17] C. Kapteyn *et al*, *to be published*

## Escape of carriers photoexcited in self-organized InAs/GaAs quantum dots

*P. N. Brunkov*<sup>†‡</sup>, *A. Patanè*<sup>‡</sup>, *A. Levin*<sup>‡</sup>, *L. Eaves*<sup>‡</sup>, *P. C. Main*<sup>‡</sup>,  
*Yu. G. Musikhin*<sup>†</sup>, *B. V. Volovik*<sup>†</sup>, *A. E. Zhukov*<sup>†</sup>, *V. M. Ustinov*<sup>†</sup>  
and *S. G. Konnikov*<sup>†</sup>

<sup>†</sup> Ioffe Physico-Technical Institute, St Petersburg, Russia

<sup>‡</sup> School of Physics and Astronomy, University of Nottingham,  
NG7 2RD Nottingham, UK

**Abstract.** Photocurrent and capacitance spectroscopy are used to investigate a Schottky barrier structure containing a single layer of self-organized InAs/GaAs quantum dots. We show that the temperature dependence of the photocurrent signal from the quantum dots is governed by thermal escape of electrons as the faster carriers.

### Introduction

InAs/GaAs self-assembled quantum dots (QDs) are of great current interest. Their zero-dimensional character has potential for new optoelectronic devices, such as low-threshold lasers, infrared detectors and high-density optical memories [1]. Carrier transport plays an important role in determining the properties of these devices. Therefore, a great deal of attention has been devoted to studies of emission and capture processes of charge carriers by the QDs using both electrical [2, 3] and optical techniques [1]. Photocurrent (PC) spectroscopy combines the advantages of both electrical and optical methods of investigation [4, 5]. The PC spectrum reflects, in part, the optical absorption in the QD layer, but carriers that are photogenerated in the QDs have to be separated in order to contribute to the PC signal. As a result, the intensity of the PC signal is governed by the interplay between the recombination and escape rates of photogenerated carriers [4, 5].

### 1. Experimental details

The QDs structures were grown by molecular beam epitaxy (MBE) on  $n^+$ -GaAs (001) substrates. The InAs layer, of average thickness 4 monolayers, was deposited at 485°C. The QDs were sandwiched between a 0.4  $\mu\text{m}$ -thick GaAs cap and a 1  $\mu\text{m}$ -thick GaAs buffer layer. The cap and buffer layers were uniformly doped with Si at  $2.0 \times 10^{16} \text{cm}^{-3}$ , except for two 10 nm thick, undoped spacers, one on each side of the QD layer. Plan-view transmission electron microscopy images reveal a uniform spatial distribution of dots, with mean diameter of 15 nm. The areal concentration was found to be  $N_{\text{QD}} = 3 \times 10^{10} \text{cm}^{-2}$ . For the PC and PL measurements, a semi-transparent, Ni-Cr Schottky barrier of diameter 100  $\mu\text{m}$  was deposited on top of the n-type structure to provide optical access to the sample. The capacitance ( $C$ ) and conductance ( $G$ ) characteristics were measured using an HP4284A LCR meter. The excitation source for the PC measurements was a tungsten-halogen lamp, dispersed by a 0.25 m monochromator and the PC signal was recorded using standard lock-in techniques. PL measurements were performed with the optical excitation provided by a He-Ne laser.

## 2. Results and discussion

Analysis of the capacitance–voltage ( $C(V)$ ) characteristics of the QD structure on the base of a quasi-static charging model indicated [2] that at  $V = 0$  V, there are two filled electron states in the QDs, at  $E_{e0} = (140 \pm 10)$  meV and  $E_{e1} = (60 \pm 10)$  meV below the bottom of the GaAs conduction band. The PL spectrum of the QD structure at  $T = 80$  K shows three QD-related bands,  $h\nu_0$ ,  $h\nu_1$  and  $h\nu_2$  peaked, respectively, at 1.150 eV, 1.222 eV and 1.281 eV. Band  $h\nu_0$  is due to ground state electron-hole transitions in the dots, whilst  $h\nu_1$  and  $h\nu_2$  are due to transitions involving the excited electron and hole states [2].

Figure 1 shows logarithmic PC spectra of the device measured at reverse bias  $V = -3$  V as a function of the temperature. At  $T = 200$  K the PC spectrum reveals features at  $\sim 1.40$  eV, due to optical absorption in the InAs wetting layer, and three features at 1.102 eV, 1.182 eV and 1.240 eV, caused by absorption in the ground and excited states of the InAs QDs. The positions of the last three features agree quite well with the energy positions of the corresponding PL peaks [2]. The temperature dependence of the PC spectra shows that the PC signal from QDs is suppressed below 200 K as shown in Figure 1.

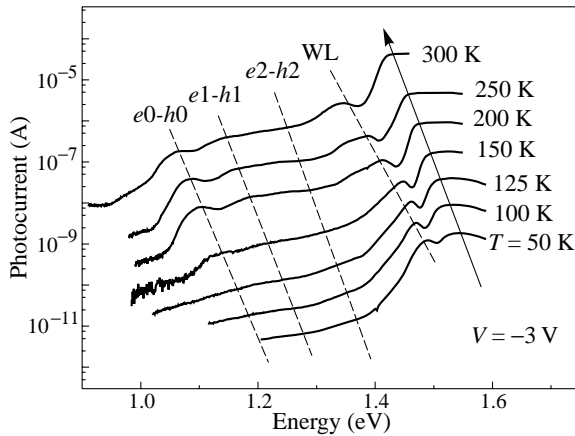


**Fig. 1.** Photocurrent (PC) spectra measured for  $V = -3$  V at various temperatures.

The amplitude of the PC signal from the QDs depends on the photon absorption. However, carriers photogenerated in the QDs can recombine before they are able to escape and contribute to the PC signal [4, 5]. Therefore, the strength of PC signal from the dots depends also on the relation between the recombination ( $1/\tau_{\text{rec}}$ ) and escape rates ( $1/\tau_{\text{esc}}$ ) of carriers. In particular, as it follows from a coupled-rate equation model, the intensity of the PC signal is mainly controlled by the escape rate of the faster carrier and can be represented in the following form [5]:

$$I_{\text{PC}} = g/(1 - \tau_{\text{esc}}/\tau_{\text{rec}}) \quad (1)$$

where  $g$  is the carrier photo-generation rate in the QDs, which is proportional to the incident photon flux ( $P$ ). Then, since the electron-hole recombination time  $\tau_{\text{rec}}$  is about 1 ns [1], for significant PC,  $\tau_{\text{esc}}$  should be smaller than 1 ns.

Since the holes are heavier and more deeply confined than the electrons [3], we estimate that their escape time is a few orders of magnitude ( $10^{-1}$ – $10^{-3}$ ) slower than that of the electrons. In this case, the photocurrent is proportional to the escape rate of electrons ( $1/\tau_{\text{esc}}^e$ ) at sufficiently low temperature when  $\tau_{\text{esc}}^e \gg \tau_{\text{rec}}$  (Eq. (1)). At high temperatures,

when the electron escape rate is very high, the current is independent of  $\tau_{\text{esc}}^e$  (and  $\tau_{\text{esc}}^h$ ) and is determined simply by the rate of photon absorption by the QDs (Eq. (1)).

The electron escape time can be expressed as:

$$\tau_{\text{esc}} = \tau_{\text{esc}}^0 \exp\left(\frac{-\Delta E_a^{e0}}{k_B T}\right) \quad (2)$$

where  $\Delta E_a^{e0}$  is the activation energy for thermal escape of carriers and  $\tau_{\text{esc}}^0$  is the escape time in the high temperature limit ( $kT \gg \Delta E_a^{e0}$ ).

In order to measure the temperature dependence of the electron escape rate out of the dots, we used admittance spectroscopy. Admittance spectroscopy involves measuring the capacitance and conductance of the device in the *ac* mode with tunable frequency,  $f$ , as a function of temperature. A step in the  $C(T)$  curve and a peak in the  $G(T)$  characteristic of the device are observed when the rate of escape of electrons,  $(1/\tau_{\text{esc}}^e)$ , out of the dots becomes comparable with measurement frequency  $f$ , according to the relation:

$$2\pi f \tau_{\text{esc}}^e = 2. \quad (3)$$

Figure 2(a) shows the Arrhenius plot of  $\tau_{\text{esc}}^e$  for  $V = -2.4$  V and a fit to the data by Eq. (2), with fitting parameters  $\Delta E_a^{e0} = 69$  meV and  $\tau_{\text{esc}}^0 = 10.9$  ps. We found that at  $V = -2.4$  V, the chemical potential  $\mu$  is in resonance with the maximum of the density of states associated to the ground state energy distribution of QDs [2]. For this bias condition, the value of  $\Delta E_a^{e0} = 69$  meV is smaller than the energy of the electron ground state ( $E_{e0} = 140$  meV) determined from the quasi-static  $C(V)$  simulations [2] and compares with the spacing between the ground state and first excited state of electrons in the QDs ( $\Delta E_a^{e0} = 80 \pm 20$  meV), as obtained from  $C(V)$  measurements. This suggests that electron emission from the QDs into the GaAs layers occurs by thermal escape, involving electron excited states of the dots. This is in agreement with the results obtained by time resolved capacitance spectroscopy [3].

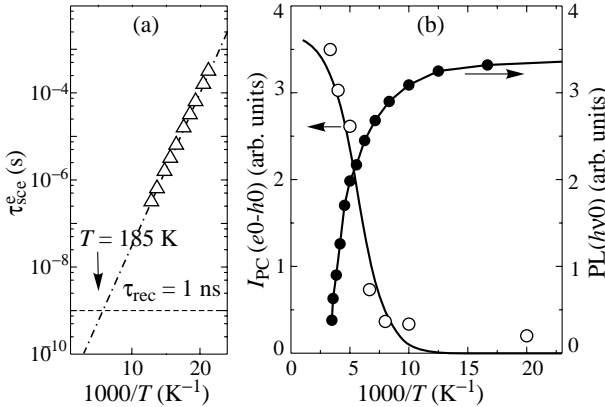


**Fig. 2.** (a) Arrhenius plot of the electron emission rate  $V = -2.4$  V. Continuous line is the fit to the data by Eq. (2). (b) Temperature dependence of the intensity of the PC peak,  $I_{\text{PC}}(e0 - h0)$ , for  $V = -3$  V (open circles) and of the PL peak,  $\text{PL}(h\nu0)$ , (solid circles) associated with the ground state transition in the QDs. The calculated temperature dependence of  $I_{\text{PC}}(e0 - h0)$  for thermal escape of electrons from QDs at  $V = -2.4$  V (solid line).

We can now interpret the observed temperature dependence of the PC signal in terms of our analysis of all measurements. Figure 2(b) shows the temperature dependence of the intensity of the PC peak associated with the QD ground state  $I_{\text{PC}}(e0 - h0)$  at  $V = -3.0$  V. The temperature dependence of the PC signal is well described by equations 2 and 3, with electron escape parameters  $\Delta E_a^{e0}$  and  $\tau_{\text{esc}}^0$  measured by admittance spectroscopy for  $V = -2.4$  V. This indicates that the electrons control the PC signal.

Figure 2(b) shows that for  $T < 110$  K there is a strong increase in the intensity of the PL peak, PL ( $h\nu_0$ ), associated with the ground state transition in the QDs. This implies that, in this temperature range, the recombination of photogenerated carriers dominates over escape processes, consistent with our description of the thermally-activated PC associated with the QDs. In particular, we estimate that the electron escape time-constant is lower than the recombination time  $\tau_{\text{rec}} = 1$  ns for temperatures  $T > 185$  K (Fig. 2a), consistent with the experimentally observed suppression of the PC signal from the QDs measured at  $V = -3.0$  V (Fig. 1).

In summary, we have found that the temperature dependence of the PC signal from the QDs is governed by thermal escape of electrons as the faster carriers. This has important implications for applications based on carrier storage in QDs where holes will be the more promising carrier type for storage devices in the given material system.

#### Acknowledgements

The work is supported by the International Russian–Ukrainian project on nanoelectronics and INTAS project 00-774. Two authors, P.N.B. and L.E., gratefully acknowledge support from the Royal Society and EPSRC, respectively.

#### References

- [1] D. Bimberg, M. Grundmann and N. N. Ledentsov, *Quantum dot heterostructures*: John Wiley and Sons Ltd., Chichester, 1998.
- [2] P. N. Brunkov *et al*, *J. Electr. Mat.* **28**, 486 (1999).
- [3] C. M. A. Kapteyn *et al*, *Appl. Phys. Lett.* **76**, 1573 (2000).
- [4] P. W. Fry *et al*, *Phys. Rev. Lett.* **84**, 733 (2000).
- [5] P. N. Brunkov *et al*, *Phys. Rev. B* **65**, (2002).

## Heterostructure optical phonons in dynamics of quantum dot electronic excitations: new experimental evidences

A. V. Baranov<sup>†‡</sup>, V. Davydov<sup>†‡</sup>, A. Fedorov<sup>†</sup>,  
H.-W. Ren<sup>‡\*</sup>, S. Sugou<sup>‡\*</sup> and Yasuaki Masumoto<sup>‡§</sup>

<sup>†</sup> S. I. Vavilov State Optical Institute, St Petersburg, 199034, Russia

<sup>‡</sup> ERATO Single Quantum Dot Project, JST Corporation, Japan

<sup>\*</sup> Opto-Electronics Research Lab., NEC Corp., Tsukuba, 305-8501, Japan

<sup>§</sup> Institute of Physics, University of Tsukuba, Tsukuba, 305-8571, Japan

**Abstract.** Unusual coupling of heterostructure optical phonons and electronic excitations in quantum dots (QD's) was observed by photoluminescence spectroscopy in strain-induced InGaAs/GaAs QD's (SIQD's) and self-assembled InAs/GaAs QD's (SAQD's). Phonon-assisted interband transitions in SIQD's were found to be governed by zone center bulk GaAs TO and LO phonons via deformation potential interaction, whereas polar interaction was inessential. For SAQD's, a n-doped GaAs substrate was found to effect on QD intraband relaxation of carriers via coupling between them and substrate LO-phonon-plasmon modes at spacing between QD's and substrate as long as 100 nm.

Dynamics of electronic excitations in QD's of different types is determined in a large extent by their interaction with optical phonons, that is subject of comprehensive studies. In most cases inherent phonons of QD's are discussed. However, QD's are usually contained in a host matrix or heterostructure with different composition and, therefore, subjected to the specific phonons in such composite media. Recently several groups reported for SAQD's systems that LO-phonons of barriers and QD/matrix interface (IF) modes can be involved in intraband carrier relaxation and/or interband optical transitions via polar Fröhlich interaction [1, 2, 3]. The problem seems should be studied in details for different types of QD heterostructures with different composition, thickness of barrier or spacer layers, etc.

We studied coupling between electronic excitations in QD's and optical phonons of surrounding media for In<sub>0.1</sub>Ga<sub>0.9</sub>As/GaAs SIQD's and InAs/GaAs SAQD's at 2 K by an analysis of excitation spectra (ES) and polarization of phonon lines in photoluminescence (PL) spectra of QD's. The spectra were measured at 2 K by the use of a cw Ti:sapphire laser and a double monochromator with combined spectral resolution down to 10  $\mu$ eV.

The sample of InGaAs/GaAs SIQD's was grown by MVPE on the semiinsulating GaAs (001) substrate and contained In<sub>0.1</sub>Ga<sub>0.9</sub>As QW (8 nm) sandwiched between epitaxial GaAs barriers. The top barrier is 6.5 nm. InGaAs QD's were formed by local strains caused by InP stressors grown on top of the structure. The stressors are 60 nm in diameter and 20 nm high with density of  $2 \times 10^9$  cm<sup>-2</sup>. The PL spectra of the sample were typical for that type of SIQD's reported before [4]. InAs SAQD's were fabricated by MBE on (001) surface of a Si-doped ( $1 \times 10^{18}$  cm<sup>-3</sup>) GaAs substrate. A 100 nm GaAs buffer layer was first grown. Then an InAs of 1.8 ML were deposited at 500 °C giving rise to lens-shaped QD's with diameter of  $\approx 22$  nm, height of  $\approx 10$  nm, and an areal density of  $\approx 1.2 \times 10^{10}$  cm<sup>-2</sup>. A thickness of GaAs cap layer was 150 nm.

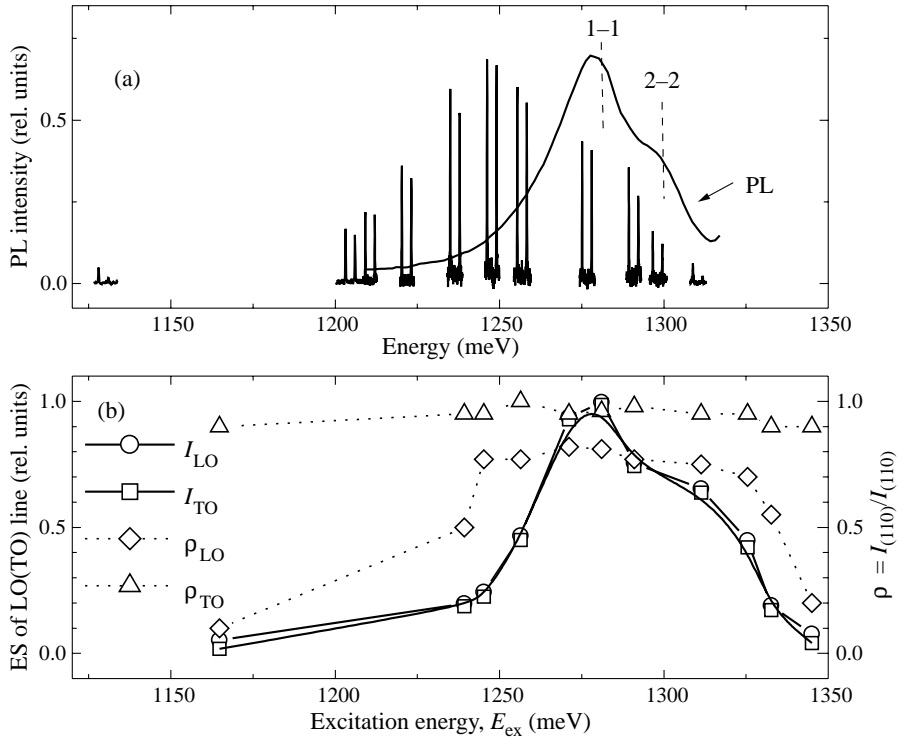


**Fig. 1.** (a) PL spectra of InGaAs/GaAs SIQD's excited above GaAs band edge (PL) and in resonance with 1–1 and 2–2 QD transitions (set of spectra with LO and TO lines). (b) ES and spectra of depolarization ratio  $\rho$  of the LO and TO lines.

**InGaAs/GaAs SIQD's.** In Fig. 1 the PL spectrum of the sample excited above GaAs band gap at state-filling conditions shows energies of the lowest (1277 meV, 1–1) and next (1293 meV, 2–2) optical transitions of SIQD ensemble. Two narrow lines (FWHM  $\simeq 120 \mu\text{eV}$ ) with Stokes shifts of 33.60 meV and 36.55 meV, refereed hereafter TO and LO, respectively, dominate the PL spectra excited in the region of the QD transitions. A set of the PL spectra in region of the lines measured in back-scattering geometry for different excitation energies  $E_{ex}$  is shown in Fig. 1(a). In Fig. 1(b) the ES of the LO(TO) lines,  $I^{LO(TO)}(E_{ex})$ , where  $I^{LO(TO)}$  is the line integral intensity, are presented together with spectra of depolarization ratio of the lines,  $\rho(E_{ex}) = I_{(110)}/I_{(110)}$ . Being excited in the region of the 1–1 and 2–2 transitions, the lines were found to be depolarized and show a strong resonant enhancement. Low-energy maximum of ES coincides with the 1–1 transition, whereas its higher energy satellite is shifted by about TO (LO)-phonon energy. Evidently, far from the resonance ( $E_{ex}$  of 1169 meV and 1345 meV) the lines result from off-resonant Raman by zone center bulk GaAs LO (36.55 meV) and TO (33.60 meV) phonons of barrier layers or substrate [5]. Due to large depolarization of the lines, they were attributed to luminescence rather than to resonant Raman. The observed features indicate that both the LO and TO phonons of GaAs are coupled with QD electronic excitations and involved in interband optical transitions.

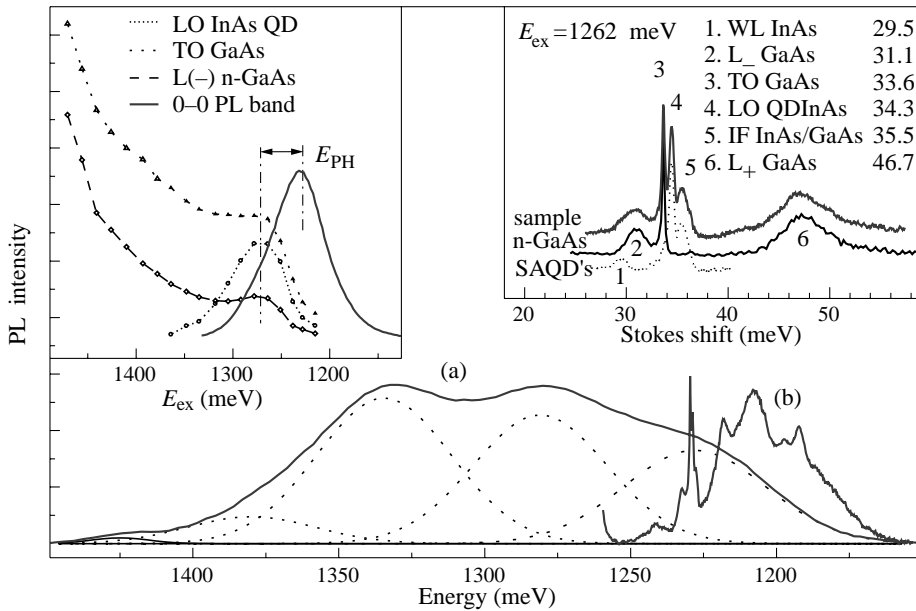


**Fig. 2.** InAs/GaAs SAQD's. (a) PL spectrum of the sample excited with 514.5 nm. (b) PL spectrum excited in the region of the QD transitions. Notations see in the text. Right insert: Enlarged portions of one-phonon region of the sample, n-GaAs substrate, and QD spectra. The table shows Stokes shifts and assignment of the lines. Left insert: ES of the TO,  $L_-$ , and LO lines. Lowest-energy PL band of SAQD's is also shown.

Energies of the ES resonances and their relative amplitudes indicate that the lines belong to phonon-assisted resonant luminescence of QD's (low-energy resonance) and luminescence excited via phonon-assisted absorption of the light (high-energy resonance). Importantly, comparable amplitudes of the LO- and TO-phonon lines as well as values of their resonance enhancement were observed. It follows that a deformation potential interaction dominates the coupling of optical phonons of GaAs host matrix with electron-hole pairs in studied SIQD's. This is in contrast to previous reports on SAQD's systems, where LO phonons of QD's [1, 3] and barrier layers [2, 3] were exclusively involved in phonon-assisted transitions through polar Fröhlich interaction. A weakness of polar coupling in the SIQD heterostructure explains the fact that we did not observe 2LO-phonon lines in the PL spectra.

**InAs/GaAs SAQD's.** The electronic energy structure of studied SAQD's was found to be typical for lens-shaped InAs SAQD's with energy of the lowest transition of 1228 meV (Fig. 2). One- and multi-phonon lines dominate its PL spectra excited in the region of the QD transitions, as shown in Fig. 2 by the spectrum excited at 1262 meV. Right insert in Fig. 2 presents an enlarged portion of the spectrum in the LO-phonon region with subtracted background due to the multi-phonon lines. The spectra of the n-GaAs substrate and QD's are also shown. The latter was obtained by subtraction of the n-GaAs and the sample spectra. It is seen that except for lines assigned to LO phonons of InAs SAQD's, InAs wetting layer (WL), and InAs/GaAs IF mode, the lines of zone center bulk GaAs TO phonons and coupled LO-phonon-plasmon modes,  $L_-$  (31.1 meV) and  $L_+$  (46.7 meV)



[6] appear to be in the spectra. It has been found that the LO phonons of InAs SAQD's, InAs WL, and InAs/GaAs IF mode are involved in intraband carrier relaxation in QD's. It follows from shift of their ES by the phonon energies ( $E_{PH}$ ) from the lowest-energy PL band of SAQD's. Left inset in Fig. 2 shows it by the example of the QD LO-phonon line. To find an evidence of coupling between the substrate phonons and electronic excitations in SAQD's we measured ES of the TO-phonon,  $L_-$ , and  $L_+$  lines. ES of the TO and  $L_-$  lines are shown in the same inset; the  $L_+$  line ES is close to the  $L_-$  one. In n-doped GaAs [7], the line intensities increase monotonically with excitation energy approaching the GaAs band gap (pre-resonant Raman). However, except for this, ES of observed lines show pronounced resonance at the same energy as that of the QD LO-phonon line. It indicates coupling between electronic excitations in SAQD's and TO phonons and LO-phonon-plasmon modes of the substrate. Shift of the ES resonances by  $E_{PH}$  as respect with the PL band shows that the lines are also caused by resonant excitation of high-energy states of SAQD's followed by phonon-mediated intraband carrier relaxation to the lowest-energy state and its annihilation.

Most intrigue finding is the fact that LO-phonon-plasmon modes of the n-GaAs substrate are involved in intraband carrier relaxation in QD's although distance between the substrate and QD's is long as 100 nm. A mechanism of such long-range interaction is analyzed at the moment. Probably, it is a result of Coulomb interaction between carriers in QD's and a charge density fluctuations in the doped substrate with frequencies of the LO-phonon-plasmon modes. In any case, the effect should be important for QD-based device where the n(p)-doped substrates are widely used.

#### Acknowledgements

Two of the authors (A.V.B. and A.V.F.) are grateful to the RFBR (Grants 99-02-16323 and 01-02-17060) and Program "Physics of Solid State Nanostructures" (Grant 99-1136) for financial support of the work.

#### References

- [1] R. Heitz, I. Mukhametzhanov, O. Stier, A. Madhukar and D. Bimberg, *Phys. Rev. Lett.* **83**, 4654 (1999).
- [2] F. Gindele, K. Hild, W. Langbain and W. Woggon, *Phys. Rev. B* **60**, R2157 (1999).
- [3] F. Findeis, A. Zrenner, G. Böhm and G. Abstreiter, *Phys. Rev. B* **61**, R10579 (2000).
- [4] H. Lipsanen, M. Sopanen and J. Ahopelto, *Phys. Rev. B* **51**, 13868 (1995).
- [5] P. Y. Yu and M. Cardona, *Fundamentals of Semiconductors* 2nd ed. (Springer) Berlin, 1999.
- [6] A. Mooradian and A. L. McWhorter, *Light Scattering Spectra of Solids*, ed. by G. B. Wright (Springer) Berlin, 1968, p. 285.
- [7] G. Abstreiter, M. Cardona and A. Pinczuk, *Light Scattering in Solids IV*, ed. by M. Cardona and G. Guntherodt (Springer) Berlin, 1984, pp. 12–182.

## Inelastic inter-valence-band scattering of photoexcited holes in quantum dot structures

*B. H. Bairamov*<sup>†</sup>, *B. P. Zakharchenya*<sup>†</sup>, *V. V. Toporov*<sup>†</sup>, *V. A. Voitenko*<sup>†</sup>,  
*F. B. Bairamov*<sup>†</sup>, and *M. Henini*<sup>‡</sup>

<sup>†</sup> Ioffe Physico-Technical Institute, St Petersburg, Russia

<sup>‡</sup> School of Physics and Astronomy, University of Nottingham, Nottingham, NG7 2RD, United Kingdom

**Abstract.** We obtain inelastic electronic light scattering for interband transitions between valence-band states of GaAs layer embedded by self-assembled InAs quantum dots (QDs). Under a low-power selective *cw* excitation above the InAs band gap but below that of GaAs at a lattice temperature  $T_l = 5.1$  K we find anomalous photoexcitation of carriers in the InAs QDs. Unusual photoinjection of the carriers to the GaAs barrier via strong Coulomb interactions results in creation of the nonequilibrium electron-hole plasma in the GaAs layer with density of  $n = p = 2.5 \times 10^{18} \text{ cm}^{-3}$  and an electron temperature  $T_e = 25$  K. Observed spectra reflects the band anisotropy and extends from zero to rather large frequency shifts with a long tail with a peak at about  $300\text{--}400 \text{ cm}^{-1}$  in good agreement with theoretical prediction.

Despite a decade of intensive theoretical and experimental work of nanometer-scale-size semiconductors embedded with quantum dots (QDs), in which electrons are confined in all three directions of space, the role of new physical mechanisms determining the efficiency of optical transitions and carrier dynamics, still remain a poorly understood issue. Electron (*e*) and hole (*h*) density in such islands is a critically important parameter that mainly controls the dynamic strength of carrier fluctuations as well as *e*–*h* interactions and determines the transport and optoelectronic properties. Due to their exceptional properties QD structures offer great potential for possible future applications. It is generally accepted that in the QD systems, the exchange interaction between electrons largely sets the amount of energy necessary to attract an additional electron to the QD [1]. Furthermore, it has been shown that multicarrier states play an important role in the formation of excitonic photoluminescence spectra of a single QD [2, 3]. Interesting data on the carrier relaxation [4] and interdiffusion within QDs as well as nature of carrier wave functions indicating the unexpected hole location towards the top of the QD, above the electron [5] have been found. A clarification of these issues requires development of efficient experimental techniques capable of probing the effects of strong interaction among the carriers, as well as their charge and real space location in the QD systems. It is clear that beyond the experimental challenge, the finding of ways to measure these properties of the QD structures by contactless methods is of particular interest. Detection of different electronic excitations in the QDs structures [6, 7] and of the fractional quantum Hall states have been successfully demonstrated by inelastic light scattering investigations [8].

In this communication we report the results of a new approach for developing a highly sensitive and stable two-channel technique [7] for detecting of *low-level* light scattering spectra in the near-infrared spectral range that is most suitable as we show for studying novel features of different electronic excitations in the QD systems. We use a low-

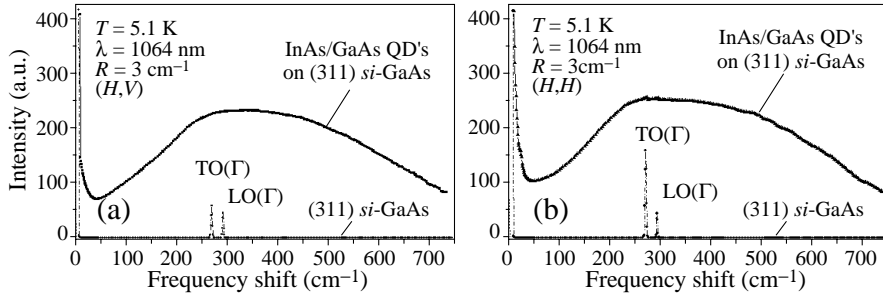


Fig. 1.

power single mode line of a continuous-wave  $\text{Nd}^{+3}$ :YAG laser with exciting photon energy  $\hbar\omega_i = 1.1650$  eV in resonance with the energy of transition between confined heavy hole and the lowest electron states of InAs QDs. It is shown clearly the anomalous photoexcitation of carriers in the InAs quantum dots and their unusual photoinjections to the GaAs barrier via strong Coulomb interaction results in creation of the nonequilibrium two-component electron-hole plasma in the GaAs layer. Apparently, the photoinjected nonthermal electron-hole gas is not a plasma unless the Debye screening length is smaller than the GaAs layer spacing. Therefore this condition for creating a plasma is thus easily fulfilled under conditions of our experiment. Using the same excitation laser we obtain inelastic electronic light scattering by intra-band charge-density fluctuations, Landau damped acoustic plasmons and inter-valence-band transitions originating from GaAs layer.

Our self-assembled QD structure with GaAs matrix embedded with arrowhead-like shape InAs QDs grown on (311)B oriented semi-insulating (*qsi*) GaAs-substrate used in this study was described previously [7]. The dot region consists of 10 periods of 1.8 monolayers of InAs and 5.1 nm GaAs. The effective diameter (base size) of InAs QDs was  $\sim 12$  nm, height  $\sim 6$  nm and density  $\sim 1.4 \times 10^{11} \text{ cm}^{-2}$ .

The spectra were excited by using a low-power single mode line of a continuous-wave  $\text{Nd}^{+3}$ :YAG laser with the excitation photon energy  $\hbar\omega_i = 1.165$  eV in resonance with the energy of transition between confined heavy hole and the lowest electron states of InAs QDs. Measurements were performed in the temperature range 5–250 K and at the excitation densities of 0.1–1.0 kW/cm<sup>2</sup>, which do not cause local heating of the sample. Polarized measurements were performed in a near-backscattering configuration from the (311) surface for the parallel (H,H) and crossed (H,V) polarizations of the incident and scattered light. The H (V)-axis corresponds to the  $[-233]$  ( $[01-1]$ ) directions, respectively. The scattered light was analyzed with an  $f/1.3$  double grating monochromator coupled to a cooled photomultiplier and using developed by us a highly sensitive two-channel photon counting system with an equal dynamic response that allows detecting rather continuous structures in the spectra with high stability. The spectral resolution was  $3 \text{ cm}^{-1}$ .

Figures 1(a) and 1(b) represent the typical polarized inelastic light scattering spectra observed from the InAs/GaAs QD structure and SiGaAs substrate at a lattice temperature as low as  $T_L = 5.1$  K for crossed (H,V) (a) and parallel (H,H) scattering configurations, respectively. Two sharp lines of GaAs transverse  $\text{TO}(\Gamma)$  and longitudinal  $\text{LO}(\Gamma)$  optical phonons are observed at  $271.6$  and  $294.9 \text{ cm}^{-1}$ , respectively in the reference spectra of the SiGaAs substrate.

It is seen that the presence of QDs enormously influences the spectra. Rather peculiar spectral features in the whole detection range presented with pronounced selection rules and enormously intense broad structure for both polarizations in the high-frequency range

are observed in the spectra of the InAs/GaAs QD structure. The spectra demonstrate also the scattering anisotropy. These findings are in striking contrast to the established characteristic features of the quasielastic single particle electronic light scattering spectra by the plasma, which is arranged by the free electron gas fluctuations in the bulk doped n-type semiconductors [9, 10] and the two-component plasma, which is arranged by photoexcited light and heavy hole gas fluctuations in the bulk p-type semiconductors [11].

The quasielastic scattering part can be attributed to the intraband single particle electronic scattering. The spectra should be detected below the characteristic cut-off frequency determined by  $\nu = q V_F$ , where  $q$  is the transfer wave number and  $V_F$  is the Fermi velocity. Bearing in mind this point, we can interpret the origin of superimposed broad second component at  $\sim 300 \text{ cm}^{-1}$  with a long tail as a consequence of the inelastic scattering by electronic transitions photoexcited from the light hole band to the intermediate state and finally to the heavy hole band. Since the region of these transitions is relatively extended, one can expect rather large tail.

The weak shoulder at  $25 \text{ cm}^{-1}$  has been attributed to the in phase acoustic plasmon mode oscillations [12] as it clearly appears only in the spectra recorded at  $T_L = 5.1 \text{ K}$  and with increasing the lattice temperature up to  $T_L = 20 \text{ K}$  cease to exist exhibiting strong Landau damping. Additional strong evidence is provided also by the existence of this structure only in the parallel scattering configuration. A first attempt to detect such a mode for e-h plasma has been performed in [13]. More recently the acoustic plasmons were observed in a gas of heavy and light holes [11,14] and in two-dimensional electron gas [15]. The experimental observation of the collective acoustic plasmons in our spectra immediately indicates creation of collisionless plasma in which the characteristic motion of the oppositely charged carriers is mostly ballistic (the probed dimension  $L \ll l$ , the electron mean free path). The detection of the acoustic plasmon mode can be used as a valuable probe of the charge density of electrons  $n$  and holes  $p$ . We find  $n = p = 2.5 \times 10^{18} \text{ cm}^{-3}$  and the local electron temperature  $T_e = 25 \text{ K}$  [12].

The differential light scattering cross section from the inter-valence-band transitions early predicted in [16, 17] for the crystals with a large spin-orbit splitting [10] can be written as

$$\begin{aligned} \frac{d^2 \Sigma}{d\omega d\Omega} = & r_0^2 \frac{3n}{2\varepsilon_{\text{Fh}}} \frac{\sqrt{\hbar\omega/\gamma_2\varepsilon_{\text{Fh}}}}{8 \left[ 1 - \exp\left(-\frac{\hbar\omega}{T}\right) \right]} \iint_0^{2\pi} \left\{ \frac{1}{\sqrt{g(\theta, \phi)}} \left[ f\left(\hbar\omega \frac{\gamma_1 - 2\gamma_2 g(\theta, \phi)}{4\gamma_2 g(\theta, \phi)}\right) \right. \right. \\ & \left. \left. - f\left(\hbar\omega \frac{\gamma_1 + 2\gamma_2 g(\theta, \phi)}{4\gamma_2 g(\theta, \phi)}\right) \right] \left[ \gamma_3^2 I_{\Gamma_{25}}(\mathbf{e}_I, \mathbf{e}_S, \theta, \phi) + \gamma_2^2 I_{\Gamma_{12}}(\mathbf{e}_I, \mathbf{e}_S, \theta, \phi) \right] \right\} \\ & \times \sin\theta d\theta d\phi. \end{aligned} \quad (1)$$

Here  $\varepsilon_{\text{Fh}}$  is the Fermi energy for holes,  $\mathbf{e}_I, \mathbf{e}_S$  are polarization vectors of incident and scattered light,  $\omega = \omega_I - \omega_S$  is Stokes frequency shift,  $(f\varepsilon)$  is Fermi distribution function,  $\gamma_1 - \gamma_3$  are Luttinger Hamiltonian parameters, and the functions  $(g\theta, \phi, I_{\Gamma'_{25}}(\mathbf{e}_I, \mathbf{e}_S, \theta, \phi)$ , and  $I_{\Gamma_{12}}(\mathbf{e}_I, \mathbf{e}_S, \theta, \phi)$  are defined as follows:

$$g(\theta, \phi) = \sqrt{1 + 3\gamma \sin^2 \theta (\sin^2 \theta \cos^2 \phi \sin^2 \phi + \cos^2 \theta)} \quad (2)$$

$$I_{\Gamma'_{25}}(\mathbf{e}_I, \mathbf{e}_S, \theta, \phi) = \sum_{i>k} \left| e_i^I e_k^{S*} + e_k^I e_i^{S*} \right|^2 \left( 1 - \frac{3\gamma_3^2 \sin^4 \theta \sin^2 2\phi}{4\gamma_2^2 g^2(\theta, \phi)} \right) \quad (3)$$

$$I_{\Gamma_{12}}(\mathbf{e}_I, \mathbf{e}_S, \theta, \phi) = \frac{2}{9} \sum_i \left| \sum_k \left( e_i^I e_i^{S*} - e_k^I e_k^{S*} \right) \right|^2 \left( 1 - \frac{3 \sin^4 \theta \cos^2 2\phi}{4 g^2(\gamma, \theta, \phi)} \right), \quad (4)$$

and  $\gamma g(\gamma_3^2 - \gamma_2^2 k^2 \gamma_2^2)$ . Eqs. (1)–(4) predict two independent so called  $\Gamma_{12}$  and  $\Gamma'_{25}$  spectra for  $\mathbf{e}_I = (1, \bar{1}, 0)/\sqrt{2}$ ,  $\mathbf{e}_S = (1, 1, 0)/\sqrt{2}$ , and for  $\mathbf{e}_I = (1, 0, 0)$ ,  $\mathbf{e}_S = (0, 1, 0)$ , respectively.

Remarkably, by solving Eq. (1) and using only the measured values  $n = p = 2.5 \times 10 \text{ cm}^{-3}$  and  $T_e = 25 \text{ K}$ , we predicted the maximum for the frequency shift in the range 250–350 in good agreement with experimental observation.

In summary, we have demonstrated that the inelastic light scattering technique in the near infrared range is efficient to study the interactions of electromagnetic waves and fluctuations of carriers in InAs/GaAs QDs structures. We find that near infrared excitation above the InAs band gap but below that of GaAs at a lattice temperature  $T_L = 5.1 \text{ K}$  produces strong additional concentration of the energy into the photoexcited e-h pairs. Unusual photoinjection of the carriers to the GaAs barrier via strong Coulomb interactions results in creation of the nonequilibrium uniform e-h two-component plasma in the GaAs barrier. Our high-sensitivity spectroscopic study allowed us to determine a photoexcited  $e-h$  density of  $n = p = 2.5 \times 10^{18} \text{ cm}^{-3}$  and electron temperature  $T_e = 25 \text{ K}$ . For both scattering polarizations we find broad structure in the high-frequency range induced by inter-valence-band transitions of photoexcited holes.

## References

- [1] M. Brodsky, N. B. Zhitenov, R. C. Ashori, L. N. Pfeifer and K. W. West, *Phys. Rev. Lett.* **85**, 2356 (2000).
- [2] E. Dekel *et al*, *Phys. Rev. Lett.* **80**, 4991 (1998).
- [3] D. Hawriliak, G. A. Narvaez, M. Bayer and A. Forchel, *Phys. Rev. Lett.* **85**, 389 (2000).
- [4] Y. Toda, O. Moriwaki, M. Nishioka and Y. Arakawa, *Phys. Rev. Lett.* **82**, 4114 (2000).
- [5] I. Kegel *et al*, *Phys. Rev. Lett.* **85**, 1694 (2000);  
P. W. Fry, *et al*, *ibid.* **84**, 733 (2000).
- [6] D. J. Lockwood *et al*, *Phys. Rev. Lett.* **77**, 354 (1996);  
R. Strenz *et al*, *ibid.* **73**, 3022 (1994);  
C. Schuller *et al*, *ibid.* **80**, 2673 (1998);  
A. A. Sirenko *et al*, *Phys. Rev. B* **58**, 2077 (1998).
- [7] B. H. Bairamov, V. A. Voitenko, B. P. Zakharchenya, V. V. Toporov, M. Henini and A. J. Kent, *JETP Lett.* **67**, 972 (1998).
- [8] M. Kang *et al*, *Phys. Rev. Lett.* **84**, 546 (2000).
- [9] G. Abstreiter, M. Cardona and A. Pinczuk, in *Light Scattering in Solids*, eds. M. Cardona and G. Guntherodt, Springer, Heidelberg, 1984.
- [10] B. H. Bairamov, I. P. Ipatova and V. A. Voitenko, *Phys. Rep.* **229**, 223 (1993).
- [11] B. Kh. Bairamov, V. A. Voitenko, I. P. Ipatova, V. K. Negoduiko and V. V. Toporov, *Semiconductors* **28**, 531(1994).
- [12] D. Pines, *Elementary Excitations in Solids*, (Benjamin, New York, 1963).
- [13] A. Pinczuk, S. Jagdeep and P. A. Wolff, *Phys. Rev. Lett.* **47**, 1487 (1981).
- [14] B. H. Bairamov, G. Irmer, J. Monecke, V. A. Voitenko, V. K. Negoduiko, V. V. Toporov and B. P. Zakharchenya, *Phys. Stat. Solidi B* **204**, 456 (1997).
- [15] D. C. Kainth, D. Richards, H. P. Huges, M. Y. Simmons and D. A. Ritchie, *Phys. Rev. B* **57**, R2065 (1998).
- [16] A. G. Aronov and E. L. Ivchenko, *Sov. Phys. - Zh. Eksp. Teor. Fiz.* **57**, 247 (1969).
- [17] M. A. Kanehisa, R.F. Wallis and M. Balkanski, *Phys. Rev. B* **25**, 7629 (1982).

## Time-resolved luminescence of self-assembled CdSe/ZnSe quantum dots

V. S. Dneprovskii<sup>†</sup>, O. A. Shaligina<sup>†</sup>, E. A. Zhukov<sup>†</sup>, V. P. Evtikhiev<sup>‡</sup>  
and V. P. Kochereshko<sup>‡</sup>

<sup>†</sup> M. V. Lomonosov Moscow State University, 119899 Moscow, Russia

<sup>‡</sup> Ioffe Physico-Technical Institute, St Petersburg, Russia

**Abstract.** Time-resolved inhomogeneously broadened spectra of CdSe/ZnSe self-assembled QDs excited by weak picosecond and powerful nanosecond laser pulses have been measured. The peculiarities of the kinetics of the CdSe/ZnSe self-assembled QDs' spectra and their changes at high excitation have been explained by different recombination times of QDs (it shortens for QDs of smaller size) and by saturation (state filling) of QDs that arises first of all for QDs of greater size.

Heteroepitaxial growth of the lattice mismatched semiconductor system offers the possibility of producing nanostructures like self-assembled quantum dots (QDs) in situ without any substrate patterning process and without having the problem to overcome current lithography limitations. QD size fluctuation, inherent in the growth process of the self-assembly of strain induced islands, results in their inhomogeneous electrical and optical properties.

Molecular-beam epitaxy has been utilized to prepare CdSe/ZnSe self-assembled QDs. The samples of two types containing QDs have been used in our experiments. Sample A nominally had about 3 monolayers of CdSe sandwiched by 40 nm ZnSe layers grown on GaAs. Transmitted electron microscopy and atomic force microscopy data [1] from similar self-assembled QDs have shown that they are approximately hemispherical with a typical base of about 20 nm and height of 2–3 nm and are dispersed with an areal density of  $10^{10} \text{ cm}^{-2}$ . These QDs were prepared in the same way and radiate in the same spectral region (2.26–2.38 eV) as in [2]. The CdSe/ZnSe sample B contained 10 layers of self-assembled QDs separated by 12 nm ZnSe barriers and sandwiched by 40 nm ZnSe layers grown on GaAs.

To study the time-resolved spectra of photoluminescence and the kinetics of luminescence the samples were excited by the focused beam of the second harmonic ( $h\nu = 3.1 \text{ eV}$ ) of the Argon-ion pumped Ti-sapphire laser (pulse duration  $\tau = 1.5 \text{ ps}$ , repetition rate 82 MHz, energy density  $0.2 \mu\text{J}/\text{cm}^2$ ). Polychromator and Hamamatsu C1587 synchroscan streak camera with a two-dimensional detector have been used for registration. The time-resolution of the system was about 10 ps. To investigate nonlinear optical properties of self-assembled QDs the third harmonic ( $h\nu = 3.45 \text{ eV}$ ) of powerful Nd:YAG laser ( $\tau = 14 \text{ ns}$ ) was used for excitation of the samples and polychromator with CCD camera for registration of the photoluminescence spectra.

The luminescence spectrum of sample B (18 K) excited by 1.5 ps pulses of the second harmonic ( $h\nu = 3.1 \text{ eV}$ ) of Ti-sapphire laser is shown in Fig. 1 together with kinetic profiles for its different spectral parts. In this case carriers were excited in the absorbing matrix (ZnSe barrier) and transported to dots. Matrix rather than QDs was photoexcited because dots are distributed in a thin layer or layers making the number of directly excited carriers in dots very small. When we excited only QDs in samples A and B by Argon laser (the energy of the exciting photons was less than the energy gap of ZnSe matrix) the intensity of CdSe QDs' luminescence was very weak. The intensity of matrix luminescence (Fig. 1)

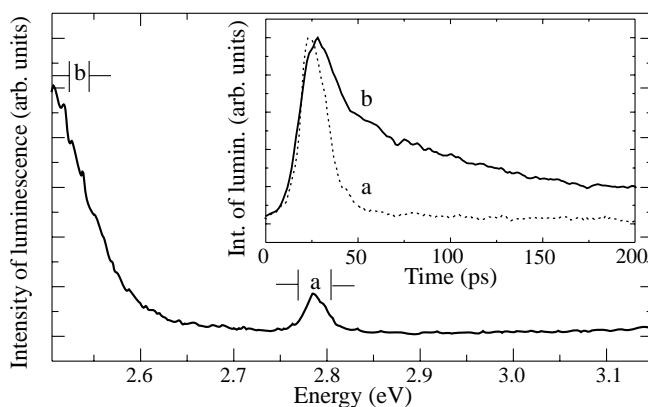


**Fig. 1.** The luminescence spectrum of CdSe/ZnSe self-assembled QDs (sample (b) and kinetic profiles (inset) of matrix (ZnSe) luminescence (a) and high-energy part of QDs' luminescence (b).

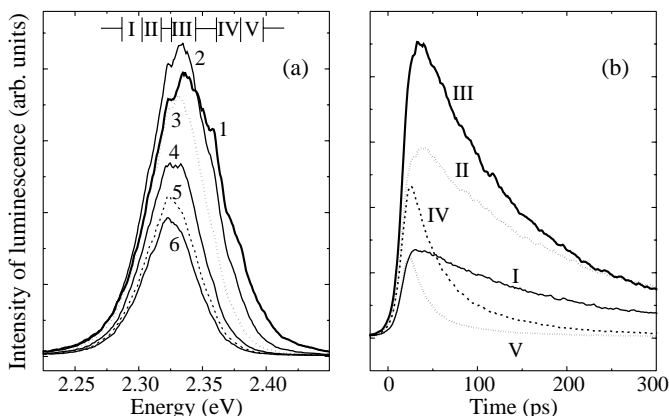


**Fig. 2.** (a) The luminescence spectra of CdSe/ZnSe self-assembled QDs (sample (A) registered at different time intervals after excitation: 1 — 0–23 ps; 2 — 23–47 ps; 3 — 48–72 ps; 4 — 87–110 ps; 5 — 122–145 ps; 6 — 145–169 ps. (b) Temporal changes of different spectral parts pointed at Fig. 2(a).

is weak compared with that of CdSe QDs and has a fast decay time. The latter and fast rise-times of the intensity of QDs' luminescence (Fig. 1, 2) may be explained by effective carrier diffusion in the ZnSe matrix and injection of carriers from matrix to CdSe QDs.

The time-resolved luminescence spectra of CdSe/ZnSe self-assembled QDs (sample A) and the temporal changes for different spectral intervals are presented in Fig. 2. Note the well-pronounced dominant changes in the high-energy parts of the spectra, the red shift of the maximum of luminescence spectra in time, and fast decay of the luminescence intensity of the high-energy spectral intervals compared with that for low-energy intervals. Inhomogeneous broadening of the luminescence spectra reflecting the variation in QD sizes must be taken into account. The energy relaxation of photoexcited electron-hole pairs in QDs is strongly redistributed between radiative and nonradiative channels of recombination. The nonradiative recombination is more effective in QDs of smaller size because of the dominant influence of the real interfaces on the electronic system. So peculiarities of CdSe/ZnSe self-assembled QDs' kinetic properties may be the result of faster recombination

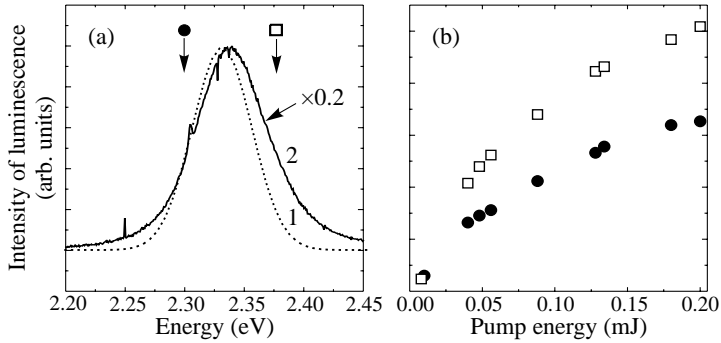


**Fig. 3.** (a) The luminescence spectra of CdSe/ZnSe self-assembled QDs (sample A at different energy of Nd:YAG laser excitation: 1 — 0.01 mJ; 2 — 0.2 mJ. (b) The dependence of the luminescence intensity upon the energy of laser pulse for different parts of the spectra pointed by arrows in Fig. 3(a).

of QDs with smaller size. The intensity of excitation was too low to explain the observed effects (Fig. 2) by any nonlinear processes.

The photoluminescence spectra of CdSe/ZnSe self-assembled QDs (sample A cooled to 80 K) registered at low and high excitation by 14 ns pulses of the third harmonic ( $h\nu = 3.45$  eV) of Nd:YAG laser are shown in Fig. 3. The blue shift of the spectral maximum and asymmetrical change of the spectrum at high excitation (high energy shoulder develops) may be explained by nonlinear absorption (it is followed by nonlinear dependence of the luminescence intensity upon the intensity of the exciting beam presented in Fig. 4) that is caused by state filling [3] in QDs. The state filling is more efficient in QDs of greater size because they have longer recombination times. It is possible to estimate the number of carriers injected in single QD that is necessary for state filling. In our case the recombination time of CdSe/ZnSe QDs  $\tau_D$  (about 100 ps) is less than the laser pulse duration  $\tau$ . So the stationary density of injected carriers per single QD:

$$n \cong \beta \frac{(1 - R)(1 - e^{-\alpha L}) W \tau_D}{\tau S h \nu N},$$

where  $\beta$  defines the efficiency of carriers injection in QDs,  $R$  and  $\alpha$  — the coefficients of reflection and absorption of the sample,  $W$  — the energy of laser pulse,  $S$  — the area of the excited spot,  $N$  — the areal density of QDs. In our case  $n > 10$ , and saturation of absorption may arise in QDs.

#### Acknowledgements

The research was made possible in part by Grants 99-02-18327 and 02-02-16167 from the Russian Foundation for Basic Research.

#### References

- [1] H. Kirmse, R. Schneider, M. Rabe, W. Neumann and F. Hennedger, *Appl. Phys. Lett.* **72**, 1329 (1998).
- [2] L. M. Robinson, H. Rho, H. E. Jackson, L. M. Smith, S. Lee, V. Dobrowolska and J. K. Furdina, *phys. stat. sol. (b)* **221**, 55 (2000).
- [3] "Nonlinear Photonics" H. M. Gibbs, G. Khitrova and N. Peyghambarian (Eds.), Springer-Verlag Berlin Heidelberg, 1990.



## Distribution of persistent currents and magnetic field in quantum wire and disc

*M. V. Entin and M. M. Mahmoodian*

Institute of Semiconductor Physics, Siberian Branch of the RAS,  
 630090 Novosibirsk, Russia

The magnetic field, applied to a quantum system produces persistent currents, which partially screen the external field. In the previous paper [1] we studied the distribution of magnetic field and current in a quantum film. Here we study the same problem for circular geometry, namely in a disc and in a circular wire. The problem is studied for the cases of weak and strong magnetic fields. Our prime interest here is the case of wide quantum discs and wires. In the magnetic field  $B_0$  along the system axis  $z$  the current has the only azimuthal component  $j_\phi$ . In the limit of weak field the current density in a pure system is described by an expression:

$$j_\phi(r) = \frac{e^2 B_0 r}{2m_e c} \sum_{m,n} \left[ f(E_{m,n}^0) + \frac{m^2}{m_e r^2} \frac{\partial f}{\partial E_{m,n}^0} \right] |\psi_{m,n}(r)|^2, \quad (1)$$

where  $f(E) = (\exp((E - \mu)/T) + 1)^{-1}$  is the Fermi function,  $\mu$ ,  $T$  are the chemical potential and the temperature,  $\psi_{m,n}(r)$  are the zero-field wave functions and  $E_{m,n}^0$  are the unperturbed energies. The summation runs over transversal  $n, m$  quantum numbers; in the case of the cylindric wire the summation includes also the longitudinal momentum  $k$ .

For the electron gas confined in a disc of radius  $R$  with hard walls, the wave functions  $\psi_{m,n}(r)$  are given by

$$\psi_{m,n}(r) = \frac{e^{im\phi} J_m(\lambda_{m,n} r/R)}{\sqrt{\pi} R J_m(\lambda_{m,n})}, \quad (2)$$

where  $\lambda_{m,n}$  is the  $n$ -th zero of a Bessel function  $J_m(x)$  and the energy levels are  $E_{m,n}^0 = \lambda_{m,n}^2 / (2m_e R^2)$ . Here  $\hbar = 1$ .

The Figures 1 and 2 show the dependence of the current distribution in the disc for selected values of a product of the Fermi momentum to the disc radius  $k_F R$  (marked on curves). For comparatively large  $k_F R$  the distribution is very sensitive to this parameter. According to the Figures, when the size grows, the surface current in a disc establishes essentially slower than in a quantum film.

The systems with cylindrical symmetry unlike the films and systems without symmetry have double degeneracy of the states with respect to the sign of  $m$ . This degeneracy is lifted by the infinitely weak magnetic field; that causes the large positive (paramagnetic) peaks in the susceptibility at the low temperature limit when the Fermi level crosses a level of transversal quantization. If the Fermi level lies between levels, the susceptibility manifests the strong diamagnetism. This diamagnetism originates from the first order correction in the term  $e^2 / 2m_e c^2 A^2 = (eB_0 r/c)^2 / 2m_e$  of the Hamiltonian, growing with the size of the system. Just this term produces the current density contribution, linearly growing with radius. Hence, the behavior of the current distribution reflects these features: when

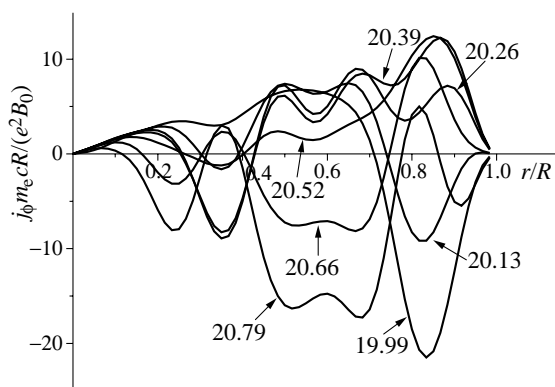


Fig. 1.

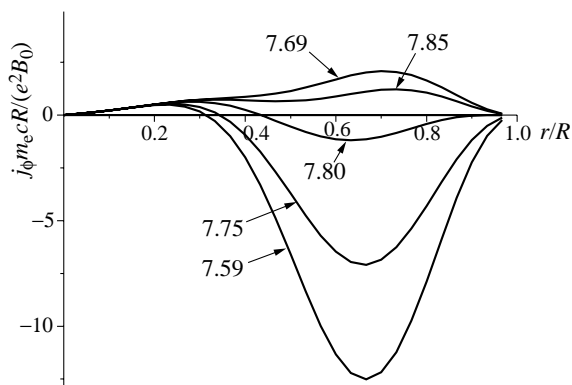


Fig. 2.

the Fermi level lies between the levels of quantization, the current has diamagnetic sign everywhere, while in a vicinity of an energy level the paramagnetic contribution prevails.

The temperature and impurity scattering washes out the current oscillations. The impurity effect was studied, basing on the impurity diagram technic.

## References

- [1] M. V. Entin, L. I. Magarill, M. M. Mahmoodian, this book, p 237.

## The influence of temperature and hydrostatic pressure on luminescence spectra of InAs/GaAs quantum dots

V. A. Gaisin<sup>†</sup>, A. Kh. Akopyan<sup>†</sup>, B. S. Kulinkin<sup>†</sup>, B. V. Novikov<sup>†</sup>, V. N. Petrov<sup>‡</sup>,  
V. M. Ustinov<sup>§</sup> and G. E. Cirilin<sup>‡</sup>

<sup>†</sup> Institute of Physics, St Petersburg State University, 198904 St Petersburg, Russia

<sup>‡</sup> Institute of Analytical Instrumentation of Russian Academy of Sciences,  
Rizhsky 26, 198103 St Petersburg, Russia

<sup>§</sup> Ioffe Physico-Technical Institute, St Petersburg, Russia

**Abstract.** The temperature dependencies of luminescence spectra of the InAs/GaAs quantum dots  $L_0$  ( $E_{L_0} = 1.235$  eV),  $L_1$  ( $E_{L_1} = 1.290$  eV) and  $I_1$  ( $E_{I_1} = 1.343$  eV) and wettings layer (WL) ( $E_{WL} = 1.408$  eV) have been investigated at  $P = 0$  and  $P = 15$  kbar. The InAs quantum dots on vicinal substrates GaAs at misorientation angle  $7^\circ$  [001] have been grown in submonolayer migration enhanced epitaxy mode (SMEE). The activation energies have been determined from the temperature quenching of luminescence. Their dependence on a value of hydrostatic pressure have been studied. The available scheme of energy levels of quantum dots has been proposed.

### Introduction

Now the physical properties of quantum dots (QD) InAs/GaAs are researched very intensively. They are used as materials for IR semiconductor lasers. The experiments with using of high hydrostatic pressure indicated to the important role of a matrix in forming of excited states [1]. The dependencies of the baric coefficients on size of QD was found out [2, 3]. In the present work the temperature dependencies of the luminescence spectra InAs/GaAs QD have been investigated.

### 1. Experimental

The temperature dependencies (80–160 K) of the luminescence spectra of samples with InAs QD grown on the vicinal substrates GaAs at misorientation angle  $7^\circ$  [001] have been investigated at pressure  $P = 0$  and  $P = 15$  kbar. The structures consist of the InAs quantum dots confined from both sides with wide-gap GaAs and  $\text{Al}_{0.25}\text{Ga}_{0.75}\text{As/GaAs}$  super-lattices (5 pairs,  $2\text{ nm} \times 2\text{ nm}$  each). Singular substrates GaAs [100], disoriented on  $7^\circ$  are used. The luminescence spectra are excited by He-Ne laser at power  $1\text{ W/cm}^2$ . The studies have been conducted at 0 and 15 kbar in the high-pressure camera with anvils of laicosapfire. Magnitudes of hydrostatic pressure are determined from displacement of R1-luminescence line of ruby, placed in driving volume of camera in the immediate vicinity of the sample under study. Samples are prepared in form of parallel-plates of size  $0.5 \times 0.5\text{ mm}^2$  and thickness 0.05 mm.

### 2. Results

In Fig. 1(a) the luminescence spectra at  $P = 15$  kbar are presented. The character of change of spectra is similar to measured one earlier at  $P = 0$  [5]. The increasing of temperature

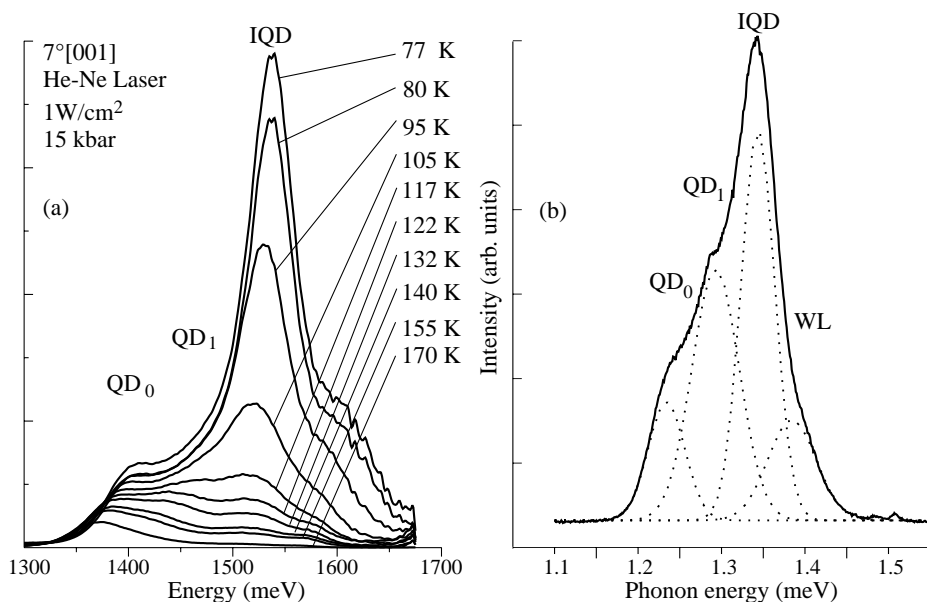


**Fig. 1.** (a) The emission spectra of 7° [001] samples at different temperature ( $P = 15$  kbar, the power of He-Ne laser is  $1 \text{ W/cm}^2$ ). 1 —  $T = 77 \text{ K}$ ; 2 —  $80 \text{ K}$ ; 3 —  $87 \text{ K}$ ; 4 —  $95 \text{ K}$ ; 5 —  $105 \text{ K}$ ; 6 —  $117 \text{ K}$ ; 7 —  $122 \text{ K}$ ; 8 —  $132 \text{ K}$ ; 9 —  $140 \text{ K}$ ; 10 —  $155 \text{ K}$ . (b) The spectrum of luminescence at  $P = 15$  kbar and  $T = 80 \text{ K}$  and its division on Gauss contours. (The power of He-Ne laser is  $1 \text{ W/cm}^2$ ).

results in decreasing total intensity luminescence, in change of spectrum form and displacement of all bands as whole to lower energy. The accurate temperature measurements are impossible due to the broadening of the photoluminescence lines, it is demonstrated by the spectra in Fig. 1(a). In this connection the division of luminescence bands on separate components has been carried out. The best agreement with experiment has been received at approximation of lines by Gaussian contours with various integrated intensity, halfwidths and energies of maxima. The example of division of one of luminescence spectra ( $P = 0$ ,  $T = 80 \text{ K}$ ) on separate components is submitted in Fig. 1(b).

For studying effect of crystal surrounding of a matrix on energy levels structure of QD the analogue studies of QD in glass and polymer matrices, in particular of QD  $\text{PbI}_2$  and  $\text{HgI}_2$ , have been carried out.

### 3. Discussion

The following results have been found out:

1. The observed earlier change of the band form with increasing hydrostatic pressure in the luminescence spectrum at  $T = 80 \text{ K}$ , is caused by relative increase of the contribution of the lines of quantum point IQD and watinglayer WL. The ratio of intensities of luminescence lines of quantum points QD<sub>0</sub>, QD<sub>1</sub> is constant at increase of pressure.

2. At  $P = 0$  and  $P = 15$  kbar the change of the form of contours of luminescence bands with increasing temperature, is caused by the distinction of speeds of temperature quenching of their component.

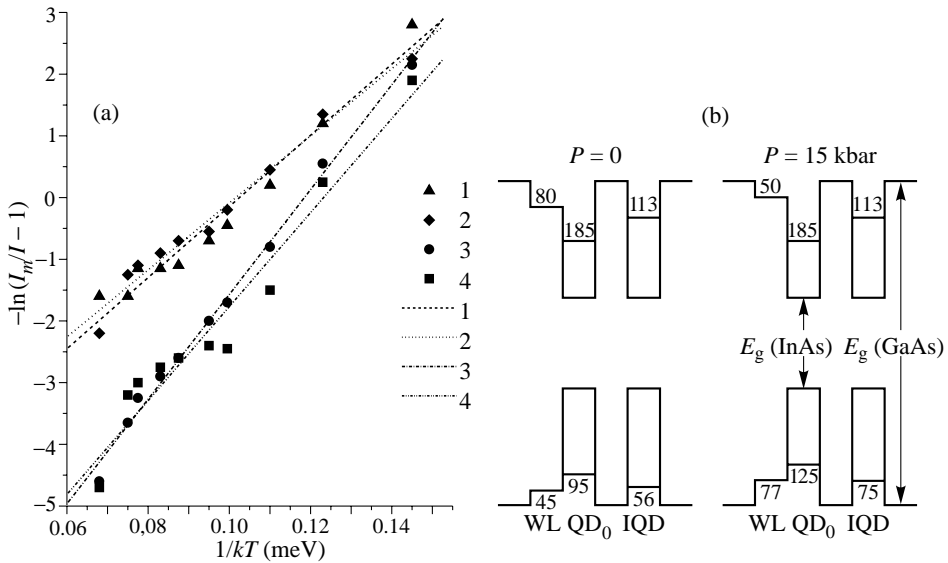


**Fig. 2.** (a) The  $1/T$  dependencies of  $-\ln(I_m/I - 1)$  for different emission lines of QD: QD<sub>0</sub> (1), QD<sub>1</sub> (2), IQD (3) and of the wetting layer WL (4) at  $P = 15$  kbar. (The power of He-Ne laser is  $1 \text{ W/cm}^2$ ). (b) The proposed scheme of energy levels of the QD. (Numbers show the energy levels shifts (in meV) relatively to the valence band top and the conduction band bottom of correspondingly bulk crystal GaAs).

For description of the temperature behavior of separate component a ratio Arrhenius:  $I/I_m = [1 + C \cdot \exp(E_a/kT)]^{-1}$  has been used, where  $C$  — constant,  $E_a$  — energy of activation. In present work the value  $E_a$  has been defined from dependence  $-\ln(I/I_m - 1)$  from  $1/kT$ , calculated with the help of a method of the least squares (Fig. 2(a)). As a result for luminescence lines of quantum points QD<sub>0</sub>, QD<sub>1</sub> and IQD and wetting layer WL the following values have been received: at  $P = 0$   $E_a = 50, 43, 56$  and  $45$  meV, at  $P = 15$  kbar —  $58, 53, 75$  and  $77$  accordingly. It has been appeared, that at increase of hydrostatic pressure from 0 up to 15 kbar energies of activation of lines QD<sub>0</sub>, QD<sub>1</sub> vary slightly, and energies of the IQD and wetting layer WL lines grow considerably. It has been proposed that the differences of activation energy and their dependencies on hydrostatic pressure are caused by the fact that the quantum points QD<sub>0</sub>, QD<sub>1</sub> are in direct contact with a wetting layer WL, and the quantum point IQD contacts directly with barrier — crystal GaAs. The temperature luminescence quenching of quantum points QD<sub>0</sub>, QD<sub>1</sub> is caused by thermal ionization of their ground states to the wetting layer WL. The temperature quenching of luminescence lines of a quantum point IQD and wetting layer WL occurs as a result of the thermal ionization hole of states directly to the barrier.

#### 4. Conclusion

On the basis of above mentioned assumptions and the values of baric coefficients of QD<sub>0</sub>, QD<sub>1</sub>, IQD quantum points and WL wetting layer received earlier, the possible scheme of levels of their electron and hole states for  $P = 0$  and  $P = 15$  kbar (Fig. 2(b)) has been proposed. As a consequence it is possible to conclude, that the reason of difference between

baric coefficient of quantum points QD<sub>0</sub>, QD<sub>1</sub>, IQD and of free excitons of GaAs crystal is due to difference of baric shifts of their hole states. For all quantum points QD<sub>0</sub>, QD<sub>1</sub>, and IQD the hydrostatic pressure does not change the value of energy distance between the ground electronic states and the conduction band bottom of the barrier GaAs. On contrary the energy distances between ground hole states and the valence band top of GaAs increase with growth of pressure.

#### *Acknowledgements*

The work is supported by Russian Foundation for Basic Research (grants 00-15-96756, 01-02-17092).

#### **References**

- [1] I. E. Itskevich, A. I. Trojan, S. G. Lyapin *et al*, *The 24th Intern. Conf. on the physics of semiconductors. August 2–7, 1998. Jerusalem, Israel*. P.TU-138.
- [2] V. A. Gaisin, D. C. Thach, B. S. Kulinkin *et al*, *Proc. 8th Int. Symp. "Nanostructures: Physics and Technology" St Petersburg*, p 406, 2000.
- [3] V. A. Gaisin, D. C. Thach, B. S. Kulinkin *et al*, *Vestnik. Sankt-Peterburgskogo Universiteta*. ser. 4. Fysika, himiya. vip. 2 (N12), 115 (2001).
- [4] V. A. Gaisin, D. C. Thach, B. S. Kulinkin *et al*, *Vestnik. Sankt-Peterburgskogo Universiteta*. ser. 4. Fysika, himiya. vip. 4 (N25), 65 (2000).
- [5] V. G. Talalaev, B. V. Novikov, S. Yu. Verbin *et al*, *Semiconductors* Is. 34, vol. 4, 453 (2000).

## Auger type relaxation of excitons in self assembled quantum dots via resonance scattering

*I. Larkin*<sup>†,‡</sup> and *A. Vagov*<sup>†,§</sup>

<sup>†</sup> Institute of Microelectronics Technology RAS Chernogolovka, Russia

<sup>‡</sup> Department of Physics and Astronomy, the University of Sheffield, UK

<sup>§</sup> Institut für Festkörpertheorie, Wilhelm-Klemm University, Munster, Germany

**Abstract.** We have investigated an Auger type mechanism of the relaxation of the carriers onto the deep levels of the self-assembled quantum dots (QD). Our analysis shows that resonant electron-hole collisions can lead to unexpectedly fast energy relaxation. Basic idea of the proposed mechanism is the Breit–Wigner type scattering of a delocalised particle with a particle trapped inside a dot. If energy of an incoming particle is close to the energy of a virtual two-particle state scattering crosssections resonantly enhanced. We show that the number of resonances is sufficiently large leading to large average crosssections. Realistic estimations for the In dots in the GaAs matrix shows that energy relaxation takes about 5–50 picosecond, which is comparable with experimental findings.

### Introduction

Typical self-assembled quantum dots have sizes of comparable to the Bohr radius of the embedding material. In the dot energy levels of single particle states for electrons and holes are well resolved and the gap between neighboring levels,  $\Delta \approx 10\text{--}20\text{ meV}$ , greatly exceeds temperature. This is essential for potential applications of dots in lasers, semiconductor sensors, quantum information systems, etc [1].

Thermolization rate of carriers in deep levels, or the time when the occupation numbers reach their equilibrium distribution, is an important characteristic of a system of dots closely related to potential applications. Experimental results suggest thermolization of deep levels is considerably faster then recombination rate for trapped excitons. For example, when carrier density is small only exciton ground state line is present in the photoluminescent spectra [2]. More direct measurements suggest thermolization time is  $\tau_T \approx 5\text{--}50\text{ ps}$  [3].

Two possible classes of mechanisms are usually considered to explain thermolization: interaction with phonons and Coulomb interaction between carriers (Auger type processes). In the case of a dot system, single phonon emission processes unlikely play a significant role in the relaxation because well resolved energy levels do not coincide with phonon frequencies considerably suppressing transition probability [4].

The role of two particle collisions in the relaxation have been investigated by Uskov [5] who considered trapping of a free particle onto lower levels of a dot as a result of such collisions. However, such mechanism is unlikely responsible for fast thermolization observed in systems with low carrier density,  $n \approx 10^8\text{ cm}^{-2}$ . Result of the calculation with help of Fermi Rule yields  $\tau_{\text{rel}} \approx (nr_0^2)^{-2}$ , where  $r_0$  is characteristic localization length of the bound wave function. Even if we assume the  $r_0$  is approximately equal to the size of a dot  $r_0 \approx a \approx 10\text{ nm}$ , the resulting time is  $\tau_{\text{rel}} \approx 10^4\text{ ns}$ . Experimental measurements, however, give for this density  $\tau_{\text{rel}} \approx 1\text{ ns}$  [6].

Analysis shows that free particle is more likely to be trapped as a result of a single collision process on a shallow level. Than scattering with a larger energy transfer involves multiple collision mechanism in a single scattering event. In the next section we consider this mechanism and evaluate energy transfer rate using a polar decomposition for scattering matrix. Then we evaluate matrix elements involved in Breit–Wigner approximation and calculate relaxation rate. In conclusion we discuss applicability of this approximation and possible scenarios of many-particle trapping.

### 1. Breit–Wigner approximation

Basic idea of Breit–Wigner approximation is resonant scattering of delocalised particle with a particle trapped in the dot. If energy of an incoming particle is close to the energy of a virtual two-particle state  $E_j$ , scattering crosssection both inelastic and elastic resonantly enhanced. Energy balance requires  $E_j = \varepsilon_a + \varepsilon_e$ , where  $\varepsilon_e$  is an energy of an incoming particle with momentum  $k$  and  $\varepsilon_a$  is an energy of localised particle. The scattering crosssection in the vicinity of such special energy exhibits a strong resonance peak. It has to be noted that trapping of second particle is only temporary, since according to Liouville theorem the volume of the phase space cannot change in the conservative system. Therefore state with real part of the energy  $E_j$  has total width  $\Gamma_j = \sum_b \Gamma_j^b$ , where  $\Gamma_j^b$  is a partial width that corresponds to the transition of localised particle to the state  $b$ . Crosssection in the channel  $a \rightarrow b$ , which means that quantum state of a particle inside a dot changes from  $a$  to  $b$  is [7]

$$\sigma_{ab}(E) = \frac{4}{k} \frac{\bar{\Gamma}_j^a \bar{\Gamma}_j^b}{(\varepsilon_e + \varepsilon_a - E_j)^2 + \frac{1}{4} \bar{\Gamma}_j^2}. \quad (1)$$

Positions of the resonances is easy to trace when the interaction is weak or absent. Then zero approximation for the two particle bound states are products of single particle bound states,  $\psi_j^e(r)$ ,  $\psi_j^h(R)$  (if particles are different). There are  $N_1$  and  $N_2$  single particle eigenstates with eigenvalues in the interval  $-U < \varepsilon_1 < 0$ . Then, there are  $N_1 \times N_2$  two-particle states with eigenvalues in the interval  $-2U < \varepsilon_2 < 0$ . It is easy to see that eigenvalues in the interval  $-2U < \varepsilon < -U$  are isolated, whereas those in the interval  $-U < \varepsilon < 0$  are embedded in the continuous spectrum formed by the states where one particle is free.

There are two reasons why resonance scattering can be much more efficient in relaxation processes than single particle collisions: 1) matrix elements of temporary capturing a free particle is not classically suppressed like transitions due to single collisions and 2) even for a two particle system number of resonances within temperature window  $0 < \varepsilon_e < T$  is large even for low temperatures.

The quantity of interest is not the crosssection (1) itself but the average rate of energy loss of a trapped particle (hole) by inelastic collisions. The rate can be written as

$$\frac{d\varepsilon}{dt} = \sum_b \int \frac{k}{m_e} (\varepsilon_a - \varepsilon_b) \sigma_{ab}(\varepsilon_e + \varepsilon_a) n_T(\varepsilon_e) d\varepsilon_e, \quad (2)$$

where  $n_T$  is Boltzmann distribution function.

In the limit  $T \gg \Gamma_j$  integration in Eq. (2) can be estimated as

$$\frac{d\varepsilon}{dt} = 2\pi \frac{n}{T} \sum_{jb} \frac{\varepsilon_a - \varepsilon_b}{\Gamma_j} \bar{\Gamma}_j^a \bar{\Gamma}_j^b \exp\left(-\frac{E_j - \varepsilon_a}{T}\right) \quad (3)$$



where

$$\bar{\Gamma}_j^b = 2\pi \sum_n \left| V_{j,n}^{j,b} \right|^2 \delta(\varepsilon_e + \varepsilon_a - \varepsilon_b - \varepsilon_{e,n}) \quad (4)$$

## 2. Coulomb matrix element and density of states

To proceed further we have to evaluate a Coulomb matrix element  $V_{j,n}^{b,a}$  between two-particle wave function  $\Psi_j^{e,h}$  of virtual state  $j$  and final wave function  $\psi_n^e \cdot \psi_b^h$ .

Complete solution is possible numerically for any chosen dot's potential. We chose analytic expression for dot's potential in the form  $U(r) = -U/(1 + r^2/a^2)$ . Result of analysis shows that

$$V_{j,n}^{j,b} \propto \exp[-\gamma_{e(h)}(\varepsilon_j - \varepsilon_b)], \quad (5)$$

where decrement  $\gamma_{e(h)} = \sqrt{a^2 m_{e(h)}/2U}$  weakly depends on the state  $j$ .

This expression has to be substituted into Eq. (3,4) and averaged over distribution of eigenvalues  $E_j$  and  $\varepsilon_b$ . We can substitute the ensemble averaging by the integration over a smooth density of states, that is  $\rho(\varepsilon) = (U + \varepsilon)/\omega^2$  for a single particle states. Since the interaction is weak the two particle density is formed by a product of two densities. Also in this approximation  $E_j$  can be simply taken as a sum of two single particle eigenvalues  $E_j = \varepsilon_a + \lambda$ . This yields for the energy loss rate (3)

$$\frac{\Delta \varepsilon_a}{\Delta t} \approx -8\pi \bar{\Gamma} n \frac{U(\varepsilon_a + U)}{\gamma^2 \omega_h^2 \omega_e^2}. \quad (6)$$

The rate disappears when energy is close to its ground state value,  $\varepsilon_0 \rightarrow -U$ , as it should.

## 3. Conclusion

Eq. (6) is strictly speaking suitable at intermediate energy  $U/\omega > (U + \varepsilon_0)/\omega > 1$ . For such levels single collision scattering probability  $\propto n\bar{\Gamma}$  is greatly enhanced by the factor  $U^2/(\gamma^2 \omega_h^2 \omega_e^2) \gg 1$ . One can easily see that this factor is in fact proportional to the total number of virtual states of the two particle system.

Numerical estimation can be done for InGaAs dots where in dimensionless atomic units ( $m_e=1$ ) with  $U \approx 20$ ,  $a \approx 1 - 2$ ,  $\omega_h \approx 1$ ,  $\omega_e \approx 3$ , and  $\gamma \approx a/\sqrt{2U} \approx 0.2$ . Total level width estimated with Eq. (4) yields  $\bar{\Gamma} \approx 10^{-3}$ . Consequently the rate for a hole sitting in a state with  $\varepsilon_0 \approx -10$  and  $n \approx 10^{-4}$  ( $n \approx 10^8 \text{ cm}^{-2}$ ) is about  $2 \times 10^{-3}$ . Therefore, it takes  $6 \times 10^3$  atomic units or 360 picoseconds for the hole to fall down to the bottom of the dot.

According to our findings, one can distinguish three stages of the energy relaxation in quantum dots. First stage is an initial capture of a carrier onto shallow localised states in the vicinity of a dot with absolute value of energy within the temperature range. For such process a standard kinetic equation analysis is applicable and relaxation rate is the same as for the weakly interacting electron gas. This stage is the fastest in the overall process. Then resonant scattering drags the trapped particle onto deeper levels of a dot. Using resonant approximation for the inelastic crosssection we found the relaxation rate that is of a standard exponential type. Finally, when particle is close to a ground state in a dot, three particle collisions become important leading to an effective capturing of the second particle into a dot. Then two-particle system relaxes to its ground state by the same resonant scattering of delocalised particles. This is generally a faster process than a single particle relaxation because the three-particle system has larger number of scattering resonances. Therefore,

the slowest time in the process is the time between the initial capture of a first particle and the capture of the second one. It is reasonable to associate this time with exciton capture time. Realistic estimations for the In dots in the GaAs matrix shows energy relaxation takes about 5–500 ps which is comparable with experimental findings [3, 6]

#### *Acknowledgements*

This work is supported by an EPSRC (UK) Grant GR/M91044.

#### **References**

- [1] D. Bimberg, M. Grundmann and N. N. Ledentsov, *Quantum Dot Heterostructures* (Wiley, New York, 1999).
- [2] S. Raymond, J. P. Reynolds, J. L. Merz, S. Fafard, Y. Feng and S. Charbonneau, *Phys. Rev. B* **58**, R13415 (1998).
- [3] R. Heitz, M. Veit, N. N. Ledentsov, A. Hoffmann, D. Bimberg, V. M. Ustinov, P. S. Kop'ev and Zh. I. Alferov, *Phys. Rev. B* **56**, 10435 (1997).
- [4] H. Benisty, C. M. Sotomayor-Torrès and C. Weisbuch, *Phys. Rev. B* **44**, 10945 (1991).
- [5] A. V. Uskov, J. McInerney, F. Adler, H. Schweizer and M. H. Pilkhun, *Appl. Phys. Lett.* **72**, 58 (1998).
- [6] S. Raymond, K. Hinzer and S. Fafard, *Phys. Rev. B* **61**, R16331 (2000).
- [7] L. Landau and E. Lifshits, *Course of Theoretical Physics v. 3 Quantum Mechanics*, Oxford Press, 1972.

## Soft collective charge mode in a 1D electron system

V. A. Sablikov and Yasha Gindikin

Institute of Radio Engineering and Electronics, Russian Academy of Sciences,  
Fryazino, Moscow District, 141120, Russia

**Abstract.** A new property of the charge collective mode in a 1D electron system is found. In the wave number region close to  $2k_F$  ( $k_F$  being the Fermi wave number) the mode frequency goes to zero, showing the soft mode behavior. In addition, the common 1D plasmon spectrum exists in the long-wave region. The soft mode is related to the short-range dynamic electron correlations in 1D and is absent in the systems of higher dimensionality. The dynamic correlations are described adequately in the frame of the Luttinger model.

### Introduction

Electron-electron interaction is known to produce the most pronounced effects in one-dimensional (1D) systems, giving rise to a strongly correlated state even if the interaction is weak [1]. Many attempts were made to treat correlations in 1D using the approaches, devised for higher-dimensional systems. They are based on the random phase approximation with various versions of the local field corrections, both static and dynamic [2]. These methods give no qualitatively new results as compared to higher dimensions, leading to the picture of charge excitations that is exhausted by common long-wave plasmons [3]. This is easy to understand since the above methods do not take correctly into account the dynamic short-range correlations, inherent in 1D. Another way to treat the dynamic correlations uses the Hartree-Fock decoupling scheme [4]. But it does not also give the correct results, since it ignores the Coulomb hole, which is important in 1D.

Presently, the most advanced way to treat dynamic electron correlations in 1D is based on the Luttinger liquid (LL) theory [5]. The short-range correlations [6, 7] appear here in a natural way, because this model takes properly into account the nesting of the Fermi surface for the wave number equal to  $2k_F$ . Owing to the short-range correlations, the LL density response contains the  $2k_F$  component (referred also to as the charge density wave, CDW), in addition to the usual long-wave one.

In the present paper we show that the CDW component of the electron density results in a qualitatively new behavior of the collective charge mode spectrum in 1D. The mode frequency goes to zero for the wave numbers close to  $2k_F$ , i.e. the soft mode appears.

### The dielectric function

Collective charge modes are given by zeros of the dielectric function  $\varepsilon(q, \omega)$ , which is related to the dynamic susceptibility  $\chi(q, \omega)$  via

$$\varepsilon^{-1}(q, \omega) = 1 + V(q)\chi(q, \omega), \quad (1)$$

$V(q)$  being the Fourier-transformed electron-electron interaction potential. The dynamic susceptibility of a 1D systems has two components, since so does the electron density

operator  $\rho(x)$ :

$$\rho(x) = -\frac{1}{\pi}\partial_x\phi + \frac{1}{2\pi}\partial_x\sin(2k_Fx - 2\phi), \quad (2)$$

$\phi(x)$  being the bosonic phase. Here the first component  $\rho_{lw}$  describes long-wave excitations and represents the sum of the densities of the right- and left-moving electrons. The corresponding excitations come about separately within each branch of electron spectrum and have momentum  $q \ll k_F$ . The second component  $\rho_{CDW}$  which rapidly oscillates in space, is due to the interference of the right- and left-moving electrons. This corresponds to excitations with momentum  $q \approx 2k_F$ . It is this term that describes the short-range electron correlations.

Two density components of Eq. (2) contribute to the density response function and to the susceptibility:

$$\chi(x, t) = \chi_{lw}(x, t) + \chi_{CDW}(x, t).$$

The dynamic susceptibilities  $\chi_{lw}(x, t)$  and  $\chi_{CDW}(x, t)$  were thoroughly investigated recently [8].

In order to find the collective modes from Eq.(1) it is sufficient to analyze the dynamic structure factor  $S(q, \omega)$ , which is the Fourier transform of the density-density correlator. At zero temperature the structure factor coincides with the imaginary part of the susceptibility:  $S(q, \omega) = -2\hbar\chi''(q, \omega)$ . The long-wave part of the structure factor,  $S_{lw}(q, \omega)$ , is universally expressed via the interaction parameter  $g(q)$  [1]:

$$S_{lw}(q, \omega) = |q|g(q)\delta(\omega - \omega_q),$$

where  $\omega_q = |q|v_F/g(q)$  is the boson dispersion. Thus, the boson dispersion results only in the shift of the  $\delta$ -peak position of  $S_{lw}(q, \omega)$ . This is clear physically, since  $S_{lw}(q, \omega)$  determines the probability to create a *single* boson when absorbing the quantum  $\hbar\omega$ , which fixes the singularity position.

The CDW structure factor  $S_{CDW}(q, \omega)$  describes the excitation of many bosons and is much more interesting. For the short-range interaction  $S_{CDW}(q, \omega)$  can be exactly calculated [7]:

$$S_{CDW}(q, \omega) = \frac{1}{v_F} \frac{g}{4g^{1/2}\Gamma^2(g)} \left(\frac{q}{k_F}\right)^2 \sum_{r=\pm 1} \left[ \left(g \frac{\hbar\omega}{\varepsilon_F}\right)^2 - \left(\frac{q}{k_F} - 2r\right)^2 \right]^{g-1},$$

$\varepsilon_F$  being the Fermi energy. The CDW structure factor is zero out of the  $q$  band  $||q| - 2k_F| < g\omega/v_F$  and diverges at the band edges.

For the Coulomb interaction the CDW structure factor can not be calculated exactly, but its general properties are qualitatively similar to the short-range interaction case [8].  $S(q, \omega)$  is non-zero inside the band  $\omega_{q-2k_F} < \omega$  and diverges at the band edges as

$$\omega S(q, \omega) \sim \frac{e^{-4\beta|\ln \epsilon|^{1/2}}}{\epsilon|\ln \epsilon|^{1/2}},$$

where  $\epsilon = \omega - \omega_{q-2k_F} \rightarrow +0$ ,  $\beta = [\pi\hbar v_F/2e^2]^{1/2}$ .

Let us return to the collective mode spectrum, which is determined by zeros of  $\varepsilon(q, \omega)$ . Eq.(1) shows that the dielectric function evidently turns to zero when the structure factor goes to infinity. Since the structure factor has singularities in two wave number regions, there are two regions, where the collective modes exist. The collective mode dispersion

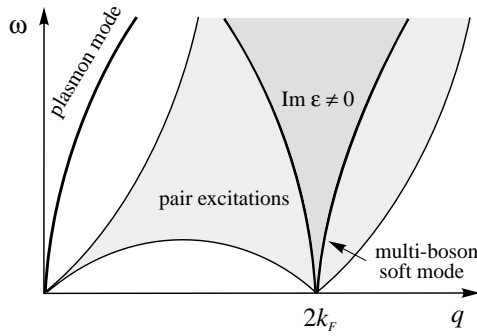


**Fig. 1.** The dispersion of charge collective modes in 1D.

is illustrated by Fig. 1. The first region corresponds to the singularity of  $S_{lw}(q, \omega)$ , which occurs at  $\omega = \omega_q$ . This mode is just long-wave plasmons. The singularities of the CDW structure factor  $S_{CDW}(q, \omega)$  give the new mode, situated near to  $q = 2k_F$ . The dispersion of this mode is  $\omega = \omega_{q-2k_F}$ . Here  $\omega$  is pure real, which means that the  $2k_F$  mode is non-decaying. An important conclusion is that the mode frequency goes to zero at  $q \rightarrow 2k_F$ , in other words, the mode is soft. It is the presence of the  $2k_F$  mode that principally distinguishes the collective excitations in the Luttinger liquid from those obtained within other approaches that do not take adequately into account the dynamic short-range electron correlations of the short-range scale.

#### Acknowledgements

This work was supported by INTAS, Russian Fund for Basic Research, and Russian Ministry of Science and Technology.

#### References

- [1] J. Voit, *Rep. Prog. Phys.* **58**, 977 (1995);
- [2] G. D. Mahan, *Many-Particle Physics*, 2nd ed. (Plenum Press, New York, 1990).
- [3] L. Calmels and A. Gold, *Phys. Rev. B* **58**, 3497 (1998).
- [4] F. Brosens, L. F. Lemmens and J. T. Devreese, *Phys. Status Solidi B* **74**, 45 (1976);
- [5] F. D. M. Haldane, *J. Phys. C* **14**, 2585 (1981).
- [6] F. D. M. Haldane, *Phys. Rev. Lett.* **47**, 1840 (1981).
- [7] V. A. Sablikov and Yasha Gindikin, *Phys. Rev. B* **61**, 12 766 (2000).
- [8] V. A. Sablikov and Yasha Gindikin, *Phys. Rev. B* **65**, 020212 (2002).

## Effects of accidental microconstriction on the quantized conductance in long wires

A. A. Starikov<sup>†‡</sup>, I. I. Yakimenko<sup>†</sup>, K.-F. Berggren<sup>†</sup>, A. C. Graham<sup>§</sup>,  
K. J. Thomas<sup>§</sup>, M. Pepper<sup>§</sup> and M. Y. Simmons<sup>§</sup>

<sup>†</sup> Department of Physics and Measurement Technology,  
Linköping University, S-581 83 Linköping, Sweden

<sup>‡</sup> Kirensky Institute of Physics, 660036, Krasnoyarsk, Russia

<sup>§</sup> Cavendish Laboratory, Madingley Road,  
Cambridge CB3 00HE, United Kingdom

**Abstract.** We have investigated the conductance of long quantum wires formed in GaAs/ $\text{Al}_x\text{Ga}_{1-x}\text{As}$  heterostructures. Using realistic fluctuation potentials from donor layers we have simulated numerically the conductance of four different kinds of wires. While ideal wires show perfect quantization, potential fluctuations from random donors may give rise to strong conductance oscillations and degradation of the quantization plateaux. Statistically there is always the possibility of having large fluctuations in a sample that may effectively act as a microconstriction. We therefore introduce microconstrictions in the wires by occasional clustering of donors. These microconstrictions are found to restore the quantized plateaux. A similar effect is found for accidental lithographic inaccuracies.

### Introduction

Long quantum wires are important objects from the view of both technology and fundamental physics (see for example [1–3] and references cited). Theory predicts that conductance through long clean wires is perfectly quantized with much sharper features than usual QPCs. However, the practical manufacturing of perfect, high quality wires is a delicate task. Thus many factors may influence the conductance in real devices and may cause deviations from theoretical predictions. Potential fluctuations from donors, small tolerance to possible inaccuracies in the lithography of gates are some of these factors. There could be two reasons for good quantization of the measured conductance in a long wire: either a superior quality of the wire or effects not connected with quantum properties of the entire wire, like local potential fluctuations from donors or defects. For example, in some samples we have observed quite well defined plateaux that degrade on thermal cycling. Does it mean that the potential landscape is changed in this process in such way that an occasional microconstriction is removed?

In this work we discuss the conductance of long wires in GaAs/ $\text{Al}_x\text{Ga}_{1-x}\text{As}$  heterostructures. We consider some accidental effects that could produce well shaped quantized plateaux. In particular, we study how donors and lithographical defects can produce QPC-like substructures and change the shape of the conductance plateaux characteristics.

### 1. Theoretical model and calculation

Long quantum wires are often fabricated in modulation-doped heterostructure with a patterned metallic top gate, see Fig. 1(a). A negative voltage applied to the gate relative to the substrate depletes the two-dimensional electron gas (2DEG) under the gated regions and

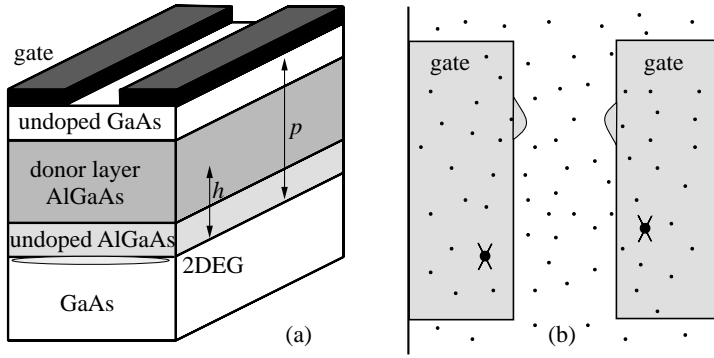


**Fig. 1.** (a) Schematic representation of a device simulating a long quantum wire; (b) Donors in the doped AlGaAs (dots), points of concentration of donors (crosses), irregularities of the shape the gates. Corresponding confinement potentials are smoothed.

leaves a conducting wire in the split gate region. The actual size of the wire can be varied lithographically by changing the geometry of the gate as well as by varying the applied voltage. The confinement potential  $U_g$  formed by the gate is determined by the well known expression [4]:

$$U_g(\mathbf{r}, z) = \frac{e}{2\pi} \int d\mathbf{r}' V_g(\mathbf{r}', 0) \frac{|z|}{(z^2 + |\mathbf{r} - \mathbf{r}'|^2)^{3/2}}, \quad (1)$$

where  $V_g(\mathbf{r}', 0)$  is the potential on the gate and  $z$  the distance between the gate and the 2DEG. To investigate possible effects in real devices we introduce the potential from random donors and mirror charges as described in [5]:

$$U_{rc}(\mathbf{r}, z) = \frac{e}{4\pi\epsilon\epsilon_0} \sum_{i=1..N} \left[ \frac{1}{\sqrt{h^2 + |\mathbf{r} - \mathbf{r}'|^2}} - \frac{1}{\sqrt{(2p - h)^2 + |\mathbf{r} - \mathbf{r}'|^2}} \right], \quad (2)$$

where the summation is over all donor positions in the plane on distance  $h$  from the 2DEG. Mirror charges are generated by the surface at distance  $p$  from the 2DEG in Fig. 1(a).

To find the electronic configuration and related properties of the system we have solved the Schrödinger equation for electrons of a mass  $m^*$  mapped on a square lattice:

$$-\frac{\hbar^2}{2m^*} \nabla^2 \Psi(x, y) + [U_g + U_{rc}] \Psi(x, y) = E_f \Psi(x, y). \quad (3)$$

The zero-temperature conductance was calculated as  $G = (2e^2/h) \text{Tr}(TT^+)$  according to the Büttiker formula;  $T$  is the transmission matrix. We use this one electron approach because we believe that brings out the essential physics in the problem.

In the following we consider four variants of long wires:

- a) a wire with uniform potential (ideal wire);
- b) a wire with a fluctuating potential  $U_{rc}$  to mimic a real device.

We also consider two additional cases associated with possible problems of manufacturing long wires. In both cases we assume that there are background potential fluctuations from random donors as in b). Thus we also have

- c) a wire with clusters of donors. We simply let more than one donor sit at the same point as shown in Fig. 1(b). The clusters represent statistical variations in donor concentration and/or impurities or other imperfections from the growth of the heterostructure;

d) the top gate has deviations from the regular shape as shown in Fig. 1(b). As a result an additional QPC microconstriction in the wire is formed.

We have studied wires formed by split gates as in Fig. 1. The lithographic length is  $4\text{ }\mu\text{m}$  and the gap between gates is  $100\text{ nm}$  wide. Typical size of the numerical grid is  $70\times 1000$ .

## 2. Results and discussion

The calculated conductance as a function of applied gate voltage is shown in Fig. 2. As indicated, the conductance for an ideal wire (dotted line) shows well-shaped sharp stairs. The dashed line on the same figure represents transport through the same long wire with potential fluctuations from random donors. In this case the quantization is degraded because of backscattering and interference effects. Depending on the particular realization of random positions of donors the conductance oscillations differ from sample to sample. The situation changes dramatically when we add two donors having larger charge, that rep-

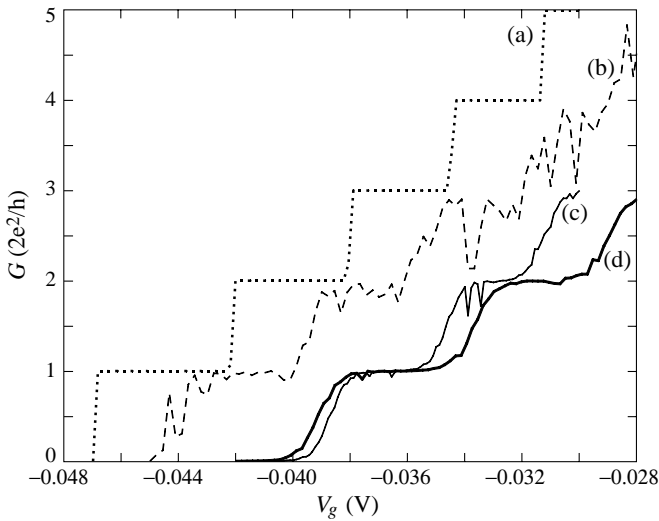


**Fig. 2.** Calculated zero-temperature conductance for long wires. (a) ideal wire; (b) wire with fluctuated potential; (c) microconstriction substructure formed by donor potential; (d) microconstriction substructure from irregular gates.

resent local concentrations/statistical clusters of donors or other imperfections. This case is shown by the bold solid line. Donors situated on the different sides of the channel may form a QPC-like structure which plays a dominant role in the transport process through the channel. The case when a QPC-like structure is formed by lithographic irregularities in the gates looks similar. However, the main difference between the two cases is the width of the plateaux which is a result of the different mechanisms behind the formation the QPC-like structures. In the case of gate irregularities the potential is more responsive to the applied voltage, it acts like a normal QPC (Fig. 2(d)). In contrast, when the narrowing is due to donor concentrations/clusters *etc.*, variation of voltage does not change the structure of local QPC-potential. Instead the voltage only shifts the entire potential landscape. In this case the plateaux are wider indicating less dependence on gate voltage (Fig. 2(c)).



In conclusion, the microconstrictions in long quantum wires may play a dominant role in transport processes. Good quantization may be observed not only in the case of well manufactured devices but also for imperfect wires with microconstrictions. Experimentally it may be a problem to recognize what kind of situation we have at hand. One possible way is to compare wires with the same geometry. Plateaux for QPC substructures are shifted with gate voltage and have different shapes which may be analyzed by means of a local saddle-point model.

#### *Acknowledgments*

This work has been supported by the the Royal Swedish Academy of Sciences (AAS) and the Engineering and Physical Sciences Research Council, UK (ACG). KJT acknowledges support from Royal Society Research Fellowship, UK.

#### **References**

- [1] S. Tarucha, T. Honda and T. Saku, *Solid State Commun.* **94**, 413 (1995).
- [2] C.-T. Liang, M. Pepper, M. Y. Simmons, C. G. Smith and D. A. Ritchie, *Phys. Rev. B* **61**, 9952 (2000).
- [3] D. J. Reilly, G. R. Facer, A. S. Dzurak, B. E. Kane, R. G. Clark, P. J. Stiles, R. G. Clark, A.R. Hamilton, J. L. O'Brien, N. E. Lumpkin, L. N. Pfeiffer and K. W. West, *Phys. Rev. B* **63**, R121311 (2001).
- [4] J. H. Davies, *Semicond. Sci. Technol.* **3**, 995 (1988).
- [5] J. H. Davies and J. A. Nixon, *Phys. Rev. B* **39**, 3423 (1989).

## Zero spin splitting of Landau levels in 2D electron systems: role of sign of Landé factor

E. E. Takhtamirov and V. A. Volkov

Institute of Radioengineering and Electronics of RAS,  
 Mokhovaya 11, 101999 Moscow, Russia

**Abstract.** The one-particle spin splitting of Landau levels in 2D electron systems is governed both by Zeeman mechanism and spin-orbit interaction. For III–V heterostructures the latter has two contributions: bulk (Dresselhaus contribution) and interface (Rashba contribution). It is analyzed the combined effect of all three mechanisms on the spectrum of Landau levels in a quantum well (001) III–V in perpendicular to plane or near to perpendicular magnetic field. The goal of the work is to find conditions when the bare spin splitting,  $\Delta_{sN}$ , of  $N$ th Landau level disappears. It is shown that 1) the Rashba and Dresselhaus mechanisms are not equivalent to each other; 2) the result depends on the sign of the Landé effective  $g$ -factor. Zero of  $\Delta_{sN}$  is induced by the Dresselhaus mechanism if  $g_{zz} < 0$ , or Rashba mechanism if  $g_{zz} > 0$ . The results are qualitatively applicable to other low-dimensional systems (quantum wires and dots).

### 1. Introduction

Recently considerable attention has been devoted to studying of spin properties in low-dimensional systems. Relating to the applied aspects, this is connected with development of the spintronics, some realizations of quantum computers, etc. Feasibility to govern the spin splitting of discrete energy levels in low-dimensional systems is of crucial importance in fundamental sense too. For example, for formation of skyrmions in a quantum Hall system it is necessary to attain the conditions when the bare splitting of Landau levels  $\Delta_{sN}$  is small, and ideally is zero. The literature data on the conditions for  $\Delta_{sN} = 0$  are contradictory. The numerical results of Lommer et al [1] indicate the existence of some magnetic field  $B_z$  when  $\Delta_{sN} = 0$ . This result is argued against, e.g., by Pfeffer [2].

We calculated analytically the bare spin splitting of Landau levels in 2D electron gas with simultaneous accounting for a) Zeeman splitting; b) bulk spin-orbit interaction proportional to quasi-momentum to the third power related to the inversion asymmetry of III–V materials (Dresselhaus contribution); c) spin-orbit interaction proportional to quasi-momentum related to the heterostructure potential asymmetry (Rashba contribution).

### 2. Effect of spin-orbit interaction on Landau level spectrum in (001) III–V quantum well

We use the following Hamiltonian for a conduction band electron in a quantum well (QW) in magnetic field  $\mathbf{B} = (B_x, B_y, B_z)$ :

$$\hat{H}^{3D} = \frac{\mathbf{P}^2}{2m^*} + U(z) + \alpha_R [\mathbf{e}_z \times \mathbf{P}] \boldsymbol{\sigma} + \hat{H}_D + \frac{1}{2} \mu_B g^{(3D)} \boldsymbol{\sigma} \mathbf{B}, \quad (1)$$

where  $\mathbf{P} = \mathbf{p} + e/c\mathbf{A}$ ,  $\mathbf{p}$  is the momentum operator, and its components are directed along the cubic axes,  $-e$  is the electron charge,  $c$  is the speed of light,  $\mathbf{A}$  is the vector potential,  $m^*$

is the effective mass,  $U(z)$  is the heterostructure potential,  $\alpha_R \equiv \alpha_R(z)$  is the function that defines the Rashba contribution [3] (for the structure with a single heterojunction it may be presented as a product of a constant and the Dirac  $\delta$ -function [4]),  $\mathbf{e}_z$  is the unit vector along  $Oz$ -axis,  $\sigma$  are the matrices of spin 1/2,  $\mu_B$  is the Bohr magneton,  $g^{(3D)} \equiv g^{(3D)}(z)$  is the bulk g-factor. The Dresselhaus contribution term  $\hat{H}_D$  is

$$\hat{H}_D = \frac{1}{2}\alpha_D \left( \sigma_x \{P_x, P_z^2 - P_y^2\} + \sigma_y \{P_y, P_x^2 - P_z^2\} + \sigma_z \{P_z, P_y^2 - P_x^2\} \right), \quad (2)$$

where  $\alpha_D$  is a constant (we assume it material independent), and the curly brackets are standing for anti-commutators.

We may rotate the coordinate axes by  $\pi/4$  around  $Oz$ -axis (the vector  $\sigma$  be transformed too) and use the gauge  $\mathbf{A} = (B_y z, -B_x z + B_z x, 0)$ . Now  $Ox$ -axis is along  $[1\bar{1}0]$ , and  $Oy$ -axis is along  $[110]$ . Averaging the resulting Hamiltonian relating to  $z$ -motion (we will use the notation  $\langle S \rangle$  for that average of an operator  $S$ ), for the ground subband neglecting interaction with others we will have the following 2D Hamiltonian (see, e.g., [5]):

$$\hat{H} = \frac{p_x^2}{2m^*} + \frac{1}{2m^*} \left( p_y + \frac{e}{c} B_z x \right)^2 + \alpha_1 \sigma_x \left( p_y + \frac{e}{c} B_z x \right) + \alpha_2 \sigma_y p_x + \frac{\mu_B}{2} \sigma \hat{\mathbf{g}} \mathbf{B}, \quad (3)$$

$$\alpha_1 = \alpha_D \langle p_z^2 \rangle - \langle \alpha_R \rangle, \quad \alpha_2 = \alpha_D \langle p_z^2 \rangle + \langle \alpha_R \rangle. \quad (4)$$

Zero energy is assumed at the bottom of the diamagnetically shifted ground subband. In the Dresselhaus term we assumed  $\langle p_z^2 \rangle$  much more than the cyclotron-motion average of  $p_x^2$  and  $p_y^2$ . The non-zero components of the effective g-factor tensor  $\hat{\mathbf{g}}$  are  $g_{xx} \neq g_{yy} \neq g_{zz}$  [5, 6]. The specific expressions for them are not essential here.

We define now the creation and destruction operators  $a^\dagger$  and  $a$  ( $\hbar = 1$ ):

$$a = \sqrt{\frac{c}{2eB_z}} (P_x - iP_y), \quad a^\dagger = \sqrt{\frac{c}{2eB_z}} (P_x + iP_y) \quad (5)$$

with the commutation rule  $[a, a^\dagger] = 1$ . Then we will have the Schrödinger equation

$$\hat{H}F = EF \quad (6)$$

with the two component eigen-function  $F = (f_1, f_2)^T$  and the Hamiltonian (3) taking the following form ( $\omega_c = eB_z/(m^*c)$ ):

$$\begin{aligned} \hat{H} = & \omega_c \left( a^\dagger a + \frac{1}{2} \right) + \frac{\mu_B}{2} \sigma \hat{\mathbf{g}} \mathbf{B} \\ & + \alpha_1 \sigma_x i \sqrt{\frac{\omega_c m^*}{2}} (a - a^\dagger) + \alpha_2 \sigma_y \sqrt{\frac{\omega_c m^*}{2}} (a + a^\dagger). \end{aligned} \quad (7)$$

Four elements of the matrix Hamiltonian (7) are

$$\hat{H}_{11} = \omega_c \left( a^\dagger a + \frac{1}{2} \right) + \frac{\mu_B}{2} g_{zz} B_z, \quad \hat{H}_{11} = \omega_c \left( a^\dagger a + \frac{1}{2} \right) - \frac{\mu_B}{2} g_{zz} B_z, \quad (8)$$

$$\hat{H}_{12} = -i\sqrt{2m^*\omega_c} \langle \alpha_R \rangle a - i\sqrt{2m^*\omega_c} \alpha_D \langle p_z^2 \rangle a^\dagger + \frac{\mu_B}{2} g_{xx} B_x - i\frac{\mu_B}{2} g_{yy} B_y, \quad (9)$$

$$\hat{H}_{21} = i\sqrt{2m^*\omega_c} \langle \alpha_R \rangle a^\dagger + i\sqrt{2m^*\omega_c} \alpha_D \langle p_z^2 \rangle a + \frac{\mu_B}{2} g_{xx} B_x + i\frac{\mu_B}{2} g_{yy} B_y, \quad (10)$$

Following [3, 7] we use series expansions

$$f_1 = \sum_{s=0}^{\infty} a_s \phi_s, \quad f_2 = \sum_{s=0}^{\infty} b_s \phi_s, \quad (11)$$

where  $\phi_s$  are oscillator functions,  $a\phi_s = \sqrt{s}\phi_{s-1}$  and  $a^\dagger\phi_s = \sqrt{s+1}\phi_{s+1}$ . Now, recalling  $a_N = b_N = 0$  if  $N < 0$ , Eq. (6) turns into set of equations

$$\left[ \omega_c \left( N + \frac{1}{2} \right) + \frac{1}{2} \mu_B g_{zz} B_z - E \right] a_N + \frac{1}{2} \mu_B g_{xx} B_x b_N - \frac{i}{2} \mu_B g_{yy} B_y b_N - i \sqrt{2m^* \omega_c} \langle \alpha_R \rangle \sqrt{N+1} b_{N+1} - i \sqrt{2m^* \omega_c} \alpha_D \langle p_z^2 \rangle \sqrt{N} b_{N-1} = 0, \quad (12)$$

$$\left[ \omega_c \left( N + \frac{1}{2} \right) - \frac{1}{2} \mu_B g_{zz} B_z - E \right] b_N + \frac{1}{2} \mu_B g_{xx} B_x a_N + \frac{i}{2} \mu_B g_{yy} B_y a_N + i \sqrt{2m^* \omega_c} \langle \alpha_R \rangle \sqrt{N} a_{N-1} + i \sqrt{2m^* \omega_c} \alpha_D \langle p_z^2 \rangle \sqrt{N+1} b_{N+1} = 0. \quad (13)$$

If  $\mathbf{B}_\parallel = (B_x, B_y) = 0$  and  $\alpha_D = 0$ , then we come to the exact result for spectrum [3, 8]. In general case the results are crucially dependent on the sign of  $g_{zz}$ . If  $g_{zz} > 0$  and  $\alpha_D = 0$  one may show that two Landau levels with numbers  $N$ -spin-up (having higher energy than the state  $N$ -spin-down) and  $(N+1)$ -spin-down interact via the Rashba mechanism, and at some critical magnetic field the Landau levels  $N$ -spin-up and  $N$ -spin-down may cross. In those conditions, but  $g_{zz} < 0$ , such a case is not possible as the state  $N$ -spin-up has lower energy than that  $N$ -spin-down. Then, if  $g_{zz} < 0$ , we come to a conclusion that only the Dresselhaus mechanism may result in zero spin splitting of a Landau level  $N$  at some critical magnetic field  $B_z$ .

These conclusions are justified with analytical solution of equations (12), (13) in the case of  $\omega_c \gg 1/2 \mu_B g_{ll} B_l$ , where  $l = x, y, z$ , and  $\omega_c \gg \alpha_j \sqrt{\omega_c m^* N}$ , where  $j = 1, 2$ . The approximate spectrum is

$$E_N^\pm = \omega_c \left( N + \frac{1}{2} \right) - \left( m^* \langle \alpha_R \rangle^2 + m^* \alpha_D^2 \langle p_z^2 \rangle^2 \right) \pm \sqrt{\left( \frac{\mu_B}{2} \mathbf{g}_\parallel \mathbf{B}_\parallel \right)^2 + \left( \frac{\mu_B}{2} g_{zz} B_z + m^* (2N+1) (\alpha_D^2 \langle p_z^2 \rangle^2 - \langle \alpha_R \rangle^2) \right)^2}. \quad (14)$$

### 3. Spin splitting for QW (001) GaAs/AlGaAs

For illustrative purposes consider QW (001) AlGaAs-GaAs-AlGaAs. For bulk GaAs  $g = -0.44$ . But the sign of effective  $g$ -factor for electrons in GaAs/AlGaAs heterostructure is very sensitive to the width of GaAs QW [6]. This answers the question why different authors came to different conclusions whether Landau levels could be spin-degenerated at some magnetic field  $B_z$ , and what mechanism of zero magnetic field spin splitting was dominant ([1, 2]). For a symmetric narrow QW  $\langle \alpha_R \rangle = 0$  and  $g_{zz} > 0$ . In this case one cannot expect to adjust  $B_z$  to come to zero spin splitting of a Landau level. The desired result may be obtained for a wide symmetric QW with  $g_{zz} < 0$ . The reliable data for the constant that governs the Rashba mechanism (that generally depends on the microscopic structure of heterointerface) are not available from the literature. So, one cannot firmly predict what grade of asymmetry of a QW is required for Rashba mechanism to overcome

that of Dresselhaus. A parallel component of magnetic field ( $B_x, B_y$ ) mixes the spin states of the same Landau level, and break the spin degeneracy once presented.

An estimate for a symmetric ( $\langle \alpha_R \rangle = 0$ ) AlGaAs-GaAs-AlGaAs QW of width 100 Å, with  $g_{zz} = -0.2$  (see Ref. [6]),  $\alpha_D = 25 \text{ eV Å}^3$  (see Ref. [9]) and  $\mathbf{B}_{\parallel} = 0$ , gives that the splitting of the Landau level  $N$  is zero at  $B_z^{\text{crit}} \approx 2 \cdot (N + 1/2)$  Tesla. The critical magnetic field  $B_z^{\text{crit}}$  strongly depends on the QW width not only via the width-dependent  $g_{zz}$ , but also via the QW width dependence of the parameter  $\langle p_z^2 \rangle^2$ . So, in narrower QWs the critical magnetic field is higher for some fixed  $N$ . Qualitatively the same conclusions about the role of the Landé factor are applicable to quantum wires and dots with parabolic confinement.

### Acknowledgments

The work was supported in part by RFBR (grant 02-02-17403), Federal Programs FTNS and PAS. E.E.T. was partially supported by the Young Scientists Support Program of RAS (Grant 43).

### References

- [1] G. Lommer, F. Malcher and U. Rössler, *Phys. Rev. Lett* **60**, 782 (1988).
- [2] P. Pfeffer, *Phys. Rev. B* **55**, R7359 (1997).
- [3] E. I. Rashba, *Fiz. Tverd. Tela* **2** 1224 (1960) [*Sov. Phys. – Solid State* **2**, 1109 (1960)]; E. I. Rashba and V. I. Sheka, in *Landau Level Spectroscopy*, Vol. 27.1, ed. by G. Landwehr and E. I. Rashba (North-Holland, Amsterdam, Oxford, New York, Tokyo, 1991).
- [4] F. T. Vasko, *Pis'ma v ZhETF* **30**, 574 (1979) [*JETP Lett.* **30**, 541 (1979)].
- [5] V. K. Kalevich and V. L. Korenev, *Pis'ma v ZhETF* **57**, 557 (1993).
- [6] E. L. Ivchenko and A. A. Kiselev, *Fiz. Tekhn. Poluprovodn.* **26** 1471 (1992) [*Sov. Phys. – Semicond.* **26**, 827 (1992)].
- [7] J. M. Luttinger, *Phys. Rev.* **102**, 1030 (1956).
- [8] Yu. A. Bychkov, V. I. Mel'nikov and E. I. Rashba, *ZhETF* **98** 717 (1990).
- [9] F. G. Pikus and G. E. Pikus, *Phys. Rev. B* **51** 16928 (1995).

## Quenching of the Hall effect in localised high magnetic field region

*S. V. Dubonos*<sup>†</sup>, *K. S. Novoselov*<sup>‡§</sup>, *A. K. Geim*<sup>‡</sup> and *J. C. Maan*<sup>§</sup>

<sup>†</sup> Institute of Microelectronics Technology and High Purity Material,  
Russian Academy of Science, Chernogolovka, Moscow district, 142432 Russia

<sup>‡</sup> Department of Physics and Astronomy, University of Manchester, Oxford Road,  
M13 9PL, Manchester, UK

<sup>§</sup> Research Institute for Materials, High Field Magnet Laboratory,  
University of Nijmegen, Toernooiveld 1, NL–6525 ED, Nijmegen, The Netherlands

**Abstract.** We report the suppression of the Hall effect in a mesoscopic Hall cross with a strong magnetic field only in the centre and vanishingly small outside. The local magnetic field is produced by placing Dy pillar on top of a structure with high-mobility two-dimensional electron gas (2DEG). The effect is found to be due to a sharp increase of the number of back-scattered and quasi-localised electron orbits. The possibility of localising electrons inside the magnetic inhomogeneity region is discussed.

### Introduction

The behaviour of electrons in micro-inhomogeneous magnetic fields continues to attract significant interest. Most recently, the research has concentrated on studying the influence of individual magnetic barriers, trying to understand how a localised region of magnetic field effects electron motion, either semiclassically or quantum-mechanically [1–8]. The experimental goal is to create a mesoscopic area inside a 2DEG with a so high (possibly, quantized) magnetic field that it alters qualitatively the electron transport inside the region. To this end, individual stripes or disks have been deposited on top of mesoscopic structures [2–6]. It creates a spike of strong magnetic field near the film edge, because the film magnetisation tends to be in plane.

We report a novel experimental system for studying a motion of ballistic electrons in microinhomogeneous magnetic fields. By depositing a ferromagnetic (Dy) pillar on a near-surface 2DEG and gradually changing its remnant magnetisation, we create a localised area of magnetic field in the 2DEG. The pillar geometry allows us, not only to increase the magnetic field strength one order of magnitude in comparison with previous experiments, but also to avoid the spike-like near edge fields. On the other hand, by studying transport in zero applied external magnetic field we avoid the contribution from skipping orbits along the edges of the 2DEG, which often short the electron transport [5]. For low magnetisation of the Dy pillar the Hall signal is proportional to the magnetic field, created by the pillar average over the Hall cross. However at the magnetic fields bigger than some critical  $B^*$  the Hall effect is strongly suppressed. Unexpectedly, the transition between the two regimes occurs in a very narrow range of magnetic fields, indicating a geometrical resonance. We attribute this effect due to the increased number of back-scattered and quasi-trapped electrons at  $B > B^*$ . A numerical simulation, based on the billiard model of a ballistic multiprobe conductor [10] is in good agreement with the observed behaviour of Hall voltage.

## 1. Experimental part and discussion

A micrograph of one of our devices is shown in Fig. 1(a). It is a set of Hall probes with the wire width  $w$  of about  $2\ \mu\text{m}$ . A shallow 2DEG with concentration  $n \approx 3.45 \times 10^{11}\ \text{cm}^{-2}$  ( $4.85 \times 10^{11}\ \text{cm}^{-2}$  after illumination) is embedded at a GaAlAs/GaAs interface located  $70\ \text{nm}$  below the surface of the sample. The initial mobility of the 2DEG heterostructure was  $\approx 1.000.000\ \text{cm}^2/(\text{V s})$ , which corresponds to an electron mean free path  $\approx 5\ \mu\text{m}$ .

Dysprosium pillars of three different diameters,  $2R$  ( $1, 1.5$  and  $3\ \mu\text{m}$ ) and of thickness  $h$  of about  $1.5\ \mu\text{m}$  were deposited in the centre of the Hall crosses. Using very high and narrow Dy dots allows us to avoid edge effects and increase the strength of magnetic field underneath of the pillars up to  $0.4\ \text{T}$ . In our experiments no external magnetic field was present. The magnetic field was created only by to the remnant magnetisation of Dy pillars (for the details see [9]).

The results of measuring the Hall resistance for the cross with  $1.5\ \mu\text{m}$  Dy pillar on top are presented in Fig. 1(b) as a function of average over the Hall cross magnetic field in plane of 2DEG. All the measurements were done at  $T = 0.3\ \text{K}$ . At low magnetic field the Hall resistance curves are nearly linear dependent on the average magnetic field, with a Hall factor approximately equal to that found on the cross with a demagnetised magnetic pillar. However, as one can see at some critical magnetic field  $B^*$  the Hall effect becomes strongly suppressed, so even  $d\rho_H/dB$  approach zero for  $B > B^*$ .

The cross with  $1\ \mu\text{m}$  Dy pillar exhibits a quite similar behaviour, although with a critical field  $\sim 50\%$  higher than for  $1.5\ \mu\text{m}$  Dy pillar.

As one can see from the Fig. 1(b) — the value of critical magnetic field differs for curves with different concentration — for high concentration curve it is  $\sim 20\%$  higher then for low concentration curve (the same relation was observed for  $1\ \mu\text{m}$  Dy pillar).

This result immediately brings us to the conclusion that the proportionality of Hall voltage to the average magnetic field around the cross [1, 2] fails. The quenching of the Hall effect is the result of the influence of the localised high magnetic field on the electron transport. Therefore, the average magnetic field is not the parameter, which can describe our system any more, but rather the actual magnetic field underneath the magnetic pillar, in

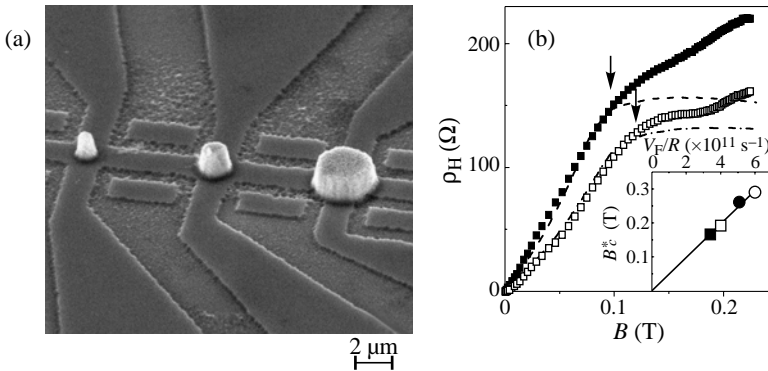


**Fig. 1.** (a) A SEM micrograph of the studied device. (b) The Hall resistance on the Hall cross with  $1.5\ \mu\text{m}$  Dy pillar on top. Solid symbols represent the measurements in dark, open — after illumination. Dash and dash-dot curves are numerical calculations for these two cases respectively. The critical magnetic fields marked by arrows. As the inset: the dependence of the critical magnetic field vs  $V_F/R$ . Squares are for  $1.5\ \mu\text{m}$  Dy pillar, circles — for  $1\ \mu\text{m}$  Dy pillar. Solid symbols — measurements in dark, open — after illumination.

the *centre* of a Hall cross  $B_c = B(0, 0)$  and the radius of this pillar. The critical magnetic field under the  $1.5 \mu\text{m}$  pillar thus determined is  $\approx 0.165 \text{ T}$  in dark and  $\approx 0.195 \text{ T}$  after illumination. For the  $1 \mu\text{m}$  pillar these values are  $\approx 0.26 \text{ T}$  and  $\approx 0.29 \text{ T}$ .

These values are plotted in the inset to Fig. 1(b) as a function of  $V_F/R$ , where  $V_F$  is the Fermi velocity. This way allows us to present the data for different  $R$  and different electron concentration (different  $V_F$ ) on the same graph. We also fitted the experimental points with a linear dependence  $B_c^* = (m^*/e) \times (V_F/\alpha R)$ , where  $m^*$  is the effective electron mass,  $e$  — the electron charge and  $\alpha$  is the fitting parameter, assuming that *the Hall effect quenches when the cyclotron radius equals to the radius of magnetic spot*. We obtain the best fit for  $\alpha = 1.26$  (close to one), which confirms our assumption.

We also calculated the conductivity tensor for our system like in Ref. [10], and show the calculated Hall resistance for  $1.5 \mu\text{m}$  Dy pillar in Fig. 1(b). At low magnetic field theory fits the experimental points very well, and it also predicts the correct value for the critical field, although the suppression of the Hall effect is much bigger.

To obtain a better physical insight, in Fig. 2 we plot the probability of finding an electron at a certain point of a Hall cross at any arbitrary instant of time when electrons are injected from the bottom lead. For zero magnetisation of the Dy pillar the probability for an electron to go left or right is the same, which gives no Hall voltage. As the magnetisation of the pillar increases — more electrons go left. However, as one can see on the last three pictures, at the magnetic fields higher the  $B_c^*$  electrons start to be localised (trapped) in the central part of the Hall cross, also the number of back-scattered electrons increases dramatically.

In our experiment the probing of real stationary states inside local magnetic inhomogeneity (like those, predicted in [7, 8]) is not possible. No electron, which comes from infinity, can be trapped in a closed orbit. Instead, in our case, electrons can be quasi-trapped — spending very long time orbiting inside the high magnetic field region, and finally scatter in a random direction, giving no contribution to the Hall signal. Also back-scattered electrons never contribute to Hall effect, which qualitatively explains the quenching of the Hall effect at magnetic field above  $B^*$ .

That the quenching of the Hall effect occurs in a very narrow magnetic field region indicates the geometrical resonance condition for Fermi-electrons. At higher temperature the suppression of the Hall effect becomes much smoother due to broadening of the thermal distribution of electron velocities on the Fermi level. In fact, the magnetic dot works like

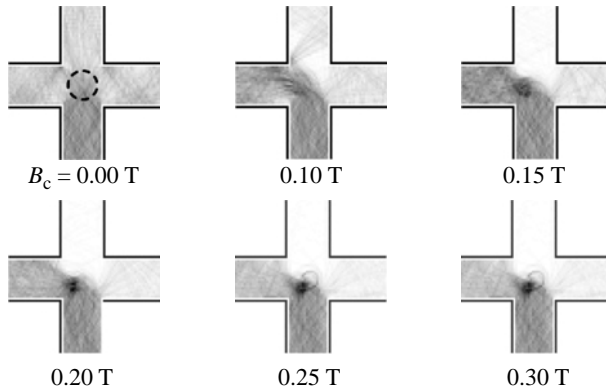


**Fig. 2.** The numerical calculations of probability of finding electron at any point of the Hall cross with  $1.5 \mu\text{m}$  Dy pillar on top at any arbitrary instant of time. The size of the Dy pillar is given as a dash circle on the first picture.



monochromator, trapping and reflecting back only electrons which velocities satisfies the condition  $V \geq (e/m^*) \times (B_c R)$ .

## Conclusions

To summarise we have reported an effect of quenching the Hall effect in system with localised high magnetic field region. Numerical calculations ascribe experimental data both qualitatively and quantitatively. The effect is found to be due to the sharp increase of a number of reflected-back and quasi-localised electrons when the cyclotron radius of an electron on Fermi surface fits inside the local magnetic field region.

## References

- [1] F. M. Peeters and X. Q. Li, *Appl. Phys. Lett.* **72**, 572 (1998).
- [2] A. K. Geim *et al*, *Appl. Phys. Lett.* **71**, 2379 (1997).
- [3] A. Nogaret, S. J. Bending and M. Henini, *Phys. Rev. Lett.* **84**, 2231 (2000).
- [4] M. Johnson *et al*, *Appl. Phys. Lett.* **71**, 974 (1997).
- [5] S. V. Dubonos *et al*, *Physica E* **6**, 746 (2000).
- [6] V. Kubrak *et al*, *Appl. Phys. Lett.* **74**, 2507 (1999).
- [7] J. Reijniers, F. M. Peeters and A. Matulis, *Phys. Rev. B* **59**, 2817 (1999).
- [8] Heung-Sun Sim *et al*, *Phys. Rev. Lett.* **80**, 1501 (1998).
- [9] K. S. Novoselov *et al*, (unpublished)
- [10] C. W. J. Beenakker and H. van Houten, *Phys. Rev. Lett.* **63**, 1857 (1989).

## Quantum interference in magnetooscillation phenomena in two-dimensional electron gas

*N. S. Averkiev and S. A. Tarasenko*

Ioffe Physico-Technical Institute, St Petersburg, Russia

**Abstract.** Effect of spin splittings on magnetooscillation phenomena is studied theoretically. It is shown that interference takes place between two types of spin splittings linear in the wave vector. The simultaneous presence of these spin terms in the Hamiltonian of the two-dimensional electron gas causes a suppression of beats in the magnetooscillation phenomena. Zeeman splitting in tilted magnetic fields is shown to be able to lead to the appearance of the oscillations with the double frequency.

### 1. Introduction

Existence of an electron spin is well known to be able to modify qualitatively a physical picture of oscillations of kinetic coefficients in magnetic fields. However, analyzing experimental data the spin effects are often ignored. We demonstrate here that the splitting of the energy spectrum depending on the spin changes drastically magnetooscillation phenomena in 2D semiconductor systems. Effect of the linear in the wave vector spin splitting originating from the lack of the center of inversion both in bulk materials (BIA) and heterostructures (SIA) as well as the Zeeman splitting role will be investigated theoretically.

### 2. Effect of $\mathbf{k}$ -linear spin splitting on magnetooscillation phenomena

The linear in the wave vector terms in the Hamiltonian of two-dimensional electron gas are known to result in beats in magnetooscillation phenomena. The  $\mathbf{k}$ -linear terms can be caused by two reasons. First, they originate from the cubic in  $\mathbf{k}$  terms in the bulk material without the inversion center. Averaging of these cubic terms over a growth direction yields the  $\mathbf{k}$ -linear terms, with  $\mathbf{k}$  being the wave vector in the quantum well plane. Besides these contributions, in asymmetrical heterostructures there is another type of  $\mathbf{k}$ -linear terms (Rashba terms). It should be emphasized that the physical nature and the symmetry of BIA and Rashba terms are different, and therefore they can not compensate each other. Moreover the papers [1, 2] showed that the additive summation of these terms also is not correct in weak localization phenomenon and spin relaxation. Below we demonstrate that the beats in the magnetooscillation phenomena disappear when the both  $\mathbf{k}$ -linear terms are of the same efficiency.

In zero magnetic field the corresponding BIA and Rashba contributions to the Hamiltonian of the two-dimensional electron gas have the form

$$\hat{H}_{BIA} = \alpha (\hat{\sigma}_x k_y + \hat{\sigma}_y k_x) \quad (1)$$

$$\hat{H}_R = \beta (\hat{\sigma}_x k_y - \hat{\sigma}_y k_x) , \quad (2)$$

where  $\hat{\sigma}_x$  and  $\hat{\sigma}_y$  are the Pauli matrices, and the crystal coordinate system  $x \parallel [1\bar{1}0]$ ,  $y \parallel [110]$  is used. In the presence of only one term, either (4) or (2), the electron spectrum

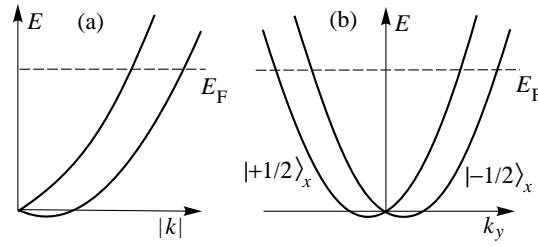


**Fig. 1.** Electron spectrum at zero magnetic field in the presence of the  $\mathbf{k}$ -linear terms. (a) the case of only one, either (4) or (2), term, (b)  $\alpha = \beta$ .

is isotropic and contains of the two different spin branches (see Fig. 1(a)). When the both types of the terms are essential the energy spectrum becomes more complicated, with the electron energy depending on the direction of the wave vector  $\mathbf{k}$ . However if the both terms are of the equal strength,  $|\alpha| = |\beta|$ , the spectrum just consists of two identical spin paraboloids shifted one with respect to the other in the  $\mathbf{k}$ -space. Fig. 1(b) sketches the case of  $\alpha = \beta$  when the spectrum is the spin paraboloids  $|\pm 1/2\rangle_x$  shifted along  $k_y$ .

At low temperatures all states are occupied below the Fermi energy. The frequencies of the oscillations in the magnetic fields are determined by a filling of the branches. As one can see from Fig. 1(a) the populations of the branches are different that leads to the appearance of the beats in the magnetooscillation phenomena. In the case of Fig. 1(b) the filling of the branches is the same and therefore the oscillations occur with the one frequency and no beat pattern is observed. It looks like the mutual compensation of the BIA and Rashba terms takes place in the magnetooscillation phenomena. However it should be emphasized that the  $\mathbf{k}$ -linear contributions do present in the Hamiltonian.

Microscopically, the oscillations are caused and determined by the pattern of the Landau levels in the magnetic field. Figure 2 shows the dependence of the arrangement of the Landau levels on the ratio  $\beta/\alpha$  calculated for the fixed value  $m^*\alpha^2/(2\omega_c\hbar^3) = 0.05$  typical for GaAs/AlGaAs structures in the magnetic field 1 T. Here  $m^*$  and  $\omega_c$  are the effective electron mass and the cyclotron frequency. When  $\alpha = \beta$  the spectrum is a set of the equidistant Landau levels with the energy distance  $\hbar\omega_c$ . It implies that the oscillations occur with the single frequency.

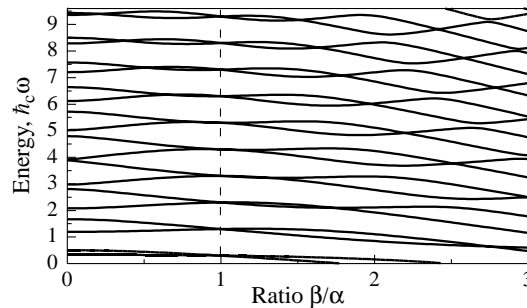


**Fig. 2.** The positions of the Landau levels at various ratio  $\beta/\alpha$  and the fixed field.

### 3. Effect of Zeeman splitting on magnetooscillation phenomena

Besides the diamagnetic (cyclotron) quantization, electron states are split into spin subbands. This Zeeman splitting,  $\Delta_Z$ , is linear in the magnetic field and depends on the  $g$ -factor. Usually in bulk semiconductors  $\Delta_Z$  is much less than  $\hbar\omega_c$  therefore the Zeeman splitting does not affect the oscillations with the small amplitude. A qualitatively new situation arises in two-dimensional systems. Applying the magnetic field tiltedly with respect to the electron gas plane, one has a possibility to change the ratio  $r = \Delta_Z/\hbar\omega_c$  in a wide range because the Zeeman splitting depends on the total magnetic field

$$\Delta_Z = \mu_0 \sqrt{g_{\parallel}^2 B_{\parallel}^2 + g_{\perp}^2 B_{\perp}^2}, \quad (3)$$

while the cyclotron frequency in the case of strong size quantization is defined only by the perpendicular component of the field,  $\omega_c = eB_{\perp}/mc$ . Here  $\mu_0$  is the Bohr magneton,  $g_{\parallel} = g_{xx} = g_{yy}$  and  $g_{\perp} = g_{zz}$  are the tensor of the electron  $g$ -factor,  $B_{\parallel}$  and  $B_{\perp}$  are the magnetic field components parallel and perpendicular to the electron gas plane.

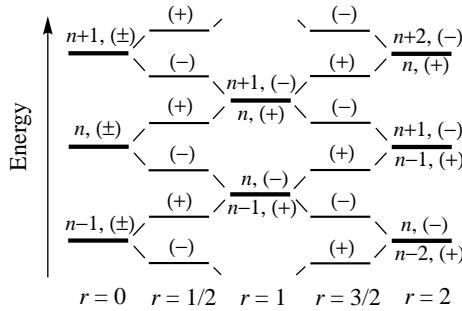


**Fig. 3.** The positions of the Landau levels at different ratio  $r$  and the fixed field.

At the absence of the spin splitting the oscillations occur with the frequency  $\cos(2\pi E_F/\hbar\omega_c)$ , where  $E_F$  is the Fermi energy. The multiple harmonics appear only in the higher fields when the amplitude of the oscillations is not small and just modify the oscillation shape. The Zeeman splitting comparable to the cyclotron energy changes qualitatively the behavior of the magnetooscillation phenomena. In the case of negligible spin relaxation the Zeeman subbands contribute additionally, and hence the oscillation parameters depend on the relative arrangement of the Landau levels from the spin subbands. Figure 3 sketches this arrangement at the fixed value of  $\hbar\omega_c$  and various ratio  $r$ . At half-integer  $r = 1/2, 3/2, \dots$  the Landau levels from the spin subbands coincide, i.e. the Landau levels from the one subband are exactly in the middle of the levels from the other subband. This arrangement leads to the suppression of the main oscillations because the phases of the main harmonic are opposite for the spin subband. Therefore the oscillations occur with the double frequency,  $\cos(4\pi E_F/\hbar\omega_c)$ , where the spin subbands contribute to equally at the half-integer ratio  $r$ . When the value of Zeeman splitting is the multiple of the cyclotron energy,  $r = 1, 2, 4, \dots$ , the coincidence of the Landau levels takes place and therefore the oscillations occur again with main harmonic,  $\cos(2\pi E_F/\hbar\omega_c)$ . However, the positions of the oscillation maxima and minima are different for the odd and even  $r$  because the energy positions of the Landau levels distinguish by the value of  $\hbar\omega_c$  [3].

In conclusion, the spin effects can qualitatively modify the magnetooscillation phenomena in 2D systems. It is shown that BIA and SIA  $k$ -linear terms in the Hamiltonian of 2DEG do not contribute additionally. Moreover, the presence of these terms of similar strengths results in the suppression of the beats in the magnetooscillation phenomena. It is shown that the Zeeman splitting in tilted magnetic fields can lead to the disappearance of the main harmonic and to the appearance of the oscillations with the double frequency.

#### *Acknowledgements*

This work was supported by the Russian Ministry of Science, the RFFI (projects 00-02-16894, 00-02-16997, and 01-02-17528), and by the Science Programme of the Presidium of RAS "Quantum low-dimensional structures".

#### **References**

- [1] F. G. Pikus and G. E. Pikus, *Phys. Rev. B* **51**, 16928 (1995).
- [2] N. S. Averkiev, L. E. Golub and M. Willander, *Fiz. Tekh. Poluprov.* **36**, 97 (2002) [*Semiconductors* **36**, 91 (2002)].
- [3] S. A. Tarasenko, *Phys. Solid State* **44**, (2002).

## Kinetic mechanism of current stratification in two-dimensional structures

*V. Yu. Kachorovskii*<sup>†</sup>, *I. S. Lyubinskiy*<sup>†</sup> and *L. D. Tsendin*<sup>‡</sup>

<sup>†</sup> Ioffe Physico-Technical Institute, St Petersburg, Russia

<sup>‡</sup> St Petersburg State Technical University, 194021 St Petersburg, Russia

**Abstract.** We study the electric field induced current instability in two-dimensional semiconductor structures with respect to formation of charge density wave (CDW). We calculate the increment of the instability and demonstrate that spatial period of the CDW is inversely proportional to the electric field.

### Introduction

In the present work we discuss stratification of current, associated with the formation of a charge-density wave (CDW) with a period depending on the electric field. Similar effects are known in the plasma physics [1] and were observed already by Faraday (see for review [2–4]) However, the understanding of the simplest striations forms was achieved only in the last decades. The main reason consists in the great diversity of the striations modes. In particular, there exist so called hydrodynamic [1, 5] and kinetic strata [6]. In contrast to hydrodynamic strata which can be described in terms of local macroscopic parameters (electron density, drift velocity, and local electron temperature), the kinetic strata do not allow macroscopic description even on the qualitative level. The hydrodynamic approach is valid only at rather high electron concentration, when the collisions between the electrons are frequent enough to restore the local Maxwellian distribution of the majority of electrons. However, at small concentrations and strong electric field the hydrodynamics description turn out to be totally wrong and the nonlocal kinetic description becomes necessary.

The hydrodynamic strata in semiconductors were investigated in many works (see for review [5]). In the present work we focus on kinetic mechanism of current stratification in semiconductors. To our knowledge, this issue was not discussed in literature.

### Kinetic mechanism of stratification

The first theoretical attempt to investigate kinetic strata in plasma was presented in Ref. [6]. The idea was put forward that in the presence of two mechanisms of inelastic scattering (strong scattering with large energy transfer  $W_0$  and weak quasielastic scattering) the current in plasma is unstable with respect to formation of periodic structure having spatial period  $L = W_0/F_0$ , where  $F_0/e$  is driven electric field and  $e$  is electron charge. In the present work we demonstrate that this mechanism of stratification can be realized under certain conditions in low-dimensional semiconductor structures as well. The conditions for realization of the effect are similar to those in gases. The main requirement, the presence of two kinds of inelastic scattering, is usually satisfied, the scattering by optical phonons with energy  $W_0$  and scattering by acoustic phonons playing the role of strong inelastic and weak quasielastic energy relaxation mechanisms, respectively.

Let us consider the motion of an electron driven by external force  $F_0$  neglecting for a moment inelastic scattering by optical phonons as well as scattering by acoustical phonons. Thus, the only scattering mechanism is elastic impurity scattering which leads to diffusion in coordinate space. As far as energy relaxation processes are “turned off” the electron heated by the field  $F_0$  will also diffuse over kinetic energy axis. This diffusion is evidently correlated with diffusion in coordinate space, since the full electron energy  $E = W - F_0 z$  is conserved (here  $W$  is electron kinetic energy). Saying by other words, the electron diffuses in  $(z, W)$  space along the line  $E = \text{const}$ . While the optical phonon scattering is taken into account, the electron motion is restricted by a shell  $0 < W < W_0$  (we assume here, that lattice temperature  $T_0$  is small compared to  $W_0$ ). Reaching the point  $W = W_0$  electron loses energy  $W_0$  and continues the diffusive motion with the energy  $E - W_0$ . A trajectory of the electron in the space  $(E, z)$  looks like “stair” with the height of step equal to  $W_0$ . Finally, let us introduce the acoustic phonons scattering, assuming for simplicity that  $T_0 = 0$ . In this case the interaction with acoustic phonons leads to decreasing of electron energy with the rate  $\kappa$  due to emission of the phonons. (one can show that for 2d system the rate of the energy losses  $\kappa$  does not depend on kinetic energy).

There are three different time scales in our problem: the transport scattering time  $\tau_{tr}$ , the characteristic time of electron heating by electric field  $\tau_0 \sim L^2/D_0$  (here  $D_0 = W_0 \tau_{tr}/M$  and  $M$  is electron effective mass), and the time  $W_0/\kappa$  which characterizes temp of energy losses due to emission of acoustic phonons. We will assume that

$$\tau_{tr} \ll \tau_0 \ll \frac{W_0}{\kappa}. \quad (1)$$

Considering the electron motion on the time scales larger than  $\tau_0$  we may deal with “stair” electron trajectories instead of dealing with individual electrons. Inequality (2) provides that acoustic phonon scattering may be considered as a small perturbation. Due to this scattering the “stair” diffusive trajectories move slowly down (along axis  $E$ ) with velocity  $\kappa$ . This means at the same time, that the trajectories slowly drift with the velocity  $s_0 = \kappa/F_0$  along axis  $z$ . Since  $s_0$  is inversely proportional to driven field, one may say that the motion of the trajectories demonstrates the negative differential mobility. It is well known, that negative differential mobility should lead to the current instability. We will see that this really happens in 2D gas under some conditions. However, our case is more complicated compared to usual Gunn instability, since we consider the motion of diffusive trajectories instead of motion of individual electrons. As for latter ones, their averaged drift velocity obeys usual Ohm’s law  $v_{dr} = F_0 \tau_{tr}/M$  and it is much larger than  $s_0$ . The fact that instability can be observed in the Ohm’s law regime indicates that the effect is purely kinetic and can not be described on the basis of macroscopic parameters.

### Basic equations

Next we consider the motion of an electron in the potential  $U(z, t)$  which includes self-consistent potential created by other electrons as well as external potential  $U_0(z) = -F_0 z$ . We argue that stationary dc solution with  $U = U_0$  is unstable with respect to formation of CDW with the spatial period  $L = W_0/F_0$ .

The most convenient variables in the problem are  $(E, z, t)$ , where  $E = W + U(z, t)$  is a full energy of the particle. The motion of the particle with a given energy  $E$  is restricted by the coordinates  $z = z_1(E, t)$  and  $z = z_2(E, t)$ , where functions  $z_1$  and  $z_2$  should be found from the conditions  $E = U(z_1, t)$  and  $E = W_0 + U(z_2, t)$ , correspondingly. One

can show that the propagation along energy axis is governed by continuity-like equation

$$\frac{\partial N}{\partial t} + \frac{\partial}{\partial E} \left( N \left[ \left\langle \frac{\partial U}{\partial t} \right\rangle - \kappa \right] \right) = J_{E+W_0} - J_E. \quad (2)$$

Here  $N = \int_{z_1}^{z_2} dz f(z, E, t)$  is electron density over energy axis,  $f(z, E, t)$  is isotropic part of electron distribution function, and angle brackets denote averaging over  $z$

$$\left\langle \frac{\partial U}{\partial t} \right\rangle = \frac{1}{N} \int_{z_1}^{z_2} dz \frac{\partial U}{\partial t} f(z, E, t). \quad (3)$$

The quantity  $J_E$  entering right-hand side of Eq. (2) represents the flux related to optical phonon emission in the point  $(E, z_2(E), t)$ .

We search the solution for self-consistent potential in the following form  $U - U_0 = \delta U \exp(-i\omega t + iqz)$ . This choice determines the energy dependence of quantities  $J_E$ ,  $N$  as follows  $J_E - J_0 = \delta J \exp(-i\omega t - iqE/F_0)$ ,  $N - N_0 = \delta N \exp(-i\omega t - iqE/F_0)$  (here  $J_0$  and  $N_0$  correspond to stationary solution). We demonstrate that for  $q \approx q_m = 2\pi m/L$  (where  $L = W_0/F_0$  and  $m = 1, 2, \dots$ ) the imaginary part of  $\omega$  is positive which implies that stationary solution of Eq. (2) is unstable. One can show that the maximal values of instability increment are reached for  $q = q_m$ . For such values of  $q$  the solution is periodic over energy with the period  $W_0$  and the right-hand side of Eq. (2) is equal to zero. Then linearization of Eq. (2) yields

$$\omega_m = s_m q_m, \quad s_m = \frac{\kappa}{F_0 + \Delta F_m} \quad (4)$$

where  $\Delta F_m$  is defined as  $\Delta F_m = N_0 \langle \delta F_m \rangle / \delta N_m = -iq_m N_0 \langle \delta U_m \rangle / \delta N_m$  (the subscript  $m$  implies that all quantities are taken at  $q = q_m$ ). We see that the physics of the problem is governed by the only parameter  $\langle \delta U_m \rangle / \delta N_m$  which has a transparent physical meaning as a response of the averaged self-consistent potential with respect to a small variation of electron density in energy space. This parameter depends on the character of electron-electron interactions in a concrete system. One can expect, however, that increasing of the electron density in a given region of energy space leads to increasing of the electron concentration in coordinate space and, correspondingly, to increasing of electrostatic potential. This hints that  $Re \langle \delta U_m \rangle / \delta N_m > 0$  and, as a consequence,  $Im(\omega_m) > 0$ . Note, that the coefficient between  $\omega_m$  and  $q_m$  can be interpreted as a velocity of propagation of  $m$ -th harmonic of self-consistent potential in the direction of axis  $z$ . What was of crucial importance for our qualitative arguments that this velocity is inversely proportional to the electric field (see Eq. (4)) demonstrating some kind of “negative differential mobility”.

In order to find the key parameter  $\Delta F_m$  one should solve linearized Boltzmann equation together with Poisson equation. The analytical solution can be found for the case when interaction with optical phonons is very strong (“black wall” boundary conditions for  $W = W_0$ ). For  $q \approx q_m$  the instability spectrum looks as follows

$$\omega(q) = \omega_m + (q - q_m)v_{dr} - i \frac{D^*}{4} (q - q_m)^2, \quad (5)$$

where  $D^* \approx D_0$  and

$$\omega_m = s_0 q_m + i \frac{\kappa}{W_0} \frac{\lambda_m |\alpha_m|^2}{1 + \lambda_m \alpha_m}. \quad (6)$$



Here  $\alpha_m = \int_0^L dy(1 - \exp(iq_my))/y$ ,  $\lambda_m = 2\pi e^2 n_0 / \epsilon q_m W_0$ , and  $n_0$ , and  $\epsilon$  are stationary concentration and dielectric constant respectively.

It is easy to check that  $Im(\omega_m) > 0$  for any  $m$ . Thus, for  $q = q_m$  the stationary solution is unstable. Eq. (5) implies that instability exists only in small regions of  $q$  near points  $q_m$ . This instability leads to formation of periodic in space structure with the period  $L$ .

The instability increment,  $Im(\omega_m)$ , is proportional to the rate of the energy losses  $\kappa$  which can be calculated in a usual way (see Ref. [7]). The result is given by  $\kappa = C_0^2 \pi^2 M / \rho a^3 \hbar$ . Here  $C_0$  is deformation potential constant,  $\rho$  is the density of the crystal, and  $a$  is a quantum well width. We see that  $\kappa$  rapidly increases with decreasing of  $a$ . As a result, the instability increment increases with decreasing  $a$  (see Eq. (6)). The critical value of  $a$  is determined from the condition  $Im(\omega_m) > 1/\tau_{ee}$ , where  $\tau_{ee}^{-1} \sim e^4 n_0 / \epsilon^2 \hbar W_0$  is the inverse characteristic time of scattering of hot electrons with characteristic energy  $W_0$ .

We conclude, that stratification of current in accordance with the mechanism described above can be observed in rather thin quantum wells with relatively low electron concentration.

### Acknowledgements

This work was supported by the INTAS and the RFBR.

### References

- [1] Yu. P. Raizer, *Physics of Gas Discharge*, Springer, Heidelberg (1990).
- [2] N. L. Oleson and A. W. Cooper, *Adv. Electronics Electron Phys.* **24**, 155 (1968).
- [3] A. V. Nedospasov, *Sov. Phys. - Usp.* **11**, 174-187, (1968).
- [4] L. Pekarek, *Sov. Phys. - Usp.* **11**, 188-208, (1968).
- [5] B. S. Kerner and V. V. Osipov, *Autosolitons*, Moscow, Nauka 1991.
- [6] L. D. Tsendin, *Sov. Phys. - Plasma Phys.* **8**, 96-109; **8**, 228-233 (1982).
- [7] F. G. Bass and Yu. G. Gurevich, *Hot electrons and strong electromagnetic waves in the plasma in semiconductors and gas discharge*, Moscow, Nauka 1975.

## Many-body lines in tunneling spectra of Al/ $\delta$ -GaAs junctions near resonant polaron threshold

*I. N. Kotel'nikov*<sup>†‡</sup>, S. E. Dizhur<sup>†</sup> and F. V. Shtrom<sup>†</sup>

<sup>†</sup> Institute of Radioengineering and Electronics, RAS, 101999 Moscow, Russia

<sup>‡</sup> International Laboratory of High Magnetic Fields and Low Temperatures,  
53-421 Wroclaw, Poland

**Abstract.** A remarkable change of LO-phonon line for tunneling from metal to 2DEG, in comparison with 3D-case, was observed. It was shown that the line shapes and the amplitudes of LO-phonon and zero-bias anomaly in tunneling spectra of Al/ $\delta$ -GaAs junctions depended on magnetic field in-plane of the 2DEG. The parameters of the lines were changed when the threshold for resonant intersubband polaron in  $\delta$ -layer was exceeded.

Last years extensive investigations of polaron effects in 2D systems have been carried out [1–3]. An important feature of these studies was the observations of resonant polaron (or magnetopolaron) effects in the high density quasi-2D system where the screening of the electron–LO-phonon interaction was predicted. In Al/ $\delta$ -GaAs tunnel junctions [3], the many-body features in the tunneling spectra (TS) have been found: a zero-bias anomaly (ZBA) near  $U = 0$  and LO-phonon lines (PhLs) at the bias  $eU = \pm \varepsilon_{\text{LO}}$ , where  $\varepsilon_{\text{LO}} \simeq 36.5$  meV is LO-phonon energy in GaAs. In 3D-case (Me/n-GaAs tunnel junctions), the PhLs have been described by the real part of the self-energy, which enter the  $E(k)$  relation of 3D-electron in the bulk of GaAs [4]. The logarithmic singularities in the self-energy, which is a result of the polaron interaction in GaAs, lead to antisymmetric (about  $U = 0$ ) structures in tunneling conductance at  $eU = \pm \varepsilon_{\text{LO}}$ . It has been shown in [5] that the PhLs at negative and positive bias have different the temperature and magnetic field dependencies. As a result, model [4] needs to be refined. There are no such studies of the PhLs in 2D tunneling systems. It may be expected that the change of the electron spectrum in 2D-case permits to get a new information about the self-energy polaron effects. In Al/ $\delta$ -GaAs tunnel junctions, for instance, the energy position of 2D-subbands may be changed by the magnetic field or by the persistent tunneling photoconductivity effect, and the resonant conditions for intersubband polaron interaction may be realized in both cases [3, 6].

The tunnel junctions with 3D-(Au/n-GaAs) and 2D-electron gas (Al/ $\delta$ -GaAs) were prepared in IRE RAS on semi-insulating (100) GaAs substrates by the method of molecular beam epitaxy [7, 3]. The method of analysis of the 2D-subband features in TS is described in [3].

Figure 1 demonstrates the TS for 3D- and 2D-cases. The TS for 2D-junctions have more complicate structure because of the size quantization in GaAs  $\delta$ -layer. The smooth minima in TS on  $eU$  scale correspond to the subband energies of 2DEG: the occupied ( $U > 0$ ) ground state energy  $E_0$  is a minimum of TS at  $eU \simeq 40$  meV and the unoccupied ( $U < 0$ ) subband  $E_1$  lies at  $eU \simeq -18$  meV. Others unoccupied subbands are beyond the scale of Fig. 1. It can be seen that the shapes of ZBA and  $\text{PhL}^+$  are almost independent on dimensionality of the electron gas in GaAs, but the shape of  $\text{PhL}^-$  ( $U < 0$ , tunneling from

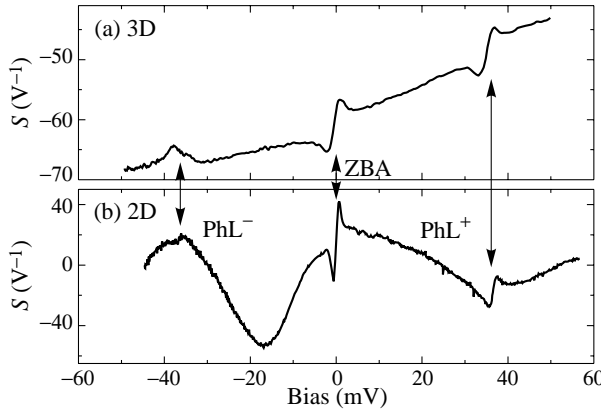


**Fig. 1.**  $S = d \ln \sigma / dU$  (or TS) as a function of the bias voltage  $U$  on the junction at  $B = 0$ . (a) TS of 3D-electron gas in Schottky-barrier Au/n-GaAs junction ( $n \simeq 3 \times 10^{18} \text{ cm}^{-3}$ ),  $T = 4.2 \text{ K}$ . (b) TS of 2DEG in Al/ $\delta$ -GaAs junction ( $n_{2D} \simeq 1 \times 10^{12} \text{ cm}^{-2}$ ) at  $T = 1.6 \text{ K}$ . Arrows point on  $\text{PhL}^-$ , ZBA and  $\text{PhL}^+$  positions.

metal to GaAs) is not. The distinction between  $\text{PhL}^-$  for 3D- and 2D-cases is clearly seen in Fig. 2, which shows the many-body features in TS after background subtraction.

Note that the shapes of PhLs for Al/ $\delta$ -GaAs are the self-energy type in contrast to inelastic phonon emission which leads to “peak” or “dip” in TS. PhLs in our samples are almost antisymmetric in  $(1/\sigma)(d\sigma/dU)$  about  $U = 0$  that gives the symmetric structure in  $\sigma = dI/dU$  — “dips” at  $eU = \pm \varepsilon_{\text{LO}}$ . The self-energy effects [4] must give a “peak” and “dip” at negative and positive bias respectively. When the in-plane magnetic field increases, the successive transformation of  $\text{PhL}^-$  from self-energy type to inelastic type

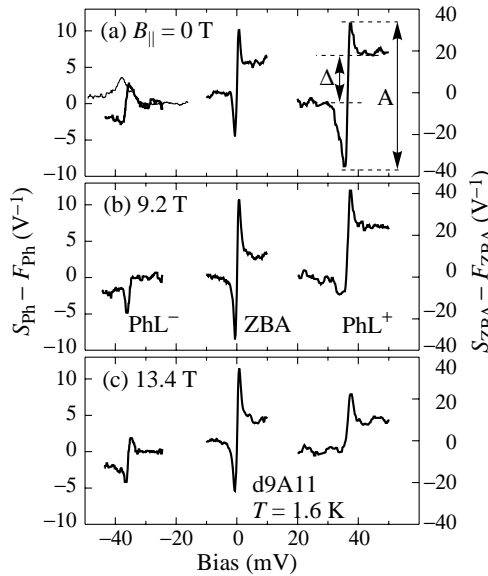


**Fig. 2.** Shapes of the  $\text{PhL}^-$ , ZBA and  $\text{PhL}^+$  at various magnetic fields in-plane of 2DEG. Thin curve on (a) shows  $\text{PhL}^-$  for the Au/n-GaAs junction at  $T = 4.2 \text{ K}$ .

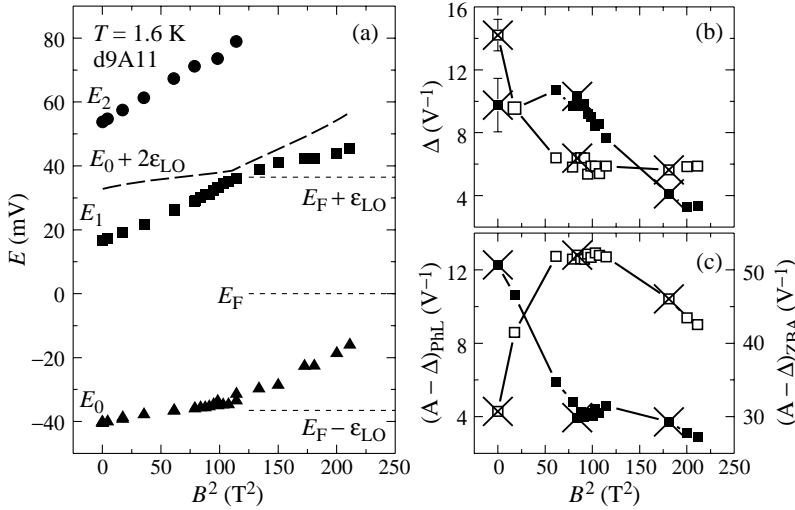


**Fig. 3.** (a) Subbands energies  $E_i$  (calculated from TS) vs. square of the magnetic field  $B^2$  in-plane of the 2DEG. Three first subbands shown. There are pinning and anticrossing for the terms  $E_1$  and  $E_0 + 2\epsilon_{LO}$  (dashed line). (b) Jumps  $\Delta$  and (c) amplitudes  $A - \Delta$  (see Fig. 2) of the many-body features in TS (ZBA — opened squares and PhL<sup>+</sup> — closed squares) as functions of  $B^2$ . Crossed symbols correspond to magnetic fields for lines shown in Fig. 2.

of line is observed as shown in Fig. 2(b). The sharp change PhL<sup>+</sup> back to the self-energy type was found when  $B$  exceeded the threshold  $B_c \simeq 11$  T (Fig. 2(a)). The phonon line at  $U < 0$  changes its shape on PhL<sup>+</sup> and *vice versa* in this case.

The  $B_c$  is a threshold field for resonant intersubband polaron interaction [3] in our sample. The picture of 2D-subbands behaviour in magnetic field is shown in Fig. 3. Here  $E_i$  is measured from Fermi level in GaAs. For the illustration of shape change in the many-body lines we used the value  $\Delta$  of the character “jump” and the amplitude of line calculated as  $A - \Delta$  (see Fig. 2(a)). The latter characterize the depth of “dip” in tunneling conductance. The dependencies of  $\Delta$  and  $A - \Delta$  on magnetic field are shown in Fig. 4 for ZBA and PhL<sup>+</sup>. It may be seen that both values ( $\Delta$  and  $A - \Delta$ ) change their behavior near the threshold  $B_c$ .

Thus, the data obtained show that the many-body lines in TS of Me/GaAs junction depend on the electron spectrum in GaAs. It concerns both the transition from 3D to 2D (only one line — PhL<sup>+</sup>) and the one-particle (in-plane medium magnetic field in 2D-case for PhL<sup>+</sup>) or quasi-particles spectrum transformation at the resonant polaron interaction (near  $B_c$  for all three lines).

For tunneling from metal to 2DEG ( $U < 0$ ), there are two subbands for an electron transfer in our case. The self-energy effects in the occupied subband  $E_0$  should renormalize  $E_1(k_{||})$  too. It may result in the PhL transformation in comparison with 3D-case. The importance of the electron tunneling transfer to  $E_1$  proved by the behavior of the PhL<sup>+</sup> at  $B < B_c$  when the transition from self-energy type to inelastic type of line is observed (Fig. 2(a) and 2(b)). Such transformation occurs at the magnetic fields when the magnetic length  $l_B = 8$  nm is close to the extent of the wave function for  $E_1$  state in the direction of tunneling. In fields exceeding the resonant polaron threshold, the self-energy effects should change drastically and the behavior of PhLs confirms it. The old model [4] should be refined for this case.

Note that the decrease of ZBA amplitude at  $B > B_c$  relates with its broadening. This effect may be described on the basis of the exchange-correlation model of ZBA [7] if we take into consideration the increase of the electron effective mass under the resonant polaron conditions.

#### *Acknowledgements*

We are grateful to V. A. Volkov for useful discussions. This work was supported by RFBR and Russian Federal Programs SAS, FTNS.

#### **References**

- [1] G. D. Hai, F. M. Peeters, N. Studart, Y. J. Wang and B. D. McCombe, *Phys. Rev B* **58**, 7822 (1998).
- [2] Y. J. Wang, Y. A. Leem, B. D. McCombe, X.-G. Wu, F. M. Peeters, E. D. Jones, J. R. Reno, X. Y. Lee and H. W. Jiang, *Phys. Rev. B* **64**, 161303(R) (2001).
- [3] I. N. Kotel'nikov, V. A. Kokin, Yu. V. Fedorov, A. V. Hook and D. T. Talbaev, *JETP Lett.* **71**, 387 (2000).
- [4] J. W. Conley and G. D. Mahan, *Phys. Rev.* **161**, 681 (1967).
- [5] A. Ya. Shul'man and I. N. Kotel'nikov, *Proc. 12th Int.Conf. High Magn. Fields in Phys. Semicond. (1996)*, World Scient. Publ., Singapore, 1997, vol. 1, p. 461.
- [6] I. N. Kotel'nikov and S. E. Dizhur, *Proc. 9th Int. Symp. Nanostr.: Physics and Technology (St Petersburg 2001)*, Ioffe Institute, St Petersburg, 2001, p. 286.
- [7] A. Ya. Shul'man, I. N. Kotel'nikov, N. A. Varvanin and E. N. Mirgorodskaya, *JETP Lett.* **73**, 573 (2001).

## The breakdown of the integer quantum Hall effect: a microscopic model with a hydronamical analogy

A. M. Martin, *L. Eaves* and K. A. Benedict

School of Physics and Astronomy, University of Nottingham,  
Nottingham, NG7 2RD, U.K.

**Abstract.** In samples used to maintain the US resistance standard the breakdown of the dissipationless integer quantum Hall effect occurs as a series of dissipative voltage steps. A mechanism for this type of breakdown is proposed and a parameter-free microscopic model is presented. In this model we calculate the rate of generation of electron-hole pairs due to charged impurity scattering and develop a simple, self-consistent, model for their motion. We thereby determine the rate of pair production and the size of the voltage steps. We then draw an analogy between this type of breakdown and vortex anti-vortex pairs formed behind a stationary obstacle in a flowing fluid.

### Introduction

In the integer quantum Hall effect regime, a two-dimensional electron fluid carries an almost dissipationless current and the ratio of the current,  $I_x$ , to the Hall voltage,  $V_H$ , is quantized in units of  $e^2/h$ . However, above a critical current value, the dissipative voltage,  $V_x$ , measured along the direction of current flow increases rapidly, leading to quantum Hall breakdown. In certain experiments, including those on the US resistance standard samples at the National Institute of Standards and Technology (NIST) [1], breakdown occurs as a series of up to twenty regular steps in  $V_x$ . This is fundamentally different from the conventional type of breakdown where one observes a single sharp increase of the longitudinal magnetoresistance.

We develop a theoretical model to account for the dissipative steps observed by the NIST group and others. We show that, in the presence of charged impurity-induced disorder, the quantum Hall fluid (QHF) is unstable when the local fluid velocity exceeds a critical value. Under these conditions, electron-hole (e-h) pair excitations (referred to as magneto-excitons) are generated spontaneously in the vicinity of the impurity. The voltage step height,  $\Delta V_x$ , is directly related to the rate of formation of the pairs, which we calculate using a model with no free parameters. We show that this type of excitation in the QHF is analogous to vortex-antivortex pair formation in classical or quantum fluid flow around an obstacle [2].

### 1. Microscopic model

The model we present can be formulated in two distinct parts. First we consider the magneto-excitation dispersion curve. This allows us to calculate, for a given electric field, at what value of the exciton wavevector it costs no energy to create e-h pairs. Secondly, we calculate the rate of generation of such excitations due to a single charged impurity. We then combine these two elements of the microscopic model using a simple model for the motion of the excitations and a self-consistent description of the electric field in the vicinity of the charged impurity.

### 1.1. Magneto-exciton dispersion

Following [3], the magneto-exciton energy is

$$\xi_{n\sigma, (n+1)\sigma'}[Q, E_y] = \epsilon_{(n+1)\sigma', (k+Q)}[E_y] - \epsilon_{n\sigma, k}[E_y] + \frac{e^2}{4\pi\kappa a_L} \Delta_{n\sigma, (n+1)\sigma'}[Q], \quad (1)$$

where  $a_L = \sqrt{\hbar/eB}$  is the magnetic length,  $\kappa$  is the dielectric constant,  $Q$  is the wavevector of the exciton,  $\epsilon_{n\sigma, k}[E_y]$  and  $\epsilon_{(n+1)\sigma', (k+Q)}[E_y]$  are the energies of the initial and final states respectively and  $E_y$  is the local electric field. The function  $\Delta_{n\sigma, (n+1)\sigma'}[Q]$  includes the exchange and Coulomb local-field corrections, which are independent of the electric field. In what follows we focus on the case when  $\sigma = \sigma'$  and hence we drop the spin notation. For Eq. (1) in the presence of an electric field we find

$$\epsilon_{(n+1), (k+Q)}[E_y] - \epsilon_{n, k}[E_y] = \hbar\omega_c - eE_y a_L (a_L Q). \quad (2)$$

Substituting Eq. (2) into Eq. (1) it is clear that for a finite electric field it is possible to find a value of  $a_L Q$  for which  $\xi_{n, (n+1)}[Q, E_y] = 0$ .

### 1.2. Scattering from an impurity

From the above it is possible to ascertain, for a given electric field, at what wavevector,  $Q$ , it costs no energy to generate an e-h pair. However, the states are orthogonal so, for the perfect system considered above, although their may well be an overlap between the wavefunction in the occupied Landau level and the unoccupied Landau level the scattering rate into the excited state will be zero. Hence, we consider the scattering rate between the two Landau levels due to the presence of a charged impurity. Following earlier work [4] we find

$$W_{0\sigma, 1\sigma} + W_{0\sigma', 1\sigma'} = W_{0,1} = \frac{4NB}{E_y} L_y \left[ \frac{e^2}{8\pi^2\kappa\hbar} \right]^2 \left| \int_{\bar{q}} d\bar{q} \frac{i\bar{q} - \alpha}{\bar{q} + \bar{q}_s} e^{-\frac{1}{4}(\alpha^2 - 2i\alpha\bar{q} + \bar{q}^2)} \right|^2, \quad (3)$$

where  $\alpha = Qa_L$ ,  $\bar{q} = q_x a_L$ ,  $\bar{q}_s = q_s a_L$ ,  $q_s$  is the screening parameter,  $L_y = V_H/E_y = I_x R_H/E_y$  and  $R_H = h/2e^2$ .

### 1.3. Model and results

Consider a local region of the sample for which, due to the proximity of an edge and the presence of a nearby charged impurity, the background electric field  $E_y$  is large enough to create e-h pairs, via scattering from an impurity, at a rate given by Eq. (3). Once an e-h pair is formed, it acts to screen electrostatically the local electric field around the impurity. The pair then moves away from the impurity, at velocity  $v$  (determined by the derivative of the magneto-exciton dispersion curve), hence generating a weaker screening electric field at the impurity. Eventually the total electric field, in the vicinity of the charged impurity is restored to a sufficiently large value to generate the next e-h pair. From this we obtain a self-consistent loop as follows. Consider a background electric field  $E_y$ ; for this field we use Eq. (1) to determine  $Qa_L$ . From this we calculate a rate ( $W_{0,1}$ ), given by Eq. (3). In conjunction with the velocity at which the e-h pair moves away from the charged impurity this rate gives us the separation ( $x_c$ ) between the generated e-h pairs. Using  $x_c$  we can obtain the screening field, at the impurity generated by a stream of e-h pairs. This in turn determines a new field  $E'_y = E_y - E_{\text{total}}^S$ . We then repeat the process replacing  $E_y$  with  $E'_y$  to find a new screening field ( $(E_{\text{total}}^S)'$ ) and hence a new total electric field  $E''_y = E_y - (E_{\text{total}}^S)'$ .

This process is repeated until a stable solution is found. Once a stable solution has been found with a given  $W_{0,1}$  we can determine the voltage drop along the sample as a function of  $E_y$ . As an e-h pair moves away from the impurity the separation of the pair also increases; i.e. due to phonon emission processes, the electron moves away from the edge where it was created towards the opposite edge of the sample and the hole thermalizes at the chemical potential at the edge. Hence, we can use  $W_{0,1}$  to deduce the strength of the dissipative current flowing across the Hall equipotentials. This gives, at  $\nu = 2$ ,

$$V_x = eW_{0,1} \left( \frac{h}{2e^2} \right). \quad (4)$$

We now compare the results of our model with two sets of experimental data which show a clear and regular series of breakdown voltage steps. The experiments of the NIST group on IQHE breakdown in the US resistance standard samples [1] were carried out on a two-dimensional electron system at  $\nu = 2$  and  $B = 12.26$  T. In Fig. 1 we have plotted the dissipative voltage as a function of the background electric field  $E_y$  (solid line).

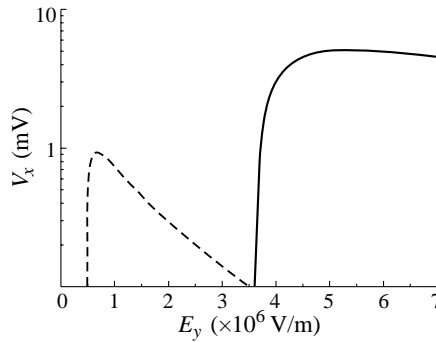


**Fig. 1.** The calculated dissipative voltage as a function of the background electric field,  $E_y$ , for an electron gas (solid line) and a hole gas (dashed line). The parameters used refer to the experimental conditions of Ref. [1] for the electron gas and Ref. [5] for the hole gas.

Recalling that  $V_x \propto W_{0,1}$  we can see that the rate of production of e-h pairs rapidly increases at a *critical* electric field. For a given  $E_y$ , for which the rate of production of e-h pairs is finite, a pair formed close to the edge will relax, i.e. the electron in the upper Landau level will relax its energy by moving towards the center of the Hall bar. This process tends to screen the Hall field in the central regions of the Hall bar. Since the Hall voltage in the NIST experiments remains constant at its quantized value when the dissipative steps occur, this screening effect tends to enhance the electric field near the edges of the Hall bar. Thus, as the *critical* electric field is reached,  $W_{0,1}$  increases rapidly, inducing an increase in  $E_y$ . For breakdown at a single charged impurity we therefore expect the system to switch between two stable states, corresponding to  $V_x = 0$  and  $V_x \approx 5$  mV. In the NIST experiments a series of steps is observed, we attribute each step to the formation of a stream of e-h pairs by other charged impurities.

It is also possible to predict the voltage step height for the breakdown of a hole gas QHF, where the observed voltage steps were considerably smaller,  $\Delta V_x \approx 1$  mV [5]. For this experiment, performed at  $B = 2.1$  T and  $\nu = 2$ , our model predicts  $\Delta V_x = 1$  mV (dashed line in Fig. 1), in good agreement with experimental data.



## 2. Hydronamical analogy

Below we show how an analogy between the above microscopic model and the breakdown of laminar fluid flow in classical fluid can be drawn [2]. For a classical fluid it is possible to write down the kinetic energy associated with a vortex as  $\xi \approx \rho K^2/4\pi$  where  $\rho$  is the density of the fluid and  $K$  is the circulation. Now consider a quantum fluid where the quantum of circulation is  $K_q = h/m$  then  $\xi = \frac{\hbar e B}{m} = \hbar \omega_c$ . From this it is clear that the energy required to generate an excitation is  $\hbar \omega_c$ . Now examining Eq. (1) we see that in the absence of interactions and electric field the energy required to generate e-h pairs is  $\hbar \omega_c$ . Now including the electric field term, but still neglecting the interactions we see that the condition to generate e-h pairs, at zero energy, is  $\hbar \omega_c - e E_y a_L (a_L Q) = 0$ . If we assume that  $a_L Q$  must be small enough such that there is an overlap between the wavefunctions in the two Landau states we find  $a_L Q \approx 2.5$ . From this it is possible to see how an analogy may be formed between e-h pair formation at the breakdown of the IQHE and vortex-antivortex pair formation in a classical fluid.

## References

- [1] C. F. Lavine, M. E. Cage and R. E. Elmquist, *J. Res. Nat. Inst. Stand. Technol.* **99** 757 (1994).
- [2] L. Eaves, *Physica B* **298** 1 (2001).
- [3] I. V. Lerner and Yu. E. Lozovik, *Sov. Phys. JETP* **51** 588 (1980);  
C. Kallin and B. I. Halperin, *Phys. Rev. B* **30** 5655 (1984);  
A. H. MacDonald, *J. Phys. C* **18** 1003 (1985).
- [4] C. Chaubet, A. Raymond and D. Dur, *Phys. Rev. B* **52** 11178 (1995).
- [5] L. Eaves *et al*, *Physica E* **6** 136 (2000).

## Pinning of Landau levels in open two dimensional electron systems

V. G. Popov<sup>†</sup>, Yu. V. Dubrovskii<sup>†</sup>, E. E. Vdovin<sup>†</sup>, Yu. N. Khanin<sup>†</sup>,  
J.-C. Portal<sup>‡§¶</sup>, D. K. Maude<sup>¶</sup>, T. G. Andersson<sup>||</sup> and S. Wang<sup>||</sup>

<sup>†</sup> Institute of Microelectronics Technology RAS, Chernogolovka 142432, Russia

<sup>‡</sup> Institut Universitaire de France, 103, Boulevard Saint-Michel,  
75005 Paris, France. <sup>§</sup> INSA, F31077 Toulouse Cedex 4, France

<sup>¶</sup> Grenoble High Magnetic Field Laboratory,  
MPI-CNRS, BP166 38042 Grenoble Cedex 9, France

<sup>||</sup> Chalmers University of Technology and Göteborg University,  
Department of Physics, S-412 96 Göteborg, Sweden

**Abstract.** Electron tunnelling between two dimensional electron systems of different electron concentration in magnetic field normal to the layers have been studied. Parallel 2DES were separated from each other by  $\text{Al}_{0.3}\text{Ga}_{0.7}\text{As}$  barrier and from highly doped  $n^+$ -GaAs contact regions by undoped GaAs-layers. In our samples each of the 2DES and adjacent contact region were in thermodynamic equilibrium provided by free carrier exchange. The measured I-V dependencies demonstrated pronounced resonant features arising when ground states of the 2DES's were adjusted by external bias. The magnetic field shifted resonant peak position. The shift on the voltage scale was linear versus magnetic field, but exhibited discontinuity in particular magnetic fields. The Landau levels pinning in the 2DES's by chemical potential in the contact region explains the experimental findings.

## Introduction

Commonly employed consideration of the two dimensional system as the system with constant electron concentration was enough successful to explain a lot of properties of two-dimensional systems in a magnetic field including integer and fractional quantum Hall (IQHE and FQHE) effects. In contrast to describe double electron systems one has to take into account essential electrons redistribution between the layers with magnetic field variation. The system where variation of the electron concentration is crucial, hereafter we call open electron system. One could expect that in magnetic field chemical potential pins Landau levels in double 2DES's with different electron concentration and the pinning manage the electron redistribution between the layers. This was observed using photoluminescence spectroscopy in studies of two 2DES separated by a tunnel barrier [1].

In this work we report the studies of the tunnelling between two 2DES's with different electron concentration in the structure with pure vertical transport, i.e. the electron transport along the layers was excluded in our samples. Parallel 2DES were separated from each other by thick  $\text{Al}_{0.3}\text{Ga}_{0.7}\text{As}$  barrier and from highly doped  $n^+$ -GaAs contact regions by undoped GaAs-layers. The Landau levels pinning in the 2DES's by chemical potential in the adjacent contact regions explains evolution of the tunnel characteristics with magnetic field.

## Experiment and discussion

Tunnel diodes under investigation were made on the base of a single barrier GaAs/Al<sub>0.3</sub>Ga<sub>0.7</sub>As heterostructure with modulated doping profile. The diodes represented cylinders with 70  $\mu\text{m}$  diameters prepared by conventional photolithography and wet etching techniques. The conduction band bottom profile is shown in Fig. 1(a).

Figure 1(b) shows the current-voltage characteristics of the diode in different magnetic fields normal to the 2DES's. The current peak and shoulder have been observed without magnetic field at bias voltage  $V_{b1} = 7.4$  mV and  $V_{b2} = -15.2$  mV accordingly. The features is related to electron resonant tunnelling between 2DES's when the 2D bound-state energies in the layers coincide. The ground bound-states (see Fig. 1(a)) coincides ( $E_{01}(V_{b1}) = E_{02}(V_{b1})$ ) at 7.4 mV and we mark this condition as 0–0 resonance. At  $V_{b2} = -15.2$  mV the condition  $E_{01}(V_{b2}) = E_{12}(V_{b2})$  is satisfied and electrons resonantly tunnel between 2D ground bound-state and first excited bound-state (0–1 resonance).

With magnetic field increase the current peak shifts as shown in Fig. 1(b). The shift of the peak means the variation of the 2D bound-state energies. The magnetic field does not affect the electron motion along its direction and therefore does not change the bound states energies. It means that shift of the resonant peak position is related with electron redistribution between 2DES's and contact electron systems only.

Figure 2(a) shows the position of the current peak related to the 0–0 resonance on voltage scale versus magnetic field with square symbols. The magnetic field dependence of the current peak position can be understood taking into account only electron redistribution between each 2DES and adjacent contact. The Fermi level in the 2DES is fixed by a chemical potential of the contact because the spacers are significantly more transparent than the barrier. Under these conditions the LL are pinned. The LL pinning means that due to the electron exchange between the 2DES and the contact the shift of the 2D bound-state compensates the cyclotron energy variation. As the result the energy of the upper populated LL doesn't vary with magnetic field increase. The resonance position is defined by difference of the energy of pinned LL (see insert to Fig. 2(a)). Neglecting the width of

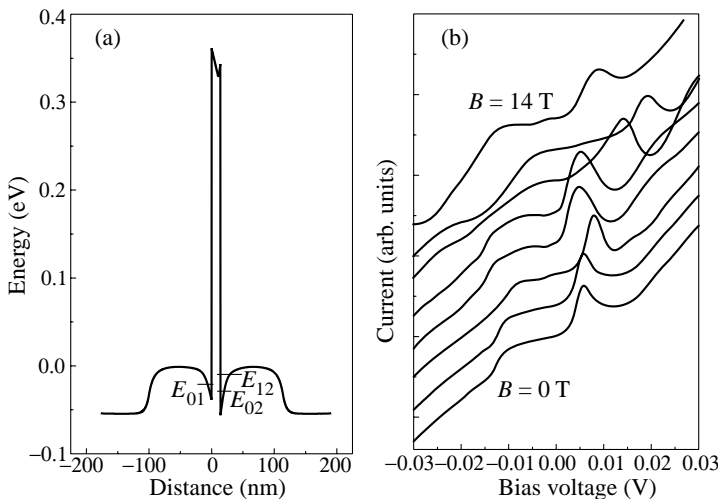


**Fig. 1.** (a) Current-voltage characteristics at different magnetic field perpendicular to the plane of the 2DES. (b) Potential profile of the conduction band bottom with 2DES subband bottoms.

the LL one has the following resonance condition  $V_p$ :

$$eV_p = (N_f - N_i)\hbar\omega_c \quad (1)$$

where  $N_i$ ,  $N_f$  are numbers of the pinned partly populated LL in the emitter ( $i$ ) and collector ( $f$ ) 2DES,  $\omega_c$  is cyclotron frequency. The filling factors in the 2DES's are the following for  $B = 3$  T:  $\nu_i(B = 3 \text{ T}) = n_i S / N_c = 4.2$ ,  $\nu_f(B = 3 \text{ T}) = 7$ . Here  $n_i$  is an electron concentration in emitter 2DES,  $S$  is a sample area,  $N_c$  is a LL degeneracy. We then obtain the following upper populated LL numbers:  $N_i(B = 3 \text{ T}) = 2$ ;  $N_f(B = 3 \text{ T}) = 3$ . According to Eq. (1) one has  $eV_p = \hbar\omega_c$ . For magnetic field  $B = 5$  T the numbers of the upper LL are the following:  $N_i(B = 5 \text{ T}) = 1$ ;  $N_f(B = 5 \text{ T}) = 2$ , so the same relation  $eV_p = \hbar\omega_c$  is valid.

The discontinuity in the peak position versus magnetic field (Fig. 2(a)) can be understood in the following way. When the pinned LL is fully depopulated with magnetic field increase, it will be pushed up and next LL with lower number will be pinned by the contact chemical potential. If it happens only in one 2DES, one should observe discontinuity found in our experiment. After first discontinuity at  $B = 5.5$  T the difference  $N_f - N_i = 0$  in magnetic field range  $B \in (5.5 \text{ T}; 7 \text{ T})$  and resonant current peak has to shift to lower voltage. With further increase of magnetic field the unsynchronized changing of the pinned LL numbers takes place and previous LL numbers difference could be restored. Assuming that LL's are infinitely narrow, one can easily obtain with the help of Eq. (1) the expected position of the resonant current peak, which is shown with solid line in Fig. 2(a).

Evidently there is a remarkable discrepancy between calculated and experimental data especially in the range of magnetic field  $B \in (5.5 \text{ T}; 7 \text{ T}) \cup (11 \text{ T}; 13 \text{ T})$ . Qualitatively the discrepancy could be explained taking into account a LL broadening because the value of the discrepancy is comparable with resonant peak width. However in this case it seems difficult to explain the linear field dependence of the resonance position.

Other possibility is to consider pinning of the spin split LL. In this case one can easily

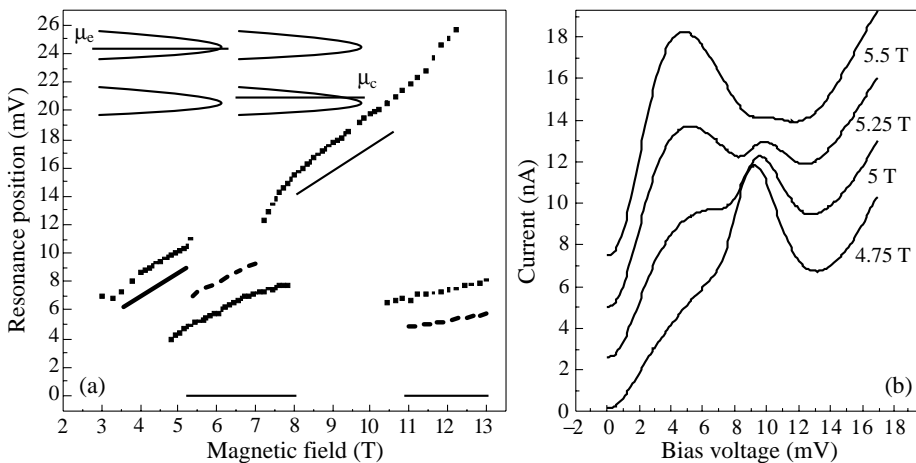


**Fig. 2.** (a) Resonance voltage position versus magnetic field. Experimental data are shown with square symbols. The solid and dashed lines correspond to calculated values in the frame of the LL pinning model without and with spin splitting of the LL accordingly. In the insert the LL are shown under pinning condition. (b) Current-voltage characteristics in magnetic fields in range of transition from one linear dependence to other (see Fig. 2(a)).

obtain the following equation:  $eV_p = (N_f - N_i)\hbar\omega_c \pm \Delta(B)$ . Here the equal value of the spin splitting  $\Delta(B)$  is supposed for both 2DES. In Ref. [2] authors have measured the value of the splitting as:  $\Delta(B) = 0.25\hbar\omega_c$ . Now expected peak positions is shown in Fig. 2(a) with dash lines.

More careful analysis shows that in the regions of the discontinuity in fact two current peaks coexist simultaneously (Fig. 2(b)). The amplitude of the one current peak decreases and that of the other increases. Such behavior can be understood if the 2DES is strongly in-plane inhomogeneous. Suppose that there are regions in the 2DES with slightly different electron concentration. It means that for these regions discontinuity appears in different magnetic fields. In this case two current peaks appears in the IV curves. With further variation of magnetic field the area of the region where the number of pinned LL has been changed increases and the area of the another region decreases. Such kind of instability should be considered taking into account the inhomogeneous and many body effects.

In summary we have investigated electron tunnelling between open 2DES. The magnetic field shifts resonant peak position. The shift on the voltage scale is linear versus magnetic field, but exhibited discontinuity in particular magnetic fields. The Landau levels pinning in the 2DES's by chemical potential in the contact region explains the experimental findings. In the regions of the discontinuity two current peaks coexist simultaneously. We argue that the peaks coexistence is the manifestation of the many body effect in the inhomogeneous 2DES.

#### *Acknowledgements*

This work was supported by the INTAS, the RFBR, the FTNS program of the Russian government, and CNRS-PICS (France).

#### **References**

- [1] D. G. Hayes, M. S. Skolnick, D. M. Whittaker, P. E. Simmonds, L. L. Taylor, S. J. Bass and L. Eaves, *Phys. Rev. B* **44**, 3436 (1991).
- [2] V. T. Dolgoplov, A. A. Shashkin, A. V. Aristov, D. Schmerek, W. Hansen, J. P. Kotthaus and M. Holland, *Phys. Rev. Lett.* **79**, 729 (1997).

## Ultra-high coulomb energy in position controlled grown carbon nanotube

*Kazuhiko Matsumoto*

Advanced Industrial Science & Technology, 1-1-1 Umezono,  
 Tuskuba, Ibaraki, 305-8568 Japan

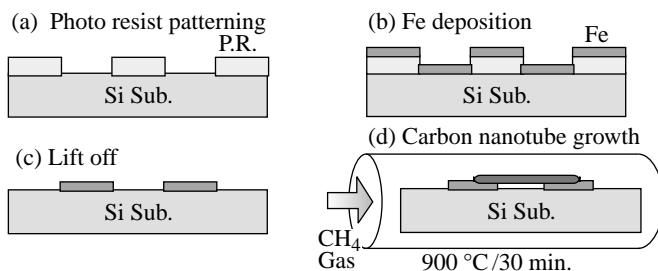
### 1. Introduction

A carbon nanotube is one of the best candidates for the nano-scale devices because of its small features. The problem of the carbon nanotube is the difficulty how to control the position and the direction of the carbon nanotube. So far, the carbon nanotube was dispersed in to the alcohol and distributed onto the substrate, and was connected to the metal electrode by moving the carbon nanotube by AFM cantilever to the electrode. This process took a lot of time and showed low yield. In order to solve this problem, we proposed the new technology that could control the position of the carbon nanotube by using the patterned chemical catalyst. The three terminal device which used the carbon nanotube as a channel was fabricated and its electrical properties were examined. The carbon nanotube three terminal device showed the single electron transistor characteristics and showed the room temperature Coulomb diamond characteristics. The Coulomb temperature of the device is as high as  $\sim 5000$  K.

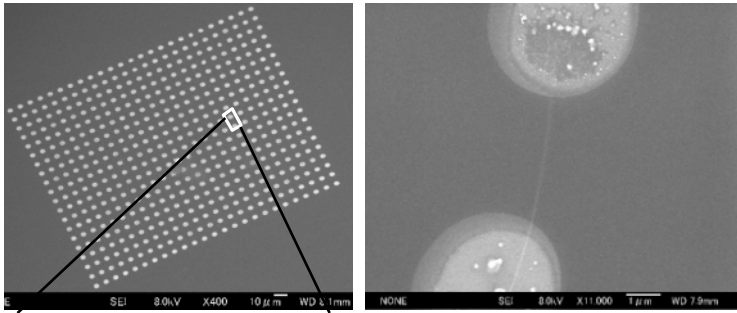
### 2. Position control growth of carbon nanotube by patterned chemical catalyst

Figure 1 shows the method of the position control growth of the carbon nanotube.

- Using the conventional photo lithography technology, photo resist was patterned on the silicon substrate.
- The iron (Fe) which worked as a chemical catalyst was deposited using the e-beam evaporator onto the patterned photo resist.
- Using the conventional technology, the Fe was lift off. Thus, the chemical catalyst, i.e., Fe, was patterned.
- The sample was then put into the thermal CVD furnace. The growth temperature is 900 centigrade for 10 minutes using the  $\text{CH}_4$  gas at 1000 sccm. Then the carbon nanotube started to grow between the chemical catalyst.



**Fig. 1.** Position controlled growth of carbon nanotube by patterned chemical catalyst.



**Fig. 2.** SEM photograph of carbon nanotube grown across patterned 2 chemical catalyst.

Figure 2 shows the SEM photograph of the patterned chemical catalyst on the silicon substrate. The 5000 white circles were patterned Fe which works as a chemical catalyst as shown in the upper SEM photograph. The lower photograph showed the enlarged area of the two chemical catalyst patterns. One carbon nanotube was grown across two chemical catalyst patterns. Thus, the position of the carbon nanotube was easily controlled by patterning the chemical catalyst using the conventional photo lithography technique.

### 3. Three terminal device using carbon nanotube as channel

Using the position controlled grown carbon nanotube shown in the previous section, the tree terminal device was fabricated. The schematic structure of the three terminal device was shown in Fig. 3. The carbon nanotube was grown using the patterned chemical catalyst on to the 100 nm thick silicon dioxide surface, which works as a channel of the device. The source and drain ohmic contacts were formed on to the patterned chemical catalyst. The back gate was also formed on to the silicon substrate.

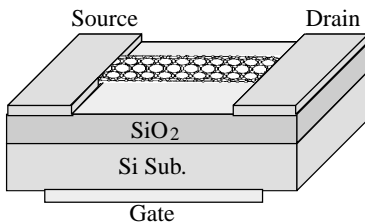


**Fig. 3.** Three terminal device using position controlled grown nanotube as channel.

The electrical properties of the device was all measured at room temperature. Figure 4 shows the drain current-drain bias characteristics using the gate bias as parameters. At 0 V gate bias, the drain current shows the Coulomb gap of about 800 mV though there is a leak components. The total energy of the device was as high as 400 meV. When the gate bias becomes 0.4 V, the Coulomb gap was completely disappeared, and the drain current increased drastically. The further increase of the drain current up to 0.72 V, however, the drain current does not increase further, but decreased. Therefore, the drain current does not increase monotonically, but oscillate by the increase of the drain bias.

The gate bias dependence of the drain current was shown in Fig. 5 with the drain bias as parameters. The gate bias was changed between +2 V to -2 V, and the drain bias also between +2 V to -2 V. The drain current oscillates with the increase of the gate bias and shows the peaks and valleys. This is the Coulomb oscillation using the carbon nanotube at room temperature. The period of the Coulomb oscillation is about 1 V. Even at the different

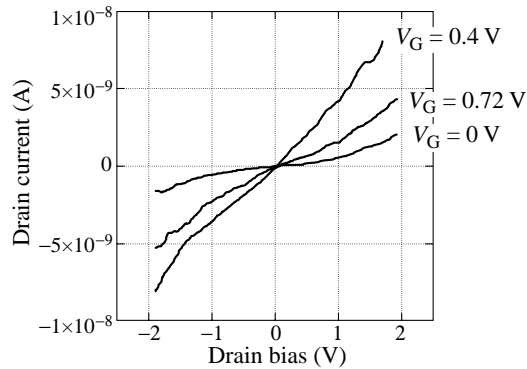


**Fig. 4.** Drain current-drain bias characteristics with gate bias as parameter at room temperature.

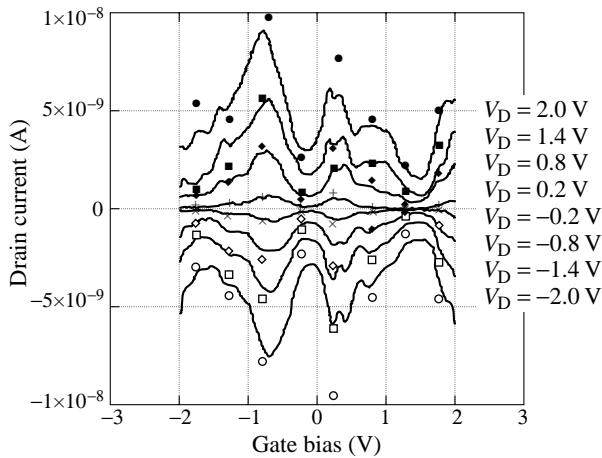


**Fig. 5.** Gate bias dependence of drain current at room temperature. Coulomb oscillation Characteristics.

drain biases, the positions of the Coulomb peak coincide quite well. The gate capacitance of the device is calculated to be  $C_g = 1.6 \times 10^{-19}$  F.

The dependence of the drain current on the gate bias and the drain bias is shown in the 3 dimensional plot as shown in Fig. 6. In Fig. 6, the clear Coulomb diamond characteristic is obtained even at such high temperature of room temperature. The black shadow area is the Coulomb blockade area where the drain current is blocked by the single electron charging energy. The size of this Coulomb blockade area is modulated by the change of the gate bias and shows the diamond structures. Figure 7 is the contour plot of the Coulomb diamond characteristics shown in Fig. 6. Four Coulomb diamond structures are seen in the figure at room temperature. The different size of the Coulomb diamond structures may attributed to the multi-dot Coulomb island structure in the carbon nanotube. The multi-dot structure may come from the defects in the nanotube or the residual metal catalyst inside the nanotube. The total Coulomb energy is as high as 400 meV and the correspondent temperature is 5000 K. Owing to such high Coulomb energy of 5000 K, the clear Coulomb diamond structure could be obtained even at such high temperature of 300 K.



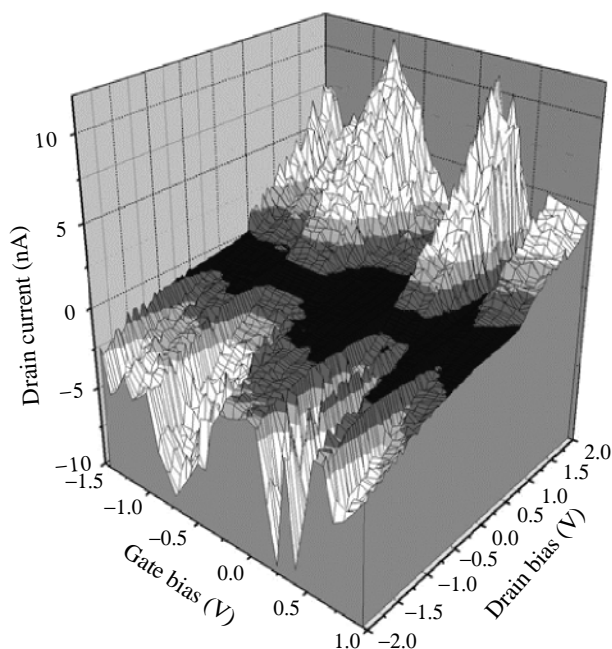


**Fig. 6.** Coulomb diamond structure at room temperature.

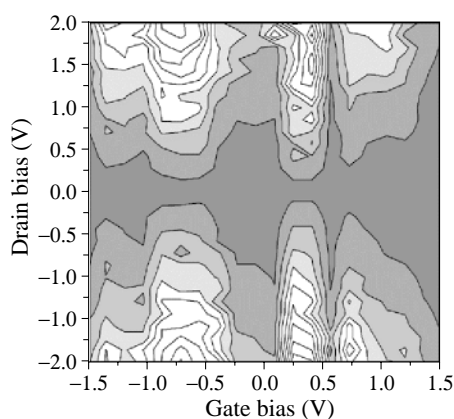


**Fig. 7.** Contour plot of Coulomb diamond at room temperature.

#### 4. Conclusions

We have succeeded in controlling the positioning of the carbon nanotube using the patterned chemical catalyst. Using this position controlled grown carbon nanotube, the three terminal device was fabricated, which worked as a single electron transistor. The single electron transistor worked at room temperature and showed the Coulomb diamond characteristics even at room temperature. The Coulomb energy is as high as 400 meV which correspondent to the Coulomb temperature of 5000 K. Owing to such high Coulomb energy, the device operated at room temperature.

## Ti/TiO<sub>x</sub>/Ti lateral tunnel junctions for single electron transistor

L. V. Litvin, V. A. Kolosnov, D. G. Baksheev, V. A. Tkachenko,  
K. P. Mogilnikov, A. G. Cherkov and A. L. Aseev

Institute of Semiconductor Physics, 13 Lavrentieva st.,  
Novosibirsk, 630090, Russia

**Abstract.** A new technique for formation of tunnel junctions from Ti stripe providing junction capacitance of about 10 aF (150 nm wide stripe) has been developed. The technique is based on through oxidizing thin sites that form when Ti stripe crosses a step previously etched in the dielectric substrate. Charge transfer through the single junctions was investigated. Inelastic tunneling via electron states localized in the barrier region was found. This results in the essential nonlinearity of junction  $I-V$  curves to a scale of bias voltage of 2–3 mV. The single electron transistor built on such junctions demonstrates the  $I-V$  curves peculiarities originating from strong nonlinearity of single junctions.

### Introduction

The contemporary single electron transistor (SET) which is used almost in all practical applications is fabricated by the shadow evaporation using about 100 nm wide Al stripe. This results in the tunnel junction area of  $100 \times 100 \text{ nm}^2$  which provides junction capacitance of 300 aF and working temperature as high as 0.15 K [1]. The tunnel junction built from metal stripe can acquire junction area being equal to its cross section. The vacuum deposited titanium layers are continuous at thickness of 3 nm therefore junction area of  $3 \times 100 \text{ nm}^2$  are accessible even for 100 nm wide lithographical design. There were attempts to built such lateral junctions in two ways: by means of step edge cut off method [2] and using the local oxidation of Ti films in scanning tunneling microscope [3]. Both methods led to huge resistance of tunnel junction ( $\geq 10^{12} \Omega$  at  $T = 77 \text{ K}$ ) and unrealistically low junction capacitance of 0.7 aF for 100 nm wide stripe [2] and 0.4 aF for that of 40 nm [3]. The latter produces a doubt whether the Coulomb blockade was indeed observed since junction capacitance can not be lower than Coulomb island self-capacitance that can be estimated by formula  $C = 4\epsilon_0\epsilon D$  producing values of 7.5 and 3 aF ( $\epsilon = 2$ ) for  $D = 100$  and 40 nm respectively. In the present work we fabricated the tunnel junctions with resistance of  $10^6$ – $10^8 \Omega$  at  $T = 4.2 \text{ K}$  employing Ti stripe of nearly 100–150 nm in width. Our junctions have capacitance of about 10 aF as it was determined from Coulomb blockade effect observed in SET built on these junctions.

### 1. Experimental details

The design of SET is depicted in Fig. 1. The details of fabrication procedure are published elsewhere [4]. The 100 nm thick Si<sub>3</sub>N<sub>4</sub> membranes having area of  $50 \mu\text{m}$  square were used as substrates to perform high-resolution control of the structure shape by transmission electron microscope. The four corners of the membrane supported by Si crystal were the alignment marks for two step electron lithography. First the Ti stripe having the length of  $4 \mu\text{m}$ , the width of 150 nm and the thickness of 6 nm was defined by the conventional "lift-off" process. This stripe acted as a mask for reactive ion etching and was dissolved

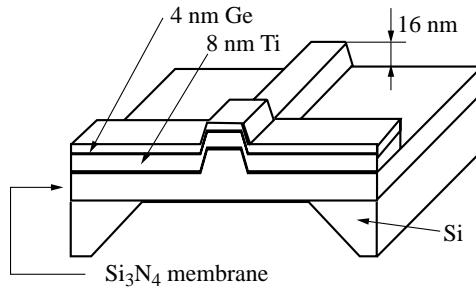


**Fig. 1.** The design of single electron transistor built on the lateral tunnel junctions. The gate is not shown (see the text).

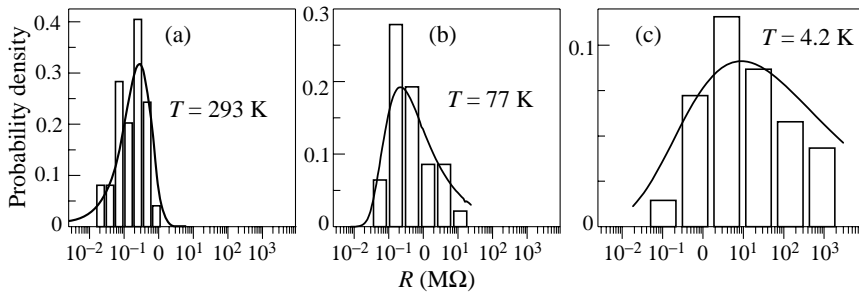


**Fig. 2.** The resistance distribution of tunnel junction at temperatures 293 K – (a), 77 K – (b), and 4.2 K – (c). The theoretical distributions obtained by Raikh and Ruzin are shown as the curves.

in HF solution after etching process. As a result the bulge defined by two steps spaced at a distance of 150 nm was arranged. In the second step the Ti nanowire with leads and self aligned gate 150 nm distant from nanowire (not shown in Fig. 1) were deposited. The nanowire was 2  $\mu\text{m}$  in length, 150 nm in width and 5–8 nm in thickness. The thin sites that form when Ti nanowire crosses the steps are through oxidized in air giving rise to formation of tunnel junction. The thickness of Ge layer deposited over Ti in the same vacuum cycle controls the degree of oxidation. Thus the SET having the Coulomb island of plain area of about  $150 \times 150 \text{ nm}^2$  was fabricated.

## 2. Results and discussion

Thirty four samples were subjected to electrical measurements at temperatures 293, 77, 4.2 K and showed resistance above 100 k $\Omega$  at  $T = 4.2 \text{ K}$  (the resistance of leads was subtracted, so the figures represent that of tunnel junction). The results reported in this paper were obtained for the samples with resistance  $12 \div 380 \text{ k}\Omega$  at  $T = 293 \text{ K}$ . At  $T = 4.2 \text{ K}$  single electron oscillations of the current as a function of gate voltage were only found for 3 samples. This results in the probability of nearly 10% for simultaneous formation of two junctions with  $R \gg h/e^2$  in two constrictions and implies the probability of 33% for formation of junction with  $R \gg h/e^2$  in each constriction.

The resistance distribution of junctions at  $T = 293 \text{ K}$  obeys the distribution function deduced by Raikh and Ruzin [5] for the randomly inhomogeneous finite-area barriers (Fig. 2(a)). At temperatures of 77 and 4.2 K this distribution transforms to distribution func-

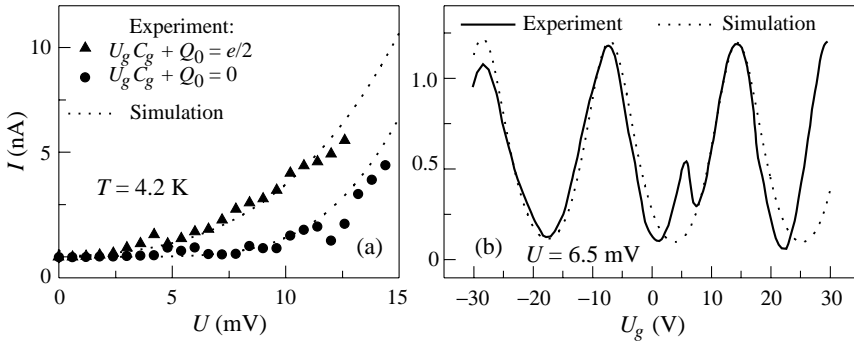


**Fig. 3.** Experimental and simulated  $I$ – $V$  curves of the single electron transistor. (a) The SET current vs bias voltage. (b) The SET current vs gate voltage.

tion of hopping conductivity of a one-dimensional chain of localized states [6] (Figs. 2(b) and 2(c)).

The idea of conduction via electron states localized in the barrier is supported by dependence of the junction resistance on temperature. In the main this dependence was found to be the power function with exponent  $4/3$  [7]. According to [8] this law corresponds to inelastic tunneling through the channels consisting of pairs of localized states. The current-voltage characteristic due to impurity channels is nonlinear  $I(V) \propto V^{n-2/(n+1)}$ , where  $n$  is the number of impurities in the channel [8]. In experiment, large number of junction  $I$ – $V$  curves are power functions (36%) and exponential ones (45%). Exponential  $I$ – $V$  curves occur when the impurities in conducting chain are positioned at distances more than  $kT$  from Fermi level [9].

The typical  $I$ – $V$  curves of SET are illustrated in Fig. 3. In samples with two tunnel junctions, Coulomb Blockade (CB) causes excessive noise (background charge fluctuations) of source-drain characteristics that switch within the region bounded by two curves corresponding to open and close state of SET (Fig. 3(a)). The source-gate characteristics exhibit single-electron oscillation of the current (Fig. 3(b)). At  $T = 4.2$  K Coulomb block-

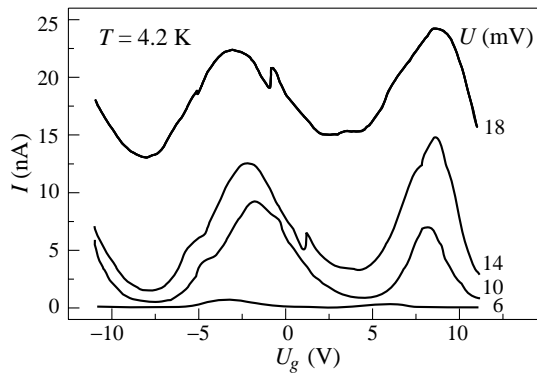


**Fig. 4.** Single electron oscillations in experimental  $I(U_g)$  plots depicted over a wide range of bias voltages.

ade effect is pronounced so the ratio  $E_c/kT = e^2/2CkT$  of about 10 can be expected, giving the estimate of junction capacitance of  $C_1 = C_2 = C/2 = 11$  aF. The same value was obtained from modeling for the sample whose characteristics are displayed in Fig. 3.

To make simulation on the basis of “orthodox” CB theory the junction nonlinearity should be implemented in the model. We described the junction resistance  $R_i$  ( $i = 1, 2$ ) by the power function  $R_i = R_{0i}/[1 + (\Delta E_i/\Delta E_{0i})^{\gamma_i}]$ , where  $\Delta E_{0i}/e$  is the voltage scale of nonlinearity for junction  $i$  and  $\gamma_i$  is the power exponent. The modeled SET parameters for Fig. 3 are  $C_1 = C_2 = 11$  aF,  $C_g = 0.0075$  aF,  $R_{01} = 5$  M $\Omega$ ,  $R_{02} = 3.3$  M $\Omega$ ,  $\Delta E_{01} = \Delta E_{02} = 2.3$  meV and  $\gamma_1 = \gamma_2 = 2$ . This set of parameters is valid for 6 different  $I-V$  curves recorded for the same SET and three of them are shown in Fig. 3.

For two fabricated SET with nonlinear  $R_1, R_2 = R_i(\Delta E_i)$  ( $R_1 \approx R_2$ ) the single electron oscillations in the  $I(U_g)$  are observed in the region of high bias voltages (Fig. 4) unlike the SET with  $R_1, R_2 = \text{const}$  [7]. This unusual behavior is simulated within the framework of “orthodox” CB theory and is supposed to originate from the junction nonlinearity under condition of  $E_c/\Delta E_{0i} \geq 1$ . Coulomb blockade in exponentially nonlinear junctions under  $E_c/\Delta E_{0i} \geq 1$  was considered in Ref. [10].

#### Acknowledgements

The work is supported by Russian Foundation for Basic Research (Grant No 01-02-17560a).

#### References

- [1] K. K. Likharev, *Mikroelektronika* **16**, 195 (1987).
- [2] S. Altmeyer, A. Hamidi *et al*, *J. Appl. Phys.* **81**, 8118 (1997).
- [3] K. Matsumoto, M. Ishii *et al*, *Appl. Phys. Lett.* **68**, 34 (1996).
- [4] L. V. Litvin, V. A. Kolosanov *et al*, *Mikroelektronika* **29**, 189 (2000).
- [5] M. E. Raikh and I. M. Ruzin, *Zh. Eksp. Teor. Fiz.* **92**, 2257 (1987).
- [6] M. E. Raikh, I. M. Ruzin, *Zh. Eksp. Teor. Fiz.* **95**, 1113 (1989).
- [7] L. V. Litvin, V. A. Kolosanov *et al*, *JETP Lett.* **72**, 264 (2000).
- [8] L. I. Glazman and K. A. Matveev, *Zh. Eksp. Teor. Fiz.* **94**, 332 (1988).
- [9] E. I. Levin, I. M. Ruzin *et al*, *Fiz. Tekh. Polupr.* **22**, 642 (1988).
- [10] A. N. Korotkov and Yu. V. Nazarov, *Physica B* **173**, 217 (1991).

## Towards superconducting molecular nanoelectronics

A. Yu. Kasumov<sup>†‡</sup>, R. Deblock<sup>†</sup>, M. Kociak<sup>†</sup>, B. Reulet<sup>†</sup>, H. Bouchiat<sup>†</sup>,  
S. Gueron<sup>†</sup>, I. I. Khodos<sup>‡</sup>, Yu. B. Gorbatov<sup>‡</sup>, V. T. Volkov<sup>‡</sup>, V. I. Nikolaichik<sup>‡</sup>,  
*Yu. A. Kasumov*<sup>‡</sup>, C. Journet<sup>§</sup>, P. Bernier<sup>§</sup>, M. Burghard<sup>¶</sup> and D. V. Klinov<sup>||</sup>

<sup>†</sup> Lab. de Phys. des Solides, Associe au CNRS, Bat 510, Universite Paris-Sud,  
91405, Orsay, France

<sup>‡</sup> Institute of Microelectronics Technology and High Purity Materials, RAS,  
142432 Chernogolovka, Moscow District, Russia

<sup>§</sup> GDPC University of Montpellier, France

<sup>¶</sup> Max Plank Institute, Stuttgart, Germany

<sup>||</sup> Shemyakin-Ovchinnikov Institute of Bioorganic Chemistry, RAS,  
Miklukho-Maklaya 16/10, Moscow 117871, Russia.

**Abstract.** Discovery of superconductivity in individual molecules of carbon nanotubes [1] and DNAs [2] opens the door for superconducting molecular nanoelectronics. From nowadays physics point of view only use of superconducting devices can satisfy the requirements of molecular nanoelectronics:

1. Ultra high level integration (10–100 billions devices per centimetre square),
2. Ultra small energy dissipation (100 picoWatt per device),
3. Ultra high operation speed (about 1 picosecond switching time).

In this report we present the following results:

1. Single ion lithography (superconducting properties of a carbon nanotube before and after modification by single 30 kV Ga ions),
2. Suppression of superconductivity in a carbon nanotube by ferromagnet electrodes (transport properties of Superconductor-Ferromagnet-Nanotube-Ferromagnet-Superconductor junctions),
3. Induced superconductivity in DNAs (superconducting properties of Re/C-DNA-Re/C junctions),
4. Nanofabrication of 3 terminal molecular devices,
5. Comparison of the experimental results with the theory [3] explaining non BCS behavior of carbon nanotubes.

In the abstract we will focus on the electron and ion beam modifications of single walled carbon nanotubes (SWNT).

### 1. Experiment

We present low temperature measurements of 3 individual SWNT mounted on Ta/Au/In superconducting contacts. Their RT resistances are  $R_N = 9\text{ k}\Omega$ ,  $28\text{ k}\Omega$  and  $41\text{ k}\Omega$ . For correct interpretation of transport measurements it is crucial to know what part of the tube resistance is due to the contacts: for a ballistic tube the entire resistance is due to the contacts, and in case of bad (low transmission) contacts the resistance can largely exceed  $R_Q$  [4]). In our case it is known for tubes SW1 and SW3. Tube SW1 was exposed to the electron beam of an electron microscope. The area of the contacts was shielded by a layer of membrane and metal opaque to electrons with an energy of 100 keV, so that only the part of the tube outside contacts (Fig. 1) was irradiated. The resistance of this sample after irradiation increased to  $20\text{ k}\Omega$  due to the radiation defects, and it is certain that this part of resistance (about  $11\text{ k}\Omega$ ) is not due to contacts. The measurements presented

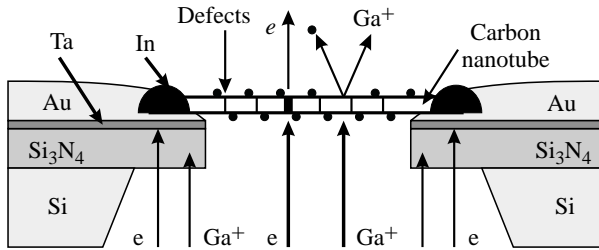


**Fig. 1.** Schematic of a real nanotube with defects, modified by electron (e) and ion ( $\text{Ga}^+$ ) beams. Defects-adsorbed atoms and structural ones are shown as black dots and partitions correspondingly. On the picture are also schematically shown the desorption of an atom by  $\text{Ga}^+$  ion, the creation of a structure defect by e-beam, and shielding effect of  $\text{Si}_3\text{N}_4$  membrane.

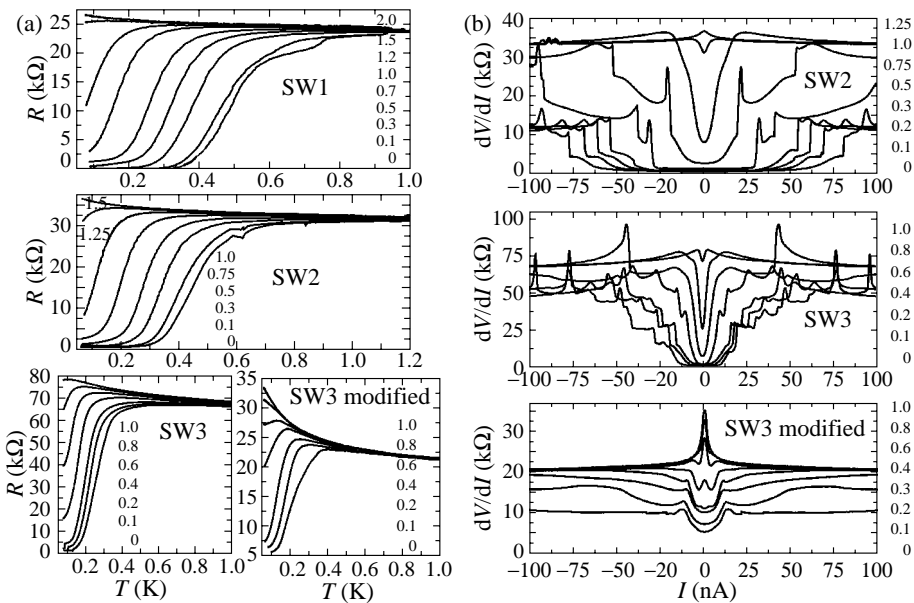


**Fig. 2.** (a) Resistance as a function of temperature for all samples, in various magnetic fields (fields are indicated in Teslas to the right of the curves). SW1 is  $0.3 \mu\text{m}$  long and is mounted on Ta/Au contacts. RT resistance of SW1 was 9 k $\Omega$  after deposition and before TEM observation, and 20 k $\Omega$  afterwards. SW2 is  $0.15 \mu\text{m}$  long and is mounted on Ta/Au/In contacts. SW3 is  $0.2 \mu\text{m}$  long and is mounted on Ta/Cr/Au/In contacts.

(b) Differential resistance as a function of current for samples SW2, SW3 and SW3m, at  $T = 70 \text{ mK}$ . (Fields are indicated in Teslas to the right of the curves).

here were obtained after this modification of the sample. Sample SW3 was exposed to the 30 kV  $\text{Ga}^+$  ion beam of a focused ion beam machine. As in the case of the electron beam, the ions did not reach the contact area, being “stuck” in the shielding membrane. The extremely small radiation dose:  $10^{13}$  ions/ $\text{cm}^2$  corresponded to 3 ions flown through a nanotube. The irradiation resulted in essential decrease of resistance of the sample down to 13 k $\Omega$ , apparently owing to the desorption of impurity atoms (in [5] all nanotubes were irradiated by Ga ions with a dose of  $2 \cdot 10^{14}$  ions/ $\text{cm}^2$ , and their resistance remained very

low, as low as 200  $\Omega$ ). This definitely proves that the most part of resistance of SW3 before irradiation, 41 k $\Omega$ , is not due to contacts. Therefore the samples are non-homogeneous one-dimensional (1D) conductors, which resistance is determined by contacts and internal defects. For sample SW2 we have no direct measurement of the influence of defects on resistance.

## 2. Results

The measurement of temperature dependence of resistance shows that all three of the samples undergo a proximity-induced superconducting transition with critical temperature  $T_c \sim 0.5$  K, which is the  $T_c$  of the superconducting electrodes (Fig. 2(a)). This is the main result of this paper. Moreover besides the  $R(T)$  dependence, the magnetic field dependence of the resistance (Fig. 2(a)), and the differential resistance Vs current curves (Fig. 2(b)) definitely show the superconducting character of the transition. For samples SW1 ( $R(T)$  dependence for this sample was presented in [1]) and SW2 the transition is complete and the resistance drops from 26 k $\Omega$  down to less than 1  $\Omega$ , defined by the sensitivity of measurements ( $I = 1$  nA,  $V = 1$  nV). Supercurrents of the order of 100 nA are measured [1]. The resistance of sample SW3 does not go to zero, but saturates at a value of 1.5 k $\Omega$ .

### Acknowledgements

This work is supported by the Russian Foundation for Basic Research and Russian State Research Program “Physics of solid state nanostructures”.

## References

- [1] A. Yu. Kasumov *et al*, *Science* **284**, 1508 (1999).
- [2] A. Yu. Kasumov *et al*, *Science* **291**, 280 (2001).
- [3] J. Gonzalez, *cond-mat/0104071*, 4 Apr.2001.
- [4] A. Bachtold *et al*, *Phys.Rev.Lett.* **84**, 6082 (2000).
- [5] T. W. Ebessen *et al*, *Nature* **382**, 54 (1996).



## Current-induced cooling of nanostructures

*E. B. Dogonkin and G. G. Zegrya*

Ioffe Physico-Technical Institute, St Petersburg, Russia

**Abstract.** A mechanism of electric current-induced cooling of nanostructures is proposed and analyzed. The conditions are studied of electric current flow through a heterostructure with two quantum wells, with electrons from one quantum well passing into the other via phonon-assisted indirect tunneling. As a result, the system is cooled by the flowing current, with the temperature of the system depending on the current nonmonotonically. A universal law for the maximal cooling temperature is derived.

### Introduction

Presently, it is possible to create practically ideal semiconductor nanoheterostructures and superlattices on their base, which are defect-free owing to lattice matching [1], with the geometric dimensions of the constituent layers and barrier heights controlled with high precision.

Let us consider the mechanism of current transport through a heterostructure with quantum wells (QWs), shown in Fig. 1. The quantum structure (QS) comprises two QWs of different widths for electrons and a QW for holes. The QW lie between the n- and p-type regions serving as emitters for, respectively, electrons and holes. The width of the second QW for electrons is chosen so that the size-quantization level  $E_2$  lies above the energy level  $E_1$  in the first QW (see Fig. 1).

Let an external bias be applied to such a structure. Then electrons from the n-type emitter can pass into the first QW by tunneling through the first barrier; however, their tunneling into the second QW is strongly suppressed by the presence of two heterobarriers.

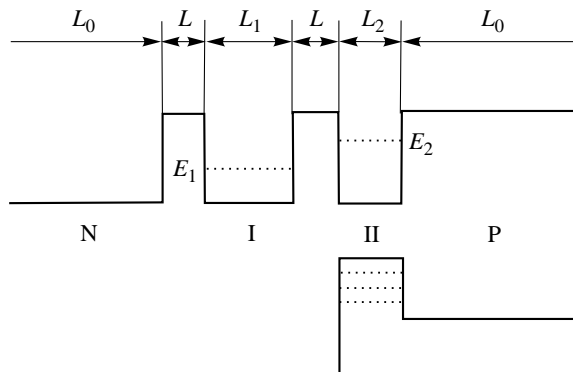


**Fig. 1.** Quantum structure. From the left to the right: (1) n-type emitter of electrons, QW I for electrons, (3) QW II for electrons and QW for holes, and (4) p-type emitter of holes.

Consequently, the probability of direct tunneling of an electron from the n-type emitter into the second QW is exponentially small, there being no resonance level in the first QW. Electrons localized in the first QW cannot tunnel into the second QW in a conventional way, either, this transition being prohibited by conservation of energy and longitudinal quasi-momentum. Electrons with the same longitudinal quasi-momentum in the first and second QWs have energies differing by  $E_1 - E_2$  (Fig. 2). Therefore, electrons pass from the first into the second QW via indirect phonon-assisted tunneling [2].

It is known that electrons in semiconductors interact rather effectively with longitudinal optical (LO) phonons at high temperatures (on the order of room temperature) [3]. Therefore, an indirect tunnel transition of an electron from the first QW into the second, with absorption of an LO phonon is rather probable. Apparently, such a tunneling process will be sufficiently effective when the difference between the size-quantization energies  $E_1 - E_2 = \hbar\omega_0$ , where  $\omega_0$  is the optical phonon frequency.

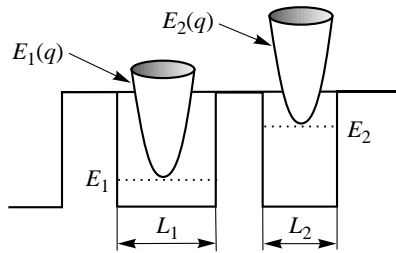


**Fig. 2.** Electron dispersion in the first and second QWs. It is seen that electrons with the same longitudinal quasi-momentum have different energies.

The aim of the present study is to analyze the mechanism of current transport through a heterostructure, with indirect tunneling of electrons from one QW into the other and their subsequent recombination with holes (see Fig. 1). With such a mechanism of current transport through the heterostructure, Joule heat is released in the n- and p-type emitters, and heat in the QS is absorbed by electrons since any passing electron takes from the lattice an energy equal to the optical phonon energy and recombines with a hole emitting a quantum of light with energy  $\hbar\omega$ . We find the current  $j_E$  through the system, corresponding to the maximum cooling temperature  $T_C$  (difference between the temperature of heat sinks,  $T_0$ , and that of the QS,  $T_Q$ ):  $T_C = T_0 - T_Q$ . A universal law is established, according to which the maximum cooling temperature is expressed solely in terms of the characteristic size-quantization energy  $E_2 - E_1$  (see (10)).

### Mechanism of phonon-assisted carrier tunneling through heterostructure

The rate  $W_{12}$  of phonon-assisted electron tunneling from the size-quantization level  $E_1$  to the level  $E_2$  can be calculated in terms of the first-order perturbation theory in electron-phonon coupling:

$$W_{12} = \frac{e^2 \omega_0 m_c \tilde{c}^2}{8\pi^2 L_2 \epsilon^* \hbar} \frac{\exp\left(\frac{\mu_1 + \hbar\omega_0 - \mu_2}{2kT}\right)}{\exp\left(\frac{\hbar\omega_0}{kT}\right) - 1} (J_1 + J_2), \quad (1)$$

where  $\mu_i$  - quasi-Fermi level in  $i$ -th QW and

$$\left\{ \begin{array}{l} J_i = \frac{1}{2A_i} \int_{\sqrt{B_i}}^{\infty} \frac{dx}{C + \cosh\left(\frac{x^2}{x_i^2} + \gamma_i\right)} \\ A_i = (k_1 \pm k_2)^2 \\ B_i = k_1(k_1 \pm k_2)(k_1^2 \pm k_1 k_2 + 2\frac{m_c \omega_0}{\hbar}) + (\frac{m_c \omega_0}{\hbar})^2 \\ C = \cosh \frac{\mu_2 - \mu_1 - \hbar \omega_0}{2kT} \\ \tilde{c} = \frac{1}{\cos(k_2 L_1) \cosh(\kappa_2 L) + \frac{\kappa_2}{k_2} \sin(k_2 L_1) \sinh(\kappa_2 L)} \\ x_i = \frac{\sqrt{2m_c kT}}{\hbar} (k_2 \pm k_1) \\ \gamma_i = \frac{2E_1 + \hbar \omega_0 - \mu_1 - \mu_2}{2kT} - \frac{B_i}{A_i}, \end{array} \right. \quad (2)$$

$k_i, \kappa_i$  are, respectively, the transverse quasi-momenta of electrons with energy  $E_i$  in the QW and under the barrier,  $L_i$  is the width of  $i$ -th QW, and  $L$  is the barrier width.

Similarly, we obtain for the rate  $W_{21}$  of tunneling from level  $E_2$  to level  $E_1$  with emission of an LO phonon:

$$W_{21} = W_{12} \exp\left(\frac{\mu_2 - \mu_1}{kT}\right). \quad (3)$$

### Stationary mode

Since the characteristic intraband carrier relaxation time  $\tau_I$  is much shorter the characteristic times of tunneling,  $\tau_T$ , and radiative recombination,  $\tau_R$ , ( $\tau_I \ll \tau_T, \tau_R$ ) [4], it can be assumed that its own quasi-Fermi level,  $\mu_1$  and  $\mu_2$ , is established in the stationary mode in each QW for electrons (Fig. 1). We assume that the process of electron tunneling from the n-type emitter into the first QW is sufficiently fast, so that the quasi-Fermi levels in the emitter and in the first QW coincide. The quasi-Fermi level for electrons in the second QW is found from the balance equation:

$$W_R = W_{12} - W_{21}, \quad (4)$$

where  $W_R$  is the rate of radiative recombination of carriers in the second QW. In what follows, we disregard the leakage currents and Auger recombination, since an optimal structure, in which these processes are suppressed, can be chosen in any given case.

### Heat balance

Let us consider the electric current transport through a system comprising a quantum structure and two emitters, of n- and p-type, each having length  $L_0$ , placed between two heat sinks with temperature  $T_0$  (Fig. 1). When current  $j$  flows through the emitters, Joule heat is released with power density  $P_J$ :

$$P_J = 2L_0 j^2 \rho, \quad (5)$$

where  $\rho$  is the emitter resistivity considered, for simplicity, to be the same for the n- and p-type regions [5].

When current flows through the quantum-confinement structure considered above (see Fig. 1), any electron passing through the system and absorbing a phonon takes away an energy  $\hbar \omega_0$  from the lattice, and, therefore, heat with power density  $P_Q$  is absorbed by the quantum structure:

$$P_Q = \frac{j \hbar \omega_0}{e}. \quad (6)$$

One's can find the spatial temperature distribution in the system:

$$T(x) = T_0 - \frac{1}{\kappa} \left[ (L_0 - |x|) \frac{j\hbar\omega_0}{2e} - (L_0^2 - x^2) \frac{j^2\rho}{2} \right]. \quad (7)$$

Thus, the following conclusions can be made. First, the system is cooled on passing current through it if  $P_J < P_Q$ , and, second, at  $P_J < 2P_Q$  the temperature of the quantum structure  $T_Q = T(x = 0)$  is lower than the ambient temperature  $T_0$ .

### Cooling temperature

The temperature of quantum system ( $x = 0$ ) is:

$$T_Q(j) = T_0 - \frac{jL_0\hbar\omega_0}{2\kappa e} + \frac{j^2\rho L_0^2}{2\kappa}. \quad (8)$$

It is noteworthy that the maximum cooling  $T_C = \max(T_0 - T_Q)$  is independent of the emitter length  $L_0$ :

$$T_C = \frac{(\hbar\omega_0)^2}{8e^2\rho\kappa}. \quad (9)$$

Using the Wiedemann–Franz law we obtain the final expression for the maximum cooling temperature  $T_C$ :

$$T_C = \frac{3}{8\pi^2} \frac{(\hbar\omega_0)^2}{T_0}. \quad (10)$$

Thus, we derived a universal law for the maximum cooling temperature of quantum structures with ohmic contacts. The maximal cooling temperature  $T_C$  depends on the single parameter of the system, namely, on the characteristic energy scale of the quantum structure, equal to  $E_2 - E_1 = \hbar\omega_0$ .

### Conclusion

A new mechanism of semiconductor nanostructure cooling by electric current is proposed. This mechanism differs from the Peltier effect [6], since in the given case the cooling temperature is independent of the difference between the kinetic coefficients, being governed solely by the difference in size-quantization energy between the first and second QWs.

With increasing temperature, both the tunneling rate and the rate of radiative recombination grow; as a result, the efficiency of cooling of the quantum system becomes higher.

The proposed cooling mechanism can be effectively used in optoelectronics, in developing LEDs and high-power semiconductor lasers [7].

### References

- [1] *Molecular Beam Epitaxy and Heterostructures*, ed. by L. Cheng and K. Ploog, (Martinus Nijhoff, Dordrecht, 1985).
- [2] L. Keldysh, *Zh. Exsp. Teor. Fiz.* **34**, p. 962–968 (1958).
- [3] V. F. Gantmakher and B. I. Levinson, *Carrier Scattering in Metals and Semiconductors* (Wiley, Amsterdam, 1987).
- [4] *Quantum Well Lasers*, ed. by P. S. Zory, Yr, (Academic, New York, 1983).
- [5] We are neglecting Thompson heat in our calculations.
- [6] A. A. Abrikosov, *Fundamentals of the Theory of Metals* (North-Holland, Amsterdam, 1988).
- [7] E. B. Dogonkin and G. G. Zegrya, submitted to *Electron. Lett.*
- [8] A. S. Polkovnikov and G. G. Zegrya, *Phys. Rev. B* **58**, 4039 (1998).

## Segment of an inhomogeneous mesoscopic loop as a dc power source

S. V. Dubonos, V. I. Kuznetsov and A. V. Nikulov

Institute of Microelectronics Technology and High Purity Materials,  
 Russian Academy of Sciences, 142432 Chernogolovka, Moscow District, Russia

**Abstract.** A dc voltage changed periodically with magnetic field is observed on segments of asymmetric aluminum loop without any external dc current at temperatures corresponded to superconducting transition. According to this experimental result a segment of the loop is a dc power source. A possibility of a persistent voltage on segments of an inhomogeneous normal metal mesoscopic loop follows from this result.

### Introduction

It is known that the persistent current (i.e. a direct current in the thermodynamic equilibrium state) can flow along a mesoscopic loop because of the quantization of the momentum circulation  $\oint_l dl p = \oint_l dl (mv + (q/c)A) = m \oint_l dl v + (q/c)\Phi = n2\pi\hbar$ . The persistent current  $I_p = sj_p$  in normal metal mesoscopic loops was predicted more than 30 years ago [1] and was observed not so long ago [2]. It is known also that a potential difference  $V = (\langle\rho\rangle_{l_s} - \langle\rho\rangle_l)l_s j$  should be observed on a segment  $l_s$  of an inhomogeneous conventional loop at a current density  $j$  along the loop if the average resistivity along the segment  $\langle\rho\rangle_{l_s} = \int_{l_s} dl \rho / l_s$  differs from the one along the loop  $\langle\rho\rangle_l = \int_l dl \rho / l$ . Therefore a possibility of a persistent voltage can be assumed at a segment of an inhomogeneous mesoscopic loop at  $j_p \neq 0$ .

The latter, i.e.  $j_p \neq 0$ , can be only if the mean free path of electrons is not smaller than the length  $l$  of loop circumference and the temperature is lower than the energy difference between adjacent permitted states  $p^2(n=1)/2m - p^2(n=0)/2m = 2\pi^2\hbar^2/ml^2$ . This difference is not large for electrons. For example, at  $l \approx 4 \mu\text{m}$ , the  $2\pi^2\hbar^2/ml^2$  value corresponds  $T \approx 1 \text{ K}$ . Therefore it is enough difficult to observe the persistent current in normal metal loop [2].

It is more easier to observe the persistent current in superconducting loop since the mean free path of superconducting pairs is infinite and the energy difference between adjacent permitted states is much higher than in normal metal loop. First experimental evidence of the persistent current at non-zero resistance — the Little-Parks experiment [3] was made as long ago as 1962. In the present work the dc voltage proportional to the  $I_p$  is observed on segments of an asymmetric superconducting loop in accordance with the analogy with a conventional inhomogeneous loop.

### 1. Experimental details

The dependencies of the dc voltage  $V$  on the magnetic flux  $\Phi \approx BS$  of some round symmetric and asymmetric Al loops (see Fig. 1) with a diameter  $2r = l/\pi = 1, 2$  and  $4 \mu\text{m}$  and a linewidth  $w = 0.2$  and  $0.4 \mu\text{m}$  at the dc measuring current  $I_m$  and different temperature close to  $T_c$  were measured. Here  $B$  is the magnetic induction produced by a superconducting coil;  $S = \pi r^2$  is the area of the loop. The Al microstructures (Fig. 1)

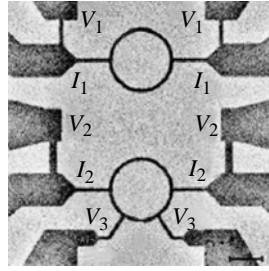


**Fig. 1.** An electron micrograph one of the aluminum loop samples.  $I_1$  and  $V_1$  are the current and potential contacts of the symmetric loop.  $I_2$  and  $V_2$  are the current and potential contacts of the asymmetric loop.  $V_3$  are the additional potential contacts of the asymmetric loop.

are prepared using an electron lithograph developed on the basis of a JEOL-840A electron scanning microscope. The sheet resistance  $R_\diamond \approx 0.5 \Omega/\diamond$  at 4.2 K, the resistance ratio  $R(300 \text{ K})/R(4.2 \text{ K}) \approx 2$  and the midpoint of the superconducting resistive transition  $T_c \approx 1.24 \text{ K}$ .

## 2. Experimental results

The voltage oscillations corresponded to the conventional Little–Parks oscillations were observed on the contacts  $V_1$  of the symmetric loop [4]. These resistance oscillations  $R_1(\Phi/\Phi_0) = V_1/I_1$  observed in the temperature region of the superconducting transition (i.e. at  $T \approx T_c$ ) are explained by the  $T_c$  oscillations  $T_c(\Phi/\Phi_0)$  because of the oscillation of the persistent current  $I_p(\Phi/\Phi_0)$  [5]. Here  $\Phi_0 = 2\pi\hbar c/q = \pi\hbar c/e$  is the flux quantum for superconducting pair,  $q = 2e$ . The voltage  $V_1 = 0$  at the measuring current  $I_1 \equiv I_m = 0$  whereas the voltage oscillations  $V(\Phi/\Phi_0)$  are observed on the contacts  $V_2$  and  $V_3$  of the asymmetric loop at  $I_2 \equiv I_m = 0$  (Fig. 2).

The apparent (with amplitude  $\Delta V \geq 0.1 \mu\text{V}$ ) oscillations without an external dc current were observed in a narrow temperature region  $\Delta T \approx 0.01 \text{ K}$  corresponds to the bottom of the resistive transition. Its amplitude increases (up to  $\Delta V \simeq 1.2 \mu\text{V}$ ) with temperature lowering down to the lowest temperature  $\approx 1.23 \text{ K}$  we could reach.

## 3. Power source

The observation of the voltage oscillations in the asymmetric loop and its absence in the symmetric loop conform to the analogy with a conventional loop. Although the oscillations  $I_p(\Phi/\Phi_0)$  [5] take place in the both cases in the symmetric loop  $\langle \rho \rangle_{I_s} = \langle \rho \rangle_I$  and therefore  $V = 0$  at  $I_m = 0$ . The difference of  $\langle \rho \rangle_{I_s}$  from  $\langle \rho \rangle_I$  in the asymmetric loop is caused by the additional potential contacts  $V_3$ .

There is an important difference from the conventional loop where the potential difference appears in accordance with the Ohm's law  $E = -\nabla V - (1/c)dA/dt = \rho j$ . The voltage in Fig. 2 is observed without the Faraday's voltage  $dA/dt = (1/l)d\Phi/dt = 0$  and consequently the electric field  $E = -\nabla V$  and the persistent current  $I_p$  should have opposite directions in a segment because  $\oint_l dl \nabla V \equiv 0$ , i.e. according to the result presented in Fig. 2 a segment of the asymmetric loop is a dc power source at  $\Phi \neq n\Phi_0$  and  $\Phi \neq (n + 0.5)\Phi_0$ . The power  $W_{\text{load}} = V^2 R_{\text{load}} / (R_{\text{load}} + R_s)^2$  can be obtained on a load with the resistance  $R_{\text{load}}$ . Because the resistance of the segment  $R_s \leq R_{sn} \approx 15 \Omega$  then  $W_{\text{load}} = V^2 / 4R_s \geq 2 \cdot 10^{-14} \text{ Wt}$  at  $R_{\text{load}} = R_s$  and  $V \approx 1 \mu\text{V}$ .

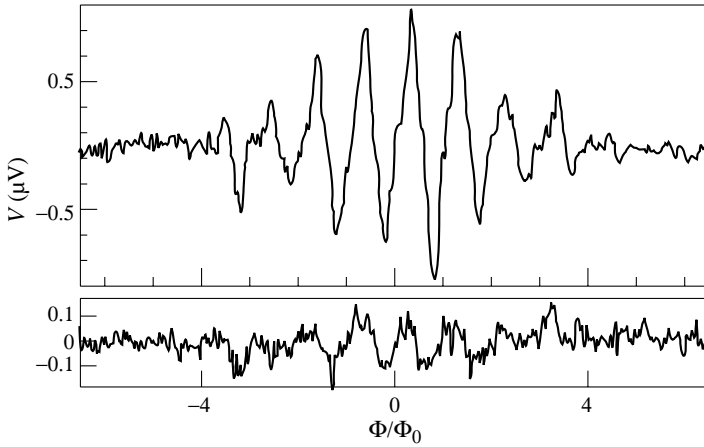


**Fig. 2.** Oscillation of the voltage measured on the  $V_2$  contacts (upper curve) and on the  $V_3$  contacts (lower curve) of the asymmetric loop with  $2r = 4 \mu\text{m}$  and  $w = 0.4 \mu\text{m}$ .  $I_m = 0$ .  $T = 1.231 \text{ K}$  corresponded to the bottom of the resistive transition.

#### 4. What energy is transformed in the power $VI_p$ ?

It should be noted that already the classical Little–Parks experiment is evidence of the dc power source. According to this experiment the persistent current  $I_p \neq 0$  is observed at non-zero resistance  $R_l > 0$  along the loop and consequently an energy dissipation with the power  $R_l I_p^2$  takes place. The persistent current is maintained in spite of this dissipation because of reiterated changes of the momentum circulation of superconducting pairs at switching of the loop between superconducting states with different connectivity [6].

Because of the quantization the momentum circulation of pair  $\int_l dl p = 2m \int_l dl v + (2e/c)\Phi$  changes from  $(2e/c)\Phi$  to  $n2\pi\hbar$  at each closing of superconducting state. The reiterated changes  $n2\pi\hbar - (2e/c)\Phi = 2\pi\hbar(n - \Phi/\Phi_0)$  with an average frequency  $\omega$  is equivalent of the action of an average force  $\int_l dl F_q = 2\pi\hbar(\bar{n} - \Phi/\Phi_0)\omega$  which maintains the circulating current instead of the Faraday's voltage.  $\bar{n}$  is the thermodynamic average of the quantum number  $n$ .  $\bar{n} - \Phi/\Phi_0 \approx (n - \Phi/\Phi_0)_{\min}$  when  $\Phi$  is not close to  $(n + 0.5)\Phi_0$  and  $\bar{n} - \Phi/\Phi_0 = 0$  at  $\Phi = (n + 0.5)\Phi_0$ , where the integer number  $n$  in  $(n - \Phi/\Phi_0)_{\min}$  corresponds to a minimum possible value  $|n - \Phi/\Phi_0|$ .

The quantum force  $F_q$  is not localized in principle in any loop segment [6], i.e.  $F_q = \int_l dl F_q/l$ . Therefore a potential difference  $V = (\pi\hbar\omega/e)(\bar{n} - \Phi/\Phi_0)(l_s/l)$  should be observed on a segment  $l_s$  remaining in superconducting state when other segment is switched in normal state with the frequency  $\omega$ . This relation explains the observed voltage oscillation (Fig. 2). Loop segments are switched in normal state at  $T \simeq T_c$  by thermal fluctuations and an external electric noise. Consequently the energy of thermal fluctuations or an external electric noise is transformed in the power  $VI_p$  observed in our work.

#### 5. Conclusion

The observation of the voltage oscillations (Fig. 2) is evidence of a possibility of an analogous observation on segments of inhomogeneous normal metal mesoscopic loop. There is an important question: thermal fluctuations or an external noise induce the dc voltage.

The temperature dependence of the amplitude  $\Delta V(T)$  observed in our work is evidence of the latter. But it is enough obvious that thermal fluctuations can also induce the dc voltage on segments of inhomogeneous mesoscopic loops [6].

#### *Acknowledgements*

This work was financially supported by the Presidium of Russian Academy of Sciences in the Program “Low-Dimensional Quantum Structures”.

#### **References**

- [1] I. O. Kulik, *Pisma Zh. Eksp. Teor. Fiz.* **11**, 407 (1970) [*JETP Lett.* **11**, 275 (1970)].
- [2] L. P. Levy *et al*, *Phys. Rev. Lett.* **64**, 2074 (1990);  
V. Chandrasekhar *et al*, *idid.* **67**, 3578 (1991);  
E. M. Q. Jariwala *et al*, *idid.* **86**, 1594 (2001).
- [3] W. A. Little and R. D. Parks, *Phys. Rev. Lett.* **9**, 9 (1962).
- [4] S. V. Dubonos, V. I. Kuznetsov and A. V. Nikulov, physics/0105059.
- [5] M. Tinkham, *Introduction to Superconductivity*. McGraw-Hill Book Company, 1975.
- [6] A. V. Nikulov, *Phys. Rev. B* **64**, 012505 (2001)



## Strongly modulated conduction in Ag/PLZT/LSCO ferroelectric field-effect transistor

I. Grekhov, L. Delimova, I. Liniichuk, D. Mashovets and I. Veselovsky  
Ioffe Physico-Technical Institute, St Petersburg, Russia

**Abstract.** A possibility of fabricating all-perovskite field effect transistor is shown, which can provide the development of a nonvolatile memory cell with a nondestructive readout of information. A thin ( $\sim 5\text{--}10\text{ nm}$ ) Sr-doped lanthanate cuprate (LSCO) film was used as a transistor channel while a ferroelectric gate insulator was a lead zirconate titanate (PLZT) film of about 100 nm thickness. The modulation of a channel conduction was found in the studied transistors to be  $\sim 70\%$ , which is an order of magnitude larger than that reported in the world literature.

### Introduction

Non-volatile memory devices are called so because they retain information when power is interrupted, therefore, they are important computer components. In this context, there has been considerable recent interest in developing non-volatile memories that use ferroelectric thin films — “ferroelectric random access memory” or FRAMs, in which information is stored in the polarization state of the ferroelectric material. A memory cell of the present FRAM is composed of a ferroelectric capacitor where the binary information is stored in terms of the signs of the stored charge, and a metal-oxide-semiconductor field effect transistor for cell selection. The stored data are destroyed during the “read” operation and it is necessary to rewrite them at the end of the operation. A radically novel approach to the memory problem is the idea of a field effect transistor with a ferroelectric gate insulator (FFET). In this case, the capacitor is not necessary because the ferroelectric gate can be considered as the information storage medium if its remnant polarization is high enough to modulate the channel conductance. The read-out of information can be done simply by pulsed control of channel conductance. Therefore, FFET is the most promising memory cell providing a high memory density, non-volatile storage, and a nondestructive read-out of information. Fabricating FFET on the basis of ordinary semiconductors was found to face with great difficulties resulting from a diffusion of Pb, Ti, and other elements into the Si substrate and forming unnecessary  $\text{SiO}_2$  layer with low dielectric constant. A structure of an all-perovskite FFET proposed as a different approach by Y. Watanabe [1] was shown to form chemically and crystallographically compatible epitaxial heterostructures. The best result found on  $\text{La}_{1.99}\text{Sr}_{0.01}\text{CuO}_4/(\text{Pb}_{0.95}\text{La}_{0.05})(\text{Zr}_{0.2}\text{Ti}_{0.8})\text{O}_3$  structure was a 10% change in the channel conduction at the gate voltage  $\pm 5\text{ V}$  [1]. In this paper, we report much deeper ( $\sim 70\%$ ) modulation of conductance in a LSCO/PLZT/Ag transistor structure.

### 1. Sample preparation

The transistor structures were produced by a sequential deposition of laser ablated films on the  $\text{NdGaO}_3$  (110) substrate, the details are given in [2]. We used two types of Sr-doped lanthanate cuprate  $\text{La}_{1.94}\text{Sr}_{0.06}\text{CuO}_4$  and  $\text{La}_{1.85}\text{Sr}_{0.15}\text{CuO}_4$  forming a transistor channel of 5–10 nm thickness, 230  $\mu\text{m}$  width, and 320  $\mu\text{m}$  length of under gate-insulator path. The gate insulator of 80–100 nm thickness was a ferroelectric  $(\text{Pb}_{0.95}\text{La}_{0.05})(\text{Zr}_{0.2}\text{Ti}_{0.8})\text{O}_3$ . Figure 1 shows a field effect transistor structure.

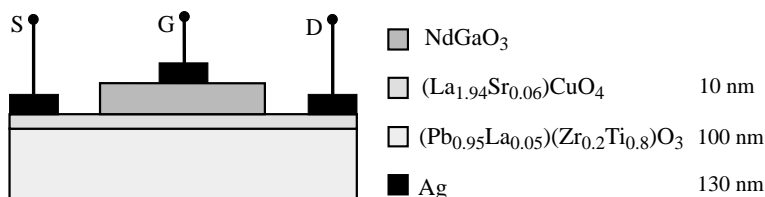


**Fig. 1.** Field effect transistor structure. Here S, G, D denote source, gate, and drain, respectively. The layer compositions and thicknesses are shown.

## 2. Results and discussion

The microstructure of PLZT and LSCO films was found from the x-ray diffraction data to show a c-oriented modification with rather good layer crystallinity and crystal lattices corresponding to the data of International Center JCPDS. The polarization hysteresis loop in Ag/PLZT/LSCO structures measured by Sawyer–Tower method at 100 Hz frequency and room temperature showed a typical character for a ferroelectric; the saturation polarization was  $P_s \sim 40\text{--}45 \mu\text{C}/\text{cm}^2$ , the maximum remnant polarization was  $P_r \sim 20\text{--}30 \mu\text{C}/\text{cm}^2$ , the coercive field strength was  $\approx (1\text{--}3) \times 10^5 \text{ V}/\text{cm}$ . According to the data on the PLZT band gap, electron affinity, and Fermi level pinning above the valence band [3], an Ag/PLZT/LSCO gate region can be considered as a Me/p/p<sup>+</sup>-structure. Indeed, the hole density in PLZT is usually assumed to be in the range of  $p = 10^{16}\text{--}10^{18} \text{ cm}^{-3}$ , the dielectric constant at zero external electric field is  $\epsilon \sim 100\text{--}300$ . The hole density in LSCO is controlled by a Sr content and, as was found from the Hall measurements of single crystals to be about  $p^+ \sim 7 \times 10^{20} \text{ cm}^{-3}$  and  $p^+ \sim 5 \times 10^{21} \text{ cm}^{-3}$  for La<sub>1.94</sub>Sr<sub>0.06</sub>CuO<sub>4</sub> and La<sub>1.85</sub>Sr<sub>0.15</sub>CuO<sub>4</sub>, respectively [4]. The Schottky barrier height at the Ag/PLZT interface is about  $\phi \sim 2.2 \text{ eV}$ . Therefore, the width of the PLZT space charge region at zero external electric field is about  $W \sim 100 \text{ nm}$  even for the carrier density  $N_A = p = 10^{18} \text{ cm}^{-3}$  and  $\epsilon = 100$ . This means that 80–100 nm thick PLZT layer in the studied structure is entirely depleted.

Figure 2 shows the total channel conductance versus the gate voltage measured relative to the drain in an Ag/PLZT/La<sub>1.94</sub>Sr<sub>0.06</sub>CuO<sub>4</sub> structure. The conductance is normalized to its maximal magnitude of  $6 \times 10^{-7} \Omega^{-1}$ .

The channel conductance modulation is seen to be  $\sim 32\%$  which is much higher than 10% observed in all-perovskite transistors [1]. The inset in Fig. 2 shows the same plot upon subtraction of the ballast resistance of the nonmodulated regions from the total channel resistance (the gate area in the studied structure covered only 20% of the total channel lengths); the effective modulation amplitude is  $\sim 73\%$ . The hole density in the La<sub>1.94</sub>Sr<sub>0.06</sub>CuO<sub>4</sub> channel was found from the data of Fig. 2 and the mobility value of  $1 \text{ cm}^2/\text{Vs}$  to be  $p \approx 3 \times 10^{18} \text{ cm}^{-3}$ , which is far lower than that of a single crystal.

We used the Atomic Force Microscopy to study the early stage of LSCO growth on a NdGaO<sub>3</sub> substrate. It was found that in the range of the 10–20 nm film thickness there is a crossover between a layer-by-layer (Frank–van der Merwe) and layer-by-layer followed by island growth (Stranski–Krastanov mode), resulting in a different surface morphology. The islands of 50 nm high and 200–600 nm in diameter, as a part of the channel, can not be modulated due to their large thickness; at the same time, they prevent the penetration of the electric field into the narrow space in between. Therefore, such surface morphology cannot provide a deep modulation of a laser-ablated FFET with the LSCO channel thickness above 10–20 nm. The channel resistance of the transistor in the “on” state was rather high ( $\sim 2 \text{ M}\Omega$ ) resulting in a limitation of the device speed. One of the possible ways to lower

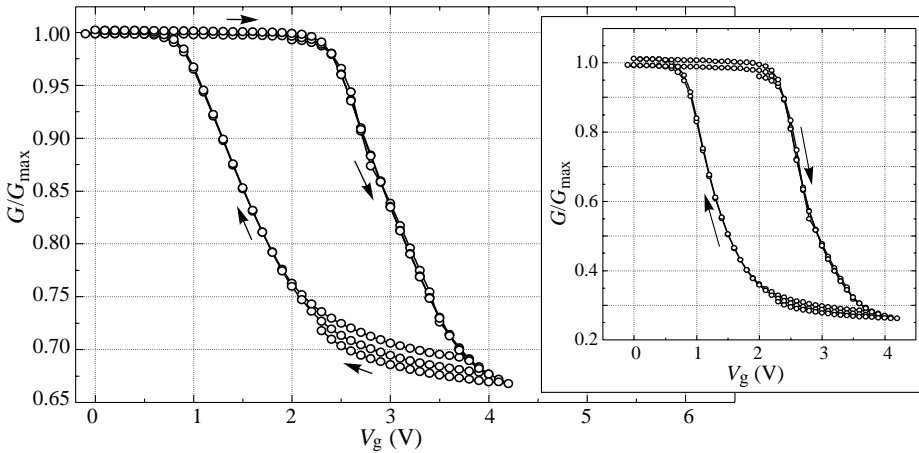


**Fig. 2.** The channel conductance  $G$  depending on the gate voltage  $V_g$ . The arrows indicate the direction of the varying voltage. Three cycles of measurements are given. The inset shows the same dependence after the subtraction of the ballast nonmodulated regions from the total resistance of the channel. The conductance is normalized to its maximal value  $G_{\max}$ .

the channel resistance is to increase the free hole density  $p$  or to increase the Sr content in LSCO. In doing so, for a favorable modulation condition to be kept, the channel thickness should be reduced as  $p^{1/2}$ , this results in the total decrease of the channel resistance as  $p^{1/2}$ .

We fabricated a FFET with a 5 nm-thick  $\text{La}_{1.85}\text{Sr}_{0.15}\text{CuO}_4$  channel where the conductance modulation on the gate voltage was 57%. The channel carrier density was found for zero gate voltage and the  $1 \text{ cm}^2/\text{Vs}$  mobility to be  $p \approx 9 \times 10^{18} \text{ cm}^{-3}$ , the channel resistance in the “on” state is about  $1 \text{ M}\Omega$ . The conductance modulation increase from 32% in  $\text{La}_{1.94}\text{Sr}_{0.06}\text{CuO}_4$  channel to 57% in  $\text{La}_{1.85}\text{Sr}_{0.15}\text{CuO}_4$  one can be accounted for by the rise of the gate width to the channel length ratio for these two structures. The ratios were about 0.2 and 0.4 for  $\text{La}_{1.94}\text{Sr}_{0.06}\text{CuO}_4/\text{PLZT}$  and  $\text{La}_{1.85}\text{Sr}_{0.15}\text{CuO}_4/\text{PLZT}$ , respectively. Of course, the structure under investigation is much larger than an intended cell size for nonvolatile memory and should be scaled properly.

### 3. Conclusions

A possibility of deep ( $\sim 70\%$ ) conductance modulation has been shown in an Ag/PLZT/LSCO all-perovskite ferroelectric field effect transistor. Relatively low carrier density ( $\sim 10^{18} - 10^{19} \text{ cm}^{-3}$ ), small thickness, and rather high surface quality of the channel have provided the penetration of the electric field into the major part of the channel and deep conductance modulation, sufficient, in principle, for operation of a non-volatile memory cell with a nondestructive readout of information.

#### Acknowledgements

The work was supported by the Program of RAS “Low-dimensional quantum Structures” and partly by RFBR grant No 00-15-96770.

### References

- [1] Y. Watanabe, *Appl. Phys. Lett.* **66**, 1770 (1995).
- [2] I. Veselovsky, I. Grekhov, L. Delimova and I. Liniichuk, *Pis'ma JTF* **27**, 39 (2001).
- [3] J. F. Scott, *et al*, *Ferroelectrics* **225**, 83 (1999).
- [4] M. Sato, T. Nishikawa, J. Takeda and H. Harashina, *J. Phys. Soc. Jap.* **63**, 1141 (1994).

## The operating modes of the Auger-transistor and the photo-field detectors under strong electric field

V. D. Kalganov<sup>†</sup>, N. V. Mileshekina<sup>†</sup> and E. V. Ostroumova

Ioffe Physico-Technical Institute, St Petersburg, Russia

<sup>†</sup> Institute of Physics, St.Petersburg State University, 198904 Petrodvorets, Russia

**Abstract.** Conditions for appearance of a self-consistent quantum well in both the near-surface region of a vacuum semiconductor field-emitter and a case of metal-insulator-semiconductor heterostructures (Auger-transistor) under strong electric field have been studied.

### 1. Introduction

The photo-field emission properties of semiconductors at a very strong electric field as well as the parallel investigation of tunnel electron emission in metal-insulator-semiconductor heterostructures with a tunnel-transparent layer of an insulator have been studied. It was found that the self-consistent quantum well near the surface of semiconductor emitter tips can change the spectral region of photosensitivity of the radiation detectors, based on a semiconductor field emitter, and leads to the significant increase in their photosensitivity [1]. Also the appearance of the self-consistent quantum well near the semiconductor surface is the key factor in the ability to use the metal-insulator heterojunction in the development of an Auger transistor based on the Al-SiO<sub>2</sub>-n-Si structure which is the fastest operation semiconductor bipolar transistor [2, 3].

### 2. Experimental and theoretical results and discussion

In the Auger transistor in particular we used a metal-insulator heterojunction instead of a wide-gap semiconductor (Fig. 1). The Auger transistor base is created by holes, which are induced on n-type silicon surface by strong electric field that exists in the thin oxide layer. The base is formed as a self-consistent quantum well for holes near the surface of n-type silicon. The base width is about 10 Å and the well depth is equal up to 0.7 eV. Auger transistor is a new type of semiconductor devices in which impact ionization or, in other words, Auger-generation of electron-hole pairs is used for generation and amplification of electrical signal. By means of impact ionization hot electrons produce additional electron-hole pairs, so that instead of one hot electron two electrons and one hole with lower kinetic energy are created in the transistor base. The characteristic time of this process is  $10^{-12} - 10^{-13}$  s. One could design a transistor in which, depending on the actual semiconductor type of the conductivity, holes rather than electrons would be the hot carriers. The advantages of the Auger transistor compared to the conventional transistors are obvious. First, the Auger transistor makes use of impact ionization, which is the fastest of all known current amplification processes. Second, the transistor current gain coefficient  $\beta$  (in the common emitter scheme) can be infinite or even negative ( $\beta \rightarrow \infty$  for  $\alpha = 1$ , and  $\beta < 0$  when  $\alpha > 1$ ). In the Al-SiO<sub>2</sub>-n-Si Auger transistor it is possible to apply to the silicon surface an electric field up to  $3 \cdot 10^7$  V/cm of any directions i.e. the electric field of the same strength as for the case of field emission structures (the tips). Thus it is possible to observe emission of electrons both from the

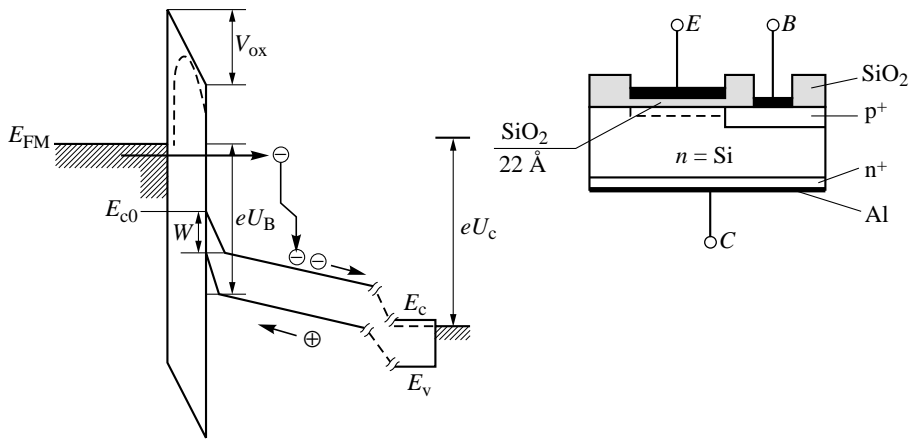


**Fig. 1.** Energy diagram of the Al-SiO<sub>2</sub>-n-Si Auger transistor with a tunnel-thin oxide layer. The self-consistent quantum well forms the transistor base.

metal to the semiconductor, and from the semiconductor to the metal. In the former case we can obtain the hot electrons, which are injected into the silicon with the kinetic energy up to 2.5 eV, that exceeds the threshold of impact ionisation in silicon. That means the generation of new electron-hole pairs is very possible. Namely these new electron-hole pairs determine an amplification of the Auger transistor [4].

The quantum size effect in the potential well of a field emitter, observed here for the narrow-gap semiconductor, for *n*-InSb structure, is used to produce the radiation detectors with a wide IR-range of the spectral sensitivity together with the known photosensitivity of the field detection structures connected with fundamental absorption of a semiconductor crystal [1, 5]. The photosensitive region location for the p-type field emitters as well as emitters mode of a high-resistivity semiconductor depends on dimension of the self-consistent quantum well also.

Photoresponse of the field emission current from the high-resistivity GaAs-tips ( $\rho = 10^6 \Omega/\text{cm}$ ) is shown in Fig. 2 for the various anode voltages corresponding to the different regions of the I-V characteristics when the light probe is moving along the field emitter. As may be seen in Fig. 2 the photoresponse depends on the electric field strength. At low voltage it does not depend on the light probe position (curve 1). The effect become more considerable and localised for the higher fields (curve 2 and 3). The photosensitive region profile is transformed when anode voltage increases and the photosensitive region shifts toward the tip base. It is very important also to estimate correctly the real value of the quantum yield for the field detection structures.

The field emitting tips from high-resistivity GaAs-crystals with the quantum yield about 120% and with a high degree of geometrical reproducibility were fabricated. Measurements of the photosensitive region profile showed that the photoresponse of the emission current can be observed under illumination of the top of a tip as well as the bulk of emitters that is quite convenient for practical purposes. The great value of the quantum yield of a semiconductor field emitter has been observed for so-called third region of the I-V characteristic when the electron multiplication processes are involved.

Experiments with both the emission of electrons from the semiconductor tips, and with the injection of hot electrons in Al-SiO<sub>2</sub>-n-Si structures show that the tunnel current of electrons from the self-consistent quantum well has appeared to be smaller, than the tunnel

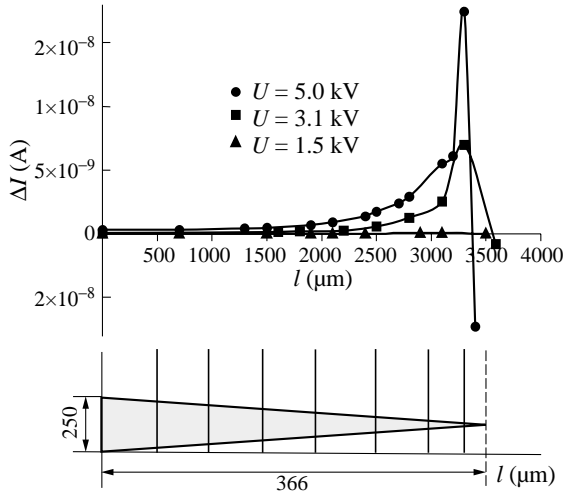


**Fig. 2.** Photoresponse profile for GaAs emitter (light probe  $d = 160\ \mu\text{m}$ ) for different anode voltages,  $T = 300\ \text{K}$ .

current of electrons from the valence band in a case of tips, and smaller, than tunnel current from the metal to the conduction band of silicon in Al-SiO<sub>2</sub>-n-Si structures.

In both cases the charge density in the self-consistent quantum wells determines the magnitude of the tunnel current of electrons from the valence band in case of tips, or the magnitude of the tunnel current of electrons from the metal into the conduction band of silicon in case of the Auger transistor. The magnitude of a tunnel current (collector current) in the Auger transistor is determined by the base voltage. In the semiconductor tips the magnitude of a tunnel emission current was determined by the illumination intensity of the semiconductor tip (Fig. 3). When the strong electric field is applied to the semiconductor surface, the steady state is installed between electrons and holes in the bulk of semiconductor and electrons or holes, which are in the surface self-consistent quantum well. In the Auger transistors the current carriers density, which are attract to the surface by the strong electric field, reach up to  $2\text{--}4 \times 10^{13}\ \text{cm}^{-2}$ . A similarity of tunnel currents of the Auger transistor and electron emission currents from semiconductor tips to vacuum is based mainly on the fact that in both cases they are electron currents but not hole currents [1]. The hole tunnel currents in the Al-SiO<sub>2</sub>-n-Si Auger transistor practically on all cases flow through the conduction band of silicon oxide. The hole tunnel current which is taking place through the silicon oxide valence band is too small due to heavy effective mass of holes in the SiO<sub>2</sub> valence band ( $m_h > 5$ ) [1, 5].

Another common problem for both of two devices is that energy levels of semiconductor

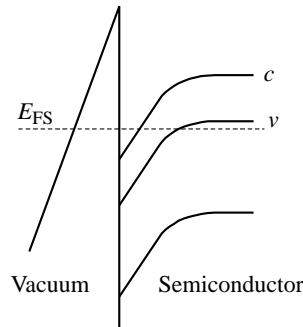


**Fig. 3.** Energy diagram of p-type semiconductor tips. On the right side are shown (from up to down) the bottom of conduction band, the top and the bottom of valence band.

valence and conduction bands may have the same energy values if the electric fields on the interfaces are strong enough. As a result the change of the electron current to the hole current may be treated as Zener breakdown. At present this problem is interesting in the investigation of emission current into vacuum by p-type semiconductor tips. When the electric field is relatively weak the p-type semiconductor tips are dielectric tips because there are no electrons in conduction band to tunnel into vacuum. The strong electric field mixtures the conduction and valence band states. As a result the current in vacuum and in thin layer of p-type semiconductor is carried out by electrons and in volume of semiconductor crystal this current has a hole nature.

The experimental studies of the field emission structures based on semiconductor tips and MIS transistor structures with a tunnel-thin oxide layer are of interest, since in both cases it is necessary to take into account only the currents of tunnel electrons both through the vacuum and through the tunnel-thin silicon oxide but not a current of holes. The reason for this is that only the electron current exists in the vacuum, and the same is true for the Al-SiO<sub>2</sub>-n-Si heterostructure, where the tunnel current is almost the electron one, since the tunneling of holes through the SiO<sub>2</sub> layer should not be taken into account because of the large effective mass of holes in silicon oxide.

### 3. Conclusions

The strong electric field applied to a surface can considerably modify the electronic characteristics of semiconductor-insulator interfaces. This gives the reason to suppose that under strong electric field conditions appropriate to the occurrence of a self-consistent quantum well near the semiconductor surface or non-equilibrium processes, the emissions properties of a semiconductor tip can be improved according to requested characteristics. Simultaneous treatment of injection currents in the Al-SiO<sub>2</sub>-n-Si Auger transistor and emission currents in case of the semiconductor tips shows that in both cases the currents are tunnel currents and carried out by electrons, not holes.

The investigation of the metal-insulator-semiconductor heterostructures allows to realize the emission of hot electrons from the metal to the semiconductor, and makes possible to create the Auger-transistor based on the Al-SiO<sub>2</sub>-n-Si structure which is the fastest operation semiconductor bipolar transistor [2, 3].

#### Acknowledgements

This research is supported by RFBR-00-02-17042 and "Integration" 326.37 and partly by "Surface atomic structures" Russian Science Programmes, and NATO's "Science for Peace" Programme.

### References

- [1] A. A. Rogachev, V. D. Kalganov, N. V. Mileschkina and E. V. Ostroumova, *Microelectronics J.* **31**, 905-911 (2000).
- [2] E. V. Ostroumova and A. A. Rogachev, in: "Fundamental Aspects of Ultrathin Dielectrics on Si-Based Devices: Towards an Atomic-Scale Understanding", NATO Science Series, 3. High Technology Vol. 47, 383-391, Kluwer Academic Dordrecht/Boston/London, (1998).
- [3] E. V. Ostroumova and A. A. Rogachev, *Microelectronics J.* **29**, 701-708 (1998).
- [4] E. V. Ostroumova and A. A. Rogachev, *Appl. Surface Sci.* **166**, 480-484 (2000).
- [5] T. Deck, V. D. Kalganov, N. V. Mileschkina, A. Moscardini and E. V. Ostroumova, *Phys. Low-Dimensional Struct.* Nov-Dec. (11/12), 147-160 (2000).

## The origin of the $1/f$ noise in GaN-based HFETs: Is it tunneling?

*M. E. Levinshtein*

Ioffe Physico-Technical Institute, St Petersburg, Russia

**Abstract.** The nature of the  $1/f$  noise in GaN/GaAlN Heterostructure Field Effect Transistors (HFETs) has been discussed. New experimental results on the  $1/f$  noise in GaN/GaAlN HFETs and different models on the flicker noise have been also described. It has been demonstrated that the  $1/f$  noise in GaN/GaAlN HFETs might be linked to the electron tunneling from the 2D gas into the tail states in GaN or AlGaIn layers.

### Introduction

GaN/GaAlN heterostructures are now in the forefront of the semiconductor research.

A low frequency noise is one of the most important characteristics of devices used in microwave and optical communication systems. The noise level in different semiconductor materials and structures is usually characterized by the dimensionless Hooge parameter,  $\alpha$  [1]:

$$\alpha = \frac{S_I}{I^2} f N \quad (1)$$

where  $N$  is the total number of the conduction electrons in the sample,  $f$  is the frequency of the analysis,  $S_I/I^2$  is the relative spectral density of noise. The values of  $\alpha$  for the same semiconductor might differ by several orders of magnitude depending on the material structural perfection.

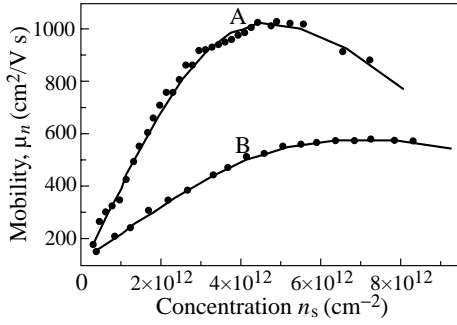
Until now, the level of the  $1/f$  noise in thin ( $\sim 0.1\text{--}3\ \mu\text{m}$ ) n-GaN epi-layers of average quality is rather high. The estimated values of Hooge constant  $\alpha$  range from 1 to 10. The level of noise is strongly correlated with the structural imperfection of the samples. Unlike GaN films, GaN/GaAlN HFETs are characterized by rather low level of the  $1/f$  noise with  $\alpha$  values of  $\sim 10^{-4}\text{--}10^{-5}$  [2, 3]. These magnitudes of  $\alpha$  are comparable with those for GaAs/GaAlAs HFETs. (Note that for GaAs epi-layers of average quality the values of  $\alpha$  lie within the range  $10^{-4} < \alpha < 10^{-5}$ ). Hence, it is obvious that the mechanism responsible for the  $1/f$  noise in thin GaN layers is suppressed in the GaN/GaAlN nano-structures.

### Results and discussion

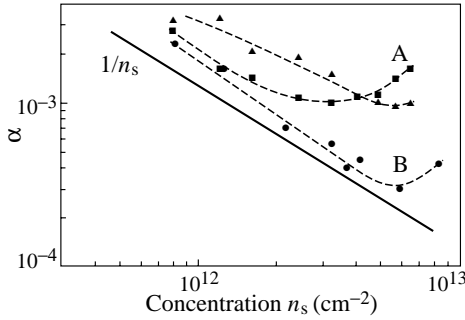
Two types of AlGaIn/GaN HFETs were investigated, both grown by metalorganic chemical vapor deposition (MOCVD) on a semi-insulating 4H-SiC substrate [4]. They consisted of a 50-nm-thick AlN buffer layer, 0.4- $\mu\text{m}$ -thick undoped GaN layer, followed by  $\text{Al}_{0.2}\text{Ga}_{0.8}\text{N}$  barrier layer, which was doped with silicon to approximately  $2 \times 10^{18}\text{ cm}^{-3}$ . The transistors had the source-drain spacing of 4–5  $\mu\text{m}$ , the gate length,  $L$ , of 1–1.5  $\mu\text{m}$ , and the gate width,  $W$ , in the range of 50 to 150  $\mu\text{m}$ . In the structures of type A, the thickness of the AlGaIn layer was 30 nm. The thickness of the AlGaIn layer in B structures was about 10 nm. All other parameters of the wafers were identical.

Fig. 1 shows the dependence of the electron mobility  $\mu_n$  in 2D-gas on channel electron concentration  $n_s$  in the structures under study. As seen in Fig. 1,  $\mu_n$  first increases with  $n_s$ , reaches a maximum value at  $n_s = (5\text{--}7) \times 10^{12}\text{ cm}^{-2}$ , and then monotonically decreases with a further increase of  $n_s$ . The increase of  $\mu_n$  with  $n_s$  is explained by increased screening of ionized impurities and dislocations in the 2D electron gas. The subsequent decrease





**Fig. 1.** The dependences of the mobility on channel concentration  $n_s$  for wafers A and B [4].



**Fig. 2.** The dependencies of the Hooge parameter  $\alpha$  on 2D sheet channel concentration  $n_s$  for A and B GaN/GaAlN HFETs. Different symbols for A transistors represent the data for different samples [4].

of  $\mu_n$  can be attributed to the electron's spillover from the 2D-channel to a parallel low electron-mobility "parasitic conduction channel" [5].

The noise spectra of current fluctuations  $S_I$  had the form of  $1/f^\Gamma$  noise with  $\Gamma$  close to unity ( $\Gamma = 1.0-1.15$ ) for both A and B structures. It was shown that neither the contact noise nor the noise from gate leakage current, contributed much to the total output HFET noise.

For the transistors of both types the relative spectral noise density  $S_{Id}/I_d^2$  increases with decreasing gate voltage,  $V_{gn}$ , faster than  $S_{Id}/I_d^2 \sim V_{gn}^{-3}$ . This effect is well known for all kinds of GaN-based HFETs and for many types of Si MOSFETs (see, for example, [6, 7]) and it can be phenomenologically described via the dependence of the Hooge parameter,  $\alpha$ , on the gate voltage.

Figure 2 represents the dependence of  $\alpha$  on the sheet channel concentration,  $n_s$ , extracted from experimental data. As seen, at high electron concentrations,  $\alpha$  is lower for the B devices than that for the A devices. This clearly shows that the low field mobility is not the only factor that correlates with the  $1/f$  noise level. At zero gate bias where devices B have a substantially lower level of the  $1/f$  noise, the values of  $n_s$  are  $6.5 \times 10^{12} \text{ cm}^{-2}$  and  $8.3 \times 10^{12} \text{ cm}^{-2}$  for structures A and B, respectively. Since the values of  $n_s$  are close for both structures, the degree of screening of the ionized impurities cannot explain the difference in the noise levels as was suggested in [6].

In spite of the difference in the absolute values of  $\alpha$ , the  $\alpha(n_s)$  dependencies are identical for both structures. At low channel concentrations,  $\alpha$  decreases with the increase of  $n_s$  as  $\alpha \sim 1/n_s$ , reaches a minimum and then increases with a further increase of  $n_s$ . The minimum value of  $\alpha$  in Fig. 2 corresponds to nearly the same concentration,  $n_s$  as the maximum in the mobility curves shown in Fig. 1.

The dependence  $\alpha \sim 1/n_s$  indicates that the spectral density of the channel resistance fluctuations,  $S_{Rch}$ , does not depend on the channel concentration. Note that such a situation

is very characteristic for Si MOSFETs, where the nature of the  $1/f$  noise is well known: noise arises from the electron tunneling from the semiconductor to traps in the oxide. Hence, the observed  $\alpha \sim 1/n_s$  dependence might be linked to the electron tunneling from the 2D gas into the tail states in GaN or AlGaIn. The amplitude of that surface noise depends only on the trap density at the Fermi level.

Until now, two mechanisms of the  $1/f$  noise suppression in the HFETs channels have been discussed. In Ref. [8] it was suggested that the  $1/f$  noise in the HFETs channels is caused by the fluctuations of the occupancy of the tail states near the band edges. Then, for degenerate semiconductors, the noise caused by the tail states decreases with an increase in the degeneracy as  $\exp((E_F - E_c)/kT)$  [9]. Hence, a high degree of degeneracy in GaN/GaAlIn HFET channels might explain such a drastic noise reduction.

Another mechanism links the  $1/f$  noise in GaN films and GaN/GaAlIn HFETs to the fluctuations in the space charge regions surrounding the dislocations [6]. Hence, this mechanism relates a high level of the  $1/f$  noise in GaN films to a very large dislocation density in thin GaN layers ( $\sim 10^8 - 10^{10} \text{ cm}^{-2}$ ) [6]. The suppression of the  $1/f$  noise in the GaN/GaAlIn HFET channels is explained by a very effective screening of the dislocations by the 2D gas. Only qualitative speculations on this mechanism of the  $1/f$  noise suppression have been discussed in Ref. [10].

The results obtained demonstrate clearly that in the conditions when the  $1/f$  noise caused by the tail states or dislocations is suppressed, a tunneling mechanism might be responsible for the residual  $1/f$  noise in the 2D gas in GaN/GaAlIn HFETs [11].

#### Acknowledgements

The author would like to thank Profs. Michael S. Shur and Segey L. Rumyantsev for helpful and stimulating discussions.

#### References

- [1] F.N. Hooge, T.G.M. Kleinpenning and L.K.J. Vandamme, *Rep. Progr. Phys.* **44**, 479 (1981).
- [2] M.E. Levinshstein, S.L. Rumyantsev, R. Gaska, J.W. Yang and M.S. Shur, *Appl. Phys. Lett.* **73**, 1089 (1998).
- [3] A. Balandin, S. Cai, R. Li, K.L. Wang, Vol. Ramgopal Rao and C.R. Viswanathan, *IEEE Electron Dev. Lett.* **19**, 475 (1998).
- [4] S.L. Rumyantsev, N. Pala, M.S. Shur, R. Gaska, M.E. Levinshstein, P.A. Ivanov, M. Asif Khan, G. Simin, X. Hu and J. Yang, *Semicond. Sci. and Technol.*, submitted for publication (2002).
- [5] X. Z. Dang, P.M. Asbeck, E. T. Yu, G. J. Sullivan, M. Y. Chen, B. T. McDermott, K. S. Boutros and J. M. Redwing, *Appl. Phys. Lett.* **74**, 3890 (1999).
- [6] J.A. Garrido, B.E. Foutz, J.A. Smart, J.R. Shealy, M.J. Murphy, W.J. Schaff and L.F. Eastman, *Appl. Phys. Lett.* **76**, 3442 (2000).
- [7] J.-M. Peransin, P. Vignaud, D. Rigaud and L.K.J. Vandamme, *IEEE Trans Electron Devices* **37**, 2250 (1990).
- [8] M.E. Levinshstein, F. Pascal, S. Contreras, W. Knap, S.L. Rumyantsev, R. Gaska, J.W. Yang and M.S. Shur, *Appl. Phys. Lett.* **72**, 3053 (1998).
- [9] A. P. Dmitriev, E. Borovitskaya, M. E. Levinshstein, S. L. Rumyantsev and M. S. Shur *J. Appl. Phys.* **90**, 301 (2001).
- [10] N. G. Weimann, L. F. Eastman, D. Doppalapudi, H. M. Ng and T. D. Maustakus, *J. Appl. Phys.* **83**, 3656 (1998).
- [11] S.L. Rumyantsev, Y. Deng, W. Knap, M.S. Shur, E. Borovitskaya, A. Dmitriev, N. Pala, R. Gaska, X. Hu, A. M. Khan, G. S. Simin, J. Yang and M.E. Levinshstein, 2001 MRS Fall Meeting, Boston, Massachusetts, November 26-30, 2001 SYMPOSIUM I GaN and Related Alloys, p. 113.

## Optimization of InGaAs/InAlAs strained multiple quantum wells for amplitude modulators

*Mauricio P. Pires*, Christiana V.-B. Tribuzy, Boris Yavich<sup>†</sup> and Patricia L. Souza  
Laboratório de Semicondutores, Centro de Estudos em Telecomunicações  
Pontifícia Universidade Católica do Rio de Janeiro,  
Rua Marquês de São Vicente 225, Rio de Janeiro, 22453-900, Brasil  
<sup>†</sup> On leave from the Ioffe Physico-Technical Institute

**Abstract.** InGaAs/InAlAs strained multiple quantum well structures for amplitude modulators based on the quantum confined Stark effect were studied in order to find the most efficient one for optical communication at 1.55  $\mu\text{m}$ . Parameters such as contrast ratio, polarization sensitivity, operation voltage and chirp are determined for structures with different InGaAs composition and thickness. Simulations of the devices' performance are carried out and are in good agreement with experiment.

### Introduction

In the past years, external optical modulators operating at 1.55  $\mu\text{m}$  have drawn much attention from researchers due to their application in optical communication [1–5]. The InGaAs/InAlAs multiple quantum well (MQW) system is of paramount importance for the development of amplitude modulators based on the Quantum Confined Stark Effect (QCSE) for telecommunication applications. This system can produce structures which operate at 1.55  $\mu\text{m}$ , it can be grown on InP substrates for optoelectronic integration and it has a lower valence band offset than the InGaAs/InP system. This last property is desirable to avoid saturation effects due to a long hole escape time from the quantum wells (QWs). Nevertheless, if the InGaAs/InAlAs system is expected to be used in the next multigigabit long haul fiber transmission systems, the MQW structure containing these materials should be further optimized.

For high frequency operation it is important to lower the operation voltage. In order to do so, the change in absorption per applied volt should be maximized. In the QCSE, the absorption threshold red-shifts with an applied reverse voltage. The wider the quantum well, the larger this red-shift is [6]. On the other hand, as the width of the QW is increased, the overlap between the electron and hole wavefunctions under an applied voltage decreases. So, a compromise between these two parameters is required. For lattice matched InGaAs/InAlAs MQW structures, the quantum well thickness for operation at 1.55  $\mu\text{m}$  is uniquely defined as 70 Å. Such quantum well thickness however, does not optimize the change in absorption. The compromise between the Stark shift and the transition oscillator strength can then only be reached with strained layers.

Other two important parameters in designing efficient amplitude modulators are the chirp and the polarization independence. The first is the dynamic wavelength broadening of the guided signal due to change in absorption which harms the long distance signal transmission because of the dispersion in the optical fibers at 1.55  $\mu\text{m}$ . The second requires that the device responds equally to TE and TM polarized signals. This condition can be achieved if the heavy and light hole energies are essentially degenerate [3, 4].

In this communication we present the results of a complete study of different InGaAs/InAlAs MQW structures for amplitude modulation. Structures containing QWs with varying alloy composition and thickness were grown. They were then processed as photodiodes for photocurrent measurements. Optimized structures were obtained with excellent figures of merit. Simulation of the device performance in terms of absorption, contrast ratio and chirp were carried out and they show good agreement with the experimental data. In addition, new structures were designed which present promising characteristics for high bit-rate optical communication.

## 1. Samples

The samples were grown by MOVPE at 100 mbar and at 635 °C on InP substrates. The active region consists of an intrinsic 20 period MQW structure with tensile strained InGaAs QWs with different  $t_{\text{QW}}$  and Ga content in the alloy,  $x$ . The InAlAs barriers are 65 Å thick and they are tensile strained between 0.05 and 0.1%. The MQW structure is inserted between  $n$  and  $p$  layers, forming the  $pin$  diode. The MQW region is separated from the  $n$  and  $p$  layers by an InAlAs spacer layer of 620 Å and 2500 Å, respectively, to avoid the diffusion of the dopants into the MQWs. Finally, the structure is topped by a  $p^+$  InGaAs contact layer.

The electron-heavy hole (e1-hh1) and electron-light hole (e1-lh1) transition energies were calculated by solving the Schrödinger equation using a one band effective mass theory where the physical parameters were interpolated from the values of the binary materials. The strain effects on the band structure were modeled using deformation potential theory. Figure 1 depicts the results of these calculations, where the solid curve corresponds to the change in  $t_{\text{QW}}$  with  $x$  so as to maintain the lowest transition energy unchanged. The transition energies involving the hh1 and lh1 will be degenerate ( $\Delta s = 0$ ) for certain  $t_{\text{QW}}$  and  $x$  pairs, represented by the dashed curve. Structures with such parameters should respond equivalently to TE and TM polarizations. The lowest optical transition of samples represented to the left (right) of the dashed curve involve heavy-(light-) holes. The characteristics of an InGaAs/InAlAs MQW structure operating at 1.55  $\mu\text{m}$  (0.8 eV), with the transition energy at 0.83 eV or 1.49  $\mu\text{m}$  (about 30 meV below the lowest MQW transition energy,  $E_1$ ), are represented by the thicker line. The solid dots in Fig. 1 represent the investigated samples and the numbers are inserted to help identifying them. Knowing the transition energy from PL and using the nominal Ga concentration  $x$ , it was possible to place the experimental points in Fig. 1 and determine  $t_{\text{QW}}$  for each sample.

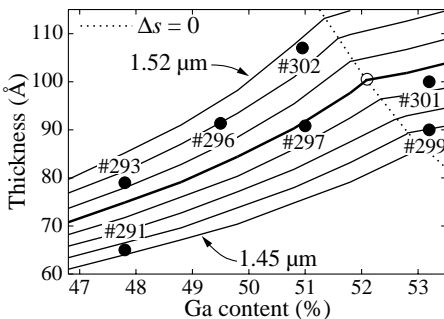


**Fig. 1.** Well width ( $t_{\text{QW}}$ ) vs. gallium concentration ( $x$ ) for the lowest transition energy of the quantum wells. Each line corresponds to a different emission wavelength differing by 10 nm from each other. The open circle shows the interception between the curve representing the 1.49  $\mu\text{m}$  emission and the  $\Delta s = 0$  curve. The dots represent the investigated samples.

## 2. Characterization

The samples were processed as photodiodes and were characterized by photocurrent (PC) with light propagating along the growth axis. The normalized PC spectra at zero bias near the band gap are illustrated for all the samples in Fig. 2. One clearly sees both the (e1–hh1) and (e1–lh1) transitions for samples 291, 293 and 296 (arrows in Fig. 2). These transitions are not resolved for samples 297, 299, 301 and 302 because the hh1 and lh1 energy levels are almost degenerate, as shown in Fig. 1. One observes by comparing Figs. 1 and 2 that the closer the sample position is to the  $\Delta s = 0$  curve the more difficult it is to resolve the e1–hh1 and e1–lh1 transitions. When a reverse voltage is applied the PC spectra are red-shifted. It is possible to quantify the PC spectra using absorption measurements at zero bias. From these results one obtains the change in absorption at the operation wavelength as a function of the reverse applied voltage. The highest change in absorption per applied voltage was obtained for samples 296 and 297, with QW thickness of about 90 Å and Ga content of 49.5% and 51%, respectively.

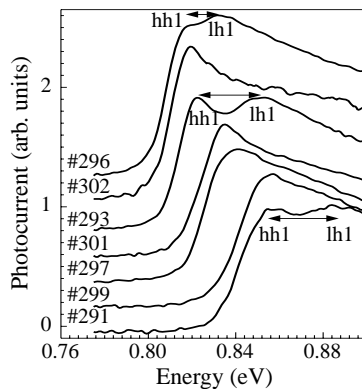


**Fig. 2.** Room temperature PC spectra of the samples depicted in Fig. 1.

Concerning the polarization sensitivity, an amplitude modulator was fabricated with the same structure as that of sample 297. The same contrast ratio (CR) as a function of reverse applied voltage was found for both polarizations. On the other hand, a lattice matched structure showed completely different for TE and TM modes.

The chirp parameter is essentially the change in refractive index caused by the change in absorption. It should always be between 0 and  $-1$  for optical communication systems. The refractive index is determined from the absorption through the Kramers–Krönig relations. The chirp parameter is then calculated and the obtained results are depicted in Fig. 3 by the solid symbols. One observes that for electric fields up to 100 kV/cm, the chirp for sample 296 is more suitable. In fact, it has already been shown that it is not possible to optimize the chirp and polarization sensitivity at the same time [7].

## 3. Simulation

Simulations were carried out by selfconsistent calculations, where effects of non-parabolicity of the bands, excitonic interaction, strain of the layers and residual doping level effects are considered. Coupling between quantum wells were not included. Since the barriers of the grown samples are thicker than 64 Å, we believe that there is no coupling effects arising from the fundamental levels in the quantum wells. In fact the calculated band-edge

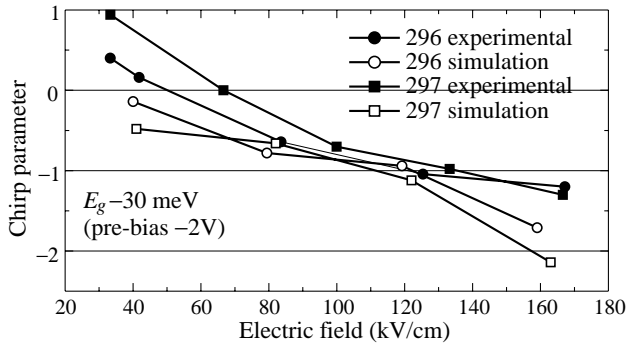


**Fig. 3.** Experimental and simulated chirp parameter for samples 296 and 297.

absorption spectra are in good agreement with that measured by photocurrent, for different values of the reverse voltage.

The refraction index variation was obtained from the theoretical absorption variation using Kramers–Krönig relation. The chirp parameter was calculated for different values of the reverse voltage for all samples, and a good agreement with experimental values is found. In Figure 3 the results of the simulation of chirp for samples 296 and 297 are represented by empty symbols.

A pre-bias of  $-2$  V was considered in both, theoretical and experimental results. Simulation of new structures point out that the chirp is very sensitive to the alloy composition. Slight changes in  $x$  (less than 0.5%) is enough for the chirp to be outside the acceptable range.

## References

- [1] T. Ido, H. Sano, S. Tanaka, D. J. Moss, H. Inoue and D. E. Knuth, *J. Lightwave Technol.* **14**, 2324 (1996).
- [2] P. Voisin, *Semicond. Sci. Technol.* **11**, 1601 (1996).
- [3] S. Chelles, R. Ferreira, P. Voisin and J. C. Harmand, *Appl. Phys. Lett.* **67** 247 (1995).
- [4] K. Wakita, I. Kotaka, O. Motomi, H. Asai and Y. Kawamura, *IEEE Photonics Technol. Lett.* **3**, 138 (1991).
- [5] G. Bastard, E. Mendez, L. Chang and L. Esaki, *Phys. Rev. B* **28**, 3241 (1983).
- [6] K. Wakita, I. Kotaka, K. Yoshino, S. Kondo and Y. Noguchi, *IEEE Photonics Technol. Lett.* **7**, 1418 (1995).
- [7] M. P. Pires, B. Yavich and P. L. Souza, *Appl. Phys. Lett.* **72**, 271 (1999).

## Metal nanoelectrodes for molecular transistor and investigation of electron transport in molecular systems

*D. B. Suyatin*<sup>†</sup>, *E. S. Soldatov*<sup>†</sup>, *I. A. Maximov*<sup>‡</sup>, *L. Montelius*<sup>‡</sup>,  
*L. Samuelson*<sup>‡</sup>, *G. B. Khomutov*<sup>†</sup>, *S. P. Gubin*<sup>§</sup> and *A. N. Sergeev-Cherenkov*<sup>†</sup>

<sup>†</sup> Faculty of Physics, Moscow State University, 119899, Moscow, Russia

<sup>‡</sup> Division of Solid State Physics and Nanometer Structure Consortium,  
Lund University, Box 118, S-221 00 Lund, Sweden

<sup>§</sup> Institute of General Inorganic Chemistry RAS, 119899, Moscow, Russia

**Abstract.** Gold nanoelectrodes with gaps of less than 10 nm were formed by conventional E-beam lithography on silicon substrates covered by Al<sub>2</sub>O<sub>3</sub>. Molecular films were deposited on the electrodes by Langmuir-Shaefer technique. The I–V curves of such systems show a suppressed conductance indicating a correlated electron tunnelling through the system. All measurements were made at room temperature.

### Introduction

The idea to use single molecules as base elements in micro and nanoelectronics is not new [1] but still actual one [2]. There are many obstacles on the way of this idea realisation and thus all investigations of the molecules usage in electronics are demonstrative or theoretical until now. Main obstacles are that large molecules are very complicated systems for a reliable control and clear understanding of physical phenomena in them. The usages of small molecules are restricted by absence of devices for reliable observation and manipulation of single molecules. At the present time usage of small molecules seems to be more realistic.

Molecular clusters are one of the most prospective molecules for future molecular electronics. The molecules have sizes from several angstroms to several nanometers. It was demonstrated by scanning tunneling microscope (STM) [3, 4] that such molecules are suitable for molecular electronics.

Investigation of electron transport through a molecular system in planar topology is very challenging from practical point of view, since a real device should to be planar. One of the main problems for experimental study is creation of appropriate system of electrodes. The electrodes have to meet the following criteria: the gap between electrodes has to be comparable with size of molecules; the leakage resistance has to be much more than resistance of the molecular system. The main goals of this work were to create the planar molecular nanostructures and to investigate an electron transport in it.

### 1. Fabrication

The metal nanoelectrodes were fabricated by a conventional E-beam lithography: 5 nm thick Ti and 20 nm thick Au were deposited on silicon substrate covered by 300 nm thick Al<sub>2</sub>O<sub>3</sub> and lifted-off in hot acetone. Fabricated electrodes were observed in a scanning electron microscope (SEM) after the lift-off process. The gap widths between electrodes depended on E-beam dose and varied in a range of 0–20 nm. The width of gaps with similar

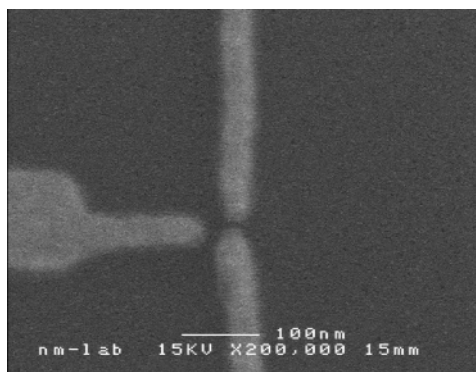


**Fig. 1.** Scanning electron micrograph of the nanoelectrodes.

doses had a deviation of 2–3 nm. The typical view of the nanoelectrodes system is shown in Fig. 1.

Molecular films were deposited on the electrodes. The films were both homogenous monolayers of molecular clusters  $\text{Pt}_5(\text{CO})_6(\text{PPh}_3)_4$  and heterogenous monolayers of mixture  $\text{Pt}_5(\text{CO})_6(\text{PPh}_3)_4$  and stearic acid in the proportion 1:20.

The  $\text{Pt}_5(\text{CO})_6(\text{PPh}_3)_4$  cluster molecules differ from other organic and inorganic molecules in that they consist of a dense, heavy metallic core, surrounded by ligand shell made up of light atoms or simple molecules.

The molecular film deposition was done by Shaefer technique described in [4]. During the deposition thin monomolecular film formed on water surface transferred on sample surface.

## 2. Results and discussion

As it was mentioned above, the essential property of nanoelectrodes is a low current leakage. The measurements of the leakage current for prepared electrodes show that the leakage current is less than 0.1 pA at 5 V. It means that the molecular systems with resistance up to teraohms can be investigated by such nanoelectrodes.

The measurements of resistance between electrodes show that some electrodes (about 15 per cent of total number of gaps) that seems to be shortened from SEM measurements have a resistance more than teraohms (about 10 per cent of total number of gaps), i.e. they are unshortened. It means that the gap between such electrodes is less than SEM resolution, i.e. 3–5 nm.

Molecular films were deposited on the electrodes after the preliminary measurements of resistance of empty gaps. After that I–V curves of obtained samples were measured at room temperature. The typical I–V curve of molecular system between nanoelectrodes is shown in Fig. 2.

On the I–V curve one can see a region with suppressed conductance near of zero voltage. The length of this region is about 500 mV. Asymptotic resistance of the I–V curve branches is about 10 GOhm.

We think that the most probable explanation of the conductance suppression is correlated electron tunneling through the molecular system. It was shown [3] that an electron transport through a system based on such single molecule can be explained by single-electron tunneling. In the first approximation the used molecules may be conceived as small metallic islands surrounded by dielectric shells. The capacitance of the single island



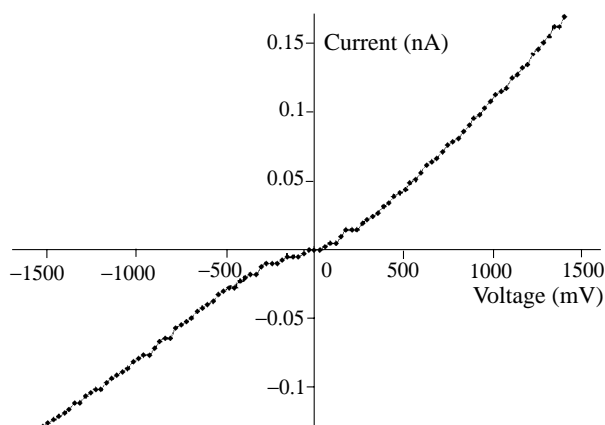


**Fig. 2.** The typical I–V curve of molecular system between nanoelectrodes.

can be estimated as approximately  $10^{18}$  F (see ref. [3]). So one can say that the investigated molecular system between electrodes resembles a system of small metallic islands separated by tunneling barriers. It is clear that the electron transport through the studied molecular system have to be single-electron tunneling due to such extremely small capacitance of the tunnel junctions between the molecules.

Noteworthy also is the fact that the I–V curves with suppressed conductance region were observed only in homogenous molecular monolayers. In all likelihood it is due to molecules of stearic acid between  $\text{Pt}_5(\text{CO})_6(\text{PPh}_3)_4$  single molecules enlarges the tunneling barrier between the islands (molecules).

### 3. Conclusions

In this work nanoelectrodes with gaps less than 10 nm have been made and the properties of such electrodes have been investigated. It was shown that such electrodes are suitable for electron transport investigations in molecular systems consisted of molecules (even single!) with diameters of about one nanometer. The technique of molecular monolayers deposition on the nanoelectrodes has been worked out. Obtained I–V curves of the molecular systems are typical for correlated electron tunneling through the arrays of tunnel barriers.

#### Acknowledgements

This work was supported by INTAS project No. 99-864 “SET transport in molecular cluster nanostructures and devices”, RFBR (No. 99-03-32218, No. 01-02-16580), Russian programs “Physics of solid-state nanostructures”, “Prospective technologies and devices of micro- and nanoelectronics”.

### References

- [1] A. Aviram and M. A. Ratner, *Chem. Phys. Lett.* **29**, 277 (1974).
- [2] Y. Wada, M. Tsukada, M. Fujihira, K. Matsushige, T. Ogawa, M. Haga and S. Tanaka, *Jpn. J. Appl. Phys.* **39**, 3835 (2000).
- [3] E. S. Soldatov, V. V. Khanin, A. S. Trifonov, D. E. Presnov, S. A. Yakovenko, G. B. Khomutov, S. P. Gubin and V. V. Kolesov, *JETP Lett.* **64**, 556 (1996).
- [4] S. A. Yakovenko, S. P. Gubin, E. S. Soldatov, A. S. Trifonov, V. V. Khanin and G. B. Khomutov, *Inorganic Materials* **32**, 1272 (1996).

## From bistability to spatio-temporal chaos in a resonant-tunneling diode

J. Unkelbach, A. Amann, P. Rodin and E. Schöll

Institut für Theoretische Physik, Technische Universität Berlin,  
 Hardenbergstrasse 36, 10623, Berlin, Germany

**Abstract.** Charge accumulation in the quantum-well of a double-barrier resonant-tunneling diode (DBRT) may result in bistability that provides a basis for formation of lateral current-density patterns. A typical pattern expected to appear is a current density front. Such fronts correspond to switching transitions and generally can not be stabilized by a conventional external circuit. In this paper we discuss formation and stabilization of stationary current density patterns in bistable DBRT. We demonstrate that the intrinsic dynamics of the DBRT can lead to the onset of regular or chaotic spatio-temporal oscillations if an attempt to stabilize unstable current density patterns by means of a simple control loop is undertaken.

### Introduction

Charge accumulation in the well of a double barrier resonant-tunneling diode (DBRT) may result in intrinsic bistability [1]. The corresponding Z-shaped current-voltage characteristic (Fig. 1) is multi-valued with respect to both current and voltage, and states on its middle branch are unstable [2]. A promising novel effect that is expected to appear due to the bistability is the formation of lateral current density patterns [3–6]. The typical pattern is a propagating current density front that switches the DBRT into the uniform on– or off–state. For a certain voltage there exists a front with zero velocity. However, similar to uniform states on the middle branch, these stationary nonuniform states turn out to be unstable for any conventional external circuit with positive load [7].

The investigation of stationary current density patterns and uniform intermediate states may give crucial insights into transport and dynamical properties of the DBRT in the regime of charge accumulation. In order to experimentally observe these unstable states a control scheme capable of stabilizing them should be implemented. The simplest control loop has been realized in [8] for uniform states by means of an active circuit that mimics a negative load resistance in series with the DBRT. It was predicted that this scheme can also be applied to nonuniform steady states [7]. In this contribution we demonstrate that in certain regimes the intrinsic dynamics of the DBRT leads to the failure of this approach: instead of desired stabilization it leads to the onset of periodic or chaotic complex spatio-temporal oscillations.

### The model

We use the DBRT model developed in [7, 9, 10]: the internal state of the device is characterized by the built-up electron concentration  $n(x, y, t)$  per unit area in the well that obeys the continuity equation

$$\frac{\partial n}{\partial t} + \frac{1}{e} \nabla \mathbf{J}_{\parallel} = \frac{1}{e} [J_{\text{ew}}(n, U) - J_{\text{wc}}(n)], \quad \nabla \equiv \mathbf{e}_x \frac{\partial}{\partial x} + \mathbf{e}_y \frac{\partial}{\partial y}. \quad (1)$$

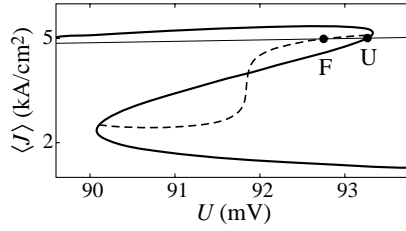


**Fig. 1.** Z-shaped current-voltage characteristic.  $\langle J \rangle$  is the current density averaged over  $x$  and  $y$ . The dashed line corresponds to lateral current-density patterns. The intersections “U” and “F” with the effective load line given by Eq. (4) are shown.

Here  $J_{ew}$  and  $J_{wc}$  are local densities of the emitter-well and well-collector currents, respectively,  $\mathbf{J}_{\parallel}$  is the density of the in-plane current in the well,  $(x, y)$  is the plane normal to the direction of the emitter-collector current,  $U > 0$  is the voltage across the device, and  $e < 0$  is the electron charge. We assume incoherent sequential tunneling for the vertical transport and Fermi distributions in the well and the emitter.

The lateral transport in the well is treated semiclassically in the drift-diffusion approximation according to [9]

$$\mathbf{J}_{\parallel} = -e D(n) \nabla n, \quad D(n) = \frac{|e|\mu n}{4\epsilon\epsilon_0} \left( \frac{4b_1b_2}{d} + \frac{r_B}{1 - \exp[-n/(\rho_0 k_B T)]} \right), \quad (2)$$

where  $\rho_0 = m/(\pi\hbar^2)$  is the two-dimensional density of states,  $m$  is the effective electron mass,  $r_B \equiv (4\pi\epsilon\epsilon_0\hbar^2)/(e^2m)$  is the Bohr radius in the semiconductor material,  $\mu$  is the electron mobility in the well,  $T$  is temperature and  $k_B$  is Boltzmann’s constant,  $\epsilon$  and  $\epsilon_0$  are the relative and absolute permittivity of the semiconductor,  $b_1$ ,  $b_2$  and  $d = b_1 + b_2$  are effective widths of the barriers and the total width of the DBRT, respectively.

The current densities  $J_{ew}$  and  $J_{wc}$  are approximated as [10]

$$J_{ew} = \frac{e}{\hbar} \Gamma_L \rho_0 \left[ \frac{k_B T}{2\pi} \ln \frac{f_w}{f_e} \right] \left[ \pi + 2 \arctan \frac{2}{\Gamma} (E_w + e\phi_w) \right], \quad J_{wc} = \frac{e}{\hbar} \Gamma_R n, \quad (3)$$

$$f_{w,e} \equiv \left( 1 + \exp \left[ \frac{E_{w,e}^F - E_w - e\phi_w}{k_B T} \right] \right)^{-1}, \quad \phi_w \equiv \frac{b_1}{d} U + \frac{eb_1b_2}{\epsilon\epsilon_0 d} n.$$

Here  $\Gamma_L/\hbar$  and  $\Gamma_R/\hbar$  are the escape rates via the emitter-well and well-collector barriers,  $\Gamma$  is the broadening of the quasi-bound well state,  $E_e^F$  and  $E_w^F$  are the Fermi energies in the emitter and the well, respectively,  $E_w$  is the energy of the quasi-bound state with respect to the bottom of the well,  $\phi_w(n, U)$  is the electrical potential at the bottom of the well with respect to the bottom of the emitter, and  $n = -\rho_0 k_B T \ln f_e$  determines  $E_e^F$ .

If the DBRT is operated in an active circuit [8] with a control loop applying an additional control voltage proportional to the device current in series with the bias  $U_0$ , it can be described by the Kirchhoff-like equation (see [2])

$$\tau_c \frac{dU}{dt} = U_0 - U + \frac{A}{L_x L_y} \int dx dy J, \quad J \equiv \frac{b_1 J_{ew} + b_2 J_{wc}}{d}. \quad (4)$$

Here  $\tau_c$  is interpreted as a characteristic relaxation time in the active circuit,  $U_0$  and  $A$  characterize the effective load line. In the conventional case of a passive circuit,  $\tau_c = RC$

and  $A = -RL_x L_y < 0$  with capacitance  $C$  and load resistance  $R > 0$ . Here we consider  $A > 0$ .

In the following we assume that the structure is symmetric and take into account only one lateral dimension. We use the following set of parameters:  $T = 4$  K,  $E_w = 40$  meV,  $E_e^F = 10$  meV,  $\Gamma = 2$  meV,  $\Gamma_L = \Gamma_R = 1$  meV,  $\mu = 10^5$  cm<sup>2</sup>/Vs,  $d = 20$  nm and the transverse dimension  $L = 3$   $\mu$ m (no-flux boundary conditions).

### Dynamics of the current-density patterns in the DBRT

For a fixed voltage  $U$  the current-density front propagates with a constant velocity whose absolute value and sign depend on the value of  $U$  [4, 7]. For a certain voltage  $U_{cr}$  the velocity is zero. Generally,  $U_{cr}$  depends on the value of the total current. We refer to the respective stationary pattern as a *filament* (Fig. 1). The differential conductance of the stationary filamentary states  $\sigma_d$  is positive in the relevant range of  $U$ . For  $U = \text{const}$  (as well as for any conventional series load resistance  $R > 0$ ) the stationary front is unstable with respect to small fluctuations and always develops into a moving front. In presence of the global constraint (4) the front is stable for  $1/A < \sigma_d$  and sufficiently small  $\tau_c$ . With increasing  $\tau_c$  the stationary front exhibits an oscillatory instability (back-and-forth motion with increasing amplitude), and eventually uniform oscillations set on.

Complex dynamics is found near the turning points of the characteristic. We observe spatio-temporal oscillations in form of *spiking* (Fig. 2(a)), where a filament completely disappears and then appears again. In a different regime we find small amplitude oscillations of a filament, termed *breathing* (Fig. 2(b)). With increasing  $\tau_c$  both modes first appear as

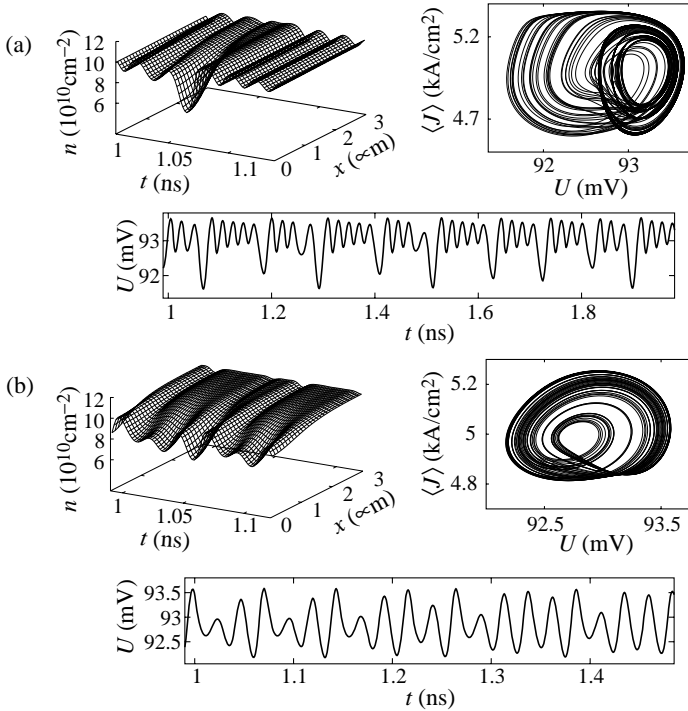


**Fig. 2.** Chaotic spiking (a) and breathing (b) of current-density patterns. Parameters:  $A = 2.45 \times 10^{-5}$   $\Omega$ cm<sup>2</sup>,  $U_0 = -29.5$  mV,  $\tau_c = 54.5$  ps (a) and  $\tau_c = 30$  ps (b).

periodic oscillations and then turn chaotic, typically via period doubling. The oscillations have a characteristic frequency  $\nu \sim 10$  GHz and appear for  $\tau_c \sim \lambda_0^{-1}$ , where  $\lambda_0$  is the unstable eigenvalue of the nonuniform state. The origin of the complex behavior is as follows. The effective load line has two relevant intersections with the current-voltage characteristic (Fig. 1): (i) the uniform state on the middle branch of the Z-shaped characteristic (state “U”), and (ii) the stationary nonuniform pattern (state “F”). Generally complex dynamics occurs when the threshold of the oscillatory instability of “F” is below that of the oscillatory instability of “U” [11]. Linear stability analysis shows that this condition is indeed satisfied for the DBRT.

The onset of complex oscillations implies failure of the stabilization technique described by Eq. (4). Let us sketch one of the possible scenarios: an attempt to stabilize the uniform state “U” in a large area structure results in current stratification and leads to the nonuniform filamentary state “F”; this state may in turn exhibit an oscillatory instability resulting in periodic or chaotic current oscillations.

#### Acknowledgments

We acknowledge support by DFG in the framework of Sfb 555. P.R. is grateful to the Alexander-von-Humboldt Foundation.

#### References

- [1] V. J. Goldman, D. C. Tsui and J. E. Cunningham, *Phys. Rev. Lett.* **58**, 1256 (1987).
- [2] E. Schöll, *Nonlinear spatio-temporal dynamics and chaos in semiconductors* (Cambridge University Press, Cambridge, 2001)
- [3] A. Wacker and E. Schöll, *J. Appl. Phys.* **78**, 7352 (1995).
- [4] B. Glavin, V. Kochelap and V. Mitin, *Phys. Rev. B* **56**, 13346 (1997).
- [5] D. Mel’nikov and A. Podlivaev, *Semiconductors* **32**, 206 (1998).
- [6] M. N. Feiginov and V. A. Volkov, *JETP Lett.* **68**, 633 (1998).
- [7] M. Meixner, P. Rodin, E. Schöll and A. Wacker, *Eur. Phys. J. B* **13**, 157 (2000).
- [8] A. D. Martin, M. L. F. Lerch, P. E. Simmonds and L. Eaves, *Appl. Phys. Lett.* **64**, 1248 (1994).
- [9] V. Cheianov, P. Rodin and E. Schöll, *Phys. Rev. B* **62**, 9966 (2000).
- [10] E. Schöll, A. Amann, M. Rudolf and J. Unkelbach, *Physica B* in print (2002).
- [11] S. Bose, P. Rodin and E. Schöll, *Phys. Rev. E* **62**, 1778 (2000).

## Temperature dependent homogeneous broadening and gain recovery dynamics in InGaAs quantum dots

*P. Borri*<sup>†</sup>, *W. Langbein*<sup>†</sup>, *S. Schneider*<sup>†</sup>, *U. Woggon*<sup>†</sup>, *R. L. Sellin*<sup>‡</sup>,  
*D. Ouyang*<sup>‡</sup> and *D. Bimberg*<sup>‡</sup>

<sup>†</sup> Experimentelle Physik IIb, Universität Dortmund,  
Otto-Hahn Str.4, D-44221 Dortmund, Germany

<sup>‡</sup> Institut für Festkörperphysik TU, Hardenbergstr. 36, D-10623 Berlin, Germany

**Abstract.** We present temperature-dependent measurements of the dephasing time in the ground-state transition of strongly-confined InGaAs quantum dots, using a highly sensitive four-wave mixing technique. At low temperature we measure a dephasing time of several hundred picoseconds. Between 7 and 100 K the polarization decay has two distinct components resulting in a non-Lorentzian lineshape with a sharp zero-phonon line and a broad band from elastic exciton-acoustic phonon interactions. We also explore the dephasing time beyond the one exciton occupation, by electrically injecting carriers. Electrical injection into the barrier region results in a dominantly pure dephasing of the excitonic ground-state transition. Once the injected carriers have filled the electronic ground state, additional filling of the excited states creates multiexcitons that show a fast dephasing due to population relaxation.

### Introduction

The dephasing time in epitaxially-grown semiconductor quantum dots (QDs) is experimentally addressed mainly by measuring the homogeneous linewidth (inversely proportional to the dephasing time) of a single dot transition isolated from the inhomogeneously broadened ensemble. Alternatively, transient four-wave mixing (FWM) spectroscopy is a powerful tool to directly measure the dephasing time even in an inhomogeneously broadened system. However, while it has been reported in GaAs islands [1] and in II–VI QDs [2, 3], FWM on self-assembled III–V QDs was found to be very difficult to measure [4].

Beyond the one exciton occupation, multiexcitons in QDs are attracting increasing interest since they provide additional degrees of freedom for quantum computation [5] and in tailoring quantum devices like lasers [6] and single photon emitters [7]. At high exciton occupancies, multiexciton spectra with a large number of emission lines are observed in single dots [8], reflecting the renormalization of the transition energies due to Coulomb interaction between carriers [9]. However, the homogeneous broadening of multiexcitonic transitions in QDs has been hardly investigated.

In this work we present FWM measurements in the excitonic ground-state transition of strongly confined InGaAs QDs in the temperature range from 7 K to 100 K. We also explore the dephasing time of multiexcitons by electrically injecting carriers.

### 1. Sample and experiment

The investigated sample is a p–i–n structure grown by MOCVD containing three layers of self-organized  $\text{In}_{0.7}\text{Ga}_{0.3}\text{As}$  QDs separated by 35 nm-thick GaAs spacers (see sketch in Fig. 1). Two AlGaAs cladding layers and a ridge structure of 5  $\mu\text{m}$  width and 500  $\mu\text{m}$  length provide optical waveguiding. The end facets were tilted to avoid multiple reflections. In the presence of an injection current ( $I_C$ ) amplified spontaneous emission (ASE) is detected and spectrally resolved, as shown in Fig. 1, at 25 K. At this temperature, thermalization among the dots does not occur and the ASE at low injection current reflects the inhomogeneous

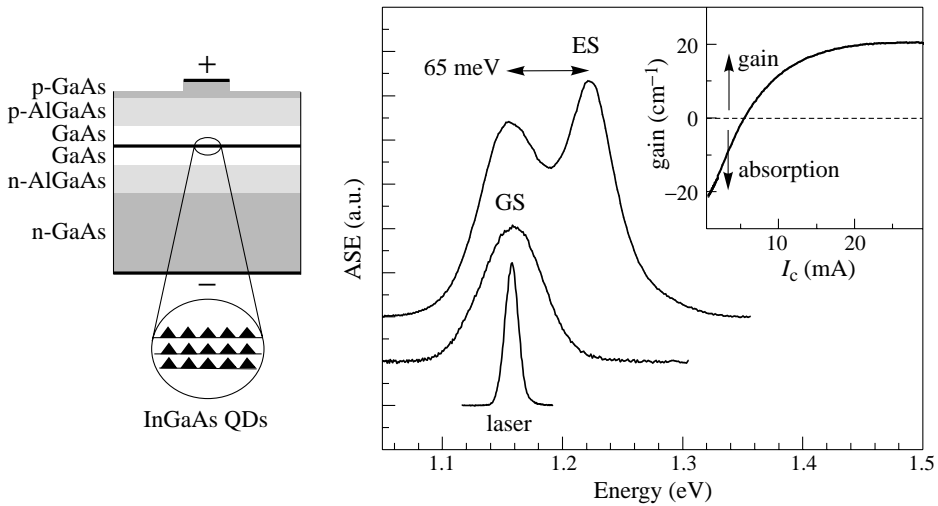


**Fig. 1.** Amplified spontaneous emission at 25 K at low (0.5 mA) and high (20 mA) injection current. The dot ground state transition (GS) is inhomogeneously broadened and separated to the first excited state transition (ES) by 65 meV. The spectrum of the pulse used in the experiment is shown. The curves are vertically displaced for clarity. A scheme of the quantum dot waveguide is also given. In the inset the gain at 1.158 eV is plotted versus injection current at 10 K.

distribution of the  $e_0h_0$  exciton recombination (GS transitions), where  $e_0$  and  $h_0$  are the lowest lying twofold spin degenerate state of electrons and holes, respectively [9]. We infer a Gaussian inhomogeneous broadening of 60 meV full width at half maximum (FWHM) attributed to fluctuations in dot size and indium concentration. At high injection current, recombination of electron and holes in the first two excited levels  $e_{1,2}h_{1,2}$  which are nearly degenerate in dots with good cylindrical symmetry [10] is visible (ES transitions). Photoluminescence on a reference sample shows a wetting layer transition  $\sim 210$  meV above the dot ground-state, evidence of the strong confinement. The small-signal gain of the GS transition (probed in the center of the inhomogeneous distribution) is shown versus  $I_C$  at 10 K in the inset of Fig. 1. With increasing  $I_C$  the optical response goes from absorption to gain and crosses transparency (i.e. one  $e_0h_0$  exciton on average) at  $I_{tr} = 5.5$  mA.

The FWM experiment is performed using an optical parametric oscillator providing Fourier-limited  $\sim 150$  fs pulses at 76 MHz repetition rate, resonant to the center of the GS transitions (as shown in Fig. 1) [11]. Two pulses are coupled into the TE waveguide mode with a relative delay time  $\tau_p$ . The energies of the exciting pulses are in the range of  $\leq 0.1$  pJ, corresponding to less than 0.1 electron-hole pair excited per dot. The FWM signal is in the third-order regime and is detected using a heterodyne technique [11]. The sample was held in a specially designed cryostat allowing for light-coupling in and out of the waveguide with high numerical aperture.

## 2. Temperature-dependent dephasing time

In Fig. 2(a) the time-integrated FWM (TI FWM) is shown versus  $\tau_p$  for different temperatures. We point out that the experiment is sensitive to three orders of magnitude FWM electric field, i.e. *six orders of magnitude FWM intensity* [11]. In the initial FWM dynamics we observe exciton-biexciton beats [12] from which we infer a biexciton binding energy of 3 meV [13]. The polarization decay clearly shows a non-exponential behavior with a

fast and a slow component evidencing a non-Lorentzian lineshape. The slow component has an exponential decay with an increasing time constant with decreasing temperature. At  $T = 7$  K the corresponding dephasing time is 630 ps, *equivalent to only 2  $\mu\text{eV}$  homogeneous broadening*. In the inset of Fig. 2(a) the Fourier transform of the TI FWM amplitude is shown where the long exponential decay results in a sharp Lorentzian line and the fast initial dephasing gives rise to a broad band. Above 100 K (not shown here) the fast dephasing dominates the TI FWM decay up to room temperature (see also Ref. [11]).

We interpret the sharp Lorentzian line as the zero-phonon line (ZPL), eventually broadened by inelastic processes like radiative recombination and phonon-assisted activation into higher energy exciton states [14]. In Fig. 2(b) the temperature dependence of the ZPL width is shown (closed squares) together with a fit (solid line) using 0.66  $\mu\text{eV}$  radiative broadening (1 ns lifetime) summed to a linear and a temperature activated broadening proportional to the Bose population number. We deduce a linear increase of  $0.22 \pm 0.02 \mu\text{eV/K}$  and an activation energy of  $16 \pm 1$  meV. This energy can be attributed to the activation of the exciton state  $e_0h_0$  into the state  $e_0h_1$  involving the first excited hole level, according to the typical energy spacings calculated in InGaAs QDs [15, 16]. The linear temperature dependence is, however, not well understood. It could be interpreted as being due to inelastic interaction with acoustic phonons of energies smaller than  $k_B T$  even at these low temperatures, due to transitions between the different spin states of the  $e_0h_0$  exciton [11]. However, recent studies on the spin-flip dynamics in InGaAs QDs would exclude the occurrence of these transitions on a time scale shorter than the exciton radiative lifetime [17]. Alternative explanations could be the broadening of the ZPL due to the elastic exciton-acoustic phonon interaction expected if virtual excitations of the excited states or a finite phonon lifetime are considered [18].

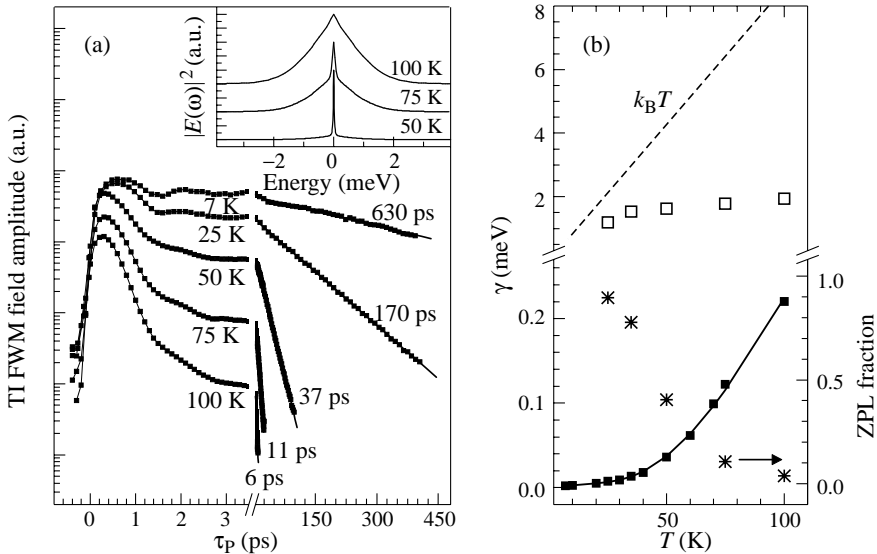


**Fig. 2.** (a) TI FWM at different temperatures as indicated. The dephasing times inferred from the exponential decays are indicated together with the exponential fits. In the inset the power spectrum of the TI FWM is shown. (b) FWHM homogeneous linewidths (closed square: ZPL, open squares: broad band) estimated from the measured dephasing. The stars are the ratio between the area of the zero-phonon line and the total area of the line.



The broad band is interpreted as the elastic acoustic–phonon broadening discussed in Ref. [14] (see also Ref. [11]). In Fig. 2(b) we show the width of the broad band versus temperature which we have inferred from the homogeneous lineshape (see inset of Fig. 2(a)). It is interesting to note that this line broadening only weakly depends on temperature [11] and tends to decrease when it approaches  $k_B T$ . Moreover, the ratio between the area of the acoustic-phonon band and that of the ZPL depends strongly on the temperature. We find that the area of the broad band is only a ten percent contribution to the total area at 25 K (see Fig. 2(b)) while it dominates at 100 K.

### 3. Dephasing time and gain recovery dynamics under injection current

The TI FWM field amplitude is shown in Fig. 3a versus the delay time between the exciting pulses at 10 K for different injection currents, as indicated [19]. Without electrical injection ( $I_C = 0$ ), the excitonic transition from the crystal ground state to  $e_0h_0$  (labelled 0-X) is probed. With increasing  $I_C$  a faster exponential decay of the FWM is observed, i.e. the ZPL broadens due to Coulomb interaction with the injected carriers. For  $I_C > 14$  mA, two  $e_0h_0$  excitons are present in the dot and the biexciton to exciton transition (labelled XX-X) is probed. The homogeneous broadening of the ZPL shows a linear increase versus  $I_C$  (see inset). For comparison, the broadening  $\gamma_c$  due to the carrier capture rate into the dot is indicated.  $\gamma_c$  is estimated from an equilibrium argument: the total capture rate, proportional to the injection current, must be balanced by the total recombination rate. At the transparency current  $I_{tr} = 5.5$  mA there is on average one exciton per dot, i.e. the total number of excitons is equal to the number of dots, and thus  $\gamma_c = \gamma_r I_C / I_{tr}$  using the exciton recombination rate  $\gamma_r = 0.67$   $\mu$ eV. Note that the homogeneous broadening due to electrical injection is more than one order of magnitude larger than the broadening arising from the capture process. In other words, electrically injected carriers in the barrier and wetting layer regions interact efficiently with the excitonic states in the QD without being captured, and give rise to a pure dephasing of the 0-X and XX-X transitions [20].

With increasing electrical injection above 15 mA, saturation of the  $e_0h_0$  excitons and filling of the excited  $e_{1,2}h_{1,2}$  excitons occurs (see Fig. 1). In presence of  $e_{1,2}h_{1,2}$  excitons the probed GS transition in the FWM experiment goes from a multiexciton ground state to a multiexciton excited state with only one  $e_0h_0$  exciton. This transition has a strong final state damping due to the relaxation of the multiexciton excited state into its ground state with two  $e_0h_0$  excitons, resulting in a fast FWM decay (see fast initial dynamics for  $I_C > 15$  mA in Fig. 3(a)). We have probed this relaxation dynamics performing differential transmission spectroscopy (DTS) on the ground-state transitions which utilizes the same heterodyne technique as the FWM experiment [21]. DTS data were taken for varying  $I_C$  from 0 mA to 30 mA.

The pump-induced change of the gain, deduced from the probe differential transmission, is shown in Fig. 3(b) at 10 K for  $I_{tr} = 5.5$  mA and for strong filling of the  $e_{1,2}h_{1,2}$  excitons ( $I_C = 30$  mA). In a QD ensemble, a macroscopic configuration for a given electrical injection is a superposition of probabilities of finding a dot in a microstate with  $n$  excitons [22]. The microstate probability varies with  $I_C$ , but each microstate has a given internal dynamics and only the capture rate is proportional to  $I_C$ . We have fitted the DTS data considering the microstates for  $n = 0, 1, 2, 3, \geq 4$ . In Fig. 3(b) a fourfold exponential fit function has been decomposed into the contributions for the different time constants, to explain the role of each microstate in the DTS signal. Moreover, an instantaneous contribution from non-resonant two-photon absorption and coherent artifacts was included [21]. All the microstates recover, after the interaction with the pump photons and the internal

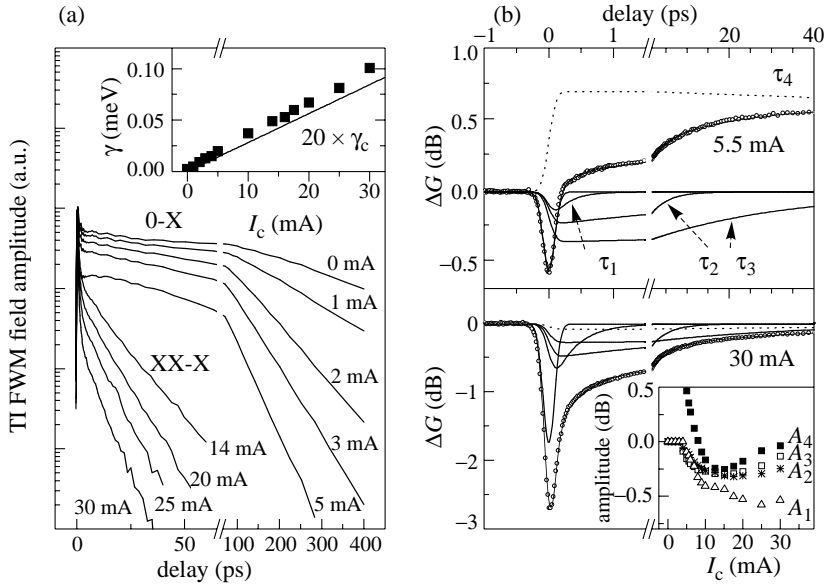


**Fig. 3.** (a) TI FWM at 10 K and different injection currents, as indicated. The dependence of the FWHM homogeneous broadening on injection current deduced from the signal decay at long delays is shown in the inset (squares), together with twenty times the estimated carrier capture rate (line). (b) Differential transmission spectroscopy at 10 K. The measured change of the gain in decibels is shown (open circles) together with its best fit (solid line). A decomposition of the fit into four exponential contributions is also shown. In the inset the dependence of the amplitudes of the four exponential contributions versus injection current is shown.

relaxation dynamics, on a long time scale, determined by the interplay between radiative recombination and capture [22], represented by  $\tau_4$  which varies from 1 ns to 200 ps going from  $I_c = 0$  mA to 30 mA. At low temperature, the excitonic configuration of each microstate is in its ground state. Consequently, the microstates with  $n = 0, 1, 2$  do not have internal relaxation dynamics since only  $e_0h_0$  excitons are present. The  $n = 3$  microstate, after the stimulated emission of a  $e_0h_0$  exciton, is left in an excited biexciton state with one  $e_0h_0$  exciton and one  $e_{1,2}h_{1,2}$  exciton. This excited biexciton relaxes into its ground-state via phonon emission, to which we attribute the two time constants  $\tau_2 = 4 \pm 0.3$  ps and  $\tau_3 = 35 \pm 4$  ps. The microstates with  $n \geq 4$  are left (after the emission stimulated by the pump) in an excited multiexciton state with two or more  $e_{1,2}h_{1,2}$  excitons, that relaxes via intradot Auger-like carrier-carrier scattering combined with phonon emission, which we attribute to the fast time constant  $\tau_1 = 0.33 \pm 0.05$  ps. The amplitudes  $A_1..A_4$  of the time constants versus injection current are shown in the inset of Fig. 3(b). Note that the fast initial dephasing observed at  $I_c = 30$  mA does indeed correspond to the relaxation dynamics given by  $\tau_1$  [19].

#### 4. Conclusions

In conclusion, we have measured a dephasing time of several hundred picoseconds at low temperatures and a non-Lorentzian homogeneous lineshape of the excitonic ground-state transition in strongly-confined InGaAs quantum dots. Moreover, we found that electrically injecting carriers decreases the dephasing time of excitonic transitions at low temperature.

In particular, a pure dephasing due to carriers injected in the barrier material and a dephasing of multiexcitonic transitions by population relaxation are distinguished. These results bring novel information in the understanding of the line broadening in III–V self-assembled quantum dots and might be of considerable importance for future applications based on a coherent optical control of the excitonic transitions in quantum dots.

### Acknowledgements

This work was supported by DFG in the frame of Wo477/17-1 and SFB296. P.B. is supported by the European Union with the Marie Curie Individual Fellowship MCFI-2000-01365.

### References

- [1] Xudong Fan, T. Takagahara, J. E. Cunningham and Hailin Wang, *Solid State Commun.* **108**, 857 (1998).
- [2] F. Gindele *et al*, *Phys. Rev. B* **60**, 8773 (1999).
- [3] H. P. Wagner *et al*, *Phys. Rev. B* **60**, 10 640 (1999).
- [4] P. Borri *et al*, *Phys. Rev. B* **60**, 7784 (1999).
- [5] Filippo Troiani, Ulrich Hohenester and Elisa Molinari, *Phys. Rev. B* **62**, R2263 (2000).
- [6] Y. Z. Hu, H. Giessen, N. Peyghambarian and S. W. Koch, *Phys. Rev. B* **53**, 4814 (1996).
- [7] D. V. Regelman *et al*, *Phys. Rev. Lett.* **87**, 257401 (2001).
- [8] E. Dekel *et al*, *Phys. Rev. Lett.* **80**, 4991 (1998).
- [9] A. J. Williamson, A. Franceschetti and A. Zunger, *Europhysics Lett.* **53**, 59 (2001) and references therein.
- [10] M. Bayer *et al*, *phys. stat. sol. (b)* **224**, 331 (2001).
- [11] P. Borri *et al*, *Phys. Rev. Lett.* **87**, 157401 (2001).
- [12] W. Langbein *et al*, *Phys. Rev. B* **55**, R7383 (1997).
- [13] O. Stier *et al*, *phys. stat. sol. (b)* **224**, 115 (2001).
- [14] L. Besombes, K. Kheng, L. Marsal and H. Mariette, *Phys. Rev. B* **63**, 155307 (2001).
- [15] D. Bimberg, M. Grundmann and N. N. Ledentsov, *Quantum Dot Heterostructures* (John Wiley and Sons, Chichester, 1999).
- [16] O. Stier, M. Grundmann and D. Bimberg, *Phys. Rev. B* **59**, 5688 (1999).
- [17] M. Paillard *et al*, *Phys. Rev. Lett.* **86**, 1634 (2001).
- [18] R. Zimmermann and E. Runge (unpublished).
- [19] P. Borri *et al*, submitted (2002).
- [20] A. V. Uskov *et al*, *Appl. Phys. Lett.* **79**, 1679 (2001).
- [21] P. Borri *et al*, *Appl. Phys. Lett.* **79**, 2633 (2001).
- [22] M. Grundmann and D. Bimberg, *Phys. Rev. B* **55**, 9740 (1997).

## Interface luminescence and lasing at a type II single broken-gap heterojunction

K. D. Moiseev<sup>†</sup>, M. P. Mikhailova<sup>†</sup>, *Yu. P. Yakovlev*<sup>†</sup> and A. Krier<sup>‡</sup>

<sup>†</sup> Ioffe Physico-Technical Institute, St Petersburg, Russia

<sup>‡</sup> Department of Physics, Lancaster University, Lancaster, LA1 4YB, UK

Type II heterostructures in the GaSb-InAs solid solution system have been intensively studied in recent years as promising candidates for the design of lasers operating in the 3–5  $\mu\text{m}$  spectral range [1–3]. An important application of these lasers is in ecological monitoring and tunable diode laser spectroscopy [4]. The main physical processes limiting high-temperature operation of conventional mid-IR lasers are non-radiative Auger recombination and carrier leakage currents, the latter arising due to poor electron and hole confinement.

We have proposed a new physical approach for the design of mid-IR lasers operating at  $\lambda = 3.2\text{--}3.26\ \mu\text{m}$  based on type II heterojunctions with a large asymmetric band-offset at the interface ( $\Delta E_C > 0.6\ \text{eV}$  and  $\Delta E_V > 0.35\ \text{eV}$ ). These high potential barriers produce effective electron-hole confinement at the interface and results in a tunnel-injection radiative recombination mechanism within the device due to reduce leakage current from the active region. The creation of high barriers for carriers leads to their strong accumulation in the active region and increases quantum emission efficiency of the spatially separated electrons and holes across the heteroboundary. Our approach also leads to the suppression of non-radiative Auger-recombination and a corresponding increase in the operation temperature of the laser. The active region of the laser structure consists of the type II heterojunction formed by narrow-gap  $\text{In}_{0.83}\text{Ga}_{0.17}\text{As}_{0.82}\text{Sb}_{0.18}$  ( $E_g = 0.393\ \text{eV}$  at 77 K) and wide-gap  $\text{Ga}_{0.84}\text{In}_{0.16}\text{As}_{0.22}\text{Sb}_{0.78}$  ( $E_g = 0.635\ \text{eV}$  at 77 K) layers lattice-matched to InAs substrate.

To begin with, we fabricated a laser structure based on a single type II broken gap P-GaInAsSb/p-InGaAsSb heterointerface. Strong interface electroluminescence was observed in the spectral range 0.3–0.4 eV at the temperature range  $T = 4.2\text{--}77\ \text{K}$ . EL spectra at  $T = 77\ \text{K}$  contained two emission bands ( $h\nu_A = 0.310\ \text{eV}$  and  $h\nu_B = 0.378\ \text{eV}$ ). In this laser structure a weak temperature dependence of threshold current, in the range 77–110 K, with a high characteristic temperature ( $T_0 = 60\ \text{K}$ ) was found [5]. The threshold current density was  $\sim 2\ \text{kA/cm}^2$  which is mainly due to electron leakage across the p-p interface of the broken-gap heterostructure.

To improve luminescent and temperature characteristics of this laser structure the radiative recombination mechanism in the single type II P-GaInAsSb/n-InGaAsSb heterojunction as an active region was studied. Intense spontaneous emission has been observed at high temperature range  $T = 77\text{--}300\ \text{K}$ . Figure 1 shows the EL spectra at  $T = 77\ \text{K}$  measured from the  $\text{P-Ga}_{0.84}\text{In}_{0.16}\text{As}_{0.22}\text{Sb}_{0.78}/\text{n-In}_{0.83}\text{Ga}_{0.17}\text{As}_{0.82}\text{Sb}_{0.18}$  heterostructure at various drive currents. Two pronounced emission bands A and B in the spectral range 3–5  $\mu\text{m}$  were observed. The low-energy emission band (A) was wider (FWHM = 53 meV) and was more prominent at low current values, with a peak photon energy of 0.260 eV (see insert in Fig. 1). This band moves towards the higher energy emission band B with increasing drive current and then the peak A reaches a constant energy of  $\sim 0.345\ \text{eV}$  above 150 mA. Band A was easily resolved up to this current, and then at high injection levels

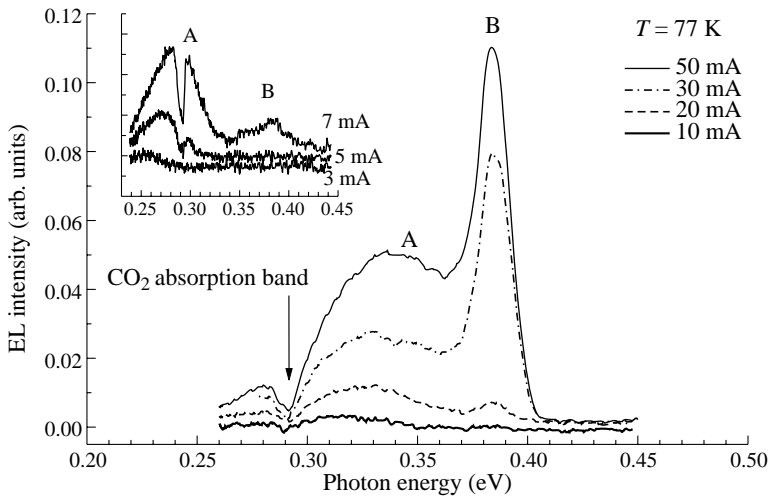


**Fig. 1.** EL spectra of the type II  $\text{P}^0\text{-Ga}_{0.84}\text{In}_{0.16}\text{As}_{0.22}\text{Sb}_{0.78}/\text{n}^0\text{-In}_{0.83}\text{Ga}_{0.17}\text{As}_{0.82}\text{Sb}_{0.18}$  heterostructure measured at low injection. Arrow indicates the atmospheric  $\text{CO}_2$  absorption region (4.25–4.27  $\mu\text{m}$ ).

one should not to exclude that it could be hidden under the emission band B which became dominant.

The emission band B appeared at higher current after the emission band A, and it should be noted that the photon energy of the emission band B ( $h\nu_B = 0.383$  eV) is the same as that observed from the PL measurements. The dependence of EL intensity on drive current for band A could be divided into two regions  $F_m \sim I^\eta$ , where  $F_m$  is the maximum spectral intensity and  $I$  is the drive current. The dependence  $F_m \sim I^2$  was established at low current but transformed to  $F_m \sim I$  at higher current. Despite this reduction in slope, no saturation was observed for the emission band A as indicated by this linear dependence and so the radiative transition A has a good prospect for the realisation of superluminescence regime and stimulated emission.

The EL spectra for this heterostructure at 300 K contained two emission bands in the spectral range 0.25–0.45 eV as well (Fig. 2). The band A with peak photon energy at  $h\nu_A = 0.320$  eV and half-width of 26 meV was more intense than the band B,  $h\nu_B = 0.355$  eV, with a half-width of 68 meV found there. The intensity of both emission bands depends linearly on drive current at  $T = 300$  K. A relative redistribution of the EL peak intensity was observed. In contrast to the low-temperature EL spectra where the emission band B was dominant, the emission, band A exhibited higher intensity than the band B at room temperature. Energy shifts towards low energy of 25 meV and 35 meV for emission bands A and B respectively, were observed with increasing temperature. According to our calculations the temperature shift of the InGaAsSb energy gap as well as interband bulk radiative recombination transitions is expected to be approximately 45 meV, similar to InAs-rich material. As mentioned above, with increasing temperature from 77 K to 300 K the decrease of the EL intensity was observed to be different for each emission band. The intensity of band B decreased by a factor of seven, while the intensity of the emission band A decreased by only two times.

The extremely low reduction of EL intensity for the emission band A with increasing temperature from 77 K to 300 K opens the way for this single heterojunction to be employed

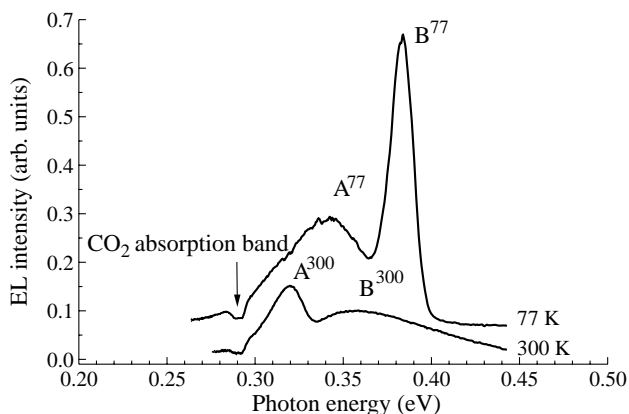


**Fig. 2.** Comparison of the EL spectra measured at 77 K and 300 K.

as a promising structure for the active region of high-efficiency light-emitting diodes and lasers operating in the mid-infrared at high temperatures. Thus, the type II heterojunction with a slight broken-gap alignment and large asymmetric band-offsets at the heteroboundary will be favourable to achieve operating temperature of mid-infrared injection lasers up to room temperature. Another one question which needs further consideration is, what is the type of the heterointerface and the energy profile there, taking into account the presence of localised states at the heteroboundary, generated by the epitaxial GaInAsSb/InGaAsSb quaternary solid solutions. The interfacial atomic structure may depend on the growth sequence i.e. GaSb-rich layer on InAs-rich, or vice versa, to give a GaAs-like or an InSb-like heterointerface.

The total EL observed on the experiment becomes more polarised with increasing drive current. The emission bands A and B are partly TM polarised at 77 K since the coherent emission observed in the laser structure based on the type II P-Ga<sub>0.84</sub>In<sub>0.16</sub>As<sub>0.22</sub>Sb<sub>0.78</sub>/n-In<sub>0.83</sub>Ga<sub>0.17</sub>As<sub>0.82</sub>Sb<sub>0.18</sub> single heterojunction was totally TM-polarised.

Following this, we prepared a p-n tunnel injection laser based on the type II P-GaInAsSb/n-InGaAsSb heterojunction as an active region instead of a p-p heterojunction (Fig. 3). We achieved a significant decrease in the threshold current and improved temperature

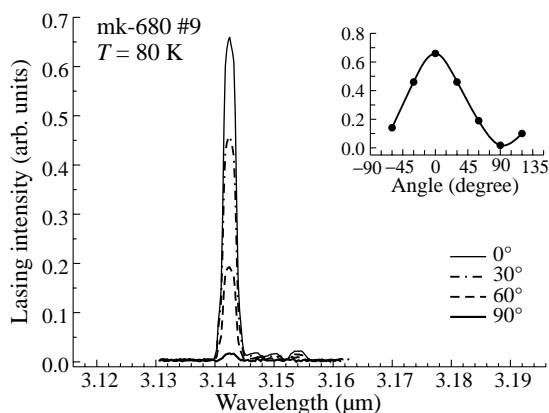


**Fig. 3.** TM-polarized lasing spectra for heterostructure based on type II single broken-gap p-n interface.

dependence. This design allows us to further improve electron confinement. We succeeded in raising the diode laser operating temperature up to  $T \sim 150$  K with a characteristic temperature of  $T_0 = 53$  K. We achieved a maximum operating temperature of 186 K under pulsed mode conditions. The threshold current density in the p-n tunnel injection laser was about  $400 \text{ A/cm}^2$  which is five times less than in the previous p-p structure.

#### *Acknowledgements*

We wish to thank the EPSRC for the award of a visiting research fellowship for K. D. Moiseev and we are also grateful for a grant from the Russian Basic Research Foundation, grant No 00-01-17047 in part support of this work.

#### **References**

- [1] D. W. Stokes, L. J. Olafsen, W. W. Bewley, Ivurgafmen, C. L. Felix, E. H. Aifer, J. R. Meyer and M. J. Yang, *J. Appl. Phys.* **86**, 4729 (1999).
- [2] A. Wilk, M. E. Gazouli, M. E. Skouri, P. Christol, P. Grech, A. N. Baranov and A. Joullie, *Appl. Phys. Lett.* **77**, 2298 (2000).
- [3] M. P. Mikhailova, K. D. Moiseev, O. G. Ershov and Yu. P. Yakovlev, *Semiconductors* **30**, 985 (1996).
- [4] A. N. Imenkov, N. M. Kolchanova, P. Kubat, K. D. Moiseev, S. Civis and Yu. P. Yakovlev, *Semiconductors*, **35**, 375 (2001)
- [5] M. P. Mikhailova, G. G. Zegrya, K. D. Moiseev, O. G. Ershov and Yu. P. Yakovlev, *Phys. Tech. Lett.* **21**, 83 (1995).

## Ultrafast switch-off of an electrically pumped InAs/GaAs quantum dot laser

A. V. Platonov<sup>†</sup>, C. Ling<sup>†</sup>, J. Feldmann<sup>†</sup>, M. Arzberger<sup>‡</sup>, M.-C. Amann<sup>‡</sup> and G. Abstreiter<sup>‡</sup>

<sup>†</sup> Optoelectronics Group, Physics Department and CeNS, University of Munich, Amalienstr. 54, D-80799 Munich, Germany

<sup>‡</sup> Walter Schottky Institut, Technical University Munich, Am Coulombwall, D-85748 Munich, Germany

**Abstract.** This paper reports on transient switch-off of the emission of an electrically pumped quantum dot laser with perturbation by a short optical pulse. This laser response is explained in terms of hot carrier absorption on intraband optical transitions leading to the transient suppression of the laser mode and, hence, to the switch-off. The switching time constant is determined to be as fast as 2 ps.

Quantum dot (QD) lasers might be favorable for highspeed optoelectronic applications due to their large differential gain, which should lead to a high modulation bandwidth [1]. Therefore, much attention has been paid to the dynamic behavior of self-assembled QDs, QD lasers, and QD amplifiers (see, e.g., Refs. [1–9]).

In this paper, we investigate the evolution of the continuous wave (cw) room temperature emission of an InAs/GaAs QD laser diode after an optical pulse impinges on one of the laser facets off-resonantly with respect to the lasing wavelength. In response to the perturbing pulse, the laser emission shows immediate switch-off (within a time of about 2 ps), formation of a train of picosecond dark pulses, and relaxation oscillations (ROs) on a sub-nanosecond time scale.

The QD laser under investigation is an edge-emitting metal clad ridge waveguide laser with InAs/GaAs QDs used as an active medium, embedded in an AlGaAs/GaAs graded-index separate-confinement heterostructure. The laser was grown by molecular beam epitaxy on a GaAs substrate. The active region consists of seven layers of self-assembled InAs QDs separated by a 10 nm thick GaAs matrix. For each of the QD layers 2.5 monolayers of InAs were deposited at a substrate temperature of 480 °C, resulting in an array of QDs with a density of about  $10^{11} \text{ cm}^{-2}$  [10]. The laser structure is 1220  $\mu\text{m}$  long and does not have a mirror or antireflection coating on the cleaved facets. Lateral confinement of the optical wave is achieved by the ridge waveguide geometry with a mesa width of 5  $\mu\text{m}$ .

Room temperature electroluminescence and lasing spectra of the free-running QD laser in the cw regime are presented in Fig. 1. They demonstrate inhomogeneous broadening with a full width at half-maximum (FWHM) of around 20 nm for  $I = 95 \text{ mA}$  bias current. Above threshold ( $I_{\text{th}} = 100 \text{ mA}$ , determined from the  $P-I$  curve in Fig. 1(b)), ground-state lasing starts with one emission line centered at 1096 nm. For higher bias currents, additional lasing lines arise [11]. Similar multiline lasing spectra have previously been observed in QD lasers [6, 12, 13], and are due to the inhomogeneous gain in the QD material. All modes are found to be TE polarized. For the pulse injection experiment, a mode-locked Ti:Sapphire laser with 80 fs pulses and 80 MHz repetition rate was used. The laser wavelength was 800 nm, which is above the band gap of the GaAs surrounding the QDs. Part of the beam was used for gating in the up-conversion setup. TE polarized Ti:Sapphire laser pulses with an energy of 0.1 nJ per pulse were focused onto the front facet of the electrically cw biased QD laser using a microscope objective. The output was collected with a second microscope



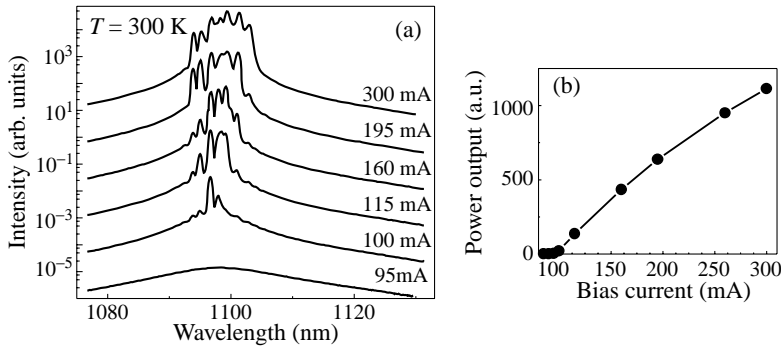


**Fig. 1.** (a) Emission spectra of the InAs/GaAs QD laser obtained for various bias currents at room temperature. The spectra have been offset vertically for clarity. (b) The total QD laser output power vs. bias current ( $P-I$  curve).

objective and up-converted with the time-delayed gating pulses in a nonlinear crystal [14]. The up-converted signal was passed through a monochromator to select the wavelength of the QD laser, and was detected by a photomultiplier tube. The long delay range of about 1 ns together with the subpicosecond time resolution allowed us to observe signal variation in a wide dynamic range.

Figure 2 shows a typical up-conversion curve of the laser output after the perturbing pulse has hit the laser facet (bias current:  $I = 350 \text{ mA} \times 3.5 I_{\text{th}}$ ). At the beginning of the curve the QD laser is shown to emit in its cw equilibrium regime. After the perturbation the laser emission drops down by one order of magnitude within a range of only 2 ps. It is worth to note here that the perturbing pulse has an energy higher than the GaAs band gap. As a result the pulse is absorbed within  $1 \mu\text{m}$  length [15], which is only a small part of the total length of the active medium. This situation is in contrast to the one described in Refs. [16, 17], where the switching dynamic of a vertical cavity surface emitting laser (VCSEL) sample with quantum wells comprising the active region was investigated. In Ref. [9] and [18] related experiments on QD lasers was performed, where the perturbing pulse had an energy close to the laser wavelength and could pass the entire cavity many

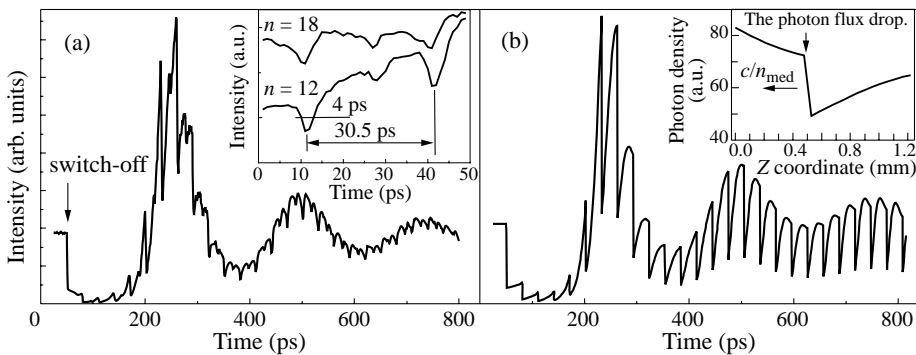


**Fig. 2.** (a) Time-resolved upconversion signal of the QD laser emission for  $I = 350 \text{ mA}$  ( $3.5 \times I_{\text{th}}$ ). The perturbing pulse energy is 0.1 nJ per pulse. The inset shows the evolution of the dark pulses after  $n$  roundtrips in the laser. The pulses have been shifted by multiples of the cavity roundtrip time (30.5 ps) and offset vertically. (b) Numerically calculated evolution of the QD laser emission. The inset demonstrates the calculated photon density within the cavity as a function of the position in the cavity at a time  $t = 500 \text{ ps}$  after pulse injection.

times. However, a comparable ultrafast switch-off of the laser diode was not observed. In our case, the small absorption length means that the local carrier density is not distributed over the whole active region immediately after the pulse. For this reason, the effect observed in this paper can neither be explained in terms of the ultrafast interdot carrier dynamics suggested in [9], nor by device heating suggested in [16, 17]. Here, the pulse creates electron-hole pairs with a high local density of  $10^{18}$ – $10^{19}$  cm<sup>-3</sup> near to the facet. A possible explanation of our results is that the large amount of free carriers absorb the QD laser light with an energy below the band gap of the GaAs due to intraband optical transitions. This mechanism can be very efficient in case of such high carrier densities, and taking into account that both kinds of carriers exist [19] and that the carriers are highly localized [20]. Therefore, this additional absorption mechanism plays the role of a photon leak, which is spatially located in the vicinity of the facet. This leak appears immediately after the perturbing pulse and creates the drop of the photon flux. When the drop reaches the other facet for the first time the switch-off of the laser emission is observed in the up-conversion signal. Then, the drop is reflected at the other facet and starts to travel back and forth in the cavity and appears as a sequence of the dark pulses with a period equal to the light round-trip time, similar to the dark pulses observed in Ref. [9]. Whereas the optically excited carriers have a finite lifetime the leak disappears on a nanosecond time-scale [15], and the laser relaxes to its equilibrium state. The relaxation oscillations (ROs) in the GHz range, which are observed in our measurements, represent a well-known effect in such pulsed experiments [9, 18]. The question arises, whether similar effects occur for quantum well lasers. However, this seems not to be the case, since an ultrafast switch-off was not observed in similar experiments on quantum well laser diodes [18]. This may be explained either by the distinction in the experimental conditions or by the fact that unique properties of the QDs play an important role for this effect. One reason may be the fast modal gain saturation in QDs [21,22]. In fact, for QD laser diodes the modal gain saturates on a bias current, which is just a bit higher than the threshold. As a result the additional optically induced carriers can not increase the gain but introduce the optical losses that lead to the lasing switch-off. Another explanation may be that strong carrier localization as present in the dots but not in the quantum wells enhances the intraband absorption cross-section as argued in Ref. [20]

Numerical calculation of the laser operation confirms the qualitative description of the laser emission modulation suggested above. The model used for the calculation is a space- and time-resolved solution of the carrier and photon density [23], including one-dimensional photon propagation, stimulated emission, facet reflection, and cw-carrier injection into the wetting layer level. The calculation starts 5 ns before the arrival of the perturbing pulse, so that the carrier and photon density in the laser have come into an equilibrium state. The material gain for the structure was measured previously [5]. To include the perturbation into the model as a leak of photons near the edge we assume the time dependent reflection coefficient of one of the cleaved facets in the form

$$R(t) = R_0 [1 - (1 - R_p) \exp(-t/t_{\text{rel}})], \quad (1)$$

where  $R_0$  is background reflectance,  $R_p$  is a part of  $R_0$ , which remains after the pulse, and  $t_{\text{rel}}$  is a lifetime of the nonequilibrium carriers.

The calculated curve shown in Fig. 2(b) demonstrates reasonable agreement with the experimental data. For this curve the following values are chosen:  $R_0 = 0.32$ ,  $R_p = 0.2$ , and  $t_{\text{rel}} = 200$  ps. We note that the resulting simulation curve is not very sensitive to the value of  $t_{\text{rel}}$  within the range of 100–400 ps. This reflects some arbitrariness in the selection

of Eq. (1). Nevertheless, the numerical data allow us to clarify the existence of the step-like drop in the photon density that propagates in the cavity. Inset in the Fig. 3 presents the calculated photon density in the cavity along the propagation axis at a time of 500 ps. The intensity drop can be easily observed in this figure. It has a sharp shape after many round trips in the cavity while its amplitude decreases with the time. This finding agrees well with the experiment, where all dark pulses have the same width (see inset in Fig. 2(a)).

However, there is a pronounced discrepancy between Fig. 2(a) and Fig. 2(b). The amplitude of the dark pulses decreases much faster in the experimental curve as compared to the calculated one. This means that at least one damping mechanism is ignored in our calculation. Carrier diffusion as well as nonlinear mode interaction are omitted as mechanisms that may be responsible for the damping of the dark pulses.

In conclusion, the ultrafast switch-off of a QD laser has been observed. The switching originates from optically induced intraband optical absorption leading to the step-like drop in the photon flux within the cavity. The recovery process after switching includes the formation of a train of dark pulses. The later reflects the fact that the drop of the photon flux exists on a sub-nanosecond scale and propagates back and forth in the cavity with a constant width in space. Finally, relaxation oscillations in the GHz range are detected.

#### Acknowledgments

Financial support by the DFG via the Gottfried-Wilhelm Leibniz Award, and by the European Union via the TMR Network "Ultrafast Quantum Optoelectronics" is acknowledged. One of us (AVP) is greatly thankful to the Alexander von Humboldt foundation for receiving a fellowship.

#### References

- [1] K. Kamath *et al*, *Appl. Phys. Lett.* **70**, 2952 (1997).
- [2] D. Bimberg *et al*, *Quantum Dot Heterostructures* Wiley, Chichester, 1999.
- [3] M. Grundmann, *Physica E* **5**, 167 (2000).
- [4] L. Zhang *et al*, *Appl. Phys. Lett.* **76**, 1222 (2000).
- [5] C. Lingk *et al*, *Appl. Phys. Lett.* **76**, 3507 (2000).
- [6] D. Bhattacharyya *et al*, *IEEE J. Sel. Top. Quantum Electron.* **5**, 648 (1999).
- [7] Y. Nambu *et al*, *Jpn. J. Appl. Phys. Part 1* **38**, 5087 (1999).
- [8] P. Borri *et al*, *IEEE Photonics Technol. Lett.* **12**, 594 (2000).
- [9] J. Zimmerman *et al*, *Appl. Phys. Lett.* **79**, 18 (2001).
- [10] L. Chu *et al*, *J. Appl. Phys.* **85**, 2355 (1999).
- [11] Note that the broadened lines observed in Fig. 1 consist of many narrowly spaced longitudinal modes not resolved by the monochromator.
- [12] L. Harris *et al*, *Appl. Phys. Lett.* **73**, 969 (1998).
- [13] A. Patanè *et al*, *J. Appl. Phys.* **87**, 1943 (2000).
- [14] J. Shah, *IEEE J. Quantum Electron.* **24**, 276 (1988).
- [15] M. C. Beard *et al*, *Phys. Rev. B* **62**, 15764 (2000).
- [16] D. Fortushì *et al*, *Appl. Phys. Lett.* **75**, 1664 (1999).
- [17] S. G. Hense and M. Wegner, *Appl. Phys. Lett.* **74**, 920 (1998).
- [18] D. H. Sutter *et al*, *Appl. Phys. Lett.* **67**, 1809 (1995).
- [19] A. V. Vinogradov, *Sov. Phys. JETP* **43**, 521 (1976).
- [20] R. Hellmann *et al*, *Phys. Rev B* **51**, 18053 (1995).
- [21] N. A. Maleev *et al*, *Semiconductors* **35**, 847 (2001).
- [22] M. V. Maximov *et al*, *Electron. Lett.* **35**, 2038 (1999).
- [23] A. Haugeneder *et al*, *J. Appl. Phys.* **85**, 1124 (1999).

## Observation of phonon bottleneck in quantum box cascade lasers

O. Drachenko<sup>†</sup>, C. Becker<sup>‡</sup>, V. Rylkov<sup>§</sup>, H. Page<sup>‡</sup>, D. Smirnov<sup>†\*</sup>, J. Leotin<sup>†</sup>  
and C. Sirtori<sup>‡</sup>

<sup>†</sup> LNCMP, 143 Avenue de Rangueil, 31432 Toulouse, France

<sup>‡</sup> Laboratoire Central de Recherches Thales, 91404 Orsay, France

<sup>§</sup> RRC Kurchatov Institute, 123182 Moscow, Russia

\* Permanent address: Ioffe Physico-Technical Institute, St Petersburg, Russia

**Abstract.** The intersubband light emission of GaAs/GaAlAs quantum cascade lasers is measured under pulsed magnetic fields parallel to the current, up to 60 T. A giant modulation of the laser intensity is observed with complete suppression of the laser emission when the energy spacing between intersubband Landau quantized states matches the GaAs optical phonon energy. When the level separation is not equal to the phonon energy, the laser output increases as a result of quenched phonon emission from the upper subband electrons. In this situation, the laser threshold current was found reduced by a factor of two.

## Introduction

Electron relaxation with longitudinal optical (LO) phonon emission is the dominant non-radiative energy relaxation process in two-dimensional (2D) system [1]. Furthermore, in zero-dimensional (0D) system with discrete energy levels, the suppression of electron-phonon scattering results in an “optical phonon bottleneck” effect [2–4]. A convenient way to prepare a 0D systems is to apply a sufficiently strong magnetic field perpendicular to the plane of a 2D electron gas. The continuum energy spectrum breaks into a Landau ladder of discrete states similar to that of a quantum dot. In this article we show that the breaking of a 2D system into ladders of 0D states substantially modifies the lifetime of the excited energy levels. In particular, we discuss the effect of an intense magnetic field on the electron scattering rates in a quantum cascade laser [5].

## 1. Experiments

The measured quantum cascade lasers based on a GaAs/AlGaAs heterostructures are described in references[6–8]. Their active region, shown in the inset of Fig. 1, consists of three coupled quantum wells. The active region displays three subbands ( $n = 1, 2$  and 3) having wave delocalised functions across this section. The laser transition occurs between the  $n = 3$  and  $n = 2$  states while the lower level ( $n = 1$ ) helps a fast depopulation of the  $n = 2$  state into  $n = 1$  level by resonant optical phonon emission. The structure includes superlattice emitter-collector regions which are designed as Bragg reflectors to prevent electrons to escape from the upper subband. We measured two sets of GaAs/GaAlAs QCL samples emitting at 11.4 and 9.2  $\mu\text{m}$ . The 9  $\mu\text{m}$  (11  $\mu\text{m}$ ) lasers include 36 (40) periods between  $n^+$  doped GaAs ohmic contact layers. The emitter-collectors are n-doped in their central part to obtain under high biases a stable uniform electric field distribution along the entire structure electrically neutral. The doping concentration is  $3\text{--}5 \times 10^{11} \text{ cm}^{-2}$ . The structures were processed into mesa-etched bars, 20  $\mu\text{m}$  wide and 1 mm long. They have

been designed to display at the laser threshold bias the intersubband energies  $E_{32}$  respectively equal to 111 and 130 meV while keeping  $E_{21}$  energy close to the LO-phonon energy. These values were confirmed by spectroscopic measurements of spontaneous emission. Measurements in a magnetic field were performed using a pulsed magnet delivering up to 62 T with total pulse duration of 120 ms [9]. All data were obtained at 4.2 K under constant current bias in a wide current range from 30 mA to 3 A, and in a longitudinal configuration  $\vec{T} \parallel \vec{B}$ . Short current pulses of 2  $\mu$ s length and 200  $\mu$ s repetition time were used in order to avoid heating effects. Light is detected with a boron doped silicon block band impurity detector (BIB) with wavelength cut-off at 33  $\mu$ m [10], mounted next to the laser facet.

## 2. Results and discussion

Figure 1 shows the light intensity and the voltage across the structure as a function of magnetic field for 11  $\mu$ m and 9  $\mu$ m lasers. Strong oscillations are observed in the entire field range. For certain fields the laser switches off, whereas the emitted power is greatly enhanced at intermediate field values. Note that the minima of the light intensity coincide with the local decrease of the voltage drop.

We will start our discussion with what is well known for 2D electron gas in a magnetic field. At  $B = 0$  T, the confined electronic states have plane wave-like energy dispersion, in the direction parallel to the layers. The corresponding energy subbands are nearly parallel because of the small nonparabolicities. In this case, optical phonon emission due

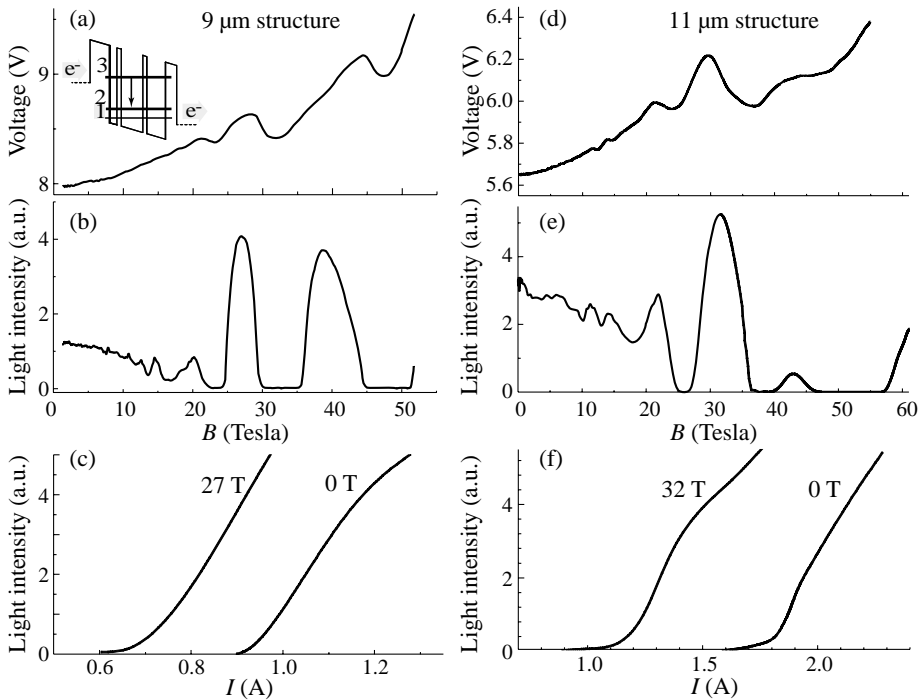


**Fig. 1.** Voltage across the device (a,d) and light intensity (b,e) as a function of the magnetic field measured at a temperature of 4.2 K on 9  $\mu$ m and 11  $\mu$ m lasers. The values of the current injected are near or slightly above the threshold current at zero magnetic field (0.95 A and 1.75 A for 9  $\mu$ m and 11  $\mu$ m structures, respectively). (c,f): Optical power as a function injected current.

to electrons scattering from the subband  $n = 3$  towards the  $n = 2$  and  $n = 1$  is always allowed, because of the nearly flat dispersion of optical phonons. Under a magnetic field, each subband breaks into a Landau ladder of highly degenerated states. Neglecting the contribution due to the spin, the energy of the electronic states reads  $E_{n,l} = E_n + (l + 1/2)\hbar\omega_c$ , where  $l$  is a Landau level (LL) index,  $\omega_c = eB/m^*$  is the cyclotron frequency and  $m^* = 0.067m_0$  the effective mass of GaAs.

Depending on the value of the magnetic field, the configuration of the Landau levels strongly influences the electron relaxation from  $|3, 0\rangle$  states with the emission of optical phonon. The relaxation is enhanced when the emission of a single LO phonon is able to relax an electron from the upper subband ground LL into one of the LLs of the lower subbands. This process describes the intersubband magneto-phonon resonance given by the equation:  $E_{3,0} - E_{n,l}(B_{n,l}) = \hbar\omega_{LO}$  with  $n = 1, 2$  [11]. In order to find the resonant fields, we calculated for both structures the LLs up to 60 T taking into account non-parabolicity effects [12]. We introduced also the broadening of the LLs as  $\sigma(B) = \sigma_0\sqrt{B}$  where  $\sigma_0$  equals 0.8 meV and 1.1 meV for 9  $\mu\text{m}$  and 11  $\mu\text{m}$  structures, respectively. The values of  $\sigma_0$  were fitted in order to reproduce the width of minima of the light intensity variations. The agreement with the experiment is quite good (within 5%) over the whole range of magnetic field for both structures. It is of interest to notice that we considered only the emission of GaAs bulk-like phonons. It means that confined phonon modes in these QW do not influence the relaxation rates. The situation can be completely different in heterostructures with larger dielectric constant difference as AlAs/GaAs.

For “non-resonant” magnetic fields, the energy and momentum conservation forbids transitions mediated by a single phonon. The relaxation of electrons injected into state  $|3, 0\rangle$  becomes inhibited. The quenching of this scattering mechanism leads to an increase of the lifetime and thus of the emitted light intensity. The final consequence of this effect is a spectacular reduction of the laser threshold current as shown in lower panels of Fig. 1. These results provide a clear observation of the so called “phonon bottleneck” in a system made of highly degenerate states.

In conclusion, we report a direct evidence of optical-phonon bottleneck in quasi quantum boxes created by the application of a high magnetic field to the quantum cascade laser structures. These results suggest also another spectroscopic tool to investigate the electron-phonon coupling in semiconductor heterostructures.

## References

- [1] U. Bockelmann and G. Bastard, *Phys. Rev. B* **42**, 8947 (1990).
- [2] H. Benisty, C. M. Sotomator-Torres and C. Weisbuch, *Phys. Rev. B* **44**, 10945 (1991).
- [3] B. N. Murdin *et al*, *Phys. Rev. B* **59**, 7817 (1999).
- [4] J. Urayama *et al*, *Phys. Rev. Lett.* **86**, 4930 (2001).
- [5] J. Faist *et al*, *Science* **264**, 553 (1994).
- [6] C. Sirtori *et al*, *Appl. Phys. Lett.* **73**, 3486 (1998).
- [7] P. Kruck *et al*, *Appl. Phys. Lett.* **76**, 3340 (2000).
- [8] H. Page *et al*, *Appl. Phys. Lett.* **78**, 3529 (2001).
- [9] O. Portugal *et al.*, *Physica B* **294-295**, 579 (2001).
- [10] S. Pasquier *et al*, *J. Appl. Phys.* **83**, 4222 (1998).
- [11] D. Smirnov *et al*, *Proceed. Physical Phenomena at High Magnetic Fields - IV Conference, 2001, Santa Fe (USA)*.
- [12] U. Ekenberg, *Phys. Rev. B* **40**, 2613 (1992)

## Gain and linewidth enhancement factor in InAs-quantum-dot and InAs-quantum-dash laser heterostructures

*P. G. Eliseev*<sup>†</sup>, A. A. Ukhanov, A. Stintz and K. J. Malloy

Center for High Technology Materials, University of New Mexico, Albuquerque

<sup>†</sup> also: P. N. Lebedev Physics Institute, Moscow, Russia

**Abstract.** Optical characteristics are investigated and compared of nanostructure semiconductor lasers with quantum dots and quantum dashes. Spectra of optical gain and of linewidth enhancement factor are obtained. Optical anisotropy in quantum dash structures is investigated.

Optical parameters of low-dimensionality laser structures are of interest because of very low threshold and operation current in QD lasers, and also because of a possibility of chirp-free operation. Low value of the linewidth enhancement factor in DWELL (dot-in-a-well) quantum-dot laser had been reported in Ref. [1]. This corresponds to theoretical expectations [2] and also confirmed by chirp-free operation of QD lasers under high-frequency direct modulation [3]. Another type of nanostructure laser is quantum-dash laser where the self-arranged nano-islands are elongated in one direction [4, 5]. Therefore these nano-islands are molecule-like formation with anisotropy of optical properties.

In this study, two types of laser heterostructure are investigated: InAs quantum dot structures at GaAs substrate and InAs quantum dash structures on InP substrates (see Table 1). The optical parameters are investigated: linewidth enhancement factor ( $\alpha$ -factor) and differential index  $dn/dN$  (where  $n$  is real part of refractive index and  $N$  is carrier density). Both types of nanostructures are grown by MBE method. The InAs QDashes were grown on an InP (001) substrate. They are inserted in a compressively strained AlGaInAs quantum well which had a thickness of 7.5 nm as described in Ref. [1]. The QDash lasers had 5 layers (quantum wells) each containing a single quantum dash plane. The dashes are elongated in the  $[1\bar{1}0]$  direction and had lengths of 300–500 nm, widths up to 25 nm, and heights up to 5 nm. Using a cleavage by plane  $(1\bar{1}0)$  diodes were fabricated with cavity axis along  $[110]$  direction therefore, the cavity axis is normal to the dashes (type A lasers). Also, using cleavage by plane  $(110)$  diodes had been fabricated with cavity axis  $[1\bar{1}0]$  parallel to the dashes (type B lasers). Samples of both types had the ridge-waveguide structure narrow enough to get a single-mode emission.

The modal gain and the linewidth enhancement factor were determined from the amplified spontaneous emission spectra. The spectral oscillations due to standing waves in the cavity were used to derive the net modal gain. Differential gain and differential index are measured at pumping of 50–80% of the threshold current. Over 500 modes are observed in typical QD laser with the cavity length of 3.6 mm. The laser was biased in pulsed mode with a Hewlett-Packard 8114A pulse generator. The pulse repetition rate was 50 kHz with a duty cycle of 1%. These parameters were chosen to avoid wavelength shift due to heating of the laser structure. The laser radiation was collimated using a  $60\times$  microscope objective and directed to the spectrometer. In our case the spectrometer used was the Fourier Transform Infrared Interferometer (FTIR) Magna-IR 760, which provides optical resolution of 9.4 pm at the laser emission wavelengths. In order to obtain spectral and current

dependence of  $\alpha$ -factor, precise measurements of spectral shift of each longitudinal mode had been performed. Measurements at different duty cycle showed that at duty cycle less than 1.5% the blue shift of modes was almost constant. At higher duty cycle it decreases and changes sign indicating predominance of thermal effect. Therefore, data at duty cycle of 1% are used to characterize an electronic effect.

Emission spectra show a tendency to the saturation of the spontaneous emission at the long-wavelength side of the emission band. In the QD lasers, the series of emission bands had been followed with progressive saturation of ground-state band and excited state bands. Because of lowest threshold current is achieved within the ground-state band (as low as 16 A/cm<sup>2</sup> in a sample with high-reflectivity mirrors), the measurement were performed in more details for ground-state emission in the range 1235–1270 nm at room temperature. From intermode spacing, the group index is  $\sim 3.4$  with very small dispersion over the range of ground-state emission. The peak of the gain is rather stable at increase of current and the laser wavelength in diodes with different cavity length (but more than 1.5 mm) is about the same in limits of 3 nm. The differential gain corresponds to the optical cross-section changing in the range from  $3.5 \times 10^{-15}$  to  $7 \times 10^{-15}$  cm<sup>2</sup>.

**Table 1.** Samples of laser structures under study.

Structure	$J_{th}$ (A/cm <sup>2</sup> )	Emission wavelength (nm)
Single InAs QD /InGaAs/GaAs,	20–80	1250
3-layer InAs QD /InGaAs/GaAs,	60–200	1250
5-layer InAsQDash/InGaAlAs/InP	400–1000	1580–1600

In QDash structures, the emission spectra are smoother than in QD ones, but here ground-state band can be singled out also. The spontaneous emission is strongly saturating along with current increase. The ground-state-related spectral peak is more mobile than in QD structures and shifts in the range 1640–1600 nm at change of current density from 200 to 400 A/cm<sup>2</sup>. The lasing occurs at current  $> 400$  A/cm<sup>2</sup> near 1600 nm (as measured in type A diode). The threshold pumping rate corresponds to  $\sim 80$  A/cm<sup>2</sup> per QDash-QW. The gain spectra are shown in Fig. 1. The peak gain in type B diode is 2.3 times lower.

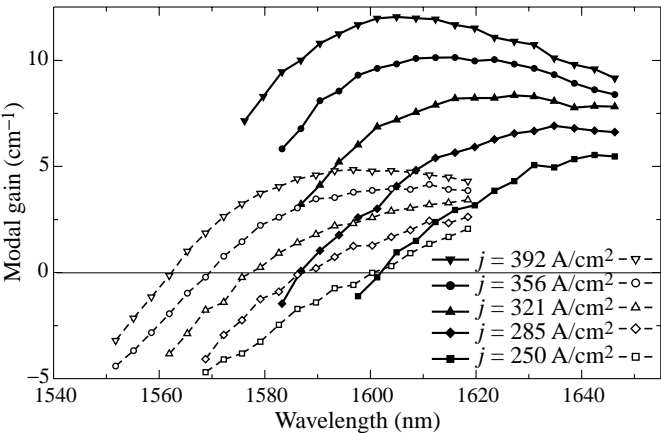


**Fig. 1.** Wavelength dependence of the modal gain of quantum-dash lasers with dashes oriented perpendicular (solid lines) and parallel to the cavity axis (dashed lines). The current density is indicated on insert for both samples with identical cavity.



This is the result of optical anisotropy that is attributed to the geometry of quantum dashes. The spectral peak of the gain is shifted to longer wavelength by  $\sim 8$  nm in type A diode as compared to type B diode. This indicates a difference in the working states responsible for optical amplification in two orthogonal directions. It suggests the transition matrix element is different in these directions. A spectral distribution of  $\alpha$ -factor is obtained in the ground-state emission range. At the gain peak of QD laser, the measured value is 0.4–0.5 with a tendency to decrease to about zero when the pumping rate approaches the laser threshold. The differential effective index  $dn_{\text{eff}}/dN$  is estimated as  $-2.6 \times 10^{-22} \text{ cm}^3$  at pumping rate between 66% and 86% of threshold current. Using the optical confinement factor of 0.03 for the quantum well we get the material differential index of  $-8.7 \times 10^{-21} \text{ cm}^3$  for an InGaAs medium containing InAs dots under the condition that all electron-hole pairs are captured into the ground states of the dots. This quantity seems to be not small but of the same order of value as in the bulk semiconductor like GaAs. Therefore the small value of  $\alpha$ -factor is associated with higher differential gain in QD laser. Spectral study of  $\alpha$ -factor in QDash lasers shows that it is different in type A (minimal value  $\sim 3$ ) and type B diodes ( $\sim 4$ ).

In conclusion, laser parameters are investigated in structures with InAs quantum dots and quantum dashes operating in spectral ranges of 1250 and 1600 nm. Spectra of modal gain, spectral mode shift, differential gain and  $\alpha$ -factor are obtained. Low values of  $\alpha$ -factor (0.4–0.5) are obtained below the laser threshold in QD lasers that explains a chirp-free performance of this type of lasers. Optical anisotropy of these parameters is obtained in quantum-dash structures. The  $\alpha$ -factor is  $\sim 3$  at the spectral peak of gain in type A QDash laser and about 4 in type B.

## References

- [1] T. C. Newell, D. J. Bossert, A. Stintz, B. Fuchs, K. J. Malloy and L. F. Lester, *IEEE Photon Technol. Lett.* **11**, 1527–1529 (1999).
- [2] Y. Miyake and M. Asada, *Jpn. J. Appl. Phys.* **28**, 1280–1281 (1989).
- [3] H. Saito, K. Nishi, A. Kamei and S. Sugou, *IEEE Photon. Technol. Lett.* **12**, 1298–1300 (2000).
- [4] V. M. Ustinov *et al*, *Appl. Phys. Lett.* **72**, 362 (1998).
- [5] R. H. Wang *et al*, *IEEE Photon. Technol. Lett.* **13**, 767–769 (2001).

## High power lasers based on submonolayer InAs-GaAs quantum dots and InGaAs quantum wells

A. R. Kovsh, A. E. Zhukov, N. A. Maleev, S. S. Mikhrin, A. V. Vasil'ev,  
Yu. M. Shernyakov, D. A. Livshits, M. V. Maximov, D. S. Sizov,  
N. V. Kryzhanovskaya, N. A. Pikhtin, V. A. Kapitonov, I. S. Tarasov,  
N. N. Ledentsov, V. M. Ustinov, J. S. Wang<sup>†</sup>, L. Wei<sup>†</sup>, G. Lin<sup>†</sup> and J. Y. Chi  
Ioffe Physico-Technical Institute, St Petersburg, Russia  
<sup>†</sup> Industrial Technology Research Institute, Taiwan

### Introduction

Development of submonolayer deposition technique can offer significant flexibility in creation of strained heterostructures of different types and material systems [1]. It was found that under certain growth conditions the deposition of InAs insertions of less than 1 monolayer (ML) thickness in GaAs matrix forms so-called submonolayer quantum dots (SML QDs) [2]. The energy spectrum of these QDs can be varied over a wide range by tuning the InAs coverage and the thickness of GaAs spacers.

Stranski–Krastanow (In,Ga)As QDs (SK QDs), which have been investigated in more details, have proved theoretically predicted lower threshold current density of 26 A/cm<sup>2</sup> in compare with QW lasers [3]. However, strong size variation of SK QDs in combination with the relatively low sheet density leads to low peak gain achievable in the ground state. This problem is the reason of typically low efficiency of SK QD-based lasers. Due to higher gain, SML QDs have proved their potential for high power laser application [2]. In this presentation we report on further progress in the technology of SML QD lasers demonstrating high output power (6 W) from 100- $\mu$ m-wide laser diode emitting at 0.94  $\mu$ m. High power QW-based lasers of the state-of-the-art performance are also presented for comparison.

### Formation of SML QDs

The epitaxial procedure to form SML InAs-GaAs QDs is shown in Fig. 1(a,b,c). There is vertical correlation between ML-height islands of different rows similar to the case of vertically coupled Stranski–Krastanow QDs [4]. It leads to formation of In-rich clusters within InGaAs QW, which are referred as SML QDs. Figure 1(d) shows the TEM image of InAs-GaAs SML QDs formed by 10 pairs of 0.5 ML of InAs and 2.5 ML of GaAs.

### Laser design

Low series resistance and narrow far-field pattern are among usual requirements for a high-power laser. To satisfy these requirements highly doped cladding layers and broad waveguiding layer are to be usually used. Relying on high gain of SML QDs we applied them as an active region of the laser structure designed in this way.

Structures were grown by solid-source molecular beam epitaxy with a high volume As-cracker cell. The waveguide was formed by 0.6- $\mu$ m-thick undoped Al<sub>0.15</sub>Ga<sub>0.85</sub>As layer sandwiched between 1.5- $\mu$ m-thick Al<sub>0.3</sub>Ga<sub>0.7</sub>As cladding layers. n- and p-type claddings were highly doped ( $\sim 1 \times 10^{18}$  cm<sup>-3</sup>) with Si and Be, respectively. The AlGaAs waveguide contained GaAs layer of 30 nm thickness with two rows of SML QDs. Distance between

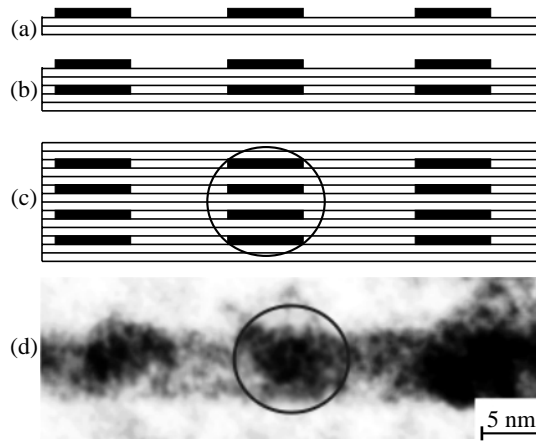


**Fig. 1.** Scheme of SML-QD formation.

rows was 12 nm. In the second type of structures each QD row was substituted for a 6.5 nm thick  $\text{In}_{0.18}\text{Ga}_{0.82}\text{As}$  QW. After formation of 100- $\mu\text{m}$ -wide stripes the wafers was thinned and metallized. The lasers were formed by cleaving into bars of different cavity lengths. Pulsed measurements were conducted on a probe station. Then individual devices were mounted p-side down on copper heatsink by In solder for continuous wave (CW) operation measurements after high- and low-reflectivity coatings of the facets.

## Results

Measurements in pulsed regime were done for both kinds of lasers with cavity length ranging from 0.5 to 2 mm. The lasing wavelength of 1-mm-long diodes based on SML QDs (SML-QD-laser) and InGaAs DQW (QW-laser) were 937 nm and 982 nm, respectively. Threshold and efficiency characteristics are shown in Fig. 2. For cavity lengths about 1 mm both lasers demonstrate high differential efficiency ( $\eta_D$ ) of about 75 ~ 80%. However, when cavity length increases  $\eta_D$  of SML-QD-laser decreases faster indicating higher internal loss ( $\alpha_i$ ). The values of  $\alpha_i$  were estimated as  $1.6 \pm 0.2$  and  $3.2 \pm 0.2 \text{ cm}^{-1}$ . We assume that two times higher loss in SML-QD-laser is due to additional light scattering originating to non-uniform In distribution.

We used data of Fig. 2 and well known lasing condition,  $g_{\text{mod}}(J_{\text{th}}) = \alpha_{\text{in}} + 1/L \ln(1/R)$ , (where the last term is mirror loss) to plot dependence of modal gain on current density in Fig. 3. We also added gain-current curve of our laser based on 10 rows of SK QDs emitting at the same wavelength (0.94  $\mu\text{m}$ ) for comparison. It is clearly seen that SML QDs offer much higher differential gain compared to SK QDs. However, this figure shows still lower differential gain of SML-QD-laser compared to QW-laser that results in higher threshold current density at all cavity lengths. Note, that gain-current dependence of QW-laser is fitted by logarithmic function characteristic for QW states, whereas the dependence for QDs is linear.

CW output power and power conversion efficiency against drive current are shown in Fig. 4. Power of SML-QD-laser (solid line) reaches the highest value of 6 W at current of 6.5 A at which point the laser fails due to the catastrophic optical mirror damage (COMD). The slope efficiency of 1 W/A ( $\eta_{\text{dif}} = 76\%$ ) remains constant till 6 A and negligibly decreases beyond this value due to thermal rollover. High doping of claddings allowed us to achieve very low series resistance of  $6.7 \times 10^{-5} \Omega \text{ cm}^2$ , which is among of the lowest

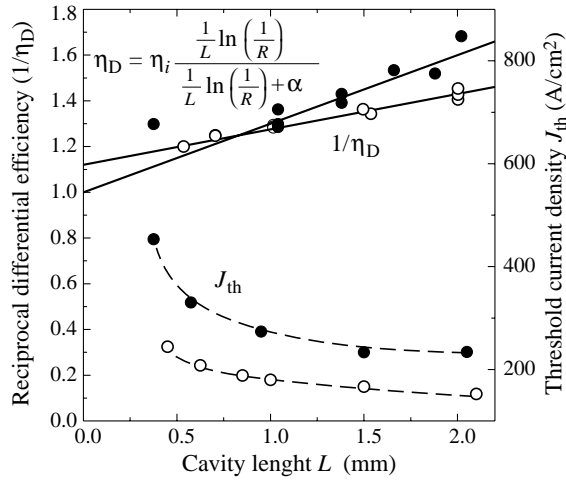


**Fig. 2.** Dependence of threshold current density and inverse differential efficiency on cavity length. Solid circles — SML-QD-lasers, open circles — QW-lasers.

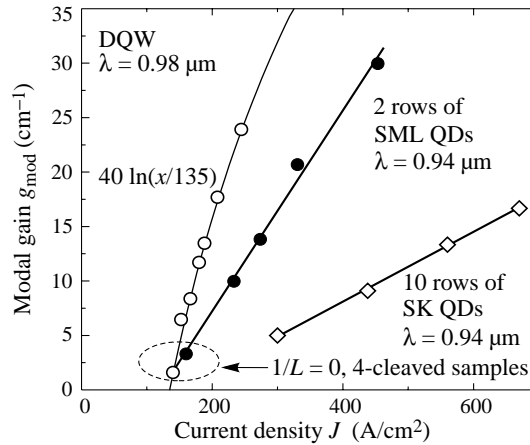


**Fig. 3.** Dependence of modal gain on current density. Solid circles — SML-QD-lasers, open circles — QW-lasers, diamonds — laser based on SK QDs.

values reported for Al-based laser diodes. As a result, conversion efficiency peaks at 58% and remains higher than 50% until laser fails. The maximum output power and efficiency shown are much higher than the best values reported for SK QD based lasers (3.5 W and 45%) [4]. Moreover, CW characteristics of these diodes are just slightly worse in compare with QW-lasers (dashed lines). QW-laser fails also because of COMD.

The calculated value of effective transverse mode size of  $0.53 \mu\text{m}$  is in good agreement with the measured beam full width at half maximum  $\Theta_{1/2}$  of  $38^\circ$ . The maximum output power of 6 W corresponds to internal power density at COMD of  $12.5 \text{ MW/cm}^2$ . We believe this relatively low value compared with the reported record for AlGaAs-based lasers [5, 6] can be improved after careful optimization of our facet coating technique.

In this context we would like to mention that low temperature sensitivity of device characteristics is essential to prevent thermal rollover at high drive currents. In the range

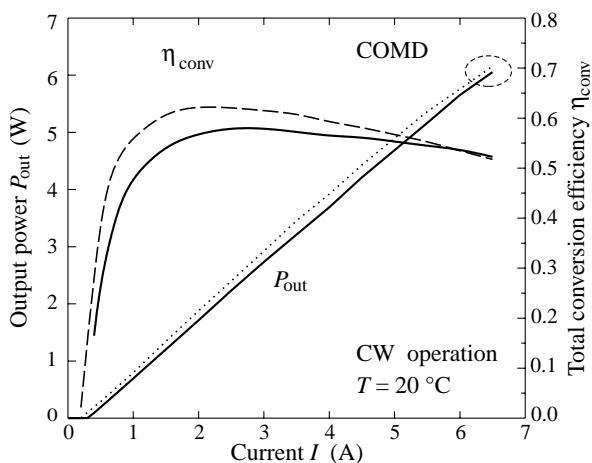


**Fig. 4.** Output power and conversion efficiency against drive current. Solid lines — SML-QD-laser, dashed lines — QW-lasers.

of 10–60°C temperature dependence of threshold current ( $\exp(T/T_0)$ ) of SML-QD-laser is described by characteristic temperature  $T_0$  of 150 K. This value is the highest for QD lasers with acceptable conversion efficiency, however it is still lower than that of the QW counterpart. QW-lasers fabricated in this work showed  $T_0$  as high as 250 K.

## Conclusion

High gain of submonolayer quantum dots allowed us to use broad waveguide design typical for high power lasers based on QWs. It resulted in the realization of high power operation of 6 W with the peak conversion efficiency of 58% and a characteristic temperature of 150 K in 100  $\mu\text{m}$ -wide diode lasers based on SML QDs. The maximum output power was limited by COMD whereas thermal rollover was found to be negligibly small. These lasers are slightly inferior to the QW-lasers fabricated in this work whose characteristics are among of the best reported for QW lasers. These results demonstrate the potential of submonolayer technique to form active region of high power laser.

## Acknowledgements

This work was supported by BMBF (grant 13 N 7231), Russian Foundation for Basic Research (grant 00-02-17039), and ITRI-Ioffe Joint Program.

## References

- [1] I. L. Krestnikov *et al*, *Phys. Stat. Sol. (a)* **183**, 207 (2001).
- [2] S. S. Mikhlin *et al*, *Semicond. Sci. Technol.* **15**, 1061 (2000).
- [3] G. T. Liu *et al*, *Electron. Lett.* **35**, 1163 (1999).
- [4] Q. Xie *et al*, *Phys. Rev. Lett.* **75**, 2542 (1995).
- [5] A. R. Kovsh *et al*, *Electron. Lett.* **35**, 1161 (1999).
- [6] X. He *et al*, *Electron. Lett.* **34**, 2126 (1998).
- [7] D. A. Livshits *et al*, *Electron. Lett.* **36**, 1848 (2000).

## MBE growth of low-threshold long-wavelength QD lasers on GaAs substrates

*N. A. Maleev, A. R. Kovsh, A. E. Zhukov, S. S. Mikhrin, A. P. Vasilev, E. S. Semenova, Yu. M. Shernyakov, E. V. Nikitina, N. V. Kryzhanovskaya, D. S. Sizov, I. P. Soshnikov, M. V. Maximov, N. N. Ledentsov, V. M. Ustinov, D. Bimberg<sup>†</sup> and Zh. I. Alferov*

*Ioffe Physico-Technical Institute, St Petersburg, Russia*

*<sup>†</sup> Technical University of Berlin, Berlin, Germany*

**Abstract.** Recent results on molecular-beam epitaxy growth of the quantum dot InGaAs/GaAs heterostructures for long-wavelength lasers on GaAs substrates are presented. As a result of optimization of the growth procedure for active region and emitter layers low-threshold current density ( $45\text{--}80\text{ A/cm}^2$ ) long-wavelength ( $1.27\text{--}1.3\text{ }\mu\text{m}$ ) laser diodes may be fabricated with high reproducibility.

### Introduction

Self-organized InGaAs quantum dots (QDs) in (Al)GaAs matrix are potential candidates for application as the active region of long-wavelength-range edge-emitting lasers and vertical-cavity surface-emitting lasers (VCSELs) on GaAs substrates [1]. Room temperature operation of QD lasers at  $1.3\text{ }\mu\text{m}$  with ultra-low threshold current densities ( $20\text{--}45\text{ A/cm}^2$ ) has been reported in [2, 3]. However, gain saturation of the ground-state QD transition associated with the low surface density of such QD array ( $\sim 1.3 \times 10^{10}\text{ cm}^{-2}$ ) forced authors to use long stripe lasers with high-reflectivity facet coatings which are principally characterized by low external differential efficiency. For  $1.3\text{ }\mu\text{m}$  QD structures this problem can not be easily solved by the use of multiple stacks of QD layers since this may enhance the formation of the nonradiative recombination centers. We have previously shown that the luminescence peak position of InAs QDs can be shifted to  $1.3\text{ }\mu\text{m}$  by covering them with thin InGaAs layer [4]. The most important advantage of this approach is that the density of such QD array is as high as  $(3\text{--}4) \times 10^{10}\text{ cm}^{-2}$ . Additional optimization of the MBE-growth procedure allows the fabrication of multiple stacks of InAs/InGaAs QD layers without any noticeable degradation in the luminescent properties for 3-layer structures [5]. As a result, continuous-wave operation was achieved for broad-area long-wavelength ( $1.24\text{--}1.28\text{ }\mu\text{m}$ ) QD lasers with threshold current density of  $90\text{ A/cm}^2$ , maximum output power of  $2.7\text{ W}$  and high differential efficiency ( $\eta_D$  higher than 50%) [5]. Recently this approach was successfully applied for the fabrication of  $1.3\text{ }\mu\text{m}$  QD VCSELs with maximum CW output power of  $0.7\text{--}0.9\text{ mW}$ , threshold current of  $1.5\text{--}2.0\text{ mA}$  and differential efficiency  $> 40\%$  [6].

In this work we focus on some critical problems in MBE growth of long-wavelength QD heterostructures and demonstrate principal possibility for fabrication of low-threshold  $1.3\text{ }\mu\text{m}$  QD lasers with large number of QD layers in active region. Proposed MBE technique provides reproducible long-wavelength lasing combined with sufficient improvements in lasers temperature stability.

### Critical problems in MBE growth of long-wavelength QD lasers on GaAs substrates

To improve the characteristics of long-wavelength QD lasers on GaAs, one has to solve several important problems. Low values of maximum single-layer modal gain for ground-state QD emission ( $3\text{--}4\text{ cm}^{-1}$ ) [5] and rapid (super-linear) increase in the laser threshold current density with increasing the number of the QD layers in active region (see Fig. 1) are among the most critical issues. For example, the lowest threshold current density in our long-wavelength QD lasers with 3-layer active region was  $70\text{--}90\text{ A/cm}^2$  whereas for 10-layer active region it was as high as  $550\text{ A/cm}^2$ . At the same time, the use of the active region with several QD layers is necessary to increase the optical gain for short-cavity edge-emitting lasers and VCSELs. Another critical issue is a significant blue-shift and non-reproducibility in the PL peak position for most of investigated laser structures (Table 1). At the same time PL spectra for test structures are quite stable and reproducible (5 test samples and 6 laser structures were investigated, full duration of the concerned MBE growth cycle was two weeks). This is serious problem because for most applications laser diodes should emit in the certain wavelength range ( $1.310\text{ }\mu\text{m}\pm 20\text{ nm}$ ). In addition, long-wavelength QD lasers usually demonstrate insufficient temperature stability (laser characteristic temperature typically less than  $50\text{--}60\text{ K}$ ).

**Table 1.** Typical PL peak positions for standard and optimized MBE technique.

Structure	Standard	Optimized
MBE technique	MBE technique	
PL max (test samples) (nm)	$1286 \pm 7$	$1292 \pm 5$
PL max (laser structures) (nm)	$1244 \pm 32$	$1282 \pm 8$
Typical blue shift (nm)	42	11

### Optimized MBE-growth technique and laser results

The main features of the developed growth technique are thorough optimization and careful control of the laser heterostructure composition in terms of growth rate, III/V fluxes ratio, layer thickness and growth temperature. The developed growth procedure provides a comparatively high area density of QDs ( $3\text{--}4 \times 10^{10}\text{ cm}^{-2}$ ) in each layer. Additionally, relatively thick GaAs spacer layers ( $20\text{--}25\text{ nm}$ ) are used to separate the QD plains. As a result area density of the self-organized InAs/InGaAs QDs is reproduced in each layer but without any noticeable spatial correlation in the dot positions and QD emission wavelength can be controllably changed from  $1.15\text{ }\mu\text{m}$  to  $1.3\text{ }\mu\text{m}$ . For InAs/InGaAs structures (2.7 ML InAs +  $55\text{ }\text{\AA}$  In<sub>0.15</sub>Ga<sub>0.85</sub>As, PL maximum at  $1.3\text{ }\mu\text{m}$ ) with different numbers of QD plains

This suggests that the radiative recombination is a dominant mechanism and that PL properties do not degrade by the developed stacking of the QD plains. It opens possibility for increasing the optical gain of the QD active region.

We also studied in details correlation between PL maximum positions for test samples and real laser heterostructures. It was found that the most critical point is the cladding layers optimization in terms of surface morphology.

We compared laser epitaxial structures fabricated by standard [5] and optimized MBE growth techniques. In both cases the same standard technology process was used for lasers fabrication. Figure 1 illustrates experimental results for longwavelength QD laser structures on GaAs substrates. Laser structures were grown by solid-source MBE on the

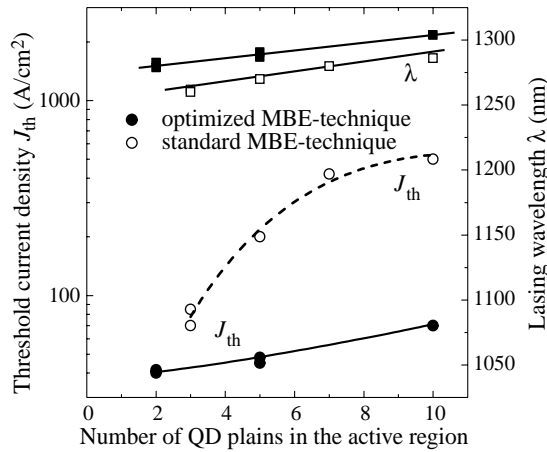


**Fig. 1.** Threshold current density and lasing wavelength for long-wavelength QD lasers MBE-grown on GaAs substrates by standard and optimized technique (best values) (up to 10) the integrated PL efficiency was studied as a function of the excitation power density. The evaluated dependence was close to linear for all test samples.

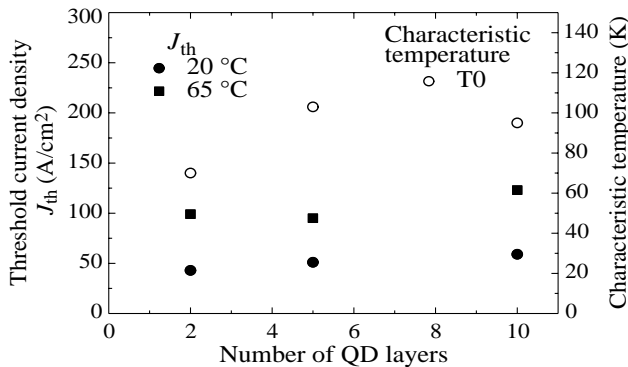


**Fig. 2.** Threshold current density and characteristic temperature for longwavelength QD lasers MBE-grown on GaAs substrates by optimized technique (typical values).

(100)-oriented n-GaAs substrate. A 0.4- $\mu\text{m}$ -thick GaAs waveguide confined by 1.4  $\mu\text{m}$  n- and p- $\text{Al}_{0.8}\text{Ga}_{0.2}\text{As}$  cladding layers contains a QD active region with different number of QD layers.

It is obviously that the optimized technique provides sufficient reduction in the threshold current densities (especially for structures with large number of QD plains). For example laser diodes with 10-layer active region demonstrate threshold current density as low as 70  $\text{A}/\text{cm}^2$  and reproducible lasing in practically important spectral range of 1.3  $\mu\text{m}$ . Careful control of MBE growth regimes for AlGaAs cladding layers provides sufficient reduction of the blue-shift in the PL peak position for laser structures and improved run-to-run reproducibility as shown in Table 1. Laser characteristic temperatures up to 85–100 K and low threshold current densities at 650 °C (100–120  $\text{A}/\text{cm}^2$ ) were achieved by using of optimized MBE technique.



## Conclusion

In conclusion, optimized MBE-growth technique for long-wavelength InGaAs/GaAs quantum dot lasers on GaAs substrates was designed. As a result low-threshold current density ( $45\text{--}80\text{ A/cm}^2$ ) long-wavelength ( $1.28\text{--}1.3\text{ }\mu\text{m}$ ) laser diodes with large number of QD plains in the active region ( $5\text{--}10$ ) were be fabricated.

## Acknowledgements

This work was supported by the Russian Foundation of Basic Research and by the Ministry of Science of Russia in the framework of the “Physics of Solid State Nanostructures” program.

## References

- [1] V. M. Ustinov and A. E. Zhukov, *Semicond. Sci. Technol.* **15**, R41-R54 (2000).
- [2] G. Park, O. B. Shchekin, S. Csutak, D. L. Huffaker and D. G. Deppe, *Appl. Phys. Lett.* **75**, 3267-3269 (1999).
- [3] X. Huang, A. Stinz, C. P. Hains, G. T. Liu, J. Cheng and K. J. Malloy, *Electron. Lett.* **36**, 41-42 (2000).
- [4] V. M. Ustinov, N. A. Maleev, A. E. Zhukov, A. R. Kovsh, A. Yu. Egorov, A. V. Lunev, B. V. Volovik, I. L. Krestnikov, Yu. G. Musikhin, N. A. Bert, P. S. Kop'ev, Zh. I. Alferov, N. N. Ledentsov and D. Bimberg, *Appl. Phys. Lett.* **74**, 2815-2817 (1999).
- [5] A. E. Zhukov, A. R. Kovsh, V. M. Ustinov, Yu. M. Shernyakov, S. S. Mikhlin, N. A. Maleev, E. Yu. Kondrateva, D. A. Livshits, M. V. Maximov, B. V. Volovik, D. A. Bedarev, Yu. G. Musikhin, N. N. Ledentsov, P. S. Kop'ev, Zh. I. Alferov and D. Bimberg, *IEEE Photonics Techn. Lett.* **11**, 1345-1347 (1999).
- [6] J. A. Lott, N. N. Ledentsov, V. M. Ustinov, N. A. Maleev, A. E. Zhukov, A. R. Kovsh, M. V. Maximov, B. V. Volovik, Zh. I. Alferov and D. Bimberg, 2000 *IEEE LEOS Annual Meeting Conference Proceedings*, Vol. 1, 13-14 November 2000, p 304-305.

## Near-threshold spectral and modal characteristics of a curved-grating quantum-well distributed-feedback laser (c-DFB)

Y. Boucher<sup>†</sup>, A. G. Deryagin<sup>‡</sup>, V. I. Kuchinskii<sup>‡</sup> and G. S. Sokolovskii<sup>‡</sup>

<sup>†</sup> ÉNIB/RESO, BP 30815, F-29608 Brest Cedex, France

<sup>‡</sup> Ioffe Physico-Technical Institute, St Petersburg, Russia

**Abstract.** We present a theoretical investigation of the spectral and modal properties of a near-threshold two-dimensional curved-grating distributed-feedback laser provided with high transverse confinement. All fields are described in the spectral domain in the frame of an extended ( $3 \times 3$ ) transfer matrix formalism which takes into account the internal sources, as well as saturation of the gain medium through amplified spontaneous emission.

### Introduction

The need for high-power, diffraction-limited, single-mode diode lasers has led in the past few years to new developments in the field of integrated structures incorporating curved-groove gratings. In particular, two-dimensional distributed-feedback lasers with a concentric corrugation inside a triangular gain section (or c-DFB) have been proposed by one of us [1, 2]. In such a configuration, the general solution  $E(\rho, \theta)$  to the (scalar) wave equation can be expressed as the product of harmonic angular function  $g(\theta)$  and radial function  $A(\rho)$  which takes the form of a linear combination of Hankel functions of the first and the second kinds, respectively converging toward and diverging from the centre of symmetry.

In what follows, we assume a metallic-like (ideal) reflection along the lateral walls, where the field should vanish [Fig. 1]. The time dependence is taken as  $\exp(+i\omega t)$ .

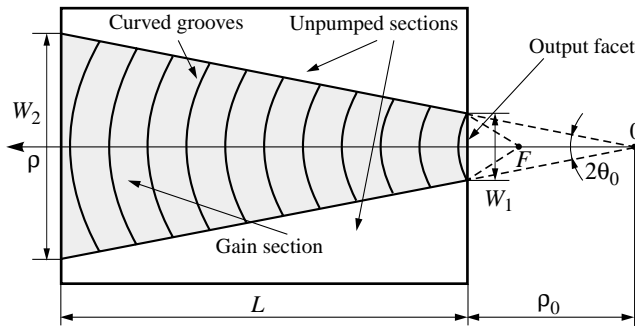


**Fig. 1.** Simplified schematic of the curved-grating DFB structure with aperture angle  $2\theta_0$ .

The angular quantification condition relative to the transverse eigenmodes enables us to distinguish between either symmetric or antisymmetric solutions:  $g_m(\theta) = \cos(m\theta)$  or  $\sin(m\theta)$ , with  $m$  respectively half-integer or integer multiple of  $(\pi/\theta_0)$ . To each value of  $m$  corresponds a radial part, written around a reference wavevector  $\beta_B$  as:

$$A_m(\rho) = S_m(\rho)H_m^{(1)}(\beta_m\rho) + R_m(\rho)H_m^{(2)}(\beta_m\rho). \quad (1)$$

The order  $m$  of the Hankel functions (the radial part) is therefore closely related to the behaviour of the harmonic angular part (the transverse mode). For a conveniently designed index modulation, these cylindrical waves appear coupled along the radial direction by coupled-wave equations (CWE), formally similar to those derived by Kogelnik and Shank in truly one-dimensional problems [3].

If we restrict ourselves to a particular  $m$ , we get:

$$R' = i(\delta + i\alpha)R + i\kappa_{RS}S \quad S' = i(\delta + i\alpha)S + i\kappa_{RS}R \quad (2)$$

with  $\delta$  — detuning from the Bragg condition,  $\alpha$  — radial amplification coefficient,  $\kappa_{RS}$  and  $\kappa_{SR}$  — coupling constants ( $\kappa_{SR} = \kappa_{RS}^*$  due to pure index-coupling).

Next, we take into account the internal sources of spontaneous emission, assumed uniform along the active zone. The relationship between the diverging and converging fields  $\{A_R, A_S\}$  at both extremities can be written under a  $(3 \times 3)$  matrix form [4–5], with or without end-facet reflections, but under the mandatory hypothesis that the concentric symmetry remains unbroken:

$$\begin{pmatrix} A_{R0} \\ A_{S0} \\ 1 \end{pmatrix} = \begin{pmatrix} M_{11} & M_{12} & M_{13} \\ M_{21} & M_{22} & M_{23} \\ 0 & 0 & 1 \end{pmatrix} \begin{pmatrix} A_{RL} \\ A_{SL} \\ 1 \end{pmatrix}, \quad (3)$$

where the  $M_{ij}$  for  $i, j = 1$  or  $2$  are that of a “classical”  $(2 \times 2)$  matrix, and the  $M_{i3}$  describe the internal sources. As a result, when no input field is present,  $A_{R0} = A_{SL} = 0$ , and the background fields emitted through both facets are:

$$A_{RL} \equiv B_{RL} = -\frac{M_{13}}{M_{11}}, \quad A_{S0} \equiv B_{S0} = \frac{M_{23}M_{11} - M_{13}M_{21}}{M_{11}}. \quad (4)$$

The corresponding emitted powers at  $\rho = \rho_0$  and  $\rho = \rho_L$  when no input field is present can be written as:

$$P_{S0/RL} = \frac{d}{\Gamma} \int \frac{\varepsilon_0}{2} cn_{0/S} \langle |B_{S0/RL} \times g_m(\theta)|^2 \rangle d\theta = \frac{d}{\Gamma} \frac{\varepsilon_0}{2} cn_0 \langle |B_{S0/RL}|^2 \rangle \frac{\rho_{0/L}}{2} \quad (5)$$

where the brackets represent a time average,  $d$  is the depth of the active zone and  $\Gamma$  the lateral confinement factor. It should be noted that these expressions give the spectral density of the emitted power, as far as all the fields appear filtered by the transfer function  $T(\omega) \propto |1/M_{11}|^2$ . For instance, when no reflecting facets are considered,

$$M_{11} = \frac{1}{\gamma L} [\gamma L \cosh(\gamma L) + i(\delta L + i\alpha L) \sinh(\gamma L)] \frac{H_m^{(2)}(\beta_B \rho_0)}{H_m^{(2)}(\beta_B \rho_L)} \quad (6)$$

with  $\gamma = [\kappa_{RS}\kappa_{SR} - (\delta + i\alpha)^2]^{1/2}$ , and:

$$T(\delta L) = \frac{|\gamma L|^2}{|\gamma L \cosh(\gamma L) + i(\delta L + i\alpha L) \sinh(\gamma L)|^2}. \quad (7)$$

This transfer function plays a leading role in imposing the spectral properties of the fields. For no or small amplification, it is responsible for a transmission forbidden band centred on  $\delta L = 0$  (Fig. 2(a)). The first transmission peak (“resonance”) is reached at  $(\delta_{\text{res}} L)$  such as:  $(\delta_{\text{res}} L)^2 = \pi^2 + |\kappa L|^2$ , so that  $\gamma L = \pm i\pi$ , the maximal value of  $T$  being therefore  $T_{\text{max}} = 1$ . Adding gain leads to an increasing  $T$ , which can become greater than unity. Besides, the resonance detuning is shifted towards  $\delta L = 0$ ; when increasing  $\alpha L$  from 0 to its threshold value  $\alpha_{\text{th}} L$  (see below),  $\delta_{\text{res}} L$  decreases from  $(\pi^2 + |\kappa L|^2)^{1/2}$  to  $\delta_{\text{th}} L$  (Fig. 2(b)).

The transmission value  $T(\delta_{\text{res}} L)$  at resonance increases, and tends towards infinite in the vicinity of the classical threshold. This divergence occurring at  $\alpha_{\text{th}} L$  should be understood as an asymptotic behaviour, devoid of physical meaning. The *saturation* of the active medium by recombination processes limits the range of values that can be actually taken by the carrier density and the gain. As a matter of fact, even when the amplification is very high

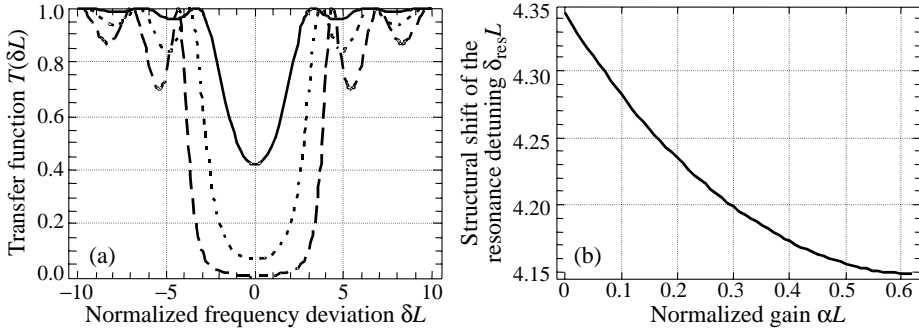


**Fig. 2.** (a) Transfer function  $T(\delta L)$  for  $\alpha L = 0$ ;  $\kappa L = 1$  (—), 2 (---) or 3 (— · —). (b) Structural shift of the resonance detuning ( $\delta_{\text{res}} L$ ) for  $\kappa L = 3$ ,  $\alpha L$  varying from 0 to  $\alpha_{\text{th}} L$ .

(for high pumping), the medium cannot deliver more energy than it has in stock. At the same time, the normalised transmission peak  $T(\delta L)/T_{\text{max}}$  becomes narrower (Fig. 3(a)). From a mathematical point of view, the bandwidth tends towards 0, but saturation mechanisms ensure that the actual line-width is finite.

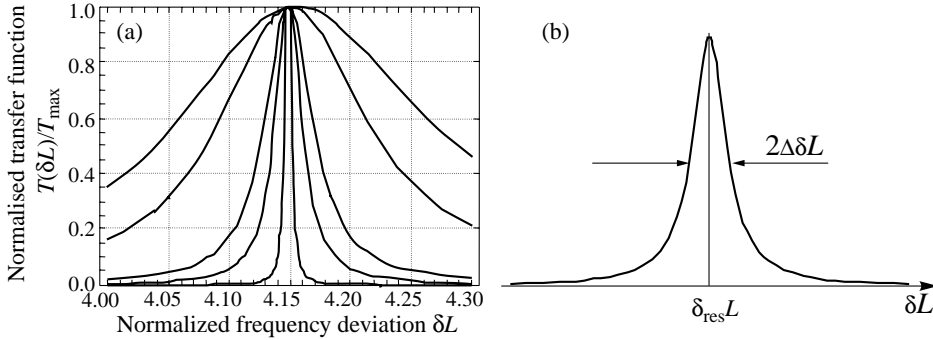


**Fig. 3.** (a) Normalised transfer function  $T(\delta L)/T_{\text{max}}$  around the transmission peak for  $\kappa L = 3$ ,  $\alpha L = 0.5$ ; 0.55; 0.6; 0.61 and 0.62. (b) Normalised Lorentzian.

As soon as the resonance peak is well defined, it becomes possible to describe it as a Lorentzian (Fig. 3(b)):

$$T(\delta L) \approx \frac{T_{\text{max}} (\Delta\delta L)^2}{(\delta L - \delta_{\text{res}} L)^2 + (\Delta\delta L)^2}, \quad (\Delta\delta L) = \left[ -\frac{1}{2} \left( \frac{1}{T} \frac{d^2 T}{d\delta L^2} \right) \Big|_{\text{res}} \right]^{-1/2}. \quad (8)$$

The “classical” threshold condition is obtained by putting  $M_{11}$  to 0:

$$\gamma \coth(\gamma L) = \alpha - i\delta. \quad (9)$$

As a matter of fact, we should take into account the saturation of the gain medium through Amplified Spontaneous Emission (ASE), looked upon as the driving source of the optical field and projected into the mode. We shall see now how the extended matrix formalism can be used to derive an expression for the line-width that remains continuously valid across threshold [6]. As far as the source terms  $M_{13}$  and  $M_{23}$  are concerned, they are best described in terms of *equivalent spontaneous fields* ( $u_{RL}$ ) emitted at  $\rho = \rho_L$  and ( $u_{S0}$ ) emitted at  $\rho = \rho_0$ . For instance, if we neglect the end-facet reflection, then:

$$M_{13} = -(u_{RL})M_{11}, \quad M_{23} = -(u_{RL})M_{21} + (u_{S0}). \quad (10)$$

The spontaneous sources are not coherent spatially: only the amplitude, not the phase, of the two fields ( $u_{RL}$ ) and ( $u_{S0}$ ) can be measured experimentally. A straightforward calculation enables one to express them through partial transfer matrices  $[L(\rho)]$  and  $[R(\rho)]$ , relating radii  $\rho_0$  to  $\rho$  and  $\rho$  to  $\rho_L$  respectively. These are completely determined in the frame of the CWE. For instance, the coefficients of the “left-hand” partial matrix  $[L(\rho)]$  are:

$$\begin{aligned} L_{11/22}(\rho) &= \frac{1}{\gamma L} \left\{ \gamma L \cosh [\gamma(\rho - \rho_0)] \pm i(\delta L + i\alpha L) \sinh [\gamma(\rho - \rho_0)] \right\} \frac{H_m^{(2/1)}(\beta_B \rho_0)}{H_m^{(2/1)}(\beta_B \rho)} \\ L_{12/21}(\rho) &= \pm \frac{i\kappa_{RS}}{\gamma} \sinh [\gamma(\rho - \rho_0)] \frac{H_m^{(2/1)}(\beta_B \rho_0)}{H_m^{(1/2)}(\beta_B \rho)} \end{aligned} \quad (11)$$

After some calculation, we obtain for the diverging emitted fields:

$$\begin{aligned} \langle |u_{RL}|^2 \rangle &\propto \frac{1}{|M_{11}|^2} \int |L_{11}(\rho) - L_{12}(\rho)|^2 d\rho \\ \langle |u_{S0}|^2 \rangle &\propto \frac{1}{|M_{11}|^2} \int |R_{11}(\rho) + R_{21}(\rho)|^2 d\rho \\ \langle (u_{RL})(u_{S0})^* \rangle &\propto \frac{1}{|M_{11}|^2} \int [L_{11}(\rho) - L_{12}(\rho)] \det [L(\rho)]^* [R_{11}(\rho) + R_{21}(\rho)]^* d\rho \end{aligned} \quad (12)$$

Similar expressions hold for the total internal fields, whatever the detuning  $\delta L$ .

We can therefore establish the complete expression for all fields, in the spectral domain, as explicit functions of the material and structural parameters of the c-DFB. In order to do that, we have only to assume that the optical parameters of the active medium (index, gain, spontaneous emission) are well defined and constant. On the other hand, they are affected by saturation. But in steady-state regime, a self-consistent determination is possible as a function of the pumping rate [7].

As far as the cylindrical symmetry remains unbroken, the extended ( $3 \times 3$ ) transfer matrix formalism provides us with a powerful tool for investigating the spectral properties of c-DFB lasers. We would like to emphasise that any radial variation of the parameters could also be described by subdividing the structure in partial zones with constant parameters. All fields appear filtered into the transfer function  $T(\delta L)$ , which enables us to derive, in normalised units, the classical threshold condition and the analytical expression of the emitted fields through both facets (even when no input field is present), as well as emitted power and lineshape.

#### Acknowledgments

Y. Boucher wishes to thank Pr. Le Bihan, Head of RESO Laboratory, for his support and encouragement.

#### References

- [1] G. S. Sokolovskii, E. U. Rafailov, D. J. L. Birkin and W. Sibbett, *J. Opt. Quant. Electron.* **31**, 215–221 (1999).
- [2] G. S. Sokolovskii, E. U. Rafailov, D. J. L. Birkin and W. Sibbett, *IEEE J. Quantum Electron.* **36**, 1412–1420 (2000).
- [3] H. Kogelnik and C. V. Shank, *J. Appl. Phys.* **43**(5), 2327–2335 (1972).
- [4] J.-P. Weber and S. Wang, *IEEE J. Quantum Electron.* **27**(10), 2256–2266 (1991).
- [5] Y. Boucher and A. Sharaiha, *IEEE J. Quantum Electron.* **36**(6), 708–720 (2000).
- [6] Y. Boucher and O. Delléa, *IEEE Proc.-Opto-electronics* **148**(1), 25–30 (2001).
- [7] Y. Boucher, *Conference on Lasers and Electro-Optics CLEO/Europe'00*, paper CWF 0068, Nice, France, Sept. 2000.

## Non-linear power-current characteristics of quantum well lasers at high injection

V. P. Evtikhiev, E. Yu. Kotelnikov, D. V. Dorofeyev and G. G. Zegrya  
Ioffe Physico-Technical Institute, St Petersburg, Russia

**Abstract.** Mechanisms causing non-linearity of power-current characteristics (PCC) of quantum-well lasers at high injection levels were studied both experimentally and theoretically. A critical injection current that switch on a nonlinear PCC mode was found to depend to a great extent on the resonator length (on the threshold concentration). The PCC non-linearity is well described within the framework of the gain saturation mechanism where a dependence of the gain coefficient on the radiation intensity at high injected carriers concentration is taken into account.

The present work deals with a study of physical processes which restrict the output power of semiconducting lasers with a wide strip at high excitation levels.

Nonlinear optical effects begin to appear at high intensities of laser radiation [1–4]. A dependence of the gain coefficient on the electromagnetic field is one of the basic nonlinear effects in semiconducting heterojunction lasers [4].

In our experiments InGaAs/AlGaAs/GaAs quantum well laser diodes were used as test samples. In order to study possible reasons for the PCC saturation, lasing and spontaneous radiation spectra were recorded under excitation by sharp current pulses with a high on-off time ratio. It was found that PCCs of laser diodes with long and short resonators differed (Fig. 1). PCCs of short-resonator lasers were sub-linear at high pumping levels, whereas PCCs of long-resonator lasers were linear at pumping currents greater than the threshold current up to the values when a catastrophic mirror degradation occurred. To be certain that the PCC saturation of lasers with short resonators was not caused by heating, spectra of the concurrent spontaneous radiation were recorded from the active area of laser

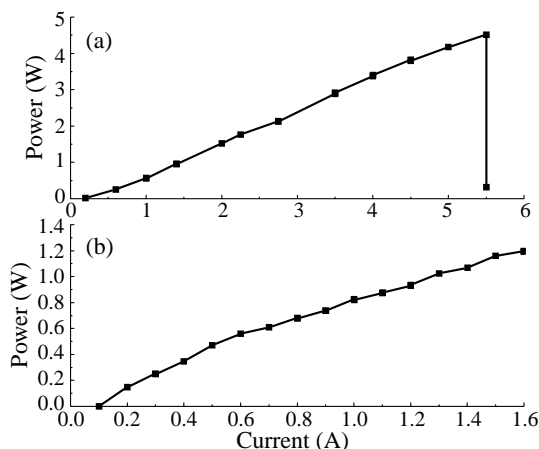


**Fig. 1.** PCC of InGaAs/GaAs/AlAs lasers with a short (0.33 mm) cavity (a) and long (1.04 mm) one (b).

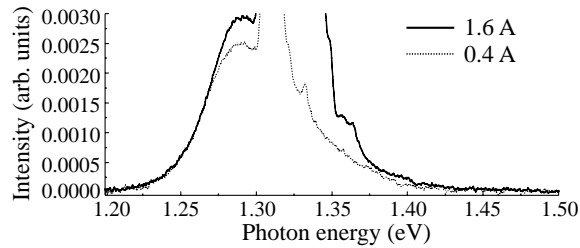


**Fig. 2.** Spontaneous emission spectra from the active layer of short cavity laser at low and high injection current.

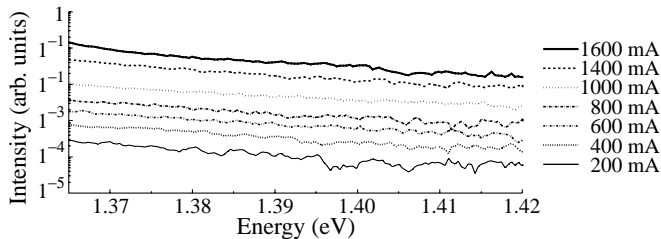


**Fig. 3.** Spontaneous emission spectral power density as a function of photon energy at different pump currents.

diodes through a window in a contact. Figure 2 demonstrates that the long-wavelength edges of the concurrent radiation spectra are independent of the pumping level. Thus, it is possible to claim that the lattice temperature in the crystal is independent of the pumping current; otherwise, a red shift would be observed resulted from decreasing the semiconductor forbidden gap with increasing temperature. According to calculations, the excitation pulse is so short that, even if the total supplied energy were transformed into heat within the laser waveguide, the temperature in this volume would rise less than by four degrees. Figure 3 shows the short-wave decays of spontaneous luminescence spectra in a semi-logarithmic coordinates. Slopes of the spectra are independent of the pumping current and demonstrate a lack of carrier heating.

Figure 4 shows generation spectra of a short-resonator laser diode. The generation spectra broaden with pumping not only toward the short-wavelengths but also toward the long-wavelengths. This fact testifies to a deformation of the gain coefficient spectrum—a decrease in the gain on the generation wavelength.

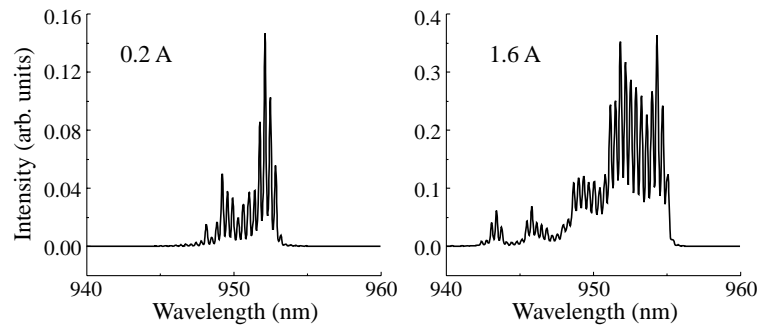


**Fig. 4.** Lasing spectra of a short-cavity laser diode at low and high pump levels.

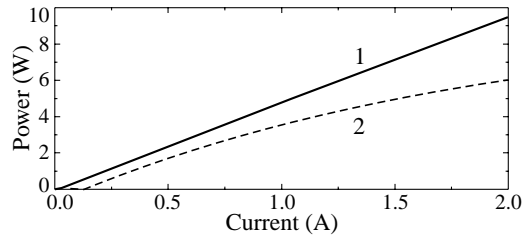


**Fig. 5.** Results of theoretical simulations of PCCs for laser diodes with short (0.33 mm) curve 1 and long (1.04 mm) curve 2 cavity lengths

To explain the above results, we propose the following model. The threshold carrier concentration in short-resonator lasers is much higher than that in long-resonator lasers. At high pumping levels and a great optical power in the resonator, a spectral dip is “burned out” in the energy distribution of carriers. Formation of such dip is caused by a high rate of the stimulated recombination. A high rate of particle-to-particle collisions hinders filling the dip at a high concentration of free carriers. To evaluate the gain coefficient in the developed generation mode, it is necessary to take into account particle collisions in higher orders of the perturbation theory; therefore, we use the density matrix formalism. The gain coefficient is defined by the imaginary part of the non-diagonal members of the density matrix which determines a probability of transitions between states in the conduction band and the valence band with the same momentum  $\mathbf{p}$ . At the resonance, where the transition probability is high, an electron and a hole with the momentum  $\mathbf{p}$  can be considered as a two-level system. At high radiation intensities resonant two-level systems become saturated; their populations become closer, the gain coefficient (as well as the threshold concentration) beginning to depend on the radiation intensity to a greater extent.

Results of theoretical simulations of PCCs for lasers with various resonator-lengths are shown in Fig. 5. Curve 1 is practically linear and corresponds to a smaller threshold concentration; curve 2 tends to saturate and corresponds to a greater threshold concentration. The calculation takes into account a dependence of the threshold concentration and, consequently, the threshold current on the radiation intensity. Theoretical results are in good agreement with the experimental data.

In summary, we have investigated power-current characteristics, lasing and spontaneous emission spectra from InGaAs/GaAs QW laser diodes at high pumping level. The obtained data demonstrate the saturation of the PCC can be caused by the violation in Fermi–Dirac distribution at high pumping levels as it was predicted in [5].

## References

- [1] N. G. Basov and V. N. Morozov, *JETP* **57**, 617–628 (1966).
- [2] N. G. Basov, *IEEE J. Quant. Electron.* **QE-4**, 855–859 (1968).
- [3] H. Hasegawa, *Phys. Rev.* **184**, 338–345 (1969).
- [4] O. N. Krohin, *Phys. Solid State* **7**, 2612–2619 (1966).
- [5] V. M. Galitskij and V. F. Elesin, *Rezonans Coupling of Electromagnetic Fields and Semiconductors* Moscow, 1986.



## Semiconductor quantum dot superlattice for coherent acoustic phonon emission

A. *Khitun* and K. L. Wang

Device Research Laboratory Electrical Engineering Department  
University of California-Los Angeles, Los Angeles, California 90095-1594

**Abstract.** We present a novel concept of using quantum dot superlattices for coherent acoustic phonon emission. Coherent lattice wave generation is proposed by collective dot vibrations in a self-assembled quantum dot array, where superlattice structure acts as a phonon resonator. The dots vibrations are synchronized by an external electric field. The proposed scheme has advantage of low phonon scattering rate in quantum dots, that enables generating high intensity phonon beams at low amplitude of the pumping electric field. The advantage is illustrated by numerical simulations carried out for Si/Ge superlattice. The proposed scheme may find many phonon applications, such as for local temperature control, phonon assisted optical transition enhancement, and characterization of low-dimensional structures.

### Introduction

The advance of epitaxial grown techniques made possible the synthesis of artificial structures — quantum dot superlattices (QDS) with high dot shape uniformity as well as ordered dot arrangement in space [1–2]. As both the size of quantum dots and the inter-dot distances decrease and become comparable with the acoustic phonon mean-free-path  $\Lambda$  ( $\Lambda \sim 90$  nm at  $T = 300$  K for Si in the Debye approximation). QDS may have attractive phonon applications. The high frequency acoustic phonons are of especial interest because of their potential applications, e.g. in the high-resolution phonon imaging and non-destructive characterization of low-dimensional structures. But the key problem for the possible phonon applications is how to generate coherent phonons with long enough coherence length. It was proposed in a number of works coherent high frequency acoustic phonon emission via electron-phonon interaction [3–4]. In these schemes electron-phonon interaction must be significant in a given material system in order to achieve substantial phonon generation. At the same time an increase of carrier concentration (doping density) inevitably increases phonon scattering and causes coherence length decrease. In the present work we describe an alternative technique for coherent acoustic phonons generation in quantum dot superlattice without evolving of electron-phonon interaction. The suggested technique allows us to achieve the same coherent phonon intensity without drastic decrease in phonon coherence length.

### 1. Phonon generation by quantum dots

There is an attractive theoretical scheme of sound amplification by stimulated emission of radiation (SASER) proposed by Zavtrak *et al.* [5–7]. In this scheme a liquid dielectric with uniformly distributed dispersed particles was suggested as an active media. And the pumping is produced by an alternating electric field via electrostriction effect due to the dielectric properties mismatch between particles and the host dielectric. Adopting the above

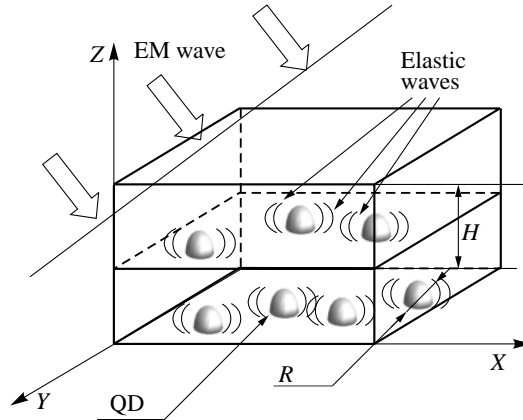


**Fig. 1.** Schematic view of QDS phonon generator. Quantum dots are depicted as semi-spheres arranged layer by layer along with Z direction. An incident electromagnetic wave EM (shown by dashed strait lines) induces dots vibrations, and, thus, generation of elastics waves EW (dotted lines). The spacer thickness and dot radius are depicted by  $H$  and  $R$ , respectively.

idea we challenge material structure to the quantum dot superlattice, where quantum dots act in analogy with the dispersed particles. The scheme of QDS phonon generator is shown in Fig. 1. QDS, grown by MBE using a self-assembled technique in the Stranski–Krastanov, contains of many periods of quantum dots separated by the spacers. The dots are regimented in the layer plane perpendicular to the Z axis (or the XY plane). In Fig. 1 the Z axis is chosen along with the superlattice grown direction. For simplicity, we assume all dots are of the same semi-spherical shape with radius  $R$ . The QDS itself is a phonon resonator. It's resonant wavelengths are defined by the interlayer distance  $H$  (Fig. 1), acoustic mismatch between host and dot materials, dot shape and mutual dot arrangement in the layers.

In order to excite synchronized dot vibrations, the QDS is radiated by an external electromagnetic wave. The electric field of intensity  $E$  causes the effective pressure acting on the dot surface as follows [8]:

$$p = \frac{3}{8\pi} \frac{\epsilon_h E^2 (\epsilon_h - \epsilon_d)}{(2\epsilon_h + \epsilon_d)} \quad (1)$$

where  $\epsilon_h$  and  $\epsilon_d$  are the dielectric constants of the host and dot materials, respectively. The effective pressure results in dot surface vibration which amplitude is defined by the dot admittance. Restricting the electric field frequency  $\omega \ll 2\pi s/a$  (where  $s$  is the speed of sound in the host material and  $a$  is the lattice constant) and taking  $(R/a) \gg 1$ , hereafter we use continuum model approximation. Following the standard approach [9], we can write the admittance for each harmonic  $\beta_m$  in explicit form:

$$\beta = i \frac{\rho c}{\rho_d c_d} \left[ \frac{j'_m(kR)}{j_m(k_d R)} \right] \quad (2)$$

where  $\rho$  is the density,  $k$  is the phonon wave vector,  $j_m$  is the spherical Bessel function of order the subscript  $d$  denotes the parameter of the dot material. The explicit form of dot acoustic admittance Eq. (3) allows as to calculate the intensity of the excited elastic wave, and also find relaxation rate associated with phonon-scattering on quantum dot boundaries. Generally, the relaxation rate is a function of phonon wave vector, quantum dot admittance,

dot density and mutual arrangement. The detailed study of phonon transport in a QDS is given in Ref. [10].

In order to achieve phonon generation, the emission intensity must exceed losses caused by different phonon scattering mechanisms (including scattering on quantum dots boundaries). In the next section we present results of numerical calculations aimed to demonstrate the advantage of the proposed scheme with respect to the schemes involving electron-phonon interaction.

## 2. Results and discussion

In Fig. 2 we had shown results of calculation of phonon relaxation rates due to the different scattering mechanisms as functions of phonon frequency. The calculations are carried out for B doped silicon with germanium quantum dots at  $T = 300$  K. The dot density is  $3 \times 10^8$  dot/cm<sup>2</sup>, the carrier concentration is  $5 \times 10^{19}$  cm<sup>-3</sup>, the spacer layer height is 20 nm, the dot radius  $R$  is 7 nm, acoustic mismatch ( $\rho c / \rho_d c_d = 0.78$ ). Calculations of phonon scattering on dots in superlattice are made after Ref. [10], taking into account given dot size and spacer layer thickness and assuming all dots to be randomly distributed within each layer. Umklapp, Mass-difference and Phonon-electron scattering rates were calculated using well-known formula [11]:

$$\begin{aligned} \frac{1}{\tau_U} &= 2\gamma^2 \frac{k_B T}{\mu V_0} \frac{\omega^2}{\omega_D} \\ \frac{1}{\tau_{Md}} &= \frac{V_0 \omega^4}{4\pi s^3} \sum f_i \left(1 - \frac{M_i}{M}\right)^2 \\ \frac{1}{\tau_{ph-e}} &= \frac{n_e D^2 \omega}{\rho s^2 k_B T} \sqrt{\frac{\pi m^* s^2}{2k_B T}} \exp\left(-\frac{m^* s^2}{2k_B T}\right) \end{aligned} \quad (3)$$

where  $\gamma$  is the Gruneisen anharmonicity parameter,  $k_B$  is the Boltzmann constant,  $T$  is the temperature,  $\omega$  is the phonon frequency,  $V_0$  is the volume per atom,  $\omega_D$  is the Debye

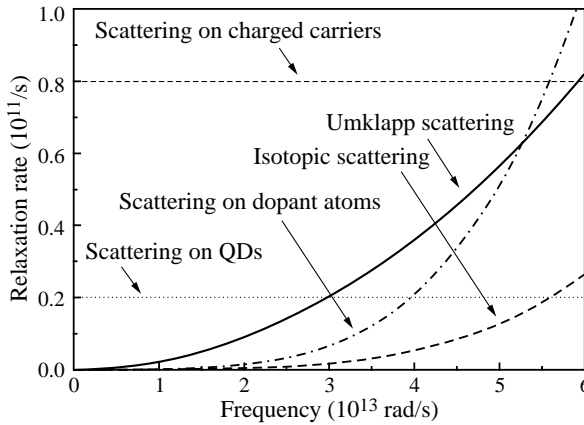


**Fig. 2.** Scattering rates caused by different mechanisms (Umklapp scattering — solid line; Isotopic scattering — dashed line; Mass-difference scattering on B dopant atoms — dash dot line, scattering on charged carriers — short dash line, scattering on quantum dots — dot line).  $T = 300$  K, dot density  $3 \times 10^8$  dot/cm<sup>2</sup> the carrier concentration is  $5 \times 10^{19}$  cm<sup>-3</sup>, the spacer layer height is 20 nm, the dot radius  $R$  is 7 nm, acoustic mismatch ( $\rho c / \rho_d c_d = 0.78$ ).

frequency,  $f$  is the fractional concentration of the impurity atoms of mass  $M_I$ ,  $n_e$  is the concentration of conduction electrons,  $D$  is the deformation potential,  $m^*$  is the electron effective mass. In Fig. 2 we plotted separately Mass-difference scattering rate caused by Si isotopes and scattering rate caused by B dopant atoms.

As it is seen from Fig. 2, the intrinsic losses of the proposed scheme may be much lower than ones of the scheme involving electron-phonon interaction. It implies lower threshold amplitude of the alternative electric field and longer coherence length of the excited phonon beam. Thus, quantum dot superlattice can be used for effective phonon beam generation and may find applications in phonon engineering for enhancing optical transitions, thermoelectricity and others.

#### Acknowledgements

This work was supported by the DoD MURI-ONR program on Thermoelectrics (Dr. John Pazik) and AFOSR MURI program on Phonon Control for Enhanced Device Performance (Dr. Dan Johnstone).

#### References

- [1] Y. S. Tang, S. Cai, G. Jin, J. Duan, K. L. Wang, H. M. Soyeze and B. S. Dunn, *Appl. Phys. Lett.* **71**, 2448 (1997).
- [2] G. Jin, J. L. Liu, S. G. Thomas, Y. H. Luo, K. L. Wang and B.-Y. Nguyen, *Appl. Phys. Lett.* **75**, 2752 (1999).
- [3] C. Rodrigues, M. A. Amato and O. A. C. Nunes, *Phys. Stat. Sol. (B)* **193**, 363 (1996).
- [4] M. E. Msall, A. Klimashov, S. Kronmuller, H. Kostial, W. Dietsche and K. Friedland, *Appl. Phys. Lett.* **74** 821 (1999).
- [5] S. T. Zavtrac, *Phys. Rev. E* **51**, 2480–2484 (1995).
- [6] S. T. Zavtrak and I. V. Volkov, *J. Tech. Phys.* **67**, 92–100 (1997).
- [7] S. T. Zavtrak and I. V. Volkov, *J. Acoust. Soc. Am.* **102** 204–6 (1997).
- [8] L. D. Landau and E. M. Lifshitz, *Electrodynamics of Homogeneous Mediums*, (Nauka, Moscow) 1985.
- [9] P. M. Morse and H. Feshbach, *Methods of Theoretical Physics*, (McGraw-Hill Book Company, Inc., New York, 1953), Part II, pp. 418–430, (1953).
- [10] A. Khitun, A. Balandin, J. L. Liu and K. L. Wang, *J. Appl. Phys.* **88**, 696–9 (2000).
- [11] P. G. Klemens, *Solid State Physics*, ed. by F. Seitz and Turnbull (Academic, New York) 1958.

## 14XX nm pump lasers for Raman and $\text{Er}^{3+}$ doped fiber amplifiers

N. V. Fetisova, N. A. Pikhtin, E. G. Golikova, A. Yu. Leshko, A. V. Lyutetskiy,  
S. O. Slipchenko, Z. N. Sokolova and I. S. Tarasov  
Ioffe Physico-Technical Institute, St Petersburg, Russia

**Abstract.** A set of high power single mode InGaAsP/InP ridge waveguide laser diodes emitting in 1440–1500 nm range on peak wavelengths used for optical fiber pumping were developed and fabricated. Room temperature continuous wave output power of 300 mW was reached. Stable operation on fundamental optical mode with only  $1^\circ$  increase of lateral far-field pattern FWHM was confirmed up to 180 mW output power.

### Introduction

Single lateral/transverse mode laser diodes emitting in the 1400–1500 nm wavelength range are widely used as pump sources for Raman amplifier systems and erbium<sup>3+</sup> doped fiber amplifiers (EDFA's). Application as EDFA pump source requires not less than 200 mW operating continuous wave (CW) output power at 1487 nm wavelength from single mode optical fiber. For recently proposed "WDM" pumping technique in Raman amplifiers it is necessary to prepare a set of pump lasers with 70–190 mW CW operating powers at different precise wavelengths (e.g. 1444, 1450, 1465, 1480 and 1495 nm) [1]. Therefore such applications of single mode laser diodes require high output power, precise peak emission wavelength, high efficiency and effective coupling into single mode optical fiber. These requirements has to be taken into account in the design of single mode laser diodes.

In our present work, we report on the fabrication and investigation of high power single lateral/transverse mode mesastructure construction laser diodes based on InGaAsP/InP separate confinement double quantum well (SC DQW) heterostructures emitting in 1440–1500 nm wavelength range.

### 1. Heterostructure and laser construction design

An achievement of maximum CW output power from single-aperture laser diodes is a complex task. It requires meeting several conditions in laser design. Laser heterostructure has to provide maximum internal quantum efficiency ( $\eta_i$ ), low internal optical loss ( $\alpha_i$ ), minimal cut-off voltage ( $V_c$ ) and series resistance. Laser diode construction has to provide the waveguide formation in the plane parallel to p-n junction (lateral direction). The maintenance of stable operation in fundamental lateral and transverse mode up to maximum output power is one of the complex problems. To provide the operation on fundamental optical mode it is necessary to chose the appropriate value of built-in refractive index step  $\Delta n$  at the active region boundary. In the mesastructure ridge waveguide lasers based on SC DQW heterostructure the effective lateral refractive index step  $\Delta n_L$  mainly depends on the following parameters: mesastructure width (W), etch depth ( $\Delta h$ ), energy bandgap ( $E_g^w$ ) and thickness ( $D_w$ ) of the waveguide. Temperature in the region of the active layer and free carrier concentration in heterostructure layers also have to be taken into account.

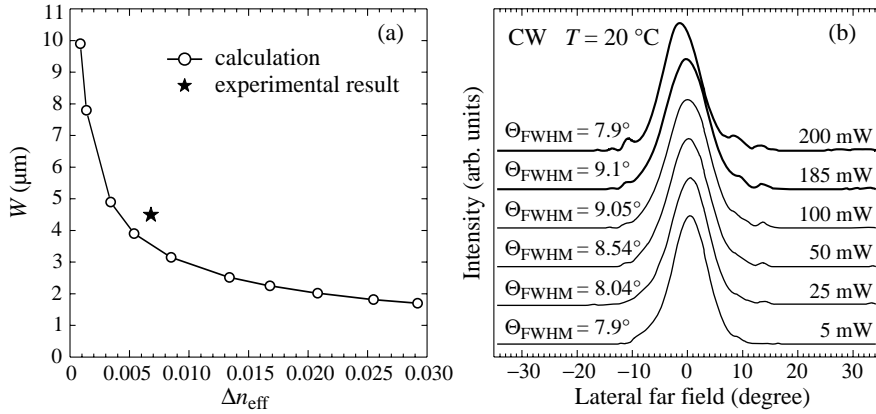


**Fig. 1.** (a) Calculated dependence of lateral effective refractive index step versus laser diode mesa stripe width under first order mode cut-off condition ( $\lambda = 1480$  nm). (b) Far-field pattern in the junction plane at different CW output powers of mesa stripe laser diode.

The effective transverse refractive index step  $\Delta n_T$  is determined mainly by  $E_g^w$  and  $D_w$  parameters.

In our calculations of the first order lateral mode cut-off condition in mesa stripe laser diode on the base of SC DQW InGaAsP/InP heterostructure, two-dimensional passive waveguide analysis was applied [2]. Calculations were carried out for different values of  $E_g^w$ ,  $D_w$  and  $\Delta h$  parameters of heterostructure. The requirements to preserve optimal  $\eta_i$ ,  $\alpha_i$ , and  $V_c$  values were also taken into account. The final results of calculation which was used for fabrication of single mode laser diodes emitting at 1487 nm peak wavelength are presented in Fig. 1(a).

On the base of carried out calculations laser diodes with optimized design of heterostructure and mesa stripe construction were fabricated. Lasers utilize 1% compressive strain double-quantum well  $\text{In}_x\text{Ga}_{1-x}\text{As}_y\text{P}_{1-y}$  active layer, two-step graded-index InGaAsP waveguide and heavily doped n- and p-InP emitters epitaxially grown on InP substrate by metalorganic chemical vapour deposition (MOCVD). To cover the 1440–1500 nm emitting wavelength range several wafers with different active layer composition were grown. Some of our recent results on structure optimization for the achievement of high output power in broad area devices were used in the design of heterostructure for narrow stripe lasers [3–6].

The grown wafers were processed into ridge construction lasers with mesa stripe width  $W = 4\text{--}5$  mm using our conventional postgrowth process in conjunction with chemical etching of channels down to the etch-stop layer [7]. Cleaved laser diode chips with cavity lengths  $L = 0.4\text{--}4$  mm were mounted junction down on copper heatsink using indium solder.

## 2. Experimental investigation

As-cleaved laser diodes fabricated from wafers with different emitting wavelengths were used mostly for heterostructures and construction characterization. The threshold current densities ( $J_{th}$ ) were measured as a function of cavity length.  $J_{th}$  deduced for infinite cavity length lasers is 350–420 A/cm<sup>2</sup> (room temperature) for all processed wafers. The values of internal stimulated quantum efficiency  $\eta_i$  and internal optical losses  $\alpha_i$  were estimated

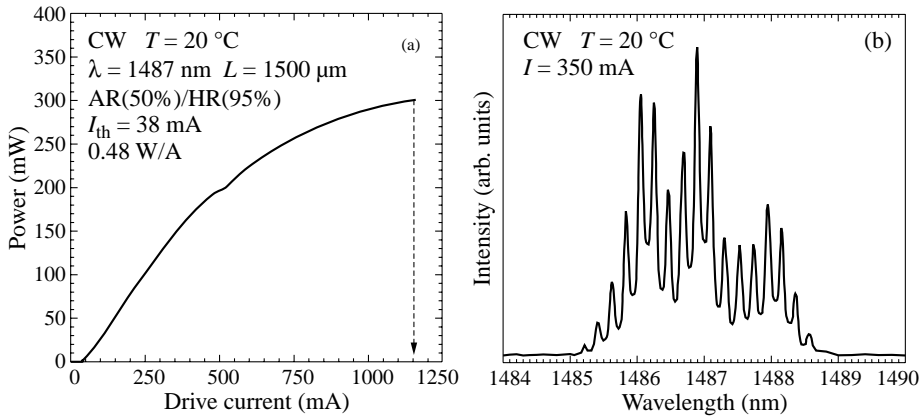


**Fig. 2.** (a) CW light-current characteristic of mesa stripe SC DQW InGaAsP/InP laser diode. (b) Emission spectra of single mode laser diode with  $L = 1.5$  mm cavity length.

from the measured dependencies of external differential quantum efficiency  $\eta_d$  versus cavity length  $L$  by conventional technique [3]. They were found to be  $\eta_i = 93\text{--}98\%$ ,  $\alpha_i = 5\text{--}7\text{ cm}^{-1}$  for all processed wafers. The external differential efficiency values of  $0.48\text{--}0.51\text{ W/A}$  for the  $1.5$  mm long devices at nearly all fabricated wavelengths ( $1444$ ,  $1465$ ,  $1487$ ,  $1495\text{ nm}$ ) are one of the highest values for  $14XX\text{ nm}$  single mode laser diodes reported elsewhere. For the achievement of high power CW at single lateral mode (SLM) operation at required peak wavelength an optimum cavity lengths were chosen from the  $\eta_d(L)$  and  $J_{th}(L)$  dependencies plotted for each wafer. Maximum attained CW room temperature SLM output power of uncoated laser diodes was  $70\text{ mW/facet}$ .

Anti-reflective/high-reflective (AR/HR =  $5\text{--}10\%/95\%$ ) Si/SiO<sub>2</sub> coatings deposited on the front/rear facets of laser diodes allowed to increase more than twice a maximum SLM optical output power. Such increase is connected not only with a slight difference of threshold current density (and therefore threshold carrier concentration) of coated and uncoated diode, but also with an influence of deposited coating material on the far field distribution [8]. Figure 1(b) shows the far-field pattern parallel to the junction plane at different CW output powers from the front facet of AR/HR coated laser diode with  $L = 1.5$  mm cavity length emitting at  $1487$  peak wavelength. It is seen that stable SLM operation is maintained up to  $185\text{ mW}$  of CW output power. The full width at half maximum (FWHM) of the far-field pattern increases only from  $8^\circ$  (threshold) to  $9^\circ$  (operating power). The measured far-field distribution in the plane perpendicular to p-n junction was found to be single transverse mode with FWHM  $35^\circ\text{--}36^\circ$  up to the highest output power. Such stable fundamental mode operation is much required to reach an efficient coupling of laser emission into single mode fiber.

The CW light current ( $L$ – $I$ ) characteristics of such laser diodes presented in Fig. 2(a) has linear kink-free dependence in the whole range of single mode operation. At further increase of output power the kink, smooth saturation and sharp “turn-off” effect are observed in series at  $L$ – $I$  curve. These corresponds to the shift of lateral far-field pattern distribution (so-called beam steering). All these effects are mostly connected with current induced effects finally resulting in the lateral waveguide collapse [9]. The observed “turn-off” effect is completely reversible and has a hysteresis-like character.

Our investigations of emission spectra of fabricated laser diode proved the SLM charac-

ter of operation. As it could be seen from the Fig. 2(b), the distance between the neighbored peaks in the emission spectra precisely corresponds to the wavelength spacing between longitudinal Fabry–Perot modes D1, determined by the well-known equation [2]. In the shown case:  $\Delta\lambda = 0.2$  nm for  $L = 1.5$  mm cavity at  $\lambda = 1487$  nm emission wavelength.

Similar results were achieved for the devices emitting at 1444, 1450, 1465 and 1495 nm peak wavelengths designed for pumping of Raman amplifiers.

Summing up, we have developed and fabricated high power narrow stripe InGaAsP/InP ( $\lambda = 1440$ – $1500$  nm) laser diodes. The optimum design of heterostructure and ridge construction allowed to attain stable single mode operation up to 170–190 mW at emission wavelengths required for Raman and EDFA fiber pumping.

#### Acknowledgements

This work was supported by the Russian Foundation for Basic Research (grants 01-02-17842, 01-02-17851) and Russian Programme “Physics of Solid State Nanostructures”.

#### References

- [1] S. Namiki, *IEEE J. of Selected Topics in QE*, **7** 3 (2001).
- [2] S. L. Chuang, *Physics of Optoelectronic Devices*, John Wiley and Sons, New York, 1995.
- [3] N. A. Pikhtin *et al*, *ECOC'01 Proceedings* **2**, 166 (2001).
- [4] E. G. Golikova *et al*, *Semiconductors* **34** 853 (2000).
- [5] A. Yu. Leshko, *Semiconductors* **34** 1432 (2000).
- [6] N. A. Pikhtin, *Semiconductors* **36** 344 (2002).
- [7] E. G. Golikova *et al*, *Tech. Phys. Lett.* **26** 913 (2000).
- [8] A. S. Scherbakov, N. A. Pikhtin *et al*, *Tech. Phys. Lett.* **22** 344 (1996).
- [9] A. Komissarov, D. Garbuzov *et al*, *CLEO'2001 Proceedings*, paper CMG1.



## Optical gain and lasing of trions in delta-doped ZnSe quantum wells

J. Puls<sup>†</sup>, G. V. Mikhailov<sup>‡</sup>, F. Henneberger<sup>†</sup>, D. R. Yakovlev<sup>‡§</sup> and A. Waag<sup>¶</sup>

<sup>†</sup> Institut für Physik, Humboldt-Universität, 10245 Berlin, Germany

<sup>‡</sup> Ioffe Physico-Technical Institute, RAS, 194021 St Petersburg, Russia

<sup>§</sup> Physikalisches Institut, Universität Würzburg, 97074 Würzburg, Germany

<sup>¶</sup> Abteilung Halbleiterphysik, Universität Ulm, 89081 Ulm, Germany

**Abstract.** The observation of optical gain at the trion transition of n-doped ZnSe quantum wells is reported. The specific optical coupling between the trion and electron band gives rise to stimulated emission on the low-energy wing of the trion photoluminescence band without degeneracy and inversion in the total particle numbers. Gain values as large as  $10^4 \text{ cm}^{-1}$  are found for excitation intensities of some  $\text{kW/cm}^2$ . A calculation of the absorption-gain crossover photon energy based on a kinetically determined equilibrium of excitons, trions and electrons with a common carrier gas temperature describes the experimental data well.

Since the experimental evidence of trions in CdTe [1] and GaAs [2] quantum wells (QWs), most of the studies on heterostructures with background carriers have been devoted to the linear optical properties. If the density of photo-excited electron-hole pairs becomes comparable with the background one, principally new effects are expected in the dense system of boson- and fermion-like excitations. This paper reports on the first observation of optical gain due to trions (charged excitons) in QWs. Compared to other laser processes in semiconductors, this gain mechanism exhibits some peculiar features. The trion consists of three carriers — for n-doping two electrons and one hole — and is hence fermion-like, whereas the optical transition is excitonic. It takes place between states of equal momentum in the electron and trion dispersion with the consequence that no degeneracy is required for achieving optical gain (see Fig. 1). Equally important is the fact that the trion band mass is by definition larger than the electron mass. Therefore, the momentum distribution of the trion  $f_t$  spreads out deeper in  $k$ -space than that of the electron  $f_e$ . As a result, optical gain can be formed even if the total number of trions does not exceed the number of electrons, i.e. without inversion in the total particle numbers.

Optical gain and lasing are studied on ZnSe QWs embedded in (Zn,Be,Mg)Se barriers with background electron densities  $n_0$  ranging from  $3 \times 10^{10}$  to  $3 \times 10^{11} \text{ cm}^{-2}$ . Additional (Zn,Be,Mg)Se cladding layers with larger gap energy are used for wave guiding purposes. Comparative studies of the nonlinear absorption at the trion transition are carried out by pumped reflection on delta-doped ZnSe/(Zn,Mg)(S,Se) QWs. The samples are quasi-stationary excited at the heavy-hole exciton resonance to minimize the heating of the carrier

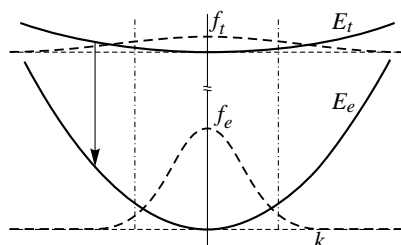


**Fig. 1.** Electron and trion band dispersion and distribution function, respectively. The dash-dotted lines mark the transition from absorption  $f_e > f_t$  to optical gain  $f_t > f_e$  for the momentum-conserving optical transition (arrow).

system by the photo-excited electron-hole pairs [3]. At low excitation intensities, the photoluminescence (PL) and reflectivity spectra show sharp lines (FWHM < 1 meV) of the heavy-hole exciton (X) and the trion (T) (Fig. 2(a)). The assignment of the lines is checked by their characteristic polarization behavior in a Faraday-oriented magnetic field [4]. With increasing  $I_{\text{exc}}$ , the X PL line grows stronger, whereas  $X^-$  line becomes a typical low-energy wing due to recombination of trions at larger  $\mathbf{k}$ -vectors. At the same time, a pronounced edge emission is found located on the low-energy wing of the  $X^-$  line. The PL is TE polarized, in accord with the selection rules for the heavy-hole trion transition. Using the stripe-length variation technique [5], the amplified spontaneous emission along the QW is used to measure the optical gain. Characteristic gain spectra for different excitation levels, excitation wavelengths, and background electron densities are summarized in Fig. 2(b). The photon energy is given with respect to the trion energy  $E_t$  at  $k = 0$  to allow for a comparison of the different samples.

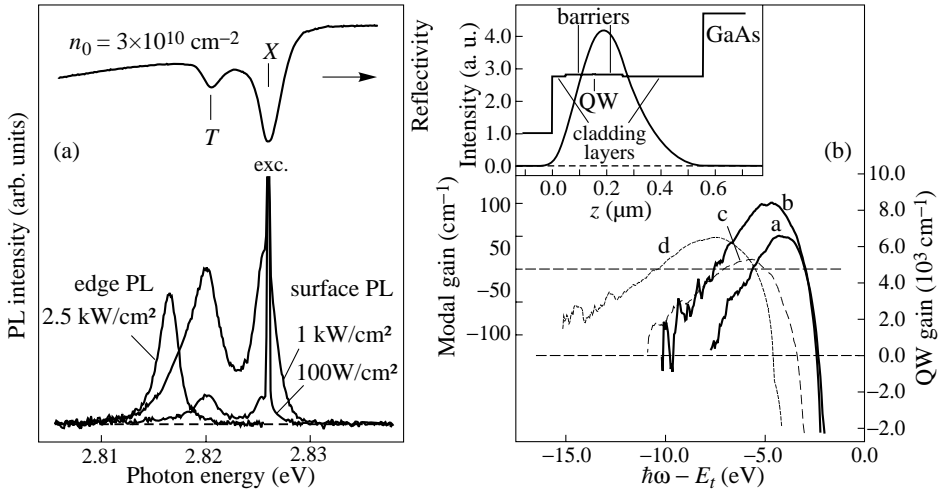


**Fig. 2.** (a) Surface and edge PL of a moderately doped ZnSe/(Zn,Mg,Be)Se single QW structure for various excitation intensities. For comparison, the low-density reflectivity spectrum is given. (b) Modal and QW gain measured for two samples: 1.  $n_0 = 3 \times 10^{10} \text{ cm}^{-2}$ : (a)  $\hbar\omega_{\text{exc}} = 2.826 \text{ eV}$ ,  $I_{\text{exc}} = 5 \text{ kW/cm}^2$ , (b)  $\hbar\omega_{\text{exc}} = 2.826 \text{ eV}$ ,  $I_{\text{exc}} = 20 \text{ kW/cm}^2$ , (c)  $\hbar\omega_{\text{exc}} = 2.87 \text{ eV}$ ,  $I_{\text{exc}} = 40 \text{ kW/cm}^2$ , 2.  $n_0 = 3 \times 10^{11} \text{ cm}^{-2}$ : (d)  $\hbar\omega_{\text{exc}} = 2.823 \text{ eV}$ ,  $I_{\text{exc}} = 40 \text{ kW/cm}^2$ . Inset: Real part of the refractive index  $n$  and intensity of the fundamental waveguide mode along growth direction  $z$ .

The stripe-length data represent merely the modal gain of the trion transition. A numerical analysis of the waveguide structure, depicted in the insert of Fig. 2, provides one fundamental TE mode, interacting efficiently with the QW. The resultant modal versus QW gain relationship is linear in good approximation and can be well fitted by  $g_{\text{mod}} = 0.0276g_{\text{QW}} - 132 \text{ cm}^{-1}$ , where the coefficient and negative offset are caused by the confinement factor of the fundamental mode and the absorption in the GaAs substrate, respectively. The calculated QW gain is given on the right-hand scale of Fig. 2. Peak values of several  $10^3 \text{ cm}^{-1}$  are obtained at very moderate excitation intensities of a few  $\text{W/cm}^2$ .

We have calculated the absorption-gain crossover  $\hbar\omega_{\text{cr}}$  given by  $f_e(k) = f_t(k)$  assuming a kinetically determined equilibrium of excitons, trions and electrons with a common carrier gas temperature [6]. A reasonable agreement with the experimental findings shown in Fig. 2(b) is obtained. In accord with the experiments,  $\hbar\omega_{\text{cr}}$  is found in a range 2 to 6 meV energetically below  $E_t$ . The experimental low-energy shift of  $\hbar\omega_{\text{cr}}$  with increasing

background density  $n_0$  (curve d) or a pure carrier heating (curve c) is correctly described. For a fixed  $n_0$ , an increase of the electron-hole pair generation rate shifts the crossover to higher energies, while heating of the carrier gas moves it in opposite direction. Our measurements demonstrate that both effects largely compensate each other for increasing excitation intensity ( $a \rightarrow b$ ).

Finally, we directly demonstrate laser action of the trion transition utilizing the feedback provided by the natural reflectivity of a cleaved sub-mm resonator structure, prepared from the  $n_0 = 3 \times 10^{10} \text{ cm}^{-2}$  sample. The respective spectra of the edge emission are drawn in Fig. 3. For  $I_{\text{exc}} \geq 4 \text{ kW/cm}^2$ , distinct laser modes appear in the region of positive modal gain. The mode spacing is in full accord with the cavity length and the dispersion of the wave guide propagation constant.

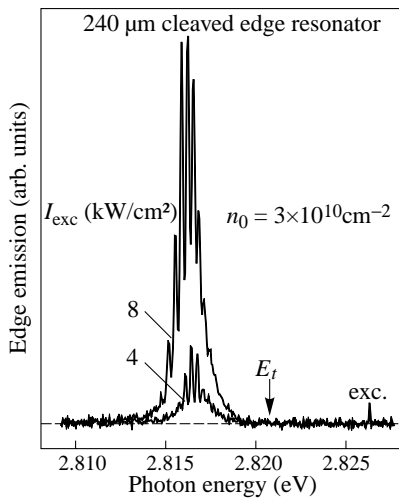


**Fig. 3.** Edge emission of a  $240 \mu\text{m}$  cleaved resonator made from the sample with  $n_0 = 3 \times 10^{10} \text{ cm}^{-2}$ . The width of the modes is limited by the spectral resolution.

In conclusion, we have observed optical gain and lasing at the trion resonance of a doped QW structure. Since the trion transition couples two band continua, the particle distributions are crucially involved. At moderate injection levels, the gain emerges on the low-energy side without degeneracy and total inversion in the trion-electron gas. Heating of the carriers is a critical factor at higher excitation.

#### Acknowledgements

This work has been funded by the Deutsche Forschungsgemeinschaft within the Project He 1939/16-1 and Russian Foundation for Basic Research within the Projects 00-02-17030 and 01-02-04010.

#### References

- [1] K. Kheng, R. T. Cox, Y. Merle d'Aubigne, F. Bassani, K. Saminadayar and S. Tatarenko, *Phys. Rev. Lett.* **71**, 1752 (1993).
- [2] G. Finkelstein, H. Shtrikman and I. Bar-Joseph, *Phys. Rev. Lett.* **74**, 976 (1995).
- [3] J. Puls, G. V. Mikhailov, S. Schwertfeger, D. R. Yakovlev, F. Henneberger and W. Faschinger, *phys. stat. sol. (b)* **227**, 331 (2001).
- [4] G. V. Astakhov, D. R. Yakovlev, V. P. Kochereshko, W. Ossau, J. Nürnberger, W. Faschinger and G. Landwehr, *Phys. Rev. B* **60**, R8485 (1999).
- [5] K. L. Shakley and R. F. Leheny, *Appl. Phys. Lett.* **18**, 475 (1971).
- [6] J. Puls, G. V. Mikhailov, F. Henneberger, D. R. Yakovlev and A. Waag, *phys. stat. sol. (b)* **229**, 637 (2002).

## SC DHS InGaAsP/InP lasers ( $\lambda = 1.5–1.6 \mu\text{m}$ ) with above-threshold internal quantum efficiency $\eta_i^{\text{st}}$ about 100%

*I. S. Tarasov, G. G. Zegrya, G. V. Skrynnikov, N. A. Pikhtin  
 and S. O. Slipchenko*

*Ioffe Physico-Technical Institute, St Petersburg, Russia*

**Abstract.** InGaAsP/InP SC DHS lasers with different waveguide design were fabricated and studied. Extremely high values of internal quantum efficiency of stimulated emission  $\eta_i^{\text{st}}$  about 97% was demonstrated experimentally in structures with step-like waveguide design which is related to lowest leakage currents above threshold and reduced threshold carriers concentration. Theoretically was shown, that it is possible to create lasers emitting at  $\lambda = 1.5 \mu\text{m}$ , with an internal quantum efficiency of stimulated emission close to 100%.  $\eta_i^{\text{st}}$  for structure with different waveguide design was calculated and prove to be in good agreement with experimental data.

### Introduction

One of the main above-threshold performance characteristics of the semiconductor laser is the optical output power. A major factor determining it, is the internal quantum efficiency of stimulated emission  $\eta_i^{\text{st}}$ . The typical values of the  $\eta_i^{\text{st}}$  is about 65–75% for SC DHS lasers emitting at  $1.55 \mu\text{m}$  [1]. The reason of so low values are the additional mechanisms of losses, such as leakage currents above threshold [2].

In this paper the experimental examinations and calculation of lasers power performances for optimization of design InGaAsP SC DHS ( $\lambda = 1.5–1.6 \mu\text{m}$ ) are carried out with the purpose of improving an internal quantum efficiency of stimulated emission  $\eta_i^{\text{st}}$ .

### 1. Experimental samples and experiment

Three SC DHS heterostructures (Fig. 1), differing by the shape of a waveguide (simple—A, one-step—C, double-steps—B), and also geometrical and energy parameters of the waveguide “steps” were chosen as basic structures. All experimental samples were grown by a MOCVD epitaxy method [3]. For laser diodes with various resonator length a CW curves was measured, on the basis of which the differential quantum efficiency  $\eta_d$  and threshold current density  $J_{th}$  was determined. From the obtained experimental dependencies of reciprocal differential quantum efficiency on resonator length the magnitude of internal optical losses  $\alpha_i$  and internal quantum efficiency  $\eta_i^{\text{st}}$  were obtained.

### 2. Theoretical model

First of all is necessary to point out that the definitions of an internal quantum efficiency before and above a threshold differ essentially. Up to a threshold the internal quantum efficiency is featured by usual expression [4] through a relation of velocities of radiative and nonradiative processes, behind a threshold is defined as a part of a stimulated emission current to a total current above a threshold [5].

$$\eta_i^{\text{st}} = \frac{I_{\text{st}}}{I - I_{\text{th}}}. \quad (1)$$

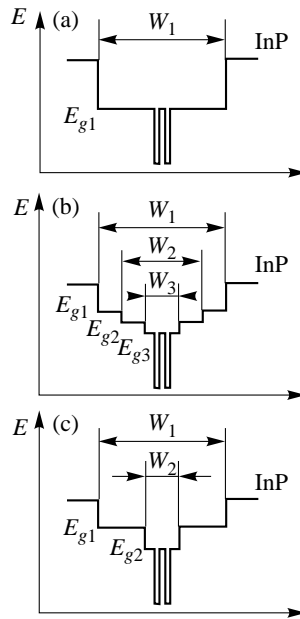


**Fig. 1.** Schematic band diagram of experimental structures (type a, b, c).

The value of  $\eta_i^{\text{st}}$  is influenced only by those currents, which continue to grow above threshold. Electrons and holes concentrations  $n_{\text{th}}$ ,  $p_{\text{th}}$  in active region, and respectively all currents monotonously dependent on these concentrations clamps at the generation threshold [5] and thus do not influence  $\eta_i^{\text{st}}$ . However, above the threshold, continue to grow concentration of carriers in a waveguide  $N_{\text{SCH}}$ . This process is accompanied by growth of spontaneous emission intensity, which are corresponding to radiative transitions in the waveguide. This effect was marked in [2, 6], in [2] experimentally was shown, that reducing of  $\eta_i^{\text{st}}$  can not be explained only by recombination in a waveguide, and related to carriers leakage into emitters. The value of these leakage is directly proportional to concentration of minority carriers at p-layer boundary- $N^*$ , and it grows with increasing of total current density. Then the leakage current density is expressed as follows:

$$J_L = \frac{e N_{\text{SCH}} L_{\text{SCH}}}{\tau_n} + N^* D_n^e (J_{\text{drift}}^* + J_{\text{diff}}^*). \quad (2)$$

Here  $L_{\text{SCH}}$  size of a waveguide,  $N_{\text{SCH}}$  — concentration of carriers in a waveguide,  $\tau_n$  — lifetime of minority carriers in waveguide layer determined by all recombination processes,  $D_n^e$  — diffusion constant of minority carriers (electrons) in p-emitter,  $J_{\text{drift}}^*$ ,  $J_{\text{diff}}^*$  dimensionless diffusion and drift components of leakage current density. Evaluating  $\eta_i^{\text{st}}$  values we assumed that quasi-Fermi levels of active region and waveguide — active region boundary vary slowly above the threshold and in SC DHS lasers with “step” like waveguide concentration on the boundary with p-layer calculated in the Boltzmann limit consistently in each of ‘steps’. Total current density can be written as:

$$J = J_{\text{st}} + J_L + J_{\text{th}}. \quad (3)$$

Here  $J_L$  and  $J_{\text{st}}$  leakage and stimulated emission current densities. Threshold current density we obtained from model [7], shown good conformity with experiment [8]. At

evaluation of a leakage in experimental structures the method similar [2] was used. The calculation was carried out with initial values on a generation threshold, up to achievement of the self-consistent solutions.

3. Results and discussion

Essential difference in  $\eta_i^{st}$  for structures of different design (Table 1) can be explained as follows. As was already marked, most essential for leakage currents density is concentration of minority carriers at p-emitter boundary, which is determined mainly by the threshold concentration. The second on importance factor is the accumulation of carriers in a waveguide layer with minimal  $E_g$  above the generation threshold, that is due to finite carriers capture time by quantum wells (QW). Thus the part of the injected carriers does not captured by QWs and contributing in  $N_{SCH}$ , and concentration grows proportionally to total current density and as a result has an effect for intrinsic losses and differential quantum efficiency.

Table 1. Parameters of experimental samples (Type A–C)

Type	$E_{g1}$ (eV)	$E_{g2}$ (eV)	$E_{g3}$ (eV)	$W_1$ ( $\mu\text{m}$ )	$W_2$ ( $\mu\text{m}$ )	$W_3$ ( $\mu\text{m}$ )	$\alpha_i^{\text{exp}}$ ( $\text{cm}^{-1}$ )	$\eta_i^{\text{exp}}$ (%)	$\eta_i^{\text{calc}}$ (%)	$\Gamma_{WG}^{\Sigma}$ (%)	$\Gamma_{ac}$ (%)
A	1.13	—	—	1.0	—	—	4.5	67	73	13	1.03
B	1.24	1.13	1.03	0.86	0.36	0.12	3.6	85	90	16	1.45
C	1.181	0.992	—	0.67	0.23	—	9	95	97	20	2

In our calculation, threshold concentration we find out from a usual threshold relation of optical amplification and losses. The optical confinement factor in active region has appeared differing in almost two times for structures (C) and (A) — 2 and 1% respectively. On the other hand with decreasing waveguide length, confinement factor in cladding layers grows twice. However, the optical confinement factor in active layer — has appeared determining for threshold concentration. Besides the structures with a stage waveguide of a type (B) and (C), because of a “double” barrier waveguide, are characterized almost on the order by smaller values of concentration of minority carriers at boundary with p-emitter, and consequently leakage current density in the emitter drops almost proportionally. Thus: the low threshold concentration in QWs from behind good optical confinement and “steplike” waveguide — is essential decreasing boundary concentration, allow to receive in structure high values of  $\eta_i^{st}$ .

To compare more particular different designs, structure C with highest  $\eta_i^{st}$  value (type 1) and two precisely same structures, but with a “nonstep” wave guide, in which of waveguide region corresponded to  $E_g$  of the first (0,992 eV — type 2) and second (1.18 eV — type 3) structure C waveguides “steps”. Concentrations of minority carriers on p-boundary,  $\eta_i^{st}$  and optical confinement factors in QWs and waveguide were calculated. As has shown, the structure of a type 1 is optimal on a leakage level of above the threshold. (Fig. 2) also is characterized by the maximum  $\eta_i^{st}$  value. Calculating  $\eta_i^{st}$  for experimental structures are given in table 1, and it is in well agreement with experimental data. Difference between calculated and measured  $\eta_i^{st}$  values is due to the additional loss mechanisms, for example such, as warming up of active region, that were not taken into account.

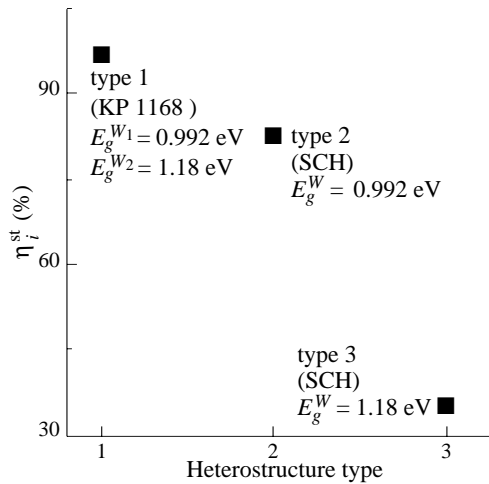


Fig. 2.  $\eta_i^{st}$ , calculated for different structure types.

#### 4. Conclusions

In this work experimentally investigated light-power characteristics of SC DHS lasers with quantum wells in InGaAsP/InP system. The threshold current densities and  $\eta_i^{st}$  were carried out for investigated structures. Maximum value of  $\eta_i^{st}$  was achieved in structure with the lowest concentration of minority carriers at boundary with p-emitter due to a double “step” waveguide and low threshold concentration. Evaluated values of  $\eta_i^{st}$  for experimental samples appears to be in good agreement with received experimental data.

#### References

- [1] A. U. Leshko, A. V. Lutezkii, N. A. Pikhtin, Z. N. Sokolova, G. V. Skrynnikov, I. S. Tarasov and N. V. Fetisova, *FTP* **34**, 7 (2000).
- [2] D. Z. Garbuzov, A. V. Ovchinnikov, N. A. Pikhtin, Z. N. Sokolova, I. S. Tarasov and V. B. Khalfin, *FTP* **25**, 5 (1991).
- [3] E. G. Golikova, *et al*, *Techn. Phys. Lett.* **26**, 913 (2000).
- [4] H. C. Casey and M. B. Panish, *Heterostructures lasers*, Academic press 1978.
- [5] L. A. Coldren and S. W. Corzine, *Diode Lasers and Photonic Integrated Circuits* Wiley Publication, New York, 1995.
- [6] H. Hirayama, J. Yoshida, Y. Miyake and M. Asada, *Appl. Phys. Lett.* **61**, 20 (1992).
- [7] L. V. Asryan, N. A. Gun'ko, A. S. Polkovnikov, G. G. Zegrya, R. A. Suris, Pey-Kee Lay and T. Makino, *Semicond. Sci. Technol.* **15**, (2000).
- [8] G. G. Zegrya, N. A. Pikhtin, G. V. Skrynnikov, S. O. Slypchenko and I. S. Tarasov, *FTP* **35**, 8 (2001).

## The use of nanostructure-cluster-based ion-implantation-induced saturable absorbers in multisection high-power 1.5- $\mu\text{m}$ picosecond laser diodes

G. B. Venus<sup>†</sup>, A. Gubenko<sup>†</sup>, E. L. Portnoi<sup>‡</sup>, E. A. Avrutin<sup>‡</sup>, J. Frahm<sup>§</sup>,  
J. Kubler<sup>§</sup> and S. Schelhase<sup>§</sup>

<sup>†</sup> Ioffe Physico-Technical Institute, St Petersburg, Russia

<sup>‡</sup> Dept. of Electronics, University of York, York YO10 5DD, England

<sup>§</sup> Advanced Photonic Systems GmbH, 12489 Berlin, Germany

**Abstract.** We report short (30–35 ps), high energy (more than 100 pJ) optical pulses at 1.5  $\mu\text{m}$  from Q-switched laser diodes with multisection implantation-induced saturable absorbers. Dramatic improvement in pulse parameters over tandem lasers is due to suppression of spatial hole-burning and amplified spontaneous emission.

### Introduction

The energy of picosecond pulses emitted by single-mode stripe Q-switched and gain-switched laser diodes typically does not exceed 10 pJ. To obtain high-brightness picosecond pulses with energies as high as 50 pJ, more complex tapered constructions [1, 2] have been used. Here, we demonstrate generation of high-energy picosecond pulses by a non-tapered, single-lobe laser by using ion-implantation induced saturable absorbers. Such absorbers are known to combine large volume (bulk rather than quantum-well materials) and short response time (down to single picoseconds) with good optical quality (low unsaturable loss) [3–7]. This unique performance, utilised in a number of ultrafast optical devices [3–7], has been attributed to structural transformation in the ion-implanted material. This involves nanostructure clusters being formed along the tracks of implantation ions; these clusters then provide fast recombination channels, whilst the undamaged bulk of the material accounts for high optical quality. An additional advantage of ion implantation for absorber formation is that, when performed from the top surface rather than facet of the laser structure [4], it allows an absorber to be fabricated in the form of multiple sections with a well-controlled length down to single microns. As shown below, this is crucial for the present work.

### 1. Fabrication

To create the 1.5- $\mu\text{m}$  single-lobed Q-switched picosecond lasers with pulse energies over 50 pJ, we used a simple InGaAsP/InP double heterostructure with a 0.25  $\mu\text{m}$  thick active layer. This choice of active layer thickness was a compromise between the capacity for storing large carrier densities in the active layer and preserving single transverse mode operation. Surface implantation by Ar ions of an energy of 3.1 MeV using a 7  $\mu\text{m}$  thick photoresist layer as the protective mask enabled us to fabricate absorber sections of a length down to 3–5  $\mu\text{m}$ .



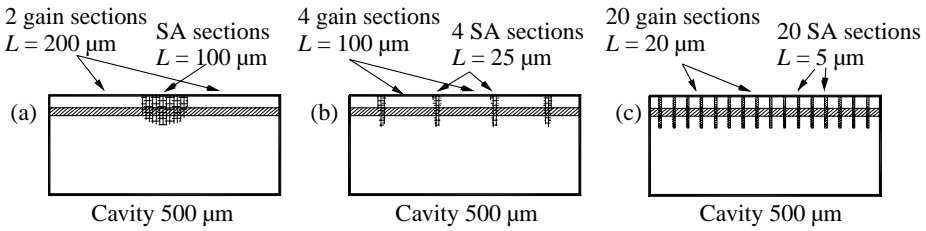


**Fig. 1.** Schematic of the longitudinal distributions of the implantation-induced saturable absorber in the lasers with: (a) single-section geometry, (b) four-section geometry, (c) multiple-section geometry.

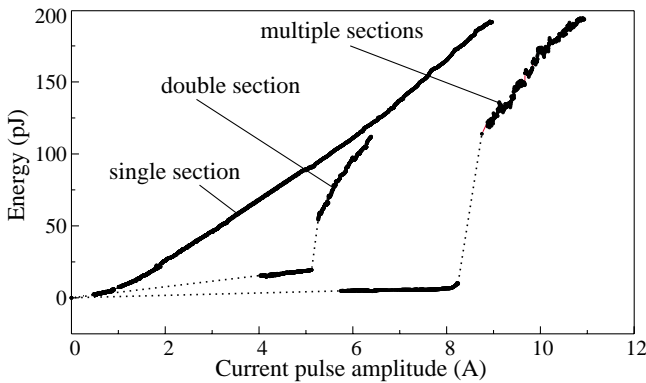


**Fig. 2.** Typical light-current characteristics for lasers with different absorber geometries, under pulsed (3 ns) pumping.

## 2. Experimental

In the experiments, we studied gain-guided lasers with a stripe width of 10  $\mu\text{m}$ . Saturable absorber sections were located symmetrically in the laser cavity, and their number was varied from one to 20 (Fig. 1). The laser was pumped by current pulses of 3 ns FWHM. Figure 2 shows the light-current characteristics of the 500  $\mu\text{m}$  long implanted lasers, with the total volume fraction of the absorber fixed at 20% and different absorber geometry.

The light-current curves for lasers with several absorber sections clearly display a characteristic kink which is the signature of the saturable absorber action and corresponds to a single pulse generation. For lasers with a single, lumped absorber, no pronounced Q-switching was observed in the entire range of currents studied. The variation in the (first) pulse energy with the number of absorber sections is shown in Fig. 3 (note that the background in the pulse energy seen at currents below the kink was attributed to amplified spontaneous emission and so was subtracted from the pulse energy). Pulse energies in excess of 100 pJ were measured for some samples with multiple absorber sections. Auto-correlation measurements give the pulse width of 30–35 ps for a 500  $\mu\text{m}$  long laser with 20 absorber sections. The lateral far field of such lasers has a half width of  $\sim 9\text{--}10.5^\circ$ , which implies a pulse power of 3–5 W in a single lobe.

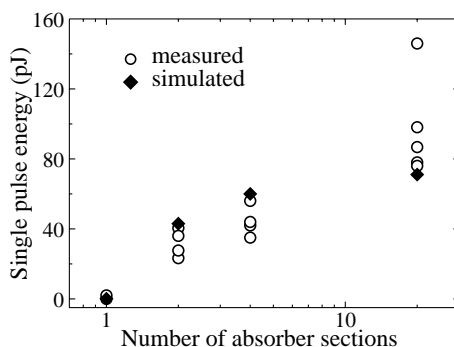


Fig. 3. Single optical pulse energy for lasers with different numbers of absorber sections.

### 3. Modelling and discussion

We used the distributed time-domain model developed earlier [8] to simulate the behaviour of the laser. The numerical parameters used (absorber cross-section  $2 \times 10^{-15} \text{ cm}^{-2}$ , relaxation time  $\sim 100 \text{ ps}$ ) reflect the unique properties of the bulk, nanostructure-cluster-based saturable absorber.

Qualitatively, the variation in the laser characteristics with the varying absorber geometry may be explained as follows. In lasers with few, and particularly single (Fig. 1(a)), absorber sections, the large absorber section length and the strong absorption in the unsaturated nanostructure absorber lead to most of the light incident on the absorber being absorbed in the outer parts of the section, leaving the inner part not saturated (Fig. 4(a)). Conversely, in the long gain sections, the photon density builds up in the regions adjacent to the absorber, causing preferential carrier, and hence gain, depletion in these regions, which in turn contributes to the decrease in the light intensity seen by the absorber. This spatially selective gain and absorption saturation (spatial hole-burning) precludes Q-switching in a single-absorber laser. An additional pulse-suppressing effect is the spontaneous emission which, in the large gain sections with high gain, can be amplified to levels significant enough to contribute to the depletion of carrier density (simulations confirm that there is no lasing at currents below the onset of the first pulse, so the measured background light energy is indeed a sign of strong amplified spontaneous emission).

The increase in the number of absorbers, and the associated decrease in the length of the individual absorber and gain sections, makes the longitudinal light profile increasingly more homogeneous. The detrimental effect of the spatial hole-burning is thus decreased until, with 20 absorbers, it is nearly totally suppressed (Fig. 4(b)).

The increase in the calculated single pulse power (shown as filled diamonds in Fig. 3) with the number of sections is in good agreement with the measurements.

Further simulations imply that, apart from increasing the power of the emitted pulses, the distributed geometry combined with the fast recombination and high differential absorption offered by the nanostructure-based absorber, may also allow to improve other parameters. For example, it may be possible to bring the repetition frequency of the self-pulsations up to the values (tens of GHz) of interest in high-bit-rate optical communications.

Further experimental and theoretical work is in progress; results will be presented at the meeting.

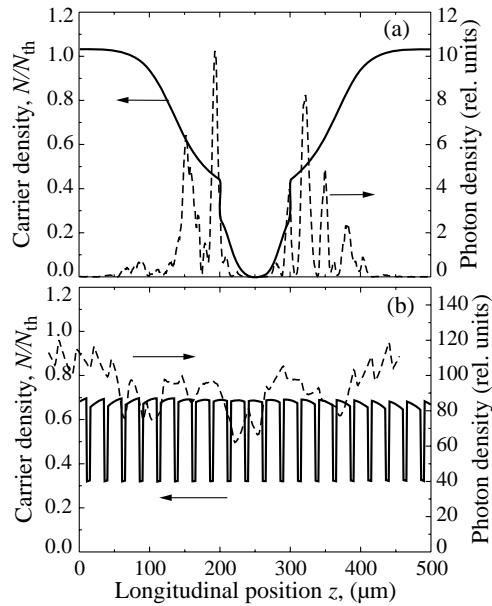


**Fig. 4.** Simulated spatial distribution of carrier density (solid lines) and photon density (dashed lines) along the cavity of a laser with a single saturable absorber (a) and a multisection saturable absorber at the time near the peak of the light pulse (b). Note the considerable spatial hole burning (inhomogeneous gain and absorption saturation) in the former case. The irregular substructure in the photon density profile is due to the multimode nature of laser emission.

## References

- [1] B. Zhu, *IEEE Photon. Technol. Lett.* **8** 503 (1996).
- [2] S. Yang, *IEEE Photon. Technol. Lett.* **9** 337 (1997).
- [3] E. Portnoi, *J. Select. Topics Quantum Electron.* **2** 256 (1997).
- [4] G. Venus, *Tech. Phys. Lett.* **25** 506 (1999).
- [5] G. Venus, *Proc. of ISLC'2000, IEEE* (2000).
- [6] Z. Bakonyi, *IEEE Photon. Technol. Lett.* **12** 570 (2000).
- [7] J. Mangeney, *Appl. Phys. Lett.* **79** 2722 (2001).
- [8] E. Avrutin, *IEE Proc. Optoelectron.* **147** 251 (2000).

## Self-focused distributed Bragg reflector QW laser diodes

D. A. Yanson<sup>†</sup>, E. U. Rafailov<sup>‡</sup>, G. S. Sokolovskii<sup>§</sup>, V. I. Kuchinskii<sup>§</sup>,  
A. C. Bryce<sup>†</sup>, J. H. Marsh<sup>†</sup> and W. Sibbett<sup>‡</sup>

<sup>†</sup> Dept. of Electronics & Electrical Engineering, University of Glasgow,  
Glasgow G12 8LT, UK

<sup>‡</sup> School of Physics & Astronomy, University of St Andrews,  
St. Andrews KY16 9SS, UK

<sup>§</sup> Ioffe Physico-Technical Institute, St Petersburg, Russia

**Abstract.** We report the first realisation of novel tapered DBR laser diodes incorporating curved gratings. The devices exhibited single-longitudinal mode operation with a side-mode suppression ratio of over 30 dB and a laterally focused beam for focal lengths around 0.5 mm. These laser sources will be suitable for applications requiring both spectrally and spatially enhanced beam quality.

### Introduction

Good quality beams are a critical requirement in many applications for high-power semiconductor lasers, such as optical computing, medicine and optical pumps for lasers/amplifiers or nonlinear crystals in frequency conversion. For these applications, a range of output characteristics that include high CW/average power and good spectral/spatial quality, is often required. Novel DBR and DFB semiconductor lasers incorporating “curved-groove” diffraction gratings afford improved control over the divergence and spectrum of the emitted light.

In theoretical studies [1, 2], novel curved-groove DFB lasers (c-DFB) were proposed, and their spatial and spectral beam characteristics were shown to be superior to those of angled-grating ( $\alpha$ -DFB) lasers. Curved-groove diffraction gratings have already been used for the enhancement of reflection from the distributed Bragg reflector of a DBR laser [3]. Here, we report the first fabricated prototype devices in a curved-groove DBR (c-DBR) configuration and demonstrate their single-mode and self-focussing operation.

The schematic of a c-DBR laser is illustrated in Fig. 1(a). The c-DBR/DFB configuration has the potential to combine the high-power capability of a broad-stripe device with the transverse mode and spectral control provided by an appropriately designed curved grating. The confocal device geometry causes the output emission in the plane of the p-n junction to be focussed at a focal point defined by the grating curvature.

### 1. Device fabrication

The c-DBR lasers were fabricated from a GaAs/AlGaAs double quantum well structure operating at a wavelength of 860 nm. The device shown in Fig. 1(a) consists of a central gain section and two passive c-DBR stacks, with individual bias control enabling the fine-tuning of the grating phase. A tapered design of the stripe contact of the cDBR laser is used to preserve the cylindrical symmetry of the device, the taper dimensions and grating curvature being a function of the design focal length. The total device length was 1.5 mm, with the each section about a third of the total length. A range of c-DBR devices were

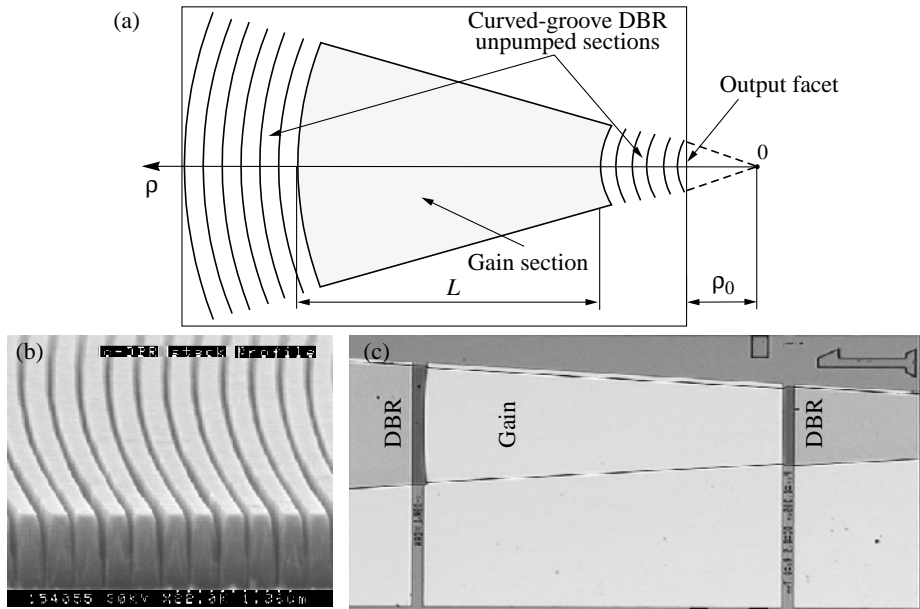


**Fig. 1.** (a) Schematic of c-DBR laser. (b) SEM photograph of a c-DBR mirror. (c) Plan view of a fabricated device.

fabricated, all with an output aperture of  $100\text{ }\mu\text{m}$  but focal lengths varying from  $0.2\text{ mm}$  to infinity (straight grating).

The third-order ( $385\text{ nm}$  period) c-DBR gratings were defined by e-beam lithography and dry-etched  $0.6\text{ }\mu\text{m}$  deep (estimated coupling strength  $\kappa = 17.5\text{ cm}^{-1}$ ). An SEM photograph of the fabricated cDBR stack is shown in Fig. 1(b), and an optical microscope image of the complete device is included as Fig. 1(c).

**2. Measurement and results**

The devices exhibited a threshold current of  $\sim 1.1\text{ A}$  as shown in Fig. 2(a), which is similar to that of identical devices but without a grating. The thresholds were high because only a third of the device was being pumped, and the two passive cDBR sections suffered a high absorption loss. A typical optical spectrum of a c-DBR laser presented in Fig. 2(b) implies single-mode lasing output with a side mode suppression in excess of  $30\text{ dB}$ .

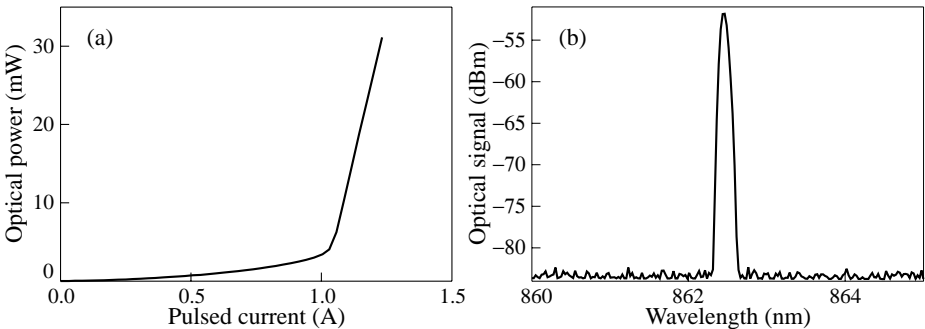


**Fig. 2.** A typical L–I curve (a) and optical spectrum (b) of a c-DBR laser.

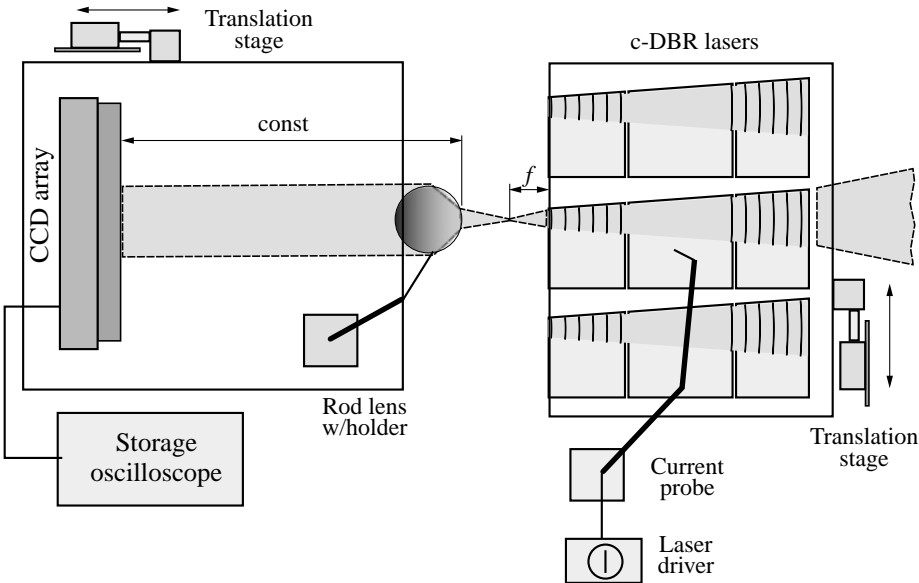


**Fig. 3.** Plan view of the experimental set-up used to measure near-field patterns and focal lengths (not to scale).

Near-field studies were performed using a high-NA rod lens mounted vertically on a micropositioner-controlled translation stage complete with a linear CCD array, which provided an image of the field distribution via a storage oscilloscope. Our experimental set-up is illustrated in Fig. 3. The distance from the lens to the CCD array was kept constant so that the optical magnification of the system also remained constant. The c-DBR devices themselves were also mounted on a lateral translation stage, which allowed the relative change in focal length to be measured when comparing adjacent devices with different gratings but all having a constant front facet width of  $100\text{ }\mu\text{m}$ .

Whilst the c-DBR devices typically had the same or wider near-field images than straight-grating DBRs (both of which showed some evidence of filamentation), there was a strong correlation between the design focal length of the grating and the lens position relative to the facet at which the sharpest (narrowest) spot in the plane p-n-junction was obtained. This relationship holds for devices with focal lengths under  $500\text{ }\mu\text{m}$ , as can be seen in Fig. 4(a). Here, the expected focal lengths (triangles) for four grating types of

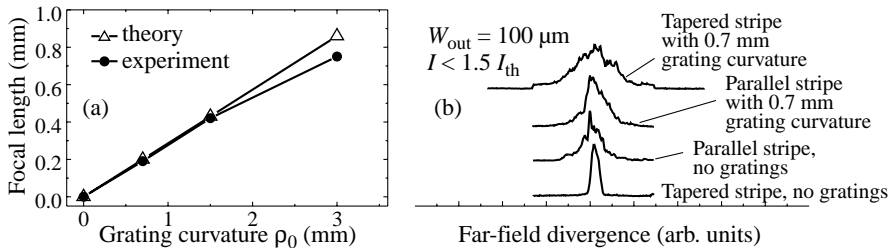


**Fig. 4.** (a) Comparison of expected and measured focal lengths as a function of the grating curvature; (b) Far-field distributions from devices with different stripe types for a fixed output aperture of  $100\text{ }\mu\text{m}$ .

varying curvature (zero focal length denoting a straight, non-focussing grating) are plotted alongside their measured focal lengths (circles).

We did not observe any position dependence in the near-fields of identical taper devices not having a grating. This fact is confirmed by Fig. 4(b), which shows the angular far-field distributions measured from lasers of different stripe geometries with and without a grating, all having a 100  $\mu\text{m}$  wide front facet. We believe that the broader far-field pattern from devices incorporating a curved grating (top two curves, focal length 200  $\mu\text{m}$ ) is due to the output beam diverging rapidly beyond the focal point located near the facet, as expected.

## Conclusions

We have reported the successful realisation of the type of a curved-grating DBR laser that was previously proposed theoretically [1]. Single-frequency generation was observed with a side-mode suppression ratio of over 30 dB and near- and far-field measurements confirmed our prediction for lateral beam focussing. Future studies will concentrate on near-field investigations and improved devices with non-absorbing c-DBR mirrors, which will be achieved using the quantum well intermixing technique. High-power operation in CW and Q-switched regimes will then be investigated.

## References

- [1] G. S. Sokolovskii, E. U. Rafailov, D. J. L. Birkin and W. Sibbett, *J. Opt. Quant. Electron.* **31**, 215–221 (1999).
- [2] G. S. Sokolovskii, E. U. Rafailov, D. J. L. Birkin and W. Sibbett, *IEEE J. Quantum Electron.* **36**, 1412–1420 (2000).
- [3] M. Uemukai, A. Yoshimoto, N. Matsumoto, T. Suhara, H. Nishihara, N. Eriksson and A. Larson, *Electron. Lett.* **33**, 1464–1465 (1997).

## Er-doped SiO<sub>2</sub> with silicon nanocrystals as a new active optical medium

*I. N. Yassievich, M. S. Bresler, O. B. Gusev and A. S. Moskalenko*

*Ioffe Physico-Technical Institute, St Petersburg, Russia*

**Abstract.** Properties of a new active optical medium, Er-doped SiO<sub>2</sub> with silicon nanocrystals, are discussed. We have considered in detail the mechanism of excitation of erbium ions by quantum confined electron-hole pairs in silicon nanocrystals, the diffusion of excitation over the erbium ions inserted into the silicon dioxide matrix and the lifetime of erbium in the excited state limited by de-excitation centers (traps, "black holes") in SiO<sub>2</sub>.

### 1. Introduction

Optical amplifiers currently used in transmission lines are based on erbium-doped silica glass (SiO<sub>2</sub>:Er). Optical amplification in these systems is achieved by pumping of the second excited state of the erbium ion followed by fast nonradiative relaxation to the first excited state (metastable state) resulting in population inversion and stimulated emission on the wavelength 1.54  $\mu\text{m}$ . Since rare earth ions have well-defined energy levels only slightly depending on the nature of the matrix, the pumping light should be in a resonance with the transition in the f-shell and therefore the pumping is done by semiconductor lasers. Besides, the pumping power should be sufficiently high, since the absorption coefficient of erbium is small. This results from the intrashell optical transition being strictly forbidden if no account is taken of the admixture from the upper states. It should be noted that Er<sup>3+</sup> ions in a dielectric matrix have fairly long lifetime in the first excited <sup>4</sup>I<sub>13/2</sub> state indicating very weak nonradiative de-excitation.

Recently erbium doped silicon attracted the attention of investigators with the aim to apply it to integrated silicon-based optoelectronic devices [1-3]. The advantage of erbium-doped silicon consists in a possibility to increase significantly effective cross section of excitation of rare earth ions [4]. This enhancement is due to a strong band-to-band absorption of the pumping light in a wide spectral range followed by an Auger process in which electron-hole pairs recombine with the transfer of energy to the f-shell of an erbium ion. The excess energy is taken away by free electrons or phonons.

However, erbium luminescence in a matrix of crystalline silicon is characterized by strong temperature quenching and can be hardly observed above 200 K. Temperature quenching in silicon is caused by de-excitation of erbium resulting from reverse Auger process accompanied by back transfer of energy which is activated by the temperature. Therefore, the optical medium favorable for excitation of rare earth ions occurs to be of insufficient quality as concerns the emission process.

In the last years a new type of optical medium was proposed which combines the advantages of rare earth doped dielectric and rare earth doped semiconductor: a heterogeneous system in which silicon nanocrystals are dispersed in a SiO<sub>2</sub> matrix [5]. The main idea of this innovation is to separate in space the regions of efficient excitation (Er-doped silicon) and emission (Er-doped silicon dioxide). It was shown experimentally that this new optical medium demonstrates strong erbium luminescence up to room temperature as expected, therefore the transfer of excitation from nanoparticles to erbium in a dielectric



matrix presumably really occurs. Though a lot of experimental results is already obtained for this important optical medium the excitation mechanism of erbium ions and transport of excitation over the dielectric matrix are understood mostly qualitatively.

In this work we present theoretical considerations of the mechanisms involved. The following topics are discussed: (i) the probability of excitation of erbium ions in silicon nanocrystals with a proper account of quantum confinement of electrons and holes (or/and excitons) for erbium transition to the second (1.24 eV) excited state from which nonradiative transition to the first excited metastable state (0.81 eV) occurs; (ii) special features of excitation processes when erbium ion is located inside the silicon nanocrystal or on its surface (the possible role of the surface electric field will be underlined); (iii) transfer of excitation between erbium ions (resonant and non-resonant mechanisms) including the case when the excitation is transmitted across the boundary between the nanocrystal and the SiO<sub>2</sub> matrix; (iv) diffusion of excitation over the dielectric matrix and nonradiative channels of erbium de-excitation.

## 2. Optical excitation of Er<sup>+3</sup> ion located in Si nanocrystal

Silicon nanocrystals with a size of 2–4 nm strongly absorb the light. Due to the effect of quantum confinement the exciton energy in nanocrystals becomes higher than the energy of the second excited state of erbium <sup>4</sup>I<sub>11/2</sub> (1.24 eV) and the selection rules for absorption are also modified increasing the absorption by nanocrystals. Later the exciton energy is efficiently transferred to erbium ions in an Auger process, the excess energy being wasted by multiphonon interaction.

Our calculations demonstrate a strong dependence of the probability of erbium excitation on the location of the ions inside nanocrystals. It can be shown that de-excitation of erbium in the nanocrystal is suppressed if the exciton energy sufficiently exceeds that of the second excited state of erbium, since in this case the back transfer process demands large activation energy. In fact, the experimental data [5, 6] show a broad band centered at ~ 0.8 μm caused by exciton emission from nanocrystals and erbium luminescence from the second excited state <sup>4</sup>I<sub>11/2</sub> at 1.0 μm and the first excited state <sup>4</sup>I<sub>13/2</sub> at 1.54 μm. This result demonstrates that excitation of erbium ions occurs to the second excited state and the reverse (de-excitation) process demands activation with a significant threshold.

The observation of <sup>4</sup>I<sub>13/2</sub> → <sup>4</sup>I<sub>15/2</sub> spectrum with the lineshape of erbium emission characteristic of dielectric matrix confirms the idea that excitation produced via silicon nanocrystals propagates thereafter among the ions inserted in silicon dioxide. Therefore we need to consider the process of excitation transfer in SiO<sub>2</sub>:Er.

## 3. Transport of excitation through Erbium ions

We have studied transport of excitation in the silicon dioxide matrix over erbium ions for resonant situation both for coherent and non-coherent transfer. The coherent transfer (proposed firstly by Davydov) is due to quantum beats between two adjacent erbium ions with strictly coinciding energies of the ground and excited states. The non-coherent transfer (the so-called Foerster mechanism) involves the ions with inhomogeneously broadened energy levels and depends on the overlap of the lineshapes of two interacting ions.

It should be stressed that in the system considered (erbium ions in a dielectric), the energy levels of the ion are broadened inhomogeneously by local fluctuations of the crystal field, and the condition of strict resonance is fulfilled only for a fairly small part of the total concentration satisfying the condition  $\delta E \leq W$ , where  $\delta E$  is the energy width in some distribution,  $W$  is the dipole-dipole interaction energy in the coherent (quantum beat)

approximation. For inhomogeneously broadened spectrum with a linewidth  $D_E$  only the fraction  $W/D_E$  of the total concentration of rare earth ions satisfies the condition of a strict resonance. This condition imposes limitation of the concentration of the “resonant” ions and, consequently, on the average distance between them  $\bar{r}$ .

Therefore, the Davydov case predominates quantum mechanically (the probability transition between two ions is proportional to  $r^{-3}$  for dipole-dipole interaction instead of  $r^{-6}$ ) but is less important statistically in the case of inhomogeneously broadened energy states. The competition of both mechanisms is actually resolved by an experiment.

We have calculated the time of excitation transfer between two adjacent erbium ions in a silicon dioxide matrix for the Davydov mechanism

$$t_{tr} = \frac{2\pi\kappa E_{n0}^3 \tau R^3}{3c^3 \hbar^3}$$

where  $R$  is the distance between the ions satisfying the condition of a strict resonance,  $\kappa$  is the dielectric constant of the medium,  $\tau$  is the lifetime of the isolated ion in the first excited state,  $E_{n0}$  is the energy of the excitation state,  $c$  is the velocity of light (in the medium).

Once coming out of the nanocrystal, the excitation will propagate over erbium ions in the dielectric matrix. We have calculated the diffusion coefficient for propagation of excitation by Davydov mechanism. The result is

$$D = \frac{1}{2} \frac{\bar{r}^2}{t_{tr}} = \frac{3c^3 \hbar^3}{2\pi\kappa E_{n0}^3 \tau} \left( \frac{4\pi \tilde{N}_{Er}}{3} \right)^{1/3},$$

where  $\tilde{N}_{Er}$  is the concentration of erbium ions being in a strict resonance. Note that  $\tilde{N}_{Er}$  can be significantly less than  $N_{Er}$ , the total erbium concentration.

For the Foerster mechanism

$$D = \frac{8}{3} \left( \frac{4\pi}{3} \right)^{1/3} C N_{Er}^{4/3},$$

where  $C$  is a constant, in agreement with our previous statement that statistically the Foerster mechanism is more favorable while the matrix element of the transition is higher for the Davydov case.

The lifetime of excitation in a dielectric for an isolated ion is  $\tau$  and will remain so if there are no additional sources of de-excitation. However, the experiment points to the existence of special traps (“black holes”) which kill the excitation after it reaches the interaction radius of the “black hole”  $r_0$ . Therefore the lifetime of excitation in a dielectric matrix with the account of its diffusion is

$$\tau_{eff} = (4\pi D r_0 N_{Tr})^{-1},$$

where  $N_{Tr}$  is concentration of traps. The dependence of the lifetime on the concentration of erbium ions  $N_{Er}$  can be presented in the form

$$\frac{1}{\tau_{de}} = \frac{1}{\tau_0} + \alpha N_{Er}^{1/3} N_{Tr}.$$

For the Foerster mechanism we arrive at another type of dependence on  $N_{Er}$ :

$$\frac{1}{\tau_{de}} = \frac{1}{\tau_0} + \beta N_{Er} N_{Tr}.$$

Luminescence will come predominantly from erbium ions in a dielectric while excitation occurs mostly in nanocrystals. Connection with the experimental results will be considered.

#### 4. Conclusion

Erbium doped  $\text{SiO}_2$  with silicon nanocrystals is a new active optical medium with ever-growing use. The Auger excitation of erbium ions by electron-hole pairs confined in silicon nanocrystals and the mechanism of excitation diffusion in the silicon dioxide matrix has been studied theoretically.

#### Acknowledgements

This work was partially supported from NWO grant 047.009.013, and grants of Russian Foundation of Basic Research, Russian Ministry of Science and Technology, the Program “Quantum Low Dimensional Structures” of the Ministry of Science and the Program “Low Dimensional Nanostructures” of the Presidium of RAS.

#### References

- [1] *Rare Earth Doped Semiconductors I*, Eds. G. S. Pomrenke, P. B. Klein and D. W. Langer, MRS, Pittsburgh, Vol. 301, 1993.
- [2] *Rare Earth Doped Semiconductors II*, Eds. S. Coffa, A. Polman and R. N. Schwartz, MRS, Pittsburgh, Vol. 422, 1996.
- [3] *Rare Earth Doped Semiconductors III*, Eds. J. M. Zavada, T. Gregorkiewicz and A. J. Steckl, EMRS, Amsterdam, 2001.
- [4] O. B. Gusev, M. S. Bresler, P. E. Pak, I. N. Yassievich, M. Forcales, N. Q. Vinh and T. Gregorkiewicz, *Phys. Rev B* **64**, 075302 (2001).
- [5] G. Franzo, V. Vinciguerra and F. Priolo, *Appl. Phys. A* **69**, 3 (2001).
- [6] P. G. Kik, M. L. Brongersma and A. Polman, *Appl. Phys. Lett.* **76**, 17 2325 (2000).

## Influence of intraband relaxation processes on threshold and power-current characteristics of quantum well lasers

G. G. Zegrya, I. A. Kostko, N. A. Gunko and E. B. Dogonkin  
Ioffe Physico-Technical Institute, St Petersburg, Russia

**Abstract.** The effect of carrier-carrier relaxation on threshold and power-current characteristics of InAs and GaAs quantum well (QW) lasers is studied. Dependence of carrier relaxation time on temperature and carrier density is considered. It is shown that in this case the gain coefficient becomes a more pronounced function of temperature and carrier density, and threshold current density increases drastically.

### Introduction

The intraband carrier relaxation determines the recombination processes both in bulk and QW semiconductor lasers [1]. Particularly, role of relaxation processes increases at higher carrier density. In this paper we show that the characteristic time of intraband relaxation considerably depends on temperature, carrier density, and parameters of a quantum well structure. Taking these dependencies into account we analyze the threshold characteristics of InAs (2.82  $\mu\text{m}$ ) and GaAs (0.81  $\mu\text{m}$ ) QW lasers. We show that in this case the threshold current density increases drastically (particularly for InAs) comparing to the case  $\tau = \infty$ .

We derive the gain and recombination rates using conventional technique of temperature Green functions [2]. We calculated wave functions taking into account a complex structure of the valence band, and Green functions for electrons and holes are assumed to be off-diagonal matrices, which gives more sophisticated analytical expressions for the relaxation times than that in [3]. The formulas for energy spectra and wave functions in a QW are given in [4]. Then, using the linear response approximations, the rates of stimulated radiative recombination are derived. Using the formula for the rate of stimulated radiative recombination, the single-well gain coefficient can be derived.

We have shown that the hole-hole relaxation is a dominant process in quantum wells at the laser threshold. In this case the spectral function is related to the imaginary part of a heavy-hole proper self-energy. The most important contribution to the imaginary part of the self-energy  $\Gamma(q, E)$  due to carrier-carrier scattering comes from ring diagrams [2]. We calculated  $\Gamma(q, E)$  using the complex structure of heavy holes. Dielectric constant in  $\Gamma(q, E)$  is calculated in a so-called random-phase approximation [2].

The role of carrier-carrier scattering increases with carrier density and temperature increase.

### 1. Results and discussion

Figure 1(a) shows temperature dependence of intraband relaxation time at  $T = 300$  K in InAs 10 nm QW structure. Calculation results for two different carrier densities are present. Intraband relaxation time dependence on temperature in InAs QW structure has non-linear form. At lower carrier density ( $n = 2 \times 10^{11} \text{ cm}^{-2}$ )  $\tau_{\text{hh}}$  decreases drastically in the temperature range 50...150 K and has minimum at  $T \sim 250\text{K}$ . For higher carrier

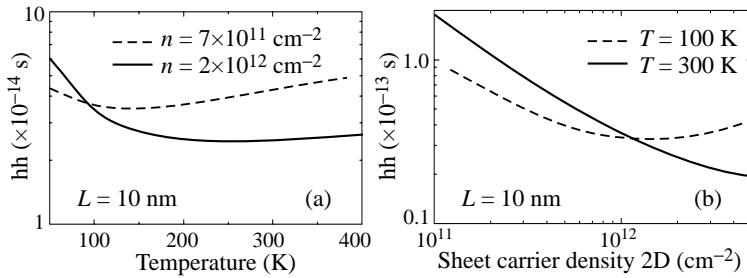


**Fig. 1.** Dependence of intraband relaxation time on temperature (a) and sheet carrier density (b) for InAs 10 nm QW structure.

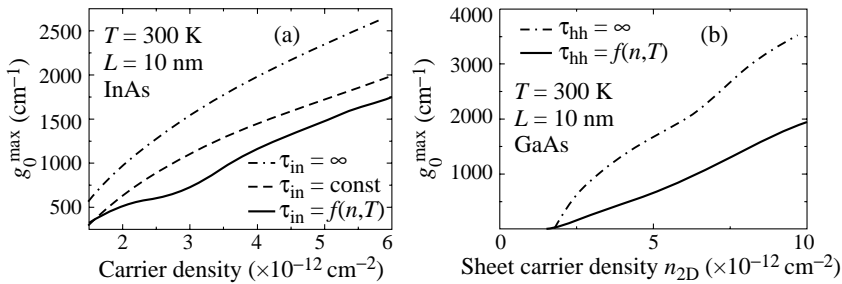


**Fig. 2.** Carrier density dependence of gain coefficient in (a) InAs and (b) GaAs 10nm QW structure at  $T = 300 \text{ K}$ .

density ( $n = 7 \times 10^{11} \text{ cm}^{-2}$ ) value of  $\tau_{hh}$  increases, dependence on temperature becomes weaker, and minimum of intraband relaxation is at  $T \sim 130 \text{ K}$ .

The dependence of intraband relaxation time on carrier density at  $T = 300 \text{ K}$  is presented in Fig. 1(b) for InAs. It is clear that at higher temperature the dependence  $\tau_{hh}(n_{2D})$  changes and becomes more non-linear.

Further in this paper we compare two methods of calculation of QW laser characteristics: (i) neglecting the carrier intraband relaxation ( $\tau_{hh} = \infty$ , dash-dot lines in Figs. 2–4) and (ii) taking into account the dependence of relaxation time on temperature, carrier density, and QW structure parameters ( $\tau_{hh} = f(n, T)$ , solid lines in Figs. 2–4).

We have analyzed the laser gain coefficient taking into account temperature dependence of the self-energy. We have shown that in this model the gain coefficient depends stronger on temperature and carrier density.

Effect of intraband relaxation processes on gain coefficient vs. carrier density in (a) InAs and (b) GaAs QW laser structure is shown in Fig. 2. Dashed curve is calculated using approximation of intraband relaxation with constant. It is clear from Fig. 2 that intraband relaxation processes affect gain dependence on sheet carrier density and gain slope, decreasing the value of  $g_0^{\text{max}}$  and decreasing the slope of the curve  $g_0^{\text{max}}(n_{2D})$ . The approximation of constant time of intraband relaxation processes is not valid and it is necessary to take into account dependencies of intraband relaxation time on temperature and carrier density.

Temperature dependence of gain coefficient is shown in Fig. 3(a). Value of maximum gain is reduced twice if intraband relaxation time is taken into account. Our analysis has shown that for the case  $\tau_{hh} = f(n, T)$ , which is usually observed experimentally, the gain

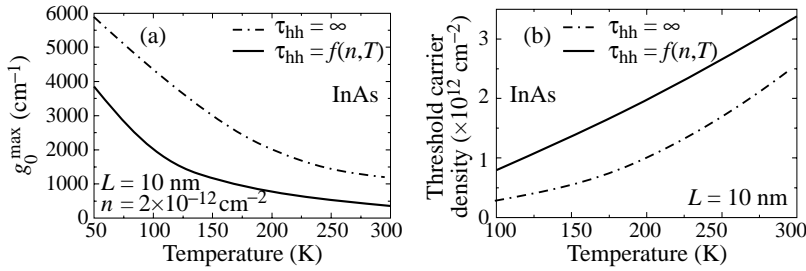


**Fig. 3.** Temperature dependence of (a) gain coefficient and (b) threshold carrier density in InAs QW structure.

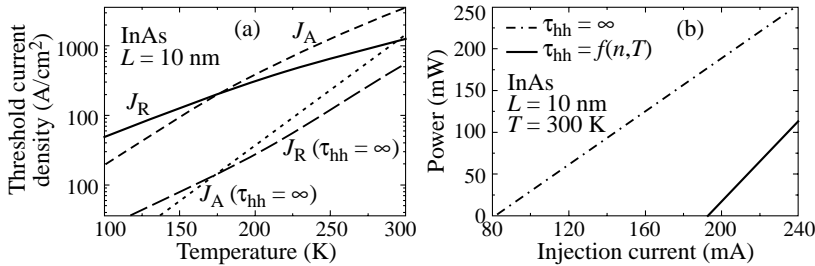


**Fig. 4.** (a) Threshold current dependence on temperature and (b) output power density vs. current density in InAs 10 nm QW structure.

coefficient is a non-linear function of the carrier density and is less than that for the case  $\tau_{hh} = \infty$ . Substituting the gain coefficient for the last case into the threshold oscillating condition  $\Gamma \cdot g(\omega) = \alpha$ , where  $\Gamma$  is the optical confinement factor,  $\alpha$  are the losses, we derive that the threshold carrier density  $n_{th}$  is higher than that for the cases  $\tau_{hh} = \infty$ . Moreover, the gain coefficient decreases with temperature increase faster than in the case of  $\tau_{hh} = \infty$ . As a result, the threshold carrier density  $n_{th}$  has more pronounced, non-linear dependence on temperature (see Fig. 3(b), solid line). This results in an increase of the threshold current and decrease of the characteristic temperature  $T_0$ . Therefore, QW laser threshold current increase at high temperatures is a result of the acceleration of hole-hole relaxation processes.

Dependence of threshold current density on temperature is presented in Fig. 4(a). Here  $j^{th} = j_R^{th} + j_A^{th}$ , where  $j_R^{th}$  is radiative current density at the threshold, and  $j_A^{th}$  is Auger current density at the threshold. The value of the threshold current increases considerably if intraband relaxation processes are taken into account. This results in changes of output power–current characteristics of the InAs and GaAs QW laser. Dependence of power density on current density at  $T = 300$  K is shown in Fig. 4(b). Proper description of intraband relaxation time drastically increases threshold current (2 kA/cm<sup>2</sup> to 4.8 kA/cm<sup>2</sup>) and limits the output power of the InAs QW laser. Our calculations have revealed that the threshold current density in GaAs QW 10 nm laser also increases twice (0.11 kA/cm<sup>2</sup> to 0.23 kA/cm<sup>2</sup>) due to intraband relaxation.

In conclusion, the analysis of influence of intraband relaxation processes on threshold characteristics of semiconductor QW lasers is performed in the paper. Our model accurately describes the dependence of threshold characteristics on temperature. In order to design

the QW lasers with high temperature stability, it is important to weaken the role of the relaxation processes. This can be achieved by optimization of a laser structure. We have shown that influence of intraband relaxation processes on threshold characteristics is more significant in long-wavelength (InAs) semiconductor QW structure comparing to the short-wavelength (GaAs) QW structure. In order to suppress intraband relaxation processes,  $n_{th}$  should be reduced. This can be achieved by optimization of number of quantum wells in the laser structure.

#### *Acknowledgments*

This work was supported by the grants RFBR 01-07-90299, 01-07-90300, Russian Scientific Programs 00-15-96812, and “Physics of Solid State Nanostructures” 97-0003.

#### **References**

- [1] M. Asada, *IEEE J. Quantum Electronics* **QE-25**, 2019 (1989); *Quantum Well Lasers*, ed. by P. Zory, Yn., Academic Press, 1993.
- [2] A. L. Fetter and I. D. Walecka, *Quantum Theory of Many Particle Systems*, McGraw-Hill, New York, 1971.
- [3] L. V. Asryan, N. A. Gun'ko, A. S. Polkovnikov, G. G. Zegrya, R. A. Suris, P-K. Lau and T. Makino, *Semicon. Sci. Technol.* **15**, 1131 (2000).
- [4] G. G. Zegrya and A. S. Polkovnikov, *Zh. Exp. Teor.Fiz.* **113**, 1491 (1998) [*JETP* **86**, 815 (1998)].

## **Terahertz emitting devices based on intersubband transitions in SiGe quantum wells**

T. N. Adam, R. T. Troeger, S. K. Ray, U. Lehmann and *J. Kolodzey*

Department of Electrical and Computer Engineering, University of Delaware,  
Newark, DE 19716, USA

**Abstract.** Terahertz electroluminescence was produced by intersubband transitions in silicon-germanium quantum wells. The devices were grown by solid-source molecular-beam epitaxy on high-resistivity silicon substrates, and were fabricated by standard photolithography and processing techniques. Using FTIR spectroscopy at a temperature of 5 K, electroluminescence was observed around 9 THz. The emission was attributed to heavy-hole-to-light-hole transitions and demonstrates the potential for SiGe technology as terahertz emitters.

### **Introduction**

Terahertz emitting devices can be useful for a wide range of applications in the areas of communication, imaging and sensing. Gunther and deLucia found a minimum attenuation in air at 30 THz [1], McClatchy et al. used THz pulses to image a scale model of a warship [2], and Nagel et al. proposed genetic diagnostics based on THz resonances of DNA molecules [3]. For decades, ternary and quaternary III–V and II–VI materials such as the In(Ga)(As)P, Ga(Al)As, or CdHg(Se)Te systems have attracted much interest as optical devices due to their direct bandgap nature and latticematched growth. However, the design and fabrication of THz-emitting devices is challenging due to free-carrier and phonon absorption of infrared radiation in semiconductors. To avoid the intense phonon absorption in the reststrahlen bands, devices of InGaAlAs on InP substrates based on surface-plasmon modes have produced wavelengths longer than 20  $\mu\text{m}$  (15 THz) [4]. The SiGe alloy system, however, has negligible infrared-active polar lattice vibrations. Thus, phonon absorption is mitigated in SiGe THz devices. SiGe quantum cascade devices have been reported with emission at 30 THz [5]. They offer monolithic integration in the well established Si integrated circuit processing. In this work, we present light emission from intersubband transitions in a superlattice of SiGe quantum wells and Si barriers.

### **Experimental**

The device structure, as displayed on the right side of Fig. 1, consisted of 16 periods of undoped  $\text{Si}_{0.7}\text{Ge}_{0.3}$  wells 1.6 nm thick separated by 3.0 nm Si barriers. The superlattice was embedded in a thin buffer and capping layer. Layers of undoped SiGe quantum wells and barriers were grown by solidsource molecular beam epitaxy (MBE) on n-type Si substrates float-zone refined with a resistivity above 2000  $\Omega\text{cm}$ . By using lightly doped substrates and quantum wells with intersubband transition energies below that of phonons, we have attempted to minimize losses in the THz region. The MBE preparation and growth procedure are described elsewhere [6]. Briefly, during the growth, the substrate was held at 400 °C and the growth rate was approximately 0.2 nm/min. Silicon was deposited with an e-beam evaporator and germanium was incorporated using an effusion cell.



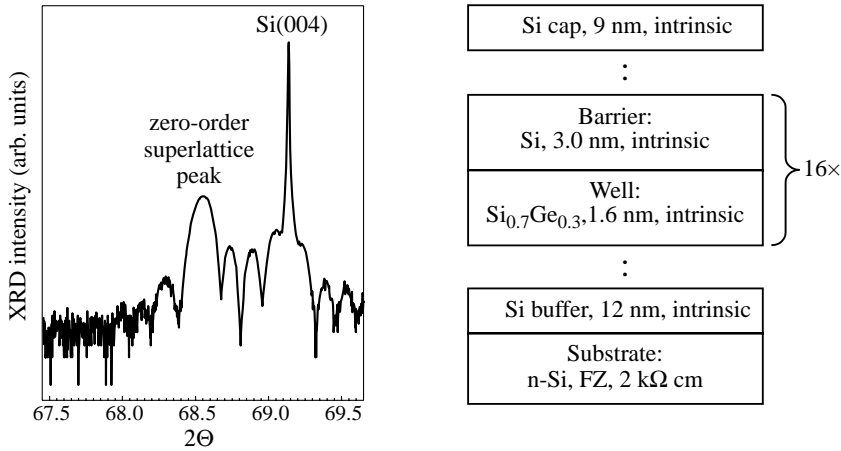


**Fig. 1.** Left: High-resolution X-ray diffraction rocking curve of our superlattice structure. Dynamical simulations confirmed 30% germanium and 3.0/1.6 nm barrier/well width. Right: Corresponding sample structure.

Crystallinity, layer thicknesses, and germanium fractions were confirmed by RHEED observations during growth and ex-situ high-resolution XRD rocking curves around the (004) silicon diffraction peak, displayed in Fig. 1. Dynamical simulations of diffracted X-rays confirmed the intended barrier and well widths, as well as germanium concentrations.

Devices were fabricated using conventional photolithography and Si processing techniques. Long 50–150  $\mu\text{m}$  wide metal fingers were fabricated using a standard lift-off technique. The fingers were spaced 70–350  $\mu\text{m}$  and connected to a large common bondpad. The device area was approximately 1  $\text{cm}^2$  and the metal contacts were Ti/Au layers with thickness of 20/250 nm respectively. A large area backside contact was achieved by evaporating Ti/Au with the same thicknesses. These emitters can be integrated with Si circuit technology and with photonic crystal elements for mode and beam control [7]. The samples were mounted to a Cu block with a thin sheet of indium and then springloaded to the cold-finger of a cryostat. Front contacts were wire-bonded. The devices were measured by Fourier Transform Infrared Spectroscopy (FTIR) with a Nicolet Nexus860 instrument in step scan mode. A helium-cooled silicon bolometer was used as the detector in combination with a lockin amplifier. During the measurement, the device was held at a temperature of 5 K. Step scan was performed by pulsing the quantum-well device with 800 ns pulses of 54 V at a 413 Hz repetition rate to prevent sample heating. A settling and stepping time of 1.5 s was allowed to reduce the background noise. During the 800 ns pulse, the total current was approximately 0.3 mA. In the resulting electroluminescence spectrum, as displayed on the left side of Fig. 2, we observed a sharp emission peak at 9.12 THz (32.9  $\mu\text{m}$ ), in good agreement with simulations. Wavefunctions, band structures, and eigenstates were calculated using Semicon-FEMB [8] — a software which solves the Schroedinger equation employing an 8-band  $\mathbf{k}\cdot\mathbf{p}$  model. Strain and applied fields are included in the calculations. The device was designed for intersubband transitions between the first heavy-hole and light-hole state centered around 9.6 THz, or 40 meV. As depicted on the right side of Fig. 2, at an applied field of 96 kV/cm, the light hole state lines up with the neighboring heavy hole state, thus cascading all 16 periods. Further evidence of resonant tunneling was found in the current-voltage characteristics at low temperatures, as shown in Fig. 3.

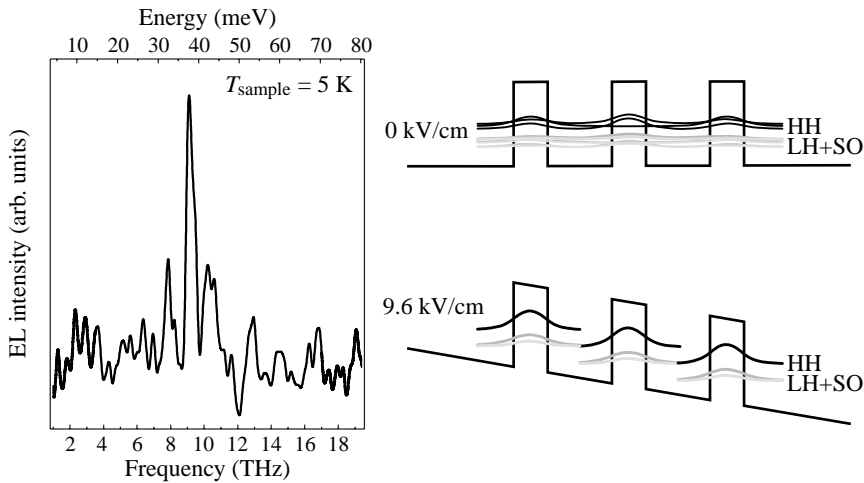


**Fig. 2.** Left: Electroluminescence spectrum with peak at 9.12 THz from SiGe quantum well device on Si substrate. The emission is due to cascaded intersubband transitions with an electrical current. Device measurement temperature was 5 K, applied current was 0.3 mA. Right: Bandstructure and wavefunction calculation with and without bias.

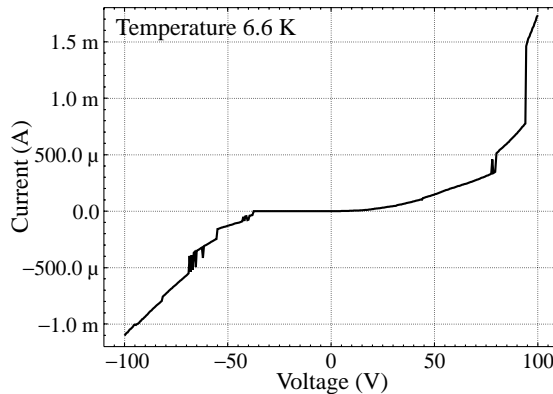


**Fig. 3.** Current–voltage measurement performed at 6.6 K in pulsed mode to prevent heating. Pulses were 1 ms wide with a repetition rate of 1 Hz. Several current steps were observed both in forward and reverse, indicating tunneling. These discontinuities disappeared above 150 K.

In summary, we have demonstrated the design, fabrication, and characterization of new promising THz-emitting SiGe quantum-well devices and found excellent agreement between the predicted and measured emission frequency. We predict feasible integration into the conventional silicon technology, offering the monolithic combination of optics and electronics on silicon.

#### Acknowledgments

The authors gratefully acknowledge support by the DARPA-funded Air Force contract number F19628-00-C-0005, and by the AFOSR grant number F49620-01-1-0042. Special thanks to Edgar Martinez, Gernot Pomrenke and Richard Soref for useful discussions and encouragement, to L. R. Ram-Mohan for help with the FEMB software, and to Claire Gmachl and Raffaele Colombelli for helpful discussions and some measurements.

## References

- [1] R. Gunther & F. DeLucia ca. 1977, Atmospheric attenuation in db/km, Private communications
- [2] K. McClatchey, M. T. Reiten and R. A. Cheville, *Appl. Phys. Lett.* **79**, 4485–4487 (2001).
- [3] M. Nagel, P. Haring Bolivar, M. Brucherseifer, H. Kurz, A. Bosserhoff and R. Buttner, *Appl. Phys. Lett.* **80**, 154–156 (2002).
- [4] R. Colombelli, F. Capasso, C. Gmachl, A. L. Hutchinson, D. L. Sivco, A. Tredicucci, M. C. Wanke, A. M. Sergent and A. Y. Cho, *Appl. Phys. Lett.* **78**, 2620–2622 (2001).
- [5] G. Dehlinger, L. Diehl, U. Gennser, H. Sigg, J. Faist, K. Ensslin, D. Gruetzmacher and E. Mueller, *Science* **290**, 2277 (2000).
- [6] M. W. Dashiell, R. T. Troeger, S. L. Rommel, T. N. Adam, P. R. Berger, J. Kolodzey, A. C. Seabaugh and R. Lake, *IEEE Trans. Electron Devices* **47**, 1707–1714 (2000).
- [7] J. Kolodzey, T. N. Adam, D. Prather, S. Shi, G. Looney and A. Rosen, *Tech. Digest of the Middle Infrared Coherent Sources International Workshop - MICS-2001*, St Petersburg, Russia, 25–29 June 2001.
- [8] L. R. Ram-Mohan, *Quantum Semiconductor Algorithms*, Northborough, MA 01532-2711, USA.

## Stimulated THz emission of acceptor-doped SiGe/Si quantum-well structures

*M. S. Kagan*<sup>†</sup>, *I. V. Altukhov*<sup>†</sup>, *E. G. Chirkova*<sup>†</sup>, *K. A. Korolev*<sup>†</sup>, *V. P. Sinis*<sup>†</sup>,  
*R. T. Troeger*<sup>‡</sup>, *S. K. Ray*<sup>‡</sup> and *J. Kolodzey*<sup>‡</sup>

<sup>†</sup> Institute of Radioengineering and Electronics, RAS, 101999 Moscow, Russia

<sup>‡</sup> University of Delaware, Newark, DE 19716, USA

**Abstract.** An intense THz emission was observed from strained SiGe/Si quantum-well structures under strong pulsed electric field. The p-type structures were MBE-grown on n-type Si substrates and  $\delta$ -doped with boron. Lines with wavelengths near 100 microns were observed in the emission spectrum. The modal structure in the spectrum gave evidence for the stimulated nature of the emission. The origin of the THz emission was attributed to intra-center optical transitions between resonant and localized boron levels.

### Introduction

Recently, the activity towards the quantum cascade THz laser on the basis of SiGe/Si heterostructures has started [1]. Here we discuss the possibility to create an alternative type of THz laser sources which could utilize a much simpler quantum well (QW) structures, i.e. a resonant-state laser (RSL) [2, 3]. Population inversion in the RSL is realized for the states of a shallow acceptor split under external stress. If the strain is high enough (above 3 kbar for Ge), the split-off acceptor state enters the light-hole branch of the valence band and creates a resonant state [4]. An applied electric field depopulates the local impurity states due to impact ionization. A population inversion of resonant states with respect to the impurity states in the gap is then formed [5] and THz lasing occurs.

Since thin layers of binary alloys like, for example,  $\text{Si}_{1-x}\text{Ge}_x$ , are strained internally due to the lattice mismatch, acceptor levels are split initially, and stimulated emission can, in principle, be obtained just by applying electric field. Acceptor-doped  $\text{Si}_{1-x}\text{Ge}_x$  is very attractive for fabricating the RSL because of its good thermal properties, low absorption in the THz range, well established, relatively cheap technology, as well as possible integration with Si-based electronics.

Earlier, we have reported on the observation of stimulated THz emission from boron-doped  $\text{Si}_{1-x}\text{Ge}_x$  quantum wells [6]. In this report, we present studies of the emission from  $\text{Si}/\text{Ge}_x\text{Si}_{1-x}/\text{Si}$  structures of various potential and doping profile. We also present evidence that the lasing is a result of population inversion between resonant and localized acceptor states similar to that in bulk p-Ge. A transverse electric field is found to affect the appearance of the resonant states.

### 1. Experimental

We studied p-type  $\text{Si}_{1-x}\text{Ge}_x$  QW structures MBE-grown pseudomorphically on n-type Si substrates. The SiGe QW was sandwiched between Si buffer and cap layers and was  $\delta$ -doped with boron in the QW middle with the concentration of  $6 \times 10^{11} \text{ cm}^{-2}$  (Fig. 1(a)). Both the buffer and cap layers were doped with one B- $\delta$ -layer.

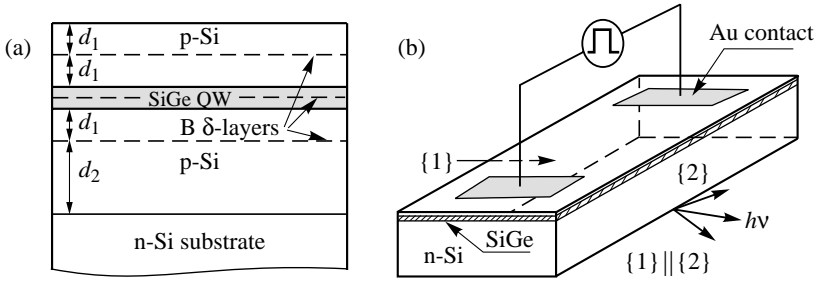


**Fig. 1.** Schematic view of structure (a) and laser design (b).

Two kinds of structures were used. In type-I QWs, the well was 20 nm thick and Ge content  $x$  in SiGe alloy was 0.15. The thickness of cap and buffer layers was 60 and 130 nm, respectively. The boron  $\delta$ -layers in the barriers, with concentration from  $4 \times 10^{11}$  to  $10^{12} \text{ cm}^{-2}$ , were positioned each at the distance  $d_1 = 30 \text{ nm}$  from respective QW interfaces. The QW thickness in type-II structures was about 13.5 nm. Other parameters (see Fig. 1(a)) were:  $x = 0.15, 0.1$ , and  $0.07$ , and  $d_1 = 19 \text{ nm}$  and  $d_2 = 62 \text{ nm}$ . The concentration of B in the  $\delta$ -layers was  $6 \times 10^{11} \text{ cm}^{-2}$ .

We used pulsed bias of 0.2 to 4  $\mu\text{s}$  duration in order to avoid overheating. Bias was applied to the SiGe layer via thermal-diffusion made Au contacts as shown in Fig. 1(b). The distance between contacts was 6 mm. Emission spectrum was measured by a grating monochromator and registered with a cooled Ga-doped Ge photodetector. Measurements were made at temperatures between 8 and 30 K. An optical resonator was formed due to the total internal reflection between the top and bottom surfaces of the sample, which were perpendicular to the growth direction, and two lateral facets (1 and 2 in Fig. 1(b)) which were parallel polished.

For the samples with the optical resonator, we observed that an intense THz emission arose at a threshold voltage above 300 V. Spectra of the intense emission were measured in the energy range 9.8 to 15.5 meV. Shown in Fig. 2(a) are parts of the spectra indicating lines for the samples of type I (Fig. 1(a)). The peak near the wavelength 104  $\mu\text{m}$  is observed.

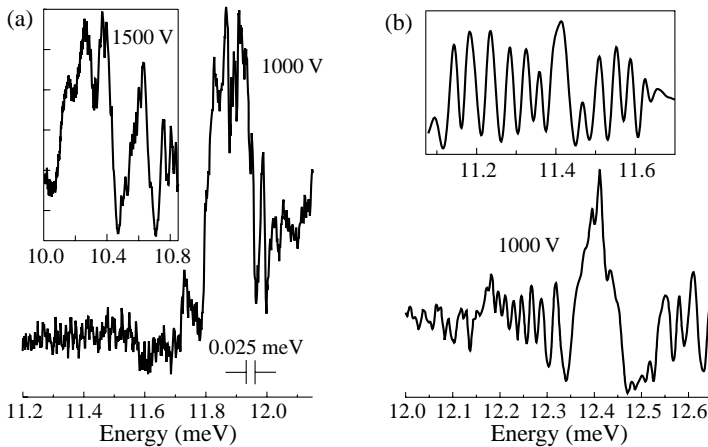


**Fig. 2.** Spectra of stimulated THz emission in structures of type I (a) and type II (b) at 1000 V. Insets: in (a) — additional lines arisen in the spectrum at 1500 V, in (b) — modal structure of the spectrum.

The spectral position of the peak varied from 103 to 108  $\mu\text{m}$  for different samples. At higher voltages, it was possible to observe additional maxima at larger wavelengths, shown in the inset of Fig. 2(a). The line near 100  $\mu\text{m}$  was observed in type-II samples with 0.15 Ge content (Fig. 2(b)). The intense emission was observed also from the type-II samples with  $x = 0.1$ . Shown in the inset in Fig. 2(b) is the modal structure of the emission. The distance between lines is near 0.04 meV and corresponds to an optical path inside the structure due to total internal reflection.

## 2. Discussion

We believe that the lasing we have observed results from a population inversion in the QW layer due to the resonant states of boron. The resonant acceptor state is created when the energy splitting between the ground and split-off acceptor states exceeds the binding energy. In the case of  $\text{Si}_{1-x}\text{Ge}_x$  structures, the splitting energy of the valence subbands is about 31 meV [7]. According to variational calculations, the binding energy of shallow acceptors is about 27 meV; the same value was obtained for the energy difference between the split-off acceptor state and the edge of higher-energy valence subband [7]. Thus, one can expect that the internal strain in the  $\text{Si}/\text{Ge}_x\text{Si}_{1-x}/\text{Si}$  layer is sufficient for the split-off state to become resonant. The situation can be improved by an existence of built-in strong electric field, as the position of space-quantization levels is controlled by electric field. We have shown [8] that the built-in transverse electric field exists in our structures due to surface charge. Additional transverse electric field arises due to thermal ionization of donors in the substrate, caused by Joule heating of the SiGe layer. Time dependence of this process is shown in Fig. 3. The intense emission arises, as a rule, at the beginning of current saturation. As a result of donor ionization, the substrate resistance decreases strongly (200  $\Omega$  for Fig. 3, see the inset). A potential drop on one of two p-n junctions (it is just a cut-off voltage in the inset) between p-contacts and n-Si substrate (Fig. 3(b)) which acts as a barrier, creates rather large transverse electric field between SiGe layer and the substrate. This field inclines the valence subbands in the QW and gives the possibility for resonant states to appear even if the internal strain is insufficient.

In conclusion, we have demonstrated THz lasing by SiGe/Si QW structures. The lasing is attributed to stimulated intracenter transitions between the resonant and localized states of

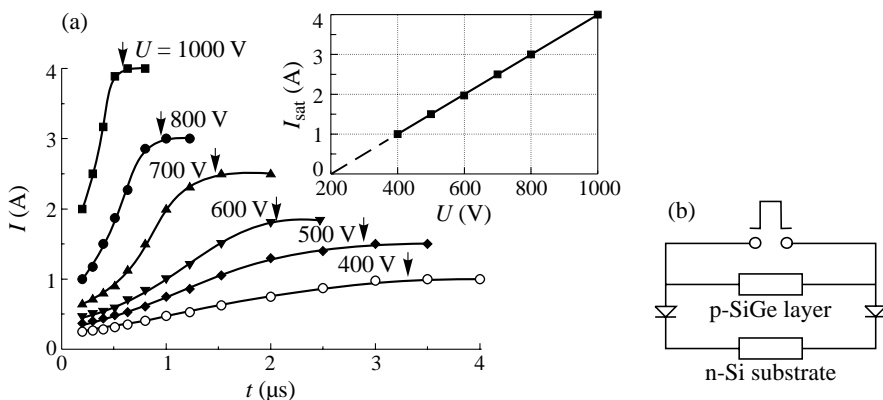


**Fig. 3.** (a) — current vs time during thermal breakdown of the substrate. Arrows show the onset of stimulated emission. Inset: voltage dependence of saturation current; (b) — equivalent circuit of SiGe/Si structure.

shallow acceptors. Thus, SiGe structures  $\delta$ -doped with boron are promising for realization of resonant-state laser (RSL) operating in THz region.

### Acknowledgements

Authors are thankful to S. G. Thomas and K. L. Wang for growing type-I structures. We acknowledge financial support by Russian Foundation for Basic Research (Grants 99-02-16169, 00-02-16066, 00-02-16093), Foundation for Leading Scientific Schools (00-15-96663), and RAS Program “Low-dimensional quantum structures”.

### References

- [1] G. Dehlinger, L. Diehl, U. Gennser, H. Sigg, J. Faist, K. Ensslin, D. Grützmacher and E. Müller, *Science* **290**, 2277 (2000).
- [2] I. V. Altukhov, M. S. Kagan, K. A. Korolev and V. P. Sinis, *JETP Lett.* **59**, 476 (1994); I. V. Altukhov, E. G. Chirkova, M. S. Kagan, K. A. Korolev, V. P. Sinis and I. N. Yassievich, *Phys. Stat. Sol. (b)* **198**, 35 (1996).
- [3] I. V. Altukhov, M. S. Kagan, K. A. Korolev, V. P. Sinis, E. G. Chirkova, M. A. Odnoblyudov and I. N. Yassievich, *JETP* **88**, 51 (1999).
- [4] M. A. Odnoblyudov, V. M. Chistyakov, I. N. Yassievich and M. S. Kagan, *Phys. Status Solidi (b)* **210**, 873 (1998).
- [5] M. A. Odnoblyudov, I. N. Yassievich, M. S. Kagan, Yu. M. Galperin and K. A. Chao, *Phys. Rev. Lett.* **83**, 644 (1999); M. A. Odnoblyudov, I. N. Yassievich, M. S. Kagan and K. A. Chao, *Phys. Rev. B* **62**, 15291 (2000).
- [6] I. V. Altukhov, E. G. Chirkova, V. P. Sinis, M. S. Kagan, Yu. P. Gousev, S. G. Thomas, K. L. Wang, M. A. Odnoblyudov and I. N. Yassievich, *Appl. Phys. Lett.* **79**, 3909 (2001).
- [7] A. Blom, M. A. Odnoblyudov, H. H. Cheng, I. N. Yassievich and K. A. Chao, *Appl. Phys. Lett.* **79**, 713 (2001).
- [8] M. S. Kagan, I. V. Altukhov, K. A. Korolev, D. V. Orlov, V. P. Sinis, S. G. Thomas, K. L. Wang and I. N. Yassievich, *Physica Status Solidi (b)* **211**, 495 (1999).

## Proposed Terahertz Bloch superlattice oscillator

A. Andronov, I. Nefedov and A. Sosnin

Institute for Physics of Microstructures Russian Academy of Sciences,  
Nizhny Novgorod GSP-105 603950 Russia

**Abstract.** Terahertz Bloch oscillator based on GaAs-GaAlAs superlattice with weak barriers is proposed. Here due to interminiband tunneling current is a rising function of electric field while the tunneling and the Bloch oscillations produce dynamic negative differential conductivity at the Terahertz frequencies. Monte-Carlo simulation demonstrates existence of the negative conductivity in 1–7 THz range in the superlattices with moderate mobility at 77 K. The oscillator should consist of the 200–600 superlattice periods sandwiched between two  $n^+$  contact regions which form also strip-line waveguide (the oscillator cavity) and could be operational at 77 K in CW mode.

### Introduction

The quantum cascade lasers cover now the high frequency part of the Terahertz range above about 10 THz. The low frequency part of the range about 0.5–5 THz is still out of the semiconductor sources (except of p-Ge lasers which are still out of wide use) [1]. One possible source for the above low part of the range are the Terahertz Bloch oscillators in superlattices (SL) with weak barriers. The oscillators are from the flock which employs dynamic negative differential conductivity (DNDC) due to electron bunching in the momentum space [2–5]. Recently the breakthrough in the utilization the bunching takes place: observation of stimulated emission in millimeter wave range in InP due to the Optical Phonon Transit Time Resonance (OPTTR) DNDC [6] and simulation of OPTTR DNDC in GaN at THz frequencies [7].

This report presents our recent results on DNDC in the Terahertz band under Bloch Oscillations (BO) and for multiminiband transport in GaAs-GaAlAs SL with weak barriers. These results are a substantial extension of the work [5] and are partially based on the work [8]. It is also worth noting here that not long ago H. Kroemer [9] discovered the DNDC in the single miniband SL transport [10] and pointed out that DNDC arises due to electron bunching in the momentum space. The DNDC implies that while (static) current-voltage ( $j - E$ ) curve has no negative slope for the ac field for the high enough frequency around  $\omega^*$  conductivity  $\sigma(\omega)$  is negative as shown in Fig. 1. The current-voltage curve without negative slope means that there is no domain formation and one can have electronic system with homogeneous electric field with negative high frequency ac conductivity: a dream of microwave engineer during the Gunn phenomena development times! Kroemer considered large signal negative conductivity which is alike LSA mode in the Gunn diodes. At small (linear) signal in single miniband SL transport there is no DNDC and the hot electron system is subject to domain formation which hinders movement of single miniband transport based SL sources toward the Terahertz range. Only microwave SL oscillators based on moving domain exist [11]. Other approaches are needed and the one discussed in this report looks quite promising.



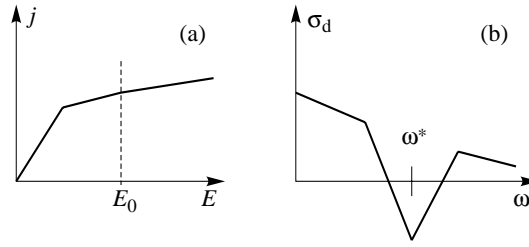


**Fig. 1.** Current–voltage curve (a) and differential conductivity versus frequency (b) for the case of dynamic negative differential conductivity.

### 1. Superlattice transport with interminiband tunneling

We consider the case of a SL with lowest miniband below an optical phonon energy and narrow minigaps. As an example one can take SL consisting of 150 Å of GaAs and 10 Å of  $\text{Ga}_{1-x}\text{Al}_x\text{As}$  with  $x$  in the range 0.05–0.2 for which the Monte-Carlo results will be given below. In such SL with moderate doping at low temperature in high electric fields the following transport processes take place:

1. The Bloch oscillations (consisting of almost free electron motion in electric field in the SL Brillouin zone followed by the Bragg scattering) with frequency

$$\omega_B = 2\pi eE/p_B = eEd/\hbar, \quad (1)$$

$p_B$  is the electron momentum on the SL Brillouin zone boundary;

2. Tunneling through narrow minigap to the second miniband with quick returning back to the first miniband due to optical phonon emission. Probability of interminiband tunneling may be written as  $P_t = \exp(-E_t/E)$ ,  $E_t = \pi^2 \varepsilon_g^2 / 4\varepsilon_B e d$ . An electron approaching boundary of the Brillouin zone at  $p_B$  by freely moving in electric field can follow the two routes: it can perform the Bragg scattering to  $(-p_B)$  and continue the BO or it can perform the interminiband tunneling to the second miniband and then return to the first miniband after emission of an optical phonon in the second miniband. Probability of the Bragg scattering is  $P_B = 1 - P_t$ . It is important that  $P_t$  and  $P_B$  strongly depend on electric field. As a result in the case both dc and ac fields are presented the probabilities of the both processes depend on the phase of the ac field, and electron bunching occur which can result in DNDC. We add the probability  $P_t$  and  $P_B$  in the standard kinetic equation and perform calculation of both current–voltage curves and differential conductivity. Results of simulation are given in Fig. 2. In the Fig. 2(a) the average drift velocity  $\langle v \rangle$  ratio to  $v_0$  ( $v_0$  is an electron velocity for energy equal to an optical phonon energy) is given versus electric field normalized to the optical phonon characteristic field  $E_0$  for different characteristic tunneling field  $E_t$ . In the simulations position of the Brillouin zone boundary  $p_B$  is chosen to be equal to  $0.8p_0$  ( $p_0$  is an electron momentum at an optical phonon energy) what corresponds to the period 160 Å of the GaAs–AlGaAs SL mentioned above: 150 Å of GaAs and 10 Å of  $\text{Ga}_{1-x}\text{Al}_x\text{As}$ . Value of the alloy composition  $x = 0.1$  corresponds to the tunneling field  $E_t = E_0$ . In GaAs  $E_0$  is of about 6 kV/cm while characteristic scattering rate  $v_0$  is of about  $5 \times 10^{12} \text{s}^{-1}$ . Changing  $x$  value in the range 0.05–0.2 changes the tunneling field in the range shown in Fig. 2(a). We see that increase of the “strength” of SL potential (increase of  $x$  and herewith  $E_t$ ) results in transformation of the curve from that of the bulk for  $E_t = 0$  to the one of single miniband transport (for  $E_t = 5.0$ ). In the latter case the rising portion of the curve in the low fields (with positive differential conductivity) is

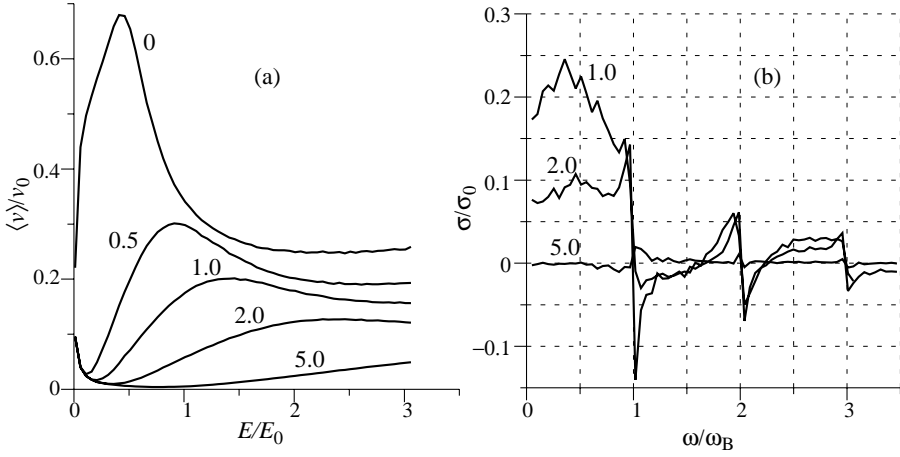


**Fig. 2.** (a) Normalized drift velocity versus normalized electric field for different values  $E_t/E_0$ ; (b) Differential conductivity versus frequency for  $E_t/E_0 = 0.75$ ;  $\sigma_0 = e^2 N / m v_0$ ;  $T = 77$  K.

not seen due to inappropriate scale. We perform also simulation of frequency dependence of the differential conductivity (Fig. 2(b)). For  $E_t/E_0 = 5.0$  standard single miniband behavior of the differential conductivity is observed [12]: negative at low frequencies up to the Bloch frequency. Differential conductivity for  $E_t/E_0 = 1.0$  and  $E_t/E_0 = 2.0$  are positive at low frequency while nearby by the Bloch frequency and its harmonics there are regions of DNDC. The Bloch frequency (angular) in this case corresponds to frequency of about 1.5 THz ( $\lambda = 200 \mu\text{m}$ ). We perform also simulation for higher fields and lower mobility in the SL. In particular for  $E/E_0 = 1.0$  when the Bloch frequency is of about 2 THz ( $\lambda = 150 \mu\text{m}$ ) the DNDC survives even for the mobility as low as  $10000 \text{ cm}^2/\text{Vs}$  for  $E_t/E_0 = 2.0$  ( $\mu$  about 0.15 for the structure mentioned). At higher fields (higher frequencies) the DNDC becomes even more pronounced with optimal for the DNDC ratio  $E_t/E$  about 2.0. The highest frequency at which the DNDC survived is determined by the condition the frequency is below the interminiband transition frequency i.e. by the condition  $\hbar\omega < \varepsilon_g$ . For  $E_t/E = 2.0$  from (1) we get:  $\omega < 8/\pi^2 \omega_0$ . From this condition we found that the DNDC limiting frequency is of about 7 THz.

## 2. The oscillator scheme

The proposed oscillator could consist of the SL layer sandwiched between two  $n^+$  contact regions what form also strip-line waveguide (which is the oscillator cavity). To estimate width of the SL layer region (number of SL periods) needed for the oscillator we should compare the strip waveguide losses with amplification coefficient in the SL. To estimate the latter we take the value of negative conductivity given in Fig. 2(b) for  $\omega \approx \omega_B$ :  $\sigma \approx 0.025\sigma_0$  and take the electron concentration  $N = 2 \times 10^{16} \text{ cm}^{-3}$ . Though we simulate the conductivity without impurity scattering the taken  $N$  value is not high and also simulation shows that the DNDC survives up to  $T = 150$  K and at moderate mobility also. For these values we have amplification coefficient  $100 \text{ cm}^{-1}$ . For estimate of the strip waveguide losses we can take data measured in [13] at  $\lambda = 75 \mu\text{m}$ : losses for  $10 \mu\text{m}$  wide strip waveguide is of about  $50 \text{ cm}^{-1}$ . The losses should follow  $\omega^{1/2}$  law. For our case  $\lambda = 200 \mu\text{m}$  we can take value of waveguide losses as  $50 \text{ cm}^{-1}$ . This figure can be even improved if one uses heavily doped (than in [13]) contact regions. From these estimates we

can conclude that the Bloch oscillator with SL region width 3–10  $\mu\text{m}$  (200–600 periods) should work. Presumably the oscillator will work in the range 1–7 THz and could be operational at 77 K in CW mode also.

#### Acknowledgement

The work is supported by State Program “Physics of Microwaves”.

#### References

- [1] Recently report is circulating about achievement of cascade lasing at about 5 THz by Neuchatel and Pisa groups.
- [2] V. L. Bonch-Bruevich and M. A. El-Sharnuby, *Vestnik of the Moscow State University* **13**, ser.3, 616 (1972).
- [3] A. Andronov and V. Kozlov, *JETF Lett.* **17**, 87 (1973).
- [4] E. Starikov and P. Siktorov, *Litov. Fiz. Sb.* **32**, 471 (1992).
- [5] A. Andronov and I. Nefedov, *Proc. 9th Inter. Conf. on Hot Carriers in Semicon.* vol 153, Plenum Press NY, (1996).
- [6] L. E. Vorobjev, S. N. Danilov *et al*, *Pisma ZETF* **73**, 253 (2001).
- [7] E. Starikov, P. Siktorov *et al*, *IEEE Trans. Electron Devices* **48**, N3, 530 (2001).
- [8] A. Sosnin, Master work, Nizhny Novgorod State University, (2001).
- [9] H. Kroemer, cond-mat/0009311
- [10] L. Esaki and R. Tsu, *IBM J. Res. Dev.* **14**, 61 (1970).
- [11] E. Schomburg, R. Scheuerer, S. Brandl, D. Pavel'ev, Yu. Koschuriniv, A. Zukov, A. Kovsh and P. S. Kop'ev, *Electron Lett.* **35**, 12 (1999).
- [12] S. A. Kitorov, G. S. Simin and V. Ya. Sandolovski, *Sov. Phys. - Solid State* **13**, 1872 (1971).
- [13] M. Rochat, M. Beck, J. Faist and U. Oesterle, *Appl. Phys. Lett.* **78**, 1967 (2001).

## Impurity induced resonant states in modulation doped heterostructures

*M. A. Odnoblyudov*<sup>†‡</sup>, A. Blom<sup>‡</sup>, I. N. Yassievich<sup>†</sup> and K.-A. Chao<sup>‡</sup>

<sup>†</sup> Ioffe Physico-Technical Institute, RAS, 194021 St Petersburg, Russia

<sup>‡</sup> Fasta tillståndets teori, Lund University, Sölvegatan 14 A, S-223 62 Lund, Sweden

**Abstract.** A study of the formation of 2D resonant states in the conduction band, induced by impurities outside heterostructure quantum wells, is presented. General expressions for the capture and scattering amplitudes are derived, and the effect on the energy spectrum and the density of states in the quantum well is calculated. The theory is applied to the Coulomb potential of donor impurity.

### Introduction

Modulation-doped semiconductor heterostructures have been under extensive experimental and theoretical study for the last few decades [1]. In such structures, impurities located in the barrier material act as the source of a long-range scattering potential for the carriers in conduction channel. The effects of elastic scattering in this framework have been studied in numerous works [1]. At the same time, impurity-induced resonant states can be formed, due to the overlap of the localized impurity orbitals with the 2D continuum states in the conduction channel, and induce strong resonant scattering. Thus, carriers from the 2D continuum states can be captured into localized states, and subsequently be re-emitted back. Such generation–recombination processes may lead to new and unexpected features of the shot noise characteristics [2] of devices based on semiconductor heterostructures. It was also shown [3], that the energy spectrum and the density of states can be strongly perturbed due to the formation of resonant states. This in turn will have consequences for optical transitions and kinetic processes [3].

In this paper we will consider resonant states induced by the Coulomb potential of donor impurities situated in the barrier region of heterostructure. Expressions for the capture and scattering amplitudes, the energy position and width of the resonant state, as well as the density of states of the perturbed spectrum are derived.

### 1. Model description

In this section we will describe a general treatment of systems which consist of a quantum well (QW) and an impurity located in the barrier region. We denote by  $V(z)$  and  $V_c(\mathbf{r})$  the potentials of the QW and the isolated impurity, respectively. The total Hamiltonian of such a system includes both these potentials. We use different zero-order Hamiltonians to describe the unperturbed localized and 2D quantum well states. Thus, the localized orbital wavefunction  $\phi(\mathbf{r})$  corresponding to the energy  $E_c$  should satisfy the Schrödinger equation with the Coulomb potential  $V_c(\mathbf{r})$ . The wavefunctions of the quantum well states  $\psi_{n\mathbf{k}}(\mathbf{r})$  with energies  $\mathcal{E}_{n\mathbf{k}}$  should be found from the solution of the quantum well problem with the potential  $V(z)$ . Here  $\mathbf{k}$  is the wavevector in the QW plane, and  $n$  enumerates the space quantization sub-bands.

The total resonant state wavefunction is constructed in the form [4]

$$\Psi_{n\mathbf{k}} = \psi_{n\mathbf{k}} + c_{n\mathbf{k}}\phi + \sum_{n'\mathbf{k}'} \frac{t_{\mathbf{k}\mathbf{k}'}^{nn'}}{E_{n\mathbf{k}} - \mathcal{E}_{n'\mathbf{k}'} + i0} \psi_{n'\mathbf{k}'}, \quad (1)$$

and should satisfy the Schrödinger equation with the total Hamiltonian. In (1),  $c_{n\mathbf{k}}$  and  $t_{\mathbf{k}\mathbf{k}'}^{nn'}$  are the capture and scattering amplitudes, respectively. Using standard procedures [4], the following expressions for the amplitudes can be obtained:

$$c_{n\mathbf{k}} = \frac{R_{n\mathbf{k}}/\mathcal{L}}{\mathcal{E}_{n\mathbf{k}} - (E_c + \Delta E_{n\mathbf{k}}) + i\Gamma_{n\mathbf{k}}/2}, \quad t_{\mathbf{k}\mathbf{k}'}^{nn'} = \frac{V_{\mathbf{k}\mathbf{k}'}^{n'n}}{\mathcal{L}^2} + \frac{c_{n\mathbf{k}}}{\mathcal{L}} X_{\mathbf{k}\mathbf{k}'}^{nn'}, \quad (2)$$

where  $\mathcal{L}^2$  is the normalization area.  $R_{n\mathbf{k}}$ ,  $V_{\mathbf{k}\mathbf{k}'}^{n'n}$  and  $X_{\mathbf{k}\mathbf{k}'}^{nn'}$  are expressed in terms of matrix elements of the QW and impurity potentials between  $\phi(\mathbf{r})$  and  $\psi_{n\mathbf{k}}(\mathbf{r})$ .

One can see from (2) that the capture amplitude  $|c_{n\mathbf{k}}|^2$ , which gives the contribution of the localized state to the hybridized one, exhibits a resonance behavior, shifted from the energy of the localized state  $E_c$  by  $\Delta E_{n\mathbf{k}}$ . The value of the shift  $\Delta E_{n\mathbf{k}}$  and the width  $\Gamma_{n\mathbf{k}}$  depend on the energy itself. We therefore define the resonance energy as the energy at which  $|c_{n\mathbf{k}}|^2$  acquires its maximum. The lifetime  $\tau_r = \hbar/\Gamma_{n\mathbf{k}}$  of the resonant state can then be found by evaluating  $\Gamma_{n\mathbf{k}}$  at this energy.

The hybridization of the continuous states with the localized orbital will also perturb the energy spectrum  $E_{n\mathbf{k}}$  and the density of states  $\rho_n(E_{n\mathbf{k}})$  in the QW. If there is a finite number  $N_d$  of impurities, the following expressions for  $E_{n\mathbf{k}}$  and  $\rho_n(E_{n\mathbf{k}})$  can be obtained

$$E_{n\mathbf{k}} = \mathcal{E}_{n\mathbf{k}} + n_{2D} \left[ \tilde{E} \frac{R_{n\mathbf{k}}^2 - 2V_{n\mathbf{k}}R_{n\mathbf{k}}}{\tilde{E}^2 + \Gamma_{n\mathbf{k}}^2/4} - V_{\mathbf{k}\mathbf{k}}^{nn} \right], \quad \rho_n(E_{n\mathbf{k}}) = \frac{1}{2\pi} \frac{k(E_{n\mathbf{k}})}{\partial E_{n\mathbf{k}}/\partial k}, \quad (3)$$

where  $\tilde{E} \equiv E_{n\mathbf{k}} - (E_c + \Delta E_{n\mathbf{k}})$  and  $n_{2D} \equiv N_d/\mathcal{L}^2$  is the sheet density of donors. This is an equation for  $E_{n\mathbf{k}}$  which should be solved to establish the relationship between the perturbed spectrum  $E_{n\mathbf{k}}$  and the corresponding wavefunction label  $\mathbf{k}$ .

By its definition in (2), the coefficient  $c_{n\mathbf{k}}$  is directly related to the probability for capture into the localized part of the resonant state [3].

## 2. Results

We now apply the theory to the system consisted of a shallow donor state with energy  $E_c = 9$  meV outside a  $\text{Al}_{0.3}\text{Ga}_{0.7}\text{As}/\text{GaAs}/\text{Al}_{0.3}\text{Ga}_{0.7}\text{As}$  quantum well.

With modulation doping, which is a dominating choice for device applications based on heterostructures [1], the charge transfer from the doping region, over the undoped spacer region into the QW, leads to the build-up of an electric field, which brings QW levels closer to the impurity level (Fig.1). Using a structure, as shown in Fig. 1, we perform calculations of the capture coefficient into the resonant states and density of states perturbed by the resonance.

In the upper panel of Fig. 2 we plot  $|c_{n\mathbf{k}}|^2$  for the lowest sub-band. One can see the Lorentzian shape and the widening of the resonance with decreasing distance  $d$ . The perturbed density of states  $\rho_n(E_{n\mathbf{k}})$ , defined by (3), is shown in the lower panel of Fig. 2. It demonstrates contributions from both the constant density of 2D states and the  $\delta$ -function-like behaviour of an isolated impurity. The increase in the density of states is by an order of

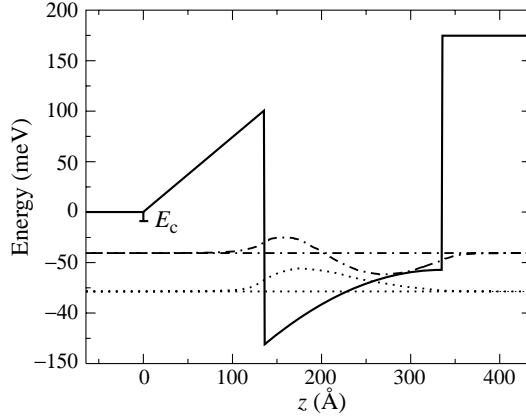


**Fig. 1.** The modulation doping profile used for the calculations with shallow donors. For this example is used a well width of  $L = 200 \text{ Å}$  and  $d = 135 \text{ Å}$ . The lowest quantization levels and their corresponding wavefunctions  $\varphi_n(z)$  are indicated.

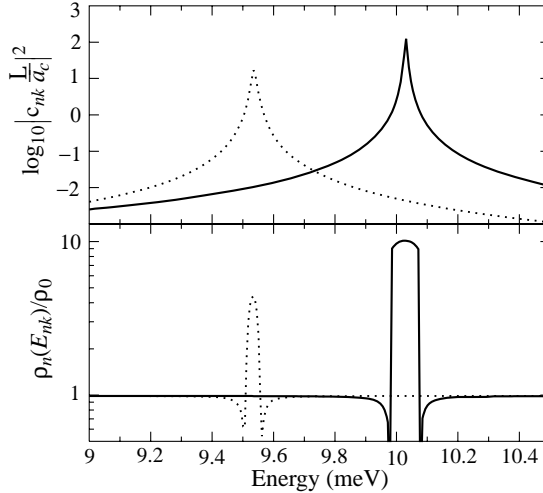


**Fig. 2.** The capture coefficient  $|c_{nk}|^2$  (upper panel) and the density of states (lower panel) as functions of the energy, for the case  $L = 200 \text{ Å}$  for the AlGaAs/GaAs QW.  $a_c$  is the Bohr radius of the donor localized state  $\phi(\mathbf{r})$ . The density of states is normalized by  $\rho_0 = m_w/2\pi\hbar^2$ . The doping concentration is taken as  $5 \times 10^{11} \text{ cm}^{-2}$ . The curves correspond to  $d = 135 \text{ Å}$  (solid) and  $d = 170 \text{ Å}$  (dot).

magnitude at the resonance at  $d = 170 \text{ Å}$  and  $n_{2D} = 5 \times 10^{11} \text{ cm}^{-2}$ . We observe an almost complete depletion of the density of states in the wings of the resonance, just before the sharp increase. This resembles a miniature band-gap, which could be possible to observe in optical absorption measurements.

We believe, that for device operation under high-field conditions, resonant scattering can be an important mechanism. The resonant scattering as presented here takes place in a very narrow energy range, where the capture and scattering probabilities vary by several orders of magnitude, and thus introduces strong scattering of carriers which have possibility to reach this energy region.

### 3. Conclusion

We have studied the formation of resonant states in the conduction band of heterostructures, induced by donor impurities situated in the barrier region.

The capture probability is found to exhibit a resonance behaviour, with a maximum at an energy shifted from the original impurity energy.

The electron distribution function and the high-field kinetic processes in the QW will be influenced by the strong resonant scattering which takes place in a narrow interval at the resonance energy. We can also expect a pronounced effect on the shot noise spectrum, due to the carrier capture and re-emission process accompanying the resonant scattering.

Optical properties are determined by the density of states, which also exhibits a resonance behaviour. A small band-gap was observed close to the resonance, and at the resonance, the density of states may be enhanced by orders of magnitude. This may have consequences for optical properties of devices based on modulation-doped heterostructures.

#### *Acknowledgements*

This work has been partially supported by the RFBR (grants 01-02-16265, 00-02-17429 and 00-15-96768), the Swedish Research Council (TFR-THZ 2000-403) and NorFA Grant.

### References

- [1] C. Weisbuch and B. Vinter, *Quantum Semiconductor Structures: Fundamental and Applications*, (Academic Press, Boston, 1991), p. 252.
- [2] Ya. M. Blanter and M. Büttiker, *Shot Noise in Mesoscopic Conductors*, Physics Reports Vol. 336, (Elsevier, Amsterdam), 2000.
- [3] M. A. Odnoblyudov, I. N. Yassievich, V. M. Chistyakov and K. A. Chao, *Phys. Rev. B* **62**, 2486 (2000).
- [4] P. A. M. Dirac, *Principles of Quantum Mechanics*, (Clarendon Press, Oxford), 4th Ed., p. 314, 1981.

## Resonant acceptor states in delta-doped SiGe nanostructures

A. A. Prokofiev<sup>†</sup>, M. A. Odnoblyudov<sup>†,‡</sup>, I. N. Yassievich<sup>†</sup> and K.-A. Chao<sup>‡</sup>

<sup>†</sup> Ioffe Physico-Technical Institute, St Petersburg, Russia

<sup>‡</sup> Fasta tillståndets teori, Lund University, Sölvegatan 14 A, S-223 62 Lund, Sweden

**Abstract.** Resonant acceptor states induced by internal strain in Si/SiGe/Si quantum wells delta-doped with boron have been investigated theoretically. Sample design of Si/SiGe/Si MQW structures for resonant state THz laser is suggested.

### Introduction

Lately great attention has been paid to Quantum Cascade Lasers (QCL), which currently can operate at wavelengths in excess of  $10\text{ }\mu\text{m}$  [1]. Recently the first attempts have been made to fabricate QCL on the basis of SiGe structures operating in THz range (1–10 THz). SiGe/Si heterostructures are very attractive for this purpose because of their good thermal properties and low lattice absorption in THz region. However, with increasing of wavelength it becomes more and more difficult to fulfill a number of conditions for operating of QCL. Resonant State Laser (RSL) which utilizes boron delta-doped SiGe QW structure has been suggested as an alternative type of THz source [2, 3]. The first RSL was realized on the basis of strained bulk p-Ge [4, 5] under condition of impurity impact ionization by an external electric field. Population inversion in the RSL is realized for the states of a shallow acceptor split under stress. If the strain is high enough, the split-off acceptor states overlap the valence band continuum forming resonant states. Under condition of impact ionization the acceptor ground states becomes depopulated but the resonant states are populated by hot carriers. In this case intracenter population inversion is formed, which is the mechanism of the THz lasing.

In boron doped Si/Si<sub>1-x</sub>Ge<sub>x</sub>/Si structures with lattice mismatch there an internal strain exists which could create the resonant states. It gives the possibility to realize the first single QW RSL without external strain [3].

In this paper we present a detailed theoretical study of acceptor resonant states in boron doped Si/Si<sub>1-x</sub>Ge<sub>x</sub>/Si structures as well as results of computer simulation of possible structures for multi quantum well resonant state lasers.

### 1. Resonant states in QW

We perform the calculation of the energy position and the width of the resonant state as well as the probabilities of resonance scattering and capture into resonant state using the method of configuration interaction. The main idea is to choose two different Hamiltonians for the initial approximation: one for localized states and the other one for continuum states. The initial approximation for wavefunction and energy of the localized states were found as variational solution of the acceptor problem in strained bulk Si<sub>1-x</sub>Ge<sub>x</sub>, which can be



presented in the form

$$\varphi^{+1/2} = \frac{1}{\sqrt{\pi a^2 b}} e^{-\sqrt{\frac{\rho_x^2}{a^2} + \frac{\rho_y^2}{b^2}}} \begin{bmatrix} 0 \\ 1 \\ 0 \\ 0 \end{bmatrix}, \quad \varphi^{-1/2} = \frac{1}{\sqrt{\pi a^2 b}} e^{-\sqrt{\frac{\rho_x^2}{a^2} + \frac{\rho_y^2}{b^2}}} \begin{bmatrix} 0 \\ 0 \\ 1 \\ 0 \end{bmatrix},$$

where  $a$  and  $b$  are variational parameters.

As zero order Hamiltonian for 2D continuum states we used the Luttinger Hamiltonian supplied by boundary conditions at QW interfaces. Those states are classified by subband number  $n$ , wave vector  $\mathbf{k}$  and parity  $\mu$ , which can be either *symmetric* or *anti-symmetric*. Corresponding wavefunctions  $\psi_{n,\mathbf{k}}^\mu$  and dispersion law  $\varepsilon_{n,\mathbf{k}}$  are found in a standard way (e. g. [6]).

In Fig. 1 we provide the scheme of localized impurity levels as well as initial approximation for resonant state energy ( $E_0$ ) superimposed on 2D dispersion curves for Si/Si<sub>0.80</sub>Ge<sub>0.20</sub>/Si QW. For that case variational parameters  $a = 27 \text{ \AA}$ ,  $b = 29 \text{ \AA}$  and  $E_0 = 5.01 \text{ meV}$  counted from the first space quantization level.

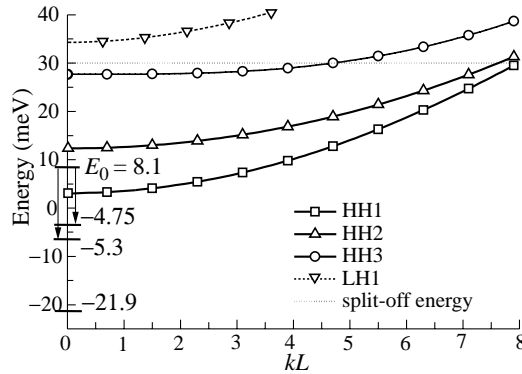


**Fig. 1.** Energy dispersion and initial approximation for impurity levels in Si/Si<sub>0.80</sub>Ge<sub>0.20</sub>/Si 200Å width QW. The kinetic energy of holes is assumed to be positive.

The wavefunction of the resonant state we present in the form

$$\Psi_{n,\mathbf{k}}^\mu = \psi_{n,\mathbf{k}}^\mu + \sum_v a_{n,\mathbf{k}}^{\mu,v} \varphi^v + \sum_{n',\mathbf{k}',\mu'} \frac{t_{\mathbf{k}\mathbf{k}'}^{n\mu,n'\mu'} \psi_{n',\mathbf{k}'}^{\mu'}}{\varepsilon_{n,\mathbf{k}} - \varepsilon_{n',\mathbf{k}'} + i\gamma}, \quad (1)$$

where  $a_{n,\mathbf{k}}^{\mu,v}$  gives the probability of capture into the resonant states, and  $t_{\mathbf{k}\mathbf{k}'}^{n\mu,n'\mu'}$  is the probability of the resonant scattering.

Substituting this wave function into Schrödinger equation one can determine  $a_{n,\mathbf{k}}^{\mu,v}$  and  $t_{\mathbf{k}\mathbf{k}'}^{n\mu,n'\mu'}$  [7, 8].

For the coefficient  $a_{n,\mathbf{k}}^{\mu,v}$  the following expression containing the resonant denominator is obtained:

$$a_{n,\mathbf{k}}^{\mu,v} = \frac{1}{\sqrt{S}} \frac{A_{n,\mathbf{k}}^{\mu,v}}{\varepsilon_{\mathbf{k},n} - (E_0 + \Delta E) + i\Gamma/2},$$

where  $S$  is the normalizing square, resonance energy shift  $\Delta E$  and width  $\Gamma$  as well as  $A_{n,\mathbf{k}}^{\mu,v}$  should be calculated numerically.

Note, that both  $\Delta E$  and  $\Gamma$  are the functions of  $\varepsilon_{\mathbf{k},n}$  and the final shift of resonance energy  $\Delta E = E_r - E_0$  is calculated at the energy  $\varepsilon_{\mathbf{k},n} = E_r$ , where the resonance energy  $E_r$  satisfies the equation:

$$E_r = E_0 + \Delta E(E_r).$$

The capture probability for the hole from the  $n$ -th subband is given by  $a_{n,\mathbf{k}}^{\mu,v}$  coefficient:

$$W_{\mathbf{k}r}^{n,\mu} = \sum_v \left| a_{n,\mathbf{k}}^{\mu,v} \right|^2.$$

The same coefficients determine the probability of elastic scattering of 2D holes.

The calculations for the case of QW width  $d = 200 \text{ \AA}$  for  $\text{Si}/\text{Si}_{1-x}\text{Ge}_x/\text{Si}$  give  $\Delta E = 0.95 \text{ meV}$  and  $\Gamma/2 = 1.6 \text{ meV}$  at  $x = 0.2$ , and  $\Delta E = 1.1 \text{ meV}$  and  $\Gamma/2 = 4.3 \text{ meV}$  at  $x = 0.25$ .

## 2. The structures for multi quantum well resonant state laser

We have performed an extensive numerical study of a  $\text{Si}/\text{Ge}_x\text{Si}_{1-x}/\text{Si}$  QW laser structures. The one of the typical structure suitable for lasing presented in Fig. 2. The i-Si buffer layer of thickness 80 nm is deposited on n-Si substrate ( $N_d = 5 \times 10^{14} \text{ cm}^{-3}$ ). The delta doping of the buffer layer with boron concentration  $8 \times 10^{10} \text{ cm}^{-2}$  should be produced at the distance 10 nm from the substrate. Then four  $\text{Si}_{0.8}\text{Ge}_{0.2}$  QW delta doped in the middle with boron concentration  $6 \times 10^{11} \text{ cm}^{-2}$  and separated by 10 nm of undoped Si are grown. The cap layer of the width 40 nm then deposited delta doped at the distance 25 nm from the last QW interface with boron concentration  $10^{12} \text{ cm}^{-2}$ . The purpose of the high concentration of doping here is to compensate the electric field produced by charge accumulation in the surface states at  $\text{Si}/\text{SiO}_2$  interface. In result, there is no band decline in the active region of the structure and all quantum wells are neutral with ground acceptor level populated by holes. Thus, the above described calculation of the resonant level position are equally applied to each QW. When an external electric field is applied along QW planes and conditions of impact ionization of localized states are realized, the resonant states become populated and we expect lasing at energy  $\hbar\omega = 14 \text{ meV}$  corresponding to the transition between resonant ( $E_0$ ) and localized states shown by arrow in Fig. 1.

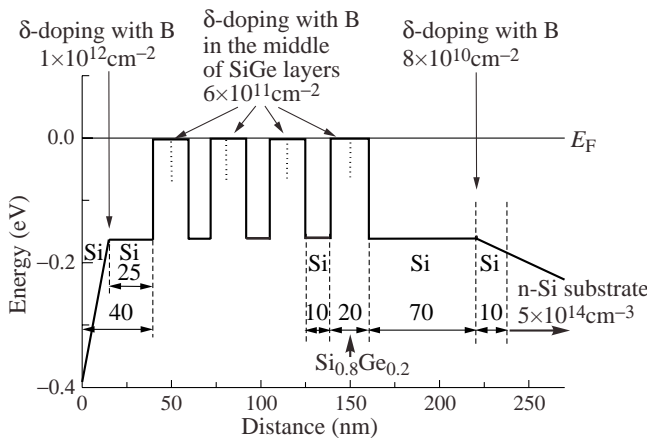


Fig. 2. Possible multi QW design for laser structure.

### 3. Conclusion

The emergence of resonant states in Si/SiGe/Si QW structures delta-doped by boron has been investigated. Energy position and width of resonant states as well as probabilities of capture on resonant state and resonant elastic scattering.

Multi QW structures suitable for THz lasing based on intracenter transition between resonant and local states are suggested.

#### *Acknowledgements*

This work has been partially supported by the RFBR (grants 01-02-16265, 00-02-17429 and 00-15-96768), The Swedish Foundation for International Cooperation in Research and Higher Education (contract 99/527 (00)) and NorFA Grant.

### References

- [1] G. Dehlinger, L. Diehl, U. Gennser, H. Sigg, J. Faist, K. Ensslin, D. Grützmacher and E. Müller, *Science* **290**, 2297 (2000).
- [2] A. Blom, M. A. Odnoblyudov, H. H. Cheng, I. N. Yassievich and K.-A. Chao, *Appl. Phys. Lett.* **79**, 713 (2001).
- [3] I. V. Altukhov, E. G. Chirkova, V. P. Sinis, M. S. Kagan, Yu. P. Gousev, S. G. Thomas, K. L. Wang, M. A. Odnoblyudov and I. N. Yassievich, *Appl. Phys. Lett.* **79**, 3909 (2001).
- [4] I. V. Altukhov, E. G. Chirkova, M. S. Kagan, K. A. Korolev, V. P. Sinis, M. A. Odnoblyudov and I. N. Yassievich, *JETPh*, **88**, 51 (1999).
- [5] Yu. P. Gousev, I. V. Altukhov, K. A. Korolev, V. P. Sinis, M. S. Kagan, E. E. Haller, M. A. Odnoblyudov, I. N. Yassievich and K.-A. Chao, *Appl. Phys. Letters* **75**, 757 (1999).
- [6] L. C. Andreani, A. Pasquarello and F. Bassani, *Phys. Rev. B* **36**, 5887 (1987).
- [7] A. A. Prokofiev, I. N. Yassievich, A. Blom, M. A. Odnoblyudov and K.-A. Chao, *Nanotechnology* **12**, 457 (2001).
- [8] M. A. Odnoblyudov, A. A. Prokofiev and I. N. Yassievich, *JETPh* (to be published in 2002).

## Circular photogalvanic effects induced by spin orientation in quantum wells

*S. D. Ganichev*<sup>†‡</sup>

<sup>†</sup> Fakultät Physik, University of Regensburg, D 93040, Regensburg, Germany

<sup>‡</sup> Ioffe Physico-Technical Institute, St Petersburg, Russia

Lately, there is much interest to use the spin of conduction electrons in semiconductor heterostructures together with their charge to realise novel device concepts [1]. It is well known that spin polarized electrons can be generated by circularly polarized light [2] and, vice versa, that the recombination of spin polarized charged carriers results in the emission of circularly polarized light [2–4]. A new property of the electron spin in a spin-polarised electron gas, is that it can drive an electrical current if some general symmetry requirements are met.

In low dimensional systems optical excitation by circularly polarized light not only leads to a spin polarized ensemble of electrons but also to a current whose direction depends on the helicity of the incident light [5]. The coupling of the helicity of the incoming photons to spin polarized final states with a net momentum is caused by angular momentum selection rules together with band splitting in  $\mathbf{k}$ -space due to  $\mathbf{k}$ -linear terms in the Hamiltonian [6]. Due to the spin selection rules the direction of the current is determined by the helicity of the light and can be reversed by switching the helicity from right- to left-handed. This effect belongs to the class of photogalvanic effects [7] and represents the circular photogalvanic effect [8].

Moreover a net in-plane spin polarisation of electrons in a quantum well based on zinc blende structure material is inevitably linked with an electric current in the well. We show that a uniform non-equilibrium spin polarisation  $\mathbf{S}$ , generated by electrical or optical spin injection, results in a current flow [9]. This we denote as ‘spin-galvanic effect’ because of its relationship to other well established transport phenomena like galvano-magnetic or thermo-galvanic effects. The microscopic origin of the effect observed in low-dimensional electron systems is an inherent asymmetry of the spin-flip scattering of electrons. This has been demonstrated by optical orientation of electron spins perpendicular to quantum wells and by Larmor precession of the spins into the plane of the wells by an external magnetic field. In contrast to zero magnetic field circular photogalvanic effect, the appearance of the current in the presence of a magnetic field is caused by the Larmor precession of optically induced magnetic momenta which results in the in-plane component of spins. This current is caused by spin relaxation due to asymmetric spin flip scattering in a two-dimensional structure with spin-split subbands in  $\mathbf{k}$ -space due to  $\mathbf{k}$ -linear terms in the Hamiltonian. The direction of current flow depends on in-plane spin orientation.

These effects occur in gyrotropic media [7]. In materials without inversion center, like III–V or II–VI, the spin degeneracy is naturally removed by reduction of the dimensionality. In materials with an inversion center, like Si or Ge, this effect is absent. However, CPGE becomes possible due to symmetry reduction in QW structures based on these materials. This is demonstrated by experiments where the inversion symmetry was broken by preparation of compositionally stepped QWs and asymmetric doping of compositionally symmetric QWs [10].

Spin photocurrents have been observed in GaAs, InAs, and SiGe QW structures at temperatures varying from 4.2 K to 300 K in a wide spectral range by using a pulsed far-infrared molecular laser delivering 100 ns pulses at wavelengths  $\lambda$  from 35  $\mu\text{m}$  to 280  $\mu\text{m}$  [11], TEA CO<sub>2</sub> laser  $\lambda = 9\text{--}11\ \mu\text{m}$  and Ti:Sapphire laser at  $\lambda = 0.777\ \mu\text{m}$ .

The conversion of spin orientation of carriers into directed motion provides two efficient methods to determine spin relaxation times of electrons in n-type materials and of holes in p-type materials. One of the proposed and realized methods is based on a magnetic-field-induced circular photogalvanic effect observed in GaAs quantum wells [9]. A pronounced peak of the current as a function of the magnetic field is observed which is caused by the Hanle effect and allows to determine directly spin relaxation times for n-type quantum wells. The second method is based on spin sensitive bleaching of the absorption of far-infrared radiation observed in p-type QW structures [12]. The absorption of circularly polarized radiation saturates at lower intensities than that of linearly polarized light due to hole monopolar spin orientation in the first heavy hole subband. Sufficiently long spin dephasing times in semiconductor QW structures are crucially needed for the realization of spintronic devices. Current investigations of the spin lifetime in semiconductor devices are based on optical spin orientation by interband excitation and further tracing the kinetics of polarized photoluminescence [1, 13–15]. These studies gave important insights into the mechanisms of spin relaxation of photoexcited free carriers. In contrast to the conventional methods of optical spin orientation, in our measurements in the terahertz range only one type of charge carriers gets spin oriented and is involved in relaxation processes. Thus monopolar spin orientation allows to study spin relaxation without electron-hole interaction and exciton formation in a condition close to the case of electron spin injection.

#### Acknowledgement

Financial support from the DFG and the RFBR is gratefully acknowledge.

#### References

- [1] S.A. Wolf, D.D. Awschalom, R.A. Buhrman *et al*, *Science* **294**, 1488 (2001).
- [2] *Optical Orientation*, F.Meier and B.P.Zakharchenya, Eds. (Elsevier Science Publ., Amsterdam, 1984).
- [3] R.Fiederling, M.Kleim, G.Reuscher, W.Ossau, G.Schmidt, A.Waag and L.W.Molenkamp, *Nature* **402**, 787 (1999).
- [4] Y.Ohno, D.K.Young, B.Beschoten, F.Matsukura, H.Ohno and D.D.Awschalom, *Nature* **402**, 790 (1999).
- [5] S.D.Ganichev, S.N.Danilov, J.Eroms *et al*, *Phys. Rev. Lett.* **86**, 4358 (2001).
- [6] S.D.Ganichev, E.L.Ivchenko and W.Prettl, *Physica E*, to be published.
- [7] E.L.Ivchenko and G.E.Pikus, *Superlattices and Other Heterostructures. Symmetry and Optical Phenomena*, (Springer, Berlin 1997).
- [8] S.D.Ganichev, H.Ketterl, W.Prettl, E.L.Ivchenko and L.E.Vorobjev, *Appl. Phys. Lett.* **77**, 3146 (2000).
- [9] S.D.Ganichev, E.L.Ivchenko, V.V.Bel'kov, S.A.Tarasenko, M.Sollinger, D.Weiss, W.Wegscheider and W.Prettl, *Proc. MRS Fall Meeting*, Boston, USA (2001).
- [10] S.D.Ganichev, U.Rössler, F.-P.Kalz, W.Prettl, R.Neumann, K.Brunner, G.Abstreiter and E.L.Ivchenko, *Proc. MRS Fall Meeting*, Boston, USA (2001).
- [11] S.D.Ganichev, *Physica B* **273-274**, 737 (1999).
- [12] S.D.Ganichev, S.N.Danilov, V.V.Bel'kov *et al*, *Phys. Rev. Lett.* **88**, 057401-1 (2002).
- [13] T.C.Damen, L.Vina, J.E.Cunningham, J.Shah and L.J.Sham, *Phys. Rev. Lett.* **67**, 3432 (1991).
- [14] L.J.Sham, *J. Phys.: Condens. Matter* **5**, A51 (1993).
- [15] J.Fabian and S.Das Sarma, *J. Vac. Sci. Technol. B* **17**, 1708 (1999).

## Spin polarization dynamics in n-doped InAs/GaAs quantum dots

O. Krebs<sup>†</sup>, S. Cortez<sup>†</sup>, A. Jbeli<sup>‡</sup>, X. Marie<sup>‡</sup>, J-M. Gérard<sup>†</sup>, T. Amand<sup>‡</sup>  
and *P. Voisin*<sup>†</sup>

<sup>†</sup> Laboratoire de Photonique et Nanostructures,  
CNRS route de Nozay, 91460 Marcoussis, France

<sup>‡</sup> Laboratoire de Physique de la Matière Condensée, INSA-CNRS  
135 Avenue de Rangueil, 31077 Toulouse Cedex 4, France

**Abstract.** We report measurements of optical orientation and spin dynamics in doped InAs-GaAs quantum boxes containing one resident electron per dot.

Because of their atomic-like energy spectrum, self assembled quantum dots (QD) appear as ideal candidates for the experimental realization of an elementary quantum gate in the condensed matter [1]. Spin relaxation processes such as motional narrowing and band mixing are supposed to become inefficient in such heterostructures. However, in non intentionally doped QD, the electron hole pair fine structure is strongly affected by the interplay between the exchange interaction and the reduced C<sub>2v</sub> symmetry of the quantum dot. The exciton ground state is characterized by two linearly polarized eigenstates along [110] and  $\bar{1}\bar{1}0$ . Recent experiments [2] performed under strictly resonant excitation demonstrated the stability of the ground-state linear polarization during the whole lifetime of the exciton up to temperatures of 30 K. Under non resonant excitation conditions, the optical orientation of excitons with circularly polarized light experiences a fast decay (a hundred of picoseconds) unless a strong magnetic field is applied. Very little is known about the spin dynamics of a single electron in a quantum dot. Here we report on the optical orientation and polarization dynamics of trions under non resonant excitation in n-doped quantum dots containing an average single resident electron per dot. The negative circular polarization of the luminescence is observed under DC excitation conditions (above the GaAs bandgap) that ensure a complete depolarization of the hole spin. In time resolved measurements, when exciting in the GaAs barrier, the initial positive circular polarization of the luminescence undergoes a fast decay and reverses sign after 10 ps, and then evolves irreversibly down to -25% during the recombination time. Similar features are observed when exciting in the wetting layer, except for a larger absolute value of circular polarization, down to -45% after 2 ns, at the end of recombination. This is simply explained by the more efficient initial polarization of the photo-electron when exciting only a heavy-hole transition. These effects are robust against temperature up to 40 K. In addition, an original non-resonant pump-and-probe experiment shows that the spin relaxation time of the resident electron is of the order of 15 ns. In order to explain these remarkable observations, we consider the dynamics of the hot trion states under the driving forces of exchange interaction, spin-orbit interaction and dot anisotropy. We find that anisotropic e-h exchange couples the triplet and singlet states, and defeats Pauli blocking of the hot trion triplet. Differences between e-h exchange in the bright and dark trions finally explain the observed irreversible evolution.

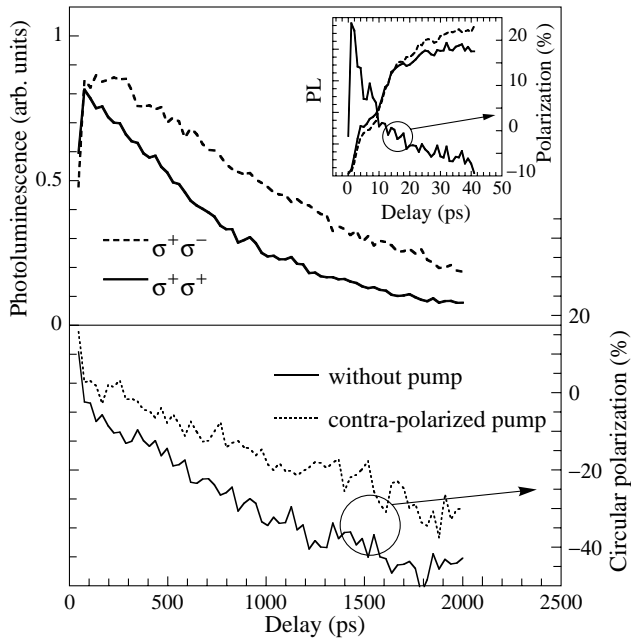


**Fig. 1.** Time dependent circularly polarized luminescence after an excitation in the wetting layer using a pulsed Ti:Sa laser. The polarization reverses sign during the first ten pico seconds (see insert), and increases (in absolute value) irreversibly during the recombination.

## References

- [1] Daniel Loss and Eugene V. Sukhorukov, *Phys. Rev. Lett.* **84**, 1035 (2000).
- [2] M. Paillard, X. Marie, P. Renucci, T. Amand, A. Jbeli and J. M. Gerard, *Phys. Rev. Lett.* **86**, 1634 (2001).
- [3] V. K. Kalevich and M. N. Tkachuk, P. Le Jeune, X. Marie and T. Amand, *Phys. Solid State* **41**, 789 (1999).

## Gateable spin memory in InP quantum dots

*I. A. Yugova*<sup>†</sup>, *I. V. Ignatiev*<sup>†</sup>, *S. Yu. Verbin*<sup>†</sup>, *I. Ya. Gerlovin*<sup>‡</sup>, *V. K. Kalevich*<sup>§</sup>,  
*A. Yu. Shiryaev*<sup>§</sup>, *K. V. Kavokin*<sup>§</sup> and *Y. Masumoto*<sup>¶</sup>

<sup>†</sup> Institute of Physics, St Petersburg State University, St Petersburg  
198904, Russia

<sup>‡</sup> Vavilov State Optical Institute, St Petersburg, 190034, Russia

<sup>§</sup> Ioffe Physico-Technical Institute, St Petersburg, Russia

<sup>¶</sup> Institute of Physics, University of Tsukuba, 305-8571, Japan

**Abstract.** In photoluminescence kinetics of the InP quantum dots, we have found a long-lived component of the degree of circular polarization, showing practically no decay during the lifetime of excitation. It is shown that this effect is observed only in the charged quantum dots. The amplitude of the long-lived PL polarization can be controlled by an applied electric field and may be as high as 50% in the case of quasi resonance excitation. The existence of the long-lived component of the polarization is the clear evidence of large lifetime of the electron spin polarization in quantum dots.

Quantum dots (QDs) structures have been suggested as the basis for making pilot devices of spin electronics [1]. Localization of carriers eliminates the impact of spatial motion on their spin state via spin-orbit interaction, and, for this reason, greatly reduces the spin relaxation rate. In the case of photocreated carriers, the spin lifetime is limited not only by spin relaxation but also by recombination of the carriers with typical times of about 1 ns. For this reason, the doped QDs, where majority (equilibrium) carriers are permanently present, attract much interest. Relatively long spin relaxation times in the presence of equilibrium electrons in the sample studied are observed recently for bulk semiconductors [2, 3] as well as for InAs QDs [4].

In this work, we studied the heterostructures with the InP QDs, whose charge state could be varied with an applied electric field. We found that the presence of excess (resident) charges in the QDs leads to appearance of long-lived spin states, which can be observed by the circularly polarized photoluminescence (PL). We show that the long-lived spin memory may be switched on and off by deliberately changing the charge state of the QDs.

We studied a heterostructure with a single layer of InP QDs sandwiched between the  $\text{In}_{0.5}\text{Ga}_{0.5}\text{P}$  barrier layers. The sample was grown by the gas source molecular beam epitaxy on an  $n^+$  GaAs substrate. The areal density of the QDs is about  $10^{10} \text{ cm}^{-2}$ . The average base diameter of the QDs is  $\approx 40 \text{ nm}$  and the height is  $\approx 5 \text{ nm}$ . In order to control the charge of the QDs, the sample was provided with a semitransparent indium tin oxide Schottky contact on the top surface and with an Ohmic contact on the bottom. Thickness of the undoped epitaxial layers, to which the electric voltage was applied, was about  $0.5 \mu\text{m}$ .

In kinetic studies, the luminescence was excited by a 3-ps pulses of a Ti:sapphire laser within the PL band (quasi-resonant excitation) as shown in the inset of Fig. 1(a). The PL kinetics was measured with a time resolution of 6 ps using a 0.25 m subtractive double monochromator and a streak camera. The measurements were made in a cryostat with a superconducting magnet. The design of the cryostat allowed us to excite the sample and to detect its emission either along the magnetic field direction (the Faraday configuration)



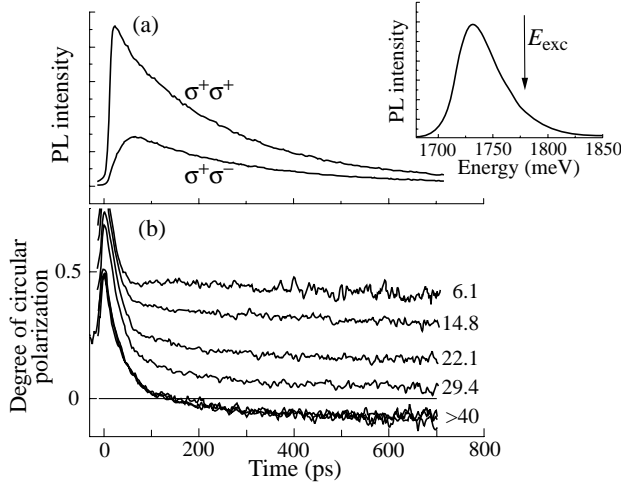


**Fig. 1.** (a) PL kinetics in co- ( $\sigma^+\sigma^+$ ) and cross- ( $\sigma^+\sigma^-$ ) circular polarizations.  $U_{bias} = 0$  V,  $E_{Stokes} = 6$  meV. (b) Degree of circular polarization of the PL at different Stokes shift shown against each curve (in meV). Inset: PL spectrum of the InP QDs. Excitation energy is shown by arrow.

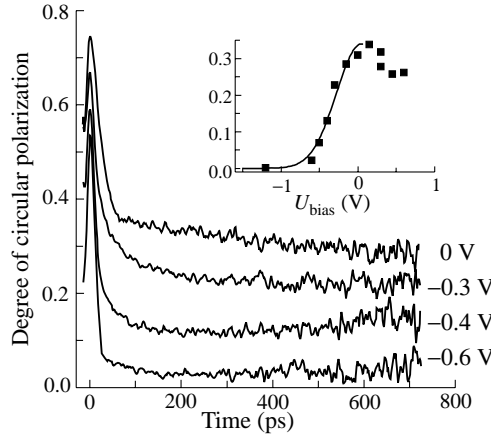


**Fig. 2.** Degree of circular polarization of the PL at different  $U_{bias}$  shown against each curve. Inset: Bias dependence of amplitude of the long-lived polarization component (squares). Solid line is the fit by a Gaussian.  $E_{Stokes} = 14$  meV.

or across the field (the Voigt configuration). The PL was detected in the backscattering geometry.

Figure 1 shows the PL kinetics of the InP QDs measured in different circular polarizations under circularly polarized excitation. The time dependence of the degree of circular polarization of the PL for different spectral points is shown in Fig. 1(b). The polarization degree is calculated in a standard manner:  $(\rho_\sigma = (I_+ - I_-)/(I_+ + I_-))$ , where  $I_+$  and  $I_-$  are the PL intensities in the co- and counter-polarized light, respectively. One can notice the long-lived polarization component, which virtually does not depend on time during the PL lifetime. The amplitude of this component lies in the range of tens of percents for small Stokes shift. It decreases with increasing Stokes shift and even becomes negative.

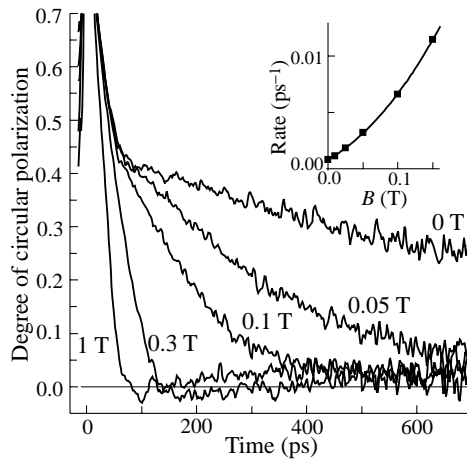


**Fig. 3.** Degree of circular polarization of the PL obtained in Voigt geometry at different magnetic fields shown against each curve.  $U_{\text{bias}} = -0.15$  V. Magnetic field dependence of decay rate of the long-lived component is shown in the inset.

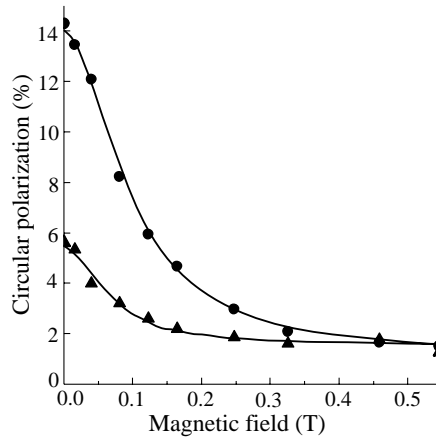


**Fig. 4.** Degree of circular polarization vs transverse magnetic field (Hanle effect) under cw excitation in the barriers ( $E_{\text{exc}} = 1.96$  eV) for the charged (circles) and neutral (triangles) QDs. Solid lines are the fits by the function  $\rho(B) = \rho(0)/(1 + (B/B_{1/2})^2)$  with  $B_{1/2} = 0.093$  T and 0.051 T for the charged and neutral QDs, respectively.

The negative circular polarization was observed in PL of the negatively charged InP [5] and InAs QDs [4].

Key result of the present work is the dependence of the long-lived component of the PL polarization,  $\rho_{\text{slow}}$ , on the applied bias (see Fig. 2). It is clearly seen that the value  $\rho_{\text{slow}}$  rapidly drops with increasing negative voltage and vanishes at  $U_{\text{bias}} < -0.5$  V. At small positive bias, the amplitude of this component remains approximately the same and slightly decreases at  $U_{\text{bias}} > 0.5$  V (see Inset in Fig. 2), which is likely to be related to abrupt increase of the current through the sample.

It has been shown in Refs. [6, 7] that the InP QDs in the structure under study contain excess charges (electrons) arrived from the doped substrate. The negative voltage removes these electrons, so that the QDs become neutral under the voltage  $U_{\text{bias}} < -0.5$  V. Therefore

one can conclude that the long-lived circular polarization of the PL is observed only for the QDs with excess charges.

The presence of the long-lived circular polarization indicates the high spin stability of the carriers in the charged QDs. The experiments have shown that the long-lived circular polarization of the PL can be efficiently suppressed by a transverse magnetic field (normal to the  $z$  axis). We have studied both the kinetics of the polarized PL (see Fig. 3), and the dependence of the degree of circular polarization on the magnetic field strength under cw excitation (the Hanle effect, see Fig. 4). In both cases, the polarization is suppressed in the fields  $B = 0.05 \div 0.1$  T. The analysis of the curves presented in Fig. 4 in the framework of the simplest model of the Hanle effect in a homogeneous ensemble of optically oriented electrons [8] yields the spin relaxation time  $\tau_s \sim 100$  ps with the known value of the electron  $g$ -factor  $g = 1.6$  [9]. Obtained value of  $\tau_s$ , however, strongly differs from the spin relaxation time (longer than 1 ns) found from kinetics of the PL polarization in zero magnetic field. It follows from here that the model of homogeneous ensemble of electrons is not applicable in this case.

We suggest that this discrepancy in relaxation times is explained by random spread of the number of resident carriers in QDs. The QDs with different number of electrons are characterized by different energy structure which exhibit different splittings in the magnetic field. A coherent excitation of the split components will produce quantum beats at different frequencies. Their destructive interference will cause a fast decay in the degree of PL polarization, which is observed in the kinetic experiments (see Fig. 3).

Thus, in this study, we demonstrate existence of a long-lived spin memory in the charged quantum dots which can be easily controlled with an applied voltage.

#### Acknowledgments

The study was supported by the Program of Presidium of the Russian Academy of Sciences "Low-Dimensional Quantum Structures", by the Program of the Ministry of Industry, Science and Technology "Physics of Solid-State Nanostructures", and by the Russian Foundation for Basic Research, projects Nos. 00-02-17354 and 00-15-96756.

#### References

- [1] A. Imamoglu, D. D. Awschalom, G. Burkard, D. P. Divincenzo, D. Loss, M. Sherwin and A. Small, *Phys. Rev. Lett.* **83**, 4204 (1999).
- [2] R. I. Dzioev, B. P. Zakharchenya, V. L. Korenev and M. N. Stepanova, *Fiz. Tverd. Tela* **39**, 1775 (1997) [*Phys. Solid State*, 39, 1765 (1997)].
- [3] J. M. Kikkawa and D. D. Awschalom, *Phys. Rev. Lett.* **80**, 4313 (1998).
- [4] S. Cortez, A. Jbeli, X. Marie, O. Krebs, R. Ferreira, T. Amand, P. Voisin and J-M. Gerard, *Proc. MSS10 Int. Conf. on Modulated Semiconductor Structures*, 23-27 July 2001, Linz, Austria, to be published in *Physica E* (2002).
- [5] R. I. Dzioev, B. P. Zakharchenya, V. L. Korenev, P. E. Pak, D. A. Vinokurov, O. V. Kovalenkov and I. S. Tarasov, *Fiz. Tverd. Tela* **40**, 1745 (1998) [*Phys. Solid State*, 40, 1587 (1998)].
- [6] Y. Masumoto, I. V. Ignatiev, I. E. Kozin, H. W. Ren and S. Sugou, *Jpn. J. Appl. Phys.* **40**, 1947 (2001).
- [7] I. E. Kozin *et al*, unpublished.
- [8] *Optical Orientation*, edited by F. Meier and B. Zakharchenya, Modern Problems in Condensed Matter Sciences Vol. 8 (North-Holland, Amsterdam, 1984).
- [9] A. A. Sirenko, T. Ruf, A. Kurtenbach and K. Eberl, *23rd Int. Conf. on the Physics of Semiconductors*, Berlin (1996), Vol. 2, P. 1385.

## Spin orientation of two-dimensional electron gas under intraband optical pumping

*S. A. Tarasenko* and E. L. Ivchenko

Ioffe Physico-Technical Institute, St Petersburg, Russia

**Abstract.** The theory of spin orientation of two-dimensional (2D) electron gas has been developed for intrasubband indirect optical transitions. The monopolar optical orientation of electrons in the conduction band is caused by the indirect scattering with virtual intermediate states in the valence band and allowance for selection rules for interband transitions. The considered mechanism of optical orientation is shown to be in an inherent relation with the special Elliot-Yafet mechanism of electron spin relaxation induced by virtual interband scattering.

### 1. Introduction

In recent years spin-dependent phenomena in low-dimensional structures attract a great attention. One of the problems of common interest is a possibility and methods of the spin polarization in systems with a two-dimensional electron gas. The conventional way to achieve the spin polarization experimentally is the optical orientation of electron spins [1]. Under optical excitation with the circularly polarized light the direct transitions from the valence to the conduction band are allowed only if the angular momentum is changed by  $\pm 1$ . These selection rules lead to the spin orientation of optically excited electrons, with the sign and the degree of polarization depending on the light helicity.

Up to now the theoretical consideration of the optical spin orientation was focused on direct interband transitions [1] and, partially, on direct intersubband transitions in the complicated valence band  $\Gamma_8$  of a zinc-blende lattice semiconductor [2]. Here we report for the first time a theory of optical spin orientation under the indirect intrasubband excitation of electron gas by circularly polarized light and give an estimate of the spin generation rate. Note that the "monopolar" optical orientation under consideration can serve as a model of spin injection because the only type of carriers, electrons, is involved.

In addition, the short-range Elliot-Yafet mechanism of electron spin relaxation considered previously only for bulk semiconductors ([1], ch. 3) is extended to quantum-well structures. This spin-relaxation mechanism is shown to be governed by the same interband matrix elements of the electron-phonon or electron-defect interaction as those which govern the indirect intrasubband optical orientation.

### 2. Monopolar optical orientation of electron gas

The light absorption under intrasubband excitation in quantum wells (Drude-like absorption) is possible only if it is assisted by a phonon or a static imperfection in order to satisfy simultaneously both the energy and momentum conservation laws.

Theoretically, these indirect optical transitions with initial and final states in the same conduction subband  $n$  are described by second-order processes with virtual intermediate states. The compound matrix element for the indirect optical transition has the standard

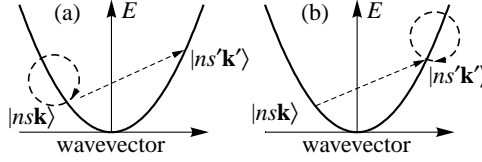


**Fig. 1.** The schematic representation of indirect intrasubband optical transitions with intermediate states in the same subband. Dashed and dotted curves indicate the electron-photon interaction and the electron momentum scattering. Figures (a) and (b) account for the first and the second terms in Eq. (1).

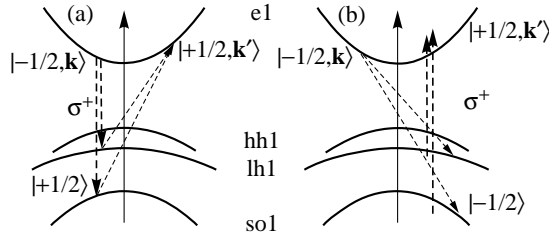


**Fig. 2.** The sketch of indirect intrasubband optical transitions with intermediate states in the valence band.

form

$$M_{ns'\mathbf{k}' \leftarrow ns\mathbf{k}} = \sum_v \left( \frac{V_{ns'\mathbf{k}', v\mathbf{k}} R_{v\mathbf{k}, ns\mathbf{k}}}{E_{v\mathbf{k}} - E_{n\mathbf{k}} - \hbar\omega} + \frac{R_{ns'\mathbf{k}', v\mathbf{k}'} V_{v\mathbf{k}', ns\mathbf{k}}}{E_{v\mathbf{k}'} - E_{n\mathbf{k}}} \right), \quad (1)$$

where  $E_{n,\mathbf{k}}$ ,  $E_{n,\mathbf{k}'}$  and  $E_v$  are the electron energies in the initial  $|n, s, \mathbf{k}\rangle$ , final  $|n, s', \mathbf{k}'\rangle$  and intermediate  $|v\rangle$  states,  $s$  is the spin index,  $\mathbf{k}$  is the electron wavevector,  $R$  is the electron-photon matrix element,  $V$  denotes the matrix element of interaction which allows the momentum transfer, e.g. scattering from impurities or phonon-assisted scattering. In the latter case the photon energy  $\hbar\omega$  is assumed to exceed the energy of an involved phonon.

The most probable processes are the transitions with intermediate states in the same subband (Fig. 1). This is the channel that determines the light absorption. However such transitions conserve the electron spin and, hence, *do not* contribute to the optical orientation.

In order to obtain the spin orientation of electron gas under intrasubband optical transitions one should take into account the virtual processes with intermediate states in the valence band, namely in the heavy, light and spin-split hole subbands. We assume that the carriers occupy the lowest electron subband  $e1$ . Then in the case of the flat QW with infinite barriers, the interband optical transitions between the  $e1$  and  $v$  states are allowed only for the hole subbands  $v = hh1, lh1$  and  $so1$ . Fig. 2 demonstrates schematically the spin orientation under the  $\sigma^+$  normal-incidence excitation. In this case only the light and spin-split hole subbands contribute to the optical orientation. Because of the selection rules for interband matrix element, the electron transitions with the spin reversal  $|e1, -1/2\rangle \rightarrow |e1, +1/2\rangle$  occur via the intermediate states  $|lh1, \pm 1/2\rangle$  and  $|so1, \pm 1/2\rangle$ ,

while the inverse processes  $|e1, +1/2\rangle \rightarrow |e1, -1/2\rangle$  are forbidden. While examining the optical orientation under oblique incidence, the heavy hole subband should also be taken into account as an intermediate state.

We consider the conduction electrons to form a nondegenerate 2D gas at the temperature  $T$  or a degenerate 2D gas with the Fermi energy  $\varepsilon_F$ , the interaction  $V$  to describe the electron scattering by bulk acoustic phonons. Then an expression for the spin generation rate at  $\hbar\omega \gg k_B T$  or  $\varepsilon_F$  ( $k_B$  is Boltzmann's constant) has the form

$$\dot{S} = \frac{1}{6} \frac{\Xi_{cv}^2}{\Xi_c^2} \frac{\Delta_{so}^2}{E_g(E_g + \Delta_{so})(3E_g + 2\Delta_{so})} \left[ \mathbf{o}_{\parallel} + \frac{a}{3} \sqrt{\frac{2m^*\omega}{\hbar}} \mathbf{o}_z \right] \eta I_0 P_{circ}. \quad (2)$$

Here  $\Xi_{cv}$  and  $\Xi_c$  denote the interband and intraband deformation potential constants,  $\Delta_{so}$  and  $E_g$  stand for the energies of the spin-splitting and the band gap,  $a$  is the width of the quantum well,  $m^*$  is the electron effective mass,  $I_0$  and  $P_{circ}$  are the light intensity and the degree of circularly polarization inside the sample,  $\mathbf{o}_{\parallel}$  and  $\mathbf{o}_z$  are the in-plane and  $z$  components of the unit vector  $\mathbf{o}$  in the light propagation direction. The factor  $\eta$  in Eq. (2) is the fraction of the light energy flux absorbed in the QW under phonon-assisted intrasubband optical transitions calculated for intermediate states in the same conduction subband, it is given by

$$\eta = \frac{3\pi\alpha}{n_\omega} \left( \frac{\Xi_c}{\hbar\omega} \right)^2 \frac{k_B T}{\rho a v_s^2} N_e, \quad (3)$$

where  $\alpha$  and  $n_\omega$  are the fine structure constant ( $\approx 1/137$ ) and the refraction index of the medium,  $\rho$  is the crystal density,  $v_s$  is the sound velocity, and  $N_e$  is the 2D carrier concentration.

An estimation for typical GaAs/AlGaAs structures shows that, at the comparable light intensities, the spin generation rate under intrasubband phonon-assisted optical transitions is by a factor of  $10^{-4} - \div 10^{-5}$  smaller than that under interband excitation. However, consideration of other mechanisms of electron scattering, e.g. by impurity-assisted coupling, can essentially increase this ratio.

### 3. Spin relaxation mechanism induced by interband scattering

Besides the monopolar optical orientation, the virtual interband scattering described by the constant  $\Xi_{cv}$  can lead to a short-range mechanism of spin relaxation of the 2D electron gas. Microscopically this mechanism is connected with the  $\mathbf{kp}$ -induced admixture of the valence band states,  $\Gamma_8$  and  $\Gamma_7$ , into the wave function of the conduction band  $\Gamma_6$  and the phonon- or defect-assisted interband coupling of these states. For bulk semiconductors this short-range Elliot–Yafet mechanism of electron spin relaxation was considered by Pikus and Titkov (see [1], ch. 3).

The spin relaxation time due to the mechanism under consideration can be calculated using the spin-flip matrix element (1) where  $v$  are the valence band states  $v = hh1, lh1$  and  $so1$  and, in the matrix element  $R_{v\mathbf{k},ns\mathbf{k}} = -(e/cm_0)\mathbf{A}p_{v,ns}$ , the vector  $(-e/c)\mathbf{A}$  is replaced by the in-plane momentum  $\hbar\mathbf{k}$ . Here  $e$  is the electron charge,  $c$  is the light velocity in vacuum and  $\mathbf{A}$  is the amplitude of the vector potential of the electro-magnetic wave.

Assuming the interband coupling  $V$  to be caused by scattering on bulk acoustic phonons one can derive the relaxation rates for the in-plane and  $z$  electron spin components which, after the averaging over the Boltzmann distribution, take the form

$$\frac{1}{\tau_{s\parallel}} = \frac{1}{6} \frac{\Xi_{cv}^2}{\Xi_c^2} \frac{\Delta_{so}^2 k_B T}{E_g(E_g + \Delta_{so})(3E_g + 2\Delta_{so})} \frac{1}{\tau_p}, \quad (4)$$

$$\frac{1}{\tau_{sz}} = \frac{2\sqrt{\pi}a}{3} \sqrt{\frac{2m^*}{\hbar^2}} k_B T \frac{1}{\tau_{s\parallel}}, \quad (5)$$

where the momentum relaxation time determined by the acoustic phonon-assisted scattering is given by

$$\frac{1}{\tau_p} = \frac{3}{2} \frac{m^* \Xi_c^2}{\rho a v_s^2 \hbar^3} k_B T. \quad (6)$$

One can see that, in case of the scattering by acoustic phonons, the spin relaxation of the 2D electron gas governed by the short-range Elliot–Yafet mechanism is very anisotropic,  $\tau_{s\parallel} \ll \tau_{sz}$ .

#### Acknowledgements

This work was supported by the Russian Ministry of Science, the RFFI (projects 00-02-16997 and 01-02-17528), the INTAS (project 99-00015), and by the Science Programme of the Presidium of RAS “Quantum low-dimensional structures”.

#### References

- [1] *Optical orientation*, eds. F. Meier and B. P. Zakharchenya, North Holland, 1984 [Russian edition: Leningrad, Nauka, 1989].
- [2] A. M. Danishevskii, E. L. Ivchenko, S. F. Kochegarov and V. K. Subashiev, *Fiz. Tverd. Tela* **27**, 710 (1985).

## The picosecond time scale spin-polarized electron kinetics in thin semiconductor layers

K. Aulenbacher<sup>†</sup>, J. Schuler<sup>†</sup>, D. v. Harrach<sup>†</sup>, E. Reichert<sup>‡</sup>, J. Röthgen<sup>†</sup>,  
A. Subashiev<sup>§</sup>, V. Tioukine<sup>†</sup> and Y. Yashin<sup>§</sup>

<sup>†</sup> Institut für Kernphysik der Univ. Mainz, J.J. Becherweg 45,  
D-55099 Mainz, Germany

<sup>‡</sup> Institut für Physik der Univ. Mainz, Staudingerweg-7, D-55099 Mainz, Germany

<sup>§</sup> State Technical University, 195251, St. Petersburg, Russia

**Abstract.** Time resolved photoemission of highly spin-polarized electrons from thin strained and unstrained GaAs<sub>x</sub>P<sub>1-x</sub> films of various thicknesses has been investigated. An upper limit for the response time of a photocathode has been found to be 1 ps for layer thicknesses less than 150 nm. We show that the electron depolarization during the electron extraction to the surface band bending region can be as low as 2% while the losses in the band bending region can contribute to 4% spin relaxation.

### 1. Introduction

The electron spin kinetics in semiconductor heterostructures is actively investigated for the development of new spintronics devices [1], the control over spin transport of the electrons through the working layer being among the priorities [2]. The other important area of the polarized electron application is for the sources of highly polarized electrons at electron accelerator facilities [3–5]. In both cases the spin depolarization mechanisms of the electrons are of interest.

In this work the depolarization factors in GaAs-based strained and unstrained layers are investigated by time-resolved photoemission. The pulse-response experiments reported here enable us to obtain direct estimation for spin relaxation during electron escape from the active layer, to evaluate depolarization in the band bending region and the capture probability of electrons at the surface to the well in the band bending region. We demonstrate that the polarization losses in the active layer are considerably lower than estimated from the polarization dependence on the active layer thickness.

### 2. Experimental

The photocathode structures fabricated at the St. Petersburg Ioffe institute were: (i) gradient doped strained layer photocathodes with an active layer of 150 nm-thick strained GaAs<sub>0.97</sub>P<sub>0.03</sub> grown on a GaAs<sub>0.72</sub>P<sub>0.28</sub> buffer layer p-doped to  $7 \times 10^{17} \text{ cm}^{-3}$  and the 10 nm top layer heavily p-doped at a level of  $1 \times 10^{19} \text{ cm}^{-3}$ ; (ii) gradient and homogeneously doped unstrained GaAs layers grown by MBE on GaAs substrate with varying thicknesses in the range from 100 to 1600 nm.

To obtain the negative electron affinity surface the samples were activated by Cs and O deposition. Quantum efficiency for the thinnest structure was about 0.5% ( $3.5 \mu\text{A/mW}$  for 850 nm radiation). All experiments were done at room temperature.

The electron pulses were generated by subpicosecond light pulses from a titanium-sapphire laser. The laser wavelength (850 nm for GaAs and 830 nm for strained GaAsP)



was chosen to be at approximately  $E_{\text{gap}} + 45$  meV which is within the polarization maximum in the emitted current. These light pulses were synchronized to the output of a klystron driving a microwave deflection cavity. By passing the cavity, the temporal (longitudinal) profile of the electron bunches was transferred into a transverse one by the deflection. To analyze the pulse profile we employed phase shifting of the laser-pulses with respect to the r.f. and then measured the current that was transmitted through a small slit at each phase point. A time-resolved polarization is obtained by measurement of the spin polarization of the transmitted electrons with a Mott-polarimeter. Details of the apparatus are described in [6].

The apparative time resolution of the measurements which was determined mainly by the finite beam size on the analyzer slit and the laser pulse width was estimated to be  $\tau_{\text{app}} = 2.0 \pm 0.4$  ps. An additional limitation stems from the electron acceleration time dispersion. The kinetic energy of electrons starting from a NEA-surface could range from zero (vacuum-level) up to the value of the negative electron affinity. Because of the finite extraction field electrons with different initial energies will show up with different arrival times at the detection system. This effect will systematically increase the detectable minimum pulse length. One of the largest widths reported for the kinetic energy distribution of GaAs is 250 meV [7]. Assuming this value the maximum possible time difference for our extraction field (0.9 MV/m) is estimated as  $\tau_{\text{atd}} = 1.8$  ps. A reduction of the energy width to 50 meV would lead to  $\tau_{\text{atd}} = 0.8$  ps. Therefore the minimum observable pulse length for a delta pulse from the photocathode  $\tau_{\text{min}} = \sqrt{\tau_{\text{app}}^2 + \tau_{\text{atd}}^2}$  depends on the photocathode surface conditions and could vary between  $\tau_{\text{min}} = 1.6$  and  $\tau_{\text{min}} = 3.0$  ps. The experimental observations suggest that the typical  $\tau_{\text{min}}$  was between 2 and 2.5 ps.

### 3. The response time of thin GaAs layers

Figure 1 shows the emission current pulse shapes for two homogeneously doped GaAs layers with different thickness. From the pulse profiles the time interval which includes 90% of the emitted charge ( $t_{90}$ ) was extracted for all structures. A strong decrease of the response time in the thin-layer samples was observed. For layer thicknesses below 200 nm the temporal structure of the electron pulse becomes nearly unobservable because of the limited temporal resolution. Taking into account the value of  $\tau_{\text{min}}$ , the upper limit for the response time of the strained layer photocathode can be determined to  $t_{90} < 2.5$  ps. The variation of  $t_{90}$  as a function of thickness is shown in Fig. 2(a). Almost quadratic increase in the

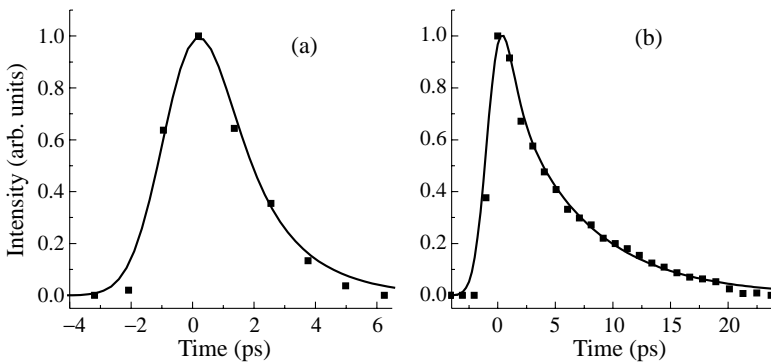


**Fig. 1.** Pulse-responses for (a) 200 nm- and (b) 400 nm-thick samples. Solid lines are the results of model calculations.

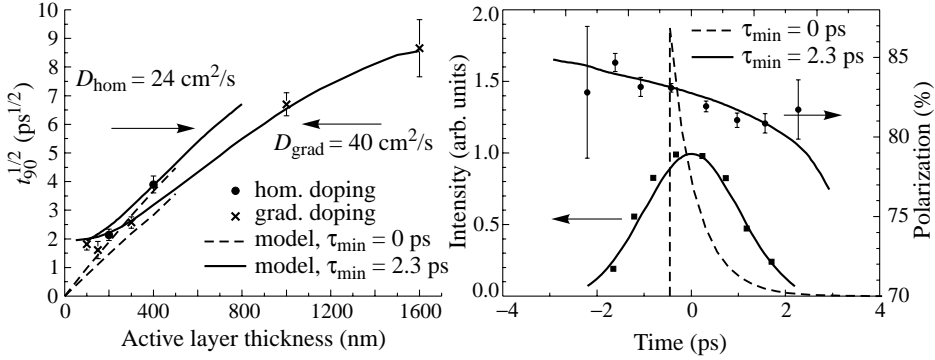


**Fig. 2.** Response-time  $t_{90}$  as a function of layer thickness (a) and time response and depolarization of a strained layer photocathode (b); solid lines: calculated intensities and polarizations based on  $I(E)$  and  $P(E)$  distributions from [9].

thickness-range between 200 and 1000 nm is observed. The small deviation from quadratic behavior can be explained by two effects. For low thicknesses experimental resolution is the major limiting factor, while for large thicknesses the response time saturates. This could be caused by carrier recombination in the sample.

The experimentally observed responses were fitted with calculations using the diffusion model of [8]. The fixed input parameters are the layer thicknesses and the absorption constant of GaAs for 850 nm radiation  $\alpha = 7 \times 10^3 \text{ cm}^{-1}$ . The diffusion constants were used as free fit parameters, but only one diffusion constant was used for a group of cathodes with the same doping level. Estimated values of the diffusion constants are  $D_{\text{hom}} = 24 \text{ cm}^2/\text{s}$  for the homogeneously and  $D_{\text{grad}} = 40 \text{ cm}^2/\text{s}$  for the gradient doped samples. To obtain a good fit for the two thickest samples the introduction of a carrier recombination time of  $\tau_{\text{rec}} = 100 \text{ ps}$  was needed, the influence of  $\tau_{\text{rec}}$  being negligible for the fitting of the thinner samples.

The other fitting result is a high effective surface recombination velocity (the lower limit for it can be estimated as  $s_{\text{min}} = 2d/t_{90}$ ). The obtained value of  $s_{\text{min}} \geq 1.2 \times 10^7 \text{ cm/s}$  correlates with the capture velocity evaluated from the electron average thermal flux to the surface indicating  $\geq 90\%$  probability for the electron capture to the band bending region.

#### 4. Strained layers and depolarization effects

In Fig. 2(b) the response in current and spin-polarization for a strained 150-nm thick layer cathode structure is presented. The depicted dependence shows a relative decrease of spin-polarization of 4.5% during 2.5 ps. Spin relaxation during the electron extraction to the surface can be estimated using the results for the emitted electron polarization observed in case of dc-operation  $P = P_0 \tau_s / (\tau_s + t_{\text{av}})$  where  $P_0$  is the initial polarization,  $t_{\text{av}}$  is the average extraction time from the layer to the surface, and  $\tau_s$  is the electronic spin-relaxation time. For the thin strained layer cathode the bulk depolarization effects cannot be disentangled from the energy correlated effects in the band bending region. This can be achieved for the thicker structures where bulk-depolarization can be measured on a much longer timescale. The shortest depolarization time measured in our apparatus was 52 ps, in agreement with values gained from photoluminescence techniques.

For the strained layer structure we have demonstrated that the average time  $t_{\text{av}} \approx t_{90}/2$  is of the order of one picosecond or even smaller, hence the contribution of conduction band transport to the relative loss of polarization is estimated to be  $\Delta P/P_0 \leq 2\%$  which

is considerably lower than the values estimated from the polarization dependence on the layer thickness possibly because of the strain relaxation with the thickness growth [10].

The observed values of the depolarization can be explained by the fact that the measurement is done on a distribution in time that is generated by the acceleration time dispersion of  $\tau_{\text{atd}}$ . The data sampled with the experimental resolution  $\tau_{\text{exp}}$  will therefore be correlated with the energy distribution of the electrons: electrons registered at early times will tend to have higher kinetic energy. Low initial kinetic energies correspond to inelastic scattering processes in the band bending region. These inelastic processes and subsequent photoemission can happen on a subpicosecond time-scale and therefore will not add an observable time dispersion. On the other hand these processes are associated with depolarization: the distribution of spin-polarization  $P(E)$  measured with an electron-spectrometer for our type of samples [9] yields total depolarization over all energy band of about 7%.

In Fig. 2(b) we have simulated the effect of the  $I(E)$  and  $P(E)$ -distributions from [9] together with the averaging that is caused by the diffusive time dispersion of the photocathode and the experimental resolution. Close fitting to the experimental results imply that the observed values of depolarization can indeed be caused by a  $P(E)$ -distribution.

## 5. Conclusions

The pulse response length of NEA-GaAs photocathodes for the thicknesses less than 200 nm is shown to decrease below 2 ps which is for the minimized doping concentration in the active region at least a factor 30 faster than the spin relaxation time in the bulk. Therefore the strained layer photocathodes with their inherent thickness limit of about 150 nm are relatively free of depolarization effects in the bulk of their active region. Strained layer photocathodes offer ultrafast response and high spin-polarization what may not only be useful in fundamental science but also for possible opto-spintronic devices.

### Acknowledgments

We want thank A. S. Terekhov for directing our attention on the kinetic energy distribution problem for experimental resolution. This work was supported by the Deutsche Forschungsgemeinschaft within the framework of the Sonderforschungsbereich 443, by the European Union through INTAS grant 99-00125 and also by the Russian Found for Basic Research under grant 00-02-16775.

## References

- [1] S. Das and B. Datta, *Appl. Phys. Lett.* **56**, 665 (1990);  
M. Oestreich, *Nature* **402**, 735 (1999).
- [2] D. Hägle, M. Oestreich *et al*, *Appl. Phys. Lett.* **73** 1580 (1998);  
M. E. Flatte and G. Vignale, *Appl. Phys. Lett.* **78**, 1273 (2001).
- [3] R. Alley *et al*, *Nucl. Instr. and Meth.* **A365**, 1 (1995).
- [4] K. Aulenbacher, Ch. Nachtigall *et al*, *Nucl. Instr. and Meth.* **A391**, 498 (1997).
- [5] Ch. Sinclair, *Intern. Workshop on Polarized Sources and Targets* eds. A. Gute *et al*, Erlangen p. 222, 1999.
- [6] P. Hartmann *et al*, *Nucl. Instr. and Meth.* **A 379**, 15 (1996).
- [7] D. Orlov, M. Hoppe *et al*, *Appl. Phys. Lett.* **78**, 2721 (2001).
- [8] P. Hartmann, J. Bermuth *et al*, *J. Appl. Phys.* **86**, 2245 (1999).
- [9] Yu. A. Mamaev, A. V. Subashiev *et al*, *Sol. State Comm.* **114**, 401 (2000).
- [10] H. Aoyagi *et al*, *Phys. Lett. A* **167**, 415 (1992).

## Spin splitting and interband photogalvanic effect in quantum wells

*L. E. Golub*

Ioffe Physico-Technical Institute, St Petersburg, Russia

**Abstract.** Circular photogalvanic effect under interband absorption in quantum wells is considered. The photocurrent is calculated as a function of light frequency for direct transitions between ground electron and hole size-quantized subbands. It is shown that the current spectrum near the absorption edge depends dramatically on the form of spin-orbit interaction: it is a linear function of photon energy in the case of structure inversion asymmetry induced spin-splitting, and it has a parabolic dependence when bulk inversion asymmetry dominates. At higher energies, the existence of a peak in the photocurrent spectrum is predicted.

### 1. Introduction

Circular photogalvanic effect is a transformation of the photon angular momentum into a directed motion of charge carriers. This leads to an appearance of electric current under absorption of a circularly-polarized light. The photocurrent reverses its direction under inversion of the light helicity, and its magnitude is linear in the absorbed radiation intensity.

Microscopically, the circular photocurrent appears owing to a correlation between the orbital and spin degrees of freedom. In bulk semiconductors and nanostructures, the correlation is a consequence of the spin-orbit interaction. This makes investigations of photogalvanic effects very important since spin properties attract now big attention in connection with interesting proposals of spintronic devices.

Photogalvanic effects in nanostructures started to be investigated recently [1]. However the experiments were performed only under intraband excitations. This technique is not commonly used, and measurements in this frequency range can be done only in a few laboratories around the world. Optical range is more suitable for optical study of semiconductors and nanostructures. The present work is devoted to a development of the corresponding theory.

### 2. Theory

Let us consider optical excitation of a quantum well (QW) by a circularly-polarized light. We investigate here the contribution to the photocurrent arising owing to the asymmetry of the momentum distribution of carriers in the moment of creation. The electric current is expressed in terms of the velocity operators and spin density matrices of electrons and holes:

$$j_i = e \sum_{\mathbf{k}} \text{Tr} \left[ v_e^i(\mathbf{k}) \rho^{(e)}(\mathbf{k}) - v_h^i(\mathbf{k}) \rho^{(h)}(\mathbf{k}) \right]. \quad (1)$$

Here  $e$  is the electron charge,  $i = x, y$  are the directions in the plane of QW, and the growth axis  $z$  coincides with the direction [001].

Density-matrix equations taking into account both direct optical transitions and elastic scattering give the following expressions for linear in the light intensity values entering

into Eq.(1)

$$\rho_{nn'}^{(e,h)} = \pm \frac{\pi}{\hbar} \tau_{e,h} \sum_s M_{ns} M_{sn'} [\delta(E_n + E_s - \hbar\omega) + \delta(E_{n'} + E_s - \hbar\omega)] . \quad (2)$$

Here  $\tau_e$  and  $\tau_h$  are the momentum relaxation times of electrons and holes,  $\hbar\omega$  is the photon energy,  $M_{ns}$  is the matrix element of the direct optical transition between the subbands  $n$  and  $s$ , and the energy dispersions  $E_{n,s}(\mathbf{k})$  are reckoned inside the bands.

Spin splittings of electron or hole subbands give rise to the circular photogalvanic effect. In order to have non-zero photocurrent, it is enough to include spin-orbit interaction for only one kind of carriers. Here we take into account spin-orbit splitting in the conduction band. In QWs, it is described by a linear in the wavevector Hamiltonian

$$H(\mathbf{k}) = \beta_{il} \sigma_i k_l , \quad (3)$$

where  $i, l = x, y, z$  for  $[[110], y, z]$ , and  $\sigma_i$  are the Pauli matrices.

Tensor  $\beta$  is determined by the symmetry of the QW. Since we consider a zinc-blende structure, there is a contribution due to bulk inversion asymmetry (BIA). It is known as the Dresselhaus term, and non-zero components of  $\beta$  in this case are

$$\beta_{xx} = -\beta_{yy} . \quad (4)$$

The QW could be asymmetrical due to inequivalence of the right and left interfaces, electric fields along  $z$  direction etc. Such structure inversion asymmetry (SIA) leads to additional contribution to the spin-orbit Hamiltonian, the so-called Rashba term:

$$\beta_{xy} = -\beta_{yx} . \quad (5)$$

Taking into account Eq. (3), the two electron states with a given wavevector have linear in  $k$  splitting  $\Delta = 2\sqrt{(\beta_{xl}k_l)^2 + (\beta_{yl}k_l)^2}$ . Two hole states with a given  $\mathbf{k}$  are assumed to be degenerate. In the spherical approximation and for infinitely-deep QW, they have the dispersion  $E_h(k)$ , and their wavefunctions are given in [2].

Calculating the reduced density of states, optical matrix elements and velocity operators, and assuming the splitting  $\Delta$  to be small, we get the expression for the interband photocurrent

$$j_i(\omega) = P_c A_0^2 \left( \frac{eP}{m_0 \hbar c} \right)^2 e \tau_e \beta_{il} o_l G(k_\omega) . \quad (6)$$

Here  $\mathbf{o}$  is the light propagation direction,  $P_c$  is the circular polarization degree,  $P$  is the Kane matrix element,  $A_0$  is the light wave amplitude, and  $k_\omega$  is the wavevector of a direct optical transition satisfying the energy conservation law

$$E_e(k_\omega) + E_h(k_\omega) = \hbar\omega - E_g , \quad (7)$$

where  $E_e(k)$  is the parabolic electron dispersion without spin-orbit corrections.

The frequency dependence of the photocurrent is given by the function  $G(k)$

$$G(k) = \frac{k}{v(k)} \frac{d}{dk} \left[ \frac{F(k)u(k)}{v(k)} \right] - \frac{F(k)}{v(k)} \left[ 2 - \frac{u(k)}{v(k)} \right] . \quad (8)$$

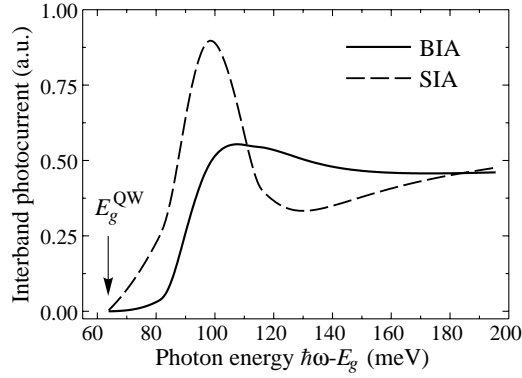


**Fig. 1.** The dependence of circular photocurrent for direct interband transitions  $hh1 \rightarrow e1$  in a 100 Å QW. Spin splitting of the electron states is due to bulk inversion asymmetry (solid line) or structure inversion asymmetry (dashed line).

Here

$$F(k) = k(NQ_+W_+)^2, v(k) = \frac{\hbar k}{m_e} + v_h(k), u(k) = \left[ \frac{\hbar k}{m_e} + v_h(k) \frac{\tau_h}{\tau_e} \right] \xi(k), \quad (9)$$

where  $v_h(k) = \hbar^{-1} dE_h(k)/dk$ ,  $m_e$  is the electron effective mass, and the expressions for the coefficients  $N$ ,  $Q_+$  and  $W_+$  are given in [2].

The first term in Eq. (8) appears because the direct transitions to the upper (lower) spin branch take place at a wavevector slightly smaller (larger) than  $k_\omega$ , and the second term appears because the two electron spin states with the same  $\mathbf{k}$  have different velocities.

The factor  $\xi(k)$  depends on the form of a spin-orbit interaction:

$$\xi_{\text{BIA}} = 1, \quad \xi_{\text{SIA}} = 1 - 1/W_+. \quad (10)$$

This difference gives rise to non-equal frequency dependences of the photocurrent. It is dramatical at the absorption edge, when  $\hbar\omega \geq E_g^{\text{QW}} = E_g + E_{e1}(0) + E_{hh1}(0)$ . For the ground hole subband  $W_+(k) \sim k^2$ , and hence

$$j_{\text{BIA}} \sim (\hbar\omega - E_g^{\text{QW}})^2, \quad j_{\text{SIA}} \sim \hbar\omega - E_g^{\text{QW}}. \quad (11)$$

This conclusion opens a possibility to distinguish experimentally which kind of asymmetry is dominant in the studied structure, BIA or SIA. This could be done by studying increase, quadratic or linear, of the circular photocurrent with light frequency near the absorption edge.

### 3. Results and discussion

Fig. 1 presents circular photocurrents caused by BIA and SIA appearing under interband transitions between the ground electron and hole subbands,  $e1$  and  $hh1$  in a 100 Å QW. The effective masses of electron, heavy- and light-holes correspond to GaAs:  $m_e = 0.067m_0$ ,

$m_{hh} = 0.51m_0$ ,  $m_{lh} = 0.082m_0$  ( $m_0$  is the free electron mass). The momentum relaxation times are taken  $\tau_e = \tau_h$  and independent of carrier energies.

One can see the linear and quadratic raising of the current near the edge in accordance to Eq. (11). At higher energy, a peak is present in the spectrum. It takes place at  $\hbar\omega - E_g \approx 100$  meV, which corresponds to excitation of carriers with  $k \approx 2/a$ . At this point the  $hh1$  energy dispersion has an anti-crossing with  $hh2$  one. This causes reconstruction of the hole wavefunctions and, hence, big changes in the dependence  $G(k)$ .

Since other size-quantized hole subbands are located near the  $hh1$ , the transitions from  $hh2$ ,  $lh1$ ,  $hh3$  states to  $e1$  in the range  $\hbar\omega - E_g \leq 200$  meV take place. This complicates the photocurrent spectrum and makes it different from one presented in Fig. 1. The relevant contributions will be calculated and published elsewhere.

#### 4. Conclusion

We have considered the two cases when either BIA or SIA dominates. However the situations are possible when both types of asymmetry are present. The analysis shows that the corresponding spin-orbit terms give non-additive contributions to the photocurrent as they do in other spin-dependent effects in QWs like weak localization and spin relaxation. We plan to investigate BIA and SIA interference in the photogalvanic effect in the near future.

#### Acknowledgements

Author thanks E. L. Ivchenko for many helpful discussions. This work is financially supported by the RFBR (project 01-02-17528), by the Programms of Russian Ministry of Science, by the Programme of Presidium of RAS "Quantum low-dimensional structures", and by INTAS (project 99-00015).

#### References

- [1] S. D. Ganichev E. L. Ivchenko, S. N. Danilov, J. Eroms, W. Wegscheider, D. Weiss and W. Prettl, *Phys. Rev. Lett.* **86**, 4358 (2001).
- [2] I. A. Merkulov, V. I. Perel' and M. E. Portnoi, *Sov. Phys. JETP* **72**, 669 (1991).

## Spin memory in the n-doped GaAs/AlGaAs quantum wells

*S. Yu. Verbin*<sup>†</sup>, *Yu. P. Efimov*<sup>†</sup>, *V. V. Petrov*<sup>†</sup>, *I. V. Ignatiev*<sup>†</sup>, *Yu. K. Dolgikh*<sup>†</sup>,  
*S. A. Eliseev*<sup>‡</sup>, *I. Ya. Gerlovin*<sup>‡</sup>, *V. V. Ovsyankin*<sup>‡</sup> and *Y. Masumoto*<sup>¶</sup>

<sup>†</sup> Institute of Physics, St Petersburg State University, St Petersburg  
198904, Russia

<sup>‡</sup> Vavilov State Optical Institute, St Petersburg, 190034, Russia

<sup>¶</sup> Institute of Physics, University of Tsukuba, 305-8571, Japan

**Abstract.** The polarized luminescence spectra and kinetics of the GaAs quantum wells with excess free electrons are studied experimentally. Quantum beats between the exciton and electron spin sublevels, split by a magnetic field, are detected. The dynamics of the degree of polarization is found to contain a long component associated with slow relaxation of electron spins.

Optical excitation of the quantum-confined semiconductor structures with free carriers may produce triple-charged particles, trions, that represent photo-excited electron-hole pairs (excitons) bound to a charged carrier. In the GaAs/AlGaAs heterostructures with a quantum well width of about 10–30 nm, the binding energy of trions makes up 1–1.5 meV, which allows one to distinguish the trion lines in the low-temperature luminescence spectra and to study dynamics of decay of the trion states [1].

Due to additional spin introduced by the charged particle, fine structure of the trion states differs essentially from that of neutral excitons [2]. The ground state of the trion, unlike that of exciton, is characterized by a nonzero spin, which provides a fundamental possibility to use trion states for the optical spin orientation of free carriers. This effect, in principle, may be used for implementation of spin memory of the quantum and optical computer.

To date, however, the trion spin dynamics, unlike that of neutral excitons and free carriers, is poorly studied. In this report, we present results of a comparative study of the spin relaxation and spin quantum beats processes in the neutral and negatively charged GaAs/AlGaAs multiple quantum wells. It is shown that the presence of free carriers drastically changes spin dynamics of the optical excitations, which shows up as a long-term (about 1 ns) component in the spin relaxation kinetics.

We studied two heterostructures with close dimensional characteristics. One of them (the reference one) contained 30 undoped quantum wells, 8 nm thick, while the second one contained 25 pairs of tunnel-coupled quantum wells (7.9 and 9.9 nm), with a thin well in each pair being doped with Si up to the carrier concentration  $7 \times 10^{10} \text{ cm}^{-2}$ . The double-well structure was grown on a doped substrate with a semitransparent InTiO-electrode deposited on its outer surface. This allowed us to vary concentration of free electrons in quantum wells by applying external voltage (bias) to the sample. The studies were performed in a magnetic field of 0–8 T. We examined spectra and kinetics of polarized luminescence of the structures versus the magnetic field and electric bias.

As has been shown in preliminary experiments, the luminescence spectrum of the double-well sample with no external electrode comprises two narrow lines (with a halfwidth



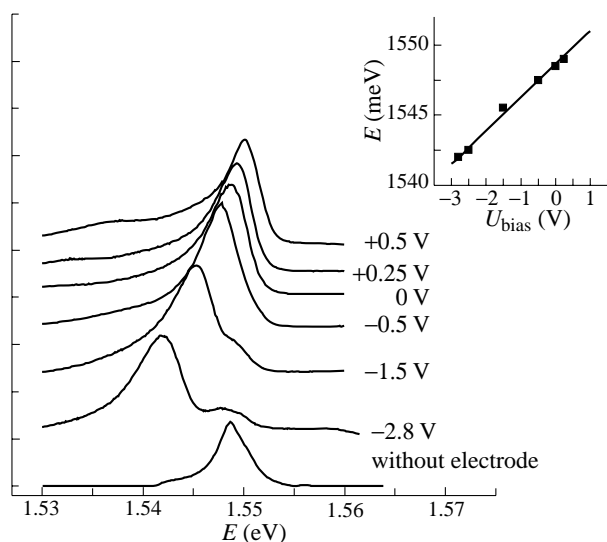


**Fig. 1.** PL spectra of undoped quantum well under different biases. Inset — bias dependence of the energy of broad PL-band.

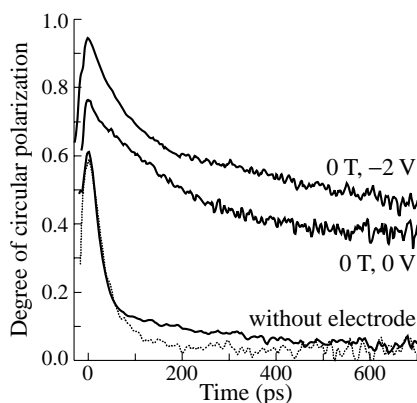


**Fig. 2.** Kinetics of the PL circular polarization degree. Values of bias and magnetic field strength are shown near each curve. Dotted curve is the kinetics of undoped sample.

of about 2 meV) corresponding to excitonic transitions in each of the wells. The most interesting for us is the low-frequency line related to the wide undoped well. After depositing the electrodes, the line substantially broadened and became asymmetric. Figure 1 shows variation of the luminescence spectrum in the region of this line when a bias is applied to the outer electrode. With increasing negative bias, the broad line is seen to shift toward lower energies. At large negative bias ( $U < -1.5$  V), the shape of the spectra substantially changes: a second line arises, with its position being independent of the bias and with its shape virtually coincident with that of the exciton line in the sample with no electrode.

Kinetics of the polarized luminescence was studied under excitation slightly above the PL band maximum of the undoped well with small Stokes shift of 2–3 meV. It was found

that the degree of circular polarization of the PL of the sample without electrode rapidly decays with the time constant of about 20 ps (see Fig. 2). In the PL of the sample with electrode, a long component arises in the decay of the degree of circular polarization (the decay time about 2 ns). Amplitude of the long component grows with increasing negative bias as it shown in Fig. 2. At a bias  $U = -2$  V, the degree of polarization, at the initial moment, approaches unity.

In the presence of magnetic field, the kinetics of the polarized luminescence essentially changes. In the Faraday configuration (magnetic field is parallel to the growth axis of the structure), rapidly-damping oscillations of the degree of linear polarization of the PL arise. The oscillation amplitude rapidly increases with increasing negative bias. The oscillation frequency increases linearly with increasing magnetic field. The slope of the field dependence of the frequency corresponds to the  $g$ -factor value 0.87. The decay time of the beats is approximately 15 ps and virtually does not depend on the magnetic field strength.

In the Voigt configuration (the field is parallel to the structure layers), much more pronounced slowly damping beats of the degree of circular polarization are observed (see Fig. 3). The beats frequency varies linearly with the magnetic field (inset in Fig. 3), but the slope of this dependence appears to be substantially smaller than in the Faraday configuration and corresponds to  $g = 0.22$ . In low magnetic fields, the decay time of the beats is about 1 ns and significantly shortens with increasing field. As in the Faraday configuration, the beats amplitude appears to be the greatest at the strong negative bias  $U \leq -2$  V.

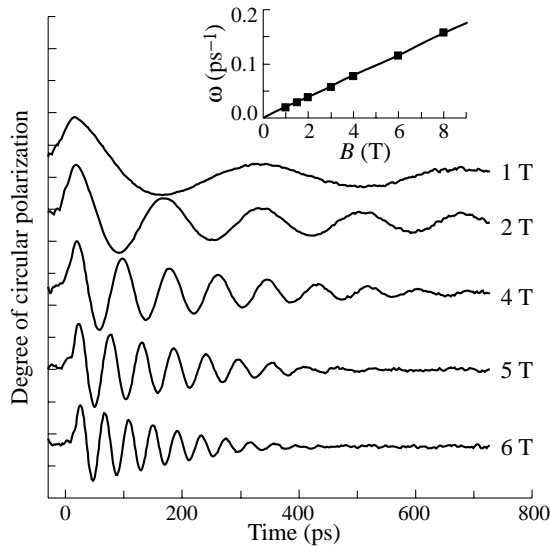


**Fig. 3.** Spin quantum beats in various magnetic field. PL is registered in the Voigt geometry.  $U_{bias} = -2$  V. Inset — magnetic field dependence of beats frequency.

The bias-induced deformation of the PL spectra, shown in Fig. 1, indicates that the spectra are formed by two essentially different processes. The broad band, whose position linearly varies with the bias, is likely to be related to the emission of free carriers, while the narrower band observed at  $U < -1.5$  V should be associated with the excitonic or trionic

transition. This band is of particular interest for us.

The most important fact is the presence of the intense long-lived component of the circular polarization in the PL of the sample with electrode. We believe that this component gives an indication of presence of free electrons in the studied quantum well. An increase of the electron density in the undoped quantum well is caused by the redistribution of the internal electric field when ITO electrode is deposited.

The presence of slow component indicates low relaxation rate of the spin states oriented by circularly polarized light. A similar effect was observed in structures with the InAs and InP quantum dots, where the n-doping dramatically reduced spin relaxation rate [3, 4]. So we can conclude that it is the presence of free electrons that favors formation of excitations with high spin stability.

It should be emphasized that it is the electron spin (rather than that of the hole) which shows stability in the system under study. This follows from the difference between the decay rates of the oscillations observed in the Faraday and Voigt configurations. The oscillations in the Faraday configuration are related to precession of the total spin of the electron-hole pair (exciton) in the magnetic field, while in the Voigt configuration the oscillations are caused by the electron spin precession. Indeed, the values of the  $g$ -factors determined experimentally in the two configurations are close to the exciton and electron  $g$ -factors measured in structures with close parameters [5].

Thus, the main result of this study is the detection of a long-term (units of ns) spin memory in the GaAs quantum wells with excess concentration of free electrons. Slowing down of the spin relaxation in such structures may be presumably ascribed to formation of trionic states. To support this suggestion, however, additional experiments are needed.

#### *Acknowledgement*

This work was supported by the Russian Foundation for Basic Research.

#### **References**

- [1] D. Sanvitto, R. A. Hogg, A. J. Shields *et al*, *Phys. Rev. B* **62**, R13294 (2000).
- [2] A. J. Shields, M. Pepper, M. Y. Simmons and D. A. Ritchie, *Phys. Rev. B* **52**, 7841 (1995).
- [3] X. Marie, A. Jbeli, M. Paillard, T. Amand and J. M. Gerard, *Nanostructures: Physics and Technology, Proc. 9th Int. Symp.*, June 18-22, 2001, Ioffe Institute, St Petersburg, Russia, p. 371-376.
- [4] I.A. Yugova, I.V. Ignatiev, S.Yu. Verbin *et al*, (unpublished).
- [5] I. Ya. Gerlovin, Yu. K. Dolgikh, S. A. Eliseev, V. V. Ovsyankin, Yu. P. Efimov, V. V. Petrov, I. V. Ignatiev, I. E. Kozin and Y. Masumoto, *Phys. Rev. B* **65**, 035317 (2002).

## Spintronics and quantum information processing in nanostructures

Guido Burkard and Daniel Loss

Department of Physics, University of Basel, Switzerland

Coherent manipulation, filtering, and measurement of electron spins in semiconducting nanostructures are new technologies which have promising applications both in conventional and in quantum information processing. In 1997 the first solid state implementation of a scalable quantum computer was proposed [1]. The qubit is defined in terms of the spin of an electron, being localized in structures such as an atom, molecule, quantum dot etc. The desired manipulation of the spins (qubits), which includes single spin rotations, spin-spin interactions, and spin read-out, can be achieved by purely electric means in terms of gates which are externally controlled by voltage pulses. I review this proposal and its further developments [2], describing possible realizations of one- and two-qubit quantum gates, state preparation and measurement, based on an all-electrical scheme to control the dynamics of spin, including spin-orbit effects [3]. I discuss recently proposed schemes for using a single quantum dot as a spin filter and spin read-out device [4], and show how the decoherence time can be measured in a transport set-up [5]. I address the issue of spin decoherence due to non-uniform hyperfine interactions with nuclei and show that for electrons confined to dots the spin decay is non-exponential [6]. Finally, I discuss methods for producing [7, 8] and detecting [9, 10] the spin-entanglement of electronic EPR pairs, being an important resource for quantum communication.

### References

- [1] D. Loss and D. P. DiVincenzo, *Phys. Rev. A* **57**, 120 (1998); cond-mat/9701055.
- [2] G. Burkard, H. A. Engel and D. Loss, *Fortschr. Phys.* **48**, 9-11, 965 (2000).
- [3] G. Burkard and D. Loss, *Phys. Rev. Lett.* **88**, 047903 (2002).
- [4] P. Recher, E. Sukhorukov and D. Loss, *Phys. Rev. Lett.* **85**, 1962 (2000).
- [5] H. A. Engel and D. Loss, *Phys. Rev. Lett.* **86**, 4648 (2001).
- [6] A. Khaetskii, D. Loss and L. Glazman, *Phys. Rev. Lett.* (May '02), cond-mat/0201303.
- [7] M.-S. Choi, C. Bruder and D. Loss, *Phys. Rev. B* **62**, 13569 (2000).
- [8] P. Recher, E. Sukhorukov and D. Loss, *Phys. Rev. B* **63**, 165314 (2001).
- [9] D. Loss and E. Sukhorukov, *Phys. Rev. Lett.* **84**, 1035 (2000).
- [10] G. Burkard, D. Loss and E. Sukhorukov, *Phys. Rev. B* **61**, R16303 (2000).

## Experimental progress in quantum-dot cellular automata

*G. L. Snider*<sup>†</sup>, *A. O. Orlov*<sup>†</sup>, *R. K. Kummamuru*<sup>†</sup>, *R. Ramasubramaniam*<sup>†</sup>,  
*G. H. Bernstein*<sup>†</sup>, *C. S. Lent*<sup>†</sup>, *M. Lieberman*<sup>‡</sup> and *T. P. Fehlner*<sup>‡</sup>

<sup>†</sup> Dept. of Electrical Engineering, University of Notre Dame, IN 46556, USA

<sup>‡</sup> Dept. of Chemistry and Biochemistry, University of Notre Dame, IN 46556, USA

**Abstract.** An overview is given of the quantum-dot cellular automata (QCA) architecture, along with a summary of experimental demonstrations of QCA devices. QCA is a transistorless computation paradigm that can provide a solution to such challenging issues as device and power density. The basic building blocks of the QCA architecture, such logic gates and clocked cells have been demonstrated. The experiments to date have used QCA cells composed of metallic islands, and operate only at low temperatures. For QCA to be practical, the operating temperature must be raised, and molecular implementations are being investigated that should yield room temperature operation.

## Introduction

For almost 40 years integrated circuits produced by the semiconductor industry have obeyed Moore's law, which predicts that the number of devices on a chip will double every 18 months. Adherence to this exponential growth curve has been a monumental task requiring rapid improvements in all aspects of integrated circuit (IC) fabrication to permit manufacturers to both shrink the size of devices and increase chip size while maintaining acceptable yields. While the use of FETs in integrated circuits has been an incredibly successful circuit paradigm, FETs are still used as current switches much like the mechanical relays used by Konrad Zuse in the 1930s. At gate lengths below  $0.05\ \mu\text{m}$  FETs will begin to encounter fundamental effects such as tunneling that make further scaling difficult. In addition, power dissipation will limit the growth of integration. A high-performance chip today dissipates more power per unit area (greater than  $30\ \text{W}/\text{cm}^2$ ) than a typical electric range-top unit. One can argue that each major shift in the basis of integrated circuits, from BJTs to FETs, and from NMOS to CMOS, was driven by the need to reduce power dissipation. Quantum-dot Cellular Automata (QCA) offers the ultra-low power dissipation and scalability to molecular dimensions that will be necessary when another paradigm shift is needed. Here, instead of fighting the effects that come with feature size reduction, these effects are used to advantage. QCA employs arrays of coupled quantum dots to implement the Boolean logic functions and clocked circuits needed for general purpose computing [1]. The advantage of QCA lies in the extremely high packing densities possible due to the small size of the dots, the simplified interconnection, and the extremely low power-delay product.

A basic QCA cell consists of four quantum dots in a square array coupled by tunnel barriers. Electrons are able to tunnel between the dots, but cannot leave the cell. If two excess electrons are placed in the cell, Coulomb repulsion will force the electrons to dots on opposite corners. There are thus two energetically equivalent ground state polarizations, as shown in Fig. 1(a), which can be labeled logic "0" and "1". If two cells are brought close together, Coulombic interactions between the electrons cause the cells to take on the same polarization. If the polarization of one of the cells is gradually changed from one state to the other, the second cell exhibits a highly bistable switching of its polarization, shown

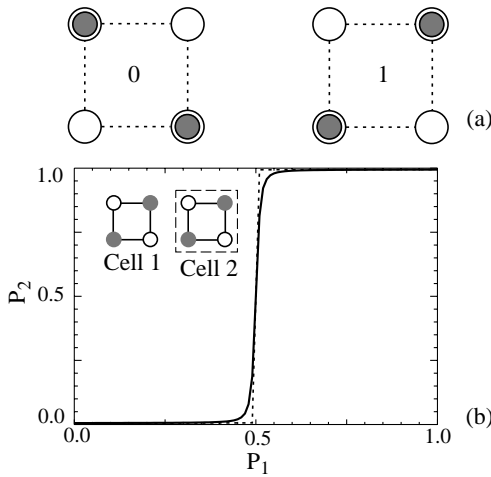


**Fig. 1.** (a) Schematic representation of QCA cells. (b) Polarization switching in cell 2.

in Fig. 1(b). In explaining the operation of QCA systems, we will begin with unlocked systems. The simplest QCA array is a line of cells, shown in Fig. 2(a). Since the cells are capacitively coupled to their neighbors, the ground state of the line is for all cells to have the same polarization. In this state, the electrons are as widely separated as possible, giving the lowest possible energy. To change the state of the line, an input is applied at the left end of the line, forcing it to a new polarization, and all subsequent cells in the line must flip their polarization to reach the new ground state.

Computing in the QCA paradigm can thus be viewed as computing with the ground state of the system. A computational problem is mapped onto an array of cells by the layout of the cells, where the goal is to make the ground state configuration of electrons represent the solution to the posed problem. The mapping of a combinational logic problem onto a QCA system can be accomplished by finding arrangements of QCA cells that implement the basic logic functions AND, OR, and NOT. An inverter, or NOT, is shown in Fig. 2(b). In this inverter the input is first split into two lines of cells then brought back together at a cell that is displaced by 45 degrees from the two lines, which produces a polarization that is opposite to that in the two lines, as required in an inverter. AND and OR gates are implemented using the topology shown in Fig. 2(c), called a majority gate. In this gate, the three inputs “vote” on the polarization of the central cell, and the majority wins. The polarization of the central cell is then propagated as the output. One of the inputs can be used as a programming input to select the AND or OR function. If the programming input is a logic 1 then the gate is an OR, but if a 0 then the gate is an AND. Thus, with majority gates and inverters it is possible to implement all combinational logic functions.

For practical QCA circuits, clocked control is necessary. In clocked circuits, the system is switched smoothly between the ground state corresponding to the old inputs and the state corresponding to the new inputs. Clocking allows cells to be locked in a particular state, performing as a latch. Thus, general purpose computing is possible, and in particular, latches make it possible to implement pipelined architectures, as required in all high-performance systems. Clocking of QCA cells is accomplished by switching the cells using a quasi-adiabatic approach [2]. This keeps the system in its instantaneous ground state during switching, which results in very low power dissipation. In metallic QCA systems, an additional dot is introduced between the top and bottom dots of a cell, as shown in Fig 2(d). The clock signal is applied to a gate coupled to this central dot to modulate the potential of the dot, and control the switching of the cell.

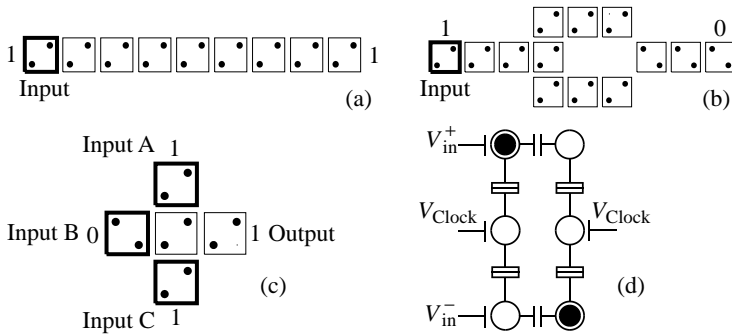


**Fig. 2.** (a) Line of cells. (b) Inverter. (c) Majority gate. (d) Clocked QCA cell.

## 1. Experiment

The experimental work presented is based on a QCA cell using aluminum islands and aluminum-oxide tunnel junctions fabricated on an oxidized silicon wafer. The fabrication uses standard electron beam lithography and dual shadow evaporations to form the islands and tunnel junctions [3]. A completed device is shown in the SEM micrograph of Fig. 3. The area of the tunnel junctions is an important quantity since this dominates island capacitance, determining the charging energy of the island, and hence the operating temperature of the device. For our devices, the area is approximately 50 by 50 nm, giving a junction capacitance of 400 aF. These metal islands stretch the definition of a quantum dot, but we will refer to them as such, because the electron population of the island is quantized and can be changed only by quantum mechanical tunneling of electrons. The device is mounted on the cold finger of a dilution refrigerator that has a base temperature of 10 mK, and characterized by measuring the conductance through various branches of the circuit using standard ac lock-in techniques. A magnetic field of 1 T is applied to suppress the superconductivity of the aluminum metal. Full details of the experimental measurements are described elsewhere [4].

The operation of a single QCA cell by abrupt switching has been previously reported [4]. We have also demonstrated the operation of a line of QCA cells [5], and a majority gate [6], all measured by abrupt switching. These experiments prove the basic principles of the QCA paradigm: the encoding of information by the position of single electrons, and the control of single-electron switching by single electrons.

In our recent experiments, we have demonstrated clocked control of QCA systems. As mentioned earlier, Toth and Lent [7] suggested a scheme for clocked control of the switching in metallic QCA cells where a central dot acts as a modulated barrier between

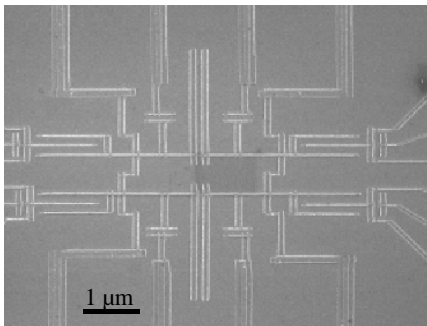


**Fig. 3.** SEM micrograph of an aluminum island QCA cell.

the two dots forming a QCA half-cell, as shown in Fig. 6(a). This half cell has no DC current connection to the external environment, so the overall cell remains electrically neutral throughout the experiment. When its gate sets the central dot's potential high, it is energetically unfavorable for an electron to be on the middle dot, so the middle dot takes on a positive net charge. An electron moves to either the top or bottom dot, depending on the input bias applied to the cell as the central dot potential is raised. Once the central dot potential is high, the electron is locked into position. If the polarity of the input signal is reversed, the electron is trapped in a metastable state [7], which does not correspond to the minimal energy configuration. If the lifetime of this state (limited by cotunneling) is long compared to the switching speed of the circuit, then the locked cell can be used as a latch.

An important feature of the clocked QCA architecture is that the polarization of the cell is changed using the clock. The small input signal only defines the final cell polarization while the clocking signal drives the electron transfer. To demonstrate QCA clocking and latching, we fabricated device where the tunnel junction between the three dots is replaced by a multi-tunnel junction (MTJ) consisting of three tunnel junctions. These extra tunnel junctions suppress the rate of co-tunneling, increasing the lifetime of the metastable state to a few seconds, sufficient for our low speed measurements. A schematic of the latching half-cell is shown in Fig. 4(a). Only one electrometer is necessary to determine the polarization of the cell.

Operation of the latching cell is shown in Fig. 4(b). The top panel shows the input voltage applied to the top dot, the clock signal in the middle panel, and the top-dot potential (output) in the bottom panel. When a small negative voltage input is applied, the cell responds with only a small change in the potential of the top dot. Next, the clock is applied (negative voltage) and the input data is latched into the cell. Note that a single half-cell inverts the input. When the input is removed at  $t = 0.3$  s the output of the latch remains in the high state until the clock is released at 1.5 s, whereupon the cell returns to its null state. At the times 1.5 to 3 s a bit of the opposite polarity is clocked into the latch. This demonstrates the operation of a latching cell.

While we have experimentally demonstrated many of the basic functions of the QCA paradigm, a number of challenges remain. Foremost is the low operating temperature required for our current metal dot implementations, set by the total capacitance of the metal islands. To reduce the total capacitance, the size of the dots must be reduced. For room temperature operation the size of the dots should be on the order of 2–5 nm. Even if we

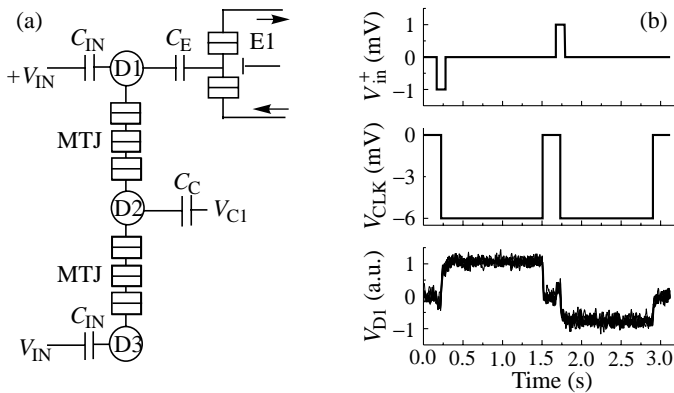


**Fig. 4.** (a) Simplified schematic of a 3-dot clocked QCA latching cell. (b) Operation of the latching cell.



could fabricate devices of this size, we must also consider the task of fabricating  $10^{11} - 10^{12}$  devices per substrate. To achieve these device quantities with the require dimensions, it will probably be necessary to use a non-traditional fabrication techniques such as molecular chemistry and self-assembly. The intent is to make molecules that implement the individual QCA cells, where the role of the quantum dots is played by redox centers within the molecule. Mixed valence molecules where the charge configuration can be changed have been demonstrated [8], and have the small size required. The advantage of molecules is that the synthesis chemistry takes care of the assembly of each cell. This reduces the requirements on the resolution of the patterning technique since we no longer need to control the placement of individual dots. However, placement of the cells must still be controlled, and will be a challenge if device densities of  $10^{12}/\text{cm}^2$  are to be achieved. We are currently investigating DNA tiling [9] as a means to obtain self-assembly. In this technique DNA will be used to produce tiles which will assemble in a unique pattern. The tiles will then be used as a backbone for attachment of the QCA molecules that will compose the desired circuit.

## 2. Conclusions

Quantum-dot cellular automata is a dramatic departure from usual digital logic devices in that information is encoded by the position of single electrons, not by the operating state of an FET current switch. We have experimentally demonstrated many of the functional elements of the QCA paradigm including individual cells, lines, logic gates, and clocking. In this paper, we have presented a short introduction to QCA and a brief overview of some experiments.

While our experiments demonstrate the feasibility of the QCA paradigm, significant challenges must be overcome before practical applications are possible. The greatest challenge, operating temperature, is also an opportunity. An important advantage of QCA is that since its basis of operation exploits quantum mechanics, scaling is possible to the molecular level. As the device is scaled down in size, the operating temperature increases, and molecular sized devices should operate at room temperature.

### Acknowledgments

This work was supported by the Defense Advanced Research Projects Agency, the Keck Foundation, the Office of Naval Research, and the National Science Foundation.

## References

- [1] C. S. Lent and P. D. Tougaw, *J. Appl. Phys.* **74**, 6227 (1993).
- [2] C. S. Lent and P. D. Tougaw, *Proceedings of the IEEE* **85**, 541 (1997).
- [3] T. A. Fulton and G. H. Dolan, *Phys. Rev. Lett.* **59**, 109 (1987).
- [4] A. O. Orlov *et al*, *Science*, **277**, 928 (1997).
- [5] A. O. Orlov *et al*, *Appl. Phys. Lett.* **74** 2875 (1999)
- [6] I. Amlani *et al*, *Science* **284**, 289 (1999).
- [7] G. Toth and C. S. Lent, *J. Appl. Phys.* **85**, 2977 (1999).
- [8] C. Creutz and H. Taube, *J. Am. Chem. Soc.* **95**, 1087 (1973).
- [9] E. Winfree, F. Liu, L. A. Wenzler and N. C. Seeman, *Nature* **394**, 539 (1998).

## Clocked quantum-dot cellular automata devices

A. O. Orlov, R. Kumamuru, R. Ramasubramaniam, C. S. Lent,  
G. H. Bernstein and G. L. Snider

Dept. of Electrical Engineering, University of Notre Dame, IN 46556, USA

**Abstract.** We present an experimental demonstration of novel Quantum-dot Cellular Automata (QCA) devices based on clocked architecture—a QCA latch and a two-bit QCA shift register. The operation of the devices is demonstrated, and sources of the digital errors occurring in clocked QCA devices are discussed.

### Introduction

Quantum-dot Cellular Automata computational paradigm [1] uses quantum dots to encode and process binary information. Logic levels in QCA are represented by the configurations of single electrons in arrays of coupled quantum-dots (cells). In the last few years, several basic QCA elements have been demonstrated [2]. However, these devices do not possess power gain needed for the operation of large QCA arrays since the only source of energy there is the signal input.

Clocked control of the QCA circuitry was proposed in [3] to overcome this obstacle. Clocked QCA systems have many advantages over edge-driven cellular architectures. Power gain in clocked systems is achievable because energy is supplied to each cell by the clock lines rather than passed from the inputs alone [4]. And since each cell can be used as a latch which acts as a short-term memory, pipelining becomes possible. The original theoretical work [3] suggested a semiconductor implementation of clocked QCA arrays, where clocking can be performed by a back gate controlling QCA array. Recently, a scheme for clocked control of QCA cells with fixed intracell barriers was proposed in [5, 6], where an extra dot placed between the two dots of the QCA cell acts as a Coulomb barrier controlled by the clock signal.

Here we present an experimental demonstration of clocked QCA devices implemented in metal system with fixed oxide barriers.

### 1. Fabrication and measurement technique

To fabricate QCA devices we use Al tunnel junction technology which combines direct E-beam lithography with a suspended mask technique [7]. The thin-film Al islands separated by tunnel junctions are thermally evaporated on the Si/SiO<sub>2</sub> substrate with in situ oxidation. The advantage of this type of QCA is relative simplicity (only 3 major processing steps: E-beam writing, development, and metal deposition/oxidation), good uniformity (junction resistance in one run typically varies by only 20–30 %), and high yield (up to 100%). The disadvantage is the small charging energy of the Al “dots”,  $E_C \sim 1$  meV. To satisfy the condition  $E_C \gg kT$  the experiments are performed in the dilution refrigerator at the temperatures 50–200 mK.

## 2. Demonstration of a QCA latch

The QCA latch consists of three micron-size Al dots (D1–D3, Fig. 1(a)), separated by multiple tunnel junctions (MTJ) with three control gates. Single-electron transistor (SET) E1 capacitively coupled to the dot D1 is used as an electrometer to readout the binary state of the latch. Figure 1(b) demonstrates the operation of a QCA latch. As the input pulse is applied (at  $t_0$ ,  $t_4$ ) no charge transfer happens (the latch remains neutral) until the clock signal is applied (at  $t_1$ ,  $t_5$ ). The clock pulse supplies energy to transfer an electron from the middle dot to the D3 (at  $t_1$ ) or D1 (at  $t_5$ ), in accordance with the polarity of the input signal. The input is then can be removed (at  $t_2$ ,  $t_6$ ) and the electron remains latched in the D3(D1) until the clock signal is set to low (at  $t_3$ ,  $t_7$ ). During the hold time the latch acts as a source of signal for the next latch. This demonstrates the operation of a QCA latch as described in [5].

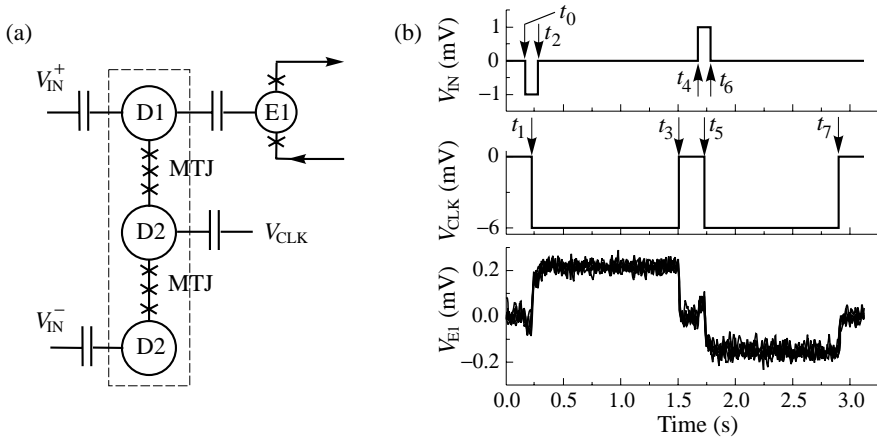


**Fig. 1.** (a) simplified circuit diagram of a QCA latch. MTJ-multiple tunnel junctions, E1-SET electrometer; (b) operation of QCA latch (several successive traces are shown).

## 3. Demonstration of a two-bit QCA shift register

A QCA shift register is assembled by capacitive coupling between adjacent QCA latches. To demonstrate a two-bit shift register, two QCA latches L1 and L2 coupled by lateral interdigitated capacitors, were fabricated (Fig. 2(a)). Operation of the QCA shift register requires the use of a three-phase clock (CLK1 and CLK2). The differential signal  $V_{IN}$  corresponding to logical “0” (logical “1”) is applied to the input IN1–IN2 at  $t_0$  ( $t_6$ ) (Fig. 2(b)). The latch L1 remains in the neutral state until CLK1 is applied at  $t_1$  ( $t_7$ ) in Fig. 2(b). When clock CLK1 is set high, the latch L1 becomes active. Once L1 is set (an electron is locked on one of the end dots), signal input is removed at  $t_2$  ( $t_8$ ) and the state of L1 does not depend on the input signal. Then the second clock CLK2 is applied to L2 at  $t_3$  ( $t_9$ ) in Fig. 2(b), and an electron in L2 switches in the direction determined by the state of the first latch. The second latch remains active when CLK1 is removed at  $t_4$  ( $t_{10}$ ) in Fig. 2(b) for as long as CLK2 is active (until  $t_5$  ( $t_{11}$ )). The cycle describing the operation of a QCA shift register is as follows: neutral → input applied → 1st clock applied and 1st latch is active → input removed → second clock applied and 2nd latch is active → 1st clock is removed. At this moment the first latch returns to a neutral and is ready to receive new information. The information encoded in the position of a single electron is shifted to a second latch and stored there. Thus, a functioning QCA 2-bit shift register is demonstrated.

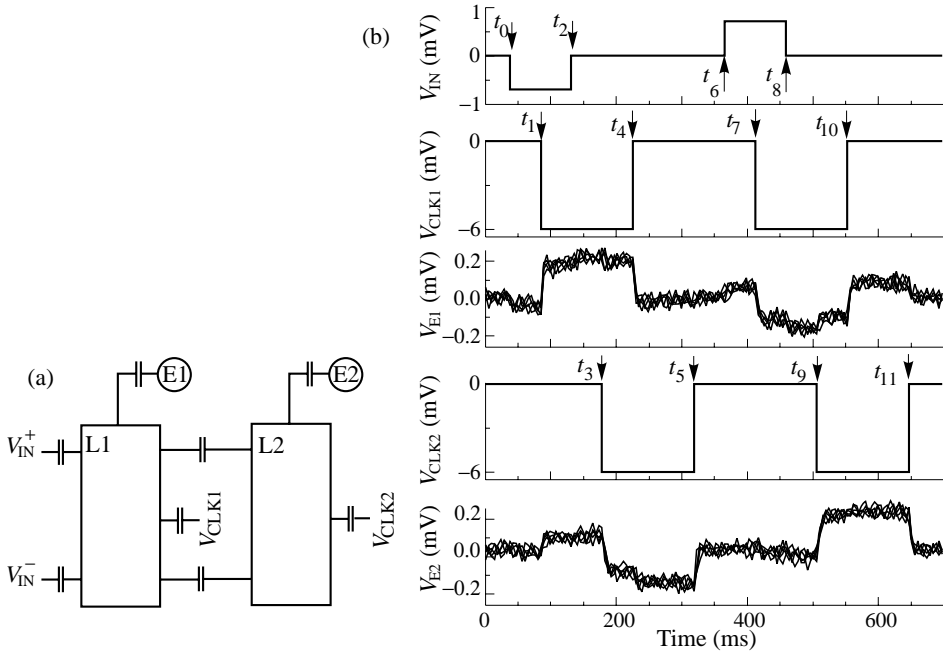


**Fig. 2.** A two bit QCA shift register: (a) simplified block-diagram; (b) operation of the register. Multiple traces are shown to demonstrate repeatability.

#### 4. Analysis of the digital errors in clocked QCA devices

For reliable operation of digital device the error in data transformations should be minimized. From the system standpoint the errors in the clocked QCA can be divided into two basic categories: (a) switching errors, which include all possible sources of errors forcing a QCA latch to switch into a “wrong” (opposite to the one suggested by the input signal) final polarization; (b) “decays,” — errors caused by the loss of information during the retention period. For a QCA latch the probability of the switching error caused by thermal fluctuations is an exponential function of  $kT$ , and for a given temperature this error could be minimized by applying larger input bias  $V_{IN}$  [6]. However, we did not find any noticeable change in the error probability for temperature varied from 50 mK to 200 mK. This is likely to be caused by the coupling of the broadband external noise to the input gates which could act as effective temperature, however more experiments need to be done to resolve this issue. Switching errors caused by the random background charge fluctuations (RBCF) are a common problem for single-electron logic devices [8]. However, for a typical timeframe of experiments ( $\sim 10$  s) the probability of this error is negligibly small. Finally, so called “dynamic errors” which occur when the switching speed is too high compared to the tunneling rate ( $\sim 10^{10}$  Hz for our junctions) [6] also lead to a switching error. The dynamic errors can also be neglected for frequencies below 100 MHz.

“Decays” in a QCA latch are events which correspond to the escape of an electron from the latched metastable state [5, 6]. We estimate the lower bound of the average lifetime of an electron in a latched state for our devices at  $T \sim 70$  mK to be greater than 100 s. For higher clock rate (say, 100 MHz) the probability of decay errors in this case falls below  $\sim 10^{-10}$ .

## 5. Summary

The operation of two QCA clocked logic devices, fabricated using Al tunnel junction technology is experimentally demonstrated. The analysis of the error rate reveals that switching to the incorrect state is the primary source of the digital errors.

A current clocked QCA prototypes operate at low temperature of 70 mK due to very small charging energies ( $\sim 1$  meV). The future generations of the QCA devices, however, are expected to work at liquid nitrogen (metal nanoclusters QCA) or even room temperatures (molecular QCA), at speeds of about  $10^{10}$  Hz, and low levels of errors.

### *Acknowledgments*

This research was supported by the W. M. Keck Foundation, DARPA, ONR (grant number N00014-95-1-1166) and NSF.

## References

- [1] C. S. Lent, P. D. Tougaw, W. Porod and G. H. Bernstein, *Nanotechnology* **4**, 49 (1993).
- [2] A. O. Orlov *et al*, *Science* **277**, 928 (1997);  
I. Amlani *et al*, *Science* **284**, 289 (1999).
- [3] C. S. Lent and P. D. Tougaw, *Proceedings of the IEEE* **85**, 541 (1997).
- [4] J. Timler and C. S. Lent, *J. Appl. Phys.* **91**, 823 (2002)
- [5] G. Toth and C. S. Lent, *J. Appl. Phys.* **85**, 2977 (1999).
- [6] K. K. Likharev and A. N. Korotkov, *Science* **273**, 763 (1996).
- [7] T. A. Fulton and G. H. Dolan, *Phys. Rev. Lett.* **59**, 109 (1987).
- [8] A. N. Korotkov, R. H. Chen and K. K. Likharev, *J. Appl. Phys.* **78**, 2520 (1995).

## Single-photon storage in a single quantum dot for the implementation of a solid-state quantum repeater

A. M. Bychkov<sup>†‡</sup> and D. Bouwmeester<sup>†</sup>

<sup>†</sup> Centre for Quantum Computation, Clarendon Laboratory,  
 Oxford University, Oxford OX1 3PU, United Kingdom

<sup>‡</sup> Moscow State Engineering Physics Institute, 115409 Moscow, Russia

**Abstract.** We propose a semiconductor quantum dot device for storage of the quantum states of individual photons. The device may be used in realistic optical quantum communication, namely, to implement a solid-state quantum repeater.

The ever-increasing demand for fast and secure computation and data transmission has over the last decade motivated extensive research into the domain of quantum physics. The idea to exploit quantum effects of the microscopic world in electronics and telecom lies behind the novel directions of research, such as spintronics and quantum information processing. Progress in physics and technology of semiconductor nanostructures, highlighted by an implementation of the source of single photons on demand [1–3], creation and control of the excitonic wave function in an 'artificial atom', or single quantum dot (QD) [4], and most recently, observations of excitonic Rabi oscillations in individual QDs [5, 6], has shown two important issues. First, physics of semiconductor nanostructures has achieved a high level of development comparable to that of atomic physics and, supported by state-of-the-art microelectronics technology, promises to develop even further. Second, at this advanced level, physics and technology of nanostructures become very closely linked, and new discoveries may offer nearly immediate device applications.

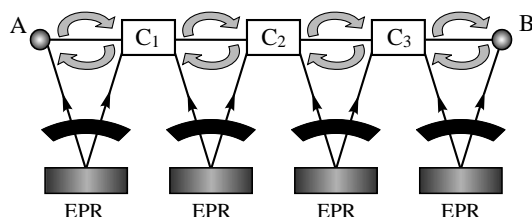


**Fig. 1.** Schematics of quantum data transmission from A to B using quantum repeaters  $C_1 - C_3$ . The protocol involves generation of entangled pairs by EPR sources, local two-photon manipulations at  $C_1$ ,  $C_2$ ,  $C_3$ , and communication of classical information between A, B, and repeaters

The proposal concerns transmission of quantum information (qubits) over a realistic communication channel containing noise and dissipation. It has been shown theoretically [7] that quantum data transmission can still be conducted by decomposing a communication channel into a sequence channels connected by quantum repeaters, see Fig. 1. The qubit to be teleported is encoded by the polarization state of a single photon, and pairs of entangled photons are generated using parametric down-conversion in non-linear crystals. The transmission procedure takes advantage of established protocols of quantum teleportation [8] and entanglement swapping [9]. Each quantum repeater is required to perform the following operations: storage of the state of two photons, local two-qubit manipulation

upon request (Bell state measurement), and classical communication. The feasibility of storage of the photon states is essential for the whole concept of quantum repeaters, and therefore the first objective of this proposal is to implement an optical quantum memory device.

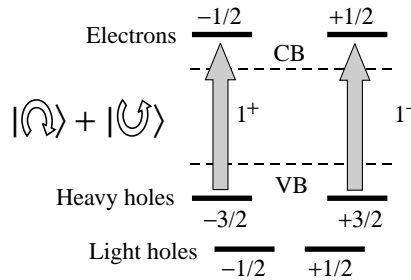


**Fig. 2.** Energy spectrum of a semiconductor nanostructure. The strain accumulated during growth splits the valence and conduction bands into discrete levels. The strongest optical transitions  $\sigma^+$  and  $\sigma^-$  correspond to absorption (emission) of a circularly co-polarised and counter-polarised photon. The two states form a basis for an arbitrary polarization state of a photon

As a prototype version of a quantum memory device, it is desirable to implement storage of the polarization state of a single photon. The proposed realization is based on resonant coupling of coherent light with semiconductor QD, see Fig. 2. In the simplest version, upon resonant excitation of the QD, an exciton is created according to the optical transitions  $\sigma^+$  and  $\sigma^-$ . In the time of electron-hole recombination, the exciton is annihilated emitting a photon of identical frequency and polarization. Thus, the memory time will be determined by the excitonic recombination time of the QD. In the longer term, the memory time may be controlled by replacing the spontaneous emission of the photon back with stimulated emission due to applied gate voltages and/or electromagnetic fields, using a more complicated geometry of the device.

The required characteristics of the samples and further experimental implications, as well as the current state of the project, will be discussed.

#### Acknowledgements

A.M.B. acknowledges the financial support of Oxford University and St. John's College.

#### References

- [1] P. Michler *et al*, *Science* **290**, 2282 (2000).
- [2] C. Santori *et al*, *Phys. Rev. Lett.* **86**, 1502 (2001).
- [3] Zh. Yuan *et al*, *Science* **295**, 102 (2002).
- [4] N. H. Bonadeo *et al*, *Science* **282**, 1473 (1998).
- [5] T. Stievater *et al*, *Phys. Rev. Lett.* **87**, 133603 (2001).
- [6] H. Kamada *et al*, *Phys. Rev. Lett.* **87**, 246401 (2001).
- [7] D. Bouwmeester, A. Ekert and A. Zeilinger (Eds), *The Physics of Quantum Information* (Springer Verlag, Berlin), 2000.
- [8] D. Bouwmeester *et al*, *Nature* **390**, 575 (1997).
- [9] J.-W. Pan *et al*, *Phys. Rev. Lett.* **80**, 3891 (1998).

## Semiconductor tunneling structure with self-assembled quantum dots for multi-logic cellular automata module

A. Khitun, S. Hong and K. L. Wang

Device Research Laboratory Electrical Engineering Department  
University of California–Los Angeles, Los Angeles, CA 90095-1594

**Abstract.** We proposed and analyzed a semiconductor multi-barrier tunneling structure, which is incorporated with a quantum dot layer for a cellular automata logic module. Both in-plane and cross-plane directions of tunneling in the self-assembled quantum dot layer were taken into consideration. Nonlinear I–V characteristics as a result of tunneling of a multi-cell system were simulated and used for the modular logic construction. Elemental units, “AND”, “OR” and “EXCHANGE” gate operations were shown. In addition, we demonstrated a set of local transition rules for use in one logic module driven by the edge bias. The stability of the scheme with respect to material structure imperfections is discussed.

### Introduction

The growing concern of scaling limit in the chip density has stimulated a great number of proposal aimed to exploit nanoscale structures for new computing paradigms [1–3]. But there is a most common problem, making a lot of proposed nanoelectronic schemes impractical, that is a demand of extreme fabrication tolerance. Being trying to achieve a large number of identically operating devices integrated in a large scale circuit, the scheme operation usually fails due to the presence of inevitable material imperfections. An appeal to the permanent progress in nanostructure fabrication unpredictably delays practical realization for many very intrigue proposals. The solution may be found in nanoelectronic architecture improvement making large scale systems resistible to the deviation in single nano-size device performances [4, 5]. In present work we demonstrate the possibility for stable operation of a cellular automata module based on semiconductor tunneling structure with self-assembled quantum dots. The stable regimes are found by numerical simulation of the structure conductance, taking into account cross layer and in-plane tunneling.

### 1. Material structure and logic module performance

In Fig. 1 we schematically depicted a five-cell fragment of a cellular automata logic module. The black layer on the bottom and the black squares on the top of the structure depict conducting substrate and metallic contacts, respectively. The core of the module consists of multiple layers of two semiconductor materials. Without the sake of generality, we depict one of these materials as silicon and another one as germanium. So, there are Si,  $\text{Si}_{1-x}\text{Ge}_x$ , Si, Ge self-assembled quantum dots, Si,  $\text{Si}_{1-x}\text{Ge}_x$  and Si layers grown in a sequence from the bottom to the top. The top contacts are the input/output edge ports providing device connection with an external circuit. Each contact represents one cell of the logic module. Input data coded into the voltage signals ( $V_{11}, \dots, V_{ij} \dots V_{NN}$ ) are applied to the ports, where  $i, j$  are the port indexes as shown in Fig. 1 and  $N$  is the total number of ports in the row. The value of  $V_{ij}$  is either  $V^0$  or  $V^1$  that corresponds to the 0 or 1 input logic state,



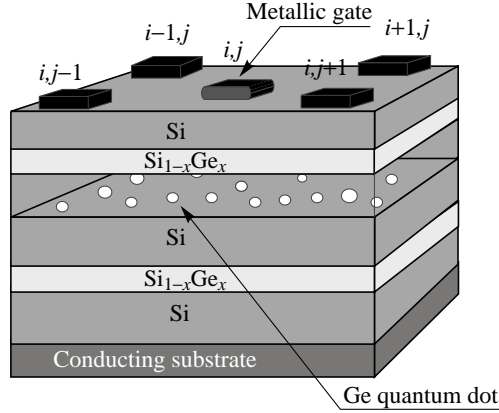


**Fig. 1.** Material structure of the logic module. The black squares on the top depict metallic contacts. The black layer on the bottom depicts common conductive substrate. There are seven layers: Si,  $\text{Si}_{1-x}\text{Ge}_x$ , Si, Ge self-assembled quantum dots, Si,  $\text{Si}_{1-x}\text{Ge}_x$  and Si grown in a sequence from the bottom to the top.

respectively. Output data are obtained as port currents ( $I_{11}, \dots, I_{ij} \dots I_{NN}$ ) stabilized at constant input voltages. The output logic state of the gate  $i, j$  is 0 if  $I_{i,j} < I_{\text{ref}}$  and 1 otherwise, where  $I_{\text{ref}}$  is the reference current. Thus, logic module can be treated here as a non-linear resistance those characteristic on  $i, i$ -th gate is a function of all neighbor inputs  $R_{ij} \equiv R_{i,j}(V_{i-1,j}; V_{i,j}; V_{i-1,j+1} \dots V_{i+1,j+1})$ . In order to build some desired local transition function  $F$  that defines logic output  $L$  from cell( $i, j$ ) as a function of all neighbors cells logic input:  $L(i, j) \equiv (F[L(i-1, j); i, j; i+1, j; i, j+1; i, j-1])$ , we have to find corresponding values of input voltages  $V^0, V^1$  and reference current  $I_{\text{ref}}$ .

In the next section we present results of numerical simulation showing the possibility to find the above parameters for different logic functions  $F$ . For each parameter we show region of permissible variation that doesn't effect on the logic functionality.

## 2. Numerical simulations

The analog circuit for the considering structure is shown in Fig. 2(a). The "Z" signs depict tunneling that is approximated by a parallel capacitance/non-linear resistance circuit. There are three different tunneling processes depicted in Fig. 2(a) by  $T_{DD}$ ,  $T_{DS}$  and  $T_{DG}$  that are dot-dot, dot-substrate and dot-contact tunneling, respectively. Each of the tunneling circuits is characterized by it's own effective non-linear resistance and capacitance. The parameters of dot-contact, dot-dot and dot-substrate tunneling are defined by Ge contain in  $\text{Si}_{1-x}\text{Ge}_x$  layers, the layers thickness, Si spacer layers thickness, Ge dot size and dot concentration.

In order to illuminate the extraordinary structure potential we present results of numerical simulation. In Fig. 3 we shown one of the central cell  $i, j$  I-V characteristics obtained for the case when all neighbor cells have the same input voltage  $V_{i-1,j} = V_{i,j-1} = V_{i+1,j} = V_{i,j+1}$ . The plot is shown in normalized units. There are 15 contours, the lighter contour color corresponds to the higher port current. In our calculations we used approximate tunneling parameters Fig. 2(b) and the dot density 16 dots per contact area. Varying the reference current and moving the voltage squares on the line (squares side length is a subject of variation too) it is possible to find the desirable input/output correlation. In Fig. 3 we

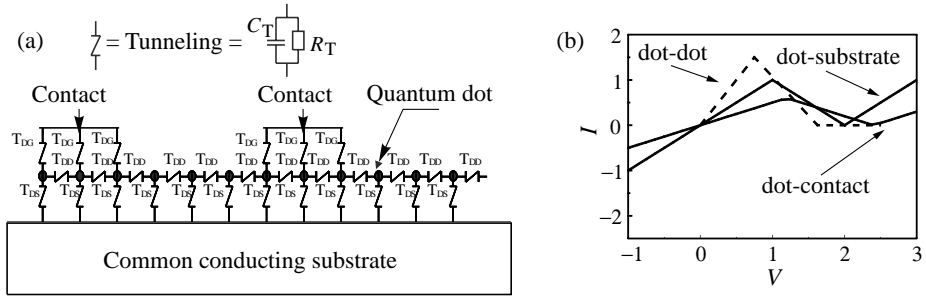


**Fig. 2.** (a) The analog circuit for the considering structure. The “Z” signs depict tunneling approximated by a parallel capacitance/non-linear resistance circuit. Three tunneling processes labeled by  $T_{DD}$ ,  $T_{DS}$  and  $T_{DG}$  are dot-dot, dot-substrate and dot-contact tunneling, respectively. (b) Tunneling resistance approximation. Two solid curves correspond to dot-contact and dot-substrate tunneling, respectively. The dashed curve corresponds to dot-dot tunneling.

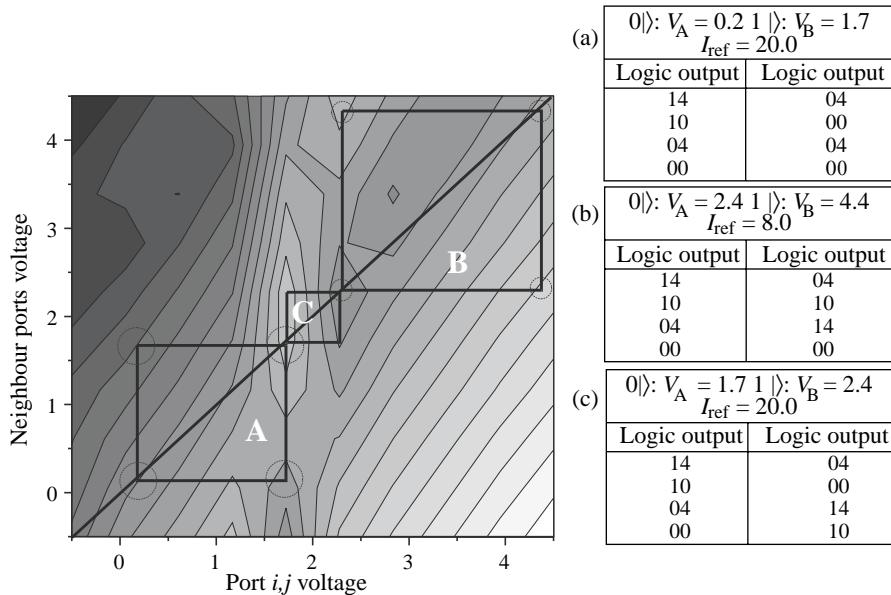


**Fig. 3.** Contours of equal cell  $i, j$  current  $I_{i,j}$  in a five-cell system (ports labeled in Fig. 1 by  $i-1, j; i, j; i+1, j; j-1, i; j+1, i$ ). All non-central cells are assumed to have the same input voltage  $V_{i-1,j} = V_{i,j-1} = V_{i+1,j} = V_{i,j+1}$ . Three true tables labeled as (a), (b) and (c) correspond to three combinations of  $V^0$ ,  $V^1$  and  $I_{ref}$  depicted graphically by three squares **A**, **B** and **C**, respectively.

shown three true tables labeled (a), (b) and (c) corresponding to the three sets of  $V^0$ ,  $V^1$  and  $I_{ref}$  depicted in Fig. 3 by three squares **A**, **B** and **C**, respectively. Each of the true tables corresponds to the one of transition rules. Thus, varying the coding voltages  $V^0$  and  $V^1$  we can switch the transition logic from one described by the true table (a) to the another described by the true table (b) and vice versa.

### 3. Discussion and conclusions

The most critical issues for the presented scheme are fluctuations of quantum dot density and size. Indeed, two neighbor cells may simply have different numbers of dot under the contacts. A loss or an add of a dot may substantially vary cell characteristics. Although one of the possible solutions is a quantum dot density increase (contact area increase) to minimize dot density fluctuation effect on cell characteristic, it is in contradiction with general demand of chip density enhancement. In our case, the effective cell unification can be achieved by proper choose of the external parameters ( $V^0$ ,  $V^1$ ,  $I_{\text{ref}}$ ). In Fig. 3 we have shown dashed circles at the each peak of the squares. The area of these circles has mean of permissible variation in the cell I–V characteristic without effect on cell logic functionality. One can see that value of the variation is a function of particular material structure, driven parameters and logic function. Thus, for the “AND” gate operation up to 30 percent variation in the cell characteristic is permissible. While for the “OR” gate, much higher accuracy is required. The “AND” gate operation has maximum resistance to the structure imperfections while other gates require much more uniform structure. In any particular case, experimental data have to be taken into consideration in order to construct logic module and optimize the edge driven parameters. The presented results based on approximated resonance tunneling characteristics are aimed to demonstrate an attractive multi-rules module potential and possible ways of module operation stability enhancement with respect to inevitable structure imperfections.

#### Acknowledgments

The authors thank Prof. V. P. Roychowdhury for valuable discussions. The work was supported by the SRC program on Integrated Nanosystems (James A. Hutchby).

#### References

- [1] C. S. Lent and P. D. Tougaw, *Proc. IEEE* **85**, 541-57 (1997).
- [2] G. H. Bernstein, I. Amlani, A. O. Orlov and G. L. Snider, *Proc. IEEE Silicon Nanoelectronics Workshop* Kyoto, Japan, p. 38-9, (1997).
- [3] C. Single, R. Augke, F. E. Prins, D. A. Wharam and D. P. Kern, *Superlattices and Microstructures*, **28**, p. (2000).
- [4] V. P. Roychowdhury, D. B. Janes, S. Bandyopadhyay and X. Wang, *IEEE Trans. Electron Dev.* **43** 1688–1699 (1996).
- [5] V. P. Roychowdhury, D. B. Janes and S. Bandyopadhyay, *Proc. IEEE* **85**, 574-88 (1997).

## Feasibility study of the spin wave quantum network

A. Khitun, R. Ostroumov and K. L. Wang

Device Research Laboratory Electrical Engineering Department  
University of California-Los Angeles, Los Angeles, California 90095-1594

**Abstract.** We propose an implementation of the spin waves for massively parallel quantum network. A spin wave based quantum network offers an advantage of random access to any qubit in the network and, consequently, the ability to recognize two qubit gates and performance gate operation between any two distant qubits. Using model simulations we illustrate the process of the two distant qubit entanglement via spin waves exchange. The utilization of spin waves allows us to avoid the most difficult single electron spin measurement procedure. Instead, qubit state recognition is accomplished by measurement of spin wave excited in a ferromagnetic layer. By estimate the proposed scheme has as high as  $10^4$  ratio between quantum system coherence time and the time of a single computational step.

### Introduction

Quantum Networks attract increasing attention due to their big promise as extremely powerful computational tools. Advantage of quantum mechanical superposition instead of classical pure states together with massive parallelism inspired from neural networks is going to revolutionize current computing technologies. The involving of quantum effects into computation procedure significantly scales down material structure. Molecules, nuclei or single electrons are considered now as potential quantum information bit carries — qubits. Each candidate is evaluated in terms of the information storage time (coherence time), the energy and the time of switching between  $|0\rangle$  and  $|1\rangle$  states and technological accessibility. Recent investigations of the electron spin relaxation in pure semiconductors have shown electron spin as a most attractive object for information to be coded. Electron spin has long enough coherence time (up to milliseconds at 1 K temperature in Si [1]) and can be easily manipulated by the applied electro-magnetic field. The problem of random access/entanglement becomes the most important issue on the present way of high parallel quantum network development. Several quantum schemes with random access entanglement capabilities have been already proposed (for example, atoms or quantum dots in the quantum electro-dynamics cavities [2, 3] and ions trapped in the laser field [4]). However, these systems have another drawbacks: short coherent interaction time and limited scalability to large number of qubits. In this work we present the feasibility study of the Spin Wave Quantum Network (SWQN) utilizing spin waves for qubit entanglement as well as qubit random access.

### 1. Material Structure

In Fig. 1 we have shown schematically the material structure of the SWQN. There are n-doped silicon substrate on the bottom, then, in a sequence, the Ferromagnetic Layer (FL) (20 nm), silicon spacer (50 nm) with implanted  $^{31}\text{P}$  atoms and metallic gate electrodes on the top of the silicon spacer.  $^{31}\text{P}$  atoms provide weakly bounded electrons, which serve as qubits (electron wave function densities are depicted in Fig. 1 by the gray spheres). Thus, the

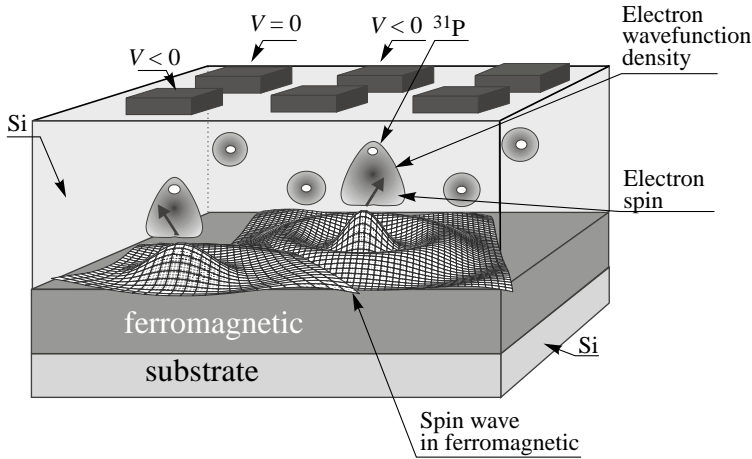


**Fig. 1.** Schematics of the material structure. There are silicon substrate on the bottom, then, in a sequence, the Ferromagnetic Layer (FL) (20 nm), silicon spacer (50 nm) with implanted  $^{31}\text{P}$  atoms and metallic gate electrodes on the top of the silicon spacer. Spins of the  $^{31}\text{P}$  atom bounded electrons are used as qubits.

proposed structure consists of simple Si-FL-Si layers with implanted atoms and electrodes deposited on the top. Here, we would like to pay attention to the ferromagnetic material to be used in the described scheme. Although deposition of a number of different antiferromagnetic and ferromagnetic films on a silicon substrate has been already demonstrated and exchange integrals of the composite materials were tabulated [5–8], metal silicides, particularly  $\text{FeSi}_2$ , is of our special interest. In the past two decades it was demonstrated that metal silicides can be grown epitaxial layers on silicon substrates. Initially, it was supposed to use metal silicides in so called post-shrink devices as well for conducting interconnects in three dimensional devices. Of the metal silicides,  $\text{FeSi}_2$  has received extensive attention because it is a semiconductor.  $\text{FeSi}_2$  exists in two thermodynamically stable phases, as theragonal, metallic  $\alpha$ - $\text{FeSi}_2$ , and as orthorhombic, semiconducting  $\beta$ - $\text{FeSi}_2$ . The phase transition occurs at 1200 K.  $\text{FeSi}_2$  atomic structure closely resembles that of Si smaller than that of Si. It has been shown that high quality epilayers of up to 200 nm thickness can be grown by MBE. For coherent epitaxial growth, there are no misfit dislocations and all lattice sites across the interface are in perfect registry. The preparation of the silicide layers is described elsewhere [9, 10].

## 2. Network operation

All qubits in the network interact with each other via spin wave exchange. The FL plays the key role as an information channel. Being of the wave nature, the collective spin oscillations in the FL present an excellent mechanism for the quantum information exchange. Any desired gate operation between two distant qubits can be decomposed into a sequence of the control qubit coupling with the FL, spin wave propagation, and coupling with the target qubit. It is important that the qubits are not in the permanent contact with the FL. The strength of the coupling is controlled by the gate voltage. At zero gate voltage the coupling between qubit and the FL is negligible, while applying a negative gate voltage we shift electron toward the FL and thus control the strength of the coupling. Varying

amplitude and duration of the gate voltage, one can excite spin wave of desired amplitude and frequency while the wave phase is defined by the qubit state.

The main requirement for any quantum computing system is that the coherence time has to be larger than the time of computation. In the described Spin Wave Quantum Network the computation time is a sum of the control qubit-FL coupling time, spin wave propagation time and the target qubit-FL wave read-out time. For the practically achievable coupling exchange integral of 0.5 meV for the qubit-FL coupling, the total interaction time is  $10^{-9} - 10^{-10}$ . The maximum spin wave propagation time is the domain length divided by the spin wave group velocity. During this time all qubits have to keep their information intact and spin waves excited from the qubits have to remain coherent. The coherence time for the electron spin in silicon at low temperature may be as high as microseconds. As to the spin waves, there are several scattering processes that can destroy spin wave coherence: scattering by phonons, spin waves, conduction electrons and defects. The strongest scattering processes are spin-spin and spin-phonon interactions, which define the coherence time of the spin wave in the defect free ferromagnetic at low temperature. The corresponding relaxation times are:

$$\begin{aligned}\tau_{mm} &\approx \frac{\hbar}{\Theta_C} \left( \frac{\Theta_C}{T} \right)^4, & T \ll \Theta_C \\ \tau_{mp} &\approx \frac{\hbar}{\Theta_D} \left( \frac{\Theta_D}{T} \right)^5, & T \ll \Theta_D\end{aligned}\quad (1)$$

where  $T$  is the temperature and  $\Theta_C$  is the Curie temperature and  $\Theta_D$  is the Debye temperature. These relaxation times have very strong temperature dependencies and are about microseconds at temperature of several K.

### 3. Conclusions

In Table 1. we summarize several characteristic times of the proposed scheme: electron spin relaxation time, spin wave coherence time, qubit-AFL coupling time and spin wave propagation time. All above times are given for the temperature of 1 K. As seen in Table 1., simultaneous utilization of the single electron for information storage and spin waves for the inter-qubit information exchange gives us favorable coherence and computation times. The proposed scheme has a high (about  $10^4$ ) ratio between system coherence time and time of a single computational step. The most attractive feature of the proposed scheme is the possibility of random access to any qubit and entanglement between any of them. The most important disadvantage is that spin wave coherence time strongly depends on temperature. Thus, the operation temperature range is restricted to 0.1–1 K.

**Table 1.**

System coherence time		Time of computation	
Electron spin relaxation time	Spin wave coherence time	Qubit coupling time	Spin wave propagation time
$10^{-6}$ s	$10^{-6}$ s	$10^{-9} - 10^{-10}$ s	$10^{-9} - 10^{-10}$ s

### Acknowledgements

The work was supported by the DARPA program on Spin-Resonance transistors (Dr. S. Wolf) and ARO program on Spin Coherent Photon Transmitter/Receiver Systems (Dr. Henry Everitt).

### References

- [1] R. Wiesendange, I. V. Svets, D. Burler, G. Tarrach, H-J. Guntherodt and J. Coey, *Europhys. Lett.* **19**, 141 (1992).
- [2] A. Imamoglu, D. D. Awschalom, G. Burkard, D. P. DiVincenzo, D. Loss, M. Sherwin and A. Small, *Phys. Rev. Lett.* **83**, (no.20), 4204–7 (1999).
- [3] J. Cirac and P. Zoller, *Phys. Rev. Lett.* **74**, 4091 (1995).
- [4] P. Pradhan, M. P. Anantram and K. Wang, LANL archive: quant-ph/0002006; also, *Bulletin of the American Physical Society* **44**, 1240 (1999) (talk no. QC41.5)
- [5] E. Giesse, J. Dengler, G. Ritter, D. Brandl and H. Voit, *Hyperfine Interactions*, vol. 93, (no.1-4), (International Conference on the Applications of the Mossbauer Effect: ICAME'93, Vancouver, BC, Canada, 8–14 Aug. 1993.) Nov. pp. 1415–19 (1994).
- [6] B. Saftic, N. Rasula, W. Zinn and J. Chevallier, *J. Magnetism and Magnetic Materials* **28**, 305–12 (1982).
- [7] A. B. Chizhik, D. N. Merenkov, S. L. Gnatchenko, K. Fronc and R. Zuberek, *Fiz. Niz. Temp.* **27**, 886–95 (2001).
- [8] M. L. Munford, L. Seligman, M. L. Sartorelli, E. Voltoini, L. F. O. Martins, W. Schwarzacher and A. A. Pasa, *J. Magnetism and Magnetic Materials* 226–230, 1613–15 (2001).
- [9] N. Cherief, C. d'Anterrosches, R. C. Cinti, T. A. Nguen Tan and J. Derrien, *Appl. Phys. Lett.* **55**, 1671 (1990).
- [10] K. Lefki, P. Muret, N. Cheriefand and R. C. Cinti, *J. Appl. Phys.* **69**, 352 (1991).
- [11] A. I. Akhiezer, V. G. Bar'vakhtar and S. V. Peletminskii, *Spin Waves* Nort-Holland Publishing Company-Amsterdam, pp 259–277, 1968.

## The proposed large-scale ensemble silicon-based NMR quantum computers

A. A. Kokin and K. A. Valiev

Institute of Physics and Technology of RAS  
34, Nakhimovskii pr., 117218 Moscow

**Abstract.** It is presented the extension of Kane's scheme [1] to ensemble approach version with strip gates. For the initialization of nuclear quantum states it is proposed to use the solid-state effect in ENDOR technique. It is suggested the possible planar silicon topology of such ensemble quantum computer and shown that the measurement with standard NMR methods signal of  $L \sim 10^3$  qubit system may be achieved. As another variant of ensemble silicon quantum computer the gateless architecture of cellular-automaton is also considered.

1. Atomic nuclei with a spin quantum number  $I = 1/2$  seem to be the *natural candidates* for qubits — two-level quantum elements in quantum computers. The early approach to NMR quantum computers was suggested in 1997 and then confirmed in experiments. In this approach it was used several diamagnetic organic liquids which individual molecules, having a number  $L$  of non-equivalent nuclear spins-qubits with  $I = 1/2$  and being nearly independent one another. The molecules act in parallel as an ensemble of *almost independent* quantum microcomputers. Computers of this type are called *bulk-ensemble* quantum computers. They can operate at *room temperature*. For measurements of qubit states the standard NMR technique is assumed. *Signal to noise ratio* is proportional to the number of molecules  $N$  and a factor that for the room temperature is scaled down as  $L2^{-L}$ . It is generally believed that for the liquid bulk-ensemble quantum computers have a *limiting value*  $L \sim 20-30$  [2].

2. For realization of *large-scale NMR quantum computers* a necessary number of qubits in quantum register should be  $L > 10^3$  that may be attained only at *very low temperatures* in *solid-state* structures. The design of solid-state quantum computer with arbitrary large value  $L$  was proposed by B. Kane in [1]. It was suggested to use an semiconductor MOS-type structure on a  $^{28}\text{Si}$  spinless substrate, into a near-surface layer of which  $^{31}\text{P}$  stable isotopes, having nuclear spin  $I = 1/2$  and producing a large quasi-one-dimensional *artificial "molecule"*, are implanted. It was suggested an electrical control and measurement of individual qubits states through the use of special gate structures.

There are *four difficulties* in implementing of Kane's quantum computer:

- (1) Signal from the spin of an individual atom is very small and requires *high sensitive measurement methods*.
- (2) For initialization nuclear spin states it is required to use of *very low nuclear spin temperature* (of order mK).
- (3) Regular donors and gates arrangement require high precision in *nanometer scale*.
- (4) It is necessary to suppress the *decoherence* of quantum states defined by *thermal fluctuations* of gate voltage.



3. As an alternative, we have proposed the variant of *an ensemble silicon-based quantum computer* [3, 4]. In this case, unlike the structure suggested by B. Kane, gates **A** and **J** form a *regular* chain of narrow ( $l_A \sim 10$  nm) and *long strips*. Under the strip gates **A** ( $y$ -axis) paramagnetic phosphorus atoms at  $l_y$  distant from each other are placed.

The separation between neighboring strip gates **A** (and phosphorus atoms), as in Kane's scheme, must be  $\leq 20$  nm. In this case the interqubit interaction is controlled by intermediate **J** gates. For  $l_y \gg l_x$  the exchange spin interaction between electrons of donor atoms under **A** gates is assumed negligibly small and as result of with the system breaks down into an ensemble of near-independent Kane's artificial "molecule", whose electronic spins at temperature  $T \leq 0,1$  K are initially fully aligned with the field of several Tesla.

Here we will give a some further development of the scheme previously considered.

4. The read-out signal from the such *ensemble in parallel acting* chains, as distinct from liquid prototype, for full nuclear polarization or for spin temperatures  $T_I \leq 10^{-3}$  K has no small factor of type  $2^{-L}L$ . The performed estimates indicate that the read-out signal in our scheme may be *available for standard NMR technique* if the number of "molecules" in ensemble will be  $N \sim 10^5$ . It may be more reduced through the use of an electron-nuclear double resonance (ENDOR) methods [5]. For the realization of an ensemble silicon quantum register we propose a variant of planar silicon topology scheme.

Consequently, high-sensitive devices for individual measurements are not needed and *the first* difficulty of Kane's scheme can be overcome.

5. The *extremely long relaxation times* of the electron and nuclear spins at low temperatures imply that the required initializing can be attained by deep cooling at short duration *only nuclear spin system* to  $T \leq 1$  mK without deep cooling of lattice. We have shown that there is the possibility to reach it at *indirect cooling* of nuclear spin system by means of *dynamic nuclear spin polarization techniques* (solid state effect) by the same ENDOR technique at the lattice temperature of order 0,1 K.

In this way the *second* difficulty of Kane's scheme can be overcome.

6. To implement an ensemble silicon quantum computer, operated on *cellular-automaton principle* [4, 6], it may be useful the previously considered system of long chains of donor atoms  $^{31}\text{P}$  disposed in silicon, but free of the **A** and **J** gates. If exchange interaction constant (it is here positive) for localized electronic spins of  $^{31}\text{P}$  along the gate **A** is more than Zeeman energy and the temperature is well below the critical temperature for electron spin ordering (Neel temperature), the one-dimensional *antiferromagnetically ordered ground state* of electronic spins is produced. For the exchange interaction constant, that correspond to the distance between donors  $l_y \sim l_x \sim 20$  nm, the electron spin critical temperature will be  $\sim 4$  K.

Due to hyperfine interaction nuclear spins will be oriented according to the electronic spin direction in the resultant field and will form array with the alternating orientation of nuclear spins. At magnetic fields  $\sim 3.5$  T and at temperatures  $\sim 10^{-3}$  K the nuclear spins  $^{31}\text{P}$  will form a periodic ground state array of ABAB... type with almost 100% opposite orientation. That is the distinct nuclear spins are *in initialized ground state*.

The using of dynamic methods makes possible the high orientation of nuclear spins also at larger temperatures and this state will be *the long-lived nonequilibrium* nuclear spin state. The dynamic methods makes possible to receive the high orientation of nuclear spins also at larger temperatures and this state will be *the long-lived nonequilibrium* nuclear spin state. We describe the organization of logic operations in this systems.

It follows that the going to ensemble quantum cellular automaton permits to overcome *the third* and *fourth* difficulty of Kane's scheme.

7. The dipole-dipole interactions of nuclear spins with polarized *random distributed* paramagnetic centre (atoms and defects) in substrate and with *nuclear spins* of impurity atoms of nuclear spin containing elements are the main mechanisms of quantum states decoherence in the ensemble quantum computers. The requirements for a *degree of cleaning* from unwanted impurities was stated. We have discussed also the other ways of decoherence suppressing.

## References

- [1] B. E. Kane, *Nature (London)* **393** 133–137 (1998).
- [2] J. A. Jones, *NMR Quantum Computation: a Critical Evaluation* LANL arXiv:quant-ph/0002085. (2000)
- [3] K. A. Valiev and A. A. Kokin, *Microelektronika* **28** 326–337 (1999) (in Russian).
- [4] K. A. Valiev and A. A. Kokin, *Quantum Computers: Reliance and Reality* Moscow-Izhevsk R&C, 2001 (in Russian).
- [5] A. Abragam and M. Goldman, *Nuclear Magnetism: Order & Disorder* (Oxford: Claren. Press.) 1982.
- [6] A. A. Kokin, *Quantum Computers & Computing* Moscow-Izhevsk, Vol. 2, p. 54–67, 2001.

## Dimensional magnetoplasma resonance in GaAs/AlGaAs heterostructures

*B. M. Ashkinadze, E. Cohen and Arza Ron*

Solid State Institute, Technion – Israel Institute of Technology, Haifa 32000, Israel

**Abstract.** The physical processes in a two-dimensional electron gas (2DEG) driven into a nonequilibrium state by light illumination or increased microwave power are studied by combined optical and dimensional magnetoplasma resonance (DMPR) spectroscopies. A hysteretic DMPR, an optical bistability of the exciton and 2DEG photoluminescence, an evolution of the photoexcited electron-hole system from exciton to metal state in modulation doped and undoped heterostructures are investigated.

The cyclotron resonance (CR) in the far-infrared (FIR) and microwave (mw) ranges is an important probe of the two-dimensional electron gas (2DEG) properties. It is known that the CR transforms into a dimensional magnetoplasma resonance (DMPR) with increasing electron density  $n_{2D}$  [1-3], if the mw (FIR) radiation wavelength is larger than the spatial dimensions of the area where the 2DEG is confined (for example, electron puddle in an inhomogeneous 2DEG). For a disk-shaped 2DEG area, the DMPR resonant frequencies are given by  $\omega_{\pm} = (\omega_p^2 + \omega_{CR}^2/4)^{1/2} \pm \omega_{CR}/2$ , where  $\omega = 2\pi f$  is the radiation frequency,  $\omega_{CR} = Be/mc$ , and  $\omega_p$  is the plasma frequency for the confined 2DEG. The two resonance branches  $\omega_{\pm}$  are the cyclotron-like magnetoplasma and edge magnetoplasma ones, respectively [3]. For a linearly polarized radiation  $\omega$ , disk diameter  $a$ , and 2DEG density  $n_{2D}$ , the DMPR magnetic field strength  $B_R$  is shifted from the classical electron CR value  $B_{CR} = \omega mc/e$ :

$$B_R = B_{CR} - 3\pi^2 ec n_{2D} / 2\kappa \omega a \quad (1)$$

where  $\kappa$  is the average dielectric constant value of the sample and free space. The cyclotron-like DMPR branch corresponds to  $B_R > 0$ . As in the CR case, the DMPR resonance line shape can be fitted to a Lorentzian that yields the 2D-electron momentum relaxation rate, and thus, the CR mobility  $\mu_{CR}$  can be estimated. A remarkable feature of the DMPR is its  $B_R$ -dependence on  $n_{2D}$ . This allows one to study the properties of the 2DEG in a nonequilibrium state.

Here, we review our recent DMPR spectroscopy studies of the physical processes in a 2DEG driven into a nonequilibrium state by light illumination or by increased microwave power. In several 2DEG studies under increased mw (FIR) power, a resonant change in the 2DEG magnetoresistance [4–6] and in the 2DEG magneto-photoluminescence (PL) (optically detected resonance, ODR) [7, 8] were observed. However, the underlying physical mechanisms of these phenomena were not specified. We show that the time-resolved mw and PL studies, under the DMPR condition, allow us to identify these mechanisms.

Two types of the GaAs/AlGaAs heterostructures (HS) were studied: a. Single-side, modulation-doped, high mobility heterojunctions (HJ's) and quantum wells (QW's), with  $n_{2D} = (0.6-3) \times 10^{11} \text{ cm}^{-2}$  and with a dc-mobility higher than  $10^6 \text{ cm}^2/\text{Vs}$  at 4K. For these HS's,  $n_{2D}$  can be reduced down to  $10^{10} \text{ cm}^{-2}$  by optical depletion (with He-Ne laser illumination). b. Undoped, mixed type I-type-II-type QW's in which  $n_{2D}$  varied from  $10^6 \text{ cm}^{-2}$  to  $3 \times 10^{11} \text{ cm}^{-2}$  by He-Ne laser illumination [9]. The following physical phenomena will be discussed:

1. Nonlinear hysteretic DMPR under 2DEG mw heating. The hysteresis and switching phenomena are observed in the mw radiation magnetotransmission of the modulation-doped QW and HJ at increased mw power. A phenomenological model based on the nonlinear DMPR (2DEG density-dependent CR), describes reasonably well the main experimental findings [10].

2. Bistability of the 2DEG-free hole photoluminescence (PL) in modulation-doped GaAs/AlGaAs QWs. A significant reduction of  $n_{2D}$  is found when the 2DEG is heated by mw irradiation at 1.8 K. The dependence of  $n_{2D}$  on the effective electron temperature  $T_e$  leads to a remarkable hysteresis of the optically detected DMPR, namely, to a bistability of the 2DEG-free hole PL spectrum as the magnetic field is scanned back and forth (Fig. 1). The PL time-resolved study shows that  $n_{2D}$  depends on the mw pulse duration and has a long recovery time ( $\sim 10^{-2}$  s). This phenomenon is attributed to an increased vertical transport of the warm electrons out of the quantum well [11].

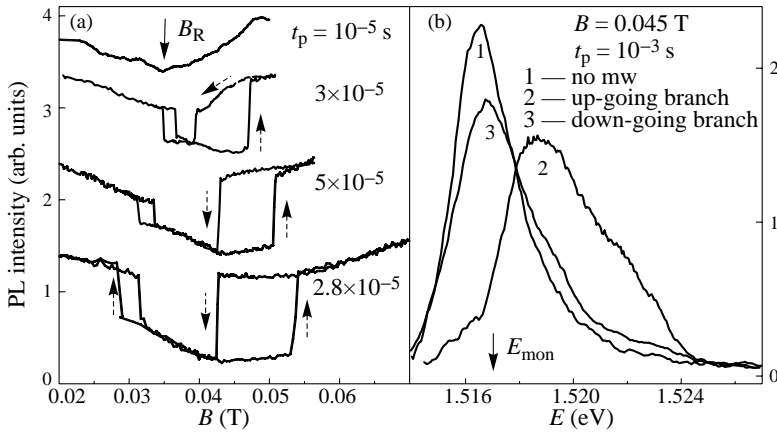


**Fig. 1.** Optically detected dimensional magnetoplasma resonance in a modulation doped 25 nm QW (0.5 mm diameter mesa,  $T = 2$  K). (a) PL intensity at  $E_{mon} = 1.517$  eV vs  $B$ . The PL is measured between mw pulses of duration  $t_p$  and repetition frequency 1 kHz (mw power  $P_{in} = 1$  mW).  $B$  is slowly scanned back and forth, as shown by arrows. The hysteresis curves are vertically shifted for clarity. (b) The PL spectra obtained at the two hysteretic branches. The difference in the PL spectra for the same  $B$  is due to different  $n_{2D}$  and  $T_e$  values on up- and down-branches.

3. Optically detected DMPR in HJ — indirect interaction between the free excitons and the 2DEG. In modulation-doped, high quality HJ, the increased vertical transport of hot electrons gives rise to the hysteretic behavior of the free exciton PL intensity. We show that the PL in such HJ's arises from free excitons that recombine radiatively in the GaAs buffer layer, far from the 2DEG. The exciton PL is affected by a mw heating of the 2DEG, and thus, its intensity exhibits a resonance and a bistability under a perpendicular magnetic field that corresponds to the 2DEG DMPR condition (Fig. 2). The PL intensity change is interpreted as being due to the interaction of the excitons with low-energy, ballistically propagating acoustic phonons that are emitted by the mw-heated 2DEG [12].

4. At low mw power irradiation, the linear DMPR or electron cyclotron resonance (CR) are used in order to measure the density and mobility of the nonequilibrium 2DEG as a function of photoexcitation intensity (Fig. 3). This allows us to study the evolution from a high mobility degenerate 2DEG into an insulating state, consisting of excitons and exciton complexes [13].

5. The results of the PL, PLE, photoinduced mw absorption (PMA) studies show that the

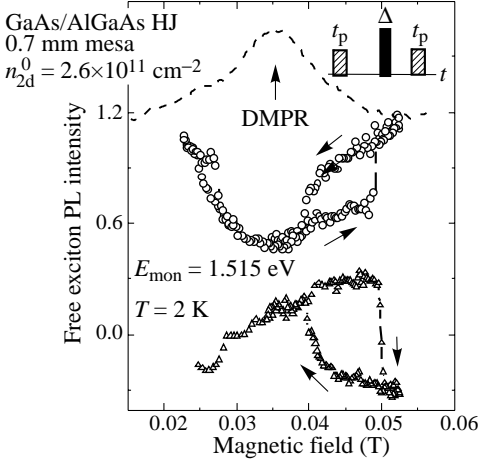


**Fig. 2.** Optically detected (by free exciton PL) DMPR of the 2DEG in a single heterojunction. Mw pulses ( $t_p$ ) and PL gating time ( $\Delta$ ) are shown in inset,  $P_{in} = 1$  mW, repetition frequency 130 Hz. Triangles — ODR obtained when  $t_p$  and ( $\Delta$ ) coincide and  $t_p = 1$  ms. Circles and dots display the ODR traces measured between mw pulses at  $t_p = 1$  ms and 0.01 ms, respectively.

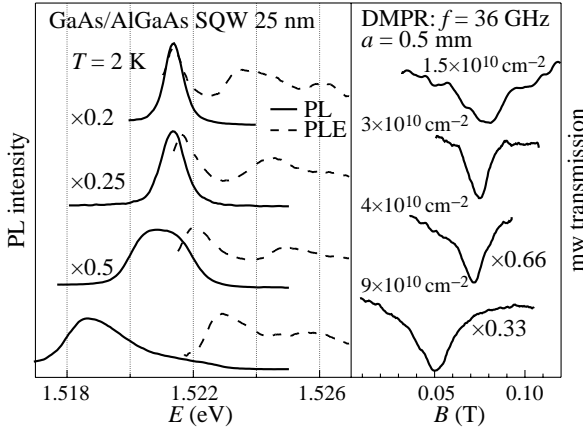


**Fig. 3.** PL, PLE and DMPR observed with decreasing 2DEG density (by increasing the He-Ne laser intensity).  $n_{2D}$  is obtained from the measured  $B_R$  values (see Eq. 1.)

photoexcited electrons and charged excitons (trions) are localized in the dilute 2DEG (in the range of  $n_{2D}$  ( $10^6 - 10^{10}$ )  $\text{cm}^{-2}$  in undoped GaAs/AlGaAs QW's [14]. Fig. 4 displays the PLE spectral evolution with increasing  $n_{2D}$  for mixed type I-II QW. The narrow exciton line (linewidth 0.5 meV) in the PLE spectrum at low  $n_{2D}$ , demonstrates high QW quality. The PLE spectra are measured after the He-Ne light pulse terminates (delay time of  $10^{-3}$  s). Photogenerated electrons (holes) have a long lifetime, and thus, they are localized in the fluctuating QW potential. In the mw absorption, we do not observe the mw CR and DMPR due to free electrons in the studied QW's. Light absorbed around these electrons, generates the localized electron-exciton complexes (trion line in the PLE spectra). One can see that the energy separation between trion and exciton lines does not increase with  $n_{2D}$  [15].

In addition, we show that free excitons can generate a significant amount of electrons due to a nonthermal Auger-like exciton dissociation in high-quality QWs [16]. This was observed by studying the excitation spectra of the photoinduced mw radiation (36 GHz) absorption (Fig. 5).

#### Acknowledgements

We thank L. N. Pfeiffer and V. Umansky for supplying us with the samples. The work was supported by the Israel Science Foundation, B.M.A. acknowledges support by a grant of Kamea Program.

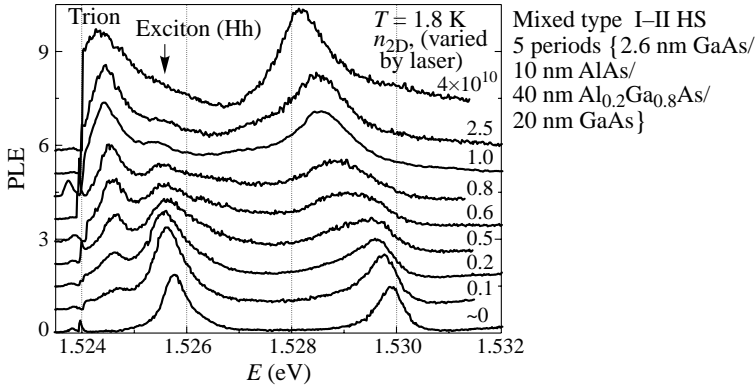


**Fig. 4.** PL excitation spectra for the mixed type I-II QW's. The pulsed He-Ne laser varies  $n_{2D}$ , and the PLE spectra are obtained with cw dye laser (PL is measured in the gates after He-Ne pulses terminate).

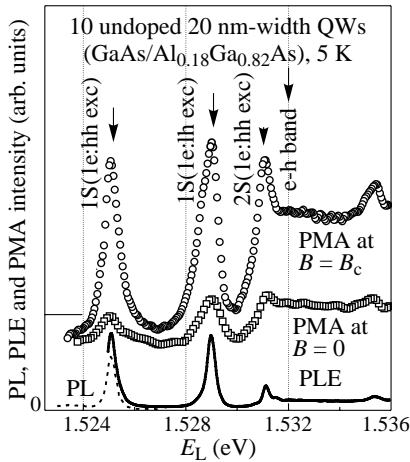


**Fig. 5.** The PL excitation (PLE) spectra and the photoinduced microwave absorption (PMA) excitation spectra for a high quality undoped 20 nm-width QW sample at 4.5 K. The mw absorption vs  $E$  is measured at  $B = B_{CR}$  and with very low mw power.

## References

- [1] G. Dresselhaus, A. F. Kip and C. Kittel, *Phys. Rev.* **98**, 368 (1955).
- [2] S. J. Allen *et al*, *Phys. Rev.* **B28**, 4875 (1983).
- [3] W. Hansen *et al*, *Semicond. and Semimetals* **35**, 279 (1992).
- [4] K. Tsujino *et al*, *Physica* **B249**, 571 (1998).
- [5] B. Meurer, *Phys. Rev.* **B49**, 16813 (1994).
- [6] M. Zudov *et al*, *Phys. Rev.* **B64**, 201311 (2001).
- [7] S. Gubarev *et al*, *JETP Lett.* **54**, 355 (1991).
- [8] G. S. Herold *et al*, *Physica* **E2**, 39 (1998).
- [9] A. Nazimov *et al*, *J. Lumin.* **85**, 301 (2000).
- [10] B. M. Ashkinadze and V. Yudson, *Phys. Rev. Lett.* **83**, 812 (1999).
- [11] B. M. Ashkinadze *et al*, *Phys. Rev.* **B64**, 161306 (2001).
- [12] B. M. Ashkinadze *et al*, *Phys. Rev.* **B62**, 16894 (2000).
- [13] B. M. Ashkinadze *et al*, *Proc. ICPS23*, (Berlin, 1996).
- [14] T. M. Yeo *et al*, *Physica E* **12**, (2002).
- [15] R. A. Suris *et al*, *Phys. Stat. Sol. (b)* **343**, (2001).
- [16] B. M. Ashkinadze *et al*, *Phys. Stat. Sol. (a)* **178**, 107 (2000).

## Magnetoresistance in long InSb nanowires

*S. V. Zaitsev-Zotov*<sup>†</sup>, *Yu. A. Kumzerov*<sup>‡</sup>, *Yu. A. Firsov*<sup>‡</sup> and *P. Monceau*<sup>§</sup>

<sup>†</sup> Institute of Radioengineering and Electronics of Russian Academy of Sciences, Mokhovaya 11, 101999 Moscow, Russia

<sup>‡</sup> Ioffe Physico-Technical Institute, St Petersburg, Russia

<sup>§</sup> Centre de Recherches sur Les Très Basses Températures, C.N.R.S., B.P. 166, 38042 Grenoble Cédex 9, France

**Abstract.** Magnetoresistance of long correlated nanowires of degenerate semiconductor InSb in asbestos matrix (wire diameter is around 50 Å, length 0.1–1 mm) is studied over temperature range 2.3–300 K. At zero magnetic field the electric conduction  $G$  and current-voltage characteristics of such wires obeys the power laws  $G \propto T^\alpha$ ,  $I \propto V^\beta$ , expected for one-dimensional electron systems. The effect of magnetic field corresponds to 20% growth of the exponents  $\alpha$ ,  $\beta$  at  $H = 10$  T that may result from breaking of the spin-charge separation in the one-dimensional electron system.

### Introduction

Electron-electron correlation effects being negligible in three-dimensional case play the dominant role in one dimension. One of the most significant consequence of the correlation effect is the absence of quasiparticle excitations in 1D metals. Instead, in 1D case the collective excitations associated with separate spin and charge degrees of freedom are developed and lead to formation of so-called Luttinger liquid (LL) [1]. Transport in LL cannot be described by the conventional kinetic equation. Charged impurity in a 1D electron system forms a tunneling barrier. Absence of single-particle excitations complicates tunneling of electrons in LL and leads to a power law dependence of tunneling density of states. Tunneling through this barrier provides the power laws for the linear conduction  $G \propto T^\alpha$ ,  $I \propto V^\beta$  [1] of impure 1D wires.

Experimental study of 1D behavior remains a challenge. Single-wall and multiwall carbon nanotubes and molecular wires are intensively studied last years. One of the most dramatical effect of reduced dimensionality on physical properties of long nanowires was reported recently for an electric conduction of InSb nanowires in an asbestos matrix [2]. It has been found that  $G$  as a function of temperature and electric field follows the power laws over 5 orders of magnitude of conduction variation. The effect was considered as a manifestation of the Luttinger-liquid-like behavior of an impure 1D electron system.

Here we present magnetoresistance data for InSb nanowires in an asbestos matrix in magnetic fields up to 10 T. The observed magnetoresistance corresponds to magnetic-field dependence of the exponents  $\alpha$ ,  $\beta$  that may result from magnetic-field-induced breaking of the spin-charge separation.

### Experimental

We studied the electrical conduction of long InSb nanowires in asbestos matrix as a function of magnetic field, temperature and electric field. Sample preparation and characterization have been described in details elsewhere [2]. The data reported below were obtained for two samples demonstrating LL-like behavior with zero magnetic field exponents  $\alpha = 2.2$ ,

$\beta = 2.11$  (sample 1),  $\alpha = 4.5$ ,  $\beta = 3.5$  (sample 2). Magnetoresistance of both samples demonstrates similar behavior.

## Results

Figure 1 shows a typical variation of the electric current,  $I$ , measured at a set of fixed voltages, vs. magnetic field. Conduction reaches a maximum at  $T \approx 1$  T and falls down by a factor of 5 at  $H = 10$  T at given temperature. For relatively small voltages (corresponding to the linear conduction regime) the effect of magnetic field on the conduction is practically independent on the voltage. For bigger voltages it is getting smaller. The observed magnetoconduction is slightly anisotropic and the ratio  $[I(H) - I(0)]/I(0)$  for  $H \perp I$  is approximately 20% bigger than for  $H \parallel I$ .

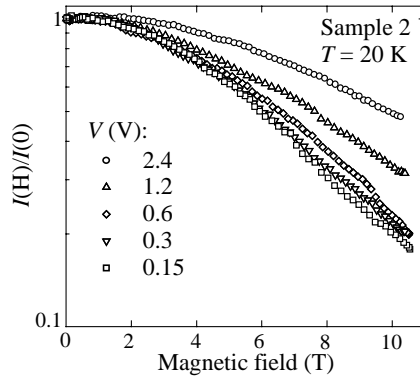


**Fig. 1.** Typical set of electric currents vs. magnetic field curves measured at different voltages.  $H \perp I$ .

Figure 2 shows the effect of the magnetic field on the shape of I–V curves. At relatively high temperatures (80 K curve) the effect of magnetic field is small. At lower temperatures the effect is much more pronounced (up to one order of current suppression was observed at  $T \leq 5$  K for  $H > 10$  T) and is smaller for bigger electric fields. For comparison: for InSb extracted from asbestos cracks a negative 20% magnetoconduction was observed at  $T = 4.2$  K and  $H = 10$  T.

Figure 3 shows a double logarithmic plot of the temperature variation of the ratio  $G(H = 10 \text{ T})/G(0)$  measured at smallest  $V$  for both studied samples. It is clearly seen that the magnetoconduction depends on temperature and grows with lowering temperature approximately as a power function of the temperature.

## Discussion

The observed magnetoresistance corresponds to a magnetic-field induced variation of the exponents for  $G(T)$

$$G(T) = G_0 \left( \frac{T}{\epsilon} \right)^{\alpha(H)} \quad (1)$$

and nonlinear I–V curve

$$I(V) = I_0 \left( \frac{V}{V_0} \right)^{\beta(H)}. \quad (2)$$

The fit by Eqs. (1), (2) gives  $d\alpha/dH = 0.05 \text{ 1/T}$ ,  $d\beta/dH = 0.06 \text{ 1/T}$  and  $\epsilon = 335 \text{ K}$  for sample 1, and  $0.11 \text{ 1/T}$ ,  $0.12 \text{ 1/T}$  and  $250 \text{ K}$  for sample 2 at  $H = 10 \text{ T}$ .



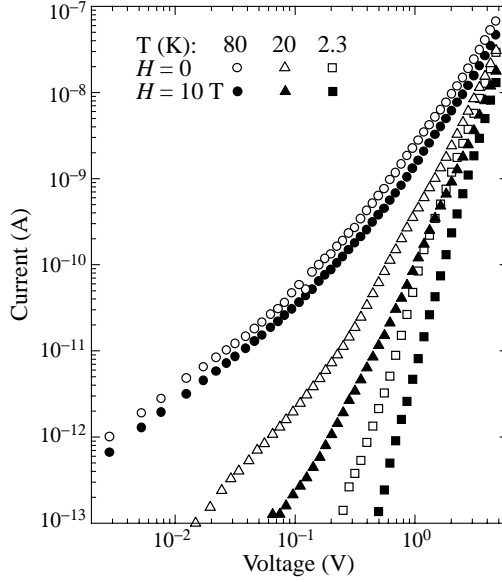


**Fig. 2.** Temperature set of I–V curves measured at zero magnetic field (empty patterns) and in  $H = 10$  T (filled patterns).  $H \perp I$ . Sample 2.

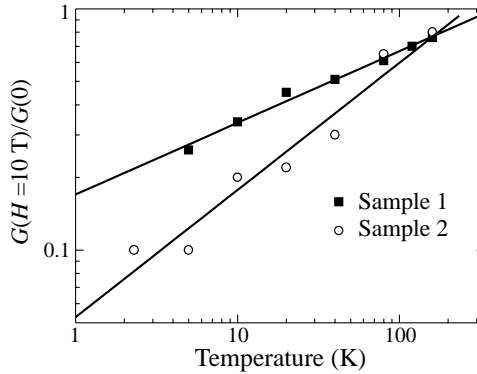


**Fig. 3.** Temperature dependence of the conduction in the magnetic field 10 T related to its value at  $H = 0$ . Lines show the least-squares fit of the data using the power law (Eq. 1).  $H \perp I$ .

At present there is no theory describing magnetoresistance in 1D correlated conductors, but we expect that magnetic field leads to variation of  $\alpha$  and  $\beta$ . It is known, that magnetic field affects correlation function critical exponents in the 1D Hubbard model [3], so  $\alpha(H)$  and  $\beta(H)$  dependences are expected. It was also shown that Zeeman splitting destroys the spin-charge separation in Tomonaga-Luttinger liquid [4]. This also leads to variation of the exponents. In Ref. [5] for a pure LL linear magnetic-field dependences for exponents of spectral functions and bulk density of states,  $\rho_{\text{bulk}}(\omega, H)$ , are obtained. However, theoretical results for  $\rho_{\text{end}}(\omega, H)$ , describing the tunneling current are still lacking. It is also worth to mention that magnetic-field-dependent exponents are observed in a temperature variation of NMR relaxation time of a spin-1/2 Heisenberg ladder [6].

## Conclusions

Thus InSb nanowires exhibit a strong positive magnetoresistance (up to 1 order in  $H = 10\text{ T}$ ) corresponding to a magnetic-field induced variation of the exponents  $\alpha$  and  $\beta$  in  $G \propto T^\alpha$  and  $I \propto V^\beta$  intrinsic to 1D case.

## Acknowledgements

One of us (S.V.Z.-Z.) is grateful to C.R.T.B.T.-C.N.R.S. for hospitality during the experimental part of research. This work has been supported by C.N.R.S. through jumelage 19 between C.R.T.B.T. and IRE RAS, the Region Rhone-Alpes through the program Temptra, the Russian Foundation for Basic Research (01-02-17771).

## References

- [1] For a review see: J. Voit, *Rep. Prog. Phys.* **58**, 977 (1995).
- [2] S.V. Zaitsev-Zotov, Yu.A. Kumzerov, Yu.A. Firsov and P. Monceau, *J. Phys.: Cond. Matter* **12**, L303 (2000).
- [3] H. Frahm and V.E. Koperin, *Phys. Rev. B* **43**, 5653 (1991);  
M. Ogata, T. Sugiyama and H. Shiba, *Phys. Rev. B* **43**, 8401 (1991).
- [4] T. Kimura, K. Kuroki and H. Aoki, *Phys. Rev. B* **53**, 9572 (1996).
- [5] S. Rabello and Q. Si, cond-mat/0008065.
- [6] G. Chaboussant *et al*, *Phys. Rev. Lett.* **80**, 2713 (1998).

## Hopping conductivity and magnetic-field-induced quantum Hall–insulator transition in InAs/GaAs quantum dot layers

V. A. Kulbachinskii<sup>†</sup>, R. A. Lunin<sup>†</sup>, V. A. Rogozin<sup>†</sup>, A. V. Golikov<sup>†</sup>,  
V. G. Kytin<sup>†</sup>, B. N. Zvonkov<sup>‡</sup>, S. M. Nekorkin<sup>‡</sup>, D. O. Filatov<sup>‡</sup>  
and A. de Visser<sup>§</sup>

<sup>†</sup> Low Temperature Physics Department, Moscow State University,  
119899, Moscow, Russia

<sup>‡</sup> Physicotechnical Research Institute, University of Nizhny Novgorod,  
603600, Nizhny Novgorod, Russia

<sup>§</sup> Van der Waals-Zeeman Institute, University of Amsterdam,  
1018 XE Amsterdam, The Netherlands

**Abstract.** We have investigated the temperature dependence of resistance in the temperature range  $T = 0.07\text{--}300$  K, the quantum Hall effect (qHe) and the Shubnikov–de Haas (SdH) effect in InAs/GaAs quantum dot structures in magnetic field up to 35 T. Two-dimensional Mott variable range hopping conductivity (VRHC) has been observed at low temperatures in samples with low carrier concentration. The length of localization correlates very well with the quantum dot cluster size obtained by Atomic Force Microscope (AFM). In samples with relatively high carrier concentration the transition qHe-insulator was observed.

### Introduction

In recent years, three-dimensional nanoscaled semiconductor islands have attracted significant attention due to their potential to act as quantum dot (QD) systems [1]. The lateral sizes and morphology, such as height, density and size distribution, of such islands can be adjusted within a certain range using appropriate growth conditions. While the optical properties of quantum dot structures are currently under intense investigation, less attention has been given to the transport properties. In this work, we report on the hopping conductivity and qHe-insulator transition of self-assembled InAs quantum dot layers, grown on GaAs substrates.

### 1. Samples

The structures were grown by atmospheric pressure metal organic vapor phase epitaxy (AP-MOVPE), using trimethylindium, trimethylgallium and arsenic, on semi-insulating (001) GaAs substrates from the (001) plane towards the [110] direction. The samples consisted of a 10–12 layers of GaAs 0.1  $\mu\text{m}$  thickness, a  $\delta$ -doping layer of Si for n-type samples (or C for p-type samples), a spacer layer (width 6 nm), an InAs quantum dot layer. The structures were capped with a cladding layer of GaAs (width 0.1  $\mu\text{m}$ ) [2]. Here we show the results for three different samples. Samples 1 and 3 were n-type with carrier concentration per layer of quantum dots  $4.0 \times 10^{10} \text{ cm}^{-2}$  and  $1.9 \times 10^{11} \text{ cm}^{-2}$ , Hall mobility 1000  $\text{cm}^2/\text{Vs}$  and 5500  $\text{cm}^2/\text{Vs}$ , respectively. Sample 2 was p-type with hole concentration per layer of quantum dots  $2.7 \times 10^{11} \text{ cm}^{-2}$  and Hall mobility 100  $\text{cm}^2/\text{Vs}$ .

The morphology of the quantum dot layers was investigated by AFM TopoMetrix<sup>®</sup> TMX-2100 Accurex<sup>TM</sup> in a contact mode. The GaAs cladding layer was etched in the

(0.8M  $K_3[Fe(CN)_6]$  in 0.3 KOH): $H_2O$ :glycerin (1:5:2), solution [3], having the etching rate for GaAs about 40 nm/min. In Fig. 1, as an example, AFM image of a quantum dot layer after etching for one of the samples is shown. Quantum dots with density  $N_S \approx 2 \times 10^{10} \text{ cm}^{-2}$  are visible. In Fig. 2 histogram of lateral base size  $L$  distribution (a) and the density of probability  $W(r)$  radial distribution of quantum dots clusters (b) are shown. (The probability  $dP(r, \Delta r)$  to find a cluster in the ring  $(r, r + \Delta r)$  is equal to  $dP(r, \Delta r) = 2\pi r W(r) \Delta r$ ).

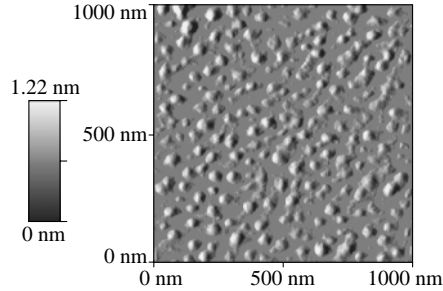


**Fig. 1.** AFM image of a surface InAs quantum dot layer after the selective etching.

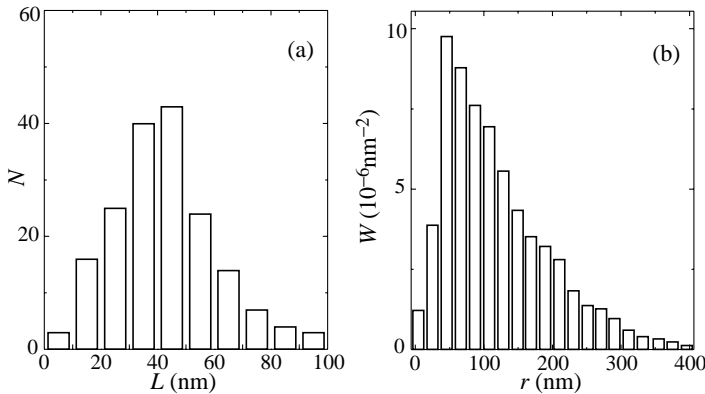


**Fig. 2.** Distribution of quantum dots by lateral base size  $L$  (a), ( $N$  – number of dots) and the density of probability  $W(r)$  radial distribution of quantum dot clusters (b).

Transport measurements were carried out on square samples with edges along the  $[110]$  and  $[\bar{1}10]$  directions. The temperature variation of the resistance was measured in the range  $T = 0.07\text{--}300$  K. The magnetoresistivity  $\rho(B)$  and Hall effect were measured in magnetic fields  $B$  up to 10 T using a superconducting solenoid and up to 35 T with help of a pulse magnet.

## 2. Variable range hopping conductivity

In Fig. 3 we show the temperature dependence of the sheet resistivity. For samples 1 and 2 the resistivity in the whole temperature interval are higher than the value  $h/e^2 \approx 25.8 \text{ k}\Omega$ , which separates metallic and insulator states in solids. For these samples the temperature dependence of the resistivity at low temperatures follows the law  $\rho(T) = \rho_0 \exp(T_0/T)^p$ ,

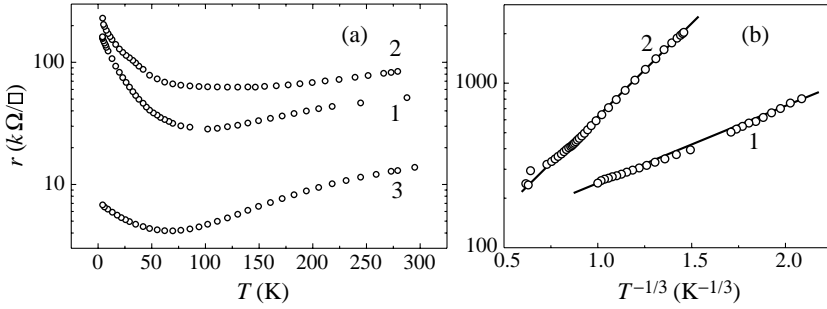


**Fig. 3.** Temperature dependence of resistance for samples 1, 2 and 3 in the whole temperature range (a) and in the low temperature interval for samples 1 and 2 (b).

where the exponent  $p$  depends on the shape of the density of states (DOS) at the Fermi level  $E_F$  [4] (variable range hopping conductivity (VRHC) regime). In 2D systems  $p = 1/3$  (Mott VRHC) for a constant DOS  $g_{E_F}$  at  $E_F$ .

Low temperature parts of the temperature dependence of the resistivity of samples 1 and 2 are shown in Fig. 3(b). Parameter  $T_0$  is equal to  $T_0 = C(g_{E_F}a^2)^{-1}$ , where  $C = 13.8$  and  $a$  is the localization length. For sample 2  $T_0 \approx 17$  K, and hence the localization length is about 80 nm. This value correlates very well with the maximum of the density of probability  $W(r)$  radial distribution of quantum dot clusters (see Fig. 2(b)).

### 3. Quantum Hall–insulator transition

In n-type samples with electron concentration  $n > 10^{11} \text{ cm}^{-2}$  (for p-type samples  $p > 5 \times 10^{11} \text{ cm}^{-2}$ ) the SdH effect and qHe is observed. Magnetoresistance measured at two different temperatures cross as it is shown in Fig. 4 for sample 3. In the crossing points derivative  $d\rho_{xx}/dT$  change the sign and quantum Hall effect–insulator transition is observed. Filling factors in these points is  $\nu = 1$  or 2. Quantum Hall effect plateau is very long and visible behind the crossing point. That is why such transition may be called “quantum Hall effect–quantum Hall insulator” [5]. The slope of the plateau is due to rather high temperature of measurements. According to the theory [6, 7] the value of  $\rho_{xx}$  in the transition point is equal to  $h/e^2$ . In the case of quantum dot layers with high density of

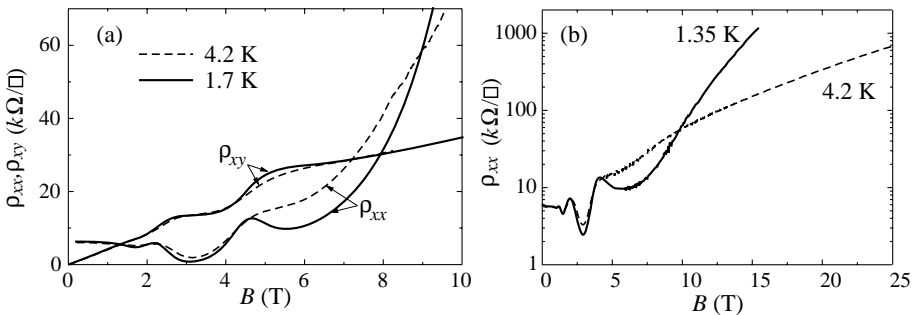


**Fig. 4.** Oscillations of the magnetoresistivity  $\rho_{xx}$  and the Hall resistivity  $\rho_{xy}$  at two temperatures at low (a) and high (b) magnetic fields for sample with electron density  $n = 1.9 \times 10^{11} \text{ cm}^{-2}$ .

dots the value of  $\rho_{xx}$  in the transition point is about two times higher. This discrepancy is explained by the morphology of the surface. 2D electrons are formed in layer due to overlapping of the electron wave functions in dots. The density of 2D electrons fluctuates with the characteristic scale of about the cluster size (see Fig. 2(b)). In magnetic field  $B = 1$  T the value of magnetic length  $l = (\hbar/eB)^{1/2} \approx 28$  nm that is less than the cluster sizes. The current flows between clusters with maximal electron concentration. In this case the effective length of conducting paths may be longer and the width less than in the uniform 2D system. In this case the calculated sheet resistivity of sample in the qHe regime may exceed the value of  $h/e^2$ , but the temperature dependence of the resistivity will be still metallic.

#### Acknowledgements

The work was supported by the Russian Foundation for Basic Research (Grants 00-02-17493, 01-02-16441) and CRDF (BRHE No. REC-001).

#### References

- [1] T. Noda, M. R. Fahy, T. Matsusue *et al*, *J. Cryst. Growth* **127**, 783 (1993).
- [2] V. A. Kulbachinskii, V. G. Kytin, R. A. Lunin *et al*, *Physica B* **266**, 185 (1999).
- [3] I. A. Karpovich, N. V. Baidus, B. N. Zvonkov, D. O. Filatov *et al*, *Phys. Low-Dim. Struct.* **3/4**, 341 (2001).
- [4] B. I. Shklovskii and A. L. Efros. *Electronic Properties of Doped Semiconductors*, Springer, Berlin, 1984.
- [5] M. Hilke, D. Shahar, S. H. Song, D. C. Tsui, Y. H. Xie and Don Monroe, *Nature* **395**, 675 (1998).
- [6] S. Kivelson, D.-H. Lee and S.-C. Zhang, *Phys. Rev. B* **46**, 2223 (1992).
- [7] D. Shahar, D. C. Tsui and J. E. Cunningham, *Phys. Rev. B* **52**, R14372 (1995).

## Persistent high-frequency hopping photoconductivity in GaAs/AlGaAs heterostructures in the quantum Hall regime

I. L. Drichko<sup>†</sup>, A. M. Diakonov<sup>†</sup>, I. Yu. Smirnov<sup>†</sup>,  
V. V. Preobrazhenskii<sup>‡</sup>, A. I. Toropov<sup>‡</sup> and Y. M. Galperin<sup>†\*</sup>

<sup>†</sup> Ioffe Physico-Technical Institute, St Petersburg, Russia

<sup>‡</sup> Semiconductors Physics Institute of SD of RAS, 630090 Novosibirsk, Russia

\* Dept. of Physics, University of Oslo, PO Box 1048 Blindern, 0316 Oslo, Norway

**Abstract.** Persistent high-frequency (hf) hopping conductivity near the middles of well developed quantum Hall plateaus has been studied in the Si modulated heterostructures GaAs/Al<sub>0.3</sub>Ga<sub>0.7</sub>As, both  $\delta$ - and modulation doped, under successive infrared irradiation in the 0.8–1.44 micron region. The conductivity has been determined by simultaneous measurement of attenuation and velocity of surface acoustic waves. With the increase of the radiation dose the conductivity decreases, whereas the carrier density in the 2D channel grows. There is a threshold of the persistent conductivity from the low energy side located between 0.86 and 0.48 eV. The observed behavior can be attributed to the so-called  $DX^-$  centers which are localized two-electron states bounded by local lattice distortion. Such states, as known, exist in Si-doped GaAs/Al<sub>x</sub>Ga<sub>1-x</sub>As with  $x \simeq 0.3$ . We believe that hf hopping is due to tunneling of electron pairs between a two-electron center and its empty neighbor.

### Introduction

GaAs/Al<sub>x</sub>Ga<sub>1-x</sub>As heterostructures are perfect objects to study quantum kinetics because of their high carrier mobility and low effective mass. They are formed from the interfaced layers of GaAs and Al<sub>x</sub>Ga<sub>1-x</sub>As, typically  $x \simeq 0.3$ . The Al<sub>x</sub>Ga<sub>1-x</sub>As layers are usually doped by Si to tune the electron density in the 2D channel. In the high mobility heterostructures, only the electrons located in the 2D channel contribute to DC conductance. Even at the quantum Hall plateaus where the  $\sigma_{xx}^{(DC)}$  is extremely small there is no evidence of the contribution of the doped region. The things go quite a different way in the case of *high-frequency* (hf) conductivity,  $\sigma_{xx}(\omega)$ . At the Hall plateaus, this quantity is latter is determined by electron hopping or tunneling between nearest localized states. As we have demonstrated earlier [1], in Si  $\delta$ -doped GaAs/Al<sub>0.3</sub>Ga<sub>0.7</sub>As heterostructures hopping contributions of both the 2D channel and the doping layer are important. This conclusion is supported by the observed dependence of  $\sigma_{xx}(\omega)$  on the *rate of cooling* in the concrete experimental run [2].

The present work reports the results of a systematic studies of  $\sigma_{xx}(\omega)$  dependences in aforementioned heterostructures on the IR irradiation in the quantum Hall regime.

### Experimental results and discussion

Surface acoustic wave (SAW) attenuation,  $\Gamma$ , and velocity variation,  $\Delta V/V$ , at a sound frequency  $f = 30\text{--}150$  MHz, in a magnetic field up to 7 T, and at temperatures 4.2 and 1.5 K have been measured in GaAs/Al<sub>0.3</sub>Ga<sub>0.7</sub>As heterostructures doped by different methods: (i) Si  $\delta$ -doped structures with electron densities in the 2D channel  $n_s \approx 1.4\text{--}4 \times 10^{11} \text{ cm}^{-2}$ ,

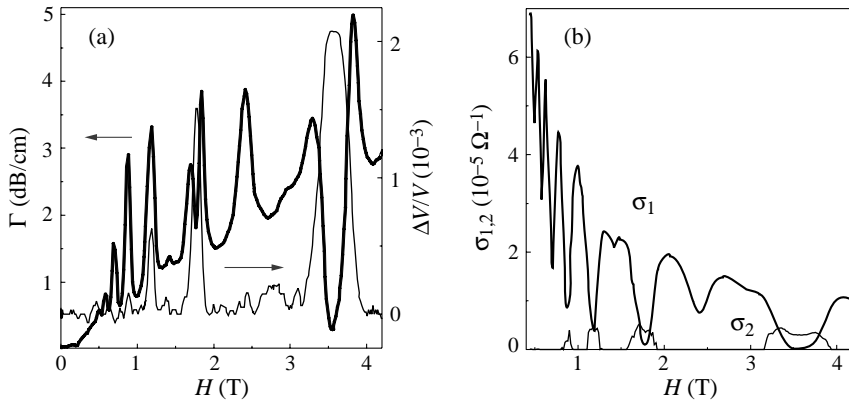


**Fig. 1.** (a) Magnetic field dependences of the SAW attenuation,  $\Gamma$ , and of the relative velocity change  $\Delta V/V$ ; (b) dependences of the  $hf$ -conductivity components  $\sigma_1$  and  $\sigma_2$  on  $H$ ,  $T = 1.5$  K,  $f = 30$  MHz.

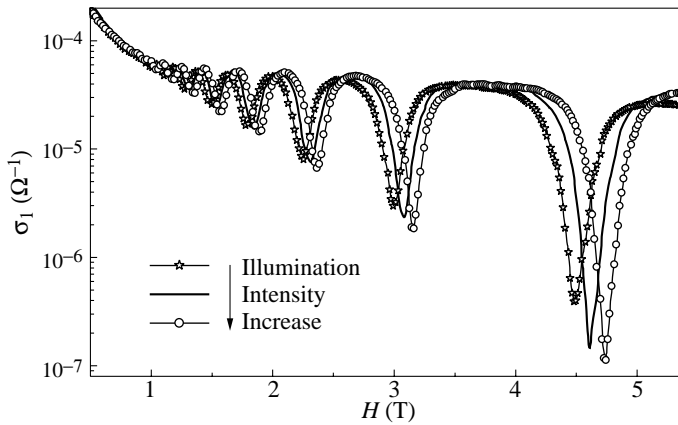


**Fig. 2.** Magnetic field dependences of the real components  $\sigma_1$  of the  $hf$ -conductivity at different illumination.  $T = 4.2$  K,  $f = 30$  MHz.

(ii) and Si modulation doped ones with  $n_s \approx 2.4\text{--}7 \times 10^{11} \text{ cm}^{-2}$ . The carrier density  $n_s$  has been determined from Shubnikov–de Haas-type oscillations of  $\Gamma$  and  $\Delta V/V$  as functions of magnetic field. Real,  $\sigma_1$ , and imaginary,  $\sigma_2$ , components of complex  $\sigma_{xx}(\omega)$  were determined from the experimentally measured  $\Gamma$  and  $\Delta V/V$  using the procedure outlined in Ref. [1]. The left panel of Fig. 1 illustrates the experimental magnetic field dependences of  $\Gamma$  and  $\Delta V/V$  at 1.5 K of the  $\delta$ -doped sample with  $n_s \approx 1.4 \times 10^{11} \text{ cm}^{-2}$ . These curves were used for calculation of  $\sigma_{1,2}$ . The results are shown in the right panel of Fig. 1.

The samples were illuminated with calibrated portions of light with different wave lengths ( $\lambda = 0.8, 1.44, 2.6$  and  $5.3 \mu\text{m}$ ) from a micro light-emitting diode (LED) located near the samples in the evacuated camera<sup>1</sup>. Magnetic field dependence of  $\sigma_1$  at 4.2 K for the  $\delta$ -doped sample with  $n_s \approx 3.3 \times 10^{11} \text{ cm}^{-2}$  illuminated with successive low portions of the  $0.8 \mu\text{m}$  LED radiation is shown in Fig. 2 (measurements are done at  $f = 30$  MHz).

<sup>1</sup>LEDs with  $\lambda = 1.44, 2.6, 5.3$  microns have been manufactured by B. A. Matveev's team at the Ioffe Institute.



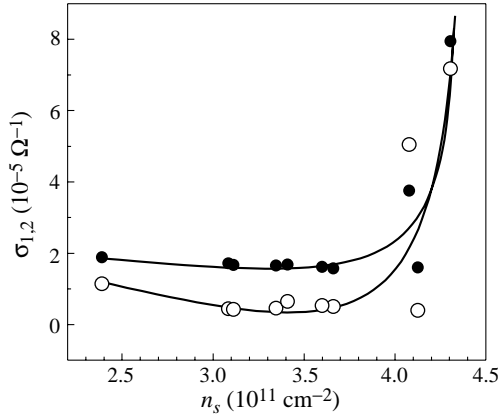


**Fig. 3.** The experimental dependences of real part of  $hf$ -conductivity  $\sigma_1$  on the sheet density  $n_s$ , tuned by an illumination ( $T = 1.5 \text{ K}$ ,  $f = 90 \text{ MHz}$ ).

One can see from the figure that after successive short ( $< 10 \text{ s}$ ) flashes of the LED the minima in  $\sigma_1$  occur at successively different magnetic fields. This means that the carrier density *increases*, while the minimal value of  $\sigma_1$  *decreases*. At the same time the conductivity maxima (determined by extended electron states) remain practically unchanged. The second important feature is that there is a *threshold* in the persistent  $hf$  photoconductivity. Namely, the persistent photoconductivity has been observed only for the radiation quantum energy exceed some value between  $0.86$  and  $0.48 \text{ eV}$  ( $1.4$  and  $2.6 \mu\text{m}$ ).

In Fig. 3, values of  $\sigma_{1,2}$  at  $\nu = 2$  and corresponding values of  $n_s$  obtained at different illuminations are plotted in the form  $\sigma_1, \sigma_2$  vs.  $n_s$  for a Si modulation doped sample ( $n_s \approx 2.5 \times 10^{11} \text{ cm}^{-2}$ ,  $T = 1.5 \text{ K}$ ,  $f = 90 \text{ MHz}$ ). One can see that the dosed successive irradiation leads to an *increase* in the 2DEG density which is accompanied by a *decrease* in  $\sigma_1$  and in slight change in  $\sigma_2$ . However, after a certain limit the density remains practically unchanged while the conductivity grows abruptly. The region of hopping conductance (identifies by the inequality  $\sigma_2 \gg \sigma_1$ ) corresponds to the decreasing part of the curve in Fig. 3.

As well known, in Si-doped  $\text{GaAs}/\text{Al}_x\text{Ga}_{1-x}\text{As}$  heterostructures, as well as in  $\text{Al}_x\text{Ga}_{1-x}\text{As}$  films with  $x > 0.22$  there exists a persistent photoconductivity at  $T < 100 \text{ K}$ . Its origin is believed to be associated with the so-called  $DX^-$  centers (see, e. g., [3] and references herein). These centers are just two-electron complexes bound by local lattice distortion which provides a negative correlation energy,  $U$ . These states can be described as *small bipolarons*. As a result, at low temperature,  $kT \leq U$ , the doped layer consists of negatively charged double-electron centers,  $D_-$ , and positively charged empty ones,  $D_+$ . The ground state is separated from the excited single-electron state,  $D_0$ , by the energy  $|U| \approx 0.8 \text{ eV}$ . As it has been demonstrated in [4] for amorphous semiconductors,  $hf$  hopping conductance in this case is due to tunneling of electron pairs between adjacent  $D_-$  and  $D_+$  defects.

We believe that a similar mechanism is responsible for our results. Indeed, in our experiments the persistent  $hf$  photoconductance is produced by the illumination with the quantum energy less than the  $\text{Al}_x\text{Ga}_{1-x}\text{As}$  bandgap. Consequently, the photoconductivity is associated with depletion of deep impurity levels. The threshold in the  $hf$  photoconductivity which is larger than the activation energy of individual impurities is consistent with general concepts of deep levels formed by  $DX^-$  centers [3].

## Conclusion

Experimentally observed persistent high-frequency hopping photoconductivity in GaAs/AlGaAs heterostructures in the quantum Hall regime has been attributed to the existence in these materials of  $DX^-$  center. These two-electron centers are formed by Si dopant in the  $Al_xGa_{1-x}As$  alloys with  $x \simeq 0.3$ . The hf hopping conductivity is in this case determined by the tunneling of electron between the two-electron  $D^-$  states and adjacent empty  $D^+$  ones.

## Acknowledgments

The work is supported by RFBR 01-02-17891, MinNauki, RF-Ukraine cooperation and Presidium RAS grants.

## References

- [1] I. L. Drichko, A. M. Diakonov, I. Yu. Smirnov, Yu. M. Galperin and A. I. Toropov, *Phys. Rev. B* **62**, 7470 (2000).
- [2] I. L. Drichko, A. M. Diakonov, Yu. M. Galperin, A. V. Patsekin, I. Yu. Smirnov and A. I. Toropov, Proc. of Int. Symp. "Nanostructures: Physics and Technology", St Petersburg, June 18–22, 582 (2001).
- [3] P. M. Mooney, *J. Appl. Phys.* **67**, R1, (1990);  
M. Hayne *et al*, A. Usher, J. J. Harris, C. T. Foxon, *Sur. Sci.* **361/362**, 574 (1996).
- [4] M. Foygel, A. G. Petukhov and A. S. Andreyev, *Phys. Rev. B* **48**, 17018 (1993).

## Ferromagnetic GaMnAs for spintronic devices

A. Koeder, W. Schoch, S. Frank, R. Kling, M. Oettinger, V. Avrutin,  
W. Limmer, R. Sauer and A. Waag  
Abt. Halbleiterphysik, Universität Ulm, Germany

**Abstract.** Ferromagnetic  $\text{Ga}_{1-x}\text{Mn}_x\text{As}$  films containing up to 5.1 at % Mn were grown by low-temperature MBE. The structural, electrical, and magnetic properties of the layers are reported. At  $x > 0.01$ , the materials show a ferromagnetic behavior. The Curie temperature reaches 80 K at 5.1 at % Mn. We propose the use of a  $n^+-\text{GaAs}/p^+-\text{GaMnAs}$  Esaki-diode (ferromagnetic Esaki-diode, FED) to provide injection of spin-polarized electrons via interband tunneling. Under reverse bias, spin-polarized electrons at the Fermi level in the valence band of GaMnAs tunnel to the conduction band of GaAs in contrast to the injection of spin-polarized holes used before.

### Introduction

In order to implement the spin of electrons for information processing and storage, spin manipulating semiconductor devices have to be developed. These device structure should ideally be based on magnetic materials compatible with conventional silicon or GaAs technology. One approach is to use diluted magnetic semiconductors (DMS), which are lattice matched to these materials. Recently, it has been possible to create a spin-polarized current and to inject it into a GaAs LED using either BeMnZnSe [1] or GaMnAs [2]. This was a first step towards the realization of semiconductor devices based on spin control rather than charge control. Both BeMnZnSe and GaMnAs materials contain magnetic ions leading to a pronounced exchange interaction between the Mn 3d states and the conduction and valence bands of the host. BeMnZnSe is paramagnetic, with a giant Zeeman splitting of the relevant bands. This leads to a complete spin polarization (as long as the Fermi energy is smaller than the Zeeman splitting). A disadvantage of using II–VI based semimagnetic semiconductors like BeMnZnSe is the temperature sensitivity of the magnetic effects. For temperatures above 10 K, the large Zeeman splitting and hence the spin polarization decreases rapidly, so that room temperature operation is excluded. In this respect, GaMnAs is more robust. Due to the high intrinsic p-type doping (Mn is an acceptor in GaAs), the Mn spin system shows a ferromagnetic phase transition. Curie temperatures  $T_c$  depend on Mn concentration, and values of up to 110 K have been reported [3].

### 1. MBE-Growth and HRXRD

The  $\text{Ga}_{1-x}\text{Mn}_x\text{As}$  films were grown in a Riber 32 MBE system equipped with an As-cracking source operating in the  $\text{As}_4$  mode. All substrates were fixed with In on the molybdenum block. First a 100 nm thick buffer layer was grown on undoped GaAs substrates at a growth temperature of  $T_s = 585^\circ\text{C}$ , then the growth was interrupted and  $T_s$  was lowered to  $250^\circ\text{C}$ . The GaMnAs layers have been grown using a V/III BEP-ratio of 30 or 10. The  $(2\times 4)$  and  $(2\times 2)$  surface reconstructions were observed for HT- and LT-GaAs, respectively. On the onset of GaMnAs growth, the surface reconstruction changed to  $(1\times 2)$ , the RHEED pattern became more streaky, and intensity oscillations were much more pronounced compared to LT-GaAs. All GaMnAs layers grown at  $250^\circ\text{C}$  with Mn

content up to  $x = 0.051$  showed mirror-like surfaces. The increase in growth temperature and/or Mn flux led to the formation of MnAs clusters in the near-surface region. In this case, the wafers showed matt surface. The Mn content was determined by high resolution X-ray diffraction (HRXRD) measurements of symmetric (004) reflections using Vegard's law,

$$a_{\text{Ga}_{1-x}\text{Mn}_x\text{As}} = a_{\text{GaAs}} + x (a_{\text{MnAs}} - a_{\text{GaAs}}) \quad (1)$$

where  $a_{\text{GaAs}} = 0.566$  nm and  $a_{\text{MnAs}} = 0.598$  nm (hypothetical zincblende MnAs [3]).

All grown GaMnAs layers (up to 900 nm thickness) were fully strained as followed from measurement of asymmetric (115) reflections.

## 2. Transport properties and ferromagnetic transition in GaMnAs

The transport properties of GaMnAs layers were studied by resistivity and Hall measurements on photolithographically defined Hall bars in the temperature range (4.2–300) K and in magnetic fields up to 22 T. All samples studied showed p-type conduction. The Mn content in GaMnAs has a strong influence on the temperature dependence of the resistivity. As the Mn fraction rises to about  $x = 0.02$ , a insulator-metal transition is observed. All measured samples showed anomalous Hall effect and a negative magnetoresistance in a wide temperature range due to magnetization of the samples. The Hall resistance  $\rho_H$  in magnetic materials can be described as [3]:

$$\rho_H = R_0 B + R_s M \quad (2)$$

where  $R_0$  is the normal Hall coefficient,  $R_s$  is the anomalous Hall coefficient, and  $M$  is the magnetization of the sample. An estimate of the hole density in the range of magnetic fields 20–22 T, when the magnetization saturates and the variation of the magnetoresistance is within 1%, gives for metallic GaMnAs  $p \sim (4-5) \times 10^{20} \text{ cm}^{-3}$  which is much smaller than the total Mn concentration.

The interaction responsible for the ferromagnetism in GaMnAs is assumed to be an indirect exchange interaction between the Mn spins mediated by holes, while in the direct exchange the Mn-Mn and the Mn-hole interactions are antiferromagnetic [3, 4]. The ferromagnetic transition in GaMnAs has a strong influence on the transport properties. Near  $T_c$  the resistivity  $\rho(T)$  shows a maximum or a kink, the negative magnetoresistance is pronounced. Below  $T_c$ , the magnetoresistance is positive in the range of small magnetic fields. The Curie temperature  $T_c$  was determined from magnetotransport measurements using the method described in [5]. Annealing of the samples has a bearing on the Mn content in the Ga-sublattice, as a consequence on the carrier concentration and Curie temperature for  $T > T_s$ . The decrease of the Mn content should be taken into account even during growth.

## 3. A ferromagnetic Esaki diode (FED) as spin-injector

The first spin injection from GaMnAs into GaAs was demonstrated recently [2], but only a very small spin injection efficiency of 2% could be achieved. One reason is likely the fast spin dephasing of holes — in contrast to electrons [6] — caused by the pronounced spin orbit coupling of states in the valence band. In order to circumvent this problem, a concept using a ferromagnetic Esaki diode has been proposed by us [7]. The idea is based on the tunnelling of spin-polarized electrons from the valence band of the p-type magnetic semiconductor (here GaMnAs) into the conduction band of the n-type non-magnetic counterpart, assuming that this tunneling is spin-conserving. In an external magnetic field, the valence band of the GaMnAs splits into different Zeeman levels, resulting in a net polarization of the hole spin.

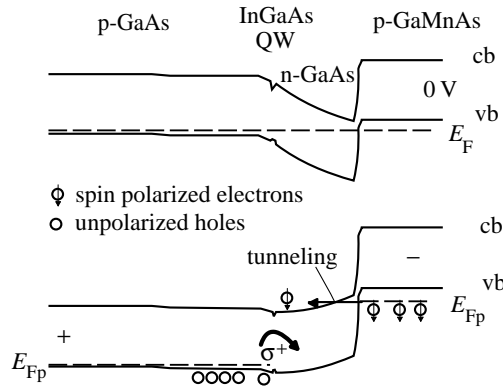


**Fig. 1.** The band diagram of FED-LED structure under (a) zero- and (b) reverse bias

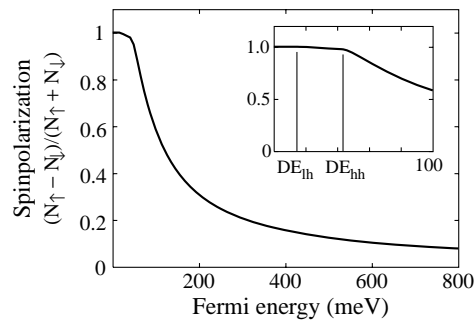


**Fig. 2.** Spinpolarization of holes in GaMnAs as a function of the Fermi energy.  $\Delta E_{lh}$ ,  $\Delta E_{hh}$  are the Zeeman splittings for light and heavy holes

The achievable spin polarization depends on the Fermi energy in the GaMnAs (given by the hole concentration) relative to the Zeeman splitting. The principle of the ferromagnetic Esaki concept is shown in (Fig. 1). The concept will be analysed taking into account the different light hole and heavy hole Zeeman splitting. The resulting spin-polarisation of holes is shown in (Fig. 2) as a function of Fermi energy assuming a  $N_0\beta$  of 1.2 eV and an external magnetic field high enough for saturation of manganese moments.

#### 4. Conclusion

We studied the transport properties of GaMnAs layers grown by LT MBE. Relatively high Curie temperatures and compatibility with conventional GaAs technology make this material promising candidate for spintronic applications. The use of ferromagnetic Esaki diodes based on GaMnAs for the spin injection in device structures is proposed, and the achievable degree of spin polarization is discussed.

#### Acknowledgements

This work was supported by Deutsche Forschungsgemeinschaft (Project Wa 860/4-1). The authors thank Dr. D. Maude (CNRS, Grenoble) for the technical assistance in Hall measurements in high magnetic fields.

## References

- [1] R. Fiederling, M. Keim, G. Reuscher, W. Ossau, G. Schmidt, A. Waag and L. M. Molenkamp *Nature* **402**, 787 (1999).
- [2] Y. Ohno, D. K. Young, B. Beschoten, F. Matsukura, H. Ohno and D. D. Awschalom, *Nature* **402**, 790 (1999).
- [3] H. Ohno, *Science* **281**, 951 (1998).
- [4] T. Dietl, H. Ohno and F. Matsukura, *Phys. Rev. B* **63**, 195205-1 (2001).
- [5] H. Ohno, H. Munekata, T. Penney, S. von Molnar and L. L. Chang, *Phys. Rev. Lett.* **68**, 2664 (1992).
- [6] J. M. Kikkawa and D. D. Awschalom, *Phys. Rev. Lett.* **80**, 4313 (1998).
- [7] *CELDIS Workshop on Dilute Magnetic Semiconductors*, Warsaw, June 2001.

## Spin-polarized transport through doped nanotube junctions in presence of applied magnetic field

A. A. Farajian, H. Mizuseki and Y. Kawazoe

Institute for Materials Reserach, Tohoku University, Sendai 980-8577, Japan

**Abstract.** The effects of different spin orientations on transport through carbon nanotubes are studied, using a simple tight-binding model within the mean-field approximation. It turns out that, in the absence of external magnetic field, the mean-field ground states of both semiconducting and metallic nanotubes are antiferromagnetic. As regards electronic/transport properties, it is observed that the conductance characteristics of spin-up and spin-down carriers are separated, and a negative differential resistance (NDR) feature in the I-V characteristics is detected, when the system is subjected to external magnetic field. NDR is particularly interesting for a wide range of applications.

### Introduction

Carbon nanotubes have shown promising features which make them potential candidates for nano-scale devices. Nonlinear transport behavior of nanotube junctions, observed from the current-voltage characteristics both experimentally [1, 2] and theoretically [3, 4], is among the most warranting properties of nanotubes as far as applications are concerned. Studying the effects of magnetic properties of carbon nanotubes is important, as it may provide yet another way to implement these materials in actual applications.

There has been some theoretical studies on magnetic properties [5], spin density wave effects [6, 7], and stable spin configurations [8] in carbon nanotubes. In the present study, we concentrate on the effects of the electron-electron interactions and spin density waves on transport through nanotubes.

### 1. Model and method

We use the following simple tight-binding Hamiltonian to model the system:

$$H = \sum_{i,\sigma} \varepsilon_i n_{i\sigma} + \sum_{\langle ij \rangle, \sigma} V_\pi c_{i\sigma}^\dagger c_{j\sigma} + \sum_i B(n_{i\uparrow} - n_{i\downarrow}) + \sum_i U_H n_{i\uparrow} n_{i\downarrow}, \quad (1)$$

with one  $\pi$  orbital per atom. (The hopping integral  $V_\pi$  is chosen as the energy unit henceforth.) Furthermore, the Hubbard term is decoupled, within the mean-field approximation, as

$$U_H \sum_i (n_{i\uparrow} \langle n_{i\downarrow} \rangle + n_{i\downarrow} \langle n_{i\uparrow} \rangle - \langle n_{i\uparrow} \rangle \langle n_{i\downarrow} \rangle). \quad (2)$$

Self-consistent calculation of the occupation numbers then determines the spin configuration of the system.

We consider two different spin density waves (SDWs) as the initial spin configurations, and compare the resulting magnetic moments and energies of the nanotubes. To this end, a metallic (4,4) and a semiconducting (7,0) nanotubes are considered. For the first

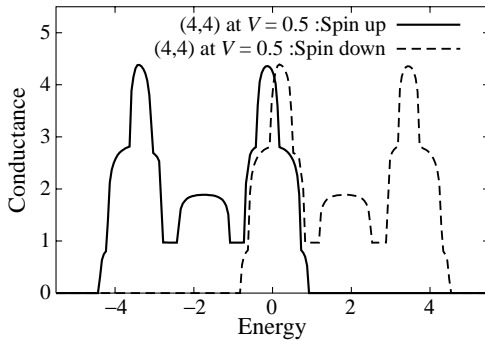


**Fig. 1.** Separation of conductance characteristics (units of  $e^2/h$ ) vs energy (hopping integral units) at a fixed external magnetic field equal to 1.0 hopping integral/Bohr magneton, for a metallic (4,4) tube at bias  $V = 0.5$  (hopping integral units). Fermi energy is shifted to zero.

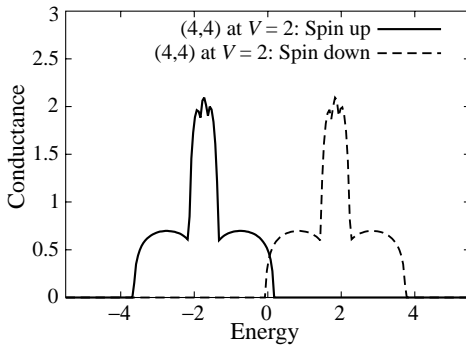


**Fig. 2.** Same as Fig. 1, but at bias  $V = 2$ .

spin configuration (SDW-1) alternating spin-up and spin-down occupations are assigned to adjacent carbon rings of the nanotube, such that all the atoms of a ring possess the same spin which is opposite to the spin of the atoms of the neighboring ring. (The rings are defined as all the carbon atoms with the same coordinate along the nanotube axis.) The spin-up configuration, e.g., for a typical site is such that 64% of the site occupation is spin up and 36% is spin down. For the SDW-2, on the other hand, neighboring atoms of each ring are assigned opposite spins (for the (7,0) nanotube, two neighboring atoms would inevitably have the same spins).

## 2. Results and discussions

The results of the self-consistent solution of the model show that for weak Hubbard couplings,  $U_H < 2$ , the solution is not spin-polarized, i.e., has net spin of zero per site. For  $3 < U_H < 6$ , the fully antiferromagnetic configuration, in which all the adjacent spins are opposite, is energetically favored for both metallic and semiconducting tubes. For strong couplings,  $7 < U_H$ , the initial spin configuration is just enhanced. As a value of  $U_H$  equal to 2.6 has reproduced the measured properties of polyacetylene [9], we set  $U_H = 2.6$  henceforth.

Having obtained the spin configurations, we turn on to transport. The total Green's function of the system projected onto the interface region determines the scattering matrix. Conductance of the system is then determined through Landauer-Büttiker approach. The same method has been used in a previous work of ours [3]. The bias voltage is simply added to the on-site terms of Eq. (1). Here, a step bias drop at the middle of the junction is assumed, as it is shown [10] that the screening length at doped nanotube junctions is of the order of a few carbon ring separations.



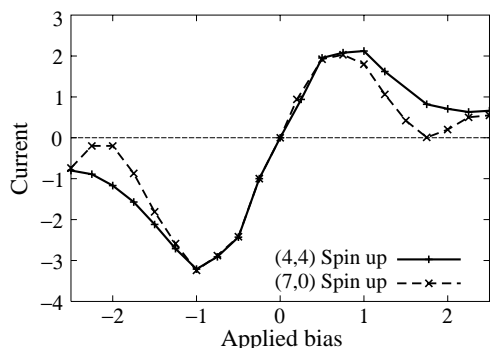


**Fig. 3.** Current (units of  $e/h \times$  hopping) vs applied bias (hopping integral units) at a fixed external magnetic field equal to 1.0 hopping integral/Bohr magneton, for doped (4,4) and (7,0) junctions. The spin-down curves (not shown) are exactly same as the spin-up curves

As an illustrative example, the conductance results of the metallic (4,4) tube under a fixed external magnetic field set to 1.0 (hopping integral/Bohr magneton), are depicted in Figs. 1 and 2 at different biases. The conductance characteristics of up- and down-carriers are observed to get separated. We also noticed the opening of a gap for this metallic tube under weak magnetic fields ( $\sim 0.1$ ), which is consistent with the previous calculations of Kobayashi [6]. The gap appears to diminish under stronger fields.

By integrating the conductance curves of the tubes under applied bias, the I-V characteristic is obtained (Fig. 3). In this calculation, initial shifts  $+0.1$  and  $-0.1$  (hopping integral) are assumed for the density of states to the left and right of the junction, respectively. These initial shifts indicate the effect of doping [3]. Furthermore, a fixed external magnetic field equal to 1.0 is assumed in the calculation. We noticed that the I-V characteristics of the up- and down-spins are identical. In addition, the I-V characteristics possess the negative differential resistance feature, which is particularly interesting for applications.

In summary, the stable spin configurations of both metallic and semiconducting nanotubes turn out to be antiferromagnetic. A gap opens for the metallic tubes in presence of weak external magnetic fields. The gap vanishes for stronger fields. Regions of negative differential resistance, with a big peak-to-valley ratio, are observed for both metallic and semiconducting tubes. Generalization of the results to include orbital magnetic effects is in progress.

### Acknowledgements

This study is supported by the Special Coordination Funds of the Ministry of Education, Culture, Sports, Science and Technology of the Japanese Government.

### References

- [1] S. J. Tans *et al*, *Nature* **386**, 474 (1997).
- [2] S. J. Tans, A. R. M. Verschueren and C. Dekker, *Nature* **393**, 49 (1998).
- [3] A. A. Farajian, K. Esfarjani and Y. Kawazoe, *Phys. Rev. Lett.* **82**, 5084 (1999).
- [4] F. Leonard and J. Tersoff, *Phys. Rev. Lett.* **85**, 4767 (2000).
- [5] J. P. Lu, *Phys. Rev. B* **74**, 1123 (1995).
- [6] K. Kobayashi, *J. Chem. Phys.* **106**, 8746 (1997).
- [7] R. Egger and A.O. Gogolin, *Eur. Phys. J. B* **3**, 281 (1998).
- [8] M. P. López Sancho, M. C. Muñoz and L. Chico, *Phys. Rev. B* **63**, 165419 (2001).
- [9] D. Baeriswyl and K. Maki, *Phys. Rev. B* **31**, 6633 (1985).
- [10] A. A. Farajian, K. Esfarjani and M. Mikami, *Phys. Rev. B* accepted.

## Super high conductivity effect in metal-polymer-metal structures

A. N. Ionov<sup>†</sup>, V. A. Zakrevskii<sup>‡</sup>, V. M. Svetlichny<sup>‡</sup> and R. Rentzsch<sup>§</sup>

<sup>†</sup> Ioffe Physico-Technical Institute, St Petersburg, Russia

<sup>‡</sup> Institute of Macromolecular Compounds, RAS, 199004, St Petersburg, Russia

<sup>§</sup> Institut für Experimentalphysik, Freie Universität Berlin,  
D-14195 Berlin, Germany

**Abstract.** We have observed that films of a polyimide precursor of poly[4,4'-bis(4"-N-phenoxy)diphenyl-sulfone] amid acid of 1,3-bis(3',4-dicarboxyphenoxy)benzene which is called type (1) polymer- or co-poly[4,4'-bis(4"-N-phenoxy)diphenyl-sulfone- $\alpha$ ,  $\omega$ -bis( $\gamma$ -amino propyl)oligodimethylsiloxane]imide of 1,3-bis(3',4-dicarboxyphenoxy)benzene type (2) polymer, placed between two metallic electrodes become highly conducting in a relatively small electric field ( $E < 1$  V/cm). If the metallic electrodes (Sn, Nb) in sandwich structures were in the superconducting state an effective resistance of zero was recorded. A typical current–voltage characteristic of an S-P-S structure looks like a Josephson type. We have experimentally shown that for a S-P-S structure, a point contact between the superconductor and the polymer film plays the role of a weak link.

### Introduction

In recent years there were reports on the super high conductivity effect in different polymers, such as polyimide and polydiphenylenphtalide [1, 2] at a thickness of the polymer of up to  $1.5\text{ }\mu\text{m}$ , which are placed between metallic electrodes in a small electrical field. If the electrodes undergo transition to the superconducting state in a small magnetic field also Josephson oscillations have been obtained. The aim of the present paper is to find other material with this anomalously high conductivity phenomena, as well as further experiments to understand their physical origin.

### 1. Preparation of the material

The effect was observed in sandwich structures M–P–M (here M is a metallic or superconducting electrode and P — polymer of type (1) or (2)) with a thickness of polyimide film up to  $2.5\text{ }\mu\text{m}$  as well as in planar geometry with a gap between two gold electrodes up to  $2.8\text{ }\mu\text{m}$ . Special care was taken to exclude tilting between the two electrodes in the sandwich structures. The conducting state in the structures is obtained with experimental conditions under which it can be excluded that electrode material was diffused into the polymer film, nor that there were micro-shortenings between the electrodes. The polyimide films were prepared by deposition of a drop of solution of type (1) or (2) in N-methyl-2-pyrrolidone on:

- (i) a polished metallic bulk electrode with sandwich structure;
- (ii) planar gold electrodes (stripes) on GaAs substrates with high resistance ( $> 10^5\text{ }\Omega\text{ cm}$ ) and with varying separation of the stripes from each other: 0.8, 1.4, 1.8,  $2.8\text{ }\mu\text{m}$ .

The films were heated in air for 2h at a constant temperature of 370–400 K to remove the major part of the polymer solvent. This heat treatment gave rise to partially imidized polyimide precursors.

## 2. Results and discussion

In our M–P–M structures, we observed a correspondence between the contact area and the total value of the resistance. The smaller the contact area, the higher the resistance of the structure. We have also observed that the effect of high conductivity vanishes non-reversibly at  $T > 500$  K. It was found that if the metallic electrodes (Sn, Nb) in sandwich structures were in the superconducting state, i.e. at  $T < T_c$ , where  $T_c$  is the bulk value of the superconducting transition temperature, in the Superconductor–Polymer(1,2)–Superconductor (S–P–S) an effective resistance of zero was recorded (Fig. 1). Two-terminal

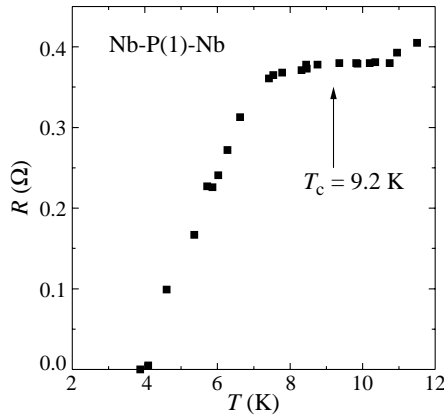


**Fig. 1.** Typical temperature dependence of the resistance in a Nb-P(1)-Nb sandwich structure with a polymer thickness of 1  $\mu\text{m}$ .

resistance measurements with constant current showed that as the temperature decreased, slow fluctuations of the resistance were observed down to the temperature  $T \geq T_c$ . At  $T < T_c$  the resistance fluctuations disappear sharply. The sharp drop in the resistance below  $T_c$  shown in Fig. 1 is similar to a superconducting transition of the S–P–S structure with reduced  $T_c$ . A typical current–voltage characteristic (CVC) of an S–P(2)–S structure is shown in Fig. 2. It looks like a Josephson CVC. The reversible behavior of the CVC excludes the existence of insulator barriers between the two superconductors. We have experimentally shown that for a superconducting S–P–S structure, a point contact between the superconductor and polymer films plays the role of a weak link. As an example for a Sn–P(2)–Sn sandwich structure with polymer film thickness of about one micron, the estimated relation of total area of point contacts to the overall area of the electrodes covered by the polymer film is  $10^{-6}$ , while the total area of all conductive channels is about  $10^{-7} \text{ cm}^2$ . The nanoscale dimension of individual conductive channels is independently estimated by the Josephson-effect behavior at a low magnetic field, which is observed in S–P–S structures due to the weak links [1, 2] connected by point contacts. We measured the voltage drop over the S–P–S sandwich structure at constant electrical current just above  $I_c$  by sweeping a small transverse magnetic field ( $H \perp I$ ); this is experimentally easier to measure as a function of the magnetic field than the critical current. The shape of the amplitude and period of the voltage oscillations shows that:

- (i) there are many conductive channels through the polymer film;
- (ii) the areas of all point contacts are nearly the same; and
- (iii) the distance between Josephson contacts is no more than 30  $\mu\text{m}$ .

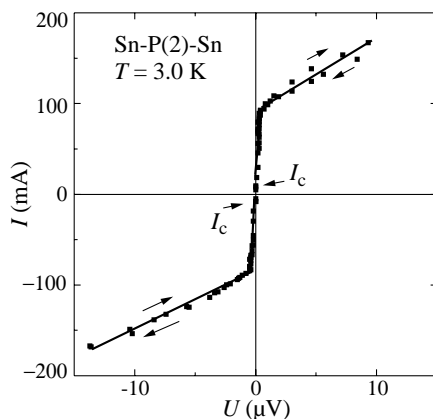


**Fig. 2.** Typical current–voltage characteristic of a Sn–P(2)–Sn sandwich.

It should be emphasized that we did not observe Josephson oscillations if one of the electrodes was in the normal state. Therefore, at first sight this seems to show that the superconducting state in the polymer channel itself could not be connected with classical pairs of the BCS-theory; instead, it could possibly be explained by ballistic transport of charge carriers in polymer channels or by an unconventionally superconductivity. The reason for the last two conclusions regarding M-P-M structures is connected with the temperature dependence of the resistance which obeys Wexler's law for point contact resistance up to room temperature [3]. The highly conducting state in polymers presupposes that there is a high concentration of charge carriers with high mobility. Electrification of polymers in contact with metals, i.e. charge transport across the interface, is a well-known phenomenon studied by various authors [4]. The charge acquired by a polymer from a metal that touches it depends on the type of polymer, on the type of the metal and on the contact area. For example, we did not observe the high conductivity in semiconductor–polymer–semiconductor structures where the semiconductor exhibited p-type conductivity with hole concentrations corresponding to the metallic side of the metal–insulator transition. At the moment there is no satisfactory explanation for the supercurrent in superconductor–polymer–superconductor sandwich structures through relatively thick polymer films.

### 2.1. Acknowledgements

This work was financially supported by the RFBR (grant No. 00-03-33060) and the programme “Low-Dimensional Quantum Structures”. One of us (A.N.I.) thanks the Freie Universität Berlin for hospitality during numerous short-term visits.

### References

- [1] A. N. Ionov, V. A. Zakrevskii and J. M. Lazebnik, *Techn. Phys. Lett.* **25**, 9 (1999).
- [2] A. N. Ionov, V. A. Zakrevskii, J. M. Lazebnik, R. Rentzsch and V. M. Svetlichny, *cond-mat/0006016*. 1. June (2000).
- [3] A. Wexler, *Proc. Phys. Soc. London* **89**, 566, 927 (1966).
- [4] J. Lowel and A. C. Rose-Innes, *Adv. Phys.* **29**, 947 (1980) and references therein.

## Ballistic effects in magnetoresistance of the planar point contact composed of single crystalline tungsten

*G. M. Mikhailov*<sup>†</sup>, *L. I. Aparshina*<sup>†</sup>, *A. V. Chernykh*<sup>†</sup>, *I. V. Malikov*<sup>†</sup>,  
*V. Y. Vinnichenko*<sup>†</sup>, *J. C. Maan*<sup>‡</sup>, *S. Olsthoorn*<sup>‡</sup>, *C. Possanzini*<sup>‡</sup> and *H. Jonge*<sup>‡</sup>

<sup>†</sup> IMT RAS, 142432 Chernogolovka, Russia

<sup>‡</sup> High Field Magnet Laboratory in Nijmegen, the Netherlands

**Abstract.** We found that a ballistic planar constriction exhibits different properties in angular dependence of the magnetoresistance in compare with that of the diffusive point contact. It shows unusual two-minima angular dependence. This behavior also differs much from that of ballistic four terminal bridges, where monotonic angular dependence of the magnetoresistance is observed.

### Introduction

Single crystalline nanostructures composed of metals attract much attention as they demonstrate new electron transport properties. In these structures conductive electrons may travel long distances without scattering, while they do not impact the boundaries. When electron mean free path (MFP) compares with the structures dimensions, ballistic properties come out.

Electron boundary scattering is the random process causing the electron trajectories to be chaotic. It was predicted [1] that the disordered wire containing a constriction much narrower than MFP ("Sharvin" point contact) is equivalent under some conditions to the unconfined wire with the width equaled to the width of the point contact and with MFP scaled by the factor  $1/\nu$ , where  $\nu$  depends on the Dyson index and the number of transverse modes of the wire and point contact. In this work we investigated magnetoresistance field effect and its angular dependence upon the direction of the magnetic field in the planar constriction, which is the W(001) nanobridge that connects two reservoirs (disordered wire). Previously [2], we found that angular dependence of the magnetoresistance for four-terminal nanobridges composed of single-crystalline tungsten exhibits sharp monotonic angular dependence. We expected to find the same results for the wire with the constriction (planar point contact), however, as it is shown below is not the case.

### 1. Experimental set-up

Investigation was made of in-plane magnetoresistance and its angular dependence under 4.2 K for planar single crystalline W(100) bridge with the different thickness ( $d$ ), width ( $W$ ) and length ( $L$ ), which is depicted in Fig. 1 together with the circuit connections. Direction of the magnetic field can be declined against the bridge axis by sample rotation using the angles  $\phi$  (out-of-plane rotation) and  $\beta$  (in-plane rotation).

### 2. Experimental results and discussion

It was found that under large magnetic field the strong and sharp  $\phi$ -angular dependence with unusual two minima is observed for the short bridge. Experimental data are presented in Fig. 2 for the long (a) and short (b) bridges. As can be seen, at low magnetic field below

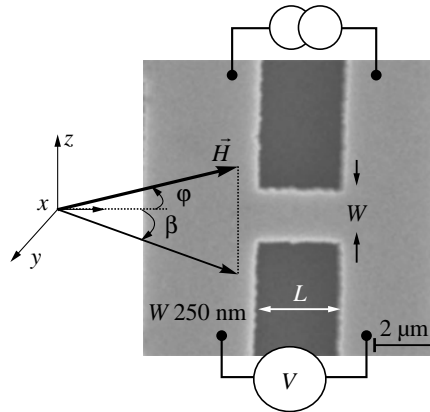


**Fig. 1.** Single-crystalline tungsten (001) bridge of the width  $W$  (ranged  $1.2\text{--}2.8\text{ }\mu\text{m}$ ) and length  $L$  (ranged  $0.3\text{--}14\text{ }\mu\text{m}$ ) connects two reservoirs. Magnetic field ( $H$ ) direction depends on  $\phi$  and  $\beta$  declination angles. Connections of AC source and microvoltmeter ( $V$ ) are depicted. Z-axis is perpendicular to the sample plane; x-axis is along  $[100]$  of W(001) film and parallel to the bridge axis.

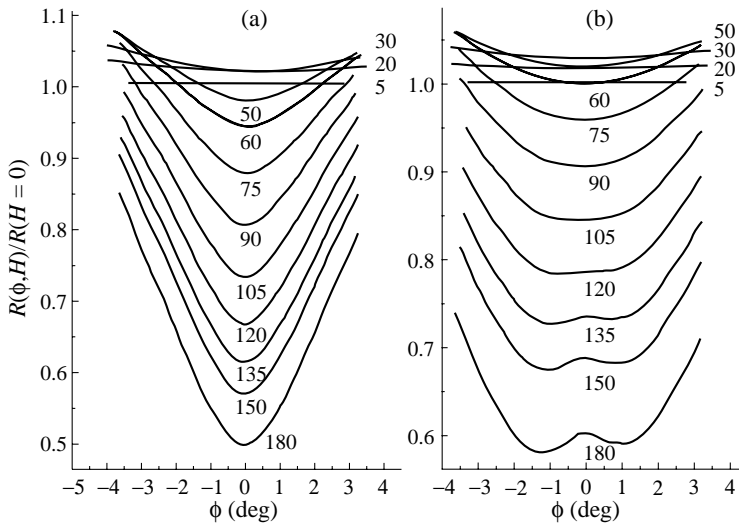


**Fig. 2.** The  $\phi$ -angular dependence of the magnetoresistance for the bridge with  $d = 350\text{ nm}$ ,  $L(W) = 14(2.8)\text{ }\mu\text{m}$  (a) and  $L(W) = 1.4(2.8)\text{ }\mu\text{m}$  (b) under different magnetic fields  $H = 5, 20, 30, 50, 60, 75, 90, 105, 120, 135, 150$  and  $180\text{ kOe}$ . In-plane rotation angle  $\beta=0$ .

90 kOe  $\phi$ -angular dependence is slow and monotonic one. However, while magnetic field increases, it becomes stronger and two minima appear for the short bridge (b, Fig. 2). The larger magnetic field is the deeper these minima are. Note, that angular dependence of the magnetoresistance upon  $\beta$  angle (in-plane rotation) is weak in the whole range of the magnetic field. Under higher sample temperatures, when MFP decreases due to electron-phonon scattering, the magnetoresistance angular dependence is weak and no two-minima are observed. Magnetoresistance field dependence at different  $\phi$ -angle is presented in Fig. 3. Curves 1–3 demonstrate magnetoresistance field effect at different  $\phi$ -angles, which

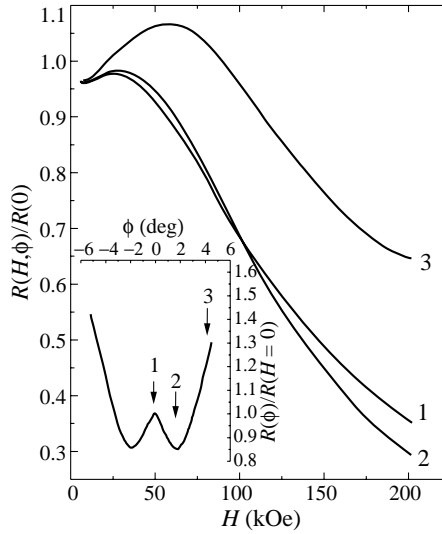


**Fig. 3.** Magnetoresistance of the bridge L1 ( $d = 350$  nm,  $W = 2.8$   $\mu\text{m}$ ,  $L = 2.4$   $\mu\text{m}$ ) at different angles  $\phi = 0$  (1),  $1.8$  (2) and  $4$  deg. (3), and angle  $\beta = 0$ . Angle dependence versus  $\phi$  is presented in the insert for  $H = 150$  kOe, where vertical arrows indicate  $\phi$ -angle positions for the curves 1–3.

are specified in the insert. These curves depend on the out-of-plane declination angle and exhibit negative magnetoresistance at the magnetic field higher than 30–70 kOe. These results also prove non-monotonic angular dependence. Note, that most deviation in the field dependence is in the high field range. This behavior should be attributed to the signature of the bulk state (spiral orbits) magnetotransport.

This has been observed recently for multi-terminal W(001) nanostructures [2], where sharp monotonic angular dependence, as it was found, is the consequence of strong anisotropy of MFP for the electrons of the bulk states. In these experiments, the characteristic angle is in the order of  $d/l_{\text{bulk}}$ , where  $l_{\text{bulk}}$  is MFP in the bulk of the nanostructure. Because the width of the bridges much exceeds their thickness,  $\phi$ -dependence is much sharper than  $\beta$ -angular dependence. We explain found two-minima angular dependence by the influence of electron transmission between the bulk (spiral orbit) and edge (skipping orbits) states. When the electrons escape the reservoir and enter the bridge (or vice versa), they have to transform their states from the edge (bulk) to bulk (edge) type. This is most important for the bridge with the length smaller than MFP (ballistic transport), because no two minima angular dependence has been observed for the long bridge (diffusive transport). Electron MFP may exceed transverse dimensions of the bridge, thus, lowering the transmission probability of electrons of the reservoir to enter the bridge at large magnetic field. Under declination of the magnetic field the electrons scatter much more with the boundaries and enhance this transmission probability. Magnetoresistance decreases. Further  $\phi$ -angular increase intensifies an electron scattering on the boundaries of the bridge itself that leads to increasing of the resistance again.

## Conclusion

We found that a ballistic planar constriction exhibits different properties in angular dependence of the magnetoresistance in compare with that of the diffusive point contact. This behavior also differs much from that of ballistic four terminal bridges, where monotonic

angular dependence of the magnetoresistance was observed. We conclude that it could not be reduced to the behavior of the disordered wire without constriction. The latter implies that nor independent transfer matrices approach nor isotropy assumption [1] could be applied to the electron transport of the investigated ballistic planar point contact composed of single-crystalline tungsten, where transmission between the edge and bulk states introduces the new features in angular dependence of the magnetoresistance and two minima angular dependence is observed.

#### *Acknowledgements*

The work was supported by Physics of solid state nanostructures program (grant 99-1126), RFBR (grant 00-02-16601) and INTAS (grant 99-193).

#### **References**

- [1] C. W. J. Beenakker, *Rev. Mod. Phys.* **69**, 731-808 (1997).
- [2] G. M. Mikhailov, A. V. Chernykh, J. C. Maan, J. G. S. Lok, A. K. Geim, D. Esteve and P. Joyez, *Nanotechnology* **11**, 379–382 (2000).



## The conductivity of disordered 2D systems: from weak to strong localization

*G. M. Minkov<sup>†</sup>, A. V. Germanenko<sup>†</sup>, O. E. Rut<sup>†</sup>, A. A. Sherstobitov<sup>†</sup>,  
B. N. Zvonkov<sup>‡</sup>, E. A. Uskova<sup>‡</sup> and A. A. Birukov<sup>‡</sup>*

<sup>†</sup> Institute of Physics and Applied Mathematics, Ural State University,  
620083 Ekaterinburg, Russia

<sup>‡</sup> Physical-Technical Research Institute, University of Nizhni Novgorod,  
603600 Nizhni Novgorod, Russia

**Abstract.** Results of detailed investigations of the conductivity and Hall effect in gated single quantum well GaAs/InGaAs/GaAs heterostructures with two-dimensional electron gas are presented. A successive analysis of the data has shown that the conductivity is diffusive for  $k_F l = 25 - 2.5$ . The absolute value of the quantum corrections for  $k_F l = 2.5$  at low temperature is not small, e.g., it is about 70% of the Drude conductivity at  $T = 0.46$  K. For  $k_F l < 2.5$  the conductivity looks like diffusive one. The temperature and magnetic field dependences are qualitatively described within the framework of the self-consistent theory by Vollhardt and Wölfle. The interference correction is therewith close in magnitude to the Drude conductivity so that the conductivity  $\sigma$  becomes significantly less than  $e^2/h$ . We conclude that the temperature and magnetic field dependences of conductivity in the whole studied  $k_F l$  range are due to changes of quantum corrections and that transition to hopping conductivity occurs at lower conductivity value.

The weak localization regime in two-dimensional (2D) systems at  $k_F l \gg 1$  ( $k_F$  and  $l$  are the Fermi quasimomentum and mean free path, respectively), when the electron motion is diffusive, is well understood from theoretical point of view [1]. In this case the quantum corrections to conductivity, which are caused by electron-electron interaction and interference, are small compared with the Drude conductivity  $\sigma_0 = \pi G_0 k_F l$ , where  $G_0 = e^2/(2\pi^2 \hbar)$ . Experimentally, this regime was studied in different types of 2D systems. Qualitative and in some cases quantitative agreement with the theoretical predictions was found. However, important questions remain to be answered: (i) what does happen with these corrections at decrease of  $k_F l$  down to  $k_F l \simeq 1$  and (ii) at decrease of temperature  $T$  when the quantum corrections become comparable in magnitude<sup>1</sup> with the Drude conductivity?

It is clear that the increase of disorder sooner or later leads to the change of the conductivity mechanism from diffusive one to hopping and another question is: when does it happen? To answer this question the temperature dependence of the conductivity is analyzed usually. It is supposed that the transition to the hopping conductivity occurs when the conductivity becomes lower than  $e^2/h$  and the strong temperature dependence arises [2]. From our point of view, it is not enough to analyze only the  $\sigma(T)$  dependence. The low conductivity and its strong temperature dependence can result from large value of the quantum corrections as well.

We have studied experimentally the quantum corrections to the conductivity in the gated GaAs/InGaAs/GaAs structures which have simplest and well-known electron energy

---

<sup>1</sup> It should be noted that the term "corrections" is not quite adequate in this case. Nevertheless, we will use it even though the correction magnitude is not small.

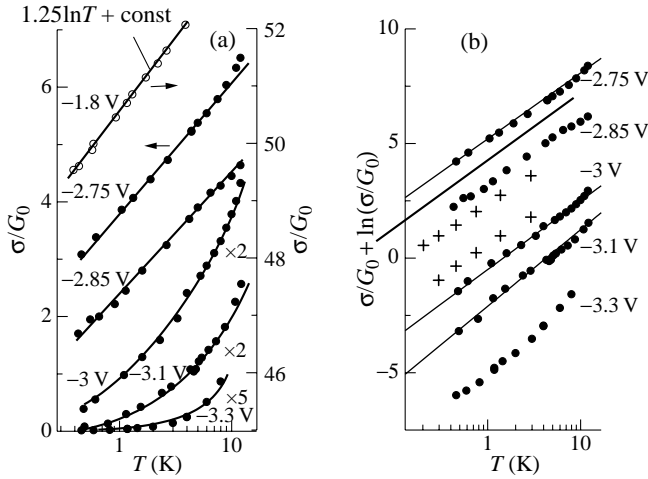


**Fig. 1.** The temperature dependences of the conductivity for different gate voltages in two different scales. The circles are our data. The values of  $k_F l$  from  $V_g = -1.8$  V to  $-3.3$  V are the following:  $k_F l \simeq 17.9$ ; 3; 2.1; 1.4; 1.0; and 0.5. The crosses are the data from the paper by Khondaker *et al* [2], where the results was interpreted as the hopping conductivity.

spectrum. The electron density at  $V_g = 0$  was about  $8 \times 10^{11} \text{ cm}^{-2}$ .

The temperature dependences of the conductivity for some gate voltages are presented in Fig. 1(a). It is clearly seen that for  $V_g \geq -2.85$  V the temperature dependences of  $\sigma$  are close to the logarithmic ones. For lower  $V_g$ , when the conductivity is less than  $e^2/h$ , the significant deviation from logarithmic dependence is evident. The conductivity in this range is usually interpreted as the hopping conductivity [2]. In this report we show that the quantum corrections can lead to such a behavior if they become close in magnitude to the Drude conductivity.

To clarify the role of quantum corrections at low conductivity when  $k_F l \simeq 1$  we have analyzed the experimental data starting from  $k_F l \gg 1$  when the conventional theories of the quantum corrections are applicable. Following the sequence of data treatment described in [3] there was shown that all theoretical predictions for temperature, low and high magnetic field behavior of the conductivity are fulfilled over  $k_F l$  range 2.5–25. These predictions are the following:

- (i) The  $\rho_{xx}$ -versus- $B$  curves taken at different temperatures are crossed at magnetic field  $B = 1/\mu$ ;
- (ii) The value of  $\sigma_{xy}$  does not depend on the temperature at  $B > 10 B_{tr}$ , where  $B_{tr} = \hbar/(2el^2)$ . This fact allows to attribute the temperature dependence of  $\sigma_{xx}$  with contribution of the EEI and determine its value;
- (iii) The low field negative magnetoresistance is well described by the theoretical expression for interference quantum correction that permits to determine the phase breaking time  $\tau_\varphi$ ;
- (iv) The temperature dependence of  $\tau_\varphi$  and its value are close to the theoretical ones;
- (v) The slope of  $\sigma(B = 0)$ -versus- $\ln T$  dependence is in accordance with summary contribution of the interference and EEI corrections.

Such accordance with the theoretical predictions allows us to determined the contributions to the conductivity due to interference and due to electron-electron interaction over

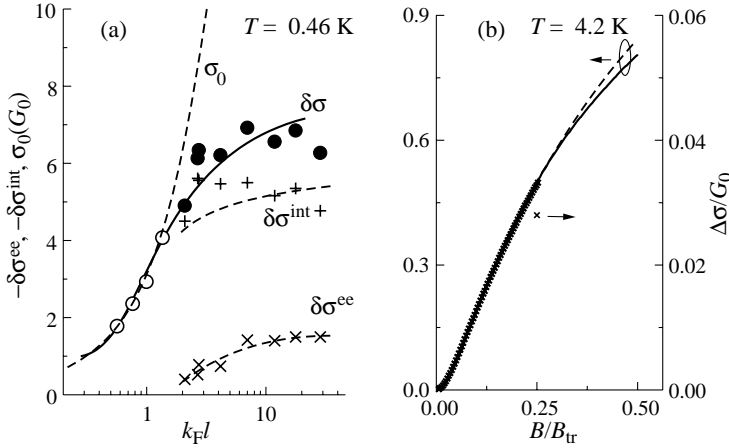


**Fig. 2.** (a) The contributions to the conductivity due to electron-electron interaction  $\delta\sigma^{ee}$ , interference  $\delta\sigma^{int}$ , and the total contribution  $\delta\sigma$  as a function of  $k_F l$ . The dotted curve is  $\sigma_0 = \pi k_F l$ , other curves are the guide for an eye. (b) The negative magnetoresistance for  $V_g = -1.8$  V ( $k_F l = 17.9$ ) (solid line) and  $V_g = -3.3$  V ( $k_F l \simeq 0.5$ ) (crosses),  $T = 4.2$  K.

the  $2.5 < k_F l < 25$  (see Fig. (a)). One can see that the main contribution to the conductivity comes from the interference correction. Moreover, the accordance with the theoretical predictions is observed down to  $k_F l = 2.5$  when quantum corrections are not small compare with Drude conductivity. At this  $k_F l$ , their value is about two-third of  $\sigma_0$  when  $T = 0.46$  K.

At gate voltage  $V_g < -2.9$  V the temperature dependence of  $\sigma$  increases and it deviates from the logarithmic one (see Fig. 1(a)). Let us compare  $\sigma(T)$  dependences in this range with self consistent theory of Anderson localization [4] which is applicable at arbitrary value of quantum correction. When  $\tau_\varphi \gg \tau$  this theory leads to the equation for the conductivity

$$\frac{\sigma_0}{G_0} + \ln \left( \frac{\sigma_0}{G_0} \right) - \left[ \frac{\sigma(T)}{G_0} + \ln \left( \frac{\sigma(T)}{G_0} \right) \right] = \ln \left[ \frac{\tau_\varphi(T)}{\tau} \right]. \quad (1)$$

In Fig. 1(a) the conductivity is plotted as  $(\sigma + \ln \sigma)$ -vs- $\ln T$  in accordance with this equation. One can see that experimental data are well described by this theory both for  $k_F l > 2.5$  and for  $k_F l < 2.5$ .

Moreover, the negative magnetoresistance is observed in this range too. Notice, the shape of  $\Delta\sigma$ -versus- $B$  dependence is the same as for large  $k_F l$ . It is illustrated by Fig. 2(b) where  $\Delta\sigma$ -versus- $B$  data for  $V_g = -1.8$  V ( $k_F l = 17.9$ ) and  $V_g = -3.3$  V ( $k_F l \simeq 0.5$ ) are presented. It is evident that both data sets practically coincide. Therewith, the values of fitting parameters of negative magnetoresistance  $\tau_\varphi$  and prefactor change slowly and monotonically over the whole  $k_F l$ -range.

From our point of view these facts indicate that at both small and large  $k_F l$ -value the conductivity mechanism remains unchanged (it is diffusion, not hopping) and the negative magnetoresistance results from the magnetic-field suppression of the interference correction to the conductivity.

Thus, down to  $k_F l \simeq 0.5$  the conductivity looks like diffusive one and its temperature and magnetic field dependence is due to that of the quantum corrections which can be comparable in magnitude with the Drude conductivity at low temperature.

It is usually supposed that at  $\sigma < e^2/h$  the conductivity mechanism is the variable range hopping [2]. It is argued by the fact that the temperature dependence of the resistivity

$\rho = \sigma^{-1}$  is well described by characteristic for this mechanism dependence:

$$\rho(T) = \rho_0 \exp\left(\frac{T_0}{T}\right)^m \quad (2)$$

with  $m = 1/2, 1/3$  depending on the ratio of the Coulomb gap width to the temperature. It should be noted that data of [2] are well described by (1) as well (see Fig. 1(b)). Thus only the temperature dependence of the conductivity does not allow to identify the conductivity mechanism reliably.

In summary, we have shown that in wide range of the low temperature conductivity starting from  $\sigma \simeq 3 \times 10^{-8} \Omega^{-1}$  the conductivity can be treated as the diffusive but not hopping one. We assume that the transition to hopping occurs at lower  $k_F l$  value.

#### Acknowledgments

This work was supported in part by the RFBR through Grants No 00-02-16215 and No 01-02-17003, the Program *University of Russia*, the Federal Program *Physics of Solid-State Nanostructures*, the CRDF through Grand No REC-005, and the Russian–Ukrainian Program *Nanophysics and Nanoelectronics*

#### References

- [1] B. A. Altshuler and A. G. Aronov, *Electron–Electron Interaction in Disordered Systems*, Eds. A. L. Efros and M. Pollak, North-Holland, 1987.
- [2] F. Tremblay, M. Pepper and R. Newbury *et al*, *J. Phys.: Cond. Matt.* **2**, 7367 (1990);  
H. W. Jiang, C. E. Johnson and K. L. Wang, *Phys. Rev. B* **46**, 12830 (1992);  
F. W. Van Keuls, X. L. Hu, H. W. Jiang and A. J. Dahm, *Phys. Rev. B* **56**, 1161 (1997);  
S. I. Khondaker, I. S. Shlimak, J. T. Nicholls, M. Pepper and D. A. Ritchie, *Phys. Rev. B* **59**, 4580 (1999).
- [3] G. M. Minkov, O. E. Rut, A. V. Germanenko, A. A. Sherstobitov, V. I. Shashkin, O. I. Khrykin and V. M. Daniltsev, *Phys. Rev. B* **64**, 235327 (2001).
- [4] D. Vollhardt and P. Wölfle, *Phys. Rev. Lett.* **45**, 842 (1980); *Phys. Rev. B* **22**, 4666 (1980);  
A. A. Gogolin and G. T. Zimanyi, *Solid State Commun.* **46**, 469 (1983).

## Magnetotransport of 2D-electrons and holes at a type II broken-gap single heterojunction doped with acceptor impurity

*K. D. Moiseev*<sup>†</sup>, *V. A. Berezovets*<sup>†</sup>, *M. P. Mikhailova*<sup>†</sup>, *V. I. Nizhankovskii*<sup>‡</sup>,  
*R. V. Parfeniev*<sup>†</sup> and *Yu. P. Yakovlev*<sup>†</sup>

<sup>†</sup> Ioffe Physico-Technical Institute, St Petersburg, Russia

<sup>‡</sup> International High Magnetic Fields and Low-Temperature Laboratory,  
 Wroclaw, Poland

The observation of the Quantum Hall effect (QHE) in a semimetal channel with coexisting electrons and holes, simultaneously, at the type II broken-gap p-GaIn<sub>0.16</sub>As<sub>0.22</sub>Sb/p-InAs single heterointerface based on unintentionally doped quaternary solid solution obtained by liquid phase epitaxy (LPE) was reported for the first time elsewhere [1]. In this report the quantum magnetotransport in the p-Ga<sub>0.84</sub>In<sub>0.16</sub>As<sub>0.22</sub>Sb<sub>0.78</sub>/p-InAs single heterostructure has been studied for a set of the samples with the both undoped and doped with Zn impurity quaternary layer at low temperatures in high magnetic fields up to 14 T.

The epitaxial layer of wide-gap GaIn<sub>0.16</sub>As<sub>0.22</sub>Sb solid solution ( $E_g = 0.635$  eV at  $T = 77$  K) with mirror-like surface was grown lattice-matched to the InAs (100) substrate by LPE. Layer lattice mismatch was as low as  $\Delta a/a = 2 \times 10^{-4}$  at room temperature. High quality of the heteroboundaries and planarity of the epitaxial growth of these solid solutions were ascertained by X-ray double diffraction measurements [2]. Abruptness of the InSb-like heterointerface as well as of subsequent 3–4 MLs ( $\sim 12$  Å) was verified by transmission electron microscopy measurements. The heavy compensate p-InAs substrate with hole concentration  $p = 8 \times 10^{16} \text{ cm}^{-3}$  at  $T = 300$  K was chosen as a semi-insulator for transport measurements at low temperature. Its low conductivity was obtained due to light doping with Zn. The unintentionally doped quaternary epilayer with the hole concentration  $p = 2 \times 10^{16} \text{ cm}^{-3}$  and the carrier mobility  $\mu_p = 2000 \text{ cm}^2/\text{Vs}$  at 77 K was used to obtain “undoped” structure (sample No 1). The sample No 2 contained quaternary solid solution doped with Zn. The parameters of the samples under study determined from low-field Hall resistance measurements are shown in Table 1.

**Table 1.**

Sample number	Epilayer doping	Hall resistance ( $\rho$ , $\Omega$ ) at $T = 1.5$ K, $B \sim 0$	Hall coefficient ( $R_H$ , $\text{cm}^2/\text{As}$ ) at $B \sim 0$	Hall mobility ( $R_H\sigma$ , $\text{cm}^2/\text{Vs}$ ) at $B \sim 0$
1	undoped	136.2	$8.72 \times 10^6$	64 000
2	Zn, 0.004 at. %	411.38 ac 191.0 dc	$1.00 \times 10^7$ ac $3.08 \times 10^6$ dc	24 000 ac 16 000 dc

The Coulomb scattering in the semimetal channel is largely reduced due to the charge separation at the heterointerface and it results in the high electron mobility at low temperatures. Existence of the electron channel at the interface in the isotype p-doped heterostruc-

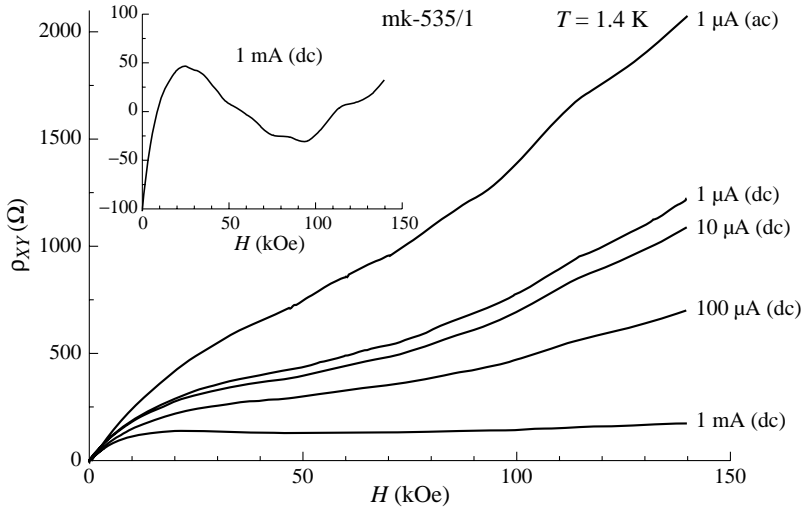


**Fig. 1.** Hall resistivity components for the sample No 2 under different drive current conditions. Insert:  $\rho_{xy}$  for  $I = 1$  mA (dc) after subtraction of monotonic background.

tures has also been clearly demonstrated in a scanning transmission microscopy study of the cross-section of the p-GaIn<sub>0.16</sub>As<sub>0.22</sub>Sb/p-InAs structures cleaved in air at room temperature. The conduction channel with high 2D-electron mobility (up to  $7 \times 10^4$  cm<sup>2</sup>/Vs at  $T = 77$  K) was observed at the interface of p-GaIn<sub>*x*</sub>As<sub>*y*</sub>Sb/p-InAs heterojunction with undoped quaternary layers in the composition range  $0.09 < x < 0.22$  and  $y = x + 0.06$  [3]. The negative sign of the Hall effect voltage indicated that the n-type conductivity was dominant. The Hall mobility observed in low magnetic fields of at  $B < 2$  T was measured on samples with the epitaxial layers lightly doped by Zn ( $p < 1 \times 10^{17}$  cm<sup>-3</sup>) in a wide temperature range (1.6–200 K) while the heavy doping level with Zn leads the depletion of the electron channel at the interface and to suppress its contribution to Hall conductivity [4].

We found out a significant 3D-holes contribution to the Hall effect and conductivity (Fig. 1) due to the transition from a low alternative current (1 μA) to high direct current (1 μA). It should be noted that bulk holes in the epilayer became more apparent under applying of direct current. Nevertheless, as it was seen in insert in Fig. 1, the behavior of the curve of  $\rho_{xy}$  is similar under both direct current and alternating current conditions. Thus, SdH oscillation positions for electrons still remain in the total current range while their intensity was reduced with drive current increasing. That means we still have a manifestation of electron channel onto the large 3D-hole background induced from the doped quaternary solid solution. Moreover, the direct current measurements can be more sensitive to the carrier sign changing. In further, we studied Hall tensor behaviour under direct current conditions.

Hall tensor components for the heterostructure based on the epilayer doped with Zn (sample No 2) are demonstrated in Fig. 2. The magnetoresistance components exhibited the SdH oscillations for electrons in the self-consistent quantum well on the InAs side for both 1.4 K and 4.2 K temperatures. Three distinct sets of the SdH oscillations were found, one of which ceases at  $B \sim 1.5$  T, where the second set begins to appear. Then, it becomes rapidly empty with increasing magnetic field and disappears in higher ( $H \sim 5$  T) magnetic fields. The third set has been clearly resolved in the magnetic field range up to

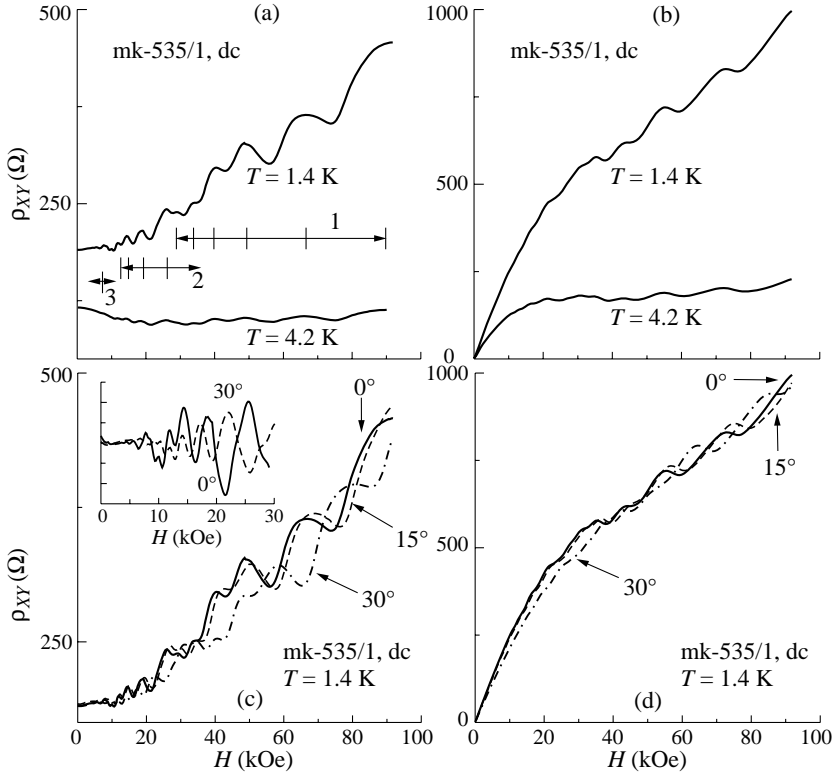


**Fig. 2.** Magnetoresistance (a) and Hall resistance (b) for the sample No 2 at various temperatures. Angular dependence of magnetoresistance (c) and Hall resistance (d).

10 T. These sets can be associated with three different quantum-size subbands ( $E_1$ ,  $E_2$  and  $E_3$ ) in the electron channel at the p-GaInAsSb/p-InAs interface. The concentrations for 2D-electron subbands  $E_1$ ,  $E_2$  and  $E_3$  were revealed as well as  $n_1 = 1.01 \times 10^{12} \text{ cm}^{-2}$ ,  $n_2 = 3.22 \times 10^{11} \text{ cm}^{-2}$  and  $n_3 = 1.01 \times 10^{11} \text{ cm}^{-2}$ , respectively.

To establish the 2D-nature of carriers for three electron subbands in the semimetal channel at the single broken-gap p-GaIn<sub>0.16</sub>As<sub>0.22</sub>Sb/p-InAs heteroboundary, the angular dependence of SdH oscillations in Hall effect ( $\rho_{xy}$ ) and magnetoresistance ( $\rho_{xx}$ ) were studied at  $T = 1.4 \text{ K}$  under magnetic fields up to 10 T. Figures 2(c,d) represent a set of the curves of  $\rho_{xx}$  and  $\rho_{xy}$  for different ( $0^\circ$ ,  $15^\circ$  and  $30^\circ$ ) angles  $\varphi$  between  $B$  and  $n$ , where  $n$  is a normal unit of the heterojunction surface. It should be noted that the shift of SdH oscillations positions towards the high magnetic fields with the angle increasing as well as  $B \cos \varphi$  is an evidence confirmation of 2D-nature of electrons at the interface. The insert in Fig. 2(c) exhibits that the low-field electron subband is also angular dependent.

The most impressive result is the demonstration of integer quantum Hall effect (QHE) plateaus in the Hall conductivity  $\sigma_{xy}$  (Fig. 3). The filling factor  $n = 2, 3$  and 6 in the magnetic field range 6–14 T for the sample No 1 was found according to the equations  $\sigma_{xy} = (n_e - n_h) \cdot e^2 / h$  and  $\nu = \nu_e(E_1) + \nu_e(E_2) - \nu_h$ , where  $h$  — Planck's constant,  $e$  — electron charge,  $\nu_e$  and  $\nu_h$  are the filling factors of the electron  $E_1$  and  $E_2$  subbands and hole subband, respectively. The filling factor is the number of the occupied Landau levels. The obtained values of the filling factor are agreed with the difference of N–P

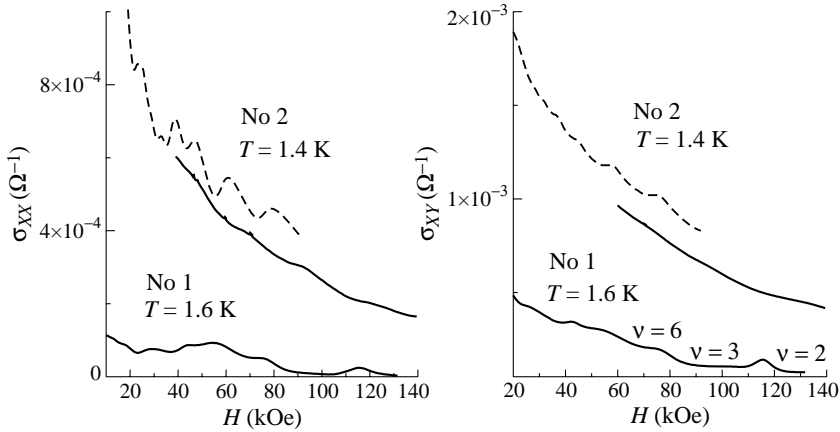


**Fig. 3.**  $\sigma_{xx}$  (a) and  $\sigma_{xy}$  (b) after substraction of monotonic background for two samples. Solid curves correspond to ac conditions while dash curves were obtained under dc conditions.

charge at the  $\text{GaIn}_{0.16}\text{As}_{0.22}\text{Sb/InAs}$  heterointerface. It inhibits that the quantum Hall effect in the presence of the electrons and holes coexisting at the single type II broken-gap heterointerface measures only the number of uncompensated carriers in a semimetal channel. As was mentioned above, direct current measurements are more sensitive to sign of carrier involving to Hall conductivity. For the sample No 2, these curves are presented as two parts: dc and ac. Unfortunately, we cannot at the moment identify the plateaus in  $\rho_{xy}$  for the sample No 2 due to strong background from 3D-holes in the epilayer. The shift of the plateaus for the sample No 2 towards high magnetic fields with Zn concentration increasing is determined by significant 3D-hole contributions to the Hall conductivity.

Doping of epilayer changes the ratio of carrier concentration of the contacting materials and results in the increasing of electron concentration in the semimetal channel due to electron transfer across the interface. It leads to different band bending for holes and electrons at the heteroboundary. For sample No 2 (doped structure) one can found that the electron quantum well became wider and shallower, and it is enough to fill three subbands. At higher magnetic fields ( $B > 16$  T) there can be realized a quantum system containing one electron and one hole subbands, where the quantum Hall effect for electrons will be observed in the presence of the hole system.

#### Acknowledgements

This work was supported by the Russian Foundation for Basic Research project No 02-02-17633, Russian Program "Low-Dimensional Nanostructures".

#### References

- [1] K. D. Moiseev, V. A. Berezovets, M. P. Mikhailova, V. I. Nizhankovskii, R. V. Parfeniev and Yu. P. Yakovlev, *Surf. Sci.* **482-485**, 1083 (2001).
- [2] K. D. Moiseev, N. N. Faleev, A. A. Sitnikova and Yu. P. Yakovlev, *Semiconductors* **34** (2000).
- [3] T. I. Voronina, T. S. Lagunova, M. P. Mikhailova, K. D. Moiseev, A. E. Rozov and Yu. P. Yakovlev, *Semiconductors* **34**, 189 (2000).
- [4] T. S. Lagunova, T. I. Voronina, M. P. Mikhailova, K. D. Moiseev, A. E. Rozov and Yu. P. Yakovlev, *Semiconductors* **32**, 215 (1998).



## Quantized acoustoelectric current in the ballistic channels

M. P. Trushin, V. A. Margulis and A. V. Shorokhov  
 Mordovian State University, 430000 Saransk, Russia

**Abstract.** The acoustoelectric current in the ballistic quantum channels is investigated. It is shown theoretically that the acoustoelectric current as a function of chemical potential (which is controlled by gate voltage itself) demonstrates either giant quantum oscillations or quantized plateaux. The conditions of such step-like behaviour have been found and investigated in detail.

### Introduction

The recent development of experimental technique has made it possible to work with higher acoustic wave frequencies and to measure currents in the pA range. To our knowledge the first observation of the acoustoelectric current in a quantum channel was reported in [1]. It was observed that a plot of current versus gate voltage shows giant oscillations having minima at those gate voltages which show plateaux in the conductance. The following experimental study [2] presents the quantized acoustoelectric current in a channel. It was observed clearly up to four plateaux in the acoustoelectric current as a function of gate voltage.

The acoustoelectric effect in the ballistic quantum channels was considered by Gurevich *et al.* [3] where the acoustic wave was represented by a phonon flux, and the electron-phonon interaction was presented as an electron-phonon collision term in the Boltzmann equation for the electrons. An interesting feature of this effect is the vanishing of the acoustoelectric current below the threshold value of the acoustic frequency  $\omega_q$

$$\omega_{th} = 2m^*s^2/\hbar. \quad (1)$$

Here  $m^*$  and  $s$  are the electron effective mass and sound velocity, respectively.

However it is important to note, that the collision picture presented in [3] is valid only when the phonon frequency is larger than the inverse finite escape time of electrons from the channel. For resonant electrons it means that the length of the channel is much larger than the acoustic wavelength. This condition together with the well-known conditions of the ballistic transport regime allows the description of the electron-phonon interaction as a scattering term in the Boltzmann equation, as used in [3]. This approach will be used below.

### 1. Acoustoelectric current in a ballistic channel

Using the formalism [3] for the acoustoelectric transport we can write down the following formula for the acoustoelectric current in a quantum channel

$$J = \frac{2em^*\Lambda^2SL}{\rho\hbar^3\omega_{th}} \frac{\partial}{\partial\mu} \sum_{nm} f^F \left( \varepsilon_{nm} + \hbar\omega_{th}/4 + \hbar\omega_q^2/4\omega_{th} - \mu \right), \quad (2)$$

where  $S$  is the sound intensity,  $\Lambda$  is the deformation potential constant,  $\rho$  is the mass density,  $f^{(F)}$  is the Fermi function,  $\mu$  is the chemical potential, and  $n, m$  are the quantum numbers of transverse quantization.

Note that Eq. (2) is valid only when the temperature is much larger than the phonon energy  $T \gg \hbar\omega_q$ . For this reason it is impossible to consider the limiting case of zero temperature by Eq. (2). Also it is important to note the present consideration is valid for not very high sound intensity when there is direct proportionality between the sound intensity and the acoustoelectric current.

Let us model the quantum channel using the asymmetric parabolic confining potential. Then the spectrum of single-electron spinless states has the simplest form

$$\varepsilon_{nmp} = \hbar\omega_x(n + 1/2) + \hbar\omega_y(m + 1/2) + p^2/2m^*. \quad (3)$$

Here  $\omega_x$  and  $\omega_y$  are the characteristic confinement frequencies,  $p$  is the electron momentum along the channel,  $n, m = 0, 1, 2, \dots$

For the following analysis it is convenient to expand Eq. (2) as a Fourier series. It can be done by means of a method similar to that used in our previous work [4] for the ballistic conductance investigations. Taking into account the characteristic parabolic confinement frequencies are much larger than the phonon frequencies we get the following formula for the acoustoelectric current

$$J = \frac{4\pi^2 em^* T S \Lambda^2 L}{\rho \hbar^5 \omega_{th}} \sum_{k=1}^{\infty} (-1)^k k \left[ \frac{1}{\omega_x^2} \frac{\sin(2\pi k \mu / \hbar \omega_x)}{\sinh(2\pi^2 k T / \hbar \omega_x) \sin(\pi k \omega_y / \omega_x)} + \right. \\ \left. + \frac{1}{\omega_y^2} \frac{\sin(2\pi k \mu / \hbar \omega_y)}{\sinh(2\pi^2 k T / \hbar \omega_y) \sin(\pi k \omega_x / \omega_y)} \right] + \frac{2em^* S \Lambda^2 L}{\rho \hbar^5 \omega_x \omega_y \omega_{th}} \mu. \quad (4)$$

As follows from this equation the dependence of the acoustoelectric current on chemical potential demonstrates two types of oscillations. The amplitudes of these oscillations are determined by the relations between the temperature and parameters of the channel (frequencies  $\omega_x$  and  $\omega_y$ ). The period of each component depends only on parameters of the channel. It is interesting to note that each maximum of giant quantum oscillations corresponds to a threshold of the ballistic conductance. It shows qualitative agreement with the aforementioned experimental results.

Now it is interesting to describe the sufficiently asymmetric quantum channel, that is  $\omega_x \gg \omega_y$ . In this case the common expression for the acoustoelectric current is the sum of two components  $J = J^{step} + J^{osc}$ . Here

$$J^{step} = \frac{2em^* S L \Lambda^2}{\rho \hbar^4 \omega_{th} \omega_y} \left[ \frac{\mu}{\hbar \omega_x} + \sum_{k=1}^{\infty} (-1)^k C_k(T) \sin(2\pi k \mu / \hbar \omega_x) \right], \quad (5)$$

where

$$C_k(T) = \frac{2\pi^2 T}{\hbar \omega_x} \frac{1}{\pi} \sinh^{-1}(2\pi^2 k T / \hbar \omega_x),$$

and

$$J^{osc} = \frac{4\pi^2 em^* T S \Lambda^2 L}{\rho \hbar^5 \omega_{th} \omega_y^2} \sum_{k=1}^{\infty} \frac{(-1)^k k \sin(2\pi k \mu / \hbar \omega_y)}{\sinh(2\pi^2 k T / \hbar \omega_y) \sin(\pi k \omega_x / \omega_y)}. \quad (6)$$

The component  $J^{\text{step}}$  is the sum of two parts, the monotonic part is a linear function on chemical potential, while the oscillating one gives a saw-toothed contribution to this dependence. As a consequence  $J^{\text{step}}$  has a step-like dependence on chemical potential. As follows from the Eq. (6) the other component gives an oscillating contribution to the acoustoelectric current. Note, that the period of these oscillations is much smaller than the length of the plateaux.

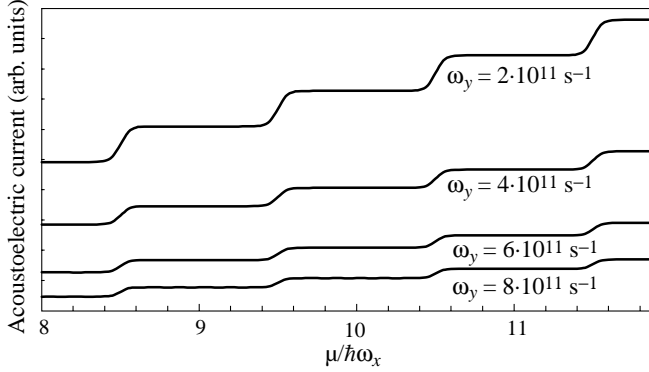


**Fig. 1.** The acoustoelectric current vs. chemical potential for different channel widths.  $T = 2$  K,  $\omega_x^{-1} = 10^{-13}$  s.

## 2. Discussion

Now let us describe some limiting cases. First of all it is interesting to consider the situation when  $\hbar\omega_y \ll 2\pi^2T \ll \hbar\omega_x$ . Then the step-like component is many times as large as the oscillating one, and the common acoustoelectric current has a step-like dependence on chemical potential. It is interesting to note that the height of the steps is inversely proportional to  $\omega_y$ , that is one is directly proportionally to the width of the channel (see Fig. 1). Also there is an inverse proportionality between the length of the plateaux and the thickness of the quantum layer (modelling by  $\omega_x$ ). It may be said that as follows from our model the existence of the acoustoelectric current steps is a consequence to the strong asymmetry of the channel. Secondly let us describe the case when  $\hbar\omega_y \lesssim 2\pi^2T \ll \hbar\omega_x$ . Then the oscillating component gives the fine structure of the acoustoelectric current steps. In the case of comparatively low temperatures  $T \ll \hbar\omega_{x,y}$  the amplitudes of the oscillation peaks is larger than the height of the steps. That is why the acoustoelectric current plateaux are destroyed by these oscillations (see Fig. 2). And finally let us describe the case  $T \gg \omega_{x,y}$ . The temperature increasing leads to the smoothing of the thresholds of the acoustoelectric current steps. This process is similar to the smoothing of the thresholds of the ballistic conductance steps. In this case there is a linear dependence of the acoustoelectric current on chemical potential

$$J = \frac{2em^*S\Lambda^2L}{\rho\hbar^5\omega_x\omega_y\omega_{th}}\mu + o\left(\frac{\hbar\omega_x}{T}, \frac{\hbar\omega_y}{T}\right). \quad (7)$$

Our conclusions focus on the following aspects such as the conditions of the step-like dependence of the acoustoelectric current versus chemical potential. In summary these conditions are as follows: firstly, the strong asymmetry of the channel, that is the thickness

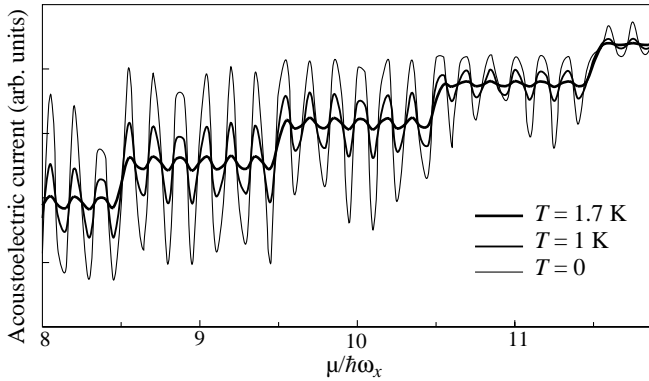


**Fig. 2.** The acoustoelectric current vs. chemical potential at different temperatures ( $\omega_x^{-1} = 10^{-13}$  s,  $\omega_y^{-1} = 1.3 \times 10^{-12}$  s).

of the quantum layer has to be very small compared to the channel width, and secondly, the temperature smearing has to satisfy the inequality  $\hbar\omega_y \ll 2\pi^2 T \ll \hbar\omega_x$ .

We have also found the acoustoelectric current in the quantum channel using the hard-wall confining potential as a model for the emulation of the quantum layer thickness. However the expressions for the Fourier coefficients are more cumbersome in this case. Nevertheless note that the conditions of the acoustoelectric current step-like behaviour remain the analogic type in this model.

And finally using the electron-phonon parameters [5] and assuming that  $L = 5 \times 10^{-4}$  cm,  $S = 10^{-3}$  erg/(cm<sup>2</sup>s) it is easy to evaluate the height of the acoustoelectric current steps

$$\Delta J^{\text{step}} = \frac{2em^*SL\Lambda^2}{\rho\hbar^4\omega_{th}\omega_y} \simeq 1 \text{ nA}. \quad (8)$$

This estimate shows agreement with experiments (see, for example, [2]).

## References

- [1] J. M. Shilton, D. R. Mace, V. I. Talyanskii *et al*, *J. Phys.: Condens. Matter* **8**, L337 (1996).
- [2] V. I. Talyanskii, J. M. Shilton, M. Pepper *et al*, *Phys. Rev. B* **56**, 15180 (1997).
- [3] V. L. Gurevich, V. I. Kozub and V. B. Pevzner, *Phys. Rev. B* **58**, 13088 (1998).
- [4] V. A. Margulis, A. V. Shorokhov and M. P. Trushin, *Phys. Lett. A* **276**, 180 (2000).
- [5] T. Brandes and A. Kawabata, *Phys. Rev. B* **54**, 4444 (1996).

## Conduction in nanocomposites: hopping on a fractal

*I. P. Zvyagin*

Faculty of Physics, Moscow State University, 119899 Moscow, Russia

**Abstract.** We discuss the mechanism of hopping conduction in nanocomposites and similar materials where the size of hopping sites is large compared to edge-to-edge separations between the sites. In this case the dominant mechanism involving transitions via virtual intermediate localized states is characterized by the increase in tunneling probabilities between distant sites; moreover the coherent tunneling path via virtual intermediate states is restricted to the fractal incipient percolation cluster. The application of percolation arguments to the calculation of the system conductivity is based on the concept of the generalized chemical distance. The resulting d.c. conductivity temperature dependence is of the form  $\ln \sigma \sim -(T_0/T)^x$ , where the exponent  $x$  is expressed in terms of the critical exponent for the chemical distance (or superlocalization exponent) and fractal dimensionality of the backbone cluster.

### Introduction

Conventional theories of electron hopping conduction in disordered solids consider the transport due to inelastic (phonon-assisted) tunneling between localized electronic states that exponentially decay away from localization points. This model was successfully applied to hopping transport in doped crystalline and amorphous semiconductors; it was also suggested to use it for granular conductors, where a nonactivated conductivity temperature dependence of the form

$$\ln \sigma = \text{const} - (T_0/T)^x, \quad (1)$$

(here  $T_0$  is a parameter and the exponent is  $x \approx 1/2$ ) was currently observed. However, for granular conductors this model is not immediately applicable due to a finite grain size that can be appreciably greater than the wave function decay length in the intergrain (barrier) region. A straightforward correction of the standard model is to take into account a decrease in the tunneling distance for transitions between a pair of sites due to the difference between the center-to-center and edge-to-edge separations [1]. For distant-neighbor hopping, however, this is not sufficient, since the most important effect comes from the involvement of intermediate virtual states [2]. If the site size is large compared to edge-to-edge separations, the intermediate virtual states can produce an exponential increase in distant-site transition probabilities compared to those for direct phonon-assisted transitions. This effect has been discussed for hopping transport in intentionally disordered superlattices [2], granular metals [3] and arrays of self-assembled quantum dots [4].

In what follows we discuss some aspects of the percolation approach to electronic transport by transitions involving virtual states related to the fractal nature of the incipient percolation cluster.

### Generalized chemical distance metric

Nanocomposites are two-phase mixtures with conducting (usually metallic) nanoparticles separated by a poorly conducting (dielectric) phase. Accordingly, a reasonable model for the system is a lattice with some of the sites occupied by metallic grains immersed in the dielectric. At metal volume fractions  $x < x_c$ , where  $x_c$  is the threshold for the appearance of the infinite metallic cluster, the conduction is due to inelastic tunneling (hopping) between

grains with size variations giving rise to fluctuations of the energy levels and charging energies.

We consider the case in which

$$a \gg w \gg \tilde{\alpha}^{-1}, \quad (2)$$

where  $a$  is the characteristic site size,  $w$  is the edge-to-edge separation between the neighboring sites and  $\tilde{\alpha}$  is the decay parameter, i.e., the inverse localization length characterizing the decay of the wave function in the dielectric; conditions (2) are usually satisfied for granular metals. Since  $a \gg w$ , we can neglect real tunneling transitions to all sites but near neighbors (NN). Therefore, the standard variable range hopping regime is not realized. At low temperatures the main contribution to the transition rate (that includes the statistical factors describing state populations) between distant sites involving intermediate virtual states is [2, 3]

$$\Gamma_{ij} = |I_{ij}|^2 \exp \{-E_{ij}/kT\}, \quad (3)$$

where

$$I_{ij} = \sum_{\beta_{ij}} \prod_{\substack{i'j' \\ i'j' \in \beta_{ij}}} \frac{t_{i'j'}}{\Delta E_{i'j'}}, \quad (4)$$

$\beta_{ij}$  denote the NN paths connecting the initial site  $i$  and the final site  $j$ , the product indices run over the successive links corresponding to the pairs  $\{i'j'\}$  along the path  $\beta_{ij}$ ,  $t_{ij}$  is the transfer integral that exponentially depends on the edge-to-edge separation  $w_{ij}$ ,  $t_{ij} = t_0 \exp \{-\tilde{\alpha}w_{ij}\}$ ,  $E_{ij} = (|E_j| - |E_i| + |E_j - E_i|)/2$  and the  $E_i$  are site energies measured from the Fermi level (in Eq. (4) we have assumed that the characteristic NN energy differences along the path are large compared to  $t_{i'j'}$ ).

Eq. (4) can be written in the form

$$I_{ij} = \sum_{\beta_{ij}} t_0 \exp \{-l(ij|\beta_{ij})\}, \quad (5)$$

where

$$l(ij|\beta_{ij}) = \sum_{\{i'j'\}} (\tilde{\alpha}w_{i'j'} + \ln |\Delta E_{i'j'}/t_0|) \quad (6)$$

is the length of the NN path  $\beta_{ij}$  connecting  $i$  and  $j$ . Of all NN paths, the main contribution to the transition rate comes from the path with the smallest  $l(ij|\beta_{ij})$ . We call the value  $l_{ij} = \min \{l(ij|\beta_{ij})\}$  the *generalized chemical distance* between  $i$  and  $j$ . Recall that the concept of the chemical distance has been studied extensively for a number of problems (growth of random aggregates, diffusion on fractals etc.) [6, 7]. Chemical distance is usually introduced as the shortest NN path connecting the two sites on the percolation cluster. The important difference of this definition from ours is that the value  $l_{ij}$ , Eq. (7), can be substantially smaller than the value  $\tilde{\alpha}a_{ij}$ , where  $a_{ij}$  is the actual path length on the structure. Accordingly, the transition rate along the NN path can appear to be much greater than the rate for direct transitions determined by the Cartesian distance  $R_{ij}$  between  $i$  and  $j$ .

For distant sites  $i$  and  $j$  we have

$$l_{ij} = n \{ \tilde{\alpha} \overline{w} + \ln (\Delta E_{i'j'}/t_0) \} = n \alpha \overline{w}, \quad (7)$$

where  $\alpha = \tilde{\alpha} + (1/\overline{w}) \ln (\Delta E_{i'j'}/t_0)$  is the renormalized decay length,  $n$  is the number of tunneling events (steps) along the shortest NN path and overline denotes the averaging along the path.

### Percolation arguments

If the scatter in transition rates is large, then we can evaluate conductivity by applying the percolation arguments. Just as in the standard percolation approach, we choose some value  $\eta$  and define a bond between NN by

$$2l_{ij} + E_{ij}/kT < \eta. \quad (8)$$

At some  $\eta = \eta_c$ , the infinite cluster of adjoining bonds apperas; the value  $\eta_c$  determines the main exponential variation of the conductivity. To find  $\eta_c$ , we can use, e.g., the bonding criterion (see [8]) that states that the threshold corresponds to the condition that the average number of bonds per site  $\bar{B}$  attains some critical value  $B_c$ . For site  $i$  the number of bonds is

$$B_i = \sum_j \int dE_j \rho(E_j) \theta\{\eta - 2l_{ij} - |E_{ij}|/kT\}, \quad (9)$$

where  $\rho(E)$  is the density of localized states. Assuming for simplicity that  $\rho(E) = \rho_0$  [3], we obtain

$$\bar{B} = \rho_0 \int_{-\eta kT}^{\eta kT} dE_j N_B(l_m(E_{ij})), \quad (10)$$

where  $N_B(l_m(E)) = \sum_j \theta(l_m(E) - l_{ij})$  and  $l_m(E) = (\eta - |E|/kT)/2$ .

We can estimate the generalized chemical distance by constructing a percolation cluster of NN links (this is the incipient percolation cluster). It is known that the incipient percolation cluster is fractal [6, 7]. As discussed above, for virtual state-mediated transitions the NN tunneling paths are restricted to the incipient percolation cluster and the transition probability depends on the generalized chemical distance. The average Carthesian distance  $R(l)$  between two sites on the fractal cluster at a chemical distance  $l$  varies as a power of  $l$ ,

$$R \sim al^{\tilde{\nu}} \equiv al^{1/\zeta}, \quad (11)$$

where  $\tilde{\nu}$  is the fractal dimensionality for the paths of minimum length; it is related to the superlocalization exponent  $\zeta$  by  $\zeta = \tilde{\nu}^{-1}$ . Obviously, conduction is determined by the bonds connecting sites lying on the backbone cluster (the backbone cluster is a part of the percolation cluster obtained after eliminating all the ‘dead ends’). Just as in [7], we can introduce the average number  $N_B(l)$  of sites on the backbone cluster with a chemical distance from a given site not exceeding  $l$ ,

$$N_B(l) \sim l^{\tilde{\nu} D_B}, \quad (12)$$

where  $D_B$  is the fractal dimensionality of the backbone cluster.

The average number of bonds can be evaluated setting  $E_i = 0$  [8]. Then Eq. (9) is easily integrated and we obtain

$$\bar{B} = \frac{2\rho_0 kT}{(\tilde{\nu} D_B + 1)(2\alpha\bar{w})^{\tilde{\nu} D_B}} \eta^{\tilde{\nu} D_B + 1}, \quad (13)$$

By the bonding criterion, for the critical value of  $\eta$  we obtain  $\eta_c = (T_0/T)^{1/(\tilde{\nu} D_B + 1)}$ , where

$$T_0 = (C/k) \frac{(2\alpha\bar{w})^{\tilde{\nu} D_B}}{\rho_0} \quad (14)$$

and the constant  $C$  is  $C \approx B_c(\tilde{\nu} D_B + 1)/2$ . Therefore, the temperature dependence of the conductivity is given by Eq. (1), where  $T_0$  is defined by Eq. (14) and the exponent is  $x = (\tilde{\nu} D_B + 1)^{-1}$ .

## Discussion

Taking the values  $D_B = 1.62$  and  $\tilde{\nu} = 1.41$  for the 2D case and  $D_B = 1.83$  and  $\tilde{\nu} = 1.88$  for the 3D case [7], we obtain  $x = 0.41$  and  $x = 0.43$ , respectively. We see that the value of  $x$  is close to 0.4 both for two- and three dimensional systems so that the conductivity temperature dependence given by Eq. (1) is close to the experimentally observed  $T^{-1/2}$ -law. The value of  $T_0$ , Eq. (14), was discussed in [3] and is reasonable for the parameters characteristic of granular metals.

An approach based on the fractal nature of the percolation cluster and superlocalization was used in [9] to describe the temperature variation of the Mott variable-range hopping conductivity. The authors obtained a conductivity variation of the type (1) with exponent  $x$  given by  $x = \zeta/(D + \zeta)$ , where  $D$  is the fractal dimensionality of the percolation cluster. The main assumption of this theory of hopping is that electron is restricted to move on a sublattice which is fractal over some range of length scales. For a standard model, in which electronic states (sites) are exponentially localized at random positions, are isotropic and have random energies, electrons are generally not restricted to the incipient cluster, since direct distant-neighbor tunneling dominates over successive tunneling events via intermediate sites. The result for the conductivity in our model differs from the corresponding result of [9]. Indeed, the expression for the exponent  $x$  contains the fractal dimensionality of the backbone cluster  $D_B$  instead of the fractal dimensionality of the percolation cluster  $D$ . Moreover, the expression (14) for the parameter  $T_0$  differs from that of [9],  $T_0^{DLS} = (C'/k\rho_0)(a/L)^D$ , where  $C'$  is a constant and  $L$  is the characteristic decay length of the superlocalized wave function at the Fermi level. Instead of  $a/L$ , Eq. (14) explicitly contains structural parameters of the material.

## Acknowledgement

The work was supported by the Russian Foundation for Basic Research (grant 00-02-16676).

## References

- [1] P. Sheng and J. Klafter, *Phys. Rev. B* **27**, 2583 (1983).
- [2] I. P. Zvyagin, *JETP Letters* **69**, 932 (1999).
- [3] I. P. Zvyagin and R. Keiper, *Phil. Mag. B* **81**, 997 (2001).
- [4] E. M. Baskin and M. V. Entin, in: *Proc. 24th International Conf. Phys. Semicond.*, Jerusalem, 1998, Ed. D. Gershoni, VII-A-23 (CD-ROM edition).
- [5] I. P. Zvyagin and M. A. Ormont, *phys. stat. sol. (b)*, **230**, No. 1 (2002).
- [6] D. Stauffer and A. Aharony, *Introduction to percolation theory*, Taylor and Francis, London, 1992.
- [7] S. Halvin and D. Ben-Avraham, *Adv. Phys.* **36**, 695 (1987).
- [8] V. L. Bonch-Bruevich, I. P. Zvyagin, R. Keiper, A. G. Mironov, R. Enderlein and B. Esser, *Electronic Theory of Disordered Semiconductors*, Nauka, Moscow 1981 [German edition: *Electronentheorie ungeordneter Halbleiter*, Deutscher Verlag der Wissenschaften, Berlin 1984].
- [9] G. Deutscher, Y. E. Lévy and B. Souillard, *Europhys. Lett.* **4**, 577 (1987).



## Tunnel spectroscopy of self-assembled quantum dots: wavefunction mapping and addressing the dots with electrostatic gates

*L. Eaves*

School of Physics and Astronomy, University of Nottingham,  
Nottingham NG7 2RD, UK

**Abstract.** This talk describes an experimental study of the distribution of the probability density of the electron wave function in InAs/GaAs self-assembled quantum dots (QDs). The carrier wave function is probed using magneto-tunnelling spectroscopy [1], which has previously proved to be a powerful technique for mapping out the energy dispersion curves of bound states in quantum wells [2] and the wave functions of confined states in quantum wires [3].

The structure used is a double-barrier GaAs/(AlGa)As resonant tunnelling diode (RTDs) in which a layer of InAs QDs is incorporated in the centre of the GaAs quantum well [4]. We observe features in the low-temperature current-voltage characteristics,  $I(V)$ , of the diode, corresponding to carrier tunnelling into 0-dimensional states of individual QDs. As discussed below, three successive features correspond to tunnelling through dot states displaying the symmetry of the ground state and first and second excited state, respectively.

We investigate the magnetic field dependence of the current resonances associated with the dot states. In the experiment, carriers tunnel through a barrier into the dots in the presence of a magnetic field,  $B$ , perpendicular to the current,  $I$ . If  $x$  and  $z$  indicate the directions of  $B$  and  $I$ , respectively, then when carriers move from the emitter into the dot, they acquire an in-plane momentum  $\Delta k_y = eB\Delta s/\hbar$  due to the action of the Lorentz force, where  $\Delta s$  is the effective distance tunnelled along  $z$ . This has pronounced effects on the tunnelling process. The intensity of the current resonances changes with increasing  $B$  and we relate this variation to the square of the Fourier transform of the electron probability density [1]. The  $I(B)$  plots provide a means of probing the characteristic form of the wave function probability density of the electron confined in the dot as a function of  $k_y$  and hence of the corresponding spatial coordinate,  $y$ . By rotating the magnetic field in the growth plane,  $(x, y)$ , we derive full two-dimensional maps of the electron wave function probability densities. These reveal clearly the elliptical symmetry of the dot ground state with quantum numbers  $(n_x, n_y, n_z) = (0, 0, 0)$ , and the characteristic lobes of the higher energy states (100) and (200).

The talk then discusses our magneto-tunnelling spectroscopy measurements of the shape and size of the wave function of an electron confined in QDs grown on a (100)- and (311)B-oriented GaAs substrate. We show that the electron wave function has a biaxial symmetry in the growth plane and that the dots are ordered along defined crystallographic directions.

Finally, it is shown that magneto-tunnelling spectroscopy on RTDs which incorporate planar gate electrodes [5] provides a means of identifying and measuring the energy levels and wave functions of an individual dot.

This work is in collaboration with A. Patanè, R. J. A. Hill, A. Levin, P. C. Main and M. Henini (University of Nottingham), D. G. Austing (NTT Atsugi), S. Tarucha (University of Tokyo and NTT Atsugi), and Yu. V. Dubrovskii and E. E. Vdovin (Institute of Microelectronics Technology, RAS Chernogolovka).

## References

- [1] E. E. Vdovin *et al*, *Science* **290**, 124 (2000).
- [2] R. K. Hayden *et al*, *Phys. Rev. Lett.* **66**, 1749 (1991).
- [3] P. H. Beton *et al*, *Phys. Rev. Lett.* **75**, 1996 (1995).
- [4] A. Patanè *et al*, *Phys. Rev. B* **62**, 13595 (2000).
- [5] R. J. A. Hill *et al*, *Appl. Phys. Lett.* **79**, 3275 (2001).

## Polarization revival of a Bloch-oscillating wave packet at resonant Zener tunneling in GaAs shallow superlattice

D. Meinhold<sup>†</sup>, V. G. Lyssenko<sup>‡</sup>, K. Leo<sup>†</sup> and B. Rosam<sup>†</sup>

<sup>†</sup> Institut für Angewandte Photophysik, Universität Dresden,  
01062 Dresden, Germany

<sup>‡</sup> Institute of Microelectronics Technology, RAS, 142432 Chernogolovka, Russia

**Abstract.** We investigate the dynamics of a Bloch-oscillating wave packet in the presence of strong coupling to delocalized above barrier states, using time-resolved intraband polarization-sensitive measurements. At a threshold electric field, the resonance of localized and delocalized states causes a quantum beating which is observed as a revival in the interband polarization. Our numerical simulation visualizes the spatial wave packet decomposition and reformation.

### Introduction

The invention of the semiconductor superlattice (SL) has allowed obtaining key experimental results, like the observation of the Wannier–Stark ladder (WSL) in linear optical spectra [1] and of Bloch oscillations (BO) [2], including the observation of tunable THz emission [3] and the harmonic spatial motion [4]. Besides these one-band phenomena, effects based on the interacting of several bands have been explored. Resonant coupling of different WSL, interminiband Zener tunneling. Field-induced delocalization of a WSL state and the damping of a BO wave packet were reported [5–9]. Much of the original interest in wave packets, and still the vast majority of research on them, has been done in atomic systems. The field-ionization of an angularly localized revolving Rydberg wave packet in an electric field has its analogue in the field-induced Zener tunneling of a Wannier–Stark wavepacket into higher bands. In this Abstract, we report the experimental observation and the numerical simulation of a polarization revival to spatial wave packet decomposition and reformation in a SL. The physical origin of this effect in the SL is somewhat different from Rydberg wave packet revivals in atomic physics. In our case, a wave packet of both localized WSL states are nearly degenerate, delocalized above barrier states are optically excited and the revival originates from a quantum beating between these few discrete states.

### 1. Results and discussion

We performed degenerate, spectrally integrated pump-probe experiments, which are sensitive to the intraband polarization [10]. Our shallow SL contains one electron miniband (30 meV width) in the below-barrier region only. We are thus able to directly address the effects of coupling to a process between localized WSL states and delocalized above-barrier states. The 90-fs laser pulse was spectrally tuned to be energetically centered between the  $hh_{-1}$  and the  $hh_0$  WSL transition, exciting a coherent, BO wave packet. By applying a voltage over the 50/54 Å GaAs/Al<sub>0.11</sub>Ga<sub>0.99</sub>As SL, the BO period was continuously tuned from 900 fs to 160 fs. Simultaneously to the pump-probe analysis, spectrally resolved four-wave mixing (SRFWM) was employed to monitor the exact excitation conditions. The excitation density was  $2 \times 10^9 \text{ cm}^{-2}$ . The sample was held at temperature 8 K.

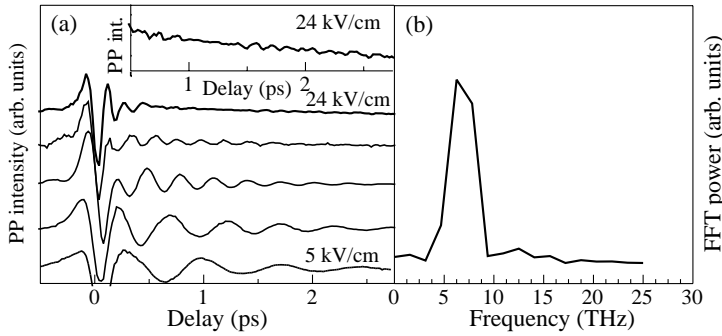


**Fig. 1.** (a) Pump-probe (PP) traces for various electric field from 5 to 24 kV/cm. Inset: enlarged PP trace for 24 kV/cm. (b) Fourier transform of the PP trace for 24 kV/cm from 1.4 to 2.5 ps with maximum at the Bloch-period 166 fs.

Figure 1(a) shows several pump-probe transients from 5 kV/cm up to 24 kV/cm. The increase in the BO frequency  $\omega_{BO}$  with applied electric field is very nicely seen:  $\omega_{BO} = eFd/\hbar$ . The internal field was calibrated using the obtained BO-frequency and the known SL period  $d$ . The results agree with the observed WSL spacing from SRFWM. Obviously, the duration of the signal modulation caused by the wave packet dynamics decreases for increasing electric field. Surprisingly, at a threshold field of 24 kV/cm, we observe a sudden drop of the intraband decay time, accompanied by the observation of a polarization revival (enlarged in inset of Fig. 1(a)). Figure 1(b) shows the Fourier transform of the 24 kV/cm trace from 1.4 ps to 2.5 ps with maximum being exactly at the initial BO frequency.

To model these experimental results quantitatively, we have calculated both the confined and the above barrier electronic states of our finite 35 well SL, subjected to an electric dc field. Our simulation shows that at this threshold electric field the confined WSL-states overlap energetically and spatially with delocalized states that lie above the barrier at

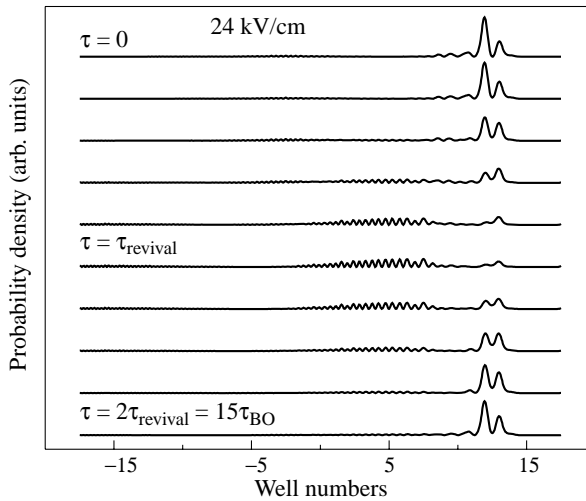


**Fig. 2.** Calculated time evolution of the spatial probability density of the BO wave packet composed of the two confined and two above-barrier states from  $\tau = 0$  and  $\tau = 2.5$  ps.

flatfield. This resonance was directly observed experimentally as an avoided crossing of the  $hh_0$  transition with a transition to an above barrier state in SRFWM (not shown). The BO wave packet resonantly Zener-tunnels into these discrete above-barrier states within a few BO periods. At this time, the electron density is spread spatially over more than 10 wells, i.e. about hundred nanometers.

Figure 2 visualized the spatial dynamics of this wave packet. While [11] we were focusing on the field-induced damping of the wave packet motion, we here show that the initially created Wannier–Stark wave packet quickly delocalizes in space, but partially reconstitutes. As this tunneling is resonant, the electronic coherence is, to some extent, conserved even though the probability density is spread over more than 100 nm. Later, the wavepacket returns into the confinement. The observed revival time of about 1.8 ps is close to the calculated one of 2.5 ps, given by the energetic splitting between confined and above barrier states.

Thus, from our results it follows that the observed initial drop in the ensemble coherence time is due to destructive interference, caused by the confined states and above barrier states. Besides the Bloch-beating, a beating of confined states with delocalized above-barrier states is observed. In other words, the Zener breakdown retains coherence when the electron tunnels to the one discrete state only.

#### Acknowledgements

We thank M. Dignam, S. Glutsh, F. Löser, F. Rossi and K. Köhler for helpful discussion and sample growth. We acknowledge Deutsche Forschungsgemeinschaft (Le 747/30), RFBR and FTN for financial support.

#### References

- [1] E. E. Mendez *et al*, *Phys. Rev. Lett.* **60**, 2426 (1988),  
R. Voisin *et al*, *Phys. Rev. Lett.* **61**, 1639 (1988).
- [2] J. Feldman *et al*, *Phys. Rev. B* **46**, 7252 (1992),  
K. Leo *et al*, *Solid State Commun.* **84**, 943 (1992).
- [3] C. Waschke *et al*, *Phys. Rev. Lett.* **70**, 3319 (1993).
- [4] V. G. Lyssenko *et al*, *Phys. Rev. Lett.* **79**, 301 (1997).
- [5] M. Ben Dahan *et al*, *Phys. Rev. Lett.* **76**, 4508 (1996).
- [6] H. Schneider *et al*, *Phys. Rev. Lett.* **65**, 2720 (1996).
- [7] M. Ben Dahan *et al*, *Phys. Rev. Lett.* **76**, 4508 (1990).
- [8] M. Nakayama *et al*, *Phys. Rev. B* **44**, 5935 (1991).
- [9] G. Bastard *et al*, *Phys. Rev. B* **50**, 4445 (1994).
- [10] M. Helm *et al*, *Phys. Rev. Lett.* **82**, 3120 (1996).
- [11] B. Rosam *et al*, *Phys. Rev. Lett.* **86**, 1307 (2001).
- [12] M. Nakayama *et al*, *Phys. Rev. B* **44**, 5935 (1991).
- [13] G. Bastard *et al*, *Phys. Rev. B* **50**, 4445 (1994).

## Tunnel gaps in the two-dimensional electron system in a magnetic field

*Yu. V. Dubrovskii*<sup>†</sup>, *P. C. Main*<sup>‡</sup>, *L. Eaves*<sup>‡</sup>, *V. A. Volkov*<sup>§</sup>, *D. Yu. Ivanov*<sup>†</sup>,  
*E. E. Vdovin*<sup>†</sup>, *Yu. N. Khanin*<sup>†</sup>, *V. G. Popov*<sup>†</sup>, *D. K. Maude*<sup>¶</sup>, *J.-C. Portal*<sup>¶+\*</sup>,  
*M. Henini*<sup>‡</sup> and *G. Hill*<sup>||</sup>

<sup>†</sup> Institute of Microelectronics Technology RAS, 142432 Chernogolovka, Russia

<sup>‡</sup> The School of Physics and Astronomy, University of Nottingham,  
Nottingham NG7 2RD, United Kingdom

<sup>§</sup> Institute of Radioengineering and Electronics RAS, Moscow, Russia

<sup>¶</sup> Grenoble High Magnetic Field Laboratory, MPI-CNRS,  
BP166 38042 Grenoble Cedex 9, France

<sup>||</sup> Department of Electrical and Electronics Engineering, University of Sheffield,  
Sheffield S3 3JD, United Kingdom

<sup>+</sup> Institut Universitaire de France

<sup>\*</sup> INSA, F31077 Toulouse Cedex 4, France

**Abstract.** We have studied the near-equilibrium tunnelling between identical two-dimensional electron systems at 0.3 K over a wide range of magnetic field applied normal to the electron layers. The magnetic field suppresses the electron tunnelling. Our results are consistent with the co-existence of two types of tunnelling gap. Moreover, at  $\nu < 2$  additional features arise in the tunnelling spectra, which we interpret in terms of the emission of some as yet unidentified quasiparticle.

It was discovered recently that a high magnetic field applied normal to the layers suppresses equilibrium tunnelling between two-dimensional electron systems [1–3] and between 2D and 3D electron systems [4, 5]. These studies were performed on samples with low [2–4] or very low disorder in the 2D electron gas [1]. Later a similar suppression was observed in tunnelling between disordered 2D electron systems [6]. It was found that, above 2 K, the suppression observed in the disordered system was similar to that found in samples with low disorder [2, 3]. There is general agreement that the observed suppression is related to the in-plane Coulomb correlation between 2D electrons in a high magnetic field.

In this work, we focus on tunnelling between two disordered, two-dimensional electron systems (2DES) at low temperature ( $T = 0.3$  K) in a magnetic field parallel to the current, that is, normal to the electron layers. The suppression of the tunnelling current becomes apparent as a dip in the tunnel conductance at zero bias, which appears [7] in a magnetic field of about 4 T. We argue that the co-existence of two tunnelling gaps of different nature could explain our experimental results.

To form the 2DES, we used sheets of Si donors ( $\delta$ -doped layers). The donor concentration was chosen to be slightly above the value for the metal-insulator transition,  $N_D$ , which was determined from  $a_B/\sqrt{N_D} = 1$ , where  $a_B$  is the effective Bohr radius. Thus, the 2DESs should be on the metal side of the transition in the absence of a magnetic field.

The MBE-grown sample was a single barrier GaAs/Al<sub>0.4</sub>Ga<sub>0.6</sub>As/GaAs heterostructure with a 12 nm thick barrier. The barrier was separated from the highly-doped, bulk contact regions by 50 nm thick, undoped GaAs spacer layers. Si donors sheets with concentration of  $3 \times 10^{11} \text{ cm}^{-2}$  were located 5 nm from each side of the barrier. The tunnelling transparency

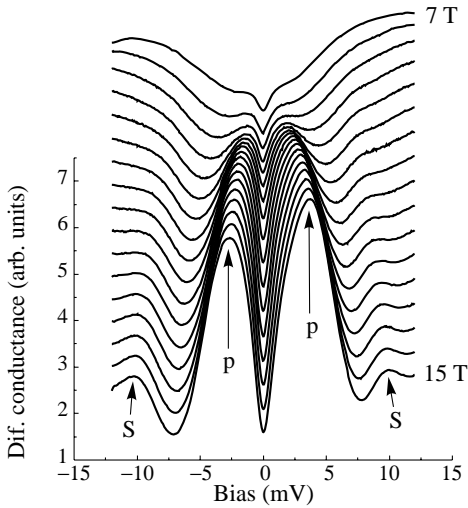


**Fig. 1.** Tunnelling differential conductance at 0.3 K as a function of external voltage in magnetic fields from 7 T up to 15 T, with 0.5 T magnetic field step between the curves. Arrows labelled “p” indicate differential conductance peaks used to determine  $\Delta_H$ . Arrows labelled “S” indicate additional peaks discussed in the text. Curves are arbitrarily shifted in the vertical direction for clarity.

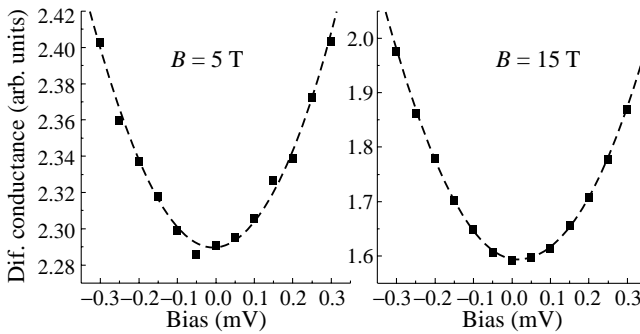


**Fig. 2.** Examples of differential conductance around zero bias in  $B = 5$  T (left), and  $B = 15$  T (right) with best fits to parabolic curves.

of the main barrier was much lower than that of the spacer regions, so that most of the applied voltage is dropped across the barrier.

The differential tunnelling conductance  $G$  versus external voltage  $V_b$  in zero magnetic field has a wide peak around zero bias [6], which reflects resonant tunnelling between the ground states of the 2DESs. The variation of the differential conductance with magnetic field,  $B$ , from 7 to 15 T is shown in Fig. 1. A narrow dip is resolved in the tunnelling spectrum at  $B = 7$  T. As can be seen, with increasing  $B = 7$ , a broad minimum with the dip at zero bias, transforms into a broad maximum. At the same time, the relative depth of the dip at zero bias is increased, as is its apparent width  $\Delta_H$ , which can be defined as the distance between maxima, as indicated in Fig. 2 by arrows. No effects due to electron spin were found. We found that the dip in differential conductance around zero bias has a parabolic dependence on bias voltage at all magnetic fields. Figure 2 shows examples of the fit of the experimental data to a parabolic dependence magnetic field 5 T and 15 T. Simple calculations of the differential tunnelling conductance, which take into account only the single-particle density of states in each layer in a magnetic field, demonstrate the transformation of the broad minimum at 7 T into a wide maximum at higher field. However, they do not predict any sharp dips at any magnetic field.

First, we concentrate on an analysis of the sharp dip. In the simplest model, the tunnelling differential conductance at low voltage reflects the joint density of states at the Fermi levels in the 2D electron layers. In this case, the dip is consistent with the “soft” gap

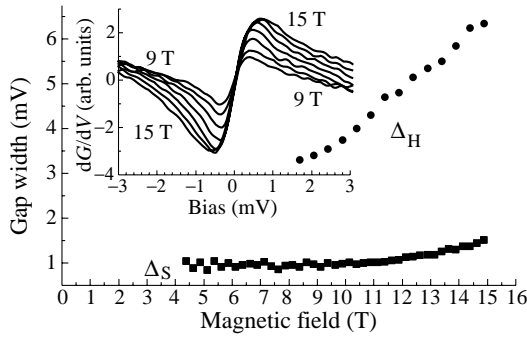


**Fig. 3.** The width of the gaps  $\Delta_S$  and  $\Delta_H$  in mV, versus magnetic field applied normal to the 2DES.

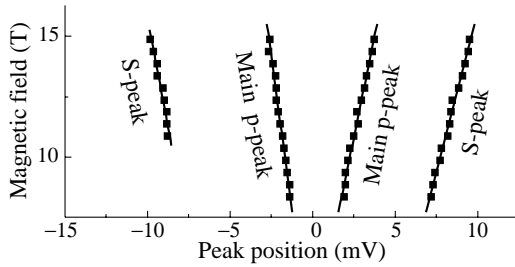


**Fig. 4.** Voltage positions of the main p-peaks and S-peaks in various magnetic fields.

in the density of states of the 2DES at the Fermi level [8]. That is, the single particle density of states in each layer around the Fermi level has the form  $D(E) = \alpha|E - E_F|$ , where  $E_F$  is the Fermi energy. It is easy to extract how the slope,  $\alpha$ , of the linear gap depends on  $B$  from data similar to that shown in Fig. 2. The slope increases with increasing field, exhibiting slow oscillations correlated with the density of states at the Fermi level (see Ref. [7]). The width of the gap ( $\approx 1$  mV) around  $\nu = 2$  (i.e.  $B \approx 7$  T) is approximately constant and is about equal to the width of the linear gap predicted by Efros and Shklovskii,  $\Delta_{ES} = g_0\pi(e^2/k)^2$  [8], where  $g_0$  is the unperturbed 2D density of states without a magnetic field. A gap of similar width to the Efros–Shklovskii gap was recently extracted from magnetotransport studies on 2DEG samples with similar disorder [9]. In the range of magnetic field where the sharp dip is visible, the tunnelling differential conductance has a broad minimum due to the low single particle density of states when the Fermi level lies between Landau levels. The dip is easily resolvable since it is much narrower than the broad minimum. With increasing  $B$ , the broad minimum transforms into a broad maximum due as the density of states at the Fermi level increases. The apparent width  $\Delta_H$  far exceeds  $\Delta_{ES}$  for  $B = 15$  T. For  $\nu < 2$ , the apparent width of the gap increases linearly with increasing magnetic field (Fig. 3) as has also been observed in tunnelling between 2D electron systems with low disorder. In that case, the gap was explained as a manifestation of a “hard” tunnel gap due to the in-plane, Coulomb correlation between electrons [1–3]. The width of this “hard” gap is of the order of the intralayer Coulomb interaction energy, an observation that is consistent with the electron sheet density in our samples.

On the other hand, for  $\nu < 2$  it is possible to determine the gap width in an alternative manner. We take the distance between the points in the differential conductance where the dependence of  $G$  on bias voltage becomes sublinear, which are just the positions of the extrema in  $dG/dV = f(V)$  (inset to Fig. 3). We have chosen this method for two reasons. First, around  $\nu < 2$ , where the gap is well-defined, it gives approximately the same width of the gap as can be determined by inspection. Secondly, at higher  $B$ , it gives the same value as that predicted theoretically, i.e.  $\Delta_{ES}$ . The width of the gap,  $\Delta_S$ , determined in this



way and  $\Delta_H$  are shown versus  $B$  in Fig. 3. As stated above, the gap width  $\Delta_S$  varies only weakly with magnetic field and is about equal to  $\Delta_{ES}$  over the whole range. However, there is an important difference between our results and the observations in systems with low disorder. We observe a parabolic dependence of  $G$  on voltage, instead of the exponential increase of the current around zero bias, which was interpreted as one of the manifestations of the “hard” gap created by  $B$ .

To explain our results, we propose that the existence of the Efros–Shklovskii (ES) gap mainly influences electron tunnelling between strongly localised 2DES at low biases. At higher bias, the intralayer Coulomb correlation still suppresses the electron tunnelling in a magnetic field but does not influence the single particle density of states. A similar co-existence of two different phenomena affecting the suppression of electron tunnelling around zero bias was recently reported [10].

For  $\nu < 2$ , in both bias polarities, additional peaks in  $G$  vs  $B$ , marked by S in Fig. 1, arise outside the main central maxima. The voltage positions of the S-peaks and the main maxima are shown in Fig. 4 as a function of  $B$ . It is evident that the S-peaks move with  $B$  at the same rate as the main maxima, but separated from them by about 6 mV. Any features related to tunnelling to higher Landau levels are located at higher biases [11]. The behaviour of the S-peaks with  $B$  is consistent with them being replicas associated with tunnelling assisted by some kind of quasiparticle emission process. At the moment, we are unable to relate the position of the peaks to any known quasiparticles in the system.

In conclusion, we have investigated equilibrium tunneling between disordered two-dimensional electron systems at 0.3 K over a wide range of magnetic field applied normal to the electron layers. The Coulomb interaction between electrons in the layers leads to tunnelling gaps in the 2DES. We argue that, at low biases, the formation of the Efros–Shklovskii (ES) “soft” gap in the density of states is the strongest influence on electron tunnelling between the 2D electron systems. At higher bias, the intralayer Coulomb interaction, similar to found in tunnelling between 2DES with low disorder, still suppresses the electron tunnelling in a magnetic field.

### Acknowledgements

This work was supported by the INTAS, the RFBR, the FTNS program of the Russian government, CNRS-PICS (France), and the EPSRC (UK).

### References

- [1] J. P. Eisenstein *et al*, *Phys. Rev. Lett.* **69**, 3804 (1992).
- [2] N. Turner *et al*, *Phys. Rev. B* **54**, 10614 (1996).
- [3] Yu. V. Dubrovskii *et al*, *JETP Lett.* **69**, 255 (1999).
- [4] R. C. Ashoori *et al*, *Phys. Rev. Lett.* **79**, 2867 (1997).
- [5] E. V. Deviatov *et al*, *Phys. Rev. B* **61**, 2939 (2000).
- [6] Yu. N. Khanin *et al*, *Physica E* **6**, 602 (2000).
- [7] Yu. V. Dubrovskii *et al*, *Physica E* **8**, (2002) to be published.
- [8] A. L. Efros and B. I. Shklovskii, *J. Phys. C: Solid State Phys.* **8**, 49 (1975).
- [9] S. I. Khondaker *et al*, *Solid State Commun.* **109**, 751 (1999).
- [10] V. Yu. Butko *et al*, *Phys. Rev. Lett.* **84**, 1543 (2000).
- [11] D. Yu. Ivanov *et al*, *Physica B* **298**, 359 (2001).

## Magnetotunnelling spectroscopy of the electron states in the quantum well with embedded self-assembled quantum dots: studies in magnetic fields up to 28 T

Yu. V. Dubrovskii<sup>†</sup>, V. A. Volkov<sup>‡</sup>, D. K. Maude<sup>§</sup>, J.-C. Portal<sup>§+\*</sup>,  
M. V. Chukalina<sup>†</sup>, *D. Yu. Ivanov*<sup>†</sup>, E. E. Vdovin<sup>†</sup>, L. Eaves<sup>¶</sup>, P. C. Main<sup>¶</sup>,  
M. Henini<sup>¶</sup> and G. Hill<sup>||</sup>

<sup>†</sup> Institute of Microelectronics Technology RAS, 142432 Chernogolovka, Russia

<sup>‡</sup> Institute of Radioengineering and Electronics RAS, Moscow, Russia

<sup>§</sup> Grenoble High Magnetic Field Laboratory, MPI-CNRS,

BP166 38042 Grenoble Cedex 9, France

<sup>¶</sup> The School of Physics and Astronomy, University of Nottingham,  
Nottingham NG7 2RD, United Kingdom

<sup>||</sup> Department of Electronic Engineering, University of Sheffield,  
Sheffield S1 3JD, UK

<sup>+</sup> Institut Universitaire de France, 103, Boulevard Saint-Michel,  
75005 Paris, France

<sup>\*</sup> INSA, F31077 Toulouse Cedex 4, France

**Abstract.** We have studied magneto-oscillations of the tunnelling current through a quantum well (QW) incorporating InAs self-assembled quantum dots in magnetic fields up to 28 T applied normal to the QW plane. We find evidence for the strong modification of the Landau levels in the host GaAs quantum well in the presence of dots embedded at the center of the well, which we attribute to electron-electron interactions.

It was shown recently that the presence of InAs self-assembled quantum dots (QDs) strongly affects the electron transport properties [1], or dramatically modifies the cyclotron resonance [2] of a two-dimensional electron gas in a GaAs quantum well (QW). Moreover, in the presence of quantum dots, the electron system undergoes a metal-insulator transition in zero magnetic field [3]. Recently, we demonstrated that QDs also modify the Landau levels structure in a QW [4]. In this work, we present an extension of our previous studies to higher magnetic field, up to 28 T, where the magnetic length is approximately equal to the average radius of the quantum dots. The usual magneto-oscillations of the tunnel current, which arise due to the presence of Landau levels in the QW and/or the emitter, are strongly modified when the areal extent of the ground Landau level state in the well was approximately equal to an integer times the average area of the quantum dots.

The AlGaAs/GaAs/AlGaAs heterostructure was the same double barrier structure as used previously [5], incorporating a layer of InAs QD in the center of the well. The presence of the dots was confirmed by photoluminescence spectroscopy. In equilibrium, the dots are charged with electrons from the contact layers. With the application of a sufficient bias to the structure, an accumulation layer is formed adjacent to the barrier, which serves as two-dimensional emitter. In a magnetic field,  $B$ , applied normal to the barriers, electrons tunnel into empty Landau level states in the well. If all tunnelling electrons have the same energy, which happens if only the lowest Landau level is occupied in the two-dimensional

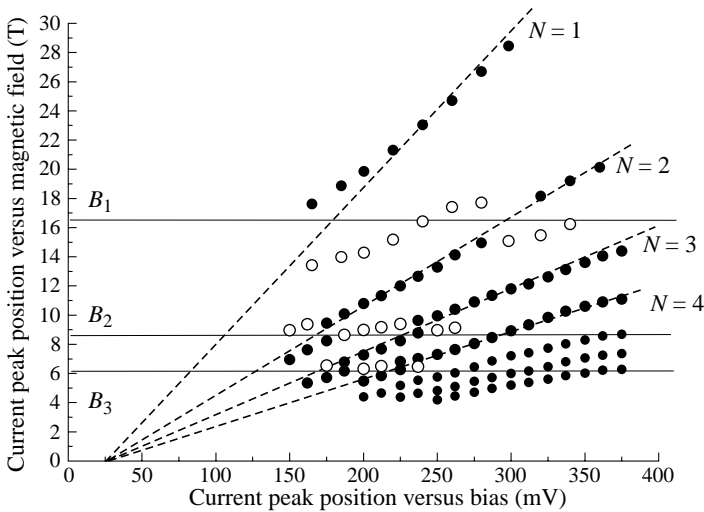


**Fig. 1.** Fan diagram of the Landau levels in the quantum well.  $N$  is the Landau level number. Other details are in the text.

emitter, the tunnelling spectra measured at different biases provide a direct mapping of the density of states in the quantum well. The energy scale may be determined from the bias voltage; the energy has an approximately linear dependence on bias.

The tunnelling current oscillates with varying magnetic field with constant bias applied to structure. We analyze only the data for fields above 5 T, when only the lowest energy Landau level is occupied in the emitter. Peaks are observed, corresponding to tunnelling into Landau states in the well. The oscillations are periodic in the inverse of the magnetic field and it is easy to determine the index of the corresponding Landau level for a given peak. The most interesting aspect of the data is that some of the features are transformed from well-defined peaks into shoulders and then back again into peaks with increasing bias voltage [4].

The figure shows a fan diagram of the observed peaks, that is the dependence of the peak position in voltage versus magnetic field. The solid circles indicate the positions of the well-defined peaks and the open circles indicate the positions of the shoulders. It is clear that in magnetic fields defined as  $B_1^*$ ,  $B_2^*$ , and  $B_3^*$ , the Landau levels are perturbed. At these particular magnetic fields, the area of the ground Landau level state in the well is approximately equal to  $S$ ,  $2S$  and  $3S$ , respectively, where  $S = 12 \text{ nm} \times 12 \text{ nm}$  is the average area of the quantum dots, determined from electron microscopy studies. An equivalent way of thinking about these conditions is that the fields correspond to  $\phi_0/n$ , where  $\phi_0$  is the flux quantum and  $n$  is an integer. Alternatively, we note that the open circles, corresponding to the shoulders, are themselves periodic in  $1/B$ . This observation may be seen most easily at  $V = 200 \text{ mV}$ , where the open circles lie precisely in between the solid circles. At this value of the voltage, the shoulders are  $\pi$  out of phase with the main set of oscillations.

At present, we do not have a quantitative model for the observed influence of the quantum dots on the Landau levels. The open circles in the Figure cannot describe any effects associated with Landau levels in the emitter. At these values of  $B$ , only the lowest Landau level is occupied in the emitter. More likely, the features are due to some sort of interaction effect. Certainly, the data in the vicinity of, say,  $B_1^*$  at around 180 mV are reminiscent of a level anti-crossing, as if there was mixing between the two Landau levels

at this value of magnetic field. For the  $B_2^*$  anti-crossing around 175 mV, one can also see the exchange of oscillator intensity, which is characteristic of this type of phenomenon. The origin of the interaction causing the anti-crossing, however, is still a mystery. It may possibly be due to some effect associated with localized charging of occupied dots leading to the formation of depleted anti-dots in the QW. However, this is very speculative and it is clear that more investigations on samples with different dot sizes are required.

In conclusion, we have used tunnelling spectroscopy to demonstrate that the presence of InAs self-arranged quantum dots modifies the structure of Landau levels in a GaAs quantum well. It is possible that a new type of commensurability effect has been identified.

#### *Acknowledgements*

This work was supported by the INTAS, the RFBR, the FTNS program of the Russian government, CNRS-PICS (France), the RS and the EPSRC (UK).

#### **References**

- [1] G. H. Kim *et al*, *Appl. Phys. Lett.* **73**, 2468 (1998).
- [2] S. Cinà *et al*, *Phys. Rev.* **B60**, 7780 (1999).
- [3] E. Ribeiro *et al*, *Phys. Rev. Lett.* **82**, 996 (1999).
- [4] Yu. V. Dubrovskii *et al*, *Proceedings of the 9th Int. Symp. "Nanostructures: Physics and Technology"*, St Petersburg, June 18–22, 2001, pp. 262–264.
- [5] Yu. V. Dubrovskii *et al*, *Nanotechnology* **12**, 491 (2001).

## Resonant broadening of two-dimensional states in semiconductors with inverted band structure

A. V. Germanenko, G. M. Minkov, V. A. Larionova and O. E. Rut  
Institute of Physics and Applied Mathematics, Ural State University  
Ekaterinburg 620083, Russia

**Abstract.** Results of tunneling studies of MOS-structures based on  $\text{Hg}_{1-x}\text{Cd}_x\text{Te}$  with an inverted band structure are reported. It has been found that the 2D states have revealed themselves at negative energies, when they are in resonance with the heavy hole valence band of bulk material. To interpret the experimental data the energy spectrum and broadening of the 2D states in a surface quantum well has been theoretically investigated in the framework of the Kane model, the finite value of the heavy hole effective mass has been taken into account.

### 1. Introduction

The broadening of 2D states which results from the resonance with the valence band states in the volume of semiconductor has been discussed for narrow gap semiconductors [1]. In these materials the 2D electron states at energies less than the energy of the top of the valence band are separated from the valence band by a barrier, which parameters are proportional to a forbidden gap. In this case the tunneling to heavy hole states is ineffective due to large value of their effective mass, and the broadening of 2D states is caused by tunneling to light hole state. A specific feature of a semiconductor with inverted energy band structure is the absence of an energy gap between conduction and valence bands. Therefore, the effect of resonance broadening due to tunneling to heavy hole states should be stronger in inverted semiconductors. This work is devoted to investigations of this effect.

### 2. Experimental results

Experimental method used here is the tunneling spectroscopy in a quantizing magnetic field. The second derivative of tunneling current with respect to voltage  $d^2j/dV^2$  as a function of bias and magnetic field in metal-insulator- $\text{Hg}_{1-x}\text{Cd}_x\text{Te}$  ( $0.095 < x < 0.105$ ) structures was investigated in magnetic fields up to 6 T at the temperature of 4.2 K. Tunnel junctions were fabricated on monocrystalline  $\text{p-Hg}_{1-x}\text{Cd}_x\text{Te}$  with the concentration of uncompensated acceptors  $N_A - N_D = (5-8) \times 10^{17} \text{ cm}^{-3}$  by a method described in [2]. Typical magnetic field dependences of  $d^2j/dV^2$  at different biases are presented in Fig. 1 for  $\mathbf{B} \parallel \mathbf{n}$ , where  $\mathbf{n}$  is the normal to the tunnel junction. The Fourier transformation (FT) was carried out to analyze the oscillation curves.

The FT-results as a bias dependence of quasimomentum, which is connected with fundamental field  $B_f$  of the Fourier spectra by the relationship  $k^2 = 2(eB_f/c\hbar)$ , is presented in Fig. 2. An inspection of Fig. 2 shows that two types of oscillations are observed:  $k^2$  increases for branches  $0^+$ ,  $0^-$ ,  $1^+$  and decreases for branches  $a$ ,  $b$  when the bias is increased. Typical angular dependences of  $B_f$  indicate that both types are connected with 2D states. The  $1^+$ ,  $0^-$  and  $0^+$  branches correspond to so called spectroscopic oscillations arising whenever the Landau levels of the 2D states coincide with the energy  $E_F + eV$ ,

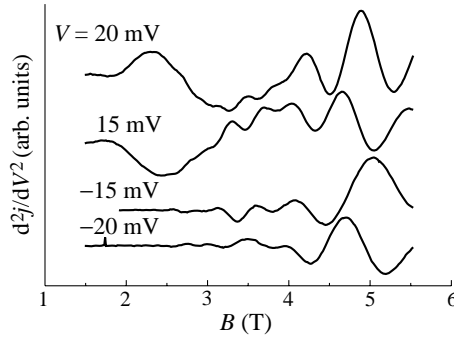


**Fig. 1.**  $d^2j/dV^2$  versus  $B$  curves at different biases.

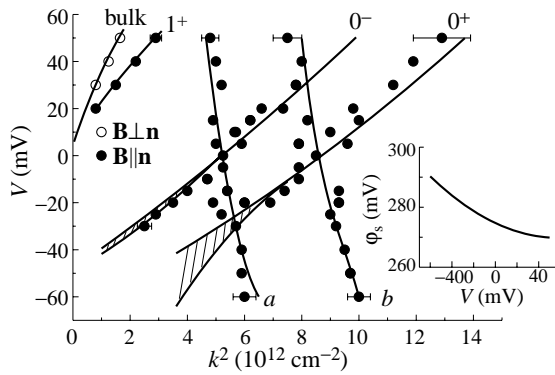


**Fig. 2.** The bias dependences of  $k^2$ . Symbols show the experimental data. The dotted curve is the dispersion law of the bulk electrons, calculated with parameters in the text. The solid curves are the theoretical bias dependences of  $k^2(E_F + eV)$  (curves  $1^+$ ,  $0^+$ ,  $0^-$ ) and  $k^2(E_F)$  (curves  $a$  and  $b$ ).

where  $E_F$  is the Fermi energy in semiconductor, and it varies in the range from  $-5$  to  $-10$  meV for different samples. The branches  $a$  and  $b$  relate to oscillations which arise whenever Landau levels of 2D states coincide with the energy  $E_F$ . So, the branches  $a$  and  $b$  give the concentration of 2D electrons, which decreases with increasing bias, as seen from the figure. It is significant that the spectroscopic oscillations are observed at negative biases down to  $V = -30$  mV. The negative biases correspond to the energies of 2D states when they are in resonance with the valence band states. This means that the resonance broadening of the 2D states is not so large to destroy the oscillation picture.

### 3. Theoretical model and discussion

To describe the energy spectrum of 2D states in a surface quantum well in an inverted semiconductor we use the Kane model. To analyze the resonance broadening of 2D states due to tunneling to heavy hole states we have to take into account the finite value of heavy hole effective mass by including in the Hamiltonian additional terms with parameters  $\gamma_1$  and  $\gamma$ , which describe the interaction with remote bands. It has been supposed in our theoretical model that the band structure of an insulator is similar to that of the semiconductor [1]. The only difference is the value of the energy gap, which is much greater for the insulator,

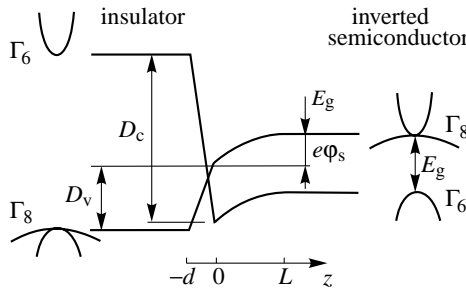


**Fig. 3.** Model of an insulator-inverted semiconductor structure.

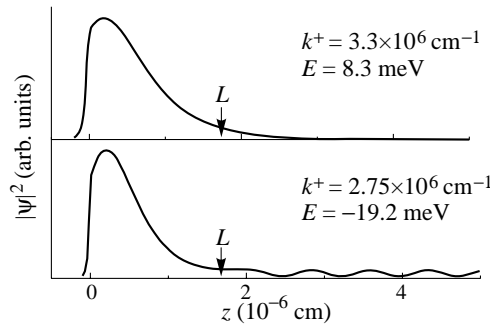


**Fig. 4.**  $|\Psi|^2$  versus  $z$  curves for nonresonant (a) and resonant (b) 2D states.

than that for the semiconductor (Fig. 3). Two additional parameters  $D_c$  and  $D_v$  (see Fig. 3) appear in this model, but the net result mainly depends on the ratio  $D_c/D_v$  [2]. The techniques of direct numerical integration has been used to solve the eigenvalue problem [3]. A behavior of the potential  $\varphi(z)$  in a space charge region of the semiconductor has been found self-consistently. Calculations have been carried out using the following parameter values  $E_g = -110$  meV,  $P = 8 \times 10^{-8}$  eV·cm,  $N_A - N_D = 8 \times 10^{17}$  cm $^{-3}$ ,  $\kappa = 20$ ,  $\gamma_1 = 2$ ,  $\gamma = 0$ ,  $D_c = 2$  eV and  $D_v = 1$  eV. Two types of solutions, which correspond to non-resonant ( $E > 0$ ) and resonant ( $E < 0$ ) 2D states, are presented in Fig. 4. It is clearly seen, that at  $E < 0$  the wave function does not decay in the volume of semiconductor. This means that the charge carrier has a non-zero probability to tunnel from the space charge region to the volume. The Levinson theorem [1, 2] has been used to find the 2D energy level position and its broadening.

Since the surface well changes with bias in our experiment, the branches  $0^+$ ,  $0^-$ ,  $1^+$ , corresponding to the spectroscopic oscillations, are not the dispersion law of 2D states directly. We have obtained the bias dependence of the surface potential (inset in Fig. 2) making the theory fit the concentration of 2D electrons at different biases, which is given by quasimomentum values at  $E = E_F$  (branches  $a$  and  $b$  in Fig. 2). Then, using this dependence we have calculated the quasimomentum values of 2D states at  $E = E_F + eV$  over the entire energy range (branches  $0^+$ ,  $0^-$ ,  $1^+$ ). A comparison between theoretical and experimental results shows that branches  $0^+$  and  $0^-$  are nothing but two branches of the ground 2D subband split by the spin-orbit interaction in the asymmetric quantum well, and

$1^+$  branch is lower spin branch of the first excited subband.

Hatched regions in Fig. 2 show the resonant broadening of the 2D energy levels calculated in the above model. It strongly depends on quasimomentum value. Being equal to zero at large quasimomentum values, when the 2D states lie above the top of the valence band ( $V > 5$  mV), the broadening increases with decreasing the quasimomentum. The increasing is stronger for  $0^+$  branch than that for  $0^-$  branch. The larger broadening of  $0^+$  states is a possible reason that we are able to detect a maximum in Fourier spectra, related to  $0^+$  branch, down to  $k^2 \simeq 6 \times 10^{12} \text{ cm}^{-2}$  only, while  $0^-$  maximum is detected down to  $k^2 \simeq 2.5 \times 10^{12} \text{ cm}^{-2}$ . For both branches maxima in Fourier spectra can be detected until the broadening exceeds 5 meV, i.e. until it is larger than the cyclotron energy at the magnetic fields, where oscillations have been observed ( $B > 1$  T). The broadening of 2D states seemingly increases when the quasimomentum tends to zero (Fig. 1). However, the calculations show that for small quasimomentum values the broadening decreases down to zero at  $k = 0$  for both branches. This agrees with analytic solution, which can be derived for  $k = 0$  [4]. It should be mentioned that the net results of calculation are not sensitive to the values of  $\gamma$ -parameters presented in literature.

#### 4. Conclusion

The investigations of 2D systems in inverted semiconductor have shown that in contrast to ordinary semiconductors the tunneling of 2D carriers to the heavy hole states of the valence band can be effective. The broadening of 2D energy levels caused by this process is different for 2D states corresponding to different spin branches of the energy spectrum, and strongly depends on quasimomentum values. The theoretical results are consistent with experimental data.

#### References

- [1] Pawel Sobkowicz, *Semicond. Sci. Technol.* **5**, 183 (1990).
- [2] G. M. Minkov, A. V. Germanenko, V. A. Larionova and O. E. Rut, *Phys. Rev. B*, to be published.
- [3] A. V. Germanenko, G. M. Minkov, V. A. Larionova, O. E. Rut, C. R. Becker and G. Landwehr, *Phys. Rev. B* **52**, 17254 (1995).
- [4] R. Stepniewski, *J. Phys. C: Solid State Phys.* **17**, L853 (1984).



## Resonant tunneling metal-oxide-silicon nanostructure

G. G. Kareva<sup>†</sup>, M. I. Vexler<sup>‡</sup>, I. V. Grekhov<sup>‡</sup> and A. F. Shulekin<sup>‡</sup>

<sup>†</sup> Institute of Physics, St Petersburg State University, 198504 St Petersburg, Russia

<sup>‡</sup> Ioffe Physico-Technical Institute, St Petersburg, Russia

**Abstract.** Some evidences for an ability of a metal-oxide-silicon (MOS) structure, widely used in the current integrated circuit electronics, to operate as a resonant tunneling diode are discussed. The energy band diagram of the MOS structure based on a highly doped p-Si ( $N_A$  in the range of  $10^{18}$ – $10^{20}$  cm<sup>-3</sup>) with an oxide thickness in the tunnel transparent range of 1–4 nm in reverse bias presents an asymmetrical double barrier with a quantum well of variable depth. Both the calculated and measured current–voltage characteristics of such nanostructures exhibit resonant tunneling features, such as steps and peaks, attesting electron resonant tunneling transport. The nanostructures have their origin in design, materials and technologies within the current integrated electronics so that they can be easily combined with its elements on one chip.

### Introduction

As development of the current integrated circuit electronics progresses, both the oxide thickness and the thickness of the silicon (Si) space charge region in MOS structures decrease significantly. Reduction in the latter dimensional parameter is attained by increasing the doping level of the Si which already approaches  $10^{18}$  cm<sup>-3</sup> in modern MOSFETs. The fundamental limitation in this development corresponds to such an increase of the p-Si dopant level that the barrier of its depletion region has become permeable for tunneling electrons. If the oxide is thin enough (1–4 nm), the oxide barrier is also tunnel transparent and the obtained MOS structures have acquired attributes of nanostructures [1, 2]. The proposed conversion takes place in a channel of developing the current electronics.

### 1. Energy band diagram

Figure 1 demonstrates the calculated energy band diagram of a studied MOS-structure in a reverse bias, the value of which ensures proper prerequisites for electron resonant tunneling. The main qualitative features of the MOS nanostructure resulting from quantitative dimensional alteration down to the nanometer scale which distinguish it from a conventional MOS structure [3, 4] and make it related to the conventional nanostructures [1, 2] are as follows:

— The energy band diagram looks like that of an asymmetrical double barrier nanostructure with a deep (more than 1.1 eV) variable quantum well. Really, the silicon space charge region may be treated and operate as a tunnel transparent barrier of the depletion layer which is the first part of the double barrier connected in series with the quantum well having a ladder of quantum subbands. The second part of the double barrier is the tunnel transparent oxide. Thus the quantum well turns out to be sandwiched between the two tunnel transparent barriers.

— The created double barrier confines the electron transport perpendicular to the surface and the electron gas in the well turns out to be 2D. Additional confinements followed by reduction of the electron gas dimension to zero may be achieved by potential fluctuations

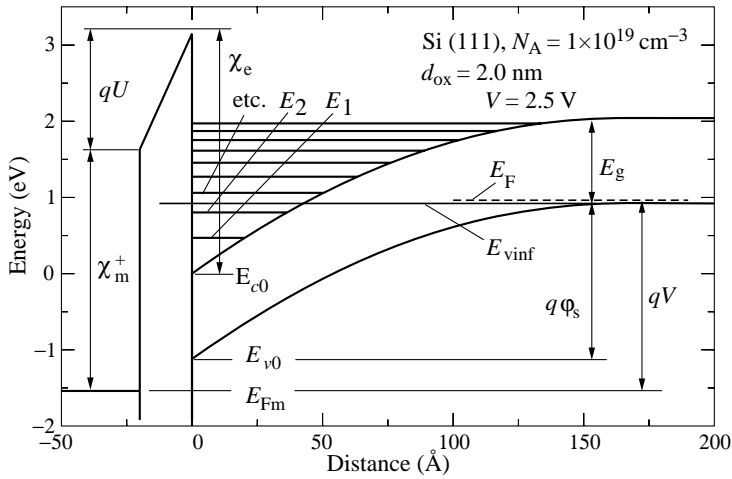


**Fig. 1.** The calculated energy band diagram of a metal-tunnel transparent oxide-p<sup>+</sup>-silicon nanos-structure in reverse bias illustrating its conversion into a double barrier resonant tunneling nanos-structure

over the surface. Sets of quantum dots arise on the Si surface, which are designed in such a manner that electrical characteristics of the nanostructures may be studied and used.

— Electron resonant tunneling through the quantized energy states in the depletion layer becomes possible in the MOS nanostructures. Therewith, the quantum well is deep and narrow enough to provide apparent energy separations between the subband bottoms ( $E_1, E_2$ , etc.), which enable the MOS nanostructure to operate at room temperature and to exhibit pronounced resonant-tunneling features in the current–voltage (I–V) characteristics. This is confirmed by the theoretical and experimental results obtained.

## 2. Calculated current–voltage characteristics

The total current in a MOS nanostructure consists of four components:

$$j = j_{v0} + j_{vdt} + j_{vrez} + j_{c0} \quad (1)$$

where  $j_{v0}$  and  $j_{c0}$  are the currents of electrons tunneling from the Si  $v$ -band and  $c$ -band through SiO<sub>2</sub> only,  $j_{vdt}$  is the current of electrons tunneling non-resonantly through the Si depletion layer and the oxide.  $j_{vrez}$  denotes the electron resonant tunneling current component through the double barrier which is the sum of the currents through the individual subbands. For each subband, it is the maximum tunneling probability  $T_{\max}$  multiplied by the maximum width  $\Delta E_i$ :

$$j_{vrez} = \frac{4\pi q}{h^3} \sum_{p,n} \left[ m_{p,\perp} \frac{v_n}{6} \sum_{i=1,2,\dots} T_{\max}^{p,n,i} \Delta E_i^{p,n} \right. \\ \left. \times \int_0^{1/2(E_{v\text{inf}} - E_i^n)} (f_p(E_i^n + E_\perp) - f_M(E_i^n + E_\perp)) \exp(-\lambda E_\perp) dE_\perp \right]. \quad (2)$$

Here,  $E_i^n$  is the bottom of  $i$ -th subband of  $n$ -th ladder ( $n = he$  or  $le$  — heavy and light electrons),  $v_n$  is subband degeneracy.  $E_\perp$  is the electron energy (not quantized) in the

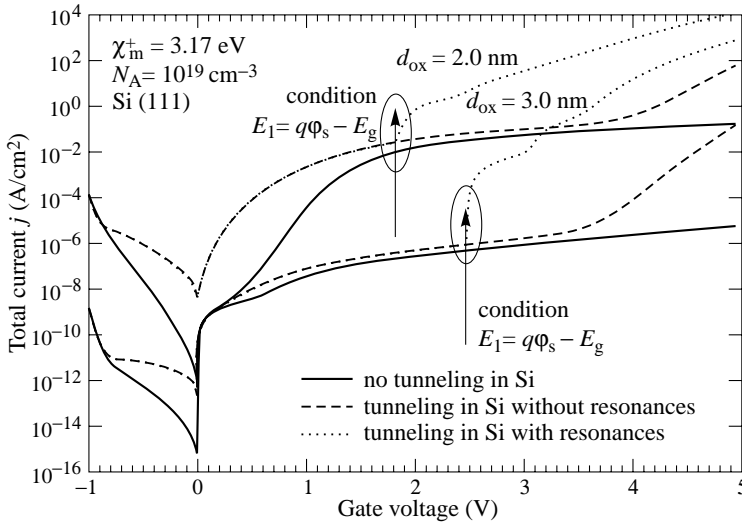


**Fig. 2.** The calculated current–voltage characteristics of the studied metal–tunnel–thin oxide–p<sup>+</sup>-Si structures with and without resonant tunneling features.

plane of Si/SiO<sub>2</sub> interface,  $f$  is for Fermi functions,  $\lambda$  is the factor of tunneling probability reduction due to the transverse energy part [3].  $m_p$  is the mass in the valence band of Si, it may be  $m_{hh}$  or  $m_{lh}$ , but the most contribution is given by lh-tunneling from the “light” band.

The calculated I–V characteristics are shown in Fig. 2.

### 3. Measured current–voltage characteristics

The measured I–V characteristic for the MOS nanostructure based on p<sup>+</sup>-Si oxidized thermally at 700 °C with Al contact is shown in Fig. 3. The two steps at  $V = 1.8$  V and  $V = 2.6$  V are due to the onset of a resonant tunneling transport. Figure 4 demonstrates more resonant tunneling features in the I–V curve along with its hysteresis for the MOS nanostructure based on p<sup>+</sup>-Si oxidized electrochemically at room temperature with InGa contact. The electrochemical oxide possesses positive charge and is less uniform than the thermal oxide. That promote to zero dimensionality of the operating electron gas.

The hysteresis starts when the reverse bias exceeds the voltage of “activation” of the

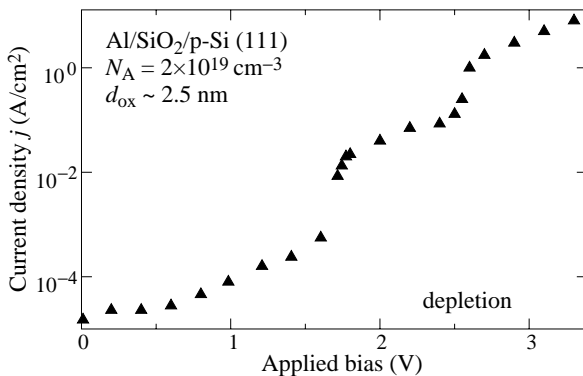


**Fig. 3.** An example of current–voltage characteristics of the Al/2.5 nm SiO<sub>2</sub>/p<sup>+</sup>-Si-nanostructure under reverse bias at room temperature exhibiting resonant tunneling features.

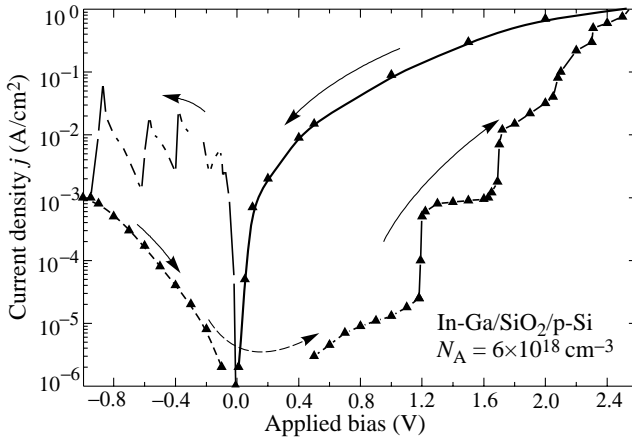


**Fig. 4.** Typical behaviour of the current-voltage characteristics of MOS-nanostructures based on p-Si (100) ( $N_A = 6 \times 10^{18} \text{ cm}^{-3}$ ), oxidized electrochemically, measured at room temperature for the sweep rate of about 10 V/min.

lowest subband  $E_1$ . With further enhancement of  $V$ , new steps appear due to higher subbands  $E_2$ ,  $E_3$  and the hysteresis loop is expanding. An interesting part of the hysteresis is the peaks in forward bias branch. The more steps were obtained in reverse bias by achieving the higher positive  $V$ , the larger number of peaks appears in forward bias. An increased positive bias causes an increased deviation from the initial smooth I-V curve (dashed curve in Fig. 4) whereas negative bias finally retrieves it. These cycles with different number of the steps and peaks can be repeated over and over again. Due to such multi-stability, the appearance of the measured characteristics may be varied by changing the bias variation program. These results bring about a rich picture of charging effects in the studied nanostructures that are beyond the scope of the present paper.

## Conclusion

Metal-oxide-silicon structures, widely used in the current integrated circuit electronics, can be converted into resonant tunneling nanostructures only due to decreasing their dimensional parameters such as: p-Si depletion layer width, oxide thickness and areas of nonuniformities, down to the nanometer scale. No additional layers or other artificial incorporations have been used. The energy band diagram of such MOS nanostructures presents an asymmetric double barrier with a deep (more than 1.1 eV) variable quantum well. The calculated and measured I-V characteristics exhibit resonant tunneling features such as steps and peaks arising from the electron resonant tunneling transport through dimensionally quantized states in the Si depletion layer. With such investigations, a bridge between the two important branches of the current electronics: nanoelectronics and integrated circuit electronics may be built up.

## Acknowledgment

This work is supported by the program "Nanostructures".

## References

- [1] F. Capasso, K. Mohammed and A. Y. Cho, *IEEE J. Quantum Electron.* **QE-22**, 1853 (1986).
- [2] F. Capasso, S. Sen and F. Beltram, *High-Speed Semiconductor Devices*, (Wiley, New York) 1990.
- [3] S. M. Sze, *Physics of Semiconductor Devices*, (Wiley, New York) 1981.
- [4] J. Požela, *Physics of High-Speed Transistors*, (Mocslas, Vilnius) 1989.

## GaAs-based tunnel junctions

C. Möller, J. Böttcher and H. Künzel

Heinrich-Hertz-Institut für Nachrichtentechnik Berlin GmbH,  
Einsteinufer 37, D-10587 Berlin, Germany

**Abstract.** The development of high quality GaAs-based tunnel junctions grown by molecular beam epitaxy was systematically studied. Fabricated Si/Be-doped GaAs tunnel junctions show record low junction resistance of less than  $7 \times 10^{-5} \Omega/\text{cm}^2$  and a peak current density of  $> 1900 \text{ A}/\text{cm}^2$ . The enhancement of lateral current spreading is demonstrated by large-area vertical-emitting LEDs.

### 1. Introduction

High-quality tunnel junctions (TJ) open new possibilities for the design of micro-cavity (MC) light sources, since they serve as an electron-hole converter. For vertically contacted devices with a semiconductor top mirror (DBR), this DBR can be doped n-type rather than p-type which eliminates optical losses as well as electrical resistance problems associated with the p-doping.

For intra-cavity contacted MC-structures with oxidised current apertures, a TJ (positioned at a node of the optical longitudinal field to minimise absorption) may be used as a high electron mobility layer to spread the carriers across the nearby aperture, ensuring improved lateral uniform current flow through the oxide-defined cavity.

The basic requirements for a TJ in a MC- light source are low resistivity, good thermal conductivity, operation temperature stability and long-term reliability. In order to accomplish low resistivity, the TJ must be very highly doped with an extreme abrupt doping profile. To handle large currents a very narrow depletion region with a large electric field across the junction is needed giving a high tunneling probability.

### 2. Experimental

All structures were grown on (100) GaAs substrates using conventional MBE (ISA/Riber 32P). To develop TJs, the maximum possible homogeneous doping has to be determined. Therefore test samples were grown using Si as donor and Be as acceptor at growth temperatures varying between  $300^\circ\text{C}$  to  $600^\circ\text{C}$ . Figure 1 shows the dependence of the effective net carrier concentration ( $N_D - N_A$ ) measured with Hall on the Silicon cell temperature ( $T_{\text{Si}}$ ) at different growth temperatures. The highest attainable net carrier concentration using homogeneous doping is  $1.8 \times 10^{19} \text{ cm}^{-3}$  for silicon. When the Si flux is further increased, the dopant starts to be incorporated on acceptor sites which results in self-compensation because of the amphoteric behaviour of Si (Fig. 1, deviation of the solid line). By choosing a low growth temperature ( $T_g \leq 400^\circ\text{C}$ ) to influence site occupancy the problem of self compensation can be reduced. Using this technique also for Be the maximum effective doping is  $2 \times 10^{20} \text{ cm}^{-3}$ . When the dopant flux is further increased the surface becomes rough. The electron and hole mobilities in these highly doped layers are still moderate (Fig. 2). An electron mobility of about  $\mu_n = 550 \text{ cm}^2/\text{Vs}$  assures high lateral current transport and low spreading resistance.

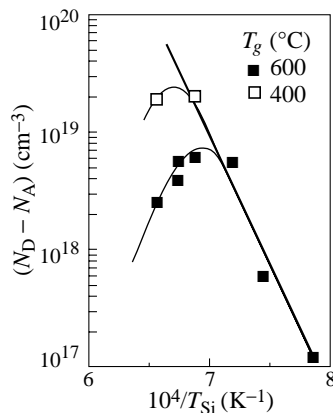


**Fig. 1.** Dependence of the effective carrier concentration ( $N_D - N_A$ ) on the Silicon cell temperature ( $T_{Si}$ ) measured with Hall (Van der Pauw—method). The growth temperature was set to  $T_g = 400$  °C ( $\nu$ ) or  $T_g = 600$  °C ( $\theta$ ).

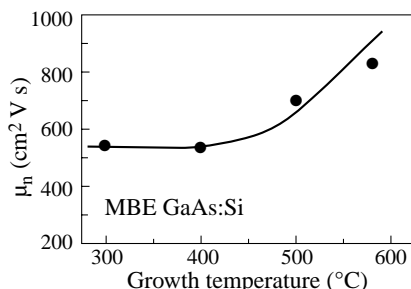
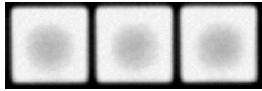


**Fig. 2.** Dependence of the electron mobility on the growth temperature at maximum Si-doping, measured with Hall (Van der Pauw—method).

Using optimised doping conditions we deposited tunnel diodes at 400 °C with very abrupt junctions. The layer sequence consisted of a 400 nm low doped GaAs:Si buffer layer followed by the tunnel region consisting of 100 nm  $n^{++}$ -GaAs:Si and 100 nm  $p^{++}$ -GaAs:Be (both layers homogeneous doped). On top we evaporated standard non-alloyed Ti/Pt/Au contacts, which we used as an etch mask to form  $30 \times 30$  m<sup>2</sup> mesas. The back-side contact was fabricated by evaporating and alloying (400 °C, 20 s) AuGe/Ni/Au contacts. The experimental I-V curves for the GaAs tunnel junction show record values: a zero-bias specific resistance of less than  $7 \times 10^{-5}$  Ω/cm<sup>2</sup> and a peak current density of  $> 1900$  A/cm<sup>2</sup>. By heat treatment of the sample at 420 °C for 3 hours we simulated additional deposition of further layers. As expected the tunnel junction moderately degrades, which may be attributed to the diffusion of dopants (the junction is no longer abrupt), but the electrical properties are still acceptable with a zero-bias specific resistance of less than  $1 \times 10^{-4}$  Ω/cm<sup>2</sup> e.g. when operating a  $30 \times 30$  m<sup>2</sup> device with a constant current density of 2000 A/cm<sup>2</sup>, the additional voltage drop by the TJ induced would increase from 0.15 V to 0.18 V.

The tunneling probability and thereby the tunnel current will increase when using materials with smaller band gaps and effective masses, as both will minimize the width and height of the tunneling energy barrier. Since  $\text{In}_x\text{Ga}_{1-x}\text{As}$  has a smaller band gap energy and lower effective masses than GaAs, a higher tunneling probability will lead to smaller specific resistances. As long as using low indium concentrations ( $x < 0.2$ ), the light absorption for 1.3 μm emitters is not critical. We tested this by replacing the n-side of the junction by 20 nm highly Si-doped  $\text{In}_{0.2}\text{Ga}_{0.8}\text{As}$ , staying close below the limit of the critical layer thickness. With a  $p^{++}/n^{++}$  GaAs/InGaAs junction we were able to reduce the resistance by a factor of 2. To demonstrate long-term stability we used aging tests under real operating conditions. The  $p^{++}/n^{++}$  GaAs/GaAs and  $p^{++}/n^{++}$  GaAs/InGaAs tunnel

junctions were forward and reverse biased with a constant current density of  $5000 \text{ A/cm}^2$  and  $85^\circ\text{C}$  operating temperature for more than 1000 hours. In case of forward bias (relevant for multi-solar cells) we see a slightly increasing resistance of approx. 0.5%, but for reverse bias (relevant for applications in LEDs, VCSEL, ...) no detectable degradation was observed.



(a) without tunnel junction



(b) with  $p^{++}/n^{++}$  GaAs/GaAs-tunnel junction



(c) with  $p^{++}/n^{++}$  GaAs/InGaAs-tunnel junction

**Fig. 3.** Intensity distribution across the  $40 \times 40 \mu\text{m}^2$  sized windows of vertical-emitting LEDs ( $\lambda = 970 \text{ nm}$ ).

The improvement in lateral current spreading was tested by growing large area vertical-emitting LEDs. The front-side emitting LED test structures (grown on n-doped (100) GaAs) consisted of a single QW active region ( $\lambda = 970 \text{ nm}$ ) and a  $p^{++}/n^{++}$  GaAs/GaAs,  $p^{++}/n^{++}$  GaAs/InGaAs or no tunnel junction. To minimize free carrier absorption in the highly doped TJ-region, the junction thickness had to be reduced to 10 nm for the p-region and 20 nm for the n-region. The LEDs, each having a size of  $350 \times 350 \mu\text{m}^2$ , were processed with a full area backside n-contact and a grid-type top p-contact. Figure 3(a) shows the inhomogeneous current and therefore light distribution across the light emitting windows of a LED without any TJ. This appears for windows larger than  $30 \times 30 \mu\text{m}^2$  and this effect is additionally amplified by increasing the current. Incorporating a TJ solves this problem (Fig. 3(b) and 3(c)), by preventing current crowding the p-contacts.

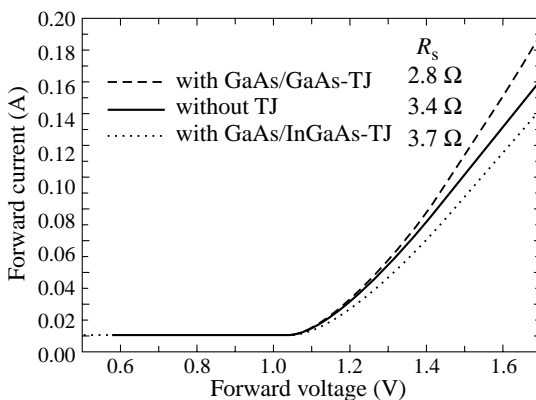


**Fig. 4.** I-U graphs of the  $350 \times 350 \mu\text{m}^2$  large vertical-emitting LEDs.

Due to this effect the series resistance for a GaAs TJ-LED is markedly lower as compared to a LED without TJ (Fig. 4). In the case of InGaAs TJ-LED the series resistance is slightly higher; presumably due to the fact that we already reached the critical layer thickness of  $\text{In}_{0.20}\text{Ga}_{0.80}\text{As}$  which leads to degraded electrical properties of this layer.

## Noise of a quantum-dot system in the cotunneling regime

*E. V. Sukhorukov*<sup>†</sup>, *G. Burkard*<sup>‡</sup> and *D. Loss*<sup>‡</sup>

<sup>†</sup> Department of Theoretical Physics, University of Geneva, Switzerland

<sup>‡</sup> Department of Physics and Astronomy, University of Basel, Switzerland

**Abstract.** We study the noise of the cotunneling current through one or several tunnel-coupled quantum dots in the Coulomb blockade regime. The various regimes of weak and strong, elastic and inelastic cotunneling are analyzed for quantum-dot systems (QDS) with few-level, nearly-degenerate, and continuous electronic spectra. We find that in contrast to sequential tunneling where the noise is either Poissonian (due to uncorrelated tunneling events) or sub-Poissonian (suppressed by charge conservation on the QDS), the noise in inelastic cotunneling can be super-Poissonian due to switching between QDS states carrying currents of different strengths.

### 1. Introduction

In recent years, there has been great interest in transport properties of strongly interacting mesoscopic systems [1]. As a rule, the electron interaction effects become stronger with the reduction of the system size, since the interacting electrons have a smaller chance to avoid each other. Thus it is not surprising that an ultrasmall quantum dot connected to leads in the transport regime, being under additional control by metallic gates, provides a unique possibility to study strong correlation effects both in the leads and in the dot itself [2]. This has led to a large number of publications on quantum dots, which investigate situations where the current acts as a probe of correlation effects. Historically, the nonequilibrium current fluctuations (shot noise) were initially considered as a serious problem for device applications of quantum dots [3, 4, 5] rather than as a fundamental physical phenomenon. Later it became clear that shot noise is an interesting phenomenon in itself [6], because it contains additional information about correlations, which is not contained, e.g., in the linear response conductance and can be used as a further approach to study transport in quantum dots, both theoretically [4, 5, 6, 7] and experimentally [8].

Similarly, the majority of papers on the noise of quantum dots consider the sequential (single-electron) tunneling regime, where a classical description (the so-called “orthodox” theory) is applicable [9]. We are not aware of any discussion in the literature of the shot noise induced by a cotunneling (two-electron, or second-order) current [10, 11], except Ref. [7], where the particular case of weak cotunneling (see below) through a double-dot (DD) system is considered. Again, this might be because until very recently cotunneling has been regarded as a minor contribution to the sequential tunneling current, which spoils the precision of single-electron devices due to leakage [12]. However, it is now well understood that cotunneling is interesting in itself, since it is responsible for strongly correlated effects such as the Kondo effect in quantum dots [13, 14], or can be used as a probe of two-electron entanglement and nonlocality [7], etc.

In this paper we present an analysis of the shot noise in the cotunneling regime. We consider the transport through a quantum-dot system (QDS) in the Coulomb blockade (CB) regime, in which the quantization of charge on the QDS leads to a suppression of the sequential tunneling current except under certain resonant conditions. We consider the



transport away from these resonances and study the next-order contribution to the current, the so-called cotunneling current [10, 11]. In general, the QDS can contain several dots, which can be coupled by tunnel junctions, the double dot (DD) being a particular example [7]. The QDS is assumed to be weakly coupled to external metallic leads which are kept at equilibrium with their associated reservoirs at the chemical potentials  $\mu_l$ ,  $l = 1, 2$ , where the currents  $I_l$  can be measured and the average current  $I$  through the QDS. The details of our calculations can be found in Ref. [15].

## 2. Shot noise of cotunneling

Before proceeding with our analysis we introduce right from the beginning all relevant physical parameters, namely the bath temperature  $T$ , bias  $\Delta\mu = \mu_1 - \mu_2$ , charging energy  $E_C$ , average level spacing  $\delta E$ , and the level width  $\Gamma = \Gamma_1 + \Gamma_2$  of the QDS, where the tunneling rates  $\Gamma_l = \pi\nu|T_l|^2$  to the leads  $l = 1, 2$  are expressed in terms of tunneling amplitudes  $T_l$  and the density of states  $\nu$  evaluated at the Fermi energy of the leads. In Fig. (1) the most important parameters are shown schematically. This variety of parameters shows that many different regimes of the CB are possible. In the linear response regime,  $\Delta\mu \ll k_B T$ , the thermal noise [16] is given by the equilibrium fluctuation-dissipation theorem (FDT) [17]. Although the cross-over from the thermal to nonequilibrium noise is of our interest, in this section we discuss the shot noise alone and set  $T = 0$ . Then the noise at zero frequency  $\omega = 0$ , when  $\delta I_2 = -\delta I_1$ , can be characterized by one single parameter, the dimensionless Fano factor  $F = S(0)/e|I|$ . The Fano factor acquires the value  $F = 1$  for uncorrelated Poissonian noise.

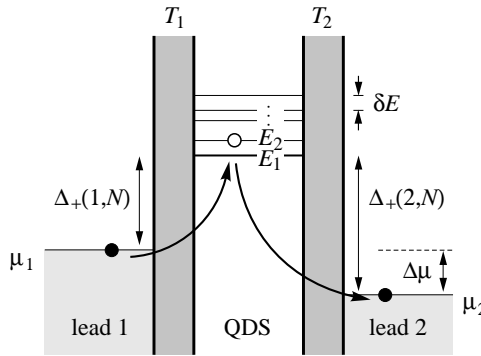


**Fig. 1.** Schematic representation of the quantum dot system (QDS) coupled to two external leads 1 and 2 (light grey) via tunneling barriers (dark grey), where the energy scale is drawn vertically. The tunneling between the QDS and the leads  $l = 1, 2$  is parametrized by the tunneling amplitudes  $T_l$ . The leads are at the chemical potentials  $\mu_{1,2}$ , with an applied bias  $\Delta\mu = \mu_1 - \mu_2$ . The (many-particle) eigenstates of the QDS with one added electron ( $N + 1$  electrons in total) are indicated by their energies  $E_1, E_2$ , etc., with average level-spacing  $\delta E$ . The energy cost for adding a particle from the Fermi level of lead  $l$  to the  $N$ -electron QDS is denoted by  $\Delta_+ > 0$  and is strictly positive in the CB regime. Note that the energies  $\Delta_-$  for removing particles from the QDS containing  $N$  electrons are positive as well, and are not drawn here.

We would like to emphasize that while the zero-frequency shot noise in the sequential tunneling regime is always suppressed below its full Poissonian value as a result of charge conservation (interactions suppressing it further), we find that, rather surprisingly,

the shot noise in the cotunneling regime is either Poissonian  $F = 1$  (elastic or weak inelastic cotunneling) or super-Poissonian  $F > 1$  (strong inelastic cotunneling). Therefore the super-Poissonian noise in QDS can be considered as being a fingerprint of inelastic cotunneling. This difference of course stems from the different physical origin of the noise in the cotunneling regime, which we discuss next. Away from the sequential tunneling peaks,  $\Delta_{\pm} > 0$ , single-electron tunneling is blocked, and the only elementary tunneling process which is compatible with energy conservation is the simultaneous tunneling of two electrons called cotunneling [10,11]. In this process one electron tunnels, say, from lead 1 into the QDS, and the other electron tunnels from the QDS into lead 2 with a time delay on the order of  $\Delta_{\pm}^{-1}$  (see Ref. [7]). This means that in the range of frequencies,  $\omega \ll \Delta_{\pm}$ , the charge on the QDS does not fluctuate, and thus in contrast to the sequential tunneling the correlation imposed by charge conservation is not relevant for cotunneling. Furthermore, in the case of elastic cotunneling,  $\delta\mu < \delta E$ , where the state of the QDS remains unchanged, the QDS can be effectively regarded as a single barrier. Therefore, subsequent elastic cotunneling events are uncorrelated, and the noise is Poissonian with  $F = 1$ . On the other hand, this is not so for inelastic cotunneling,  $\delta\mu > \delta E$ , where the internal state of the QDS is changed, thereby changing the conditions for the subsequent cotunneling event. Thus, in this case the QDS switches between different current states, and this creates a correction to noise  $\Delta S$ , so that the total noise is non-Poissonian, and can become super-Poissonian. The other mechanism underlying super-Poissonian noise is the excitation of high energy levels (heating) of the QDS caused by multiple inelastic cotunneling transitions and leading to the additional noise  $\Delta S_h$ . Thus the total noise can be written as  $S = eI + \Delta S_h + \Delta S$ .

According to this picture we consider the following different regimes of the inelastic cotunneling. We first discuss the weak cotunneling regime  $w \ll w_{in}$ , where  $w \sim \Gamma_1 \Gamma_2 \Delta\mu / \Delta_{\pm}^2$  is the average rate of the inelastic cotunneling transitions on the QDS, and  $w_{in}$  is the intrinsic relaxation rate of the QDS to its equilibrium state due to the coupling to the environment. In this regime the cotunneling happens so rarely that the QDS always relaxes to its equilibrium state before the next electron passes through it. Thus we expect no correlations between cotunneling events in this regime, and the zero-frequency noise is going to take on its Poissonian value with Fano factor  $F = 1$ , as first obtained for a special case in Ref. [7].

Next, we consider strong cotunneling, i.e.  $w \gg w_{in}$ . In the case of a few-level QDS,  $\delta E \sim E_C$  [18], noise turns out to be non-Poissonian, as we have discussed above, and this effect can be estimated as follows. The QDS is switching between states with the different currents  $I \sim ew$ , and we find  $\delta I \sim ew$ . The QDS stays in each state for the time  $\tau \sim w^{-1}$ . Therefore, for the positive correction to the noise power we get  $\Delta S \sim \delta I^2 \tau \sim e^2 w$ , and the estimate for the correction to the Fano factor follows as  $\Delta S / eI \sim 1$ . A similar result is expected for the noise induced by heating,  $\Delta S_h$ , which can roughly be estimated by assuming an equilibrium distribution on the QDS with the temperature  $k_B T \sim \Delta\mu$  and considering the additional noise as being thermal [16],  $\Delta S_h \sim \Gamma k_B T \sim (eI / \Delta\mu) k_B T \sim eI$ . The characteristic frequency of the noise correction  $\Delta S$  is  $\omega \sim w$ , with  $\Delta S$  vanishing for  $\omega \gg w$  (but still in the classical range,  $\omega \ll \Delta\mu$ ). In contrast to this, the additional noise due to heating,  $\Delta S_h$ , does not depend on the frequency.

Finally, we discuss the case of a multi-level QDS,  $\delta E \ll E_C$ . In this case the correlations in the cotunneling current described above do not play an essential role. In the regime of low bias,  $\Delta\mu \ll (\delta E \cdot E_C)^{1/2}$ , elastic cotunneling dominates transport [10], and thus the noise is Poissonian. In the opposite case of large bias,  $\Delta_{\pm} \gg \Delta\mu \gg (\delta E \cdot E_C)^{1/2}$ , the transport is governed by inelastic cotunneling. We find three universal regimes where  $I \sim \Delta\mu^3$ ,

and the Fano factor does not depend on the bias  $\Delta\mu$ . The first is the regime of weak cotunneling,  $\tau_{in} \ll \tau_c$ , where  $\tau_{in}$  and  $\tau_c$  are time scales characterizing the single-particle dynamics of the QDS. The energy relaxation time  $\tau_{in}$  describes the strength of the coupling to the environment while  $\tau_c \sim e v_D \Delta\mu / I$  is the cotunneling transition time. We find that  $F = 1$ . The other two regimes of strong cotunneling  $\tau_{in} \gg \tau_c$  are determined by the electron-electron scattering time  $\tau_{ee}$ . For the cold-electron regime,  $\tau_c \ll \tau_{ee}$ , we find the distribution function by solving the integral equation, while for hot electrons,  $\tau_c \gg \tau_{ee}$ , the distribution  $f(\varepsilon)$  is given by the Fermi distribution function with an electron temperature obtained from the energy balance equation. We use  $f(\varepsilon)$  to calculate the Fano factor, which turns out to be very close to 1. On the other hand, the current depends not only on  $G_1 G_2$  but also on the ratio,  $G_1 / G_2$ , depending on the cotunneling regime.

## References

- [1] L. P. Kouwenhoven, G. Schön and L. L. Sohn, *Mesoscopic Electron Transport*, NATO ASI Series E: Applied Sciences Vol. 345, (Kluwer Academic Publishers, 1997).
- [2] See, e.g., *Electron transport in quantum dots*, L. P. Kouwenhoven *et al*, in Ref. [1].
- [3] For a review, see: M. H. Devoret and R. J. Schoelkopf, *Nature* **406**, 1039 (2000).
- [4] A. N. Korotkov, D. V. Averin, K. K. Likharev and S. A. Vasenko, *Single-Electron Tunneling and Mesoscopic Devices*, ed. by H. Koch and H. Lübbig, Springer Series in Electronics and Photonics, Vol. 31, p. 45 (Springer-Verlag, Berlin), 1992.
- [5] A. N. Korotkov, *Phys. Rev. B* **49**, 10381 (1994).
- [6] For a recent review on shot noise, see: Ya. M. Blanter and M. Büttiker, *Phys. Rep.* **336**, 1 (2000).
- [7] D. Loss and E. V. Sukhorukov, *Phys. Rev. Lett.* **84**, 1035 (2000).
- [8] H. Birk, M. J. M. de Jong and C. Schönenberger, *Phys. Rev. Lett.* **75**, 1610 (1995).
- [9] For an early review, see D. V. Averin and K. K. Likharev, *Mesoscopic Phenomena in Solids*, ed. by B. L. Al'tshuler, P. L. Lee and R. A. Webb (North-Holland, Amsterdam), 1991.
- [10] D. V. Averin and Yu. V. Nazarov, *Single Charge Tunneling*, eds. H. Grabert and M. H. Devoret, NATO ASI Series B: Physics, Vol. 294, (Plenum Press, New York) 1992.
- [11] For experiments on single dots in the cotunneling regime see, D. C. Glatelli *et al*, *Z. Phys. B* **85**, 375 (1991).
- [12] D. Estève, *Single Charge Tunneling*, eds. H. Grabert and M. H. Devoret, NATO ASI Series B: Physics, Vol. 294, (Plenum Press, New York) 1992;  
D. V. Averin and K. K. Likharev, *ibid*.
- [13] L. I. Glazman and M. E. Raikh, *Pis'ma Zh. Eksp. Teor. Fiz.* **47**, 378 (1988) [*JETP Lett.* **47**, 452 (1988)].
- [14] T. K. Ng and P. A. Lee, *Phys. Rev. Lett.* **61**, 1768 (1988).
- [15] E. V. Sukhorukov, G. Burkard and D. Loss, *Phys. Rev. B* **63**, 125315 (2001).
- [16] J. B. Johnson, *Phys. Rev.* **29**, 367 (1927); H. Nyquist, *ibid.* **32**, 110 (1928).
- [17] H. B. Gallen and T. A. Welton, *Phys. Rev.* **83**, 34 (1951).
- [18] This condition does not necessarily mean that the QDS is small. For example, it can be easily satisfied in carbon nanotubes which are 30 nm long and contain 102 electrons; see e.g., L. C. Venema *et al*, *Science* **283**, 52 (1999).

## Tunneling of photogenerated holes through Landau levels in GaAs/AlGaAs double barrier diodes

A. Vercik<sup>†</sup>, M. J. S. P. Brasil<sup>‡</sup>, Y. G. Gobato<sup>†§</sup> and G. E. Marques<sup>†</sup>

<sup>†</sup> Grupo de Semicondutores, Universidade Federal de Sao Carlos  
CP 676, Sao Carlos - SP, 13560-970, Brazil

<sup>‡</sup> Grupo de Propriedades Opticas, Instituto de Fisica Gleb Wataghin  
Universidade de Campinas, CP 6165, Campinas-SP, 13083-970, Brazil

<sup>§</sup> Also at Universidade Federal de Santa Catarina

**Abstract.** The experimental observation of Landau levels due to the quantization of the transverse moment of holes in resonant tunneling diodes is reported in this work. At very low bias, the photocurrent versus voltage curves, measured under a magnetic field perpendicular to the barrier planes, exhibited several peaks associated to this phenomenon. The analysis of the peak position as a function of the magnetic field reveals several interesting features as non-parabolicity of the valence band, diamagnetic behavior and repulsion between levels with the same Landau-level index.

### Introduction

The two-dimensional (2D) hole systems has attracted great interest due to the rich variety of phenomena found in such systems. In contrast to the 2D electron systems, which have been extensively studied both theoretically and experimentally, much less information on 2D hole systems is known. Furthermore, the complexity of the valence band structure which strongly influence the properties of 2D hole systems makes the access to information obtained from experiments difficult. Most of the theoretical studies of 2D systems are based on the use of the Luttinger Hamiltonian [1, 2]. Although dealing with different structures, some theoretical results reveal several features characteristic of the 2D hole systems, like the non-parabolicity of the subbands and the repulsion between subbands with the same Landau-level index [3]. Experimentally, the formation of valence-band levels was recently reported by using optical techniques in two-terminal structures such as modulated-doped quantum wells [4, 5], quantum wells with superlattice buffers [6], and structures with more than two terminals [7].

In this work, we report the direct experimental observation of the formation of Landau levels, due to the quantization of the transverse moment of holes, in resonant tunneling diodes.

### 1. Experimental setup

The structures used in this work are symmetric GaAs/Al<sub>0.35</sub>Ga<sub>0.65</sub>As double barrier diodes. The barriers are 10 nm thick and the well width is 5 nm. The double barrier system is enclosed by a 60 nm undoped GaAs and a 300 nm Si-doped n<sup>+</sup>-GaAs (10<sup>18</sup> cm<sup>-3</sup>) layers grown on both sides of the structure. Annular contacts on the top of 500×600 μm mesas allow photocurrent measurements under applied voltage. The 488 nm line of a Coherent Ar<sup>+</sup> ion laser was used as the carrier photoexcitation source. Current voltage (I–V) curves were measured at 2 K and under magnetic fields up to 15 T provided by an Oxford superconducting magnet. The optical power was kept below 2mW to avoid an

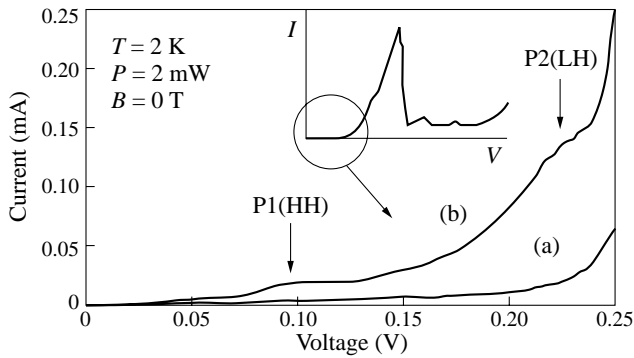


**Fig. 1.** (a) Dark current-voltage curve; (b) illuminated current-voltage curve, exhibiting two peaks corresponding to resonant tunneling through heavy and light hole levels. The inset shows the I–V region of interest.

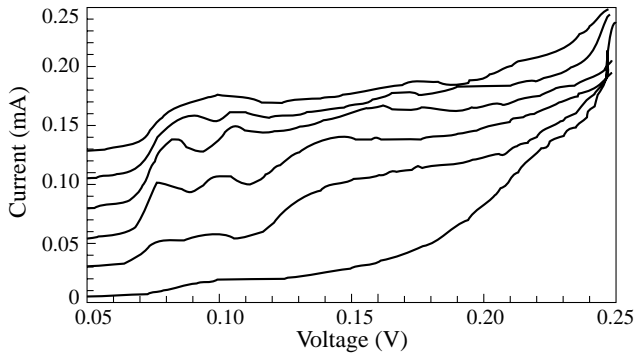
earlier (at lower voltage) increase of the electron tunneling current which would screen the hole current.

## 2. Results and discussion

The dark current in the used n-i-n sample is dominated by electrons and symmetrical under positive and negative bias. When the top contact is positively biased, electrons are injected from the substrate (the electron emitter), tunneling to the top contact (the electron collector). At voltages lower than 0.25 V, which is the tunneling onset, the current is negligible, and no effect of the magnetic field on the curve shape is observed. The measured dark current is shown in curve (a) of Fig. 1. However, when the sample is illuminated, an appreciable increase of the current is observed in this voltage region [Fig. 1, curve (b)]. These new current peaks are associated to holes that were photocreated in the top contact, drifted and diffused towards the barrier surface, where they accumulated, and then tunneled to the substrate [8]. This fact is also corroborated by a shift of the main resonance peak toward lower voltages, produced by the higher population of holes which increases the voltage drop across the intrinsic part of the sample. In this case, the I–V curve at zero magnetic field presents two peaks at 0.1 V and 0.22 V labeled P1 and P2 respectively, which correspond to resonances of heavy and light hole levels, as reported previously in the literature [8].

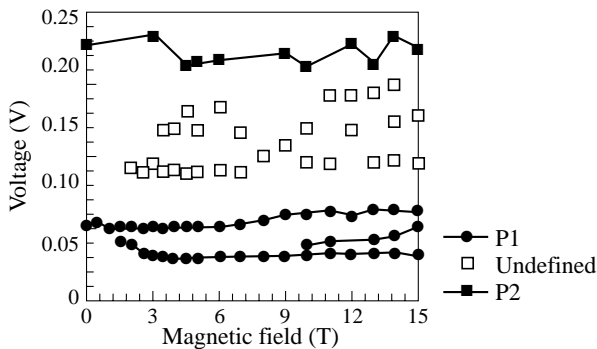
When the measurements are performed under magnetic fields, new features become observable. Figure 2 shows the photocurrent response for magnetic fields between 0 T and 15 T, in a bias range between 0.05 and 0.25 V. The curves for the different values of magnetic field are vertically shifted for a better visualization. These curves show a splitting of the lower hole level as the magnetic field is increased and the appearance of new peaks between those observed at zero magnetic field. This structure can be attributed to the quantization of the transverse moment of holes into Landau levels in the quantum well. Thus the peaks correspond to holes that tunnel resonantly with each subband splitted by the magnetic field.

Figure 3 shows the peak positions as a function of the applied magnetic field. In this plot it is possible to identify clearly the evolution of the P1 peak, which exhibits an initial splitting up to 4 T, and a secondary bifurcation of the lower branch at 10 T. Theoretical calculations previously reported only predicts an increase of the lowest level energy with the magnetic field [3]. Thus, between 0 T and 4, the lower branch of the P1 level exhibits and unexpected diamagnetic behavior. The non-linear behavior of these curves is related to a non-parabolic subband dispersion relation for holes in the quantum well. It can also be



**Fig. 2.** Illuminated current-voltage curve at different magnetic fields (indicated in the figure). Peak features appear in the curves due to the formation of Landau levels.

seen a tendency of the levels to become horizontal. This fact was attributed to a repulsion between levels belonging to different subbands with the same Landau-level index [3]. The features of the higher levels are not so clear due to noise in the measurements and because of the expected level crossing which makes the interpretation cumbersome.



**Fig. 3.** Peak position versus magnetic field. The structure of the lowest level (circles) is clear showing bifurcations. The highest level are not so well defined.

#### Acknowledgements

The authors are grateful to J. Nagle, B. Vinter, and Y. Guldner, for providing of samples and to FAPESP (Fundação de Amparo à Pesquisa do Estado de São Paulo) for the financial support.

#### References

- [1] J. M. Luttinger and W. Kohn, *Phys. Rev.* **97**, 869 (1955).
- [2] J. M. Luttinger, *Phys. Rev.* **102**, 1030 (1956).
- [3] U. Ekenberg and M. Altarelli, *Phys. Rev. B* **32**, 3712 (1985).
- [4] S. Glasberg, H. Shtrikman and I. Bar-Joseph, *Phys. Rev. B* **63**, 201308 (2001).
- [5] S. Wongmanerod *et al*, *Phys. Rev. B* **62**, 15952 (2000).
- [6] B. E. Cole *et al*, *Phys. Rev. B* **55**, 2503 (1997).
- [7] S. C. Dultz, H. W. Jiang and W. J. Schaff, *Phys. Rev. B* **58**, R7532 (1998).
- [8] H. Y. Chu, P. W. Park, S. G. Han and E. Lee, *Jpn. J. Appl. Phys.* **34**, 1355 (1994).

## Entangled exciton states in quantum dot molecules

*M. Bayer*<sup>†‡</sup>, *G. Ortner*<sup>†‡</sup>, *A. Larionov*<sup>†</sup>, *A. Kress*<sup>†</sup>, *A. Forchel*<sup>†</sup>, *P. Hawrylak*<sup>§</sup>,  
*K. Hinzer*<sup>§</sup>, *M. Korkusinski*<sup>§</sup>, *S. Fafard*<sup>§</sup>, *Z. Wasilewski*<sup>§</sup>, *T. L. Reinecke*<sup>¶</sup>  
and *Yu. Lyanda-Geller*<sup>¶</sup>

<sup>†</sup> Technische Physik, Universität Würzburg, Am Hubland, D-97074 Würzburg

<sup>‡</sup> Experimentelle Physik II, Universität Dortmund,  
Otto-Hahn-Straße 4, D-44227 Dortmund, Germany

<sup>§</sup> Institute for Microstructural Sciences, NRC, Ottawa, K1A 6N5, Canada

<sup>¶</sup> Naval Research Laboratory, Washington DC, USA

Currently there is strong interest in realizing implementations of quantum computation and quantum cryptography [1] in a solid state environment. One of the systems that are actively studied are semiconductor quantum dots (QDs). Due to their discrete energy level structure, they are often called artificial atoms, and they attract immediately interest of quantum information science since they allow to mimic the design developed for atomic physics systems such as ions in traps or atoms in cavities. However, despite of the similarities, one has to keep in mind that any elementary excitation in a QD has a generic many-body character.

An essential building block of a quantum processor is a quantum gate which entangles the states of two quantum bits. Recently it has been proposed that a pair of vertically aligned QDs could be used as an optically driven quantum gate [2]: The quantum bits are individual carriers either on dot zero or dot one. The different dot indices play the same role as a "spin", therefore we term them "isospin". Quantum mechanical tunneling between the dots rotates the "isospin" and leads to superposition of two quantum dot states. The quantum gate is built when two different particles, an electron and a hole, are created optically. The two particles form entangled isospin states. The entanglement can be controlled by application of an electric field along the heterostructure growth direction.

Here we present spectroscopic studies on single quantum dot molecules (QDMs) with different vertical separation between the dots that support the feasibility of this proposal. The comparison of the evolution of the excitonic recombination spectrum with the results of calculations allows us to demonstrate coherent tunneling of electrons and holes across the separating barrier and the formation of entangled exciton states. For a given barrier width, we find only small variations of the tunneling induced splitting between the entangled states demonstrating a good homogeneity within the obtained QDM ensembles.

### 1. Experimental data

A key requirement towards this demonstration of entanglement is the development of a growth technique allowing the fabrication of vertically aligned QDs with the same geometries. A promising technique in this respect is the Stransky–Krastanov epitaxy, for which the strain field of a QD in a first layer facilitates the growth of a second QD above it. This technique was supplemented by an indium-flush procedure which allows for a shape engineering of the QDs: The first layer of dots having the form of lenses with a height of  $\sim 4$ – $6$  nm is grown on a wetting layer of less than two monolayers of InAs on GaAs. Subsequently, the dots in this first layer are covered with 3 nm of GaAs, at which time the

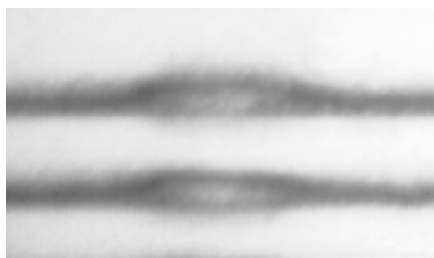


**Fig. 1.** Transmission electron micrograph of a QDM consisting of two disk-shaped InAs self-assembled quantum dots separated by a GaAs barrier.

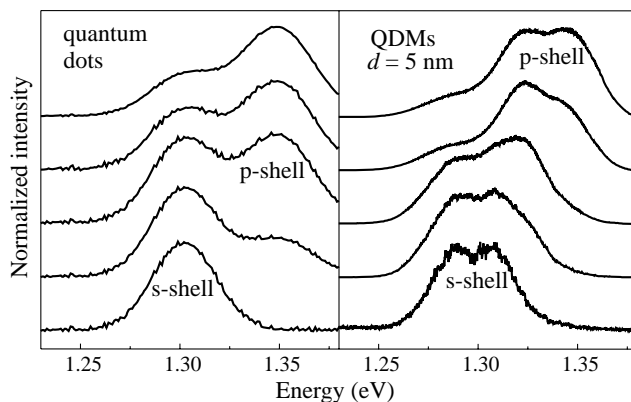


**Fig. 2.** Photoluminescence spectra recorded at  $T = 2$  K on ensembles of quantum dots (left panel) and quantum dot molecules (right panel) for varying excitation powers (increasing from bottom to the top). The barrier thickness in the quantum dot molecules was 5 nm.

indium-flush leaves all the dots with the same height. The dots are subsequently covered by a GaAs layer with a total thickness  $d$  measured from the wetting layer, and the same process is repeated for the second dot layer. The width of the GaAs barriers was varied from 4 to 8 nm.

From transmission electron microscope images such as the one shown in Fig. 1, we find only small variations of the geometries of the two QDs in a molecule. The dot shapes can be well approximated by disks with heights between 1–2 nm and radii between 8–12 nm. For narrow barrier widths the vertical alignment between the dots is perfect. With increasing barrier width we find besides molecules with perfect alignment structures, for which a lateral displacement of the dots with respect to each other occurs. This is well conceivable, because for wide barriers the influence of the strain from the dot in the first layer will be reduced.

From the coupling of two system with a discrete electronic shell structure we expect a splitting of each state into ‘bonding’ and an ‘anti-bonding’ orbitals, in analogy to the binding observed for molecules found in nature. Figure 2 shows state filling spectroscopy performed on ensembles containing  $\sim 10^6$  QDs (left panel) and QDMs (right panel) where  $d$  was 5 nm. For the QDs at low excitation only emission from the s-shell is observed. With increasing excitation, higher dot shells are occupied with electron-hole pairs according to the Pauli principle and emission from the p-shell appears in the spectra. The energy splitting between these shells is about 50 meV. For the QDMs, already at very low excitation two features separated by almost 25 meV are observed, which can be attributed to the expected coupling induced splitting of the s-shell exciton. Note, that the higher lying line cannot be



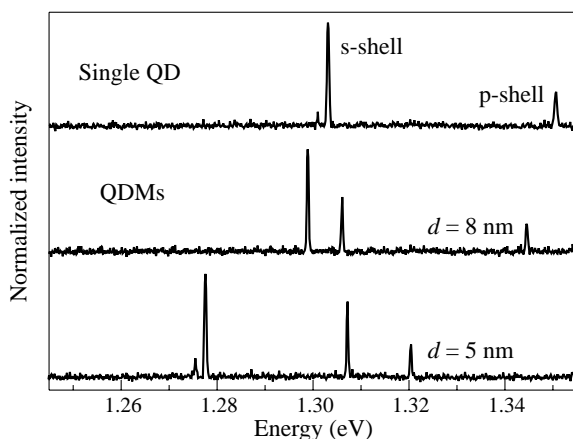


**Fig. 3.** Low excitation photoluminescence spectra recorded at  $T = 60$  K on a single QD (upper trace) and on single QDMs (lower traces) with barrier widths of 5 and 8 nm [3].

attributed to p-shell emission, because the splitting between p- and s-shell is mainly given by the lateral confinement and therefore is approximately the same for the QDMs: p-shell emission can be observed 50 meV above the s-shell when increasing the optical excitation. For it, also a splitting by  $\sim 30$  meV is observed which is slightly larger than the splitting in the s-shell. The larger splitting is well conceivable because of the larger penetration of the carrier wave functions into the GaAs barrier for higher lying states.

Still detailed information about the electronic shell structure cannot be obtained from these ensemble spectra because of their inhomogeneous broadening. Therefore we have isolated single QDMs in lithographically fabricated mesa structures with lateral sizes of about 100 nm. Figure 2 shows corresponding photoluminescence spectra for molecules with barriers of 5 and 8 nm width in comparison to the spectrum from a single dot. The sample temperature was 60 K, which allows for thermal excitation of carriers into higher lying shells. Therefore excitonic emission from the s- and p-shells are observed for the single dot. For the QDMs a splitting of the s-shell emission is observed that increases strongly with decreasing barrier width.

The left panel in Fig. 4 shows the measured energy splitting of the s-shell exciton

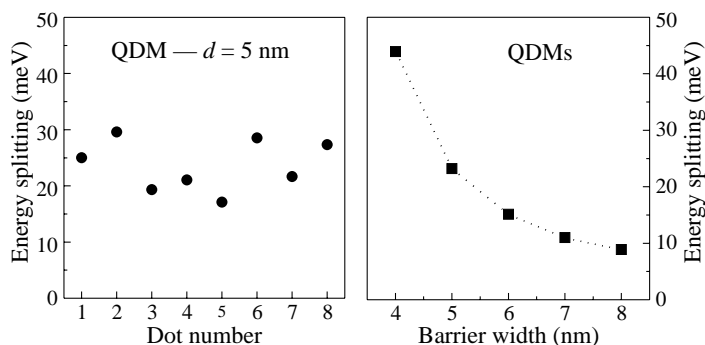


**Fig. 4.** Left panel: Energy splitting between the s-shell exciton states for different quantum dot molecules with a barrier width of 5 nm. Right panel: Average energy splitting (determined from single QDM studies) of the s-shell exciton versus barrier width.

states for different QDMs having a GaAs barrier thickness of 5 nm. For all structures a considerable splitting of  $24 \pm 6$  meV is observed. Its rather small variation indicates a good sample homogeneity, in particular a good vertical alignment of the dot structures. We note however, that for large barrier widths we find also QDMs whose spectra give clear indications for an asymmetry of the QDMs [4]. The right panel of Fig. 4 shows the dependence of the average energy splitting of the s-shell exciton on the barrier width  $d$ . With decreasing  $d$  a strong increase of the splitting is observed. Most importantly, for  $d < 5$  nm the splitting becomes larger than the thermal energy at room temperature which makes it insensitive on thermal perturbations and the system of QDMs attractive for quantum information applications.

## 2. Theoretical analysis

In a symmetric QDM structure the tunneling causes a splitting of the single particle states into symmetric (bonding) and antisymmetric (anti-bonding) orbitals. Because we generate electron-hole pairs in the QDMs, excitonic effects have to be taken into account. There are four different ways to distribute electron and hole among the two coupled dots with isospin indices 0 (upper dot) and 1 (lower dot):  $|0, 0\rangle$  and  $|1, 1\rangle$  (optically active (bright states) as well as  $|0, 1\rangle$  and  $|1, 0\rangle$  (optically inactive/dark states). To take the symmetry of coupling to the light field into account, a transformation into a basis of entangled isospin states is useful [3]. These entangled basis states are:

$$\begin{bmatrix} |a\rangle \\ |b\rangle \\ |c\rangle \\ |d\rangle \end{bmatrix} = \frac{1}{\sqrt{2}} \begin{bmatrix} |0, 0\rangle + |1, 1\rangle \\ |0, 1\rangle + |1, 0\rangle \\ |0, 1\rangle - |1, 0\rangle \\ |0, 0\rangle - |1, 1\rangle \end{bmatrix}.$$

States  $|c\rangle$  and  $|d\rangle$  are antisymmetric and therefore optically inactive. States  $|a\rangle$  and  $|b\rangle$ , on the other hand, are the excitonic analogs of the symmetric and antisymmetric single particle states. The splitting between them is given by the tunneling matrix elements of the carriers, which are renormalized by the Coulomb interaction between electron and hole.

### Acknowledgements

This work has been carried out under the Canadian European Research Initiative on Nanostructures supported by IMS NRC, NSERC, and EC. The Würzburg group acknowledges financial support by the DFG, the DARPA and the State of Bavaria. The Washington group acknowledges the support by the Office of Naval Research.

## References

- [1] See, for example, *The Physics of Quantum Information*, eds. D. Bouwmeester, A. Ekert and A. Zeilinger (Springer, Berlin, 2000).
- [2] P. Hawrylak, S. Fafard and Z. R. Wasilewski, *Cond. Matter News* **7**, 16 (1999).
- [3] M. Bayer, P. Hawrylak, K. Hinzer, S. Fafard, M. Korkusinski, Z. R. Wasilewski, O. Stern and A. Forchel, *Science* **291**, 451 (2001) and in preparation.
- [4] G. Ortner, M. Bayer, A. Larionov, V. B. Timofeev, A. Forchel, P. Hawrylak, M. Korkusinski, S. Fafard and Z. Wasilewski, in preparation.

## Magneto-optical properties of self-assembled (Cd,Mn)Se quantum dots

*J. Puls, P. Kratzert, A. Hundt, M. Rabe and F. Henneberger*

Institut für Physik der Humboldt-Universität zu Berlin  
Invalidenstr. 110, D-10115 Berlin, Germany

**Abstract.** A systematic study of the magneto-optical properties of semimagnetic (Cd,Mn)Se quantum dots is performed. The data proves the successful incorporation of the magnetic Mn ions into the QDs providing zero-dimensional magnetic entities for controlling single carrier spins.

Low-dimensional magnetic heterostructures are key components for the development of spin sensitive devices. Recently, II–VI semimagnetic quantum dot (QD) structures have attracted much interest [1]. From the sp-d coupling between the localized moments of the  $\text{Mn}^{2+}$  ions and the interior QD states, a huge Zeeman effect is expected, allowing the control of individual carrier spins on a nm-length scale. In this paper, the optical properties of semimagnetic (Cd,Mn)Se QDs embedded in a non-magnetic ZnSe environment are studied by photoluminescence (PL) in a Faraday-oriented magnetic field  $B$ . Measurements on the inhomogeneously broadened dot ensemble as well as on single quantum dots are carried out by macro- and micro-PL techniques, respectively.

The samples are grown by molecular beam epitaxy on a ZnSe buffer layer on top of a GaAs substrate, applying the thermally activated surface reorganization well established for non-magnetic QDs [2]. As shown very recently [3], this technique enables to accomplish a distinct Stranski–Krastanov morphology of three-dimensional islands with a core of pure CdSe. For the growth of semimagnetic QDs, three monolayers of  $\text{Cd}_{1-x}\text{Mn}_x\text{Se}$  are deposited instead of a pure CdSe film. The Mn content  $x$  calibrated via the Mn flux by X-ray diffraction and electron micro-probe on  $\text{Zn}_{1-x}\text{Mn}_x\text{Se}$  epilayers is varied between 0.03 and 0.10. Ultra-high vacuum atomic force microscopy proves that, in the whole  $x$ -range studied, the thermally activated reorganization results in a monomodally distributed dot ensemble. With increasing  $x$ , a continuous reduction of the QD density and a slight decrease of the average height is observed [4] yielding dots with an average height of 1.2 nm and densities of about  $600 \mu\text{m}^{-2}$  for  $x = 0.05$ . For comparison, three monolayer single quantum wells (SQWs) are grown without the activation process.

In Fig. 1(a), magneto-PL spectra are shown for a typical (Cd,Mn)Se QD structure with  $x = 0.07$ . Compared to CdSe QDs, the zero-field PL is high-energy shifted in accord with the increased bandgap. In a magnetic field, the PL moves to the low-energy side and becomes strongly  $\sigma^+$  polarized, both signifying occurrence of a giant Zeeman effect. In Fig. 1(b), the field dependence of the Zeeman components and the polarization degree are detailed. The Zeeman splitting resembles the Brillouin function-like magnetization of the Mn ions. A  $g$ -factor as large as 350 is derived from the linear part at low fields. Accordingly, the polarization degree of the QD exciton spin reaches already 90% at fields ( $B = 0.5$  T) attainable by permanent magnets. Another feature, seen in Fig. 1(a), is the much lower PL yield of the Mn-containing QD structures at  $B = 0$  T. We attribute this to a non-radiative transfer to intra-Mn transitions. Since the energy of the confined exciton is close to the Mn excitation energies, such Auger processes are quite probable here. With increasing  $B$ , the quantum yield partly recovers with saturation similar as the Zeeman

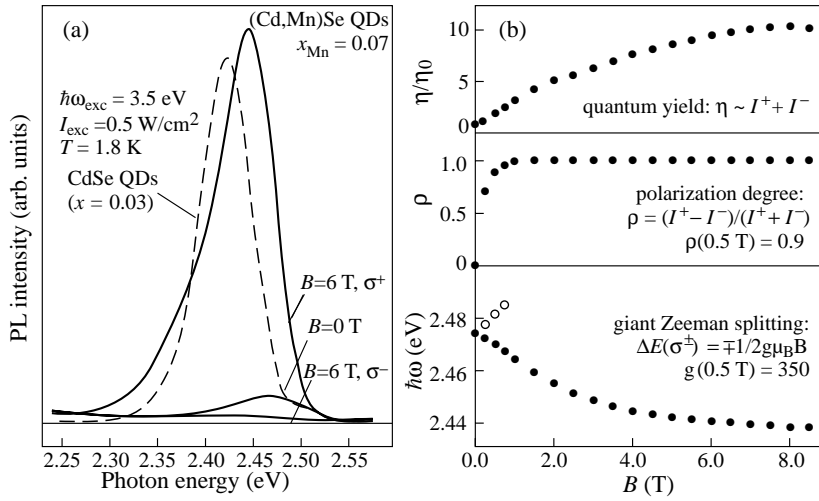


**Fig. 1.** Macro-PL data for (Cd,Mn)Se/ZnSe quantum structures. (a) PL spectra of a QD sample with  $x = 0.07$  at  $B = 0$  and  $B = 6$  T for both direction of circular polarization ( $\sigma^\pm$ ). Dashed line: scaled down spectrum of pure CdSe QDs. The spectra are corrected for interference effects. (b) Magnetic-field dependence of the Zeeman components, the polarization degree, and the quantum yield normalized to  $B = 0$  T.

splitting (see upper part of Fig. 1(b)). This is related to the increasing population of the  $m_s = -5/2$  Mn spin state, where transitions to higher shells of the  $3d^5$  Mn electrons are forbidden by spin-projection selection rule [5]. We emphasize that the reduced quantum yield has no relevance for unipolar spin-sensitive devices.

In Fig. 2, experimentally derived exciton  $g$ -values at a fixed field of  $B = 6$  T are drawn for SQW and QD structures with various Mn content. After initial rise the  $g$ -factors saturate for  $x \approx 0.1$  with slightly larger values for the QW structures. To conclude about the successful incorporation of the magnetic Mn ions, the data are compared in the following with model calculations. Whereas for the SQWs a standard quantum well calculation is used, reliable assumptions have to be made for the QDs. They are supposed to be a spherical lens with an aspect ratio of 1:3, located on a two monolayer wetting film. The electron-hole Coulomb interaction is accounted for by an effective electron potential. The field dependence of the band edge energies in the semimagnetic materials are described in mean field approximation using bulk parameters for the spd exchange interaction. The pairing of Mn ions is accounted for by the fraction  $r(x)$  of magnetically active single spins depending on the nearest neighbor coordination. This yields in a bulk-like environment  $r_{\text{bulk}} = (1 - x)^{12}$ , while  $r_{\text{QW}} = 1/3(1 - x)^{12} + 2/3(1 - x)^8$  is appropriate for a three monolayer QW.

The QW data are indeed well described by the expected spin fraction  $r_{\text{QW}}$ , while the QD  $g$ -factors are located between the curves calculated for  $r_{\text{bulk}}$  and  $r_{\text{QW}}$ . This is in accord with the slightly higher probability of pair formation in QDs, more extended in growth direction. The about 10% smaller  $g$ -factors in the QDs originate from the higher confinement and hence larger penetration of the wavefunction into the nonmagnetic barrier. In a reference calculation, we have also computed the  $g$ -factor of a pure CdSe QD on top of a semimagnetic wetting layer. This yields values significantly smaller than in the experiment (see dashed line in Fig. 2).

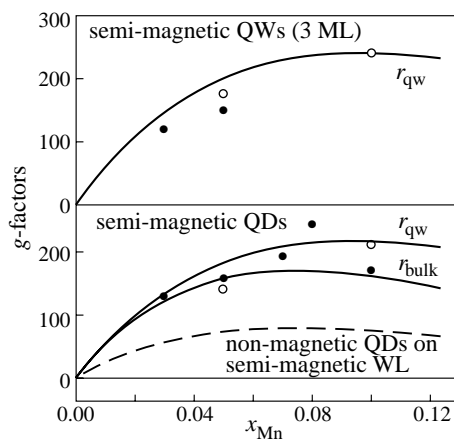


**Fig. 2.** Experimental  $g$ -factors of (Cd,Mn)Se QD and SQW samples grown on sub- (open symbols) and supercritical (filled symbols) buffer in dependence on the nominal Mn content  $x$ . The solid lines represent the calculated data for  $r_{\text{QW}}$  and  $r_{\text{bulk}}$ , the dashed line refers to a non-magnetic dot on a semimagnetic wetting layer. For simplicity, effects of alloying, exciton magneto-polaron formation, and the changes of masses due to incorporation of Mn have been neglected in the calculations.

Since based on the bulk exchange constants, our analysis has not provided evidence for a reduced sp-d interaction in low-dimensions. We attribute this to the dominant role of the heavy hole, the contribution of which is less affected by confinement.

In conclusion, the magneto-optical studies have proven the anticipated giant Zeeman effect in reasonable agreement with calculations assuming a homogeneous incorporation of the magnetic ions across QD and wetting layer. While the  $g$ -factor is not enhanced in comparison with SQWs, the QD structures have the potential for control of individual carrier spins.

#### Acknowledgements

This work was supported by the Deutsche Forschungsgemeinschaft in the framework of Sfb 296.

#### References

- [1] C. S. Kim, M. Kim, S. Lee, J. Kossut, J. K. Furdyna and M. Dobrowolska, *J. Cryst. Growth* **214/215**, 395 (2000),  
N. Takahashi, K. Takabayashi, I. Souma, J. Shen and Y. Oka, *J. Appl. Phys.* **87**, 6469 (2000),  
Y. Terai, S. Kuroda and K. Takita, *Appl. Phys. Lett.* **76**, 2400 (2000),  
G. Bacher, H. Schömig, M. K. Welsch, S. Zaitsev, V. D. Kulakovskii, A. Forchel, S. Lee, M. Dobrowolska, J. K. Furdyna, B. König and W. Ossau, *Appl. Phys. Lett.* **79**, 524 (2001).
- [2] M. Rabe, M. Lowisch and F. Henneberger, *J. Cryst. Growth* **184/185**, 248 (1998).
- [3] D. Litvinov, A. Rosenauer, D. Gerthsen, P. Kratzert, M. Rabe and F. Henneberger, submitted to *Appl. Phys. Lett.*
- [4] P. Kratzert, J. Puls, M. Rabe and F. Henneberger, *Appl. Phys. Lett.* **79**, 2814 (2001).
- [5] M. Nawrocki, Yu. G. Rubo, J. P. Lascaray and D. Coquillat, *Phys. Rev. B* **52**, R2241 (1995).

## Singlet and triplet states of charged excitons in ZnSe-based QWs probed by high magnetic fields

*D. R. Yakovlev*<sup>†‡</sup>, *G. V. Astakhov*<sup>†</sup>, *W. Ossau*<sup>‡</sup>,  
*Q. McCulloch*<sup>§</sup>, *S. A. Crooker*<sup>§</sup> and *A. B. Dzyubenko*<sup>¶</sup>

<sup>†</sup> Ioffe Physico-Technical Institute, St Petersburg, Russia

<sup>‡</sup> Physikalisches Institut der Universität Würzburg, 97074 Würzburg, Germany

<sup>§</sup> National High Magnetic Field Laboratory, Los Alamos, NM 87545, USA

<sup>¶</sup> Department of Physics, SUNY at Buffalo, Buffalo NY 14260, USA

**Abstract.** Singlet and triplet states of negatively ( $X^-$ ) and positively ( $X^+$ ) charged excitons (trions) in ZnSe-based quantum wells have been studied by means of photoluminescence in pulsed magnetic fields to 50 Tesla. Singlet state binding energies of  $X^-$  show a monotonic increase with growing magnetic fields with a tendency to saturation. Contrary to that a decrease of  $X^+$  binding energy is found. A crossover of the triplet and singlet states is observed in magnetic fields 35–50 T.

### 1. Introduction

Charged excitons (trions) are bound states consisting of three carriers: two electrons and one hole in case of negatively charged exciton ( $X^-$ ) and two holes and one electron for positively charged excitons ( $X^+$ ). Their binding energy in quasi-two-dimensional structures is about an order of magnitude smaller than the binding energy of neutral excitons. In analogy with  $H^-$  and  $H_2^+$  trions have singlet and triplet states. Singlet is a ground state at weak and moderate magnetic fields. Triplet is unbound in weak magnetic fields, but its binding energy increases faster than changes of the singlet binding energy, and in sufficiently high fields the triplet state becomes the ground state of the trion. Here we report the high-magnetic-field studies of singlet and triplet states in ZnSe-based quantum wells (QWs), where the excitonic effects are very distinct compared to GaAs QWs [1, 2].

### 2. Experimental

Results for three structures with  $X^-$  are presented. They are ZnSe/Zn<sub>0.82</sub>Be<sub>0.08</sub>Mg<sub>0.10</sub>Se single QWs ( $L_z = 48, 67$  and  $190$  Å) grown by MBE on (100) GaAs substrates. The structures were nominally undoped and electron density in the QW has been tuned by above-barrier illumination [3]. An  $X^+$  has been studied in a  $105$  Å ZnSe/Zn<sub>0.89</sub>Mg<sub>0.11</sub>Se<sub>0.18</sub>Se<sub>0.82</sub> QW modulation doped with Nitrogen in the barriers. In all structures concentration of free carriers was relatively small and does not exceed  $1-2 \times 10^{10}$  cm<sup>-2</sup>.

Experiments in a capacitor-driven 50 T mid-pulse magnet ( $\sim 400$  ms decay) at the National High Magnetic Field Laboratory (Los Alamos, USA) were performed at 1.6 K. Magnetic fields were applied perpendicular to the QW plane (Faraday geometry). Photoluminescence (PL) excited with a cw He-Cd laser and reflectivity spectra were detected in two circular polarizations, which allows to resolve spin components of excitons and trions.

### 3. Singlet trion states

Modification of exciton and trion PL lines in high magnetic fields is displayed in Fig. 1. Additionally to the singlet trion state ( $X_s^-$ ) the triplet state ( $X_t^-$ ) became visible as a separate line at  $B > 15$  T. Energies of the PL maxima vs magnetic field are plotted in Fig. 2. Exciton ( $X$ ) shows a regular behavior with two well-resolved spin components (spin splitting corresponds to the exciton  $g$  factor  $g_X = +0.84$ ) and a diamagnetic shift. As expected the spin splitting of the singlet state is similar to the exciton splitting, except

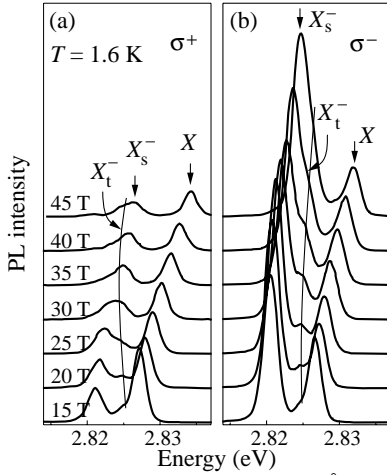


**Fig. 1.** PL spectra for a 67 Å ZnSe/Zn<sub>0.82</sub>Be<sub>0.08</sub>Mg<sub>0.10</sub>Se QW detected in two circular polarizations.

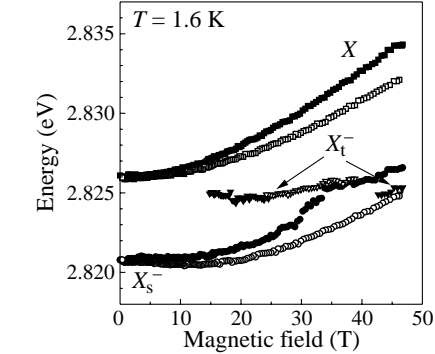
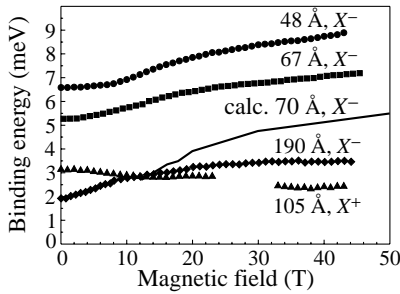


**Fig. 2.** Field dependence of the PL energy of a 67 Å ZnSe/Zn<sub>0.82</sub>Be<sub>0.08</sub>Mg<sub>0.10</sub>Se QW. Circular polarized components are shown by closed symbols for  $\sigma^+$  polarization and by open symbols for  $\sigma^-$  polarization.

**Fig. 3.** Trion binding energy vs magnetic field for ZnSe/Zn<sub>0.82</sub>Be<sub>0.08</sub>Mg<sub>0.10</sub>Se QWs of different width. The solid line shows results of calculations for a 70 Å QW, for parameters see Ref. [5].  $X^+$  binding energy is given for a 105 Å ZnSe/Zn<sub>0.89</sub>Mg<sub>0.11</sub>S<sub>0.18</sub>Se<sub>0.82</sub> QW (stars).  $T = 1.6$  K.

for a deviation in the field range 30–40 T. The latter is caused by the crossing of the  $\sigma^+$  polarized component with the triplet state.

Binding energy of trions  $E_B(X^-)$  and  $E_B(X^+)$  (measured as an energy distance between exciton and trion PL lines) are plotted in Fig. 3 vs magnetic field strength. In order to avoid uncertainties caused by spin splittings, data for the center-of-gravity of exciton- and trion spin doublets are given. The binding energy of the “bare” trions which exhibit no contribution from the Fermi energy is presented (for details see [4]).

Binding energies of  $X^-$  in all studied QWs show a monotonic increase with growing magnetic fields and a tendency to saturation in high fields  $B > 25$  T. The increase is stronger in wider QWs with smaller  $E_B(X^-)$ , e.g. it amounts to 150% in a 190 Å QW and has only 35% in a 48 Å QW. Being more compact in narrow QWs the singlet state becomes less sensitive to compression by external magnetic fields. Qualitatively  $E_B(X^-)$  dependencies from Fig. 3 are consistent with theoretical predictions for the singlet state [5]. The energies of the singlet and “dark” ( $M_z = -1$ ) triplet state have been computed for a 70 Å QW. Experimentally determined binding energies for a 67 Å QW are larger than theoretical. Possible reasons for that are discussed in Ref. [5].

Magnetic field dependence of the positively charged exciton differs drastically from  $X^-$  behavior. Binding energy of  $X^+$  shows no dependence on magnetic fields for  $B < 6$  T and decreases by 25% at higher fields (see stars). We are not aware of theoretical attempts to model  $X^+$  behavior in magnetic fields. However, it is clear that the difference in magnetic

field behavior of  $X^+$  and  $X^-$  binding energies is due to the very different structure of wave functions of these complexes (see discussion in Ref. [6]).  $X^-$  is constructed of two light particles (electrons) rotated around one heavy particle (hole). This complex has one center and magnetic field will localize the electron wave functions around the hole, thus inducing an increase of the binding energy. In contrast  $X^+$  has two heavy particles, i.e. two centers, and one light particle moving between two centers. In this case shrinking of electron wave function by magnetic fields hinders it from optimal adjustment for two centers, which results in decreasing binding energy of  $X^+$  complex.

#### 4. Triplet trion states

Being unbound at zero magnetic field, the triplet state of  $X^-$  appears on the low energy side of the exciton line for  $B > 15$  T and it approaches the singlet from below in fields up to 47 T (Figs. 1 and 2).

The triplet trion state has six spin sublevels. According to the *spin* optical selection rule  $\Delta S_z = \pm 1$ , four of them (with  $S_z = \pm 1/2 \pm 3/2$  are optically active and can decay radiatively. Sometimes such states are called “bright” states. Note that this should not be confused with the appearance of “dark” and “bright” triplet states because of the *orbital* selection rule [7]. Two other states with  $S_z = \pm 5/2$  could optically decay only by a spin-scattering assisted process. When spins are conserved, these triplet states are optically inactive, no matter what orbital wave functions they have. A separation of the triplet line from the exciton transition increases relatively fast with magnetic field and at about 35 T it crosses the upper spin component of the singlet. Theoretical calculations predict such a behavior for the “dark” ( $M_z = -1$ ) triplet [8–10]. Based on this, we assign the observed line to the “dark” triplet ( $M_z = -1$ ).

It is seen from Fig. 2 that the binding energy of the triplet state grows faster than that of the singlet state. The crossover of center-of-gravity of these states is expected in magnetic fields of about 50 T. We would like to indicate an interesting behavior of the  $\sigma^+$  polarized singlet state, which crosses with the “dark” triplet state. A clear deviation from the monotonic energy shift of the singlet state is observed in the field range 30–40 T, i.e. at the crossing range. Such experimental behavior indicates the interaction between the singlet and triplet state. Theoretically, such singlet-triplet interaction (that may lead to a singlet-triplet anticrossing) may be expected when the spin-scattering mechanisms are operative.

#### Acknowledgements

The authors are thankful to V. P. Kochereshko for useful discussions. This work was supported in part by the mutual grant of Russian Foundation for Basic Research (00-02-04020) and the Deutsche Forschungsgemeinschaft (Os98/6 and SFB 410).

#### References

- [1] G. V. Astakhov *et al*, *Phys. Rev. B* **60**, R8485 (1999).
- [2] G. V. Astakhov *et al*, *Phys. Rev. B* **62**, 10345 (2000).
- [3] G. V. Astakhov *et al*, *Phys. Rev. B* **65**, 15 February (2002) in press.
- [4] G. V. Astakhov *et al*, *Phys. Rev. B* **65**, 15 March (2002) in press.
- [5] D. R. Yakovlev *et al*, *Phys. Stat. Sol. (b)* **227**, 353 (2001).
- [6] R. A. Sergeev and R. A. Suris, *Phys. Solid State* **43**, 746 (2001).
- [7] A. B. Dzyubenko and A. Yu. Sivachenko, *Phys. Rev. Lett.* **84**, 4429 (2000).
- [8] D. M. Whittaker and A. J. Shields, *Phys. Rev. B* **56**, 15185 (1997).
- [9] A. Wojs *et al*, *Phys. Rev. B* **62**, 4630 (2000).
- [10] C. Riva *et al*, *Phys. Rev. B* **63**, 115302 (2001).



## Combined exciton and trion excitations in modulation doped quantum well structures

V. P. Kochereshko<sup>†</sup>, G. V. Astakhov<sup>†‡</sup>, D. R. Yakovlev<sup>†‡</sup>, W. Ossau<sup>‡</sup>,  
G. Landwehr<sup>‡</sup>, T. Wojtowicz<sup>§</sup>, G. Karczewski<sup>§</sup> and J. Kossut<sup>§</sup>

<sup>†</sup> Ioffe Physico-Technical Institute, St Petersburg, Russia

<sup>‡</sup> Physikalisches Institut der Universität Würzburg, 97074, Würzburg, Germany

<sup>§</sup> Institute of Physics, Polish Academy of Sciences, PL-02608 Warsaw, Poland

**Abstract.** Photoluminescence, photoluminescence excitation (PLE) and reflectivity spectra of CdTe-based modulation-doped quantum well (QW) structures with 2DEG have been studied in magnetic fields. Resonant lines corresponding to combined optical transitions in which the photo-generation of excitons as well as trions is accompanied by the excitation of an additional electron from states below the Fermi level to states above the Fermi level were observed and analyzed.

### Introduction

Elementary optical processes such as photo-excitation of electrons between discrete levels of impurity centers, photo-creation and the radiative annihilation of an exciton, exciton scattering by impurities *etc.* are usually under observation in the optical spectra of semiconductors. Apart from such basic processes one can consider combined resonances, which involve several of these elementary ones. One of the best known examples of such combined process is the exciton absorption in an indirect gap semiconductor, where the exciton photo-creation is accompanied by the absorption of a phonon.

In doped semiconductors and semiconductor heterostructures which contain a two-dimensional electron gas (2DEG) new elementary and combined processes with the participation of additional electrons could be observed. For example the optical transition to bound exciton-electron states (trions) was found recently in quantum well structures [1]. Since this pioneering work many papers devoted to trions have been published. Trions were observed in a number of quantum well (QW) structures based on different semiconductor heterosystems, such as, CdTe/CdZnTe, CdTe/CdMgTe, CdTe/CdMnTe, GaAs/AlGaAs, ZnSe/ZnMgSSe [2–5]. Trions, both negatively as well as positively charged, trions related to heavy as well as to light holes were found and studied experimentally [6, 7].

In addition to bound exciton–electron states, resonant combined exciton–electron processes involving three-particles have been observed in the presence of magnetic fields [8]. Such combined processes were called *Exciton Cyclotron Resonance* (ExCR), meaning that in an external magnetic field an incident photon creates an exciton in its ground state and simultaneously excites one of the background electrons from the lowest to one of the higher Landau levels. The energy of these transitions is equal to the sum of the exciton energy and a multiple of the electron cyclotron energy.

The present paper is concerned with combined processes of excitons and trions interacting with electronic transitions in modulation doped quantum well structures based on CdTe.

### Experiment

In this study we investigate CdTe/Cd<sub>0.85</sub>Mg<sub>0.15</sub>Te single quantum well structures. Typical structures contain a 120 Å QW where the modulation doping is spaced in the barriers

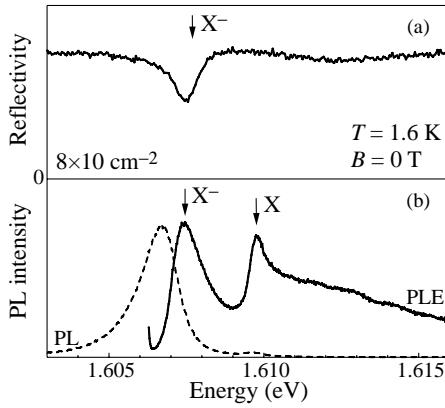


**Fig. 1.** Reflectivity (a) and Photoluminescence Excitation (b) spectra taken from an 120 Å CdTe/Cd<sub>0.85</sub>Mg<sub>0.15</sub>Te QW with 2D electron concentration of  $8 \times 10^{10} \text{ cm}^{-2}$ . Dashed line shows the photoluminescence spectrum.

at a 100 Å distance from the QW. The structure design allows us to control the electron concentration by keeping constant all other QW parameters (QW width, barrier height, background impurity concentration, *etc.*). Photoluminescence (PL), photoluminescence excitation (PLE), reflectivity and transmission spectra of these modulation-doped quantum well structures with 2DEGs of low and moderate concentrations ( $n_e$  varied from  $5 \times 10^{10}$  to  $2 \times 10^{12} \text{ cm}^{-2}$ ) have been studied in magnetic fields up to 7.5 T.

Figure 1 shows reflectivity, PL and PLE spectra taken from a QW structure CdTe/Cd<sub>0.85</sub>Mg<sub>0.15</sub>Te with a 2DEG concentration of  $8 \times 10^{10} \text{ cm}^{-2}$  at 1.6 K at zero magnetic field. This electron concentration corresponds to the Fermi energy of the 2DEG of 1.8 meV. In the PLE spectrum (Fig. 1(b)) a trion line and an exciton line are observed. Only the trion line ( $X^-$ ) can be recognised in the reflectivity spectrum (Fig. 1(a)). The exciton line in this spectrum is very broad and is difficult to distinguish.

Apparently one can observe a very large width of the X line in the PLE spectrum which is broadened at the high energy site. This high-energy tail of the line appears due to a combined exciton–electron process in which the photo-creation of an exciton is accompanied by the excitation of an additional electron from states below to states above the Fermi level of the 2DEG. A similar combined process in which the photo-generation of trions is accompanied by the excitation of an additional electron also results in an additional broadening of the trion line.

Strong modifications of the spectra are observed in magnetic fields. Figure 2(a) shows

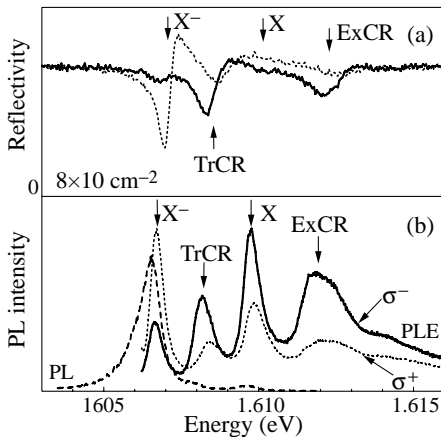


**Fig. 2.** Reflectivity (a) and Photoluminescence Excitation (b) spectra taken from an 120 Å CdTe/Cd<sub>0.85</sub>Mg<sub>0.15</sub>Te QW with 2D electron concentration of  $8 \times 10^{10} \text{ cm}^{-2}$  in  $\sigma^+$  (dotted line) and  $\sigma^-$  (solid line) circular polarization. Dashed line shows the photoluminescence spectrum.

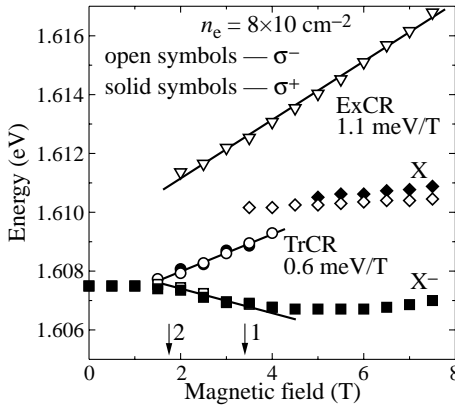


**Fig. 3.** Magnetic field dependence of exciton (X), trion ( $X^-$ ), ExCR and TrCR photon energies.

the modifications of reflectivity and Fig. 2(b) of PLE spectra for the SQW structure with an electron concentration of  $8 \times 10^{10} \text{ cm}^{-2}$  at the field of 3 T.

The trion reflectivity line becomes completely circularly polarized in the presence of the magnetic field. It can be observed in  $\sigma^+$  polarization only. This strong polarization of the line reflects the fact that the trion ground state is a singlet. Consequently, in a magnetic field, in which all background electrons are spin-polarized, the trion can be created for one circular polarization of the incident photon only, namely, for those in which the background electron and the electron in the exciton have opposite spin alignment.

In addition to the exciton (X) and the trion ( $X^-$ ) reflectivity lines two new lines appear in external magnetic fields, i.e., the *Combined Exciton Cyclotron Resonance* line (ExCR) and the *Combined Trion Cyclotron Resonance* line (TrCR). The ExCR line appears in the spectra as a transformation of the high energy tail of the exciton line with increasing magnetic field [7]. In magnetic fields the exciton line becomes narrow and the high-energy tail of the line splits into several ExCR lines. We attribute these lines with combined exciton electron processes in which the photo-creation of the exciton is accompanied by the excitation of an additional electron from the lowest filled to an empty Landau levels.

The TrCR line is observed between the exciton and the trion reflectivity features. This line can be observed in the spectra of QWs with rather high electron concentrations and at filling factors between 2 and 1 only [9]. The TrCR line appears as a “splitting” of a broad band at  $B = 0$  into two lines (trion line and TrCR line) when a magnetic field is applied. The magnetic field dependence of the observed line positions is presented in Fig. 3.

One can see that the ExCR line shifts linearly with a slope of 1.1 meV/T. The expected slope of the ExCR line for the studied QW is equal to  $\hbar\omega_c[1+m_e/(m_e+m_h)] = 1.35 \text{ meV/T}$ , where  $\hbar\omega_c = 1.16 \text{ meV/T}$  is the electron cyclotron energy,  $m_e = 0.1m_0$  and  $m_h = 0.5m_0$ . The TrCR line is situated between the trion and exciton resonances (see Fig. 3). It becomes resolvable from the trion resonance at a certain magnetic field of 1.7 T, corresponding to the 2DEG filling factor  $\nu = 2$ . The TrCR loses its intensity and disappears in higher magnetic fields when the filling factor becomes smaller than 1. The slope of the TrCR line of 0.6 meV/T is equal to  $\hbar\omega_c/2 = 0.58 \text{ meV/T}$ . In analogy with the ExCR line we attribute the TrCR line to a combined process in which the trion participates.

## Discussion

The trion absorption (reflection) line is formed by the binding of one photo-created exciton and one electron from the 2DEG. In the initial state of this process we have an electron  $e$  and in the final state we have a trion  $Tr$ . This means that an electron and the absorbed

photon ( $ph$ ) forms a trion:

$$e + ph \rightarrow Tr. \quad (1)$$

The energy of this transition is therefore:

$$E_{ph} = E_{Tr} - E_e. \quad (2)$$

As electrons in the 2DEG have energies (measured from the bottom of conduction band) in the range from zero to the Fermi energy:  $0 \leq E_e \leq E_F$ , the trion absorption (reflection) band should be spread within the energies from  $(E_{Tr} - E_F)$  to  $E_{Tr}$ .

One can easily see that the same energy range has to correspond to the trion combined process in which an incident photon creates a trion and simultaneously excites an additional electron from states below the Fermi level to states above that. This means, in the initial state we have two electrons  $e1$  and  $e2$  with energies  $0 \leq E_{e1(e2)} \leq E_F$  and in the final state we have a trion and one electron  $e3$  with an energy  $E_{e3} \geq E_F$ :

$$e1 + e2 + ph \rightarrow Tr + e3. \quad (3)$$

Therefore, the photon energy of this transition is

$$E_{ph} = E_{Tr} + E_{e3} - (E_{e1} + E_{e2}). \quad (4)$$

Hence, the trion combined band can be spread in the energy range from  $(E_{Tr} - E_F)$  to  $+\infty$ . So, in the absence of magnetic fields the trion absorption (reflection) band overlaps with the band of combined trion–electron process.

In external magnetic fields when the filling factor becomes less than 2 (or when the cyclotron energy becomes larger than the Fermi energy) these the trion and TrCR bands cannot overlap anymore. At these conditions the trion band shifts with magnetic fields to low energies as  $-\hbar\omega_c/2$  [see Eq. (2)] and the trion combined band shifts to high energies as  $+\hbar\omega_c/2$  [see Eq. (4)].

In conclusion, photoluminescence, photoluminescence excitation and reflectivity spectra of CdTe/CdMgTe modulation-doped QW structures with a 2DEG have been studied in magnetic fields. Resonant lines corresponding to combined optical transitions in which the photo-generation of excitons as well as of trions is accompanied by the excitation of an additional electron from states below- to states above the Fermi level were observed and analyzed as a function of the magnetic field strength.

#### Acknowledgments

This work has been supported by the mutual grant of the RFBR No. 01-02-16999 and the Deutsche Forschungsgemeinschaft (Nos. Os98/6 and 436 RUS 113/557).

#### References

- [1] K. Kheng *et al*, *Phys. Rev. Lett.* **71**, 1752 (1993).
- [2] K. Kheng *et al*, *Superlatt. & Microstruct.* **15**, 253 (1994).
- [3] G. Finkelstein, H. Shtrikman and I. Bar-Joseph, *Phys. Rev. Lett.* **74**, 976 (1995).
- [4] A. J. Shields *et al*, *Phys. Rev. B* **51**, 18049 (1995).
- [5] G. V. Astakhov *et al*, *Phys. Rev. B* **60**, R8485 (1999).
- [6] G. Finkelstein, H. Shtrikman and I. Bar-Joseph, *Phys. Rev. B* **53**, R1709 (1996).
- [7] A. Haury *et al*, *Superlatt. & Microstruct.* **23**, 1097 (1998).
- [8] D. R. Yakovlev, V. P. Kochereshko, R. A. Suris *et al*, *Phys. Rev. Lett.* **79**, 3974 (1997).
- [9] V. P. Kochereshko *et al*, Proc. NATO Workshop on Optical Properties of Semiconductor Nanostructures, Ser. 3, Vol. 81 (Kluwer Academic Publishers, the Netherlands 2000) p. 299.

## Modeling of the photoluminescence spectra of localize excitons in $\text{Zn}_{1-x}\text{Cd}_x\text{Se}$ quantum wells

*P. Díaz-Arencibia* and I. Hernández-Calderón

Physics Department, CINVESTAV, Apdo. Postal 14-740, 07000 Mexico, D.F. Mexico

**Abstract.** We present a model for the calculation of the emission spectra of localized excitons in  $\text{Zn}_{1-x}\text{Cd}_x\text{Se}$  quantum wells (QWs). The model takes into account the dependence of localization energy ( $E_{\text{loc}}$ ) on (i) the lateral size of the islands, (ii) the island size distribution, and, (iii) the exciton island population as a function of temperature. The model includes exciton migration assisted by acoustical phonons. The calculation is illustrated for the case of a 10 ML thick  $\text{Zn}_{0.8}\text{Cd}_{0.2}\text{Se}/\text{ZnSe}$  QW.

### Introduction

We consider a QW with thickness equal to  $N$ -monomolecular layers ( $1 \text{ ML} = a/2$ ) and thickness fluctuations of  $\pm 1 \text{ ML}$  forming  $(N+1)$  and  $(N-1)$  islands. The energy  $E_{1S}$  of a localized exciton depends not only on the thickness of the QW at the island but also on its lateral dimension. We have calculated the localization energy  $E_{\text{loc}}(L)$ , as a function of the island size;  $L$ , of square islands of an  $N = 10 \text{ ML}$  thick QW of  $\text{Zn}_{1-x}\text{Cd}_x\text{Se}$  with  $x = 0.2$  [2, 3].

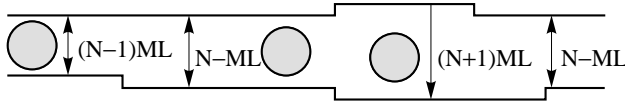


**Fig. 1.** Scheme of the  $N$ -ML thick QW with  $N \pm 1$  thickness fluctuation.

### Island distribution

It is described by means of the distribution function:

$$F(L) = \nu_N f_N(L) + \nu_{N+1} f_{N+1}(L) + \nu_{N-1} f_{N-1}(L). \quad (1)$$

The  $N$ -region is represented by a Dirac delta function  $f_N(L) = \delta(L)$ , while the distribution function of the  $(N-1)$  and  $(N+1)$  islands is given by:

$$f_m(L) = A_m (L/u_m)^4 \{ \exp[(L - L_m)/w_m] + 1 \}^{-1}. \quad (2)$$

Here,  $A_m$  is a normalization factor to ensure that  $\int_0^\infty f_m(L) dL = 1$ , where  $m = N-1$  or  $N+1$  and  $u_m$  and  $w_m$  are fitting parameters.  $L_m$  — represents the more probable island size.

$\nu_N$ ,  $\nu_{N+1}$  and  $\nu_{N-1}$  are the fraction of the total area corresponding to each region of the QW. Note that:  $\nu_N + \nu_{N+1} + \nu_{N-1} = 1$ .

## Migration

Excitons are created after the generation of electron-hole pairs in a time interval much shorter than the recombination time.  $\tau_{\text{exc}} \ll \tau_R$ . At very low temperatures excitons created at the  $(N+1)$  islands remain and recombine there. A fraction of the excitons created at the  $N$ -region can migrate to the  $(N+1)$  islands and contribute to their emission. This migration process involves exciton diffusion towards an  $(N+1)$  island and depends on the density of  $(N+1)$  islands. The exciton relaxes into the island emitting an acoustical phonon. It is found that: [4]

$$\tau_{n,m} = \tau_{m,n} \exp[(E_m - E_n)/k_B T]. \quad (3)$$

## Inhomogeneous broadening due to the island size distribution

Employing the inverse relation of  $E_{\text{loc}}(L)$ , [2,3]; i.e.,  $L(E_{\text{loc}})$ , a similar expression to Eq. (1) is obtained in the energy domain:

$$F(E) = v_N f_N(E) + v_{N+1} f_{N+1}(E) + v_{N-1} f_{N-1}(E) \quad (4)$$

where  $E$  refers to the localization energy  $E_{\text{loc}}$ . Fig. 2 shows  $F(E)$ . The width of the peaks represent the contribution of the island size distribution to the inhomogeneous broadening, i.e. the spectral density distribution of the emission. Now, in order to obtain the temperature dependent intensity it is necessary to take into account the exciton population of the m-ML thick island as a function of temperature;  $N_m(T)$ . The intensity of the emission that we observe in the experiment is proportional to the  $f_m(E)$  in Eq. (4) multiplied by the respective exciton population.

$$I(E, T) = \eta_{\text{int}} [f_{N+1}(E)N_{N+1}(T) + f_N(E)N_N(T) + f_{N-1}(E)N_{N-1}(T)]. \quad (5)$$

We have included  $\eta_{\text{int}}$  the internal quantum efficiency of the emission process, defined as:  $\eta_{\text{int}} = (1 + \tau_{\text{rad}}/\tau_{\text{nr}})^{-1}$ , where  $\tau_{\text{rad}}$  and  $\tau_{\text{nr}}$  are the radiative and non-radiative recombination times.

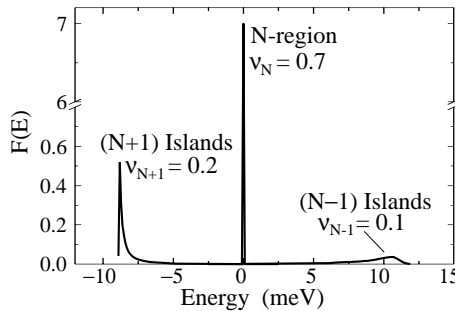


**Fig. 2.** Island size distribution in the energy domain. This can be interpreted as a spectral density distribution of the emission. The peaks give the broadening due to the presence of islands at the interfaces.

### Exciton population

The rate equations that give the exciton population in each QW region can be written as:

$$\begin{cases} \frac{\partial N_{N+1}}{\partial t} = G_{N+1} - \left( \frac{1}{\tau_R} + \frac{1}{\tau_{N+1,N}} + \frac{1}{\tau_{N+1,N-1}} \right) N_{N+1} + \frac{N_N}{\tau_{N,N+1}} + \frac{N_{N-1}}{\tau_{N-1,N+1}} \\ \frac{\partial N_N}{\partial t} = G_N + \frac{N_{N+1}}{\tau_{N+1,N}} - \left( \frac{1}{\tau_R} + \frac{1}{\tau_{N,N+1}} + \frac{1}{\tau_{N,N-1}} \right) N_N + \frac{N_{N-1}}{\tau_{N-1,N}} \\ \frac{\partial N_{N-1}}{\partial t} = G_{N-1} + \frac{N_{N+1}}{\tau_{N+1,N-1}} + \frac{N_N}{\tau_{N,N-1}} + \left( \frac{1}{\tau_R} + \frac{1}{\tau_{N-1,N}} + \frac{1}{\tau_{N-1,N+1}} \right) N_{N-1} \end{cases} \quad (6)$$

Here  $G_m$  are the generation rates of excitons at the  $m$ -region.  $G = \sum_m G_m$ ,  $m = N, N \pm 1$ ,  $\tau_R$  is the total recombination time, defined as:  $\tau_R^{-1} = \tau_{\text{rad}}^{-1} + \tau_{\text{nr}}^{-1}$ . Under steady state conditions ( $\partial/\partial t = 0$ ), we solve (6) in order to obtain the population of excitons as a function of temperature.

Additional inhomogeneous and homogeneous contributions to the line broadening (intrinsic sample properties and temperature effects) are taken into account by the Gaussian convolution of the spectrum of Fig. 2. Each  $f_m(E)$  is transformed to:

$$\psi_m(E) = \left( \sigma_E \sqrt{\pi/2} \right)^{-1} v_m \int_0^\infty f_m(\varepsilon) \exp \left[ -(\varepsilon - E)^2 / \sigma_E^2 \right] d\varepsilon \quad (7)$$

$\sigma_E$  enters in the model as a fitting parameter that can be estimated from the experiment.

Finally, the emission spectra of localized excitons can be expressed as:

$$I(E, T) = \eta_{\text{int}} \left[ \psi_{N+1}(E) N_{N+1}(T) + \psi_N(E) N_N(T) + \psi_{N-1}(E) N_{N-1}(T) \right]. \quad (8)$$

The results are presented in Fig. 3 for the case of a 10 ML thick  $\text{Zn}_{0.8}\text{Cd}_{0.2}\text{Se}/\text{ZnSe}$  QW. We have chosen arbitrary values of  $L_m$ ; 18  $a_B$  and 7  $a_B$  for the  $N+1$  and  $N-1$  islands, respectively. Here  $a_B$  is the exciton Bohr radius. Note that the contribution from the  $(N-1)$  region is negligible even at relatively high temperatures. We have observed a similar temperature behavior of the spectra lineshape in  $\text{ZnCdSe}$  QWs. [5], a detailed comparison of the experiment with the calculation will be published elsewhere.

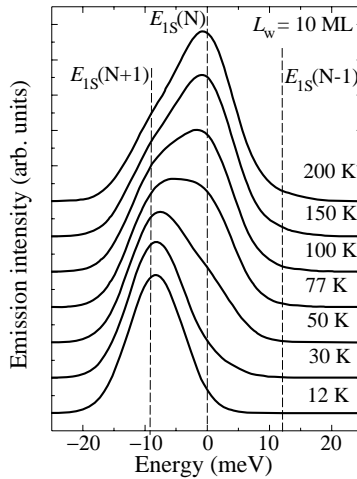


**Fig. 3.** Calculated emission spectra of localized excitons in  $\text{ZnCdSe}/\text{ZnSe}$  QW with  $\pm 1$  ML thickness fluctuation. Results of the calculation of the PL spectra of a QW with the island distribution given above. The calculations were made for different sample temperature.

## Conclusion

We developed a model for the calculation of the luminescence spectrum of QWs due to localized excitons. The localization is produced by  $\pm 1$  ML thickness fluctuations of the QW. The model takes into account the dependence of localization energy ( $E_{\text{loc}}$ ) on the lateral size of the islands, the island size distribution and the exciton island population as a function of temperature. The model includes exciton migration assisted by acoustical phonons. The calculation was illustrated for the case of a 10 ML thick  $\text{Zn}_{0.8}\text{Cd}_{0.2}\text{Se}$  QW. The evolution of the calculated spectra exhibits the behavior experimentally observed in the PL of QWs.

## References

- [1] D. S. Citrin, *Phys. Rev.* **B47**, 3832 (1993).
- [2] P. Díaz Arencibia and I. Hernández Calderón, *Proc. 9 Int. Symp. Nanostructures: Physics and Technology*, Ioffe Institute, St Petersburg, p 546, 2001.
- [3] P. Díaz-Arencibia and I. Hernández-Calderón, *Microelectronics Journal* in press (2002).
- [4] Er-Xuan Ping, *Appl. Phys. Lett.* **62**, 2569 (1993).
- [5] P. Díaz-Arencibia, I. Hernández-Calderón, L. M. Hernández-Ramírez and M. C. Tamargo, *J. Vac. Sci. & Techn. B* **18**, 1526 (2000).



## Pauli blockade in spin-flip Raman scattering via donor bound excitons

A. V. Koudinov<sup>†</sup>, Yu. G. Kusrayev<sup>†</sup>, B. P. Zakharchenya<sup>†</sup>, D. Wolverson<sup>‡</sup>,  
J. J. Davies<sup>‡</sup> and J. Kossut<sup>§</sup>

<sup>†</sup> Ioffe Physico-Technical Institute, St Petersburg, Russia

<sup>‡</sup> University of Bath, Bath, UK

<sup>§</sup> Institute of Physics, Polish Academy of Sciences, Warsaw, Poland

**Abstract.** We have investigated spin-flip Raman scattering by manganese ions in (001)-CdTe/CdMnTe quantum wells. The intensity of the SFRS obtained in resonance with the donor bound exciton in the Voigt geometry was found to depend strongly on the orientation of the crystal with respect to the magnetic field: Raman intensities for field parallel to  $[110]$  and  $[1\bar{1}0]$  directions differ by about a factor of 8. The observed phenomenon is interpreted in terms of an electron spin blockade in the  $D^0X$  complex. The role of double resonance is discussed.

### Introduction

The unusual properties of diluted magnetic semiconductors (DMS) and DMS-based nanostructures allow one to manipulate the energy spectrum and spin splittings of electrons and holes. Due to the enhancement of the magnetic properties of carriers by the strong exchange interaction with magnetic ions, the  $g$ -factors of carriers in quantum well (QW) structures of, for instance, CdTe/CdMnTe depend on the well width and manganese concentration. One of the most powerful methods of investigation of spin effects in semiconductors is spin-flip Raman scattering (SFRS) [1, 2]. This technique was successfully used to study the exchange interactions in bulk DMSs [3] and QW structures [4, 5]. These investigations gave useful information about  $g$ -factors of free and localized carriers. Recently, another technique, polarized photoluminescence spectroscopy, was used to study the in-plane anisotropy of the heavy-hole  $g$ -factor in CdTe/CdMnTe QWs [6]. It was found that the QWs under study possessed  $C_{2v}$  symmetry, and the heavy hole  $g$ -factor is extremely anisotropic. Its lateral components along  $[110]$  and  $[1\bar{1}0]$  directions have opposite signs:  $g_{xx} = -g_{yy}$ . In this paper, we report the study of spin-flip Raman scattering in (001)-CdTe/CdMnTe QWs, where Zeeman splittings of the band carriers are close to those of Mn spins — the case when exchange scattering is expected to be the most effective.

### 1. Results and discussion

The structures under study were non-magnetic CdTe QWs with thicknesses  $L = 40, 60$  and  $100 \text{ \AA}$  surrounded by wide ( $500 \text{ \AA}$ ) semimagnetic  $\text{Cd}_{1-x}\text{Mn}_x\text{Te}$  barriers with  $x = 0.3$  (sample 1) and  $0.5$  (sample 2), grown on (001)-GaAs substrates. The measurements were performed at  $T = 1.6 \text{ K}$  in the backscattering Voigt geometry (direction of excitation was  $z$  and of observation  $\bar{z}$ , where  $z$  is the growth axis). The incident light was linearly polarized in either  $\pi$  ( $\mathbf{E}_i \parallel \mathbf{B}$ ) or  $\sigma$  ( $\mathbf{E}_i \perp \mathbf{B}$ ) direction. To study the angular dependences of SFRS intensity, we rotated the crystal around the growth axis.

Figure 1 shows the spectra of SFRS in the backscattering Voigt geometry from the CdTe/CdMnTe QW (sample 1) for two orientations of the crystal —  $\varphi = 0^\circ$  and  $90^\circ$ .

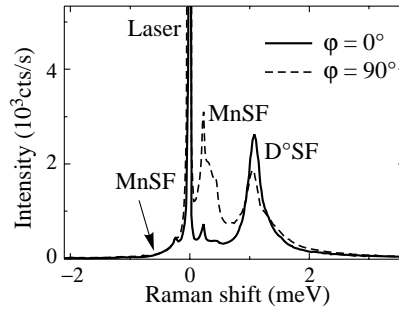


**Fig. 1.** Spin-flip spectra in the Voigt backscattering geometry and crossed polarization configuration  $z(\pi, \sigma)\bar{z}$ , in 60 Å CdTe/CdMnTe QW (sample 1). Spectra are recorded under excitation energy  $E = 1.66008$  eV, magnetic field  $B = 2$  T, for  $\varphi = 0^\circ$  (solid line) and  $\varphi = 90^\circ$  (dotted line), where  $\varphi$  is an angle between magnetic field and  $[110]$  direction. As usual,  $\pi$  means linear polarization along-while  $\sigma$  — perpendicular to the magnetic field.

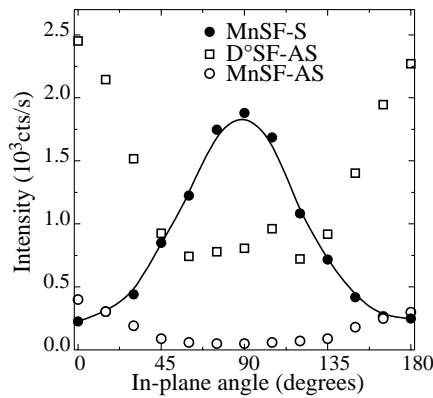


**Fig. 2.** Angular dependences of MnSF intensity in CdTe/CdMnTe QW (sample 2,  $L = 60$  Å),  $z(\pi, \sigma)\bar{z}$  configuration,  $B = 2$  T, for Stokes (closed circles) and anti-Stokes (open circles) lines. Angular dependence of  $D^0\text{SF}$  (squares) is also shown for comparison.

The spectra are recorded in the crossed  $(\pi, \sigma)$  polarization configuration, where the first and the second indices stand for the linear polarization of the exciting and scattered light, respectively. The narrower lines correspond to the Raman process with a flip of one or more spins of manganese electrons with  $g = 2$  (MnSF), while the broader ones originate from spin-flip of donor electron ( $D^0\text{SF}$ ). One can see from Fig. 1 that the Raman intensities for the cases where the magnetic field is directed along  $[110]$  ( $\varphi = 0^\circ$ ) and  $[1\bar{1}0]$  ( $\varphi = 90^\circ$ ), which are equivalent for an ideal QW, are different. Resonance profiles for the two Raman features reveal two distinct bands: one of them is located in energy close to the exciton weakly localized by the fluctuations of QW potential (X) and the other one is close to the donor bound exciton ( $D^0\text{X}$ ) [7]. These are (X and  $D^0\text{X}$ ) the states which serve as intermediate ones for the resonant Raman processes. The spectra shown in Fig. 1 were recorded under excitation in resonance with the  $D^0\text{X}$  complex. Qualitatively similar spectra were observed under the resonant excitation in the region of weakly localized excitons (X).

In Fig. 2 we plotted the angular dependences of SFRS intensities for MnSF and  $D^0\text{SF}$

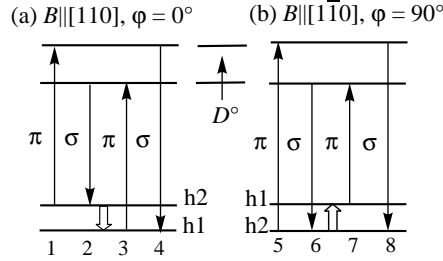


**Fig. 3.** Schematic diagram illustrating the spin-flip Raman scattering via donor bound exciton in two cases: (a)  $\varphi = 0^\circ$  and (b)  $\varphi = 90^\circ$ . The allowed optical transitions 1, 2...8 are shown by standard arrows; double arrows show the hole spin-flip accompanied by the simultaneous flip of manganese spin.

lines in sample 2 under the excitation into the  $D^0X$  complex. In case of  $D^0SF$ , a variation of intensity by a factor of 3 is observed, while the intensity of  $MnSF$  shows much sharper angular dependence (about a factor of 8). Surprisingly, these dependences turned out to be in antiphase. Earlier, we explained the anisotropy of  $D^0SF$  intensity in terms of the angle-dependent lifetime of the intermediate state [7], which is a consequence of the heavy-hole  $g$ -factor anisotropy. However such an interpretation is inapplicable for  $MnSF$ , because of its antiphase angular dependence.

The resonant paramagnetic Raman scattering is the third-order process consisting of the three stages (see Fig. 3): (i) absorption of an excitation photon and creation of an exciton in the intermediate state, (ii) flip of the manganese spin by the exciton, and (iii) emission of a photon. In the Stokes scattering process, the energy of the emitted light is reduced with respect to the exciting light by the amount spent to reorient the Mn spin. Despite the fact that we observe similar SFRS spectra under excitation close to  $X$  and  $D^0X$ , the mechanisms underlying in these two cases can be quite different. If the  $D^0X$  complex consisting of two electrons in singlet state and hole serves as an intermediate state for the process, then only the hole spin can be responsible for the flip of Mn spin since electron spin is blocked ( $S = S_1 + S_2 = 0$ ). However this restriction is removed when the exciton ( $X$ ) works as an intermediate state. In what follows, we focus on the case of Mn spin-flip provided that the donor bound exciton serves as an intermediate state in the Raman process, i.e. excitation light is in close resonance with  $D^0X$ .

Let us consider the Mn SFRS transitions at  $\varphi = 0^\circ$  and  $90^\circ$ . For  $\pi$ -polarized light exciting resonantly a  $D^0X$  complex, the appropriate optical transitions at  $\varphi = 0^\circ$  are 1 and 3 (see Fig. 3). However, since the ground state of the complex corresponds to the antiparallel spins of two electrons the lower electron sublevel at low temperatures is occupied by the donor electron so that transition 3 is blocked. Process 1–2 is also ruled out since it does not correspond to a Mn electron spin-flip. Thus for  $\varphi = 0^\circ$  the process must go via the 1–4 channel. Consider now the right-hand part of Fig. 3,  $\varphi = 90^\circ$ . The hole  $g$ -factor has an opposite sign for this angle and therefore the hole spin sublevels change places. Eliminating, for analogous reasons, the  $\pi$ -transition 7 (the lower electron sublevel is blocked) and process 5–8 (not the Mn-electron spin-flip), we infer for  $\varphi = 90^\circ$  to the path 5–8. Comparing now channels 1–4 ( $\varphi = 0^\circ$ ) and 5–8 ( $\varphi = 90^\circ$ ) for the Stokes process [8] (Mn spin increases by 1) we conclude that the efficiency of path 5–8 should be higher because double resonance conditions are fulfilled provided that hole and Mn Zeeman

splittings are close to each other. The experimentally-observed angular dependence of the MnSF intensity (see Fig. 2) entirely agrees with this prediction. Note that the opposite arguments are applicable for anti-Stokes process, i.e. in this case SFRS intensity at  $\varphi = 0^\circ$  should be larger. It can be seen from Figs. 1 and 2 that this is indeed the case.

## 2. Conclusions

To conclude, we have shown that the intensity of MnSF displays a strong lateral anisotropy. It has been demonstrated that, due to the Pauli exclusion principle, spin-flip Raman scattering is blocked in unfavourable conditions. On the contrary, in favourable conditions, the SFRS efficiency is dominated by the double resonance.

### Acknowledgements

This work has been supported by the Royal Society and Russian Foundation for Basic Research within the Projects 00-02-16941, 01-02-17906.

## References

- [1] D. G. Thomas and J. J. Hopfield, *Phys. Rev.* **175**, 1021 (1968).
- [2] V. F. Sapega, T. Ruf, M. Cardona, K. Ploog, E. L. Ivchenko and D. N. Mirlin, *Phys. Rev. B* **50**, 2510 (1994).
- [3] A. K. Ramdas and S. Rodrigues, *Topics in Applied Physics*, vol 68, p 137, Berlin-Heidelberg.: Springer-Verlag, 1990.
- [4] J. Stühler, G. Schaak, M. Dahl, A. Waag, G. Landwehr, K. V. Kavokin and I. A. Merkulov, *Phys. Rev.Lett.* **74**, 2567 (1995).
- [5] M. P. Halsall, P. J. Boyce, D. Wolverson, J. J. Davies, D. E. Ashenford and B. Lunn, *Phys. Rev. B* **50**, 11755 (1994).
- [6] Yu. G. Kusrayev, A. V. Koudinov, I. G. Aksyanov, B. P. Zakharchenya, T. Wojtowicz, G. Karczewski and J. Kossut, *Phys. Rev. Lett.* **82**, 3176 (1999).
- [7] Yu. G. Kusrayev, A. V. Koudinov, D. Wolverson and J. Kossut, *Phys. Stat. Sol. (b)* **229** (2002) (to be published).
- [8] Isotropic manganese-band carrier exchange interaction allows only flip-flop transitions raising one spin and lowering another. It is supposed, however, that due to the hole spin anisotropy in QWs under study flip-flip exchange transitions are also possible.

## Molecular states of 2D excitons in the GaAs-SQW-structures and the coherent transient spectroscopy of the phase-conjugate response

V. V. Ovsyankin<sup>†</sup>, Yu. K. Dolgikh<sup>†</sup>, B. V. Stroganov<sup>†</sup>, V. S. Zapasskii<sup>†</sup>,  
S. A. Eliseev<sup>‡</sup>, Yu. P. Efimov<sup>‡</sup> and V. V. Petrov<sup>‡</sup>

<sup>†</sup> S. I. Vavilov State Optical Institute, 199034, Birzhevaya 14, St Petersburg, Russia

<sup>‡</sup> Institute of Physics, St Petersburg State University

**Abstract.** The spectra, dynamics of excitation, and excitation spectra of the time-integrated transient coherent phase-conjugate response, generated by the HH-excitons ( $X$ ) of a high-quality GaAs quantum well are studied experimentally at 8 K. The spectra of the bound ( $BXX$ ) and anti-bound ( $AXX$ ) states of the biexcitonic molecules are identified. It is shown that both systems of the optically active molecular states are not elementary and require the energy of exciton rotation around the common center of mass to be included into the model two-exciton Hamiltonian to describe them properly. The equilibrium inter-exciton distance in the bound state is found. The  $AXX$  states mainly decay with creation of two nonradiative excitons with  $\mathbf{k}_X \rightarrow \mathbf{k}_{opt}$  i.e. of surface polaritons.

### Introduction

The spectrum and dynamics of the 2D exciton states excited within the area of their spatial coherence is of great interest both for the fundamental physics of collective states of weakly coupled quasi-particles with quasi-bosonic statistics [1], and for application of the SQW structures as nonlinear quantum mirrors in the systems of parallel classical (or quantum) processing of photonic information [2]. For operation of these devices, the spectra of the cascaded  $X \rightarrow XX$  transitions into the bound and anti-bound two-excitonic states should show an optical gap at the frequency of one-exciton transition. In the perfect 2D structures, this gap may arise only as a result of inter-excitonic (correlative) interaction, capable of splitting the two-excitonic states into a system of bound ( $BXX$ ) and anti-bound ( $AXX$ ) biexcitonic states. One of the goals of this paper was to elucidate feasibility of such gap structures within the GaAs/AlGaAs-type systems. Note that though the idea about the correlation interaction as a source of excitonic anharmonism is commonly recognized and widely used in the analysis of spectra and dynamics of the resonant nonlinear photoresponse of semiconductor 2D structures [3, 4, 5, 6], no computational models are available nowadays that allow one to reliably predict the eigenstates and eigenvectors of the biexcitonic molecules for real quasi-2D structures. This is why become so important experimental data on the spectrum and symmetry of the  $XX$ -states and probabilities of the optical and non-optical  $X \rightarrow XX \rightarrow X_k + X_{-k}$  transitions between the one- and two-excitonic states. Obtaining these data was the main goal of the study.

### Experimental

We studied a GaAs/Al<sub>0.3</sub>Ga<sub>0.7</sub>As structure with a single 8-nm GaAs quantum well grown using the molecular beam epitaxy technique. The sample was held in a closed-cycle cryostat at 8 K. The luminescence spectrum of the sample in the expected region of the HH-exciton is characterized by an isolated peak at 1.566 meV with a half-width at half-maximum of

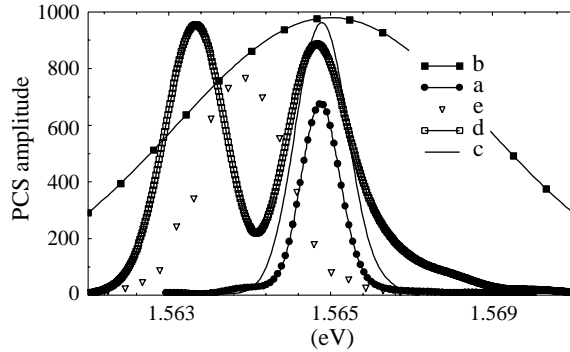


**Fig. 1.** The luminescence spectrum (a) and spectrum of the exciting PCS pulses (b). The normalized PCS spectra measured at  $\tau_{12} = 0$  for collinear polarizations of the 1 and 2 pulses and for the pulse intensities  $I_1 = I_2 = I_0$  (c) and  $I_1 = I_2 = 10I_0$  (d), where  $I_0$  is the intensity corresponding to the calculated exciton density ( $5 \times 10^8 \text{ cm}^{-2}$ ). The excitation spectrum of the low-frequency excitonic PCS resonance for orthogonal linear polarizations of the pulses 1 and 2 with the spectral width  $\delta\omega = 1.6 \text{ meV}$  (e).

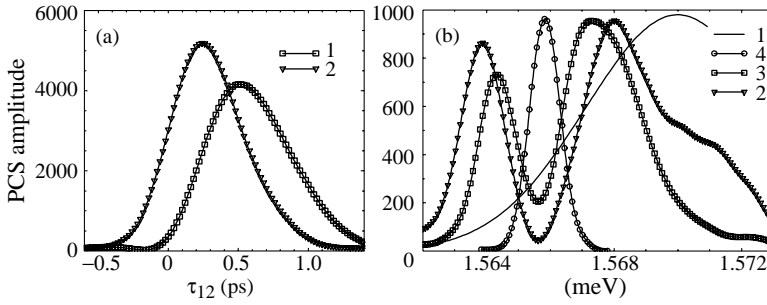
0.7 meV (Fig. 1). The spectra and dynamics of the nonlinear transient photoresponse were studied using the method of nonlinear wave mixing of delayed wave packets in the geometry of phase conjugation on a surface. This geometry differs from the most popular geometry of double-pulse four-wave mixing in that the reference momentum ( $\mathbf{k}_2$ ) in the former is exactly normal to the surface of the structure, while the measured phase-conjugation signal (PCS) is traveling in the direction ( $-\mathbf{k}_1$ ) opposite to the direction of propagation of the phase-conjugate pulse ( $\mathbf{k}_1$ ). The time-integrated intensity was measured with a detector located either in front of or after the spectral device. In the degenerate version of the technique, we employed, the pulses with the needed spectro-temporal characteristics were obtained by spectral selection of emission of the 100-fs pulses of a mode-locked Ti:sapphire laser down to a spectral width of  $\delta\omega = 6 \text{ meV}$  or  $\delta\omega = 1.6 \text{ meV}$  depending on the type of the experiment.

Figure 1 shows spectral characteristics of the PCS detected at zero delay between the pulses ( $\tau_{12} = 0$ ). The low-frequency resonance, additional to the resonance  $0 \rightarrow X$ , spaced apart by  $\sim 2 \text{ meV}$  and arising at higher pump power (see Fig. 1(d)), is uniquely associated with the PCS induced by the polarization related to the transition  $BXX \rightarrow X$ . This is further confirmed by spectral position of the PCS excited by pulses with orthogonal polarizations at  $\omega = 0.5(\omega_{0X} + \omega_{XB})$  (Fig. 1(e)).

### Structure of bound and anti-bound states of the biexcitonic molecules

In a short-wavelength region (with respect to the  $0 \rightarrow X$  resonance) of the PCS spectrum (Fig. 1(d)), one can notice a spectral feature which may be presumably attributed to the PCS generated by the polarization associated with the transitions  $AXX \rightarrow X$ . By choosing the delay time at which the processes of single-quantum ( $0 \rightarrow X$ ) and triple-quantum ( $0 \rightarrow X \rightarrow XX \rightarrow X$ ) population of single exciton states interfere destructively, the contribution of the  $0 \rightarrow X$  transition to the PCS can be totally suppressed, as seen from Fig. 2(a) for the delay time  $\tau_{12} = 0.18 \text{ ps}$ .

By shifting the frequency of the exciting pulses to shorter wavelengths, as shown in



**Fig. 2.** The dependence of PCS intensity at frequencies  $\omega_{0X}$  [a(1)] and  $\omega_{XB}$  [a(2)] on the time delay  $\tau_{12}$  between the pulses of collinear polarizations of the pulses and  $I_1 = I_2 = 20I_0$ . b(1) is the spectrum of the exciting pulses, b(2) is the PCS spectrum, b(3) is the same as b(2), but for the circularly co-polarized exciting pulses, and b(4) is the reference spectrum of the single-exciton resonance.

Fig. 2(b) (1), and by choosing the delay time for which the single-exciton contribution to the PCS appears to be suppressed, we obtained the spectrum of the transitions  $AXX \rightarrow X$  and  $BXX \rightarrow X$  in the form shown in Fig. 2b (2), convenient for the analysis.

The fact that the structure of optically active transitions into the anti-bound states is not elementary follows from the data presented in Fig. 2. It, however, does not look surprising because, according to systematics of the singlet excitonic states, the  $AXX$  state should be represented by three levels with the components of the total angular momentum  $M = \pm 2, \pm 1$ , and 0. The  $BXX$  state, on the contrary, is usually considered to be elementary, because the ground singlet state should be definitely characterized by zero angular momentum. One can see that, contrary to the anticipated (for  $M = 0$  in the  $BXX$  state) total forbiddenness for the  $BXX \rightarrow X$  transition to be revealed in the PCS spectrum for the circularly co-polarized exciting pulses, this band is nearly as intense as (though slightly narrower than) a similar band observed under collinear polarizations and is shifted to shorter wavelengths by  $\delta \approx 0.46$  meV. The only possible explanation for these facts is that, in the biexcitonic system under study, the rotational motion of the excitons around their common center of mass essentially controls the energy characteristics of the bound molecular state. By relating the shift  $\delta$  to spacing between the rotational levels with  $l = 0$  and  $l = 2$ :  $\delta = l(l + 1)\hbar^2/2m^*r^2$ , and by taking, for the effective mass of the exciton  $m^* = 0.44m_0$ , we come to a reasonable value of the equilibrium inter-excitonic distance of the biexcitonic molecule  $r = 33.5$  nm.

### Dynamics and relaxation channels of the anti-bound states

As has been shown experimentally, the dephasing rate of the anti-bound states grows with increasing detuning from the single-exciton transition frequency and rapidly reaches the instrumental limit determined by duration of the transform-limited pulses with  $\delta\omega = 1.6$  meV. This growth correlates with opposite behavior of the PCS [b(2)]. Such a behavior definitely shows that the process of emission into free space in the transition  $AXX \rightarrow X$  is shunted by a more effective process. A simple analysis, based on the energy and in-plane momentum conservation laws allows us to conclude that the main channel of decay of the  $AXX$  states is the decomposition into two surface polaritons with opposite momenta.

### Acknowledgements

This work was financially supported by the Russian Foundation for Basic Research, grant 00-02-17354.

### References

- [1] A. Griffin, D. W. Snoke and S. Stringari, *Bose-Einstein Condensation*, Cambridge University Press, Cambridge, 1995.
- [2] I. Ya. Gerlovin, V. V. Ovsyankin, B. V. Stroganov and V. S. Zapasskii, *Nanotechnology* **11** 383–386 (2000).
- [3] J. Shah, *Ultrafast Spectroscopy of Semiconductors and Semiconductor Nanostructures* Springer, Berlin, Chap. 2, 1996.
- [4] A. L. Ivanov, H. Wang, J. Shah, T. C. Damen, L. V. Keldysh, H. Haug and L. N. Pfeiffer, *Phys. Rev. B* **56**, 1 (1997).
- [5] V. M. Axt, K. Victor and T. Kuhn, *Phys. Status Solidi B* **206**, 189 (1998).
- [6] Th. Ostreih, K. Schonhammer and L. J. Sham, *Phys. Rev. B* **58**, 12920 (1998).



## Exciton states of nano-islands in ZnCdSe quantum wells

A. Reznitsky<sup>†</sup>, A. Klochikhin<sup>†‡</sup>, S. Permogorov<sup>†</sup>, I. Sedova<sup>†</sup>, S. Sorokin<sup>†</sup>,  
S. Ivanov<sup>†</sup>, M. Schmidt<sup>§</sup>, H. Kalt<sup>§</sup> and C. Klingshirn<sup>§</sup>

<sup>†</sup> Ioffe Physico-Technical Institute, St Petersburg, Russia

<sup>‡</sup> Petersburg Nuclear Physics Institute, 188350, St Petersburg, Russia,

<sup>§</sup> Universität Karlsruhe, Institut für Angewandte Physik, 76128 Karlsruhe, Germany

**Abstract.** The photoluminescence (PL) and PL excitation (PLE) spectra of quantum wells (QWs) formed by CdSe insertions in ZnSe matrix reveal the states of heavy and light excitons localized in CdSe-rich islands, and the energy  $E_{ME}$  which is associated with the percolation threshold over the entire lateral plane of QW. The model calculations are performed which result in evaluation of the island mean size and composition of ZnCdSe solid solution within and outside of islands.

### Introduction

Structural and spectroscopic studies has established that the QWs formed by MBE insertion of CdSe in ZnSe demonstrate strongly inhomogeneous distribution of composition along the QW plane resulting in formation of ZnCdSe nano-islands strongly enriched in CdSe content. In spite of the intensive studies of these quantum objects during last years, the interpretation of exciton spectra of QWs with islands still remains controversial.

As it was shown by different structural techniques, CdSe is distributed over several atomic planes perpendicular to the growth direction ( $z$ ) even for sub-monolayer depositions, forming the ZnCdSe QWs with diffusion profile[1, 2]. The increase of the amount of deposited CdSe do not change strongly the  $z$ -profile of QW. Instead, the formation of ZnCdSe nano-islands (with lateral dimensions about 5–10 nm), imbedded in ZnCdSe solid solution with much smaller CdSe content, takes place in ( $x,y$ ) QW plane.

In present paper we discuss a new insight into the internal electronic structure of QWs with islands based on the study of PL and PLE spectra and complementing data on the QW microscopic structure.

### Experimental results

We have studied ZnCdSe single QWs formed by the migration enhanced epitaxy using the multi-cycled deposition of CdSe on the ZnSe surface[3] with the total deposited CdSe amount between 1.5 and 3 monolayers (ML). Average CdSe mole fraction within the QWs ranges within 35–50%. As it is established by HRTEM, the mean spatial extension of the ZnCdSe QW in the growth direction is about 5 ML, the mean lateral island size is about 3–5 nm, and the mean island separation exceeds by two times the lateral island size. The micro-PL spectra has revealed the fine structure of sharp lines corresponding to the emission of exciton states confined in particular islands, which is mostly evident on the low energy wing of the PL band.

The PLE spectra presented in Fig. 1 show that the shape of the spectrum strongly depends on the detector position in the PL band.

For high energy part of the PL band the PLE spectra exhibit pronounced oscillating structure which indicates the relatively short life-times of the emitting states and can be

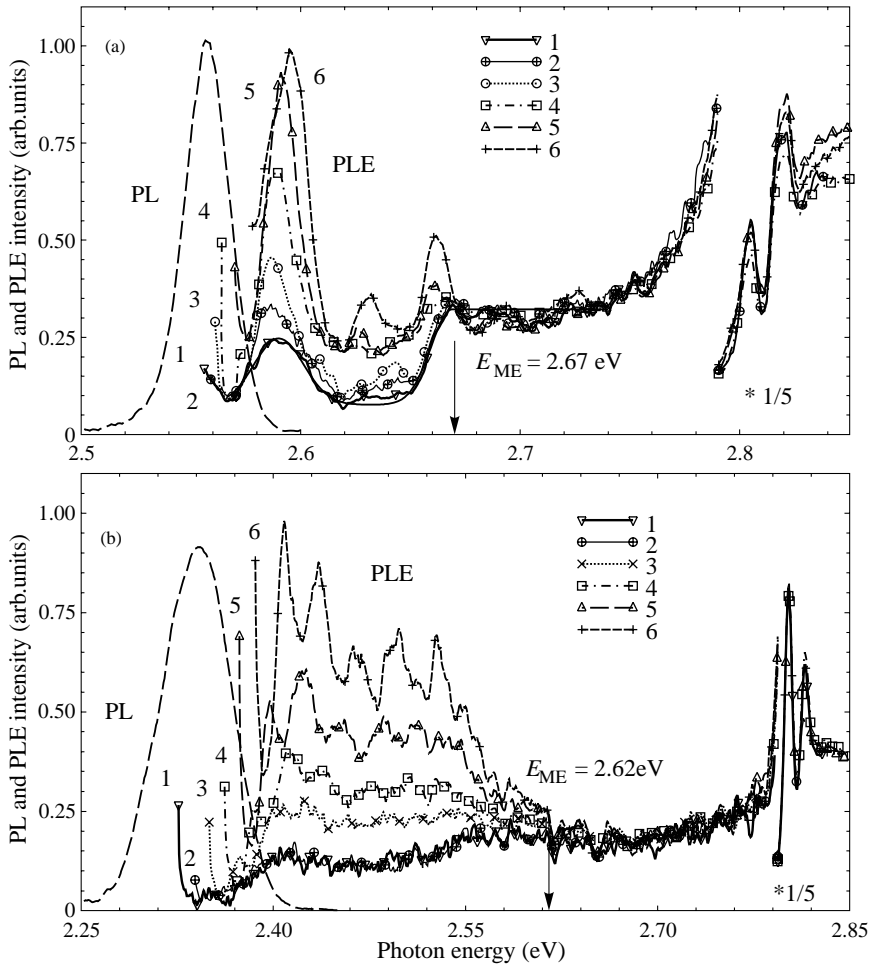


**Fig. 1.** PL and PLE spectra of SQWs formed by MBE insertion in ZnSe of  $5 \times 0.3$  ML CdSe (a) and  $8 \times 0.37$  ML CdSe (b). PLE spectra are taken for detector positions (in eV): (a) 1 — 2.545; 2 — 2.550; 3 — 2.555; 4 — 2.560; 5 — 2.565; 6 — 2.570; (b) 1 — 2.316; 2 — 2.328; 3 — 2.340; 4 — 2.352; 5 — 2.364; 6 — 2.376; Arrows  $E_{ME}$  indicate the position of exciton mobility edge in the corresponding systems (see text). Note the change of intensity scale at 2.79 eV.

assigned to the recombination of excited island states[4]. The PLE spectra of the low energy wing of PL band show no oscillating structure and contain relatively broad bands (2.59 and 2.41 eV for spectra shown in Fig. 1(a) and (b), respectively) the shape of which is much less sensitive to the position of detector. We have attributed this band to absorption by s-type LHE island states for which a large oscillator strength is expected. Our model calculations confirm this assignment.

As it was shown in Ref. [4], the PLE spectra being normalized at a proper energy practically coincide above a definite energy  $E_{ME}$  situated well below the band gap of ZnSe barrier. The shape of PL band is sensitive to excitation energy at excitation below  $E_{ME}$  and do not depend on it when excited above  $E_{ME}$ . The excitation at  $\omega < E_{ME}$  creates excitons

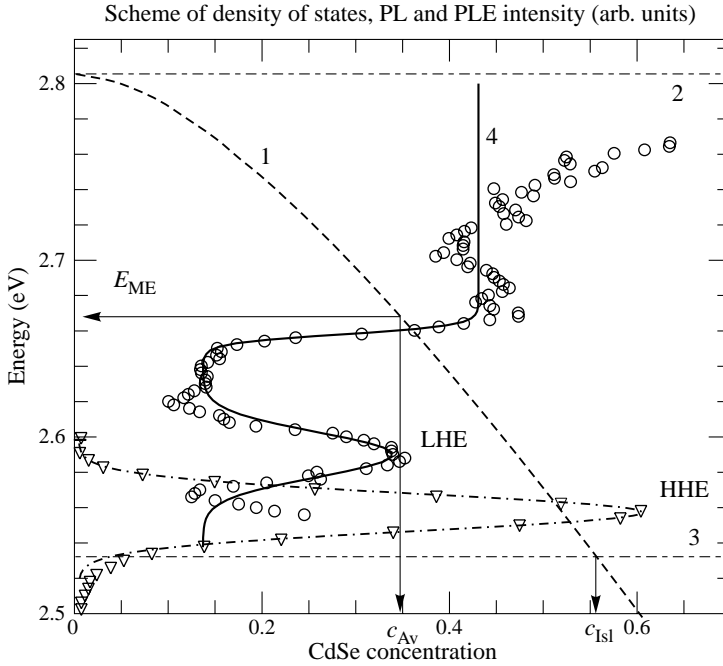


**Fig. 2.** Schematic representation of exciton states in ZnCdSe QWs with islands for sample in Fig. 1(a). Dashed curve 1 shows the size-quantized energy for the center of mass of 2D exciton in 5ML ZnCdSe QW as a function of average CdSe concentration. Lines 2 and 3 are the ZnSe barrier exciton energy and the bottom energy of islands, respectively. Curve 4 represents schematically the density of exciton states responsible for excitation of ground states in PL. Arrow  $E_{ME}$  indicates the position of the mobility edge. The experimental points show PL band (triangles) and trace 1 in PLE (circles) spectra from Fig. 1(a).

localized within particular islands whereas excitons produced at  $\omega > E_{ME}$  are able to move along the entire QW plane. At excitation via the localized states the PL spectrum is formed by the selected set of the islands having the electronic levels at proper energies. On contrary, the exciton states extended along the QW plane can be further captured by any of the available islands. On these grounds the energy  $E_{ME}$  can be considered as an exciton percolation threshold in QW containing nano-size islands with enhanced content of the narrow-gap component of the solid solution.

### Model for the energy spectrum of ZnCdSe QWs with islands

We have calculated the concentration dependence of size quantization energy for the QW with 5 ML FWHM having a diffusional profile (curve 1 in Fig. 2).

The average concentration of CdSe  $c_{Av}$  in the ZnCdSe regions surrounding the islands governs the energy position of the mobility edge  $E_{ME}$ . Above this level the motion of 2D excitons in (x,y) plane of QW can be considered as free, while below  $E_{ME}$  all exciton states are localized in potential wells of CdSe enriched islands. The exciton states in these wells are confined in (x,y) plane with the level positions being determined both by the mean CdSe concentration within the islands  $c_{Isl}$  and the island (x,y) dimensions. The calculation shows

that the heavy hole exciton (HHE) ground state energy is close to potential well bottom for island size and well depth more than 3 nm and 0.1 eV, respectively. At the same time, the energy level position of excitons formed by light hole (LHE) is more sensitive to island size. The different dependence of HHE and LHE localization energy on island lateral (x,y) size and composition  $c_{\text{Isl}}$  can be used to determine the mean island size and composition by fitting the experimental results.

We have performed the model calculations of exciton energy levels in the systems studied. As an energy of HHE level we have used the position of PL band maximum while the PLE band located at high energy side of PL band was considered as LHE position. Fitting of these values by the model has allowed us to obtain the self-consistent values of mean concentration of CdSe inside the islands and mean lateral dimensions of the islands. Using the ratio  $M_{\text{HHE}}/M_{\text{LHE}} = 5$  we have obtained  $c_{\text{Isl}} = 0.56$  and lateral dimensions of 3.7 nm for the sample shown in Fig. 1(a) and 0.9 and 4.1 nm for the sample in Fig. 1(b) which is in good agreement with the results of HRTEM studies. The mean concentration of CdSe in ZnCdSe solution between the islands in QWs, estimated by the  $E_{\text{ME}}$  positions, are  $c_{\text{Av}} = 0.35$  and 0.4 for these two samples, respectively.

## Conclusion

In conclusion, we have shown that the optical spectroscopy in conjunction with a rather simple model can be used for estimation of the mean CdSe concentrations in islands and in the surrounding solution, as well as for determination of the mean lateral dimensions of the islands in highly inhomogeneous ZnCdSe QWs. The obtained estimations should be considered as a first approximation and a proper account for influence of strains on the level positions is necessary to obtain more reliable values.

## Acknowledgments

Authors are thankful to D. Litvinov, A. Rosenauer and D. Gerthsen for preliminary information on HRTEM data. This work is partly supported by Russian Foundation for Basic Research, Russian program "Low-Dimensional Quantum Structures" and Deutsche Forschungsgemeinschaft.

## References

- [1] R. N. Kyutt *et al*, *Appl. Phys. Lett.* **75**, 373 (1999).
- [2] N. Peranio *et al*, *Phys. Rev. B* **61**, 16015 (2000).
- [3] S. Sorokin *et al*, *J. Cryst. Growth* **201/202**, 461 (1999).
- [4] A. Reznitsky *et al*, *phys. stat. sol. (b)* **229**, n.1/2 (2002).

## Inhomogeneous luminescence of slow polaritons from near-surface two-dimensional excitonic system

T. V. Teperik and V. V. Popov

Institute of Radio Engineering and Electronics, RAS, 410019 Saratov, Russia

**Abstract.** The problem of spontaneous emission of free polaritons from two-dimensional (2D) excitonic system is solved for the case of asymmetric dielectric environment of 2D excitonic system. The dispersion and radiative decay rates of resonant polaritons are calculated. The most of attention is given to slow resonant polaritons whose phase velocity is less than the speed of light in the ambient medium. The conclusion is drawn that the slow resonant polaritons can be observed in time-resolved photoluminescence experiments on near-surface 2D excitonic systems at grazing angles of emission.

### Introduction

The properties of resonant (radiative) polaritons in two-dimensional (2D) excitonic systems were theoretically studied in [1–4]. All cited papers were restricted to the case of symmetric dielectric environment of 2D excitonic system and a photon quasi-continuum was actually represented by a spectrum of electromagnetic (EM) eigen-modes of a cavity of infinite size. This implies that both incoming and outgoing homogeneous plane EM waves are present at the plane of 2D excitonic system. There are three optically active exciton-polariton modes were found, which are called T, L and Z modes [2]. These modes are distinguished by their electric field polarisation. The T mode has a  $s$  (or TE) polarisation whereas L and Z modes have  $p$  (TM) polarisation. In a symmetric dielectric environment, L and Z modes exhibit even and odd distributions of in-plane components of electric field across 2D excitonic layer, respectively. The resonant excitons and exciton-polaritons in GaAs/AlGaAs quantum wells (QWs) were experimentally observed [5, 6].

In this paper we consider the case of asymmetric dielectric environment of 2D excitonic system. Such a situation is typical for near-surface excitonic layers where the dielectric constant of an ambient medium is much less than that of a substrate [7]. In contrast to [2–4], we represent the radiation field in each surrounding medium (in the ambient one and in the substrate) as a single outgoing plane inhomogeneous EM wave that satisfies the scattering conditions at infinity away from 2D excitonic system. The adoption of this ansatz for EM field allows us to cover the region of slow polaritons, i.e. of those whose phase velocity is less than the speed of light in the ambient medium. We conclude that slow resonant polaritons may be observed in time-resolved photoluminescence (PL) experiments at grazing angles of emission.

### 1. Model and basic equations

Let a thin excitonic layer locate at the  $x$ – $y$  plane of the interface between two optically inactive media with dielectric constants  $\varepsilon_1$  and  $\varepsilon_2$  (the  $z$  axis is directed from medium 2 to medium 1). We search for a solution of the Maxwell equations with a spatio-temporal dependence of EM field in the form of a plane wave  $\exp[i(k_{\parallel}x + k_z^{(j)}z - \tilde{\omega}t)]$  in the

$j$ th medium ( $j = 1, 2$ ), where  $k_{\parallel}$  and  $k_z$  are the in-plane and transverse wavevectors, respectively, which are related by the relationship

$$\left(k_z^{(j)}\right)^2 + k_{\parallel}^2 = \left(\frac{\tilde{\omega}}{c}\right)^2 \varepsilon_j. \quad (1)$$

Here  $c$  is the speed of light in the vacuum. We describe the response of excitonic material by a local dielectric function of the Lorentzian type  $\varepsilon(\tilde{\omega}) = \varepsilon_b[1 + \omega_{\text{LT}}/(\omega_0 - \tilde{\omega} - i\gamma_d)]$ , where  $\varepsilon_b$  is a background dielectric constant,  $\omega_0$  and  $\omega_{\text{LT}}$  are the exciton frequency and longitudinal-transverse (LT) splitting, respectively,  $\gamma_d$  is the exciton damping due to all relaxation processes except radiative decay.

We approximate the discontinuity of in-plane components of electric and magnetic fields across a thin excitonic layer with effective boundary conditions (EBCs) at  $z = 0$ :

$$\mathbf{E}_{\parallel}^{(1)} - \mathbf{E}_{\parallel}^{(2)} = \frac{i}{2} \chi_z \mathbf{e}_x k_{\parallel} \left( \varepsilon_1 E_z^{(1)} + \varepsilon_2 E_z^{(2)} \right), \quad (2)$$

$$\mathbf{H}_{\parallel}^{(1)} - \mathbf{H}_{\parallel}^{(2)} = \frac{i\tilde{\omega}}{2c} \chi_{\parallel} \mathbf{e}_z \times \left( \mathbf{E}_{\parallel}^{(1)} + \mathbf{E}_{\parallel}^{(2)} \right), \quad (3)$$

where  $\chi_z = [\varepsilon_b - \varepsilon(\tilde{\omega})]L_z/\varepsilon_b\varepsilon(\tilde{\omega})$ ,  $\chi_{\parallel} = [\varepsilon(\tilde{\omega}) - \varepsilon_b]L_z$ ,  $\mathbf{e}_x$  and  $\mathbf{e}_z$  are the unit vectors of the  $x$  and  $z$  co-ordinate axes,  $L_z$  is the thickness of excitonic layer. Boundary conditions (2) and (3) are just an obvious generalisation of EBCs used in [4] to the case of different dielectric constants of surrounding media. Implication of the boundary conditions (2) and (3) produces the following dispersion relations:

$$k_z^{(1)} - k_z^{(2)} = i\chi_{\parallel} \left( \frac{\tilde{\omega}}{c} \right)^2 \quad (4)$$

for TE (or T) mode and

$$\frac{ik_{\parallel}^2 \varepsilon_1 \chi_z + k_z^{(1)}}{ik_{\parallel}^2 \varepsilon_2 \chi_z - k_z^{(2)}} = \frac{ik_z^{(1)} \chi_{\parallel} - 2\varepsilon_1}{ik_z^{(2)} \chi_{\parallel} + 2\varepsilon_2} \quad (5)$$

for TM modes.

Bearing in mind the experimental situation of spontaneous EM emission from coherent polariton modes in 2D excitonic system we assume that the in-plane wavevector  $k_{\parallel}$  is a real-valued quantity. Then we have to treat the frequency and transverse wavevectors in Eqs. (1) to (5) as a complex-valued quantities  $\tilde{\omega} = \omega - i\gamma$  and  $k_z^{(j)} = \text{Re}k_z^{(j)} + i\text{Im}k_z^{(j)}$ . The real part of the complex-valued frequency gives the polariton eigen-frequency and the imaginary part  $\gamma$  is the total decay rate. It is obvious that  $\gamma = \gamma_r$ , the radiative decay rate, if we neglect all non-radiative relaxation processes ( $\gamma_d = 0$ ). The scattering conditions at  $z \rightarrow \pm\infty$  are satisfied with choosing  $\text{Re}k_z^{(1)} > 0$  and  $\text{Re}k_z^{(2)} < 0$  that corresponds to the waves outgoing away from the excitonic layer into media 1 and 2. We evaluate the index of exponential inhomogeneity of the emitted wave in the plane of the wave front as  $\alpha_{\text{inh}}^{(j)} = k_{\parallel} \text{Im}k_z^{(j)} / \sqrt{k_{\parallel}^2 + (\text{Re}k_z^{(j)})^2}$  in the  $j$ th medium ( $j = 1, 2$ ).

## 2. Results and discussion

One can see from Figure 1(a) that in asymmetric environment  $\varepsilon_1 \neq \varepsilon_2$  all modes exhibit non-zero radiative decay in the slow-wave region of the  $\omega$ - $k_{\parallel}$  plane for the ambient medium

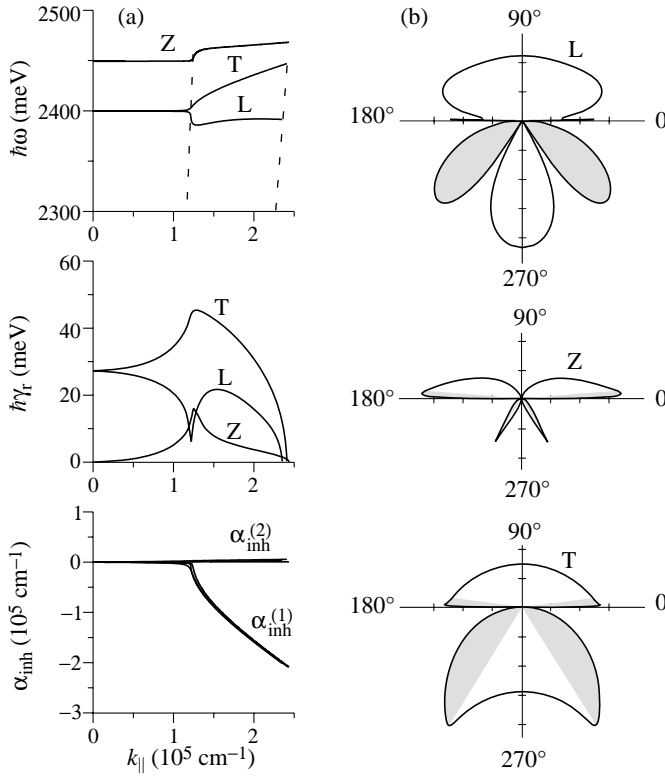


**Fig. 1.** (a) Resonant exciton-polariton dispersion  $\omega(k_{||})$ , radiative decay rate  $\gamma_r$  and inhomogeneity of emitted EM wave  $\alpha_{\text{inh}}^{(j)}$  as functions of in-plane wavevector. Dependencies  $\alpha_{\text{inh}}^{(j)}(k_{||})$  for different polariton modes are scarcely resolved on a choosing scale. Straight dashed lines mark dispersions of bulk photons in media 1 and 2. (b) Angular patterns of EM emission from resonant polariton modes. The angle of emission  $\theta$  is reckoned from the plane of 2D excitonic system. Angles  $0 < \theta < 180^\circ$  correspond to emission into the ambient medium whereas angles  $180^\circ < \theta < 360^\circ$  correspond to emission into the substrate. Parameters used are as follows [8]:  $\hbar\omega_0 = 2400 \text{ meV}$ ,  $\hbar\omega_{\text{LT}} = 50 \text{ meV}$ ,  $\varepsilon_b = 4.41$ ,  $L_z = 30 \text{ nm}$ ,  $\varepsilon_1 = 1$ ,  $\varepsilon_2 = 3.8$  (quartz).

(the one with lower dielectric constant). Of course, in this case L and Z modes have no definite parities of their electric field distributions about the  $z$  axis. Nevertheless, we will continue to denote the lower and upper TM branches as L and Z modes, respectively. The inhomogeneity of EM wave emitted into the ambient medium increases drastically in the slow-wave region. The phase velocity of inhomogeneous plane EM wave appears to be less than the speed of light in corresponding medium. The stronger the inhomogeneity of the wave the slower the wave. Thus it is just the strong inhomogeneity of the emitted EM wave what makes the radiative decay of slow polaritons into ambient medium possible. Note that the inhomogeneity of emitted wave acquires opposite signs in different media.

Figure 1(b) shows angular patterns of the EM energy emission flux density for the resonant polariton modes. Slow polaritons luminesce at angles inside the shaded regions of emission patterns. The side lobes of the emission pattern for L mode owe their origin

entirely to the luminescence of slow polaritons. These side lobes are strongly developed in the substrate while in the ambient medium they look just like thin needles directed nearly parallel to the plane of 2D excitonic system. We conclude that slow resonant polaritons can be observed in time-resolved PL experiments on near-surface 2D excitonic systems at grazing angles of emission. The slow polaritons can be identified by an angular dependence of the emission frequency that arises from pronounced dispersion of polaritons in the slow-wave region.

#### *Acknowledgements*

We are grateful to S. G. Tikhodeev for stimulating discussions. This work was performed under the Russian Research Program "Physics of Solid State Nanostructures".

#### **References**

- [1] E. L. Ivchenko, *Sov. Phys. Solid. State* **33**, 1344 (1991).
- [2] F. Tassone, F. Bassani and L. C. Andreani, *Phys. Rev. B* **45**, 6023 (1992).
- [3] S. Jorda, U. Rössler and D. Broido, *Phys. Rev. B* **48**, 1669 (1993).
- [4] R. Atanasov, F. Bassani and V. M. Agranovich, *Phys. Rev. B* **49**, 2658 (1994).
- [5] M. W. Berz, L. C. Andreani, E. F. Steingmeier and F. K. Rein, *Solid State Commun.* **80**, 553 (1991).
- [6] B. Deveaud, F. Clérot, N. Roy, K. Satzke, B. Sermage and D. S. Katzer, *Phys. Rev. Lett.* **67**, 2355 (1991).
- [7] N. A. Gippius, A. L. Yablonskii, A. B. Dzyubenko, S. G. Tikhodeev, L. V. Kulik, V. D. Kulakovskii and A. Forchel, *J. Appl. Phys.* **83**, 5410 (1998).
- [8] T. Fujita, Y. Sato, T. Kuitani and T. Ishihara, *Phys. Rev. B* **57**, 12428 (1998).



## Nanostructures on flexible substrates

*M. S. Shur*<sup>†</sup>, *S. L. Rumyantsev*<sup>‡</sup> and *R. Gaska*<sup>†</sup>

<sup>†</sup> Electrical, Computer and Systems Engineering Department  
Rensselaer Polytechnic Institute, Troy, NY 12180-3590

<sup>‡</sup> Ioffe Physico-Technical Institute, St Petersburg, Russia

**Abstract.** We report on fabrication, characterization, and properties of nanocrystalline semiconductor films and thin-film devices chemically deposited on fibers, cloth, and large area flexible substrates at low temperatures (close to room temperature). We also describe the photovoltaic effect in CdS/CuS films deposited on viewfoils and trylene threads. CdS films deposited on viewfoils exhibit unique behavior under stress and UV radiation exposure with reproducible resistance changes of several orders of magnitude with bending up to 10 mm curvature. The measurements of the  $1/f$  noise in these nanocrystalline structures indicate a high quality of nanocrystallites.

## Introduction

The progress in microelectronics has been associated with scaling of the minimum feature size of integrated circuits. This trend described by the famous Moore's law is now running out of steam as this minimum feature size approaches the values where limitations related to non-ideal effects become important or even dominant. At the same time, the opposite trend of increasing the overall size of integrated circuits has emerged stimulated primarily by the development of flat panel displays. Emerging technology of nanostructures on flexible substrates promises to merge these opposing trends and lead to the development of ultra large area integrated circuits embedded into electrotexiles or into stretchable and flexible "sensitive skin". The "sensitive skin" [1, 2] will revolutionize robotics by enabling the creation of robots functioning in unstructured environments, such as school yards, nursing homes, or battle fields and will find many other applications in medicine, biotechnology, home security, and defense. Electrotextile technology that aims to scale up the size of electronic circuits to the size of a human being and beyond exemplifies this merging of scaling-up trend with nanostructures. We can distinguish three distinct directions in this field that might eventually merge together in electrotextile systems: conducting textiles, wearable electronics, and semiconducting films and devices embedded into electrotexiles. This paper deals with the latter technology that will benefit from using nanostructures. In Section 1, we discuss  $A_2B_6$  and  $A_4B_6$  nanostructured semiconducting films. Section 2 reviews emerging semiconductor devices on flexible substrates and cloth using  $A_2B_6$  and  $A_4B_6$  semiconducting films.

### 1. $A_2B_6$ and $A_4B_6$ semiconducting films for electrotextile applications

Our approach to fabricating semiconductor films for electrotexiles is based on the process of depositing nanocrystalline CdSe (1.75 eV), CdS (2.4 eV), PbS (0.4 eV), PbSe (0.24 eV) and  $Cu_xS$  (semiconductor/metal) films on flexible substrates or threads at temperatures close to room temperature [3]. Large area surfaces can be covered. We have covered areas up to  $8 \times 11$  inches but the process can be scaled up. These semiconducting and metal films will serve as building blocks for thin-film technology, which will enable us to develop the sensitive skin and/or electrotextile arrays.

The chemical deposition of the films is very simple and reproducible. Low deposition temperature allows for the thin film deposition on thermally unstable substrates.

The basic deposition scheme is described in Ref. [4] using CdSe films as an example. Thin films of CdSe, CdS, PbS and CuS are deposited using the water solutions of the corresponding complex-salt compounds containing the relevant elements. References [4, 5] describe properties of chemically deposited CdSe films. Typical thickness of the films deposited in one cycle at room temperature was approximately 0.5 mm. The films exhibited nanocrystalline structure with the average grain size around 0.12–0.15 mm. The results of X-ray studies showed that the inter-grain material consists of CdSe nanocrystals with the size ranging from 0.007 mm to 0.01 mm. This inter-grain material plays a very important role for the improved adhesion and stability of the films deposited on flexible substrates. After the deposition, CdSe films exhibited a significant photosensitivity in a visible spectral range. Also, a large persistent photoconductivity was observed after a UV illumination.

Using a similar process, we have also deposited  $\text{Cu}_x\text{S}$  on flexible substrates. (The type of conductivity depends on the molar fraction of Cu.) Metallic CuS films are expected to be suitable for fabrication of interconnects for sensor arrays.

The CdS films were deposited at temperatures 60–70 °C from solutions containing cadmium citrate complex-ions and thiourea. A Scanning Electron Microscope (SEM) study revealed that the CdS films deposited on the viewfoil are very homogeneous. No distinguishable structure of the layers has been found with the characteristic dimension of the fraction of microns. The structure of the layers deposited on the threads was more complicated: CdS films deposited on threads are not uniform and contain some insertions and cracks.

To investigate the crystal structure further, the CdS films with reduced thickness were deposited on a nickel grid [6]. Since this grid was transparent for the electron beam of the High Resolution Transmission Electron Microscope (HRTEM), we were able to study the CdS structure in the corner of the grid. Figure 1 shows the HRTEM picture with a high magnification, such that single crystallites and atomic layers can be distinguished. The size of the crystallites is about 3 to 5 nm. The crystallites are separated from each other by amorphous CdS.

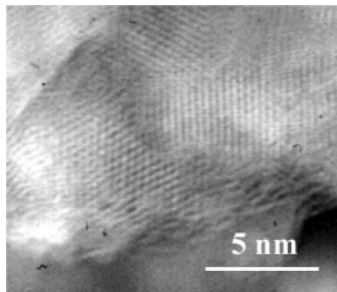


**Fig. 1.** HRTEM picture [6].

The CdS films are very sensitive to illumination. The resistance change under UV illumination is over seven orders of magnitude. The measurements of the spectral responsivity indicated that the spectral response is consistent with the bandgap of the hexagonal CdS (2.45 eV). All films demonstrated a slow response to the illumination. We also found that the characteristic time of the photoconductivity increase depends on the light wavelength: the shorter is the wavelength, the slower is the current increase under illumination.

These CdS films are also very sensitive to the stress (tension) under UV illumination.

In order to study the stress sensitivity we bent the viewfoil with the deposited CdS film as shown in the inset in Fig. 2.

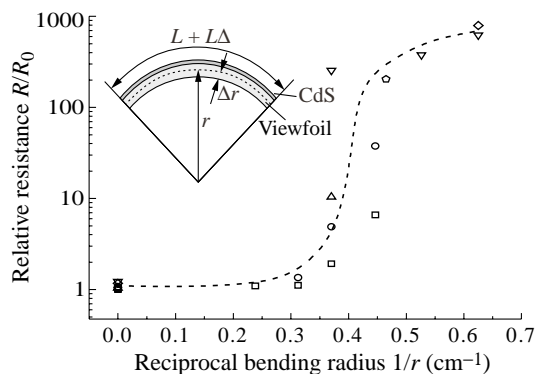


**Fig. 2.** Relative change in the film resistance under UV illumination versus reciprocal bending radius. The inset shows how the film was bent [6].

The dependence of the structure resistance normalized to the unstressed resistance as a function of the reciprocal radius  $r$  of the film bending is shown in Fig. 2. Different symbols correspond to different measurement sessions on the same sample. The sample was illuminated with the diffused light of the xenon lamp. As seen, the resistance under tension increases by several orders of magnitude. Symbols at  $1/r = 0$  (no strain) show the value of the initial resistance ( $R/R_0 = 1$ ) and the value of the resistance after every measurement. These data show that the change in the resistance under stress is reproducible. This reproducibility might be explained by the film structure, which consists of nanocrystallites separated by elastic amorphous CdS (see Fig. 1).

One of the most important characteristics of the piezoresistive sensors is the gauge factor defined as:  $G = (\Delta R/R_0)/(\Delta L/L_0)$ , where  $L$  is the sensor length. As follows from the inset in Fig. 2,  $\Delta L/L \approx \Delta r/r$ , where  $\Delta r = 50 \mu\text{m}$  is the half of the viewfoil thickness. We found the maximal value  $G \approx 10^5$  for our CdS films, that is several orders of magnitude larger than that for metal ( $G = 1-2$ ) and regular semiconductor piezoresistive sensors ( $G \approx 10^2$ ).

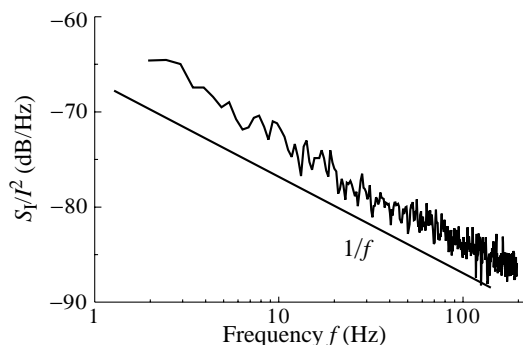


**Fig. 3.** Low frequency noise spectrum for CdS film.

Figure 3 shows the low frequency noise spectra of CdS film measured under illumination by a low noise halogen lamp. As seen, the spectrum has the  $1/f$  form. In order to estimate

the Hooge parameter  $\alpha = (S_I/I^2)fN$ , the total number of carriers  $N$  was found from the sample resistance as  $N = L^2/Rq\mu$  (Here  $L$  and  $R$  are the sample length and resistance, respectively, and  $\mu$  is the mobility.) We estimated the electron mean free path,  $l$ , to be on the order of the nanocrystallite size, e.g. 5 nm. This allowed us to estimate the electron mobility,  $\mu = ql/m^*v = 100 \text{ cm}^2/\text{Vs}$ , where  $q$  is the electron charge,  $m^*$  is the effective mass, and  $v$  is the thermal velocity. Using this value of  $\mu$ , we found  $\alpha = 3 \times 10^{-3}$ . This value indicates the level of the  $1/f$  noise of the same order of magnitude as in good quality polycrystalline films (Si, CdSe) deposited on nonflexible substrates.

## 2. $\text{A}_2\text{B}_6$ and $\text{A}_4\text{B}_6$ semiconductor devices on flexible substrates and cloth

A solar cell on a flexible substrate was fabricated by depositing a set of the CuS and nickel contact stripes on a viewfoil. These sets of contacts represented “ohmic” and “non-ohmic” contacts, respectively. Then CdS films of approximately 0.5  $\mu\text{m}$  thick were deposited on top using the water solutions of complex-salt compounds.

Figure 4 shows typical current-voltage characteristics under UV illumination. As seen from the figure, both the open circuit voltage and the fill factor are quite low. As shown in [7] the reason for the low fill factor is a high series resistance.

These results clearly demonstrate a feasibility of fabricating CdS solar cells on flexible substrates that also might cover surfaces of complex geometry. These cells might find applications for autonomous power sources, especially for naval and marine applications, where such autonomous source placed, for example, on a buoy might collect sunlight for different sun orientations throughout the day.

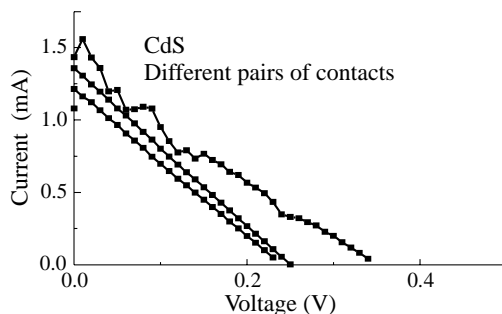


**Fig. 4.** Measured current-voltage characteristics under light [7].

In Reference [8], we reported on the photovoltaic effect in CdS/CuS films deposited on trylene threads. This technology should lead to the development of solar cells on textiles for harvesting solar energy using electro textiles and for providing renewable power source for wearable electronics.

In Fig. 5, line 1 shows the current-voltage characteristic of the semiconducting thread with two different contacts (aluminum and nickel) under illumination with the xenon lamp. For comparison, we also show the current-voltage characteristics of a conventional CdS solar cells [9] (lines 2 and 3) and of the CdS photovoltaic element fabricated on the viewfoil [7] (line 4). In this figure, the light generated current is normalized to its maximum value (the actual measured values at  $V = 0$  were 5 nA, 1 mA and 50 mA for thread, viewfoil and conventional photovoltaic element, respectively). As can be seen, the photovoltaic voltage for the semiconducting thread is close to that for the CdS solar cell. A relatively low fill factor can be explained by a large series resistance. These results clearly demonstrate a feasibility of fabricating CdS solar cells on cloth.

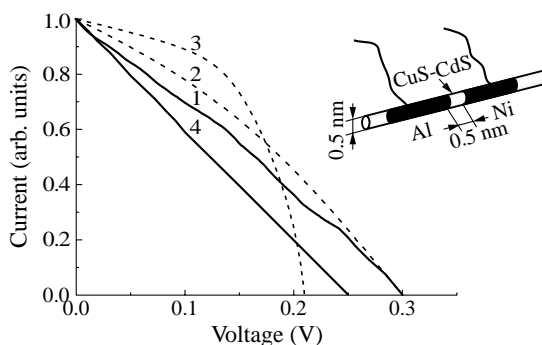


**Fig. 5.** Current voltage characteristics under illumination for semiconducting thread (curve 1), conventional CdS-based solar cells (curves 2 and 3), and for semiconducting viewfoil (curve 4). The current is normalized to its maximum value at  $V = 0$  [8].

### 3. Conclusions

Many challenges have to be addressed to develop practical nanostructure technology on flexible substrates. These challenges include the development of reliable low temperature deposition technology for depositing semiconducting films on threads and cloth, the development of flexible/stretchable metal and transparent metal films, the demonstration of semiconductor heterostructures on threads and cloth, the development of ultra large area (length) continuous material deposition and processing. As the first step, basic device building blocks have to be demonstrated and optimized. These device building blocks include flexible, stretchable ohmic and Schottky contacts, p-n junctions, Metal-Insulator-Semiconductor structures, and heterostructure diodes. Our group recently demonstrated field effect in PbS deposited on a flexible metal wire. The development of thin film transistors is now under way. Once the materials and device problems are solved, a variety of important issues related to systems, subsystems, energy harvesting, and communication on cloth and on “sensitive skin” will have to be addressed. Some of these problems have been discussed in Ref. [1, 2]. However, the work has just begun. Quoting Samuel Butler, “Our minds want clothes as well as our bodies”.

### References

- [1] V. Lumelsky, M. S. Shur and S. Wagner, Editors, *Sensitive Skin*, World Scientific, ISBN 981-02-4369-3, 2000
- [2] V. Lumelsky, M. S. Shur and S. Wagner, *IEEE Sensors Journal* **1**, 41 (2001).
- [3] J. Sinius et al., *Radio electronics, Vilnius, Technika* **30**, 170 (1994).
- [4] J. Soltys, J. Sinius and A. Sinius, *Surface Science* (1994).
- [5] R. Baltramiejunas, R. Gaska, E. Kuokstis and J. Sinius, *Fifth Conference on Physics and Applications of A<sup>2</sup>B<sup>6</sup> Compounds*, Vilnius, Lithuania, June 1983.
- [6] M. S. Shur, S. Rumyantsev, R. Gaska, B. Q. Wei, R. Vajtai, P. M. Ajayan and J. Sinius, *accepted for publication in Solid State Electronics* **1**, 41 (2001).
- [7] M. S. Shur, J. Sinius, R. Gaska and S. Rumyantsev, *Electron. Lett* **37**, 518 (2001).
- [8] M. S. Shur, G. Gaskiene, S. L. Rumyantsev, R. Rimeika, R. Gaska and J. Sinius, *Electron. Lett.* **37**, 1036 (2001).
- [9] R. K Pandey, S. Mishra, S. Tiwari, P. Sahu and B. P. Chandra, *Solar Energy Mater. and Solar Cells* **60**, 59 (2000).

## Author Index

**Abstreiter G.**, 2, 187, 385

Adam T. N., 441

Aderhold J., 78

Akasaki I., 72

Akopyan A. Kh., 292

Alam A., 82

Alekseenko M. V., 168

Aleshkin V. Ya., 203, 221, 229

Alferov Zh. I., 399

Alshanskii G. A., 210

Altukhov I. V., 445

Amand T., 463

Amann A., 245, 371

Amann M.-C., 385

Amano H., 72

Andersson T. G., 331

Andreev A. D., 229

Andronov A., 449

Aneeshkumar B., 249

Ankudinov A., 157

Aparshina L. I., 534

Arapov Yu. G., 210

Arseev P. I., 154

Arzberger M., 385

Aseev A. L., 339

Ashkinadze B. M., 508

Astakhov G. V., 93, 594

Aulenbacher K., 473

Averkiev N. S., 249, 315

Avrutin E. A., 425

Avrutin V., 524

**Baidakova M. V.**, 164

Bairamov B. H., 283

Bairamov F. B., 283

Baksheev D. G., 339

Banshchikov A. G., 22

Baranov A. V., 279

Baryshev A. V., 120

Bauer G., 147

Bayer M., 584

Bazhenov N., 157

Bechstedt F., 78

Becker C., 389

Bel'kov V. V., 187

Benedek G., 199

Benedict K. A., 327

Berezovets V. A., 542

Berggren K.-F., 303

Bergman J. P., 72

Bernier P., 343

Bernstein G. H., 486, 491

Bigenwald P., 97

Bimberg D., 12, 271, 375, 399

Bird J. P., 57

Birkedal D., 124

Birudavolu S., 20

Birukov A. A., 538

Blagnov P. A., 175

Blom A., 453

Bobyl A. V., 26

Borri P., 375

Boucher Y., 403

Bouchiat H., 343

Bouwmeester D., 495

Böttcher J., 574

Brasil M. J. S. P., 581

Bresler M. S., 433

Brett M. J., 112

Brunev D. V., 30

Brunkov P. N., 275

Brunner K., 187

Bryce A. C., 429

Brysgalov V. V., 168

Burbaev T. M., 195

Burdov V. A., 206

Burghard M., 343

Burkard G., 485, 577

Bychkov A. M., 495

**Cao Y.**, 57

Chao K.-A., 453, 457

Chaparo S., 57

Chaplik A. V., 270

Chemakin A. V., 34

Cherepanov V. A., 53

Cherkov A. G., 339

Chernykh A. V., 534

Chernyshova M., 160

Chirkova E. G., 445

Chi J. Y., 45, 175, 395

Christianen P. C. M., 249

- Chukalina M. V., 563  
 Cicoira F., 5  
 Cirlin G. E., 60, 179, 229, 271, 292  
 Citrin D. S., 266  
 Cohen E., 508  
 Cortez S., 463  
 Crooker S. A., 93  
**D**  
 Danilov S. N., 229  
 Davies J. J., 602  
 Davydov V., 279  
 Davydov V. Yu., 78, 164  
 de Visser A., 516  
 Deblock R., 343  
 Delimova L., 354  
 Demikhovskii V. Ya., 233  
 Deryagin A. G., 403  
 Deych L. I., 127  
 Diakonov A. M., 520  
 Dikme Y., 82  
 Dizhur S. E., 323  
 Díaz-Arencibia P., 598  
 Dneprovskii V. S., 287  
 Dogonkin E. B., 346, 437  
 Dolgikh Yu. K., 481, 606  
 Dorofeyev D. V., 407  
 Drachenko O., 389  
 Dremín A. N., 116  
 Drichko I. L., 520  
 Drozdov Yu. N., 183  
 Dubonos S. V., 311, 350  
 Dubrovskii Yu. V., 256, 331, 559, 563  
 Dvurechenskii A. V., 191  
**E**  
 Eastman L., 101  
 Eaves L., 256, 275, 327, 554, 559, 563  
 Efimov Yu. P., 481, 606  
 Efremov M. D., 179  
 Efros A. L., 105  
 Egorov V. A., 60, 179, 229  
 Ehehalt J., 271  
 El-Emawy A. A., 20  
 Eliseev P. G., 392  
 Eliseev S. A., 481, 606  
 Emtsev V. V., 78  
 Entin M. V., 237, 290  
 Erland J., 241  
 Evtikhiev V. P., 157, 287, 407  
**F**  
 Fafard S., 584  
 Farajian A. A., 528  
 Fedorov A. V., 279  
 Fedosov N. K., 229  
 Feick H., 77, 78  
 Feldmann J., 385  
 Felhner T. P., 486  
 Fernée M. J., 38  
 Fetisova N. V., 414  
 Filatov D. O., 516  
 Firsov D. A., 229  
 Firsov Yu. A., 512  
 Forchel A., 584  
 Fossard F., 229  
 Frahm J., 425  
 Frank S., 524  
 Fujiwara Y., 16  
 Furthmüller J., 78  
**G**  
 Gaikov D. V., 131  
 Gaisin V. A., 292  
 Gajiev G., 134  
 Galperin Yu. M., 520  
 Ganichev S. D., 187, 461  
 Gaponova D. M., 221, 229  
 Gaquiere C., 101  
 García-Rocha M., 89  
 Gaska R., 618  
 Gavrilenko V. I., 203, 221  
 Geim A. K., 311  
 Gerlovin I. Ya., 465, 481  
 Germanenko A. V., 538, 566  
 Gerstenbrandt G., 82  
 Gerthsen D., 49, 68  
 Gérard J-M., 463  
 Gindikin Ya., 300  
 Gippius N. A., 116, 138  
 Gladyshev A. H., 45, 60  
 Gobato Y. G., 581  
 Golikova E. G., 414  
 Golikov A. V., 516  
 Golubev V. G., 108, 134  
 Golub L. E., 477  
 Goncharuk I. N., 164  
 Gorbatov Yu. B., 343  
 Gorbenko O. M., 68  
 Gordeev Yu. S., 168  
 Goupalov S. V., 266  
 Graham A. C., 303  
 Grandjean N., 97  
 Graul J., 78

- Grekhov I., 354  
Grigoriev V. N., 241  
Grimmeiss H., 168  
Gubenko A., 425  
Gubin S. P., 368  
Gueron S., 343  
Gunko N. A., 437  
Gurevich A. S., 93  
Gurevich S. A., 41  
Gurtovoi V., 101  
Gurylev D. I., 252  
Gusev O. B., 433  
**H**  
Haller E. E., 78  
Haratizadeh H., 72  
Harima H., 78, 164  
Harrach D. v., 473  
Hashimoto A., 78  
Hawrylak P., 584  
Håkanson U., 263  
Heitz R., 271  
Henini M., 256, 283, 559, 563  
Henneberger F., 49, 418, 588  
Hernández-Calderón I., 89, 598  
Heuken M., 82  
Hill G., 256, 559, 563  
Hinzer K., 584  
Hirayama Y., 147  
Hoffmann P., 5  
Hong S., 497  
Hovenier J. N., 221  
Huffaker D. L., 20  
Huhtinen H., 157  
Hundt A., 588  
Hvam J. M., 124, 241  
**I**  
Ignatiev I. V., 465, 481  
Ikaida T., 147  
Il'inskii A. V., 108  
Ionov A. N., 531  
Ipatova I. P., 199  
Ivanov D. Yu., 559, 563  
Ivanov S. V., 78, 85, 610  
Ivchenko E. L., 187, 261, 469  
Iwaya M., 72  
**J**  
Jacobson M. A., 97  
Jansen R. H., 82  
Jappsen A.-K., 245  
Jbeli A., 463  
Johansson M. K.-J., 263  
Johnson S. R., 57  
John S., 112  
Jonge H., 534  
Journet C., 343  
Julien F., 229  
**K**  
Kachorovskii V. Yu., 319  
Kagan M. S., 445  
Kalevich V. K., 465  
Kalisch H., 82  
Kalt H., 610  
Kamiyama S., 72  
Kapitonov V. A., 395  
Kaplyanskii A. A., 120  
Kapteyn C., 271  
Karczewski G., 93, 594  
Karpov A. N., 30  
Karpov S. V., 164  
Kartenko N. F., 22  
Kasumov A. Yu., 343  
Kasumov Yu. A., 343  
Kaveev A. K., 22  
Kavokin A., 97  
Kavokin K. V., 465  
Kawazoe Y., 528  
Kazakov I. P., 195  
Kennedy S. R., 112  
Khanin Yu. N., 256, 331, 559  
Khitun A., 410, 497, 501  
Khodos I. I., 343  
Khomitsky D. V., 233  
Khomutov G. B., 368  
Kirienko V. V., 191  
Klingshirn C., 147, 610  
Kling R., 524  
Klinov D. V., 343  
Klitzing K. von, 1  
Klochikhin A. A., 78, 610  
Kochereshko V. P., 93, 287, 594  
Kocherscheidt G., 217  
Kociak M., 343  
Koeder A., 524  
Kokin A. A., 505  
Kolesov B. A., 179  
Kolobkova E. V., 131  
Kolodzey J., 441, 445  
Kolosanov V. A., 339  
Konnikov S. G., 26, 275  
Kop'ev P. S., 85



- Korkusinski M., 584  
 Korolev K. A., 445  
 Kosobukin V. A., 120  
 Kossut J., 594, 602  
 Kostko I. A., 437  
 Kotel'nikov I. N., 323  
 Kotelnikov E., 157  
 Kotelnikov E. Yu., 407  
 Koudinov A. V., 602  
 Kovalchuk A., 101  
 Kovsh A. R., 68, 175, 395, 399  
 Kowalczyk L., 160  
 Kozhevnikov V. M., 41  
 Kozlov D. V., 203, 221  
 Krasilnik Z. F., 183  
 Kratzert P., 49, 588  
 Krebs O., 463  
 Kress A., 584  
 Krier A., 381  
 Krizhanovskii D. N., 116  
 Kryzhanovskaya N. V., 45, 60, 395, 399  
 Kubler J., 425  
 Kuchinskii V. I., 403, 429  
 Kulakovskii V. D., 116  
 Kulbachinskii V. A., 516  
 Kulinkin B. S., 292  
 Kummamuru R., 491  
 Kummamuru R. K., 486  
 Kumzerov Yu. A., 512  
 Kunert R., 12  
 Kurbatov V. A., 195  
 Kurdyukov D. A., 108, 134  
 Kurtz E., 147  
 Kusrayev Yu. G., 602  
 Kuznetsov O. A., 210  
 Kuznetsov V. I., 350  
 Künzel H., 574  
 Kytin V. G., 516  
 Kyutt R. N., 164  
**L**  
 Laiho R., 157  
 Landwehr G., 594  
 Langbein W., 217, 375  
 Larionova V. A., 566  
 Larionov A., 584  
 Larkin I., 296  
 Lavallard P., 266  
 Ledentsov N. N., 60, 68, 229, 271, 395, 399  
 Lee C. P., 225  
 Lee H. C., 225  
 Lee W. S., 16  
 Lehmann U., 441  
 Lent C. S., 486, 491  
 Leotin J., 389  
 Leo K., 556  
 Leshko A. Yu., 414  
 Levinshtein M. E., 361  
 Levin A., 275  
 Leys M. R., 249  
 Lieberman M., 486  
 Limmer W., 524  
 Limonov M. F., 120  
 Ling C., 385  
 Liniichuk I., 354  
 Lin G., 395  
 Lipovskii A. A., 131  
 Lisyansky A. A., 127  
 Litvinenko U. L., 241  
 Litvinov D., 49  
 Litvin L. V., 339  
 Livshits D. A., 395  
 Lobanov D. N., 183  
 Loss D., 485, 577  
 Lozovik Yu. E., 172, 214  
 Luenenbuerger M., 82  
 Lundin W. V., 164  
 Lunin R. A., 516  
 Lyanda-Geller Yu., 584  
 Lyssenko V. G., 124, 241, 556  
 Lyubinskiy I. S., 319  
 Lyutetskiy A. V., 414  
**M**  
 Maan J. C., 311, 534  
 Magarill L. I., 237  
 Mahmoodian M. M., 237, 290  
 Main P. C., 256, 275, 559, 563  
 Makhonin M. N., 116  
 Maleev N. A., 395, 399  
 Malikov I. V., 534  
 Malloy K. J., 392  
 Margulis V. A., 546  
 Marie X., 463  
 Marques G. E., 581  
 Marsh J. H., 429  
 Martin A. M., 327  
 Mashovets D., 354  
 Maslova N. S., 154

- Masselin P., 172  
Massies J., 97  
Masumoto Y., 279, 465, 481  
Matsuda Y. H., 147  
Matsumoto K., 335  
Maude D. K., 331, 559, 563  
Maximov I. A., 368  
Maximov M. V., 395, 399  
Medvedev A. V., 108  
Meinhold D., 556  
Meixner M., 12  
Melehin V. G., 131  
Merkulova S. P., 172  
Merz J. L., 175  
Mikhailova M. P., 381, 542  
Mikhailov G. M., 534  
Mikhailov G. V., 418  
Mikhaylov A. N., 206  
Mikhrin S. S., 395, 399  
Mikoushkin V. M., 168  
Minkov G. M., 538, 566  
Mintairov A. M., 175  
Miura N., 147  
Mizuseki H., 528  
Mogilnikov K. P., 339  
Moiseev K. D., 381, 542  
Moisseeva M. M., 22  
Monceau P., 512  
Monemar B., 72  
Montelius L., 368  
Moskalenko A. S., 433  
Möller C., 574  
Mudryi A. V., 78  
Muljarov E. A., 138  
Musikhin Yu. G., 60, 275  
**N**  
Naser B., 57  
Nazarov M. M., 172  
Nefedov I., 449  
Neizvestny I. G., 30, 34  
Nekorkin S. M., 516  
Nelson D. K., 97  
Neumann R., 187  
Neverov V. N., 210  
Nikiforov A. I., 53, 191  
Nikitina E. V., 399  
Nikolaichik V. I., 343  
Nikulov A. V., 350  
Nizhankovskii V. I., 542  
Novikov A. V., 183  
Novikov B. V., 292  
Novoselov K. S., 311  
**O**  
Odnoblyudov M. A., 453, 457  
Oettinger M., 524  
Oga R., 16  
Olsthoorn S., 534  
Ono K., 147  
Orehov D. A., 179  
Orlov A. O., 486, 491  
Ortner G., 584  
Ossau W., 93, 594  
Ostroumov R., 501  
Ouyang D., 375  
Ovchinnikov I. V., 214  
Ovsyankin V. V., 481, 606  
**P**  
Page H., 389  
Pal D., 229  
Panevin V. Yu., 229  
Panov V. I., 154  
Parfeniev R. V., 542  
Paskov P. P., 72  
Patanè A., 275  
Pchelyakov O. P., 53  
Pepper M., 303  
Permogorov S., 610  
Petrikov V. D., 131  
Petroff P. M., 260  
Petrov V. N., 292  
Petrov V. V., 481, 606  
Pevtsov A. B., 108, 134  
Pikhtin N. A., 252, 395, 414, 421  
Pinczolit M., 147  
Pires M. P., 364  
Pistol M.-E., 263  
Platonov A. V., 385  
Pokrovsky A. L., 105  
Polyakov N. K., 60  
Popov V. G., 331, 559  
Popov V. V., 614  
Portal J.-C., 331, 559, 563  
Portnoi E. L., 425  
Possanzini C., 534  
Pozina G., 72  
Preobrazhenskii V. V., 520  
Prettl W., 187  
Prokofiev A. A., 457  
Proshina O. V., 199

- Protzmann H., 82  
 Puls J., 418, 588  
**R**  
 Rabe M., 49, 588  
 Rafailov E. U., 429  
 Ramamoorthy A., 57  
 Ramasubramaniam R., 486, 491  
 Ray S. K., 441, 445  
 Reichert E., 473  
 Reinecke T. L., 584  
 Rentzsch R., 531  
 Ren H. -W., 279  
 Reulet B., 343  
 Revin D. G., 229  
 Reznitsky A., 610  
 Roberts J. S., 116  
 Rodin P., 371  
 Rogozin V. A., 516  
 Ron Arza, 508  
 Rosam B., 556  
 Rosenauer A., 49  
 Rostovshchikova T. N., 41  
 Rössler U., 187  
 Röthgen J., 473  
 Rubinsztein-Dunlop H., 38  
 Rumyantsev S. L., 618  
 Rut O. E., 538, 566  
 Rylkov V., 389  
 Rzaev M. M., 195  
**S**  
 Sablikov V. A., 300  
 Sachkov V. A., 179  
 Sadofyev Yu. G., 57  
 Sakharov A. V., 78  
 Samsonenko Yu. B., 60  
 Samuelson L., 263, 368  
 Samusev K. B., 120  
 Sauer R., 524  
 Savinov S. V., 154  
 Scheglov M. P., 164  
 Schelhase S., 425  
 Scherbakov A. V., 108  
 Schmidt J., 140  
 Schmidt M., 610  
 Schmidt S. R., 229  
 Schneider S., 375  
 Schoch W., 524  
 Schoen O., 82  
 Schomburg E., 245  
 Schöll E., 12, 245, 371  
 Schuler J., 473  
 Sedova I., 610  
 Seifert W., 263  
 Seilmeier A., 229  
 Sel'kin A. V., 108  
 Sellin R. L., 375  
 Semenova E. S., 399  
 Sergeev-Cherenkov A. N., 368  
 Shadrin E. B., 108  
 Shaligina O. A., 287  
 Shalygin V. A., 229  
 Shantsev D. V., 26  
 Shapiro N., 77  
 Shapoval S., 101  
 Shastin V. N., 221  
 Shchukin V. A., 12  
 Shernyakov Yu. M., 395, 399  
 Sherstobitov A. A., 538  
 Shiraki Y., 147  
 Shiryayev A. Yu., 465  
 Shkurinov A. P., 172  
 Shorokhov A. V., 546  
 Shtrom F. V., 323  
 Shubina T. V., 85  
 Shur M. S., 618  
 Shwartz N. L., 30, 34  
 Sibbett W., 429  
 Silov A. Yu., 249  
 Simmons M. Y., 303  
 Sinis V. P., 445  
 Sipatov A. Yu., 160  
 Sirtori C., 389  
 Sitnikova A. A., 26  
 Sizov D. S., 45, 60, 395, 399  
 Skolnick M. S., 116  
 Skrynnikov G. V., 421  
 Slipchenko S. O., 414, 421  
 Smirnov A. N., 164  
 Smirnov D., 389  
 Smirnov I. Yu., 520  
 Smirnov M. B., 164  
 Smirnov V. V., 41  
 Snider G. L., 486, 491  
 Sokolova Z. N., 252, 414  
 Sokolovskii G. S., 403, 429  
 Sokolov N. S., 22, 64  
 Soldatov E. S., 368  
 Sorokin S., 610

- Soshnikov I. P., 68, 399  
Sosnin A., 449  
Souza P. L., 364  
Springholz G., 147  
Starikov A. A., 303  
Stintz A., 392  
Story T., 160  
Strelchuk V. V., 85  
Stroganov B. V., 606  
Subashiev A., 473  
Sugou S., 279  
Sukhorukov E. V., 577  
Sun K. W., 225  
Suris R. A., 26, 93, 266  
Suturin S. M., 64  
Suyatin D. B., 368  
Svetlichny V. M., 531  
**T**  
Takeda Y., 16  
Takhtamirov E. E., 307  
Tarasenko S. A., 315, 469  
Tarasov I. S., 252, 395, 414, 421  
Tartakovskii A. I., 116  
Teperik T. V., 614  
Tetelbaum D. I., 206  
Theron D., 101  
Thomas K. J., 303  
Tikhodeev S. G., 138  
Tioukine V., 473  
Titkov A., 157  
Tkachenko V. A., 339  
Toader O., 112  
Tonkih A. A., 60  
Toporov V. V., 283  
Toropov A. I., 520  
Towe E., 229  
Travnikov V. V., 134  
Tribuzy C. V.-B., 364  
Troeger R. T., 441, 445  
Trushin M. P., 546  
Trushin S. A., 206  
Tsatsul'nikov A. F., 45, 60, 68  
Tsendin L. D., 319  
**U**  
Uchida K., 147  
Ukhanov A. A., 392  
Ulin V. P., 26, 64  
Unkelbach J., 371  
Uskova E. A., 221, 538  
Ustinov V. M., 45, 60, 68, 175, 229, 271, 275, 292, 395, 399  
Usvyat D. E., 120  
Utke I., 5  
**V**  
Vagov A., 296  
Valakh M. Ya., 85, 183  
Valiev K. A., 505  
van der Meer A. F. G., 221  
Vasil'ev A. V., 395  
Vasilev A. P., 399  
Vdovin E. E., 256, 331, 559, 563  
Vdovin V. I., 195  
Vekshin V. A., 78  
Venus G. B., 425  
Verbin S. Yu., 465, 481  
Vercik A., 581  
Vertjachih A., 101  
Veselovsky I., 354  
Vinnichenko V. Y., 534  
Vlasov A. S., 175  
Voisin P., 463  
Voitenko V. A., 283  
Volkov V. A., 307, 559, 563  
Volkov V. T., 343  
Volodin V. A., 179  
Voloubev V. V., 160  
Volovik B. V., 68, 275  
Vorobjev L. E., 229  
Vostokov N. V., 183  
Vuychik M. V., 85  
**W**  
Waag A., 418, 524  
Wacker A., 245  
Wang J. S., 45, 175, 395  
Wang K. L., 410, 497, 501  
Wang S., 331  
Warner J., 38  
Wasilewski Z., 584  
Watt A., 38  
Weber E. R., 77  
Wei L., 45, 175, 395  
Werner P., 68, 179  
Woggon U., 375  
Wojtowicz T., 594  
Wolter J. H., 249  
Wolverson D., 602  
Wu J., 78  
**Y**  
Yablonskii A. L., 138  
Yablonsky A. N., 183

- Yakimenko I. I., 303  
Yakimov A. I., 191  
Yakovlev D. R., 93, 418, 594  
Yakovlev Yu. P., 381, 542  
Yakunin M. V., 210  
Yamamoto A., 78  
Yanovitskaya Z. Sh., 30, 34  
Yanson D. A., 429  
Yashin Y., 473  
Yassievich I. N., 41, 433, 453, 457  
Yasuhira T., 147  
Yavich B., 364  
Yavsin D. A., 41  
Yugova I. A., 465  
Yukhymchuk V. A., 183  
**Z**abelin M. A., 41  
Zabrodskii A. G., 168  
Zaitsev-Zotov S. V., 512  
Zakharchenya B. P., 283, 602  
Zakharov N. D., 68, 179  
Zakrevskii V. A., 531  
Zapasskii V. S., 606  
Zavarin E. E., 164  
Zegrya G. G., 157, 346, 407, 421, 437  
Zhang Y.-H., 57  
Zhukavin R. Kh., 221  
Zhukov A. E., 68, 229, 275, 395, 399  
Zhukov E. A., 287  
Zimmermann R., 217  
Zverev A. V., 34  
Zvonkov B. N., 221, 516, 538  
Zvyagin I. P., 550